LEGIBILITY NOTICE

A major purpose of the Technical Information Center is to provide the broadest dissemination possible of information contained in DOE's Research and Development Reports to business, industry, the academic community, and federal, state and local governments.

Although a small portion of this report is not reproducible, it is being made available to expedite the availability of information on the research discussed herein.

3-87 JT (1) (5)

DR 0339-5

ORNL/FMP-87/4

CONF-8705103--

U.S. Department of Energy
Fossil Energy
Advanced Research and Technology Development
and
Morgantown Energy Technology Center

FOSSIL ENERGY MATERIALS PROGRAM CONFERENCE PROCEEDINGS

Fossil Energy Materials Program Office

OAK RIDGE NATIONAL LABORATORY
OPERATED BY MARTIN MARIETTA ENERGY SYSTEMS, INC.
FOR THE U.S. DEPARTMENT OF ENERGY

Fossil
Energy
Program

Printed in the United States of America. Available from
National Technical Information Service
U.S. Department of Commerce
5285 Port Royal Road, Springfield, Virginia 22161
NTIS price codes—Printed Copy: A99 Microfiche A01

ORNL/FMP--87/4

DE88 002250

FOSSIL ENERGY MATERIALS PROGRAM CONFERENCE PROCEEDINGS

Compiled by R. R. Judkins

Sponsored by U. S. Department of Energy
Office of Fossil Energy
Office of Technical Coordination
and Morgantown Energy Technology Center

Held at Pollard Auditorium
Oak Ridge Associated Universities
Oak Ridge, Tennessee
May 19-21, 1987

Date Published: August 1987

Prepared by the
OAK RIDGE NATIONAL LABORATORY
Oak Ridge, Tennessee 37831
operated by
MARTIN MARIETTA ENERGY SYSTEMS, INC.
for the
U.S. DEPARTMENT OF ENERGY
under Contract DE-AC05-84OR21400

TABLE OF CONTENTS

PREFACE

The U. S. Department of Energy Office of Fossil Energy has recognized the need for materials research and development to assure the adequacy of materials of construction for advanced fossil energy systems. The principal responsibility for identifying needed materials research and for establishing a program to address these needs resides within the Office of Technical Coordination. That office has established the Advanced Research and Technology Development (AR&TD) Fossil Energy Materials Program to fulfill that responsibility. In addition to the AR&TD Materials Program, which is designed to address in a generic way the materials needs of fossil energy systems, specific materials support activities are also sponsored by the various line organizations such as the Office of Coal Gasification.

Management of the AR&TD Materials Program has been decentralized to DOE Oak Ridge Operations, with the Oak Ridge National Laboratory (ORNL) as the technical support contractor. Management of the Surface Gasification Materials Program has been decentralized to the Morgantown Energy Technology Center. Field office management is by DOE-ORO with ORNL as the technical support contractor. Work on these two programs is conducted at national and other government laboratories, universities, not-for-profit research centers, and industrial research centers.

Formal program reviews are conducted at least annually for the various projects. Previously, the formal reviews have been conducted in closed sessions by the DOE-Headquarters, ORO, and ORNL management team, and, on occasion, by *ad hoc* peer review panels convened by the DOE-Office of Energy Research. For several reasons, not the least of which were increased program exposure and transfer of developed technology to the public, we decided to conduct this year's reviews in an open forum.

A conference was held at Oak Ridge, Tennessee on May 19-21, 1987, to present and discuss the results of program activities during the past year. The conference program was organized in accordance with the research thrust areas we have established. These research thrust areas include structural ceramics (particularly fiber-reinforced ceramic composites), corrosion and erosion, and alloy development and mechanical properties. Three one-day sessions devoted to these research thrust areas were held, and principal investigators presented the results of their research. Both slide and poster presentations were included in the program. This format was chosen to assure maximum interaction of the principal investigators with program managers, the other principal investigators, and other attendees at the conference.

Eighty-six people attended the conference. Based on the favorable response of those in attendance, we anticipate that this format will be used in subsequent annual reviews. Subsequent reviews will be held either in Washington, D. C. (Germantown, Maryland), or in Oak Ridge, Tennessee.

These conference proceedings include papers for both the slide and poster presentations that were made. These papers were provided in camera-ready form by the authors, and they have not been subjected to peer reviews nor have they been edited prior to compilation (in some instances, editing may have been performed by the submitting organization).

Appendix A to these proceedings provides the conference program and session agenda. Appendix B provides the names and addresses of conference participants and attendees. As is indicated in the frontispiece, copies of these proceedings are available from the National Technical Information Service. There are no restrictions on distribution of these proceedings.

ACKNOWLEDGEMENTS

The Fossil Energy Materials Program expresses sincere appreciation to the many fine researchers on the program for the excellent work they are doing in support of the program and for their efforts and support in making this conference a success. Special thanks are extended to Bonnie Reesor of the ORNL Conference Coordination office for her help in organizing and conducting this conference. Wanda Gilliam is hereby thanked for the many thankless jobs she had to perform in assuring the success of this conference. We appreciate the help of Alma McDonald in the rush at the registration desk. As is always the case, we are indebted to many other people who helped us in conducting this conference, but this acknowledgements section would never end if we cited each of you and the jobs you did. We are indebted to you for your help, however.

Wanda Gilliam and Barbara Lovelace must be mentioned for their efforts in the final preparation and assembly of these proceedings for publication. Last but not least, we thank the conference attendees for their interest in the Fossil Energy Materials Program.

SESSION I - STRUCTURAL CERAMICS

PROCESSING AND PROPERTIES OF SiC/NICALON COMPOSITES

R. A. Lowden, A. J. Caputo, D. P. Stinton,
and T. M. Besmann

Metals and Ceramics Division

and

M. D. Morris

Engineering Physics and Mathematics Division

Oak Ridge National Laboratory
P. O. Box X
Oak Ridge, Tennessee 37831

ABSTRACT

A statistically designed experiment was performed to evaluate the effects of process variables on fiber-reinforced SiC composites fabricated by chemical vapor infiltration. Response surface methodology was applied to study the influence of temperature, pressure, reactant supply rate, and gas ratios on the deposition process and the properties of the produced material. Deposition temperature and total gas flow rates had inverse effects on density and strength, while the effect of pressure was statistically insignificant. Low H_2:CH_3SiCl_3 ratios evoked a positive response in all dependent variables.

INTRODUCTION

Fiber-reinforced ceramic composites are being developed as potential candidates for high-temperature structural materials. High-strength ceramic fibers incorporated into brittle matrices prevent catastrophic failure by improving fracture toughness through energy dissipation processes such as fiber pull-out and crack deflection.[1-3] Ceramic composite systems exhibiting improved strength and fracture toughness over monolithic ceramics have been reported,[4-6] but many of the conventional ceramic manufacturing techniques used to produce them tend to

mechanically, thermally, or chemically damage the fibers. Procedures have been developed to fabricate fiber-reinforced ceramic composites by depositing a matrix within a fibrous structure using relatively low-temperature, low-stress chemical vapor deposition techniques,[7] reducing fiber degradation. Termed chemical vapor infiltration, the technique has been applied to a variety of fiber-matrix combinations, which has resulted in material with favorable mechanical properties, but the process has been dependent on diffusion and thus involves long processing times.[8-16] An improved infiltration process, reducing processing times from weeks to hours, has now been developed combining thermal-gradient and pressure-gradient approaches.[17-23]

A major portion of our early investigations involved the infiltration of Nicalon* fibrous structures with SiC. Uniform deposition throughout cloth preforms was achieved utilizing the pyrolysis of methyltrichlorosilane (MTS or CH_3SiCl_3) in the presence of hydrogen with a furnace temperature of ~1475 K and atmospheric pressure. These conditions resulted in comparatively high-density composites exhibiting high strength and fracture toughness in completion times of less than 30 h for a 45-mm-diam × 12.5-mm-thick disk sample.

The purpose of the study reported here was to analyze the combined effect of temperature, pressure, gas ratios and total gas flow on the thermal-gradient, pressure-gradient process as applied to the SiC/Nicalon system. Infiltration time, strength, and final density were selected as the initial response variables to be examined. The information obtained can be used to choose the optimum conditions required to achieve a final product with the highest density and strength and uniform infiltration in the shortest time.

STATISTICAL DESIGN

An experiment was statistically designed using response surface methods to study the effects of temperature, pressure, H_2:MTS ratio, and total gas flow on various properties. Response surface methodology

---

*Nippon Carbon Company, Tokyo, Japan.

consists of a group of methods used in the empirical study of the relationships between one or more measured responses and a number of input variables.[24,25] The methods were used to determine what sets of experimental variables are required to produce the best combination of strength, density, and uniform infiltration in the shortest time. The experimental parameters, temperature, pressure, total gas flow, and the volume ratio of H_2:MTS, were statistically combined in a four-dimensional array utilizing a central composite design.[26]

A minimum of 30 experimental sets of conditions were necessary to provide the required data to evaluate the contributions and interactions of the four factors. The nominal levels of the four experimental parameters are summarized in Table 1. The region to be explored is defined by the following minima and maxima; temperatures from 1375 to 1575 K, pressures from 10 to 100 kPa, total gas flows from 275 to 1100 cm^3/min, and H_2:MTS from 10 to 35. The central point was placed at a temperature of 1475 K, a pressure of 55 kPa, a total gas flow of 550 cm^3/min and H_2:MTS = 20:1. Four runs at the central point verified the reproducibility. Two points were added to assess the response of a higher-temperature value and of a lower H_2:MTS ratio.

EXPERIMENTAL

PROCESSING

The experiments were carried out in a water-jacketed furnace resistively heated using a graphite element. The critical components of the infiltration apparatus, the water-cooled injector and the graphite holder, have been described previously.[17-23] A schematic of the system is shown in Fig. 1. Fibrous preforms are retained within a graphite holder that contacts a water-cooled copper gas distributor, thus cooling the bottom and side surfaces of the substrate. The top of the fibrous preform is exposed to the hot zone of the furnace, creating a steep temperature gradient across the preform. The reactant gases initially pass into the cooled area of the preform but do not react because of the low temperature. The gases continue from the cooled region of the preform into the hotter regions, where the MTS decomposes and SiC deposits on and around the

Table 1. Summary of experimental input conditions

Experimental design

Temperature	Pressure	H_2:MTS ratio	Total flow[a]
-	+	+	-
+	+	-	+
+	+	+	-
-	+	+	+
-	-	-	+
-	+	-	+
0	0	0	0
0	0	+	0
0	0	--	0
0	+	0	0
+	-	+	+
0	0	0	0
-	-	+	+
+	+	+	+
+	0	0	0
0	0	0	0
+	-	+	-
0	0	-	0
-	-	+	-
0	0	0	+
+	+	-	-
++	0	0	0
-	-	-	-
0	0	0	0
0	-	0	0
0	0	0	-
-	-	-	-
-	+	-	-
-	0	-	-
+	-	-	+

	Factor levels				
Factor	Very low (--)	Low (-)	Median (0)	High (+)	Very high (++)
Temperature (K)	-	1375	1475	1575	1675
Pressure (KPa)	-	10	55	100	-
H_2:MTS ratio	5	10	20	35	-
Total flow	-	275	550	1100	-

[a]All flows in cm^3/min (STP) at 300 K and 100 KPa.

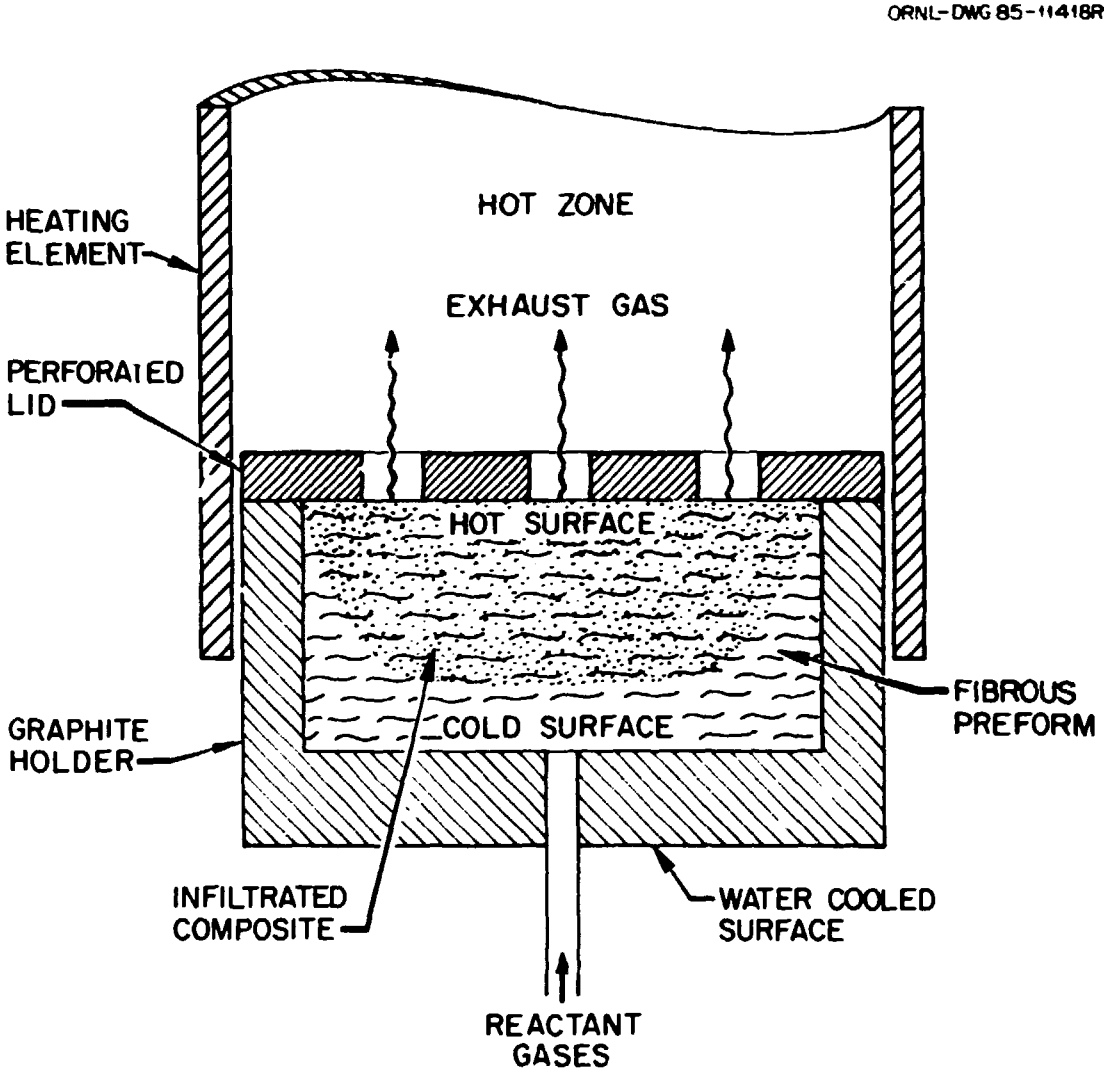

Fig. 1. Schematic of infiltration system.

fibers to form the matrix. When the top surface becomes coated and is no longer permeable, the gases flow radially through the substrate to the preform circumference and exit through the perforated retaining lid.

The gas/vapor flow, pressure, and temperature control systems are automated to facilitate uninterrupted operation and eliminate daily cycling. Mass flow controllers* were used to set and maintain gas flows

*Type 1259A, MKS Instruments, Inc., 34 Third Ave., Burlington, MA 01803.

and ratios. Methytrichlorosilane was carried to the reactor by a flow of hydrogen through an evaporator and metered using a vapor source controller.* Pressure control was accomplished using a gas ballast technique, injecting argon gas into the pump inlet to regulate effective pumping speed.† The corrected optical temperature at the top surface of the specimen was measured and controlled by a single-wavelength automatic optical pyrometer‡ equipped with a time-proportioning controller. A predetermined pressure differential across the sample designated complete infiltration.

Fibrous preforms were fabricated by stacking multiple layers of plain-weave Nicalon cloth in a 30-60-90° orientation sequence into the cavity of a graphite holder. The layers were compressed and held in place by a perforated graphite lid pinned to the holder. The average fiber content was 41.2 ± 0.8 vol %, 52 layers, with sample dimensions of 45 mm in diameter and 12.5 mm thick. The sizing was then removed from the cloth through multiple washings in acetone. The preform was precoated with a thin layer of pyrolytic carbon to protect the fibers from reactants and products containing chlorine and reduce interfacial bonding to enhance fiber pull-out.[23] The carbon was deposited isothermally by the decomposition of propylene in argon at 1375 K and 5 kPa.[27-29]

The prepared preform had an average theoretical density of 2.91 ± 0.01 g/cm^3. The theoretical density is defined as the sum of the products of volume fraction and reported density of each component of the composite (fibers, pyrocarbon, and, after infiltration, SiC). The matrix phase was then deposited from the specified mixtures of H_2 and MTS at the appropriate temperatures and pressures defined by the design.

TESTING

Twelve bend bars [four each from the top, middle, and bottom areas (Fig. 2)] were prepared from each sample to evaluate each one and also to

---

*Source V, Tylan, 23301 South Wilmington Ave., Carson, CA 90745.

†Type 250B, MKS Instruments, Inc., 34 Third Ave., Burlington, MA 01803.

‡Modline 2000, Ircon, Inc., 7301 N. Caldwell Ave., Niles, IL 60648.

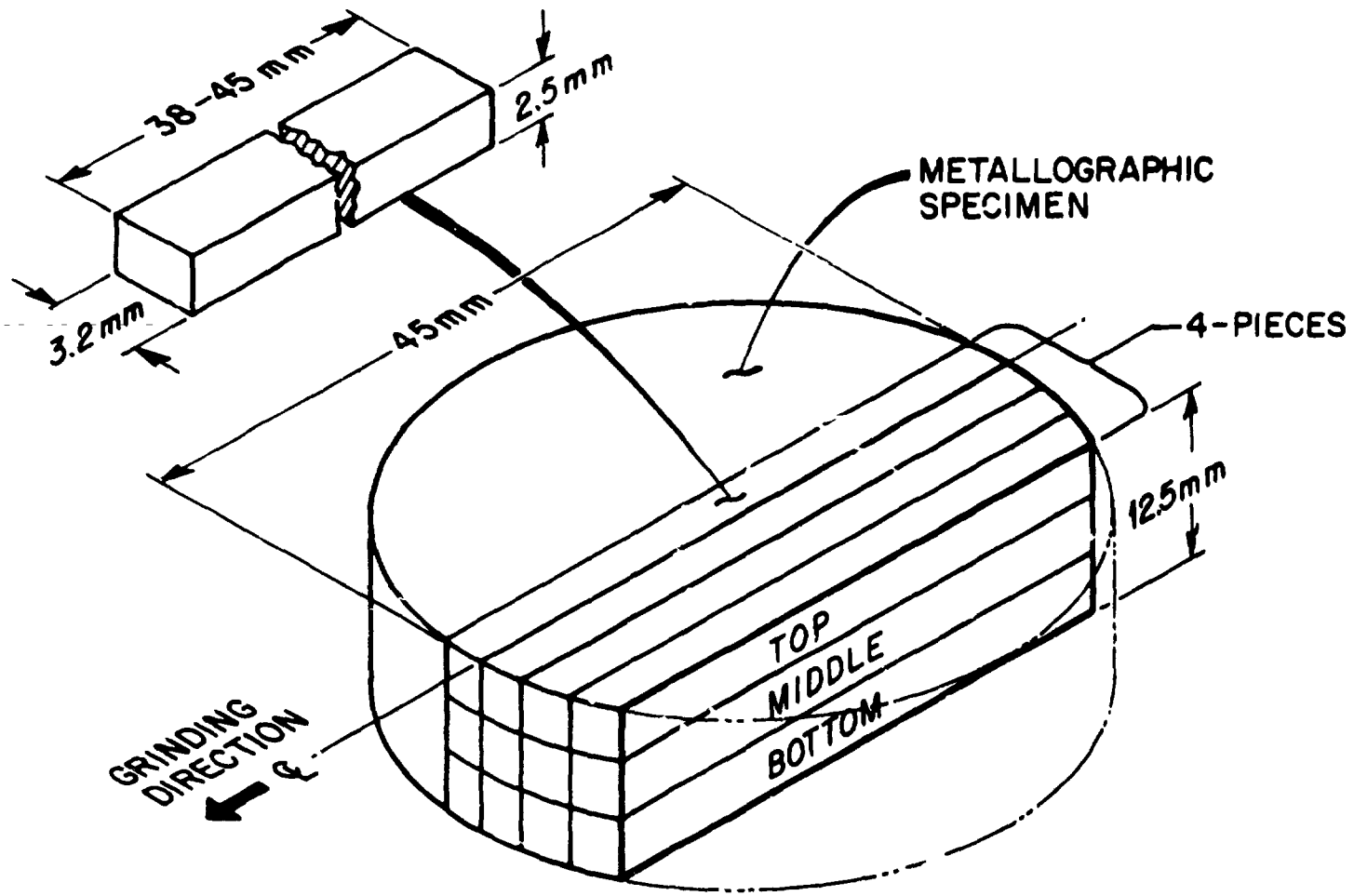

Fig. 2. Location of test specimens within sample.

determine variation due to location in the sample. The bars were cut from the samples parallel to the 0-90° orientation of the top layer of cloth using a diamond saw, and tensile and compression surfaces were ground parallel to the long axis of the specimen. The average dimensions of the bars were 2.5 × 3.3 × 45 mm, and all were measured and weighed to determine densities. Flexural strengths were measured at room temperature employing four-point bend methods and using a support span of 25.4 mm, a loading span of 6.4 mm, and a crosshead speed of 0.51 cm/min. The load was applied perpendicular to the layers of cloth. Metallographic examination of polished cross sections taken 5 mm off the centerline provided an overall view of the infiltrated sample and coating morphologies.

RESULTS

The results of the experiment are summarized in Tables 2 and 3. Only 28 of the 30 runs were completed. Two runs were deleted when it was recognized that the projected infiltration times were significantly greater than 8 days. A goal of the temperature-gradient forced-flow technique is to decrease processing times.

PROCESSING TIME

The infiltration parameters and resulting completion times for the 28 completed experimental runs are given in Table 2. Three of the four factors considered, temperature, H_2:MTS ratio, and total gas flow rate, appear to affect infiltration times. Times ranged from 5 h to over 8 days. Examination of the data indicates that time was most effectively reduced by increasing temperature and total gas flow rate, while pressure had little influence. Temperature was the most significant variable, since the majority of the runs processed with a furnace temperature above 1475 K were completed in less than 20 h.

DENSITY

Bulk densities were measured and percentage of theoretical density values were calculated for each of the specimens obtained from the 28

Table 2. Infiltration parameters and resulting processing times

Run	Temperature (K)	Pressure (KPa)	MTS flow[a]	H_2 flow[a]	H_2:MTS ratio	Total flow[a]	Time (h)
1	1375	100	8.0	267	35	275	202.7
2	1575	100	100.0	1000	10	1100	5.3
3	1575	100	8.0	267	35	275	49.0
4	1375	100	31.0	1069	35	1100	50.0
5	1375	10	100.0	1000	10	1100	28.0
6	1375	100	100.0	1000	10	1100	32.0
7	1475	55	26.0	524	20	550	43.6
8	1475	55	15.0	535	35	550	39.3
9	1475	55	92.0	458	5	550	12.0
10	1475	100	26.0	524	20	550	34.4
11	1575	10	31.0	1069	35	1100	12.0
12	1475	55	26.0	524	20	550	24.1
13	1375	10	31.0	1069	35	1100	57.8
14	1575	100	31.0	1069	35	1100	16.8
15	1375	55	26.0	524	20	550	21.5
16	1475	55	26.0	524	20	550	26.8
17	1575	10	8.0	267	35	275	72.0
18	1475	55	50.0	500	10	550	46.4
19	1375	10	8.0	267	35	275	0.0
20	1475	55	52.0	1048	20	1100	12.8
21	1575	100	25.0	250	10	275	18.5
22	1675	55	26.0	524	20	550	7.5
23	1575	10	25.0	250	10	275	17.4
24	1475	55	26.0	524	20	550	26.1
25	1475	10	26.0	524	20	550	63.5
26	1475	55	13.0	262	20	275	53.1
27	1375	10	25.0	250	10	275	0.0
28	1375	100	25.0	250	10	275	51.3
29	1375	55	26.0	250	10	275	112.5
30	1575	10	100.0	1000	10	1100	14.1

[a]All flows in cm^3/min (STP) at 300 K and 100 KPa.

Table 3. Density and flexure strength results[a]

Run	Position	Density (g/cm³)	Std. dev.	%T.D.[b]	Strength (MPa)	Std. dev.
1	Top	2.53	0.01	86.8	301	32
1	Middle	2.48	0.01	85.2	294	13
1	Bottom	2.28	0.03	78.5	247	5
2	Top	2.42	0.01	82.8	265	21
2	Middle	2.32	0.02	79.6	248	15
3	Top	2.33	0.03	80.0	334	30
3	Middle	2.14	0.03	73.6	286	18
3	Bottom	2.21	0.03	75.9	263	46
4	Top	2.48	0.02	85.5	299	13
4	Middle	2.34	0.01	80.8	278	14
5	Top	2.47	0.02	85.1	394	18
5	Middle	2.29	0.01	78.8	300	8
5	Bottom	2.03	0.02	70.1	156	10
6	Top	2.55	0.02	87.3	359	44
6	Middle	2.44	0.01	83.3	268	9
7	Top	2.52	0.01	86.5	313	11
7	Middle	2.50	0.02	85.9	346	22
7	Bottom	2.50	0.02	85.8	385	43
8	Top	2.35	0.02	80.9	277	19
8	Middle	2.44	0.04	84.3	311	22
8	Bottom	2.57	0.02	88.6	371	13
9	Top	2.53	0.02	87.2	436	4
9	Middle	2.45	0.01	84.4	354	11
9	Bottom	2.28	0.01	78.6	311	14
10	Top	2.49	0.01	85.6	325	18
10	Middle	2.51	0.02	86.0	349	14
10	Bottom	2.49	0.02	85.4	343	30
11	Top	2.29	0.03	78.7	260	14
11	Middle	2.46	0.02	84.8	345	14
11	Bottom	2.42	0.02	83.4	348	50
12	Top	2.54	0.02	87.4	324	18
12	Middle	2.51	0.01	86.5	410	34
12	Bottom	2.30	0.02	79.2	303	6
13	Top	2.49	0.01	86.4	450	16
13	Middle	2.35	0.05	81.4	405	24
14	Top	2.41	0.02	83.0	283	27
14	Middle	2.48	0.03	85.3	357	28
14	Bottom	2.05	0.03	70.6	162	13
15	Top	2.48	0.03	85.5	318	30
15	Middle	2.51	0.02	86.5	320	18
15	Bottom	2.01	0.03	69.3	120	34
16	Top	2.51	0.01	86.5	351	25
16	Middle	2.43	0.09	83.9	447	20
16	Bottom	1.84	0.02	63.4	158	23
17	Top	2.44	0.02	83.5	236	25
17	Middle	2.34	0.03	80.1	252	9
17	Bottom	1.80	0.08	61.6	145	49
18	Top	2.61	0.01	89.9	344	46
18	Middle	2.22	0.02	76.6	216	3
18	Bottom	1.87	0.02	64.4	104	10
20	Top	2.53	0.01	86.9	450	12
20	Middle	2.43	0.01	83.5	403	25
20	Bottom	2.11	0.04	72.8	315	13
21	Top	2.52	0.01	87.2	417	18
21	Middle	2.47	0.02	85.5	406	30
21	Bottom	2.44	0.02	84.4	390	14
22	Top	2.32	0.01	79.5	321	22
22	Middle	2.35	0.01	80.8	353	10
22	Bottom	2.27	0.03	77.8	350	24
23	Top	2.58	0.03	88.2	396	30
23	Middle	2.57	0.01	87.8	354	44
23	Bottom	2.49	0.03	85.4	308	26
24	Top	2.59	0.01	88.8	471	3
24	Middle	2.54	0.01	87.1	410	22
24	Bottom	2.33	0.01	80.1	344	7
25	Top	2.43	0.02	84.1	333	13
25	Middle	2.24	0.02	77.7	274	10
26	Top	2.53	0.02	86.9	274	25
26	Middle	2.42	0.04	83.1	272	38
26	Bottom	2.06	0.06	70.8	142	10
28	Top	2.62	0.02	90.1	430	10
28	Middle	2.56	0.01	88.0	421	28
28	Bottom	2.40	0.06	82.7	478	34
29	Top	2.64	0.01	90.9	447	46
29	Middle	2.63	0.01	90.6	440	23
29	Bottom	2.56	0.01	88.2	422	18
30	Top	2.48	0.03	85.0	343	13
30	Middle	2.52	0.02	86.5	337	14
30	Bottom	2.27	0.09	78.0	228	19

[a]Average of four values for each layer.
[b]Density of SiC = 3.21 g/cm³, Pyc = 2.00 g/cm³, and Nicalon = 2.55 g/cm³.

samples. The average values for the top, middle, and bottom layers are reported in Table 3. In some cases, uninfiltrated bottom sections delaminated; thus only 8 of the 12 specimens from a sample were available for examination. In most instances, the highest densities occurred in the top positions, although runs 7 and 10 resulted in radial and axial density gradients of <1% for an average density of 2.50 g/cm^3. Values as high as 2.65 g/cm^3, 91.2% of theoretical density, were measured, but the density frequently decreased toward the bottom (cooled side) of the preform. A typical polished cross section of a completed composite sample is shown in Fig. 3.

ROOM-TEMPERATURE FLEXURE STRENGTH

Flexure strengths of the composite specimens were measured by four-point bending and ranged from 83 to 517 MPa. All specimens exhibited composite behavior during testing, as demonstrated by fiber pull-out and by the appearance of the load-crosshead displacement curves (Fig. 4). The results are reported in Table 3 as the average values across each layer. Examination of the data reveals a modest positive correlation between density and strength. A plot of these two values for all specimens tested is shown in Fig. 5. The correlation coefficient is 0.764, and the corresponding p value is <0.0001. Although buckling at the compressive surface and cracking parallel to the tensile surface occur during testing and thus failure occurs not in simple tension but by a complex combination of tension, compression, and shear, flexure strengths are adequate to obtain a relative measure of the strength of the composites fabricated under different infiltration conditions.

PROCESS RELATIONSHIPS

The experiments were designed to evaluate the effects of controlled input variables on the infiltration process. In order to predict given responses across a range of variables, each point must be itself reproducible. Reproducibility within the experimental design was verified by repeating the central point four times. These are run numbers 7, 12, 16, and 24 in the sequence (Table 3). Neglecting the bottom locations,

ORNL-PHOTO 3153-87

HOT FACE

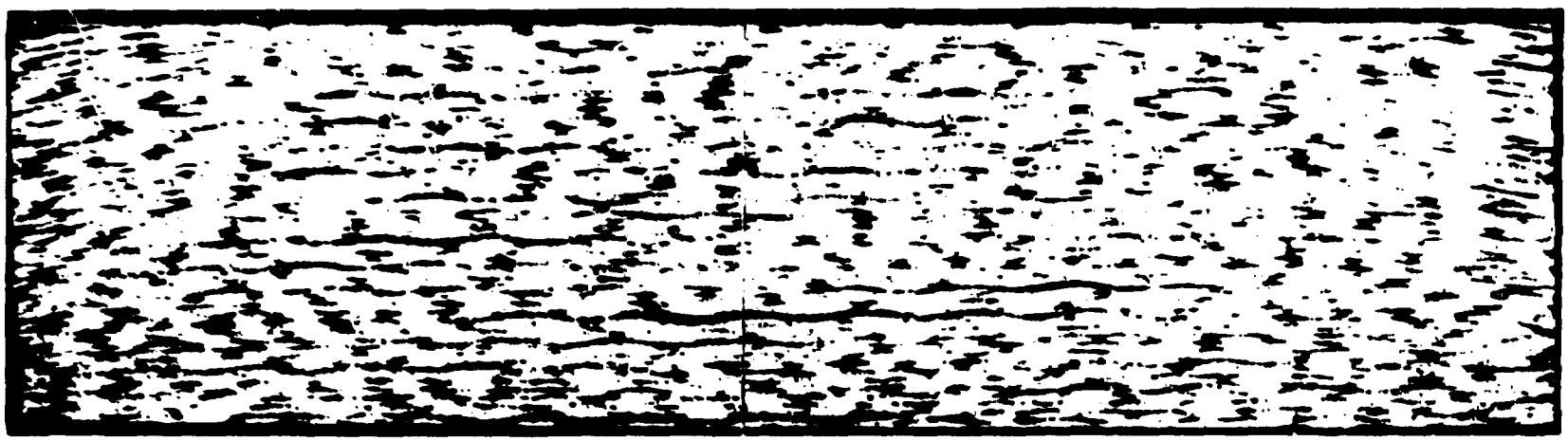

COLD FACE

5 mm

Fig. 3. Cross section of an infiltrated sample.

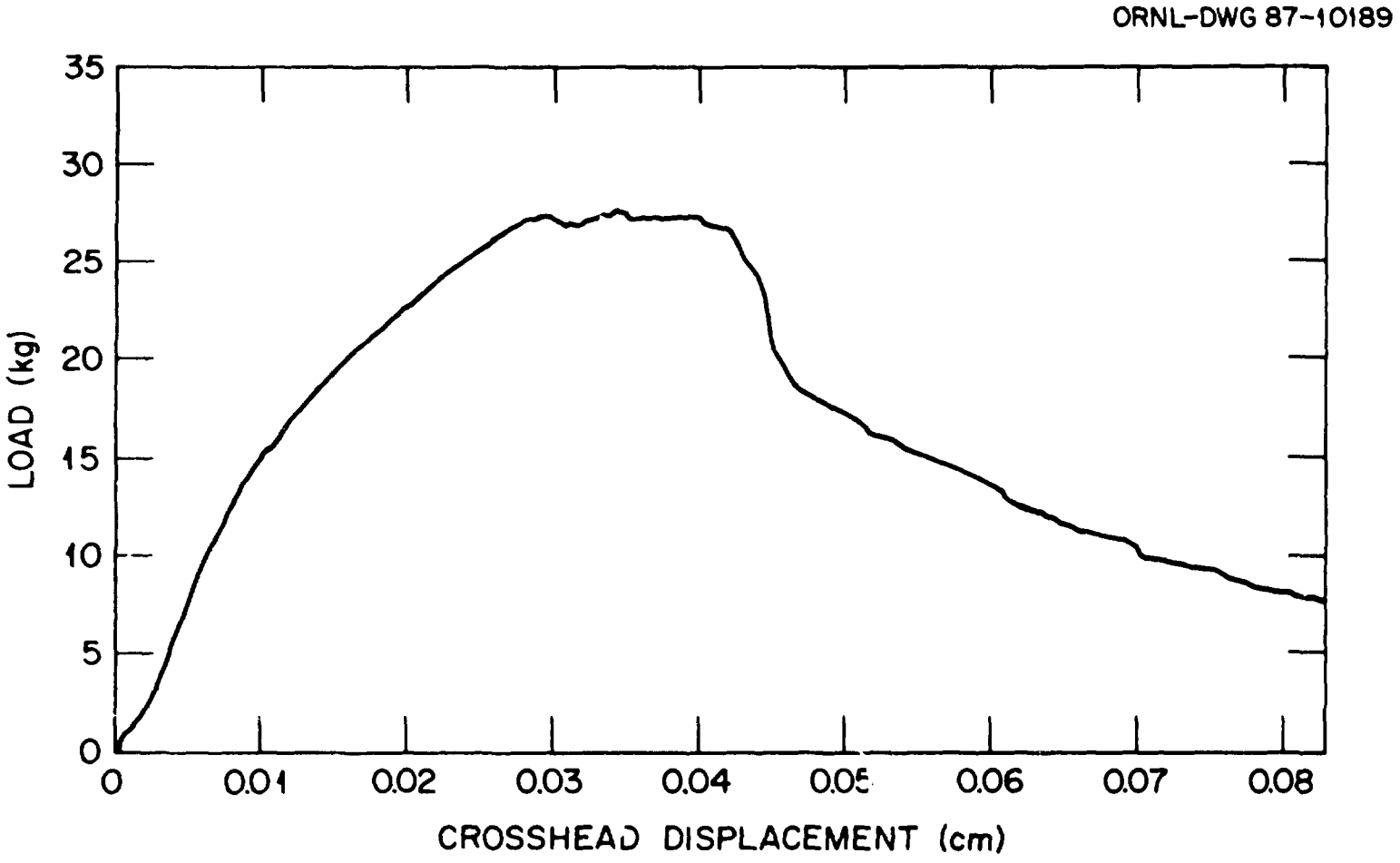

Fig. 4. Curve of load vs crosshead displacement for SiC/Nicalon composite tested in 4-point flexure at room temperature.

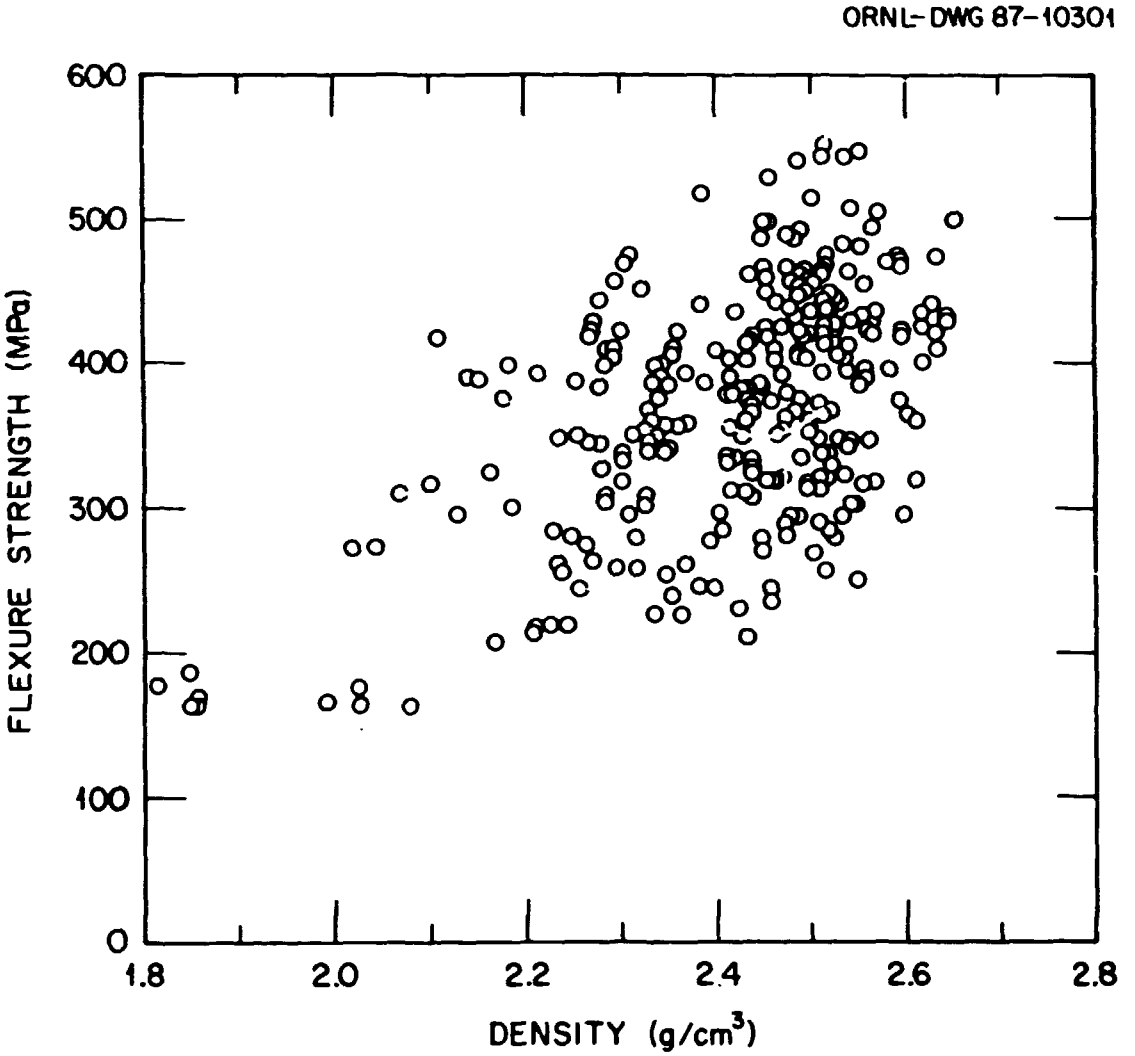

Fig. 5. Plot of room-temperature flexure strength vs density for all specimens tested.

examination of the standard deviations of density and strength within these four shows that the variability within the group was <2% for density and <15% for strength, making it possible to relate them to the response variables, time, density achieved, and strength, as a function of the input parameters, temperature, pressure, H_2:MTS ratio, and total gas flow.

Using multiple linear regression, an equation relating infiltration time and the process parameters was derived and shown to be statistically significant but lacked precision, with an R^2 of 59%. The precision of the relationship was considerably improved by utilizing the natural logarithm

of time, resulting in an R^2 of 82%. The final form of the time equation is:

$$\begin{aligned}\ln[\text{time (h)}] = {} & 12\ (\pm 1) - 6.8\ (\pm 0.8) \times 10^{-3}\ [T\ (K)] \\ & - 4.3\ (\pm 3.6) \times 10^{-5}\ [P\ (kPa)] \\ & + 3.3\ (\pm 0.7) \times 10^{-2}\ [\text{vol ratio } (H_2\text{:MTS})] \\ & - 1.4\ (\pm 0.2) \times 10^{-3}\ [\text{flow rate } (cm^3/min)].\end{aligned}$$

The gradient of this fitted surface at the central point indicates that infiltration time is decreased not only by increased temperature and total flow rate but also by reduced H_2:MTS ratios. The shortest time, 5.3 h, resulted from a furnace temperature of 1575 K, a pressure of 100 kPa, a total flow of 1100 cm^3/min, and an H_2:MTS ratio of 10:1. The conditions for the longest, 202.7 h, were 1375 K, 100 kPa, a total flow rate of 275 cm^3/min, and an H_2:MTS ratio of 35:1.

Statistical analysis of the densities as a function of the experimental variables indicated that the only values that could be related with any accuracy were the top-row averages. The bottom layers were unpredictable for many sets of conditions, leading to an R^2 of <30%. In addition, first-order linear regression did not fit well, and thus mixed quadratic terms were added to account for the interactions of the four process parameters. The equation for top-row average density thus derived has an R^2 of 82% and is given in Table 4. Evaluation of the gradient of the equation at the central point suggests that density is most effectively increased by reducing temperature, H_2:MTS ratio, and total flow rate. Again, pressure had little influence. This trend is supported by the facts that runs 28 and 29 produced the highest top-row densities and that both of these had temperature, H_2:MTS ratio, and total gas flow rate at their respective lowest values.

The same fitting procedure used to relate density was also used to correlate flexural strength with the four process parameters. As with density measurements, the bottom areas yielded the greatest variations and were deleted during analysis. The relationship for top-row average strength has an R of 83% but contains high standard errors for individual estimates due to a combination of possible redundancies in the equation and the exclusion of undetermined factors.

Table 4. Relationship for top row average density

Parameter	Estimate
Intercept	118 (±13) %
a	−0.02 (±0.01) % / K
b	0.16 (0.16) % / KPa
c	1.02 (0.61) %
d	−0.03 (0.02) % /cm³/min
e	1.15 (1.30) × 10^{-4} % / K KPa
f	−7.37 (3.47) × 10^{-3} % / K
g	2.14 (1.45) × 10^{-5} %/K cm³/min
h	−8.50 (10.2) × 10^{-4} % / KPa
i	6.40 (3.18) × 10^{-5} % / KPa cm³/min
j	5.92 (1.11) × 10^{-5} % / cm³/min

$$T.D.\ (\%) = 118 + (a \times T) + (b \times P) + (c \times R) + (d \times F) + (e \times T \times P) + (f \times T \times R) + (g \times T \times F) + (h \times P \times R) + (i \times P \times F) + (j \times R \times F)$$

T = temperature (K),
P = pressure (KPa),
R = molar ratio of H_2/MTS,
F = total gas flow (cm³/min).

DISCUSSION

THERMODYNAMICS AND KINETICS

The chemical vapor deposition of SiC from MTS is a relatively simple process and has been extensively examined.[30-34] Methyltrichlorosilane contains silicon and carbon in stoichiometric proportions and is a liquid with a reasonable vapor pressure, making it a good reactant for vapor deposition. Thermodynamic analyses of the Si-C-H-Cl system (using SOLGASMIX-PV[35-37]) have been previously reported,[37,38] but an analysis was made in this study to include conditions bounded by the experimental design. The thermodynamic analysis was conducted using the EQUILIB computer program of the F*A*C*T system.* The equilibria were defined by specifying temperature, pressure, and the molar ratio of H_2:MTS. Three

*EQUILIB, F*A*C*T, W. T. Thompson, Royal Military College of Canada, and A. D. Pelton and C. W. Bale, Ecole Polytechnique, Montreal.

condensed phases (Si, α-SiC, and β-SiC) and 81 gas species were considered. Previous investigators have shown that the formation of carbon is kinetically hindered under the conditions considered; thus it was omitted in this analysis.[37,39] The results of the thermodynamic calculations were used to calculate theoretical deposition efficiencies by dividing the equilibrium yields by the yield as determined from the molar quantity of MTS (Figs. 6 and 7).

PRESSURE

Pressure appeared to have little or no effect on the response variables. It was originally assumed that reducing the processing pressure would decrease deposition rates and, therefore, increase infiltration times due to increased gas velocities and decreased residence times.[40] At the reduced pressures considered (55 and 10 kPa), the linear gas velocities are 1.8 and 12.7 times higher, respectively, than at local atmospheric pressure. This implies greatly reduced residence times of the gases within the preform. At the central-point total gas flow rate of 550 cm^3/min, the residence time is 3.7×10^{-2}, while the residence times for the reduced pressures are calculated to be 2.0×10^{-2} and 2.9×10^{-3} s, respectively. Thus, these factors should decrease coating rates, but this was not observed.

Different mechanisms associated with reduced pressure may affect deposition efficiency. Figure 6 displays the equilibrium deposition efficiency of SiC as a function of H_2:MTS ratios at various pressures as predicted by thermodynamic calculation. The graph indicates an increase in deposition efficiency with reduced pressure. An isothermal decrease in pressure shifts equilibrium toward the products SiC and HCl. These combined with higher diffusion rates, also associated with reduced pressure, could counteract the effects of increased gas velocities.

TEMPERATURE

A plot of predicted deposition rates with respect to gas composition at the different furnace temperatures used in the statistical study is shown in Fig. 7. Increasing the furnace temperature increases the

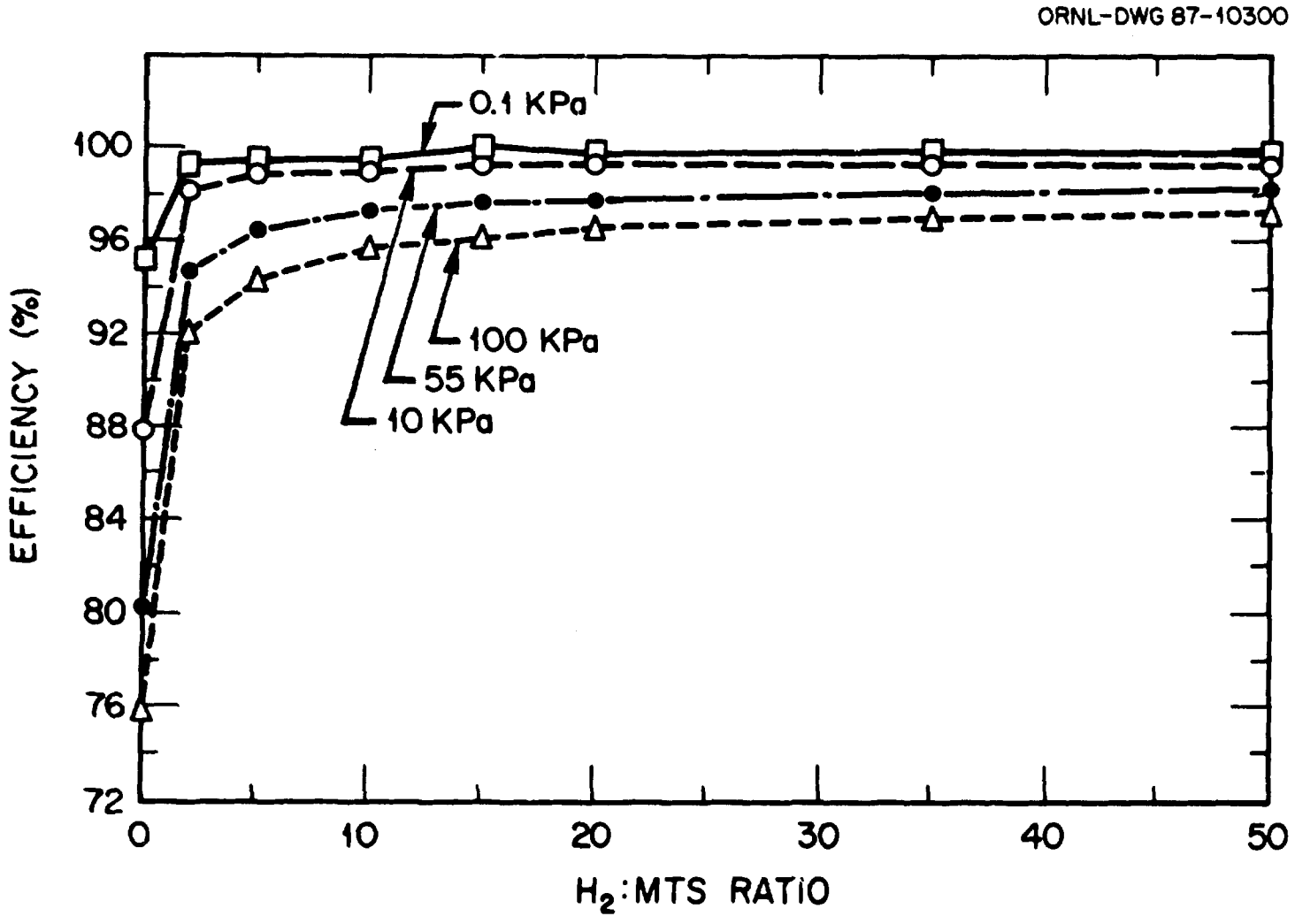

Fig. 6. Calculated deposition efficiencies as a function of H_2:MTS ratio and pressure.

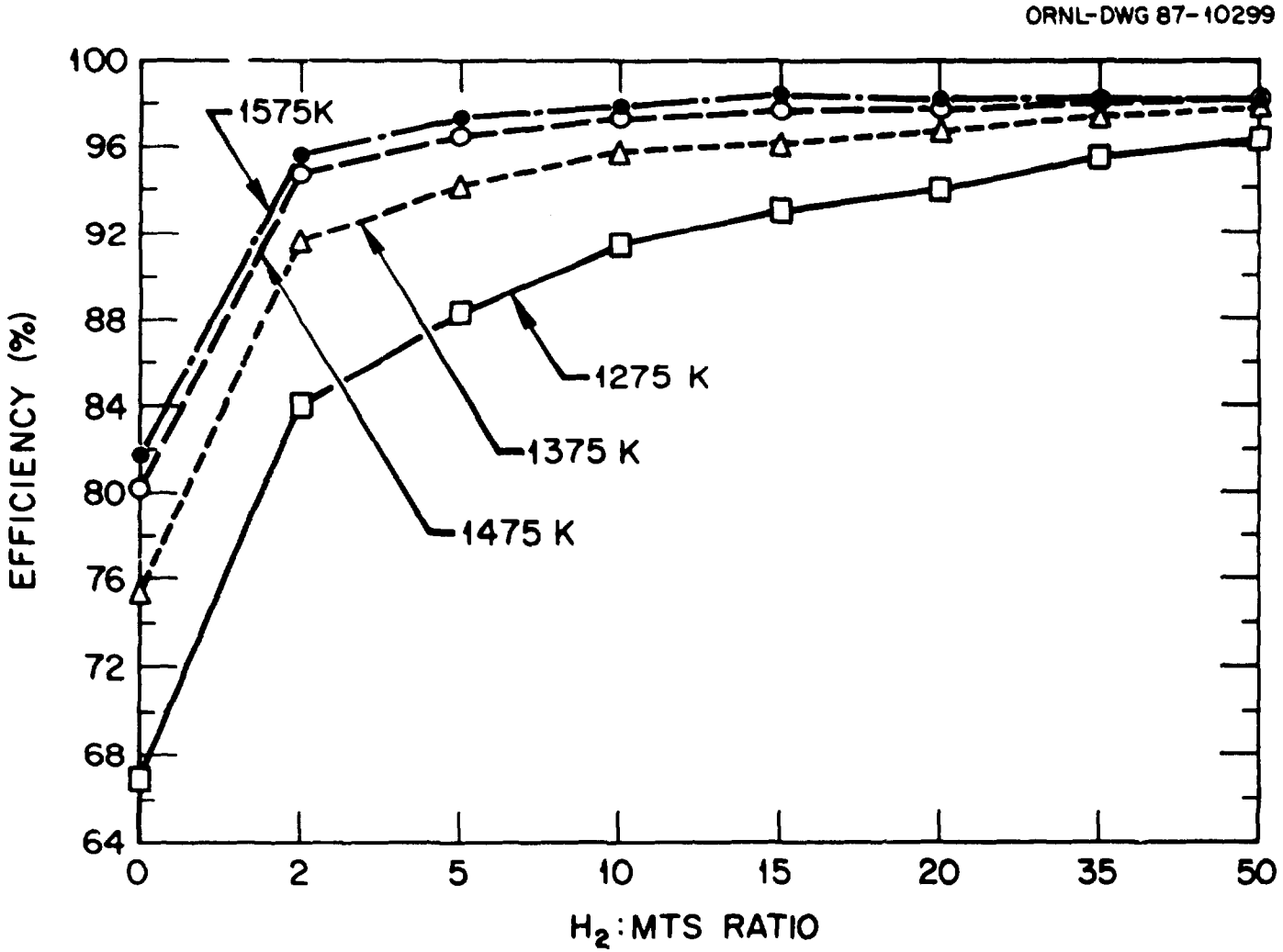

Fig. 7. Calculated deposition efficiencies as a function of H_2:MTS ratio and temperature.

deposition efficiency, and this is reflected in the observed reduction of infiltration times at higher temperatures. The average flexure strengths of the samples processed at 1575 K were lower than those of samples infiltrated at 1375 and 1475 K. A reduction of strength in the final material is expected, since Nicalon fibers degrade at elevated temperatures.[41,42]

An increase in achieved density was noted in the respective low-temperature runs. The decrease in deposition rates at this condition may allow open porosity in the upper areas to remain for a longer fraction of the run time. Reactant gases are thus able to permeate a larger percentage of the volume, resulting in more complete and uniform infiltration.[39]

TOTAL FLOW RATE

In general, the total gas flow had the same contributive effect as temperature. Time was decreased as the flows were increased, and higher densities were attained at lower gas flow rates. Early studies of SiC coatings from chlorosilanes determined that the rate-controlling factor was the reactant supply rate.[31] High deposition rates occur at high levels of flow and low ratios of hydrogen to methyltrichlorosilane.

A detrimental effect of high gas flows in the temperature-gradient pressure-gradient process was the lack of deposition in the bottom layers. The increased flow rate of gas cools the lower surface and disturbs the temperature gradient. This is enhanced by the basic principles and designs present in the gas injection and distribution systems, which cause the reactant gases and graphite holder to be cooled at the same rate regardless of deposition conditions.

HYDROGEN:MTS RATIO

In Figs. 6 and 7 it is evident that increasing the ratio of hydrogen to MTS has a positive effect on the deposition efficiency up to a ratio of 12:1, where leveling occurs. In the series of experimental runs, a decrease in the ratio resulted in a favorable response with respect to all three output variables. A decrease in H_2:MTS ratio corresponds to an increase in reactant concentration; thus, lowering the H_2:MTS ratio also decreased the likelihood of codepositing silicon. Codeposition occurs

when the ratio of hydrogen to silicon in the Si-C-H-Cl gas mixture is high or the reaction is carried out at low temperature.[38] Several investigations have determined that deposition of single-phase SiC occurs at H_2:Si = 5 or less at a temperature of 1473 K, Si:C = 1, and Cl:Si = 3 (ref. 37). Higher-quality material is therefore produced at the lower ratios.

CONCLUSIONS

The thermal-gradient pressure-gradient process for the fabrication of ceramic-fiber-reinforced ceramic-matrix composites was studied in response to the following experimental variables: temperature, pressure, total gas flow, and H_2:MTS ratio. These parameters influenced achieved density, flexure strength, and infiltration time. The information obtained has advanced the progress toward developing an efficient method for producing high density and high strength composites.

Runs 7 and 10 produced samples with density variations throughout of less than 1% of the average 86.1% and 85.6% of theoretical, confirming that uniform infiltration is attainable. The statistical analysis indicated that within the boundaries of the experiment, a temperature of 1473 K, an H_2:MTS ratio of less than 10:1, and a total gas flow of 550 cm^3/min would result in high strength, density, and uniformity in a comparatively short processing time. The operating pressure was found to be statistically insignificant; thus infiltration at atmospheric pressure simplifies processing. Combining these results and trends, material with uniform physical properties can be produced.

Multiple linear regression techniques were employed to relate the response of the process and the properties of the fabricated composite material to the experimental variables. The relationships of infiltration time, density, and room-temperature flexure strength to the input parameters of temperature, pressure, H_2:MTS ratio, and total gas flow were determined. Relatively accurate responses can be calculated from the predictive equations.

REFERENCES

1. J. Aveston and A. Kelly, "Theory of Multiple Fracture of Fibrous Composites," *J. Mater. Sci.* **8**, 352-62 (1973).

2. D. B. Marshal and A. G. Evans, "Failure Mechanisms in Ceramic-Fiber/Ceramic Matrix Composites," *J. Am. Ceram. Soc.* **68**, 225-31 (1985).

3. R. W. Rice, "Mechanisms of Toughening in Ceramic Matrix Composites," *Ceram. Eng. Sci. Proc.* 2(7-8), 661-701 (1981).

4. K. M. Prewo and J. J. Brennan, "High-Strength Silicon Carbide Fiber-Reinforced Glass-Matrix," *J. Mater. Sci.* **15**, 463-68 (1980).

5. K. M. Prewo and J. J. Brennan, "Silicon Carbide Yarn Reinforced Glass Matrix Composites," *J. Mater. Sci.* **17**, 1201-6 (1982).

6. J. J. Brennan and K. M. Prewo, "Silicon Carbide Fiber-Reinforced Glass-Matrix Composites Exhibiting High Strength and Toughness," *J. Mater. Sci.* **17**, 2371-82 (1982).

7. W. A. Bryant, "The Fundamentals of Chemical Vapour Deposition," *J. Mater. Sci.* **12**, 1285-1306 (1977).

8. W. H. Pfiefer et al., "Consolidation of Composite Structures by CVD," pp. 463-85 in *Second Int. Conf. Chem. Vapor Dep.*, ed. J. M. Blocher, Jr., and J. C. Whithers, Electrochemical Society, New York, 1970.

9. H. O. Pierson and J. F. Sarrana, "Carbon Composites from Wool Substrates," pp. 487-505 in *Second Int. Conf. Chem. Vapor Dep.*, ed. J. M. Blocher, Jr., and J. C. Whithers, Electrochemical Society, New York, 1970.

10. J. C. Whithers, "Chemical Vapor Deposition of Ceramic Composites Containing Whisker and Fiber Reinforcements," pp. 507-19 in *Second Int. Conf. Chem. Vapor Dep.*, ed. J. M. Blocher, Jr., and J. C. Whithers, Electrochemical Society, New York, 1970.

11. L. R. Newkirk et al., "Chemical Vapor Deposition Fabrication of Filament Reinforced Composites for High Temperature Applications," pp. 82-101 in *Chemically Vapor Deposited Coatings*, ed. H. O. Pierson, American Ceramic Society, Columbus, Ohio, 1981.

12. J. J. Gebhart, "CVD Boron Nitride Infiltration of Fibrous Structures: Properties of Low Temperature Deposits," pp. 469-72 in *Fourth Int. Conf. Chem. Vapor Dep.*, ed. G. F. Wakefield and J. M. Blocher, Jr., Electrochemical Society, Princeton, N.J., 1973.

13. F. Christin, R. Naslain, and C. Bernard, "A Thermodynamic and Experimental Approach of Silicon Carbide-CVD Application to the CVD-Infiltration of Porous Carbon-Carbon Composites," pp. 499–514 in *Proc. Seventh Int. Conf. Chem. Vapor Dep.*, ed. G. F. Wakefield and J. M. Blocher, Jr., Electrochemical Society, Princeton, N.J., 1973.

14. R. Naslain, H. Hannache, L. Heraud, J. Rossignol, F. Christin, and C. Bernard, "Chemical Vapor Infiltration Techniques," pp. 293–304 in *Euro-CVD-Four*, Eindhoven, Netherlands, 1983.

15. H. Hannache, R. Naslain, and C. Bernard, "Boron Nitride Chemical Vapour Infiltration of Fibrous Materials from BCl_3-NH_3H_2 or BF_3-NA_3 Mixtures: A Thermodynamic and Experimental Approach," *J. Less-Common Met.* 95, 221–46 (1983).

16. J. Rossignol, I. Langlais, and R. Naslain, "A Tentative Modelization of Titanium Carbide CVI Within the Pore Network of Two-Dimensional Carbon-Carbon Composite Preforms," pp. 596–614 in *Ninth Int. Conf. Chem. Vapor Dep.*, ed. M. Robinson, G. Cullen, C. Van den Brekel, and J. M. Blocker, Jr., Electrochemical Society, Princeton, N.J., 1984.

17. A. J. Caputo and W. J. Lackey, "Process for the Preparation of Fiber-Reinforced Ceramic Composites by Chemical Vapor Deposition", U.S. patent 4,580,523, April 8, 1986.

18. A. J. Caputo and W. J. Lackey, *Fabrication of Fiber-Reinforced Ceramic Composites by Chemical Vapor Infiltration*, ORNL/TM-9235, October 1984.

19. A. J. Caputo and W. J. Lackey, "Fabrication of Fiber-Reinforced Ceramic Composites by Chemical Vapor Infiltration," *Ceram. Eng. Sci. Proc.* 5(7–8), 654–67 (1984).

20. A. J. Caputo, W. J. Lackey, and D. P. Stinton, "Development of a New, Faster Process for the Fabrication of Ceramic Fiber-Reinforced Ceramic Composites by Chemical Vapor Infiltration," *Ceram. Eng. Sci. Proc.* 6(7–8), 694–706 (1985).

21. A. J. Caputo, R. A. Lowden, and D. P. Stinton, *Improvements in the Fabrication of Ceramic-Fiber-Ceramic-Matrix Composites by Chemical Vapor Deposition*, ORNL/TM-9651, June 1985.

22. D. P. Stinton, A. J. Caputo, and R. A. Lowden, "Synthesis of Fiber-Reinforced SiC Composites by Chemical Vapor Infiltration," *Am. Ceram. Soc. Bull.* 65(2), 347-50 (1986).

23. A. J. Caputo, R. A. Lowden, and D. P. Stinton, "Fiber-Reinforced SiC Composites With Improved Mechanical Properties," *Am. Ceram. Soc. Bull.* 66(2), 368-72 (1987).

24. G. E. P. Box, W. G. Hunter, and J. S. Hunter, *Statistics for Experimenters*, Wiley, New York, 1978.

25. W. G. Cochran and G. M. Cox, *Experimental Designs*, Wiley, New York, 1950.

26. R. H. Myers, *Response Surface Methodology*, Allyn and Bacon, Inc., Boston, 1971.

27. W. V. Kotlensky, "Deposition of Pyrolytic Carbon in Porous Solids," *Chem. Phys. Carbon* 9, 173-262 (1973).

28. B. Dacic and S. Marikovic, " Carbon Fiber/Carbon Composites by CVD from Propylene," pp. 616-63 in *Carbon '80 (Int. Carbon Conf., 3rd)*, 1980.

29. H. O. Pierson and M. L. Lieberman, "The Chemical Vapor Deposition of Carbon on Carbon Fibers," *Carbon* 13, 159-66 (1975).

30. T. D. Gulden, "Deposition and Microstructure of Vapor Deposited Silicon Carbide," *J. Am. Ceram. Soc.* 51(8), 424-27 (1968).

31. T. D. Gulden, "Mechanical Properties of Polycrystalline BetaSiC," *J. Am. Ceram. Soc.* 52(11), 585-90 (1969).

32. R. J. Price, "Structure and Properties of Pyrolytic Silicon Carbide," *Am. Ceram. Soc. Bull.* 48(9), 859-62 (1969).

33. D. P. Stinton and W. J. Lackey, "Effect of Deposition Conditions on the Properties of Pyrolytic SiC Coatings for HTGR Fuel Particles," *Am. Ceram. Soc. Bull.* 47(6), 568-73 (1978).

34. J. I. Federer, *Fluidized Bed Deposition and Evaluation of Silicon Carbide Coatings on Microspheres*, ORNL/TM-5152, January 1977.

35. G. Eriksson, "Thermodynamic Studies of High-Temperature Equilibria," *Chem. Scr.* 8(3), 100-03 (1975).

36. T. M. Besmann, *SOLGASMIX-PV, A Computer Program to Calculate Equilibrium Relationships in Complex Chemical Systems*, ORNL/TM-5775, April 1977.

37. J. Chin, P. K. Ganzel, and R. G. Hudson, "The Structure of Chemical Vapor Deposited Silicon Carbide," *Thin Solid Films* **40**, 57-72 (1977).

38. G. S. Fischman and W. T. Petuskey, "Thermodynamic Analysis and Kinetic Implications of Chemical Vapor Deposition of SiC from Si-C-Cl-H Gas Systems," *J. Am. Ceram. Soc.* **68**(4), 185-90 (1985).

39. P. Krautwasser, G. M. Begun, and P. Angelini, "Raman Spectral Characterization of Silicon Carbide Nuclear Fuel Coatings," *J. Am. Ceram. Soc.* **66**(6), 424–34 (1983).

40. E. Fitzer and R. Gadow, "Fiber-Reinforced Silicon Carbide," *Am. Ceram. Soc. Bull.* **65**(2), 326–35 (1986).

41. T. Mah et al., "Thermal Stability of SiC Fibers," *J. Mater. Sci.* **19**, 1191-1201 (1984).

42. H. H. Moeller and J. H. Worley, "Tensile Testing of Ceramic Fiber Tows," *Ceram. Eng. Sci. Proc.* **6**(7-8), 558-66 (1985).

DEVELOPMENT OF ADVANCED FIBER REINFORCED CERAMICS

T. L. Starr and J. N. Harris
Georgia Tech Research Institute
Georgia Institute of Technology
Atlanta, Georgia 30332

ABSTRACT

Silicon nitride composites with random, short fiber reinforcement have been fabricated using reaction sintering techniques. Large diameter fiber yields high density composites but degradation of fiber during nitriding limits property gains. Small diameter whiskers with better high temperature stability yield low density composites using currently available silicon powders. Future work will focus on coatings to stabilize fibers, new fibers with better high temperature stability and finer silicon powders for whisker composites.

INTRODUCTION

A fundamental problem in the processing of ceramic composites is the fact that the incorporated fibers tend to reinforce the green structure, preventing the volume reduction and densification that usually can be obtained by free sintering. Hot pressing is a direct approach to overcoming this problem, providing the necessary densification by application of pressure. An alternative approach, more appropriate for fossil energy system components, is to maximize the green density of composite preforms and to utilize volume filling techniques for final densification. Earlier work, reported at the past two program reviews, has

focused on processing techniques consistent with this approach.

For blends of ceramic powder and chopped fiber, a new packing model was developed to better understanding the critical parameters for achieving high green density[1]. At a particular fiber loading, the density is determined by the packing density of the powder, the aspect ratio of the fiber and the ratio of the fiber length to particle diameter.

Two volume-filling techniques for composite densification have been studied. For silica matrix composites we used a resin-like silica precursor material to impregnate the preform[2]. After firing, dense silica fills the pores and the composite density is increased without volume reduction. Several cycles of impregnation and firing yields a final high density3.

A second volume-filling technique is reaction sintering for production of nitride ceramics. In the reaction sintering process, a preform of silicon is converted to the nitride by sintering in nitrogen to 1400°C. The solid volume of the preform increases by 23% with no change in bulk volume, yielding a density increase.

SILICON NITRIDE COMPOSITES

In the work since the last review we have used this process to prepare silicon nitride composites with silicon carbide fibers and whiskers, and to characterize these with respect to microstructure and mechanical properties.

CHOPPED FIBER COMPOSITES

Six composites were prepared using two silicon slips (low and high solids) and chopped SiC fibers (Nicalon fiber, Nippon Carbon Co., Tokyo, Japan) with three types of processing (as-received, chopped and crushed). High and low solids slips were prepared from milled silicon powder. One powder (Union Carbide Corp., USA) was dry milled for 17 hours and used for a 72% solids slip. Another powder (Kemanord Corp., Sweden) was dry milled for 3 and 27 hours and an 86% solids slip was prepared using equal parts of these fractions. One-half the silicon powder is added to distilled water

and roll overnight. Ten percent of the remaining powder is added each day for the next five days. Typically, ten additional days are required to reach minimum viscosity and for outgassing to cease. At this point, the pH of the suspension is near neutral.

Fiber was blended into each slip in small increments until the viscosity of the blend started to increase. This composition is different for each combination of fiber and slip. After de-airing, each composition was cast on plaster to form 2" x 2" x 1/4" plates. As seen in Table 1, the crushed fiber yielded a composite with high fiber loading and green density comparable to the monolithic material.

Table 1. Composites with Nicalon in silicon nitride

		AS - CAST		SINTERED	
Fiber	L/D	% fiber	% TD	% TD	% nitride*
Low solids slip					
None	---	0	70.4	82.1	90.8
As-received	112	10.4	67.0	79.3	92.1
Chopped	108	11.1	65.7	77.3	92.8
Crushed	33	25.6	69.1	79.3	94.1
High solids slip					
None	---	0	79.7	86.7	40.8
As-received	112	5.1	78.5	85.9	40.8
Chopped	108	6.5	79.7	87.0	40.8
Crushed	33	10.0	80.7	88.7	39.1

*Estimated from weight gain. No residual silicon detected by XRD for samples greater than 90%.

A standard five day reaction sintering cycle resulted in full conversion of the four compositions using the low solids silicon slip. The high solids slip yielded parts that were too dense to fully nitride due to the surface porosity closing, restricting the access of nitrogen to the interior of the part.

Overall, the most promising composition appeared to be the composite with 25% fiber and full conversion to nitride. A fracture surface of this material (figure 1) shows intact fibers and apparent fiber pull-out although some damage of the fiber surface is apparent (Figure 2).

Test bars were machined for flexure strength and fracture toughness measurement at room temperature and at 1000 and 1200°C. Flexure strength testing utilized four-point loading with an 4x8x50 mm bar. Fracture toughness was measured using three point loading of a single edge notched beam specimen (SENB). The results are plotted in Figures 3 and 4 along with reference values for monolithic reaction sintered silicon nitride. The strength of the composite material is somewhat lower than that of monolithic material of comparable density. The SENB fracture toughness is similar for the two materials.

WHISKER COMPOSITES

The fiber/powder packing model indicates that the approximately 0.6 micron diameter SiC whiskers (Silar SC-9, ARCO Chemical Co., Greer. SC) require a silicon powder with a sub-micron particle size in order to achieve good packing density. Forty grams of a fine silicon powder was supplied by Tokyo Tekko Company, Tokyo, Japan. This powder is produced by a patented hydride decomposition process which produces a sub-micron particle with a range of diameters. The powder was shipped under nitrogen although the manufacturer states that it is "slightly nitrided" and stable in air. A small sample was exposed to air and weighed over a period of six hours. After an initial weight gain of approximately 0.4% in thirty minutes, no further increase was observed. This air stability simplifies handling and processing as compared to other fine silicon powders.

The powder was characterized by X-ray diffraction, transmission electron microscopy and BET surface area analysis. The X-ray diffraction

Figure 1. Fracture surface of chopped fiber composite (200x)

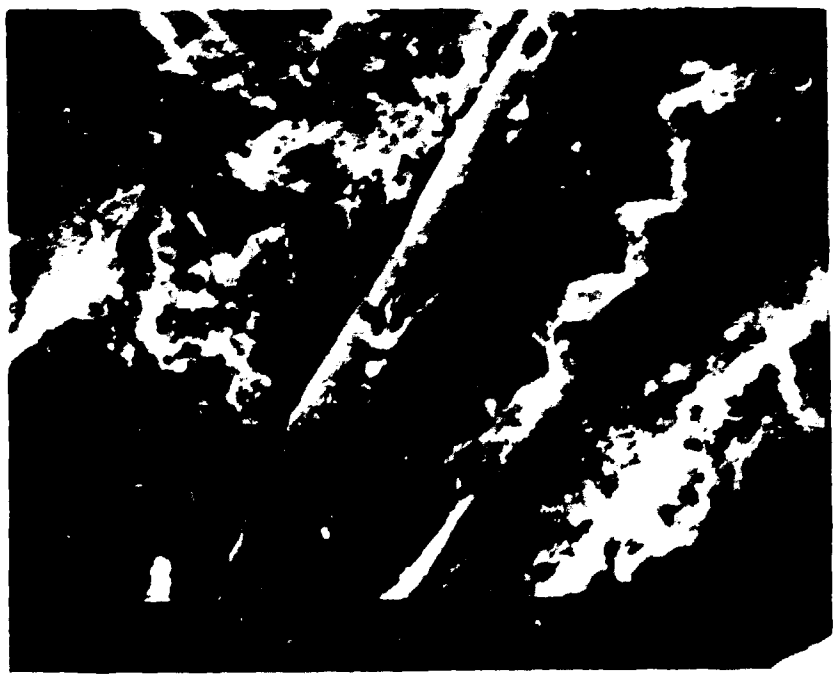

Figure 2. Degradation of Nicalon after Nitriding

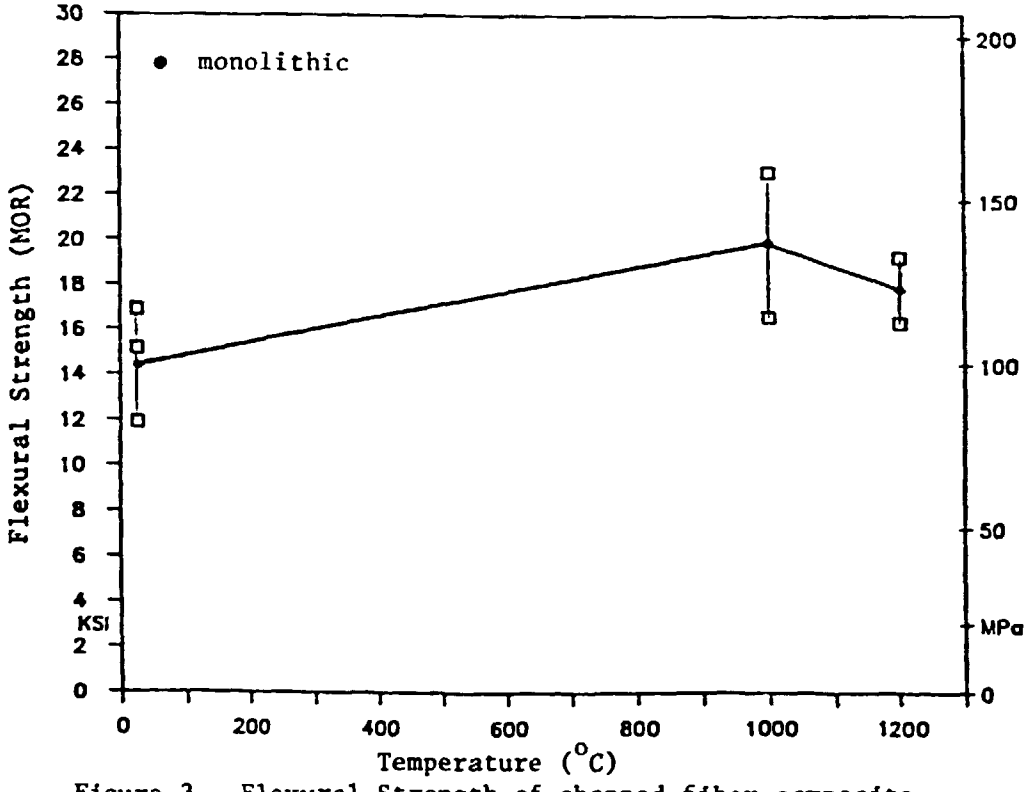

Figure 3. Flexural Strength of chopped fiber composite

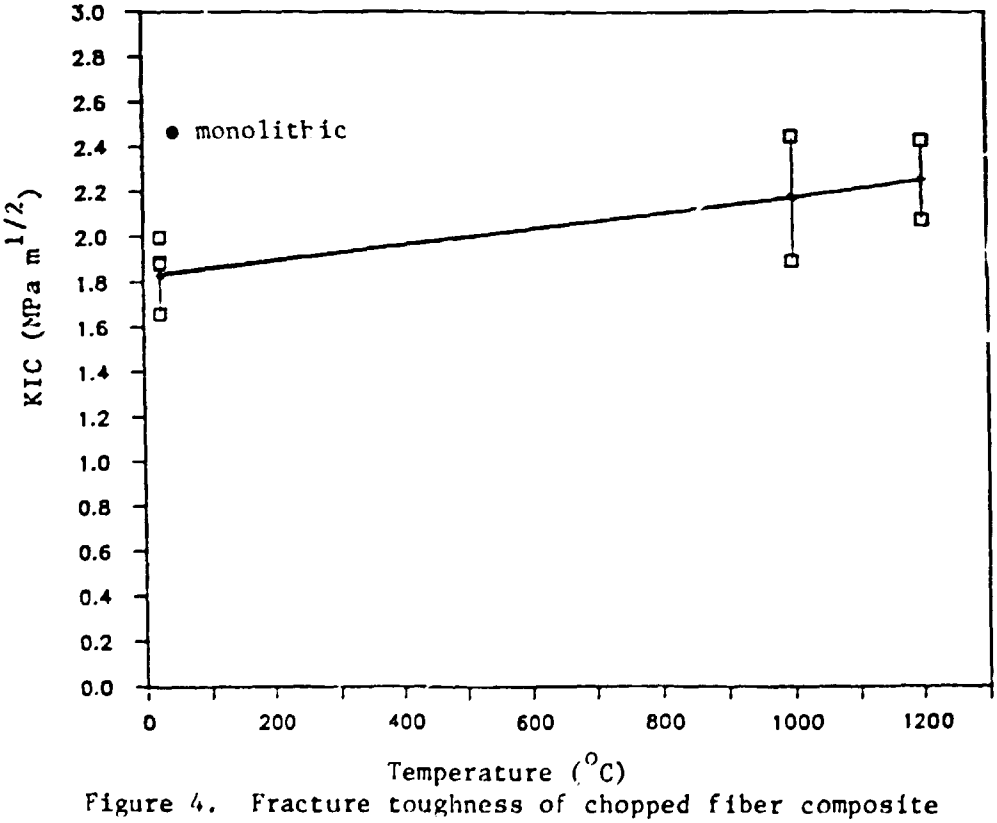

Figure 4. Fracture toughness of chopped fiber composite

showed silicon metal as the only crystalline phase. The TEM micrograph in figure 5 shows spherical particles with diameters ranging from 0.01 to 0.1 um. The TEM sample was prepared by mulling the powder between glass slides with methanol and evaporating a drop of this dispersion on a microscope grid. Under these conditions the particles are highly agglomerated. The BET surface area is 84 m^2/g, equivalent to an average spherical diameter of 0.03 um, in good agreement with the microscopy results. The relative sizes of the two materials can be seen in Figure 6.

The powder was dispersed in isopropanol using ultrasonics. Due to the large surface area, a dispersion with adequate fluidity contained only 35% (by weight) of silicon. This is contrasted to typical powder loadings of 70-90% for coarser powders. Whiskers were blended with the silicon dispersion at a loading of 18% (by volume), again using ultrasonics.

Such low solids dispersions are not suitable for slip-casting. Instead, the dried dispersion was lightly ground to form fine pellets and pressed into a disc under uniaxial pressure. Pressed density for the silicon alone was 1.11 g/cc and for the composite 1.35 g/cc. The improved packing efficiency with the fine powder is apparent when contrasted to earlier results with coarse powder. In this case, the pressed density went from 1.60 to 0.90 g/cc with addition of 15% chopped fiber.

Pellets of the composite and of the silicon powder alone were nitrided. A small amount of iron oxide (2.9% by weight) was added to one pellet of each composition. Iron is known to accelerate the nitridation of milled silicon powder. The nitrided samples were characterized by weight gain and by X-ray diffraction.

These results are shown in table 2, along with results for a coarse powder/Nicalon fiber composite and two monolithic materials. Significant differences are apparent among these materials. These include conversion efficiency, alpha/beta ratio and fiber reactions.

All four samples made with the ultra-fine powder were completely converted to alpha-silicon nitride, that is, no detectable silicon metal remained. This is in contrast to the gravimetric estimated of percent converted for the composite sample with Fe which indicates an apparent conversion of only 20%. This discrepancy must be due to concurrent weight

Figure 5. Ultrafine silicon powder (115,000x)

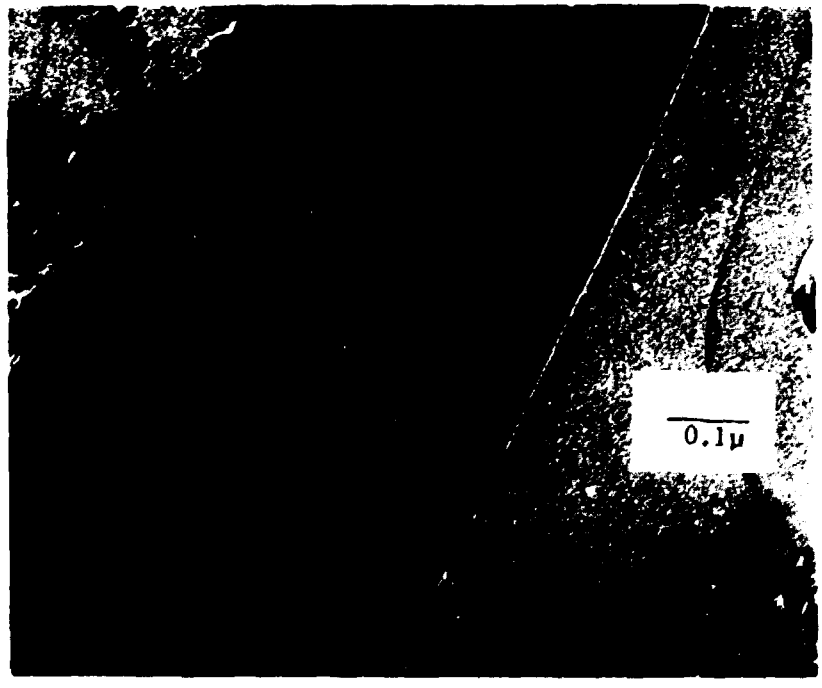

Figure 6. Ultrafine silicon with Silar whisker (115,000x)

loss occurring during nitriding. The effect of green density is also apparent in the conversion efficiency. None of the samples with greater than 25% porosity showed any residual silicon while the sample with 20% porosity showed considerable unconverted metal.

The alpha/beta ratio for the ultra fine silicon is quite different than that for the coarse powder, with no beta phase detected in the former. Studies of the nitridation reaction indicate that the alpha phase forms from a gas phase reaction, while beta-silicon nitride forms from vapor-solid (V S) or vapor- liquid-solid (VLS) reactions[4].

Since insufficient powder was available for preparation of test bars, mechanical properties could not be determined for the whisker reinforced composites.

Table 2. Characterization of silicon carbide whisker composites

		X-Ray Peak Height				
	green porosity	alpha	beta	silicon	other	gravimetric % nitrided
Ultrafine silicon	0.52	100	ND	ND	--	79
+ Fe	0.43	100	ND	ND	--	97
+ Silar	0.44	100	ND	ND	SiC	78
+ Fe + Silar	0.43	100	ND	ND	--	21
Coarse silicon #1	0.20	13	6	100	--	41
Coarse silicon #2	0.29	69	92	ND	--	95
+ Nicalon	0.32	97	25	ND	--	94

ND = not detected

CONCLUSIONS

Although the microstructure of the fracture surface of the chopped fiber composite suggested improved toughness, this was not borne out in the

mechanical testing. This may be due to the test method (SENB) which measures initial crack opening resistance. Chopped fiber reinforcement is expected to promote crack deflection and, thus, primarily to increase the total work of fracture. Also, the fiber may not provide toughening due to its degradation during nitriding. A weakened fiber cannot effectively bridge the crack and resist opening.

The better high temperature stability of the whisker reinforcement should lead to effective toughening. While the ultrafine silicon powder packs efficiently with these whiskers, the overall density still must be improved. A silicon powder with a somewhat larger average particle size is desirable.

This work shows the potential for practical fabrication of a ceramic composite having a reaction sintered silicon nitride matrix and a silicon carbide fiber or whisker reinforcing phase. Preform fabrication issues have been addressed and high density composites can be prepared. Development of improved mechanical properties will require optimization of the nitriding process to obtain high conversion and high density with minimal fiber degradation, use of more stable fibers or whiskers, and control of the fiber-matrix interface to improve fiber stability and increase the fiber contribution to the work-of-fracture.

REFERENCES

1. T. L. Starr, "Packing Density of Fiber/Powder Blends" Ceram. Bull. 65(9) 1293-6 (1986).

2. T. L. Starr and J. N. Harris, in AR&TD Fossil Energy Materials Program Quarterly Progress Report for Period Ending December 31, 1983, Oak Ridge National Laboratory Report ORNL/FMP-84/1, pp. 407-418 (March 1984).

3. T. L. Starr and J. N. Harris, in AR&TD Fossil Energy Materials Program Quarterly Progress Report for Period Ending March 31, 1984, Oak Ridge National Laboratory Report ORNL/FMP-84/2, pp. 365-380 (May 1984).

4. A. J. Moulson, "Reaction Bonded Silicon Nitride: Its Formation and Properties" J. Mater. Sci. 14(5) 1017-51 (1979).

FRACTURE TOUGHNESS BEHAVIOR OF A SILICON CARBIDE WHISKER-REINFORCED ALUMINA CERAMIC AT SELECTED POROSITIES

Ralph F. Krause, Jr. and E. R. Fuller, Jr.

National Bureau of Standards
Gaithersburg, MD 20899

The fracture toughness behavior of a silicon carbide whisker-reinforced alumina ceramic has been characterized at porosities, ranging from 0.6 to 11.5 percent. The composite material consisted of alumina that was hot pressed with 25 weight percent silicon carbide whiskers. Controlled flaws of increasing size were produced on polished surfaces of specimens by Vickers indentation loading from 2 to 200 N. The flexural strength measured as a function of indentation load indicates that the resistance to fracture of these materials increases as a function of crack extension. The results are analysed in terms of a fracture model containing ligamentary tractions in the wake of the crack.

I. INTRODUCTION

The achievement of higher efficiency heat engines and heat recovery systems requires the availability of high temperature, high performance structural materials. Structural ceramics, and more recently, ceramic matrix composites have received particular attention for these applications due to their high strength, corrosion resistance, and thermal shock resistance. Even with these positive attributes, improved reliability and extended lifetime under service conditions are necessary for structural ceramics to gain industrial acceptance. These materials have mechanical

and chemical limitations especially when they are subjected to high temperatures, reactive environments, and extreme thermal gradients. An important property needed for structural design is the fracture resistance of a material which characterizes the limitation of crack extension under applied stress.

Silicon carbide whisker-reinforced alumina is a newly developed ceramic composite which shows considerable promise as a high strength structural ceramic [1, 2, 3]. As part of a program to investigate the critical factors which influence mechanical and microstructural behavior, a recent method of analysis [4] of strength-indentation measurements was adapted to characterize the fracture resistance of this material at selected porosities.

II. EXPERIMENTAL PROCEDURE

Billets of a silicon carbide whisker-reinforced alumina ceramic, whose porosities ranged from 0.6 to 11.5 percent, were provided for this investigation through the courtesy of J. F. Rhodes [1,2]. A fine-grained alumina powder was hot pressed with 25 weight percent silicon carbide whiskers to form the billets of the composite material. The billets were rectangular plates, 150 mm x 150 mm x 12 mm, except for the highest density billet (0.6 percent porosity) which was a cylindrical puck, 110 mm diam x 15 mm. The silicon carbide whiskers were produced in a carburization process at 1600°C where the sources of silicon and carbon were rice hull ash and rice hull hydrocarbons, respectively [3]. Nominal whisker dimensions were 0.45 to 0.65 μm diam and 10 to 80 μm length [3].

The billets were diamond-sawed to fabricate flexure specimens, nominally 3 mm x 4 mm x 50 mm, with the prospective tensile surface, 4 mm x 50 mm, normal to the hot press direction. The sides of the specimens were diamond-ground flat and parallel by a 30 μm diamond wheel, and the prospective tensile surfaces of the flexure specimens were polished with 9 μm diamond paste. The specimens were soaked and rinsed in ethyl alcohol to remove the wax needed to mount them for polishing, and they were dried in a hot air flow.

The porosity, p, of a flexure specimen was calculated by

$$p = 1 - \rho_b/\rho_t \tag{1}$$

where ρ_b and ρ_t are the bulk and theoretical densities, respectively. The bulk density was determined from the mass and bulk dimensions of the specimen. The theoretical density, ρ_t = 3.762 g/cm^3, was calculated from

$$1/\rho_t = w_1/\rho_1 + w_2/\rho_2 \tag{2}$$

where w_i is the weight fraction and ρ_i is the x-ray density of the ith component: ρ_1 + 3.987 g/cm^3 for Al_2O_3 and ρ_2 = 3.217 g/cm^3 for SiC.

A flaw of variable size, controlled by Vickers indentation loading between 2 and 200 N, was placed in the center of the prospective tensile surfaces of several of the flexure specimens. Care was taken to orient one set of the radial cracks of an indentation flaw in the direction of prospective rupture. The indentations were made in air at room temperature with a steady loading rate that required 15 s to produce a full load. The diamond pyramid contacted the specimen surface for about 30 s before it was

withdrawn to complete the loading cycle. The lengths of surface cracks were measured by optical microscopy, using a calibrated scale accurate within 2 μm.

Strength tests were conducted on specimens under 4 point flexure in dry nitrogen at room temperature. The gear-driven crosshead of a universal testing maching was operated at a constant load-point displacement speed of 5 mm/min, producing a loading rate of 145 N/s on the material, until the applied load attained its maximum value, F, required to rupture the specimen. The load was transmitted to the specimen through 6 mm diam rollers. Loading was measured by a linear load transducer and was recorded on a constant speed chart. The load transducer was calibrated at the full scale of the chart with a known 10 kg mass, which was converted to force units by the local acceleration of gravity, 9.801 m/s^2. The flexural strength, S, was calculated by

$$S = 3(\ell_1 - \ell_2)F/2BW^2 \qquad (3)$$

in which the loading spans were ℓ_1 = 40 mm and ℓ_2 = 10 mm and in which the nominal dimensions of the specimen were B = 4 mm and W = 3 mm. Following rupture of a specimen, it was examined by optical microscopy to confirm whether or not the fractured surface passed through a radial crack of the indentation flaw.

III. DATA ANALYSIS

According to the energy principle, incremental crack extension, dc, can occur when the applied stress-intensity factor, K, is equal to or

greater than the fracture resistance of a material, K_R. An equilibrium position will be attained at $K = K_R$, if $dK/dc < dK_R/dc$. The criterion for the onset of crack-extension instability, leading finally to failure, is the point of common tangency,

$$dK/dc = dK_R/dc \tag{4}$$

This point defines the critical stress-intensity factor, K_c, or fracture toughness for a given configuration of the material.

To facilitate analysis of the data, a parametric representation of the fracture resistance as a fractional power function in crack extension, Δc, is used [4]

$$K_R = K_o(\Delta c/c_o)^{1/r} \tag{5}$$

where K_o, c_o, and $r \geq 1$ are constants. The exponent $1/r$ measures the susceptibility to R-curve behavior, that is, the susceptibility for fracture resistance increasing with crack extension. When $1/r = 0$, Eq. (5) gives completely brittle behavior, namely, $K_R = K_o = K_c$. The nature of R-curve behavior represents the situation that besides the energy needed to propagate a crack at its tip, additional energy is required to overcome perhaps the tractions of aggregate interlock and pullout or the restraining forces of ligaments in the wake of the crack. In general, $\Delta c = c - c_p$, where c is the total crack length and c_p is a traction-free portion such as exists in a prenotched specimen.

When a sufficient load, P, is applied to a sharp indenter in contact with a material, and the indenter is then unloaded, semi-circular radial

cracks will develop in the material [5]. The driving force of the crack system may be characterized by a residual stress-intensity factor,

$$K_r = \chi P c^{-3/2} \tag{6}$$

where χ is a constant dependent on the material and indenter geometry. At the equilibrium position, $K_r = K_R$, a tractioned crack length, $\Delta c = c_I$, is produced by the indentation load, P. Thus, the constants c_o and χ are characterized by

$$c_o = c_I (P_o/P)^{2r/(3r+2)} \tag{7}$$

and

$$\chi = (K_o/P_o) c_o^{3/2} \tag{8}$$

The crack length, c_I, is assumed to be the half-length of indentation surface crack.

When a freshly indented material is subsequently subjected to a small bending stress, σ, a bending stress-intensity factor, K_b, will be superposed upon K_r. The tractioned crack system will grow as long as $(K_r + K_b) \geq K_R$. The bending stress-intensity factor may be characterized by

$$K_b = Y\sigma c^{1/2} \tag{9}$$

where Y is a configuration coefficient which is dependent on specimen and flaw geometry. Catastrophic failure ensues when the criterion of Eq. (4) is satisfied. Under this condition the tractioned crack has extended to

the onset of instability, c_T, and by definition $\sigma = S$. Solution of the fracture mechanics equations gives [4]

$$c_T/c_I = [4r/(r-2)]^{2r/(3r+2)} \tag{10}$$

and

$$S = S_o(P/P_o)^{-\beta} \tag{11}$$

where

$$r = 2(1+\beta)/(1-3\beta) \tag{12}$$

and

$$K_o = YS_o\beta^{-\beta}(1+\beta)^{(1+\beta)}c_o^{1/2} \tag{13}$$

The maximum flexural strength, S_o, represents the situation that a crack has extended from an intrinsic traction-free flaw, c_p, to the onset of instability, c_t, under the conditions of $K_b = K_R$ and $dK_b/dc = dK_R/dc$. Solution of the fracture mechanics equations in this case gives

$$c_p/c_t = 4\beta/(1+\beta) \tag{14}$$

and

$$c_t/c_o = \beta^{-(1+\beta)/2}\ (1-3\beta)^{(1-3\beta)/4\beta}\ (1+\beta)^{(\beta/2+1/4\beta+7/4)} \tag{15}$$

Generally, an indentation crack, c_I, will dominate over an intrinsic flaw, c_p, to cause specimen failure at a point of instability of crack-extension, $\Delta c = c_T$, if $c_I > c_o$.

IV. EXPERIMENTAL RESULTS

Three billets at separate porosities of the whisker-reinforced alumina ceramic have been characterized. Table 1 gives the mean porosity, p, and

Table 1. Values of parameters that define crack-extension in a 25 wt percent silicon carbide whisker-reinforced alumina ceramic at selected porosities. The uncertainty for each value is its standard deviation.

	Parameter	Billet (a)	Billet (b)	Billet (c)
A.	Porosity			
	p, percent	11.48 ± 0.16	4.89 ± 0.14	0.60 ± 0.03
	No. of measurements	24	24	24
B.	Intrinsic Strength			
	S_o, MPa	421 ± 11	559 ± 12	681 ± 15
	No. of measurements	11	6	6
C.	Indented Beam Strength			
	β	0.276 ± 0.015	0.266 ± 0.009	0.262 ± 0.014
	P_o, N	8.5 ± 1.3	4.7 ± 0.5	4.9 ± 0.7
	No. of measurements	13	18	18
	Percent $\langle \log_e(S) \rangle$	± 1.7	± 1.3	± 2.0
	Student's t for 95 % confidence interval	1.80	1.75	1.75
D.	Indented Crack Length			
	c_o, μm	28.9 ± 2.4	18.1 ± 1.2	18.8 ± 1.6
	χ	0.095 ± 0.003	0.088 ± 0.002	0.110 ± 0.005
	No. of measurements	6	6	6
E.	Fracture Resistance			
	r	14.8 ± 4.0	12.5 ± 1.8	11.8 ± 2.6
	K_o, MPa·m$^{1/2}$	5.17 ± 0.25	5.35 ± 0.17	6.61 ± 0.32
	c_T/c_I	2.66 ± 0.04	2.69 ± 0.03	2.70 ± 0.04
F.	Intrinsic Flaw Size			
	c_p/c_t	0.86 ± 0.04	0.84 ± 0.02	0.83 ± 0.04
	c_t/c_o	3.41 ± 0.10	3.32 ± 0.06	3.29 ± 0.09
	c_p, μm	85 ± 17	50 ± 7	51 ± 9

the standard deviation of the mean from measurements on 24 flexure specimens from each billet. In general, specimens from the edges of the billets tended to be slightly less porous.

Figure 1 shows the bending strength as a function of indentation load at the selected porosities of the material. The open circles which are arbitrarily plotted at $\log_{10}(P) = 0$ correspond to strengths of non-indented specimens. A plateau of strength, S_o, which is invariant with indentation load exists over a region of small indentation flaws at each porosity, but the range of this plateau decreases with decreasing porosity of the material. Figure 2 shows S_o as a function of the porosity, p. A straight line, the logarithm of Eq. (11), was fitted by a method of least squares to evaluate the coefficients β and P_o at each porosity, Table 1, using the mean values of S_o to calculate the respective P_o. Only those indentation loads which correspond to the fractured surface having passed through a radial crack of an indentation flaw are considered valid points for the fit. The dashed line describes a slope of -1/3 which a fracture toughness invariant with crack size in the region of large cracks would indicate.

Figure 3 shows the half-length of surface crack as a function of indentation load at the selected porosities of the material. The dashed line is a least-squares-fit to the observed data. In principle an alternative value of β could be deduced from the slope of this fit, $(1+\beta)/2 = 2r/(3r+2)$. However, evaluation of β from Eq. (11) is preferred because the variance of $(1+\beta)/2$ would have to be 0.25 of the variance of β from the slope of the strength data to provide the same variance of r. The solid lines in Fig. 3 describe the slope $(1+\beta)/2$ at the respective porosities of the material where β was deduced from the strength data. Clearly, there is a bias in the small crack region of indentation loads due to the failure to

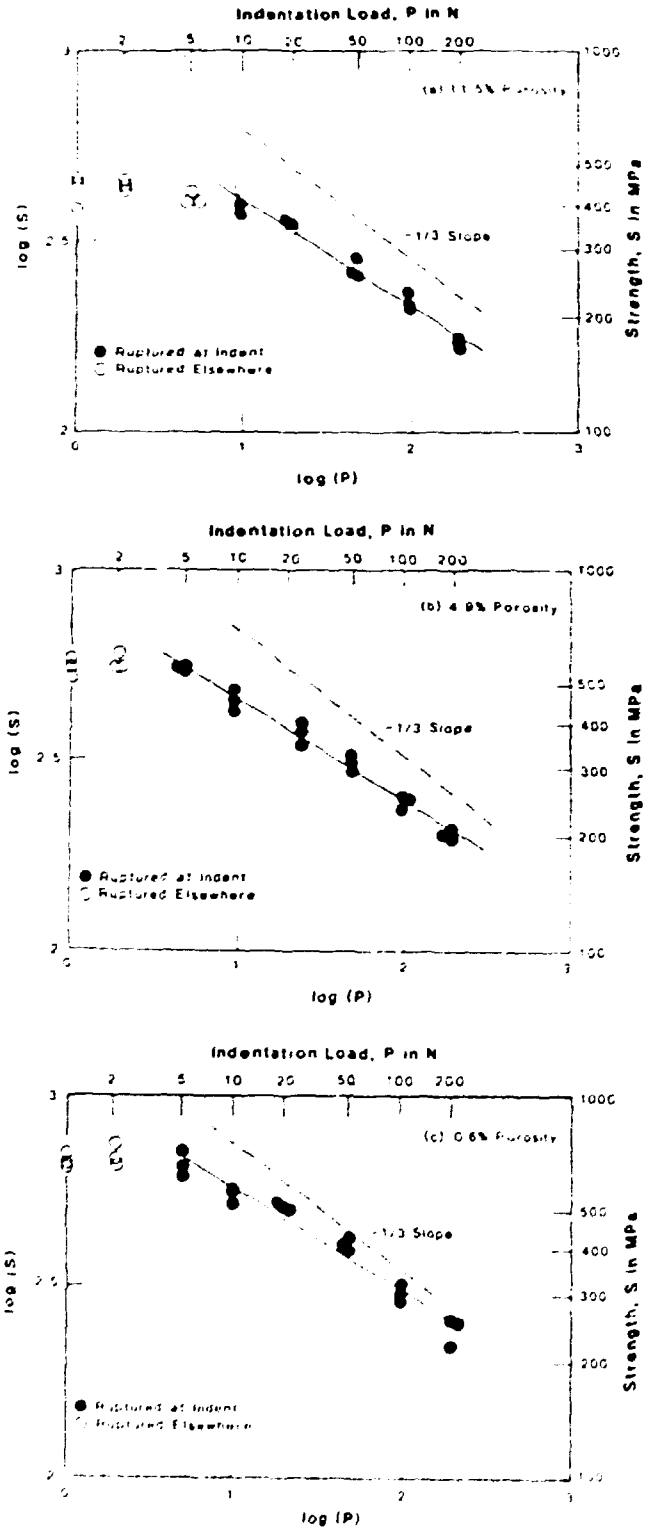

Figure 1. Bending strength, S, as a function of indentation load, P, for a 25 wt percent silicon carbide whisker-reinforced alumina ceramic at selected porosities. The solid line is a least-squares-fit for the solid points.

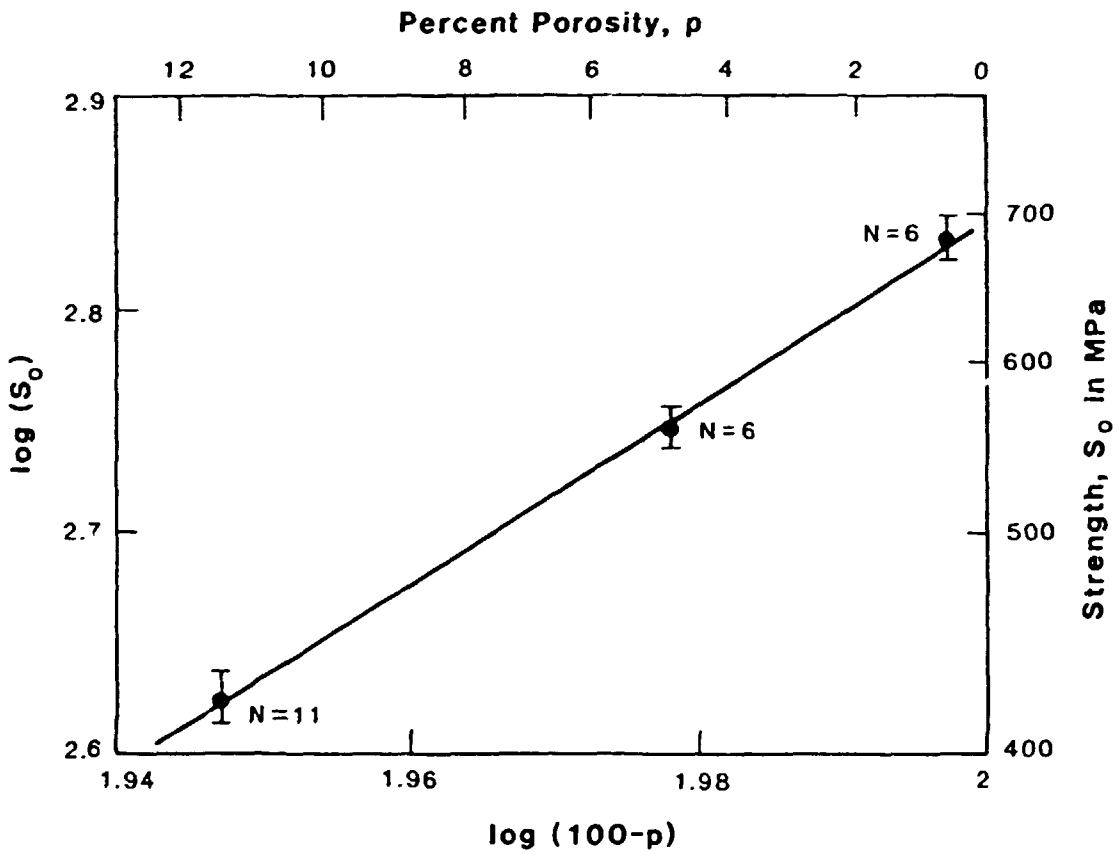

Figure 2. Intrinsic strength, S_o, as a function of porosity of a 25 wt percent silicon carbide whisker-reinforced alumina ceramic.

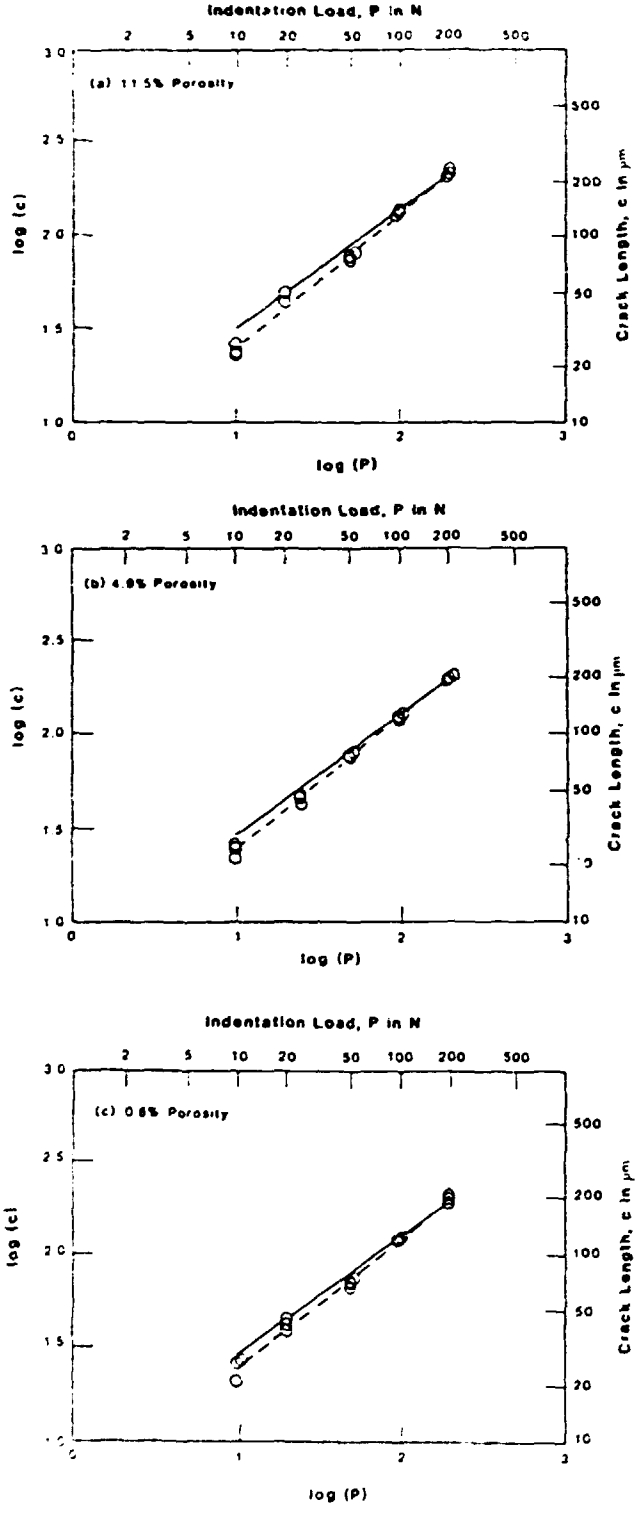

Figure 3. Half-length of surface crack, $c = c_f$, as a function of indentation load, P, for a 25 wt percent silicon carbide whisker-reinforced alumina ceramic at selected porosities. The dashed line is a least-squares-fit, and the slope of the solid line is derived from the strength measurements.

observe the complete crack length by optical microscopy. Using r and P_o from the indentation-strength data, the constant c_o was evaluated by Eq. (7) with c_I only from the large crack region of indentation load, P. Table 1 gives the mean value of c_o at each porosity.

Since Eq. (11) is believed to provide a reasonable fit to the observed strength data, the supposition of Eq. (5) is confirmed as a reasonable representation of the fracture resistance at the selected porosities of the material. Table 1 gives the values of r and K_o deduced from Eqs. (12) and (13), respectively, using Y = 1.174 [4]. Figure 4 shows the fracture resistance, K_R, as a function of Eq. (5). The length of the shaded region at a given porosity describes the range of values of the critical stress-intensity factor, K_c, at the onset of crack-extension instability, c_T, deduced from the analysis of the experiments.

While the R-curve of the material at a given porosity was evaluated from the indentation-strength measurements with $P > P_o$, the intrinsic flaw size, c_p, was evaluated from the strength measurements on non-indented specimens, including those with $P < P_o$. Figure 5 shows typical stress-intensity factors generated as a function of crack length, c. The intersection of the K_r and K_R curves describes in general the indentation crack size, c_I. When the applied flexural stress is increased to the strength value, $\sigma = S$, K_b is superposed on K_r and the crack is extended to the onset of instability, $\Delta c = c_T$. Table 1 gives the values of c_T/c_I at the selected porosities. When the applied flexural stress is increased to $\sigma = S_o$ in cases where $P < P_o$, the crack is extended to the onset of instability, $\Delta c = c_t - c_p$. In this case the intrinsic flaw, c_p, which is considered traction-free dominates over the indentation crack, $c_I < c_o$, to

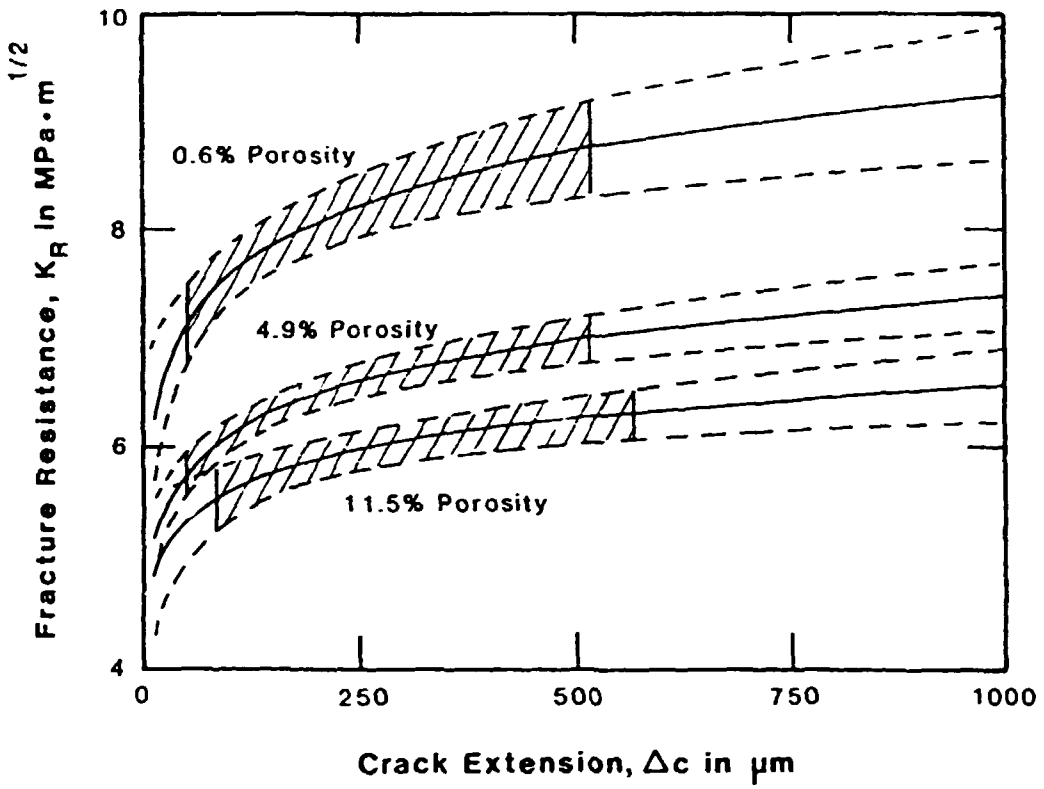

Figure 4. Fracture resistance as a function of crack extension of a 25 wt percent silicon carbide whisker-reinforced alumina ceramic at selected porosities. The shaded region at a given porosity represents the 95 percent confidence interval of K_R.

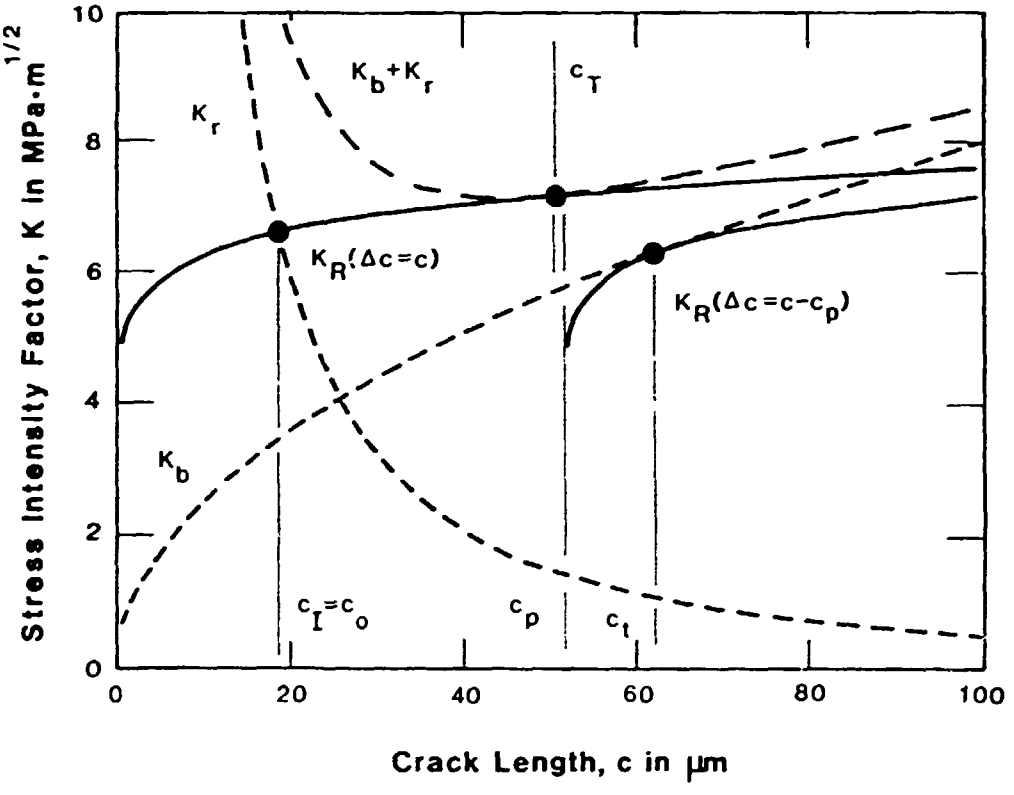

Figure 5. Typical stress-intensity factors as functions of crack length in a 25 wt percent silicon carbide whisker-reinforced alumina ceramic. This example depicts the K_r curve at indentation load, P_o, and the K_b curve at intrinsic strength, S_o, for the 0.6 percent porosity of the ceramic.

cause material failure. Table 1 gives the values of c_p/c_t, c_t/c_o, and c_p at the selected porosities.

V. PROPAGATION OF ERRORS

Analysis of the random errors in the strength measurements will elucidate whether or not the K_R curves themselves, appearing to increase with crack-extension, and the apparent difference in the K_R curves at the selected porosities of the material are significant. While the uncertainties listed in sections A and B of Table 1 are the standard deviations of the mean p and of the mean S_o, respectively, the standard deviations of β and of the mean log(S) in the indentation-strength measurements follow the statistical analysis of a straight line [6]. The standard deviations of the other parameters in Table 1 were estimated by the law of propagation of errors. According to the principle of least squares applied to the logarithm of Eq. (11), the ordinate intercept is

$$[\log(S_o) + \beta \cdot \log(P_o)] = \langle \log(S) \rangle + \beta \cdot \langle \log(P) \rangle \qquad (16)$$

where $\langle \log(S) \rangle = \Sigma \log(S_i)/N$ and where P is assumed not subject to error. The variables $\langle \log(S) \rangle$ and β can be shown to be statistically independent [6], a necessary requirement for the validity of the law of propagation of errors. Using Eq. (16), variances of the parameters were derived as listed in Table 2. The standard deviation of a given parameter is the square root of its variance. The 95 percent confidence interval is the product of the standard deviation and the Student's t [6].

Table 2. Propagation of Errors Formulas: $Var(Z) = \sum[\delta Z/\delta x_i]^2 \, Var(x_i)$

Z	$[\delta Z/\delta x_i]$ at respective x_i			
	β	$\langle\log(S)\rangle$	$\log\langle S_o\rangle$	$\log\langle c_I\rangle$
r	$8/(1-3\beta)^2$			
$\log(P_o)$	$[\langle\log(P_s)\rangle - \log(P_o)]/\beta$	$1/\beta$	$1/\beta$	
$\log(c_o)$	$[(1+\beta)\langle\log(P_S)\rangle - \log(P_o) - \beta\log\langle P_c\rangle]/2\beta$	$(1+\beta)/2\beta$	$(1+\beta)/2\beta$	1
$\log(\chi)$	$\log(1+1/\beta)+\langle\log(P_S)\rangle - \log\langle P_c\rangle$	1		2
$\log(K_o)$	$\log(1+1/\beta)+[(1+\beta)\langle\log(P_s)\rangle - \log(P_o) - \beta\log\langle P_c\rangle]/4\beta$	$(1+\beta)/4\beta$	$(3\beta-1)/4\beta$	1/2
$\log(K_R)$	$\log(1+1/\beta)+\langle\log(P_s)\rangle - \log\langle P_c\rangle + 2[\log\langle c_I\rangle - \log(c)]/(1+\beta)^2$	1		$2\beta/(1+\beta)$
$\log(c_T/c_I)$	$[\log(1+1/\beta) - 1/\beta]/2$			
$\log(c_p/c_t)$	$4/(1+\beta)^2$			
$\log(c_t/c_o)$	$1/(1+\beta) - \log(\beta)/2 - \log(1-3\beta)/4\beta^2 + (1-1/2\beta^2)\log(1+\beta)/2$			
$\log(c_p)$	$[(1+\beta)\langle\log(P_s)\rangle - \log(P_o) - \log(1-3\beta)/2\beta]/2\beta + 1/\beta + [(1-1/2\beta^2)\log(1+\beta) - \log(\beta) - \log\langle P_c\rangle]/2$	$(1+\beta)/2\beta$	$(1+\beta)/2\beta$	1

$\langle\log(P_s)\rangle$ = mean $\log(P_s)$ of indentation-strength measurements
$\langle P_c\rangle$ = mean P_c of crack length measurements
$\log(N)$ = $\log_e(N)$

Figure 4 shows the 95 percent confidence intervals of K_R, being ± 3.8, ± 3.3, and ± 5.2 percent for a crack-extension of Δc = 0.5 mm at the selected porosities of 11.5, 4.9, and 0.6 percent, respectively.

VI. REFERENCES

1. J.F. Rhodes, private communication, ARCO Chemical Company, Greer, SC, May 14, 1986.

2. J.F. Rhodes, H.M. Rootare, C.A. Springs, and J.E. Peters, "Whisker-Reinforced Structural Ceramic Composites," American Ceramic Society Meeting, Chicago, April 28, 1986.

3. J.F. Rhodes, H.M. Rootare, and J.L. Cook, "Silicon Carbide Whiskers," American Ceramic Society Meeting, Chicago, April 28, 1986.

4. R.F. Krause, Jr., "Rising Fracture Toughness from the Bending Strength of Indented Alumina Beams," submitted to the J. Amer. Ceram. Soc., August 1986.

5. D.B. Marshall and B.R. Lawn, "Residual Stress Effects in Sharp Contact Cracking, Part 1, Indentation Fracture Mechanics," J. Materials Science 14 (1979).

6. J. Mandel, The Statistical Analysis of Experimental Data, Dover Publications, Inc., New York, 1984.

Acknowledgment

This work was funded by the US Department of Energy, Structural Ceramics Project, Oak Ridge National Laboratory, Oak Ridge, TN.

CERAMIC FILTER FAILURE ANALYSIS

R. Chang, J. Sawyer, and C. Okoh

Acurex Corporation
Environmental Systems Division
485 Clyde Avenue, P.O. Box 7044
Mountain View, California 94039

ABSTRACT

Ceramic filters offer a promising approach for particulate control from high temperature gas streams. The major concern is the long-term durability of these filters in the hostile environment of the hot corrosive gas stream. The objective of the program is to determine the causes of ceramic filter failure during use and to propose development work needed to improve the reliability of these filters.

A literature search was conducted to determine the major types of ceramic filters. Manufacturers and users of the filters were contacted to determine their application experience with various filter types and to obtain samples for further analysis.

Failure analysis was conducted on different samples using a combination of surface and structural analysis techniques including SEM, EDX, EPMA, AES and X-ray diffraction. Stress analysis was performed to relate filter mechanical properties with areas of stress concentration during use. This paper summarizes the effort to date on failure analysis.

INTRODUCTION

The need to control particulates that result from the combustion or gasification of coal is an essential issue that affects the viability of advanced coal-use technologies, such as gasification,

pressurized fluidized-bed combustion and direct coal-fueled heat engines. Particulates from the hot-gas stream from these processes must be controlled to protect components of the energy system and to meet environmental emissions requirements. High-temperature ceramic filters offer a promising approach for the removal of particulates from these hot-gas streams. Tests with different types of ceramic filters have shown they can tolerate high-temperature (>850°C) exposures and collect particulates efficiently. However, durability problems encountered during the use of the filters at high temperatures led to concerns over the long-term reliability of ceramic filters.

The objective of the present project is to determine the principal causes of failure of ceramic filters used for the removal of fine particulates from high-temperature, high-pressure (HTHP) gas streams in coal conversion and utilization systems, such as fluidized-bed combustors, direct coal-fired gas turbines, and coal gasification systems. Materials research and development to improve the reliability of these filters and design features of current filters which contribute to material failure will then be identified.

In the present paper, a summary of the findings to date on the project will be presented.

MAJOR TYPES OF CERAMIC FILTERS

The major types of ceramic filters currently under development can be classified into three groups:

Ceramic fabric filters -- These are flexible filters made from ceramic fibers which are formed into a mat or woven as a cloth. In the mat form, the fibers are short and the structure is too weak to be self supporting. The mat is therefore supported by screens on each side.[1] The short fibers tend to be unstable and would gradually be lost into the gas stream. As a result, recent emphasis has been in the development of woven filters.[2]

In the woven form, continuous filament yarns or yarns twisted from staple fibers (short fibers) are made into cloths with different weave patterns. Continuous filament cloths tend to form filters with smooth, slick surfaces while staple yarns form cloths with a texturized appearance. The filters are generally tubular in shape and are designed like conventional bag filter units. The current approach is to produce seamless filter tubes since earlier versions of seamed filter bags which were constructed like conventional filter bags encountered seam durability problems.

The most common filter fiber materials include continuous filaments of silica-alumina-boria and staple fibers of silica alumina. Other materials such as silicon carbide, quartz, different compositions of fiberglass, zirconia, zirconia-silica, and alumina have been used but only limited data is available because of the short test durations.

Ceramic candle filters -- These rigid tubular filters are made by bonding ceramic fibers or grains or a combination of these.[3,4] Candles are produced commercially for filtration applications. The most common forms are made of silicon carbide or alumina-silica grains held together with a clay binder. In one type, alumina-silica fiber tufts are added to the silicon carbide grain structure to improve air permeability.

In more recent approaches, the filter candles are produced in two layers. The outer layer, or filtration surface, consists of a dense, thin layer of small pore openings. This surface layer is the primary filtration surface and can be formed from small grains or fine fibers.[5] The thin outer layer is supported by a thick, highly porous grain structure used mainly to impart overall strength.

An alternative to granular filter candles is the formation of candles composed of fine ceramic fibers bonded with clay binders. The fibers are alumina or alumina-silica based material.[3,6]

Ceramic monolith filters -- The monolith filter is the most compact of the different filter geometries and consists of multiple filter cells packaged into a honeycomb shape. There are two types

currently under development. One type is a honeycomb shape formed by the extrusion of a ceramic mixture (with cordierite or mullite as the major component) which is then fired into a rigid structure.[7] Alternate upstream and downstream cells are blocked so that the dirty gas stream is forced to flow across the porous cell walls. These filters are mainly developed to remove particulates from diesel engine emissions and has not been applied for coal-fired applications.

The major monolith filter type currently under development for coal-fired applications is a cross flow filter.[8] The basic concept is similar to the honeycomb filter with the exception that the inlet and outlet flows travel crosswise instead of parallel to one another. Because of the cross flow configuration, the filter cannot be extruded as a single piece but instead has to be formed from individual filter "tiles" bonded to form a monolithic structure. The filter material is basically cordierite.

Besides the three major ceramic filter categories, efforts are underway to develop new ceramic filter types and configurations. Some of the more interesting types include:

- Ceramic sponge
- Fiber reinforced silicon carbide composite filters
- Fabric filters with high-temperature coatings

Since these are developmental filters, little performance information is available.

FILTER STRESS ANALYSIS

A significant number of filter failures to date can be attributed to excessive stresses being imposed on the filter, often as a result of improper design. If the magnitude of stresses encountered by the filter can be estimated and compared with estimates of the failure strength of the ceramic material, steps can be taken to select proper materials and design conditions where the filter material will hold up.

Each of the filter types are sensitive to different stresses. A fabric filter is flexible and therefore less susceptible to thermal shock and vibrational perturbations compared to rigid filter types. However, it is sensitive to damage from flexing and abrasion. The different stresses which can be damaging to a fabric filter are shown in Figure 1.

The tensile break strength of different filter fabric materials range from 20 to 200 lb/in.[9] The axial stress due to the weight of the filter and dust and the hoop stress imposed by the cleaning pulse

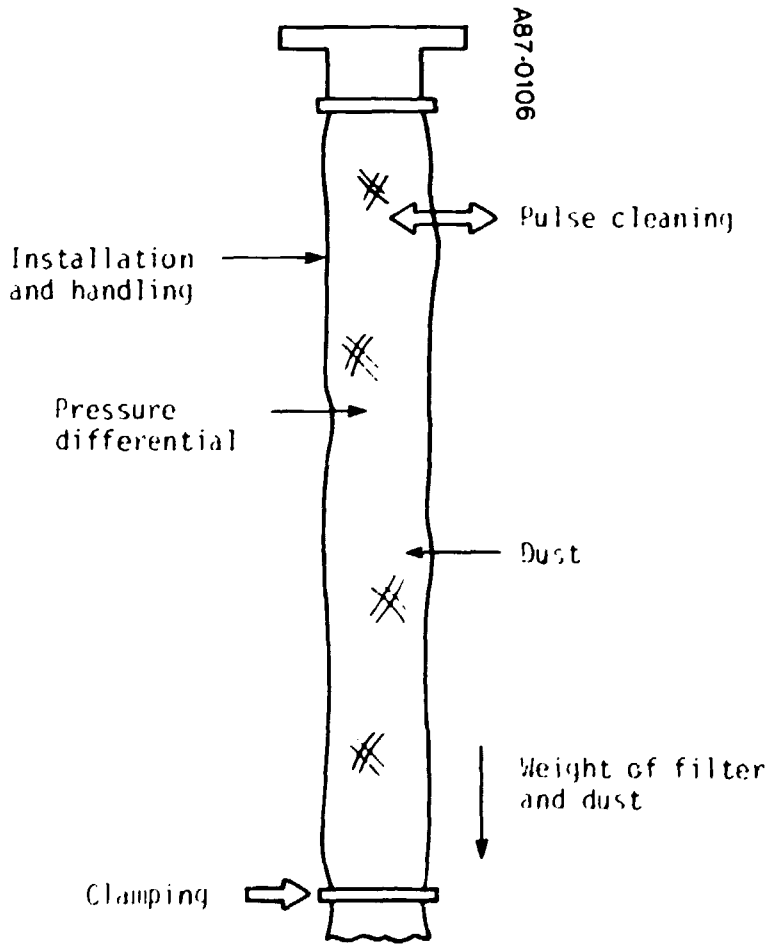

Figure 1. Source of Stresses in a Bag Filter

ranges from 1 to 2 lb/in. under normal operating conditions.[10] In general, these stresses should not cause any problems. However, in some cases, the tensile break strength of the filter fabric can be quite low because of a flaw in the weave or degradation of the ceramic material. For example, a few filter tubes have been observed to split axially in what is considered as a "seam" failure. In these filters, it was determined that the "seam" region was an order of magnitude lower in tensile break strength compared to the rest of the fabric and the 1 to 2 lb/in. stresses encountered is close to the break strength.

In some applications[3], the filter was degraded severely by the environment during use. The break strength of the material was acceptable at the beginning but was too weak at the end. Information on fabric materials properties such as strength as a function of time, temperature, and gas phase components would be valuable in the design of filters for specific applications.

Localized high stress concentrations can be exerted by sharp instruments or excessive folding of the fabric during handling and installation or by pressure from clamping. In many cases, the damage is not noticeable until actual use. It is difficult to estimate the magnitude of these stresses. Proper installation procedures and design should be incorporated to avoid these stress conditions. For example, the clamps can be rounded at the edges to prevent sharp corners and a flexible gasket material should be used between the clamps and the support cage.

There is also no good method for estimating the abrasion damage caused by dust impinging on the filter surface or in passing across the filter. Results to date show no observable damage. In fact, the presence of dust in the filter appears to improve the flex-abrasion resistance of some filters.[9,10] There are also no data to date to indicate filter failure caused by flexing and self-abrasion.

Candle filters are rigid structures and susceptible to thermal shock and vibrations. These are probably the major causes for any damage observed to date on this otherwise strongest of the different

ceramic filter types. The different stresses in a candle filter are shown in Figure 2.

Available data on ceramic candles made of silicon carbide, show break strengths around 2,000 psig.[3] The stresses in the candle caused by the weight of the candle and accumulated dust are on the order of several psig and those, due to the pressure differential across the filter, are less than system pressure.

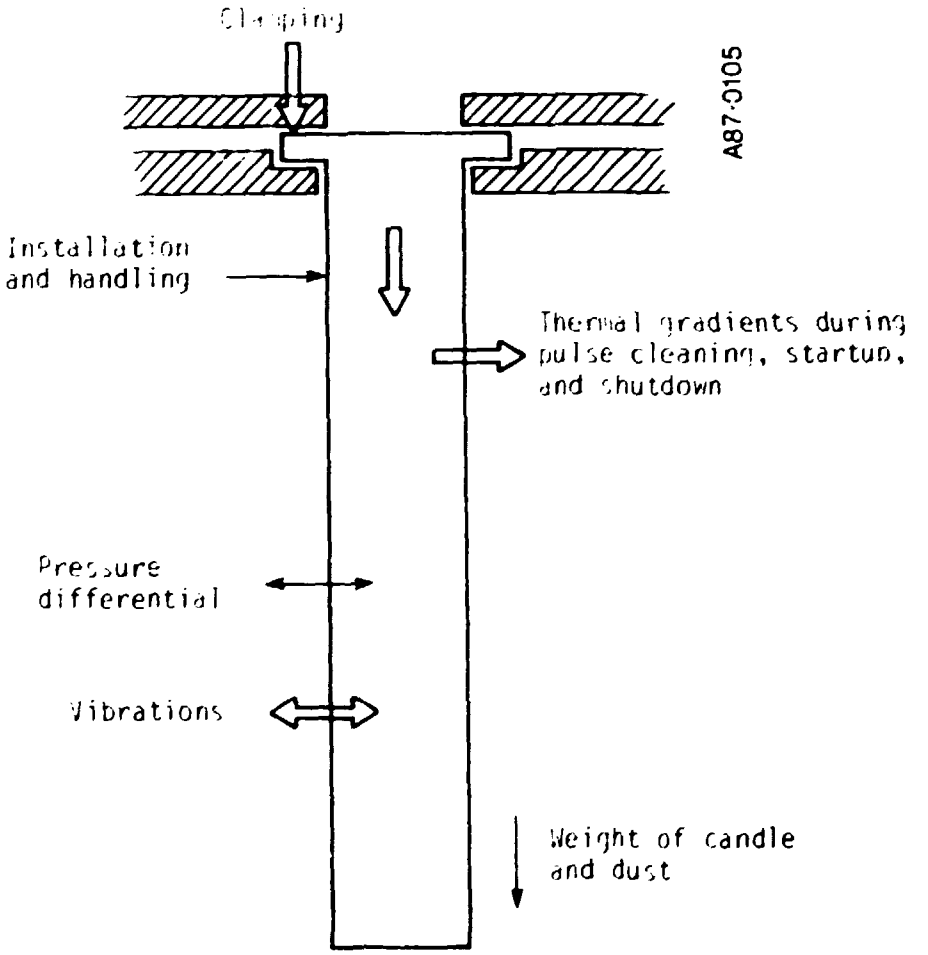

Figure 2. Source of Stresses in a Candle Filter

The maximum stress induced in the candle filter during pulse cleaning with room temperature gas can be estimated by:

$$\sigma = \frac{\alpha \Delta T E}{1 - \mu} \qquad (1)$$

σ = Stress

α = Coefficient of thermal expansion

ΔT = Temperature differential between pulse gas and filter wall

E = Young's modulus

μ = Poisson's ratio

Assuming $\alpha = 5 \times 10^{-6}$ in./in. °F, $\Delta T = 1{,}500$°F, $E = 10^6$ psi, and $\mu = 0.3$, the stress σ has a value of 10^4 psi. This maximum stress value actually exceeds the measured break strength of the candle.

This maximum stress occurs at the moment the cold pulse gas enters the filter candle. In practice, some heating of the pulse gas will have occurred as the gas travels down the pulse tube as well as when some of the gas mixes with the hot gases in the candle. Also, the candle will begin cooling fairly quickly as the pulse gas reverses flow across the filter. Another problem is the lack of data on the various properties of the ceramic candle. The calculation above was based mostly on estimated values.

It can be seen that the stresses caused by the thermal shock can be very high. This is especially severe near the entrance region where the temperature differences are the greatest. The candle is generally not permeable near the flange region so that any thermal gradients remain fairly steep due to slower cooling. The flange collar is also an area of stress concentration. Some candles are fabricated with rounded flanges to minimize this stress concentration.

The tubular, symmetrical candle structure is sensitive to vibrations induced by the cleaning pulse or any movements in the filter vessel. The pulse can in the worst case set up a resonant frequency in the candle much like blowing into a tube. Or the pulse can be misaligned so that part of the jet impinges on one side of the

candle wall. Any small displacements can impose significant stresses as estimated by the equation:

$$\sigma_t = \frac{u}{r} \frac{E}{(1 - \mu)} \qquad (2)$$

where

σ_t = tangential or hoop stress

u = small displacement due to vibration

Assuming a small displacement of u = 20 microns due to vibrations so that $(u/r) = 10^{-3}$, σ_t = 1,400 psi.

Combinations of thermal and vibrational stresses could even be more severe and have order of magnitudes close to the yield strength of the candle. Any perturbations from normal operation such as high pulse flow or any deterioration of filter strength with time can cause filter failure. Proper design should eliminate most of these problems.

Ceramic cross flow filters have problems similar to candles although their monolithic structure and fabrication method could present some unique situations. A sketch of the different stresses is given in Figure 3.

The measured rupture strength of the cross flow filter is about 1,400 psig.[9] Using equation 2, the maximum thermal stress is estimated to be around 10,000 psig for a temperature differential of 1,400°F. This stress is in excess of the yield strength of the filter material. The actual temperature differentials are lower since the pulse gas will get partially heated up before it contacts the ceramic filter surface. Like the other types of ceramic filters, there is a general lack of useful data on ceramic material properties. In any case, the stresses can be significant, especially near the entrance to the filter and regions where the filter thickness varies.

The monolithic structure of the filter creates nonuniform temperature distributions during pulse cleaning, startup, and shutdown since different parts of the filter heats up quite differently. This is accentuated by the nonuniform thickness and permeability of the

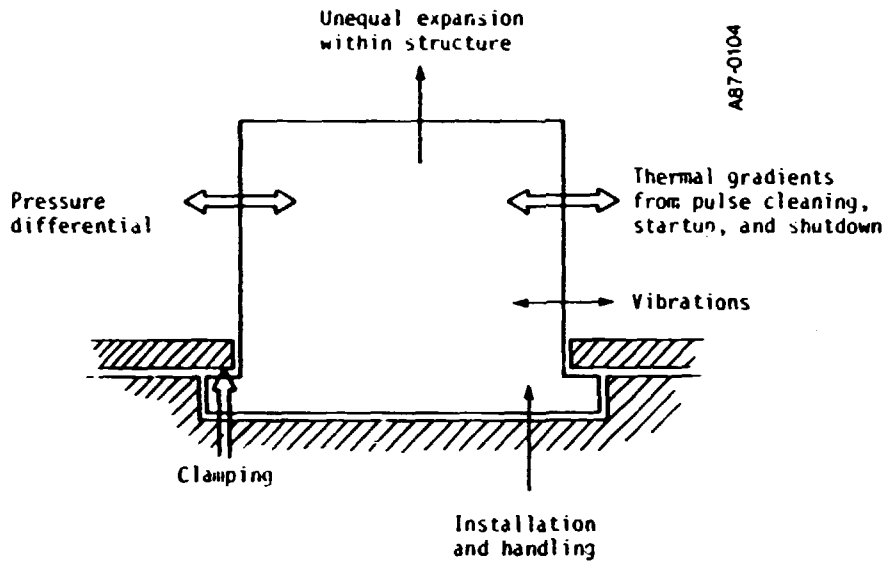

Figure 3. Source of Stresses in a Cross Flow Filter

structure. The filter is also formed from individual tiles held together by a different refractory material. Any incompatibilities in the cement and the tile material such as different coefficients of thermal expansion (CTE) could produce localized stress concentrations. A result of this is delamination of the tiles.

STRUCTURAL ANALYSIS

Results of analysis with SEM, EDX and x-ray diffraction, show significant variations in the structure and surface of different filter types and the effect of flyash components on the surface.

Figures 4 and 5 show the surface of a silica-alumina-boria based fabric which has been exposed to a high-temperature gasifier atmosphere.[3] The fabric lost 99 percent of its strength after exposure. There is significant fusion of ash on the filter fibers which can cause embrittlement. The surface appears pitted, perhaps as a result of gas phase or ash component attack. The fibers are being studied further with x-ray diffraction and electron probe microanalysis. X-ray diffraction studies of the same material heated

Figure 4. Surface of a Silica-Alumina-Boria Based Fabric

Figure 5. Ash Fusion on Fabric

to 1,000°F and 1,600°F in air, show definite changes in the phase composition and crystalline size (Figure 6) with much sharper diffraction peaks after heating at the higher temperatures. Thus, even in air, there is evidence of significant changes in the ceramic structure.

The surface of a layered candle is shown in Figures 7 and 8. Figure 7 shows the unique construction of this filter which has a thin surface layer of dense fibers on top of a porous substrate of silicon carbide grains. The dense surface layer serves as the primary filter for dust. Figure 8 shows the filter surface after application in a gasifier. The filter sample was cleaned thoroughly by vacuuming and immersion in an ultrasonic bath. This was followed by heating in air at 1,000°F for 4 hours to drive off residual carbon deposits. There still appears to be significant dust attachment to the filter. This dust adhesion could lead to eventual blinding of the filter.

An example of the cross flow filter surface is shown in Figure 9. Unlike the other filter types, the surface contains a very nonuniform pore size distribution with pores of several hundred microns evident. These large pores, however, are not continuous across the filter wall. After use, the pores can be seen to be filled with dust (Figure 10). There did not appear to be any significant loss in permeability or cleanability during the test period in which this filter was exposed.[8] However, there is evidence of ash fusion (Figure 11).

SUMMARY

From the results and analysis to date, some of the preliminary conclusions derived are:

- Filter failure generally occurs when stress levels encountered by the filter during use exceed the yield/rupture strength of the weakest point in the filter. This excessive stress level can be encountered under various conditions such as:
  - -- Improper clamping or mounting design

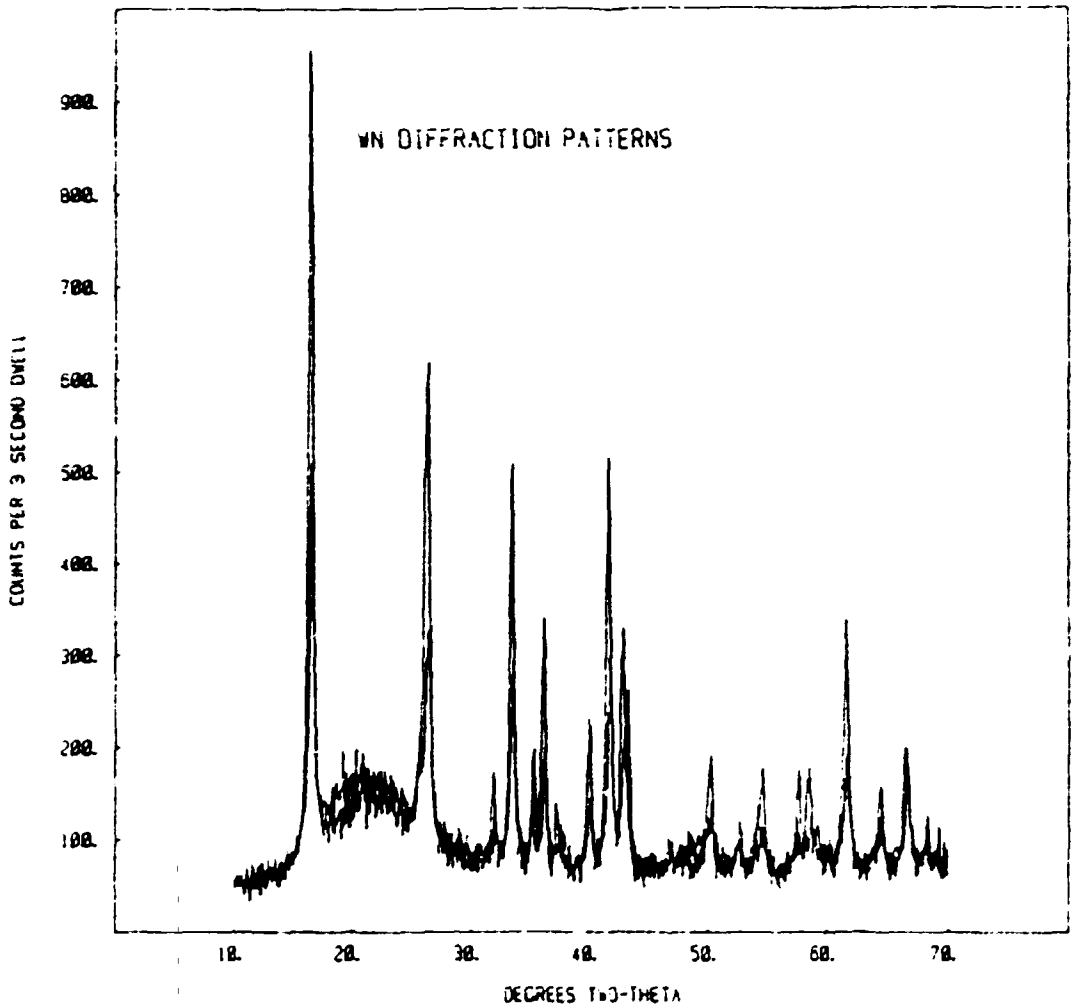

*Upper curve: After heating at 1,600°F
Lower curve: After heating at 1,000°F

Figure 6. Silica-Alumina-Boria Based Fabric Diffraction Pattern*

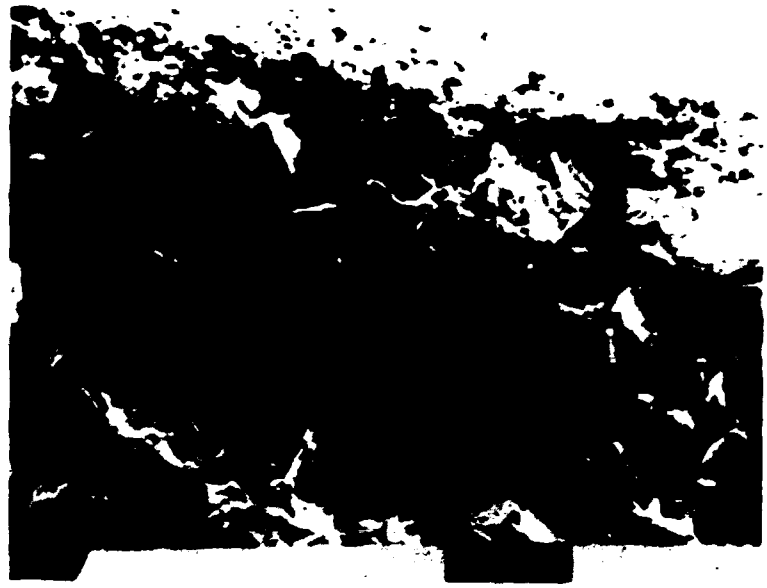

Figure 7. Surface of Layered Candle

Figure 8. Surface of Used Candle

Figure 9. Surface of Cross Flow Filter

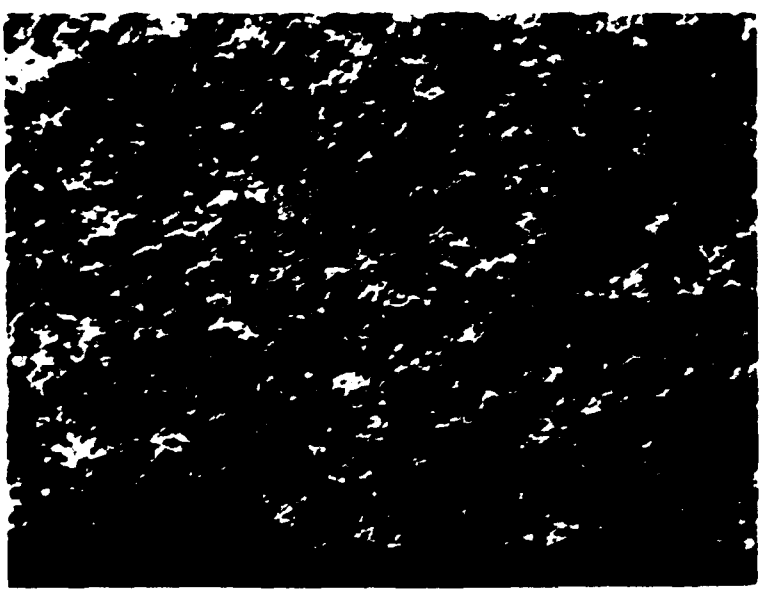

Figure 10. Surface of Used Cross Flow Filter

Figure 11. Ash Fusion on Cross Flow Filter

-- Excessive pressure drop across the filter
-- Vibrations
-- Excessive pulse cleaning pressure
-- Thermal gradients set up during startup and shutdown
-- Thermal shock from cleaning with cold pulse gas

- The microstructure of some of the ceramic filter materials, such as phase composition and crystalline size, changes with time and temperature. This has a direct effect on the overall mechanical properties of the filter such as yield strength and modulus of elasticity. In general, the filter material turns weaker and more brittle on exposure to temperature.
- Some of the filters are made of strong and inert material such as silicon carbide but are held together by clay-based binders which can limit the effective range of application. For example, there is evidence of attack of flyash components on the binder material in ceramic candles. Another example is cross flow filter delamination as a result of

incompatibility of the "glue" holding the different filter layers.

- Gas phase and ash components can affect the filter material by interacting with some of the components in the material. Alkali components can be especially active. One of the major problems is the formation of local fluxes which can cause flyash to sinter on the filter and eventually cause blinding. Other problems include the weakening of the filter structure on exposure to temperature and gases.

ACKNOWLEGEMENT

This work would not have been possible without the support of groups supplying ceramic filter samples from their test facilities. Special thanks are due to the following people:

Mr. Chris Bower, National Coal Board, Coal Research Establishment

Dr. David Ciliberti, Westinghouse

Mr. Jim Zievers, Industrial Filter and Pump

Dr. Lloyd White, 3M Company

REFERENCES

1. Shackleton, M., et al., "High-Temperature High-Pressure Gas Cleanup with Ceramic Bag Filters," DOE/ET/17092-1504, January 1984.
2. White, L. R., et al., "Ceramic Fabrics for Filtration at High Temperatures, 290-870°C," I ChemE Symposium Series No. 99, p. 263, September 1986.
3. Oakley, J.E. and G.P. Reed, "The Behavior of High Temperature Filter Materials in Hot Gasifier and Combustor Gas Atmospheres," I ChemE Symposium Series No. 99, p 421, September 1986.
4. Lippert, T.E. and D.F. Ciliberti, "Ceramic Filter Elements for High-Pressure, High-Temperature Gases," EPRI CS-4382, January 1986.

5. Zievers, J. F., et al., "Porous Ceramics -- Dust Penetration," presented at 17th Annual Meeting of the Fine Particle Society, San Francisco, CA, July 1986.
6. Schmidt, D., R. Schulz, and J. Bender, "Long-Term Tests with Ceramic Dust Separators at Gas Temperatures between 800°C and 1000°C," I ChemE Symposium Series No. 99, p. 245, September 1986.
7. Weaver, C. S., "Particulate Control Technology and Particulate Emissions Standards for Heavy-Duty Diesel Engines," Report to EPA under Contract 68-01-6543, December 1984.
8. Ciliberti, D.F., et al., "Hot Gas Cleanup Using Ceramic Cross Flow Membrane Filters," COE/ET/1591-1565, December 1983.
9. Chang, R. and H. Lips, "Ceramic Fabric Material Testing," DOE/MC/20110-1895, June 1985.
10. Chang, R., J. Sawyer, and H. Lips, "Performance Evaluation of Ceramic Fabric Bag Filter on a Bench-Scale Coal Gasifier," Acurex Final Report to DOE under Contract DE-AC21-84MC21337.

IMPROVED CERAMIC COMPOSITES THROUGH FIBER-MATRIX INTERACTION

J.L. Bates, C.W. Griffin, W.J. Weber, and E.L. Courtright

Materials Sciences Department
Pacific Northwest Laboratory(a)
P.O. Box 999
Richland, Washington 99352

ABSTRACT

Preliminary analyses of matrix/fiber interactions between Si_3N_4 matrix with 5 wt.% MgO added as a sintering aid, and Nicalon™(b) silicon carbide fibers have been performed. Specimens with 0, 10, and 30 vol.% fibers were prepared by hot pressing at 1750°C in one atmosphere of nitrogen. Specimen characterization revealed that a significant amount of magnesium diffuses into the silicon carbide fibers during fabrication. Free carbon on the surface of the Nicalon™ appears to play an important role in debonding. No evidence of Si enrichment or SiO_2 formation have been found at the interfaces.

INTRODUCTION

Fiber-matrix interfaces play key roles in the performance of ceramic matrix composites. Since ceramic composite systems are a relatively new field, the nature of these interfaces and their relationship to mechanical properties, microstructure, process history, or environmental exposure are not yet well understood. The work reported in this paper represents the start of a program aimed at understanding and controlling the fiber-matrix interface. The ultimate objective is to control properties in a way that will

---

(a) Pacific Northwest Laboratory is operated by Battelle Memorial Institute for the U.S. Department of Energy under Contract DE-AC06-76RLO 1830.

(b) Nicalon is the registered tademark of Nippon Carbon Co.

enhance the use of ceramic matrix composites in fossil energy applications. Principal objectives include: (1) develop a basic understanding of fiber-matrix interface reactions; (2) relate this understanding to process history and service behavior, and (3) develop methodologies to modify or otherwise control the fiber-matrix interface in a way that will improve bulk composite behavior.

The initial research work, as reported herein, investigates the microstructure and chemical interactions at the fiber/matrix interface of a silicon nitride/silicon carbide reinforced composite. Our initial goal is to determine the effect of interfacial chemistry on fracture behavior and, if possible, relate these effects to process history or matrix phase additions. With this knowledge, modifications can hopefully be made to the matrix and fiber components, or in the fabrication process, in order to further improve bulk composite properties.

BACKGROUND

The composite system chosen for these initial studies consisted of a MgO doped Si_3N_4 matrix reinforced with SiC fibers. Silicon nitride exhibits several important characteristics such as high strength at high temperatures, good oxidation resistance, and good thermal shock resistance that are attractive for use in fossil energy applications. This work complements other Fossil Energy Materials Programs where process technologies for fabricating Si_3N_4/SiC composite systems are currently under development.

A major processing concern in fabricating any ceramic composite system is the difference in properties between the reinforcing fiber and matrix phases that can influence the integrity of the densified composite. For example, the thermal expansion of silicon carbide is greater than silicon nitride. When a composite prepared from these two materials cools from a high sintering temperature, the silicon carbide fibers contract more than the silicon nitride matrix. If the fiber-matrix bond is

sufficiently strong, the fiber contraction should pre-stress the matrix in compression and the fibers in tension. This could potentially increase the composite's strength under conditions where matrix fracture is the controlling process. On the other hand, if the interfacial bond is too strong, and no relative slippage between fiber and matrix can occur, the composite may behave more like a monolith with increased susceptibility to fracture. Improved knowledge of the fiber/matrix interface will be essential to the ultimate development and optimization of all ceramic composite systems.

EXPERIMENTAL APPROACH

MATERIALS

An x-ray fluorescence analysis of the starting materials is presented in Table 1. The matrix was a LC-10 grade Si_3N_4 powder produced by HC Starck Company in West Germany. Five weight percent magnesium oxide was added as a sintering aid by dry mixing the two powders for 4 hours in a Turbula blender. X-ray diffraction (XRD) analysis of the starting matrix powder revealed mostly alpha-Si_3N_4 with less than 10% beta-Si_3N_4.

The silicon carbide fibers were ceramic grade Nicalon^{TM}, obtained from Nippon Carbon Company, and were typically 15 to 20 microns in diameter. These fibers have been reported to contain both free carbon and up to 10% Oxygen as SiO_2.[1,2] A chemical composition of $SiC_{1.4}O_{0.3}$ has been suggested for the ceramic grade material.[2] Our XRD analysis revealed broad peaks near the beta-SiC positions indicating amorphous or very fine crystallites. No evidence of crystalline SiO_2 was found, which suggests that this phase could be present as a glass.

COMPOSITE SPECIMEN FABRICATION

The general procedure used to make fiber reinforced specimens is illustrated in Figure 1. The chopped fibers were first washed in acetone to remove any sizing or small particles created during

Table 1. X-Ray Fluorescence Analysis of Composite Starting Materials

Elements	Units	SiC[a] Fibers	Si_3N_4[b] + 5 wt.% MgO[c]
Al	wt.%	< 0.25	< 0.25
Mg	"	< 0.04	4.5
Na	"	0.85	0.05
P	"	< 0.44	< 0.49
Si	"	58.1	55.9
Ti	"	0.01	< 0.01
S,Cl,K,Ca,P	"	< 0.20	< 0.20
Co	ppm	6	< 6
Ni	"	3	4
Cu	"	9	3
Zn	"	2	< 2
Se	"	1	< 1
Sr	"	19	< 1
Zr	"	13	5
Mo	"	3	< 1
Ba	"	62	< 18
Mn	"	27	< 10
As	"	< 1	2
Others	"	< 20	< 20

(a) Nicalon™ fibers, P-1 mm, Lot AP010029, Nippon Carbon Co., Tokyo, Japan
(b) Si_3N_4 Grade LC-10, H.C. Starck, Berlin, West Germany
(c) 99.9% MgO Semi-Elements, Inc., Saxonburg, Pennsylvania

the chopping operation. A scanning electron micrograph of the washed fibers is shown in Figure 2. The fibers were then disbursed in alcohol using a high speed blender before the pre-mixed silicon nitride powder was added. After one minute of blending, the mixture was poured into a vacuum casting apparatus. This process leaves a solid cake when the excess liquid is removed from the slurry. The cake then becomes the feed material for subsequent consolidation. Unreinforced Si_3N_4 and composites containing 10 and 30 vol.% chopped SiC fibers were hot pressed in a 76 mm (3 inch) diameter graphite die at 1 atmosphere of nitrogen. Movement of the hot press pistons began at 1600°C and the pressure was increased to 24.1 MPa (3500 psi). The composite was then heated to a final temperature of 1750°C under load and held at temperature and

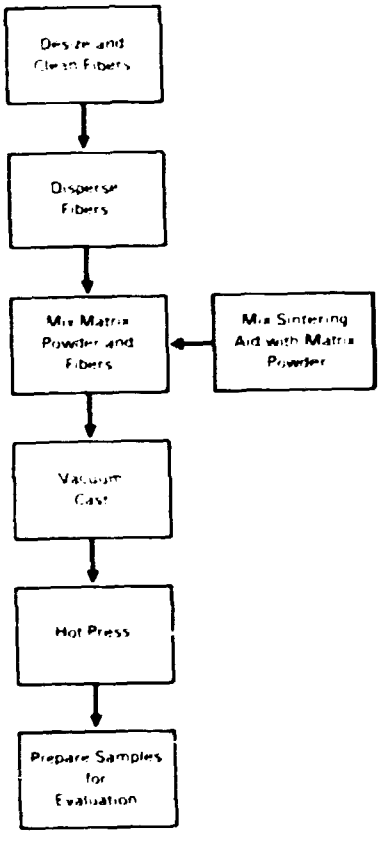

Figure 1. General Composite Fabrication Procedure

pressure for 30 minutes. The specimens were then hot ejected from the die and cooled to room temperature at a rate of approximately 300°C per hour. After hot pressing, the billets were cut into individual samples for evaluation purposes.

The hot pressing conditions had been preselected to obtain good consolidation and maximize fiber/matrix contact in order to study potential interfacial reactions. Some loss in fiber strength due to thermal treatments in nitrogen at or above 1400°C may occur.[3] However improved toughness has been reported in hot pressed Si_3N_4/SiC at 1750°-1850°C.[4]

The density of the hot pressed composites and the volume fraction of beta-Si_3N_4 are listed in Table 2. Density decreased as the volume fraction of fibers increased, because the lower density

Table 2. Density and β- to α-Si_3N_4 Ratio of Hot Pressed Si_3N_4/SiC Composites

Fiber Volume %	Density gm/cm^3	β-Si_3N_4/α-Si_3N_4
0	3.16	4.00
10	3.10	2.33
30	3.02	1.50

fibers (2.55 g/cm^3) replace the higher density Si_3N_4+ MgO matrix (3.18 g/cm^3). X-ray diffraction analysis showed that the fraction of the beta-Si_3N_4 decreased as the fiber volume increased.

RESULTS AND DISCUSSIONS

MICROSTRUCTURAL ANALYSIS

The microstructure of an unreinforced silicon nitride specimen is shown in Figure 3. High density areas and porous regions can readily be seen in the optical micrograph. Scanning Electron Microscopy and Energy Dispersive X-ray (SEM-EDX) analysis revealed that the porous regions have a lower concentration of the MgO sintering aid. The concentration was apparently too low to provide a sufficient quantity of the $MgO{\cdot}SiO_2$ liquid phase needed for complete densification. These results suggest that dry blending did not uniformly disperse the sintering aid.

The microstructure of a 10 vol.% fiber composite is shown in Figure 4. The distribution of fibers was very uniform throughout the composite cross-section. During hot pressing, the fibers tended to align perpendicular to the pressing direction which results in two dimensional reinforcement. Matrix phase porosity was also more evenly distributed in the 10 vol.% composite than in the unreinforced sample as shown in Figure 3.

Energy Dispersive X-ray analysis showed that the fibers may contain up to 14 wt.% MgO (calculation based on Mg concentration)

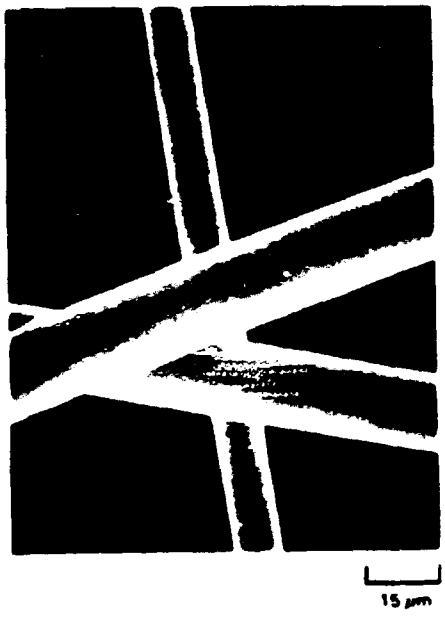

Figure 2. Scanning Electron Micrograph of Washed Fibers

and that the magnesia concentration in the matrix close to the fibers was below the initial 5 wt.% addition. The impurity level reported in Table 1 and supporting SEM-EDX analysis of the Nicalon fibers prior to fabrication indicate less than .04 wt.% Mg in the starting fibers. Thus, the mobility of Mg is sufficient to allow significant amounts of this element to diffuse from the matrix into the fibers.

Depletion of MgO in the matrix may account for regions of lower porosity observed in the matrix phase itself as illustrated in Figure 4. In addition, the fibers appear to have dark centers. This optical contrast may be due to a second phase or to a magnesium gradient across the fiber radius. Analysis of the latter possibility has not yet been completed.

Herron and Risbud[5] observed a similar result in Ba-Si-Al-O-N glass ceramic composites. They reported that Ba diffused into the SiC fibers (Nicalon™) from a barium containing glass matrix and also observed dark circles at the center of their fibers surrounded

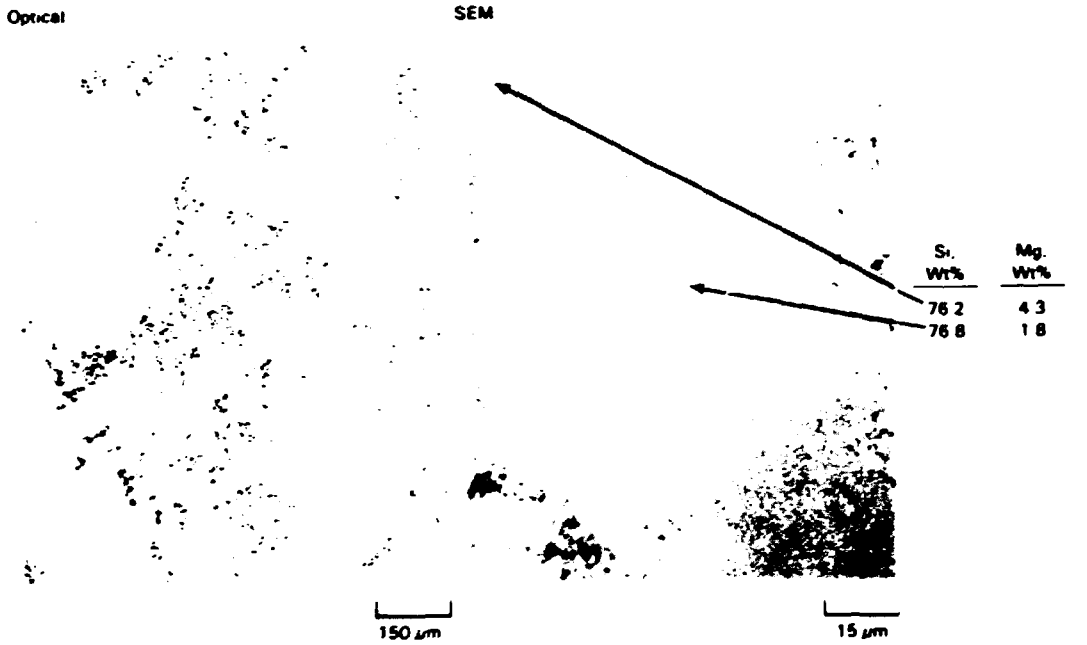

Figure 3. Microstructure and SEM-EDX of Unreinforced Si_3N_4 + 5 wt% MgO

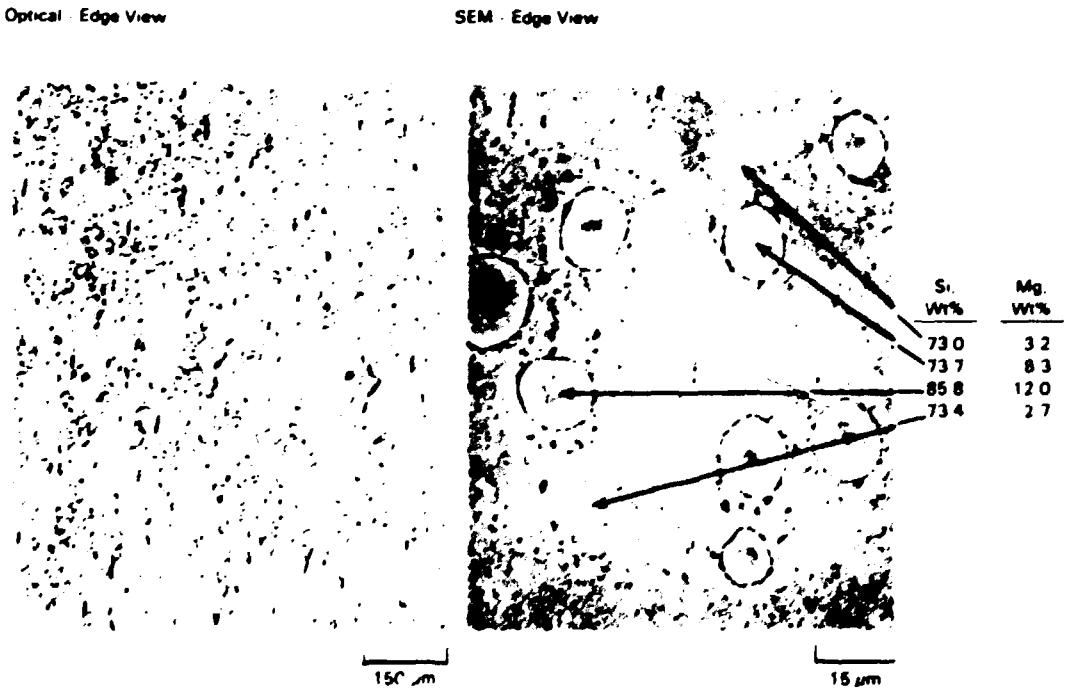

Figure 4. Microstructure and SEM-EDX Analysis of 10 vol% Fiber Composite

by lighter rings. The dark centers contained only silicon and carbon whereas the lighter rings contained barium along with silicon and carbon.

The microstructure of the 30% composite is shown in Figure 5. While the field of view shown appears to be reasonably uniform, the bulk hot pressed composite exhibited segregation on a macroscopic scale. No further analysis was performed on the 30% material and plans have been made to re-fabricate the composite.

FRACTURE ANALYSIS

A specimen of the 10 vol.% SiC composite was notched and fractured to provide a fracture surface for examination by SEM. This fracture surface is shown in Figure 6, and appears to be typical of many ceramic fiber reinforced composites. There is evidence of both fiber pull-out and debonding at fiber/matrix interfaces. The fiber ends appear to have fractured cleanly. There is very little evidence of microcracking or preferred crack propagation paths through the matrix itself. The grain size in the silicon nitride matrix is relatively small compared to the fiber diameter, and appears to be equiaxed as opposed to the fibrous beta-Si_3N_4 microstructure reported by Shalek and co-workers for magnesia doped silicon nitride hot pressed at the same 1750°C temperature.[4] The surface of the individual fibers are noticeably rougher as compared to the pre-hot pressed condition. (Figure 2) There is evidence of grain growth and of matrix phase grain imprints along the full length of the exposed fiber surfaces. This condition was also reported by Shalek, et al.[4] A mechanically rough surface like this would be expected to limit interfacial movement and explains the low number of pull-outs observed in the fracture surface.

To obtain more detailed information on the chemistry of the interfaces, a second 10 vol.% SiC specimen was fractured in-situ under high vacuum and examined by Auger Electron Spectroscopy (AES). A line trace of relative oxygen and carbon concentrations across the diameter of a fractured fiber is shown in Figure 7.

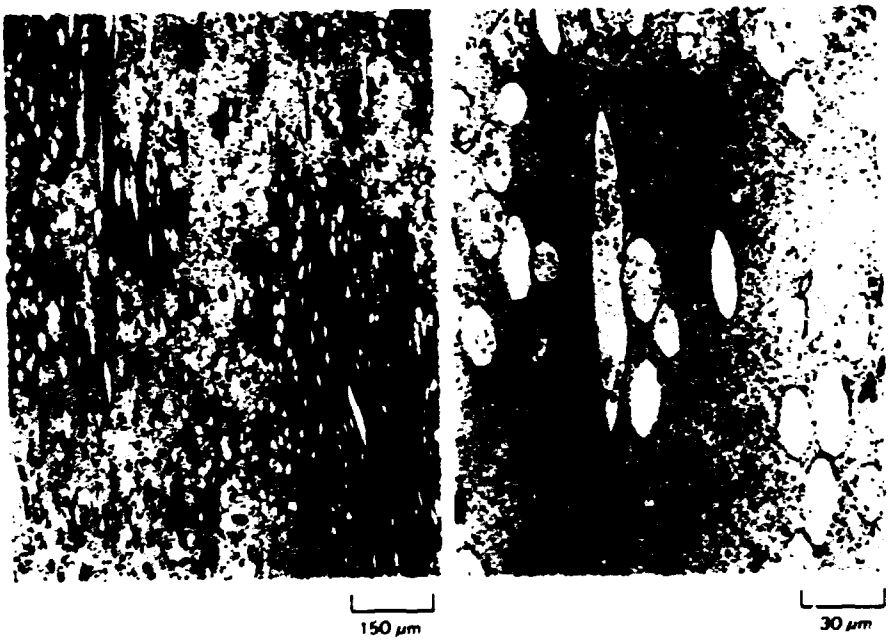

Figure 5. Microstructure of a 30 vol% Fiber Composite

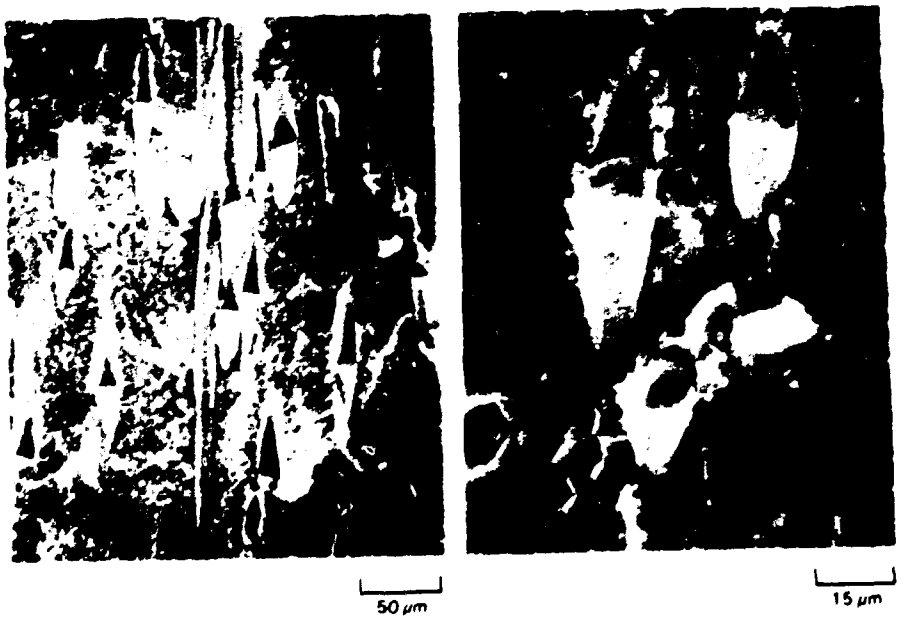

Figure 6. Scanning Electron Micrograph of the Fracture Surface of a 10 vol% Fiber Composite

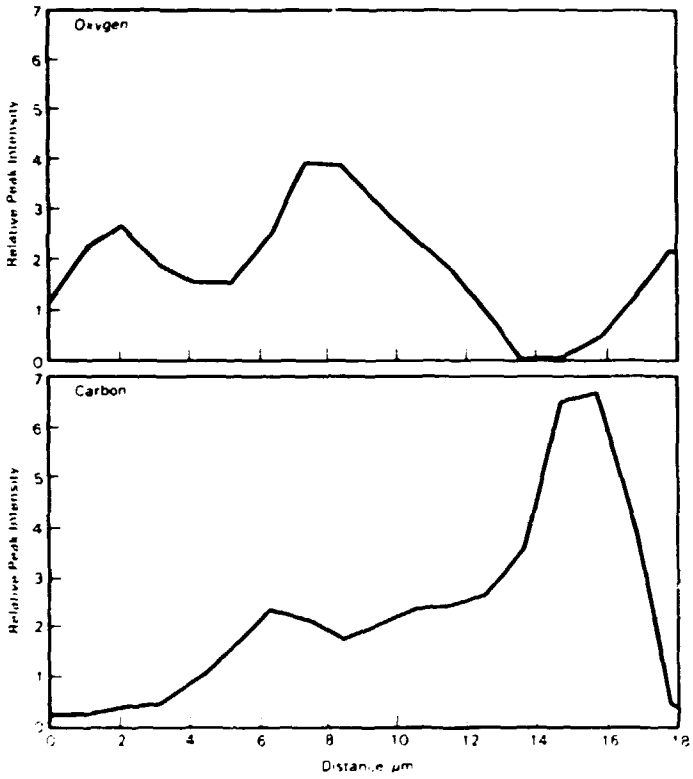

Figure 7. Oxygen and Carbon Trace Across a Fiber by AES

There is a trend shown in this and other AES traces for the high oxygen concentrations to be associated with low carbon concentrations; however, this trend was not rigorously established. It was apparent that the O/C ratio varied across the fiber. The edges of the fibers,within 2 μm of the surface, generally display higher carbon peaks. Future analyses using a new fine-spot AES instrument with a resolution of 25 nm will greatly improve our ability to determine silicon, oxygen, carbon, and magnesium distributions both within fibers and at interfaces.

Analysis of the fiber surface also revealed even concentrations of carbon, which may be elemental carbon. This carbon layer (thickness currently undefined) was apparently instrumental in the fibers debonding from the matrix phase during fracture. This carbon may be associated with incomplete removal of

the sizing. Chemical analysis of the valley or trough regions in the matrix where fibers had once been in contact with the matrix exhibited very high carbon and typically very low concentrations of oxygen and magnesium. The silicon/nitrogen ratio was on the order of 0.75 consistent with stoichiometric Si_3N_4. In the matrix area, the carbon content was low (~ 3 a/o), and the oxygen concentration was on the order of 15 a/o.

Analysis of the debonded fiber surface revealed two different chemistries. One was similar to that found in the matrix valleys and the other exhibited low carbon with high magnesium and oxygen concentrations. The latter analysis was more typical of that found near the center of the fibers where the magnesium was on the order of 10-16 a/o and the silicon/carbon ratio varied between 0.6 to 1.2.

The AES analysis performed on the fractured specimen corroborated the prior evidence of significant magnesium migration from the matrix to the fiber. There was also noticeable depletion in the magnesium content on the matrix side of the matrix/fiber interface. No indications of silicon rich regions or SiO_2 were found at the interface. The relative chemical concentrations did not clearly show development of compositions like Mg_2SiO_4, $MgSiN_2$, or Si_2N_2O in the interface region. Further refinement of the sensitivity factors used in the Auger analysis is underway and will hopefully shed additional light on the phases present.

Previous analysis of AVCO silicon carbide fibers (SCS-6) by Corbin and coworkers indicated a high free carbon surface region and delamination at the interface.[6] The high carbon layer was divided between the matrix and the fiber. The analysis performed in our work suggests that there is also a carbon rich layer that adheres partly to the fiber and partly to the matrix. The SEM results showed some fibers with light appearance and others with a dark cast that appeared to correlate with the two different chemistries. A high magnification photograph of one fiber revealed what appeared to be a thin interface layer, but more detailed analysis is needed to confirm this observation.

CONCLUSIONS

While this work is just beginning, a few preliminary conclusions appear appropriate.

Magnesium added as MgO to aid in densifying silicon nitride diffuses across the matrix/fiber interface into the silicon carbide fiber. There appears to be a corresponding depletion in the magnesium concentration on the matrix side of the matrix/fiber interface.

The high free carbon concentration found on the surface of the Nicalon™ fibers used in these studies appears to contribute to fiber debonding. Preferential control of this layer may provide a means of enhancing toughness and/or strength in the bulk composite.

Although both the matrix and fiber materials appear to contain significant amounts of oxygen, there appears to be no preferential formatio of SiO_2 at the fiber interface or evidence of silicon migration across the interface.

FUTURE DIRECTION

The migration of magnesium from the Si_3N_4 matrix into the silicon carbide fiber may alter the fiber strength and affect mechanical behavior of the composite. Tests will be performed to determine if this effect is detrimental. The influence of other hot pressing additives such as yttria and aluminia will also be explored.

Lower hot pressing temperatures can be used to reduce both grain growth in the fiber and the degree that silicon nitride matrix grains imprint the surface of the fiber. However, previous studies show that lower hot pressing temperatures also reduce fracture toughness.[4] The microstructural effect that hot pressing has on strength, degree of fiber pull-out and fracture toughness needs to be better understood.

The role that free carbon at the interface has on fiber debonding and its relative effect on fracture toughness needs to be studied more thoroughly. Techniques will have to be employed to provide better resolution of the interfacial chemistry.

REFERENCES

1. Mah, T., M.G. Mendiratta, A.D. Katz, K.S. Mazdiyasni. 1987. "Recent Developments in Fiber-Reinforced High Temperature Ceramic Composites". Am. Ceram. Soc. Bull., Vol. 66, No. 2, 304-312 (1987).

2. Clark, T.J., M. Jaffe, J. Rabe, and N.R. Langley. 1986. "Thermal Stability Characterization of SiC Ceramic Fibers: I, Mechanical Properties and Chemical Structure Effects." in Proceedings of the 10th Annual Conference on Composites and Advanced Ceramic Materials, D.R. Messier, Program Chairman, 901-913, American Ceramics Society, Columbus, Ohio.

3. Sawyer, L.C., R.T. Chen, F. Haimbach, P.S. Harget, E.R. Prack, M. Jaffe. 1986. "Thermal Stability Characterization of SiC Ceramic Fibers: II, Fractography and Structure." in Proceedings of the 10th Annual Conferen on Composites and Advanced Ceramic Materials, D.R. Messier, Program Chairman, 914-830, American Ceramics Society, Columbus, Ohio.

4. Shalek, P.D., J.J. Petrovic, G.F. Hurley, F.D. Gac. "Hot-Pressed SiC Whisker/Si_3N_4 Matrix Composites." A. Ceram. Soc. Bull., Vol. 65, No. 2, 351-356 (1986).

5. Herron, M.A. and S.H. Risbud. "Characterization of SiC-Fiber-Reinforced Ba-Si-Al-O-N Glass-Ceramic Composites." Am. Ceram. Soc. Bull., Vol. 65, No. 2, 342-346 (1986).

6. Corbin, N.D., G.A. Rosseti, S.D. Hartline, 1986. "Microstructure Property Relationships for SiC Filament-Reinforced RBSN." in Proceedings of the 10th Annual Conference on Composites and Advanced Ceramic Materials, D.R. Messier, Program Chairman, 958-968, American Ceramics Society, Columbus, Ohio.

EFFECT OF FLAWS ON THE FRACTURE BEHAVIOR OF STRUCTURAL CERAMICS

J. P. Singh, R. A. Roberts, J. J. Vaitekunas, and W. A. Ellingson

Materials and Components Technology Division
Argonne National Laboratory
9700 South Cass Avenue
Argonne, Illinois 60439

ABSTRACT

Fracture studies and nondestructive evaluation (NDE) were performed to detect and assess the effect of flaws on the fracture behavior of hot-pressed Si_3N_4 with Fe inclusions. The NDE methods used were through-transmission and backscatter ultrasound and low-kV contact radiography. The addition of 5 and 0.5 wt % Fe inclusions of 88 to 250 μm size reduced the strength of Si_3N_4 specimens by approximately 40 and 15%, respectively. Fractography indicated that failure occurred primarily from internal flaws which included Fe- and Si-rich inclusions and/or regions of Si_3N_4 matrix that were degraded as a result of reaction between Si_3N_4 and molten Fe. For Fe inclusion-induced internal flaws, the critical flaw sizes calculated by fracture mechanics were always larger than the fractographically measured flaw sizes. This observation suggested a local degradation in fracture toughness of Si_3N_4 matrix. A ratio, K, of ~3.5 to 4.2 appeared to exist between the calculated and measured values of the critical internal flaw sizes. The ratio K will have important implications for strength prediction based on observed flaw size.

A comparison of the fractography and NDE results for the location of critical flaws indicated that the backscatter ultrasound method may be more suitable than through-transmission ultrasound or low-kV contact radiography for the detection of near-surface flaws.

INTRODUCTION

Si_3N_4 has been recognized as a candidate for structural applications in advanced heat engines (gas turbine, diesel)[1,2] and many other

devices[3] because of its potentially excellent mechanical integrity and resistance to oxidation and corrosion at high temperatures. However, the mechanical behavior of Si_3N_4 and other polycrystalline ceramics, in general, has been observed to be controlled by the size, number, and distribution of extrinsic and intrinsic flaws[4-6] such as machining flaws, pores, agglomerates, inclusions, and other microstructural irregularities. These flaws are, in many cases, introduced during various stages of fabrication, machining and service. The nature and the density of these flaws will depend upon the fabrication techniques (green pressing, slip casting, sintering, hot-pressing, etc.). Evaluation of the effect of these flaws on fracture properties of specimens made by different techniques will provide information for the control of fabrication and machining procedures. The detection of these flaws by nondestructive evaluation (NDE) methods will ensure greater reliability for ceramic materials.

This paper gives the results obtained with nondestructive flaw detection methods and evaluation of the effect of well-characterized flaws on fracture behavior of hot-pressed Si_3N_4. Since inclusions rich in Fe and Si have been observed to cause substantial strength degradation of Si_3N_4 material, this initial study was conducted on Si_3N_4-Fe systems. Two different NDE techniques, low-energy contact x-radiography and focused ultrasonic imaging, were used. Failure-initiating flaws were located by NDE and fractography and were correlated with strength by means of a fracture mechanics approach. The flaw detection data obtained by NDE were compared with fractographic observations to evaluate the relative effectiveness of the NDE techniques. Finally, strength data were statistically analyzed to see if NDE screening of specimens improved the Weibull modulus of the strength distribution.

EXPERIMENTAL PROCEDURES

SPECIMEN PREPARATION

Dense specimens of Si_3N_4 were hot pressed from two commercial powder, designated Si_3N_4-A and Si_3N_4-B. Each powder was wet milled in 30% isopropyl alcohol + 70% water solution for 16 h; Al_2O_3 balls served

as the grinding medium. Microstructures of the powders were obtained by electron microscopy. Si_3N_4 powders were mixed with 6 wt % Y_2O_3 as a densification aid and the mixtures were again wet milled for 16 h and then spray dried. The spray-dried powder mixtures were hot pressed in a boron-coated graphite die at 1750°C and 22 MPa for 2 h in a high-purity N_2 atmosphere. Some Si_3N_4 specimens were seeded with Fe inclusions by hot-pressing a powder mixture of Si_3N_4-A with 6 wt % Y_2O_3 and appropriate amounts (0.5 and 5 wt %) of Fe powder (88 to 250 μm) at 1725°C for 2 h with the same die, pressure, and gas atmosphere described above.

The density of the hot-pressed disks was measured by the buoyancy method. The disks were ground to a standard surface finish on a 45 to 32 μm diamond wheel. Modulus of rupture (MOR) bars (~3.8 x 0.4 x 0.3 cm) were subsequently machined from the disks. The cut faces of the bars were ground on a 32-μm diamond wheel and the edges were bevelled. The bars were used for mechanical properties measurement and fractographic studies.

NDE APPROACH

Nondestructive evaluation was performed on the hot-pressed and surface-finished Si_3N_4 specimens before and after machining of MOR bars from the disks. The techniques used were low-energy contact x-radiography and ultrasonic imaging. NDE data obtained on hot-pressed disks were used as a guide to establish the orientation of cutting lines for MOR bars. The objective was to put the critical flaws (major silicon, silicon-rich, iron, and/or iron-rich inclusions) in the constant-moment section of the MOR bars, which would then be fractured in the four-point bending mode. The details of the NDE procedures have been given elsewhere.[7,8]

MECHANICAL PROPERTIES MEASUREMENTS AND FRACTOGRAPHY

To measure flexural strength, the MOR bars were fractured in the four-point-bending mode with a support span of 3.18 cm, loading span of 0.953 cm, and a crosshead speed of 0.13 cm/min. The bars were positioned in such a way that the apparent critical flaws (specifically Fe, Fe-rich, Si, and/or Si-rich inclusions) detected by NDE were located in a tensile region. The fracture surfaces of the broken bars were

examined by optical and electron microscopy to establish fracture modes and to locate failure-initiating critical flaws. At low magnification, optical microscopy was used to find the general location of the critical flaws by identifying fracture markings such as fracture mirrors and river patterns.[9-10] Subsequently, scanning electron microscopy was used to find the exact location and details of the critical flaws. Fracture toughness (K_{IC}) was measured by indentation techniques[11] and the elastic modulus was evaluated by the pulse-echo technique.[12]

RESULTS AND DISCUSSIONS

MECHANICAL PROPERTIES AND FRACTOGRAPHY

Although this study focused primarily on specimens of Si_3N_4 seeded with Fe inclusions, limited results for unseeded Si_3N_4-A and Si_3N_4-B specimens will also be presented to establish a data base for the purpose of comparison.

The densities of hot-pressed Si_3N_4-A and Si_3N_4-B specimens were measured to be 3.234 and 3.224 g/cm^3, respectively. The measured values of fracture stress (σ_F), fracture toughness (K_{IC}), and elastic modulus (E) for Si_3N_4 specimens are summarized in Table 1.

Table 1. Mechanical Properties of Hot-pressed Si_3N_4

Material	Fracture Stress, σ_F (MPa)	Fracture Toughness, K_{IC} (MPa$\sqrt{m}$)	Elastic Modulus, E (GPa)
Si_3N_4-A + 6% Y_2O_3	839 ± 25	6.7 ± 0.09	296 ± 2
Si_3N_4-B + 6% Y_2O_3	1049 ± 118	6.4 ± 0.03	307 ± 6

The fractographic observation of the fracture surfaces of the broken MOR bars indicated a mixed trans- and intergranular failure mode in both Si_3N_4-A and Si_3N_4-B specimens (see Fig. 1). The largest grains in Si_3N_4-A and Si_3N_4-B specimens were ~7 and 3 μm in diameter, respectively. The failures were observed to initiate primarily from surface

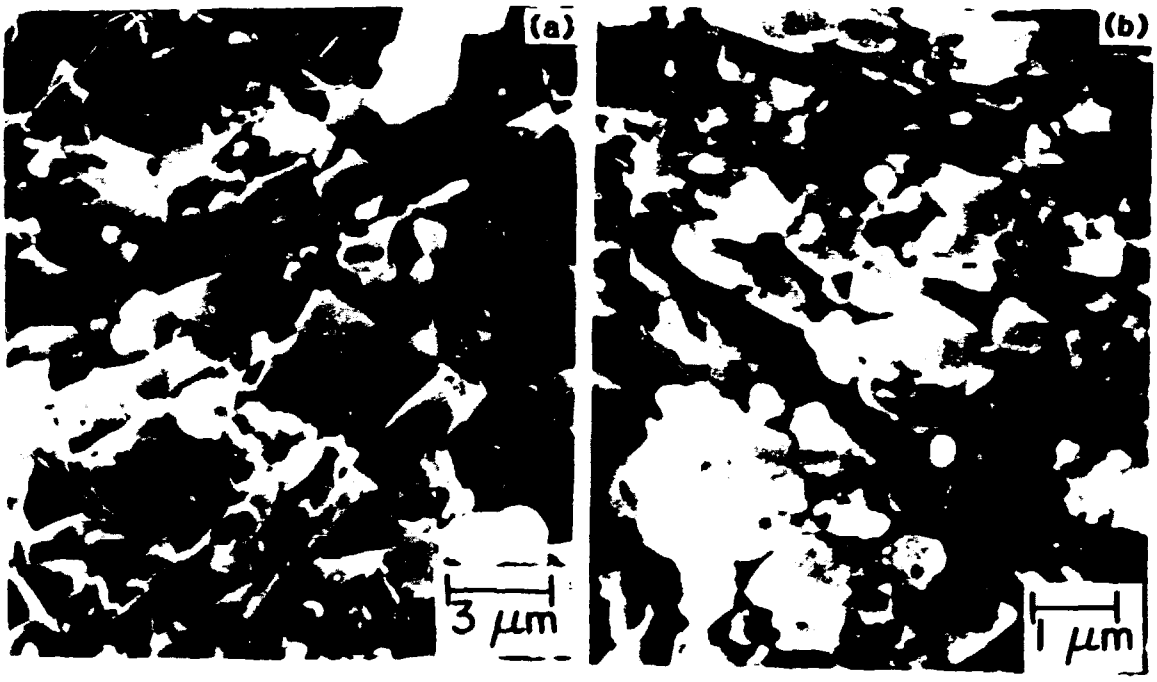

Fig. 1. Scanning Electron Micrographs of Fracture Surfaces of (a) Si_3N_4-A + 6% Y_2O_3 and (b) Si_3N_4-B + 6% Y_2O_3 Specimens Hot-pressed for 2 h at 1750°C and 22 MPa.

flaws introduced during surface machining. The failure-initiating flaws were generally semielliptical in shape and were located in polycrystalline regions in both Si_3N_4-A and Si_3N_4-B specimens.

Figure 2 shows micrographs of a fracture surface of a hot-pressed Si_3N_4-A + 6% Y_2O_3 specimen; an outer fracture mirror and a failure-causing flaw are indicated. According to the experimental observation of Mecholsky et al.,[10] the outer fracture mirror radius (A_o) is related to the critical flaw size (C_c) by

$$\frac{A_o}{C_c} = 13. \qquad (1)$$

The critical flaw size obtained from Eq. (1) by fracture mirror measurements agreed very well with the measured depth of the surface flaw. The flaw sizes measured by fractography for Si_3N_4-A and Si_3N_4-B specimens generally ranged from 25 to 81 μm.

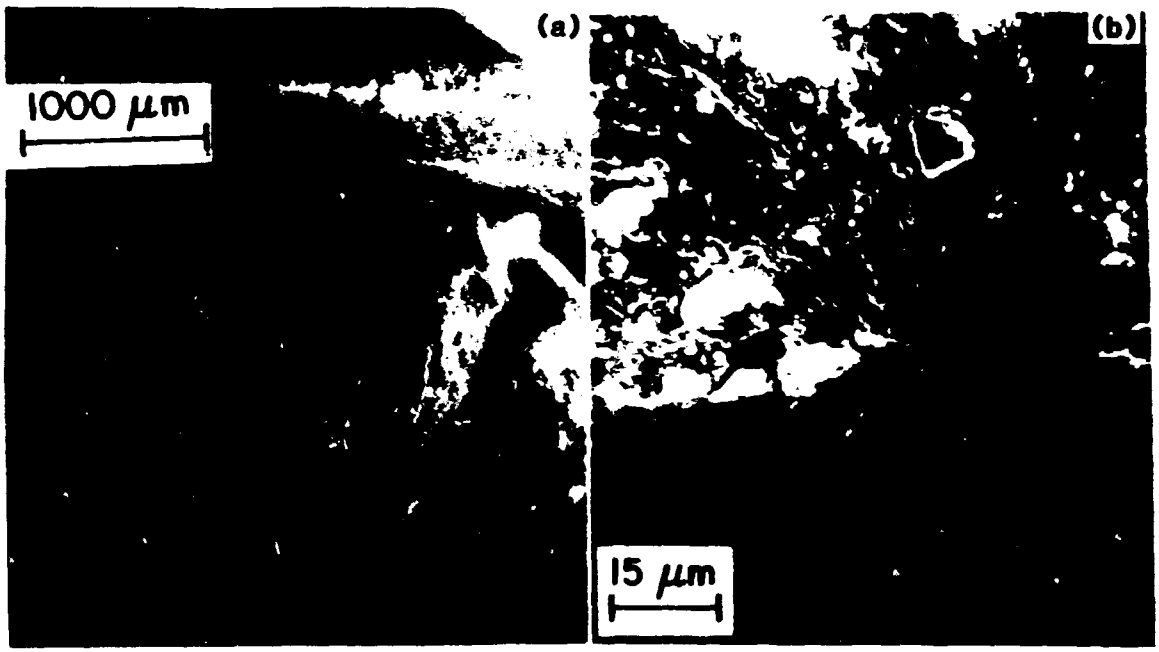

Fig. 2. Scanning Electron Micrographs of Fracture Surface of a Hot-pressed Si_3N_4-A + 6% Y_2O_3 Specimen Showing (a) Outer Fracture Mirror Boundary (Dashed Line) and (b) a Typical Surface Flaw.

Table 2 shows the mechanical properties of Si_3N_4-A specimens with 0.5 and 5 wt % Fe inclusions ranging in size from 88 to 250 μm. The measured densities of the specimens with 0.5 and 5 wt. % Fe were 3.21 and 3.25 g/cm^3, respectively. The data in Tables 1 and 2 show that Fe inclusions have little effect on the fracture toughness (K_{IC}) of Si_3N_4 specimens. On the other hand, the strength (σ_F) of Si_3N_4 specimens is decreased by ~15 and 40% when 0.5 and 5 wt % Fe inclusions, respectively, are present. These reductions in strength are due to the formation of large critical flaws caused by Fe inclusions. Figure 3 shows typical critical flaws observed by fractography in Si_3N_4-Fe specimens. These flaws were generally located within 150 μm of the tensile surface and primarily included Si-and/or Fe-rich inclusions and regions of degraded Si_3N_4 matrix due to interaction between molten Fe and the matrix. The flaw size, which was defined as half the width (smallest dimension) of the internal flaws, ranged from ~14 to 84 μm.

Table 2. Measured Mechanical Properties of Hot-pressed Si_3N_4-A + 6% Y_2O_3 with Fe Inclusions

Property	Fe Content (wt %)	
	0.5	5
Flexural Strength, σ_F (MPa)	716 ± 84	507 ± 29
Fracture Toughness, K_{IC} (MPa$\sqrt{m}$)	6.53 ± 0.9[a]	6.53 ± 0.9
Elastic Modulus, E (GPa)	289 ± 2	303 ± 6

[a]This value was assumed.

CORRELATION OF NDE AND FRACTOGRAPHIC OBSERVATIONS

Correlations were made between NDE predictions and fractographic observations of the location of critical flaws in Si_3N_4-Fe specimens. Through-transmission ultrasound and low-kV x-radiography were used to locate critical flaws nondestructively. The NDE-indicated features presumed to be Fe, Fe-rich, Si, and/or Si-rich inclusions are shown in Fig. 4. The largest inclusions were assumed to be the critical flaws, and MOR bars were machined from the disks (Fig. 5) in such a way that these flaws were included in the bars. These bars were again interrogated by NDE methods in two orthogonal directions to determine the exact locations of the flaws. Subsequently, these bars were broken in the four-point-bending mode with the largest inclusions positioned in the tensile region. The fracture surfaces of the broken bars were examined by fractography to identify and evaluate critical flaws. Good agreement between NDE predictions and fractographic observations of the location of critical flaws was observed for ~7 out of the 21 specimens tested. In these specimens, the NDE (low-kV radiography and through-transmission ultrasound) data indicated the largest flaw to be at or near the tensile surface. In the other specimens (in which fractography and NDE results did not agree), NDE indicated the largest inclusions to be further away from the tensile surface than the surface or near-surface inclusions that actually caused failure. In these specimens, although radiography

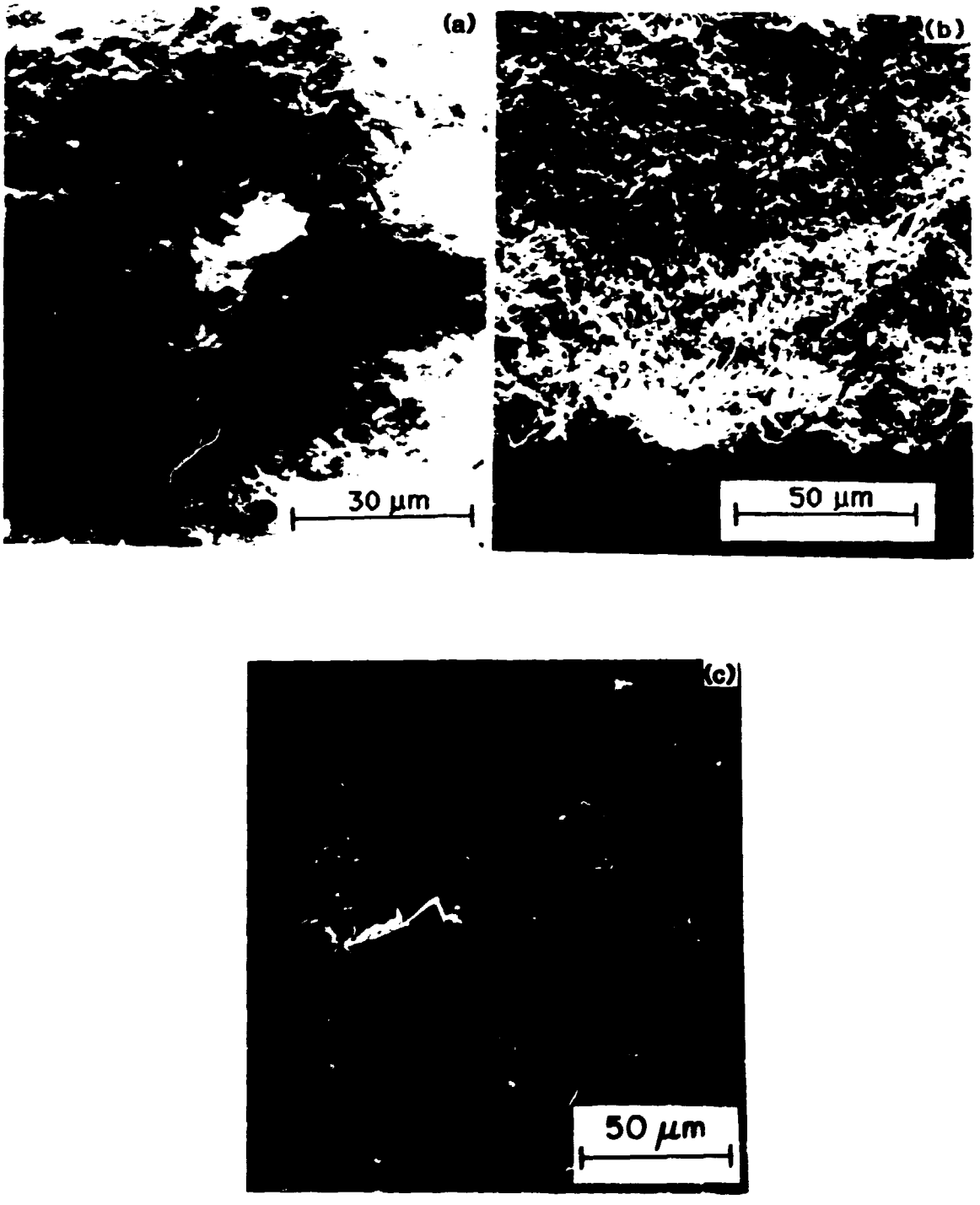

Fig. 3. Scanning Electron Micrographs of Si_3N_4-Fe Fracture Surface Showing Typical Internal Flaws. (a) Fe-rich inclusion; (b) degraded Si_3N_4 matrix; and (c) Si-rich inclusion.

Fig. 4. Low-kV Contact X-Radiograph of Hot-pressed Si_3N_4-A + 6% Y_2O_3 + 5% Fe Specimen Showing Fe, Fe-rich, Si, and/or Si-rich Inclusions.

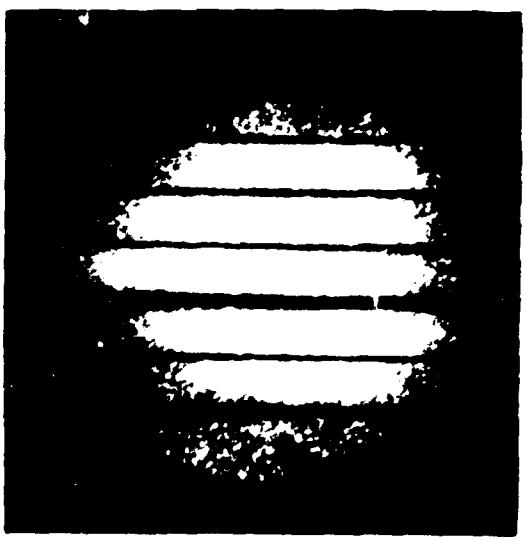

Fig. 5.
An X-Ray Image of One of the Si_3N_4 Disks with 5% Fe Inclusions, Showing the Relative Orientation of Modulus of Rupture Bars.

and through-transmission ultrasound located the largest flaws (inclusions), the stress and stress intensity at these flaws were not sufficient to cause failure.

The above observations suggest that for specimens in which failure is expected from surface or near-surface flaws, surface NDE (backscatter ultrasound) data may be more appropriate for failure prediction. A comparison of through-transmission ultrasound, backscatter ultrasound and low-kV x-ray images is shown in Fig. 6. These images demonstrate the effectiveness of ultrasonic backscatter in detecting near-surface flaws as opposed to internal flaws. Subsequently, a set of 20 bar specimens (Si_3N_4 + 6% Y_2O_3 + 0.5% Fe) was evaluated by low-kV x-radiography and backscatter ultrasound to predict the locations of critical flaws (largest near-surface inclusions), and these predictions were compared with the fractographic observations. Good agreement between the NDE predictions and fractographic observations was obtained for 13 out of 20 specimens. This represents a 65% success rate with surface NDE, as compared to an ~33% success rate with through-transmission NDE. Further improvement in NDE predictions is expected with refinements in NDE techniques.

Fig. 6.
Comparison of (a) Through-Transmission Ultrasound, (b) Backscatter Ultrasound, and (c) Low-kV X-Ray Images of a Modulus of Rupture Bar. Common image features are indicated.

CORRELATION BETWEEN MEASURED CRITICAL FLAW SIZE AND MECHANICAL PROPERTIES

In order to find a correlation between mechanical properties and critical flaw sizes measured by fractography, a fracture mechanics analysis was used to calculate an effective critical flaw size based on measured mechanical properties. Subsequently, a comparison was made between the effective and measured critical flaw sizes to evaluate the above correlation. For the semielliptical surface flaws, the effective critical flaw size C_e was calculated from the measured values of flexural strength σ_F and fracture toughness K_{IC} (Table 1) by use of the relationship[13,14]

$$K_{IC} = 1.35\ \sigma_F \sqrt{C_e}. \tag{2}$$

Since the internal flaws were of irregular shape, radii of hypothetical circular cracks that would fail at the same applied stress were calculated for the purpose of comparison with measured flaw sizes. The radius (a) of this effective critical circular flaw was calculated by the use of the relationship[15]

$$K_{IC}^2 = (4/\pi)\ a\ \sigma_a^2, \tag{3}$$

where σ_a is the applied stress at the critical internal flaw. The value of σ_a was calculated from the measured flexural strength σ_f, specimen thickness, and distance of the flaw from the tensile surface.

A comparison of the measured and calculated values of the critical surface flaw sizes in Si_3N_4 + 6% Y_2O_3 specimens is shown in Table 3. The good agreement obtained between the measured and calculated flaw sizes substantiates the validity of fracture mechanics calculations and fractographic observations. A similar comparison between the measured and calculated values of the critical flaw size for Si_3N_4 specimens with Fe inclusions is shown in Fig. 7. It is to be noted that unlike the case of surface flaws, values of the critical internal flaw size calculated by fracture mechanics analysis were always greater than the measured ones. Similar observations were made by Baumgartner and

Table 3. Calculated and Measured Values of the Critical Flaw Size

Material and Specimen No.	Critical Flaw Size (μm)	
	Measured	Calculated
Si_3N_4-A		
1	48	41
2	51	56
3	25	33
4	81	76
5	72	74
Si_3N_4-B		
1	30	26
2	33	31

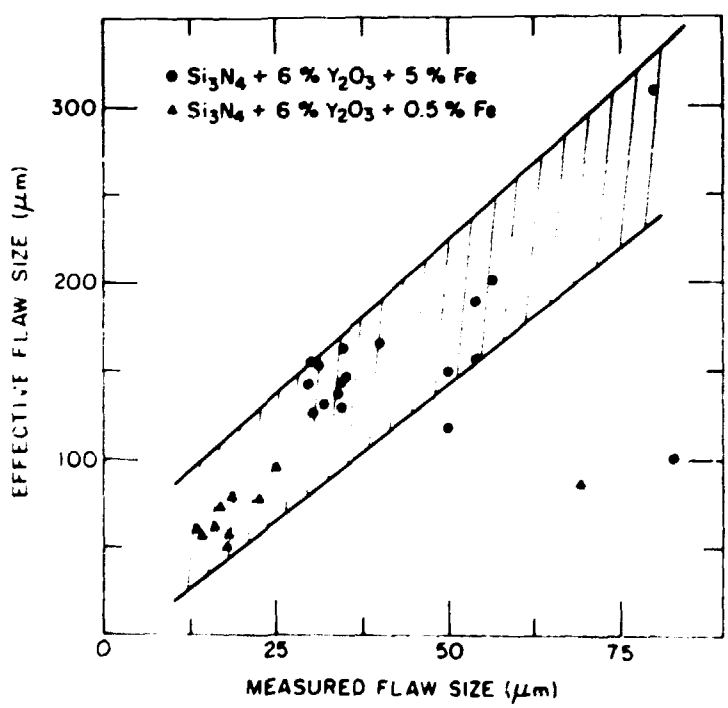

Fig. 7. Comparison of the Measured and Calculated (Effective) Values of the Critical Flaw Size for Si_3N_4-Fe Specimens.

Richerson[16] for inclusion-initiated fracture in hot-pressed Si_3N_4. The tendency of fracture mechanics calculations to overestimate the critical internal flaw sizes associated with these inclusions appears to be due partly to the inaccurate assumption of circular cracks and the corresponding K_{IC} for irregularly shaped internal flaws, and partly to the local degradation in fracture toughness (K_{IC}) at the matrix-inclusion interface. As suggested by Baumgartner and Richerson[16] and Singh,[17] the reduction in local K_{IC} amounts to as much as 50% of the bulk value. Therefore, fracture mechanics prediction based on a bulk K_{IC} value (which is higher than the local K_{IC}) results in an overestimate of the critical internal flaw size and may provide misleading conclusions unless caution is exercised. The data shown in Fig. 7 also suggest the existence of a definite ratio, K, between the calculated and measured flaw sizes. In general, the value of K ranges from 3.5 to 4.2. Assuming that NDE-predicted flaw size (C_I) agrees with fractographically measured flaw size, it is proposed that for a given Fe inclusion size (C_I), an "effective flaw size" C_{eff} ($C_{eff} = KC_I$) can be obtained to predict the strength degradation due to inclusions more precisely. Determination of an "effective flaw size" will have important implications for failure prediction in ceramics based on the inclusion size indicated by NDE data.

STATISTICAL EVALUATION OF STRENGTH DATA

In order to evaluate the effectiveness of NDE screening procedures, Weibull plots of strength data for the Si_3N_4-Fe specimen population before and after NDE screening were constructed. The Weibull analysis included data for both Si_3N_4 + 6% Y_2O_3 + 0.5% Fe and Si_3N_4 + 6% Y_2O_3 + 5% Fe specimens. The results indicate that the Weibull modulus for strength distribution increases from 3.1 to 17.2 and from 11.3 to 12.1, respectively, for these specimens as a result of NDE screening. This demonstrates the validity of NDE screening in improving strength distribution. Further improvements are expected with refinements in NDE techniques.

SUMMARY

- The addition of 5 and 0.5 wt % Fe inclusions of 88 to 250 μm size reduced the strength of Si_3N_4 specimens by approximately 40 and 15%, respectively. This is believed to be due to formation of large flaws resulting from the interaction between molten Fe and Si_3N_4 matrix.

- Failure in Si_3N_4-Y_2O_3-Fe specimens occurred primarily from internal flaws located within ~150 um of the tensile surface. These flaws included Fe- and Si-rich inclusions and/or regions of Si_3N_4 matrix that were degraded as a result of reaction between Si_3N_4 and molten Fe.

- A comparison of fractographic observations and NDE data on the location of failure-initiating flaws suggests that for specimens in which failure is expected from surface or near-surface flaws, a surface NDE method such as backscatter ultrasound may be most appropriate for the detection of failure-initiating flaws.

- For surface flaws, good agreement was observed between the critical flaw sizes calculated by fracture mechanics analysis and measured by fractography. On the other hand, for inclusion (Fe)-induced internal flaws, the calculated flaw sizes were always larger than the measured sizes. This observation suggests a local degradation in fracture toughness of the Si_3N_4 matrix. A ratio K (~3.5 to 4.2) appears to exis between the calculated and measured values of the critical internal flaw sizes. Assuming an agreement between fractographically measured and NDE-predicted flaw sizes, an "effective flaw size" C_{eff} can be determined from the NDE-predicted flaw size C_I (i.e., $C_{eff} = KC_I$) to predict strength degradation due to inclusions.

- A Weibull analysis of strength data suggests that initial NDE screening has improved the strength distribution of the Si_3N_4-Y_2O_3-Fe specimens.

ACKNOWLEDGMENTS

The research was supported by the U. S. Department of Energy, Advanced Research and Technology Development Fossil Energy Materials Program, under contract W-31-109 Eng-38. Thanks are extended to J. Lucas of the Quality Assurance Division for helping with the radiographic imaging and to R. B. Poeppel, Manager of the Ceramics Section, for frequent discussions and helpful comments.

REFERENCES

1. D. W. Richerson, "Evolution in the U. S. of Ceramic Technology for Turbine Engines," Ceram. Bull. 64(2), 282-286 (1985).

2. D. C. Larsen and J. W. Adams, Property Screening and Evaluation of Ceramic Turbine Materials, Air Force Wright Aeronautical Laboratories Report AFWAL-TR-83-4141, April 1984.

3. Katsutoshi Komeya, "Development of Nitrogen Ceramics," Am. Ceram. Soc. Bull. 63(9), 1158-1159 (1984).

4. Reliability of Ceramics for Heat Engine Applications, National Materials Advisory Board Report NMAB-357, 1980.

5. H. P. Kirchner, R. M. Gruver, and W. A. Sotter, "Characteristics of Flaws at Fracture Origin and Fracture Stress-Flaw Size Relations in Various Ceramics," Mater. Sci. Eng. 22(2), 147-156 (1976).

6. F. F. Lange, "Processing-Related Fracture Origins: 1. Observations in Sintered and Isostatically Hot-Pressed Al_2O_3/ZrO_2 Composites," J. Am. Ceram. Soc. 66(6), 396-398 (1983).

7. J. P. Singh, R. A. Roberts, J. J. Vaitekunas, and W. A. Ellingson, "Failure Prediction of Hot-Pressed Si_3N_4 Ceramics by NDE," ASME Paper No. 87-GT-7 (1987).

8. R. A. Roberts, J. P. Singh and J. J. Vaitekunas, "NDE and Fracture Studies of Hot-Pressed Si_3N_4," Ceramic Engineering and Science Proceedings (in press).

9. J. W. Johnson and D. G. Holloway, "On the Shape and Size of Fracture Zones on Glass Fracture Surfaces," Phil. Mag. 14, 731-743 (1966).

10. J. J. Mecholsky, Jr., S. W. Freiman, and R. W. Rice, "Fracture Surface Analysis of Ceramics," J. Mater. Sci. 11, 1310-1319 (1976).

11. A. G. Evans, "Fracture Toughness: The Role of Indentation Techniques," in Fracture Mechanics Applied to Brittle Materials, S. W. Freiman, ed., ASTM STP 678, pp. 112-135 (1979).

12. J. Krautkrämer and H. Krautkrämer, Ultrasonic Testing of Materials, Springer-Verlag, New York (1983).

13. A. S. Kobayashi "Crack Opening Displacement in a Surface Flawed Plate Subjected to Tension or Plate Bending," in Proc. Second Int. Conf. on Mechanical Behavior of Materials, Boston, MA, pp. 1073-1077 (August 1976).

14. C. A. Andersson and R. J. Bratton, "Effect of Surface Finish on the Strength of Hot-Pressed Silicon Nitride," in Science of Ceramic Machining and Surface Finishing II, R. R. Hockey and R. W. Rice, eds., NBS Publication 562, pp. 463-476 (1979).

15. I. N. Sneddon, "The Distribution of Stress in the Neighborhood of a Crack in an Elastic Solid," Proc. R. Soc. London, pp. 229-260, 187A (1946).

16. H. R. Baumgartner and D. W. Richerson, "Inclusion Effects on the Strength of Hot-Pressed Si_3N_4," in Fracture Mechanics of Ceramics, Vol. 1, R. C. Bradt, D. P. H. Hasselman and F. F. Lange, eds., Plenum Press, New York, pp. 367-386 (1973).

17. J. P. Singh, "A Review of the Effect of Flaws on the Fracture Behavior of Structural Ceramics," Argonne National Laboratory Report ANL/FE-86-3 (1986).

MATERIAL AND SYSTEM CHARACTERIZATION OF REFRACTORY LININGS FOR SLAGGING GASIFIERS

F. Tamer and O. Buyukozturk

Massachusetts Institute of Technology
Department of Civil Engineering
Cambridge, Massachusetts 02139

ABSTRACT

In this paper thermomechanical tests conducted for sintered high-alumina, and sintered and hot-pressed high-chromia refractories are reported. The tests characterize the stress-strain behavior of the materials under short-term uniaxial loadings. The parameters of the experiments include pre-selected constant temperature levels T in the range of 70°F to 2400°F with monotonically increasing mechanical loads (or cyclic mechanical loads between two fixed load levels), increasing temperatures from 70°F to 2400°F with pre-selected constant load levels, slag-impregnation, and partial oxygen pressures (P_{O_2}) of 10^{-8} atm representative of slagging gasifiers environment.

Two different behavioral regions are identified: a low temperature mechanism for temperatures below approximately 1/2 T_m (T_m is the melting temperature of the material) where a linear elastic behavior with a brittle failure is observed, and a high temperature mechanism for temperatures above approximately 1/2 T_m where large non-linear inelastic deformation prior to failure is observed. The strength (defined as the peak stress on the stress-strain curve) of the materials in the low temperature range is found to be decreasing proportionally to $T^{1/2}$, while in the high temperature range the strength appears to be decreasing proportionally to T.

Peak strains show higher rates of increase, and the initial modulus of elasticity show higher rates of decrease, for temperatures above approximately 1/2 T_m. P_{O_2} values of approxiamtely 10^{-8} atm seem to have little effect on the thermomechanical

behavior of high-alumina sintered refractory, but affect the behavior of high-chromia sintered refractory at high temperature levels. Slag impregnated specimens show increased strength and stiffness up to the temperature level of approximately 1/2 T_m compared to as-manufactured specimens. An increased rate of stiffness degradation with temperature is observed in the slag-impregnated specimens. Finally, the ratio of the strengths of hot-pressed materials to those of sintered materials at temperatures approximately below 1/2 T_m is consistently found to be a constant for the same loading conditions.

INTRODUCTION

BACKGROUND

Refractory materials are used in large reactor vessel linings such as those used for coal gasification vessels, blast furnaces, ammonia plants, petroleum refinery units, liquid metal fast breeder reactors, and vessels for the glass and cement-making industries[1-18]. The vessels are usually composed of an outside steel shell and layers of refractories. Refractory linings protect the steel shell from high temperatures, attack of slags and process gases. Cooling systems are frequently used to keep the shell temperature at certain predetermined levels. With the slagging gasifiers the refractory layers are composed of dense bricks next to the hot-face and of insulating material next to the steel sheel. The bricks are usually jointed together using mortar material. The bricks are in the form of trapezoidal blocks with either a straight edge (Fig. 1a), or a circular edge (Fig. 1b). The bricks may sometimes be keyed together for mechanically interlocking them anticipating an improvement in the system integrity (Fig. 1b).

Generally, the range of operating temperatures in slagging gasifiers is 2500°F - 3300°F. Ash is usually present as molten slag that runs down the walls of the gasifiers, and is corrosive to the linings. Gas pressures in the gasifier usually range from atmospheric

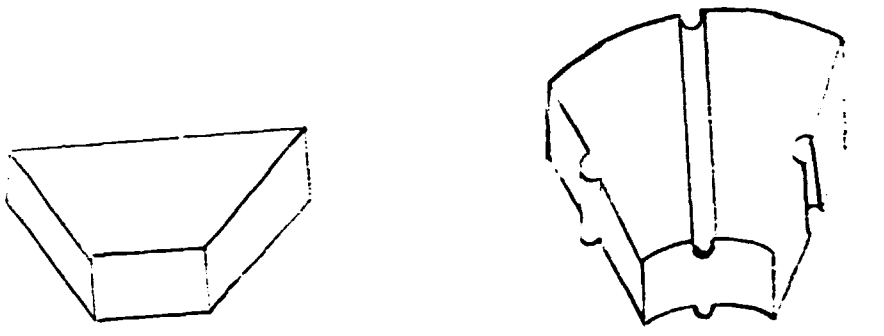

(a) straight edge brick

(b) circular edge brick with grooves and keys

Figure 1 - Bricks Shapes

to 1000 psi. Gases present consist of H_2O (steam), H_2, CO, CO_2 and small amounts of CH_4, N_2, NH_3 and H_2S [20]. These gases are usually reducing in nature, and a typical value of the partial oxygen pressure during operation is 10^{-8} atm.

Different modes of failure of the brick-mortar lining systems have been observed and studied[12,13,19-38]. Failure can occur by degradation of the mechanical properties of refractories at elevated temperatures through cracking, crushing, and spalling of the refractory materials under thermomechanical loadings, by joint failure of the brick-mortar system, by disintegration of the refractories under gas attack, and by corrosion or erosion due to slag attack. Present design methods for these systems generally use empirical methods based on over-simplified assumptions.

The analysis and design of refractory linings is complicated primarily due to the complexity in modeling the material behavior. Such an analysis should consider the refractory material behavior with respect to the effects of monotonic and cyclic mechanical loads,

elevated temperatures and thermal cycling, environmental interaction such as slags and process gases, and history of thermomechanical loadings. Therefore, there is a need to develop a comprehensive set of material data representative of the material behavior in the process environment of the vessel.

GENERAL OBJECTIVES OF WORK AT MIT

The general objectives of the current work at MIT are: (a) to generate and compile experimental data on the thermomechanical behavior of selected candidate materials in the categories of high-Cr_2O_3 and high-Al_2O_3 refractories for the linings in slagging gasifiers, and (b) based on the obtained data to expand the material and numerical analysis models previously developed at MIT to predict the thermomechanical behavior of various lining systems under transient temperature loadings.

Previous Work

Previous work at MIT[12,13,19] concentrated on material and system modeling of the behavior of refractory linings for slagging gasifiers. Data was collected from the literature on the thermomechanical and thermophysical properties of high alumina and high-chromia refractories. Temperature dependent material models were developed to represent the material behavior. Emphasis was on the development of a time-independent constitutive model to predict the material response to multiaxial, non-proportional and cyclic loads. The temperature effect is introduced by scaling the stress-strain curves at different levels, with respect to the peak stress and the associated axial peak strain. A power law creep model, a conductivity model for cracked media, and polynomial representations of the thermophysical properties were also proposed. The different models were incorporated in a finite element program. A predictive corrosion model was proposed to study the long-term corrosion process of lining systems. Based on this model, sensitivity studies were performed to identify the

important factors characterizing the long term behavior of the linings. Using the finite element program, the thermomechanical behavior of linings with various material combinations, lining geometries, and heating schemes was studied. Based on the findings from the thermomechanical and corrosion analyses, tentative recommendations were made for the design and operation of lining systems.

Focus of Present Work

The numerical analysis capability developed from the thermomechanical analysis of mortar-brick systems is a powerful tool to predict stress and strain distributions, cracking and deterioration. However, the developed capabilities suffer from the lack of data for candidate refractory materials. Therefore, the present work concentrates on testing of selected high-alumina and high-chromia refractories manufactured by sintering, hot-pressing, or fusion-casting. Table 1 shows the classes of materials under investigation within the current work scope. The scope of the testing program includes short-term uniaxial monotonic and cyclic mechanical load tests at room and constant elevated temperatures; and constant load tests under constant or varying temperatures. Table 2 summarizes the test program undertaken. In this paper, the results of 148 tests corresponding to the tests completed (Table 2) will be presented for materials identified as A, B, and D. Each test case presented has been confirmed by generally three and at least two tests, except those for slag-impregnated material B at 2200°F and under a P_{O_2} of 10^{-8} atm, and for the short-term creep tests.

MATERIALS AND EQUIPMENT

MATERIALS TESTED

The results discussed in this paper refer to a sintered high-alumina (Material A) and sintered high-chromia (Material B) and a

Material Classification	Chemical Composition	Manufacturing Process	Testing of Slag Impregnated Material	%Apparent Porosity	Closed Pores
A	90% Al_2O_3 10% Cr_2O_3	Sintering	Yes	17	No
B	82% Al_2O_3 18% Cr_2O_3	Sintering	Yes	12	No
C	90% Al_2O_3 10% Cr_2O_3	Hot-Pressing	Yes	4	Yes
D	80% Al_2O_3 20% Cr_2O_3	Hot-Pressing	No	8	Yes
E	78% Al_2O_3 8% Cr_2O_3 + ...	Fusion-Casting	No	-	-

Table 1

Materials under investigation

	Short-Term Uniaxial Compression Tests			
	$\dot{\epsilon}$ is constant in the range 10^{-3} sec^{-1} to 10^{-4} sec^{-1}			$\dot{\epsilon}$ is variable
	Constant T in the range 70°F to 2400°F			Increasing T from 70°F to 2400°F
	Monotonic P to failure		Cyclic P	Constant P between 70%f_p to 95%f_p
	Air	P_{O_2} = 10^{-6} atm.	Air	Air
Material A As-Manufactured	X	X	X	X
Material A Slag-Impregnated	X	X		
Material B As-Manufactured	X	X	X	O
Material B Slag-Impregnated	X	X		
Material D	O			

$\dot{\epsilon}$ = strain rate

f_p = monotonic material strength

P = applied compressive load

T = temperature

P_{O_2} = partial oxygen pressure

X testing essentially complete

O testing in progress

Table 2 Test Program

hot-pressed high-chromia (Material D) refractories. The high-alumina refractory was selected for its known good resistance to thermal shock[22]. The high-chromia refractory was selected for its good resistance to corrosion by slags[10,23,30,33]. Both materials are low-silica containing refractories to resist hydrogen attack, and carbon monoxide disintegration.

Material A is composed of 90% Al_2O_3 and 10% Cr_2O_3, forming a solid solution with 17% open pores. It has some lattice structure. There is no free Al_2O_3 or Cr_2O_3 present. There are two minor phases present: coarse Al_2O_3 penetrated by Cr_2O_3 exhibiting a white color, and Cr_2O_3 grains penetrated by Al_2O_3 exhibiting a pink color. Its average bulk density is 206 lbs/ft^3 (3300 Kg/m^3). The manufacturer's suggested maximum use temperature is 3450°F. Material B is composed of 82% Cr_2O_3, and 18% MgO. It has 12% open pores. It is mostly picochromite, and free Cr_2O_3 exists as a second phase. It has a spinel structure. Its average bulk density is 235 lbs/ft^3 (3800 Kg/m^3). The manufacturer's suggested maximum use temperature is 3272°F. Material D is composed of 80% Cr_2O_3 and 20% MgO. It has 8% closed pores. Only one phase exists.

SPECIMEN PREPARATION

Specimen preparation is critical to insure that (1) the test results represent the material behavior, and not just the behavior of laboratory specimens; and (2) any variability in the results is an inherent material property, and is not caused by the specimen preparation.

Specimen preparation of sintered materials is described first for both as manufactured and slag-impregnated materials. The refractory materials were received as bricks. The specimens were cored out of the bricks, and the end surfaces were prepared for testing. Some specimens were slag-impregnated.

Factors affecting the specimen preparation are: (1) specimen's shape and dimensions; (2) the direction and location of coring from

the brick; (3) the coring speed; (4) end surface preparation; and (5) the slag-impregnation procedure.

Cylindrical specimens of 1" diameter and 2.5" to 3" height were adopted as standard. The circular cross-section was preferred over the rectangular one to insure the uniformity of stress and temperature applied on the specimen. The height to diameter ratio of 2.5 to 3.0 was adopted to minimize the end zone effect in compression testing[43]. The 1" diameter was chosen to comply with the minimum imposed by ASTM, of 3 to 4 times the size of the maximum aggregate. Figure 2 shows the strength (defined as the peak stress on the stress-strain curve) variation with specimen's diameter for Material A from our preliminary tests. A diameter of 0.875" leads to a consistently lower strength than that of a diameter of 1". The largest size aggregate being 1/3" for Material A, one notices that the 0.875" diameter does not comply with the ASTM requirement. Testing of specimens with a diameter much larger than 1" is expected to give a reduced strength.

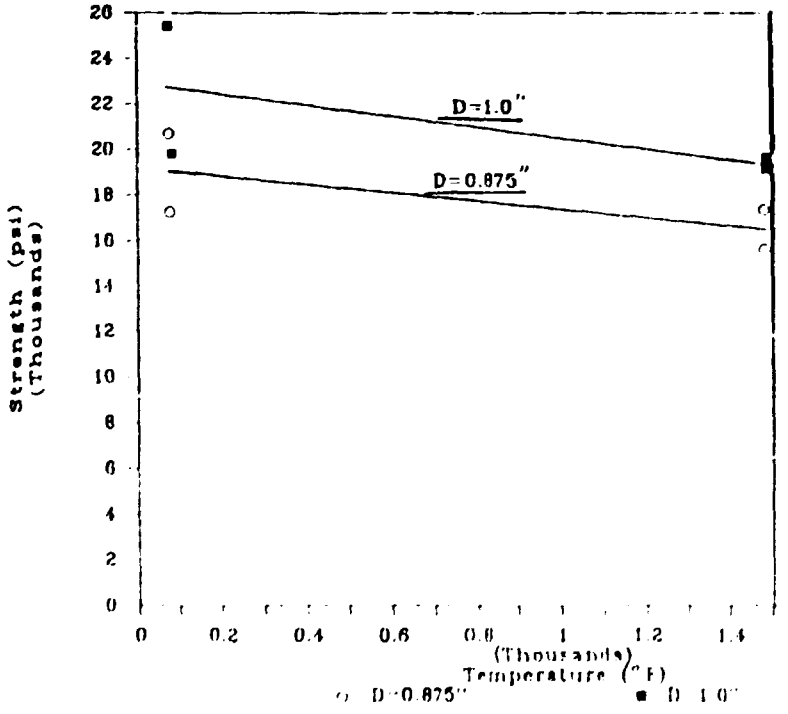

Figure 2 - Strength Variation with Specimen's Diameter for Material A

The next step was to minimize the damage due to the coring operation, as well as the end surface preparation. After conducting preliminary tests, a coring speed of 375 RPM, along with grinding of the specimen end surfaces were found to be adequate, and adopted as standard. An average uniaxial compressive strenght of 20700 psi was found for specimens cored out along the pressing direction. The specimens cored in the direction perpendicular to the pressing direction exhibited an average strength of 17470 psi and a greater ductility. These tests revealed an anisotropic material behavior. This is attributed to the nature of the sintering process where the pressing force is uniaxial. To limit the number of tests, and for consistency within the present test program as well as with the tests conducted by other researchers in the field, it was decided to examine only specimens cored out with their axis parallel to the pressing direction.

The next parameter examined was the specific location of the specimen on the brick. Figure 3 shows typical stress-strain curves for specimens cored out from the corner and interior of a material B brick. The corner specimen exhibits a weaker strength. This behavior was consistently reproduced, and confirmed. Generally, the specimens cored out from corner locations are weaker than specimens cored out from the interior of the brick. This is related to the sintering process, and can be explained by stress concentrations developing at the corners during the pressing operation. Figure 4 shows average strengths for the specimens from different directions and locations of coring. The brick is thus not only anisotropic, but also inhomogeneous. Interior specimens cored out with their axis parallel to the pressing direction were adopted as standard for testing.

To study the effect of slag-impregnation, specimens were impregnated with western-acid slag[33,38] of the following composition: 52.4% SiO_2, 22.5% Al_2O_3, 10.1% CaO, 6.0% Fe_2O_3, 2.0% C, 1.9% Na_2, 1.8% MgO, 1.1% TiO_2, 0.5% K_2O, and less than 0.5% of other constituents. The specimens were packed in an alumina crucible with

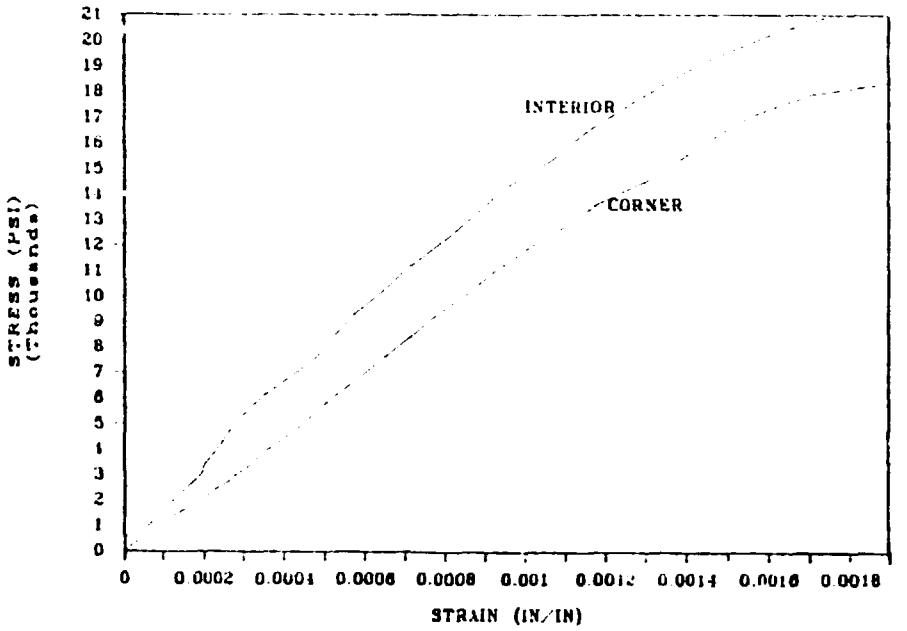

Figure 3 - Variation in Material Behavior with Core Location On the Brick, for Material B

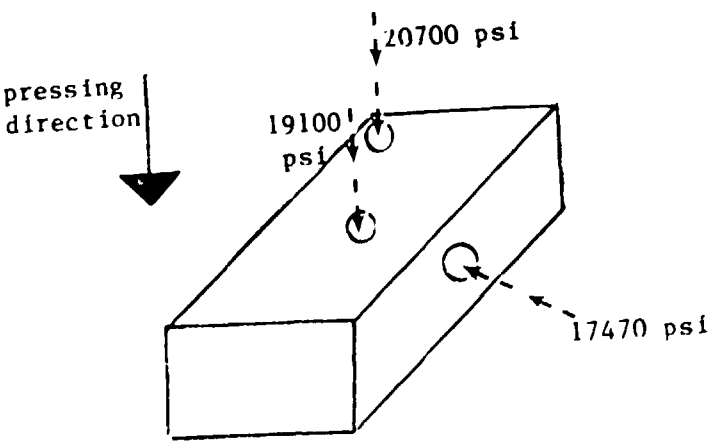

Figure 4 - Average Strengths for Different Directions of Coring and Location on the Brick for Material B

slag powder. The specimens were kept for 10 hours in slag at 2822°F (1550°C) under an atomosphere of N_2 and NH_3, with an estimated P_{O_2} of 10^{-3} to 10^{-4} atm. Material A was slag-saturated, while Material B was slag-impregnated but not saturated. Two positions of the specimens were tried in the crucible: a horizontal position that resulted in uniform impregnation over the length of the specimen but with distorted cross sections, and a vertical position that produced a uniform impregnation over its cross sections. The horizontal position resulted in an average strength of 11500 psi for chromia specimens at room temperature, compared to an average strength of 21900 psi for specimens impregnated in the vertical position. The method of horizontal impregnation was not used for further testing. Test results from vertically slag-impregnated specimen were consistent.

Hot-pressed materials have a much smaller maximum grain size allowing a choice of smaller specimens for testing. Furthermore, since hot-pressed materials are expensive and difficult to get in large block size for coring, square specimens with a 0.3" by 0.3" cross-section, and a height of 0.9" (giving a side to height ratio of 3) were chosen. The end surfaces were ground flat and parallel for testing.

THERMOMECHANICAL TEST EQUIPMENT

A thermomechanical testing equipment for testing under compressive loads and controlled gas environment was developed for conducting the proposed testing program. The muffle tube and retort system, along with the furnace are shown in Fig. 5. The system is designed to apply 50,000 lbs at 2800°F, under a controlled P_{O_2} as low as 10^{-15} atm. The furnace has a 10 inch-long circular heat zone. It is heated by SiC heating elements connected in series, and arranged in a symmetrical circular pattern around the specimen. The furnace is controlled using a K-thermocouple (chromel-alumel) up to 2000°F, and a B-thermocouple (platinum - 6% rhodium vs. platinum - 30% rhodium) for temperatures above 2000°F. Both thermocouples are connected to a

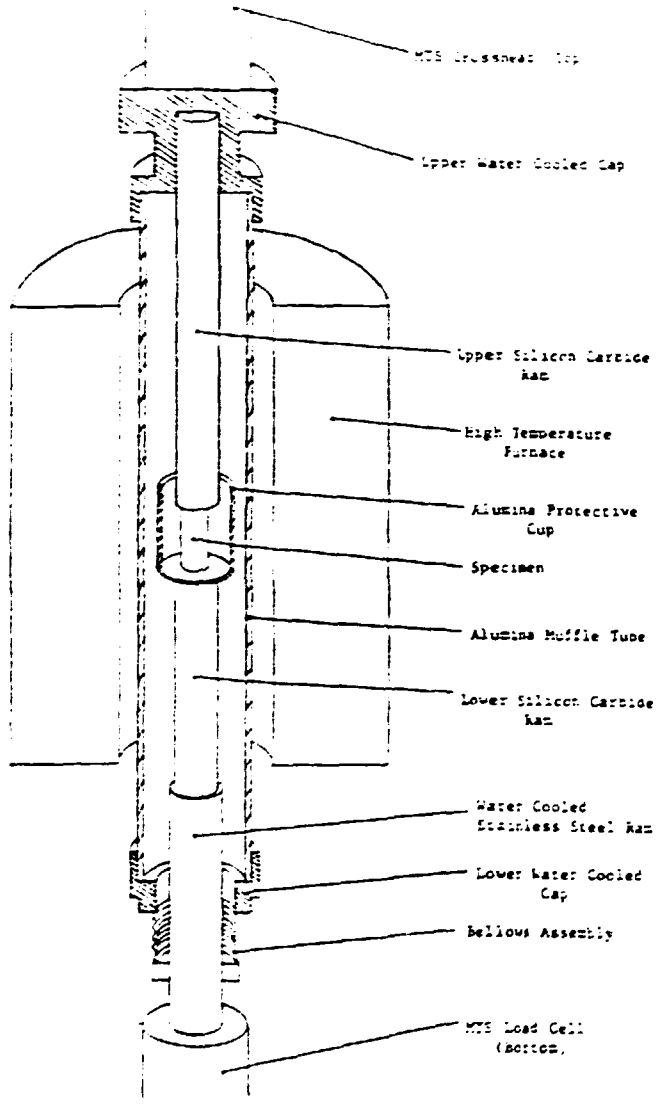

Figure 5 - Furnace, Retort System, and Muffle Tube for Thermomechanical Testing Under Controlled Gas Environment

microprocessor for control. The load train consists of SiC loading tubes, and recrystalyzed SiC caps. The lower SiC tube frames into a water cooled stainless steel (grade 347) loading rod. The load train is connected to water cooled vacuum flange assemblies to provide tight seal around the muffle tube. Bellows assembly around the stainless

steel rod provides a moving seal to allow for piston movement. The entire retort assembly is connected to a 110 kips loading frame. The data acquisition and control is fully automated, and the facility is shown in Fig. 6. A PDP-11 computer is used for control. A Fluke 2400B linked to an IBM-XT is used for data acquisition. A user-friendly software has been developed to carry out these tests.

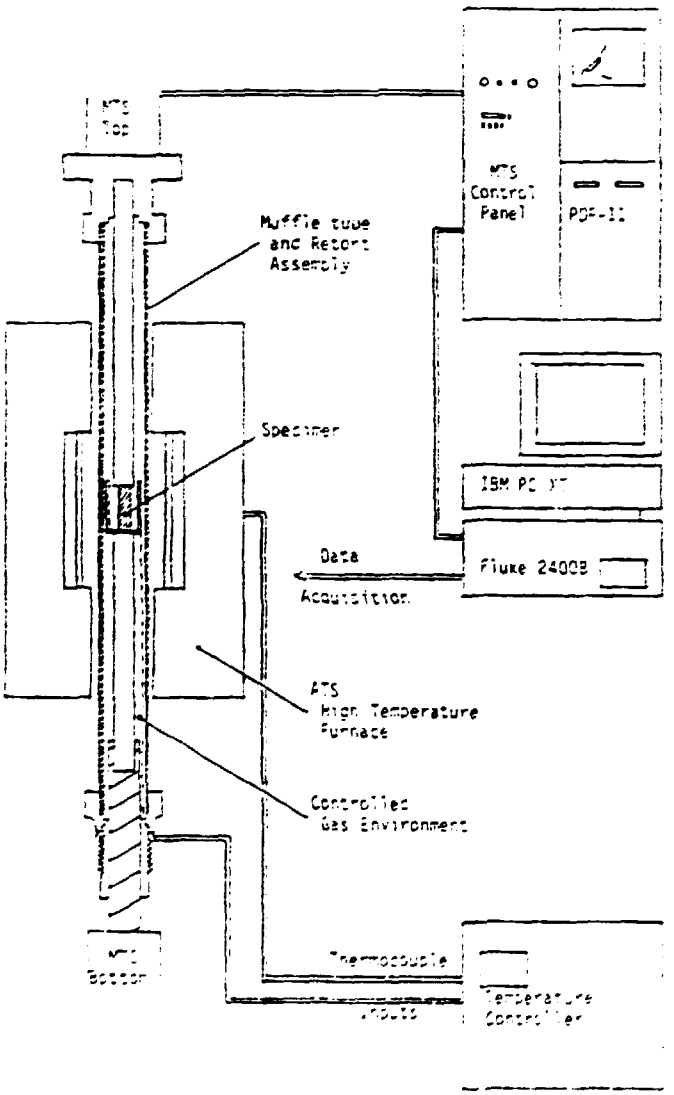

Figure 6 - Test System Facility at MIT

BEHAVIOR OF REFRACTORY MATERIALS UNDER SHORT-TERM THERMOMECHANICAL LOADS

Extensive room temperature, short-term monotonically applied compression tests were performed on refractory specimens taken from a manufacturer's production line for over a one year period, and prepared according to the standard preparation procedure previously outlined. A larger variation in the material behavior was found to occur in specimens taken from different batches of bricks received at different periods in time, than in specimens taken from the same batch of bricks. To get consistent results all further tests were performed on specimens taken from bricks belonging to the same batch. Typical test results and main behavioral aspects of short-term compression tests on refractory specimens taken from the same batch of bricks are discussed in the next sections.

The first section concentrates on tests on as-manufactured materials, conducted in air atmosphere. Monotonic and cyclic mechanical load tests under constant predetermined temperature levels, and constant mechanical load tests under different temperature variations are examined. The second section focuses on the effect of environmental factors, such as partial oxygen pressure and slag-impregnation.

TESTS ON AS-MANUFACTURED MATERIALS IN AIR ATMOSPHERE

Room Temperature Testing

The behavior of as-manufactured and slag-impregnated Materials A and B, and as-manufactured Material D at room temperature is examined first.

The behavior of as-manufactured and slag-impregnated specimens at room temperature are compared. Typical results for Materials A, B and D are shown in Fig. 7. The materials with and without slag-impregnation behave in a linear elastic manner up to the maximum stress (defined as strength) on the stress-strain curve, where brittle failure occurs with negligible amounts of inelastic strains. The

strength of slag-impregnated specimens is higher than those of as-manufactured specimens. This may be attributed to the slag penetrating into the pores and solidifying at room temperature and acting as a glassy bond. The slag-impregnated material is, thus, less porous with stronger bond between its grains. Material A exhibited a larger increase in strength with slag-impregnation than Material B. This is attributed to the fact that Material A was impregnated to a higher degree than Material B, thus having less empty pores after slag-impregnation.

The hot-pressed material (Material D) is about 7.5 times stronger than the sintered one (Material B) with about the same chemical composition. This factor seems to relate to the grain size as will be discussed in the next section.

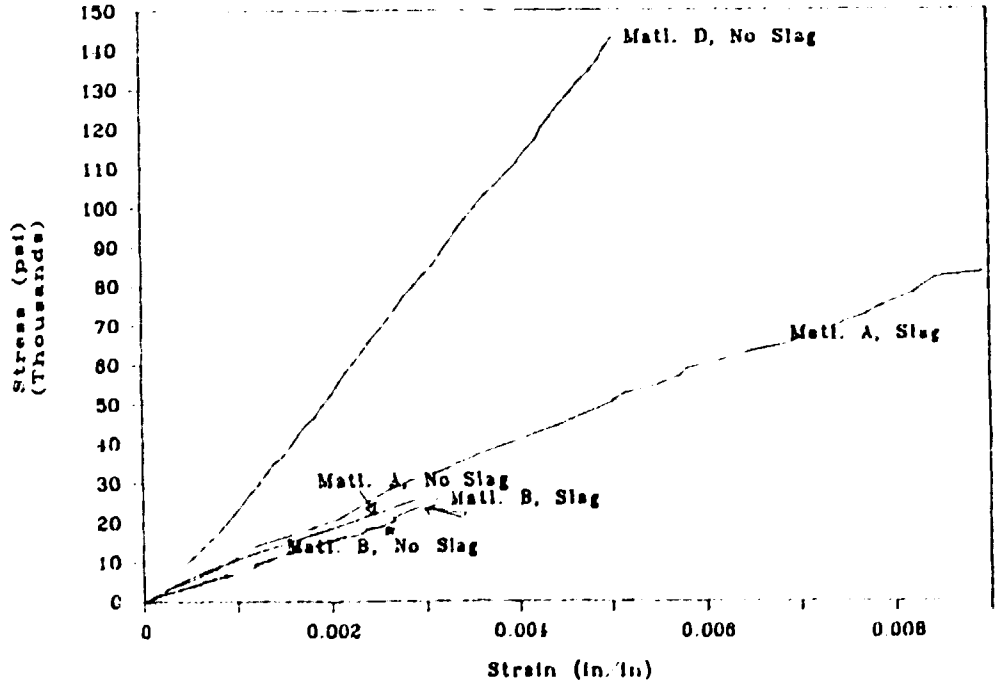

Figure 7 - Typical Behavior of As-Manufactured and Slag-Impregnated Material A, and B, and As-Manufactured Material D at Room Temperature

Low-cycle high-stress cyclic mechanical tests were carried out at room temperature. In the preliminary testing stage, two types of tests were conducted: cycling between two fixed load levels as shown in Fig. 8a, and cycling with a fixed load increment per cycle as shown in Fig. 8b. Only low-cycle high-stress cyclic tests between zero and fixed load levels (in the range of 70% to 95% of the monotonic strength) were carried out on standard specimens. Figure 9 shows the variation of the average number of cycles to failure for Material B with respect to the value of the fixed load level. Results of cyclic tests exhibited a larger variation than those in monotonic tests, and characterization of material behavior under cyclic mechanical loads is difficult.

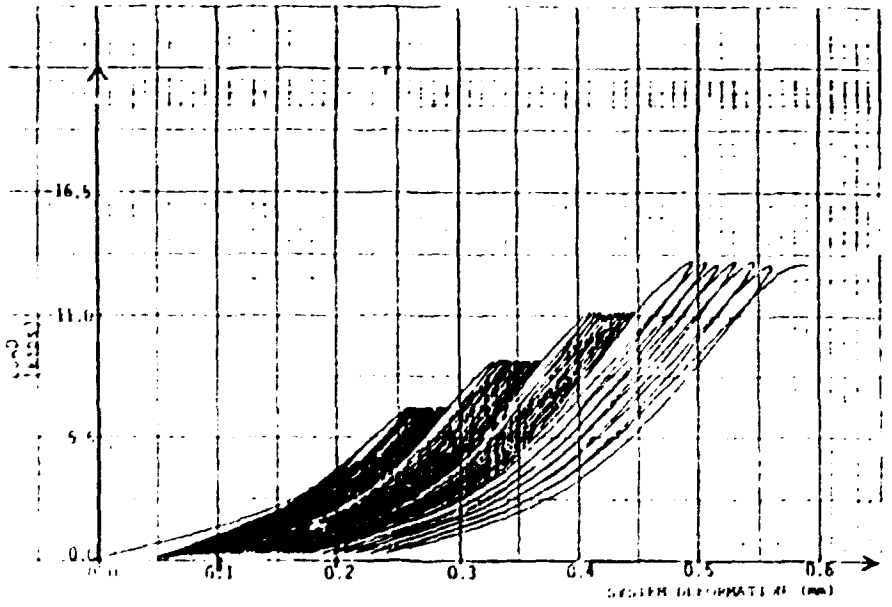

(a) Cycling Between Two Fixed Load Levels

Figure 8 - Cyclic Mechanical Tests

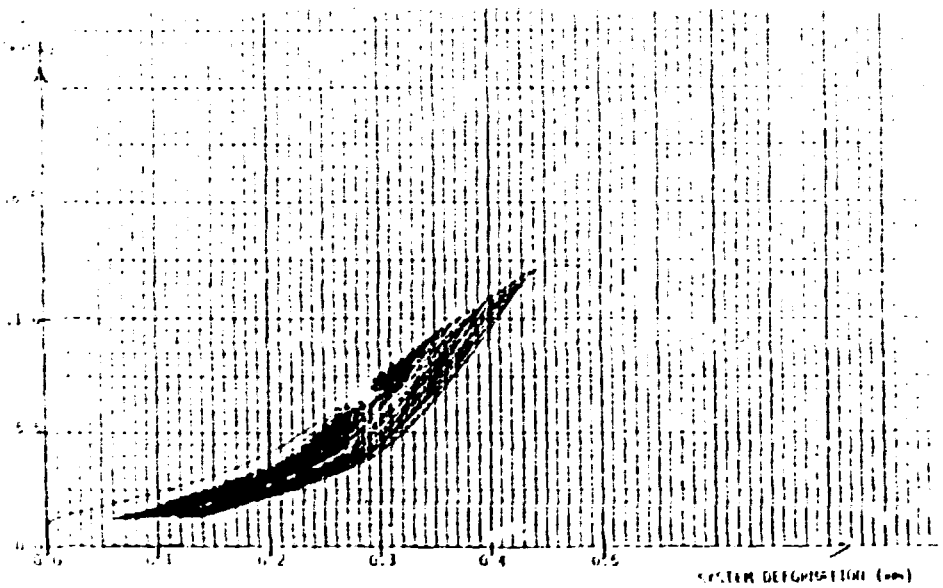

(b) Cycling With A Fixed Load Increment Per Cycle

Figure 8 - Cyclic Mechanical Tests

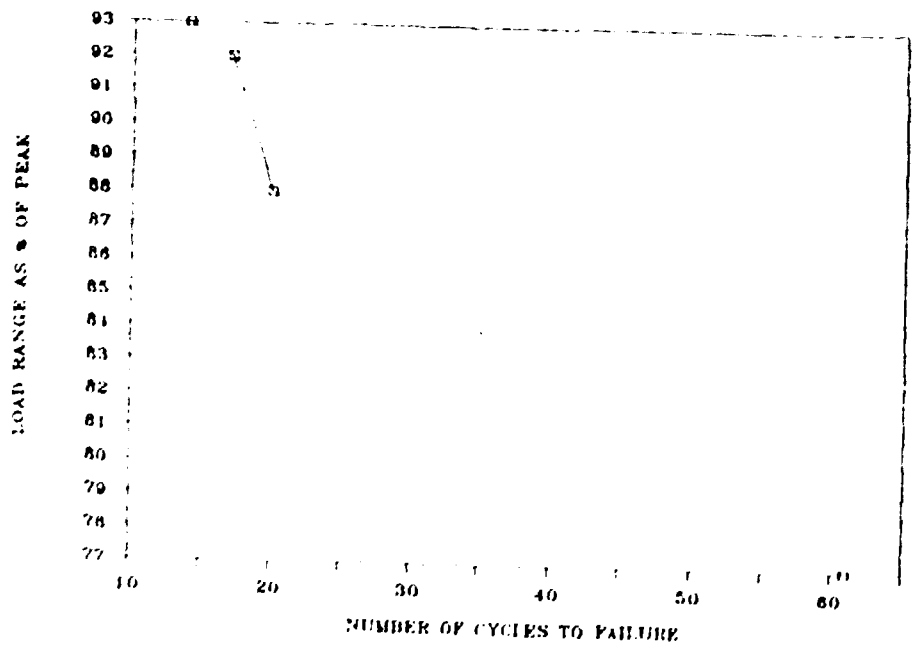

Figure 9 - Average Number of Cycles to Failure for Material B for Different Fixed Load Levels

Constant Temperature, Varying Load Tests

Short-term uniaxial compression tests conducted on as-manufactured Materials A, B and D are discussed in this section. Two types of tests are examined: the system displacement is monotonically increased (under displacement controlled tests), or the loads are cycled between two predetermined fixed load levels (under load controlled tests). The temperature was maintained constant during the test. The following temperature levels were adopted: 73°F (room temperature), 500°F, 1000°F, 1500°F, 2000°F, 2200°F, and 2400°F. The behavior of as-manufactured specimens of Materials A, B and D under monotonically increasing loads, and constant predetermined temperature levels is discussed first. The stress-strain curves for different temperature levels, are shown in Figs. 10, 11 and 12 for Materials A, B, and D respectively.

Two deformation mechanisms are identified. At temperature levels below roughly 1/2 T_m (where T_m is the melting temperature of the material), the deformation behavior is linear elastic with a brittle failure. At temperatures above 1/2 T_m the material deformation is initially linear elastic, and exhibits significant non-linearities prior to the peak strength. Inelastic deformations continue to occur in the post-peak region. Clearly, there is a transition temperature from the low to the high temperature deformation behavior. This transition temperature is found to correspond to about one-half the melting point of the material. This is observed for both Materials A and B. Material A having a higher melting temperature exhibits a higher transition temperature. For Material D tests above 1/2 T_m are in progress. The source of the inelastic strains is believed to be primarily due to creep effects, and is discussed later.

This transition temperature, with brittle fracture at temperatures below it, and more ductile behavior at temperatures above it, has also been observed for alumina ceramic[40] for which at 2300°F (1260°C) the failure is by fracture, and at 2318°F (1270°C) an upper field stress and a lower yield plateau are observed.

The parameters that are going to be examined in further detail are the strength, the initial modulus of elasticity, the associated peak

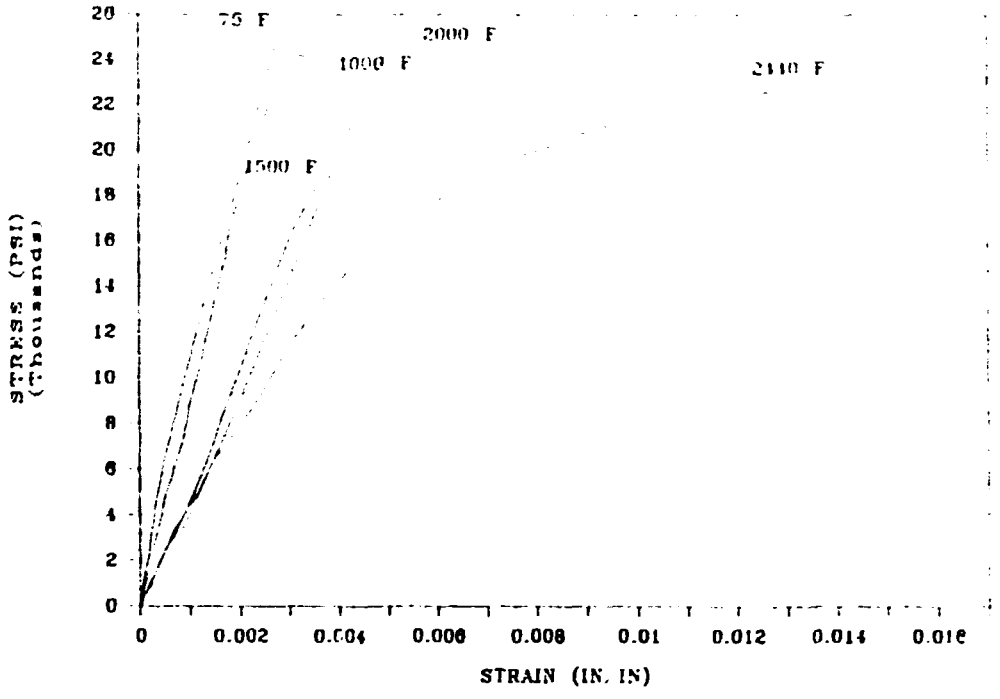

Figure 10 - Stress Strain Curves for Material A at Different Temperature Levels

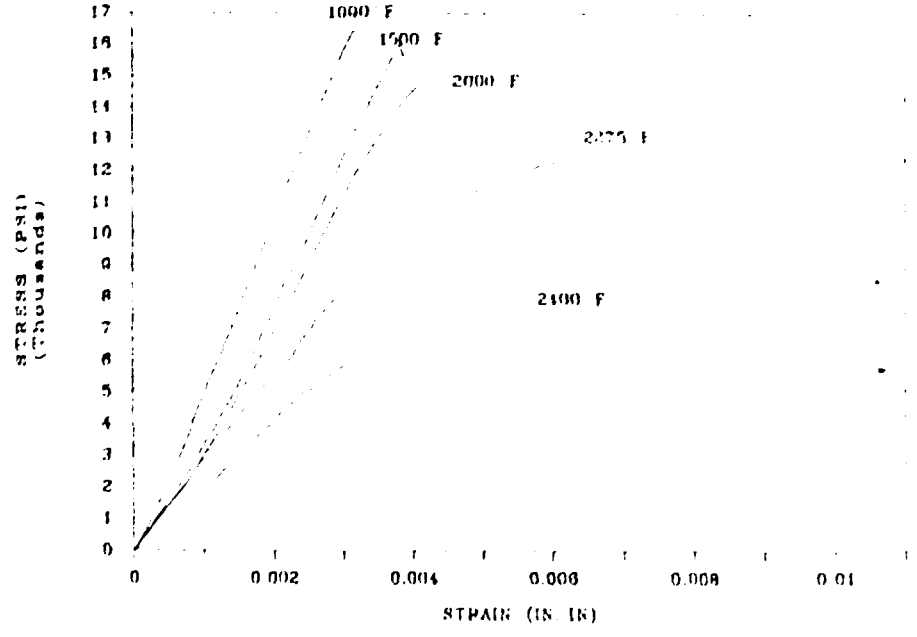

Figure 11 - Stress Strain curves for Material B at Different Temperature Levels

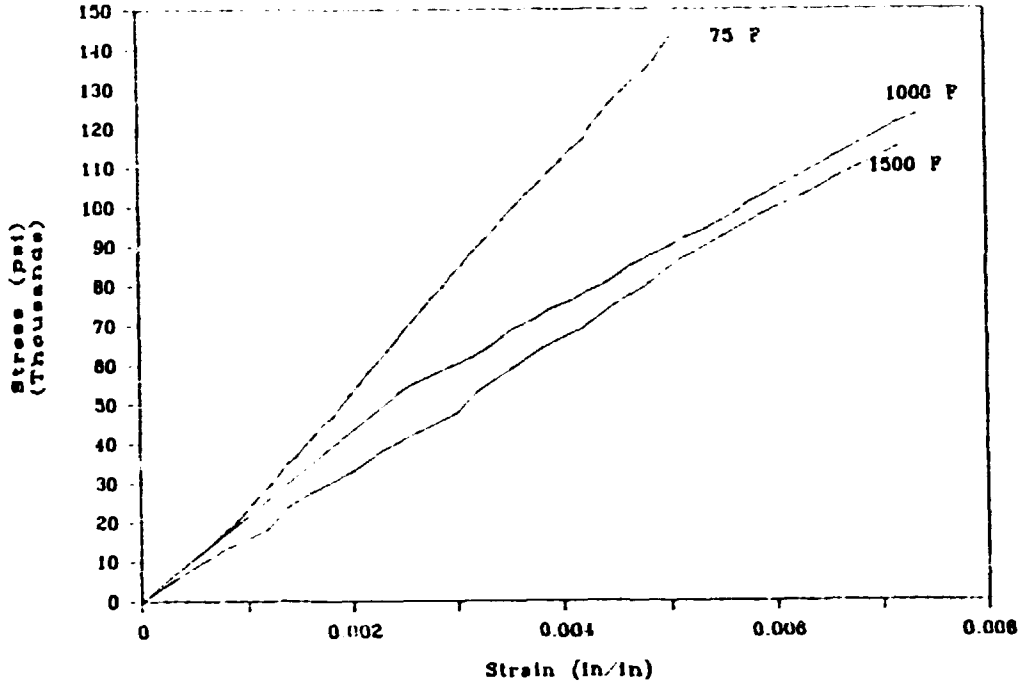

Figure 12 - Stress Strain Curves for Material D at Different Temperature Levels

strain, the variation of the material's density after testing, and the effect of cyclic mechanical loads.

The strength of the material, similarly to the failure behavior, follows two different mechanisms: one below a transition temperature (roughly equal to 1/2 T_m), and one above this transition temperature. Decrease in the material's strength with temperature is proportional to the square root of T below the transition temperature; and is proportional to T above the transition temperature. This is shown in Fig. 13 for Material B. For the temperature levels below the transition temperature, the strength is found to degrade as a function of the square root of temperature, governed by an equation of the type:

$$S = \hat{\tau} \left[1 - (T / T_0)^{1/2}\right] \qquad (1)$$

where S is the strength of the material, and T_0 and $\hat{\tau}$ are fitting parameters. $\hat{\tau}$ is linked by some researchers to inherent material properties[39], and represent the ideal strength of the material at 0°K. T_0 is the temperature (in °K) at which the strength is reduced to zero.

For temperatures above the transition temperature, the strength degradation is found to be proportional to the temperature, and is governed by an equation of the type:

$$S = \hat{\tau} \left[1 - (T / T_0)\right] \qquad (2)$$

where the symbols are as defined for Equation (1).

This strength behavior has been reported for ceramics in general[41] where the fracture stress decreases slowly at low temperatures, controlled by a simple crack propagation. At intermediate to high temperatures, the fracture stress decreases much faster, governed by a deformation assisted brittle fracture. And finally, there is a third region, where ductile fracture occurs at higher temperatures. Our tests represent the first two behavioral regions.

Tests were conducted on Material D at temperatures below the transition temperature. The behavior is similar to that found for the sintered materials, and the strength is governed by Equation (1). This is shown in Fig. 14. The strength of hot-pressed high-chromia to sintered high-chromia is a constant, which is roughly equal to the inverse ratio of the maximum grain size to the 1/4 power. This is given by:

$$S\, d_{max}^{1/4} = \text{constant} \qquad (3)$$

where S is the strength of the material, and d_{max} is the maximum grain size. Assuming that below the transition temperature weak grain boundaries act as initial flaws, one can assume that: $2c = d$, where $2c$ is the crack length, and d the grain size. Assuming that below the transition temperature failure is governed by a constant fracture toughness criterion the following expression is obtained:

$$S\, d^{1/2} = \text{constant}. \qquad (4)$$

The discrepancy between Equation (3) and Equation (4) can be explained by the fact that the tested sintered high chromia does not

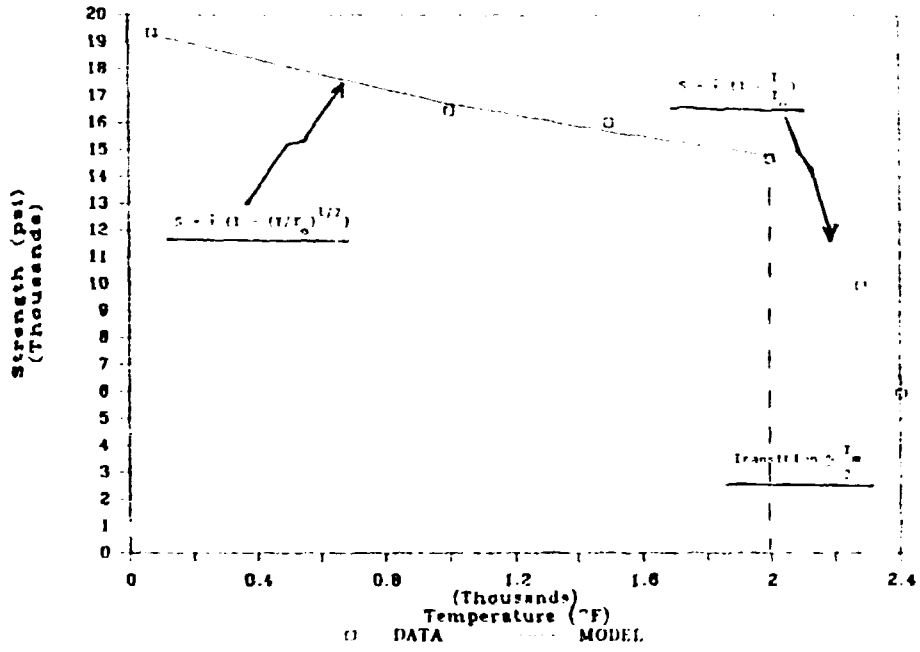

Figure 13 - Strength Variation with Temperature for Material B

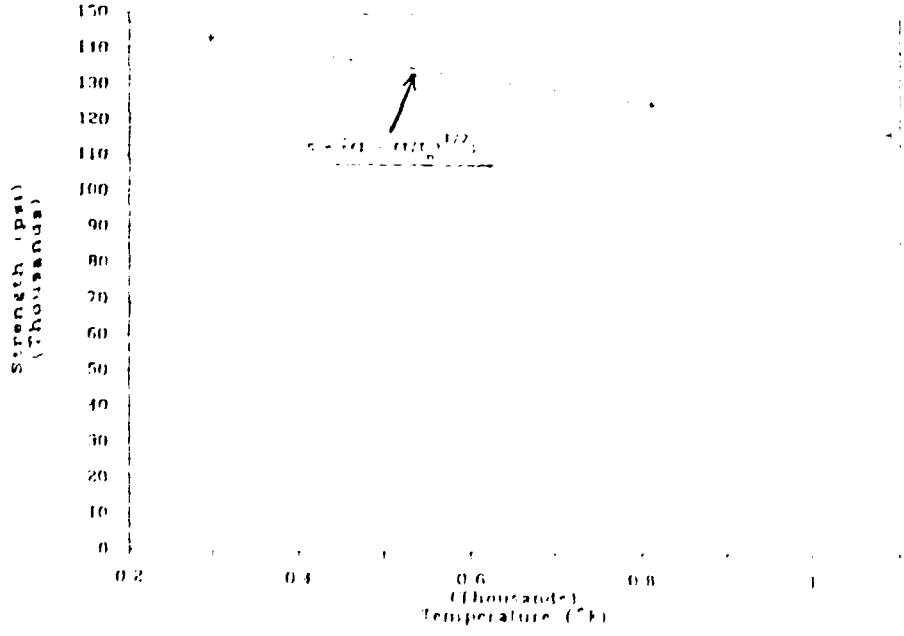

Figure 14 - Strength Variation with Temperature for Material D

have a uniform grain size, but that it is made by a gradation of different grain sizes. The maximum grain size might not be the controlling factor, but rather the grain size distribution. The hot-pressed material has a roughly uniform grain size distribution. Thus, if instead of considering the maximum grain size, one considers the average grain size, it will lead to a higher exponent in Equation (3).

The next parameter of interest, is the initial slope of the stress strain curve. The variation of the initial modulus of elasticity with temperature is shown in Fig. 15. The rate of decrease of the modulus with temperature is noticeably higher at temperatures above the transition. It is found that the ratio of the material's strength to the cubic root of the initial modulus is a constant, for temperature levels below the transition temperature. This is shown in Fig. 16 for Material B. Similar results are obtained for Material A.

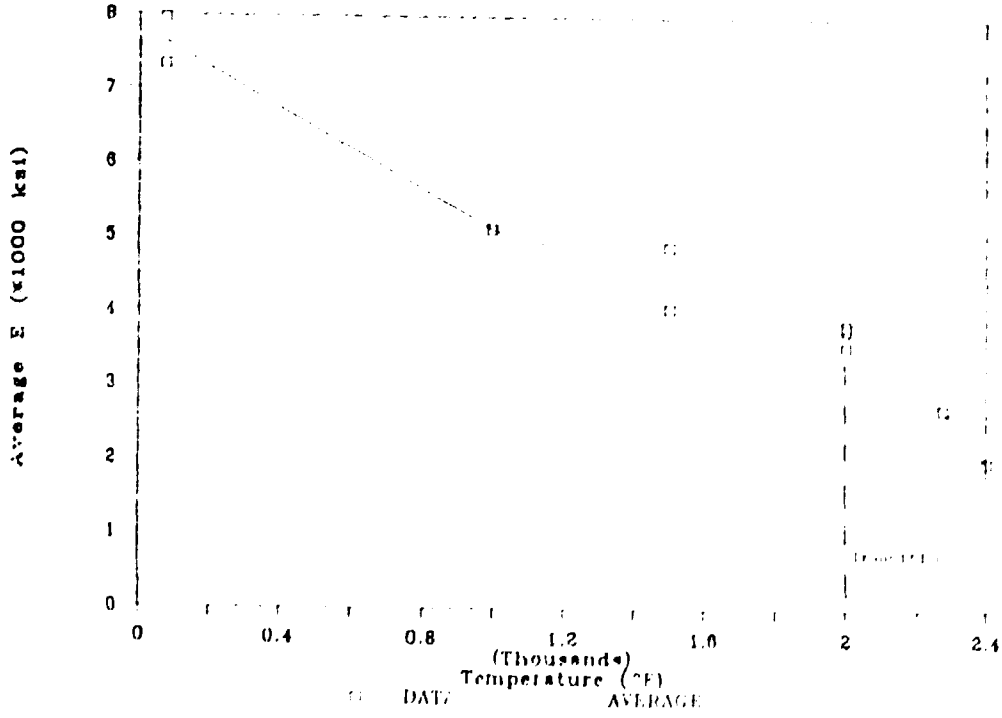

Figure 15 - Variation of the Initial Stiffness with Temperature for Material B

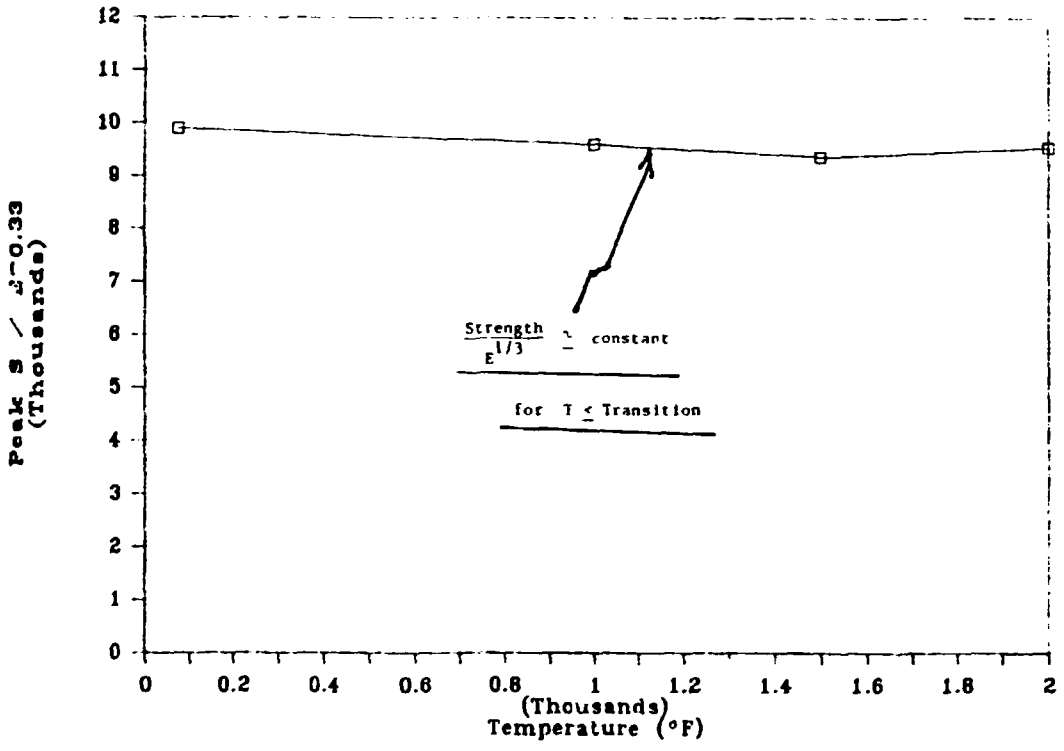

Figure 16 - Variation of the Ratio of Strength to Cubic Root of Initial Stiffness, with Temperature, for Material B

The variation with temperature of the peak strain values associated with the peak stress, for Material A, is shown in Fig. 17. The rate of increse in the peak strain is lower for temperatures below the transition level than those above the transition temperature.

Below the transition temperature, the specimen fails in a brittle mode, and the fracture strain is fitted by the following expression:

$$\varepsilon_f = C_1 \exp\left(\frac{-C_2 S (1 - (S / \hat{\tau})^2)}{T}\right) \quad ; \qquad (5)$$

where S is the material strength given by Equation (1), T is the temperature in °K, $\hat{\tau}$ is defined in Equation (1), and C_1 and C_2 are constants. This behavior is shown in solid line in Fig. 18. In materials such as metallic glasses[39] Equation (5) applies for temperatures below $0.6T_g$ (T_g defined as the glass transition temperature) and C_1 and C_2 are related to well-known material properties.

The density of tested specimens was measured after testing at elevated temperatures, and compared to density after room temperature testing. At elevated temperatures the density decreases, which indicates that more cracking is developing at high temperatures. Below the transition temperature, the fracture strain is related to the density decrease by the following relationship:

$$\frac{\varepsilon_f}{\varepsilon_{room}} = 1 + (\Delta\rho)^{3/2} \qquad (6)$$

where ε_f is the fracture strain below the transition temperature, ε_{room} is the fracture strain at room temperature, and $\Delta\rho$ is the density decrease in percent. This is shown in Fig. 19. At temperature levels above the transition temperature, Equation (6) predicts lower fracture strains than those observed. This is due to the increased ductility of the material above the transition temperature.

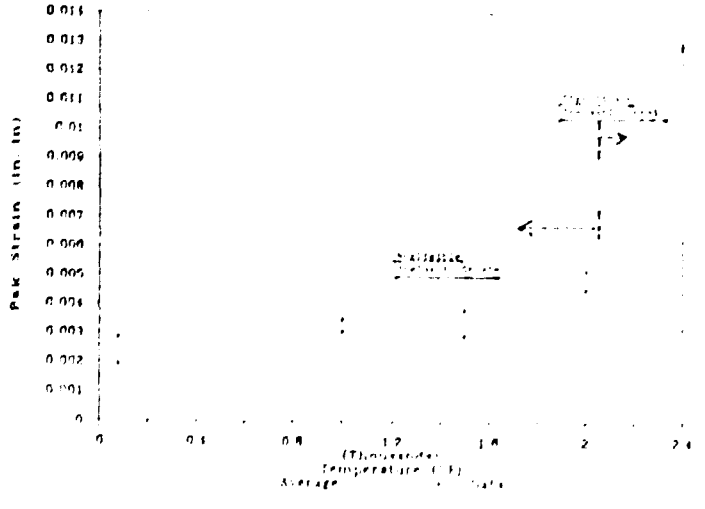

Figure 17 - Variation of the Associated Peak-Strain with Temperature, for Material A

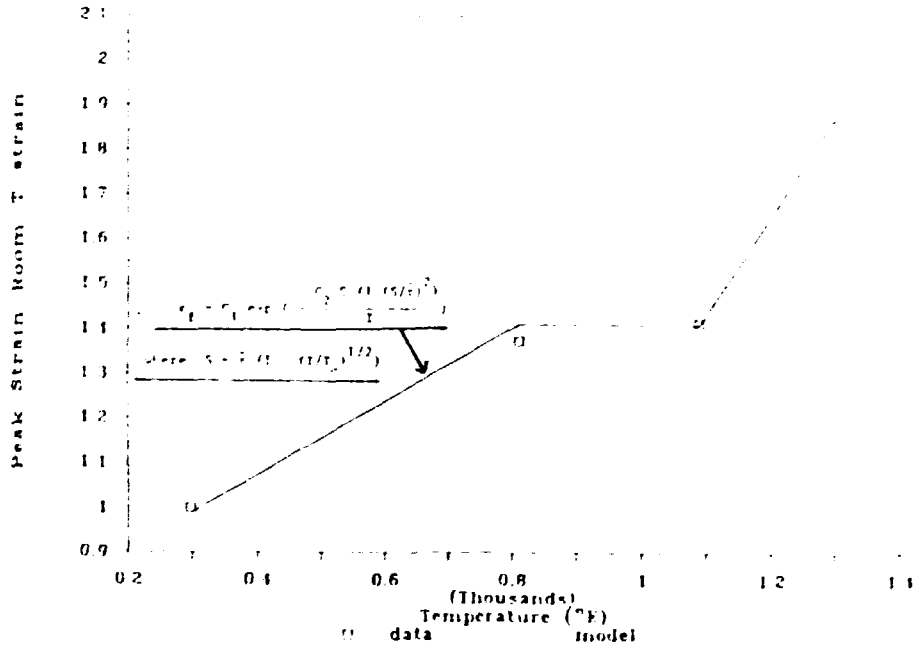

Figure 18 - Fitting of Associated Peak-Strains for Temperatures Below the Transition Temperature, for Material A

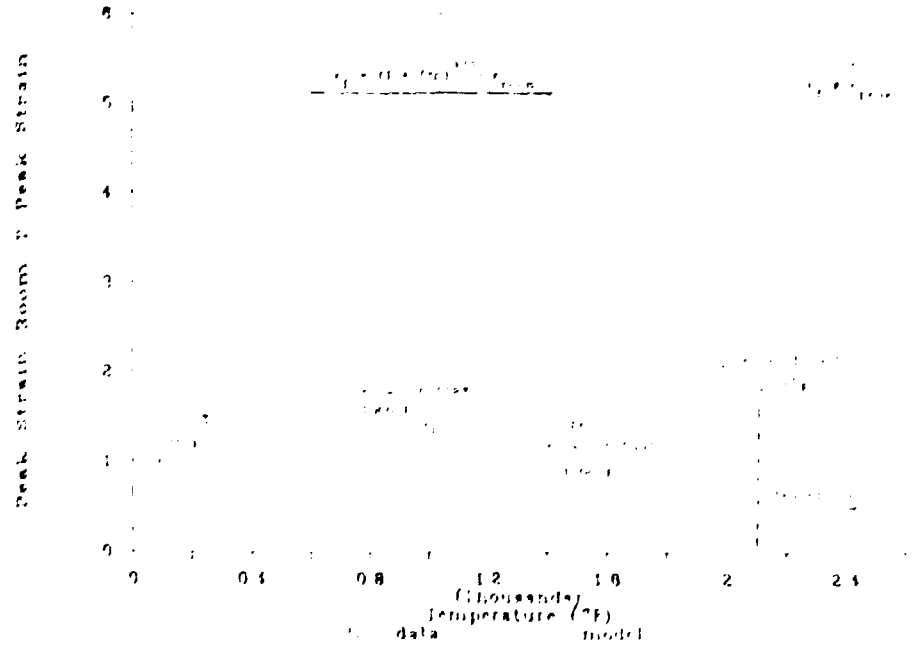

Figure 19 - Variation of Fracture Strain (below 1/2 T_m) and Associated Peak Strain (above 1/2 T_m) with Temperature and Density Decrease After Testing

Cyclic mechanical load tests were conducted on Material A at different temperature levels. A typical cyclic test is shown in Fig. 20. Initial cycles (cycles 0 to 18) accumulate significant amounts of inelastic strain. Later cycles (cycles 23 to 36) accumulate less inelastic strain. Large amounts of accumulated inelastic strains usaually form immediately before final failure. The specimen shown in Fig. 20 was cycled to 75% of the monotonic strength, at 1500°F. It did not fail after 60 cycles. High-temperature cyclic tests are still underway to confirm the results.

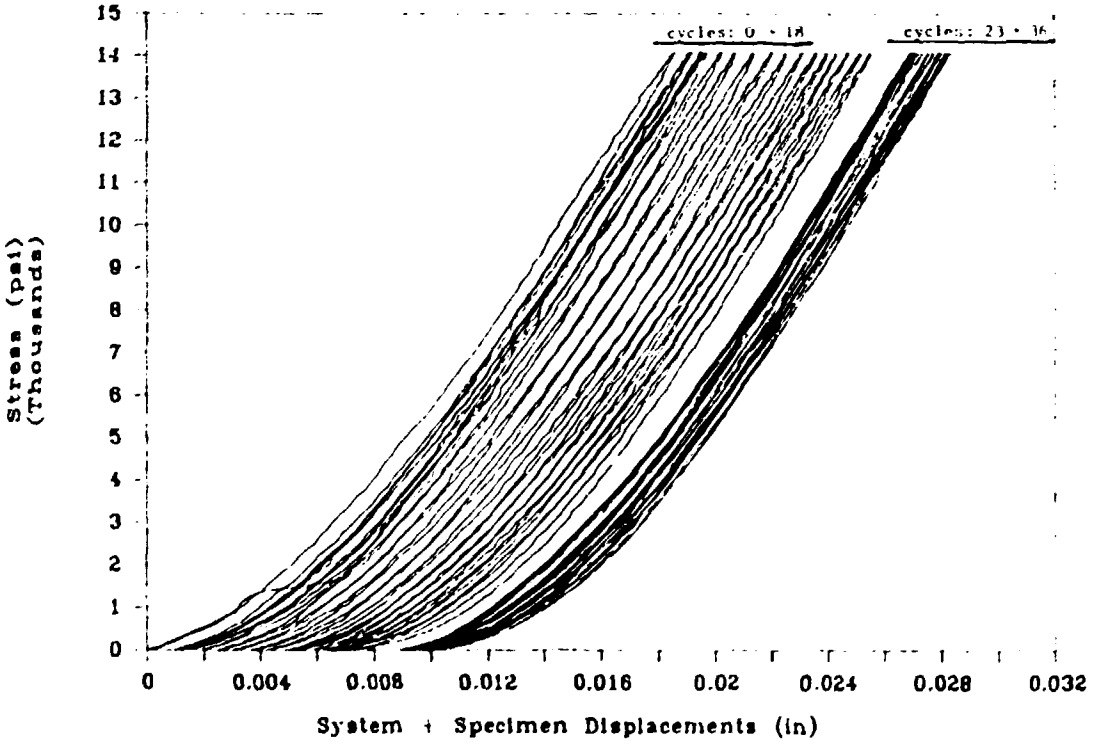

Figure 20 - Cyclic Mechanical Test Up to 75% of Monotonic Strength, at 1500°F, for Material A

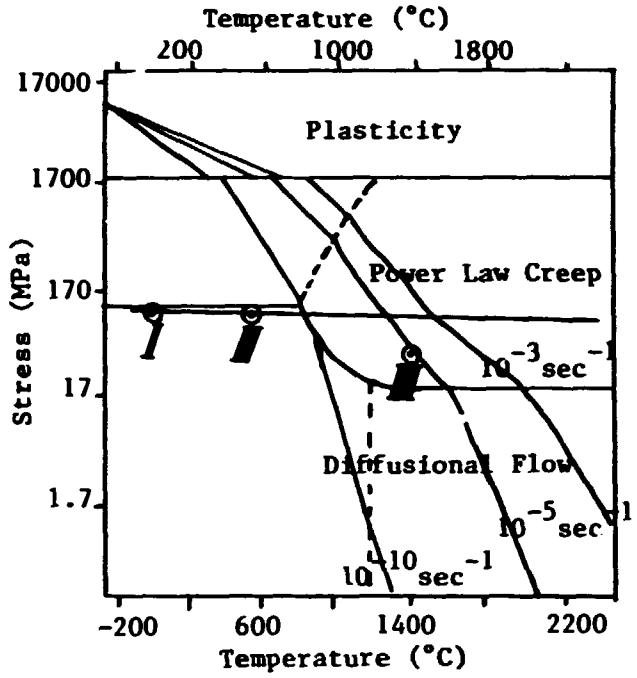

Figure 21 - Stress-Temperature Map of Cr_2O_3 with a Grain Size of 10 μm (from Ref. 42), with Comparison to Material B

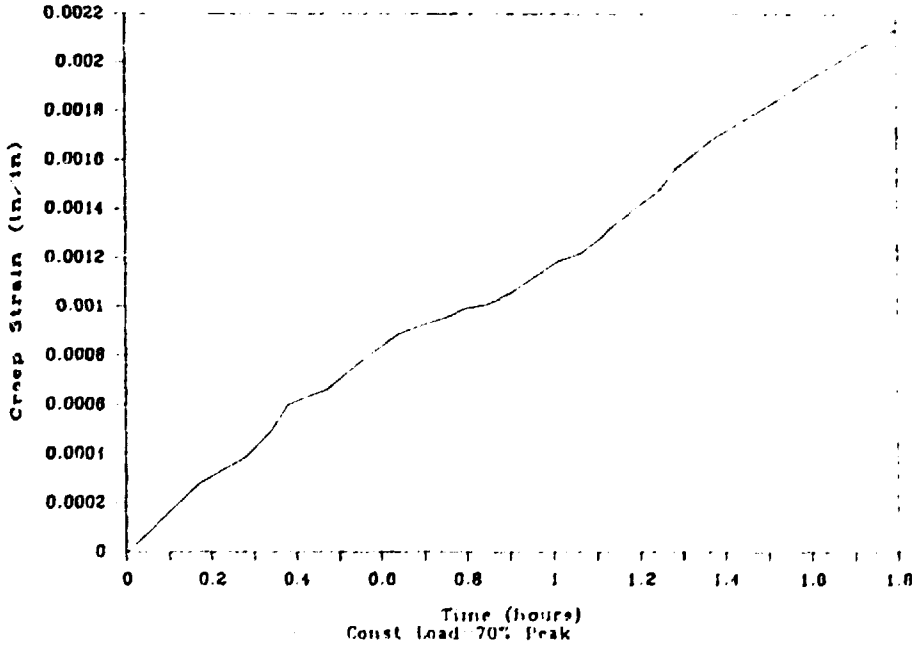

Figure 22 - Short-Term Creep Tests at 70% of Monotonic Strength, at 1500°F, on Material A

Constant Load, Varying Temperature Tests

In this section constant load tests accompanied with constant predetermined, or monotonically increasing temperature levels are examined. Comparison with published deformation maps is made.

A stress temperature-map for Cr_2O_3 with a grain size of 10 μm is extracted from Ref. 42, and the features relevant to the present discussion are shown in Fig. 21. It is interesting to study, using this map, the behavior of tested sintered high-chromia (Material B), keeping in mind that there is 18% MgO in Material B, and that the grain size and porosity are different. Two points are used to define the brittle fracture line on the map, and they are: point I at room temperature: 23°C (73°F) and a strength of 133 Mpa (19300 psi) and point II at 538°C (1000°F) and a strength of 113 Mpa (16461 psi). Point III is then added to the map, at 1346°C (2400°F), and a strength of 45 MPa, (6500 psi). Point I and II clearly are outside the creep regime, while point III falls in the power law creep region, below the brittle fracture line defined by points I and II. The stress-temperature map predicts a strain rate of 10^{-5} sec^{-1}. The test strain rate was 4×10^{-3} sec^{-1} which is close enough, since the map is for pure Cr_2O_3, and a different porosity. This seems to indicate that the inelastic strains present at higher temperatures may be due to creep.

Creep data available in the literature for sintered high-chromia and high-alumina refractories is generally for small creep load levels (usually less than 1000 psi). To be able to interpret the results of current tests, short-term creep tests at high loads (in the range of 75% of the peak strength) are needed. Preliminary creep tests at 1500°F, and 70% of the monotonic strength showed that the contribution of the short-term creep deformation (during the 5 to 10 minutes duration of monotonic tests) to the total deformation is negligible (Fig. 22) at temperatures below 1/2 T_m. Tests at higher temperatures are being carried out, and effect of creep is expected to be determined, especially in the zone above the transition temperature.

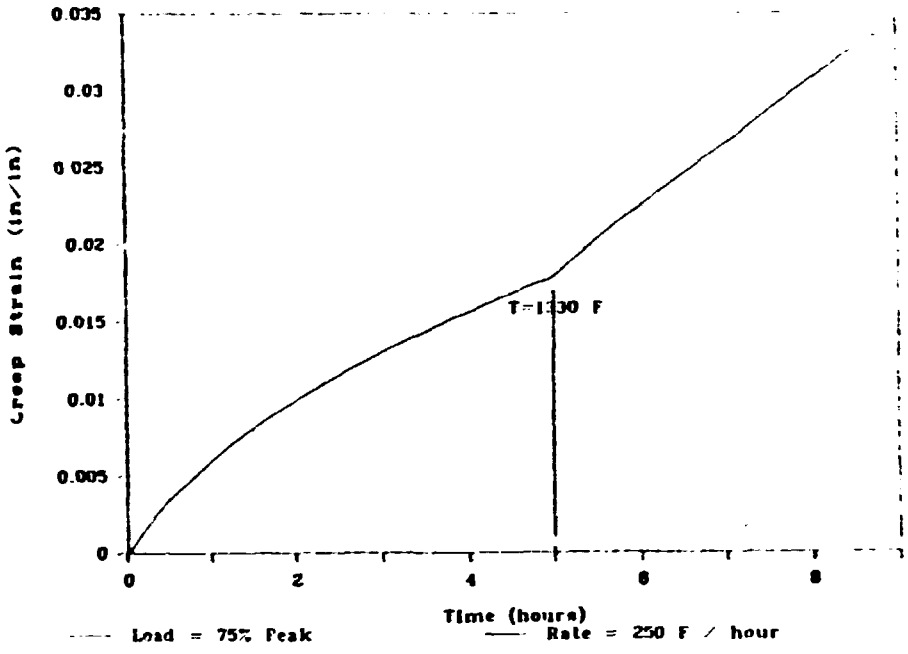

Figure 23 - Creep Strain Under 75% of Monotonic strength, Under an Increasing Temperature at a Rate of 250°F

Constant load, increasing temperature tests were also conducted on sintered refractories. Figure 23 shows the strain after application of the load, vs. time, for Material A, under 75% of the monotonic strength, and a heat-up rate of 250°F/hour. It appears that the creep strain rate at low temperatures reduces with time until a transition temperature level. At high temperatures, above this new transition temperature (determined to be 1330°F for this combination of load and heat-up rate), the creep strain rate reaches a steady state value. This is an interesting result, and could prove useful in the design of refractory linings.

ENVIRONMENTAL EFFECTS

Effect of Partial Oxygen Pressure

The effect of partial oxygen pressure on the behavior of as-manufactured materials is examined first. The specimen is tested in a muffle tube in which the gas environment is controlled. Helium gas is first used to flush the system and drive the air out. A mixture of

95% N_2 - 5% NH_3 is then used to achieve a low P_{O_2}. The P_{O_2} value inside the muffle tube has been calibrated by measuring the voltage across a zirconia tube with one of its ends in the output gas, and the second end in air. The P_{O_2} is then calculated using the Nernst equation:

$$P_{O_2} = (P_{O_2})_{ref} \, e^{-4fV/RT} \qquad (7)$$

where T is the temperature, $(P_{O_2})_{ref}$ is 0.21 atm for air, V is the measured voltage, and R and f are constants. Partial oxygen pressures of 10^{-15} atm were measured using the gas mixture described above (5% NH_3/N_2).

During testing a P_{O_2} value of 10^{-8} atm was used to represent the gasifiers' environment for sintered as-manufactured refractories. The initial elastic modulus in low P_{O_2} environment was compared to the one in air. The low P_{O_2} atmosphere used was found not to affect the behavior of Material A. For Material B an effect was observed at higher temperatures. Figure 24 shows the ratio of the initial elastic modulus in low P_{O_2} environment to the one in air for different temperature levels, for Material B. At low temperatures the low P_{O_2} atmosphere does not have any effect. But at 2200°F, under a P_{O_2} of 10^{-8} atm, a 35% increase in modulus is consistently observed for Material B. This might suggest that at high temperatures, under reducing atmosphere, a subtle change of phase of Material B is happening. It is difficult to observe the change of phase, because it is expected that it reverses when the specimen is brought back to air (i.e. oxidizing atmosphere).

Effect of Slag-Impregnation

Slag-impregnated specimens were tested under both air and low P_{O_2} atmospheres. The purpose of duplicating the same thermomechanical loading conditions, in two different gas environments, is to be able to separate the slag effect from the P_{O_2} effect, for modeling purposes. This section describes testing of slag-impregnated specimens in air. As discussed previously, slag-impregnated specimens show an increased strength at room temperature, but the strength at higher temperature drops below the value corresponding to that of

as-manufactured strength. Figure 25 shows the stress-strain curves for as-manufactured and slag-impregnated material A at 75°F and 2400°F. The strength at 2400°F is below the strength of the as-manufactured specimen. At room temperature the slag-impregnated material fails in a brittle manner. As temperature increases, a ductile post-peak behavior is observed, such as the stress-strain curve at 2400°F in Fig. 25. The rate of decrease in the initial slope of the stress-strain curve is also lower for the slag-impregnated specimens than that for as-manufactured ones. As-manufactured specimens exhibit a linear-elastic behavior initially at all temperature ranges while slag-impregnated specimens deviate from the initial elastic behavior at high temperatures. Similar work has been completed on Material B in air atmosphere. The behavior of slag-impregnated Material B is similar to that of slag-impregnated Material A.

Combined Effect of Slag and P_{O_2}

Finally, slag-impregnated materials tested under controlled P_{O_2} atmosphere are studied. The low P_{O_2} atmosphere did not have much effect on the behavior of slag-impregnated Material A. But as in the case of as-manufactured specimens, the low P_{O_2} atmosphere had an effect on slag-impregnated Material B at high temperature. A substantial strength decrease is observed for slag-impregnated Material B at 2200°F and a P_{O_2} of 10^{-8} atm. This is shown in Fig. 26. This result still needs to be further verified.

SYSTEM ANALYSIS

The developed data represents a substantial and complemetary contribution to the existing data on the thermomechanical behavior of materials used in refractory linings. Previous work at MIT[12,13,19], has led to the development of extensive predictive capabilities for the analysis of refractory lining systems. The main drawback to the use of this capability for predictive analysis has been the lack of reliable material data.

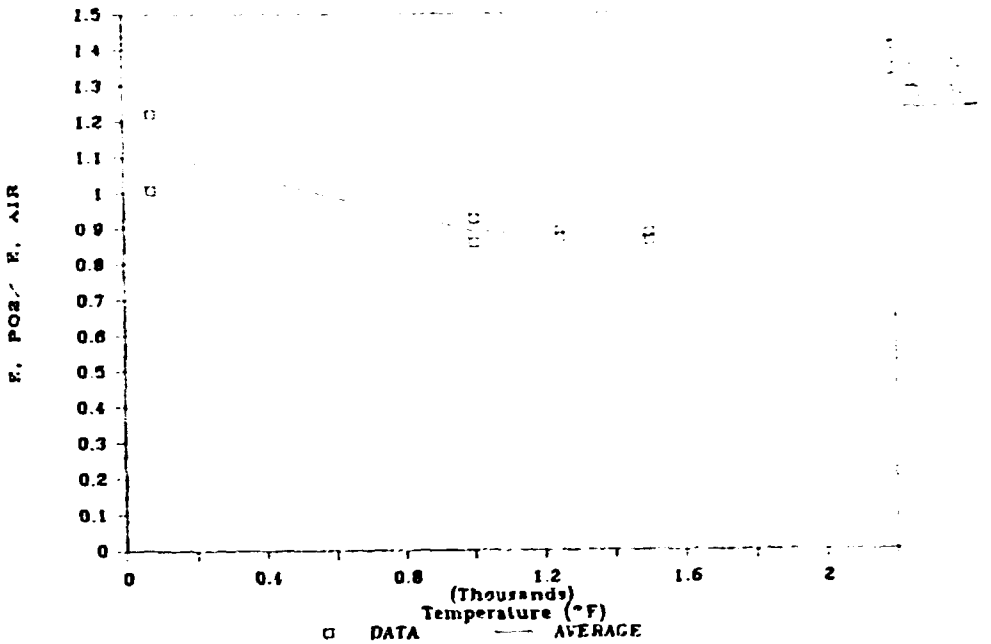

Figure 24 - Ratio of Initial Stiffness in a P_{O_2} of 10^{-8} atm to Initial Stiffness in Air, for Material B

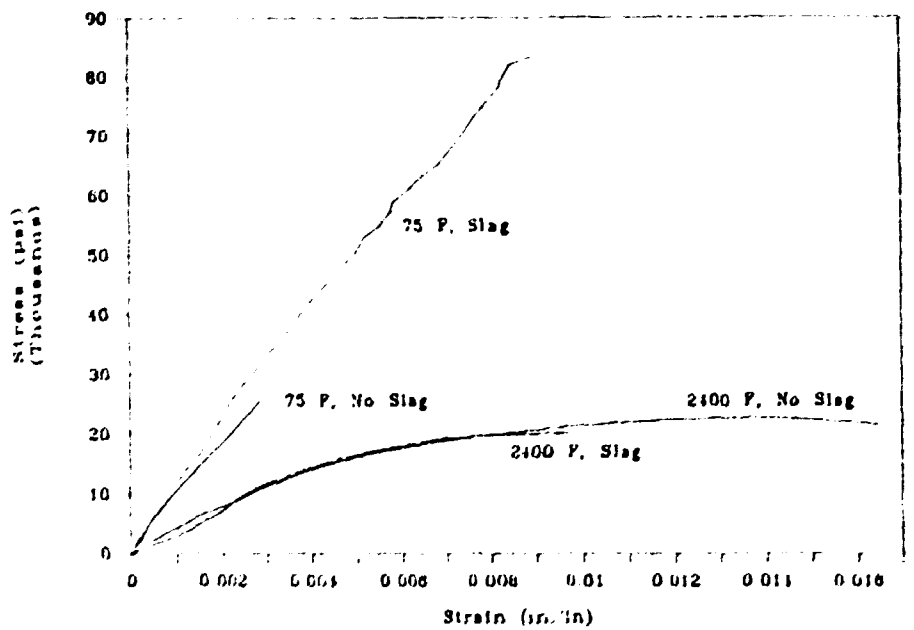

Figure 25 - Stress Strain Curves for Slag-Impregnated Material A at 75°F and 2400°F, in Air

The newly acquired data described in this paper, therefore, constitutes an essential part of this predictive capability, on the basis of which calibration of the model and refinement of the analysis for more accurate predictions will be possible.

SUMMARY, CONCLUSIONS AND FUTURE WORK

SUMMARY AND CONCLUSIONS

A high temperature testing facility, including a furnace, retort system, and a fully computerized automatic data acquisition and control system was developed. Various techniques were studied and further developed for preparing as manufactured and slag-impregnated refractory specimens.

A total of 148 tests (excluding the tests made for the trial purposes and those that were not successful) were performed on selected refractory materials. Compressive stress-strain response of the materials in room and elevated temperatures up to 2400°F was obtained. Deformation and failure mechanism, short-term creep

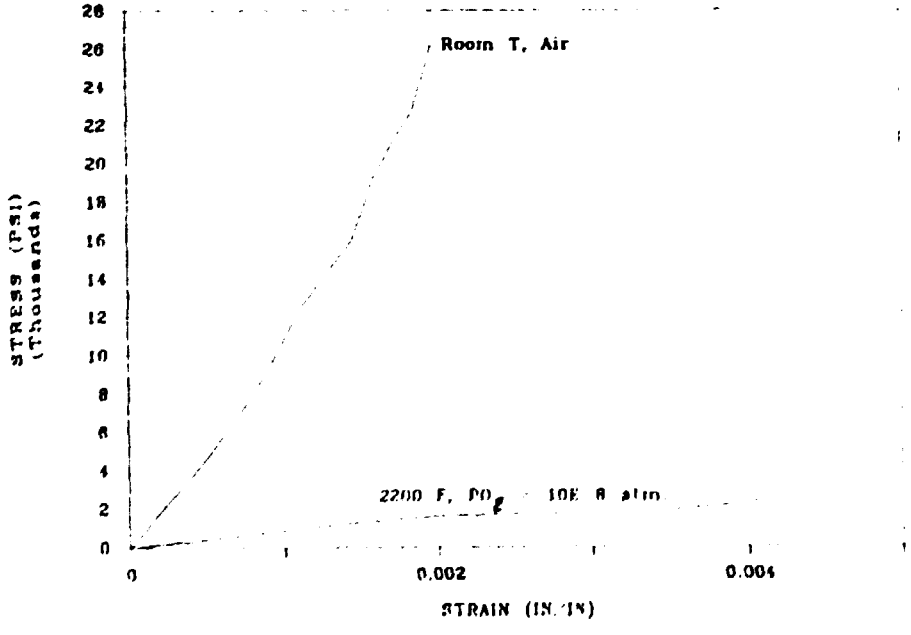

Figure 26 - Stress Strain Curves for Slag-Impregnated Material B, Under Different Temperatures and P_{O_2} Combinations

response, the effects P_{O_2} and slag impregnation were studied. The following are the highlights of the findings from this work at the present time.

(1) Essentially two deformation mechanisms were identified: (a) low temperature mechanism for temperature below approximately 1/2 T_m (T_m is the melting temperature of the material) where a linear elastic behavior with a brittle failure was obtained and (b) high temperature mechanism for temperatures above approximately 1/2 T_m where a non-linear inelastic deformation response with a ductile failure was obtained.

(2) Strength (maximum stress levels on the stress-strain curve) decreased with temperature. The strength for temperatures below a transition level (approximately equal to 1/2 T_m), is found to be decreasing proportionally to $T^{1/2}$, and for temperatures above the transition level the strength appears to be decreasing proportionally to T.

(3) Peak strains associated with the peak stress levels on the stress-strain curve showed higher rates of increase with temperatures above approximately 1/2 T_m.

(4) Initial Young's modulus of the materials showed higher rates of decrease with temperatures above approximately 1/2 T_m.

(5) The contribution of short-term creep deformation (approximately 10 minutes) under high stress (approximately 70 to 75 percent of the peak stress) to the total deformation was found to be negligible at temperatures below 1/2 T_m. Short term creep tests have to be run at higher temperatures (above 1/2 Tm).

(6) P_{O_2} values of approximately 10^{-8} atm representative of a coal gasifier environment seemed to have little effect on the thermomechanical material behavior of high-alumina sintered refractory, but affected the behavior of high chromia refractory.

(7) For temperature levels up to below 1/2 T_m the specimens impregnated with the western acid slag showed increased strength and

stiffness compared to as-manufactured specimens. However, in the same range of temperatures, an increased rate of stiffness degradation with temperature was observed in the slag-impregnated specimens in comparison to the as-manufactured ones. Combination of higher temperatures and reducing atmospheres seem to have a critical effect on the strength of refractories.

(8) For temperatures below 1/2 T_m, the ratio of the strength of hot-pressed material to the one of sintered material with similar chemical composition is a constant. This constant is related to the maximum aggregate size in the material.

(9) Our experience from this experimental program indicates that adoption of a standard specimen preparation technique is necessary to get consistent and representative data. Variability in material data may occur due to differences in the methods of preparing the specimen, the specific location of the specimen from a block, and the coring direction of the specimen in a block from which the specimen was extracted.

The test program conducted led to the development and evaluation of new material data which provides insight into the understanding of the thermomechanical behavior of refractories. The quantitative information developed constitutes a part of the data base necessary for use in the development of predictive design methods.

FUTURE WORK

Future work is needed to focus on the thermomechanical behavior of hot-pressed and fused-cast refractories. Additional testing will concentrate on the behavior of as-manufactured and slag-impregnated Material C, and as manufactured Material E. Obtained results will be compared with the tests performed on Materials A, B and D. Experience we have gained from the experimental work will be utilized to produce most relevant and comprehensive set of data. The new data will be added to our current material database. Additional analytical

parameter studies on refractory linings will be performed to include the new materials tested.

ACKNOWLEDGEMENTS

The work described in this paper was sponsored by the U. S. Department of Energy, Advanced Research and Technology Development, Fossil Energy Materials Program.

The authors would like to express their appreciation to Mr. R. A. Bradley, Dr. R. R. Judkins, and Dr. P. T. Carlson of Oak Ridge National Laboratory for their support and many useful comments. Thanks are due to Prof. A. S. Argon of the Massachusetts Inscitute of Technology and Prof. M. P. Ashby of Cambridge University for stimulating and helpful discussions.

Thanks are also due to Dr. L. Trostel and Mesrs. T. Butkus and M. E. Washburn of Norton Company for their helpful suggestions. The authors appreciate the assistance provided by Mesrs. C. Taylor, and S. Martin of Norton Company in specimen preparation and P. Moon of M.I.T. in experimentation.

REFERENCES

1. Gilchrist, J.D. (1977), Fuels, Furnaces and Refractories, Pergamon Press, Oxford, England.

2. Duffy, J.I. (1980), Refractory Materials, Noyes Data Corporation, Park Ridge, N.J.

3. Shaw, K. (1972), Refractories and Their Uses, John Wiley & Sons, New York, N.Y.

4. Norton, F. H. (1968), Refractories, McGraw-Hill, N.Y.

5. Budnikov, P. P. (1964), The Technology of Ceramics and Refractories, The MIT Press, Cambridge, MA.

6. ISI Publication 116, (1968), Blast-Furnace Refractories, Iron and Steel Institute, London, England.

7. Babcock & Wilcox Experimental Report (initial report, not formally published).

8. Air Force Materials Lab (1963), Refractory Ceramics of Interest in Aerospace Structural Applications - A Materials Selection Handbook, Report No. ASD-TRD-63-4102, Wright-Patterson Air Force Base, Ohio.

9. Bakker, W. T., and Stringer, J. (1981), "Materials for Coal Gasification Combined Cycle Power Plants," Sixth Annual Conference on Material for Coal Conversion and Ultilization, October.

10. Bakker, W. T., Greenberg, S., Trondt, M., and Gerhardus, U. (1984), "Refractory Practice in Slagging Gasifiers," American Ceramic Society Bulletin, Vol. 63, No. 7.

11. Buyukozturk, O., and Tseng, Tsi-Ming (1982), "Thermomechanical Behavior of Refractory Linings," Journal of the American Ceramic Society, Vol. 65, No. 6.

12. Chen, E. S., and Buyukozturk, O. (1985), "Methodology for Thermomechanical Analysis of Brittle Systems," American Ceramic Society Bulletin, Refractories Issue.

13. Chen, E. S., and Buyukozturk, O. (1985), "Thermomechanical Behavior of Refractory Linings in Slagging Gasifiers," American Ceramic Society Bulletin, Refractories Issue.

14. Crowley, M. S. (1984), "Refractory Usage in the Process Industries," Standard Oil Campany, Indiana.

15. Kennedy, C. R. (1979), "Refractories for Application in Slagging Gasifiers," Fourth Annual Conference on Materials for Coal Conversion and Utilization, October.

16. Crowley, M. S., and Johnson, R. C. (1972), "Guidelines for Installing and Drying Refractory Concrete Linings in Petroleum and Petrochemical Units", American Ceramic Society Bulletin, Vol. 51, No. 3.

17. Hugget, L. G. (1966), "Lining of Secondary Reformers", Proc. Mat. Tech. Symposium, Pergamon Press.

18. McGannon, E. (1964), "The Making, Shaping and Treating of Steel," United States Steel Corporation, Eighth Edition.

19. Chen, E. S., and Buyukozturk, O. (1985), "Methodology for Thermo-mechanical Analysis of Brittle Systems," American Ceramic Society Bulletin, Refractories Issue, July.

20. Chen, E. S. (1984), "Behavior of Refractory Linings for Slagging Gasifiers," Ph.D. Thesis, Massachusetts Institute of Technology.

21. ACI Publication SP 74 (1982), Monolithic Refractories, Lankard, D. R., Editor, American Concrete Institute, Detroit, Michigan.

22. Bandyopahyay, G., Chen, J., Kennedy, C. R., and Diereks, D. R. (1983), "Thermal-Shock Damage of Refractories for Application in Slagging Coal Gasifiers," Journal of Materials for Energy Systems, Vol. 4, No. 4, March.

23. Bonar, J. A., Kennedy, C. R., and Swaroop, R. G. (1980), "Coal-Ash Slag Attack and Corrosion of Refractories," American Ceramic Society Bulletin, Vol. 59, 1980.

24. Bray, D. J., Smyth, J. R., and McGee, T. D. (1980), "Creep of 90% Al_2O_3 Refractory Concrete," American Ceramic Society Bulletin, Vol. 63, No. 7.

25. Buyukozturk, O. and Tseng, Tsi-Ming (1983), "Heat Conduction through Layered Refractory Linings," Journal of Engineering Mechanics, Vol. 109, No. 4.

26. Cooper, A. R. (1981), "Kinetics of Refractory Corrosion", Ceramic Engineering and Science Proceedings, Published by American Ceramic Society, Vol. 2, No. 11-12.

27. Crowley, M. S. (1975), "Refractory Problems in Coal Gasification Reactors," Ceramic Society Bulletin, Vol. 51, No. 12.

28. Greenberg, S. et al. (1984), "The Corrosion of Ceramic Refractories Exposed to Synthetic Coal Slags by Means of the Rotating-Cylinder Technique: An Interim Report," Argonne National Laboratory, Argonne, Illinois.

29. Greenberg, S., and Peoppel, R. B. (1985), "The Corrosion of Ceramic Refractories Exposed to a Synthetic Coal Slag By Means of the Rotating-Drum Technique," Argonne National Laboratory, Argonne, Illinois.

30. Kennedy, C. R. (1980), "Compatability of Water-Cooled Refractories with a Basic Coal-Ash Slag at 1500°C," Journal of Materials for Energy Systems, Vol. 2, September.

31. Kennedy, C. R. (1981), "Coal Slag-Refractory Compatability Studies: Progress to Date," American Ceramic Society Proceedings, Vol. 2, 1981.

32. Kennedy, C. R. (1981), "Compapatability of Water-Cooled Chromia Containing Refractories with a High Iron Oxide Acidic Coal Ash Slag at 1575°C," Journal of Materials for Energy Systems, Vol. 3, No. 3.

33. Washburn, M. E. (1982), "Rotating Sample Slag Test for Refractories," Seventh Annual Conference on Materials for Coal Conversion and Utilization, November.

34. Wygant, J. F., and Crowley, M. S. (1964), "Designing Monolithic Refractory Vessel Linings," American Ceramic Society Bulletin, Vol. 43, No. 3.

35. Easler, T. E. et al. (1985), "Influence of Oxidizing and Reducing Environments on Coal-Slag-Induced Corrosion of Silicon Carbide Ceramics," Argonne National Laboratory, Argonne, Illinois.

36. Lim, K. H. (1983), "Investigations and Design Considerations for the Refractory Lining of Coal Gasifiers", Interceramics, Vol. 33.

37. Robbins, C. R., and Mauer, F. A. (1981), "Chemical Degradation of Castable Refractories in Coal Gasification Process Environments," Journal of Materials for Energy Systems, Vol. 3.

38. Washburn, M. E. (1983), "Comparative Rotating Sample Slag Test," Presented on April 25, 1983 at the Ceramic Society 85th Annual Meeting, Chicago, IL.

39. Megusar. J., Argon, A. S., and Grant, N.J. (1979), "Plastic Flow and Fracture in $Pd_{80}Si_{20}$ near T_g," Materials Science and Engineering, 38, pp. 63-72.

40. Kingery, W. D., Bowen, H. U., and Uhlmann, D. R. (1976), Introduction to Ceramics, John Wiley & Sons, New York, N.Y.

41. Evans, A. G., and Langdon, T. G. (1976), Structural Ceramics, Progress in Materials Science, Vol. 21, pp. 171-441.

42. Frost, H. J., and Ashby, M. F. (1982), Deformation Mechansism Maps, Pergamon Press, Elmsford, N.Y.

43. Kotsovos, M. D. (1983), "Effect of Testing Techniques on the Post-Ultimate Behavior of Concrete in Compression", Materiaux et Constructions, Vol. 16, No. 91, pp. 3-12.

MATERIALS DEVELOPMENT FOR SOLID OXIDE OXYGEN PRODUCTION UNIT

T. E. Easler and R. B. Poeppel

Materials and Components Technology Division
Argonne National Laboratory
9700 South Cass Avenue
Argonne, Illinois 60439

ABSTRACT

The implementation of a solid oxide oxygen pump in coal gasification systems is believed to have the potential for significantly reducing the cost of oxygen generation for the gasification process. The solid oxide oxygen pump concept is based on the oxygen-ion conducting behavior of zirconia ceramics. The approach being taken to fabricate the oxygen pump involves fabrication of thin multilayer structures of ceramic electrode and electrolyte materials by the tape casting process. It is desired to make the laminated structures as thin as possible to minimize internal power losses which are the result of the high resistances of the individual ceramic oxide layers. Both the air and oxygen electrodes are made of strontium-doped lanthanum manganite. The particular ceramic electrolyte under development in this project is zirconia doped with 8 mol % Y_2O_3. This study is particularly concerned with determining the types of failure modes that may be associated with the very thin ceramic layers. The fabrication of the layers, and the initial failure mode identification tests, are described in this paper.

INTRODUCTION

The development and implementation of a solid oxide ceramic oxygen pump in coal gasification systems is believed to have the potential for reducing cost, when compared to other oxygen production systems such as cryogenic pumping. However, the economic success of the solid oxide oxygen pump is dependent on the reduction of internal power losses caused by high internal resistances in the individual ceramic oxide

components. For a given component, in particular the electrolyte, the power loss is directly proportional to the electrical resistance, which in turn is proportional to the resistivity of the material multiplied by the thickness of the component.

The electrolyte may be the single most critical material in the solid oxide oxygen pump. In addition to being a conduit for oxygen ions, the electrolyte must prevent the intermixing of the depleted air and enriched oxygen streams. Yttria-stabilized zirconia has been chosen for the electrolyte because it has the best combination of chemical stability, low resistivity, and low parasitic losses of all known oxygen ion conductors. The internal resistance of the electrolyte may be reduced by reducing its thickness. The minimum practical thickness, however, is determined by the mechanical integrity of the electrolyte.

The results discussed in this paper include the characterization of the ceramic powders used for the electrode and electrolyte, the development of a tape casting slip formulation, and characterization of the tapes. In addition, the initial results of the first failure mode identification test, which was the clamping bend test, are discussed.

CERAMIC LAYER FABRICATION

TAPE CASTING

Tape casting is a fabrication process which is used extensively in the ceramic industry for manufacturing substrates, capacitors, and microelectronics. It is the technique that has been chosen for forming the thin ceramic layers required for the oxygen pump. Tape casting involves incorporating a ceramic powder of the desired composition into a slurry or slip which can be poured out onto a suitable substrate, such as glass or a Teflon surface, and spread into a thin layer with a knife-edge or doctor blade. The slip formulation, including the choice of binder, is critical to the process. Many types of binder systems are commercially available. The binders are typically thermoplastic resins or plastics, or cellulosic materials. Each type of binder is compatible with different types of solvents, and the choice of binder system must be made with consideration to its compatibility with the ceramic powder

characteristics, and the properties required of the tapes that will be derived from it. In addition to the binder and solvent, other components of the slip include a dispersant to deflocculate the ceramic particles, and a plasticizer to change the glass transition temperature of the binder. In some systems, a lubricant or release agent is incorporated to facilitate release of the tape from the substrate after the solvent has evaporated.

CERAMIC POWDER CHARACTERIZATION

Several characteristics of the ceramic electrode and electrolyte powders must be known in order to successfully develop tape casting slips for the fabrication not only of single layers of these components, but also of successively cast layers for single oxygen-pump cells comprising air-electrode/electrolyte/oxygen-electrode. One of the most important characteristics is the particle size distribution of the powder. The range of particle sizes and their number distribution are directly related to the surface area of the powder, which dictates the amounts of binder and other organic slip components required. The particle size distributions for the electrolyte and electrode powders are given in Fig. 1. The zirconia electrolyte material has an average grain size of about 5 μm. Very few grains are larger than about 20 μm in size, and a sizable volume fraction (~30 vol %) is finer than 1 μm The lanthanum manganite electrode powder is considerably different. An average grain size of approximately 35 μm is observed, with a relatively small volume fraction less than 5 μm. Because of the differences in these distributions, the surface area of the zirconia powder is substantially larger than that of the lanthanum manganite powder. As a result, a greater amount of binder is required for the zirconia tape casting slip.

When necessary, particle size distributions can be altered to some extent by milling the powder to reduce particle sizes, or by calcining the powder to increase the particle sizes as a result of agglomeration. When the sensitivity to changes in organic components is not sufficient to produce the desired tape characteristics, alterations in the ceramic powder particle size distributions are another means of effecting changes.

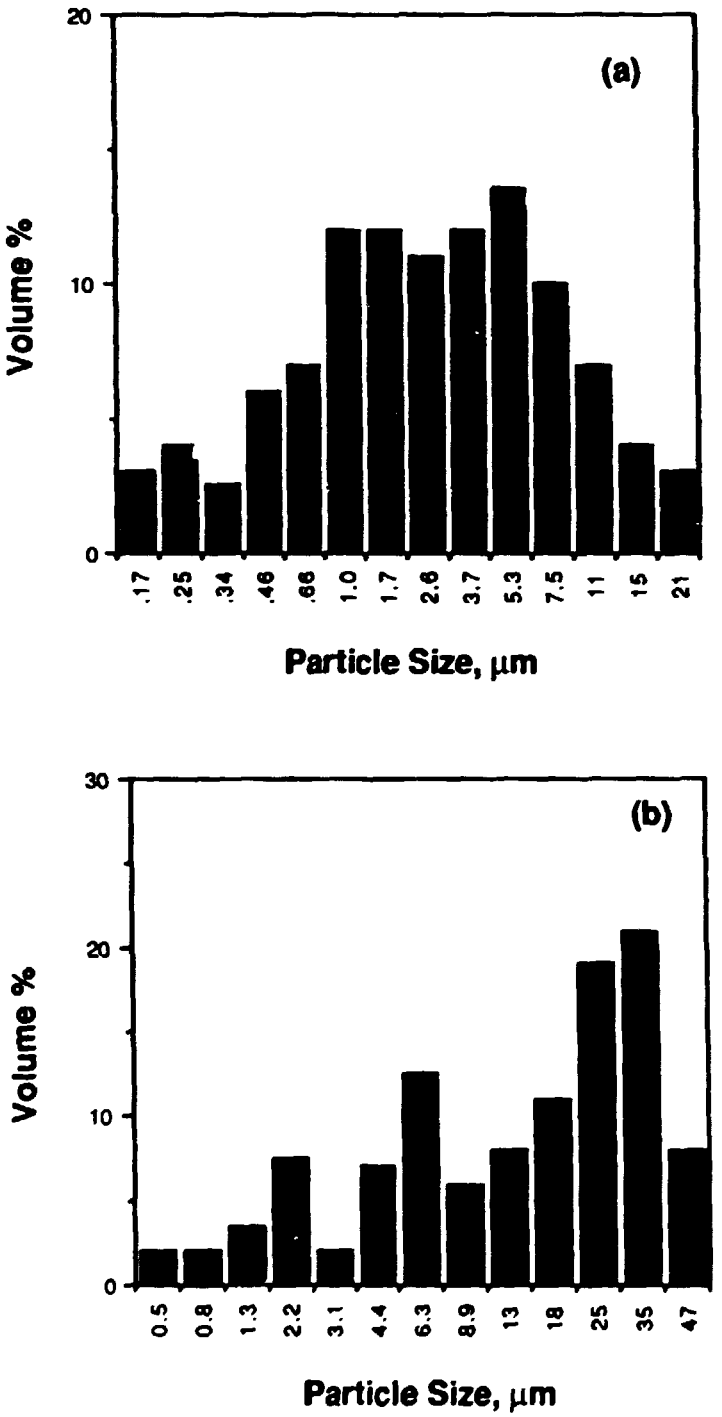

Fig. 1. Particle Size Distributions for (a) the Zirconia Electrolyte Powder and (b) the Lanthanum Manganite Electrode Powder.

TAPE-CASTING SLIP FORMULATION

The slip formula used for fabrication of the electrolyte tapes is given in Table 1. The binder system is a thermoplastic acrylic ester resin from Rohm and Haas Company, designated Acryloid B-98. This binder is used with a toluene/ethanol solvent system and a plasticizer designated PX316 (manufactured by USX Corporation). The lubricant and release agent is UCON 50-HB-2000 from Union Carbide. Solsperse 9000 dispersant from ICI Americas was used to deflocculate the slip. Yttria-stabilized zirconia (8 mol % Y_2O_3) from Toyo Soda Company, designated TZ-8Y, has given the best sintering results to date. This slip is cast on a glass substrate and dries relatively quickly, such that the tapes may be stripped from the glass after about 20 min. The flexibility of the tapes can be altered by changing the amount of plasticizer in the slip.

The slip formula for the electrode tapes is given in Table 2.

CHARACTERIZATION OF TAPES

After the tapes are stripped from the substrate, disk-shaped specimens are cut with a punch and sintered to allow the determination of firing shrinkage and density. The unfired specimens are approximately 1.5 in. in diameter and 0.004 in. thick. Total firing shrinkages of about 28 to 30% were observed. The densities of the electrolyte specimens were at least 97% of theoretical. In addition to measuring the total shrinkage of the disks, a dilatometer was used to investigate the shrinkage behavior as a function of temperature. Such a shrinkage profile is illustrated in Fig. 2. Two regions of shrinkage behavior are exhibited: that which occurs at low temperatures (200 to 300°C) when the organic components burn out, and that which occurs during high-temperature sintering. Generally, a burnout shrinkage in the range of 2 to 4% is observed when the amount of binder is at its optimal level. Excess binder results in greater shrinkages at low temperature, which may be difficult to tolerate in multilayer systems. The amount of shrinkage during sintering is dictated by the degree of densification of the sample; when densification ceases, shrinkage no longer occurs.

Table 1. Electrolyte Tape Casting Slip Formulation

Supplier	Component	Amount, g
Rohm and Haas	B-98 Binder	3.4
J. T. Baker	Toluene Solvent	18.4
J. T. Baker	Ethanol Solvent	12.2
USX Corp.	PX316 Plasticizer	1.1
Union Carbide	UCON Lubricant	2.7
ICI Americas	Solsperse 9000 Dispersant	1.0
Toyo Soda	TZ-8Y Zirconia	50.0

Table 2. Electrode Tape Casting Slip Formulation

Supplier	Component	Amount, g
Rohm and Haas	B-98 Binder	3.25
J. T. Baker	Xylene Solvent	17.8
J. T. Baker	Ethanol Solvent	9.5
USX Corp.	PX316 Plasticizer	1.0
Union Carbide	UCON Lubricant	2.0
ICI Americas	Solsperse 9000 Dispersant	1.6
Anderson Tech.	$(La_{0.8}Sr_{0.2})MnO_3$	35.0

FAILURE MODE IDENTIFICATION

Several anticipated failure modes have been identified for study. The disk-shaped specimens described above will be used to test the effects of various internal and external stress fields on the failure behavior of both single-layer and multilayer samples. One of the anticipated failure modes for thin ceramic layers is related to stresses that may arise when the membranes are clamped between manifolding surfaces. Although the ceramic layer and the clamping surfaces should be flat, typically some curvature is expected. The first type of failure mode investigation that was carried out was a clamping bend test, which measures the ability of the electrolyte to conform to the shape of a clamping surface. For this test, curved electrolyte disks were compressed between flat clamping surfaces and loaded to failure.

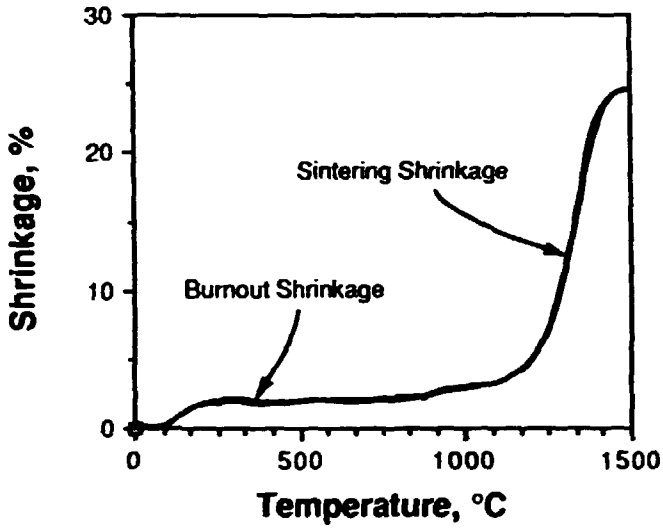

Fig. 2. Firing Shrinkage Profile for a Typical Zirconia Electrolyte Tape.

Curved specimens were obtained by placing the disks on zirconia setter plates during firing. Since tape-cast specimens frequently do not fire flat without some type of restraint during firing, the lack of restraint on these samples allowed them to warp slightly, such that varying amounts of curvature resulted.

The test data are presented in Fig. 3, which is a plot of the load at failure as a function of the degree of nonlinearity of the disks. The values on the x-axis were obtained by measuring the gap between the loading surfaces at the point where they first came into contact with the specimen. This value is largest for the specimens with the greatest degree of curvature. A trend of increasing load at failure was observed with increasing flatness of the disks. The equation on the plot corresponds to a logarithmic fit of the data, which yields a coefficient of determination of 82%. These data are being analyzed, with consideration given to existing theories for stress distributions in cylindrical plates and shells. A micrograph of a typical fracture surface is shown in Fig. 4 to illustrate the microstructure of the electrolyte material.

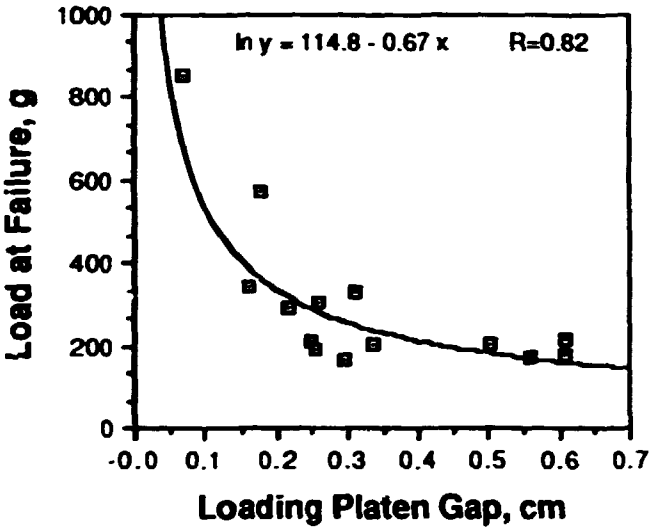

Fig. 3. Load at Failure Determined by Clamping Bend Test, as a Function of the Loading Platen Gap.

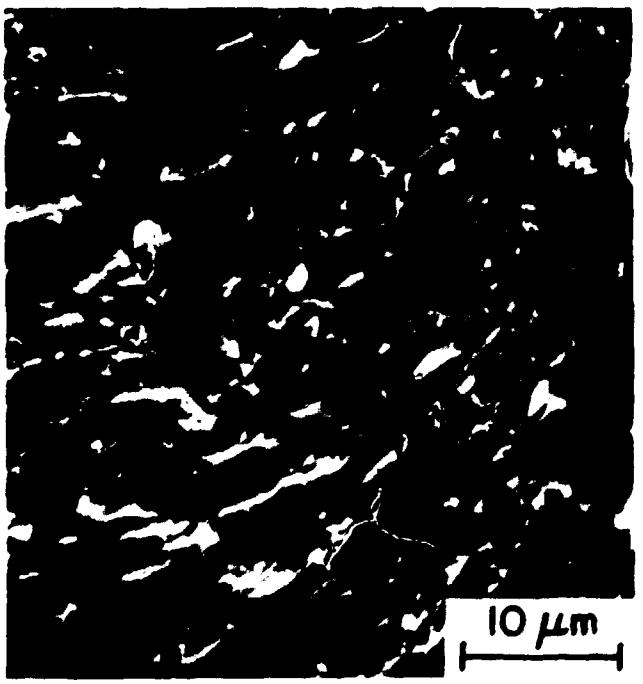

Fig. 4. Micrograph of Typical Fracture Surface of the Zirconia Electrolyte Material. Average grain size about 5 μm.

SUMMARY

The first months of effort on this project have yielded the following accomplishments

1. Characterization of the electrolyte and electrode ceramic powders was completed. Powder analyses included particle size distributions, surface areas, and powder morphology.
2. Tape casting slips were developed with the aid of the results of the powder characterization analyses. Single layers of electrolyte and electrode tapes were successfully cast.
3. Specimens were cut from the electrolyte and electrode tapes, and fired densities and shrinkages were determined.
4. Firing shrinkage rates were determined by dilatometry to investigate firing shrinkage behavior as a function of temperature. Values for the binder burnout shrinkage and sintering shrinkage components of the total tape shrinkages were obtained.
5. On the basis of the firing shrinkage results described above, slip formulations were adjusted to allow multilayer tape casting of electrode/electrolyte/electrode composites.
6. The first of six failure mode identification tests was carried out. This was the clamping bend test, which involved the investigation of the dependence of load at failure on the degree of curvature of thin layers of the electrolyte material. Higher failure loads were observed for specimens with smaller amounts of curvature.

ACKNOWLEDGMENTS

The work was supported by the U. S. Department of Energy, Office of Fossil Energy, Morgantown Energy Technology Center, and Oak Ridge Operations Office as part of the Surface Coal Gasification Materials Development Program (FTP/A 49677), under Contract W-31-109-Eng-38.

FIBER-REINFORCED COMPOSITE HOT-GAS FILTERS

D. P. Stinton, R. A. Lowden and R. Chang*

Metals and Ceramics Division
Oak Ridge National Laboratory
P. O. Box X
Oak Ridge, Tennessee 37831

ABSTRACT

A chemical vapor deposition process was developed for the fabrication of high-temperature particulate filters. Fibrous materials such as Nicalon (SiC) felt and aluminosilicate papers were used as the filter material. Preliminary evaluation of filter specimens fabricated from Nicalon revealed extremely encouraging results. Cleanable filters with collection efficiencies of >99.9% were recorded for both PFBC flyash and gasifier char.

INTRODUCTION

The Department of Energy Office of Fossil Energy is providing support for the development of several technologies which will utilize coal in an environmentally acceptable manner. Several of the technologies being developed, such as combined cycle coal gasification, combined cycle pressurized fluidized bed combustion (PFBC), direct coal-fired gas turbines, and coal gasification molten carbonate fuel cell systems, would benefit significantly from the development of hot-gas cleanup technology. Sulfur, alkali metals, NO_x, and solid particulates must be removed from the gas stream to protect metallic components of the turbines from corrosion and erosion. A number of techniques are being investigated for the removal of particulates from hot gas streams, including ceramic bag filters, ceramic cross-flow filters, particle bed filters, and ceramic candle filters.

---

*Acurex Corporation, Mountain View, California.

Composites consisting of a silicon carbide matrix reinforced with continuous Nicalon* fibers have been developed by the AR&TD Fossil Energy Materials Program.[1,2] Composites of this type are light, chemically inert in fossil energy systems at 1000°C, and exhibit high strength and exceptional fracture toughness. The goal of this work is to produce a composite filter that has the requisite strength and toughness as well as sufficient porosity to be permeable to the gas stream with a pore size distribution necessary for an effective filter.

EXPERIMENTAL

High-temperature particulate filter specimens (7.5-cm-diam disks) were fabricated at ORNL by a chemical vapor deposition process that placed a free-standing fibrous material (felt) within a constant temperature region (~1200°C) of the resistively heated deposition furnace (Fig. 1). The reactants, methyltrichlorosilane (CH_3SiCl_3) plus hydrogen, were forced through the felt and deposited a thin layer of SiC on the individual fibers. The process has been developed to the extent that SiC is uniformly deposited across the diameter and thickness of the felt.

Filter medium designs being investigated include free-standing fibrous Nicalon felt, or felt with Nicalon cloth applied to the inner (upstream) surface, the outer (downstream) surface, or both the inner and outer surfaces (Fig. 2). The felt functions as the filter medium and the thin layer of silicon carbide bonds the fibers together providing the necessary mechanical strength to stabilize the felt (bond individual fibers together) to prevent fiber movement or loss during pressure-pulse cleaning. Deposition of SiC on the fibers also firmly bonds the cloth to the felt. Interlocking of fibers as demonstrated in Fig. 3 not only provides the mechanical strength but also gives the composite filter very high fracture toughness. In order to minimize the weight of the filter, thin layers of felt were used with a minimum deposition of SiC.

---

*Nicalon, Nippon Carbon Co., Tokyo, Japan.

ORNL-DWG87-19732

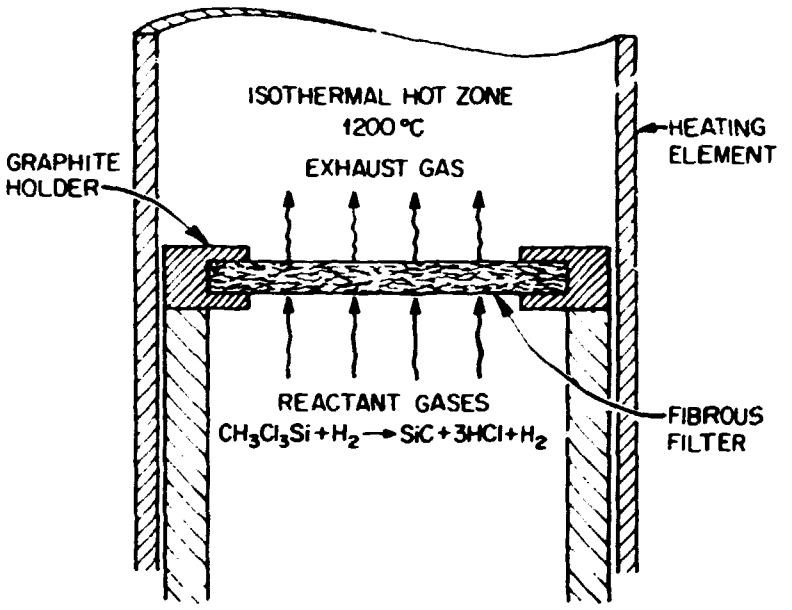

Fig. 1. Schematic of chemical vapor deposition process.

ORNL-DWG87-10734

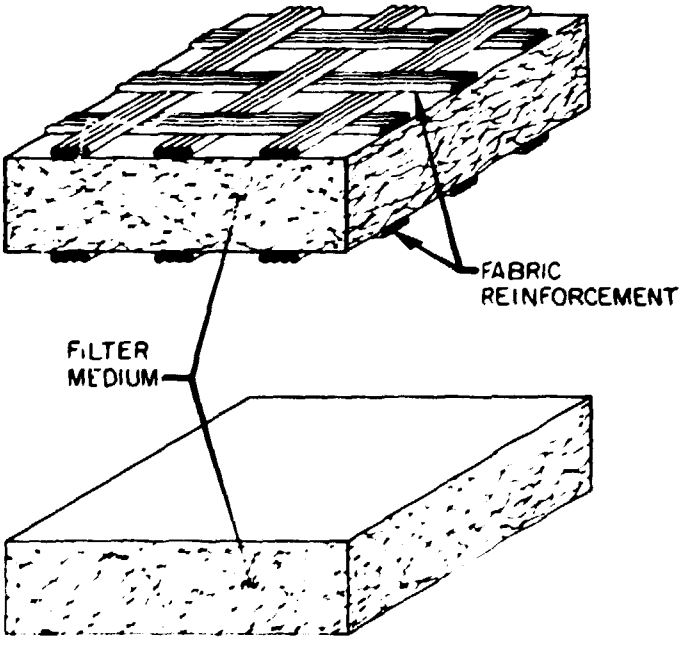

Fig. 2. Filter designs being investigated.

ORNL-PHOTO 3090-87

Fig. 3. Photograph showing the interlocking of Nicalon fibers with CVD SiC. The deposition of SiC in this photo is much greater than that needed for filter applications but better illustrates the interlocking of fibers.

Screening tests of composite filters were undertaken at Acurex Corporation to assess their filter efficiency and cleanability.[3] Figure 4 shows a sketch of the filter holding arrangement. The filter specimen was loaded in a horizontal position with the contaminated gas flowing up through the filter. Six specimens (7.5-cm-diam flat disks) were screened using both PFBC flyash and gasifier char at 200°C and 800°C. Note that there was no other structural support for the filter disk.

When the first specimens were tested, the edges of the filter were sometimes broken by the restraining fixture. This was corrected by using a ceramic gasket that expanded when heated. With this arrangement, the room-temperature clamping force could be reduced significantly. The gasket also prevented the edge of the fixture from cutting into the filter.

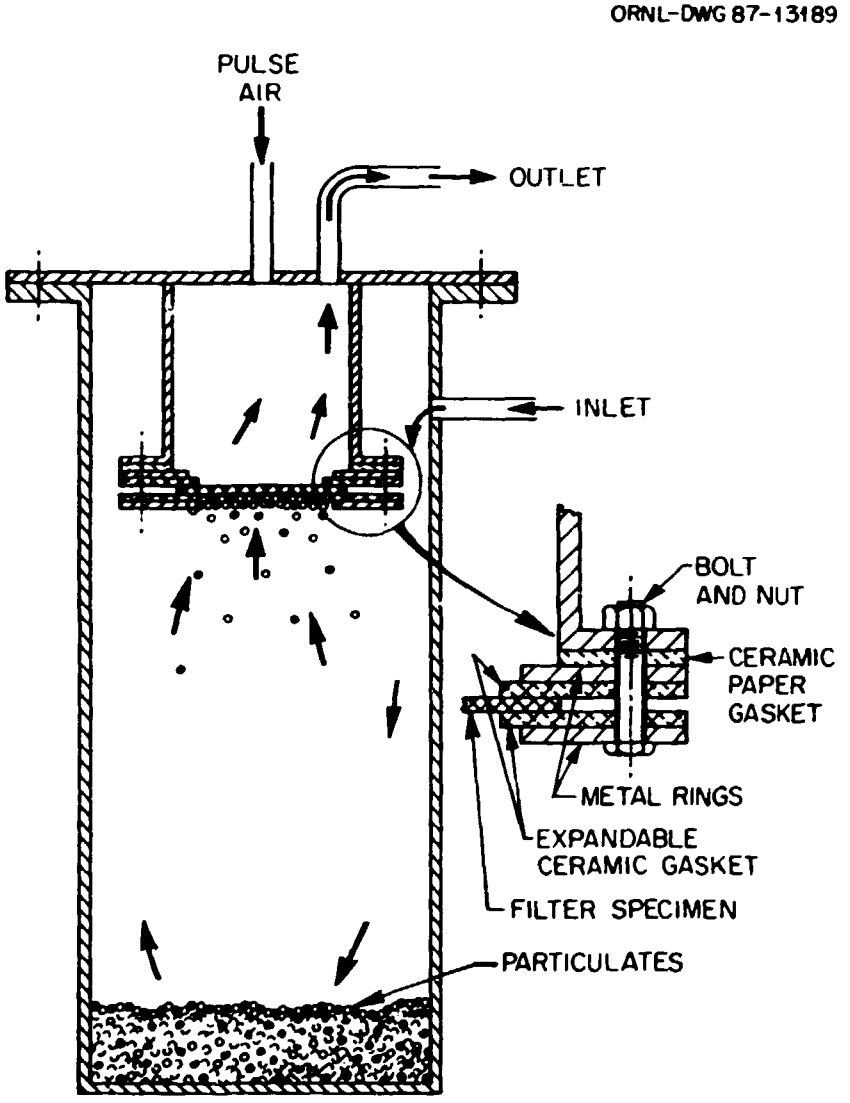

Fig. 4. Filter specimen clamping arrangement.

Filter specimens were constructed of a layer of Nicalon felt sandwiched between two layers of Nicalon cloth, with the exception of one sample which had the cloth on one side only. Nicalon felt consists of a three-dimensional array of continuous filaments 15 μm in diameter. The average pore size as shown in Fig. 5 is about 100 μm. Because of bridging and agglomeration of the particulates, the Nicalon felt can effectively filter particles significantly smaller than 100 μm. Table 1 describes the conditions under which the various filters were prepared.

ORNL-PHOTO 3093-87

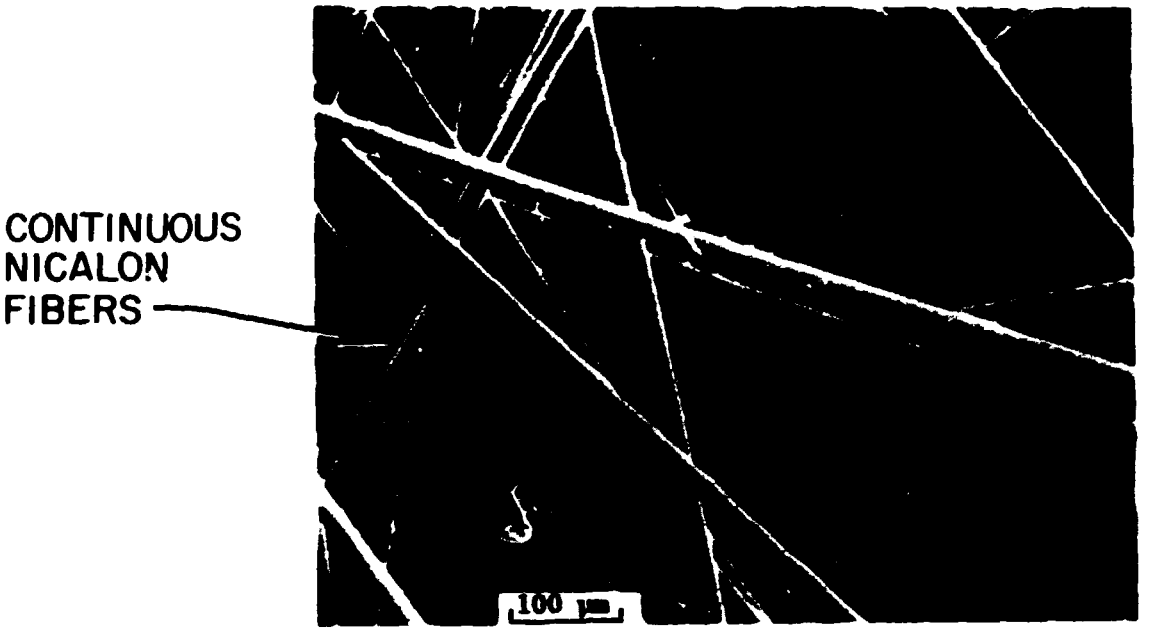

Fig. 5. Nicalon felt showing a pore size of about 100 microns.

Table 1. Composite Filter Samples

Number	Reactant gas concentration (g/min)	Run time (h)	Deposition temperature (°C)	Filter design
23	0.21	2	1200	Plain weave Nicalon upstream and downstream, felt in middle
20	0.42	4	1200	Plain weave Nicalon upstream and downstream, felt in middle
17	0.42	4	1200	Open Satin weave upstream only, felt backing
24	0.21	4	1200	Plain weave Nicalon upstream and downstream, felt in middle
16	0.24	4	1200	Plain weave Nicalon upstream and downstream, felt in middle
21	0.42	2	1300	Plain weave Nicalon upstream and downstream, felt in middle

RESULTS

PFBC flyash and gasifier char as described in Table 2 were used as test dusts. The PFBC flyash has a higher particle density, a smaller particle size, and, as revealed by optical microscopy, a rougher surface. Earlier tests had shown the gasifier char to be less efficiently filtered than the PFBC flyash.[4,5] The char did not form a cohesive filter cake, which is probably the reason for less efficient collection.

Table 2. Description of Test Dusts

	PFBC flyash	Gasifier char
Particle density	2.87 g/cm^3	2.18 g/cm^3
Particle diameter	4.5 μm	5.5 μm

The initial tests described in Table 3 were performed at face velocities of 11 to 22 cm/s using PFBC flyash at 200°C. The test specimen with the highest amount of deposited silicon carbide (No. 20) and the specimen with the least amount (No. 23) showed about the same results at these high face velocities. For specimen 20, decreasing the face velocity from 22.2 cm/s to 11.0 cm/s did not appear to have any major effect on dust removal efficiency or cleanability of the fabric. At the end of testing both filter specimens had areas on the clean side which showed evidence of some dust penetration, probably through pinholes in the felt. The edges of the filters had cracked and the layers were starting to delaminate. However, measured collection efficiencies were high considering the high filter face velocities.

Specimen 17 had woven fabric on the upstream side only. The pressure drop across the filter increased rapidly after about 3 h of testing. Use of a higher cleaning pulse pressure (0.36 MPa versus 0.18 MPa) or increasing the cleaning frequency did not slow the increase in the pressure drop.

Table 3. Summary of Test Results*

Test number	Specimen number/ test dust	Test conditions	Collection efficiency	Test time (h)
1	23/PFBC flyash	200°C 21.7 cm/s	99.7%	4
2	20/PFBC flyash	200°C 22.2 cm/s	99.3%	4
3	20/PFBC flyash	200°C 11.0 cm/s	99.4%	4
4	17/PFBC flyash	200°C 20.5 cm/s	99.5%	4
5	24/PFBC flyash	200°C 2.5 cm/s	99.2%	4
6	24/PFBC flyash	800°C 2.5 cm/s	>99.9%	4
7	24/PFBC flyash	200°C 2.7 cm/s	>99.9%	4
8	24/Gasifier char	200°C 2.7 cm/s	97.0%	5
9	20/Gasifier char (Retest)	200°C 3.0 cm/s	99.7%	5
10	16/Gasifier char	200°C 3.0 cm/s	99.4%	11
11	21/Gasifier char	800°C 3.5 cm/s	>99.9%	50

*Tests were conducted at 200°C with dust-laden air rather than combustion products. Air or nitrogen (room temperature) was used as the pulse gas for periodically removing dust from the filter surface. A pulse pressure of 0.18 MPa was generally used with a pulse duration of 0.05 s.

Specimen 24 was tested at a lower face velocity of about 2.5 cm/s and at 200°C and 800°C. With the exception of the first four hours of testing (test 5), the collection efficiency was higher at the lower face velocities (>99.9% for tests 6 and 7). At the end of testing with PFBC dust, specimen 24 was reused for testing with gasifier char. The collection efficiency kept dropping during the test, and later it was found that the edge of the filter had broken. There was also a large amount of char between the woven material and the felt on the upstream side. The restraint arrangement was then modified with an expandable gasket material, which extended beyond the edge of the clamp to prevent excessive stress on the filter.

Specimen 20 was also retested using gasifier char at 200°C and at a face velocity of 3.0 cm/s. The initial collection efficiency of 99.5% gradually improved to 99.7%. When the filter specimen was removed, no char was noticeable on the downstream side.

Specimen 16 was tested with gasifier char at 200°C and a face velocity of 3.0 cm/s. Specimen 16 was a new sample as compared to specimen 20 which had been used for testing with PFBC dust prior to testing with char. Slightly lower collection efficiencies were measured.

After the short duration tests showed promising results, a specimen was selected for longer duration testing at high temperatures. Specimen 21 was tested at 800°C for 50 h. After an initial collection efficiency of about 99.6%, the filter collection efficiency improved to >99.9%. There was no noticeable damage to the filter and no char was observed on the downstream side of the filter.

DISCUSSION

The ideal filter should retain 100% of the particulates at the surface since particulates that penetrate the filter medium could not likely be removed during the cleaning cycle. Results from testing the first set of composite filter specimens are very encouraging since collection efficiencies were uniformly high even at very high face velocities. There did not appear to be cleanability problems with the small filter specimens.

Edge fractures occurred in the first few filter specimens tested. A slight change in the fixture and gasketing material appeared to resolve the problem. The edge weakness can be partially attributed to reduced deposition of silicon carbide at the edge during fabrication of the filter. The rest of the filter, although unsupported, had no cracks or other structural failures. Delamination of the felt from the cloth layers was also observed. Better bonding between layers could be obtained with heavier deposits of silicon carbide.

Use of simpler base filter construction will make fabrication of commercial-scale filters easier. Besides the multiple-layered construction used, single-layer construction will also be examined. Use of ceramic paper material or a single layer of texturized ceramic cloth as the base material for chemical vapor deposition of silicon carbide are possible approaches. Filters fabricated from aluminosilicate papers have been prepared but not yet tested. The papers offer the additional advantage of having controlled pore sizes. Figure 6 shows ceramic papers fabricated from continuous filaments 1 to 2 μm in diameter. These papers have pore sizes between 1 and 10 μm. Eventually, tubular preforms consisting of a cylinder of felt, possibly wrapped with continuous filaments, will be infiltrated to produce candle filters.

The use of different base fiber material and different materials for deposition will also be investigated for composite filter construction. In any case there needs to be a better understanding of how the interaction of the different components of the composite filter effect the performance of the filter.

Chemical compatibility of the filter materials with hot combustion gases must be determined. Composite filters are currently being tested by the National Coal Research Establishment at Stoke Orchard, England, in a coal gasification system. After testing, the filters will be returned for further testing and evaluation. Potential problems could arise because silicon carbide is susceptible to attack by alkali metals at elevated temperatures. For example, sodium could form a low melting (870°C) eutectic with the protective SiO_2 film that forms on the surface of the SiC at elevated temperatures. Attack of the protective layer leads to rapid degradation of the SiC. If the reaction causes a significant problem, another material less susceptible to alkali attack will be deposited by CVD in place of the SiC.

Fig. 6. Aluminosilicate papers with reduced pore sizes.

CONCLUSIONS

A process utilizing chemical vapor deposition was developed for the fabrication of high-temperature particulate filters. Fibrous materials such as Nicalon felt with a pore size of about 100 μm were evaluated as filter mediums. For additional strength Nicalon felt was sandwiched between layers of Nicalon cloth. Preliminary evaluation of the initial Nicalon filters revealed that cleanable filters with collection efficiencies of >99.9% for either PFBC flyash or gasifier char could be produced. Simpler filter designs need to be investigated since particulates were often trapped between the cloth layer and felt and delamination of the filters was occasionally observed. Filters consisting of aluminosilicate papers with pore sizes ranging from 1 to 10 μm were successfully prepared but have not been tested. The relationships between filter efficiency, cleanability, strength, toughness, preform design, and deposition conditions need to be established to optimize the properties of the filter materials.

REFERENCES

1. D. P. Stinton, A. J. Caputo, and R. A. Lowden, "Synthesis of Fiber-Reinforced SiC Composites by Chemical Vapor Infiltration," Am. Ceram. Soc. Bull. 65(2), 347-50 (1986).

2. A. J. Caputo, D. P. Stinton, R. A. Lowden, and T. M. Besmann, "Fiber-Reinforced SiC Composites with Improved Mechanical Properties," Am. Ceram. Soc. Bull. 66(2), 368-72 (1987).

3. R. Chang and H. Lips, Ceramic Fabric Material Testing, DOE/MC/20110-1895, June 1985.

4. R. Chang, J. Sawyer, and H. Lips, Performance Evaluation of a Ceramic Fabric Bag Filter on a Bench-Scale Coal Gasifier, Acurex Final Report FR-86-113/ESD for DOE/Morgantown Energy Technology Center, October 1986.

5. M. Shackleton, R. Chang, J. Sawyer, W. Kuby, E. Turner-Tamiyasu, High-Temperature High-Pressure Gas Cleanup with Ceramic Bag Filters, DOE/ET/17092-1504, January 1984.

NONDESTRUCTIVE EVALUATION OF ADVANCED CERAMIC COMPOSITE MATERIALS

J. B. Walter and L. A. Lott

Idaho National Engineering Laboratory
EG&G Idaho, Inc.
P.O. Box 1625
Idaho Falls, Idaho 83415

ABSTRACT

Ceramic composites are an important new type of material being developed for applications requiring high strength at high temperatures. Considered here are composites of a SiC matrix reinforced with SiC fabric which is formed by chemical vapor infiltration of the fabric. An important aspect of this process is the formation of extensive porosity which limits the strength of the material. Effective methods of nondestructively detecting and characterizing porosity in the material are needed. This is a challenging task for ultrasonic techniques because of the high levels of porosity (typically 10-50%) found in the material and because of the intrinsic heterogeneity and anisotropy of the material, all of which strongly affect ultrasonic wave propagation. Through-transmission techniques for measuring ultrasonic properties are described, including the use of time delay spectrometry and laser generation of ultrasound. Acoustic properties and area scans are presented for samples containing a range of porosity. It is concluded that the techniques are adequate to form a technical basis for developing effective ultrasonic NDE methods.

INTRODUCTION

The objective of this program is to evaluate and develop nondestructive evaluation (NDE) techniques for advanced ceramic composite materials. The capabilities of current state-of-the-art NDE techniques to reliably detect and characterize defects will be determined. New and/or improved techniques will be developed as the needs are identified.

NDE is needed in applications where material failure is critical and no basis for lifetime prediction exists, as, for example, in ceramic composite heat exchangers. It is important to develop NDE methods in concert with material development so that the techniques can be used as material process development tools, be available when in-service problems occur, and be used for in-process sensing and control.

A large technology base exists for NDE of monolithic materials (primarily metals). However, NDE of ceramic composites is a significantly more complex problem requiring research and development. Ultrasonic techniques are considered the most promising and are being investigated first. Other techniques, primarily radiography, are being used to complement ultrasonics and corroborate the results.

SiC-reinforced SiC is the first material system being studied. Porosity is of primary concern, because its formation is inherent in the production of the material, and because it reduces the strength of the composite. Thus techniques to detect and characterize porosity are being investigated first.

During the reporting period, test samples of SiC cloth-reinforced SiC matrix material containing varying degrees of porosity have been obtained. Through-transmission ultrasonic techniques have been developed to measure the acoustical properties of the coupons, and correlations of the ultrasonic properties with the porosity in the samples have been observed. A pulse/echo method for measuring ultrasonic properties and detecting individual pores or groups of pores has also been examined. Laser-generated ultrasonic waves have been investigated and found to significantly increase the ultrasonic energy coupled into these highly porous materials. Time delay spectrometry has also been found to improve the signal-to-noise ratio, and was especially useful for through-transmission attenuation measurements.

COMPOSITE SAMPLES

The first material system being addressed consists of continuous SiC fibers in a SiC matrix. A preform is built up from layers of Nicalon[a]

[a]Nippon Carbon Co., Tokyo, Japan

cloth. A matrix of SiC is added to the preform by a chemical vapor infiltration (CVI) process. These samples typically have high porosity content, because as more and more of the matrix is deposited on the fibers in the preform, further infiltration of the gasses which react to form the matrix is inhibited.

Test coupons have been received from Refractory Composites Inc. (RCI) and the AR&TD program at ORNL, which produce the composites by different CVI processes. The samples include 5 different fiber volume fractions, and have porosity volume fractions ranging from 10 to 50%, as shown in Figure 1. The majority of the specimens were manufactured by RCI; a few low porosity, high fiber samples were contributed by ORNL to help fill out the sample set.

ULTRASONIC ATTENUATION

Through-transmission measurements of the ultrasonic attenuation have been made using both pulsed and continuous-wave (CW) techniques. The through-transmission arrangement of the transducers and sample are shown in Figure 2. The SiC-SiC samples were typically 3.3 mm thick, with bulk porosity between 26 and 42 vol.%. Standard piezoelectric, broadband, 12 mm diameter transducers were used in both cases. The attenuation values were determined from the response of the receiving transducer with and without the sample present. A correction for reflection at the surfaces of the sample was applied, treating the sample as homogeneous.[b]

The pulsed work used a standard pulser/receiver which delivered a voltage pulse to the transmitter, generating an acoustic pulse. The pulse traveled through the water bath and the sample to the receiver. The voltage output of the receiver (standard A scan) was digitized by a transient recorder and transferred to a computer. The A scan was Fourier transformed to the frequency domain, where the attenuation was calculated.

[b]The samples are of course anisotropic. However, the wave length in the sample generally exceeds 2 mm, which is large compared to the thickness of the layers. For the higher porosity samples, where the wavelength at 2 MHz can be as short as 1 mm, the correction for reflection is small compared to the attenuations observed.

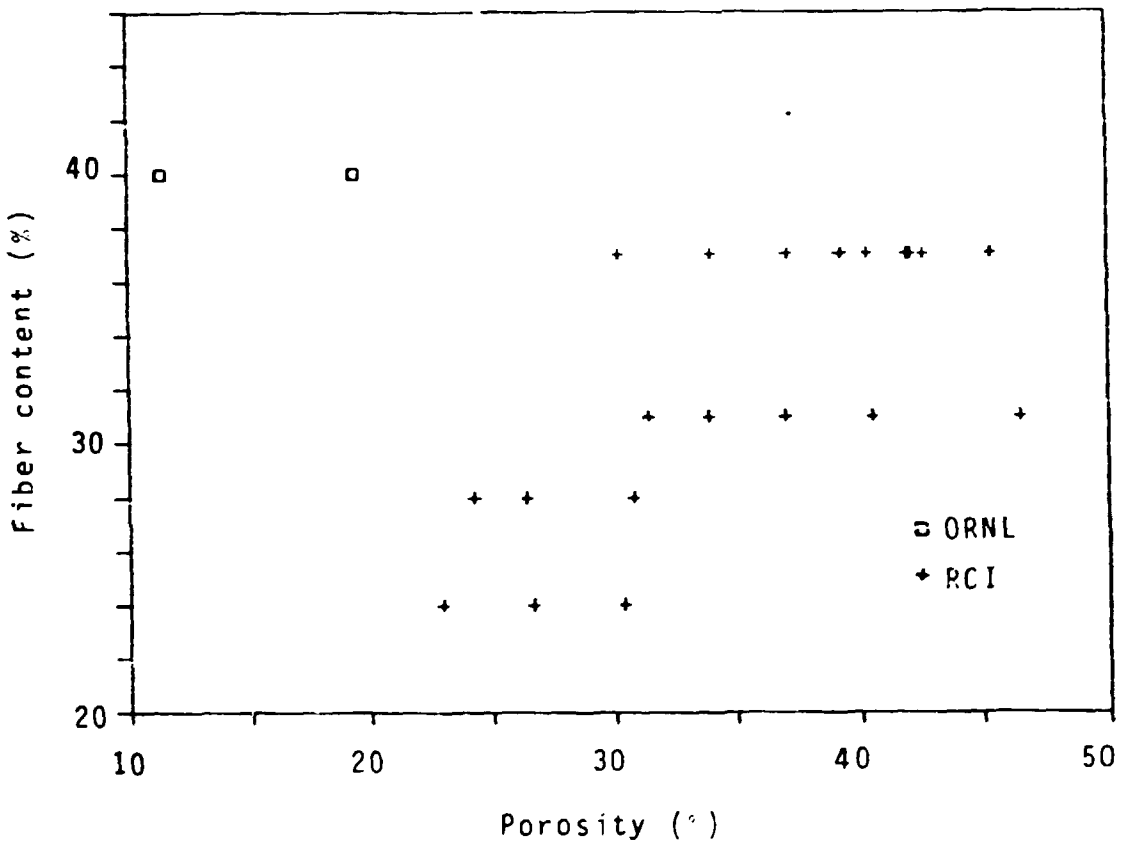

Fig. 1. Fiber and porosity fractions of test coupons of SiC fabric reinforced SiC acquired for investigation of NDE techniques for characterization of porosity content.

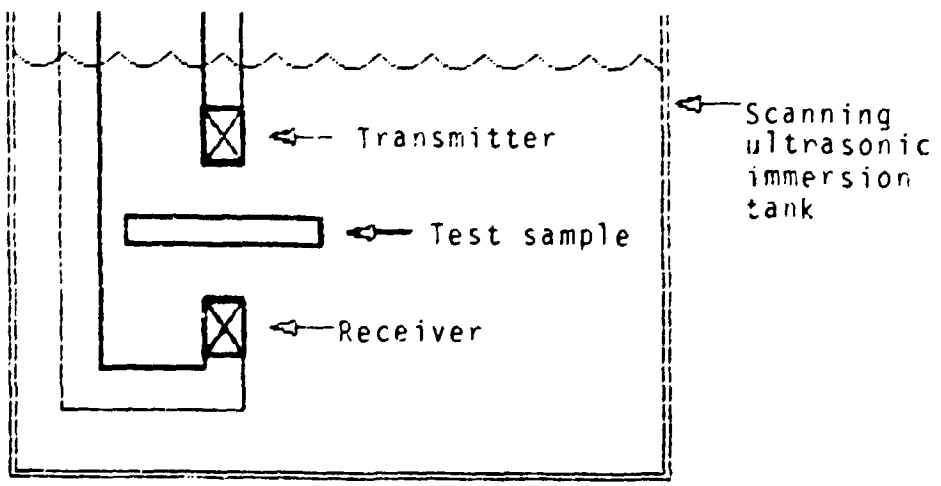

Fig. 2. Through-transmission measurement system using two piezoelectric transducers coupled to the sample by the water bath.

Measurements were made at an array of points distributed over the central area of the sample to obtain an attenuation which could be compared with the overall sample porosity. Figure 3 shows the measurements with 2.25 MHz transducers for six samples with 37% fiber reinforcement. The coupon with 26% porosity shows an attenuation varying from 3-12 dB/mm, and the coupon with 39% porosity has about 10 dB/mm greater attenuation. Figure 4 shows that at 1.6 MHz the attenuation increases by about 0.5 dB for each percent porosity.

The CW work was a collaborative effort with P. M. Gammell, Naval Surface Weapons Center, Silver Spring, Maryland.[c] Time delay spectrometry (TDS) uses a long duration CW signal, and has been effective with other highly attenuating materials.[1] This is because the ultrasonic signal is being continuously transmitted and received, providing a duty factor near 1, in sharp contrast to pulsed systems. The frequency of the transmitter is swept through a range of frequencies which the receiver tracks, allowing for the travel time of the ultrasonic signal. An added benefit occurs because the received signal is envelope detected, providing a slowly varying signal which can be recorded with a 100 kHz, 12 bit digitizer, in contrast to pulsed systems which record signals in the megahertz range with at best 8 bit accuracy. This translates to 24 dB added dynamic range. TDS provides directly a frequency domain display of the amplitude of the ultrasonic signal transmitted through a sample, because for any portion of the signal, the time it is received is a linear function of frequency. Figure 5 shows attenuation measurements for two samples with 35% and 42% porosity measured with 10 MHz transducers. The measurements were done for only a single location on the sample, however the benefits of using TDS are clear. The measurements are useful at frequencies as high as 4 MHz for the 35% porosity sample, and as high as 3 MHz for the 42% porosity sample, which transmitted insufficient ultrasonic energy for measurements with the pulsed technique. The cusps evident, particularly for the 42% porosity sample, are not actual changes in attenuation, but are measurement

[c]Supported by the Materials Block Program and the Internal Exploratory Development Program at the Naval Surface Weapons Center.

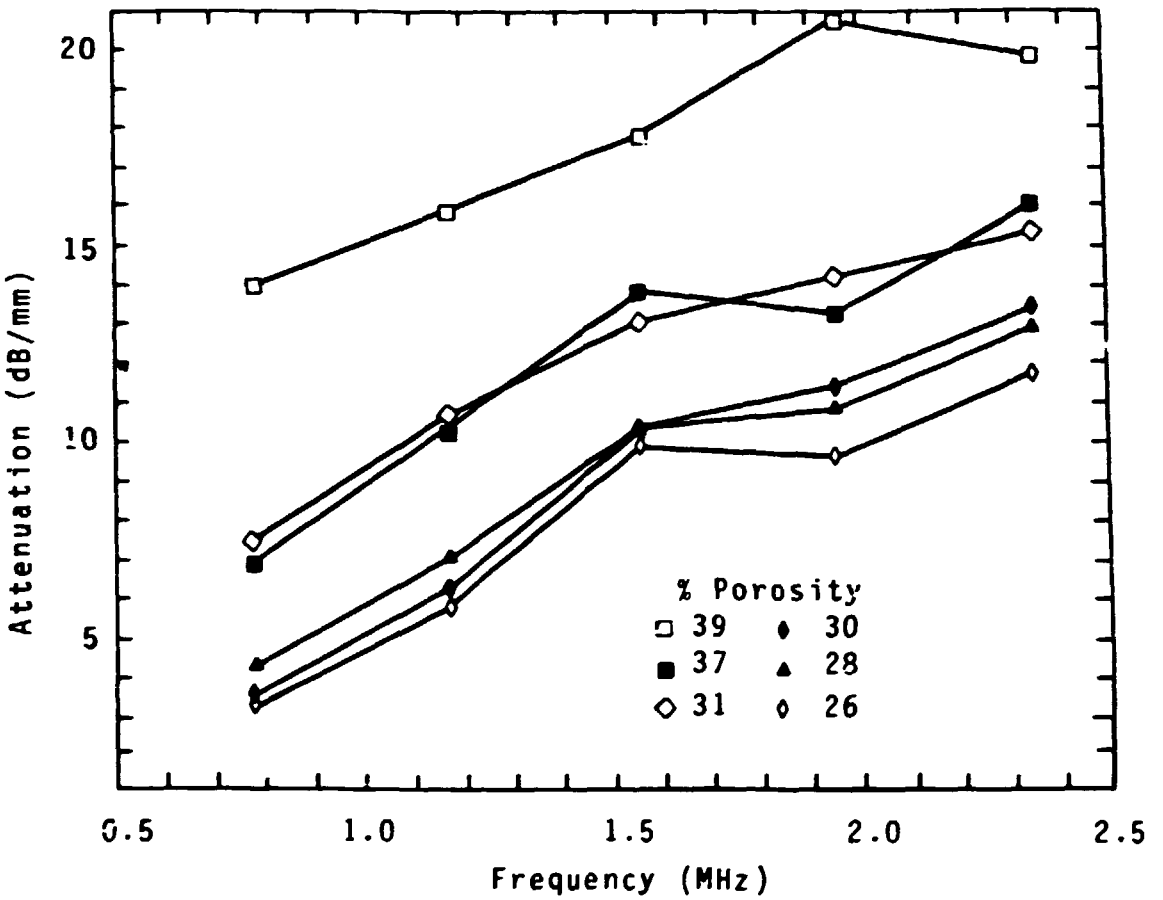

Fig. 3. Attenuation measured for six SiC-SiC samples with porosity content ranging from 26 to 39 vol.%. The attenuation increases by about 5 dB/MHz.

artifacts due to destructive interference between portions of the ultrasound which travel through the sample with different velocities.

PROPAGATION VELOCITY

The velocity of the ultrasonic pulse in the samples was also studied with the through-transmission arrangement in Figure 2, using the pulsed technique. Figure 6 shows ultrasonic pulses at the receiving transducer with and without the sample interposed between the two transducers. The delay evident for the sample absent reflects the faster velocity in the sample. The appearance of the ultrasonic pulse is distorted by the sample, because the higher frequencies are preferentially attenuated.

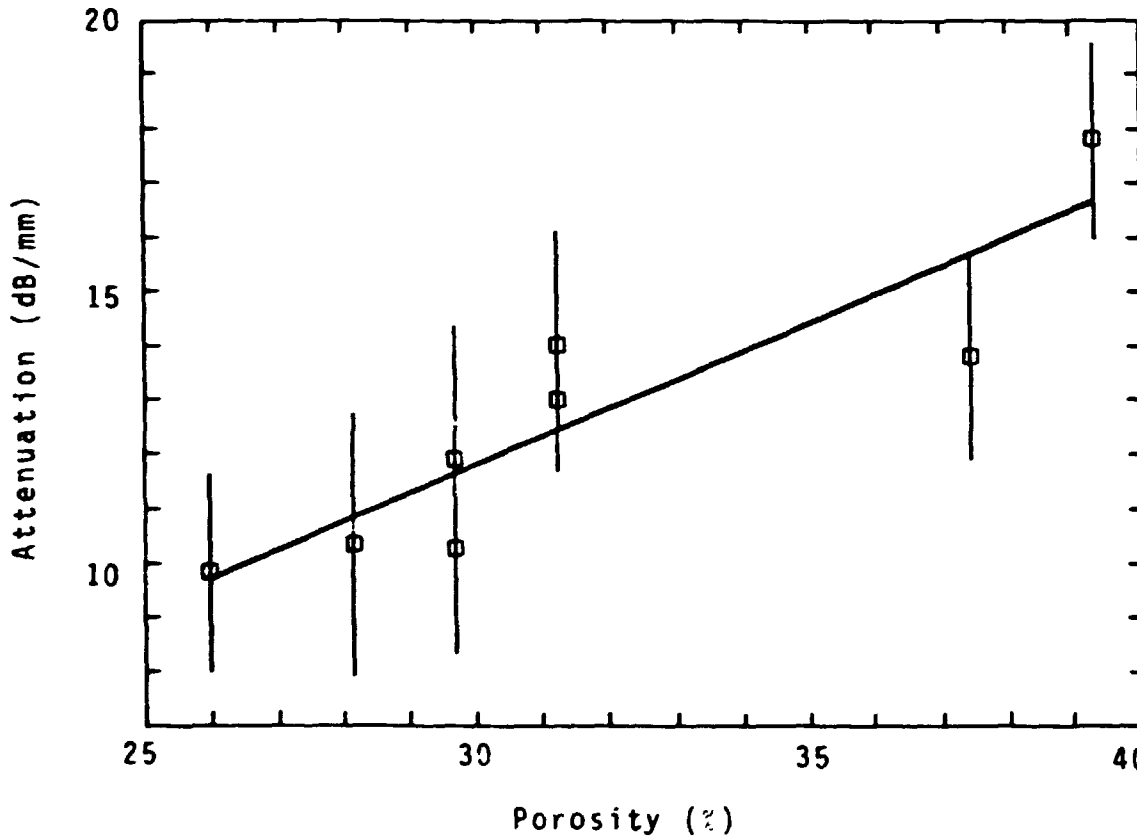

Fig. 4. Attenuation at 1.6 MHz as a function of sample porosity. The attenuation increases at about 0.5 dB/% porosity. The error bars are the standard deviation values measured at different points on the sample. Two sets of measurements are shown for two of the samples.

The delay was measured between the leading edges of the pulses, indicated by the arrows. The accuracy of the delay measurement was about 10 ns, the digitizing period of the transient recorder used, which corresponds to an accuracy in the velocity of a few percent.

Figure 7 shows a strong dependence of propagation velocity on porosity for 6 samples having porosities ranging from 25% to 40%. The error bars show the standard deviation of the measurements for an array of points distributed over the central region of the sample, and indicate the degree of variability in the sample. Porosity was calculated from the bulk density of the sample, and represents the average porosity in the sample.

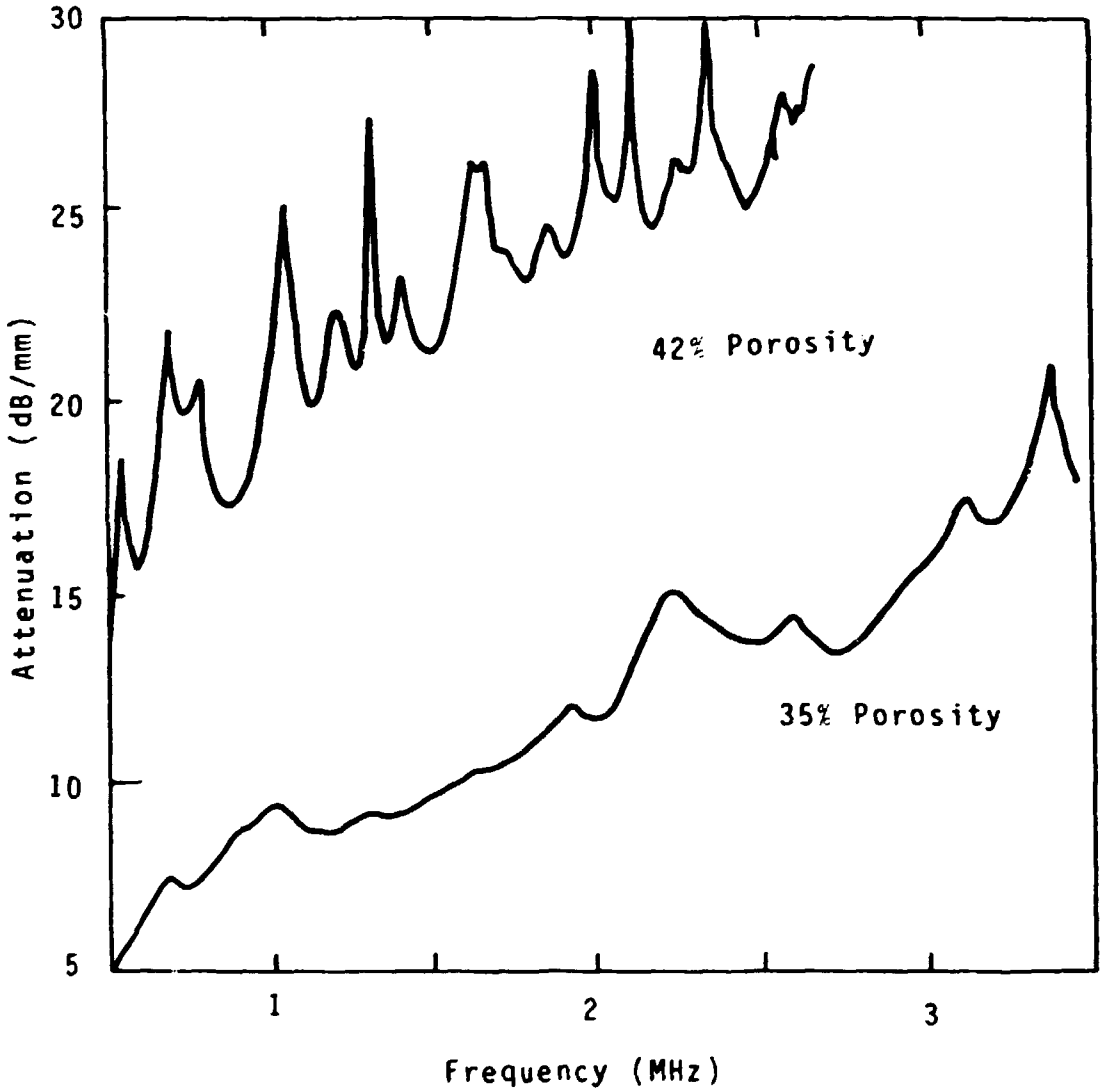

Fig. 5. Attenuation measured by time delay spectrometry for SiC-SiC samples with 35% and 42% porosity. The inherent averaging in the technique provided more accurate measurements, at higher frequencies than was possible with a conventional pulsed technique. Interference effects are evident in the cusps present for the 42% porosity sample.

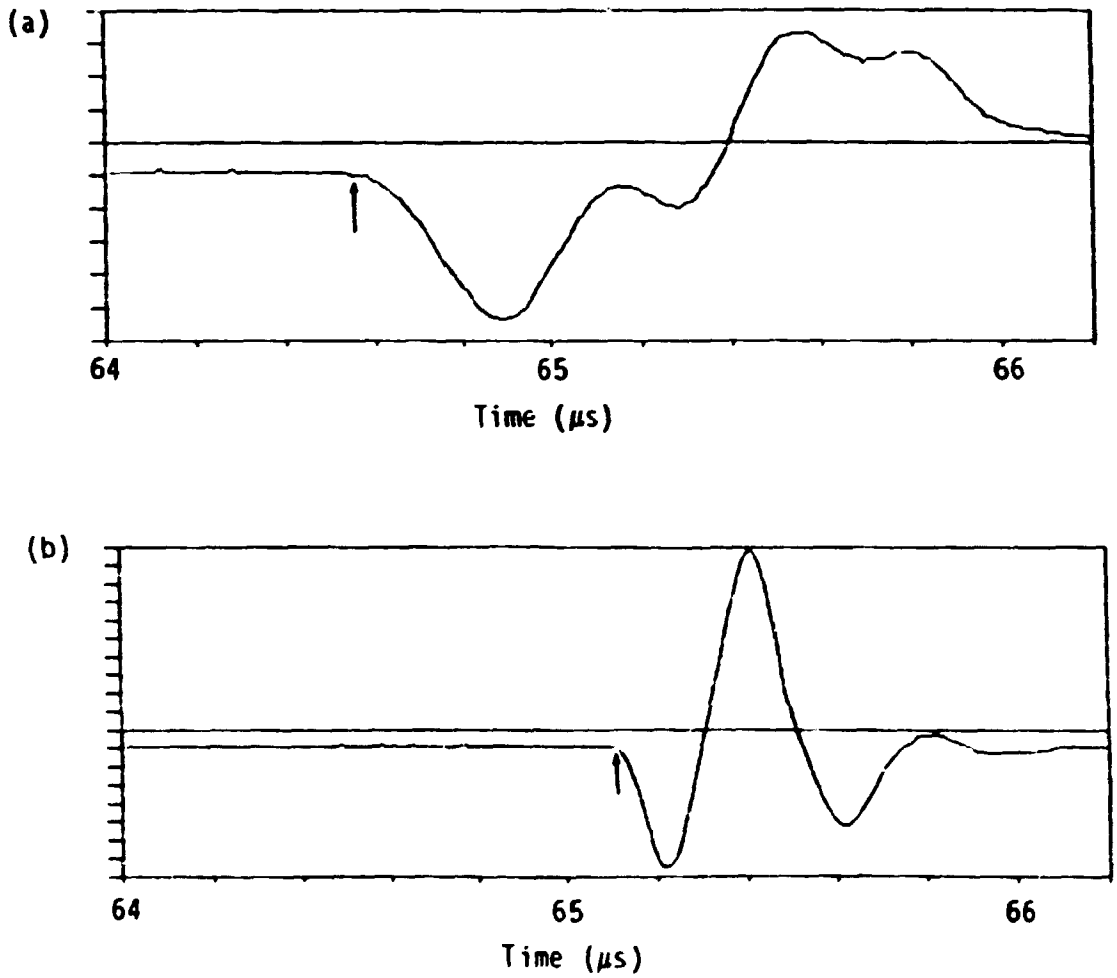

Fig. 6. Typical examples of the recorded ultrasonic pulses for the conventional, pulsed, through-transmission system with the sample (a) interposed and (b) not interposed between the transmitter and the receiver. The distortion in the ultrasonic pulse is caused by the frequency dependent attenuation in these highly attenuating SiC-SiC samples. The arrows indicate the arrival times of the pulses at the receiver.

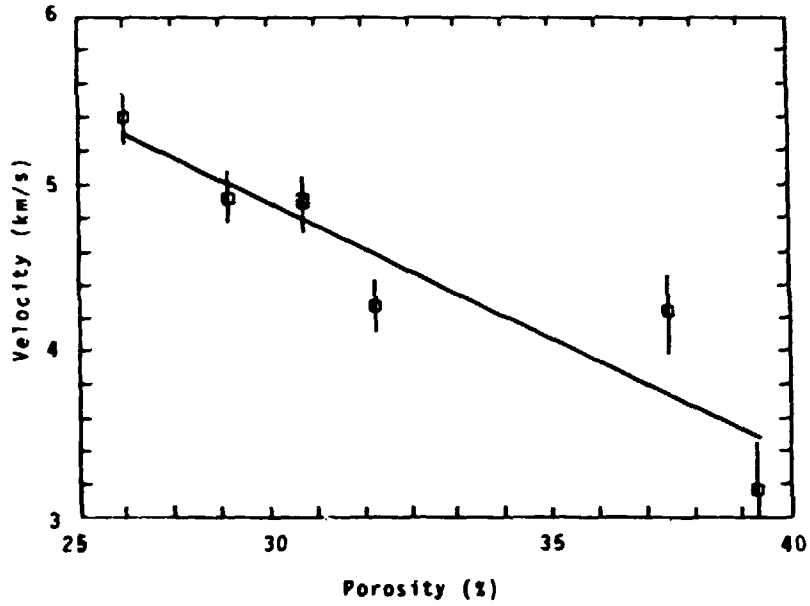

Fig. 7. Acoustic velocity measured with the conventional pulsed system. Velocity is seen to depend strongly on the sample porosity. The error bars are the standard deviation of measurements at different points on the sample. Two sets of measurements are shown for one sample.

ULTRASONIC TRANSMITTANCE

The ultrasonic energy transmitted through a sample has been examined using both the conventional arrangement in Figure 2 and the thermoelastic setup in Figure 8, where the transmitting transducer is replaced with a laser. The transmitted energy includes all the ultrasonic energy in the pulse which reaches the receiving transducer. It is determined by the content of the initial ultrasonic pulse, the thickness and frequency dependent attenuation of the sample, and the coupling efficiency of the ultrasonic pulse into and out of the sample. The content of the ultrasonic pulse and the coupling efficiency will not change with position on the sample. The technique is intended for samples of uniform thickness, for which variations in the transmitted energy will reflect differences in the attenuation.

Good correlation has been noted between the transmitted energy and the porosity of the material using the piezoelectric setup, however the thermoelastic arrangement couples more acoustic energy into the sample and

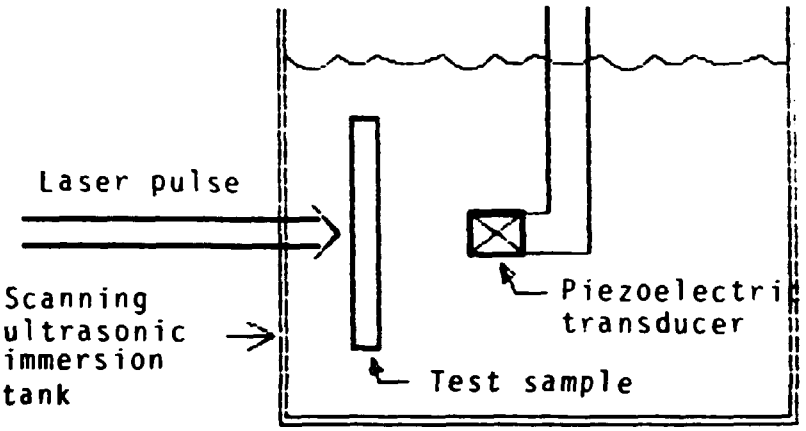

Fig. 8. Through-transmission measurement system using a pulsed laser to generate an acoustic pulse at the surface of the sample by thermoelastic conversion. The transmitted acoustic pulse is detected by a conventional piezoelectric transducer, coupled to the sample by a water bath.

provides much better results. A pulsed, Nd:YAG laser is used to deliver a 10 ns, 90 mJ pulse to the surface of a sample. An ultrasonic pulse is generated by thermoelastic conversion of the deposited heat energy.[2] Increases of approximately 20 dB have been observed in the received signal levels compared to the piezoelectric setup, resulting in improved characterization of all samples.

Samples representing a range of porosities have been characterized using the laser generation system. The laser beam was defocused to about a 6 mm spot size to minimize effects from surface roughness (and inhomogeneities on the order of the fiber bundle spacing of 1 mm). Figure 9 shows the measured correlation between transmitted energy and porosity. Each point represents an average of 15 measurements for the sample, distributed across the width of the sample at 2 mm intervals. The error bars show the standard deviation of the values measured for the sample. The line is a least squares fit to the points.

AREA SCANS

The transmitted energy and propagation velocity measurements have been employed in scans of samples, resulting in maps of the sample which can

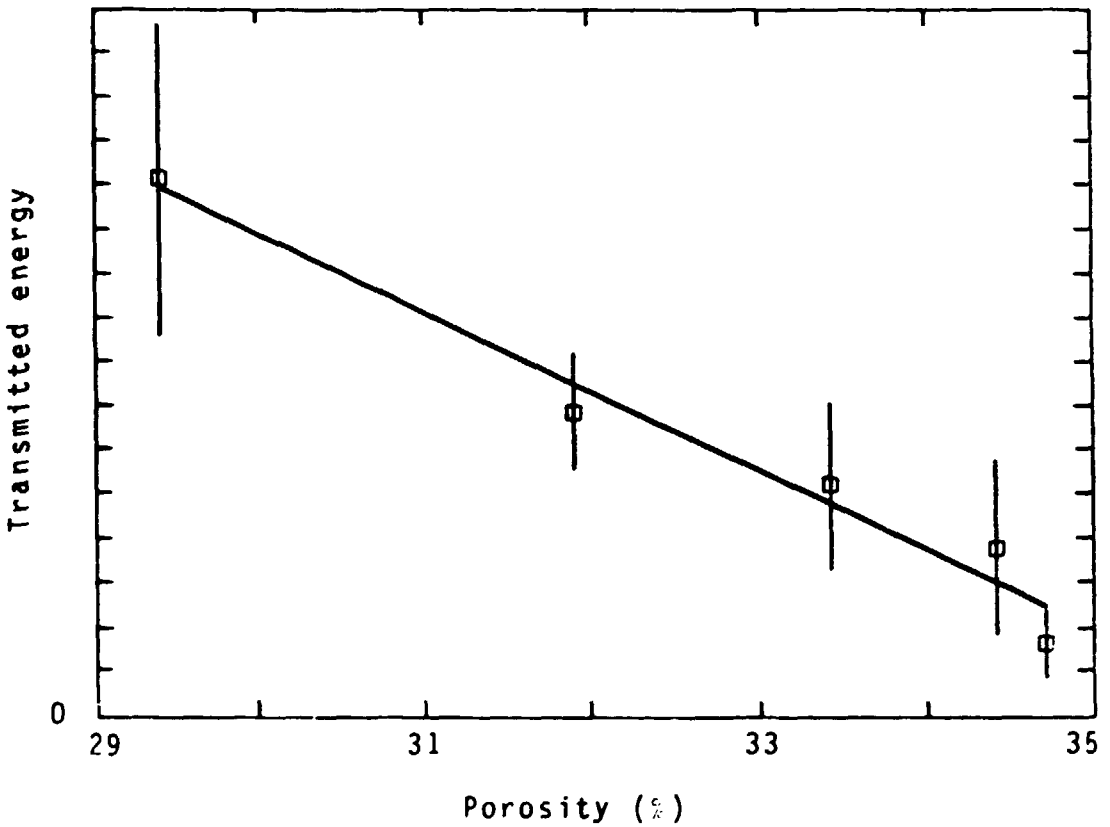

Fig. 9. Transmitted acoustic energy measured with the thermoelastic system. The dependence of ultrasonic transmission on porosity is clear. The error bars are the standard deviation of values measured at different points on the sample, and reflect the point-to-point variation in the ultrasonic transmission.

be correlated with radiographic examinations. Figure 10 shows a positive print of an x-ray radiograph of a sample having large variations in porosity. Measurements of the film density, calibrated with penetrameters included in the exposure, reveal that the porosity varies from 31% in the dark region to 43% in the light region. Ultrasonic scans with 2.25 MHz, 6 mm diameter transducers show the same pattern. Figure 11 shows a map of the transmitted energy, with regions of higher ultrasonic transmittance appearing darker. Figure 12 shows a map of the propagation velocity, with regions of higher velocity appearing darker. In all three, a darker band is seen which curves from the upper left, across the middle, to the upper right.

Fig. 10. Positive image of X-ray radiograph of a SiC-SiC sample containing large variations in porosity. Porosity varies from 31% to 43%.

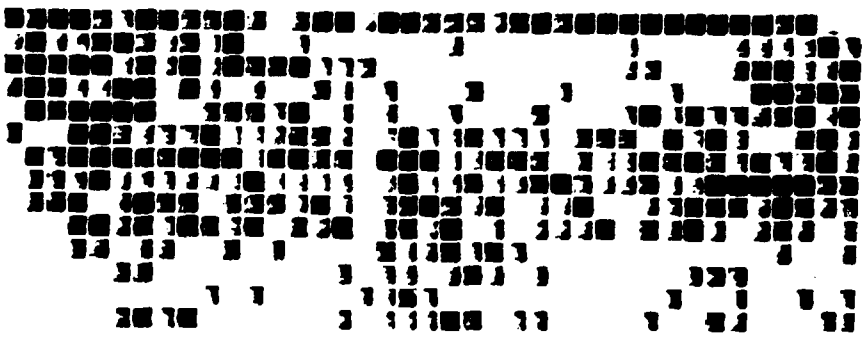

Fig. 11. Map of the transmitted ultrasonic energy for the sample in Figure 11. The darker areas have higher transmitted energy.

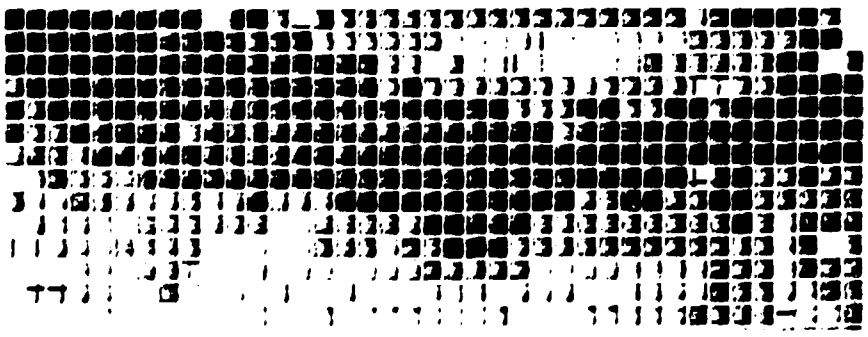

Fig. 12 Map of the ultrasonic propagation velocity for the sample in Figure 11. The darker areas have higher velocity.

Despite the clear correlations evident between the radiographic and ultrasonic measurements, it should be noted that the techniques do not measure exactly the same properties. While radiography measures density, the ultrasonic techniques measure how well and how fast ultrasonic energy is propagated through the material and thus depend on the structure of the material in addition to the overall density. Ultrasonics is potentially capable of providing additional detailed information about the characteristics of porosity which radiography can only locate.

ULTRASONIC PULSE/ECHO

The potential use of a pulse/echo ultrasonic technique has been investigated using both conventional piezoelectric and thermoelastic laser generation of ultrasonic pulses, as shown in Figure 13. The use of the laser in pulse/echo is similar to its use above in through-transmission, with two added benefits. Since in the thermoelastic configuration the ultrasonic pulse is generated at the surface of the sample, the large front surface echo is absent. The first signal arriving at the receiver is a pulse which travels back into the water away from the sample. It was experimentally observed that besides being much smaller, it is also shorter than the front surface echo obtained with typical piezoelectric transducers. Figure 14 compares these two cases, showing the improvement obtained with the thermoelastic generation. The laser produces a shorter, cleaner pulse, important for near-surface investigation.

This technique is promising for ultrasonic backscatter and flaw detection in denser samples. The high attenuation observed in Figure 3 has serious implications for application of pulse/echo techniques with these highly porous SiC-SiC samples. An attenuation of 4.5 dB/mm, corresponding to the least attenuating sample at 1 MHz, means that half of the ultrasonic energy which enters the sample penetrates only to a depth of 0.7 mm. Since the propagation velocity is 5.4 km/s in this sample, half of the energy is removed from the ultrasonic pulse in an eighth of a wavelength, or 99.6% in one wavelength. The attenuation per wavelength is about the same at 2 MHz. For the data in Figure 6b, the ultrasonic activity at 5 MHz for times corresponding to echoes at depths between 0.75

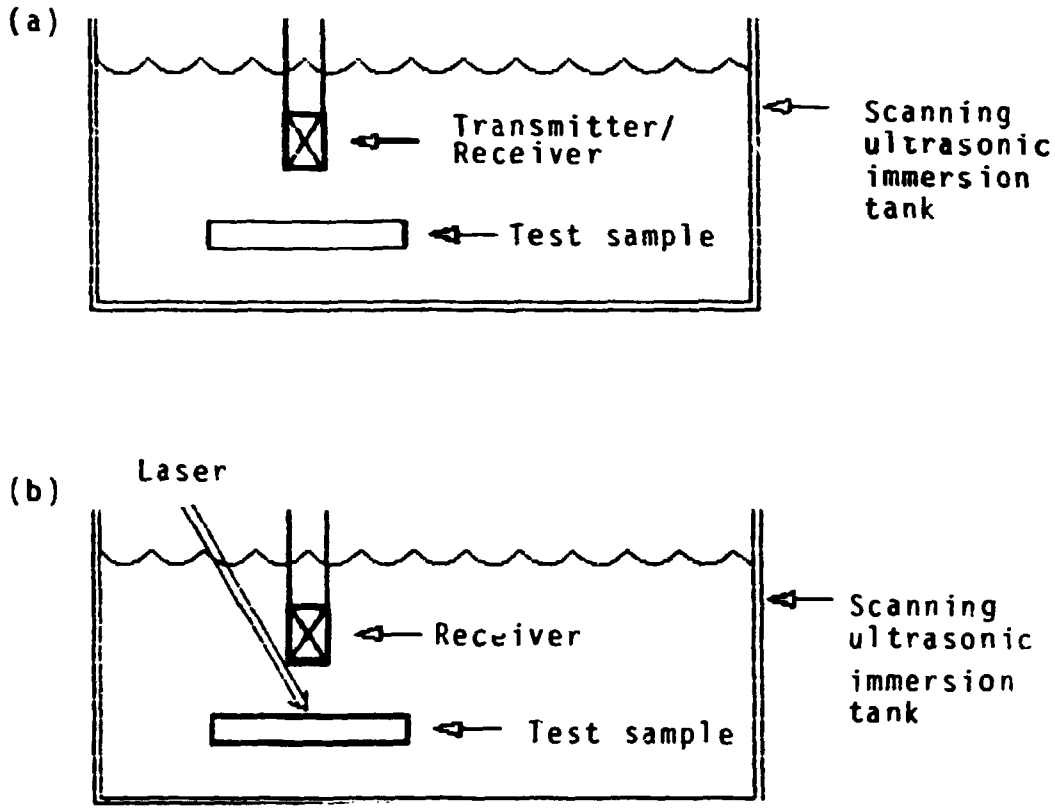

Fig. 13. Pulse/echo measurement systems using (a) conventional piezoelectric and (b) thermoelastic laser generation of ultrasonic pulses. In both systems, the reflected and scattered ultrasonic pulse is received by the piezoelectric transducer, coupled to the sample by a conventional water bath.

and 2 wavelengths is down by only 24 dB from the front surface. An echo from a back surface at 0.75 wavelengths would have travelled through 1.5 wavelengths of material, and be down by 36 dB, insignificant compared to the 24 dB observed. Pulse echo techniques may be viable for wavelengths which are long compared to the depths of interest, or for examining the initial signal for interference between a flaw signal and the front surface signal.

SUMMARY AND CONCLUSIONS

In order to develop ultrasonic NDE techniques for advanced ceramic/ceramic composites, the basic ultrasonic properties of the material must be known, as well as how they are affected by material properties and

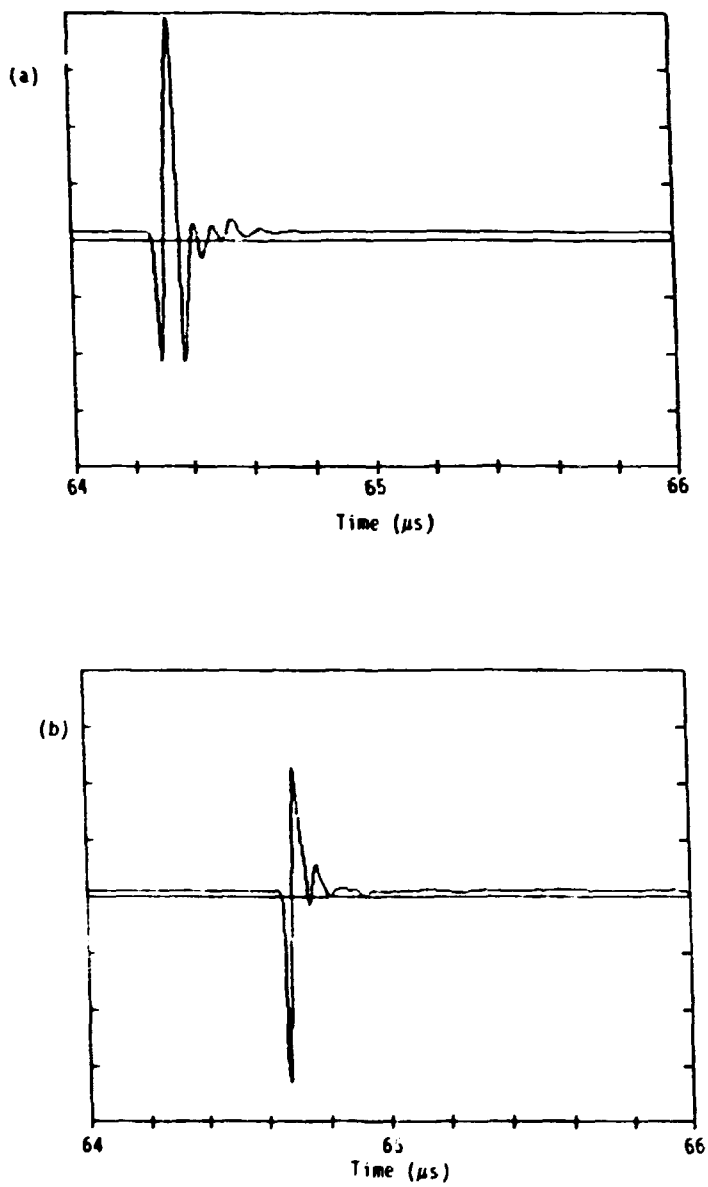

Fig. 14. Typical examples of the recorded ultrasonic pulses for the (a) conventional and (b) thermoelastic pulse/echo systems. The thermoelastic generation technique produces a shorter, cleaner pulse, important for near surface investigation.

conditions of interest. Because of the nature of ceramic composites, ultrasonic measurements are difficult to make, requiring special measuring techniques to be developed. Several experimental measuring techniques have been developed to measure ultrasonic propagation velocity, attenuation, and transmitted energy.

Because of high attenuation in the inhomogeneous and porous material, measurements are restricted to relatively low frequencies (<5 MHz) in order to transmit sufficient acoustic energy through samples for meaningful measurements. In addition, measurements are restricted to through-transmission methods using separate pulsing and receiving transducers. This requires the acoustic wave to make only one transit through samples, in contrast to conventional pulse-echo measurements where two or more transits can normally occur. For the most porous, highly attenuating samples, conventional piezoelectric generation of ultrasound is inadequate. However, laser thermoelastic generation of ultrasound directly in the samples was found to produce approximately 20 dB higher ultrasonic amplitudes, making measurements of ultrasonic properties possible in these samples.

Techniques were successfully applied to a set of samples containing a range of porosity, enabling correlations to ultrasonic properties to be made. It is concluded that the techniques developed are adequate to determine the ultrasonic properties of ceramic composites and to form a technical basis for developing effective ultrasonic NDE methods.

REFERENCES

1. Gammell, P. M., "Ultrasonic Characterization of Highly Attenuating Materials with Time Delay Spectrometry," Proceedings of the 15th Symposium on Nondestructive Evaluation April 23-25, 1985, San Antonio, TX.

2. R. J. Dewhurst, et al., "Quantitative Measurements of Laser-Generated Waveforms," J. Appl. Phys. 53, 1982, pp. 4064-4071.

ADVANCED MATERIALS FOR SOLID OXIDE FUEL CELLS

C.W. Griffin and J.L. Bates

Materials Sciences Department
Pacific Northwest Laboratory[a]
P. O. Box 999
Richland, Washington 99352

ABSTRACT

Materials based on the In_2O_3-$PrO_{1.83}$-ZrO_2 system were examined as potential electrodes and current interconnects for solid oxide fuel cells (SOFC). The electrical transport, thermal, and electrochemcial properties are described in relationship to structure, phase equilbria, and composition. The electrical conductivity was dependent on structure and composition, and can exceed the conductivity of the state-of-the-art electrode/interconnect materials. The instability of the In_2O_3 in reducing environments may eliminate this system as SOFC anodes or interconnects. This system may be used as cathodes if indium does not diffuse into the electrolyte and degrade fuel cell performance.

(a)Pacific Northwest Laboratory is operated by Battelle Memorial Institute for the U.S. Department of Energy under Contract DE-AC06-76RLO 1830.

INTRODUCTION

Solid oxide fuel cells (SOFC) are direct energy conversion devices requiring materials to operate at high temperatures for long times. High-temperature oxide materials based on rare-earth (Re_xO_y) stabilized ZrO_2 (HfO_2) are being studied as advanced SOFC electrode and interconnect materials. The objective is to develop high-electronically conducting oxide materials with thermal and fabrication characteristics similar to the solid electrolyte. Ionically conducting Y_2O_3 or Re_xO_y stabilized ZrO_2 (HfO_2) solid electrolytes are made electronically conducting with additions of other oxides, e.g., In_2O_3, while retaining structures similar to the electrolyte and interconnects. These structures may provide: 1) thermal expansion match with the electrolyte, 2) simultaneous fabrication of electrode and electrolyte as an integral cell component, 3) compositions that minimize material interactions between SOFC components, and 4) improved electrode/electrolyte reaction rates. This paper describes the research and development of materials based on the In_2O_3-$PrO_{1.83}$-ZrO_2 system as potential electrodes and current interconnect for SOFC. The electrical transport, thermal, and electrochemical interaction properties are described in relationship to structure, phase equilibria and composition.

EXPERIMENTAL PROCEDURES

Sample fabrication and the techniques used to determine the electrical and thermal phase equilibria and electrochemical properties are described. Property measurements included electrical conductivity, Seebeck coefficient, ionic transference

numbers, thermal expansion, and thermal stability. Electrochemical interdiffusion tests were also performed.

SAMPLE FABRICATION

Samples were fabricated by pressing and sintering coprecipitated powders. Sulfate solutions with desired cationic (In, Pr, Zr) ratios were sprayed into ammonium hydroxide to coprecipitate mixed oxide powders. The precipitate was filtered, washed sequentially with water, acetone, toluene, and acetone, dried in air at 373 K before being calcined in air for 5 hours at 973K. The calcined powders were cold-pressed and granulated through a 45 mesh screen before pressing uniaxially at 152 MPa as parallelepipeds and isostatically pressed at 228 MPa. The pressed bars were sintered for 12 hours at 1823K in air. A cover powder prevented the loss of In_2O_3 during sintering. The furnace was rapidly cooled to 1273K before cooling to room temperature at 300°/h.

PHASE EQUILIBRIA

Quantitative energy dispersive x-ray (EDX) analysis coupled with scanning electron microscopy (SEM), ceramography, and x-ray diffraction (XRD) were used to determine the In_2O_3-$PrO_{1.83}$-ZrO_2 ternary phase diagram. The crystal structure and quantitative estimate of each phase was determined by XRD. The overall composition and the composition of each individual phase was determined by quantitative EDX analyses of large, representative areas. The weight percent of each element[a] was computer calculated from the EDX peak height and width. The EDX system was calibrated with oxides of known compositions.

(a) Present EDX capabilities only detects elements with atomic number greater than 11.

ELECTRICAL CONDUCTIVITY

The electrical conductivity was measured in air using a four-contact dc probe method in a resistance-heated furnace with platinum knife-edge contacts. The temperature of the furnace was measured and controlled with calibrated Pt-Pt 10% Rh thermocouples to within ± 1K from 500 to 1500K. The direct current and voltages were measured in both directions using a high-impedence digital voltmeter and a digital microammeter. The electrical conductivity measurements were accurate to ± 10%.

SEEBECK COEFFECIENT

The absolute Seebeck coefficients were determined on similar samples by applying a temperature gradient along the length of a sample and measuring the potential difference (ΔV) and temperature difference (ΔT) at points along the length of the specimen bar. The absolute Seebeck coefficient determined from a least squares analysis of six ΔV versus ΔT data points. This technique minimized radial temperature gradients and composition changes and provides optimum control of the temperature gradients. This technique was used previously to determine the Seebeck coefficient in the In_2O_3-SnO_2 system.[1]

IONIC TRANSFERENCE NUMBER

The transference numbers were measured using a half cell technique to 1275K in high oxygen pressures using the emf induced by an oxygen gradient maintained across the sample. The ionic transference number (t_i) was calculated from the Nernst equation:

$$t_i = \frac{E}{E_o} = \frac{4FE}{RT} \cdot \ln \; Po_2^{I}/Po_2^{II}$$

where E and E_o are the measured and theoretical emfs respectively, expected at temperature, T(K), across an oxygen gradient Po_2^I and Po_2^{II}. The gas constant is R and the Faraday constant is F.

THERMAL EXPANSION AND STABILITY

Thermal expansion was measured using a high temperature push-rod dilatometer to 1275K with a linear variable differential transducer, sensitive to ± 0.25 μm with temperatures accurate to ±5 K. The coefficient of thermal expansion (CTE) was determined from a linear regression analysis of the expansion versus temperature data points.

The thermal stability was determined from the weight change after prolonged exposure in air or hydrogen at temperatures up to 1473 K. The samples were heated to the test temperature and held for a predetermined time, cooled and weighed. The weight change was determined to 0.01 wt %.

ELECTROCHEMICAL INTERDIFFUSION TESTS

Electrochemical interdiffusion (EID) tests were performed on simple half-cells consisting of an In_2O_3-$PrO_{1.83}$-ZrO_2 cathode and yttria stabilized zirconia electrolyte. The half-cells were fabricated by simultaneously pressing layers of the cathode and electrolyte together into half-cell discs. The disc was sintered in air at 1823K for 12 h. The disc was reduced in thickness and Pt leads attached to both surfaces and connected to a dc power supply outside the EID test furnace. At temperature, a constant current was maintained across the half-cell disc by adjusting the voltage with current and voltage monitored during the test. After the EID test, the disc was examined to determine interfacial interactions, compositional changes, and interdiffusion of cations.

The phase equilbria, electrical and thermal properties, and electrochemical tests are presented below. The relationships

between the phase equilbria and the electrical and thermal properties are discussed.

PHASE EQUILIBRIA

The isothermal ternary phase diagram at 1823K for the In_2O_3-$PrO_{1.83}$-ZrO_2 system is shown in Figure 1 where each triangle represents a measured composition. The individual components form three different phases within the In_2O_3-$PrO_{1.83}$-ZrO_2 ternary. Indium oxide forms a body-centered cubic (BCC, B) phase and praseodymium oxide forms a face centered cubic (FCC, C) phase. Zirconia forms an unstable monoclinic phase (M), but a stable ZrO_2 FCC (F) phase forms when sufficient amounts of In_2O_3 and/or $PrO_{1.83}$ are present.

In addition, two binary compounds were found. A single orthorhombic phase (O) forms when the Pr:In ratio is 1:1 or 67 mol% $PrO_{1.83}$ and 33 mol% In_2O_3 and appears similar with the orthorhombic pattern for $InNdO_3$.[2] When the Pr:Zr ratio is 1:1, a second binary compound with a pyrochlore (P) structure forms. The XRD pattern matches that for $Pr_2Zr_2O_7$.[2] The addition of ZrO_2 to $PrO_{1.83}$ appears to reduce the Pr to the 3^+ state (Pr_2O_3) to form the pyrochlore composition.

The exact boundaries between the C, C+P, and P phase regions were difficult to define because of structural similarities. Pyrochlore is a FCC fluorite structure with a defective fluorite super structure ($A_2B_2X_7V_X$) containing anion vacancies (V_X) very similar to cubic $PrO_{1.83}$.[3] These structural similarities allow a gradual transition between the pyrochlore and fluorite structures, which results in additional x-ray diffraction lines that are resolved by doubling the size of the unit cell. These additional lines are difficult to detect until a large quantity of the pyrochlore phase is present. The phase boundaries are represented

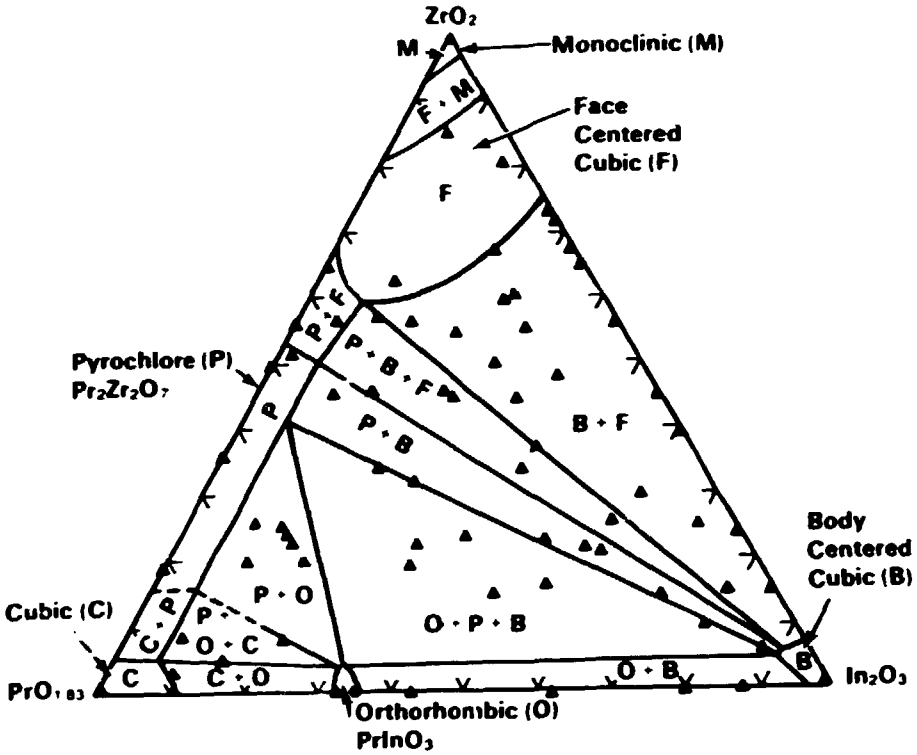

Figure 1. In_2O_3-$PrO_{1.83}$-ZrO_2 Phase Diagram at 1823K

by dashed lines to indicate a gradual transition between the cubic $PrO_{1.83}$ and pyrochlore phases without a definite phase boundary.

ELECTRICAL CONDUCTIVITY

The electrical conductivity varied with composition and structure over eight orders of magnitude between 500 and 1500 K. The electrical conductivity increased with the BCC phase, Figure 2 and was dependent on the presence of second and/or third phases. For example, comparing compositions with equal amounts of the In_2O_3 BCC phase, higher conductivities result for compositions with the pyrochlore or ZrO_2 FCC second phases than with an orthorhombic second phase. The electrical conductivity also increased at all temperatures with the concentration of In_2O_3 as shown at 1300K in Figure 3. This trend was not as dependent on structure as was seen for the In_2O_3 BCC phase in Figure 2.

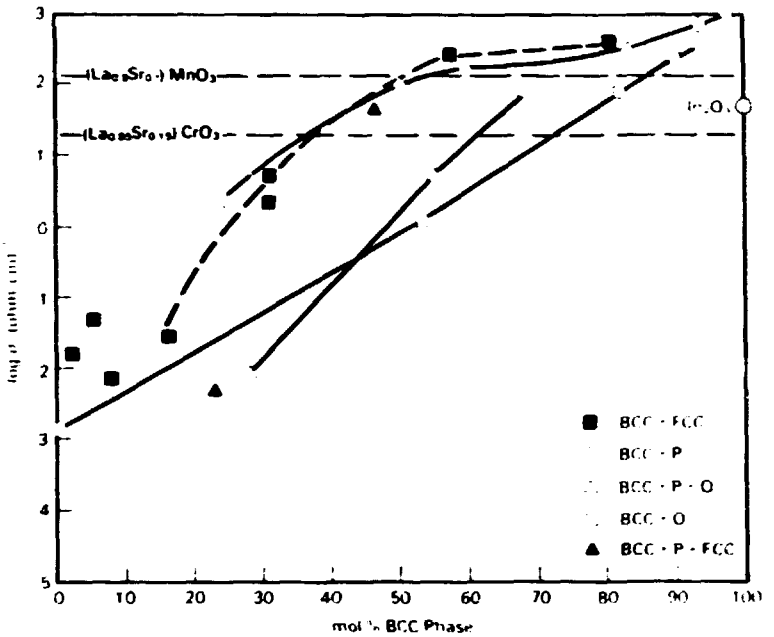

Figure 2. Electrical Conductivity as Function In_2O_3 BCC Phase at 1300K

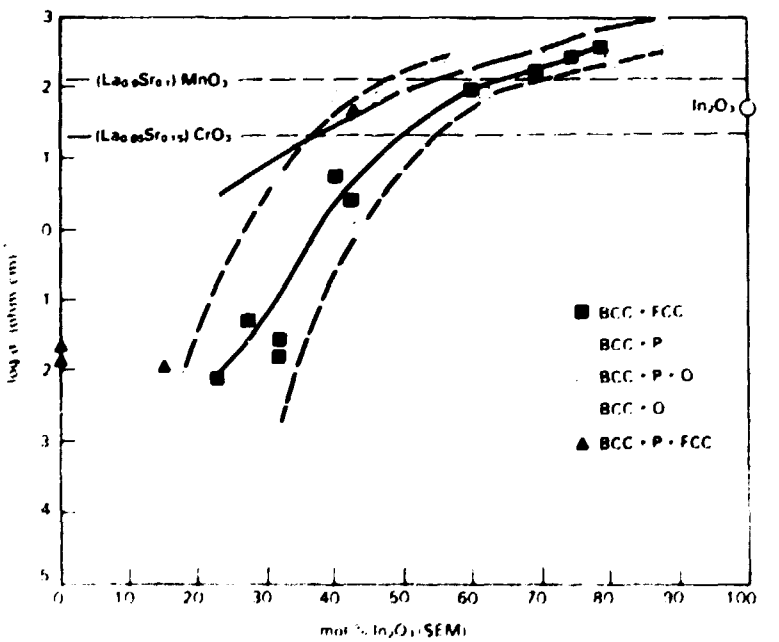

Figure 3. Electrical Conductivity as a Function of In_2O_3 Content at 1300 K

There are a number of compositions within the In_2O_3-$PrO_{1.83}$-ZrO_2 system with higher electrical conductivities than the present cathode $(La_{0.9}, Sr_{0.1})MnO_3$ and interconnect $(La_{0.85}, Sr_{0.15})CrO_3$ materials, Figures 2 and 3. However, compositions containing between 35 and 50 mol% In_2O_3 BCC phase are required.

SEEBECK COEFFICIENT

The Seebeck coefficients for compositions containing In_2O_3 BCC and ZrO_2 FCC phases are shown in Figure 4. Compositions containing a large fraction of In_2O_3 and the BCC phase exhibit negative Seebeck coefficients (n-type conduction) that become more negative at higher temperatures. The sign of the Seebeck coefficient changed from negative at low temperatures to positive at high temperatures as the fraction of the ZrO_2 FCC phase increased. The sign change suggests mixed ionic and electronic conduction with predominately oxygen ion conduction at higher temperatures. As the amount of the FCC phase increased further, the Seebeck coefficient was positive over the entire temperature range.

TRANSFERENCE NUMBERS

Transference numbers define the relative amounts of ionic and electronic conduction. The electrolyte should be a total ionic conductor and the electrodes should be predominately electronic with some ionic conduction. Mixed conduction of the electrode can potentially improve oxygen adsorption and charge transfer at the electrode-electrolyte interface thereby improving fuel cell efficiency.

The transference number was determined for a number of compositions within the B + F phase field. The ZrO_2 FCC phase exhibited >99% ionic conduction (t_i = >0.99). As the fraction of the In_2O_3 BCC phase increased, the ionic transference number decreased to 1% as shown in Figure 5. Within the In_2O_3-$PrO_{1.83}$-ZrO_2

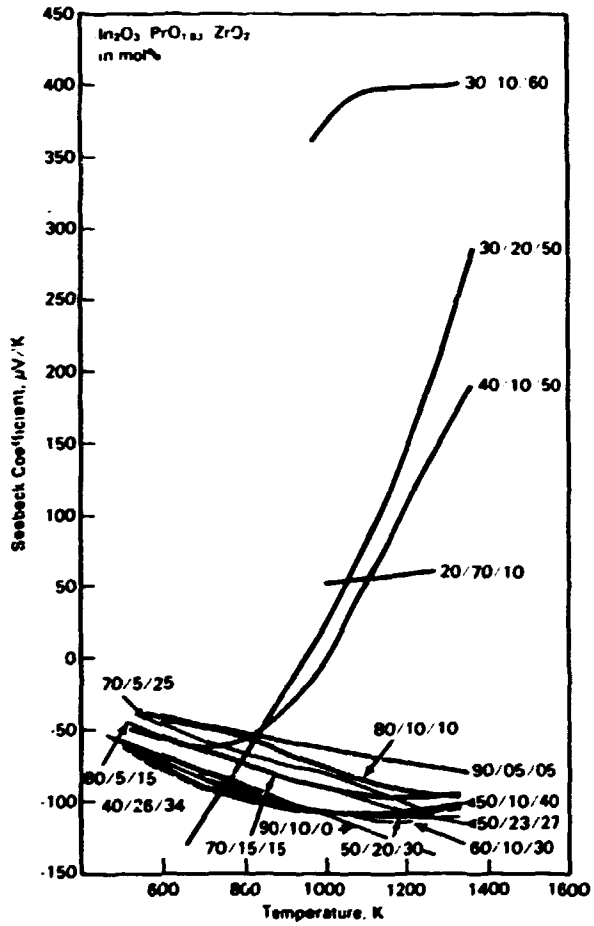

Figure 4. Seebeck Coefficients as a Function of Temperature

system, compositions with high electrical conductivity (>60 mol% BCC phase) are predominately electronic conductors with ionic transference numbers less than 0.01. However, the absolute ionic conduction in these electronic conductors may actually be as great as the nearly 100% ionically conducting ZrO_2 FCC phase. The total conductivity (σ_T) of these electronic conductors (t_i = 0.01) is more than 100 times higher than the ionically conducting FCC phase (T_i = 0.99). Therefore, the ionic contribution (σ_i) can be greater ($\sigma_i=\sigma_T t_i=1.0$ ohm^{-1}-cm^{-1}) in the electronic conductor than in the ionic conductor ($\sigma_i=\sigma_T t_i$-1.0 ohm^{-1}-cm^{-1}). High absolute ionic conduction makes these predominately electronic conductors attractive electrode materials for solid oxide fuel cells.

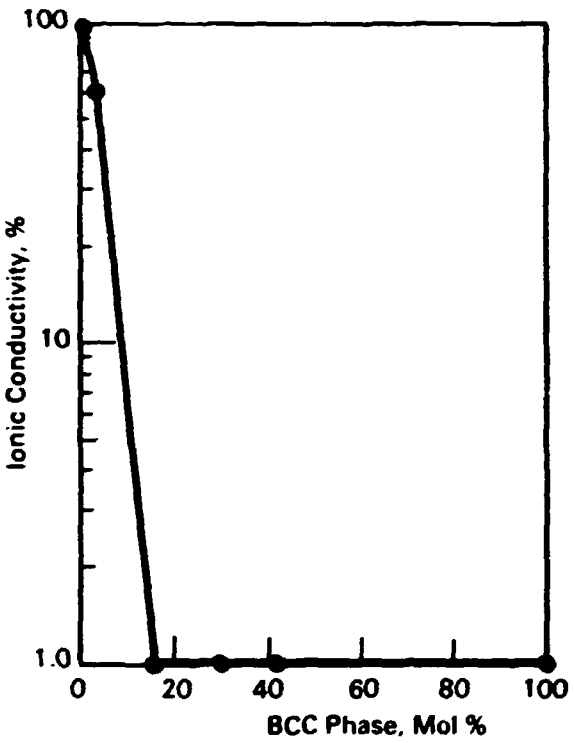

Figure 5. Ionic Transference Number as a Function of In_2O_3 BCC Phase

THERMAL EXPANSION AND STABILITY

The thermal expansion of electrodes must match the electrolyte to minimize thermally induced stress during fabrication and operation. The thermal expansion of the compositions shown in Table 1 were linear over the entire temperature range. The coefficients of thermal expansion (CTE) are shown in Table 1. The measured CTE of an 9.4 mol% Y_2O_3 - 90.6 mol% ZrO_2 electrolyte was higher, 11 x 10^{-6}/K, than reported by Feduska et al[4] for yttria stabilized zirconia and may be attributed to different electrolyte compositions. The thermal expansion of the In_2O_3 BCC phase was lower (9.2 x 10^{-6}/K) than yttria stabilized zirconia. As the pyrochlore fraction increased, the CTE increased to 9.6 x 10^{-6}/K for a composition containing 50 mol% pyrochlore. The CTE also

Table 1. Thermal Expansion of In_2O_3-$PrO_{1.83}$-ZrO_2 and Y_2O_3 Stabilized ZrO_2

Composition, mol%			Structure, mol%(a)			Coefficient of Thermal Expansion
In_2O_3	$PrO_{1.83}$	ZrO_2	Pyrochlore	BCC	FCC	10^{-6}/K
100				100		9.2
78	12	10	10	90		9.4
70	16	14	25	75		9.1
50	26	24	50	50		9.6
79	6	15		80	20	9.3
69	6	25		51	49	9.7
40	12	48		31	69	10.2
					100	11.0
9.4 mol% Y_2O_3 - 90.6 mol% ZrO_2						

(a) Determined from the In_2O_3-$PrO_{1.83}$-ZrO_2 phase diagram or by x-ray diffraction.

increased from 9.3 to 10.2 x 10^{-6}/K as the fraction of the ZrO_2 FCC phase increased from 20 to 69 mol%. The compositions containing FCC + BCC have the closest thermal expansion match to the Y_2O_3 stabilized ZrO_2 electrolyte.

Compositions containing B + F and B + P phases have thermal expansions similar to the electrolyte providing a sufficient amount of the ZrO_2 FCC or pyrochlore second phase is present. The ratio between the In_2O_3 BCC and second phases would have to be adjusted to balance the thermal expansion and electrical conductivity requirements for SOFC components.

THERMAL STABILITY

The In_2O_3-$PrO_{1.83}$-ZrO_2 compositions shown in Table 2 are thermally stable in air up to 1473 K, Table 2. After 98 h at 1273 K and 1473 K in air, the samples weight changed less than 0.1 wt %. The stability of these materials in air makes them potential candidates for the cathode.

The In_2O_3-$PrO_{1.83}$-ZrO_2 samples shown in Table 3 were held at 1473K for one hour in a reducing environment of 4%H_2 - 96%Ar. During these tests, samples were reduced to In metal with 25 and 64 wt% weight loss. These compositions with high In_2O_3 can not, therefore, be used as anodes or interconnectors because they are unstable in a reducing environment.

ELECTROCHEMICAL INTERDIFFUSION

Two EID tests were performed using a cathode with an overall composition of 43 mol% In_2O_3, 24 mol% $PrO_{1.83}$, 33 mol% ZrO_2 and yttria stabilized zirconia electrolyte containing 9.4 mol% Y_2O_3. This particular cathode was chosen because it has high electrical conductivity and a structure similar to the electrolyte. The microstructure of a pretest sample is shown in Figure 6. A significant amount of porosity is found at the cathode-electrolyte interface, which could result in localized, higher current densities than the overall average current den[illegible] The cathode contains equal molar amounts of two phases: [illegible] ZrO_2

Table 2. Weight Change After 98 h at 1273 K and 1473 K in Air

Composition, mol%			1273 K Weight Change,[a] %	1473 K Weight Change, %
In_2O_3	$PrO_{1.83}$	ZrO_2		
40	60		+0.02	+0.13
60	40		+0.01	+0.05
30.6	28.6	34.8	-0.06	+0.01
23	34.3	42.7	+0.03	+0.02
20.1	39.6	40.3	0.00	-0.04
75		25	-0.02	-0.09
50	20	30	+0.04	-0.05
30	50	20	-0.01	-0.05
50	10	40	-0.01	-0.05
40	10	50	+0.01	-0.03
90	5	5	+0.01	-0.03
80	10	10	+0.02	-0.06
70	15	15	+0.01	-0.05

(a) Plus sign indicates a weight gain and a minus sign a weight loss.

Table 3. Weight Loss of Ar-4%H_2 at 1473 K

Composition, mol%			Structure, mol%			
In_2O_3	$PrO_{1.83}$	ZrO_2	Pyrochlore	BCC	FCC	Weight Loss,%
70	15	15	17	83		44
50	23	27	46	54		34
80	5	15		80	20	50
75		25		57	43	64
60	10	30		74	36	25
70	5	25		51	49	48
50	10	40		31	69	40

FCC phase composed of 16 mol% In_2O_3, 56 mol% $PrO_{1.83}$, and 28 mol% ZrO_2 and a discontinuous In_2O_3 BCC phase composed of 92 mol% In_2O_3, 2 mol% $PrO_{1.83}$, and 6 mol% ZrO_2. The BCC phase exhibits elongated shape with a major axis 5 to 10 μm and and a minor 1 to 2 μm.

The electrolyte is composed of a single FCC phase of yttria stabilized zirconia containing a significant amount of In_2O_3. For example, an area in the electrolyte 150 μm from the interface contained 5.6 mol% In_2O_3. Apparently, the In_2O_3 mobility is great enough to diffuse into the electrolyte from the electrode during sintering.

One EID test (5) was conducted at a constant current density of 0.3 A/cm^2 for 316 h as summarized in Table 4. The voltage increased slowly from 1.7 to 3.2 V during the test. There were no

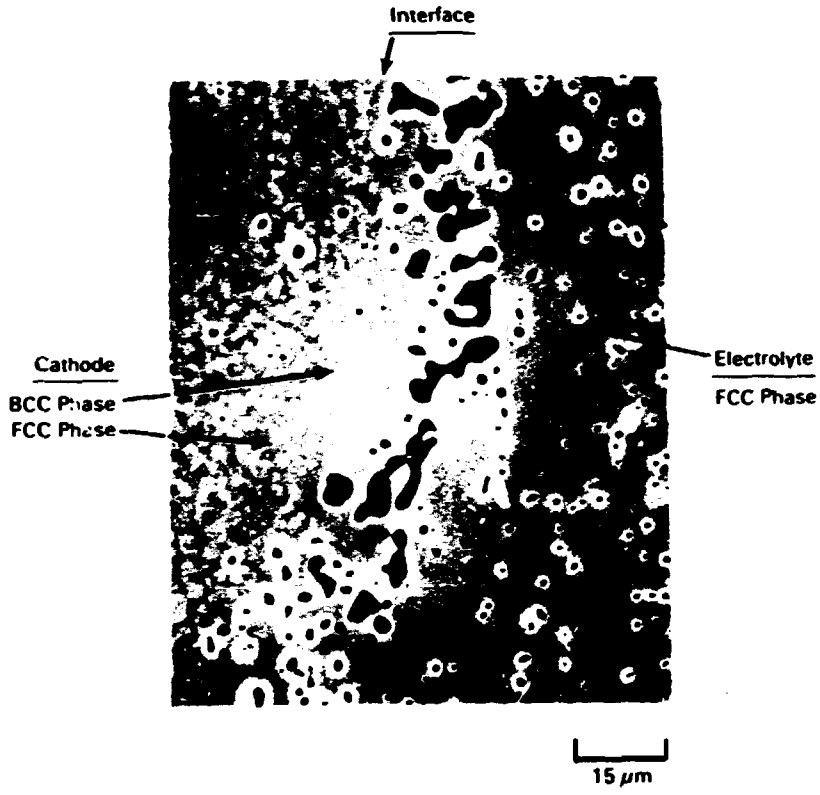

Figure 6. Half-cell Microstructure Before Electrochemical Interdiffusion Test

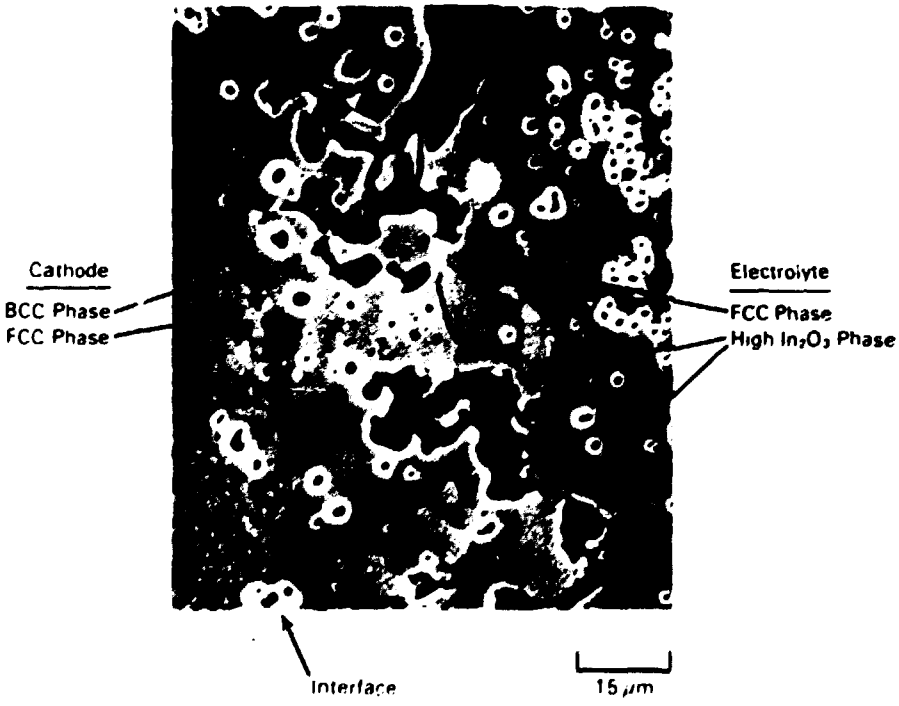

Figure 7. Half-cell Microstructure Following Electrochemical Interdiffusion Test 5

Table 4. Electrochemical Interdiffusion Test Conditions and Results

EID #	Current Density, (a) A/cm^2	Voltage Start	Voltage Finish	Temperature Range, C	Duration, h.
5	0.3	1.7	3.2	979 - 1004	316
6	0.5	1.8	4.0	924 - 1027	332

(a) Localized current densities in areas of contact were significantly larger.

visible degradation of the disc following this test. A small portion of the sample disc was sectioned for analysis; the remainder was used to conduct EID test 6.

The microstructure of the disc following EID test 5 is shown in Figure 7. About 3 mol % In_2O_3 was found in the electrolyte 150 μm from the interface; slightly less than found in the pretest disc. The large second phases observed in the electrolyte near the interface contained 96 to 98 mol% In_2O_3 with 2 to 4 mol% $PrO_{1.83}$ and ZrO_2. Y_2O_3 was not found in this phase. This phase is probably the In_2O_3 BCC phase based on the In_2O_3-$PrO_{1.83}$-ZrO_2 phase diagram. This large In_2O_3 phase was not found in the pretest disc and was much larger than the In_2O_3 BCC phase found in the cathode. This In_2O_3 phase may result from a consolidation of the smaller BCC In_2O_3 phases in the cathode.

The second EID test (6) was conducted at a higher current density (0.5 A/cm^2) for 332 h, Table 4. This test was similar to EID test 5 in that the voltage increased with time and the disc wa:

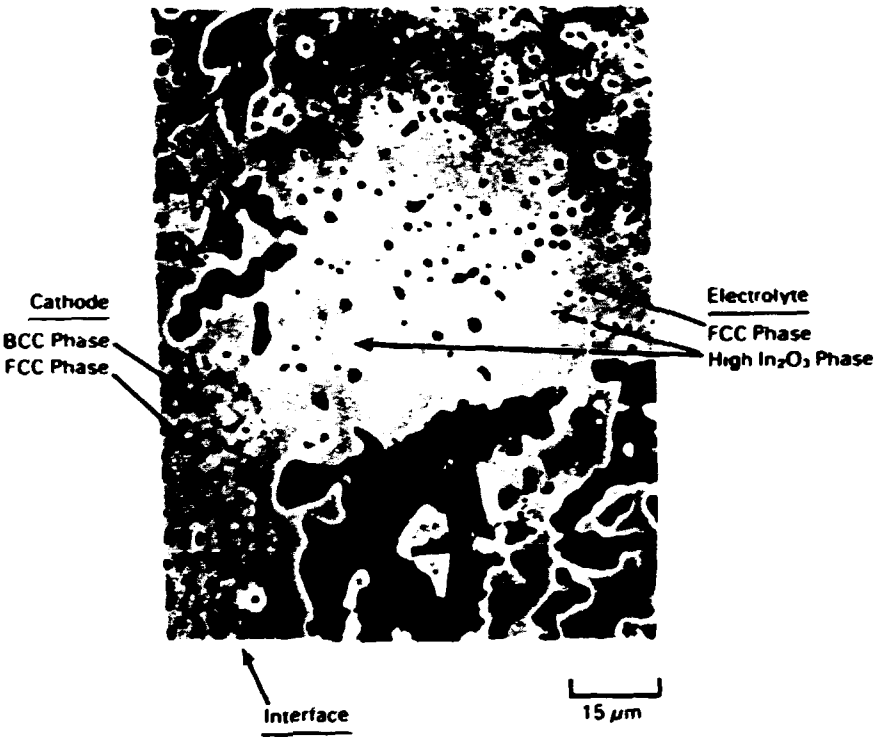

Figure 8. Half-cell Microstructure Following Electrochemical Interdiffusion Test 6

not visibly degradated. The interface microstructure shown in Figure 8 was similar to the microstructure after the lower current density test, Figure 7. In_2O_3 was found in the electrolyte about 150 μm from the interface, although the concentration (1.2 mol%) was less than either EID test 5 or the pretest disc. The postest In_2O_3 concentration in the electrolyte suggest the electric field is driving the In_2O_3 toward the cathode. The large high In_2O_3 phases observed after EID test 5 were also observed following EID test 6. The In_2O_3 appears to be very mobile in the FCC phase, which could be a problem if it diffused to the anode-electrolyte interface. At the anode, In_2O_3 will be reduced to the metal and volatalize in the reducing atmosphere. The large high In_2O_3 phases observed at the electrolyte interface following the EID tests are due to either prolonged time at high temperatures or to an electrochemical process.

CONCLUSIONS

Material properties required the electrode and interconnects in a SOFC were measured for compositions in the In_2O_3-$PrO_{1.83}$-ZrO_2 system. Electrical conductity was dependent on structure and composition and exceed the conductivity of present electrodes and interconnects. In addition, the high absolute ionic conductivity of these materials will result in mixed electronic and ionic conductivity and improve the efficiency of SOFC.

For all their attractive features, In_2O_3-$PrO_{1.83}$-ZrO_2 compositions cannot be used for the anode or interconnect components because the In_2O_3 was unstable in the reducing environment these components must operate. Compositions in this system could be used for the cathode. However, the effect of the In_2O_3 diffusion into the electrolyte on the operation of the fuel cell would have to be determined.

REFERENCES

1. J. L. Bates, C. W. Griffin, D. D. Marchant and J. E. Garnier, "Electrical Conductivity, Seebeck Coefficient and Structure of In_2O_3-SnO_2", Bull. A. Cer. Soc., 65, No. 4. 673-678 (1986).

2. Joint Committee on Powder Diffraction Standards. 1971. Power Diffraction Files. Joint Committee on Powder Diffraction Standards, Swarthmore, Pennsylvania.

3. A. F. Wells, Structural Inorganic Chemistry, Fourth Edition Clarendon Press, Cambridge (1975) pp. 209, 499-508.

4. Feduska, W., et al. 1985. High-Temperature Solid Oxide Electrolyte Fuel Cell Power Generation System. DOE/ET/17089, Westinghouse Research and Development Center, Pittsburgh, Pennsylvania.

WHISKER REINFORCED STRUCTURAL CERAMICS (PROGRESS IN THE VLS GROWTH AND USE OF LONG SILICON CARBIDE WHISKERS)

F. D. Gac and P. D. Shalek
Materials Science & Technology Division

W. J. Parkinson
Design Engineering Division

Los Alamos National Laboratory
Los Alamos, New Mexico 87545

C. Edwards and J. B. Price

Textile Research Center
Texas Tech University
P.O. Box 5888
Lubbock, Texas 79417-5888

ABSTRACT

A VLS whisker growth process, optimized for the production of short (~10 mm lengths) SiC whiskers, was modified to produce $\geq$ 25 mm long whiskers. In conjunction with this modification, a plan was developed for incorporating an AI system to enhance the whisker growth process. An oriented whisker ribbon was produced from the long whiskers, as a step toward the development of a staple whisker yarn.

INTRODUCTION

It has long been recognized that there is a need for a high strength fiber that is resistant to high temperature oxidizing environments. Hence, one reason why the Dow Corning Corporation was awarded a contract in 1983 by the Defense Research Projects Agency (DARPA) to develop a silicon-carbon based fiber whose properties surpassed the Nicalon fiber developed in Japan.[a,b] The need for such a fiber was again emphasized in January 1987 by two keynote

---

[a]Air Force Contract F33615-83-C-5006; DARPA funding administered by Major Steven G. Wax through Dr. Allan P. Katz of the Air Force Wright Aeronautical Laboratories (AFWAL).

[b]Product of the Nippon Carbon Co., Tokyo, Japan; distributed in the U.S. by the Dow Corning Corp., Midland, MI 48686-00995.

speakers, Persh and Stein, at the 11th Annual Conference on Composites and Advanced Ceramic Materials.[1,2] Most recently, in March 1987, AFWAL published a Program Research and Development Announcement[3] in which the requirements for a high temperature fiber were outlined.

Los Alamos has been involved in the synthesis[4-7] and use[8-10] of silicon carbide (SiC) whiskers, produced by a vapor-liquid-solid (VLS) crystal growth process, since 1982. These whiskers display an average tensile strength in the range of 8.4-14.6 GPa (1.2-2.1 Mpsi) and an elastic modulus of 578 GPa (83.8 Mpsi).[11,12] These tensile strengths are markedly higher than the 2 GPa (0.3 Mpsi) average reported for Nicalon.[13] The whiskers are normally grown in ∿10 mm lengths but experimentation revealed that the whiskers could be grown in 25-75 mm lengths. Consequently, it was concluded that the long VLS SiC whiskers might lend themselves to the fabrication of a staple yarn which could be evaluated as a candidate high temperature "fiber."

Review of staple yarn theory showed that, depending upon the length and twist of discontinuous fibers within a staple yarn, one can observe up to ∿90% of the modulus of a continuous fiber.[14] Therefore, the potential exists to achieve staple yarn strengths that represent a considerable fraction of the strength of the discontinuous fiber, or whisker, in this case. Assuming this translated to only 25% of the tensile strength of the whiskers, this would still represent a minimum average value of 2.1 GPa (0.3 Mpsi), which would be equivalent to the Nicalon. However, it should be noted that the single crystal, highly stoichiometric nature of the whiskers lends itself to enhanced elevated temperature resistance, compared to that expected for the predominantly amorphous Si-C-O Nicalon fiber.

The remainder of this paper addresses the VLS growth of long SiC whiskers and initial attempts at producing a staple yarn from such whiskers. In addition, plans for incorporation of an artificial intelligence (AI) system in the whisker growth process are discussed. An AI system offers the potential for further improving the yield, quality and reproducibility of the whisker growth process at a fraction of the human resources. Such a payoff is especially attractive from the standpoint of technology transfer. The timing for incorporation of the AI system is ideal since a new, more meaningful database is being generated in conjunction with the shift from growing short whiskers to growing long whiskers.

PROGRESS DURING FISCAL YEAR 1987

LONG SIC WHISKER GROWTH

Growth of long VLS SiC whiskers required a modification of the well understood, controllable process for growing short whiskers. A brief review of the short whisker growth process is presented as background information. The process makes use of the reactor shown in Fig. 1. The whiskers are grown from a metallic catalyst distributed

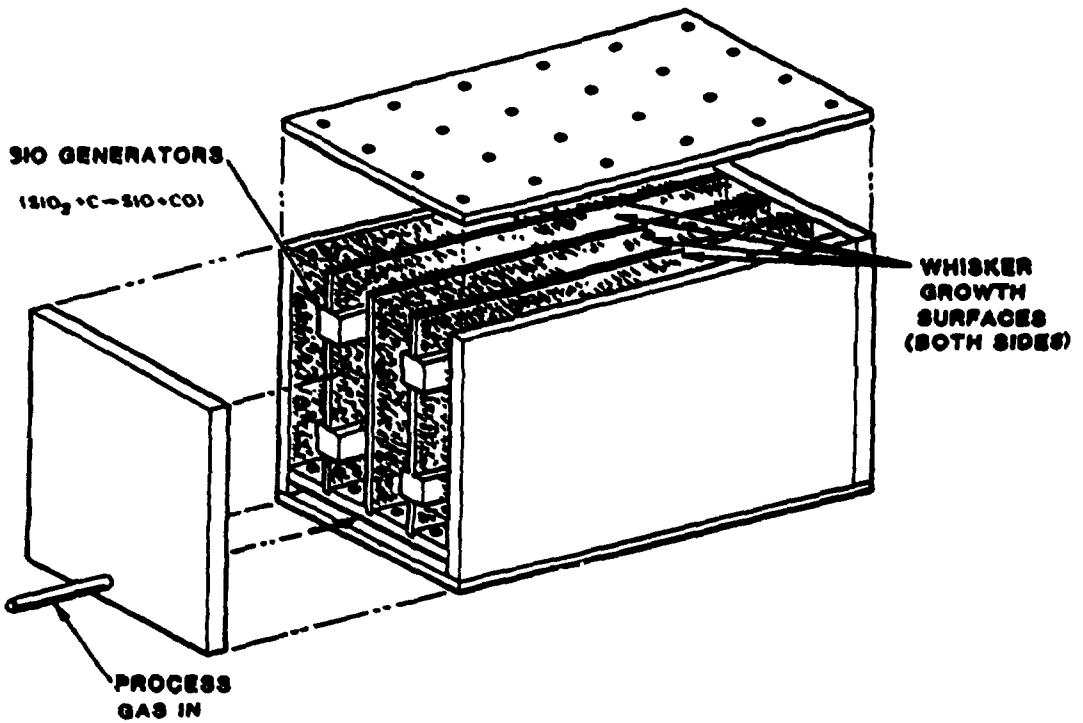

Fig. 1. Type of reactor used in growing short VLS SiC whiskers.

on vertical graphite plates. The methane (CH_4) reactant in the process gas stream mixes with the silicon monoxide (SiO) reactant being generated in situ to nucleate whisker growth. Figure 2 illustrates the uniform yield of prime whiskers (4-8 μm diameter) that could be obtained throughout the reactor when the process parameters were optimized. These whiskers were produced from the Alloy 62[c] (manganese-based) catalyst, which always gave the highest weight yield.

In order to obtain the prime whiskers, it was necessary to control the reactant gas composition so as to nucleate whiskers in the appropriate portion of phase area A of the phase diagram shown in Fig. 3. In this diagram, the reactant composition (carbon-to-silicon (C/Si) ratio) is on the horizontal axis, the reactant pressure (silicon (Si) supersaturation) is on the vertical axis, and the phase areas represent different morphologies of SiC whiskers that are nucleated and grow there.

One of the most important factors contributing to good whisker growth was the homogeniety of the reactant gas (SiO, CH_4) mixing. Flow visualization studies showed that vigorous jet action was needed to achieve optimum mixing. In actual practice, it was found that diffusion of the process gases through the plenum porosity was necessary, in concert with the jet action, for optimum mixing (Fig. 4). The plenum porosity, however, was not stable over a long period of time, as it progressively filled with SiC reaction product with an eventual deterioration in the quality and amount of whisker growth. A new plenum designed for long term stability is under evaluation, where the bulk porosity is purposely sealed and then simulated with a pattern of fine holes, as shown in Fig. 5.

Numerous modifications were made to the short whisker reactor configuration in an attempt to grow long whiskers. The modification shown in Fig. 6 has proven to be the best thus far; the center of the reactor has been opened up and the same generator weight is used but in a vertical rather than horizontal array. A stainless steel catalyst is used instead of Alloy 62 because it has proven to grow the longest whiskers. Other process conditions such as heating cycle, gas composition and flow rate remain essentially the same.

Some long whiskers grown in the modified reactor are shown in Fig. 7. At the end of the run, they were almost perpendicular to the plates with some of about 76 mm in length extending to the center of the reactor, having since settled. Yields of up to 6 grams per run have been obtained, compared to about 12 grams per run for the short whisker setup, in the same, small developmental reactor.

---

[c]Product of Coast Metals Inc., Little Ferry, N.J (no longer a supplier).

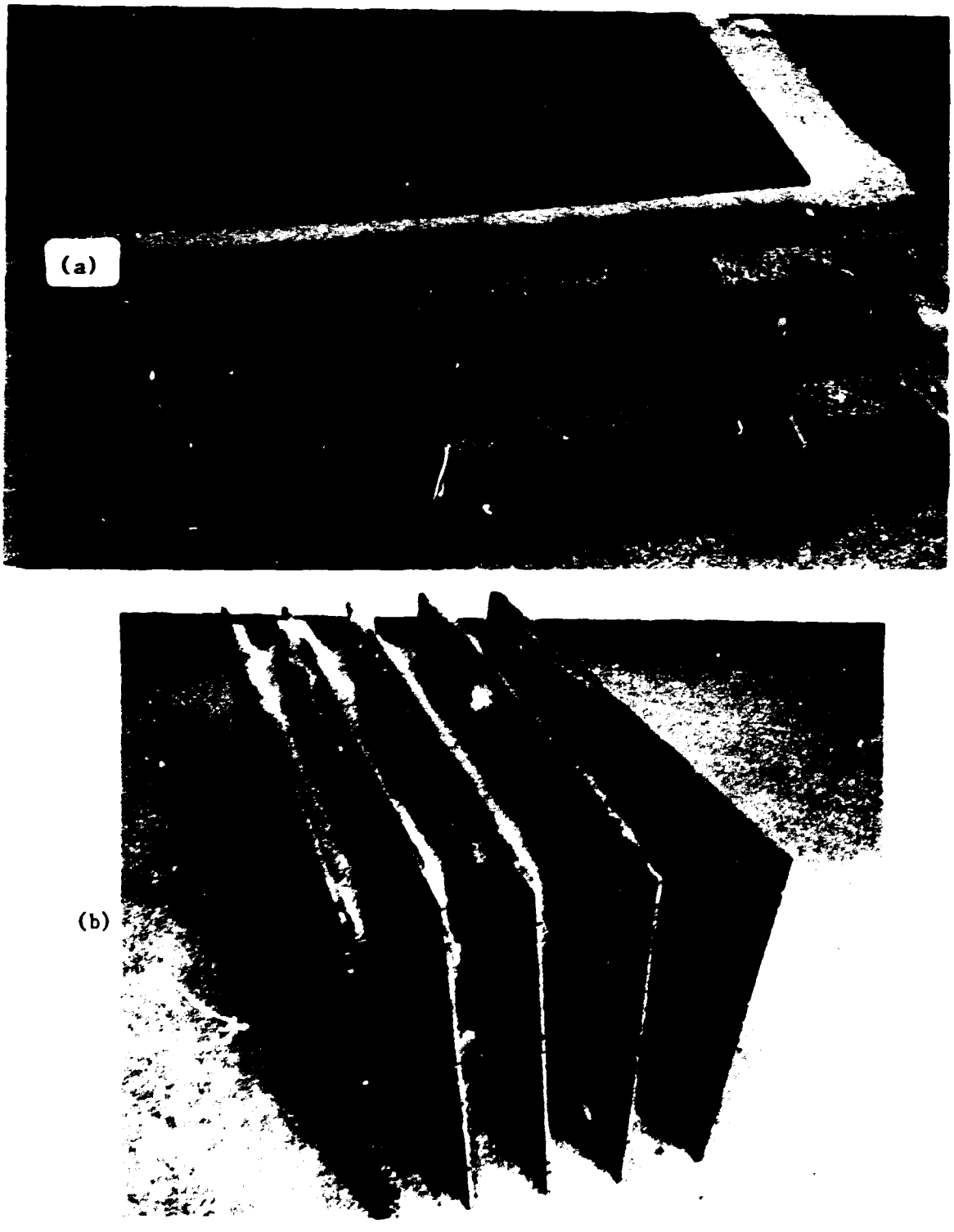

Fig. 2. Copious, uniform growth of prime VLS SiC whiskers resulting from optimized process, as seen (a) across plates and (b) across reactor.

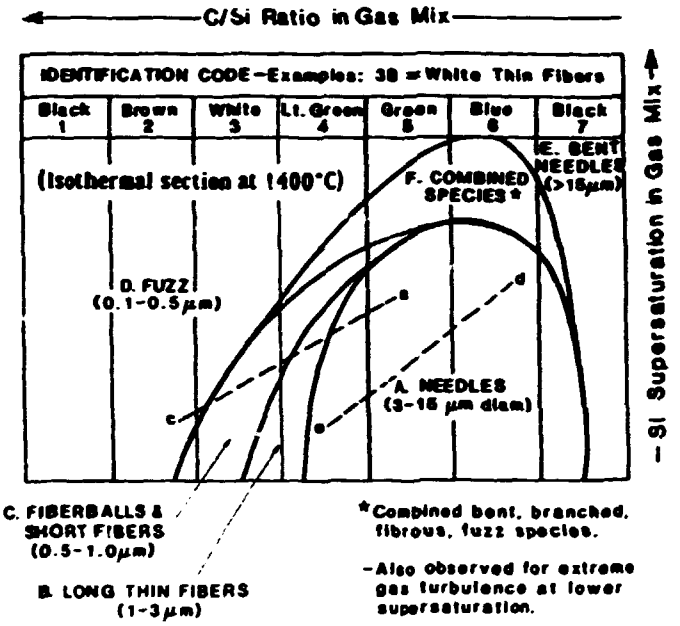

Fig. 3. Empirical phase diagram for VLS SiC whisker growth (1400°C, Alloy 62 catalyst).

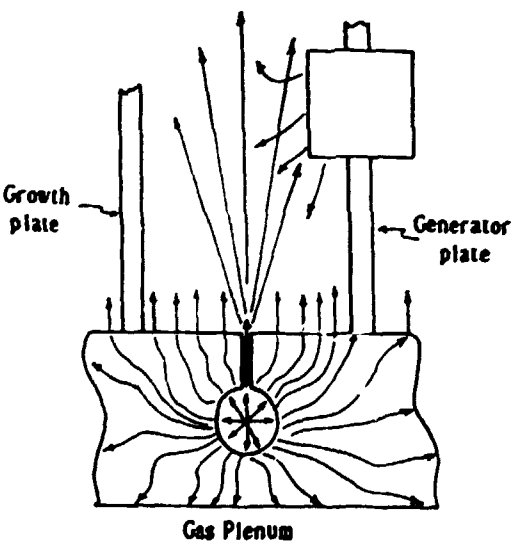

Fig. 4. Jet action coupled with diffusion through a porous plenum has given the most favorable reactant gas mixing for whisker growth.

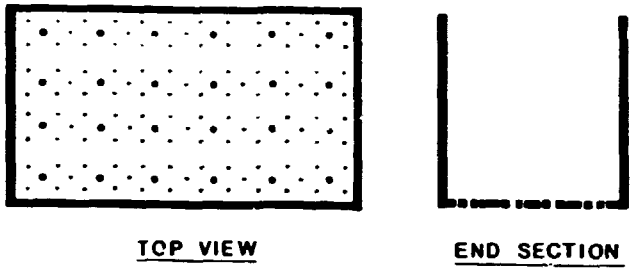

- Jets
- Simulated Bulk Porosity

Fig. 5. Stable VLS SiC whisker growth reactor design (under evaluation) utilizing a bored plenum, jet mixing and simulated diffusion.

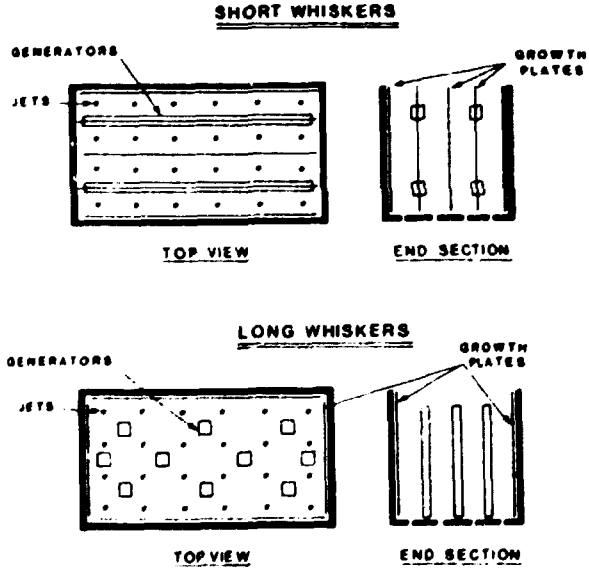

Fig. 6. Current reactor configurations (semi-stable) for VLS SiC whisker growth; both utilize a bored plenum, jet mixing and natural diffusion.

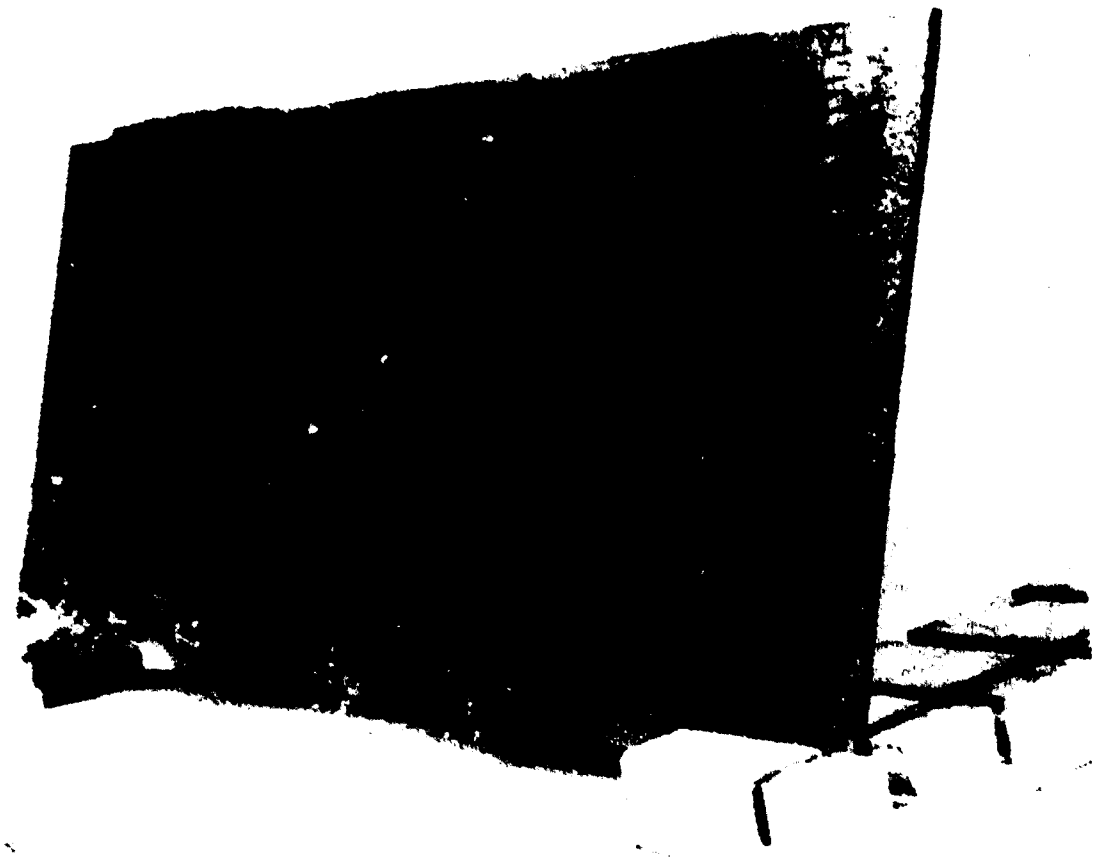

Fig. 7. Long whiskers grown in modified reactor of Fig. 6.

In order to increase the yield of long whiskers, a higher SiO concentration must be maintained in the reactor. The in situ generator process presents a problem in that the SiO generation starts at a very high level, then falls off rapidly with time, as shown in Fig. 8. The reactant composition thus follows the paths shown by dotted lines a-c and d-e in Fig. 3. Good growth, as shown in Fig. 2, is obtained when the reactant composition stays within phase area A for the entire run (path d-e). A path such as a-c, however, can result in the nucleation of secondary phases on the prime whisker growth, as shown in Fig. 9.

Two approaches are presently being investigated to increase long whisker yield and eliminate secondary growth. One involves tailoring the SiO concentration-time profile by programming the partial pressure of carbon monoxide (CO) to give constant SiO generation, and therefore a constant C/Si ratio. This will eliminate secondary growth and will allow an increase in generator weight for significantly increased yield. A numerical program is in place for determining the CO overpressure profile. The second approach entails programming the partial pressure of CH_4 to match the decline in the partial pressure of SiO. This will eliminate secondary growth but gives only a small increase in yield. This approach is the easier of the two to implement.

INCORPORATION OF ARTIFICIAL INTELLIGENCE

An AI scheme will be applied to the VLS SiC whisker growth process by developing two expert systems, or more precisely, one expert system in two stages that will do two distinct jobs. Work has commenced in laying the groundwork for a whisker growth consultant, the first expert system or the first stage of the final product. The whisker growth consultant will help the current user set up whisker growth experiments and future users set up production runs. The second expert system will be a control program for the whisker growth process that will be piggy-backed upon the knowledge base of the whisker growth consultant. This two phase plan is illustrated in Fig. 10.

Artificial intelligence programs, or in this case expert systems (which are a subset of AI programs), differ from conventional programs in several ways. The most significant difference is that expert systems use symbol manipulation to solve problems that require heuristic solutions, whereas conventional programs manipulate numbers to solve problems that can be solved algorithmically.

Some of the reasons why AI will be particularly useful for VLS whisker growth are as follows:

1. The process cannot be described adequately with a mathematical model. Therefore, one cannot develop a control algorithm for the whisker growth process. Control will have to be rule-based.

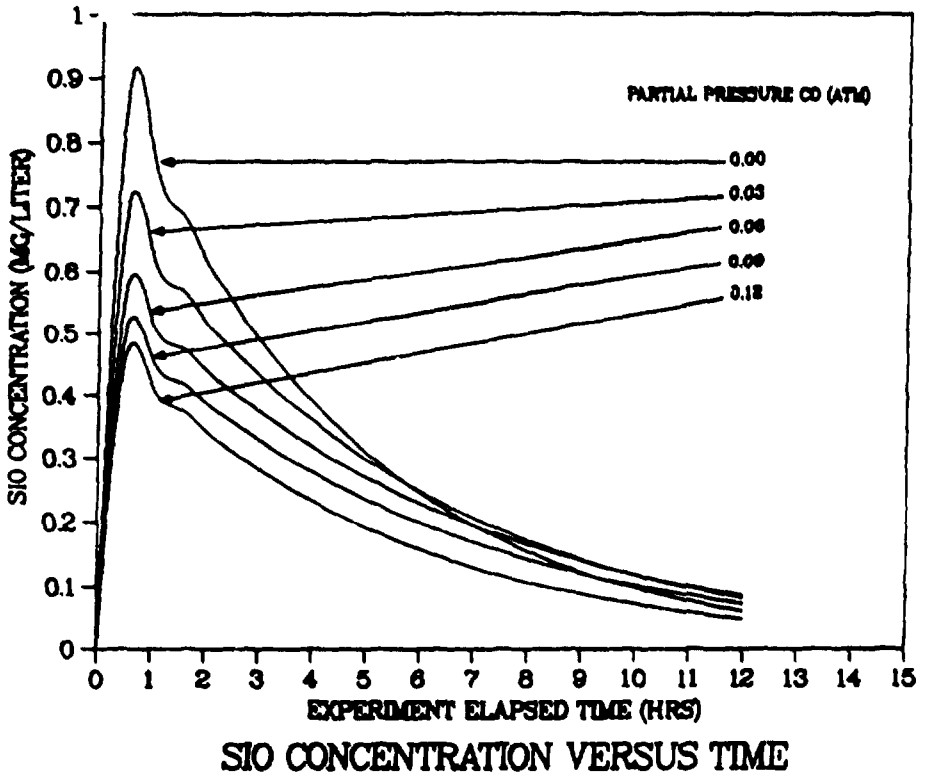

Fig. 8. Change in SiO concentration with time for reactor with in situ generators.

(a)

(b)

Fig. 9. Whisker growth along path a-c in Fig. 3 showing secondary phase overgrowth after (a) 5 hours and (b) 7.5 hours at 1400°C.

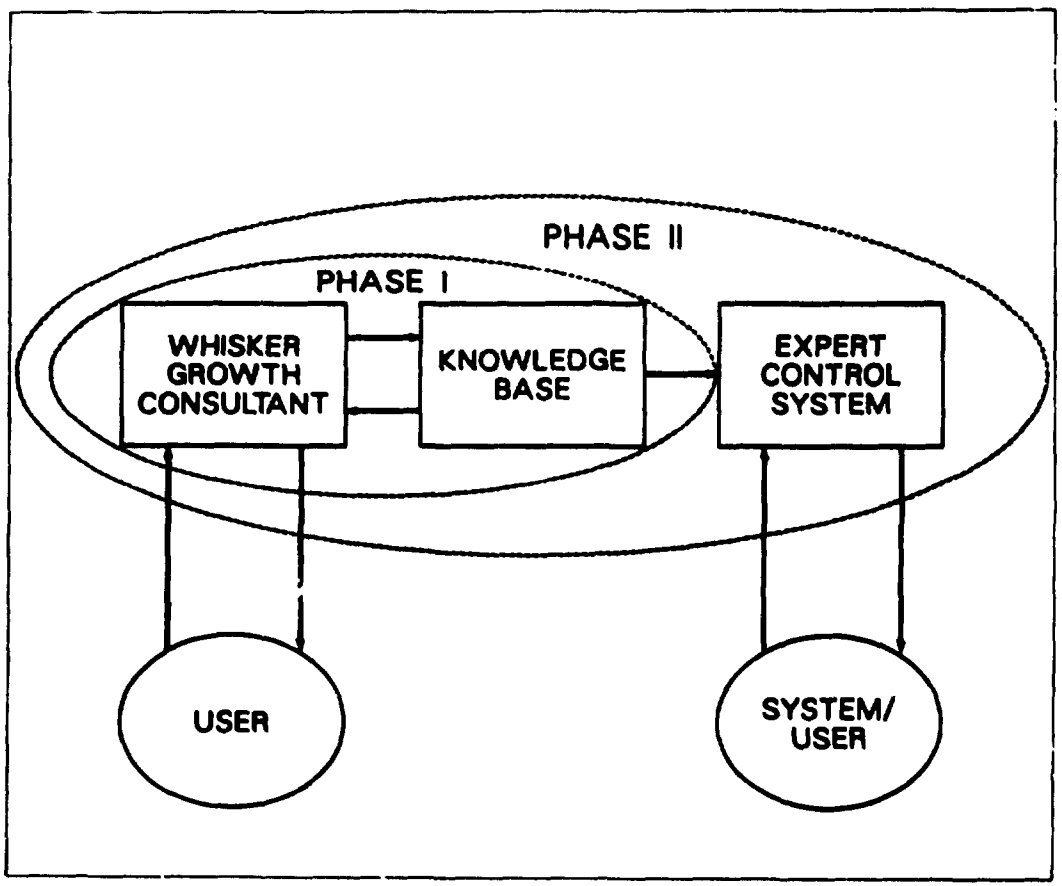

Fig. 10. Conceptual representation of expert systems envisioned for the VLS SiC whisker growth process.

2. We can make the process work because we have experienced experts who use heuristic rules in addition to understanding the physics and chemistry of the process. The AI system would function in the same way.

3. Technology transfer of a rule-based process will take place easier if the rule set and knowledge base are defined and computerized. In other words, we cannot readily transfer the actual experts.

The major challenge impeding the development of an expert system for the VLS whisker growth process is that all of the rules have yet to be identified and defined. The first step toward remedying this situation entailed building a relational database using the INGRES[d] database management system. Correlations, obtained by manipulation of the database, will be used to develop rules and confidence levels for those rules. A partial list of categories from that database that will be examined is as follows:

1) amount of SiO generation,
2) catalyst characteristics,
3) substrate characteristics,
4) inlet gas composition and flow rate,
5) reactor characteristics, and
6) exit gas composition as a function of time.

When the whisker growth consultant is completed, a dialogue between a user and the expert system may proceed like this:

USER:

"I have catalyst X and reactor Y, and I wish to produce Z grams of whiskers of type W. What should my initial conditions be?"

COMPUTER:

"The initial temperature should be A, the initial flow rate B, and the initial composition C, with an initial peak concentration of CO of D."

OR

"If I know more about the substrate I could answer that question with greater confidence."

---

[d]Product of Relational Technology, Inc., Berkeley, CA 94705.

The control system will be a direct outgrowth from the consultant, and in fact, will use the same knowledge-base. The expert control system will sense the reactor temperature and exit gas composition, use the information provided to the whisker growth consultant, and adjust the inlet gas composition and possibly the reaction temperature to achieve the required results.

VLS SIC WHISKER STAPLE YARN DEVELOPMENT

Progress in developing a staple yarn from VLS SiC whiskers has proceeded along two paths. The first attempt entailed folding ~25 wt% of as-grown (i.e., not beneficiated) VLS SiC whiskers, measuring $\leq$ 20 mm long, into the core of a rayon sliver. The purpose of the rayon was to serve as a carrier and lubricant during subsequent yarn processing. The handmade "composite" sliver is shown in Fig. 11; the dark gray material is the whiskers and the white fibers are the rayon. Scanning electron microscope (SEM) examination of this sliver, Fig. 12, revealed that the whiskers (the slender, straight rods) were quite disoriented while the rayon fibers (the thicker, curved fibers) displayed considerable orientation. This sliver was then rotor spun to produce the yarn shown in Fig. 13. This proved to be too aggressive a treatment for the whiskers in that the whisker length was reduced to $\leq$ 4 mm and ~60% of the whiskers was lost as powder that accumulated in the rotor spinner. A high magnification view of the rotor spun yarn is presented in Fig. 14. Few whiskers could be easily identified amongst the rayon and those that were present, though displaying some orientation, were quite short.

In view of these results, it was concluded that a second, much less aggressive, non-conventional approach would have to be explored to develop an acceptable staple whisker yarn. To that end, three basic processing steps were identified. The first was to disrupt the as-grown whisker bundles in such a way so as to not reduce the whisker lengths. This was accomplished by air agitating the whiskers while immersed in glycerine. The second step was to orient and collect the whiskers in a form that would facilitate the production of a yarn. This was accomplished by vacuum casting onto a translating piece of filter paper to produce the oriented whisker ribbons shown in Fig. 15. Concurrent with the vacuum casting operation, the whiskers were washed with water to remove the glycerine. SEM examination of the ribbon revealed that the whiskers displayed a considerable degree of orientation and that not all of the glycerine was removed during washing, as shown in Fig. 16. The third step is envisioned to involve rolling up and rayon wrapping the ribbon to produce a yarn.

Fig. 11. Handmade "composite" sliver consisting of ∿25 wt% VLS SiC whiskers folded into the core of a rayon sliver.

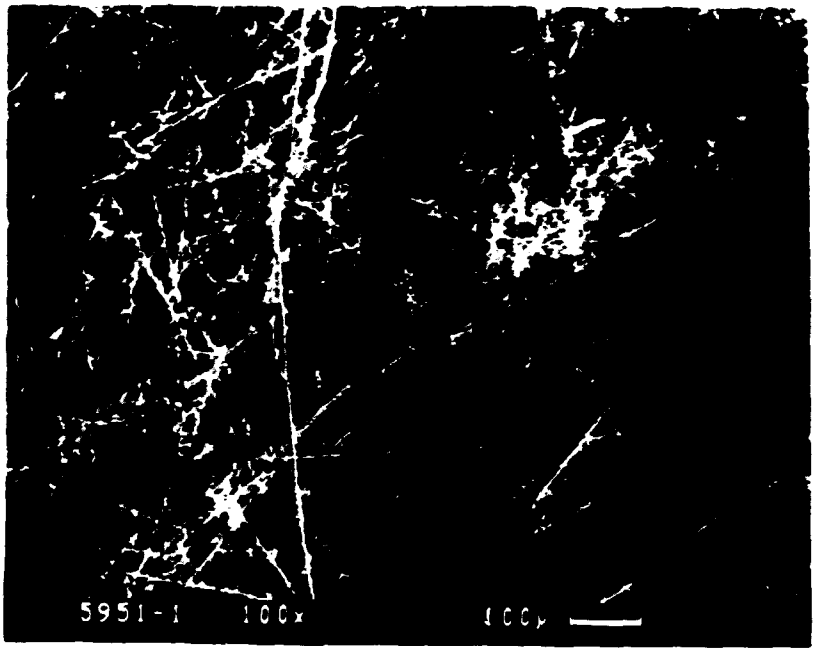

Fig. 12. SEM photomicrograph of handmade whisker-rayon sliver; whisker length is $\leq$ 20 mm.

SUMMARY

A VLS whisker growth process, optimized for the production of ~10 mm long SiC whiskers, was modified to produce longer whiskers measuring $\geq$ 25 mm in length. Efforts are underway to tailor the partial pressure of CO and/or the partial pressure of CH_4 to 1) achieve more stable SiO generation, 2) increase the yield of long whiskers, and 3) eliminate undesirable secondary whisker growth. A plan was developed for incorporating an AI system to enhance the quality and reproducibility of whisker growth. Attempts at producing a staple whisker yarn by rotor spinning revealed that this technique was too aggressive. A non-conventional approach was developed in which an oriented whisker ribbon was produced as a predecessor to a staple yarn. Future work in this area will focus on twisting the ribbon and incorporating a fugitive rayon fiber around the ribbon to facilitate subsequent handling and actual yarn production.

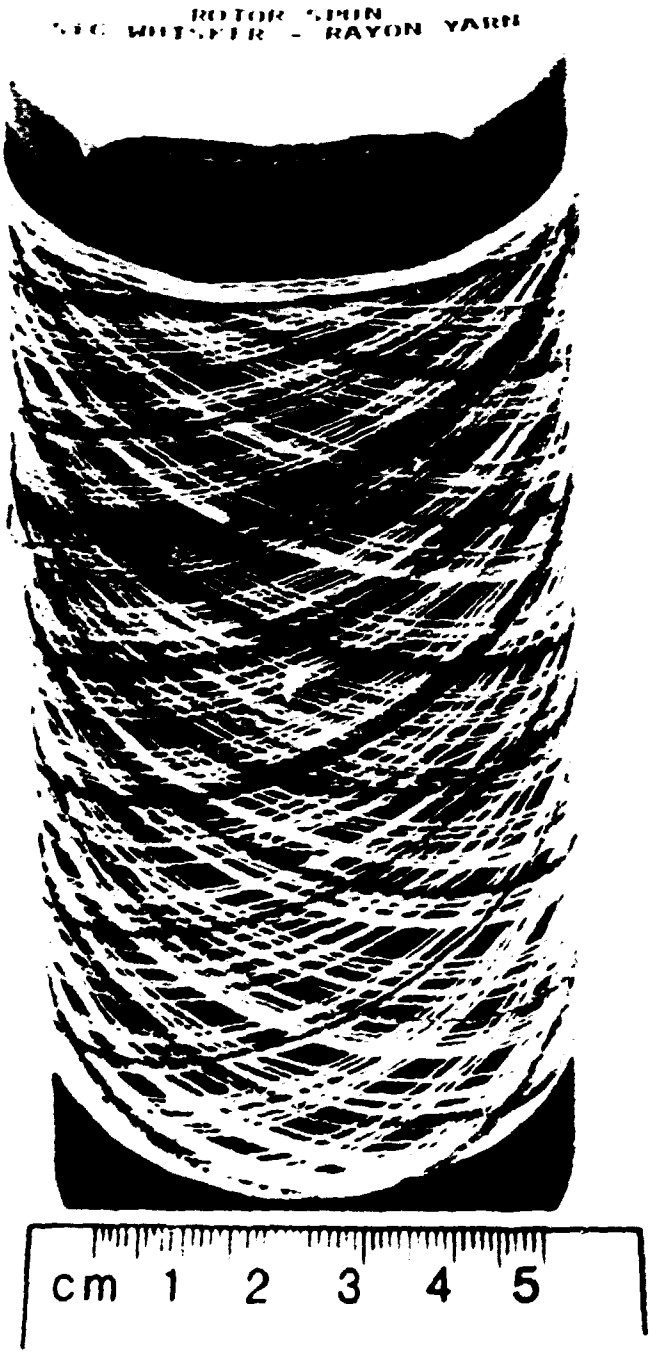

Fig. 13. First iteration staple whisker yarn with rayon carrier.

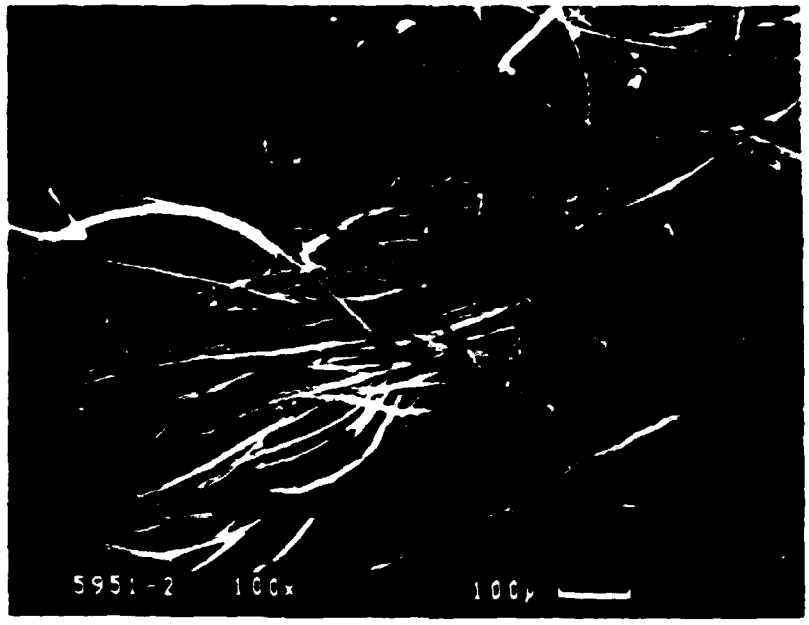

Fig. 14. SEM photomicrograph of whisker-rayon rotor spun yarn; whisker length is $\leq$ 4 mm.

ACKNOWLEDGEMENTS

The authors wish to express their thanks to P. D. DeVargas for assisting with the whisker growth; J. R. Bradberry for performing the scanning electron microscopy; S. R. Skaggs, W. Miller, R. Pusch and J. S. Parker for orchestrating the staple yarn development; and G. A. Montoya for typing the manuscript. The authors also gratefully acknowledge the support of the DOE Fossil Energy Office of Technical Coordination and the DARPA/Los Alamos IMA Program.

REFERENCES

1. J. Persh, "The U.S. Is Meeting the Ceramics Challenge," James I. Mueller Memorial Lecture, 11th Annual Conference on Composites & Advanced Ceramic Materials, January 18-23, 1987, Cocoa Beach, FL, to be published in Ceram. Eng. Sci. Proc., 8 [7-8] (1987).

2. B. A. Stein, H. G. Mahs and W. D. Brewer, "Airframe Materials for the National Aerospace Plane," Keynote Address, to be published in the Proceedings of the 1987 Joint NASA/DoD Conference on Metal Matrix, Carbon, and Ceramic Matrix Composites, January 22-23, 1987, Cocoa Beach, FL, by the Metals & Ceramics Information Center, Battelle Columbus Division.

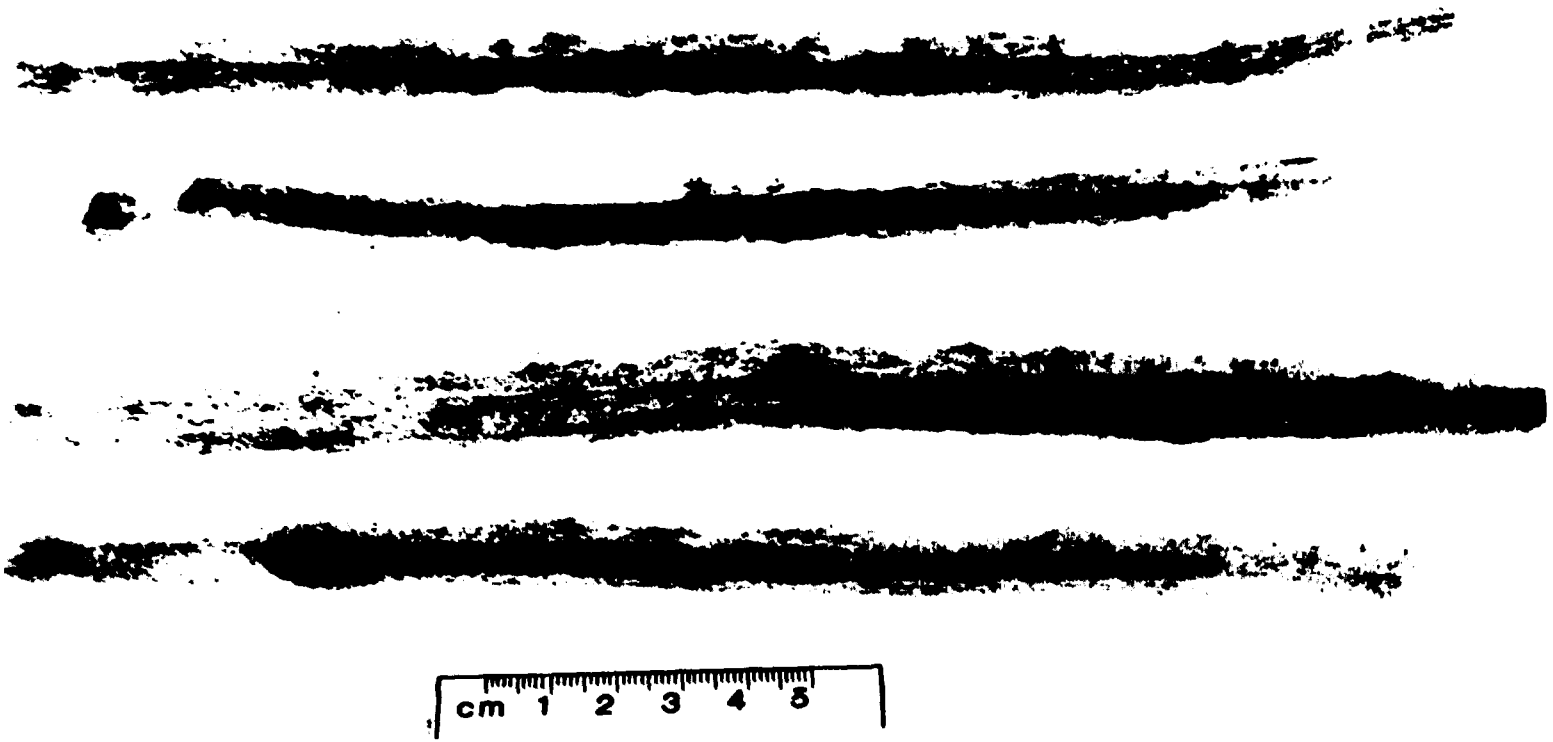

Fig. 15. VLS SiC whisker ribbons produced by glycerine dispersion and vacuum collection.

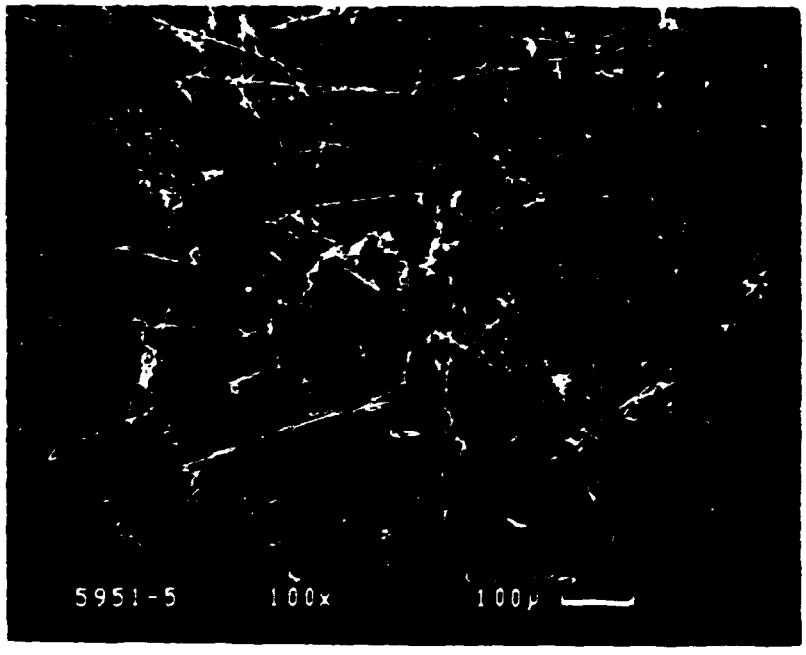

Fig. 16. SEM photomicrograph of VLS SiC whisker ribbon; the clumps are residual glycerine.

3. "Ultra-High Temperature Composite Materials and Process Screening," Program Research and Development Announcement 87 4 PMRR, in Commerce Business Daily, Wednesday, March 11, 1987.

4. J. V. Milewski, F. D. Gac and J. J. Petrovic, "Production and Characterization of Beta-Silicon Carbide and Alpha Silicon Nitride Whiskers for Ceramic Matrix Composites," pp. 177-186 in Proc. of the Seventh Annual Conference on Materials for Coal Conversion and Utilization, November 16-18, 1982, DOE/EPRI/GRI/NBS, Gaithersburg, MD.

5. J. V. Milewski, F. D. Gac, J. J. Petrovic and S. R. Skaggs, "Growth of Beta-Silicon Carbide Whiskers by the VLS Process," J. Mater. Sci., 20 [4] 1160-66 (1985).

6. G. F. Hurley, D. E. Christiansen, J. D. Katz, W. J. Parkinson and P. D. Shalek, "Progress in VLS Growth of SiC Whiskers," pp. 1-14 in Metal Matrix, Carbon and Ceramic Matrix Composites 1986, NASA Conference Publication 2445, Cocoa Beach, Florida, January 21-24, 1986.

7. J. D. Katz, G. F. Hurley and P. D. Shalek, "Influence of Catalyst Size on the Rate of Nucleation and Growth of Silicon Carbide Whiskers by the Vapor-Liquid-Solid Method," pp. 15-25, ibid.

8. F. D. Gac and J. J. Petrovic, "Feasibility of a Composite of SiC Whiskers in an $MoSi_2$ Matrix," Comm. Am. Ceram. Soc., 68 [8] C200-C201 (1985).

9. P. D. Shalek, J. J. Petrovic, G. F. Hurley and F. D. Gac, "Hot-Pressed SiC Whisker/Si_3N_4 Matrix Composites," Am. Ceram. Soc. Bull., 65 [2] 351-356 (1986).

10. F. D. Gac, J. J. Petrovic, J. V. Milewski and P. D. Shalek, "Performance of Commercial and Research Grade SiC Whiskers in a Borosilicate Glass Matrix," Cer. Eng. Sci. Proc., 7 [7-8] 978-982 (1986).

11. J. J. Petrovic, J. V. Milewski, D. L. Rohr and F. D. Gac, "Tensile Mechanical Properties of SiC Whiskers," J. Mater. Sci., 20 1167-77 (1985).

12. J. J. Petrovic and R. C. Hoover, "Tensile Fracture Behavior of long SiC Whiskers," J. Mater. Sci., 22 517-22 (1987).

13. J. A. DiCarlo, "Fibers for Structurally Reliable Metal and Ceramic Composites," J. Metals, 37 [6] 44-49 (1985).

14. J. W. S. Hearle, P. Grosberg and S. Backer, Structural Mechanics of Fiber, Yarns, and Fabrics - Volume 1, (Wiley-Interscience, New York, 1969), p. 273.

MODELING OF FIBROUS PREFORMS FOR CVD INFILTRATION

T. L. Starr
Georgia Tech Research Institute
Georgia Institute of Technology
Atlanta, Georgia 30332

ABSTRACT

Chemical vapor infiltration using combined pressure and temperature gradients results in dramatically shorter fabrication times for ceramic composites. A microstructural model for the fibrous preform and the intermediate, partially densified composite is used to predict gas flow and temperature throughout the body. Combined with kinetics data, the model allows calculation of the density distribution during the infiltration process. Predicting the effect of modifications to the process and of changes in preform structure, the model aids optimization of processing conditions, structure and properties.

INTRODUCTION

Ceramic matrix composites can be fabricated by chemical vapor infiltration (CVI) of a fibrous preform. Recent development of a forced flow, thermal gradient technique can reduce infiltration time to several hours[1]. In this technique, the reactant gas is forced to flow through the preform from the cool face to the hot face as indicated in Figure 1. While successful composites have been produced, a fundamental understanding of the process and its critical parameters is lacking. In order to gain this insight an analytical model of this process is being developed.

The overall scheme for this model is shown in Figure 2. The starting point is a geometric description of the microstructure of the fibrous preform prior to infiltration. Gas permeability and thermal conductivity are calculated from this structure model and fiber material properties. These, combined with the appropriate boundary conditions, are used to calculate the pressure and temperature variation across the preform. The deposition rate is determined as a function of position within the preform, resulting in a partially dense composite microstructure. Iteratively, this intermediate structure is used to calculate new temperature, flow and deposition rate values.

STRUCTURE MODEL

Initial development has focused on random short fiber preforms. The model used for such a preform and the partially densified composite structure consists of an array of intersecting cylinders with cubic symmetry (Figures 3 and 4). The density of such a structure depends only on the ratio of fiber diameter to unit cell length:

$$c = \frac{3\pi}{4}\left(\frac{d}{L}\right)^2 - \sqrt{2}\left(\frac{d}{L}\right)^3$$

where c = the fraction dense volume
d = the fiber diameter
and L = unit cell length

For a known preform density and fiber diameter, the average unit cell length can be calculated. This is used to calculate other microstructural parameters such as surface area per unit volume and pore size[2]. To better represent the microstructure of real random, short fiber preforms, one additional constraint is placed on the model. A range of cell sizes is assumed, following a log-normal distribution[3]. As infiltration proceeds, the effective fiber diameter increases while the unit cell lengths remain constant. New values for pore size and surface area can be calculated for any value of density.

GAS PERMEABILITY

The pressure drop across a porous preform is proportional to the gas viscosity, the material thickness and the flow rate, and is inversely proportional to the permeability of the preform. The permeability depends on the preform microstructure,

$$K = B\frac{(1 - c)^3}{S^2}$$

where K = permeability,

S = surface area per unit volume,

and B = constant related to the microstructure

For the initial preform the surface area is inversely proportional to the fiber diameter. (Thus, a preform made with 15 micron diameter fibers will be 900 times more permeable than one with 0.5 micron fibers.) As density increases the surface area initially increases but then decreases as the smaller pores are filled or closed (Figure 5). Permeability decreases, resulting in an increase in the pressure rise across the preform.

THERMAL GRADIENT

The thermal gradient through the preform can be calculated assuming that the temperatures are fixed at the boundaries and that solid state conduction is the dominant mode of heat flow. In this case, the temperature profile depends only on the relative thermal conductivity of different regions of the preform, not on its absolute value. For solid state conduction the thermal conductivity increases with density. The temperature profile depends on the density gradient through the preform and

changes as infiltration proceeds.

In the particular experimental arrangement used in the Oak Ridge CVI process the cool face of the preform is separated from the water cooled gas injector by a graphite holder. Thus the temperature of this face is not controlled directly but depends on the temperatures at the hot face and injector, and on the relative thermal conductivities of the holder and the preform. Since the latter will change with density, the cool face temperature will change as infiltration proceeds. For the case where the holder thickness is equal to the preform thickness, the cool face temperature is given by

$$T_c = T_i + \frac{T_h - T_i}{1 + \lambda_h/\lambda_p}$$

where T_h, T_c, and T_i are the hot face, cool face and injector temperatures and $_h$ and $_p$ are the holder and preform thermal conductivities. The variation in this temperature can be illustrated by assuming reasonable values for thermal conductivities, 100 W/mK for the graphite holder and 1 and 100 W/mK at the initial and final densities for the preform. Injector and hot face temperatures are constant at 60 and 1200°C. This gives an initial temperature at the cool face of 71°C, rising to 630°C at the final density. Comparable variation in temperature is expected within the preform as infiltration proceeds.

The deposition kinetics depend critically on temperature. The uncertainty in the thermal conductivity of the partially densified composite is a major factor in the overall uncertainty in the CVI model.

DEPOSITION KINETICS

Micrographs of partially densified preforms show clearly that the CVI proceeds as an extended fiber coating process, building up successively thicker layers of relatively uniform thickness. This is the basis of the

structure model described above. In seeking kinetic data, the work of Brennfleck et al. in coating of continuous fibers appears to be transferable to CVI[4]. In this work, SiC was deposited from methyltrichlorosilane (MTS) in excess H_2 at temperatures from 800 to 1000°C. They found a linear dependence on MTS concentration and an exponential dependence on temperature giving an overall rate equation of

$$D_l = 2.8 \times 10^{-2} M_{MTS} e^{-E_a/RT}$$

where D_l = the deposition rate in cm/s
M_{MTS} = the mole fraction MTS
R = the gas constant
T = the temperature in K
and E_a = the activation energy and is equal to 120 kJ/mole.

This can be converted to a volume deposition rate by multiplying both sides of the equation by the surface area available to deposition, S, and to a molar deposition rate using the density and molecular weight of SiC. This gives

$$D_m = 2.3 \times 10^{-3} M_{MTS} S e^{-E_a/RT}$$

for the molar deposition rate in moles/s/cm.

A one-dimensional model of the forced flow, thermal gradient CVI process is a reasonable approximation to the actual experimental arrangement and allows straightforward calculation of flow, temperature and reaction rates. This model, shown in Figure 6, represents a cylindrical section through the preform and is divided into a finite number of disc shaped elements. Each element is considered homogenrous, and temperature, density, permeability and pressure gradients through the preform are approximated by varying these properties from element to element.

The deposition rate within an element can be calculated knowing the temperature, surface area and MTS concentration. The temperature is calculated using standard heat flow techniques and the hot face and gas injector temperatures and the thermal conductivity of each element. (The graphite holder is included as the first element in the model.) Surface area is calculated from the structure mode' The MTS concentration is

computed stepwise for each element using the gas flow rate and initial concentration, diminished by the deposition occurring in the preceding elements.

While the uncertainty in thermal conductivity does not allow quantitative calculations at this time, the model provides considerable insight into the effect of process variables on infiltration. Several trial calculations have been performed for a preform of fifteen micron diameter fibers packed to 20% density, a hot face temperature of 1200°C, a gas injector temperature of 60°C, and 10:1 H_2 to MTS ratio. The preform is 1.27 cm thick and 4.51 cm in diameter. The graphite spacer is 1.10 cm thick.

The effect of the temperature gradient can be seen in Figure 7 for a gas flow rate of 550 cc/min STP. Assuming a linear temperature gradient through the preform, the deposition rate is calculated as a function of position for four different cool face temperatures. In the isothermal case (T_c = 1200°), the deposition is most rapid at the inlet, decreasing through the preform as MTS is depleted from the reaction gas. At the lowest cool face temperature the deposition rate continually increases through the preform as the temperature rises. Depletion of the reactant gas is not great enough to reverse this trend. In the intermediate cases, the two opposing factors, thermal gradient and gas depletion, are of comparable importance and the deposition rate shows less variation.

The effect of gas flow rate also is shown in Figure 8 where the deposition rate profile is calculated for a 600° cool face temperature and two different gas flows. The effect of MTS depletion is seen in the reduced deposition rate near the hot face at the lower flow. These model calculations suggest that fine tuning of the infiltration process is possible by controlling the cool face temperature and the gas flow rate.

Continued development of this model is in progress. Comparison of predictions with experimental results will allow adjustment of model parameters and result in quantitative calculations. Extension to

three-dimensional modeling will allow optimization of the infiltration process for general shapes.

REFERENCES

1. A. J. Caputo, D. P. Stinton, R. A. Lowden, and T. M. Besmann, "Fiber-Reinforced SiC Composites with Improved Mechanical Properties," Am. Ceram. Soc. Bull., 66 (2) 368-72 (1987).

2. G. W. Scherer, "Sintering of Low-Density Glasses: I, Theory" J. Amer. Ceram. Soc., 60 (5-6) 236-246 (1977).

3. H. W. Piekaar and L. A. Clarenburg, "Aerosol Filters - Pore Size Distribution in Fibrous Filters," Chem. Eng. Sci., 22 1399-1408 (1967).

4. Brennfleck, E. Fitzer, B. Schoch, M. Dietrich, "CVD of SiC-Interlayers and Their Interaction with Carbon Fibers and with Multi-layered NbN-Coatings", Proc. of 9th Int. Conf. on CVD, pp. 649-662 (1984).

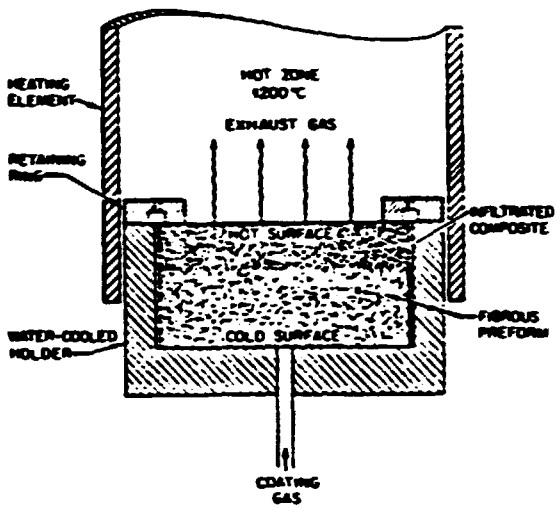

Figure 1. Schematic of forced flow, thermal gradient CVI system.

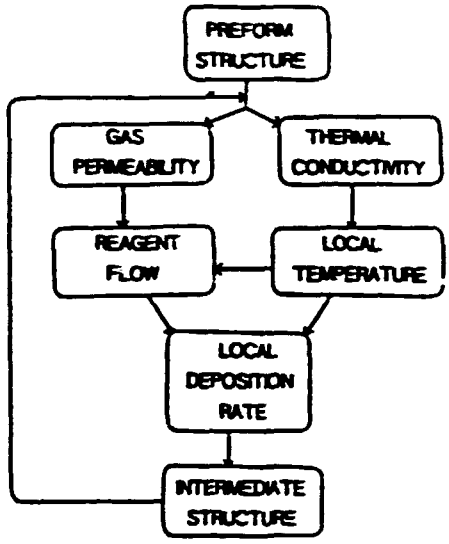

Figure 2. Overall scheme of CVI model.

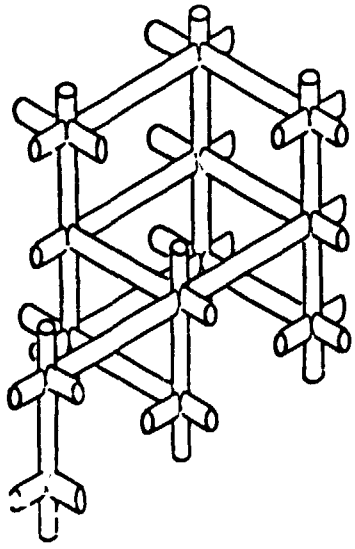

Figure 3. Model for micro-structure of random fiber preform.

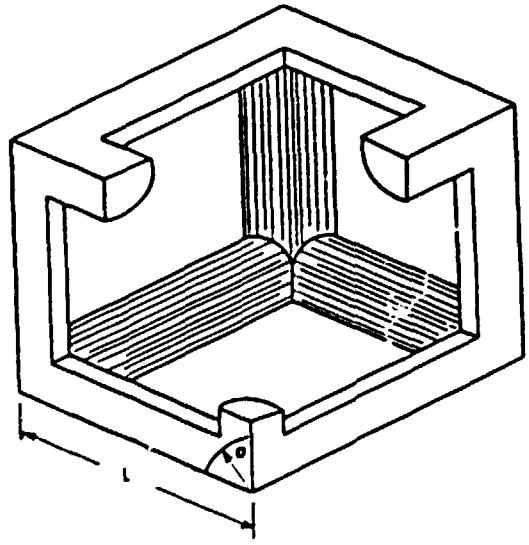

Figure 4. Unit cell for of random structure model.

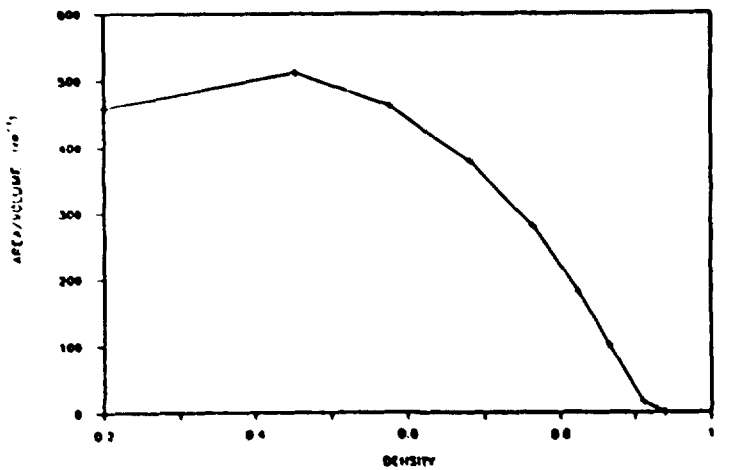

Figure 5. Surface area/volume for fifteen micron fiber preform.

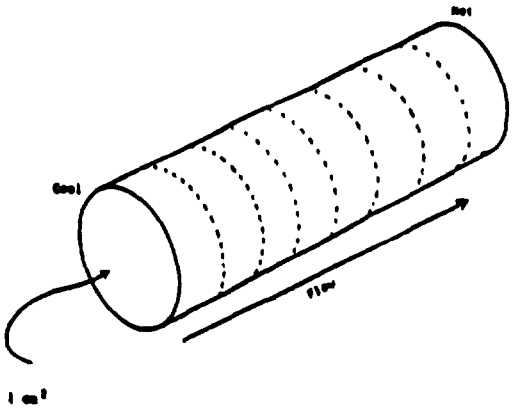

Figure 6. One-dimensional model for CVI process.

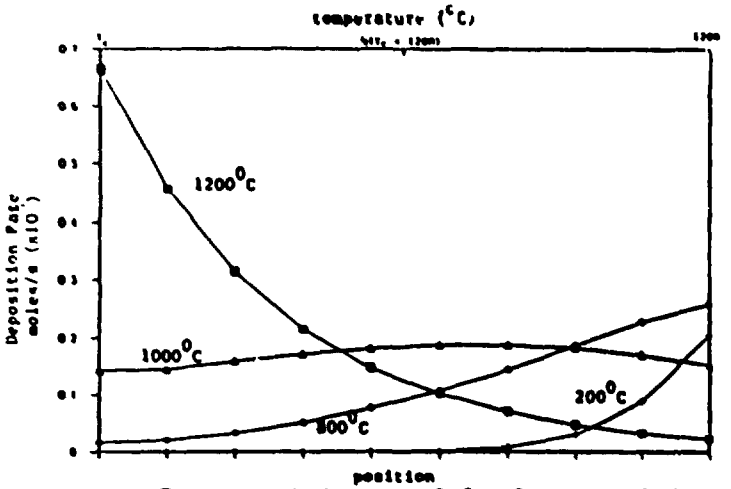

Figure 7. Deposition profile for initial preform depends on cool face temperature.

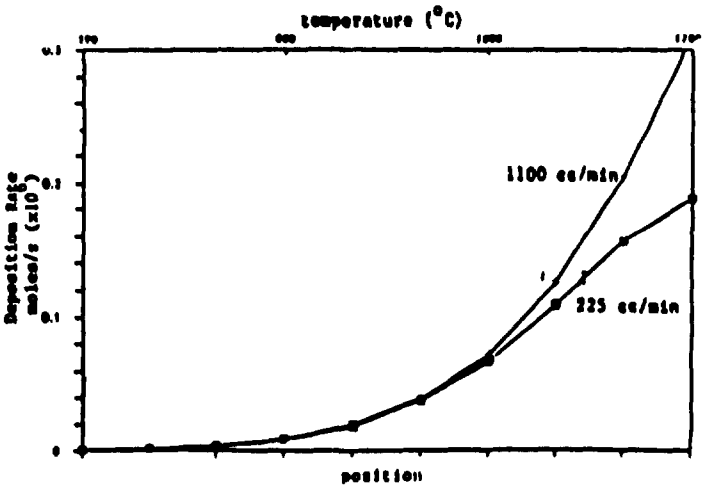

Figure 8. Deposition profile depends on gas flow rate.

JOINING OF SILICON CARBIDE-REINFORCED CERAMICS

Dennis N. Coon and Robert M. Neilson, Jr.

Idaho National Engineering Laboratory
EG&G Idaho, Inc.
P. O. Box 1625
Idaho Falls, ID 83415

INTRODUCTION

Recent advances in polymer and metal matrix composites have elevated them to the status of practical engineering materials. These advances have also prompted intensive research efforts to develop advanced ceramic fiber/ceramic matrix composites for high temperature applications. To fully realize their potential in these applications, reliable and practical joining techniques must be developed that will permit the use of engineering designs. Such joints require sufficient strength and toughness for projected applications as well as resistance to environmental and thermal degradation comparable to that of the composite joined.

This research program will identify and develop techniques for joining silicon carbide fiber-reinforced ceramic composites of tubular geometries, primarily through the use of glass joining materials. The general tasks of this program include: identifying, preparing, and characterizing glass compositions suitable for joining ceramic/ceramic composites; developing a joining methodology an evaluating the effects of process parameters on joint characteristics; fabricating and characterizing joints; and determining physical/mechanical properties and failure behavior of joints under ambient conditions, elevated temperatures, and simulated service environments.

The majority of the effort in this research program during the last year has been directed towards characterization of glass compositions for use as joining materials. The following requirements for the glass brazing material were identified early in the program:

1. The glass joining material should melt and flow at temperatures below those reported to degrade the properties of the composite material (approximately 1200°C).

2. The glass joining material should not exhibit excessive chemical reactivity with SiC.

3. Ideally, the devitrified glass joint should exhibit good mechanical properties to 1000°C.

4. The glass composition should devitrify to crystalline phases which exhibit low thermal expansion and good chemical resistivity to promote thermal and chemical stability of the resulting joint.

This review discusses the results of characterization studies of candidate joining glasses with respect to the above criteria. Also discussed are the results of some initial joining experiments.

EXPERIMENTAL PROCEDURE

The batch compositions of glasses prepared in this study are given in Table 1. These compositions represent systematic variations of MgO, Li_2O, Al_2O_3, and SiO_2. Nucleating agents (TiO_2 and ZrO_2) were also added to selected compositions. These variations permit the examination of the effects of compositional changes and nucleating agents on the characteristics of the glass.

Glasses were prepared by mixing reagent grade powders for 2 h in polyethylene bottles using alumina mill balls. The mixed powders were melted in alumina or platinum crucibles at 1400°C in air for 1 h. The resulting glasses were crushed, remixed, and remelted for 6 h at 1400°C in air. The melts were poured into preheated boron nitride molds, placed in an oven, and held at the appropriate annealing temperature for 4 h. After annealing, the oven was shut off and the glasses allowed to cool to room temperature. Glass of each composition was mechanically crushed into a powder (38-63 μm) for differential

TABLE 1. MAGNESIUM-LITHIUM-ALUMINOSILICATE GLASS COMPOSITIONS PREPARED FOR USE AS JOINING MATERIALS (wt%)

Composition Number	SiO_2	Al_2O_3	Li_2O	MgO	TiO_2[a]	ZrO_2[a]
3a-T	60	20	20	0	3	--
3b-T	60	20	15	5	3	--
3c-T	60	20	10	10	3	--
3d-T	60	20	5	15	3	--
3e-T	60	20	0	20	3	--
3b	60	20	15	5	--	--
3b-Z	60	20	15	5	--	3
4a	65.2	19.2	15.6	--	--	--
5a	65	10.5	14	10.5	--	--
5a-T	65	10.5	14	10.5	3	--
5a-Z	65	10.5	14	10.5	--	3
6a	60	10	10	20	--	--
6a-T	60	10	10	20	3	--
6a-Z	60	10	10	20	--	3
7a	65	10.5	10.5	14	--	--
7a-T	65	10.5	10.5	14	3	--
7a-Z	65	10.5	10.5	14	--	3

a. TiO_2 and ZrO_2 are in addition to 100%.

thermal analysis (DTA), quench tests to determine the crystalline phases evolved during devitrification, and examination of the compatibility between the glass compositions and SiC at high temperature. Selected glass compositions were prepared as slices (2.5 x 12.7 x 12.7 mm), cubes (1.75 x 1.75 x 1.75 mm), and flexure bars (3 x 4 x 45 mm) by diamond sawing. All samples were stored in a desiccator until used.

DIFFERENTIAL THERMAL ANALYSIS

Glass powders were examined by differential thermal analysis (DTA) to identify glass transition, crystallization, and melting temperatures. The DTA thermograms were obtained using approximately 45 mg of glass powder and an alumina reference material. A constant 10°C/min heating

rate and static air environment were employed. A thermogram of kaolinite was obtained and compared to reference patterns to ensure the DTA was in proper working condition prior to examining the glass materials.

QUENCH TESTS

Based on results of the DTA thermograms, selected glass powders were encapsulated in platinum foil, placed in a preheated furnace, held for a finite length of time, and quenched to room temperature in air. The crystallization temperatures were identified by the DTA results. The treated powder was examined by x-ray diffraction to determine the crystalline phases evolved.

COMPATIBILITY TESTS

Selected glass powders were mixed with ethyl alcohol to form a slurry, and a drop of the slurry was placed on the surface of a slice of monolithic silicon carbide. This slice was then dried to remove the alcohol, and the dried samples were heat treated. The treated samples were cross sectioned, polished, and examined by scanning electron microscopy (SEM) to determine the extent of any chemical reaction with the silicon carbide, and the nature of any crystalline phases evolved.

WETTING BEHAVIOR

The wetting behavior of glass compositions 5a-T, 6a-T, and 3b-T was examined by sessile drop experiments as a function of time and temperature in air. Glass cubes were placed on a silicon carbide slab (the surface of the silicon carbide in contact with the glass was polished) and placed in a furnace preheated to the desired temperature. After holding for a specified time, the specimen was lowered out of the furnace on an elevator, and a photograph of the drop geometry was taken while the specimen was still hot. The time from removal from the furnace until the photograph was taken was less than two seconds in each case. The furnace was allowed to equilibrate to the test temperature before another specimen was tested. Each time-temperature-composition datum point represented a separate specimen. The photographs were used to measure drop geometry,

i.e. contact angle (Figure 1). The contact angle was measured on each side of the drop and the results averaged. The maximum difference in contact angle observed between the two sides was 3°.

CRYSTALLIZATION RATES OF GLASS COMPOSITION 5a-T

Crystallization experiments were conducted by heat treating slices (3 x 12 x 12 mm) of glass composition 5a-T at temperatures between 700 and 900°C. Since no low temperature nucleation treatment was used, crystallization occurred predominately from the surface. The specimen was cross sectioned and the thickness of the crystalline surface layer was measured as a function of time. The crystallization rate was calculated according to:

$$X = kt \qquad (1)$$

where: X = the thickness of crystalline surface layer
t = time
k = crystallization rate.

STRENGTH OF DEVITRIFIED GLASS COMPOSITION 5a-T

Billets of glass composition 5a-T were machined into flexure bars with a surface finish of approximately 230 grit, and the tensile edges were beveled. Selected bars were heat treated to obtain approximately 70-80 vol.% crystalline content. The strength of both treated and untreated bars as a function of temperature was tested in three-point bending with a lower span of 40 mm.

The heat treatment schedule used to crystallize the flexure bars is shown in Figure 2. A low temperature nucleation treatment (4 h at 600°C) was used to promote uniform bulk crystallization. The furnace temperature was then increased to 750°C for 30 min. This amount of time was expected to yield the desired crystalline content. After the high temperature heat treatment, the bars were transferred to an annealing oven at 500°C, held for 2 h, and allowed to cool to room temperature overnight.

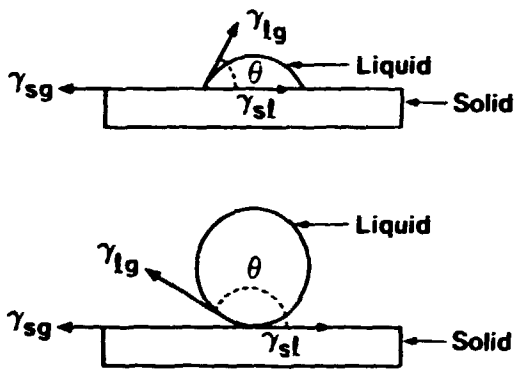

Fig. 1. Geometry of liquid drops on solid surfaces showing wetting (top) and nonwetting (bottom).

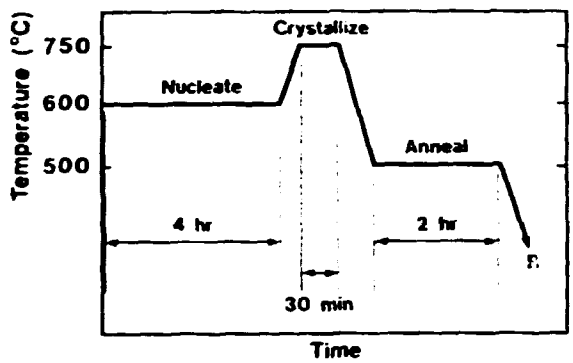

Fig. 2. Heat treatment schedule used to devitrify flexure bars of glass composition 5a-T.

SIMULTANEOUS CRYSTALLIZATION AND SINTERING OF A GLASS POWDER

Two alternative routes in the preparation of a glass-ceramic from a glass powder are possible, as shown in Figure 3. The three-step process (melting, nucleation, and crystallization) is the preferred route since the melting step enhances glass flow and minimizes potential defects (strength limiting flaws) in the joint. The melting step also provides a degree of tolerance to surface imperfections on the composite surface. However, if the brazing materials are amenable to the single-step process (simultaneous crystallization and sintering), more refractory joining compositions could be used without degrading the composite properties. Also, the possibility of reduced time at temperature could result in potentially large energy savings.

Crystallization-sintering experiments were conducted with glass composition 5a-T. Glass powder (<63 μm) was pressed at 20 ksi into pellets (2.5 mm in height x 12.7 mm in diameter) without using a binder. The density of the pellets was determined from the dimensions and mass to be 1.64 g/cm^3. The density of glass composition 5a-T was determined to

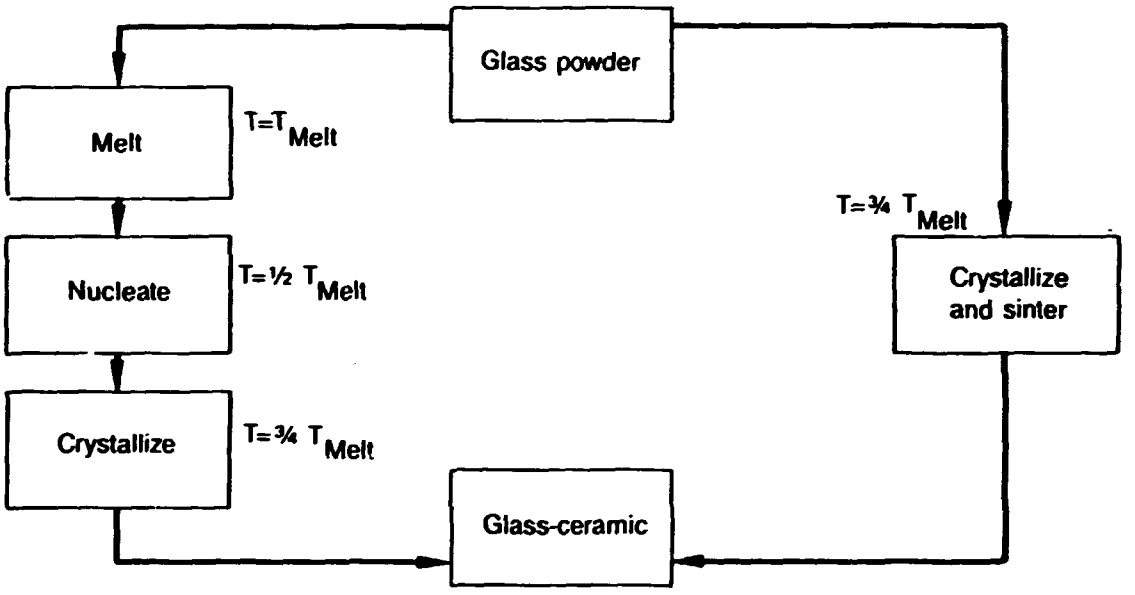

Fig. 3. Alternative methods for the preparation of a glass-ceramic from a glass powder.

be 2.46 g/cm^3 by the Archimedes' immersion method. The pellets were then dried at 400°C for 10 min and treated at 750°C for times ranging from 15 min to 6 h. The density of the treated pellets was determined by the Archimedes' immersion method. The densification behavior of a soda-lime-silica standard glass (NBS 710) was also determined.

JOINING EXPERIMENTS

Two hundred and twenty-two composite bars (5 x 6 x 48 mm) were procured from Refractory Composites, Inc. with either 37 or 41 vol.% fiber. The density of each type of bar was determined by the bulk density method (measure dimensions and weight) and the Archimedes' immersion method.

The composite bars will be cut in half, perpendicular to the 48 mm dimension, and the two halves rejoined to form a butt joint. A fixture to maintain alignment of the halves during joining and post-joining heat treatments was fabricated from boron nitride. Flexure tests will be used to examine joint properties because they are simple (both at room

temperature and high temperature) and amenable to the butt joint geometry. Shear testing will be conducted to provide supplemental information as appropriate.

Initial joining experiments have concentrated on glass composition 5a-T. The glass was prepared as a powder with particle sizes between 38 and 63 μm. The powder was mixed with acetone to form a paste and applied to the surface with a spatula. The coated composite was then dried at 125°C for 15 min to remove the acetone. The composite halves were removed from the drying oven, placed in the joining fixture, and heated in air to 1150°C and held for 15 min. After joining, the sample was transferred to an annealing oven, held at the appropriate annealing temperature for 2 h, and cooled to room temperature in the oven.

RESULTS AND DISCUSSION

CHEMICAL ANALYSES

The analyses of the glass compositions prepared are given in Table 2 along with the compositions expected from batch calculations. For simplicity, the concentrations of TiO_2 and ZrO_2 are not listed. Compositions 3a-T through 3e-T showed about 4-5 wt.% increases in the Al_2O_3 concentration. These Al_2O_3 additions are due to limited dissolution of alumina crucible material during melting. Minor decreases in the SiO_2, Li_2O, and MgO concentrations were also observed, which are consistent with decreases expected as a result of simply adding more Al_2O_3. The small losses of Li_2O and MgO observed indicate that volatilization of alkali oxides and alkaline earth oxides was not a major problem.

Compositions 3b through 7a-Z show some interesting trends. Compositions 3b and 3b-Z exhibited large increases of Al_2O_3, presumably due to exaggerated attack of the crucible during melting. Large decreases in SiO_2, Li_2O, and MgO were observed, and are consistent with the large Al_2O_3 increase. The TiO_2 addition to series 3 compositions (3b-T) limited the attack, resulting in smaller Al_2O_3 increases. Compositions 5a, 5a-T, 5a-Z, 6a, 6a-T, 6a-Z, 7a, 7a-T, and 7a-Z exhibited Al_2O_3 additions and SiO_2, Li_2O, and MgO

TABLE 2. ANALYZED COMPOSITIONS OF GLASSES PREPARED IN THIS STUDY (wt%)

Composition Number	SiO_2		Al_2O_3		Li_2O		MgO	
	Batch	Analyzed	Batch	Analyzed	Batch	Analyzed	Batch	Analyzed
3a-T	60	57.7	20	24.9	20	17.4	0	0
3b-T	60	57.7	20	24.4	15	13.7	5	4.1
3c-T	60	59.7	20	23.6	10	8.2	10	8.4
3d-T	60	59.1	20	23.5	5	4.6	15	12.8
3e-T	60	58.9	20	24.2	0	0	20	16.8
3b	60	47.4	20	38.7	15	10.4	5	3.6
3b-z	60	46.0	20	38.9	15	10.5	5	3.4
4a	65.2	62.4	19.2	23.1	15.6	14.4	0	0.1
5a	65	57.2	10.5	21.8	14	12.6	10.5	8.4
5a-T	65	62.9	10.5	14.4	14	12.6	10.5	10.1
5a-Z	65	59.3	10.5	20.7	14	11.5	10.5	8.5
6a	60	54.9	10	20.7	10	8.6	20	15.7
6a-T	60	54.1	10	19.1	10	9.7	20	17.0
6a-Z	60	57.9	10	13.9	10	9.3	20	19.3
7a	65	64.6	10.5	13.5	10.5	9.2	14	12.7
7a-T	65	63.6	10.5	14.8	10.5	8.9	14	12.7
7a-Z	65	60.0	10.5	20.0	10.5	8.7	14	11.4

reductions. The TiO_2-containing composition, 5a-T, appeared to limit attack of the crucible, resulting in smaller Al_2O_3 increases. On the other hand, ZrO_2 additions to series 6 compositions, 6a-Z, exhibited lower Al_2O_3 increases than either 6a or 6a-T. In the series 7a compositions, a ZrO_2 addition (7a-Z) exhibited a larger Al_2O_3 increase than either 7a or 7a-T.

The addition of Al_2O_3 due to attack of the crucible was eliminated by melting in platinum crucibles. The degree of attack was dependent on glass composition (Table 2).

DIFFERENTIAL THERMAL ANALYSIS

The transition, crystallization, and melting temperatures identified from the DTA thermograms are given in Table 3 for all glass compositions. These results have been discussed in detail elsewhere;[1] here we will concentrate on the results for glass compositions 3a-T through 3e-T. Figure 4 shows that the glass transition temperature increased nonlinearly with MgO additions from 490°C for the MgO-free composition (3a-T) to 780°C for the Li_2O-free composition (3e-T). The devitrification temperature increased from 620°C for composition 3a-T to 975°C for composition 3e-T. Figure 5 shows the effect of MgO additions on the melting temperature. Initial MgO additions depress the melting temperature slightly; however, continued MgO additions increase the melting temperature dramatically. Additions of 10 wt.% MgO or more increase the melting temperature above the proposed joining temperature range.

The composition changes investigated with glass compositions 3a-T through 3e-T can have two effects on the glass structure. First, the nonbridging oxygen (NBO) concentration can be altered. Second, the strength of the modifying ion-oxygen bond can be altered. It has been proposed that both of these effects will alter the transition temperature since they affect the viscosity-temperature relationship.[2] Previous investigators have suggested that each change alone has a dominant effect on the glass transition temperature (T_g).

TABLE 3. THERMAL CHARACTERISTICS OF GLASSES PREPARED IN THIS STUDY AS DETERMINED BY DTA

Composition Number	Transition Temperature (°C)	Crystallization Temperature (°C)	Onset of Melting (°C)
3a-T	490	620	1040
3c-T	565	720	1125
3d-T	640	810	1260
3e-T	780	975	1325
4a	485	615	1015
3b	540	645	1075
3b-T	505	640	975
3b-Z	595	705	1175
5a	505	660/690[a]	925
5a-T	505	675	925
5a-Z	515	695	1000
6a	550	710/735[a]	940
6a-T	555	725	1025
6a-Z	550	750/735[a]	930
7a	525	705	920
7a-T	530	700	920
7a-Z	545	735	910

a. Two exothermic peaks were observed. The maximum peak is listed first.

Gutzow[2] derived the following relationship for polystyrene·

$$(T_g)^{-1} = a + b(P)^{-1} \qquad (2)$$

where P defines the degree of polymerization. This indicates that as the structure becomes more "cross-linked" the transition temperature (T_g) increases.

Eisenberg and Takahasi[2] defined P for alkali-silicate systems in the following way:

$$\frac{[M_2O]}{[SiO_2]} = \frac{P + 1}{P} \qquad (3)$$

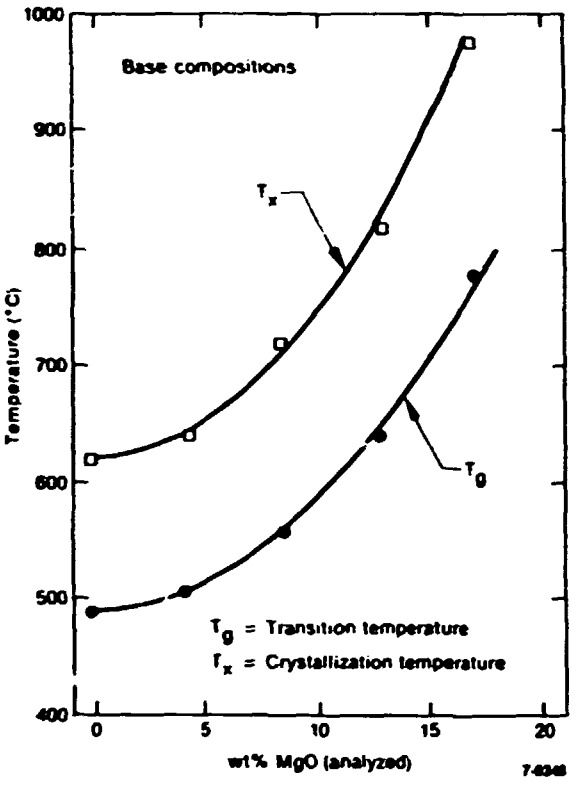

Fig. 4. Effect of MgO content on the crystallization and transition temperatures for glass compositions 3a-T, 3b-T, 3c-T, 3d-T, and 3e-T.

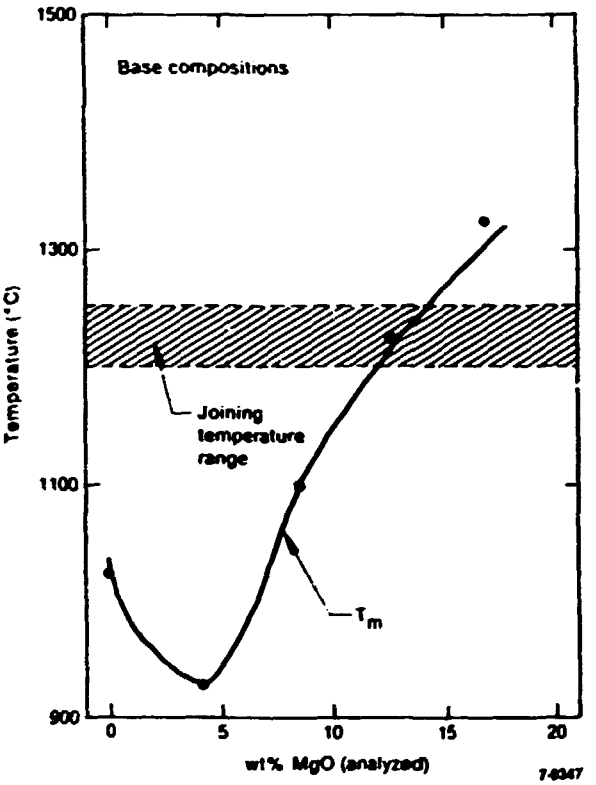

Fig. 5. Effect of MgO additions on the melting temperatures (T_m).

where the concentration of alkali oxide is given by $[M_2O]$ and the concentration of silica is given by $[SiO_2]$.

Using Equations 2 and 3 along with the glass compositions, the following relationship was developed:

$$(T_g)^{-1} = A + B(\overline{NBO}) \qquad (4)$$

This equation predicts the expected trend that as more NBO are present in the structure, the transition temperature decreases. As can be seen from Figure 6, which gives data for compositions 3a-T, 3b-T, 3c-T, 3d-T, 3e-T, 5a-T, 6a-T, and 7a-T, this relationship describes the data well for $\overline{NBO}<0.5$ but yields unsatisfactory results at higher $\overline{NBO}$ values.

Eisenberg and Takahasi[2] related the transition temperature to the coulombic force between the modifying ion and oxygen:

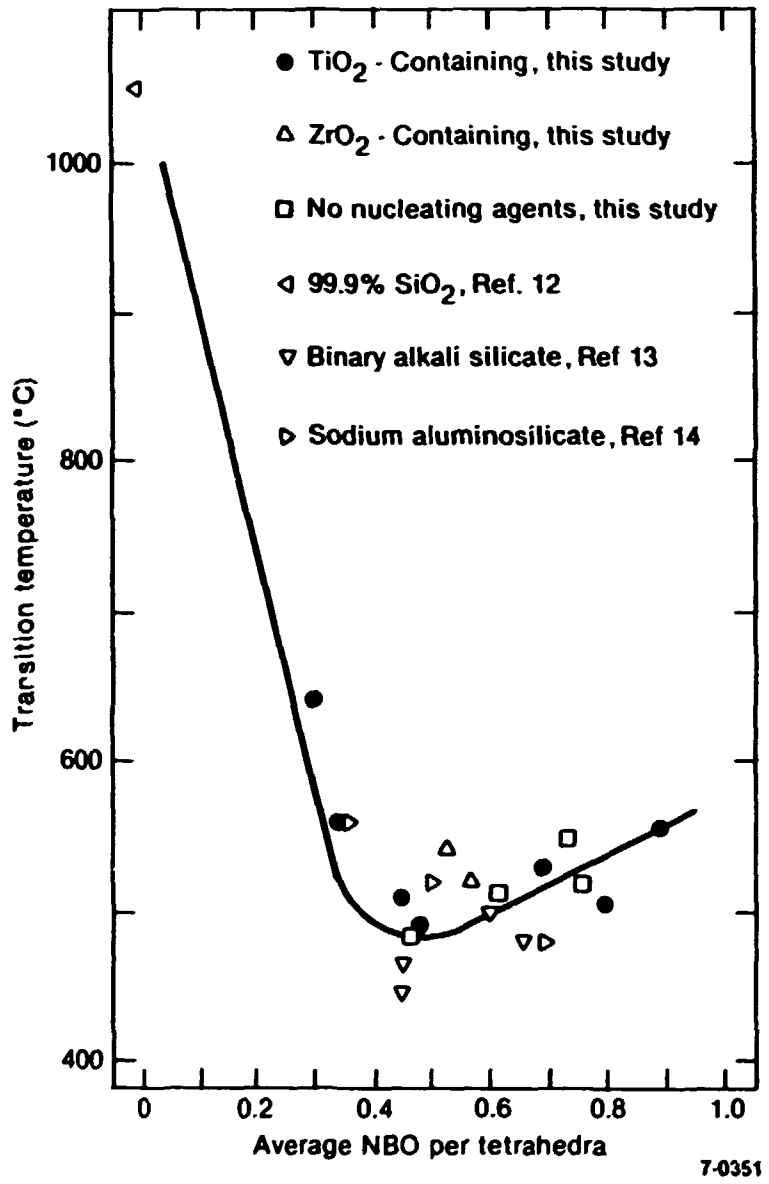

Fig. 6. Effect of the calculated nonbridging oxygen concentration on the glass transition temperature.

$$T_g = C(Z/r) + D \qquad (5)$$

The coulombic force between the modifying ion and oxygen ion is proportional to (Z/r), where Z is the charge on the modifying ion and r is the ionic radius. This relationship was shown to hold for silicate and phosphate glasses.

A similar relationship was developed[3] which suggests that T_g is proportional to the average work required to break a modifying ion-oxygen bond ($\bar{W}$):

$$T_g = a + b(\bar{W}) \quad (6)$$

The data for compositions 3a-T, 3b-T, 3c-T, 3d-T, 3e-T, 5a-T, 6a-T, and 7a-T are plotted in Figure 7. There is a significant amount of scatter in the data as indicated by the correlation coefficient of 0.74 for the linear regression.

Since NBO correlates well to T_g for $\overline{NBO}<0.5$, and $\bar{W}$ gives a fair correlation over the entire range, it is reasonable to expect that both parameters affect the transition temperature to some extent. With this in mind, the data were fit to the two-parameter linear relationship:

$$T_g = a + b(\overline{NBO}) + c(\bar{W}) \quad (7)$$

Using standard regression techniques, the constants were determined to be:

$a = 252.5 \pm 1.0$

$b = -115.8 \pm 0.7$

$c = 146.5 \pm 0.4$

The plus-or-minus value indicates the 95% confidence interval. The correlation coefficient of the multivariate regression was 0.96, indicating an excellent fit to the experimental data. These constants indicate that as the average nonbridging oxygen concentration increases, the transition temperature decreases. Also, as the average strength of the modifying ion-oxygen bond increases, the glass transition temperature increases. These trends are consistent with the effect of MgO additions on the transition temperature (Figure 4).

QUENCH TESTS

The results of x-ray analyses for selected compositions which have been heat treated are given in Tables 4 and 5. The crystallization temperature listed in the tables is that identified by the maximum on the

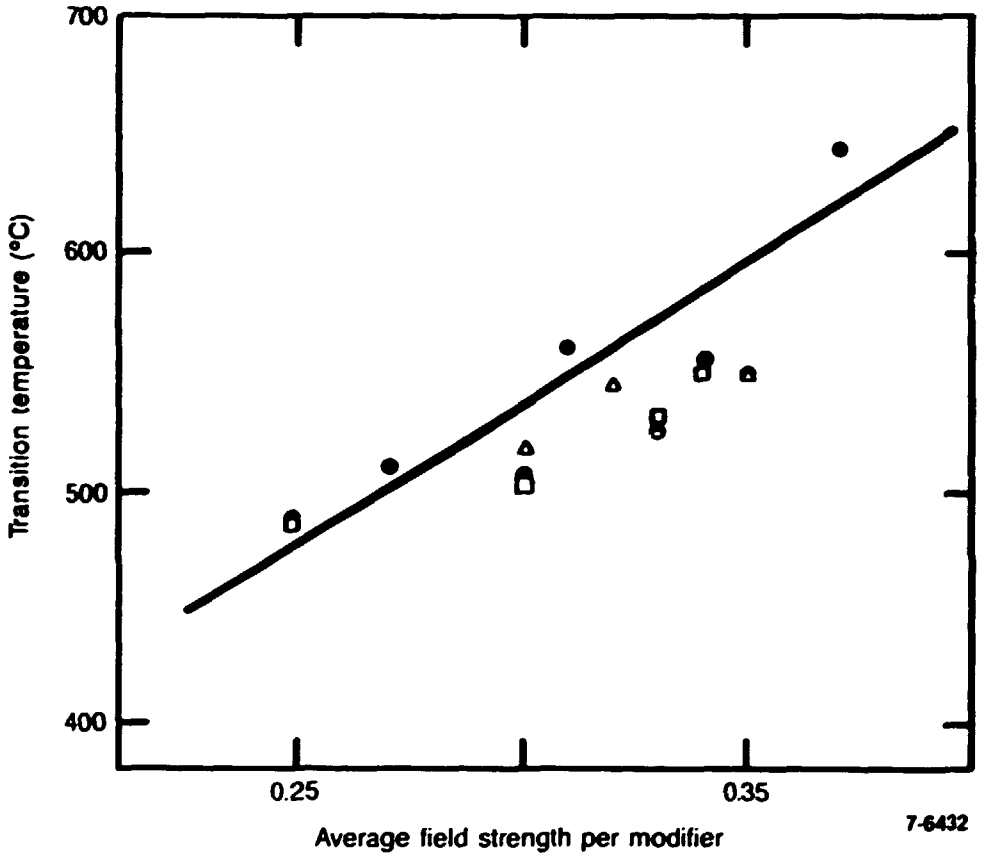

Fig. 7. Effect of the calculated average strength of the modifying ion-oxygen bonds on the glass transition temperature.

TABLE 4. RESULTS OF X-RAY ANALYSES OF CRYSTALLINE PHASES IN BASE COMPOSITIONS

Composition Number	Crystallization Temperature (°C)	Hold Time	Crystalline Phases	
			Major	Minor
3b-T	640	1 h	$Li_2Al_2Si_3O_{10}$	Li_2SiO_3
3c-T	720	1 h	$LiAlSi_2O_6$	$Li_2Al_2Si_3O_{10}$
				Mg_2SiO_4
				Li_2SiO_3
3d-T	910	2 min	$Mg_2Al_4Si_5O_{18}$	$MgSiO_3$
		1 h	$LiAlSi_2O_6$	$MgSiO_4$

TABLE 5. RESULTS OF X-RAY ANALYSES OF CRYSTALLINE PHASES IN MODIFIED COMPOSITIONS

Composition Number	Crystallization Temperature (°C)	Hold Time	Crystalline Phases	
			Major	Minor
4a	615	1 h	$Li_2Al_2Si_3O_{10}$	Li_2SiO_3
5a	650	2 min.	Amorphous	
		5 min.	$Li_2Al_2Si_3O_{10}$	+ glass
		15 min.	$Li_2Al_2Si_2O_{10}$	Li_2SiO_3
		30 min.	$Li_2Al_2Si_2O_{10}$	Li_2SiO_3
		1 h	$Li_2Al_2Si_3O_{10}$	Li_2SiO_3
		6.5 h	$Li_2Al_2Si_3O_{10}$	Li_2SiO_3
				$MgSiO_3$
6a	700	1 h	$Li_2Al_2Si_3O_{10}$	Li_2SiO_3
				$MgSiO_3$

DTA thermogram. Each sample was heated to 1250°C and held for 15 minutes before lowering the temperature to the crystallization temperature and holding for the listed time. The high temperature heat treatment (1250°C) was used to simulate expected joining cycles.

The major phase evolved from composition 3b-T after treating at 640°C for one hour was $Li_2Al_2Si_3O_{10}$. Chemically, this phase is equivalent to a solid solution of β'-spodumene ($LiAlSi_2O_6$) and β'-eucryptite ($LiAlSiO_4$). A minor amount of lithium metasilicate (Li_2SiO_3) was also observed. When composition 3c-T was held at 720°C for one hour, β'-spodumene was the major phase analyzed, and minor phases ($Li_2Al_2Si_3O_{10}$, Mg_2SiO_4, and Li_2SiO_3) were also detected. Heat treating composition 3d-T for two minutes at 910°C resulted in the presence of cordierite ($Mg_2Al_4Si_5O_{18}$) and enstatite ($MgSiO_3$). A treatment time of one hour resulted in the presence of $LiAlSi_2O_6$ and forsterite ($MgSiO_4$).

Heat treating compositions 4a, 5a, and 6a at the appropriate temperatures for various times resulted in $Li_2Al_2Si_3O_{10}$ as the primary crystalline phase. A minor amount of Li_2SiO_3 was observed when composition 4a was held at 615°C for one hour. Similarly, when composition 6a was held at 700°C for one hour Li_2SiO_3 and Mg_2SiO_4 were observed in minor amounts. Composition 5a was x-ray amorphous after being held for two minutes at 650°C; after five minutes at 650°C, $Li_2Al_2Si_3O_{10}$ began to appear. This phase, along with Li_2SiO_3, was detected for heat-treatment times of 15 min, 30 min, 1 h, and 6.5 h. The x-ray pattern of the samples held for 6.5 h also indicated small amounts of $MgSiO_3$.

Two results of the quench tests are of interest. First, for glass compositions which melt in the appropriate range, $Li_2Al_2Si_3O_{10}$ is the predominant crystalline phase evolved. In the temperature range 25 to 1000°C, this phase exhibits a slightly negative linear thermal expansion. The crystallization of this low expansion phase will lower the overall expansion of the glass-ceramic as crystallization proceeds. The reduced thermal expansion of the devitrified material provides some built in resistance to thermal shock during temperature cycling.

Second, the effect of crystallization on the residual glass composition is of concern since mechanical properties at high temperature are dependent on the refractory nature of the residual glass. The more refractory the glass, the greater the strength retention, and the higher the possible application temperatures. Figure 8 illustrates the effect of devitrification on the residual glass composition as the crystalline phases $Li_2Al_2Si_3O_{10}$, Li_2SiO_3, and $MgSiO_3$ are evolved, in that order, assuming that crystallization goes to completion for one phase before the nest phase begins to evolve. The amount of $Li_2Al_2Si_3O_{10}$ which develops is limited by the available aluminum concentration, which decreases to zero. A slight decrease in the silicon concentration, a slight increase in lithium concentration, and a relatively large increase in magnesium concentration of the residual glass results. The amount of the second phase evolved (Li_2SiO_3) is limited by the available lithium concentration, which decreases to zero. A slight increase in the silicon concentration of the residual glass is

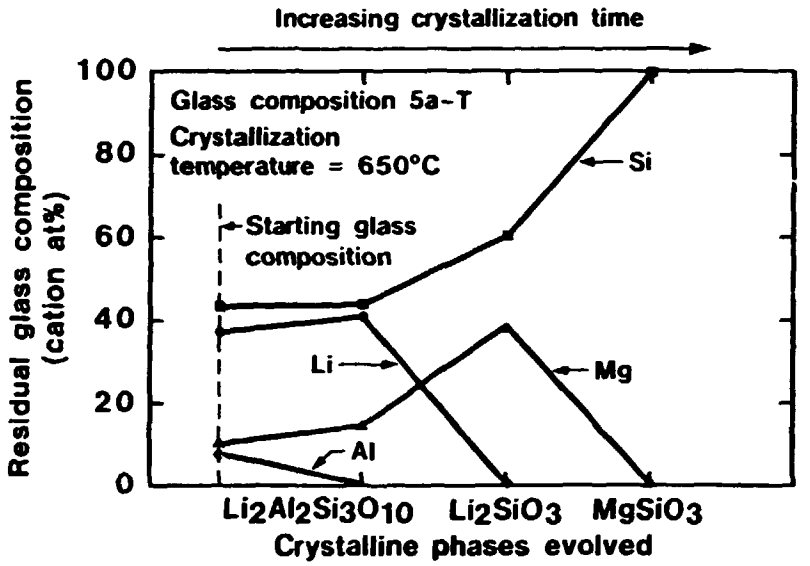

Fig. 8. Effect of crystallization of 5a on the residual glass composition.

anticipated, along with a very large increase in magnesium concentration. The third phase evolved ($MgSiO_3$) is limited by the available silicon concentration, which decreases to zero leaving magnesium as the only cation present in the residual glass. At this point, the residual glass is chemically equivalent to MgO. Although Figure 8 assumes that all crystallizations go to completion, this would rarely be the case in reality; however, the general trends are valid. As lithium-containing phases evolve from the parent glass, the composition of the residual glass must be higher in magnesium. These results, coupled with the effect of composition changes on the transition temperature, suggest that the residual glass component becomes more refractory as crystallization proceeds.

COMPATIBILITY TESTS

Composition 3b-T exhibited complete melting and flow when held at 1250°C for 15 min on the silicon carbide surface. Optical examination indicated that the glass contained cracks resulting from thermal expansion mismatch and/or thermal shock damage due to the rapid quench. Some bubbles remained in the glass. Figure 9 shows a scanning electron microscopy (SEM) photograph of the glass/SiC interface obtained from a

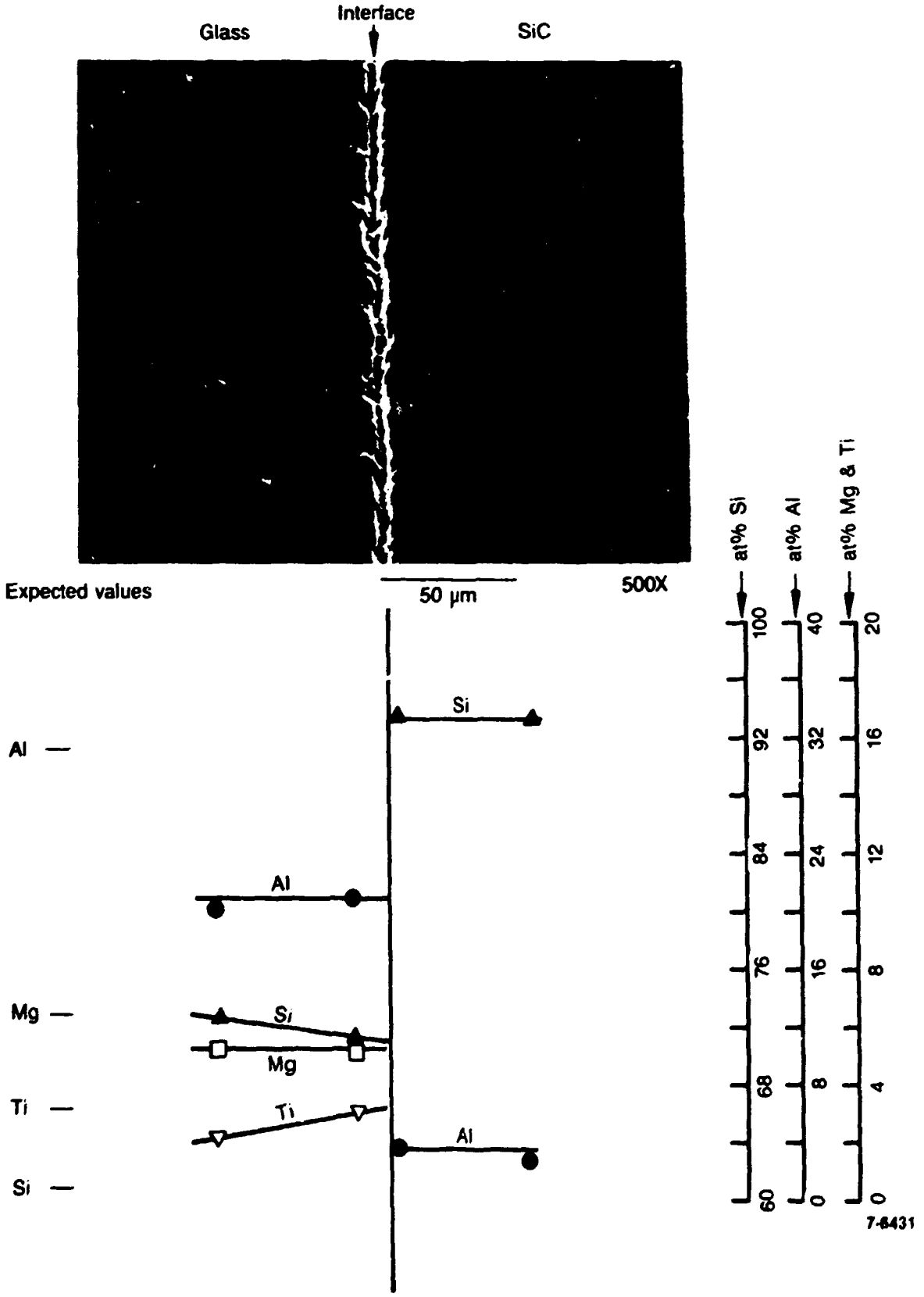

Fig. 9. SEM photomicrograph and EDS data from glass (3b-T)/silicon carbide (NC-203) interface after holding at 1250°C for 15 min and then quenching.

polished cross section. Also shown in Figure 9 are data obtained from this sample by energy dispersive spectroscopy (EDS). The EDS data are given in cation atom percent, but lithium is not shown because it cannot be detected by EDS. The silicon carbide contains predominately silicon with small amounts of aluminum. The aluminum observed probably is residue of the alumina polishing compound. Also detected in the silicon carbide, but not shown in Figure 9, was 3-4% tungsten. The tungsten was incorporated as an impurity during comminution of the silicon carbide powders before densification.

On the glass side of the interface, reduced silicon, and increased aluminum are observed. The expected values listed were calculated from the analyzed composition of the glass, and show fair agreement with those obtained by EDS. At the interface itself, the glass appeared to delaminate from the silicon carbide. These results suggest that the glass is chemically compatible with silicon carbide. Extensive reaction was not observed at 1250°C in 15 min.

Similar results have been obtained for compositions 3c-T, 4a, and 5a. The details of those results have been reported elsewhere.[1] None of the compositions investigated exhibited extensive reaction with silicon carbide at 1250°C in 15 min. Glass composition 3c-T was observed to be partially crystalline after this heat treatment cycle. These experiments did indicate that the onset of melting, as determined by DTA, must be 1150°C or less to ensure complete melting and flow at 1250°C in 15 min.

WETTING BEHAVIOR

The effect of time on the contact angle of glass composition 5a-T in contact with silicon carbide at 950, 975, and 1000°C is shown in Figure 10. The temperatures given in Figure 10 are normalized to the onset of melting, T_m, as determined from the DTA thermogram. As expected, the contact angle decreased from that of a cube (90°) to some equilibrium value. The equilibrium contact angle was 30.5, 32, and 44° for temperatures of 1000, 975, and 950°C respectively. A slight increase in the contact angle was observed for specimens heated at 950°C for long times. It is hypothesized that such a change in

geometry occurred because limited crystallization occurred over these long times. The expectation of limited crystallization is reasonable since the test temperature was only slightly above the onset of melting. At the higher temperatures, no crystallization effects were observed. It has been noted that crystallization of this composition results in surface distortion, and, hence, changes in the drop geometry.

Figure 11 shows the effect of time on the contact angle for glass composition 3b-T at temperatures of 1100, 1125, and 1150°C. Again the temperature has been normalized to the onset of melting observed on the DTA thermogram. The contact angle decreased from the initial 90° to an equilibrium value after some time, with equilibrium contact angles of 35, 40 and 50° observed at temperatures of 1150, 1125, and 1000°C respectively. The time required to reach the equilibrium value decreased with increasing temperature.

Changes in the contact angle with time at 1100, 1125, and 1150°C for glass composition 6a-T are shown in Figure 12. As before, the test temperatures are normalized to the DTA melting temperature, and the contact angle decreases from 90° to an equilibrium value after some finite time. Equilibrium contact angles of 44, 39, and 33° were

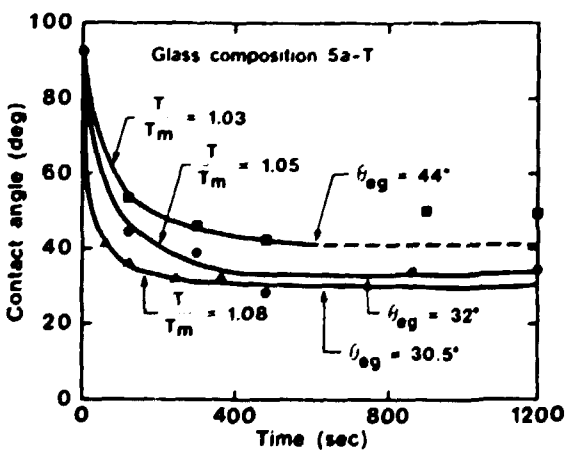

Fig. 10. Effect of time and temperature on the contact angle of glass composition 5a-T in contact with SiC. The onset of melting (T_m) in composition 5a-T was determined to be 925°C.

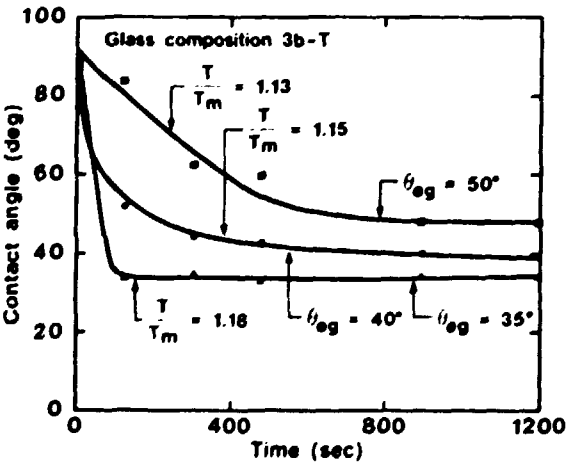

Fig. 11. Effect of time and temperature on the contact angle of glass composition 3b-T in contact with SiC. The onset of melting in composition 3b-T was determined to be 975°C.

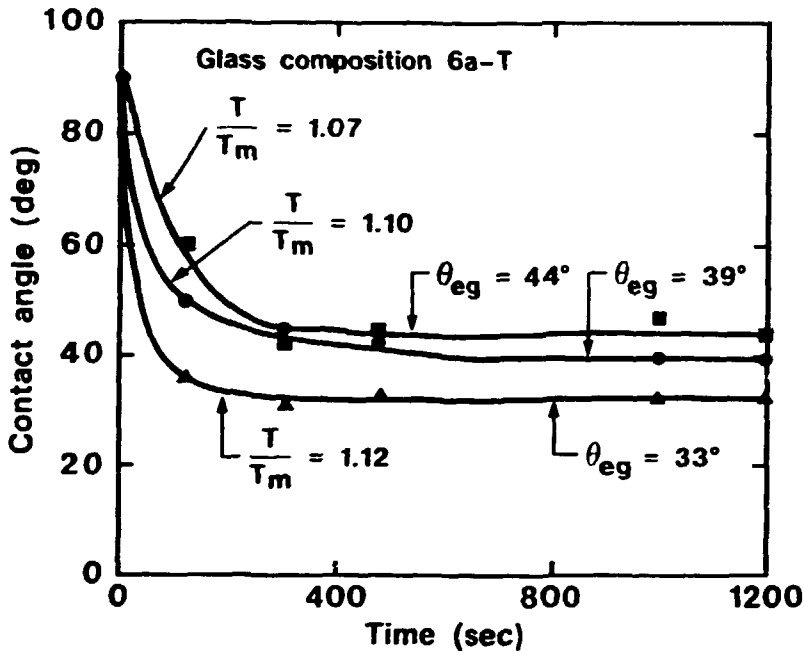

Fig. 12. Effect of time and temperature on the contact angle of glass composition 6a-T in contact with SiC. The onset of melting (T_m) in composition 6a-T was determined to be 1025°C.

observed at test temperatures of 1100, 1125, and 1150°C respectively. Interestingly, the data indicate that the equilibrium contact angle is obtained after 300-400 s, and is essentially independent of test temperature.

The equilibrium contact angle is a measure of the ability of the glass to wet a silicon carbide surface, and is determined by the thermodynamic interfacial energies of the surfaces in contact.[4] The interfacial energies are represented by forces acting at the triple point along the interface in question (Figure 1). The interfacial energy between the solid and the gas (atmosphere) is shown by a force acting away from the drop along the solid surface (γ_{sg}). The interfacial energy between the solid and liquid is represented by a force acting along the solid-liquid interface (γ_{sl}). The force γ_{sg} acts in a direction opposite to that of force γ_{sl}. A force representing the third interfacial energy, that between the liquid and gas (γ_{lg}) and acts in a direction parallel to the liquid-atmosphere interface. The force vector which represents the liquid-gas interfacial energy can be projected on the the plane of the substrate or solid. The projection is calculated numerically as $\gamma_{lg}(\cos\theta)$.

The sum of all forces acting at the triple point must be zero to maintain equilibrium. The following equation (Young's equation) describes the drop geometry at equilibrium:

$$\gamma_{sg} = \gamma_{sl} + \gamma_{lg}\cos\theta \qquad (8)$$

If the energy of the solid/gas interface is larger than the energy of the solid/liquid interface, the liquid/gas energy must act as shown in Figure 1a. In this case, the equilibrium contact angle is less than 90°, and the liquid is said to wet the solid. If the energy of the solid/gas interface is less than the energy of the solid/liquid interface, the liquid/gas interface energy must act as shown in Figure 1b. In this case, the liquid is said not to wet the solid, and equilibrium contact angles of greater than 90° are observed.

All of the glasses used in this investigation wet the silicon carbide as evidence by equilibrium contact angles of 50° or less. It has been shown that no severe chemical interaction between the glass compositions under investigation and SiC was detected at 1250°C. Therefore, it is unlikely that a reaction at lower temperatures would exist and confuse the results of wetting.[5] Figure 13 illustrates that the equilibrium contact angle decreased with increasing test temperature for all glass compositions studied. All of the glass compositions resulted in equilibrium contact angles between 30 and 50°. The temperatures required to obtain these angles were dependent on the composition of the glass. Glass composition 5a-T produced the measured contact angles at temperatures just above its DTA melting point ($1.03<T/T_m<1.08$). Glass composition 6a-T required slightly higher temperatures relative to its DTA melting point ($1.07<T/T_m<1.12$) to yield the same contact angles. Glass composition 3b-T had to be heated well above its DTA melting point ($1.13<T/T_m<1.18$) to produce similar equilibrium contact values. The actual test temperatures required to produce similar equilibrium contact angles were similar for compositions 6a-T and 3b-T (1100-1150°C). The actual test temperature required to produce similar equilibrium contact angles with composition 5a-T was much lower (950-1000°C). These results suggest that wetting behavior as a function of temperature is directly related to the glass chemistry.

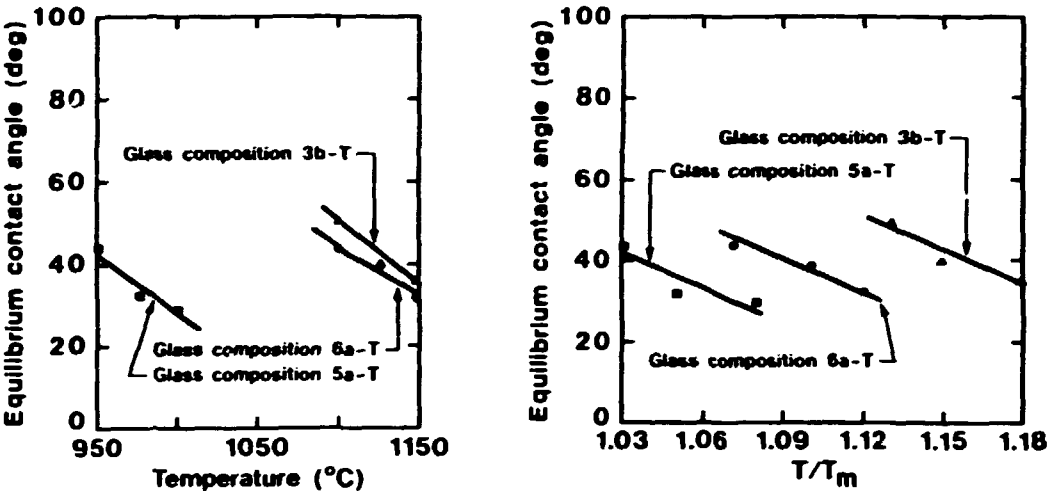

Fig. 13. The variation of the equilibrium contact angle for glass compositions 5a-T, 6a-T, and 3b-T as a function of (left) the actual test temperature, and (right) the normalized test temperature.

Comparing the chemistries of glass compositions 5a-T and 6a-T (Table 1), composition 6a-T is higher in MgO and lower in both Li_2O and SiO_2 contents than composition 5a-T. The glasses used to study the wetting behavior were melted in platinum crucibles and are expected to have a composition similar to that expected from the batch materials. This difference in composition resulted in a shift to temperatures farther above the melting point to obtain contact angles between 30 and 50° with composition 6a-T. These trends would be observed if the increase in MgO content, accompanied by decreases of Li_2O and SiO_2, resulted in a less thermodynamically favorable system. In other words, the energy of the glass composition 5a-T interface is less than that of the glass composition 6a-T interface at the same temperature, relative to its melting point.

Comparing the chemistries of glass compositions 5a-T and 3b-T (Table 1), composition 3b-T is lower in MgO content and higher in Al_2O_3 content. The SiO_2 and Li_2O contents of compositions 5a-T and 3b-T are similar with 3b-T being slightly lower in SiO_2 content and slightly higher in Li_2O content. These compositional changes resulted in a large shift to higher temperatures, relative to the melting point (Figure 6b), to obtain similar equilibrium contact angles. Again, these

results indicate that a composition 5a-T-SiC interface is more thermodynamically favorable (lower interface energy) than a composition 3b-T- SiC interface at similar temperatures relative to their respective melting points.

An additional relationship can be developed to describe the interfacial energies of the sessile drop experiment.[4]. The adhesive energy (E_{ad}) can be describe as:

$$E_{ad} = \gamma_{sg} - \gamma_{sl} + \gamma_{lg} \tag{9}$$

This relationship says that the adhesive energy is simply the amount of energy reduction due to the replacement of a solid/gas interface with a lower energy solid/liquid interface plus the addition a new interface, the liquid/gas interface. Substituting Equation 8 in to Equation 9 and rearranging, the Young-Dupre relationship is obtained:

$$E_{ad}/\gamma_{lg} = 1 + \cos\theta \tag{10}$$

The term E_{ad}/γ_{lg} describes a normalized adhesive energy, and in a sense is a multiplier. This term quantitatively addresses the amount of adhesive energy expected relative to the introduction of a liquid/gas interface into the system. In terms of forming a bond between the liquid and solid, the term E_{ad}/γ_{lg} should be as large as possible, and must be larger than one for wetting to occur.

Figure 14 shows the effects of glass composition and temperature on the data plotted according to Equation 10. The normalized adhesive energy, E_{ad}/γ_{lg}, ranges from 1.64 to 1.86 for the glass compositions studied. The effect of glass composition on the normalized adhesive energy (Figure 14b) is analogous to the effect of glass composition on the equilibrium contact angle. Glass composition 6a-T, with an addition of MgO and reductions of Li_2O and SiO_2 relative to composition 5a-T, results in a shift to higher temperatures, relative to the melting point, to obtain similar normalized adhesive energies. Glass composition 3b-T, with an addition of Al_2O_3 and reduction of MgO relative to composition 5a-T, resulted in a large shift to higher

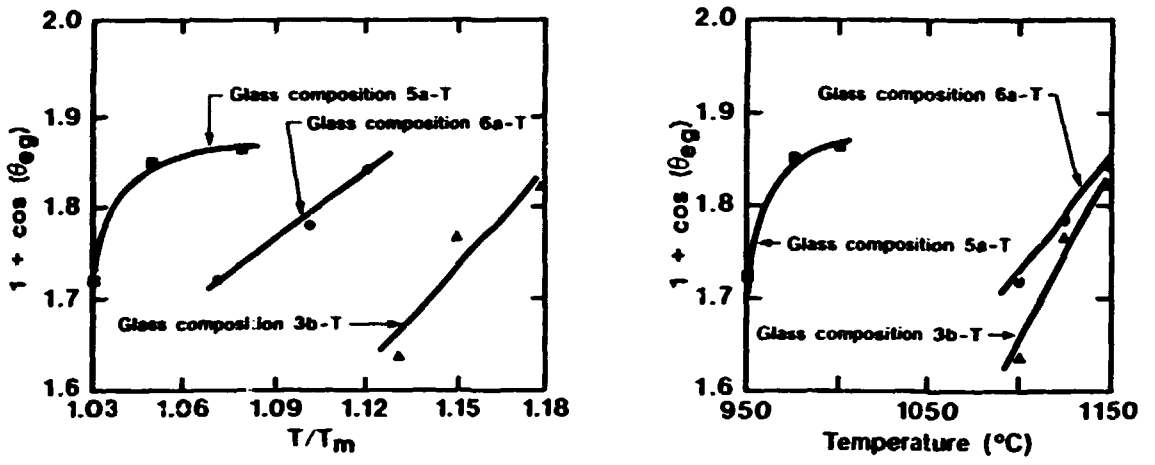

Fig. 14. The effect of (left) the actual test temperature, and (right) the normalized test temperature on the parameter $1+\cos\theta_{eq}$ for compositions 5a-T, 6a-T, and 3b-T.

temperatures to obtain similar adhesive energies. These results suggest that the composition changes made to 5a-T result in a less thermodynamically favorable system with lower adhesive energies.

Summing all of these results, the following conclusions can be made. The addition of MgO to a $MgO\text{-}Li_2O\text{-}Al_2O_3\text{-}SiO_2$ glass moderately reduced its wetting ability at any given temperature relative to its melting point, and lowered the expected adhesive energy of the liquid/solid interface. The addition of Al_2O_3 to a $MgO\text{-}Li_2O\text{-}Al_2O_3\text{-}SiO_2$ glass greatly reduced its wetting ability at any given temperature relative to its melting point, and greatly lowered the expected liquid solid adhesive energy.

CRYSTALLIZATION RATES OF GLASS COMPOSITION 5a-T

The thickness of crystalline surface layers formed on slices of glass composition 5a-T as a function of temperature and time are shown in Figure 15. The regression lines were forced to pass through the origin, which corresponds to no crystal growth at time t = 0. The growth rates are plotted in Figure 16 as a function of temperature, and are observed to increase with increasing temperature. The growth rate appears to be levelling off and the scatter in the data is more extreme at the higher temperature. The increased scatter in the data indicates a crystallization process which is more difficult to control at the higher

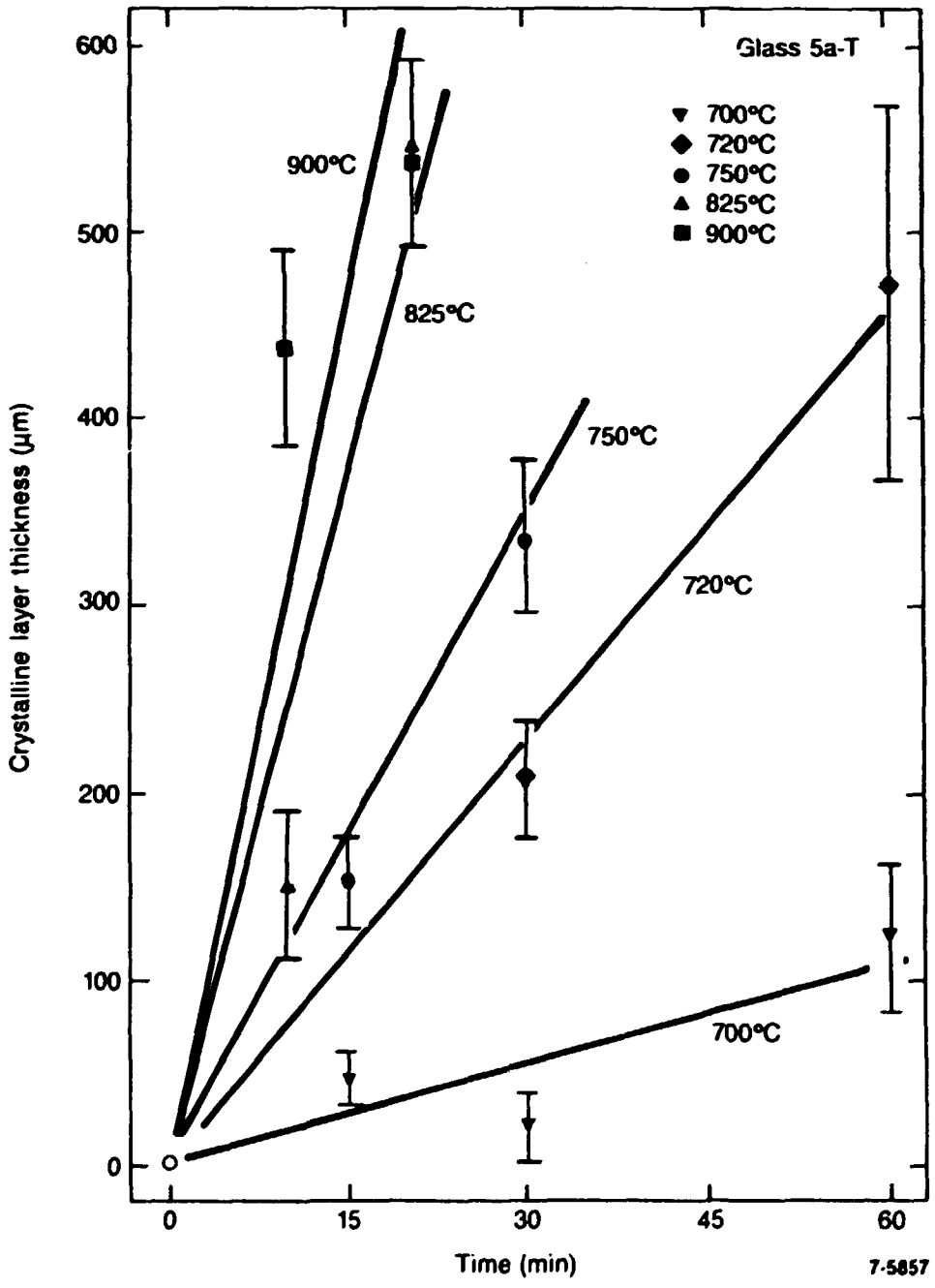

Fig. 15. Crystalline layer thickness as a function of time at temperature for glass composition 5a-T.

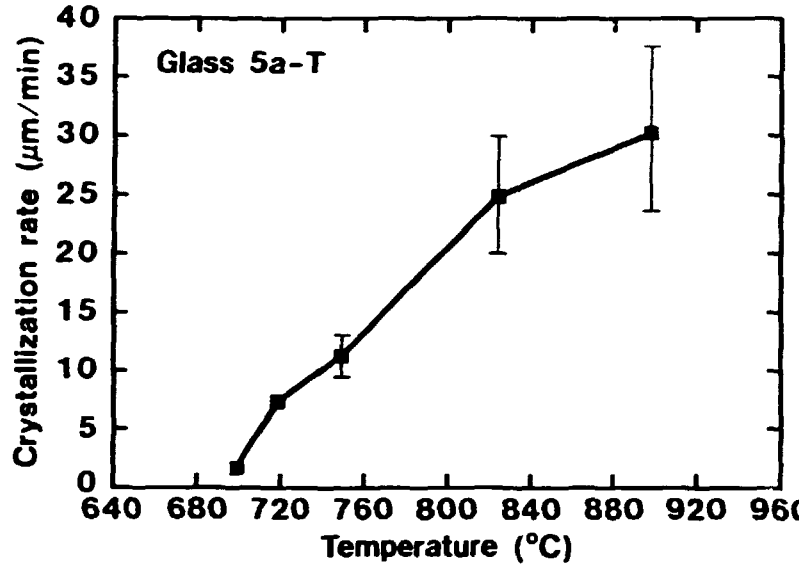

Fig. 16. Variation of crystallization rate as a function of temperature for glass composition 5a-T.

temperatures where the kinetics are faster. It is expected that the growth rate maximizes at some temperature just below the onset of melting (925°C).

In the lower temperature region, the growth rate can be modelled by an Arrhenius-type law:

$$k = A \exp[-E/RT] \qquad (12)$$

where: E = activation energy of the crystallization process
R = gas constant
T = temperature
A = constant

Equation 12 can be linearized such that a plot of ln(k) vs. T^{-1} permits calculation of the activation energy as shown in Figure 17. The activation energy for the crystallization of 5a-T is 294 kJ/mole. The low activation energy suggests that the magnesium modified lithium-aluminosilicate prepared in this study will crystallize readily as expected.

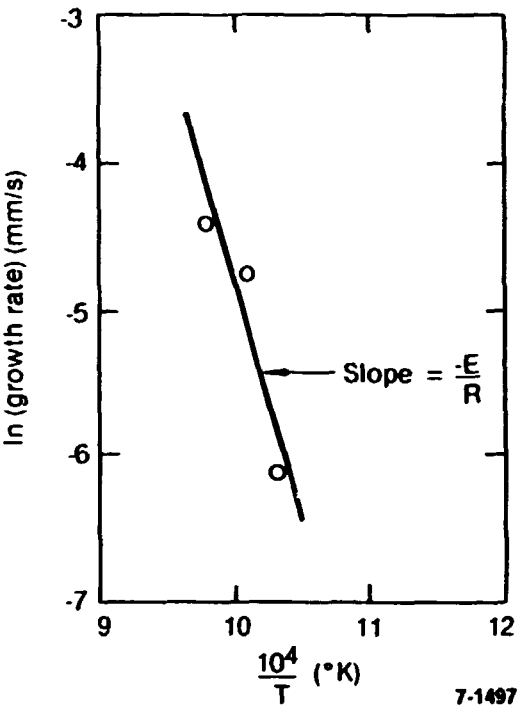

Fig. 17. Ln growth rate as a function of T^{-1} for glass composition 5a-T.

Samples of glass 3b-T were heat treated at 640 and 725°C for various times. After approximately 60 min at 640°C and 30 min at 725°C, the specimens were observed to fracture into small pieces. It is hypothesized that the surface crystallization combined with a volume change upon crystallization resulted in mechanical stresses which exceeded the fracture stress. Similar fractures were observed with attempts to crystallize glass composition 6a-T at 725°C. Both sets of experiments were designed to promote surface crystallization. Experiments are underway to determine if glass compositions 3b-T and 6a-T can be uniformly crystallized throughout the bulk to prepare a glass-ceramic.

STRENGTH OF DEVITRIFIED GLASS COMPOSITION 5a-T

The thermal expansion of the phase $Li_2Al_2Si_3O_{10}$ has been reported to be very low. Mechanical stresses result from the expansion mismatch and cause some cracking. The annealing treatment minimized transient stresses due to thermal fluctuations and limited the amount of cracking.

The variation of fracture stress with temperature for the treated and untreated bars is shown in Figure 18. Two to five bars were tested at each temperature; the data represent the average and the range (minimum and maximum values). Each specimen was allowed to equilibrate to the furnace temperature for 5 min before testing at a crosshead speed of 8.5×10^{-3} mm/s. Since the crystallization treatment was performed on machined bars, and some cracking resulted from expansion mismatch, the flaw size distributions in the treated and untreated bars do not correspond. The fracture stresses are normalized to the respective room temperature values. For this reason, the fracture stresses of the treated bars are normalized to the average room temperature fracture stress of the treated bars, and the fracture stresses of the untreated bars are normalized to their average room temperature fracture stress. The treated bars had about 15-20% of the strength of the untreated bars at room temperature due to a change in flaw population.

The untreated bars exhibited about a 25% reduction in strength when heated to 450°C. Viscoelastic deformation was observed in these materials at 490°C, which is very close to the transition temperature. It can be concluded that the useful maximum temperature for mechanical stability of the untreated material is less than 490°C.

The treated bars showed a 40% increase in strength upon heating to 500°C. Large increases in strength, compared to the room temperature values, were observed upon heating to 710 and 785°C. The treated bars tested at 785°C were as strong or slightly stronger than the untreated bars at room temperature. The increase in strength is presumably due to a change in flaw characteristics at the high temperature. The important thing to remember is not the strength values, but that no deformation was observed in the treated bars at temperatures at least as high as 785°C. The loading curves were perfectly linear indicating brittle behavior throughout the entire range.

SIMULTANEOUS CRYSTALLIZATION AND SINTERING OF A GLASS POWDER

The densification behavior of powdered glass composition 5a-T at 750°C is shown in Figure 19. The data suggest that densification occurred very rapidly. The slight decrease in density at long times is

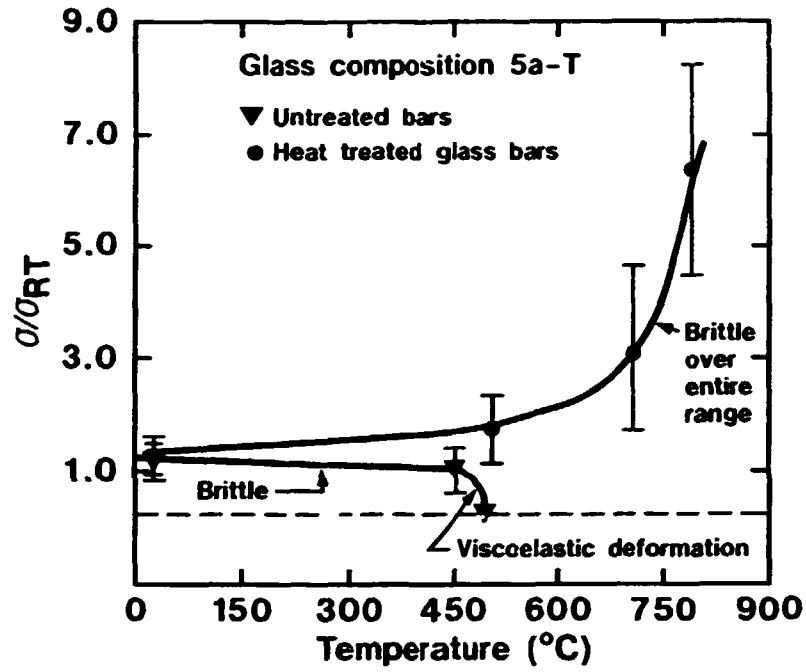

Fig. 18. Normalized fracture stress of treated and untreated flexure bars as a function of temperature for glass composition 5a-T.

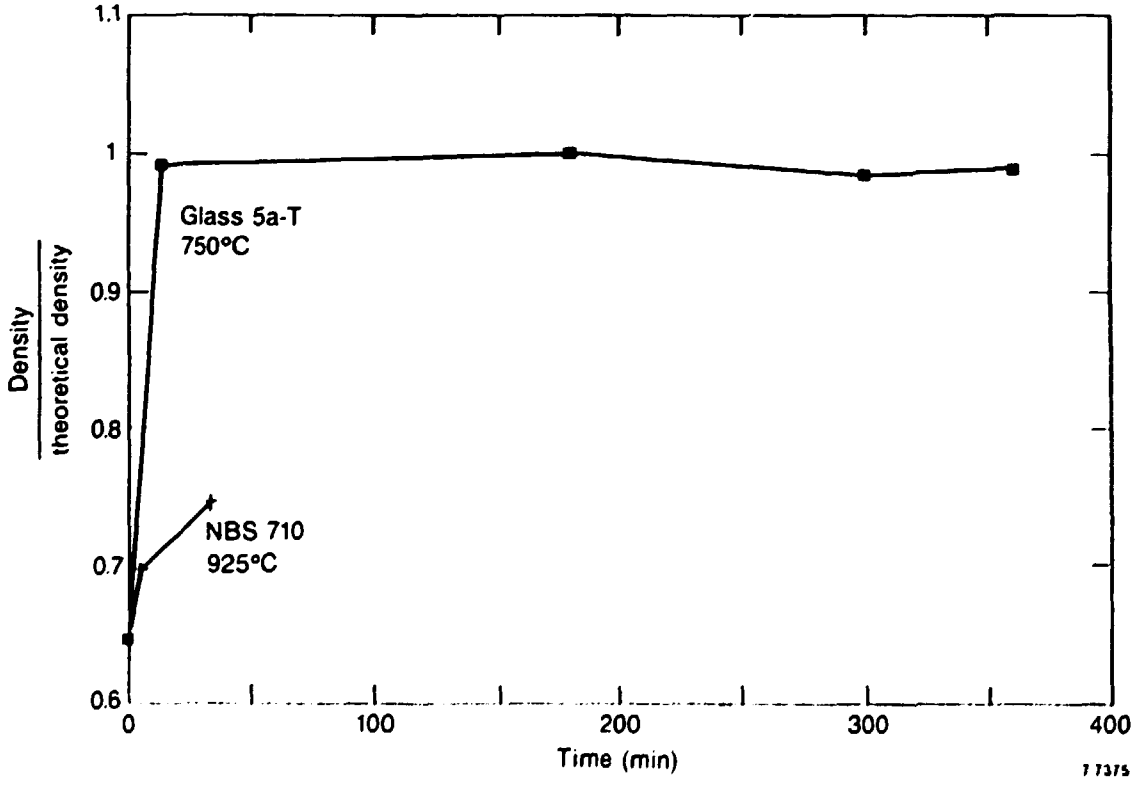

Fig. 19. Densification of powder compacts of 5a-T and NBS 710 glasses as a function of time at temperature.

associated with the formation of small pores during crystallization. Also shown in Figure 19 are the densification data for a NBS 710 glass. The densification rate calculated from the NBS 710 data was 15.2 x s^{-1}. This densification rate is in excellent agreement with number reported in the literature[6] and confirms the validity of the experimental approach and results observed for glass composition 5a-T.

While the possibility of a single-step joining process is apparent, initial joining experiments will utilize the more conventional three-step process. The "proof-of-concept" of vitreous brazing of silicon carbide reinforced composites will be accomplished in this manner. The use of the single-step process to allow more refractory brazing compositions will be pursued as appropriate.

JOINING EXPERIMENTS

Initial experiments indicated that glass composition 5a-T did melt at 1150°C in 15 min. Large bubbles remained in the glass after heat treatment. More satisfactory results were observed when the pieces to be joined were pretreated at 1050°C to melt the glass powder and coat the surfaces prior to the joining heat treatment. However, small bubbles were still observed in the glass. Experiments are continuing to optimize the time-temperature relationship required to eliminate these bubbles.

CONCLUSIONS

The following conclusions are based on experiments performed during the preceding year:

1. The transition, crystallization, and melting temperatures of glasses in the MgO-Li_2O-Al_2O_3-SiO_2 system can be adjusted by altering the glass composition.

2. Although limited dissolution of alumina crucible material occurred during melting, large losses of Li_2O and MgO due to volatilization were not observed. Melting in platinum crucibles eliminated compositional changes.

3. Low expansion lithium-aluminosilicate phases were observed to crystallize from compositions which melt in the appropriate range for joining. These phases will provide inherent thermal shock resistance of the joint.

4. As lithium-containing phases crystallize from the glass compositions of interest, the residual glass phase becomes more concentrated in MgO and SiO_2. This observation implies that the residual glass phase shifts to more refractory compositions as crystallization proceeds.

5. None of the glass compositions examined exhibit severe chemical reaction with hot-pressed silicon carbide at temperatures to 1250°C. Melting temperatures as determined by DTA must be 1150°C or less to ensure complete melting in contact with silicon carbide at 1250°C in 15 min.

6. Equilibrium contact angles between 30 and 50° were observed for glass compositions 5a-T, 3b-T, and 6a-T in contact with silicon carbide at temperatures between 950 and 1150°C. Low MgO and Al_2O_3 concentrations resulted in the lowest equilibrium contact angles, and, hence, the largest expected adhesive energy, at temperatures just above the melting point.

7. Glass composition 5a-T crystallized readily at temperatures between 700 and 900°C. The activation energy associated with the crystallization process was 294 kJ/mole.

8. The segregation of magnesium and silicon into the residual glass phase with crystallization shifts the onset of viscoelastic deformation to higher temperatures. The end result is that higher application temperatures of joined silicon carbide composites can be obtained by crystallizing the braze material.

9. Although MgO and Al_2O_3 additions inhibited the wetting ability of the glass, Al_2O_3 is necessary for crystallization of $Li_2Al_2Si_3O_{10}$, and MgO is necessary to increase the refractory nature of the residual glass.

10. The possibility of simultaneously crystallizing and sintering the glass composition from a powder to a glass-ceramic was demonstrated and will be pursued as appropriate.

11. A joining geometry has been selected to prepare butt joints for flexure testing, and a joining fixture to maintain alignment of the composite during joining has been demonstrated.

REFERENCES

1. Coon, D. N., Neilson, R. M., Jr., and Landini, D. J., "Characterization of MgO-Li_2O-Al_2O_3-SiO_2 Glasses For Use as Brazing Materials," EGG-MS-7523, February 1987.

2. Balta, P. and Balta, E., Introduction to the Physical Chemistry of the Vitreous State, Abacus Press, 1976, pp. 154-165.

3. Coon, D. N. and Neilson, R. M., Jr., "Effect of MgO Additions on the Glass Transition Temperature of Li_2O-Al_2O_3-SiO_2 Glasses," submitted to the Journal of Materials Science Letters.

4. Murr, L. E., " Interfacial Energetics in Metal-Metal, Metal-Ceramic, Metal-Semiconductor, and Related Solid-Solid and Liquid-Solid Systems," Surfaces and Interfaces in Ceramic and Ceramic-Metal Systems, ed. by Pask, J. A. and Evans, A. G., Plenum Press, 1981, pp. 107-119.

5. Hoge, C. E., Brennan, J. J., and Pask, J. A., "Interfacial Reactions and Wetting Behavior of Glass-Iron Systems," Journal of the American Ceramic Society, [56]2, pp. 51-54, 1973.

6. Clark, T. J. and Reed, J. S., "Kinetic Processes Involved in the Sintering and Crystallization of Glass Powders," Journal of the American Ceramic Society, [69]11, pp. 837-846, 1986.

DEVELOPMENT OF NONDESTRUCTIVE EVALUATION METHODS FOR STRUCTURAL CERAMICS

W. A. Ellingson, R. A. Roberts, M. W. Vannier, J. L. Ackerman,
B. D. Sawicka, S. Gronemeyer, and R. J. Kriz

Materials and Components Technology Division
Argonne National Laboratory
Argonne, Illinois 60439

ABSTRACT

Advanced nondestructive evaluation methods are being developed to characterize ceramic materials and allow improvement of process technology. If one can spatially determine porosity, map organic binder/plasticizer distributions, measure average through-volume and in-plane density, as well as detect inclusions, process and machining operations may be modified to enhance the reliability of ceramics. Two modes of X-ray tomographic imaging -- advanced film (analog) tomography and computed tomography -- are being developed to provide flaw detection and density profile mapping capability. Nuclear magnetic resonance imaging is being developed to determine porosity and map the distribution of organic binder/plasticizer. Ultrasonic backscatter and through-transmission are being developed to measure average through-thickness densities and detect surface inclusions.

INTRODUCTION

The sensitivity of ceramics to flaws necessitates carefully controlled processing and finishing operations. The flaw sizes that affect load-bearing capabilities are dependent upon the stress levels in the part, but are frequently on the order of 10-100 μm. Nondestructive evaluation (NDE) methods (methods which detect flaws of interest without damage to the part) are being developed for defect screening as well as for characterization of ceramic materials: e.g., mapping of density gradients, binder/plasticizer (B/P) distribution in the green state, and porosity distributions.

Since ceramic materials compete with metal materials for many market applications, the need to hold down fabrication costs becomes a driving force for the development of effective NDE methods. Finishing (grinding, machining, etching, etc.) can be a costly step in ceramic processing. Any NDE method that can be used to screen parts prior to densification or final machining may increase yield by allowing final operations to be done only on parts that have a high probability of being acceptable (i.e., flaw-free). NDE techniques, therefore, must be developed with the following in mind: (a) What is the sensitivity (i.e., minimum detectable flaw size)? (b) What is the cost of the inspection system? (c) How difficult is the system to implement? and (d) What throughput can be handled? At this time, few of these questions can be adequately answered. However, several advanced NDE methods are being developed which appear to be very promising and these will be discussed here. To date, our NDE efforts have concentrated on characterization of monolithic ceramics after the forming step (see Table I); however, we have also conducted a significant amount of work on densified monolithic and SiC/SiC composites.

Porosity

Porosity is a characteristic of ceramics formed from compaction of the powder. Measurement of open porosity (volume fraction, size, shape, and distribution) can yield information on how the body will densify. A common method currently used to characterize open porosity is mercury porosimetry.[2] However, this method does not yield information on the spatial distribution of porosity. A method currently being developed to map porosity distribution is nuclear magnetic resonance (NMR) imaging.[3] To image the open porosity of green-state (or partially densified) ceramics, a "filler" fluid is used as a marker. Fluid is introduced into the test samples by vacuum impregnation to ensure adequate penetration into all the internal volumes of interest. The fractional open porosity is related to the fractional image intensity (NMR signal strength).

Table I Common Processing Operations for Advanced Ceramics[1]

Operation	Method	Examples
Powder preparation	Synthesis	SiC
	Sizing	Si_3N_4
	Granulating	ZrO_2
	Blending	
	Solution chemistry	Glasses
Forming	Slip casting	Combustors, Stators
	Dry pressing	Cutting tools
	Extrusion	Tubing, honeycomb
	Injection molding	Turbocharger rotors
	Tape casting	Capacitors
	Melting/casting	Glass ceramics
Densification	Sintering	Al_2O_3
	Reaction bonding	Si_3N_4
	Hot pressing	Si_3N_4, SiC, BN
	Hot isostatic pressing	Si_3N_4, SiC
Finishing	Mechanical	Diamond grinding
	Chemical	Etching
	Radiation	Laser, electron beam
	Electric	Electric discharge

Exploratory work[4,5] was performed with samples of several different ceramic materials. Sample 1 was a green-state MgO compact containing 309 g of MgO powder and 20% polyethylene glycol (PEG) binder (mw = 3200), cold pressed at 345 MPa (5000 psi) into a 31-mm-diam x 27-mm-high cylinder. Six holes, ranging in diameter from 330 μm to 1390 μm, were drilled parallel to the cylinder axis to provide recognizable void features, as shown in the diagram of Fig. 1. Sample 2 was a 25-mm-diam green-state SiC compact, similarly prepared and drilled. Sample 3 consisted of three partially sintered Al_2O_3 disks, 25 mm in diameter, with densities of 1.648, 1.703, and 1.720 g/cm^3, respectively. Sample 4

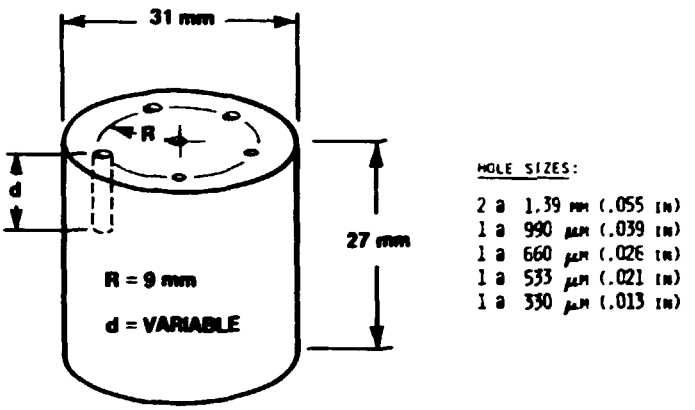

Fig. 1. Schematic Diagram of Ceramic Test Phantom Used for Initial NMR Imaging Studies.

consisted of two sets of Al_2O_3 disks specially prepared by ALCOA. The powders used in the two sets had mean particle sizes of 4.5 and ~0.4 μm, respectively. Each set consisted of three sample groups with a green-state diameter of nominally 25 mm and length/diameter ratios of 0.17, 0.58, and 1.13, respectively. (Different powder sizes and different L/D ratios were used to see whether the NMR porosity measurements were sensitive to these parameters.) Each group consisted, in turn, of three different types of specimens with nominal densities as follows: (a) green, 56.4% theoretical density; (b) bisque-fired, 54.9% theoretical density; and (c) partially sintered (prepared by heating bisque-fired compacts), 86.5% theoretical density. All samples were prepared in a single-ended press at a pressure of 689 MPa (10,000 psi).

All preliminary NMR imaging work was done with a filler fluid consisting of benzene, paramagnetically doped with 10.3 ± 0.6 mM chromium acetylacetonate [$Cr(CH_3COCH_2COCH_3)_3$] or 20.6 ± 1 2 mM $Cr(acac)_3$ to give proton T_1's of 237 ± 12 or 122 ± 11 ms, respectively.

Figure 2 shows a 2-mm-thick transaxial NMR image of the hole pattern (see Fig. 1) of the MgO sample, taken about 1 mm from the face of the sample. The smallest hole, 330 μm in diameter (on the order of the pixel size), is imaged.

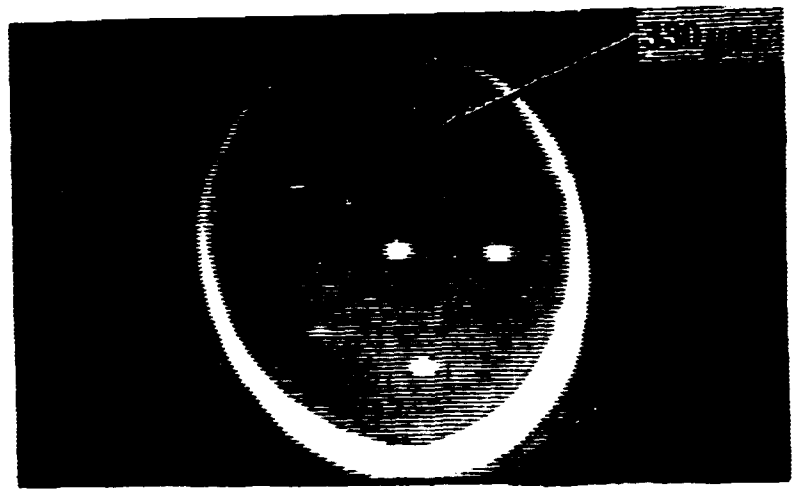

Fig. 2. Transaxial Spin-Echo NMR Image of An MgO/20% Polyethylene Glycol Green Ceramic Compact with the Hole Pattern Shown in Fig. 1. Benzene was used as the filler fluid. The bright rim is pure benzene. The bulk of the ceramic body exhibits an NMR-derived porosity of 15.5 ± 6.2%, and the dark, round patch has a porosity of 7.4 ± 1.7%. The background (noise) value is 2.1 ± 1.1%.

An NMR image was taken of the three partially densified Al_2O_3 disks of Sample 3; the image plane approximately contained the axes of all three disks. NMR signal intensities for each disk were measured near the disk axes and near the peripheries. Figure 3 shows the relationship between the NMR-derived fractional porosities and the densities of the Al_2O_3 specimens. The vertical bars on the experimental points represent standard deviations within each region of interest, and the solid lines are linear least-squares fits. The higher porosity and increased porosity variance at the periphery are roughly in accord with what is known about density distributions after compaction.[6]

An experiment was conducted on one Al_2O_3 specimen from Sample 4. Specimen 1-F-3 (set number 1, particle size ~0.4 μm), partially sintered to 86.5% of theoretical density, was vacuum impregnated with the paramagnetically doped benzene. A sagittal NMR image (image taken along the longitudinal axis) of this sample is shown in Fig. 4. The gray scale values of the individual pixels of the sagittal NMR image correspond to the filler fluid concentration, and hence to the local porosity. The bright region outside the specimen represents the gray-scale value of the pure benzene.

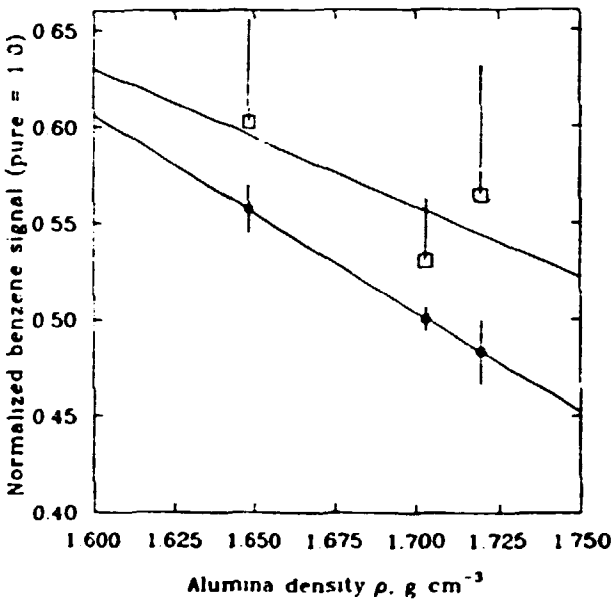

Fig. 3. Relationship of NMR Signal Intensity vs Measured Density of Partially Sintered Al_2O_3 Disks. , peripheral region; , on-axis region. Solid lines are least-squares fits; error bars are standard deviation about the mean pixel intensity within each region of interest. (Half-error bars are used where necessary to avoid overlap.)

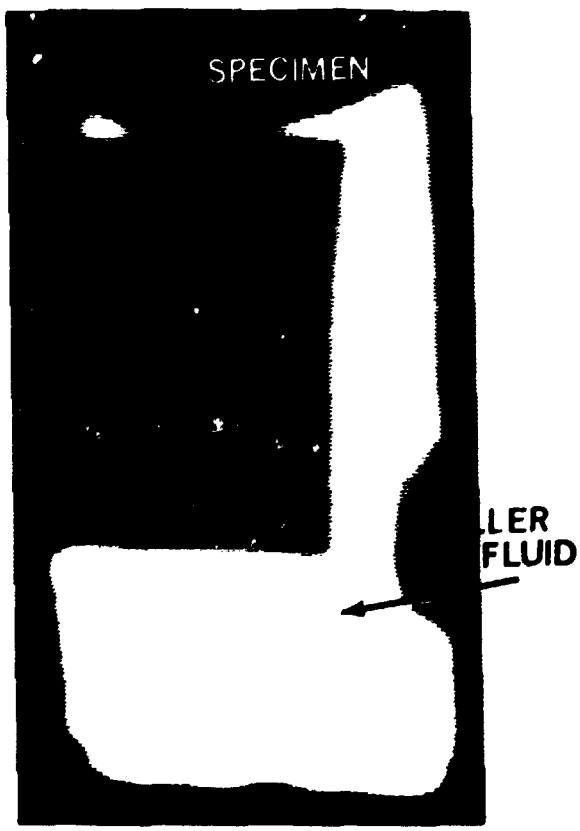

Fig. 4. Sagittal NMR Image of Partially Densified Al_2O_3 (ρ = 3.47, 86.5 %TD, slice thickness = 2 mm).

In order to better display the NMR-measured porosity, a surface diagram was made to display the gray scale (porosity) in three dimensions. In the 3-D map of Fig. 5, the surface represents the relative gray scale (porosity) of the sample. Two important observations can be made from this map: (1) the radial distribution of porosity, as measured by NMR, changes along the axis of the cylinder; and (2) the apparent porosity is significantly different at the two ends of the sample (one end was at the fixed end of the ram, and the other at the movable end). This is in agreement with previous work[6] relative to measuring pressure variation along the axis of a right-circular cylinder that was compacted with a single-acting ram. Figure 6 shows a typical pressure distribution (in percent of applied load) in a granular compact for an L/D ratio of 1.75.[7] Note that as one proceeds towards the fixed end of the specimen, the pressure gradient changes significantly.

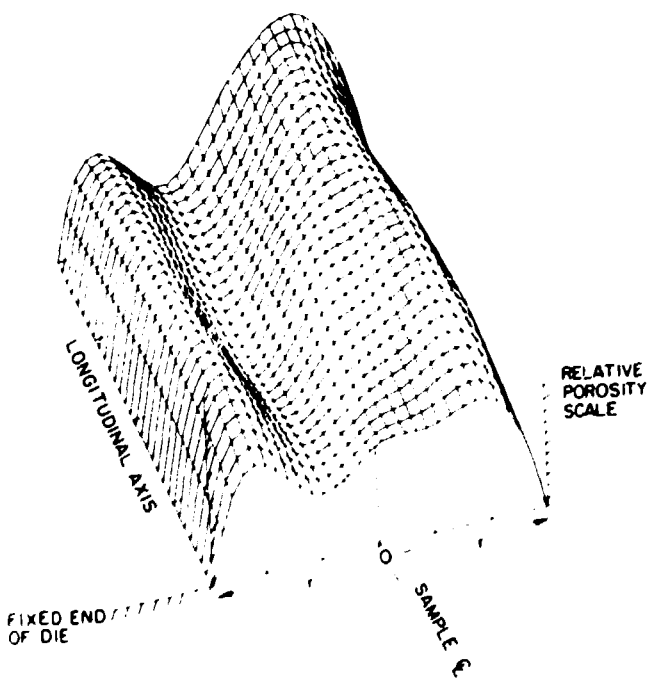

Fig. 5. Three-Dimensional Surface Diagram of NMR Signal Intensity (Porosity) for Sagittal Image Shown in Fig. 4.

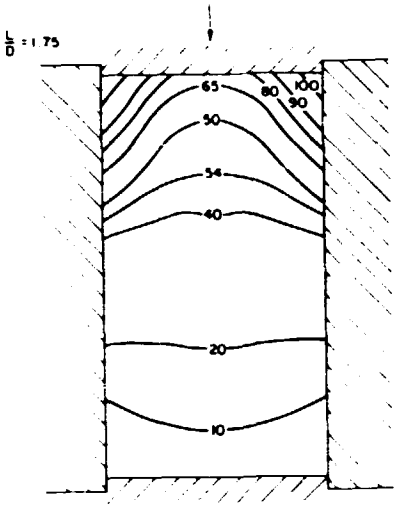

Fig. 6. Typical Pressure Distribution (Percent of Applied Load) in Right Circular Cylinder of Granular Material Compacted Green Ceramic with Single-acting Ram [from Ref. 7].

Binder/Plasticizer Distribution

Injection molding problems have been identified[8] which can cause defects in final parts. Table II lists typical defects and some of the potential causes of these defects, many of which can be traced to a poor distribution of organic B/P. For example: (a) incomplete parts, due to an improper feed material which is the result of poor mixing of the ceramic powder and the B/P; (b) large failure-causing pores, caused either by large pockets of the B/P itself (left by poor mixing) or by agglomerates lines (regions within the part where injected material folds on itself but does not join completely), possibly caused by improper feed material; and (d) cracks in the final product, perhaps caused by a high local concen-tration of B/P (low ceramic green packing density) with resulting locally high differences in densification rate and thermal expansion. Clearly, the ability to map the distribution of organic B/P would improve the under-standing of the injection molding process.

Table II. Injection Molding Defects and Causes[9]

Type of Defect	Causes
Incomplete part	Improper feed material Poor tool design Improper material and/or tool temperature Inadequate tool lubrication
Large pores	Entrapped air Improper material flow and consolidation during injection Agglomerates Large pockets of the organic due to incomplete mixing
Knit lines	Improper tool design or feed material Incorrect temperatures
Cracks	Sticking during removal from tool Improper tool design Improper extraction of the organic

We recently used a medical 1.5-T superconducting-magnet NMR imaging system (Siemens Magnetom™) to evalute the feasibility of imaging the B/P directly.[10] A green-state test specimen was made by mixing 25 wt.% binder with SiC powder. Stark SiC powder was used as the starting powder. The binder was PEG with mw = 8000, which has a higher molar concentration of hydrogen protons than the lower-mw form. The SiC/PEG mixture was cold-pressed to 517 MPa (7500 psi) at room temperature to obtain a 25-mm-diam, 25-mm-high right circular cylinder. Five 5-mm-diam glass beads were incorporated at the midsection of the specimen to simulate defects, as shown in Fig. 7.

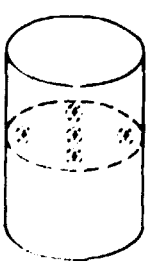

Fig. 7. Schematic of SiC/25% Polyethylene Glycol Used in Initial Test of Direct NMR Imaging of Binder/Plasticizer.

T_1-weighted, proton-density weighted, and T_2-weighted images were obtained with standard (medical imaging) spin-echo and inversion-recovery pulse sequences. The slice thickness was 5 mm and the in-plane resolution was 0.59 mm. Figures 8 and 9 are axial and sagittal images obtained with a T_1-weighted spin-echo sequence (repetition time = 0.5 s, echo time = 17 ms, pixel size = 600 μm).

The imaging time for Figs. 8 and 9 was 4.3 min (4 excitations x 128 matrix x 0.5 s). Not only are the five glass beads well visualized, but the image inhomogeneity in the surrounding B/P suggests nonuniformity in its distribution. The T_2-weighted (second echo) images had very low S/N ratios, indicating a relatively short T_2 relaxation time for the B/P. The S/N ratios were also low for the proton-weighted images.

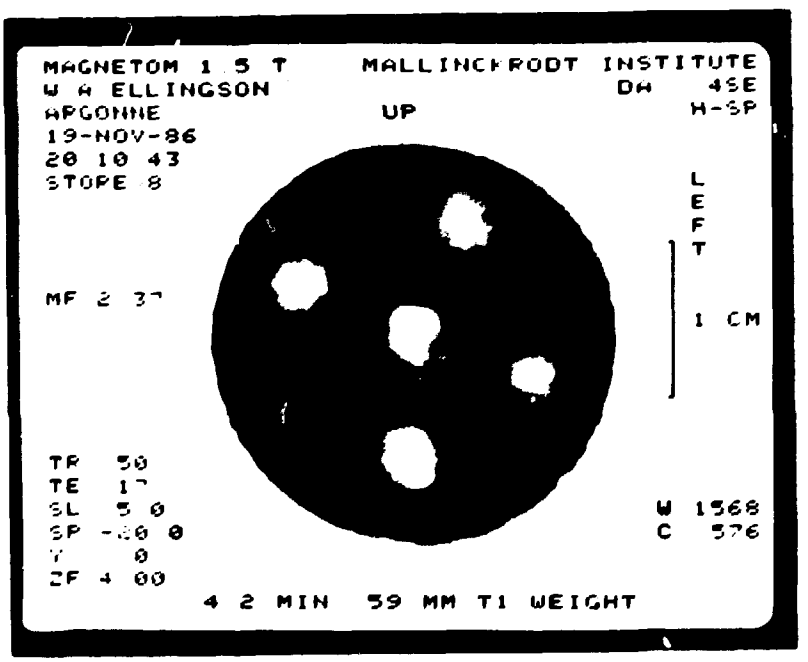

Fig. 8. Tomographic NMR Image of Binder Distribution and Defects at Midsection of Specimen Shown Schematically in Fig. 7. The light-colored circles are the 5-mm-diam glass beads intentionally introduced at the midsection to simulate known defects.

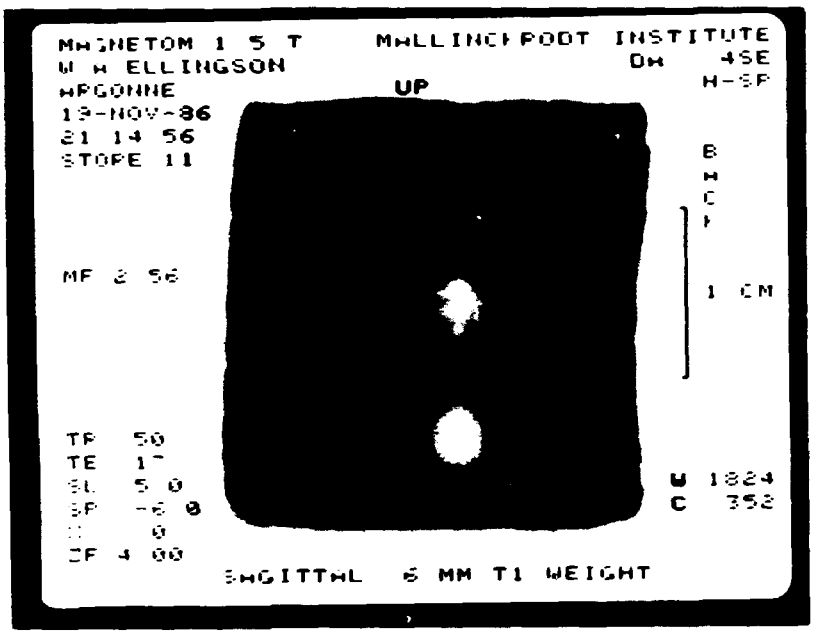

Fig. 9. Direct NMR Image of Binder Distribution and Intentional Defects in the Same Specimen Shown in Fig. 8. In this case, the image is taken sagittally (see Fig. 8 for sagittal plane location). The axial location of the 5-mm glass beads is clearly detected.

Density

Density gradients are of fundamental importance to ceramic processing. They are responsible for many of the problems with "shrinkage" cracking, warping, and deviations from near-net shape that have traditionally frustrated the ceramic engineer. X-ray computed tomography offers a method of nondestructively mapping the density gradients in green (unsintered) or sintered ceramic parts without tedious sectioning, measuring, and weighing.

Accurate two-dimensional attenuation mappings of cross sections through an object can be produced; from these, density variations can be obtained within the limits of the contrast of the computed tomographic (CT) image.[7,11-13] Since small density gradients and small defects are to be observed, X-ray CT imaging for industrial ceramics must provide images that have very good attenuation resolution and no artifacts. The attenuation can be measured within each pixel of the image with an accuracy equal to the noise of the image. The pixel-to-pixel statistical

noise, which determines the attenuation resolution, depends on several factors. The contrast of the CT image (i.e., the inverse of the noise) for fixed scan parameters depends on the value of the absorption coefficient (and therefore the energy of the source) and the intensity of the radiation transmitted through the object (and therefore the source intensity and the sample thickness). Thus, for industrial CT applications, one would like to both optimize the photon (X-ray) energy and increase the beam intensity (photon flux). Polychromatic X-ray sources are generally considered preferable to isotopic sources because of their greater intensity.

The optimum photon energy choice can be estimated by using the relationship $\mu \cdot x = 2$, where μ is the attenuation coefficient at a given photon energy and x is the part thickness. This relationship, which, comes directly from the formulas for the CT noise,[7] yields an optimum photon energy of about 1.25 MeV for 10-cm-thick objects of both Al_2O_3 (ρ = 3.95 g/cm^3) and zirconia (ρ = 4.65 g/cm^3); this value is approximately equal to the photon energy of a ^{60}Co source. In comparison, the use of a photon energy of 60 keV, which is about the peak effective energy of a 120-kVp X-ray tube, decreases the S/N ratio (for the same scan parameters, source intensity, and scan time) by a factor of 10 in the case of Al_2O_3, and by ~8 orders of magnitude in the case of zirconia. For a 10-cm Al_2O_3 object, this increase in noise can be compensated for by using a source 100 times as intense, which is possible for an X-ray source relative to an isotopic source. However, for a 10-cm zirconia object, the lowest practical energy is about 150 keV (which corresponds to a tube voltage of ~300 kV), and thus the intensity must be a factor of 10^4 greater in comparison to an isotopic source.

In order to examine the quantitative capability of X-ray CT imaging, two 146 x 146-mm densified Al_2O_3 tiles (ρ = 3.93 g/cm^3), one 6 mm thick and one 23 mm thick (see Fig. 10), were examined. As part of this study, low-kV contact radiographic images were obtained with a Picker 110 Hot-Shot X-ray imaging system. The system was operated at 70 kVp and 8 mA, with a 76.2-cm (30-in.) source-to-film distance, type M-8 Ready Pack film, and a 0.05-mm (0.002-in.) Pb screen to reduce radiation scatter; the resulting film densities were 3.2.

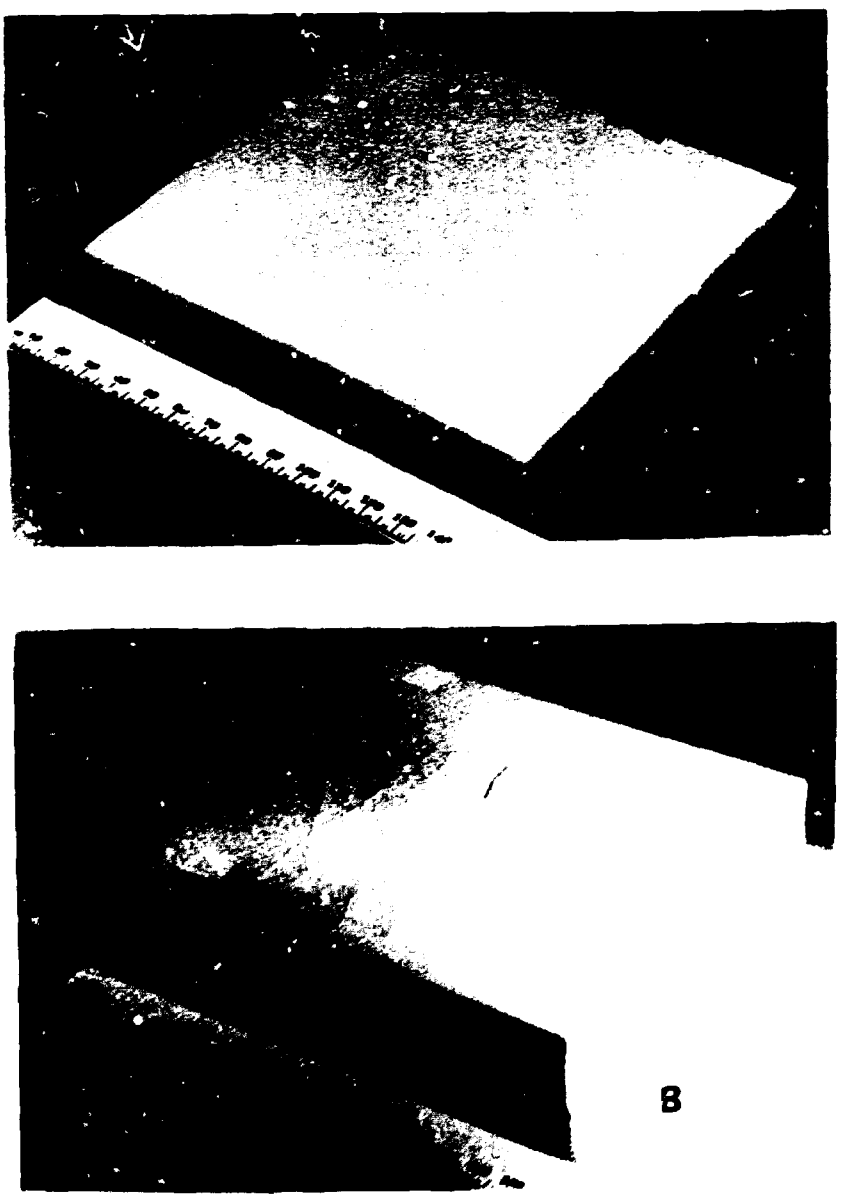

Fig. 10. Photograph of Sintered Al_2O_3 Ceramic Tiles Used for X-Ray CT Imaging Tests. Tiles are 146 mm square, with thicknesses of (A) 6 mm and (B) 23 mm.

Low-kV radiographs of the 6-mm-thick tile (see Fig. 11) suggested that this tile had three regions with either somewhat lower density or decreased thickness. Thickness measurements showed no appreciable change in dimension; thus, the change in optical film density indicated regions of lower ceramic density. From the radiographs, one cannot determine the absolute density to quantify the density decrease in the three regions, nor can one determine how far these regions extend through the tile thickness.

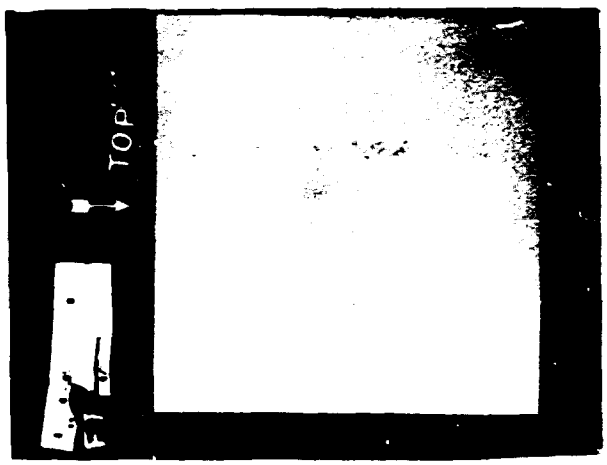

Fig. 11. Low-kV Contact Radiographic Image of 6-mm-thick Al_2O_3 tile.

CT scans of this tile were made in two planes, one parallel and one normal to the square face. A ^{192}Ir source was used. Figure 12 shows a CT image of a section parallel to the large face at the midplane. The image is presented with a thresholded scale, so that the dynamic range of the scale extends only from 98% to 100% of the nominal density (i.e., densities below 3.85 g/cm^3 are presented as black, those above 3.93 g/cm^3 are white, and the densities between these limits are shown by various tones of gray). The three lower-density regions observed in the radiograph of Fig. 11 are clearly visible. The average density obtained from the CT image in various locations outside of these regions is 3.92-3.93 g/cm^3, which agrees perfectly with the nominal density of the tile determined by weighing. In the three lower-density regions, the average densities determined from the CT data over an area of 10-20 pixels were 3.87, 3.81, and 3.84 g/cm^3, respectively, with an uncertainty of less than ±0.01 g/cm^3. The three low-density regions therefore have a density that is lower than the nominal density of the tile by 1, 3, and 2%, respectively. To examine whether the density variation extended through

the tile thickness, a cross-sectional CT scan was made across the 3.81-g/cm^3 region. The pixel size in this scan was 0.7 mm. Figure 13 shows the image of this cross section (6 x 146 mm). The data show that the low-density region extends throughout the thickness of the sample and is not just in the midplane.

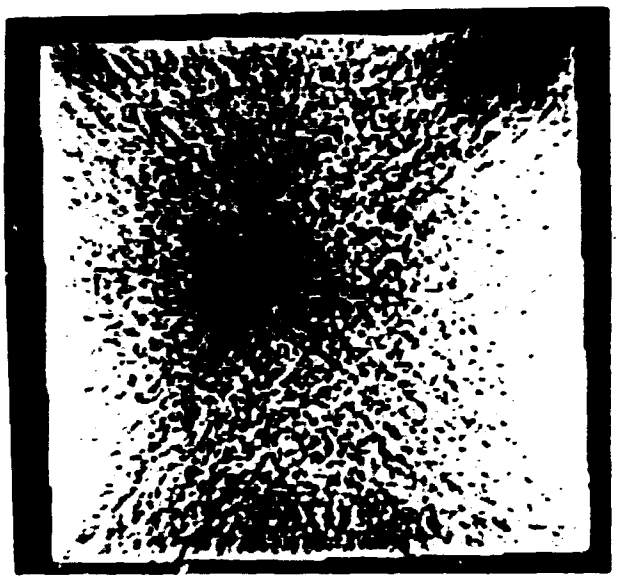

Fig. 12. CT Image Through the Midplane of the Same Tile Shown in Fig. 11. The gray scale of the image is adjusted so that the range from black to white encompasses densities between 98% and 100% of the average specimen density.

Fig. 13. Cross Sectional CT Image of the Tile of Figs. 11 and 12, Taken Through Midline of Tile. The gray scale of the image is thresholded to cover densities between 97% and 100% of the maximum density.

Visual examination of the 23-mm-thick tile (see Fig. 10b) showed significant surface-breaking cracks. Not known was the depth to which the cracking extended or whether the cracking was caused by a significant density gradient in the specimen. Low-kV contact radiographic images were obtained (Fig. 14). Cracks are visible, but the depths are unknown. A CT image (Fig. 15) was obtained at the midplane of the 23-mm-thick tile in a similar manner to the image shown in Fig. 12. In this case, the gray scale ranges from about 90% to 100% of the maximum density (i.e., densities below 3.7 g/cm^3 are black, and those above 3.95 g/cm^3 are white).

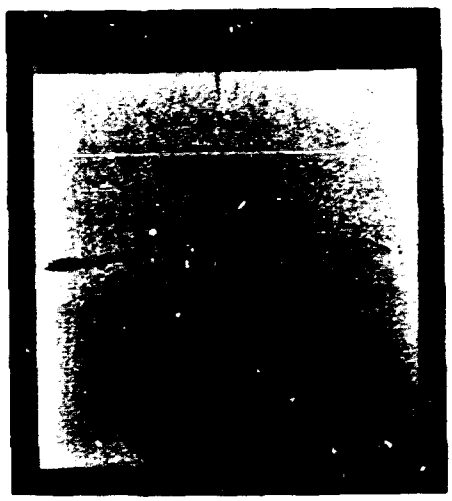

Fig. 14. Low-kV Contact Radiographic Image of 23-mm-thick Al_2O_3 Tile.

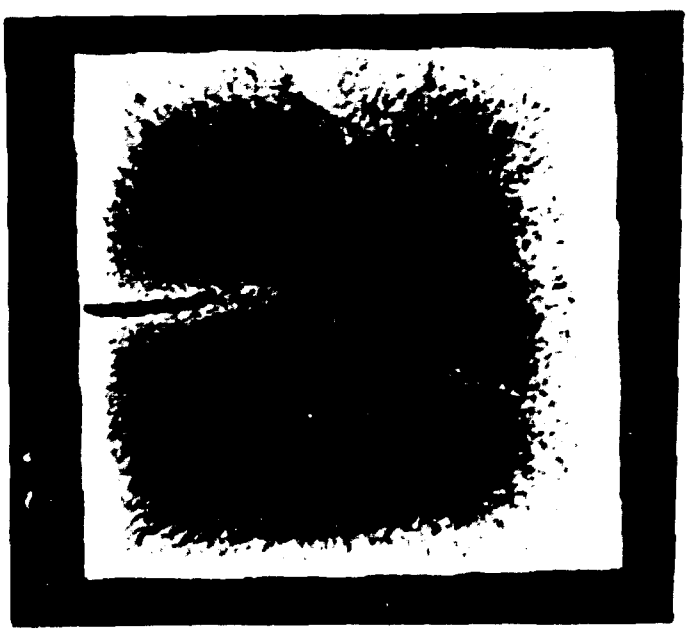

Fig. 15. CT Image of the 23-mm-thick Tile, Displayed on a Scale that Covers a Density Range from about 3.7 to 3.95 g/cm^3.

From the CT image, densities in various regions of the tile were calculated as before. The density is generally higher at the edges of the tile (3.93 g/cm^3) and decreases towards the center to form two large low-density regions separated by an S-shaped ribbon of denser material. The high-density ribbon is quite narrow in the center of the tile (5 pixels, i.e., 5 mm or less), and widens towards the edges of the tile. A crack is seen in the CT image, running along the center of the high-density ribbon. It is estimated to be 4 cm long and ~0.4 mm wide.

A comparison of the CT image with the low-kV contact radiograph shows several interesting features. First, the three cracks observed in the CT image are more clearly observed in the radiograph (indicating that a higher CT spatial resolution would be desirable). Second, the low-kV radiograph is not as sensitive to density gradients as the CT image, which shows that the cracks lie along high-density ribbons. Third, the smaller cracks in the radiograph are not visible in the CT image. Either these cracks are not located in the midplane or the resolution of the CT image is too low.

Inclusions

Another NDE method for detecting flaws (e.g., inclusions) within a body is analog tomography.[14] It is similar to computed tomography in that only a single plane is imaged within a body. The general principle of a linear analog tomogram is illustrated in Fig. 16, in which aa denotes the plane of interest (sometimes called the fulcrum plane) in an object O. A photographic plate lies in the plane ZZ (parallel to aa). In the production of a "conventional" two-dimensional X-radiograph, the X-ray source, s, is fixed at a particular point, say s_o. The X-ray beam passes through A and B and impinges on the photographic plate at the point p_o. The optical transmittance of p_o on the developed plate is related to the sum of the X-ray absorptivities at all points along the line s_op_o. In the production of a linear analog tomogram, the source s is moved along the linear path QQ while the photographic film undergoes coordinated motion in the opposite direction, such that an X-ray beam passing through point A maintains a constant position relative to the film. The coupled linear motion of s and the film ensures a one-to-one correspondence between points on the film and points on the plane aa.

However, as S moves, the X-ray beams passing through a given point on any other plane (exemplified by point B on plane bb) will impinge at different positions on the film; consequently, all planes other than the one of interest are blurred. Thus, unlike an ordinary X-radiograph, the linear tomogram contains a selectively focused image of the fulcrum plane. However, it also contains the deliberately blurred X-ray information from other planes parallel to the fulcrum plane; this complicates the interpretation of its diagnostic content.

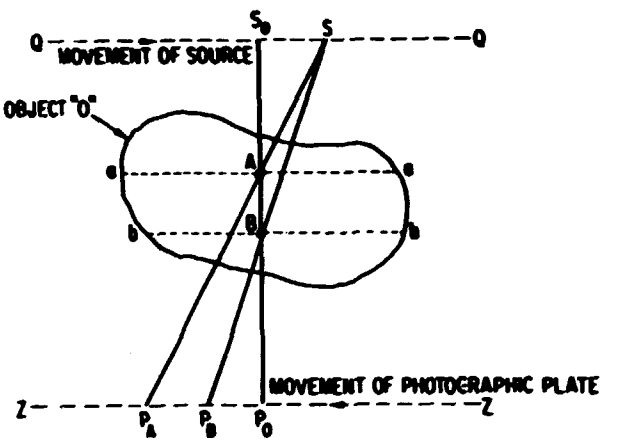

Fig. 16. Schematic Diagram of Arrangement Used to Make Linear Analog Tomographic X-Ray Images.

In an initial experiment with a medical analog tomographic imaging system (a Siemens Optiplanimat), we used a special Kodak AR film with no Pb screen. The X-ray head had a 300-μm focal spot size set to a 40° circular orbit (at 2.5 s) and was operated at 44 kvp at 250 mA•s. The nominal in-plane slice thickness for this setup was estimated to be 1 mm. The test specimen was a green-state Si_3N_4 billet 5.1 x 5.1 x 0.5 cm in size, containing seeded inclusions as shown in Fig. 17. Figure 18 shows a series of tomographic images taken at four different planes parallel to the face of the billet, with 1-mm depth increments. The reason for the blurring of certain features at different "cuts" can be seen from a conventional X-ray image taken of the object on its side (Fig. 19). The side-view X-ray shows that the inclusions do not lie in a single plane, but vary in depth near the midsection. To date, we have been able to detect inclusions down to 100 μm in size with analog tomography.

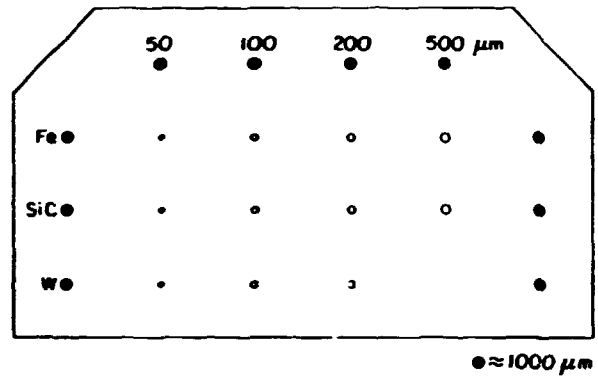

Fig. 17. Schematic Diagram of Green-state Si_3N_4 Test Piece, Showing Pattern of Seeded Inclusions.

Backscatter ultrasonic imaging[15] is an NDE technique that is sensitive primarily to near-surface inclusions. The technique exploits the generation of surface waves occurring when an ultrasonic beam is incident on a water/ceramic interface at a critical (Rayleigh) angle. The experimental configuration for this technique is presented in Fig. 20. A single focused transducer is positioned such that the focal zone is located slightly below the specimen surface, and the central axis of the focused beam is oriented at approximately the critical angle for surface waves (~75° for Si_3N_4). The transducer is used in a pulse-echo mode. The propagating surface-wave pulses are reflected by any near-surface defects, and the reflected pulses propagate back toward the transducer. The surface-wave pulses are coupled to the fluid medium; hence, the pulses are continuously radiating or "leaking" energy back into the water at the critical angle. The transducer thus detects the reflected surface-wave pulses as the pulses pass beneath the transducer. The surface waves penetrate the specimen to a depth of approximately one wavelength (~200 μm at 25 MHz). Images of the ceramic surface are formed by mechanically scanning the focal zone over the surface of the specimen, and recording the amplitude of the reflected surface-wave pulses at each scan position.

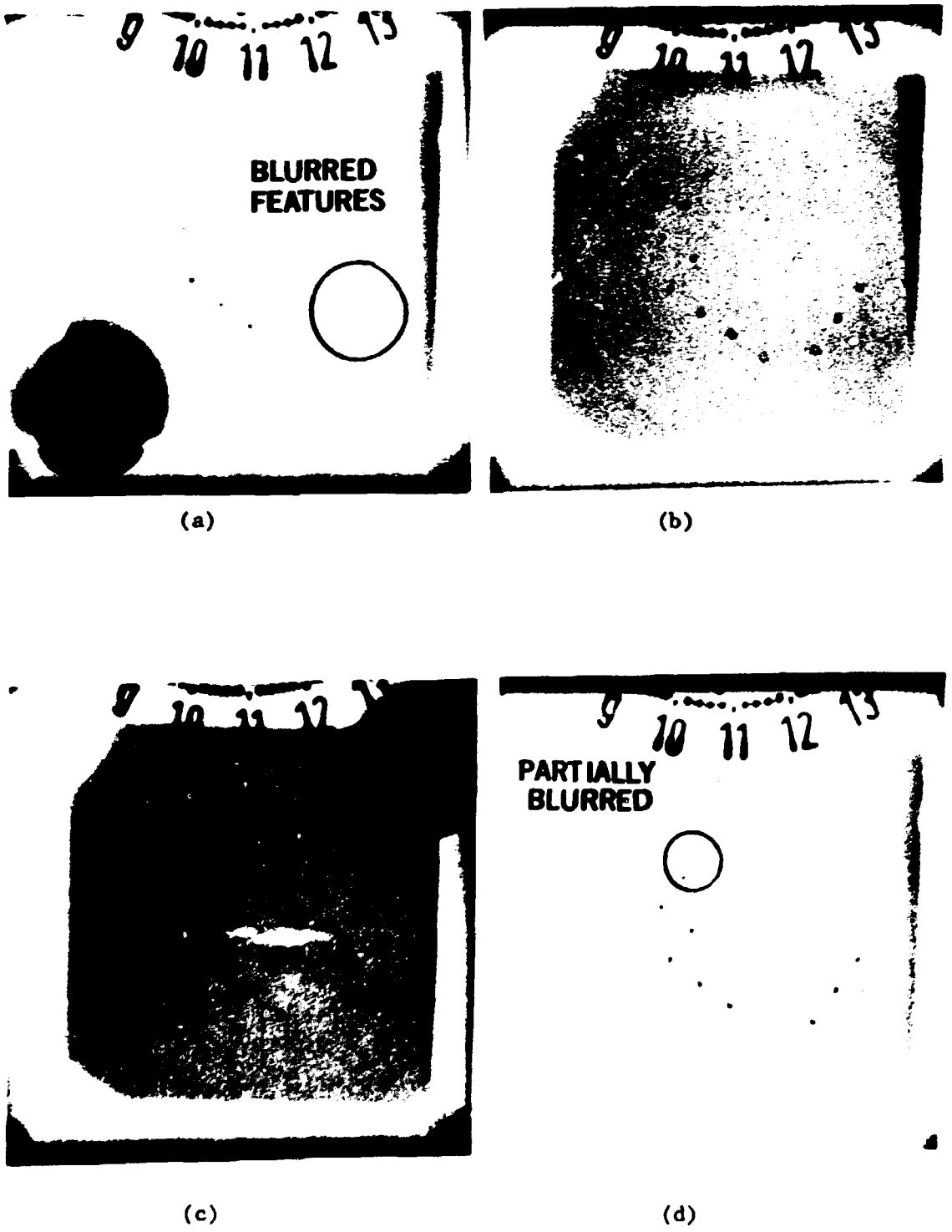

Fig. 18. Series of X-Ray Tomographic Images of Test Piece Shown in Fig. 17. (a) 2 mm above major defects, (b) 1 mm above major defects, (c) in-plane of major defects, (d) 1 mm below plane of major defects.

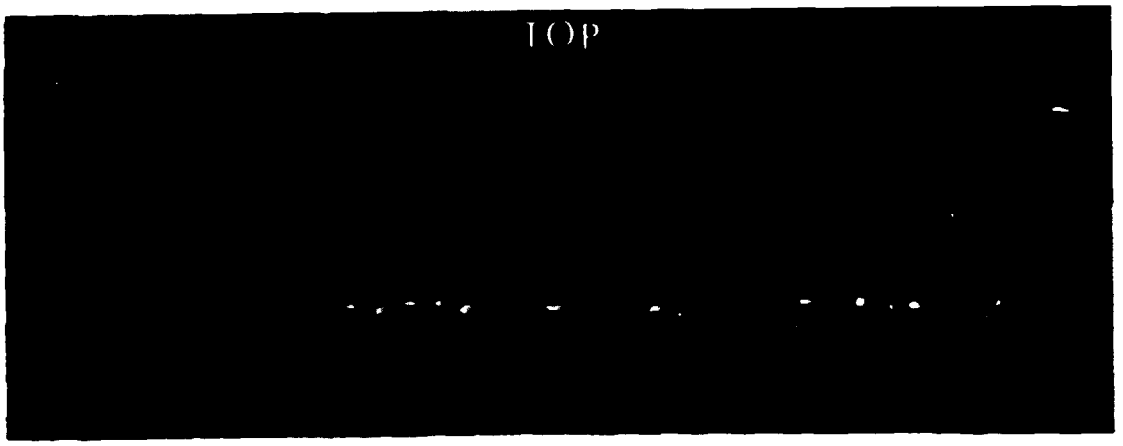

Fig. 19. Side-View X-Ray Image of Test Piece Shown in Fig. 17.

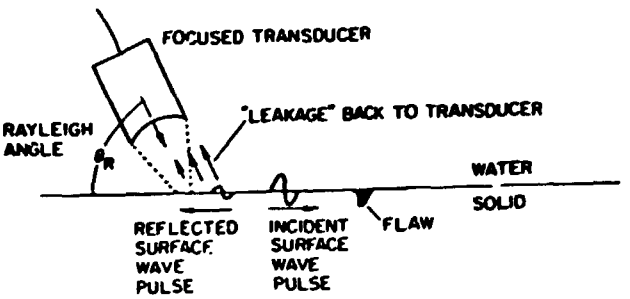

Fig. 20. Schematic Diagram of Ultrasonic Backscatter Arrangement (Ref. 15).

Surface-wave images of five MOR bars (Si_3N_4 + 6 wt.% Y_2O_3 + 0.5 wt.% Fe) are presented in Fig. 21. The images were obtained withg a 25-MHz transducer having a 1.0-in. focal length in water, and a 100-μm scanning step (pixel) size. Several indications of near-surface inclusions were obtained. As before, three or four of the largest indications located within the constant-moment cross section in the four-point bending were identified as potential failure-initiating flaws. Fractography data obtained on these bars after fracture reveal that the surface-wave NDE data identified, a priori, the failure site in all five specimens. The observed failure sites are circled in Fig. 21.

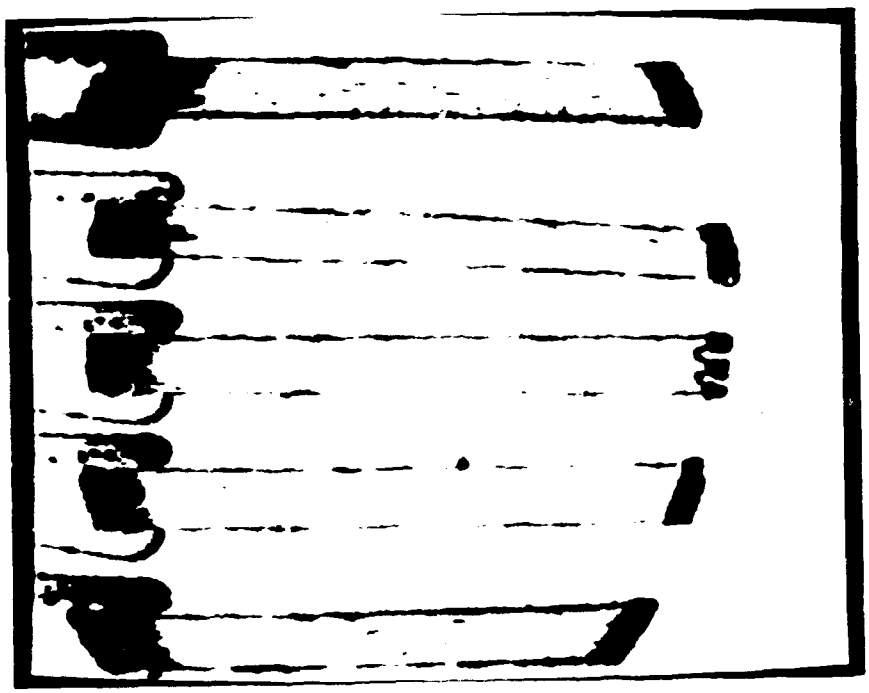

Fig. 21. Backscatter Ultrasonic Images of MOR Bars Cut from an Si_3N_4 Specimen Seeded with 0.5 wt.% Fe. The circled indications were the failure sites in subsequent four-point-bending fracture tests.

CONCLUSIONS

Encouraging results have been obtained in applying several advanced nondestructive evaluation methods to the characterization of porosity distribution, binder/ plasticizer distribution, density distribution, and inclusions in structural ceramics. These methods have the potential of helping to reduce costs associated with ceramic processing.

REFERENCES

[1]U.S. Congress, Office of Technology Assessment, New Structural Materials Technologies: Opportunities for the Use of Advanced Ceramics and Composites - A Technical Memorandum, OTA-TM-E-32, U.S. Government Printing Office, Washington, DC, September 1986.

[2]W. D. Kingery, H. K. Bowen, and D. R. Uhlmann, Introduction to Ceramics, 2nd Edition, John Wiley and Sons, New York (1976).

[3]W. S. Moore and G. N. Holland, Br. Med. Bull. 36(3) 297-299 (1980).

[4]J. L. Ackerman, W. A. Ellingson, J. A. Koutcher, and B. R. Rosen, "Development of Nuclear Magnetic Resonance Imaging Techniques for Characterizing Green-State Ceramic Materials," to be published in the Proceedings of the 2nd Intl. Symposium on the Nondestructive Characterization of Materials, Montreal, Canada, July 21-23, 1986.

[5]W. A. Ellingson, J. L. Ackerman, J. D. Weyand, R. A. DiMilia, and L. Garrido, "Characterization of Porosity in Green-State and Partially Densified Al_2O_3 by Nuclear Magnetic Resonance Imaging," to be published in the Ceramic Engineering and Science Proceedings, 11th Annual Conference on Composites and Advanced Ceramics, American Ceramic Society, Cocoa Beach, Fl, January 18-23, 1987.

[6]R. A. Thompson, Am. Ceram. Soc. Bull. 60(2) 237-243 (1981).

[7]B. D. Sawicka and B. J. F. Palmer, Density Gradients in Ceramic Pellets Measured by Computed Tomography, AECL-9261, Atomic Energy of Canada Limited, Chalk River, Canada, 1986.

[8]H. C. Yeh, J. M. Wimmer, M. E. Huang, M. E. Rorabaugh, J. Schienle, and K. H. Styhr, Improved Silicon Nitride for Advanced Heat Engines, Annual Technical Report submitted to NASA by AiResearch Casting Company, A Division of the Garrett Corporation, published as NASA-CR-175006, October 1985.

[9]H. C. Yeh, AiResearch Casting Company, private communication, 1986.

[10]W. A. Ellingson and S. Gronemeyer, unpublished work.

[11]G. T. Herman, Image Reconstruction from Projections, Academic Press, New York (1980).

[12]R. A. Brooks and G. Di Chiro, Phys. Med. Biol. 21, 689 (1976)

[13]A. C. Kak, Proc. IEEE 69, 1245 (1979).

[14]W. A. Ellingson, "Three-Dimensional Radiographic Imaging Methods," in Research Techniques in NDT, R. S. Sharpe, ed., Academic Press, New York (1986).

[15]R. A. Roberts, J. P. Singh, J. J. Vaitekunas, "NDE and Fracture Studies of Hot-Pressed Si_3N_4," to be published in Ceramic Engineering and Science Proceedings, 11th Annual Conference on Composites and Advanced Ceramics, American Ceramic Society, Cocoa Beach, Fl, January 18-23, 1987.

SESSION II - CORROSION AND EROSION

CORROSION OF ALLOYS IN MIXED-GAS AND COMBUSTION ENVIRONMENTS

K. Natesan

Materials and Components Technology Division
Argonne National Laboratory
9700 South Cass Avenue
Argonne, Illinois 60439

ABSTRACT

Extensive research has been performed over the past 10 years to evaluate the compatibility of engineering materials and model alloys in oxygen-sulfur mixed-gas environments that are relevant to both coal gasification and coal combustion schemes. This paper briefly summarizes the available information to give insight into the development of protective oxide scales in high-temperature alloys exposed to complex gas atmospheres. Results from ongoing research activities on the corrosion of high-chromium alloys are used to examine the roles of several factors such as cation and sulfur transport through the scales, mechanical effects, sulfur segregation, and time-dependent morphological changes in the scale, in the onset of breakaway corrosion in structural alloys. From current knowledge of the combustion and gasification environments and of the behavior of structural alloys exposed to them, several requirements that a suitable alloy should meet are presented, and possible avenues for modification of alloys to achieve improved corrosion resistance are discussed.

INTRODUCTION

Corrosion of materials at elevated temperatures is a potential problem in many systems within the chemical, petroleum, and power-generating industries. The corrosion phenomenon involves an interaction between a metal or an alloy and its environment. The interactions are generally undesired chemical reactions which can lead to wastage and altered structural integrity of the materials. Therefore, alloy selection for high-temperature applications is based not only on the

strength properties of the material, but also on its resistance to complex atmospheres that are prevalent in the anticipated exposure environment.

The gas environments that result from the reaction of coal with steam and oxygen in syngas processes consist predominantly of CO and H_2, with minor amounts of CO_2, H_2O, H_2S, and NH_3. An understanding has been developed of the environments prevalent in various gasification processes to explain material behavior in such environments.[1-3] In coal gasification atmospheres that involve species such as oxygen, sulfur, and carbon, it has been well established that the reliable performance of various components strongly depends on the sulfur content of the gas phase and on the duration and temperature of exposure.[4] On the other hand, combustion of coal in a fluidized bed (FBC) generates an environment that includes O_2, N_2, SO_2, CO_2, and small amounts of CO. One of the major material concerns in FBC systems is the oxidation-sulfidation behavior of the in-bed heat exchanger tube alloys and uncooled structural supports. Over the past several years, a number of investigations have been conducted to evaluate the corrosion/erosion performance of engineering materials. These investigations have been conducted with either small-scale fluidized beds[5-12] or laboratory setups with simulated combustion gas chemistry.[13,14]

Figure 1 depicts the oxygen-sulfur-temperature conditions in coal gasification and FBC schemes and those prevalent in gas-cooled reactors and oil-refining processes. In coal combustion and gas turbine systems, the oxygen partial pressure (p_{O_2}) in the gas phase is generally high, and the sulfur partial pressure (p_{S_2}) (present as SO_2) is generally low. The gas itself has very little effect on the material behavior under these conditions; however, the environments are conducive to formation of solid sulfates ($CaSO_4$) in FBC systems and liquid alkali sulfates and chlorides in turbine systems, which deposit on the metallic components and lead to material degradation in service. In both oil refinery and coal gasification processes, the prevalent environments have negligible to low p_{O_2} and moderate to high p_{S_2}. The contrasting feature is that the temperature range in the former is ~300 to 600°C, while in the latter it is ~400 to 1500°C.

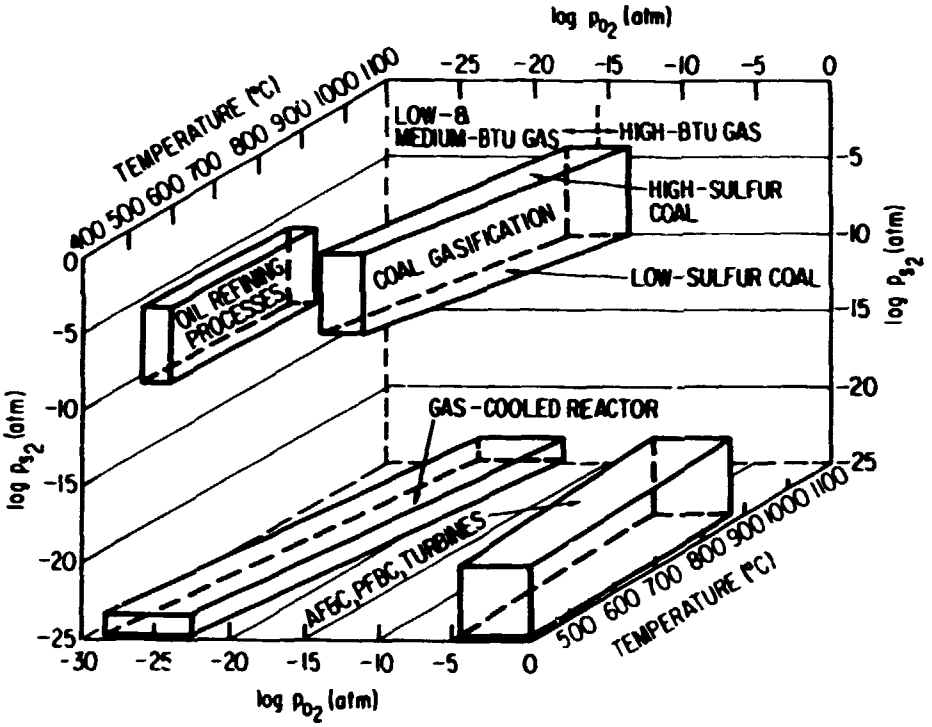

Fig. 1. Oxygen-Sulfur-Temperature Diagram Indicating Operating Conditions Prevalent in Coal Gasification, Combustion, Gas-cooled Reactors, and Oil Refining Systems.

The expected or desired lifetimes of various plant components are important in assessing the performance of different materials. For conceptual commercial plant design studies, a plant life of at least 20 years has been assumed for major vessels and piping. In dry-ash gasifiers, metallic alloys must have lifetimes of at least 20,000 h if they are to be used for such gasifier internal components as solid transfer lines, valves, dip legs, grid supports, refractory anchors, and for such external components as hot-gas piping and cyclones. In the case of entrained slagging gasifiers, no metallic internal components will be used because the reaction temperatures are in the range of 1400 to 1600°C; however, cyclones, piping, and refractory anchors will be required in these processes. Although the majority of internal components will be refractory lined, the metal temperatures can range from ~500 to 1000°C in these applications.

A major metallic component with a desired lifetime of 10 years or more is the heat exchanger required in both gasification and FBC schemes. In this case, the metal itself is subjected to lower temperatures (because of internal cooling of the tubes by the working fluid), while the gas temperatures can approach the gasifier outlet or the FBC bed temperature. The actual metal temperature can range from ~370°C in systems designed to produce saturated steam, to 650°C in systems designed to generate superheated steam at elevated pressures, and to ~900°C in in-bed air heater applications in cogeneration plants. As a result, material wastage by sulfidation, corrosion induced by deposition of condensed phases, and changes in mechanical properties of tube materials are of concern.

The purpose of the present paper is to briefly summarize the available information on metallic materials to give insight into the development of protective scales on alloy surfaces and causes of breakdown. In addition, corrosion test results from ongoing research activities are used to establish the mechanisms of oxidation/sulfidation of materials exposed to both coal gasification and FBC environments.

CHARACTERIZATION OF GASIFICATION AND FBC ENVIRONMENTS

Figure 2 shows the dependence of the p_{O_2} and p_{S_2} on temperature at the design pressure of 30 atm for several oxygen-blown medium-Btu gasification processes. The calculated results show that the temperature dependence of p_{O_2} is almost the same for all of the medium-Btu processes; the variation in p_{S_2} with temperature of these processes depends directly on the H_2S content of the raw product gas generated, which, in turn, is predominantly determined by the sulfur content of the coal feedstock. The results show that the p_{S_2} can vary by at least two orders of magnitude, while the p_{O_2} value remains the same as the H_2S content of the gas increases from 0.11 vol % (typical of low-sulfur coal feedstocks) to 1.30 vol % (typical of high-sulfur feedstocks). Several important observations have been made from an analysis of the gasifier characteristics in various process schemes. On an absolute basis, the p_{O_2} decreases with a decrease in temperature at a much higher rate

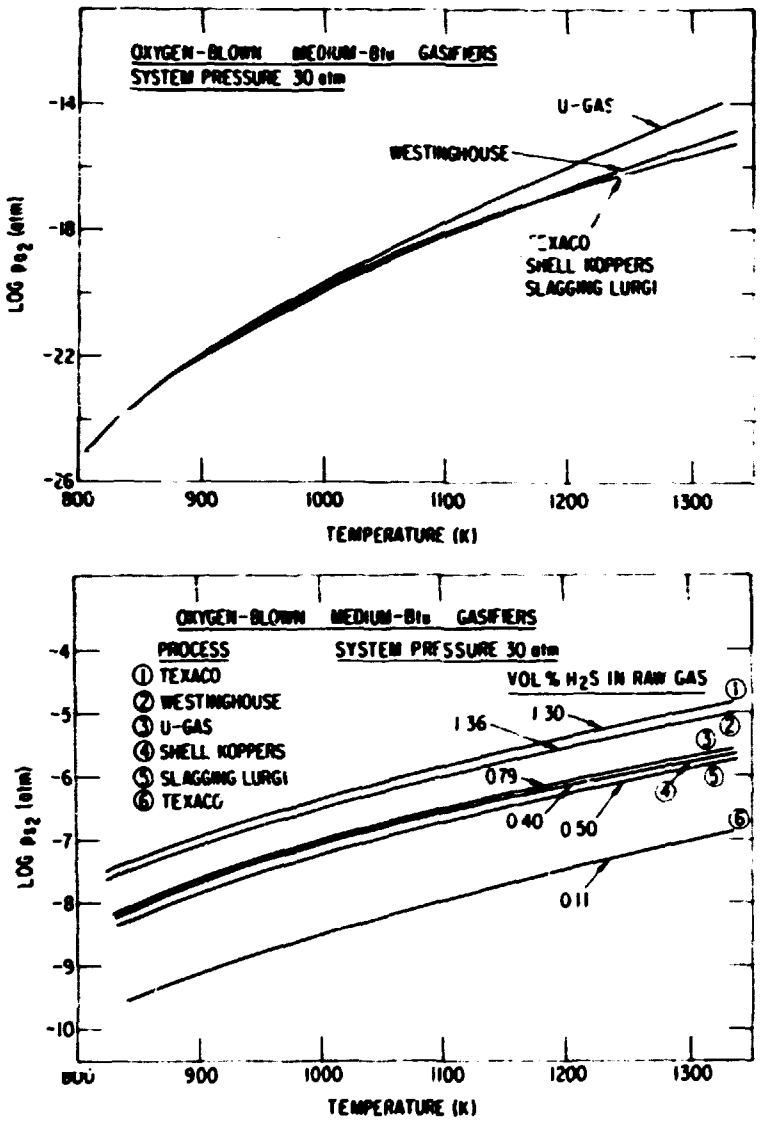

Fig. 2. Oxygen and Sulfur Partial Pressures as Functions of Temperature for Several Medium-Btu Gasifiers.

than does the p_{S_2}. At a given temperature, the p_{O_2} is generally higher in medium-Btu processes than in low-Btu systems; this difference is more pronounced at lower temperatures. A comparison of gaseous environments in high-Btu gasification schemes with those of medium- and low-Btu systems showed that the p_{O_2} can be lower by a factor of 10 in the latter systems.[1-3] This is particularly important because it suggests that both medium- and low-Btu processes have, in general, more reducing

atmospheres and higher p_{S_2}, values a combination that can lead to more severe material degradation by sulfidation than is experienced in high-Btu atmospheres.

In contrast with coal gasification systems, the FBC systems generally are operated under excess air conditions, and the combustor flue gas usually contains 5 to 10% oxygen. However, when in-situ oxygen probes have been used to evaluate the local chemistry in the beds of a number of FBC systems, the results indicate that the time-averaged p_{O_2} values ranged between 10^{-2} and 10^{-14} atm for extended time periods.[15-18] The calculated p_{S_2} in the gas phase is determined largely by the thermodynamic equilibrium between calcined limestone (CaO) and sulfated lime ($CaSO_4$), both of which are present in significant quantity during the bed operation. Figure 3 shows the CaO-CaS-$CaSO_4$ phase stability fields calculated for temperatures of 704, 840, and 900°C. Superimposed on this plot is the p_{O_2}-p_{S_2} curve (dashed line) calculated using thermodynamic equilibria between various gas species in the combustion environment at 900°C. It is evident that, at a given p_{O_2} in the environment, the p_{S_2} established in the gas phase will be orders of magnitude higher in the absence of sulfur sorbent. Since the $CaSO_4$ and CaO are always present in the in-bed environment, the p_{O_2} and p_{S_2} in the bed will follow along the CaO-$CaSO_4$ equilibrium line. On this basis, the lowest value of p_{O_2} that can be attained is $\sim 2 \times 10^{-12}$ atm at 900°C, and the corresponding sulfur pressure is $\sim 10^{-6}$ atm. The combination of a low-p_{O_2} environment and the presence of deposits on the tube surface can lead to sulfidation corrosion of in-bed materials. Extensive studies are in progress at Argonne National Laboratory to understand the mechanisms of corrosion and the effect of several key variables on the corrosion process.

SCALING OF ALLOYS IN OXYGEN-SULFUR ATMOSPHERES

The formation and maintenance of protective surface oxide scales are essential in preventing rapid degradation of structural alloys used in elevated-temperature applications. In principle, one of three oxides, Cr_2O_3, Al_2O_3, or SiO_2, will constitute the major component of a

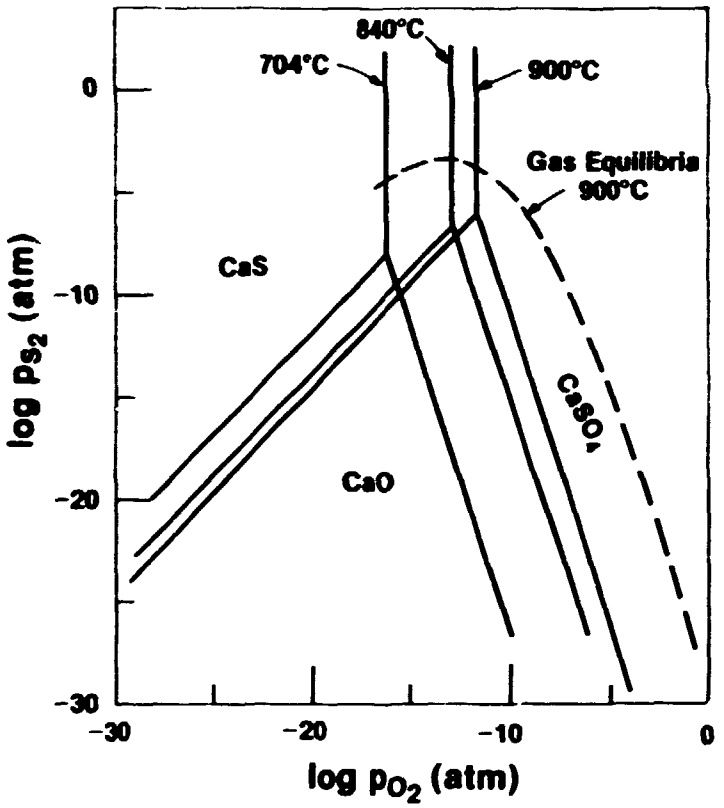

Fig. 3. CaO-CaO-$CaSO_4$ Phase Stability Fields Calculated at Several Temperatures Along with Calculated Oxygen-Sulfur Curve for Combustion of Coal at 900°C.

thermally formed surface scale. Extensive research has been conducted on Cr_2O_3-forming alloys and the present paper addresses the oxidation/sulfidation behavior of only these alloys when they are exposed to both gasification and combustion environments.

Cr_2O_3 is the predominant constituent of surface scales formed on heat-resistant austenitic Fe-Cr-Ni alloys. Under isothermal conditions, alloys containing a minimum of about 14 wt % Cr can be expected to form protective Cr-rich oxide scales in oxygen-rich (single oxidant) environments at temperatures in the range 600 to 800°C, while about 20 wt % Cr is required at temperatures near 1000°C. In oxygen-sulfur mixed-gas environments, typical of those encountered in gasification atmospheres, experience shows that a thermodynamically stable protective oxide may not form, owing to the presence of sulfur originating in the coal feedstock.[19] In practice, an excess of oxygen above the level defining thermodynamic equilibrium between Cr_2O_3 and "CrS" is required to form

Cr_2O_3 as a continuous surface layer.[20,21] As shown in Fig. 4, results indicate that the "transition" or "kinetic" boundary for oxide formation in the high-Cr alloys is at a threshold p_{O_2} ~10^3 times the p_{O_2} value for Cr oxide/Cr sulfide equilibrium at a temperature of 750°C or above, and increases to 10^5 times the equilibrium value at 650°C. The consequences of oxygen pressures lower than the threshold value in the environment are increased rates of scale growth and substantially deeper penetration of sulfur into the alloy substrate. On the basis of the morphological information developed on a number of commercial engineering alloys, advanced highly alloyed metallic materials, and model alloys exposed to oxygen-sulfur mixed-gas environments that simulate coal gasification atmospheres, three regimes have been defined to describe the oxidation-sulfidation behavior of the alloys at elevated temperatures.[19]

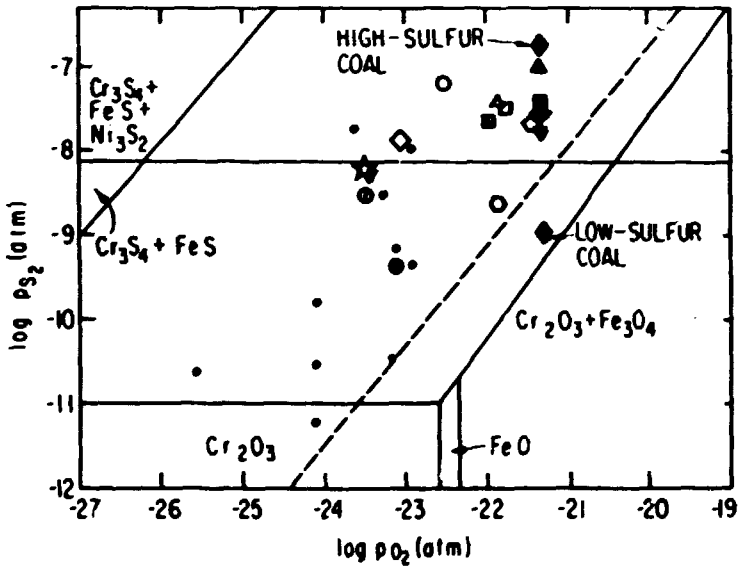

Fig. 4. Calculated Thermochemical Diagram for Type 310 Stainless Steel at 923 K, Showing the Experimental Gas Potential, Experimental Kinetic Boundary, and the Low- and High-Btu Gasifier Conditions at 923 K.

In contrast to the gasification atmospheres that have generally low p_{O_2} and moderate to high p_{S_2} resulting in sulfidation of the alloys, the p_{O_2} range in FBC systems is generally high enough to develop iron

and/or chromium oxide scales on heat-resistant alloys. The oxygen-sulfur thermochemical diagrams shown in Fig. 5 for Fe, Cr, and Ni at several temperatures indicate the thermodynamic stability of various oxide and sulfide phases. Superimposed on these diagrams are the CaO-CaS-$CaSO_4$ phase fields at the corresponding metal temperatures. In FBC systems, due to the presence of large quantities of $CaSO_4$ and CaO, the deposit on the tube surfaces is generally comprised of CaO and $CaSO_4$ and the p_{O_2}-p_{S_2} range in the exposure environment is dictated by the CaO/$CaSO_4$ phase boundary line. As a result, the extent of interaction between the deposit and the substrate, or the deposit and the scale, depends on three factors: the porosity of the deposit layer and the transport of gaseous molecules containing sulfur; the dissociation of $CaSO_4$ to establish a sulfur pressure at the underside of the deposit; and the rate of reaction between the underlying alloy elements and the reactants such as oxygen and sulfur to form oxide/sulfide scales and internal penetration of oxygen/sulfur into the substrate. Extensive research has been conducted at Argonne National Laboratory to evaluate the roles of key variables such as gas chemistry, sorbent, metal temperature, and gas-cycling conditions, in the corrosion of candidate heat exchanger materials; the results have been reported elsewhere.[22,23] In the case of high-chromium alloys exposed to combustion atmospheres, the dominant reaction between the $CaSO_4$-rich deposit and the substrate is

$$Cr + CaSO_4 \rightarrow CaCr_2O_4 \text{ or } Cr_2O_3 + \text{sulfur}.$$

The sulfur that is released by this reaction migrates into the substrate alloy leading to intergranular sulfidation.

BREAKDOWN OF SCALES IN OXYGEN-SULFUR ATMOSPHERES

The mechanism by which the corrosion process proceeds in a given alloy strongly depends on both the alloy chemistry and the oxygen/sulfur partial pressures in the exposure environment. The threshold p_{O_2} values for oxide formation are temperature dependent, but are influenced little

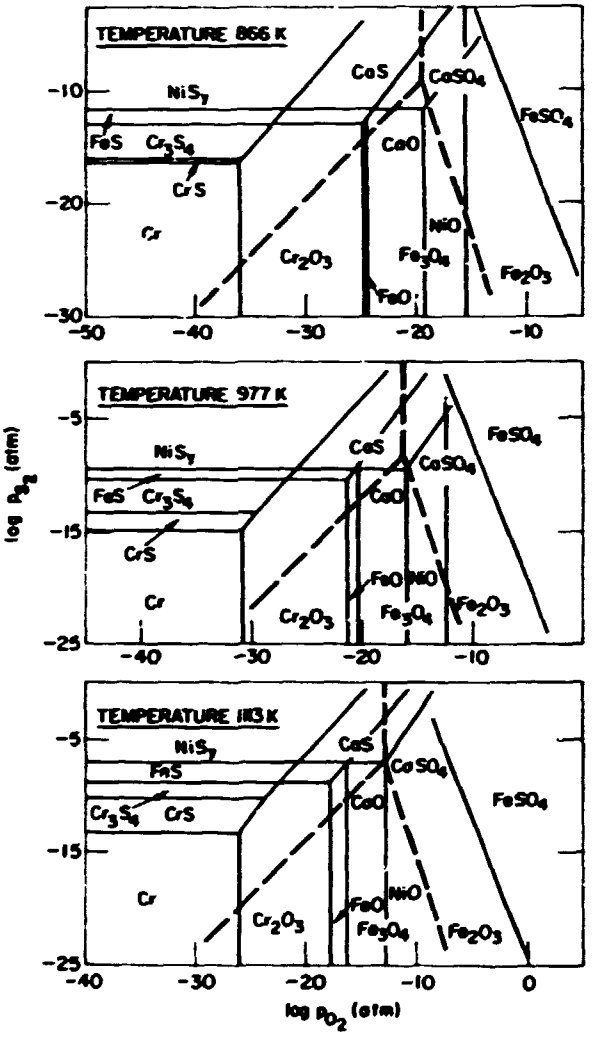

Fig. 5.
Oxygen–Sulfur Thermochemical Diagrams at 866, 977, and 1113 K Depicting Regions of Stability of Various Oxide and Sulfide Phases. The phase fields for the CaO–CaS–$CaSO_4$ system (dashed lines) are also shown.

by the Cr content of the alloy in the range 20 to 50 wt %. Minor alloying additions primarily influence the type (binary oxides, spinels, and duplex layers) and porosity of the scales as well as the adhesion of the oxide scale to the substrate material. Even if an alloy develops a protective oxide scale after short-term exposures to mixed-gas environments, the long-term behavior and thus, life expectation for the alloy, is strongly dependent on whether the alloy exhibits "breakaway" or "accelerated" corrosion.

Several possible breakaway processes can be identified, including the following:

1. Mechanical and thermal-cycling damage.

2. Development of short-circuit and impurity transport paths in the oxide scale.

3. Changes in the oxide composition with time.

4. Depletion of the protective scale-forming element in the substrate as a result of repeated spalling and reforming of the protective scale.

5. Transport of base-metal cations through the oxide scale to the gas/scale interface and subsequent sulfidation of these elements.

6. Transport of sulfur through the oxide scale into the substrate and sulfidation of the Cr- or Al-depleted (Fe, Ni, Co) region in the vicinity of the scale/metal interface.

In general, most of the alloys exhibit breakaway corrosion, especially in oxygen-sulfur mixed-gas atmospheres; the exposure time at which it occurs is dependent on temperature, gas chemistry, alloy composition, and microstructure of scales. In most applications of heat-resistant alloys, the materials are subjected to temperature cycling conditions. Breakdown of scales can occur as a result of the difference in thermal properties between scales and alloy substrates and as a result of growth stresses that are generated during oxidation. Baxter and Natesan[24] have discussed various mechanical considerations in the degradation of structural materials exposed to several environments at elevated temperatures.

In the presence of oxygen-sulfur mixed-gas atmospheres, processes 2 through 6 listed above can play dominant roles in the development of breakaway corrosion in structural alloys. The effect of initial composition of preformed oxide scale on subsequent sulfidation has been studied by Natesan[25,26] using Incoloy 800 and pure Cr specimens. In this study, the preformed oxide scales in Incoloy 800 consisted of (Cr,Mn) spinel, while those in pure Cr specimens were Cr_2O_3. Exposure of the preoxidized specimens to sulfur-oxygen mixed-gas atmospheres resulted in the formation of (Mn,Cr) sulfide crystals on the external surface. Figure 6a shows the surface morphology of preformed oxide scale on an Incoloy 800 specimen, and Figs. 6b-d show specimen surfaces after exposure to sulfur-containing environments. X-ray analysis showed that the crystals on these specimens were (Mn,Cr) sulfide, whereas the oxide underneath consisted of (Cr,Mn) oxide. Figure 7 shows the SEM photomicrograph and elemental mapping for Cr, Mn, O, and S for the specimen in Fig. 6d, mounted in a tapered section; it should be noted that in these pictures the thicknesses of the sulfide and oxide scales are exaggerated significantly as a result of the taper mounting of the specimen. The figure shows that the (Mn,Cr) sulfide crystals were located predominantly at the preformed-oxide/gas interface; virtually no sulfur was detected either in the oxide itself or in the substrate alloy. In the case of pure Cr specimens in which the preoxidized layer consisted of Cr_2O_3, subsequent exposure of the specimens to sulfur-containing environments only resulted in Cr sulfide particles at the Cr oxide/gas interface. Although the scale structure exhibited discrete particles of Cr_2O_3 with some porosity, no sulfur was detected in the interior of the scale, indicating that the scale formation in mixed gas is largely determined by the Cr rather than by sulfur diffusion in the Cr_2O_3 scale.

Another aspect to the oxidation-sulfidation of structural alloys is the transport of the more noble base-metal elements such as Fe, Ni, and Co from the substrate to the gas/scale interface. Recently, Natesan and Veal[27] have examined the influence of sulfur in the gas environment on the chemical changes in Cr oxide scales that were preformed on high-purity Fe-25 wt % Cr-20 wt % Ni alloy. The x-ray photoelectron

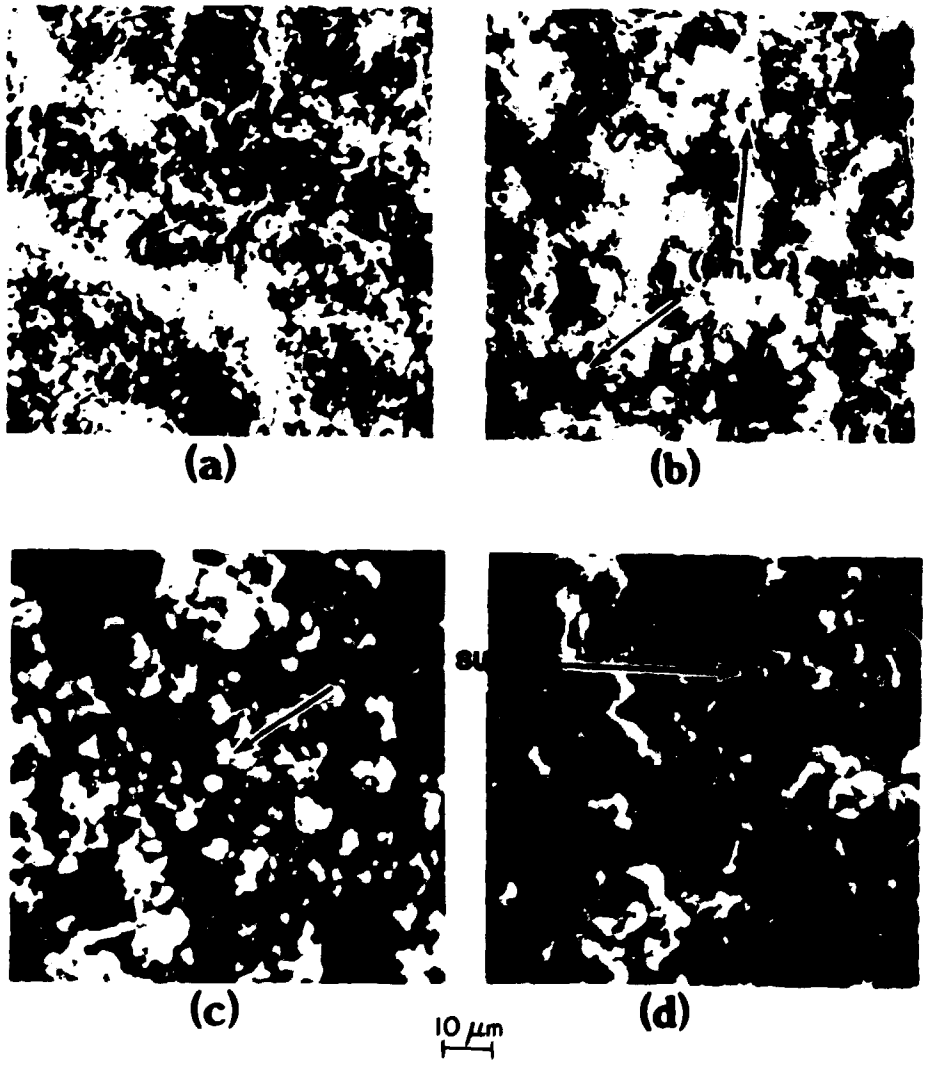

Fig. 6. SEM Photomicrographs of Incoloy 800 Specimens that were Preoxidized at $p_{O_2} = 9 \times 10^{-18}$ atm (a) and Subsequently Exposed to Oxygen-Sulfur Mixed-Gas Atmospheres at $p_{O_2}/p^e_{O_2}$ Values of (b) 1834, (c) 234, and (d) 331.

spectroscopy (XPS) technique was used to evaluate the compositional changes at the scale surfaces. Figure 8 shows the XPS spectra of the surfaces of preformed oxide layers before and after exposure to sulfur-containing environments. For comparison, the spectra for the Cr_2O_3 and Cr_2S_3 phases are also shown. The data, with a lineup of Cr 3p peaks, show that the counts for Fe 3p increase with an increase in time of exposure in a sulfur-containing atmosphere. Further, there exists a shift in the energy level for the Fe 3p peak as the time of exposure

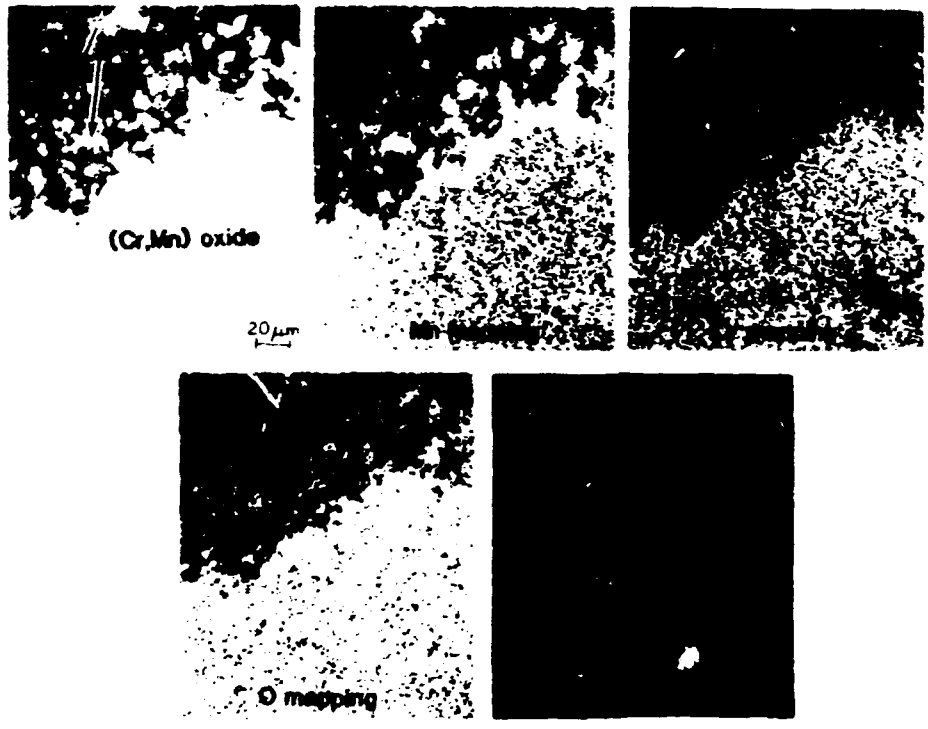

Fig. 7. SEM Photomicrograph and Elemental Mapping for Mn, Cr, O, and S of the Specimen Shown in Fig. 6d, Taper Mounted to Accentuate the External Scale and Preformed Oxide Layer.

increases, which will be correlated at a later date with the chemistry of the interactions at the oxide surface. In addition, with an increase in the Fe 3p peak, the S 3s peak also increases, indicating that the sulfur adsorption is associated with the iron content of the oxide surface. Figure 9 shows the counts as a function of binding energy for Fe 2p in the two states, normalized with respect to the Cr peak. With such a normalization procedure, the Fe/Cr ratio at the surface of the oxide scale can be quantified as shown in the figure. With an increase in exposure time to a sulfur-containing environment, the Fe/Cr ratio increases by a factor of 4.5 after 24 h. The enrichment of iron at the gas/oxide scale interface of the scale is an essential step in the eventual breakdown of the scale in the bioxidant environments.

In general, the diffusivities of various elements in decreasing order are as follows: $D_{Mn} > D_{Fe} > D_{Cr} > D_{Co} > D_{Ni}$. As a result, even among chromia-forming alloys, high Fe- and Mn-containing alloys are much more susceptible to sulfidation than are the Co- and Ni-base alloys;

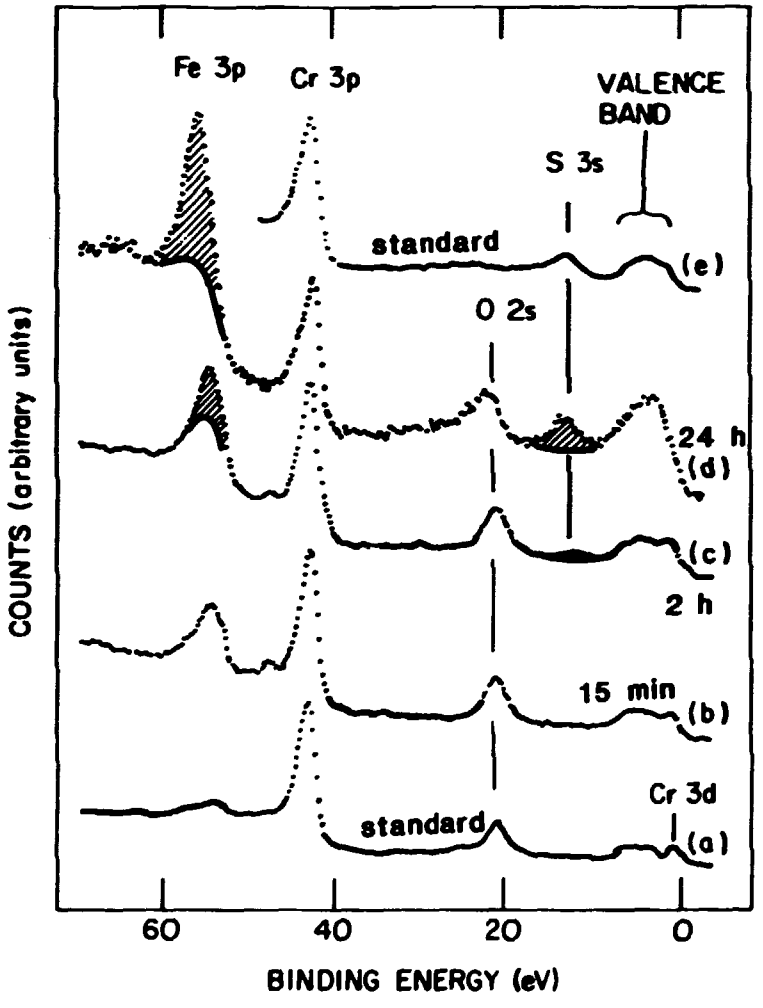

Fig. 8. X-Ray Photoelectron Spectroscopy (XPS) Data of the Surfaces of Preformed Oxide Layers Before and After Exposures to Sulfur-containing Atmospheres.

however, sulfur can and does transport through the Cr_2O_3 scales, and formation of low-melting Ni-Ni sulfide eutectic in the scale/substrate interface can lead to catastrophic corrosion in Ni-base alloys.

MORPHOLOGICAL DEVELOPMENTS LEADING TO BREAKAWAY CORROSION

Although the onset of breakaway corrosion is difficult to predict, the influence of alloy and gas chemistries on the catastrophic nature of the corrosion process is of concern in the application of materials at elevated temperatures. The scale morphologies that develop on alloys

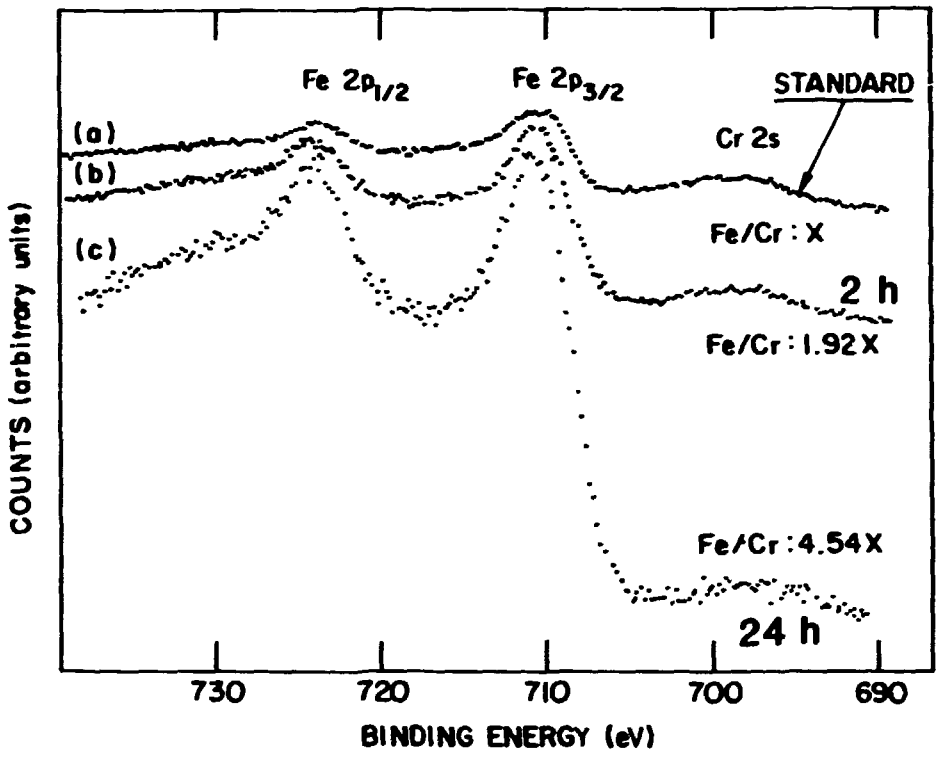

Fig. 9. XPS Counts as a Function of Binding Energy for Fe 2p in Two States, Normalized with Respect to Chromium Peak.

exposed to mixed-gas atmospheres strongly depend on the amount of sulfur present as H_2S or SO_2 in the gas phase. Nucleation and subsequent growth of tenacious protective oxide scales can be affected by the adsorption onto, and transport of sulfur through, the scale layers. Further, a knowledge of time-dependent variations in the composition of scale layers and the development of new reaction-product phases, as well as changes in the physical properties of the scale, is needed to establish the susceptibility of an alloy to breakaway corrosion.

Based on available information on the oxidation-sulfidation behavior of structural alloys discussed thus far, one can categorize the alloys in terms of two distinct corrosion scale morphologies. For example, Fig. 10 shows the scale morphology in specimens of Fe-25 wt % Cr-20 wt % Ni alloy that have been preoxidized for 72 h at 875°C in a sulfur-free atmosphere with p_{O_2} ~2 x 10^{-18} atm and subsequently exposed to an H_2-H_2S atmosphere (p_{S_2} ~4 x 10^{-8} atm) for 5, 7, and 22 h. The preoxidation of the alloy in a low-p_{O_2} environment resulted in an

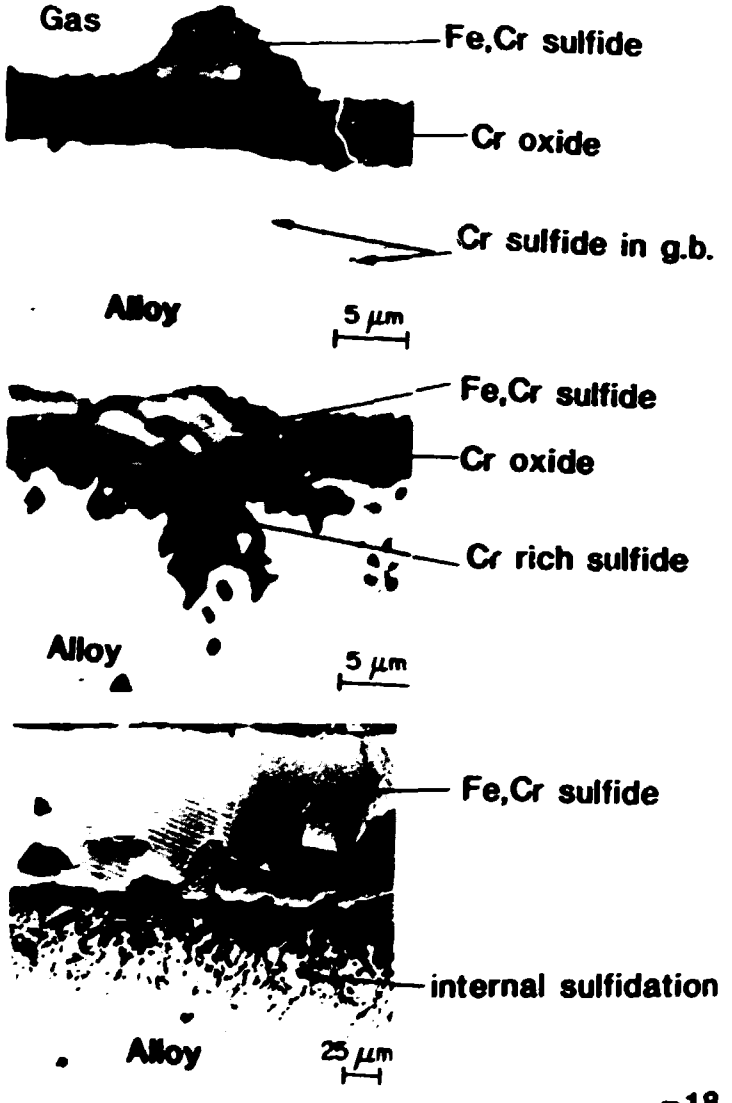

Fig. 10. Morphological Changes Observed in an Fe-25Cr-20Ni Alloy Preoxidized in Low-p_{O_2} Atmosphere and Subsequently Exposed to H_2-H_2S Atmosphere for Different Times at 875°C.

external Cr_2O_3 scale of ~4 μm in thickness. After a 5-h exposure to H_2-H_2S atmosphere, the preoxidized specimen developed a (Fe,Cr) sulfide phase at the gas/oxide interface, indicating significant transport of Fe

and Cr through the oxide scale and subsequent sulfidation of the transported elements. Small precipitates of Cr-rich sulfide particles can also be observed at the grain boundaries in the substrate material, indicating some transport of sulfur inwards. After a 7-h exposure, the continuous oxide scale was breached, and sulfidation at the substrate/oxide interface was noted. The sulfide particles at the grain boundaries became larger due to increased sulfur penetration. After 22 h of exposure, the oxide scale was virtually destroyed, and the scale consisted of predominantly (Fe,Cr) sulfide accompanied by substantial internal sulfidation of the alloy.

The morphological features that develop in high-Cr alloys exposed to O_2-SO_2 mixed-gas environments are somewhat different compared to those obtained in an H_2-H_2S environment described above. In general, the O_2-SO_2 gas mixtures establish much higher p_{O_2} values in the gas phase (than those of H_2-H_2O-H_2S mixtures); as a result, the alloys exposed to such environments develop predominantly oxide scales. However, the oxide scales are porous in nature and also generally contain a sulfide phase that results from the reaction between the base-metal constituents and the sulfur released from the oxidation of Cr or Al with SO_2. The porous oxide scale enables SO_2 gas molecules to permeate to the scale/substrate interface and cause internal sulfidation. Figure 11 shows the morphological features that developed on Type 310 stainless steel and Incoloy 800, respectively, after a 500-h exposure at 840°C to O_2-SO_2 gas mixture with $p_{O_2} = 7 \times 10^{-3}$ atm and $p_{SO_2} = 1.7 \times 10^{-3}$ atm. The p_{S_2} corresponding to this O_2-SO_2 gas mixture is 2.6×10^{-28} atm, which is extremely small for sulfidation of Cr or any of the other elements in the alloy. However, the p_{SO_2} value is orders of magnitude larger than that required for sulfidation of Cr and Fe in the alloy, and the internal sulfidation of the substrate material occurs via reaction between SO_2 gas transported through the porous oxide and the substrate elements. In such environments, deep internal sulfidation of the material prevents the alloy from developing protective oxide scale and eventually leads to breakaway corrosion.

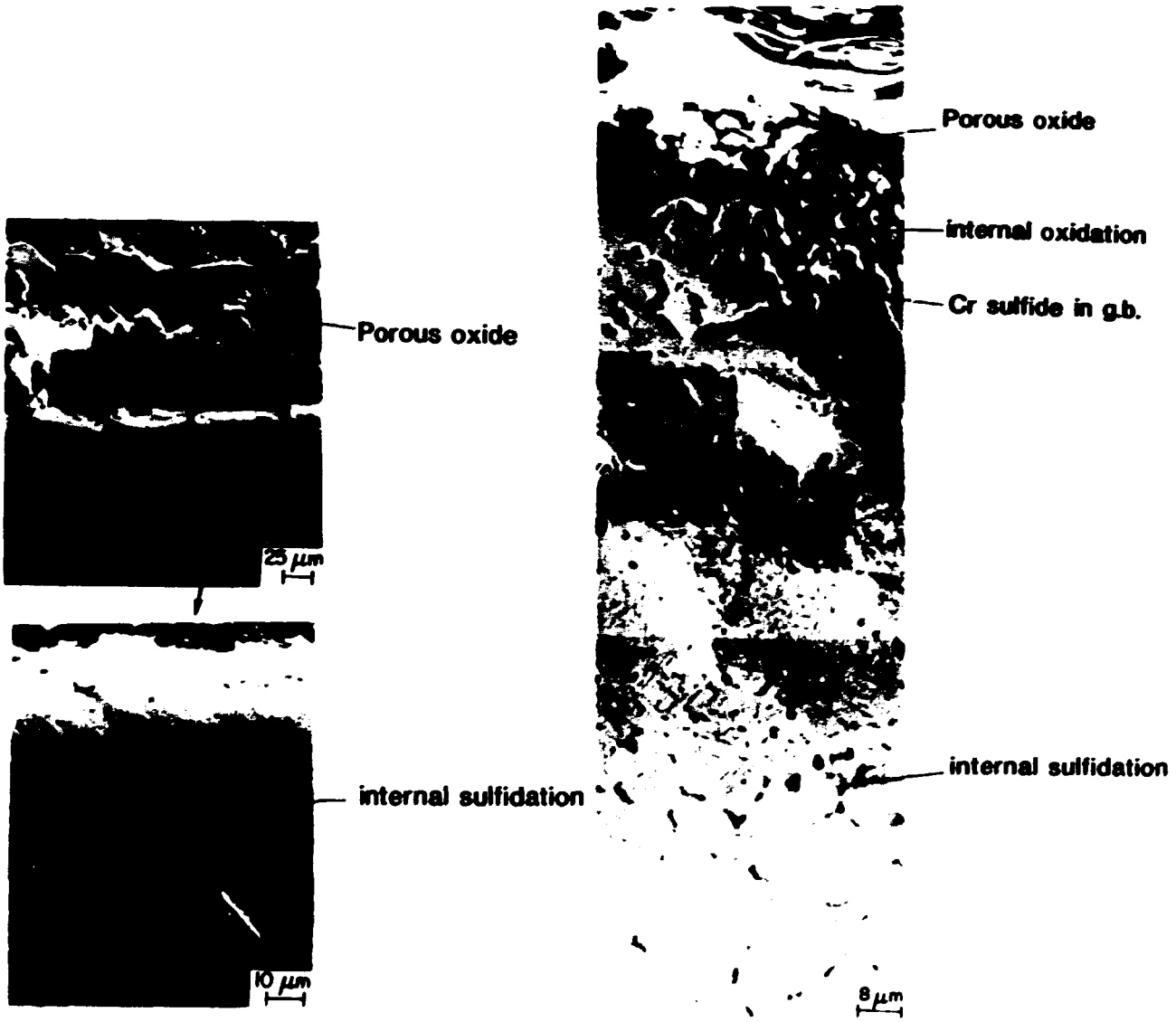

Fig. 11. Morphological Changes Observed in a Type 310 Stainless Steel (Left) and an Incoloy 800 (Right) Specimen after 500-h Exposure to O_2-SO_2 Atmosphere at 840°C.

Figures 12 and 13 are schematic representations of corrosion scale development and morphological changes that occur in Cr_2O_3-forming alloys exposed to low-p_{O_2} (with H_2S) and high-p_{O_2} (with SO_2) atmospheres, respectively, at elevated temperatures. In the former atmosphere (at p_{O_2} values above the threshold value), the alloy in the early stages

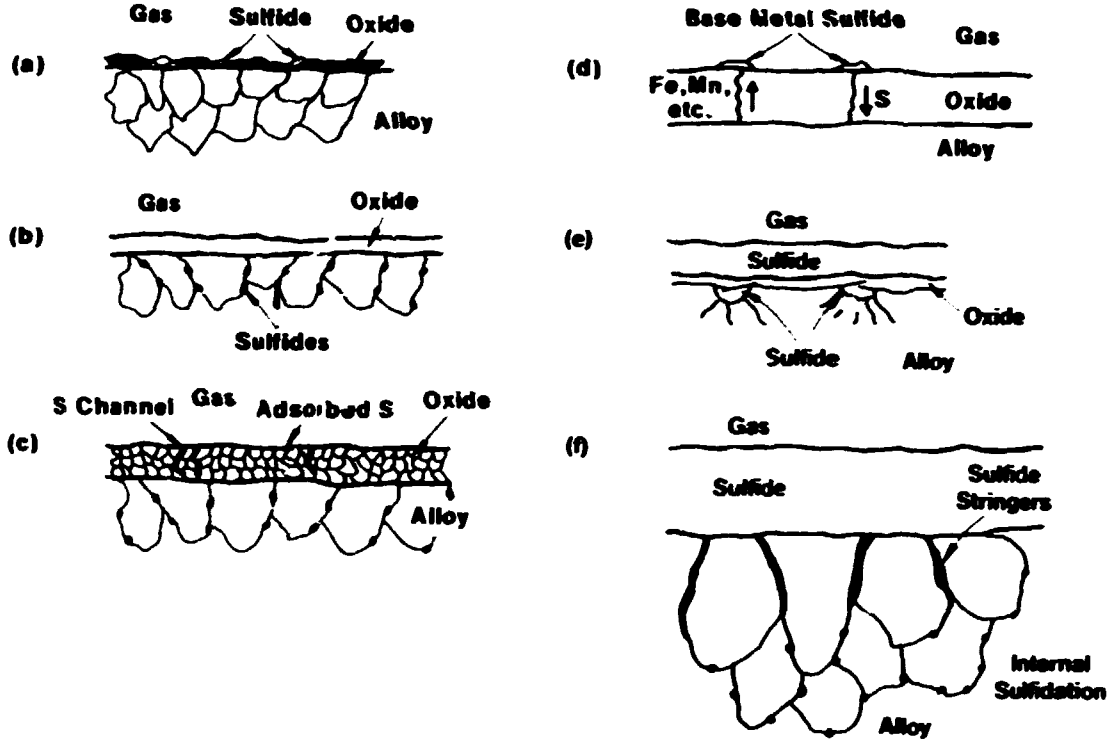

Fig. 12. Schematic Representation of Reaction Sequence for Cr_2O_3-forming Alloys Exposed to Low-P_{O_2} Environments Containing H_2S.

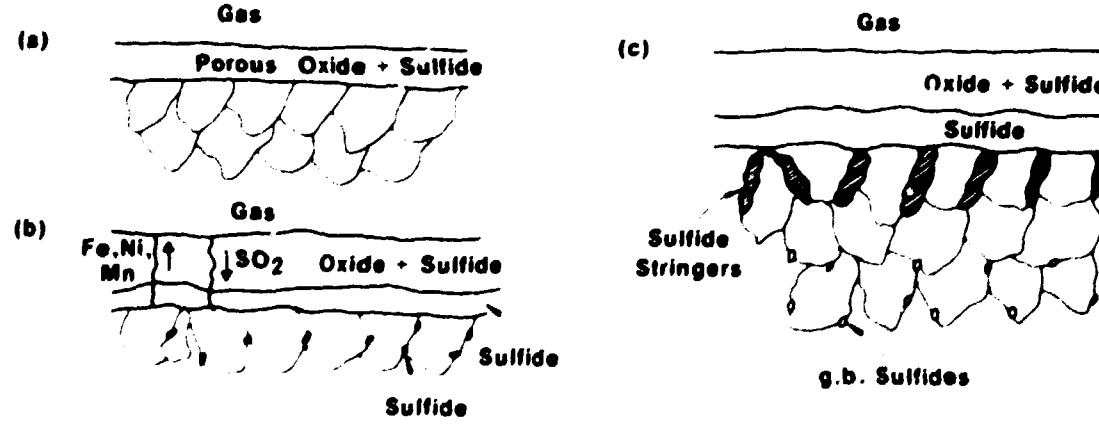

Fig. 13. Schematic Representation of Reaction Sequence for Cr_2O_3-forming Alloys Exposed to High-P_{O_2} Environments Containing SO_2.

of exposure develops oxide and sulfide nuclei. Eventually, the thermodynamic conditions establish a continuous Cr_2O_3 scale via reoxidation of sulfide particles, while the sulfur released is driven into the substrate along the grain boundaries. The oxide growth occurs via Cr transport across the scale to the scale/gas interface, where it is oxidized, leading to increased thickness. At the same time, the sulfur in the gas phase is adsorbed onto the scale/gas interface, and channels are established in the fine-grain oxide scale through which the transport of base-metal cations (Cr, Fe, Ni, Co, etc.) to the scale/gas interface is accentuated. If the sulfur pressure in the gas phase exceeds the metal/metal sulfide equilibria for the base-metal elements, their sulfides form at the oxide scale/gas interface. As the sulfide grows, stresses develop in the oxide scale, which eventually fails and leads to sulfidation at the oxide scale/substrate interface. Since the transport rates of cations and sulfur through the sulfide phase are orders of magnitude faster than those through the oxide scale, the sulfidation attack continues in an accelerated manner. At longer exposure times, the oxide is virtually destroyed, and a massive sulfide scale develops -- a condition that represents breakaway corrosion for the alloy.

In the case of high-p_{O_2} (with SO_2) atmospheres, the high-Cr alloys generally develop porous oxide scales, and some sulfides are observed in the inner portions of the scale (in the vicinity of scale/substrate interface). The sulfides form via reactions between substrate elements and sulfur that is released when Cr reacts with SO_2 to form external oxide scale. The porosity present in the scale enables further molecular transport of SO_2 in the gas phase to the scale/substrate interface, leading to further oxidation/sulfidation. The sulfur that is released is transported along the grain boundaries in the metal, leading to internal sulfidation of the alloy. Generally, the acceptable lifetimes for high-Cr alloys exposed to these atmospheres are determined by the depth of internal sulfidation, which is largely determined by the alloy chemistry, temperature, and SO_2 content of the gas phase.

ALLOY MODIFICATION FOR IMPROVED CORROSION RESISTANCE

Based on the information presented thus far, it is evident that an alloy suitable for application in oxygen-sulfur environments at elevated temperatures should develop protective oxide scales in the exposure environment. The long-term performance of an alloy, even if it initially develops an oxide scale, will be determined by the onset of breakaway corrosion in the service environment. Four avenues to minimize the outward transport of cations and inward transport of sulfur can be envisioned: (1) develop a scale whose growth rate is faster than the transport rate of either base-metal elements or sulfur, (2) control the scale microstructure (grain size, grain boundary distribution, porosity, beneficial segregation, etc.) to minimize cation and sulfur transport through the scales, (3) develop a barrier layer, which may or may not be oxide, with an inherently lower diffusivity for cations and sulfur, that possesses adequate adhesion to the external scale and the substrate material, and (4) apply a corrosion-resistant coating that is chemically compatible with the substrate while maintaining adequate physical and mechanical integrity in a service atmosphere. In general, avenue 1 can rarely be achieved in Cr_2O_3-forming alloys. Other scales such as refractory metal oxides should be examined; however, a higher growth rate of oxide will lead to thicker scales which may be susceptible to mechanically or thermally induced spallation. Control of scale microstructure (avenue 2) has potential as a means to minimize breakaway corrosion, and the influence of various physical and chemical parameters on the scale morphology and microstructure needs to be quantified. The concept of a barrier layer (avenue 3) is being examined in the oxidation/sulfidation studies of Fe-Cr-Ni alloys with either Zr or Nb additions in a concentration range of 1 to 6 wt %.[28,29] Both Zr and Nb promote the formation and maintenance of chromium-rich oxide scales. Thermogravimetric studies have shown that the alloys with 3 wt % addition of either Zr or Nb exhibit protective oxide scales, while the commercial Type 310 stainless steel exposed to the same oxygen-sulfur atmosphere underwent breakaway corrosion (see Fig. 14). In addition,

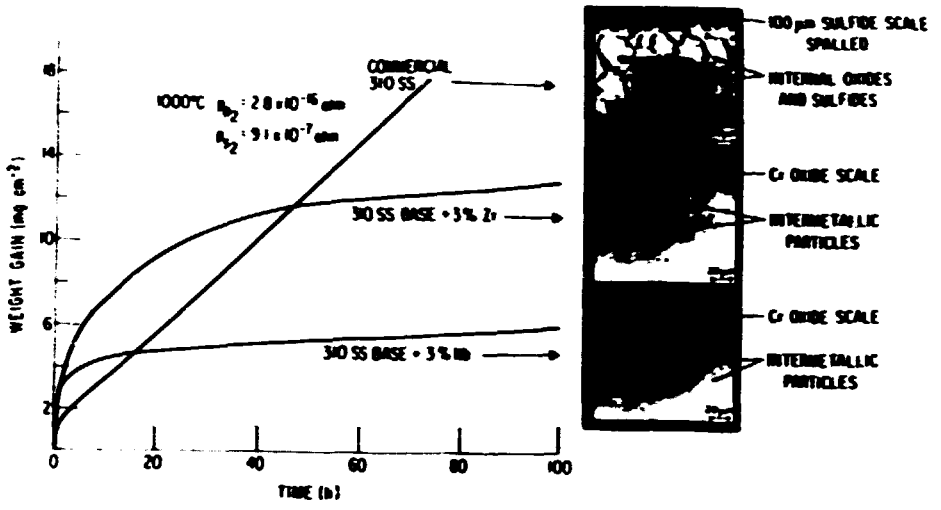

Fig. 14. Thermogravimetric Test Data for Commercial Type 310 Stainless Steel and Fe-25Cr-20Ni Alloys Containing 3 wt % Zr or Nb after Exposure to Oxygen-Sulfur Atmospheres at 1000°C.

the long-term studies have shown that these alloying additions form a Zr- or Nb-rich interfacial layer at the chromium oxide/substrate interface, thereby extending the time for the onset of breakaway corrosion in Fe-Cr-Ni alloys exposed to mixed-gas environments.

Several MCrAl coatings and electrospark-deposited coatings (avenue 4) have been evaluated for their resistance to oxidation/sulfidation at elevated temperatures in mixed-gas atmospheres. The results have been reported elsewhere.[30,31] Among the MCrAl coatings evaluated, the high aluminum Co-Cr-Al-Y and Ni-Co-Cr-Al-Y exhibited superior sulfidation resistance over a wide range of p_{S_2}. Electrospark deposition of chromium carbide coating seemed to decrease the parabolic rate of oxidation/sulfidation while maintaining a high hardness value in the surface region of the coated material. Additional research effort is needed in the coating areas to establish the gas/coating and coating/substrate interactions and to correlate the beneficial effects of coated layers with the chemistry of exposure environment, temperature, and time.

SUMMARY

Oxidation of alloys exposed to mixed-gas environments is a complex process in view of multiple reactants present in the exposure atmospheres and time-dependent transport of various substrate elements to the reaction front. The research results from this program show that thermochemistry is a viable and important tool for understanding and evaluating corrosion processes in these environments. The requirements for protective scale development and causes of scale breakdown have been examined in detail. While molecular transport of SO_2 inward through a porous oxide scale is responsible for sulfidation attack of materials exposed to SO_2-containing atmospheres, the transport of base-metal cations outward through the scale and subsequent sulfidation of them seems to initiate breakaway corrosion in H_2S-containing atmopsheres. Several avenues have been considered for modification of bulk compositions of alloys and alloy surfaces to achieve improved corrosion resistance for materials exposed to mixed-gas environments.

ACKNOWLEDGMENTS

This work was supported by the U. S. Department of Energy, Advanced Research and Technology Development Fossil Energy Materials Program [WBS Elements ANL-3(A) and 3(B)], under contract W-31-109-Eng-38. The author acknowledges the assistance of D. L. Rink in the performance of corrosion tests and R. Puccetti in the microstructural evaluation of various specimens.

REFERENCES

1. K. Natesan, Proc. Conf. on Scientific Problems of Coal Utilization, Morgantown, WV, B. R. Cooper, Ed., DOE Symp. Series No. 46, p. 146, 1978.

2. T. C. Tiearney, Jr. and K. Natesan, J. of Mater. for Energy Syst. 1, 13 (1980).

3. K. Natesan, Proc. Conf. on Corrosion-Erosion Wear of Materials in Emerging Fossil Energy Systems, Berkeley, CA, A. V. Levy, Ed., NACE, Houston, TX, p. 100, 1982.

4. K. Natesan, "Corrosion and Mechanical Behavior of Materials for Coal Gasification Applications," Argonne National Laboratory Report ANL-80-5, May 1980.

5. T. A. Godfrey and J. H. DeVan, "Corrosion of High-Temperature Materials in AFBC Environments," Oak Ridge National Laboratory Report, ORNL/TM-7734/P2, 1981.

6. A. J. Minchener et al., "Materials Problems in Fluidized-Bed Combustion Systems," Electric Power Research Institute Report, EPRI CS-1853, 1981.

7. P. L. Daniel and J. Stringer, Mater. Perform. 20(9), 9 (1981).

8. J. Stringer, A. J. Minchener, D. M. Lloyd, and H. R. Hoy, High-Temp. Technol. 1, 27 (1982).

9. C. J. Spengler, "Evaluation of Heat Exchanger and Turbine Materials for Use in a Coal-Fired Fluidized-Bed Combustion Environment, Final Report," Westinghouse R&D Center Report, WAD-10613-CE, 1981.

10. S. Cohen, J. Mogul, and S. Wolosin, "Materials Experience in a Fluidized-Bed Coal Combustion System at Curtiss-Wright Corporation," Preprint, Paper No. 161, Corrosion/80, NACE, 1980.

11. H. R. Hoy and A. G. Roberts, Proc. Sixth Intl. Conf. on Fluidized Combustion, Atlanta, GA, CONF-800428, Vol. 2, p. 241, 1980.

12. C. J. Lane, "Studies of In-Bed Corrosion in a Pressurized Fluidized-Bed Combustor, Final Report," Electric Power Research Institute Report, EPRI CS-1935, 1981.

13. K. Natesan, Corrosion 38(7), 361 (1982).

14. P. J. Ficalora, "Hot Corrosion Reactions of $CaSO_4$ with Cr, Ni, Fe, and Several Alloys," Oak Ridge National Laboratory Report, ORNL/TM-8735, 1983.

15. A. Minchener, "Fluidized-Bed Combustion: Corrosion/Erosion Tests," Program Book, DOE/EPRI/GRI/NBS Fifth Annual Conf. on Materials for Coal Conversion and Utilization, Gaithersburg, MD, p. V-14, 1980.

16. A. A. Boiarski, V. Nagarajan, I. G. Wright, and H. E. Carlton, J. Inst. Energy, Vol. LVII, No. 430, p. 252 (1984).

17. E. B. Ljungstrom, Proc. Eighth Intl. Conf. on Fluidized-Bed Combustion, Houston, TX, DOE/METC-85/6021, Vol. II, p. 853, July 1985.

18. R. G. Vincent, ibid., Vol. I, p. 218.

19. T. C. Tiearney, Jr. and K. Natesan, Oxid. Met. 17, 1 (1982).

20. K. Natesan and M. B. Delaplane, Proc. Symp. on Corrosion-Erosion Behavior of Materials, New York, NY, K. Natesan, Ed., Fall Mtg. of TMS-AIME, October 1978, AIME, p. 1, 1980.

21. R. A. Perkins and S. J. Vonk, "Materials Problems in Fluidized-Bed Combustion Systems," Electric Power Research Institute Report, EPRI-FP-1280, 1979.

22. K. Natesan, Proc. FBC Materials Workshop, Nova Scotia, Canada, July 29-August 1, 1985, to be published by Electric Power Research Institute, Palo Alto, CA.

23. K. Natesan, High-Temp. Technol. 4(4), 193 (1986).

24. D. J. Baxter and K. Natesan, Rev. High-Temp. Mater. 5(344), 149 (1983).

25. K. Natesan and S. J. Dapkunas, Proc. JIMIS-3 Conf. on High-Temperature Corrosion of Metals and Alloys, Supplement to Trans. Jpn. Inst. of Met., Vol. 24, p. 411, 1983.

26. K. Natesan, Corrosion 41(11), 646 (1985).

27. K. Natesan and B. W. Veal, Argonne National Laboratory, unpublished work, 1986.

28. D. J. Baxter and K. Natesan, Corros. Sci. 26, 153 (1986).

29. D. J. Baxter and K. Natesan, Proc. Third Berkeley Conf. on Corrosion-Erosion Wear of Materials at Elevated Temperatures, Berkeley, CA, January 29-31, 1986, to be published by NACE.

30. K. Natesan, J. Mater. Sci. & Eng. 87, 99 (1987).

31. K. Natesan and R. N. Johnson, paper presented at the Intl. Symp. on Metallurgical Coatings, San Diego, CA, March 23-27, 1987.

CORROSION-RESISTANT SCALES ON IRON-BASED ALLOYS

H. S. Hsu

Metals and Ceramics Division
Oak Ridge National Laboratory
P.O. Box X
Oak Ridge, Tennessee 37831

ABSTRACT

Corrosion tests were conducted at 800°C on iron-based alloys in a H_2-H_2S-H_2O-Ar gas mixture with $P_{S_2} = 10^{-6}$ and $P_{O_2} = 10^{-20}$ atm that simulates severe coal gasification environments. Al_2O_3-forming iron-based alloys were more corrosion resistant than Cr_2O_3-forming iron-based alloys in this environment. Rapid sulfidation of Al_2O_3-forming iron-based alloys with and without preoxidation proceeded initially by nucleation and growth of chromium-rich sulfides and later by formation of iron-rich sulfides. To increase the corrosion resistance of Al_2O_3-forming iron-based alloys, the formation of fast-growing sulfides, such as CrS, FeS, and sulfide mixtures containing CrS and/or FeS, should be minimized or avoided completely. A new iron-based alloy developed in this study has shown very good corrosion resistance. Only small metal sulfide particles formed on the alloy surface with no observable internal sulfidation.

INTRODUCTION

Because of high temperatures and the presence of sulfur, chlorine, and other impurities in coal-derived environments, metal components in coal utilization and coal conversion systems are subject to severe corrosion. These components include gas coolers in coal gasification systems, superheaters and reheaters in pulverized-coal boilers and industrial coal-fired boilers, and heat exchangers in fluidized-bed combustors, hot-gas cleanup systems, and direct-coal-fired heat engines. Both ferritic and austenitic iron-based alloys are frequently employed in these coal-related applications.

Most high-temperature alloys or metallic coatings designed to withstand oxidizing environments rely on the formation of protective Cr_2O_3 or Al_2O_3 scales. However, when operating in mixed-oxidant environments containing sulfur, protective oxide scales may not form or may eventually break down thus allowing rapid corrosion of the base alloy. Therefore, the protective oxide scale formed on high-temperature alloys exposed to mixed-gas environments must be chemically stable and an effective barrier to sulfur/chlorine transport. For long-term applications it must also resist mechanical breakdown. Previous work on the development and breakdown of protective oxide scales on alloys exposed to coal-derived atmospheres have recently been reviewed in detail.[1]

Although extensive studies have been conducted in the past few decades to characterize the corrosion behavior of heat-resistant alloys in coal-derived environments, protective scales with optimum performance in mixed-gas environments have not yet been found. The purpose of this study is to develop corrosion-resistant scales on iron-based alloys that are effective in mixed-oxidant (oxygen-sulfur) environments at 500 to 800°C. In this paper results of corrosion tests at 800°C on Fe-25Cr-20Ni and Fe-17Cr-6Al alloys exposed to a H_2-H_2S-H_2O-Ar mixed-gas of a composition yielding equilibrium values of $P_{S_2} = 10^{-6}$ and $P_{O_2} = 10^{-20}$ atm will be discussed. Based on experience gained during testing of the Fe-25Cr-20Ni and Fe-17Cr-6Al alloys in the mixed-gas environment, two new iron-based alloys were developed. Corrosion results of these two iron-based alloys exposed to the same mixed-gas environment will also be addressed.

EXPERIMENTAL

Four iron-based alloys including a chromia and alumina former and two proprietory alloys were studied. Compositions of the first two alloys are listed in Table 1; however, because of patent restrictions, compositions of the alloys designated as C and D cannot yet be disclosed. Alloy A (Fe-25Cr-20Ni), which simulates the composition of type 310 stainless steel, was used as a model for Cr_2O_3-forming iron-based alloys. Alloy B (Fe-17Cr-6Al) was used as a model for Al_2O_3-forming iron-based

Table 1. Nominal composition of alloys (wt %)

Alloy	Fe	Cr	Ni	Al	Si	Mn	Mo	Cu	C	P	S
A	balance	24.87	19.83	0.01	0.04	<0.01	<0.01	<0.01	0.002	0.003	0.006
B	balance	17.36	0.05	5.51	0.02	0.04	0.02	0.02	0.003	0.004	0.004
C	iron-based alloy (4 components)										
D	iron-based alloy (3 components)										

alloys. These alloys were prepared by arc melting and drop casting. They were then homogenized at 1200°C in high-purity argon for 4 h and hot swaged at 1120°C to 12.7-mm-diam bars. After hot swaging, the materials were annealed at 1120°C for 20 min. Alloys C and D exhibited surface cracks when swaged at 1120°C; they were subsequently swaged and then annealed at 1200°C. Specimens cut from the bar were about 0.7 mm thick. The specimens were ground with 600-grit SiC paper, cleaned with acetone, and rinsed with distilled water.

During exposure to the mixed gas atmosphere weight changes of samples were continuously measured by an Ainsworth microbalance. In order to prevent separation due to thermal diffusion, the gas mixture was preheated and flowed upward within the reaction tube at a linear flow rate of about 1.55 cm/s. Platinum foil was located inside the hot zone of the reaction tube to enhance the gas mixture reaching its equilibrium state. To control the sample's position, a magnetic device was used to lower the specimen into the hot zone of the furnace which was purged with the gas mixture for at least 2 h prior to the start of the corrosion experiment.

Gas mixtures used in this study contained hydrogen, hydrogen sulfide, and argon that were premixed to the desired compositions by the Matheson Gas Products Company. Moisture was added to the gas mixture by bubbling the gas through a temperature-controlled water bath. The oxygen partial pressure in the gas was continuously monitored by a Y_2O_3-stabilized ZrO_2 oxygen sensor. The equilibrium partial pressures of sulfur at the reaction temperature were calculated from known compositions of the gas mixture by using thermodynamics data in the JANAF Tables.[2] The compositions of the gas mixtures and their equilibrium pressures of oxygen and sulfur used in the present work are given in Table 2. The gas mixture and test temperature were selected to simulate severe coal gasification environments.[3]

Table 2. Compositions of the gas mixtures employed

% H_2	% H_2S	% H_2O	Ar	log P_{S_2}[a]	log P_{O_2}[a]
8.33	0.55	1.12	90.0	−6.0	−20.0
0.83	0.055	1.12	98.0	−6.0	−18.0

[a]Calculated at 800°C.

Experiments were begun by lowering a cold specimen into the hot zone of the furnace, and stopped by quenching the specimen to room temperature in high-purity argon. Both optical and scanning electron microscopes (SEM) were employed to examine the morphology of corrosion scales, while energy-dispersive x-ray spectroscopy (EDS) was used to determine the chemistry of scales.

RESULTS AND DISCUSSION

Results of thermogravimetric analyses (TGA) from alloys A and B are shown in Fig. 1. Alloy B corroded at a much slower rate than alloy A. Since Cr_2O_3 is thermodynamically unstable in this environment, it may not form or may rapidly convert to fast-growing chromium sulfides or sulfide mixtures containing chromium. Alloys that rely on the formation of Cr_2O_3 for protection in high-temperature oxidizing environments are not necessarily corrosion resistant in high-temperature aggressive atmospheres with high P_{S_2} and low P_{O_2}. Similar results have been reported in coal-gasification pilot plant components by Danyluk and Diercks[4] (Table 3). Material failures due to severe sulfidation were all Cr_2O_3-forming alloys. Thus, Cr_2O_3-forming alloys cannot be used in high-temperature aggressive environments with high P_{S_2} and low P_{O_2}. In addition, because of their potential for forming low-melting metal-metal sulfide eutectics, nickel- and/or cobalt-containing alloys are also unsuitable for application in high-temperature aggressive environments with high P_{S_2} and low P_{O_2}.

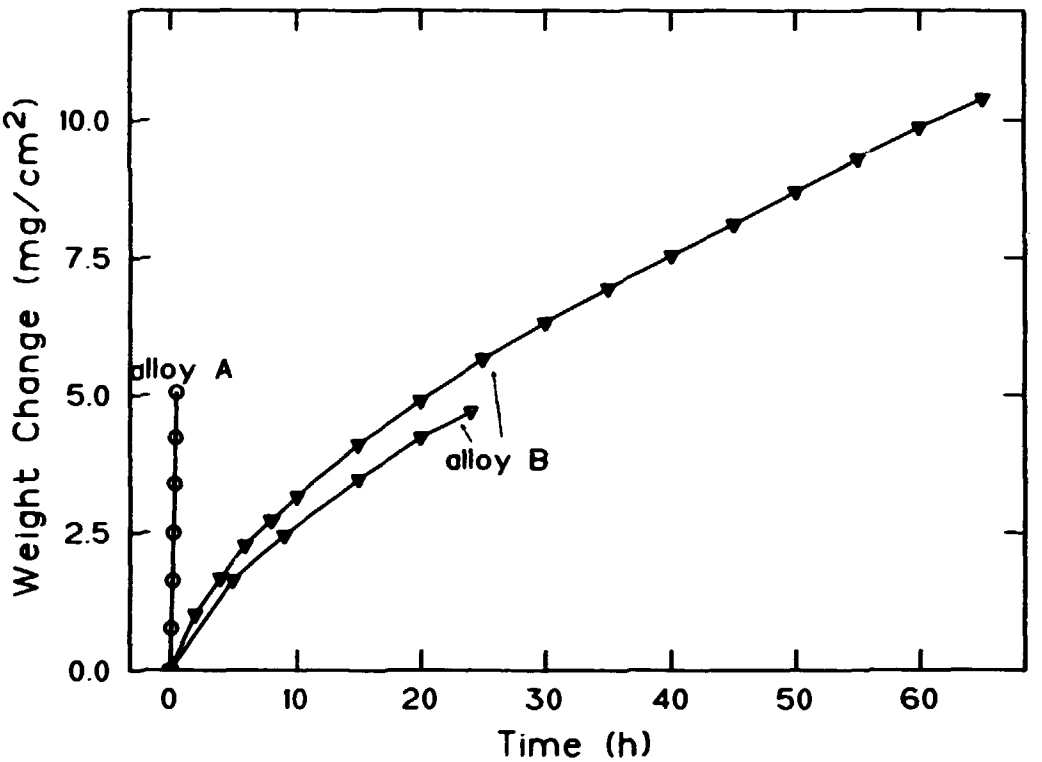

Fig. 1. TGA data from corrosion of alloys A and B to the gas mixture with $P_{S_2} = 10^{-6}$ and $P_{O_2} = 10^{-20}$ atm at 800°C.

Table 3. Material failures reported in coal-gasification pilot plant components[4] due to severe sulfidation

Material failures reported in	Composition (wt %)					
	Fe	Ni	Cr	Mn	Mo	Si
Ni-based alloys						
Inconel 182	8	bal	14	8	-	1
Inconel 600	8	bal	16	1	-	-
Hastelloy C	20	bal	22	2	6	1
Fe-based alloys						
310 SS	bal	20	25	2	-	2
347 SS	bal	11	18	2	-	1
(Fe,Ni)-based alloys						
Incoloy 800	46	33	21	1	-	-
RA 330	43	35	19	2	-	1

The equilibrium oxygen partial pressure of Al_2O_3/Al_2S_3 is more than seven orders of magnitude lower than that for Cr_2O_3/"CrS" at the same partial pressure of sulfur, and Al_2O_3 is thermodynamically stable in most coal-related environments. ("CrS" is used here to represent chromium sulfides with different stoichiometries.) However, due to significant stress build-up in the oxide during corrosion, Al_2O_3 scales crack easily and allow rapid reaction between other elements in the base metal and sulfur from the gas. Additionally, because the presence of aluminum in an alloy generally tends to diminish its mechanical properties, aluminum concentrations are normally kept at the lowest possible level. As a result, once the Al_2O_3 scale cracks or spalls, it is very difficult to reform new Al_2O_3 on the surface. Even so, Al_2O_3-forming iron-based alloys (alloy B) should, in general, have better corrosion resistance than Cr_2O_3-forming iron-based alloys (alloy A) in mixed-gas environments containing sulfur (such as coal gasification systems). Unfortunately, few Al_2O_3-forming alloys have been actually used in coal-related applications with high-temperature aggressive environments. In order to better understand the development of corrosion-resistant scales on Al_2O_3-forming alloys, a study of both the nucleation and growth of corrosion scales and the breakdown of preformed Al_2O_3 scales in the mixed-gas environment is essential.

Figures 2(a) and (b) show surface topographies of alloy B exposed to the mixed gas ($P_{S_2} = 10^{-6}$ and $P_{O_2} = 10^{-20}$ atm) at 800°C for 5 and 10 min, respectively. During the early stage of corrosion, only spherical or crystalline sulfide nuclei formed on the alloy surface. Nonstandard semiquantitative EDS analysis indicated that the sulfide nuclei contain $(Cr_{0.48}Fe_{0.3}Al_{0.22})S$, where the total of cations in the sulfide is normalized to one. Because of the inability to detect light elements by EDS, the oxygen content of the nuclei is not known. Therefore, the corrosion product formed on alloy B can be a mixed sulfide (Cr,Fe,Al)S or a mixture of (Cr,Fe)S and Al_2O_3. Further verification of the form of the corrosion product is needed.

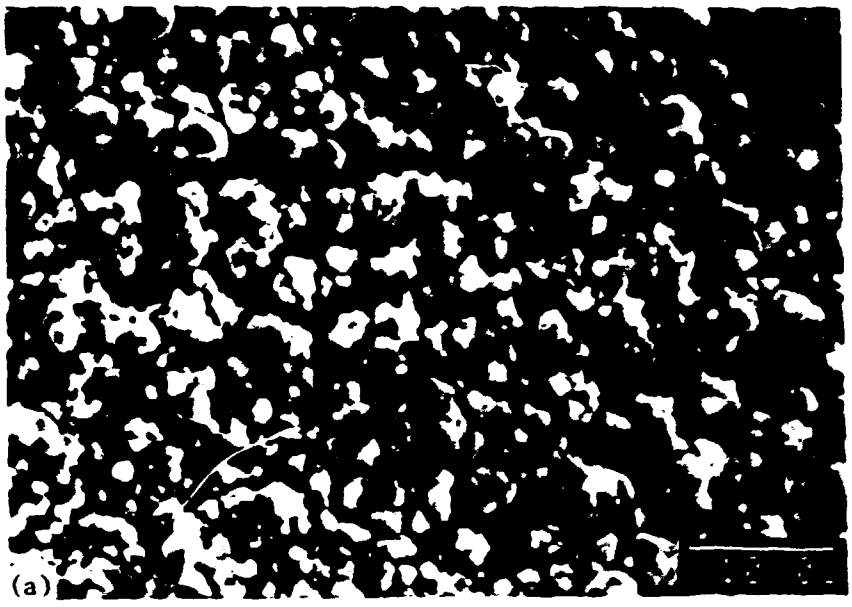

5 min

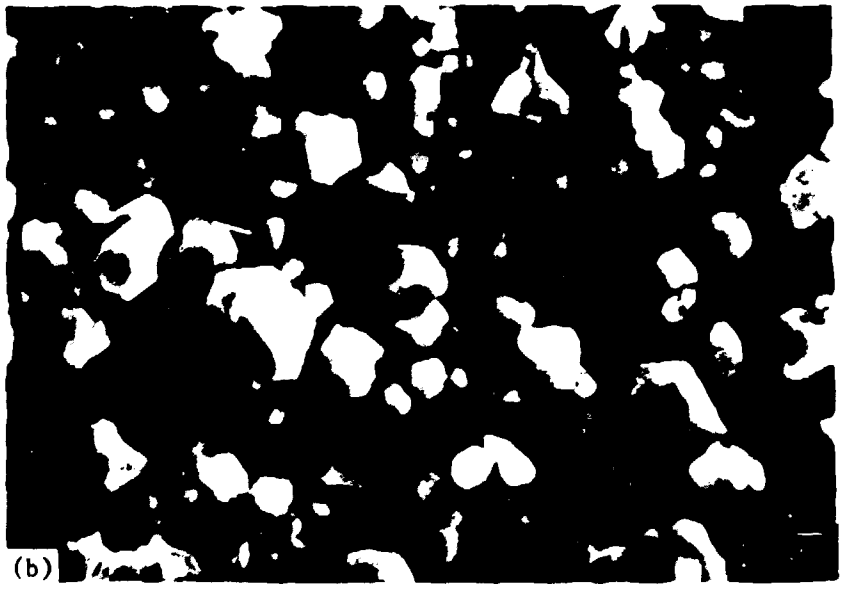

10 min

Fig. 2. Surface topographies of alloy B exposed to the gas mixture with $P_{S_2} = 10^{-6}$ and $P_{O_2} = 10^{-20}$ atm at 800°C. (a) 5 min. (b) 10 min.

After a 30-min exposure to the mixed gas with $P_{S_2} = 10^{-6}$ and $P_{O_2} = 10^{-20}$ atm at 800°C, platelet sulfides began to form as shown in Fig. 3(a). These platelet sulfides, $(Fe_{0.72}Cr_{0.2}Al_{0.08})S$, have a much higher concentration of iron compared to the spherical sulfides formed during the early stage of exposure. Besides the formation of iron-rich sulfide platelets, an iron-rich sulfide, $(Fe_{0.72}Cr_{0.2}Al_{0.08})S$, has also grown on some surfaces of the crystalline chromium-rich sulfide. $(Cr_{0.44}Fe_{0.36}Al_{0.2})S$ can be seen in the upper left of the micrograph in Fig. 3(b), but the chromium-rich sulfide grain in the lower right of the micrograph is covered almost entirely with the iron-rich sulfide. Apparently, the growth of the iron-rich sulfide is faster than that of the chromium-rich sulfide. Therefore, after a long period of exposure of alloy B to the mixed gas, the iron-rich sulfide outgrows the chromium-rich sulfide and becomes the major corrosion product in the scale.

Figures 4(a) and (b) show the topography and the cross section of the scale, respectively, after a 24-h exposure of alloy B to the same mixed gas. The iron-rich sulfide, $(Fe_{0.73}Cr_{0.24}Al_{0.03})S$, continued growing into a thick, porous layer on alloy B. Only a relatively thin layer of sulfide enriched with chromium and aluminum was detected between the iron-rich sulfide scale and the metal substrate. In addition, some internal sulfidation can also be observed in Fig. 4(b).

One approach being widely used to increase corrosion resistance of alloys is preoxidation: the alloy is exposed to an oxidizing environment in order to develop a protective oxide scale prior to exposure to an aggressive atmosphere. In general, such preoxidation treatments have, at least initially, improved the subsequent resistance to sulfur-containing environments. Upon exposure to sulfur-containing gases, the preformed oxide scale results in an initial incubation period during which the scale remains protective, followed by relatively rapid growth of sulfides. It was found that preoxidation only extends the useful life of many alloys from a few hundred to perhaps a thousand hours.[5,6] Although preoxidation may have only limited advantages for practical applications in mixed-gas environments, it can be a useful means to understand the breakdown of corrosion scale exposed to mixed-gas environments.

Fig. 3. (a) Surface topographies of alloy B exposed to the gas mixture with $P_{S_2} = 10^{-6}$ and $P_{O_2} = 10^{-20}$ atm at 800°C for 30 min. (b) A higher magnification of (a).

Fig. 4. (a) Topography of the scale. (b) Cross section of the scale from alloy B exposed to the gas mixture with $P_{S_2} = 10^{-6}$ and $P_{O_2} = 10^{-20}$ atm at 800°C for 24 h.

Comparison of results of corrosion of alloy B with no preoxidation and with preoxidation at either 800 or 1000°C for 20 h in Ar-1CO-1H_2O (P_{O_2} ~ 10^{-15} atm) followed by exposure to the mixed gas at 800°C are shown in Fig. 5. The alloy B with preoxidation shows much better corrosion resistance than the same material with no preoxidation. The corrosion of alloy B with a 1000°C preoxidation is slower than that with an 800°C preoxidation. The primary difference between preoxidations at 800 and 1000°C of alloy B is the difference in the amount of stress build-up in the scale as well as stress-relaxation processes. At 1000°C, the oxidation stresses in the oxide can be partially relieved by the wrinkling of the scale. At lower oxidation temperatures, however, the oxide tends to crack and spall instead (see Fig. 6).

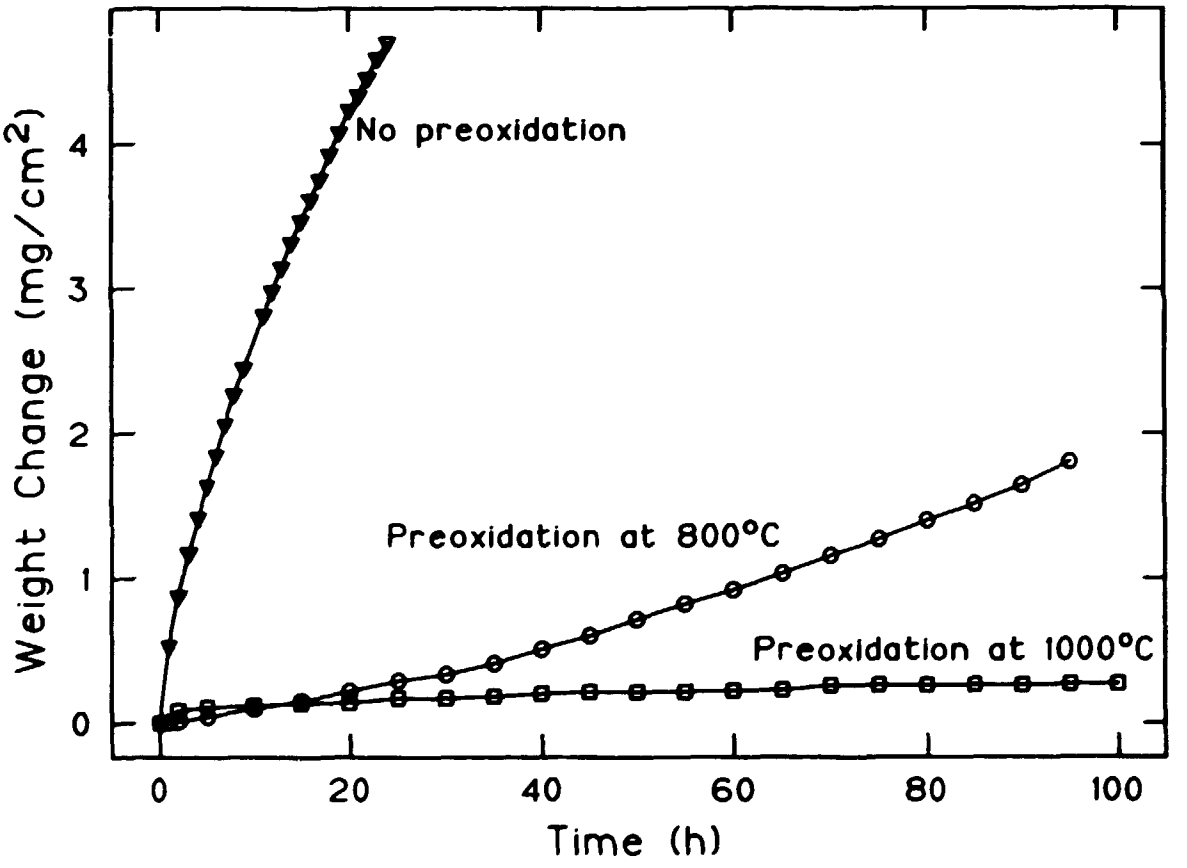

Fig. 5. TGA data from corrosion of alloy B with no preoxidation and with preoxidation at 800 and 1000°C exposed to the gas mixture with P_{S_2} = 10^{-6} and P_{O_2} = 10^{-20} atm at 800°C.

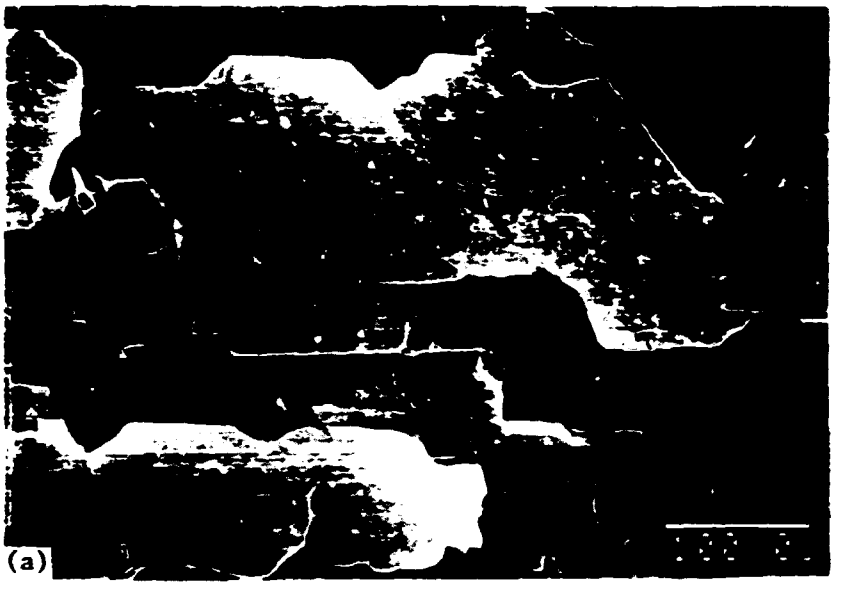

900°C

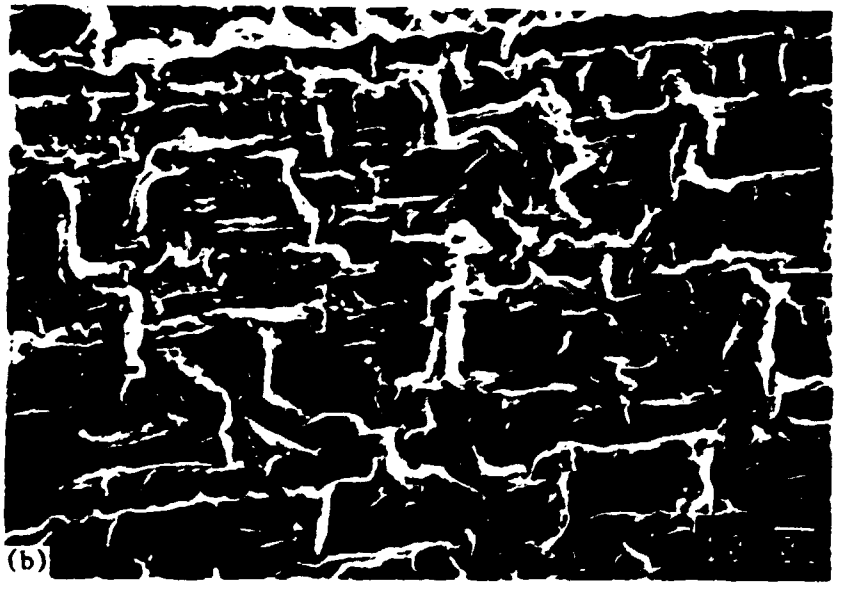

1000°C

Fig. 6. Scale topographies from alloy B preoxidized in Ar-1CO-1H_2O (log P_{O_2} ~ −15) for 20 h. (a) 900°C. (b) 1000°C.

Although alloy B preoxidized at 1000°C showed very good corrosion resistance for a 100-h exposure to the mixed gas, some catastrophic sulfidation was observed on a microscopic scale. Figure 7 shows the scale topography of an alloy B specimen that was preoxidized at 1000°C in Ar-1CO-1H_2O for 20 h and then exposed to the mixed gas atmosphere at 800°C for 100 h. Most sulfides formed on the preformed alumina scale have the same pattern. Small sulfide nodules, which formed for only a relatively short period of time, were primarily chromium-rich sulfides. Meanwhile, large sulfide particles, which formed over a much longer period of time, were composed of iron-rich sulfide platelets, $(Fe_{0.71}Cr_{0.24}Al_{0.05})S$, surrounded by cauliflower-shape chromium-rich sulfide crystallites, $(Cr_{0.61}Fe_{0.34}Al_{0.05})S$. These results indicate that initially small chromium-rich sulfide nodules are nucleated on the preformed alumina scale and later iron-rich sulfide starts to overgrow the chromium-rich sulfide nodules.

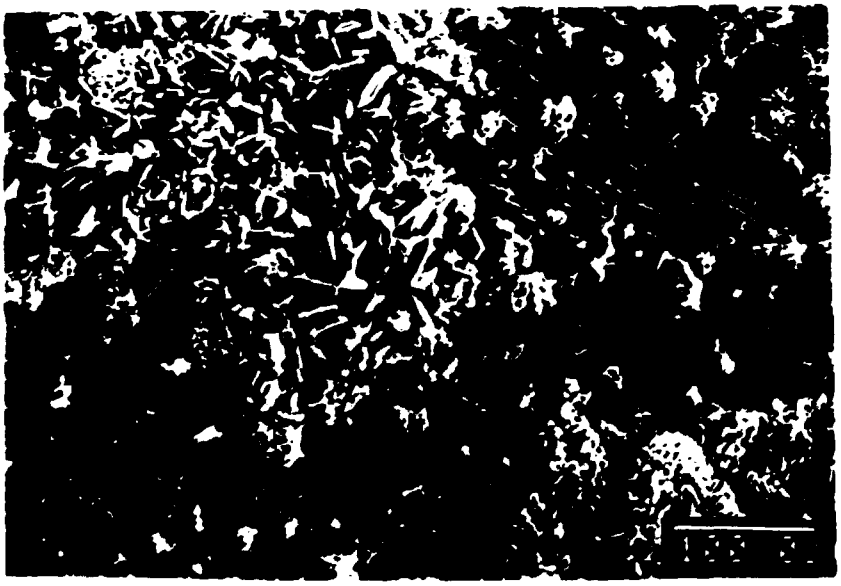

Fig. 7. Scale topography from alloy B that was preoxidized in Ar-1CO-1H_2O (log $P_{O_2} \sim -15$) for 20 h at 1000°C and exposed to the gas mixture with $P_{S_2} = 10^{-6}$ and $P_{O_2} = 10^{-20}$ atm at 800°C for 100 h.

Two major modes for initiation of rapid sulfidation on the preformed alumina in the mixed-gas environment are cracks in the oxide scale and the conversion of alumina to mixtures of alumina and metal sulfides. Examples of breakdown of preformed alumina scales are shown in Fig. 8. Cracks in the oxide scale generally occur in the area with high stress density such as the crossing of two wrinkles, where sulfide nodules begin to grow as shown in Fig. 8(a). The conversion of alumina to alumina plus metal sulfides normally occurs at preformed oxides that contact the metal substrate. The cause of the conversion of alumina is not known. It could be due to inward sulfur diffusion through microfissures or short-circuit diffusion paths that allow the formation of metal sulfides in the oxide. However, if the preformed oxide separates from the metal substrate, the supply of metal ions to the oxide is interrupted, and the conversion of alumina to alumina plus metal sulfides will not occur (as shown in Fig. 9). The conversion of alumina to alumina plus metal sulfides decreases the protectiveness of alumina scales, and sulfide nodules start to form eventually [as shown in Fig. 8(b)].

In conclusion, the corrosion study of both unoxidized and preoxidized alloy B exposed to the mixed gas with $P_{S_2} = 10^{-6}$ and $P_{O_2} = 10^{-20}$ atm at 800°C showed that chromium-rich sulfides form initially on the surface of the alloy or on the preformed alumina scale but later are outgrown by iron-rich sulfides. Because the growth rate of "CrS" is more than six orders of magnitude greater than that of Cr_2O_3, the fast-growing "CrS" or chromium-rich sulfides provide no protection to the alloy. This is also true for FeS and sulfide mixtures containing FeS and/or "CrS." Thus, if the formation of the fast-growing FeS, "CrS," or their sulfide mixtures can be minimized or eliminated completely, the corrosion resistance of Al_2O_3-forming iron-based alloys to mixed gas containing sulfur can be improved greatly. It is also believed that if the initially formed "CrS" or chromium-rich sulfides can be suppressed, catastrophic sulfidation due to the outgrowth of iron-rich sulfides can be subsequently reduced.

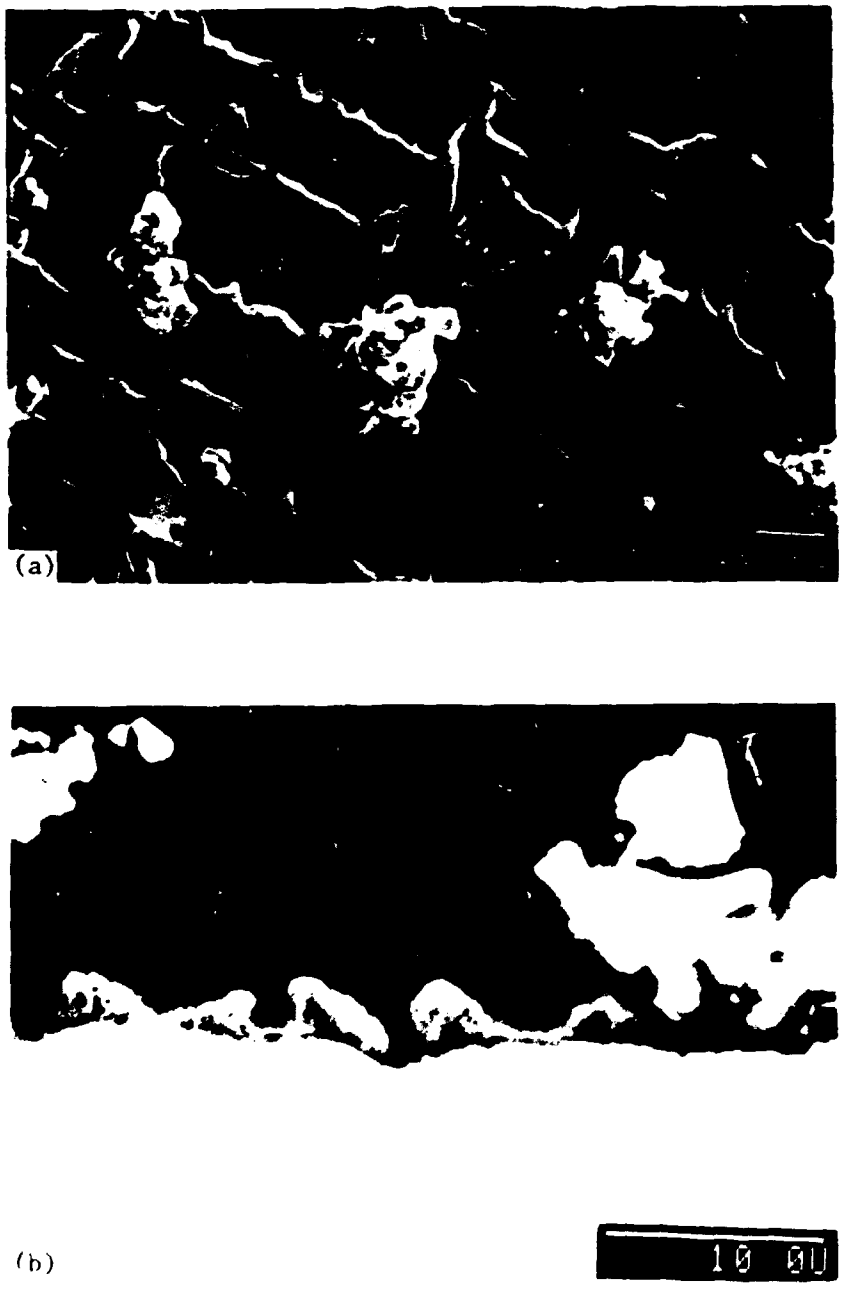

Fig. 8. After preoxidation in Ar-1Cr-1H_2O (log $P_{O_2} \sim -15$) for 20 h at 1000°C and exposure to the gas mixture with $P_{S_2} = 10^{-26}$ and $P_{O_2} = 10^{-20}$ atm at 800°C for 100 h. (a) Cracks where wrinkles intersect provided nucleation sites for sulfides. (b) Alumina became alumina plus metal sulfides.

10 0U

Fig. 9. After preoxidation in Ar-1CO-1H_2O (log $P_{O_2} \sim -15$) for 20 h at 1000°C and exposure to the gas mixture with $P_{S_2} = 10^{-6}$ and $P_{O_2} = 10^{-20}$ atm at 800°C for 100 h, areas where Al_2O_3 separated from metal did not undergo sulfidation while areas where Al_2O_3 remained attached underwent a conversion to alumina plus metal sulfides.

In order to minimize the nucleation and growth of fast-growing sulfides, iron-based alloys C and D were developed. For comparison, corrosion results from alloys A, B, C, and D exposed to the mixed gas ($P_{S_2} = 10^{-6}$ and $P_{O_2} = 10^{-20}$ atm) at 800°C are plotted in Fig. 10. Corrosion of alloy C is only slightly less than alloy B. Figure 11 shows the scale cross section of alloy C exposed to the mixed gas at 800°C for 24 h. It formed an outer iron-rich sulfide $(Fe_{0.8}Cr_{0.2})S$ layer and an inner porous sulfide layer. Formation of the inner porous layer is caused by internal sulfidation which is more severe in alloy C than in alloy B. Therefore, alloy C cannot be considered as a good corrosion-resistant material.

Alloy D is significantly more corrosion resistant in severe sulfidizing environments. Corrosion of alloy D is about a factor of five slower than that of alloy B and proceeds by the formation of metal sulfide particles on a thin sulfide layer as shown in Fig. 12. The growth of these metal sulfide particles is responsible for most of the corrosion reactions on alloy D. No internal sulfidation was observed.

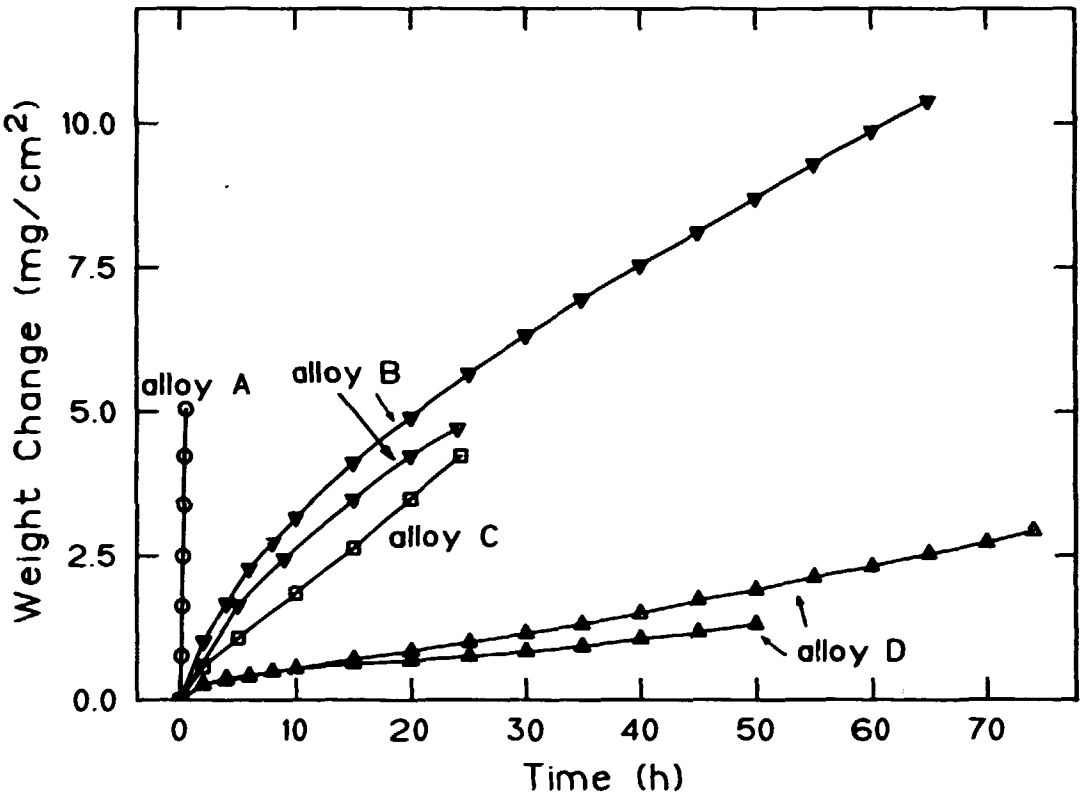

Fig. 10. TGA data from corrosion of alloys A, B, C, and D exposed to the gas mixture with $P_{S_2} = 10^{-6}$ and $P_{O_2} = 10^{-20}$ atm at 800°C.

Fig. 11. Corrosion of alloy C in the gas mixture with $P_{S_2} = 10^{-6}$ and $P_{O_2} = 10^{-20}$ atm at 800°C for 74 h forms metal sulfide particles on the surface of sample.

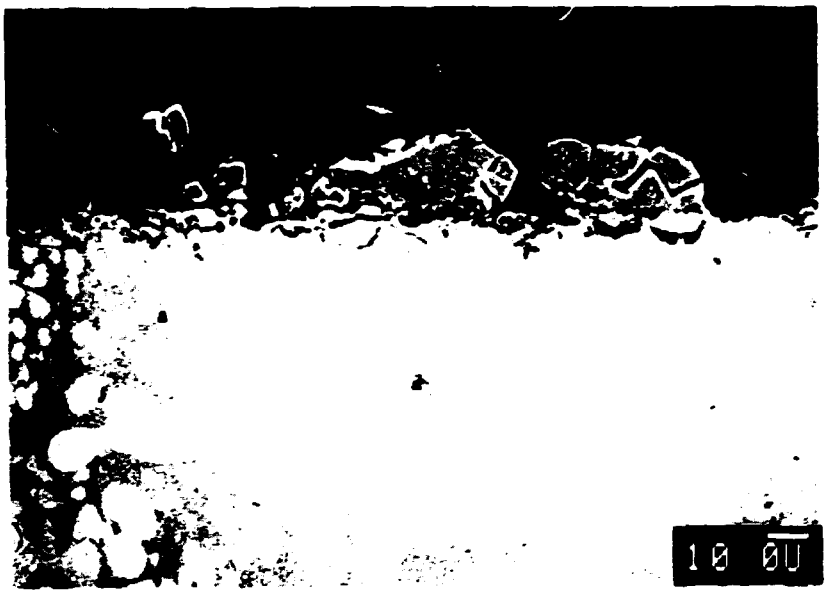

Fig. 12. Corrosion of alloy D in the gas mixture with $P_{S_2} = 10^{-6}$ and $P_{O_2} = 10^{-20}$ atm at 800°C for 74 h forms metal sulfide particles on the surface of sample.

To understand how alloy D corrodes in mixed gas environments, the alloy was exposed to a less aggressive gas mixture. The TGA data from alloy D exposed at 800°C to the gas mixture with $P_{S_2} = 10^{-6}$ atm and two different oxygen partial pressures of 10^{-18} and 10^{-20} atm are shown in Fig. 13. Topography and cross section of the scale formed on alloy D exposed to the mixed gas with $P_{S_2} = 10^{-6}$ and $P_{O_2} = 10^{-18}$ atm at 800°C for 92 h are shown in Fig. 14(a) and (b), respectively. Figure 14(a) indicates that some metal sulfide particles also formed on the surface of alloy D under this less aggressive environment. Figure 14(b) shows that alloy D is a two-phase material and the metal sulfide particles formed primarily on only one of the phases. If the corrosion resistance of the phase in alloy D that is responsible for the formation of metal sulfide particles can be improved, the corrosion resistance of this material will increase significantly. Further development of corrosion-resistant Al_2O_3-forming iron-based alloys is in progress.

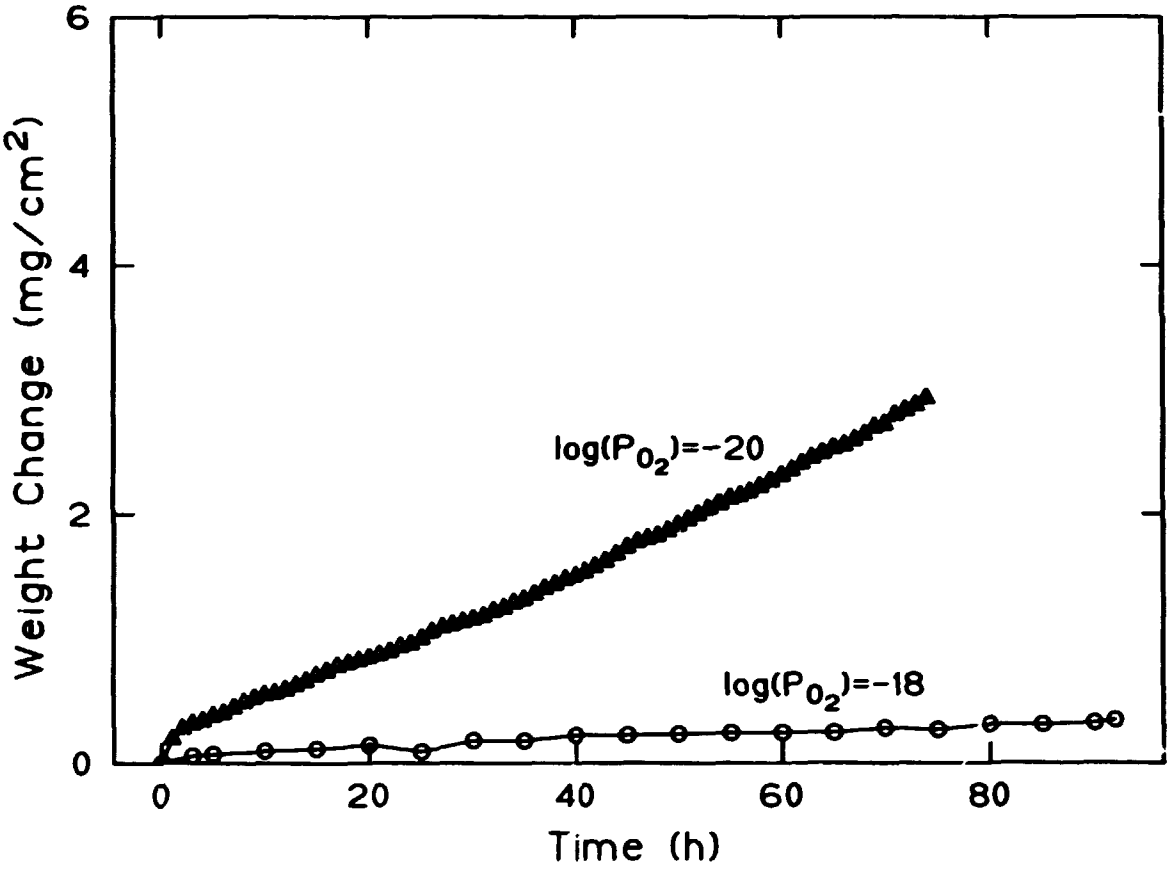

Fig. 13. TGA data from corrosion of alloy D exposed to the gas mixture with $P_{S_2} = 10^{-6}$ atm with two different P_{O_2} at 800°C.

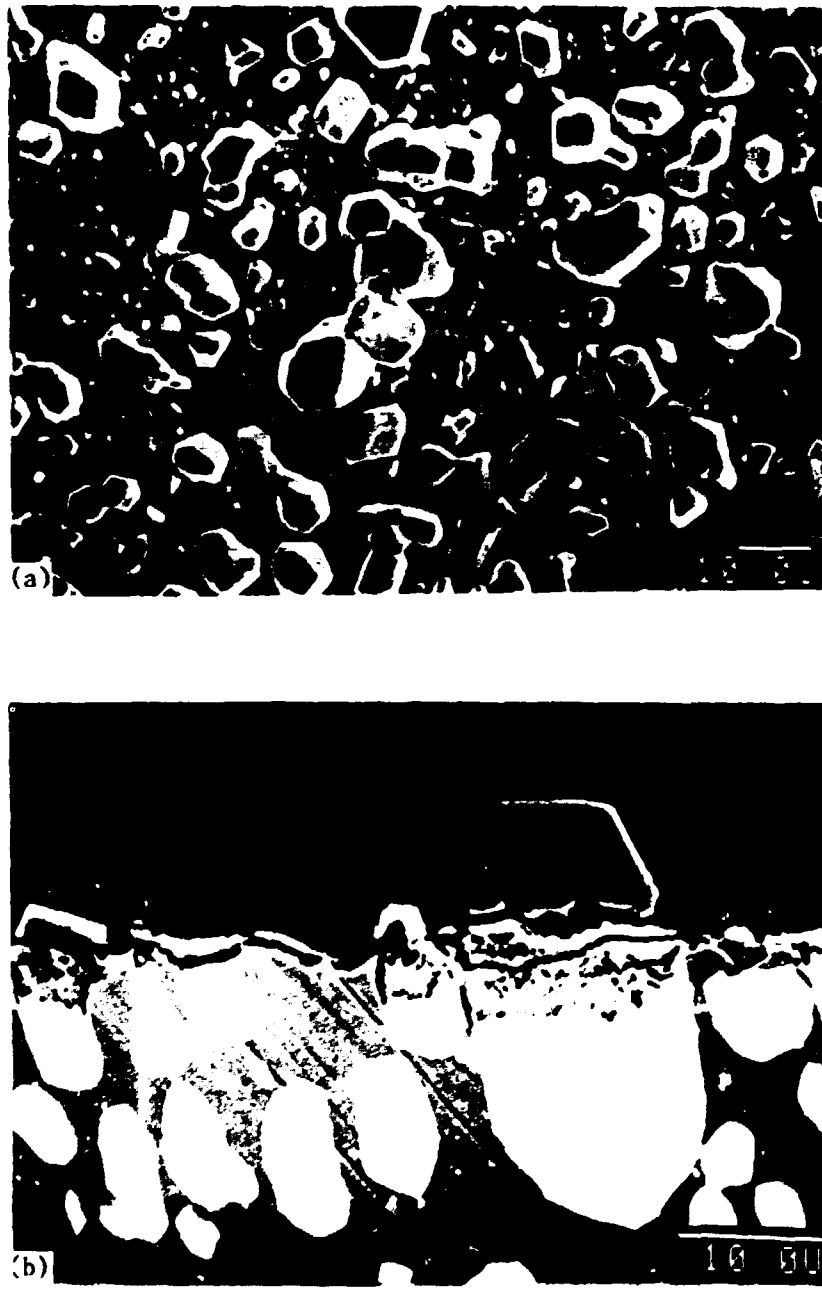

Fig. 14. (a) Topography of the scale. (b) Cross section of the scale from corrosion of alloy D in the gas mixture with $P_{S_2} = 10^{-6}$ and $P_{O_2} = 10^{-18}$ atm at 800°C for 92 h.

CONCLUSIONS

Cr_2O_3-forming alloys (such as alloy A) cannot be used in high-temperature aggressive environments with high P_{S_2} and low P_{O_2} because Cr_2O_3 is thermodynamically unstable. Due to their potential for forming low-melting metal-metal sulfide eutectics, nickel- and/or cobalt-containing alloys are also not suitable for application in high-temperature aggressive environments containing sulfur.

Rapid sulfidation on Al_2O_3-forming alloys (such as alloy B) with and without preoxidation proceeds initially with nucleation and growth of chromium-rich sulfides and later with formation of iron-rich sulfides. In order to develop corrosion-resistant scales, the formation of fast-growing sulfides, such as CrS, FeS, and their mixtures, must be prevented.

Two iron-based alloys were developed as corrosion-resistant materials. Alloy D, one of those, was significantly more corrosion resistant to the mixed gas with $P_{S_2} = 10^{-6}$ and $P_{O_2} = 10^{-20}$ atm at 800°C. The corrosion rate of alloy D was about a factor of five lower than that of alloy B. By improving the corrosion resistance of the phase in alloy D that is responsible for corrosion, the resistance of this material to mixed gas environments could be increased significantly. Further development of more corrosion-resistant iron-based alloys is in progress.

REFERENCES

1. H. S. Hsu, A Review of the Development and Breakdown of Protective Oxide Scales on Alloys Exposed to Coal-Derived Atmospheres, ORNL-6323, October 1986.

2. JANAF Thermochemical Tables, NSRDS-NBS 37, U.S. Department of Commerce, Washington, DC, 1971.

3. K. Natesan, "High Temperature Corrosion in Coal Gasification Systems," J. Corros. 41, 646 (1985).

4. S. Danyluk and D. Diercks, The Properties and Performance of Materials in the Coal Gasification Environment, V. L. Hill and H. L. Black, eds., American Society for Metals, Metals Park, Ohio, p. 155 (1981).

5. R. A. Perkins and S. J. Vonk, Materials Problems in Fluidized-Bed Combustion Systems, EPRI-FP-1280, Electric Power Research Institute, Palo Alto, Calif., 1979.

6. F. H. Stott, F.M.F. Chong, and C. A. Stirling, The Effectiveness of Preformed Oxides for Protection of Alloys in Sulphidizing Gases at High Temperatures, 9th ed., International Congress on Metallic Corrosion, p. 1, (1984).

CORROSION MECHANISMS OF COAL COMBUSTION PRODUCTS ON ALLOYS AND COATINGS

G. M. Kim, E. A. Gulbransen and G. H. Meier
Department of Materials Science and Engineering
848 Benedum Hall
University of Pittsburgh
Pittsburgh, PA 15261

ABSTRACT

The ferrous alloys (Fe-18Cr-6Al, Fe-18Cr-6Al-1Ti, Fe-18Cr-6Al-1Hf, Fe-25Cr and Fe-20Si) were studied between 700 and 1100°C in an oxidizing (air or H_2/H_2O) atmosphere. Then the breakdown of preformed oxide scales on these alloys was studied in a sulfidation/oxidation ($H_2/H_2O/H_2S$) atmosphere at the same temperatures.

The resistance to isothermal oxidation, thermal cycling in air at 950°C, and sulfidation/oxidation increases in the order of SiO_2 former > Al_2O_3 former > Cr_2O_3 former. The addition of Ti to Fe-18Cr-6Al improves the resistance to cyclic oxidation and sulfidation/oxidation at 950°C. The addition of Hf to Fe-18Cr-6Al improves cyclic oxidation resistance but also provides rapid transport paths for sulfur through the scale.

The breakdown of Cr_2O_3 films on Fe-25Cr initiates at the scale/gas interface.

Silica scales formed on Fe-20Si are extremely resistant to sulfur penetration but may break down eventually due to the outward transport of Fe through the scale.

Key Words; isothermal and cyclic oxidation, sulfidation/oxidation, ferrous alloys.

INTRODUCTION

The development of high temperature alloys which are resistant to surface degradation has been based upon the desirability of forming protective oxide scales in which the transport of cations and anions is extremely slow. The most commonly used protective oxides are Cr_2O_3, Al_2O_3 and SiO_2. The alloys and metallic coatings in coal gasification processes are exposed at high temperature to a low potential of oxygen and a high potential of other reactant gases (mainly sulfur).[1,2] The oxygen potential in these environments is sufficiently high for Al_2O_3, Cr_2O_3 and SiO_2 to remain thermodynamically stable.[1,2] Therefore, preformed oxide scales are expected to grow in these environments at least until the scales break down due to the formation of less protective reaction products. It is necessary to understand how the preformed oxide scales are degraded by the reactive species (especially sulfur) of the coal gasification processes.

Basically three types of ferrous alloys were chosen.

Cr_2O_3 former : Fe-25Cr

Al_2O_3 former : Fe-18Cr-6Al, Fe-18Cr-6Al-1Hf, Fe-18Cr-6Al-1Ti

SiO_2 former : Fe-20Si

The oxidation and mixed gas corrosion of these ferrous alloys have been the subject of numerous investigations.[3-13]

The objective of this research is directed toward studying the mechanisms by which preformed oxide layers are degraded in the high P_{S_2} and low P_{O_2} environments.

EXPERIMENTAL

The alloys(Fe-25Cr, Fe-18Cr-6Al-1Ti, Fe-18Cr-6Al-1Hf, Fe-18Cr-6Al and Fe-20Si)* were prepared from 99.9% pure raw materials by arc melting in argon and drop casting in a chilled copper mold, 9.5 x 25.4 x 152.4 mm in size. The ingots were homogenized at 1100°C for 100 hours in an argon gas stream. Test specimens, approximately 12 x 9 x 2 mm in size, were ground on all surfaces through 600 grit on wet silicon carbide papers and ultrasonically cleaned in methanol.

* Alloy compositions are given in weight percent.

The specimens were oxidized isothermally and the weight changes due to the oxidation were monitored continuously by a Cahn 2000 microbalance in conjunction with a strip chart recorder. The cyclic oxidation tests were carried out by cyclically oxidizing the specimens in an apparatus which periodically removed the specimens from the furnace and reinserted them. Sulfidation/oxidation experiments were carried out at 950°C in $H_2/H_2O/H_2S$ gas mixtures with $P_{S_2} = 10^{-6.1}$ and $P_{O_2} = 10^{-13.7}$ atm. For reference, the position of this gas composition has been indicated on the thermodynamic stability diagrams for Al, Ti, Si, Cr, Fe and Hf in Figure 1.[14,15] (The thermodynamic data for HfS_2 are not available and have been estimated.) The experimental setup for sulfidation/oxidation has been described elsewhere.[16]

Most of the reaction products were identified by X-ray diffraction (XRD) techniques. The surface morphology and cross section of the scales were examined by scanning electron microscopy (SEM) with energy dispersive x-ray analysis (EDX) and wave length dispersive analysis (WDX). Observation of the underside of the scale and alloy substrate were carried out on scales spalled from the alloys during cooling or mechanically pulled from the alloy by a Sebastian adherence test machine. Prior to examination in the SEM, specimens were coated with palladium by evaporation to prevent charging effects and to increase contrast.

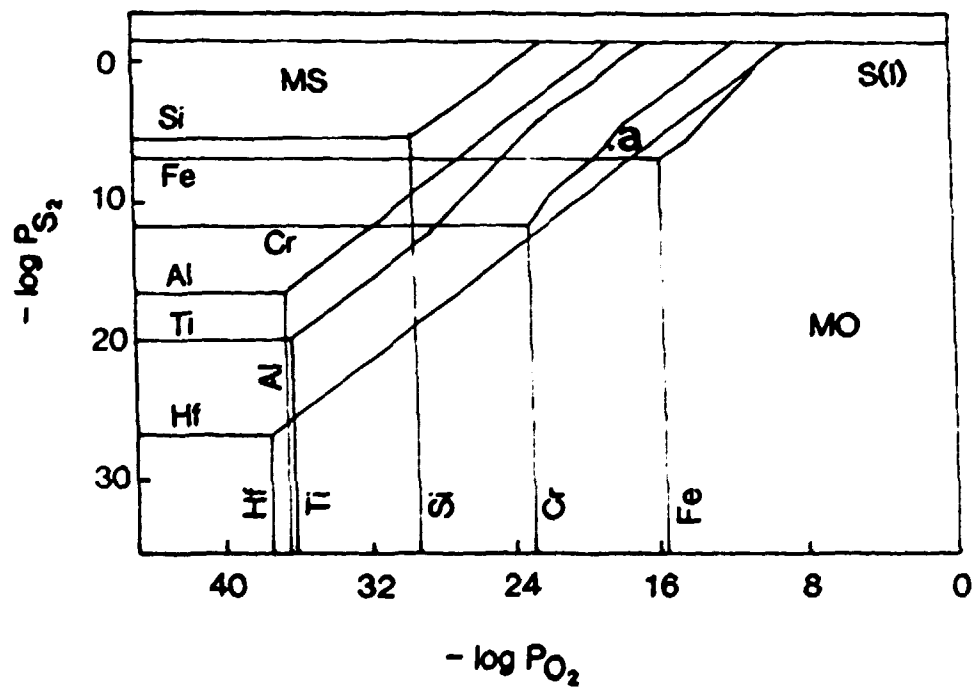

Figure 1:Stability Diagrams for the M (Al, Ti, Si, Cr, Fe and Hf)-S-O systems at 950°C. Gas composition is illustrated.

RESULTS AND DISCUSSION

Oxidation in Air

Specimens were oxidized isothermally for a week at 950°C in flowing air. The weight changes of the specimens were continuously recorded during oxidation using a Cahn 2000 microbalance. The results are shown in Figure 2. Differences in the rates of scale growth were significant depending on the types of oxide scales formed on the alloy surface. The relative growth rates of the scales were in the order of Cr_2O_3 forming > Al_2O_3 forming > SiO_2 forming alloys.

Fe-20Si exhibited the best oxidation resistance among the alloys, but the rate of scale growth on Fe-20Si was significantly larger than that on Ni-20Si. It has been reported that Ni-20Si formed a vitreous silica layer with a small amount of transient oxides of Ni_2SiO_4 during oxidation.[16] A vitreous SiO_2 layer was also reported to form on Fe-Si alloys[17] along with a significant amount of Fe_2O_3. It is believed that the larger weight gain for Fe-Si as compared to Ni-Si is due to the formation of Fe_2O_3.

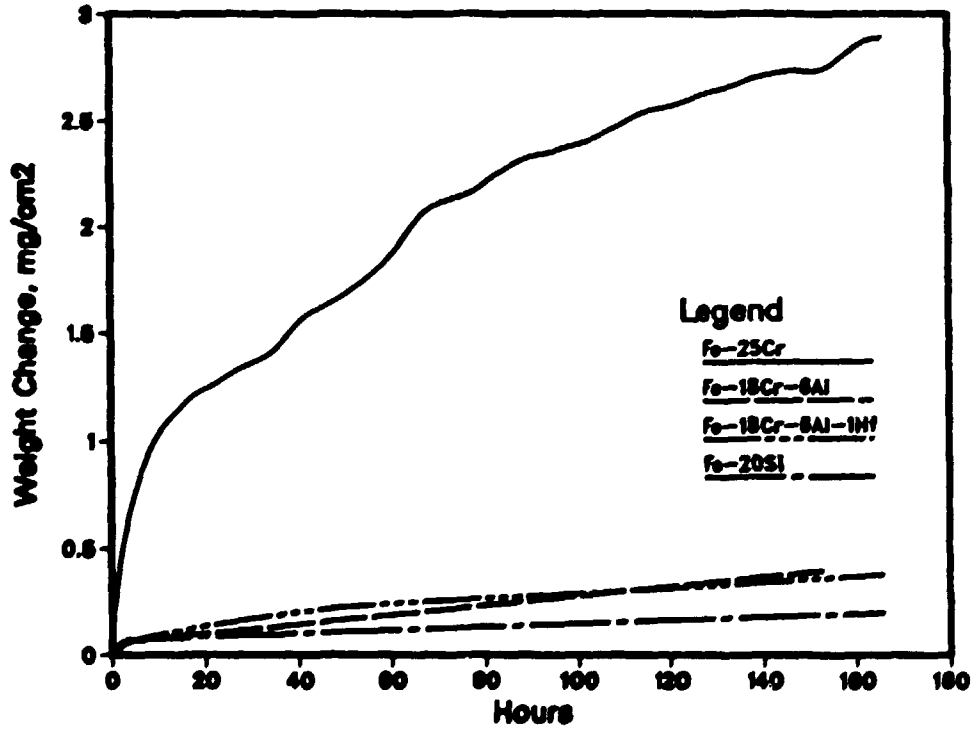

Figure 2: Weight changes vs. time for the alloys during oxidation in air at 950°C.

The scale growth rate of Fe-18Cr-6Al-1Hf was greater than that of Fe-18Cr-6Al in the early stage of oxidation (up to 100 hours) and then both rates became comparable. The increase in weight during the early stage of oxidation of alloys containing Hf has been attributed to the development of oxide pegs at the scale/alloy interface, providing rapid diffusion paths for oxygen through the oxide scale.[8] Loss of contact between the alloy and the oxide on Fe-18Cr-6Al may be one of the reasons for the lower growth rate, due to the reduced transport of elements across the scale/alloy interface.[11] Fe-18Cr-6Al formed an α-Al_2O_3 layer on the alloy surface after a week of oxidation in air at 950°C. Convoluted, wrinkled scale and voids at the scale/alloy interface were observed, as presented elsewhere.[8,9,11] The Al_2O_3 scale formed on Fe-18Cr-6Al-1Hf contained a small amount of Hf-rich oxides in the Al_2O_3 layer after a week of oxidation at 950°C. This scale was relatively flat and nonwrinkled. The addition of Hf to Fe-18Cr-6Al provides a more flat scale surface and results in the formation of less porosity at the scale/alloy interface. However, the Al_2O_3 scales formed on both Fe-18Cr-6Al and Fe-18Cr-6Al-1Hf remain protective during isothermal oxidation at 950°C in the range of one week.

Fe-25Cr formed a Cr_2O_3 layer after a week of oxidation in air at 950°C and showed the fastest scale growth rate among the alloys.

Cyclic Oxidation in Air

These tests were conducted to study the integrity and adherence of the oxide scale during thermal cycling. Each cycle consisted of 45 minutes of isothermal oxidation at 950°C in flowing air followed by 15 minutes of cooling to room temperature. The weight changes per unit area (mg/cm^2) versus the number of cycles (hours) are plotted in Figure 3.

Fe-20Si and Fe-18Cr-6Al-1Hf exhibited excellent cyclic oxidation resistance. Furthermore, although this test was extended to over 3000 cycles in a separate experiment with the same experimental conditions for Fe-18Cr-6Al-1Hf, these alloys maintained good resistance to thermal cycling. Initially the thermal cycling of Fe-18Cr-6Al shows a similar weight gain trend as Fe-18Cr-6Al-1Hf, but after 300 cycles, Fe-18Cr-6Al continues to gain weight until breakdown. During the initial stage of thermal cycling of Fe-18Cr-6Al, the processes of scale damaging and rehealing continue as long as the supply of Al is enough to reheal the Al_2O_3 scales. When Al is depleted in the alloy (about 300 cycles), non-protective

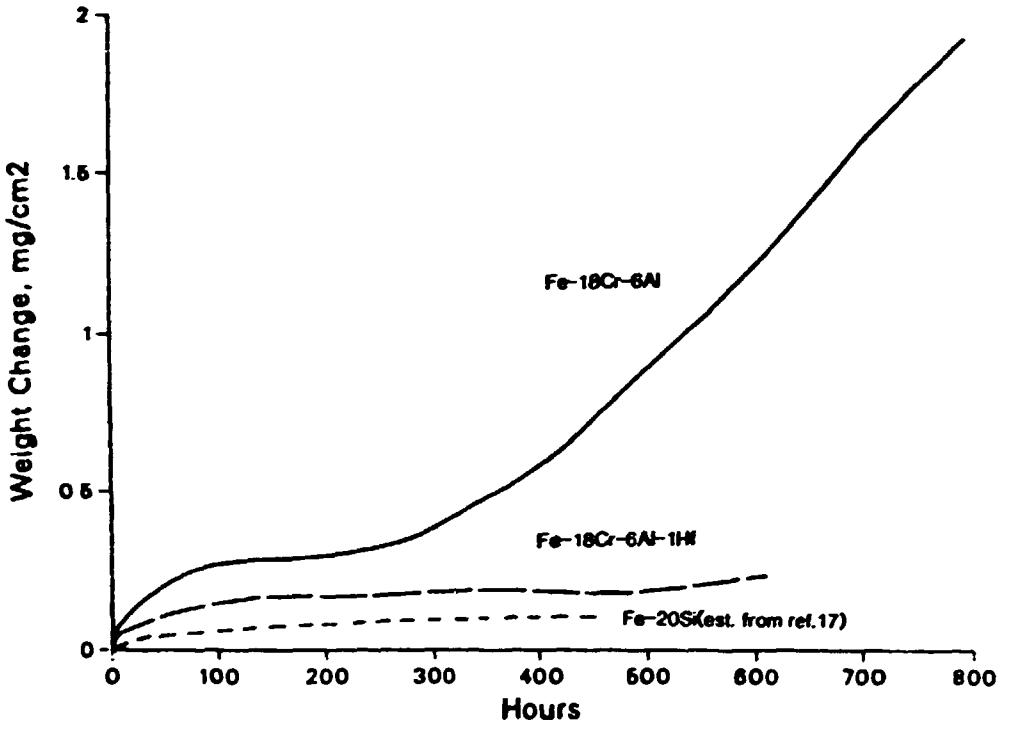

Figure 3: Weight changes versus time for cyclic oxidation (one hour cycles) for the alloys in air at 950°C.

base metal oxides are developed, leading to large weight gains. It is apparent from kinetic measurements and morphological examination, that the addition of Hf to Fe-18Cr-6Al improved the scale adherence and integrity. Figure 4 shows the effects of the addition of Ti and Hf to Fe-18Cr-6Al on thermal cycling at 1100°C. Ti and Hf greatly improve cyclic oxidation resistance. There are several mechanisms to account for the improved adhesion of alumina layers due to the reactive elements. These include: i) reduction of growth stresses in the oxide scale due to the formation of new oxide in the oxide scale, ii) elimination of the interfacial porosity, iii) the formation of a stronger scale/substrate interface, and iv) mechanical keying. The present data indicate that the formation of oxide pegs (mechanical keying) is not essential for good adherence since the oxides of Ti are not stable enough to form beneath Al_2O_3. Metallographic analysis indeed shows the complete absence of oxide protrusions for FeCrAl + Ti whereas profuse peg formation was observed for FeCrAl + Hf.

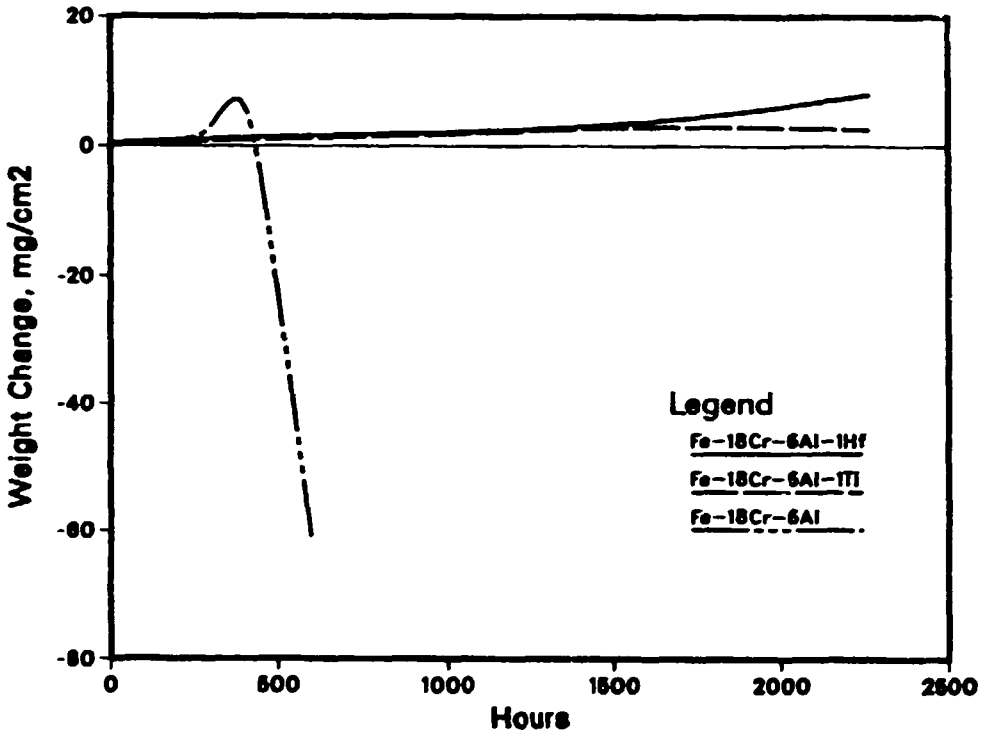

Figure 4: Weight change versus time for cyclic oxidation (one hour cycles) for Fe-18Cr-6Al, Fe-18Cr-6Al-1Hf and Fe-18Cr-6Al-1Ti in air at 1100°C.

Fe-20Si showed good cyclic oxidation resistance but underwent a marked shape change and eventually fractured. The cause of this shape change is not clearly understood, but is believed due to gradual shape changes from repeated eutectoid decomposition at 825°C upon cooling and heating during thermal cycling.[19]

Sulfidation/Oxidation

The degradation resistance of high temperature alloys and coatings can be improved by the preformation of protective oxide scales prior to exposure to sulfur bearing gases. In these experiments, all specimens were preoxidized for 30 minutes at 950°C in a H_2/H_2O gas mixture (P_{O_2} = 1.95×10^{-19} atm) to provide preformed oxide scales on the alloy surface prior to exposure to a $H_2/H_2O/H_2S$ gas mixture (P_{S_2} = 8×10^{-7}, P_{O_2} = 1.95×10^{-19} atm) unless otherwise specified. Table 1 shows how oxide scales formed on the different alloys compare in sulfur bearing gases in

Table 1: Weight changes after 4 hours of sulfidation/oxidation at 950°C.

Alloy	H_2/H_2O for 30 min. (mg/cm^2)	$H_2/H_2O/H_2S$ after 30 min. of preox. (mg/cm^2)
Fe-18Cr-6Al	0.11	1.65(3H)
Fe-18Cr-6Al-1Hf	0.10	0.30
Fe-18Cr-6Al-1Ti	0.10	0.15
Fe-25Cr	0.15	5.20
Fe-20Si	negligible	0.04

terms of weight gain. The relative resistance of preformed oxide scales to this sulfidation/oxidation atmosphere is in the order of SiO_2 former > Al_2O_3 former > Cr_2O_3 former. Figure 5 shows Fe-20Si which was preoxidized in a H_2/H_2O gas mixture at 700°C for 30 minutes and subsequently exposed to a $H_2/H_2O/H_2S$ gas mixture for 4 hours at the same temperature. Small particles of iron sulfides were

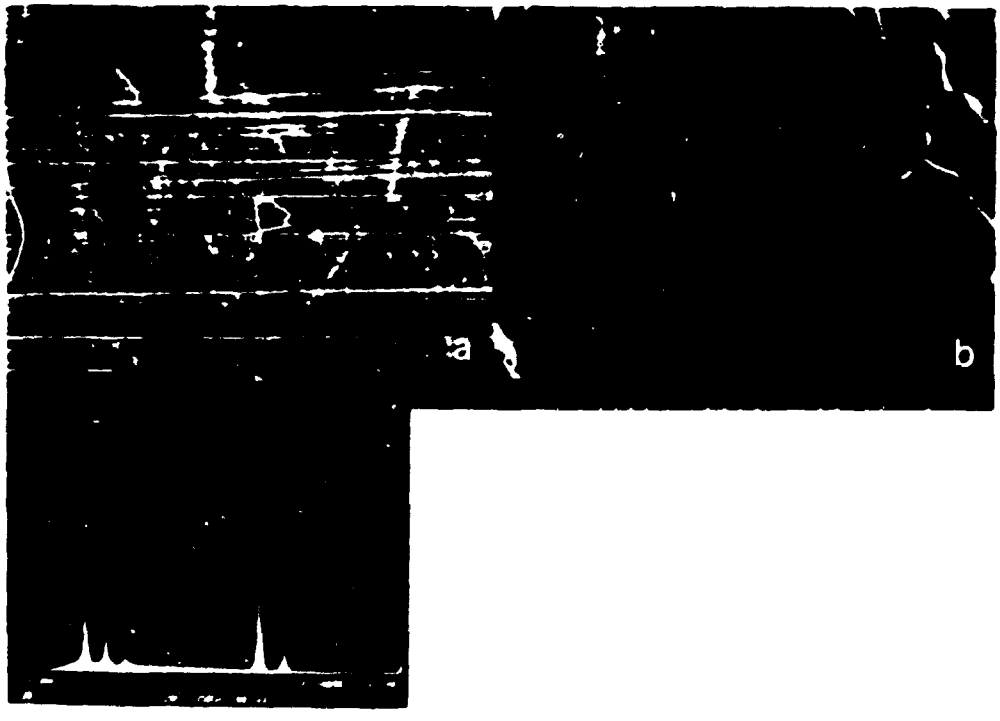

Figure 5: Fe-20Si exposed to a H_2/H_2O mixture for 30 minutes and subsequently exposed to a $H_2/H_2O/H_2S$ mixture for 4 hours at 700°C. (a) external oxide scale, (b) underside of the oxide scale and (c) EDX of particles in (a).

observed at the scale/gas interface but not at the scale/alloy interface. Overall sulfidation attack was not significant. The long term stability of these alloys in high-p_{S_2}, low-P_{O_2} atmospheres still must be determined as considerable outward diffusion of Fe through the SiO_2 surface scales has been observed for exposures in pure O_2[17]. This transport may eventually result in scale breakdown initiating at the scale/gas interface.

Breakdown of preformed Al_2O_3 scale on Fe-18Cr-6Al-1Hf and Fe-18Cr-6Al in sulfur bearing gases has been studied at 950°C.[16] The oxide scale adherence and the sulfidation/oxidation resistance of Fe-18Cr-6Al was improved by hafnium addition. The addition of Ti to Fe-18Cr-6Al improved the sulfidation/oxidation resistance in addition to the resistance to thermal cycling, as shown in Table 1. Figure 6 shows a comparison of the effect of Ti and Hf in Fe-18Cr-6Al on sulfidation/oxidation resistance. Fe-18Cr-6Al-1Ti shows better resistance in sulfur bearing gases than Fe-18Cr-6Al-1Hf. The corresponding surface morphologies of Fe-18Cr-6Al-1Ti and Fe-18Cr-6Al-1Hf after 12 hours of sulfidation/oxidation in a $H_2/H_2O/H_2S$ gas mixture following 30 minutes of preoxidation in a H_2/H_2O gas mixture at 950°C are shown in Figure 7. The Al_2O_3 scales on both Fe-18Cr-6Al-1Ti and Fe-18Cr-6Al-1Hf were cracked and spalled during cooling. The alloy substrate of Fe-18Cr-6Al-1Ti was smooth and appeared to be intact but that of Fe-18Cr-6Al-1Hf was significantly degraded. It has been shown that the HfO_2 oxide pegs formed in FeCrAl + Hf provide rapid transport paths for sulfur through the Al_2O_3 scale and initiate scale breakdown. Thus, while Hf additions extend the life of FeCrAl alloys by improving adherence they also provide phases in the scale which are vulnerable to sulfur penetration. Additions of Ti to FeCrAl, on the other hand, provide improved scale adherence without providing paths for sulfur ingress. This is believed to be responsible for the difference in corrosion rates shown in Fig. 6.

Fe-25Cr exhibited the worst sulfidation/oxidation resistance among the alloys, shown in Table 1. Figure 8 shows Fe-25Cr which was preoxidized in a H_2/H_2O gas mixture at 700°C for 30 minutes and subsequently exposed to a $H_2/H_2O/H_2S$ gas mixture for 4 hours at the same temperature. The sulfides at the scale/gas interface are considerably larger than those at the scale/alloy interface and by all indications, form first. This observation has been reported by Stirling[18] and by Perkins[19] and is in contrast to the breakdown of Cr_2O_3 scales on Ni-Cr alloys which initiates at the scale/alloy interface.

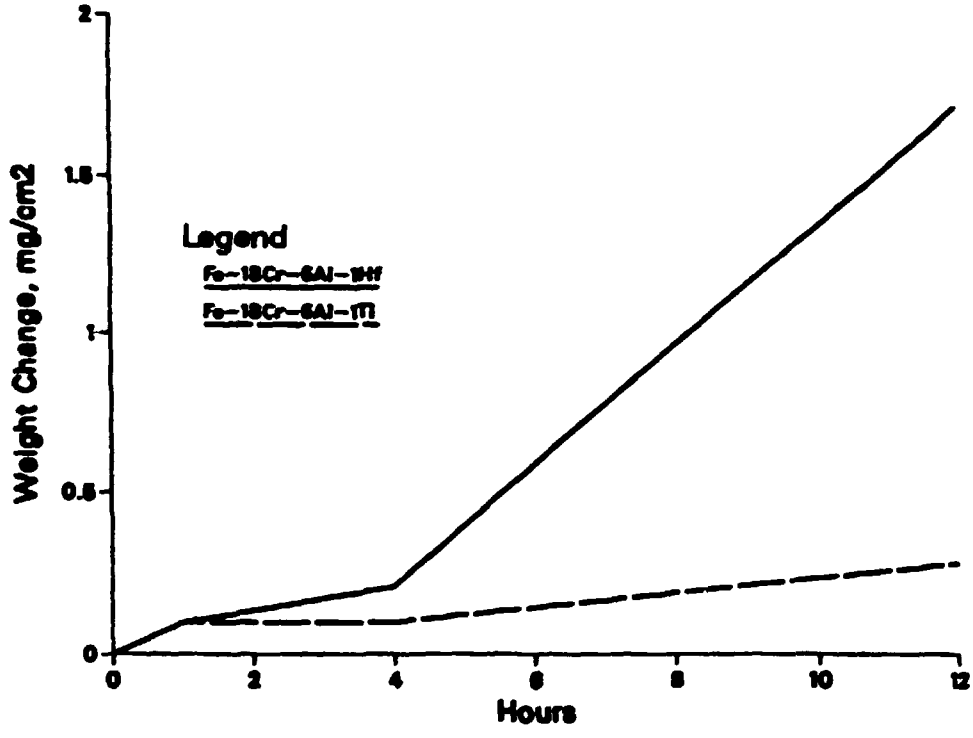

Figure 6: Weight changes vs. time for Fe-18Cr-6Al-1Ti and Fe-18Cr-6Al-1Hf which were preoxidized in a H_2/H_2O mixture and subsequently exposed to a $H_2/H_2O/H_2S$ mixture at 950°C.

a) Fe-18Cr-6Al-1Ti b) Fe-18Cr-6Al-1Hf

Figure 7: Surface morphologies of (a) Fe-Cr-Al-1Ti and (b) Fe-Cr-Al-1Hf which were preoxidized in a H_2/H_2O gas mixture for 30 minutes and subsequently exposed to a $H_2/H_2O/H_2S$ gas mixture for 12 hours at 950°C.

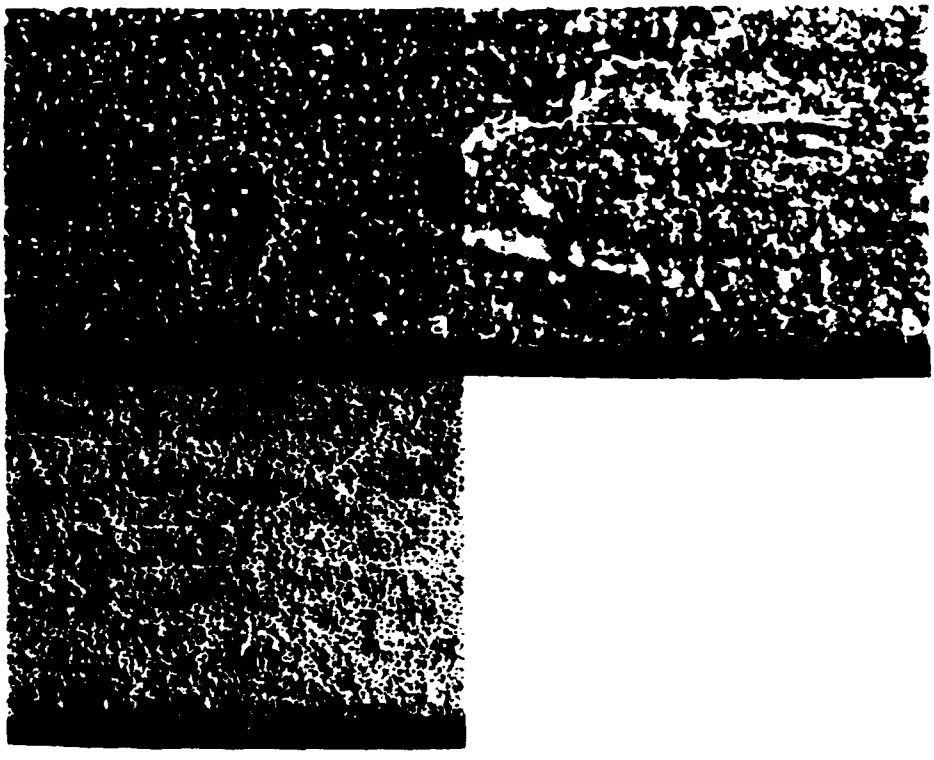

Figure 8:Fe-25Cr which was preoxidized in a H_2/H_2O gas mixture for 30 minutes and subsequently exposed to a $H_2/H_2O/H_2S$ gas mixture for 4 hours at 700°C.

CONCLUSIONS

The ferrous alloys (Fe-18Cr-6Al, Fe-18Cr-6Al-1Ti, Fe-18Cr-6Al-1Hf, Fe-25Cr and Fe-20Si) were studied between 700 and 1100°C in an oxidizing (air or H_2/H_2O) atmosphere. Then the breakdown of preformed oxide scales on these alloys was studied in a sulfidation/oxidation ($H_2/H_2O/H_2S$) atmosphere at the same temperatures.

1. The resistance to isothermal oxidation and thermal cycling in air at 950°C increases in the order of SiO_2 former > Al_2O_3 former > Cr_2O_3 former.

2. The addition of Ti to Fe-18Cr-6Al improves the resistance to cyclic oxidation and sulfidation/oxidation at 950°C. The addition of Hf improves cyclic oxidation resistance but provides rapid transport paths for sulfur through the scale.

3. The breakdown of Cr_2O_3 scales on Fe-25Cr in high-pS_2, low-pO_2 atmospheres initiates at the scale/gas interface.

4. The SiO_2 scales formed on Fe-20Si are resistant to sulfur penetration but the outward transport of Fe through the scales raises questions concerning their long term stability in high-pS_2, low pO_2 atmospheres.

REFERENCES

1. K. Natesan, "High Temperature Corrosion in Coal Gasification Systems", Corrosion, Vol. 18, 1985, pp. 646.
2. R. A. Perkins and S. J. Vonk, "Corrosion Chemistry in Low Oxygen Activity Atmospheres", Tech. report 979-6, Lockheed Palo Alto Research Laboratory, December 1979.
3. T. T. Huang, B. Peterson, D. A. Shores and E. Pfender, "XPS and AES Studies of High Temperature Corrosion Mechanism of Fe-30Cr Alloys", Corrosion Science, Vol. 24, 1984, pp. 167.
4. G. J. Yurek, M. H. LaBranche and Y. K. Kim, "Oxidation of Cr and Fe-25Cr Alloy in H_2-H_2O-H_2S Gas Mixtures at 900°C, High Temperature Corrosion in Energy Systems, M.F. Rothman, ed., AIME, 1985, pp. 295.
5. F. H. Stott, F. M. Chong and C. A. Stirling, "Preoxidation for Protection of High Temperatuare Alloys in Environments of High Sulfur and Low Oxygen Potentials Pertinent to Gasification Processes", High Temperatuare Corrosion in Energy Systems, M. F. Rothman, Ed., AIME, 1985, pp. 253.
6. A. Atkinson and J. W. Gardner, "The Diffusion of Fe^{3+} in Amorphous SiO_2 and Protective Properties of SiO_2 Layer", Corrosion Science, Vol. 21, 1981, pp. 49.
7. I. Svedung and N. G. Vannerberg, "The Influence of Silicon on the Oxidation of Iron", Corrosion Science, Vol. 14, 1974, pp. 391.
8. J. K. Tien and F. S. Pettit, "Mechanism of Oxide Adherence on Fe-25Cr-4Al (Y or Sc) Alloys", Metallurgical Transactions, Vol. 3, 1972, pp. 1587.

9. F. A. Golightly, G. C. Wood and F. H. Stott, "The Early Stage of Development of α - Al_2O_3 Scales on Fe-Cr-Al and Fe-Cr-Al-Y Alloys at High Temperature", Oxidation of Metals, Vol. 14, 1980, pp. 217.
10. F. H. Stott, F. A. Golightly and G. C. Wood, "The Influence of Yttrium Additions on the Oxide Scale Adhesion to an Iron-Chromium-Aluminum Alloy", Oxidation of Metals, Vol. 10, 1976, pp. 163.
11. F. A. Golightly, F. H. Stott and G. C. Wood, "The Influence of Yttrium Additions on the Oxide Scale Adhesion to an Iron-Chromium-Aluminum Alloy", Oxidation of Metals, Vol. 10, 1976, pp. 163.
12. F. H. Stott and M. F. Chong, "The Influence of Preoxidation on the Degradation of Alloys in Sulfur-Containing Gases at High Temperature", Corrosion Resistant Materials for Coal Conversion Systems, D. B. Meadowcroft and M. I. Manning, ed., Applied Science Publishers, London and New York, 1983, pp. 491.
13. F. H. Stott, G. C. Wood and F. A. Golightly, "The Isothermal Oxidation Behavior of Fe-Cr-Al and Fe-Cr-Al-Y Alloys at 1200 C^o, Corrosion Science, Vol. 19, 1979, pp. 869.
14. G. H. Meier and E. A. Gulbransen, "Thermochemical Stability Diagrams for Condensed Phases and Volatility Diagrams of Volatile Species over Condensed Phases in Twenty Metal-Sulfur-Oxygen Systems Between 1150 -1450^{o}K", DOE Report on Contract No DE-AC-01-79-ET-13547, 1980
15. O. Kubaschewski and C. B. Alcock, Metallurgical Thermochemistry, Pergamon Press, New York, 1979.
16. G. M. Kim, The Breakdown of Preformed Oxide Scales on Ni-30Cr, Fe-18Cr-6Al-1Hf and Ni-20Si in Sulfur and Carbon-Bearing Gases, PhD Dissertation, University of Pittsburgh, 1986.
17. T. Adachi and G. H. Meier, to appear in Oxidation of Metals, 1987.
18. C. A. Stirling, The Influence of Preformed Cr_2O_3 Scales on the High Temperature Corrosion of Alloys in Sulfur-Containing Gases, PhD. Dissertation, University of Manchester, 1985.
19. R. A. Perkins "Corrosion Chemistry in Low Oxygen Activity Atmospheres", Final Report on EPRI Project 979-6 (1982).

THE EFFECTS OF MICROALLOY CONSTITUENTS ON THE FORMATION AND BREAKDOWN OF PROTECTIVE OXIDE SCALES ON HIGH-TEMPERATURE ALLOYS FOR USE IN THE FOSSIL ENERGY INDUSTRY

I. G. Wright and J. A. Colwell

Battelle Columbus Division
505 King Ave., Columbus, Ohio 43201

OBJECTIVES

The objectives of this program are (1) to gain an improved understanding of the effects of alloying constituents present at low levels on the development and mode of breakdown of protective oxide scales in conditions representing those encountered in combustion and gasification processes, and (2) to achieve better control over the growth of scales which will contribute to improvements in long-term high-temperature corrosion resistance of heat exchanger and heat recovery materials.

ISSUES

The intended operating conditions of the alloys studied in this program are the temperature range of 500 to 700C, in an environment representative of the most severe encountered in projected combustion or gasification processing. These raise two major issues. The first concerns the compatibility of the information to be produced with the existing database for alloys of the type considered: essentially all of the mechanistic understanding for microalloying effects was developed at temperatures above 800C, with most studies concentrated in the range 1000 to 1100C. It is therefore likely that the accepted mechanisms of oxidation will be significantly modified in the temperature range of interest, since the relative kinetics of the competing

reactions may be different. This will affect the assumptions based on the oxidation behavior of alloys known to reliably form given protective scales at higher temperatures (minimum alloying levels to form particular oxides), and will directly impact the tentative understanding of the ways in which the often powerful effects of microalloying additions are brought about. The second issue concerns the choice of environment to be used in this study. It is imperative that the gas mixtures used be sufficiently well characterized that mechanistic interpretations can be made from the results, while maintaining a close relationship with real process environments. As discussed later, this forces some difficult choices, which must be resolved by initial experimentation.

APPROACH

The approach adopted involves the evaluation of the effects of a range of elements used as minor additions to three base alloy compositions. The effects of these additions on the development of protective scales will be assessed through comparison with the corrosion kinetics and scale morphologies of the base alloys developed in exposures in specific gas mixtures. In addition, limited comparisons will be made of the initial stages of scale development on the base alloys, and of the effects of some of the minor additions, using an Auger electron spectroscopy/X-ray photoelectron spectroscopy (AES/XPS) analytical chamber equipped with a scanning electron microscope. In this, the surface composition and chemical bonding in the scales will be monitored as a function of time in a constant gaseous environment, and as a function of variations in a changing gaseous environment. Experiments are also planned to provide links with the more conventional thermobalance studies, to ensure the validity of these in situ studies.

The effects of selected additions on the breakdown of protective scales will be characterized from the exposure in aggressive gas mixtures of pre-formed scales on the base alloys and on alloys containing these alloying, additions, using a combination of thermobalance and muffle furnace exposures.

The rationale for the choices of base alloys, additions, and exposure conditions is discussed in the following sections.

BASE ALLOYS

The base alloys chosen for study contain 25 percent by weight of chromium to ensure that continuous, protective scales of Cr_2O_3 are reliably formed. The 18Cr-based stainless steels are widely used in practice in the temperature range of interest, but 18% Cr is considered marginal for the formation and maintenance of a continuous, protective scale. In this program it was considered prudent to select alloys with an effective reservoir of the basic scale-forming element. It is noted that the choice of 25% Cr as a baseline does not allow for the exploitation of the possible effects of some microalloy additions to reduce the bulk chromium level necessary for the formation of a protective scale; such effects, if suggested by results, could be further explored later in the program if warranted by considerations such as alloy fabricability.

The base alloy compositions are:

(a) Fe-25Cr, which is essentially an analogue of type 446 stainless steel,
(b) Fe-25Cr-20Ni, an analogue of type 310 stainless steel, and
(c) Fe-25Cr-6Al, which is based on the basic Kanthal-type chemistry.

While alloys (a) and (b) are expected to form continuous, protective chromia scales, alloy (c) is intended to be an alumina-former. Alloys of the FeCrAl-type intended for use at temperatures of 1000C or higher typically contain up to 4% Al; information from the literature indicates that such alloys do not form a continuous film of alpha alumina at temperatures below 800C or so. The aluminum content of alloy (c) was boosted to 6% in an attempt to increase the probability of forming an alumina scale, although there is little evidence to suggest that this will occur. In addition, 6% Al is near to the practical limit in a wrought alloy.

ALLOYING ADDITIONS

The alloying additions of interest in this program can be categorized as:

(i) Common alloying additions, which include those typically present as a result of refining operations and elements added for high-temperature strenghtening purposes. Elements chosen in this category are Mn, Si, and Al (Al added to alloys (a) and (b)). All three of these elements have a high affinity for oxygen, while Mn forms very stable sulfides and may play a key role in determining the sulfidation resistance of alloys.

(ii) Reactive elements added for their special effects on grain refining or on oxidation resistance. Additions representative of this class are Y and Hf.

(iii) Stable oxide dispersions, initially incorporated for improved high-temperature creep strength, but also found capable of exerting significant beneficial effects on oxidation behavior, especially for chromia-formers. Yttria, Y_2O_3, was chosen in this category.

(iv) Other elements chosen for specific effects. Examples are Pt, which has been used to improve the performance of protective aluminide coatings for gas turbine blades, ostensibly by increasing the activity of aluminum in the coatings, and Nb (as NbC) which is employed to stabilize the carbides in some austenitic stainless steels, and which becomes effectively distributed in the alloy grain boundaries, possibly modifying their character.

OTHER CONSIDERATIONS

The sequence of kinetic events which occurs in the initial stages of high-temperature corrosion has a large influence on the detailed morphology of the scale, hence on the subsequent corrosion behavior of the alloy. Among other factors besides bulk alloy chemistry which can affect this sequence of events, are the distribution of reactive elements in the alloy surface, and the alloy surface finish. In order to exert control over the distribution of the microalloy constituents in the experimental alloys, different methods will be used to incorporate some of them into the base alloys. These include:

(1) bulk alloying, of elements at levels above and below their solubility limits in the base alloys,

(2) rapid solidification followed by consolidation, with levels of elements significantly above, as well as below their solubility limits, to obtain controlled microstructures with uniform distributions of the elements of interest,

(3) solid state alloying through high-energy milling and consolidation of alloy powders, to introduce controlled dispersions of yttria,

(4) ion implantation to achieve uniform surface distributions of yttrium, hafnium, and platinum, and

(5) overlay coating by sputtering of platinum (followed by a diffusion treatment) or by physical vapor deposition of yttrium- or hafnium-containing base alloys, to achieve high concentrations and uniform distributions of the desired elements.

Details of the elemental additions to be made to the base alloys, alloy compositions, and methods of incorporation are given in Table 1.

Table 1
NOMINAL COMPOSITIONS OF MICROALLOYED MATERIALS

	Concentration, weight percent						
Base Alloy	Y	Hf	Si	Al	Mn	NbC	Pt
(a) Bulk Alloying							
Fe-25Cr	0.1, 1.0	0.1, 1.0	1.0, 3.0	1.0, 2.0	2.0	--	--
Fe-25Cr-20Ni	0.1, 1.0	0.1, 1.0	1.0, 3.0	1.0, 2.0	2.0	--	--
Fe-25Cr-6Al	0.1, 1.0	0.1, 1.0	1.0, 3.0	--	2.0	--	--
(b) Rapid Solidification							
Fe-25Cr-20Ni	0.1, 1.0	--	1.0, 6.0	--	--	1.5	--
Fe-25Cr-6Al	0.1, 1.0	--	1.0, 6.0	--	--	--	--
(c) High Energy Milling							
Fe-25Cr-20Ni	2.0 (Y_2O_3)	--	--	--	--	--	--
Fe-25Cr-6Al	2.0 (Y_2O_3)	--	--	--	--	--	--
(d) Ion Implantation							
Fe-25Cr-20Ni	10^{17}	10^{17}	--	--	--	--	10^{16}
Fe-25Cr-6Al	10^{17}	10^{17}	--	--	--	--	10^{16}
(e) Overlay Coating							
Fe-25Cr	--	--	--	--	--	--	TBD
Fe-25Cr-20Ni	1.0	1.0	--	--	--	--	TBD
Fe-25Cr-6Al	1.0	1.0	--	--	--	--	TBD

The effects of surface finish on the development of scales on these alloys will not be investigated in any detail this program. A single surface finish, for instance 0.5 micron diamond, will be used as a basis for comparison.

PROGRESS

LITERATURE REVIEW

As mentioned above, the majority of the studies of high-temperature corrosion reported in the open literature are concerned with temperatures significantly higher than those of interest in this program. Nevertheless, it is anticipated that there is a mechanistic thread that can be traced back from these studies to provide at least some guidelines for use at lower temperatures. The literature survey was organized so that a detailed search was made for the last ten years, while reliance was placed on available reviews and compilations for earlier work.

Information of direct relevance was found in three areas: oxidation studies of FeCrAl-type alloys by Bennett and co-workers at Harwell, UK[1], mixed gas (coal gasification) studies by Natesan and co-workers at Argonne National Labs.[2], and by Japanese groups[3], and alloy development programs for improved steam boilers, particularly by Rehn et al at Foster Wheeler[4] and by Babcock-Hitachi[5] and Mitsubishi[6] in Japan. Essentially no information was found to allow comparisons of the extent of the effects to be expected of microalloy additions on the high-temperature corrosion behavior of austenitic versus ferritic alloys, with or without microalloy additions, in the 500 to 700C temperature range.

At higher temperatures, there have been significant advances in approaches to explaining some of the effects of rare earth and rare earth oxide additions. In particular, Nagai's group at Osaka University has made some valuable contributions[7], using electrical conductivity measurements to demonstrate the types of effects exerted by dopants such as NiO, CeO_2, and Gd_2O_3 on the oxygen pressure dependence

of the conductivity of Cr_2O_3. A number of studies has made use of modern surface analytical tools in the characterization of scales formed in various environments, but in general these have not been linked to questions raised by mechanisms proposed to explain critical high-temperature corrosion issues.

Little progress was reported in the measurement of stresses or strains experienced by growing oxide scales, or in understanding the interactions between corrosion and applied stress.

ALLOY PREPARATION

Master heats of the three base alloys were prepared by Carpenter Technology Corp. for use by all participants in the program. These were nominally 60 kg. heats which were produced by induction melting in vacuum, followed by electro-slag remelting, casting into 7.6 to 8.3 cm round ingots, and hot forging into bar stock of 2.5 x 2.5 cm cross section. The analyses of the finished alloys are given in Table 2; the desired compositions were accurately met, and the content of tramp elements (especially Mn, Si, and S) was commendably low.

The alloys containing the microalloying additions specified in Table 1, which are to be added by bulk alloying, will use the master alloy stock as starting material. These alloys will be produced by the Ames Laboratory Materials Preparation Center by vacuum tungsten arc remelting and drop casting into 1.5 cm x 9.0 cm ingots. The master alloys will also be used as the starting materials for those alloys to which additions are to be made by ion implantation, and by overlay coating. Pure elemental sources have been used for the alloys prepared by rapid solidification processing and by powder processing in order to expedite their production.

EXPOSURES

In order to assess the likely oxidation rates, and the composition, morphology and mechanical behavior of the scales formed on the base alloys, isothermal and cyclic oxidation runs were made in dried

oxygen at 700C using samples of types 310 and 446 stainless steels. The compositions of these alloys are shown in Table 2. The isothermal oxidation kinetics at 700C in 0.13 atm. dry oxygen for both alloys were very slow, with rates approximating to a parabolic rate constant of about 2.5×10^{-13} gcm^{-4}s^{-1}, and scale thicknesses after 25hr. of about 0.25μm. Exposure to thermal cycling, in which each cycle comprised 0.75hr. at 700C and 0.25 hr. cooling to about 100C and then reheating to 700C, resulted in some scale spallation from both alloys, with the greatest effect on type 446 stainless steel. Examples of the cyclic oxidation kinetics and of the oxide scales formed are shown in Figs. 1 and 2. Note the very small weight changes experienced by type 310 stainless steel, and the thin (about 0.3μm) uniform external oxide formed. While type 446 stainless steel suffered relatively more scale spallation, which resulted in the formation of some iron-rich transient oxide, protective chromium-rich scales always reformed after the maximum exposures of 300 hr which were made. Based on these results, it is clear that relatively short duration cyclic runs in air will not be sufficient to develop easily discernible differences between the various microalloy additions on the type 310 analogue. Consequently, future work will concentrate on more aggressive environments which contain sulfur.

As a means of selecting a sulfidizing environment which is consistent with the goals of this program, namely that the corrosion conditions be sufficiently well defined and controlled to allow unambiguous interpretation of the corrosion morphologies and the effects of the alloying additions, the Ellingham-Pourbaix phase stability diagrams for the Fe-O-S, Ni-O-S, and Cr-O-S systems at 700C were constructed. These are shown in Fig 3. A gas mixture that has the same general oxygen and sulfur partial pressures as those generated in combustion and gasification processes, that is sufficiently removed from the thermodynamic phase boundaries that the expected corrosion products can be identified with some confidence (while taking note of the concept of kinetic phase boundaries), and that can be experimentally attained with good accuracy, is represented by oxygen and sulfur partial pressures of 10^{-20} and $10^{-6.5}$ atm., respectively. This is noted by the star on each

Table 2
BASE ALLOY COMPOSITIONS

Alloy	Heat No.	Producer	Weight Percent							
			Ni	Cr	Al	C	Mn	Si	P	S
Fe-25Cr	T08007	Carpenter Technology	<0.01	25.04	<0.01	0.001	<0.01	<0.01	<0.005	0.003
Fe-20Ni-25Cr	T08008	Carpenter Technology	19.91	24.84	0.01	0.004	<0.01	<0.01	<0.005	0.002
Fe-25Cr-6Al	T08009	Carpenter Technology	<0.01	24.62	5.88	0.004	<0.01	<0.01	<0.005	0.003
AISI 310			19.02	24.71	--	0.06	1.76	0.72	0.027	0.017
AISI 446	6050210	Republic Steel	0.26	24.00	--	0.146	0.78	0.44	0.020	0.011

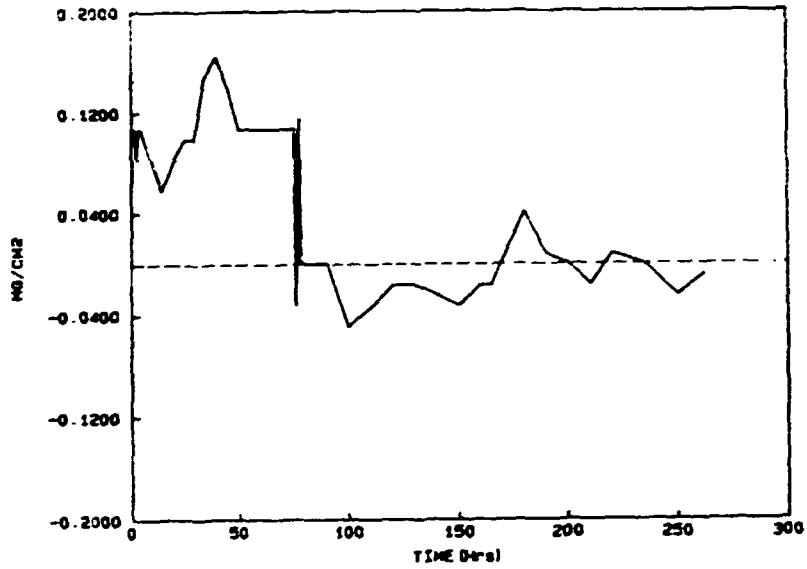

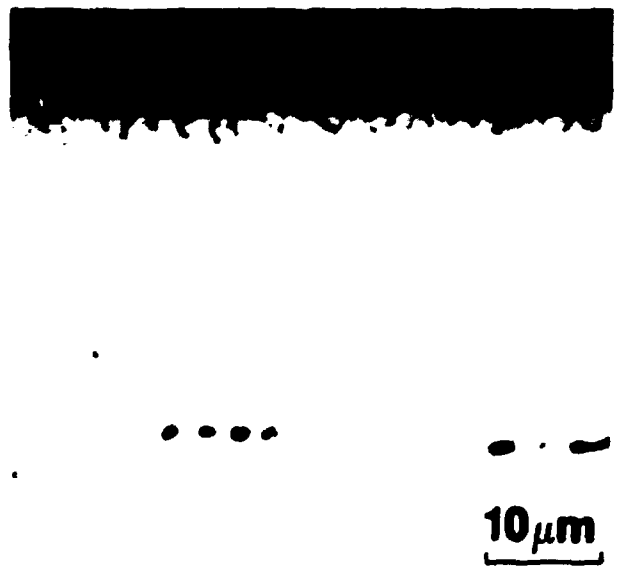

Figure 1. Oxidation kinetics and cross section of final scale on type 310 stainless steel subjected to cyclic oxidation at 700°C in 0.13 atm dry oxygen for 262 hr. (One cycle = 0.75 hr at 700°C, then cooled to ~100°C for 0.25 hr.)

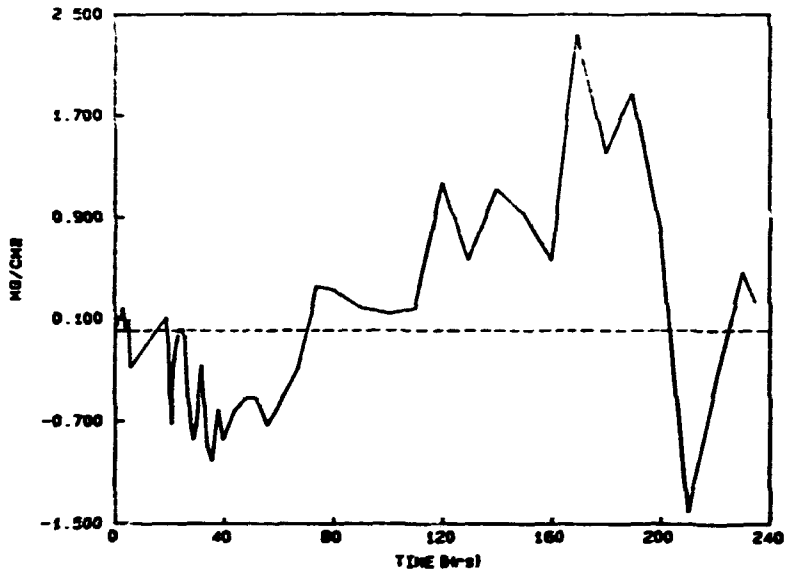

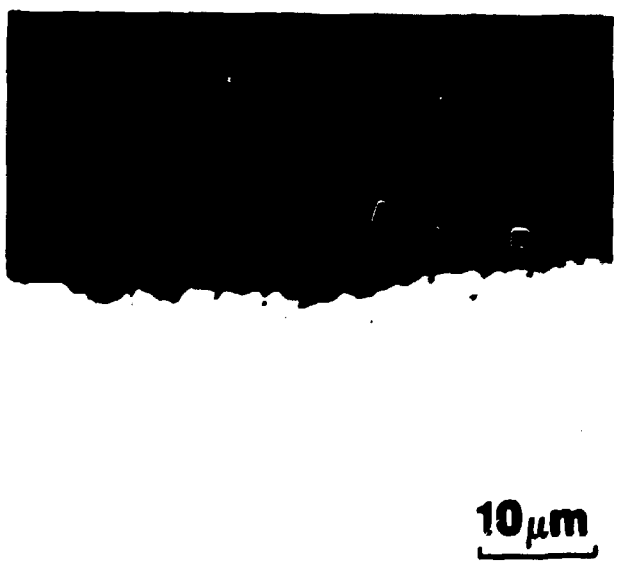

Figure 2. Oxidation kinetics and cross section of final scale on type 446 stainless steel subjected to cyclic oxidation at 700°C in 0.13 atm dry oxygen for 235 hr. (One cycle = 0.75 h at 700°C, then cooled to ∿100°C for 0.25 hr.)

(A) Fe-rich
(B) Cr-rich

of the diagrams in Figure 3. Such conditions are most simply attained through the use of gas mixtures of $H_2/H_2O/H_2S$ or $CO/CO_2/COS$, which can be equilibrated in typical laboratory corrosion apparatus by standard techniques. A point of considerable interest is that, for the desired gas partial pressures, the total number of moles of sulfur required by the $H_2/H_2O/H_2S$ mixture is ten times that required by the $CO/CO_2/COS$ mixture. This difference, together with the possibility of the reaction of carbon in the latter mixture with the alloys at some point in the corrosion process, suggests that there is the possibility that the kinetics of the corrosion process in the $CO/CO_2/COS$ mixture may significantly modify the corrosion morphologies expected from thermodynamic considerations. These gas mixtures with nominally equivalent oxidizing and sulfidizing potentials may, in fact, lead to quite different corrosion morphologies. Since all of the gaseous species represented in these mixtures are likely to be present in process gases, careful justification is required before one of these mixtures is rejected from further consideration.

FUTURE PLANS

The next series of corrosion exposures will involve a comparison of the isothermal kinetics and scale morphologies resulting from reaction of the three base alloys with $CO/CO_2/COS$ and $H_2/H_2O/H_2S$ gas mixtures intended to have identical oxygen and sulfur partial pressures (10^{-20} and $10^{-6.5}$ atm. respectively) at 700C. Analysis of these results will be used to select the exposure conditions to be used for the initial characterization of the corrosion behavior of the range of alloys listed in Table 1. It is intended that the conditions selected will be sufficiently severe to discriminate among the effects of the various alloying additions, while being sufficiently well-controlled to facilitate characterization and interpretation of the reactions which have occurred. The exposures will be made at 700C. The first runs will employ isothermal conditions; if the use of only one gas mixture can be justified for screening the corrosion behavior, consideration will be given to additional runs under thermal cycling conditions. The

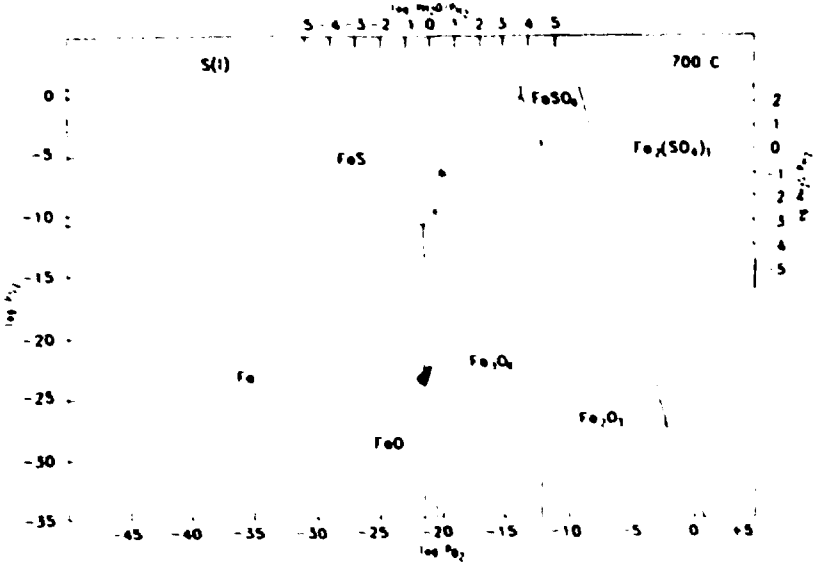

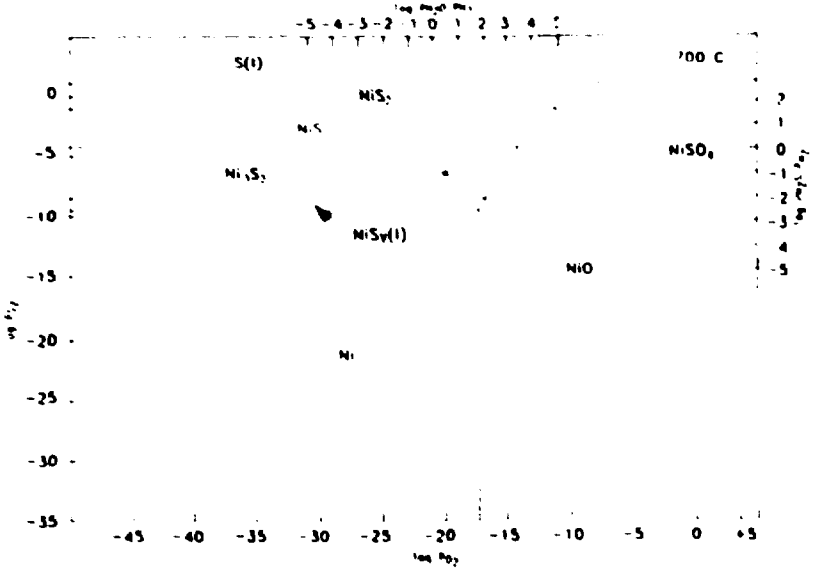

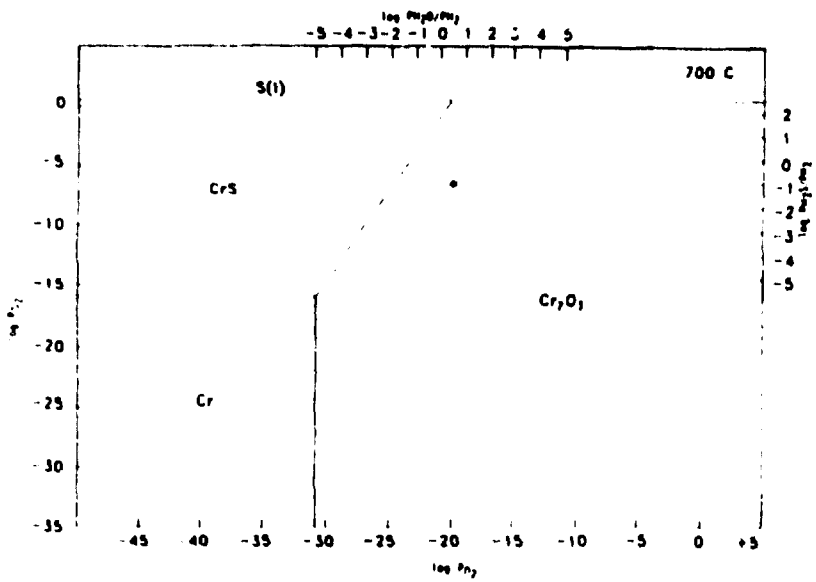

Figure 3. Phase stability diagrams for the Fe-, Cr-, and Ni-O-S systems at 700°C.

techniques to be used for characterization of the scales are standard optical metallography (where sufficiently thick scales are formed), X-ray diffraction analysis of specific areas or layers, and energy dispersive X-ray analysis/electron microprobe analysis of polished or fractured cross sections.

REFERENCES

(1) M.J.Bennett, private communication with I.G.Wright, Battelle Columbus Division, Nov. 1986.

(2) See, for instance, D.J.Baxter and K.Natesan, Corr. Sci., 26(2) 153 (1986).

(3) See, for instance, S.Kihara et al, "Corrosion Resistance of High Chromium Steels in Coal Gasification Atmospheres", paper no. 101, CORROSION/86, NACE (1986).

(4) I.M.Rehn, "Laboratory Fireside Corrosion Evaluation of Improved Superheater Tube Alloys and Coatings", EPRI CS3184, June 1983.

(5) K.Tamura et al, "Study on Applicability of Tubing and Piping Materials for Improved Coal-Fired Power Boiler", Proc. First Int. Conf. on Improved Coal-Fired Power Plants, EPRI, (1986).

(6) F. Masuyama and H.Haneda, "Update Survey and Evaluation of Materials for Steam Generators for Improved Coal-Fired Power Plants", ibid.

(7) H.Nagai, S.Ishikawa, N.Amano, and K.Shoji, Trans. Jap. Inst. Metals, 26 (10) 753 (1985).

INVESTIGATION OF THE EFFECTS OF MICROALLOY CONSTITUTENTS, SURFACE TREATMENT AND OXIDATION CONDITIONS ON THE DEVELOPMENT AND BREAKDOWN OF PROTECTIVE OXIDE SCALES

K. Vedula, G. M. Michal, T. E. Michell, G. Welsch,
I. Grobis and S. Chang

Department of Metallurgy and Materials Science
Case Western Reserve University
Cleveland, Ohio 44106

ABSTRACT

The initial results of a program designed to define the factors that effect the protectiveness of oxide scales formed in mixed S_2/O_2 atmosphere environments are presented. Scale formations on Fe-25Cr and Fe-25Cr-20Ni alloys which are chromia formers and an Fe-25Cr-6Al alloy which is an alumina former have been determined at 700°C under an SO_2 atmosphere. These preliminary results indicate that the alumina forming alloy is superior to the chromia forming alloy under the conditions examined. An analysis of the thermodynamic activities of the major constitutents of the three alloys has been conducted, and oxide/sulfied stability diagrams for the elements Fe, Cr, Ni and Al at these activity levels have been constructed.

INTRODUCTION

The focus of the current program is to obtain a better understanding of material behavior in fossil energy environments. The particular emphasis is on the effects of reactive element additions or the protectiveness of oxide scales formed in atmospheres containing high pS_2/pO_2 ratios. Iron based alloys, including Fe-25Cr and Fe-25Cr-20Ni which are Cr_2O_3formers and Fe-25Cr-6Al which is an Al_2O_3 formers, are the base alloys for this investigation.

Conventional alloying as well as ion-implantation will be the techniques for incorporating the reactive elements into the base alloys.

The results of preliminary testing of the three base alloys are presented and discussed herein. Scale formation on the base alloys subjected to an atmosphere of pure SO_2 at 700°C has been determined using optical and scanning electron microscopy (SEM) and energy dispersive X-ray spectrocopy (EDS). Also included is an analysis of the theremodynamic activities of the major constituents of the base alloys and oxide/sulfide stability diagrams for those elements determined for those activity levels.

MATERIALS AND EXPERIMENTAL PROCEDURES

The three base alloys were obtained from Carpenter Technology Corporation. The alloys were prepared by Vacuum Induction Melting (VIM) followed by Electro-Slag Refining (ERS) to minimize undesirable contaminants. After VIM the alloys were cast into 3.25" round ingots. The chemical analyses of these ingots (provided by Carpenter Technology) is shown in Table 1:

Table 1. Chemical Analyses of VIM Ingots (weight per cent)

Alloy	C	Mn	Si	P	S	Cr	Ni	Al
Fe-25Cr	.001	<.01	<.01	<.005	.003	25.04	<.01	<.01
Fe-25Cr-20Ni	.004	<.01	<.01	<.005	.002	24.84	19.91	.01
Fe-25Cr-6Al	.004	<.01	<.001	<.005	.003	24.62	<.01	5.88

After ESR, the alloys were cast into 5.80" round ingots. These ingots were then soaked at 1176C (2150F) for the Fe-25Cr-20Ni alloy and at 1065C (1950F) for the other two alloys for two hours, before forging into 2.25" squares. The forged alloys were hot cut and reheated to the soaking temperature, except for the Fe-25Cr-6Al alloy which was cold cut before reheating. The reheated alloys were soaked for half an hour, hot rolled into 1" suqares and slowly cooled into vermiculite.

Two sets of experiments were conducted on coupons from the as-hot-rolled alloys 1mm thick, sliced perpendicular to the rolling direction. In the first set of experiments, one coupon of each alloy was tested. One side of each coupon was polished to 600 micron grit paper and the other side was polished to 0.25 micron diamond paste. The coupons were placed in an alumina crucible in an inclined position. In the second set of experiments, three coupons of each alloy were tested. Each coupon was given the identical surface polish on both sides this time. One coupon of each alloy was polished to 600 micron grit paper, another coupon to the 0.25 micron diamond paste and the third coupon to a 0.05 micron Al_2O_3 paste finish. For both sets of experiments the coupons were exposed to SO_2 at atmosphereic pressure at 700°C for 162 hours in a horizontal tube furnace.

EXPERIMENTAL RESULTS

FIRST SERIES OF COUPONS

The major observation was that the Cr_2O_3 forming alloys (Fe-25Cr and Fe-25Cr-20Ni) corroded severely, whereas the Al_2O_3 forming alloy (Fe-25Cr-6Al) remained almost unaffected. Figure 1, which is a macro picture comparing the 600 grit surfaces of the three coupons illustrated some of the differences, although the contrast is lost to some extent in the pictures. Another significant observation was that the 600 micron surface showed much more severe reaction than the 0.25 micron surface in the Cr_2O_3 forming alloys.

Scanning electron micrographs of the Fe-25Cr-20Ni alloy after testing show that the morphology of the scale is somewhat different on the two sides of the coupon as shown in Fig. 2, suggesting that the corrosion process is very sensitive to the surface preparation. However, the 600 micron surface was directly exposed to the flowing gas, whereas the 0.25 micron surface may have been sheltered due

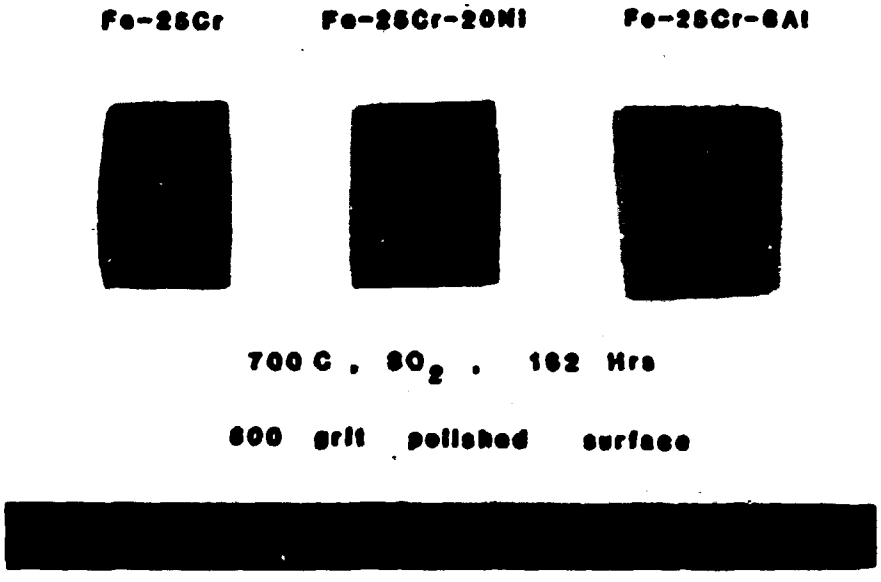

Figure 1. Tested specimens from first experimer

to the positioning of the coupon in the crucible. The origin of the differences in the scale formed on the two sides of the coupon needs to be investigated further, particularly since the differences were not as dramatic in the second experient to be described later.

The EDS sulfur map of the areas in the micrographs in Fig. 2 show that the protrusions on scale surface are sulfur rich and hence, probably sulfides. The background on the 0.25 micron surface shows evidence of cracking.

The corroded sample of Fe-25Cr-20Ni was fractured to reveal the transverse morphology of the scale. Figure 3 shows a portion of the cracked, partially adherent scale sitting on the 600 micron side of the alloy substrate along with some of the obviously spalled regions on the alloying surface. EDS analysis shows that the alloy substrate away from the interface (region A) contains the expected elements Fe, Ni and Cr. The alloy substrate adjacent to the scale (region B) reveals a significant depletion of chromium. The exposed surface of the spalled region (region C) also indicates a depletion

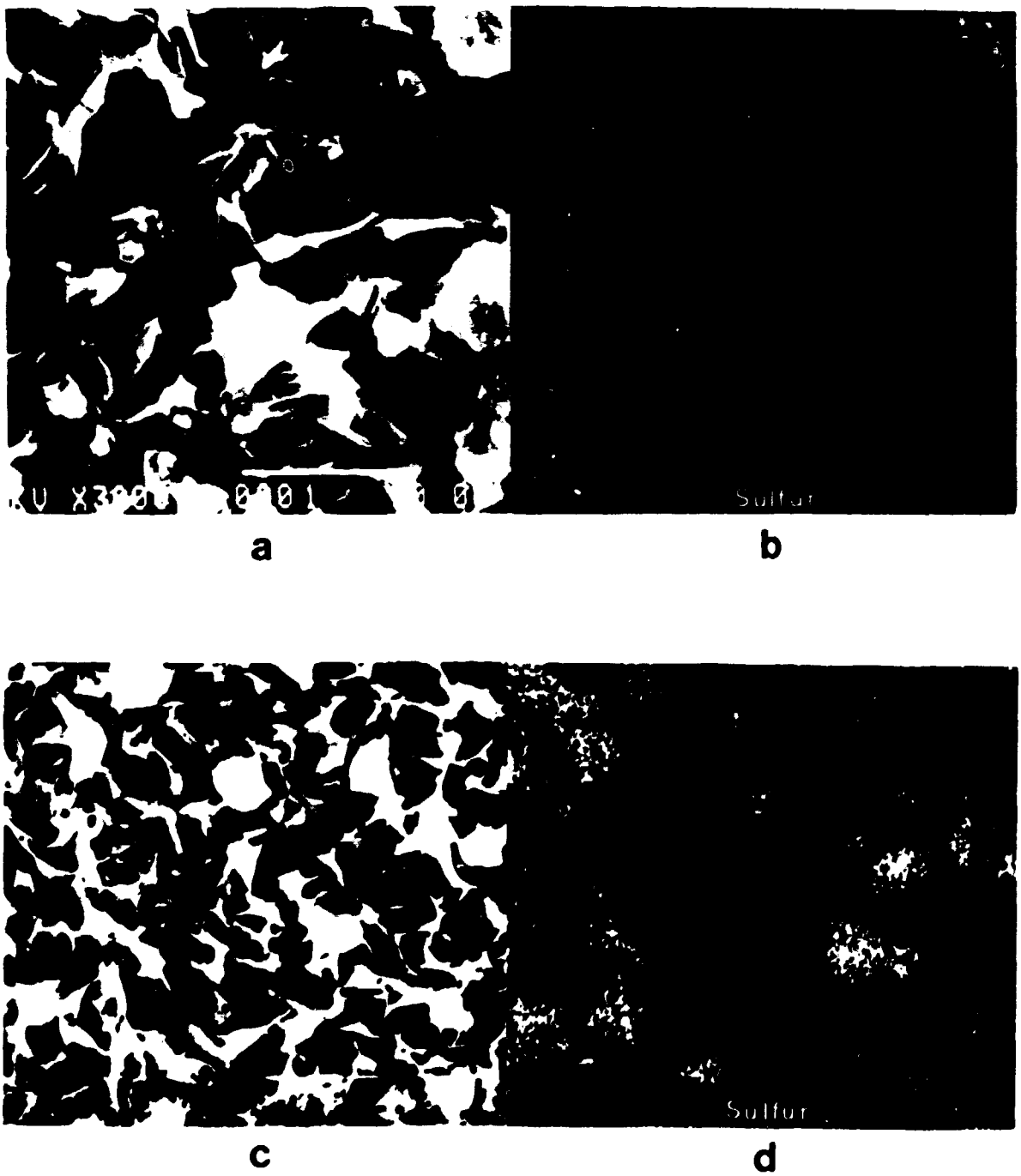

Figure 2. SEM micrographs and corresponding EDS sulfur maps for Fe-25Cr-20Ni specimen surface tested at 700C for 162 hours in SO_2 at 1 atmosphere: (a,b) 0.25 micron side and (c,d) 600 grit side.

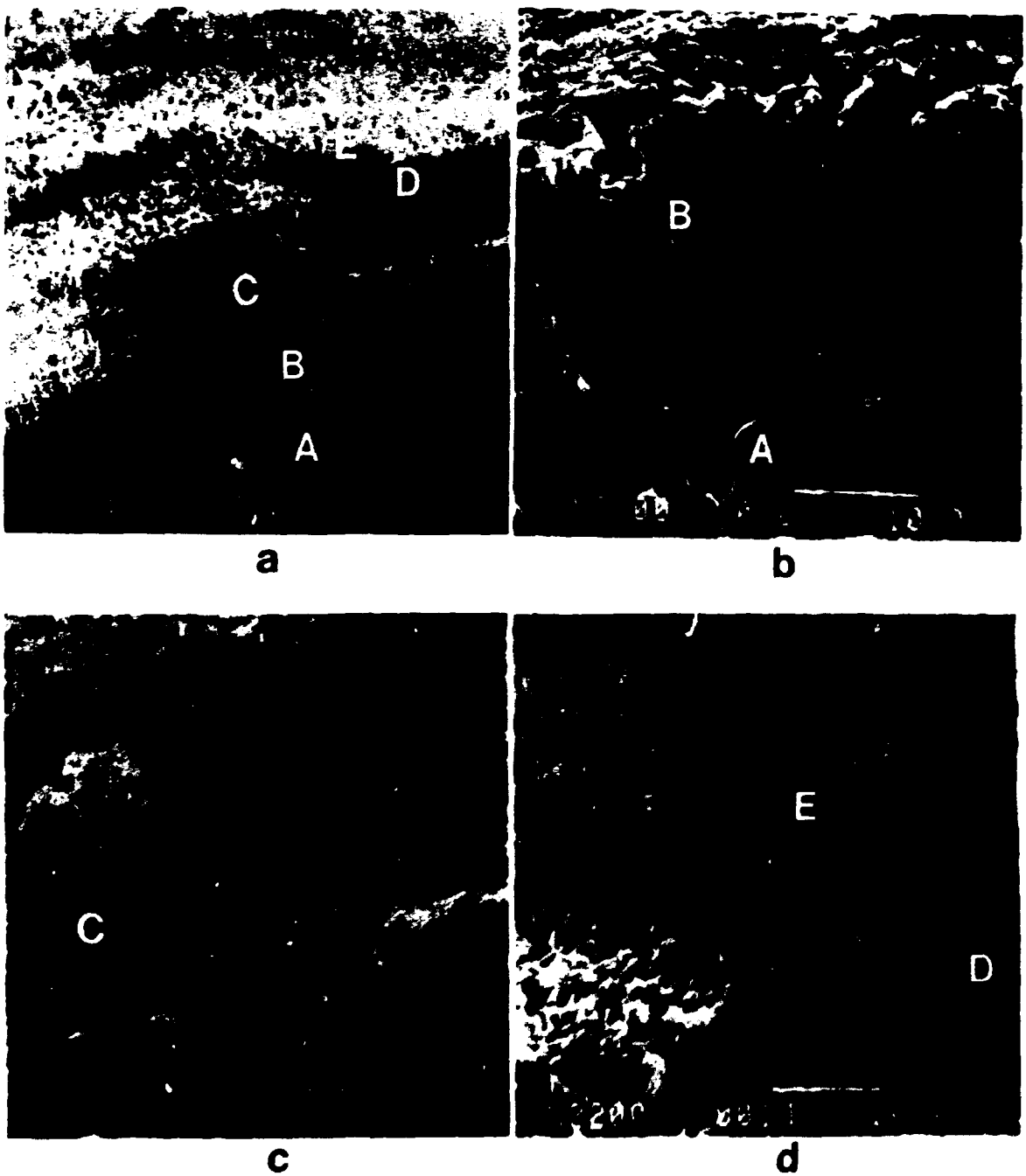

Figure 3. SEM micrographs of transverse fracture of Fe-25Cr-20Ni tested at 700C for 162 hours in SO_2 at 1 atmosphere. (a) Low magnification view of the scale layers. (b) Enlargement of regions A and B, (c) Enlargement of region C, (d) Enlargement of region D and E.

of chromium along with a small amount of sulfur. The actual scale consists of two layers (as shown in the enlarged Fig. 4 as well): i) a more compact inner layer which is chromium rich and has only a small amount of sulfur (region D) and ii) a layer on top of it which consists of nodules and blades (region E). The top layer consisting of blades and noduules is very rich in sulfur as well as in chromium.

These observations suggest that chromium has diffused out of the alloy substrate and formed a scale which appears to be a chromium rich sulfide on the outside and an inner layer which may be a chromium rich oxide or a mixture of chromium rich oxide and sulfide. The gaps between the scale and the alloy as well as the cracks in the scale suggest that the scale is very unprotective. The cracks and gaps may have formed during the cooling of the specimen or during the fracture of the specimen.

The scale on the Fe-25Cr alloy appe. to have features similar to that on the Fe-25Cr-20Ni alloy described above, whereas the scale on the Fe-25Cr-6Al alloy is almost non-existent except for a few aluminum rich nodules (presumably oxides). Figure 5 illustrates the scales of these two alloys on the 600 grit side of the coupons.

SECOND SERIES OF COUPONS

The dramatic differences between the Cr_2O_3 forming alloys and the Al_2O_3 forming alloy were reproduced as shown in macro pictures of the 0.25 micron surface of the three alloys in Fig. 6. The Fe-25Cr-6Al alloy remained intact, whereas the other two alloys corroded badly. In fact, a distinct difference between the two Cr_2O_3 forming alloys was observed in this experiment. The ferritic Fe-25Cr alloy developed a uniform dark bluish green scale which remained intact during cooling of the specimen, whereas the austenitic Fe-25Cr-20Ni alloy developed a more greyish scale which spalled extensively during the cooling to room temperature.

Figure 4. SEM micrograph (4000X) of transverse surface of scale including regions D and E from Fig. 3 for Fe-25Cr-20Ni specimen tested at 700C for 162 hours in SO_2 at 1 atmosphere.

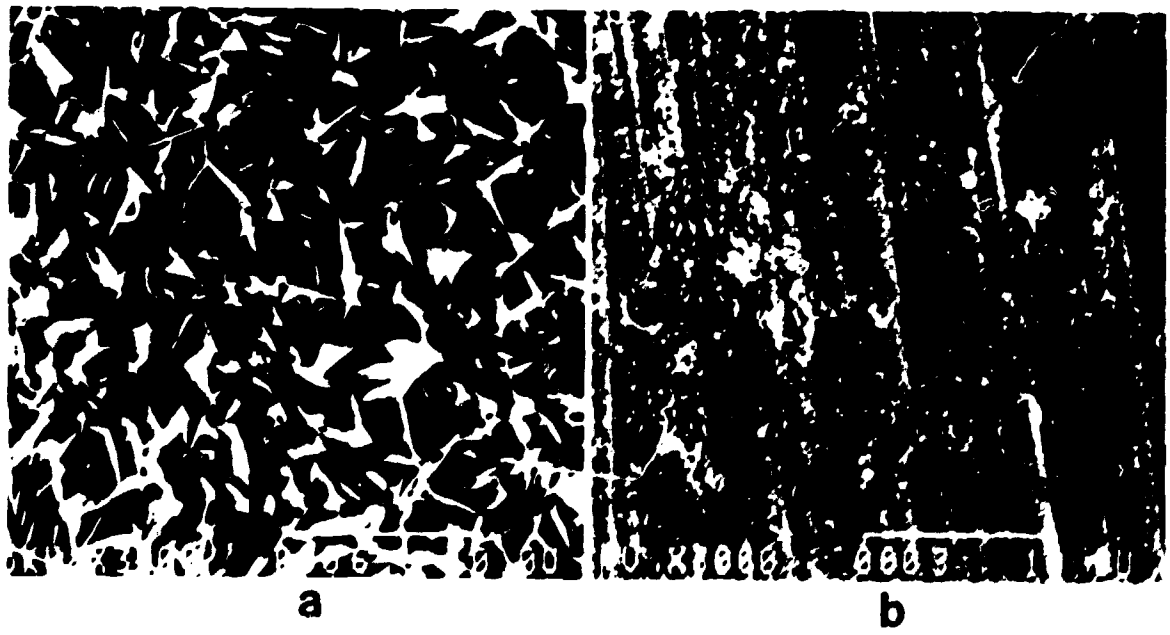

Figure 5. SEM micrographs of (a) Fe-25Cr and (b) Fe-25Cr-6Al specimens tested at 700C for 162 hours in SO_2 at 1 atmosphere.

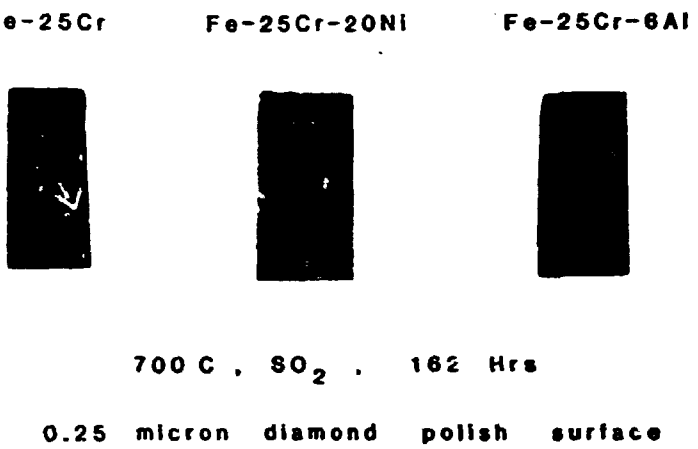

Figure 6. Tested specimens from second experiment.

It is interesting that the different types of surface finish did not result in any dramatic differences in the corrosion of the three alloys in this expiment. The undersides of each of the Cr_2O_3 forming alloys, however, showed somewhat less degradation compared to the upper sides which were more openly exposed to the flowing gas. These observations suggest that surface finish may not have been the major cause for the differences observed on two sides of the coupons in the first experiment.

DISCUSSION OF THERMODYNAMIC FACTORS

Oxide/sulfide stability diagrams for the base alloys have been constructed. Diagrams of this type form the cornerstone for predicting possible scale constituents under combined oxidation/ sulfidation conditions. Such diagrams for pure metals, iron, chromium, nickel and aluminum are well established. In those cases, the metal has unit thermodynamic activity by definition. In the base alloys used in this study, the activities of the four major elements are reduced by various degrees depending upon their concentrations and whether they are in a BCC or a FCC matrix. Through a review of the thermodynamic data on solutions of iron, chromium, nickel and aluminum,

the activities of these four elements at 700C in the three base alloys were estimated. These activity values are listed in Table 2 below:

Table 2. Thermodynamic Activity Data for the Base Alloys at 700C

Alloy	Element	Weight percent	Atomic percent	Activity Coeff.	Activity
Fe-25Cr	Fe	74.96	73.3	1.05	0.770
	Cr	25.04	26.7	1.58	0.432
Fe-25Cr-20Ni	Fe	55.25	54.6	1.00	0.546
	Cr	24.84	26.4	1.72	0.454
	Ni	19.91	19.0	1.00	0.190
Fe-25Cr-6Al	Fe	69.50	64.3	0.95	0.611
	Cr	24.62	24.6	1.42	0.351
	Al	5.88	11.1	0.001	0.00011

This table shows that the activities of nickel and iron are nearly ideal[1,2]. Chromium exhibits a small positive deviation from ideality in both the BCC[3,4] and FCC[2] solid solutions. Aluminum exhibits a strong negative deviation from ideality[2,3].

Based upon the activity data listed in Table 2, the oxide/sulfide stability diagrams for Fe, Cr, Ni and Al in each of the three base alloys were calculated. These diagrams are shown in Fig. 7 along with the superimposed diagrams for the pure elements. The shaded regions between the alloys and the corresponding oxides and sulfides indicate the extent to which these boundaries shift due to changes in the activities in the alloys compared with the pure metals. The diagrams show that the driving force for the formation of a particular oxide or sulfide phase is reduced depending on the deviation from unit activity. The relatively low stability of aluminum in one base alloy causes a significant shift in the stability lines for aluminum sulfide or oxide. In fact, the sulfide phase, AlS, becomes unstable at the activity level of aluminum in the base alloy and disappears from the stability diagram.

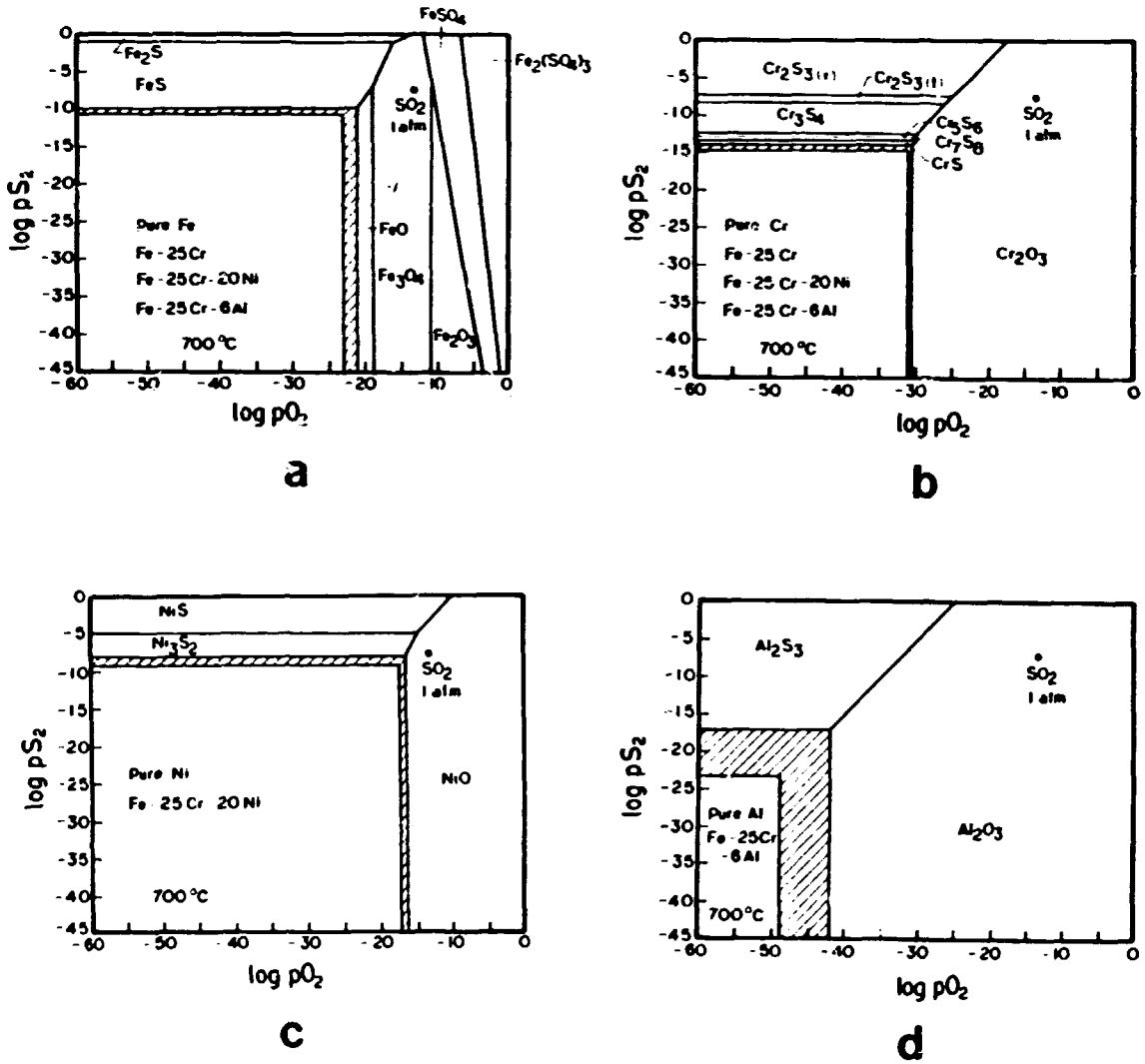

Figure 7. Changes in the Stability Diagrams for (a) Fe, (b) Cr, (c) Ni and (d) Al in the base alloys compared to the pure element at 700°C. The S_2/O_2 activity of dissociated SO_2 is indicated.

The oxygen and sulfur partial pressures at equilibrium with SO_2 gas at 700C are also indicated on each of the four diagrams. In the case of nickel the atmosphere used in the preliminary experiments discussed before, is in the oxide field but close to the triple point between the metals, the oxide and the sulfide.

In the case of Al, Cr and Fe, the SO_2 atmosphere is well within the respective oxide phase fields. Hence at thermodynamic equilibrium, only oxides should form when the base alloys are exposed under the conditions used.

However, it is well known that the kinetic boundaries can be shifted substantially from the thermodynamic equilibrium, and the preliminary experimental indications of sulfide formation on the Cr_2O_3 forming base alloys must be due to kinetic factors.

SUMMARY

The preliminary results indicate that the alumina forming alloy is far superior to the chromia forming alloys under the conditions of interest. The thermodynamic boundary between oxides and sulfides is not valid, at least for the chromia formers, since the atmospheres used should have only resulted in the formation of oxides under equilibrium conditions.

In the Fe-25Cr-20Ni alloy, the scale formed in SO_2 at 700C after 162 hours is very non adherent and consists of blades and nodules of predominantly chromium rich sulfides on top of a more compact scale which may be predominantly chromium rich oxide.

The surface conditions and exact positioning of the specimens in the flowing gas may play an important role in the kinetics of attack.

ACKNOWLEDGEMENT

The support of this project by the Department of Energy, through Martin Marietta Energy Systems, Inc., Subcontract Number 86-95900C, is appreciated.

REFERENCES

1. R. A. Oriani, Acta Met., Vol. 1, 448 (1953).
2. E. A. Gulbransen and K. F. Andrew, Trans. TMS of AIME, Vol. 221, 1247 (1961).
3. Y. Yeannin, C. Mannershanty and F. D. Richardson, Trans. TMS of AIME, Vol. 227, 300 (1963).
4. R. Hultgren et al., in Selected Values of Thermodynamic Properties of Binary Alloys, ASM, 1973, p. 147, 156, 694, 708, 847.

THE EFFECTS OF MICROALLOY CONSTITUENTS, SURFACE TREATMENT AND OXIDATION CONDITIONS ON THE DEVELOPMENT AND BREAKDOWN OF PROTECTIVE OXIDE SCALES

V. Srinivasan

Universal Energy Systems, Inc.
4401 Dayton Xenia Road
Dayton, Ohio 45432

INTRODUCTION

A major material problem in superheaters, reheaters, syngas coolers and heat exchangers or recovery systems in coal - derived energy systems is gaseous corrosion in the temperature range of 500° to 700°C induced by the multioxidant environment. These components are made of ferritic or austenitic steels that have adequate mechanical Strength in the above temperature span. They depend for their corrosion resistance on the formation of continuous scales with protective Al_2O_3 or Cr_2O_3 layers as major components. Such protection does not long last as the mechanical breakdown of the protective oxide scales and the penetration of corrosive species soon follow. Both of the above degradation processes depend on the scale microstructure, morphology and adhesion, substrate chemistry and microstructure and the environment. An understanding of their dependencies is essential for the development of new generation of corrosion-resistant alloys for long term applications in coal combustion or conversion systems.

Much of our current knowledge on the oxidation and corrosion behavior of Fe , Ni- and Co base alloys comes from investigations at temperatures above 850°C (Ref. 1). An important contribution of these investigations is the discovery of the beneficial effects of oxygen active elements and oxide dispersoids on scaling[2].

Minor additions of these elements or dispersoids improve the oxidation resistance considerably by enhancing the scale adhesion and modifying the scale morphology and growth process. These improvements are likely to provide resistance to scale breakdown and the transport of corrosive reactants.

Extrapolation of the results of oxidation/corrosion studies at temperatures well above 850°C will not lead to a meaningful understanding of the corrosion behavior of ferritic and austenitic steels with and without oxygen active elements in the temperature range of 500° to 700°C. Kinetic factors are likely to dominate the oxidation/corrosion behavior in this temperature range with possible changes in the mechanisms of reactant transport across the scale and in the substrate. It is therefore, the purpose of this program to investigate the effect of additions of several microalloy constituents, their concentration, the method of incorporation, the surface pretreatment and the oxidizing conditions on the nucleation, growth and breakdown of Al_2O_3 and Cr_2O_3 scales on ferritic and austenitic steels. The ultimate goal of this program is to identify the factors that lead to corrosion resistant microstructures and morphology of protective oxide scales and implement the findings in alloy development.

EXPERIMENTAL MATERIALS AND METHODS

Commercial ferritic steel, AISI 446 was chosen for this preliminary study. Model alloys that will be extensively investigated are Fe 25Cr-20Ni, Fe 25Cr-6Al and Fe 25Cr. The chemical compositions of these materials are given in Table 1. Coupons of nominal size 1 cm x 1 cm x 0.2 cm were machined from annealed bars and had holes for suspension into a reaction quartz tube. They were metallographically polished upto 0.05μm and washed throughly. After measuring the dimensions and initial weights they were exposed to flowing O_2 at 1 atm. and to 700 and 850°C. Thermogravimetric measurements were made using Cahn

balance. A few coupons were implanted with Ce on both sides. The implantation was carried out in an high current implanter at 160 KeV, and the fluence was 4 E 15 ions per sq.cm.

TABLE I

NOMINAL CHEMICAL COMPOSITIONS, WT.%

Designation	Cr	Ni	Al	C	P	S	Mn	Fe
Fe-25Cr	25-04	<0.01	<0.01	0.001	<0.005	0.003	<0.01	Bal
Fe-25Kr-20Ni	24-84	19.91	0.01	0.004	<0.005	0.002	<0.01	Bal
Fe-25Cr-6Al	24.61	<0.01	5.88	0.004	<0.005	0.003	<0.01	Bal
AISI 446	24.0	0.26	-	0.146	0.02	0.011	0.78	Bal

°F Mixed gas corrosion tests were run on unimplanted and Ce-implanted coupons at 850°C for 4 hours. The gas mixture consisted of $H_2/H_2S/H_2O/Ar$ in the ratio by Vol.% 19.03: 0.33: 3.74: 76.9 to give partial pressures, $Ps_2 = 10^{-7}$ atm. and $Po_2 = 10^{-19.07}$ atm. at the test temperature. The gas mixture was equilibrated by passing through a platinum honeycomb at 850°C placed upstream to the sample.

Scales and the substrates were examined using optical microscopy, SEM/EDX, Rutherford backscattering (RBS), sputter Auger electron spectroscopy (AES) and x-ray diffraction (XRD).

RESULTS AND DISCUSSION

Thermogravimetric data showed insignificant weight gain at 700°C after about 120 hours while the weight gain was significant at 850°C in flowing O_2 at 1 atm. Figure 1 shows the result of thermogravimetric measurements. The same data were plotted in log-log scale in Figure 2. The oxidation kinetic was not parabolic.

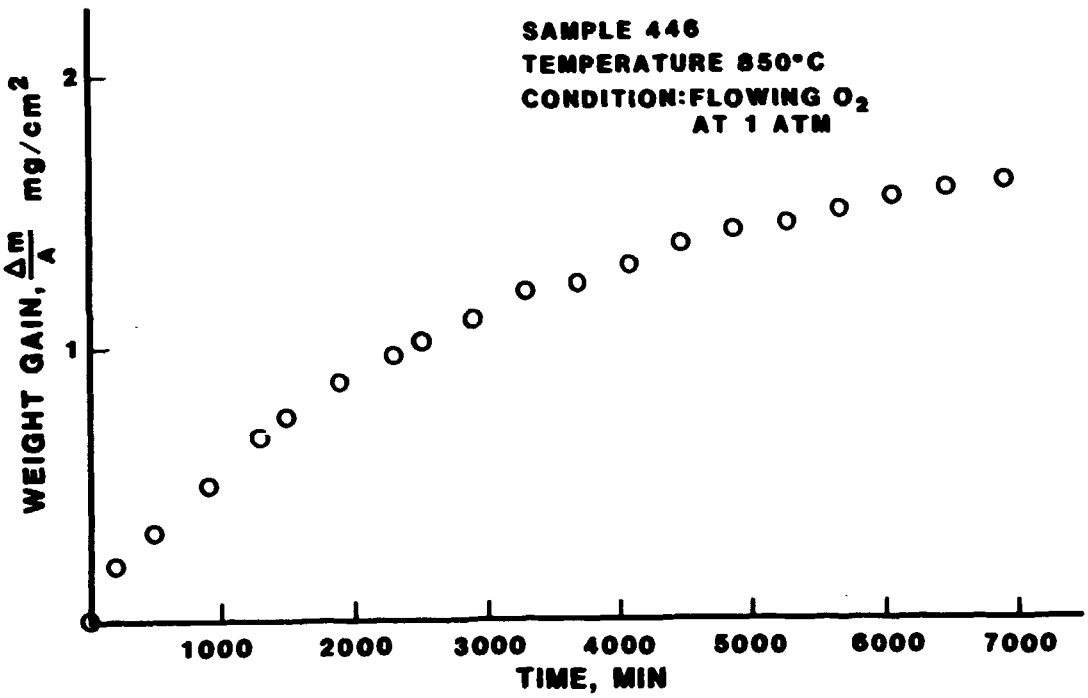

Figure 1. Weight gain as a function of time.

The x-ray diffraction peaks observed on the sample exposed to 700°C contained those corresponding to Fe and Cr, the major alloying elements in the substrate suggesting very thin scale. However, the XRD peaks obtained from the sample exposed to 850°C contained a set identified as those of Cr_2O_3. The diffraction peaks forming the second set seem to have been shifted from positions corresponding to possible mixed oxides to be expected on alloys of similar composition.

Figure 3-5 show oxide scale surface and the transverse section of the oxide scale. At 700°C thick scale growth was seen along the grain boundaries and nodules were present on the oxide surfaces.

RBS spectra taken from the pretest coupon and coupons oxidized at 700° and 850°C are shown in Figure 6. RBS analysis suggested that the outer scale was rich in metal-deficit oxides suggesting mixed or non-stoichiometric oxides.

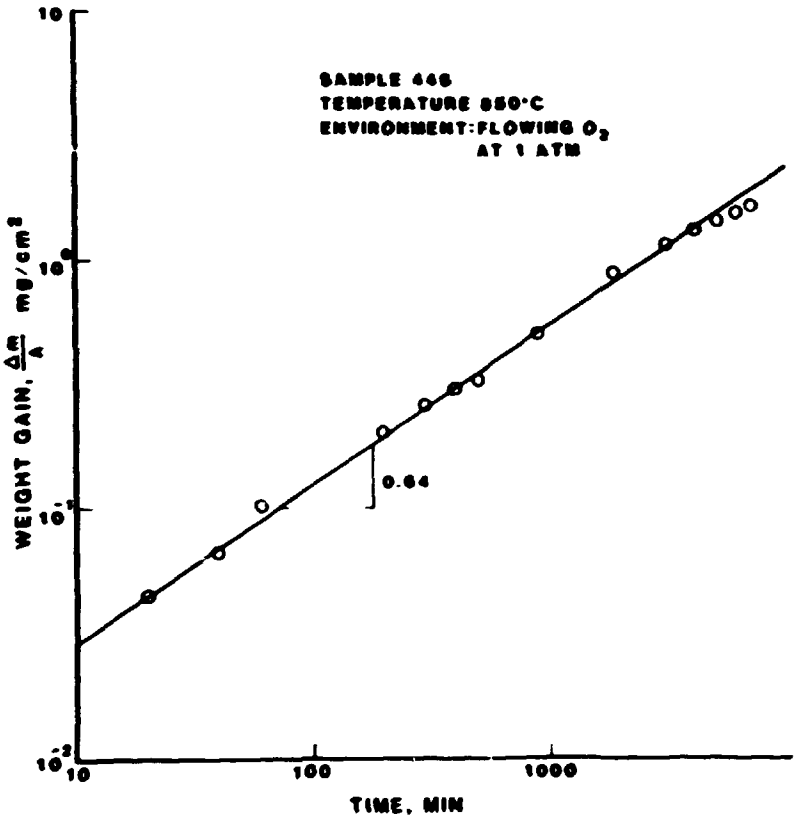

Figure 2. Weight gain as a function of time.

The results of sputter AES analysis on the sample oxidized at 850°C are shown in Figure 7-9. The outer oxide scale is rich in Mn, and the scale thickness was estimated about 8μm.

This preliminary work suggests that oxidation kinetics is very slow at 700°C even in unimplanted AISI 446 and therefore, corrosion tests besides cyclic oxidation test may have to be used to assess the effect of microalloy constituents. However, scale growth at 850°C was faster, and the scale formed in 120 hours was thick consisting of Cr_2O_3 scale near the scale/substrate interface and metal deficit non stoichimetric scale rich in Mn at the gas scale interface.

Figure 3. SEM of oxide scales thermally grown at 700°C on AISI 446 in flowing O_2 at 1 atm. for 120 hrs.

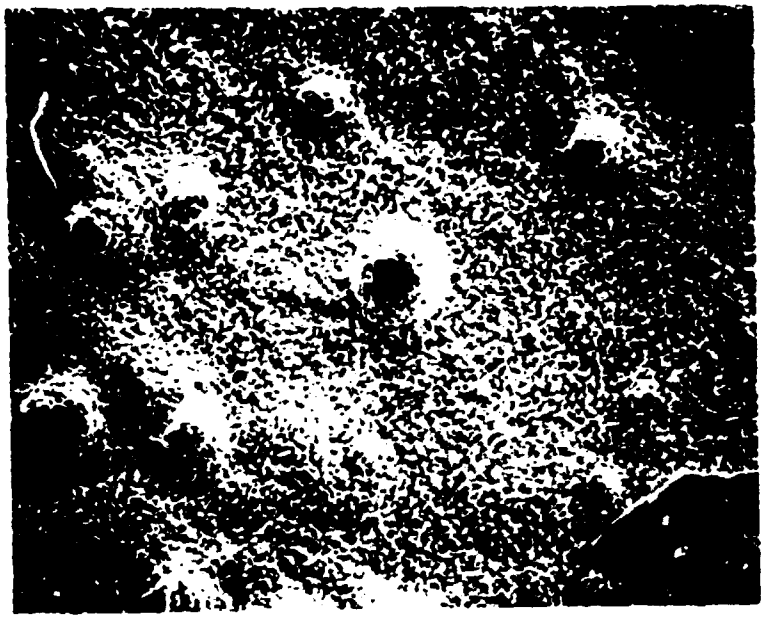

Figure 4. SEM of oxide scales thermally grown at 850°C on AISI 446 in flowing O_2 at 1 atm. for 120 hrs.

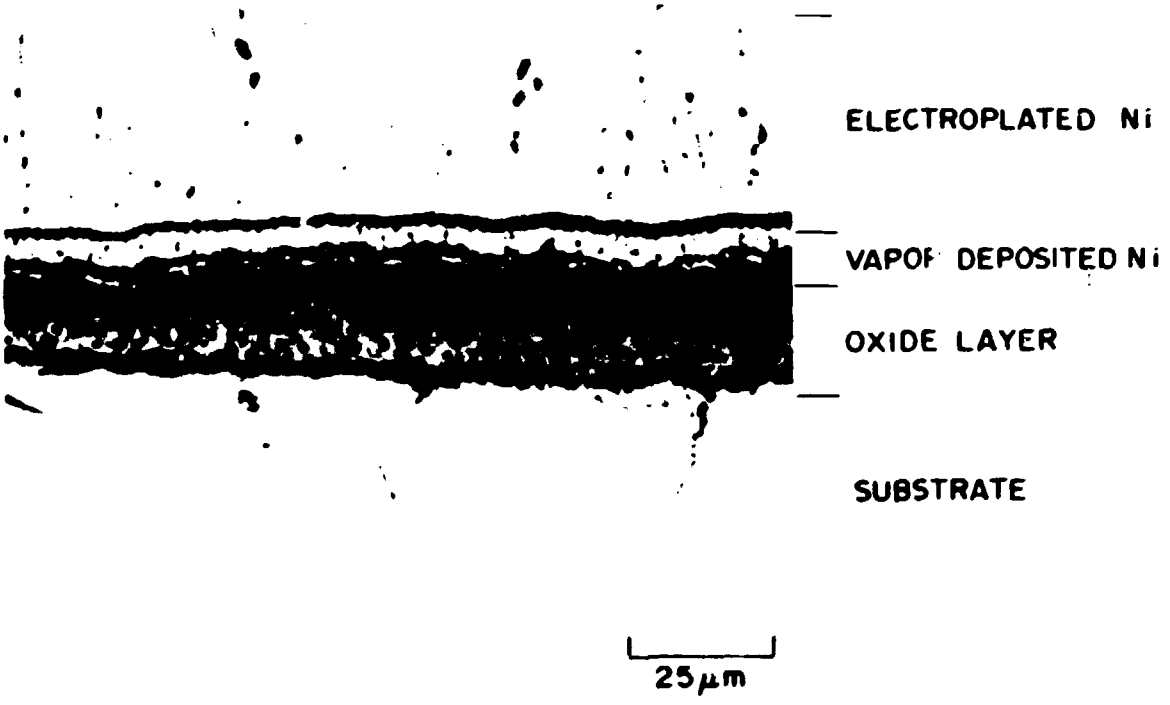

Figure 5. Optical micrograph of transverse section showing the oxide scale and the substrate, AISI 446 after 120 hrs. exposure at 850°C in flowing O_2 at 1 atm.

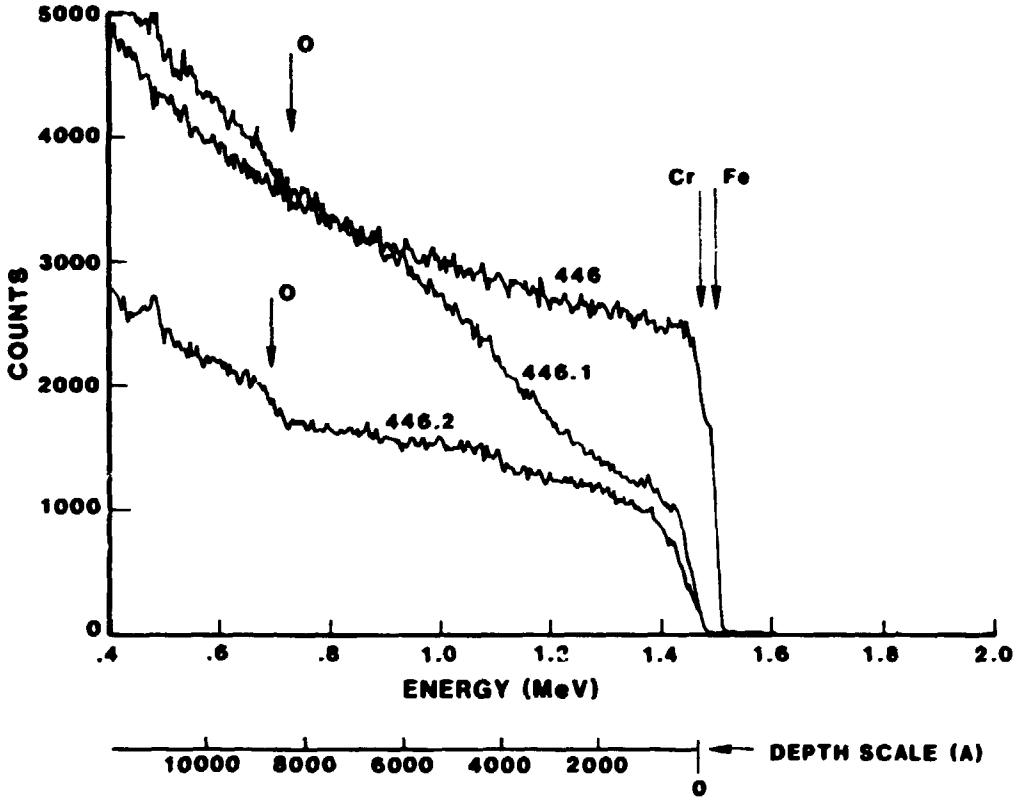

Figure 6. RBS Spectra from pretest, 446, and oxidized coupons, 446.1 and 446.2. 446.1 and 446.2 oxidized respectively at 700°C and 850°C for 120 hrs. in flowing oxygen at 1 atm.

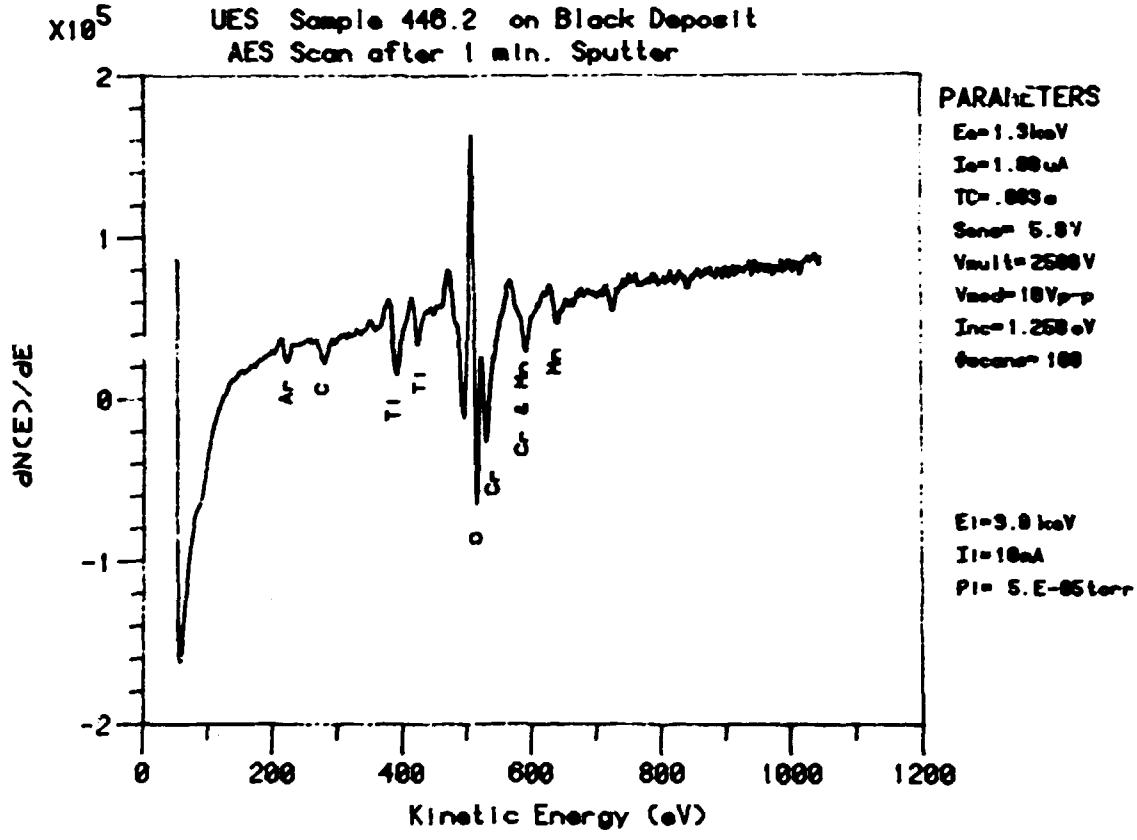

Figure 7. AES spectrum after 1 min. sputtering on the scale of 446 exposed to 850°C for 120 hrs. in flowing O_2 at 1 atm.

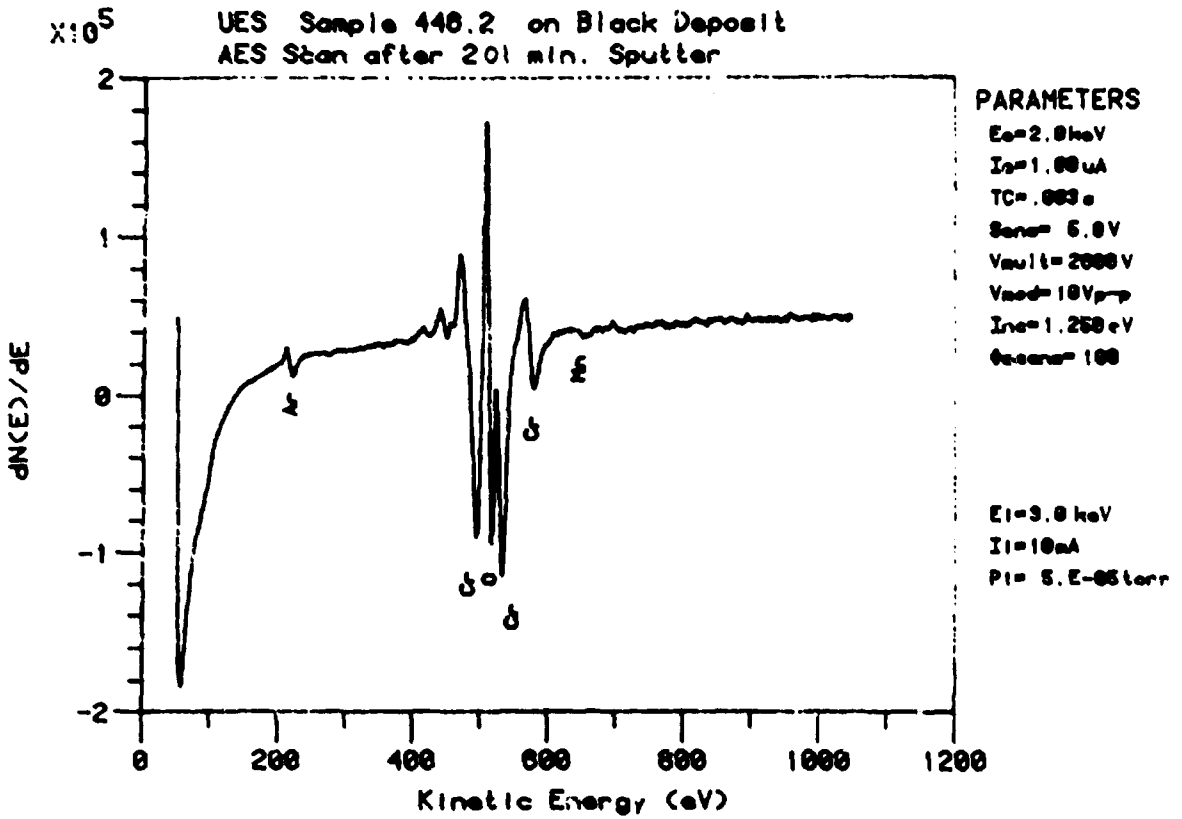

Figure 8. AES spectrum after 201 min. sputtering of the scale of 446 exposed to 850°C for 120 hrs. in flowing O_2 at 1 atm.

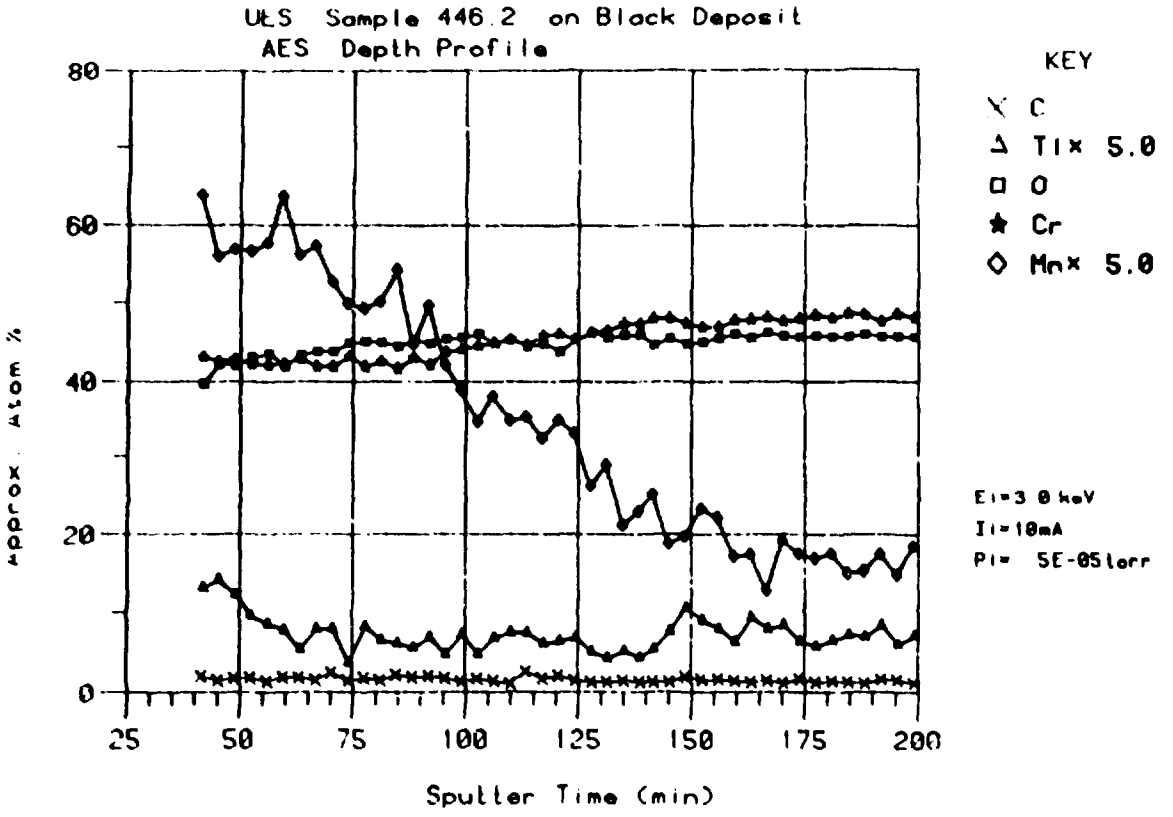

Figure 9. AES depth profile of elements across the oxide scale of 446 exposed to 850°C for 120 hrs. in flowing O_2 at 1 atm.

REFERENCES

1. H. Hindam and D.P. Whittle, Oxid. Metals, 18 (1982), 245-284.

2. D.P. Whittle and J. Stringer, Phil. Trans. R. Soc. London, A Ser. 295 (1980), 309-329.

1514M

MECHANISMS OF GALLING AND ABRASIVE WEAR

L. K. Ives, M. B. Peterson, and E. P. Whitenton

Metallurgy Division
National Bureau of Standards
Gaithersburg, MD 20899

ABSTRACT

Galling is a severe form of wear which has been recognized as a serious problem affecting the operation of control valves and other components used in fossil energy conversion systems. Recent results obtained in a program of research aimed at advancing the basic understanding of the process of galling are presented. The galling test method and a method which has been developed to measure quantitatively the amount and character of galling damage are described. Data on the galling behavior of pure metals, experimental alloys, and commercial alloys are presented. The influence of hardness, crystal structure, stacking fault energy and other materials properties are discussed.

INTRODUCTION

Galling is a form of severe wear that occurs at sliding contacts. It is recognized by the development of a significant increase in surface roughness as a result of local plastic deformation, fracture, and often the transfer of material from one surface to the other. The onset of galling is usually sudden and is accompanied by a large and varying coefficient of friction. Continued sliding once galling has occurred may result in seizure. Whether or not galling occurs at a sliding contact is determined by such operating variables and conditions as load, sliding speed, temperature, the type of lubricant, and the chemistry of the surrounding

environment. The nature of the materials in contact can also have a substantial influence on the tendency to gall and on the severity of the damage that occurs should galling take place. The composition, microstructure, crystal structure, and mechanical properties of each member of the sliding pair are of great importance.

As was pointed out in a recent review of the literature,[1] relatively few publications are available that deal strictly with the subject of galling. However, this apparent neglect is largely a consequence of terminology. In studies of the fundamental mechanisms of friction and wear, the term adhesive wear is commonly used even though the damage process may be that of galling. In field service situations damage processes that could be described as galling are frequently referred to as scoring, scuffing, or even seizure. The term scuffing is favored when the system is lubricated, such as between the piston ring and cylinder wall of an internal combustion engine. The term galling is frequently preferred when the damage is sufficiently gross to be easily visible to the unaided eye. If one is not restricted by some rather arbitrary considerations pertaining to the scale of the damage and exposure conditions, then there is in fact a fairly large body of literature concerned with the process of galling.

A principle means to prevent galling is to apply a suitable lubricant and to operate under design conditions that do not exceed the load carrying capacity of the lubricant. In many applications it is not possible to apply a lubricant. An important example is that of valves used for fluid flow control. The valve face and seat usually can not be lubricated and the fluid itself may not act as a lubricant. If galling occurs, the roughened surface may prevent proper sealing and leakage can result. Additional damage may develop if abrasive particles are present in the fluid steam, such as is often the case in fossil energy conversion systems.

High velocities may be attained in the leakage path and severe solid particle erosion can occur. Under these circumstances the best approach is to employ valve designs that minimize sliding and to select materials that are resistant to galling. Unfortunately, there is a serious lack of information regarding the galling behavior of different materials and almost no information on the relationship between material properties, exposure conditions and the severity of the damage should galling take place.

The purpose of this project has been to develop an improved understanding of the galling process, particularly as it relates to materials properties. An important aspect of the work has been the development of a method to measure quantitatively the amount and character of galling damage. In what follows, a brief review will be given of some of the work carried out in this project with emphasis on current results. The galling test procedure, the method developed to measure surface damage, the mechanism of galling, and the influence of various materials properties on galling will be discussed. Representative results obtained on high purity experimental metals and on selected commercial alloys will be presented.

GALLING TEST METHOD

The galling test used in the majority of the experiments has consisted of a spherically tipped pin sliding on a specimen flat. The test specimen configuration is illustrated schematically in Fig. 1. A number of other configurations have been employed by investigators in the study of galling. Perhaps the most widely used is the button on block arrangement[2] illustrated in Fig. 2. Recently, in a study of the galling behavior of two steels[3], experiments were conducted to compare the pin-on-flat and the button-on-block tests. Although some differences were noted, both

tests gave the same relative ranking of the steels in terms of the severity of the galling damage.

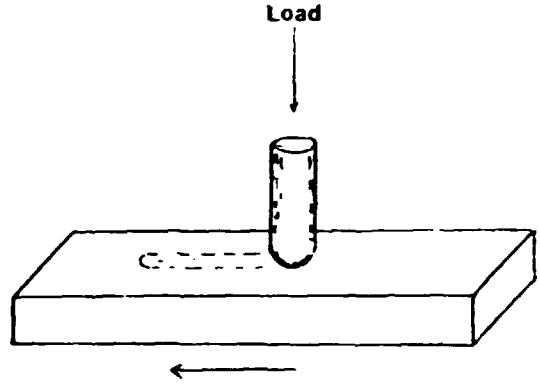

Fig. 1. Schematic drawing of the pin-on-flat test specimen configuration.

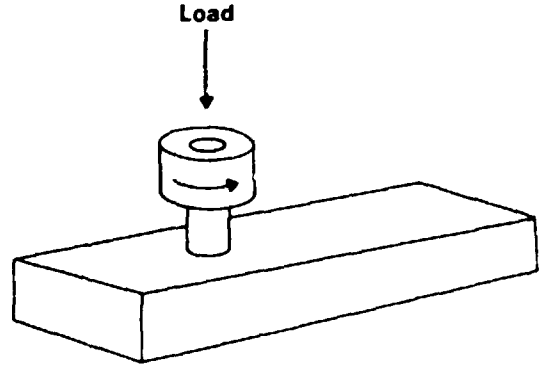

Fig. 2. Schematic drawing of the button-on-block test specimen configuration.

The pin on flat configuration was selected for several reasons. First, there is no problem in obtaining precise alignment between the contacting specimens as there is with many designs involving the sliding of one flat surface against another. Second, the location on the flat where galling is first initiated is easily recognized. With the button on block test, as well as with other tests that involve large

area contact, galling may begin at more than one site, and, unless the sliding distance is small, the initial site may be obliterated by subsequent contact. In the pin on flat test this assumes that only a single pass is employed. Repeated passes over the same track would also alter the evidence of previous events. The experiments carried out in this investigation have all consisted of a single pass, with a sliding distance of 4-5 cm.

Two different galling test machines have been employed. They are a hydraulically operated machine suitable for loads in the range 1500 N to 100,000 N and a mechanical screw driven machine for loads of from about 1 N to 1500 N. Dead weight loading is employed with the screw driven machine. With the hydraulic machine the desired load is applied by means of a hydraulic cylinder and indicated by a load cell. There is no provision for maintaining this load constant during the test. However, the load is carefully monitored and in most tests variations were no more than a few percent of the selected load. Both machines are equipped for continuous monitoring of friction force and specimen translation distance.

SPECIMEN PREPARATION

The specimens are prepared to near final dimensions by machining or surface grinding as required. The radius of the spherical tip at the end of the pin is 2.54 cm while the pin diameter and length are typically 1.2 cm and 2.0 cm, respectively. Typical dimensions of the flats are 6 cm long, 1.2 cm wide, and 1 cm thick. After machining, the specimens are heat treated or given the desired surface treatment, as was the case for two steels that were studied in the carburized[3] and nitrided[4] conditions. In a few cases additional surface grinding has been carried out after the latter stage of treatment. The final preparation of the

test surfaces consists of grinding on SiC abrasive papers to 600 grit followed by lapping with 6 μm diamond compound. The specimens are then carefully cleaned by ultrasonic agitation in solvents and exposed to ultraviolet light as a further means to eliminate contaminants. The above cleaning procedure is regarded as the standard preparation procedure. For certain experiments, however, etching, chemical polishing, electropolishing, or machining to obtain a particular texture[5] have been used to prepare the surface.

CHARACTERIZATION OF DAMAGE

Most reported investigations of galling have been concerned with determining the conditions for the onset of damage, with load being the primary variable of interest. Whether or not galling has occurred is usually assessed by visual examination of the surfaces with the unaided eye. With few exceptions[6,7] quantitative measurements have not been employed to determine the amount or character of the damage. A major feature of galling is the development of a significant increase in surface roughness. It follows that parameters based on surface topography might logically be chosen to measure the damage due to galling.[5] This has been the approach taken in this program.

A detailed description of the damage measurement method can be found in reference 8 so only a brief outline will be given here. Surface topography measurements are made with a computer controlled stylus profilometer system. Only damage on the specimen flat is measured, although the method could be adapted to measure damage on the pin. A series of parallel, equally spaced profile traces is made across the wear track. These traces yield the x-, y- and z-coordinates of the surface topography. A number of different parameters to represent the amount and character of the damage are calculated from these topography data.

One parameter that has been found useful is the average maximum peak to valley parameter, $\bar{R}_t$, defined by

$$\bar{R}_t = (1/n) \Sigma (R_t)_j \qquad (j = 1 \text{ to } n) \qquad (1)$$

Here, the specimen surface is the xy-plane with the y-axis parallel and the x-axis perpendicular to the direction of sliding. $(R_t)_j$ is the maximum peak to valley distance for the j^{th} trace, and $\bar{R}_t$ is the average for all n traces.

Another parameter, $R_t(rms)$, that has been used is the root mean square deviation of the R_t values. A relatively hard slider might produce a deep but smooth groove in the flat without appreciable damage due to galling. However, the resulting $\bar{R}_t$ value would be large. On the other hand, $R_t(rms)$ would be small giving in this case a better representation of the actual amount of damage due to galling.

A third parameter that has been used to indicate the severity of the damage is the displaced volume, DV, defined by

$$DV = \Delta x \Delta y \sum_{j=1}^{n} \sum_{i=1}^{m} |z_{ij}|, \qquad (2)$$

where z_{ij} is the elevation of the ij^{th} point on the surface measured with respect to the original surface plane and Δx and Δy are the spacing between points in the x- and y-directions, respectively. The displaced volume is the sum of the volume of the peaks above the original surface plane and the volume of the valleys below that plane.

The above parameters measure the amount of damage. A parameter that has been employed to provide information on the shape of topographic features is the aspect ratio parameter, AR. This parameter is defined by

$$AR = \frac{\Delta x \sum_{i=1}^{m} \sum_{j=1}^{n-1} |z_{ij} - z_{i,j+1}|}{\Delta y \sum_{j=1}^{n} \sum_{i=1}^{m-1} |z_{ij} - z_{i+1,j}|} \qquad (3)$$

A value of AR≅1 would be obtained if the damage consisted of peaks and/or valleys with dimensions approximately equal in the x- and y-directions. Damage that consisted primarily of long grooves or ridges parallel to the direction of sliding would give a value <<1 while a predominance of grooves or ridges perpendicular to the sliding direction would give a value >1.

In addition to the profilometry measurements which are employed for the quantitative measurement of damage, further analyses of the damaged surfaces have been conducted using optical microscopy, scanning electron microscopy, transmission electron microscopy, and micro-indentation hardness methods. These latter characterization methods are indispensible for the analysis of galling mechanisms, particularly with respect to studying the details of the deformation, fracture, and transfer behavior of different materials.

RESULTS AND DISCUSSION

Studies have been conducted on a variety of pure metals, experimental alloys and commercial alloys. The effects of materials properties and various test conditions have been investigated. Some recent results will be presented and discussed here.

GALLING OF PURE METALS

Figure 3 shows the sliding damage on specimen flats of eleven different pure metals. In each case the pin was of the same material as the flat. The applied load for all metals was 130 N. Sliding commenced at the top of each flat shown in the figure and was terminated after a single

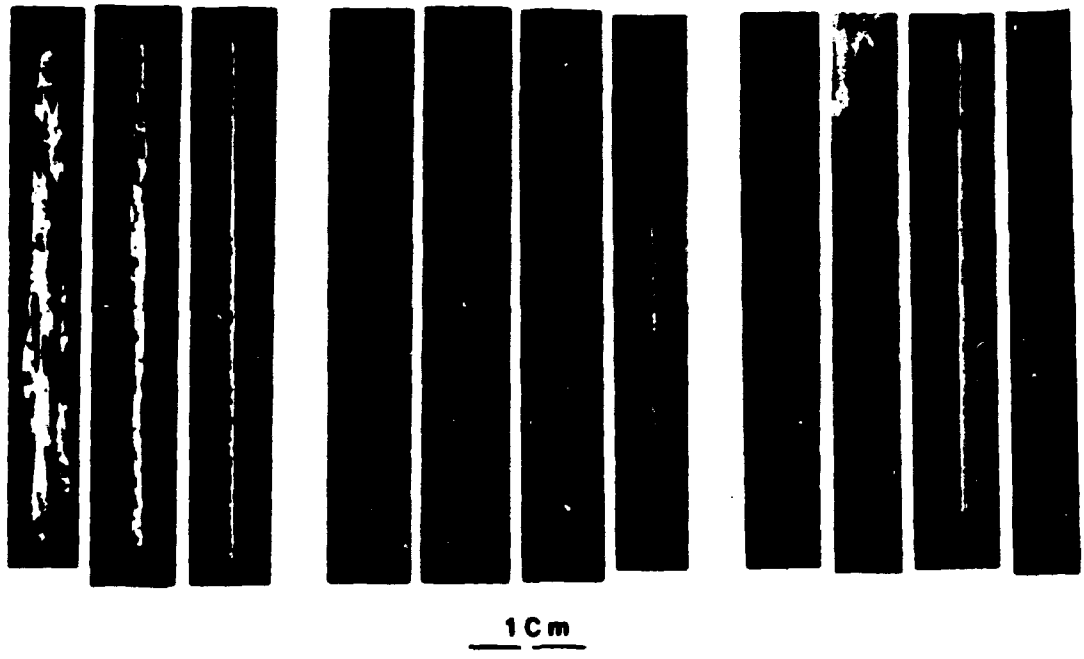

Fig. 3. Photograph of specimen flats of pure metals after sliding with pins of like materials at a load of 130 N.

stroke at the bottom. There are three fcc metals (Al, Cu, Ni), four bcc metals (Fe, Mo, Nb, Ta), and four hcp metals (Co, Mg, Ti, Zn). Some important properties of these metals are listed in Table 1. The last column in the table gives the critical Hertz load for each metal. This is the load computed from Hertz's equations for a spherical indentor at which the maximum shear stress, occurring at a depth of about one half the radius of the contact circle below the surface, just equals the yield stress of the material.[9] In each case the applied load of 130 N employed in the tests is

substantially greater than the critical Hertz load and as a consequence plastic deformation of the specimens occurred as a result of the application of this load.

Although the pattern of damage differs somewhat among the various fcc and bcc metals, all exhibit features that are characteristic of galling. Damage to the hcp metals is significantly less than for the fcc and bcc metals, and in two cases, for Mg and Co, there was essentially no evidence of galling.

Table 1. Pure metals and properties.

Metal	Purity (wt.%)	Crystal Structure	c/a	Hardness (kg/mm^2)	Elastic Modulus (Kg/mm^2)	Critical Hertz Load (N)
Al	99.99	fcc	1.633	28	7.4E3	9.7
Cu	99.99	fcc	1.633	123	12.3E3	30
Ni	99.5	fcc	1.633	318	21.4E3	55
Fe	99.98	bcc	--	179	21.1E3	31
Mo	99.5	bcc	--	259	29.5E3	36
Nb	99.9	bcc	--	108	10.5E3	29
Ta	99.9	bcc	--	182	19.0E3	34
Ti	99.2	hcp	1.587	216	11.2E3	57
Co	99.998	hcp	1.624	243	21.1E3	43
Mg	99.95	hcp	1.624	34	4.6E3	16
Zn	99.995	hcp	1.856	45	9.8E3	12

As a typical example of galling in these experiments, the damage to the Fe specimen will be examined in more detail here using the SEM micrographs shown in Fig. 4 and 5. In Fig. 4a the initial part of the track on the flat is shown. The observed damage can be accounted for as follows: As sliding began, a cap of material within the flat below the pin was plastically deformed and was displaced to form a prow. Fracture as a result of tensile and shear stresses behind the prow accompanied the motion of the prow. However, the growth in size of the prow and work hardening of the deformed material caused an increasing resistance to motion. Eventually, the resistance became so great that the prow

could no longer be moved by the pin. The pin then slid over the prow, probably leaving some prow material attached to the pin and perhaps transferring pin material to the prow. In addition, a lip of material at the rear of the prow, clearly visible in Fig. 4a, was caused to curl away from the flat.

With continued sliding, the deep groove shown in Fig. 4b was formed by a prow being translated along the surface of the flat by the pin. Again, there are raised lips of material left in the groove. This process continued until, at approximately 3 cm sliding distance, the entire prow was torn away from the pin and left behind, Fig. 4c. Finally, the prow that was being moved along with the pin when the experiment was terminated is shown in Fig. 4d. At higher

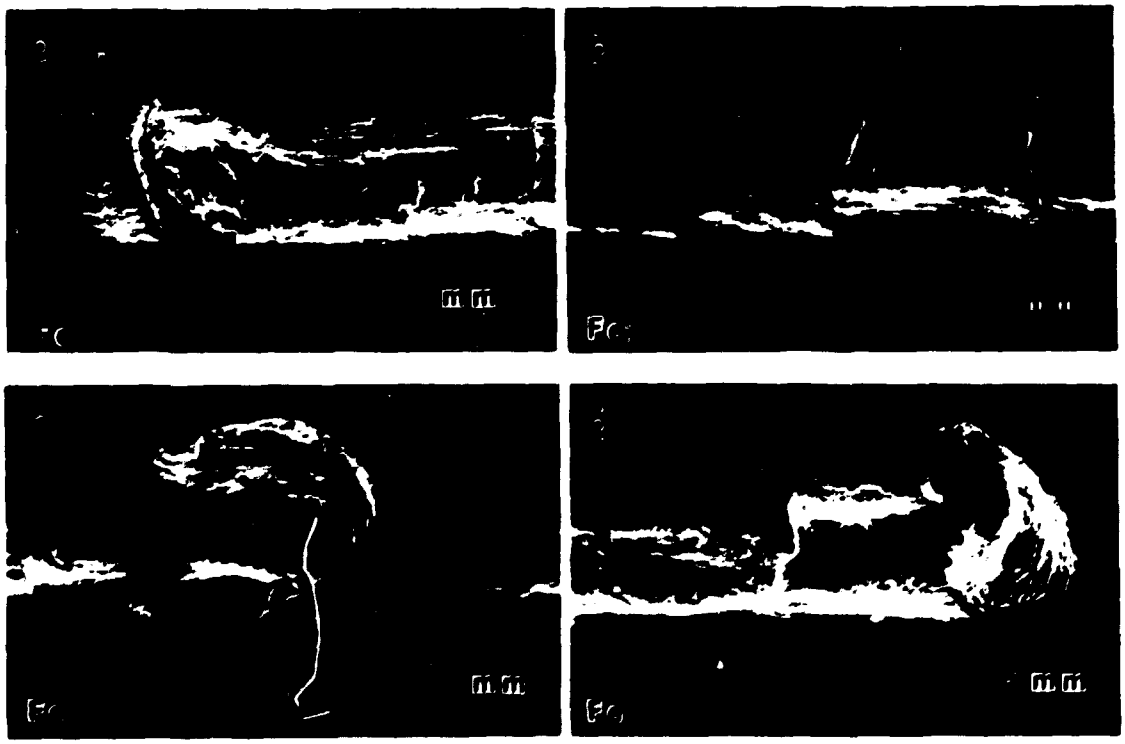

Fig. 4. SEM micrographs of sections of track on Fe specimen flat. a) At beginning. b) After 0.5 cm sliding distance. c) After 3 cm sliding distance. d) At terminus.

magnifications the details of the damage vary. Grooves and lamellar features are present as a result of the sliding and shearing action. In addition, areas with somewhat elongated dimples were seen, Fig. 5. Dimples are a characteristic feature of ductile fracture in tension.

Among the hcp metals that were studied, Ti and Zn were found to gall, but the damage, particularly for Zn, was less than for the bcc and fcc metals. Furthermore, for Zn the character of the damage was somewhat different. A SEM micrograph of a section of the track on the Zn specimen is shown in Fig. 6. The damage consists of numerous small prows. Each prow was sustained for only a short distance and was then left behind. The process appeared to have occurred simultaneously on both the flat and the pin.

Figure 7 shows an optical micrograph of a section of the track on the Co specimen. The damage consists of smooth grooves. The micrograph in Fig. 7 was taken under Nomarski interference contrast conditions to reveal the

Fig. 5. SEM micrograph showing dimple features in track on Fe specimen flat.

Fig. 6. SEM micrograph of section of track on Zn specimen flat.

Fig. 7. Optical micrograph of section of track on Co specimen flat. Nomarski interference contrast.

slight differences in topography. This Co specimen surface was electropolished prior to testing. A small amount of grain relief was present and this is visible in the micrograph. There was no evidence of galling in this test. Even when a test was conducted at a load of 1400 N (compared to 130 N for Fig. 7) galling did not occur.

In Fig. 8, damage severity indicated by the average maximum peak to valley parameter $\bar{R}_t$ is plotted as a function of hardness for the pure metals. It is clear that there is no correlation between damage severity and hardness. The $\bar{R}_t$ value for Al is very high while that for Mg is very low and Mg is nearly as soft as Al. Similarly, Mo and Co differ only slightly in hardness but have significantly different

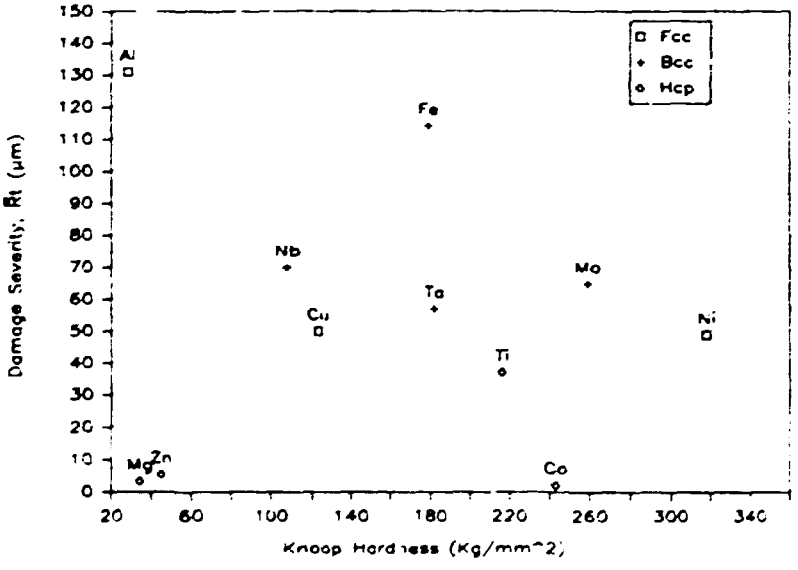

Fig. 8. Damage severity measured in terms of $\bar{R}_t$ plotted as a function of hardness for pure metal specimens.

$\bar{R}_t$ values. In connection with these data it should be pointed out that all specimens were tested in the as-received condition. The grain sizes and amount of work hardening introduced during processing were not all the same. Both of these factors could affect damage severity.

The main factor which appears to influence galling severity in Fig. 8 is crystal structure. The galling severity for the hcp metals is, in all cases, lower than for the fcc and bcc metals, although for Ti it is only slightly lower. Ti differs from the other hcp metals studied here in that the lowest critical resolved shear stress is on the pyramidal planes rather than on the basal plane.

MECHANISM OF GALLING

The study of the pure metals has provided a clear demonstration of the primary mechanism of galling. Although it was recognized early that a high coefficient of friction and plastic deformation were associated with severe adhesive wear, it was not until the work of Cocks[10] that the damage mechanism was studied in any detail. In experiments involving the sliding of copper pins on the surface of a copper cylinder, Cocks recognized that sliding took place beneath the pin in a wedge of metal from the cylinder. The process is illustrated schematically in Fig. 9. At about the same time as Cocks' work, Antler[11], in studying the same phenomenon, used the

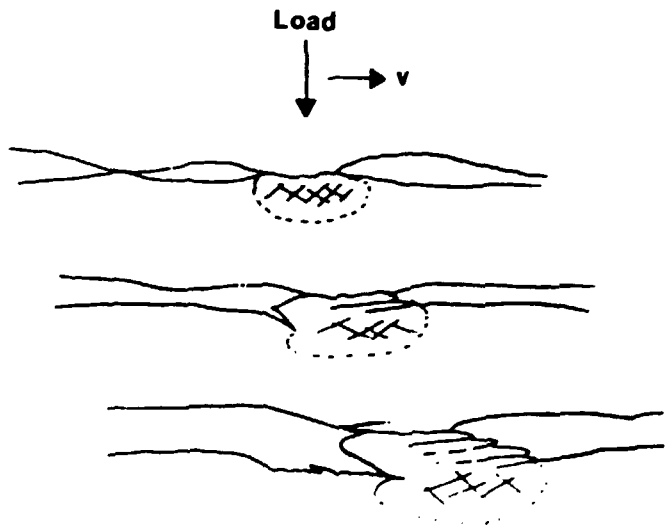

Fig. 9. Schematic illustration of prow (wedge) formation mechanism. Upper body is assumed to be harder than lower. Prow formation progresses from top to bottom of figure.

term prow instead of wedge. The term prow now appears to be used more often than wedge in describing the damage feature. It should also be pointed out that, in his early work, Antler considered the growth of prows to be the result of the accretion of material by repeated events rather than by a single event as was proposed by Cocks. In later work, Antler[12] considered several mechanisms including that of Cocks. In the single pass experiments employed in this investigation, the primary damage event was the wedge formation process described by Cocks and illustrated in Fig. 9.

THE INFLUENCE OF STACKING FAULT ENERGY

Bhansali and Miller[13] hypothesized that materials with low stacking fault energies (SFE) should be more resistant to galling than materials with high stacking fault energies. In order to test this hypothesis in the present work, experiments were conducted on a series of Cu-Al and Cu-Ge alloys with different stacking fault energies. The alloys studied are listed in Table 2. Galling tests on these alloys were conducted at a load of 130 N. Pins and flats were of the same alloy in each test. The damage, measured in terms of the parameters discussed above, is plotted as function of stacking fault energy in Fig. 10a-d. In Fig.

Table 2. Alloys for the study of galling vs. SFE.

Metal	Solute Concentration (at.%)	SFE (mJ/m^2)	Hardness (Kg/mm^2)
Cu - 6 Al	13.07	7	74
Cu - 8 Al	17.00	4	100
Cu - 2 Ge	1.75	35	50
Cu - 6 Ge	5.29	16	60
Cu - 10 Ge	8.86	6	88
Cu - 15 Ge	13.38	-	182

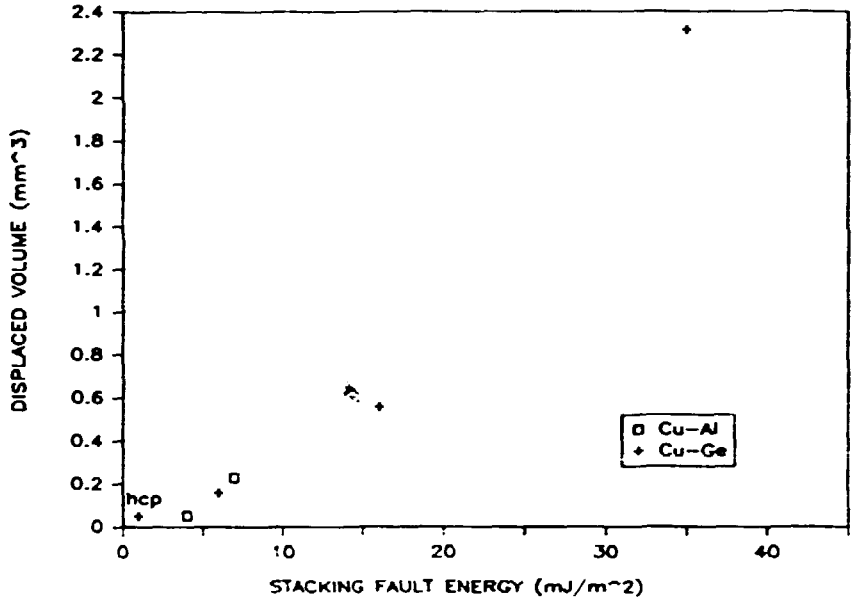

Fig. 10a

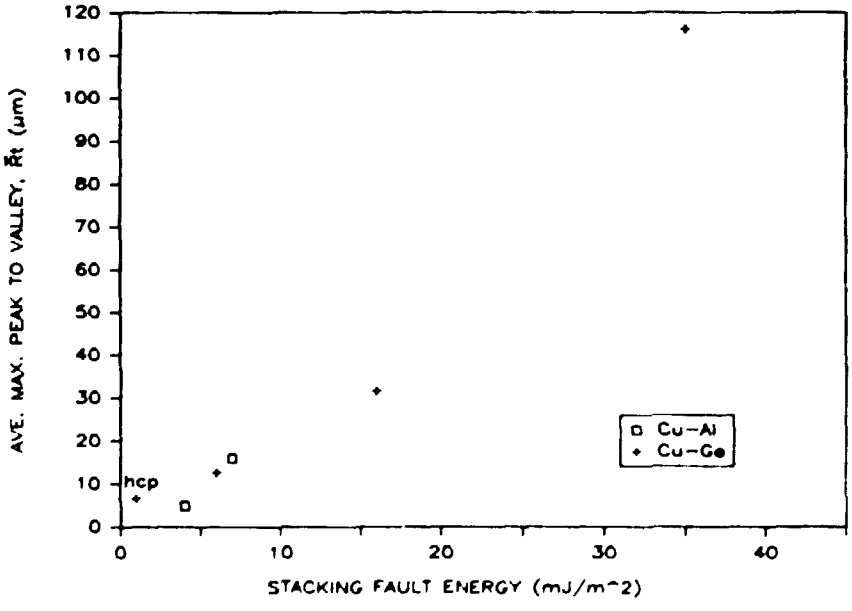

Fig. 10b

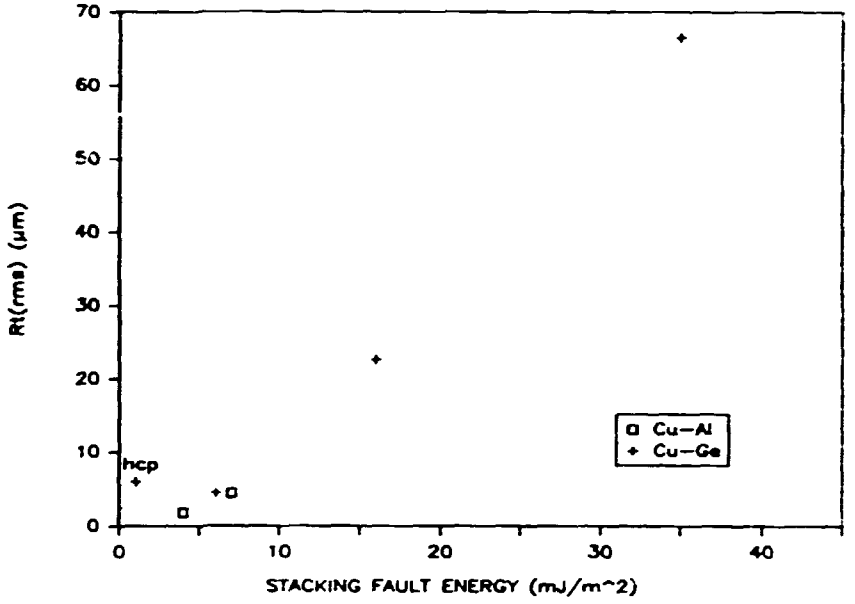

Fig. 10c

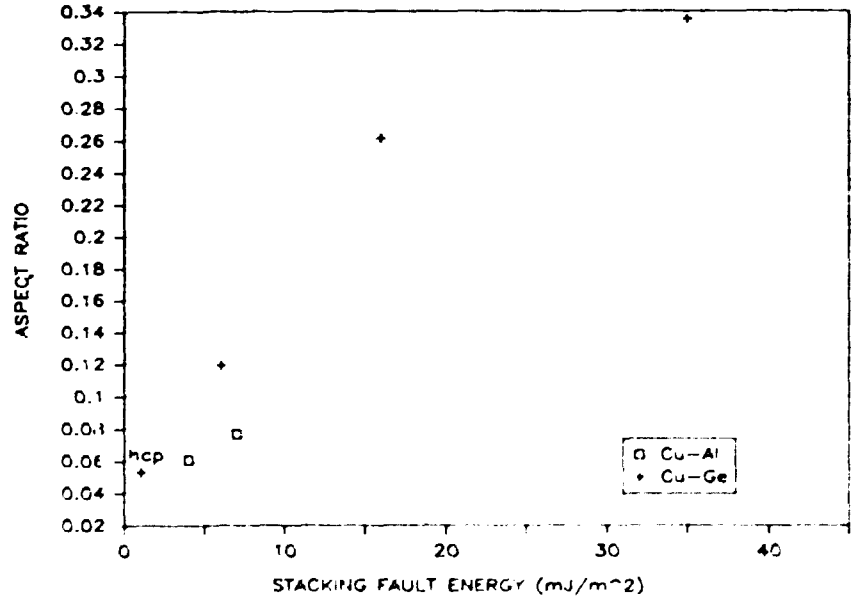

Fig. 10d

Fig. 10. Variation of damage parameters as a function of stacking fault energy for Cu - Al and Cu - Ge alloys after tests at 130 N. a) Displaced volume parameter. b) $\bar{R}_t$ parameter. c) R_t (rms) parameter. d) Aspect ratio parameter.

10a-c, it can be seen that each damage parameter decreases in about the same manner with decreasing stacking fault energy. One of the alloys, Cu - 15 Ge, has the hcp structure and in this respect does not belong with this comparison among fcc alloys. It is included, however, because one effect of decreasing the stacking fault energy is to increase the tendency towards coplanar slip. Coplanar slip in fcc alloys can be compared to the preference for basal slip in many hcp metals. Thus, fcc alloys with very low stacking fault energies tend to behave like hcp metals exhibiting primarily basal slip. For the purpose of plotting the data, the stacking fault energy of the Cu - 15 Ge alloy has been assigned arbitrarily the low value of 1 mJ/m^2. The actual stacking fault energy for this alloy could, of course, be determined for extended dislocations lying on the basal plane, but it would not be the relevant quantity for use in this comparison.

In Fig. 10d the aspect ratio parameter is plotted as a function of stacking fault energy. Values $<<1$ are obtained for alloys with low stacking fault energies. The damage on specimen flats of these materials consisted of fine grooves parallel to the direction of sliding, similar in appearance to the damage on Co shown in Fig. 7. For higher stacking fault energies, the aspect ratio parameter in Fig. 10d remains less than one but has increased significantly in magnitude compared to the low stacking fault energy alloys. In this case, microscopy examination of the surfaces showed that the damage consisted of lumps and grooves, commensurate with the occurrence of galling.

In Table 2 it may be noted that as the stacking fault energy decreases the hardness increases. The $\bar{R}_t$ parameter is plotted as a function of hardness in Fig. 11. As was found for the stacking fault energy, the damage decreases with increasing hardness. Although an increase in hardness probably contributes some to the reduction in damage severity,

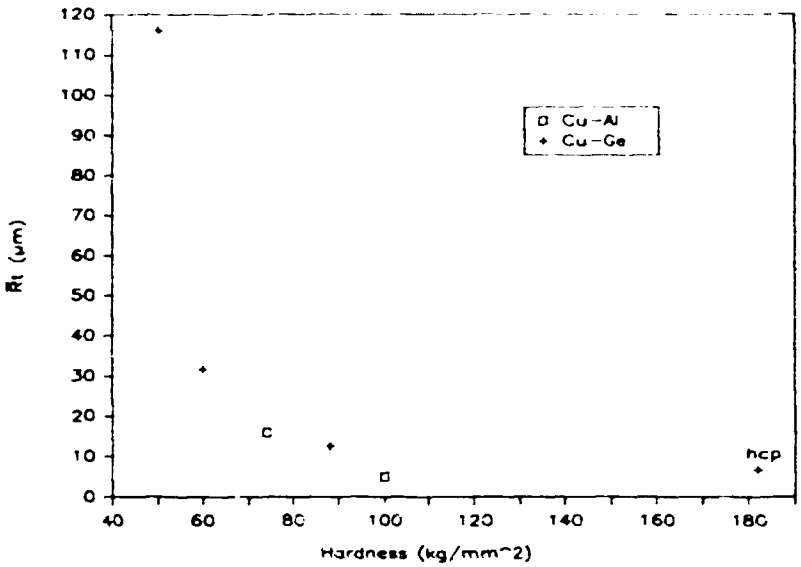

Fig. 11. Variation of $\bar{R}_t$ parameter as a function of hardness for Cu - Al and Cu - Ge alloys.

we attribute the majority of the effect to the decrease in stacking fault energy which influences the mode of deformation. For the pure metals, it was clear that the mode of deformation was the predominant factor influencing galling behavior, for example, compare Zn or Mg with Al. The former two metals deform primarily by basal slip while the latter metal deforms more or less homogeneously because of easy cross slip among the {111} glide planes. Also, it is difficult to explain solely on the basis of hardness the sharp drop in damage that occurs between 50 and 70 kg/mm^2 and the relative insensitivity to hardness thereafter.

GALLING OF COMMERCIAL ALLOYS

The galling severity of a number of commercial alloys has been measured. For example, a comparison was made of AISI 1541 steel in the soft, hot rolled condition (94 HRB) and the hard, quenched condition (54 HRC).[3] The results are shown in Fig. 12 where damage severity, in terms of $\bar{R}_t$,

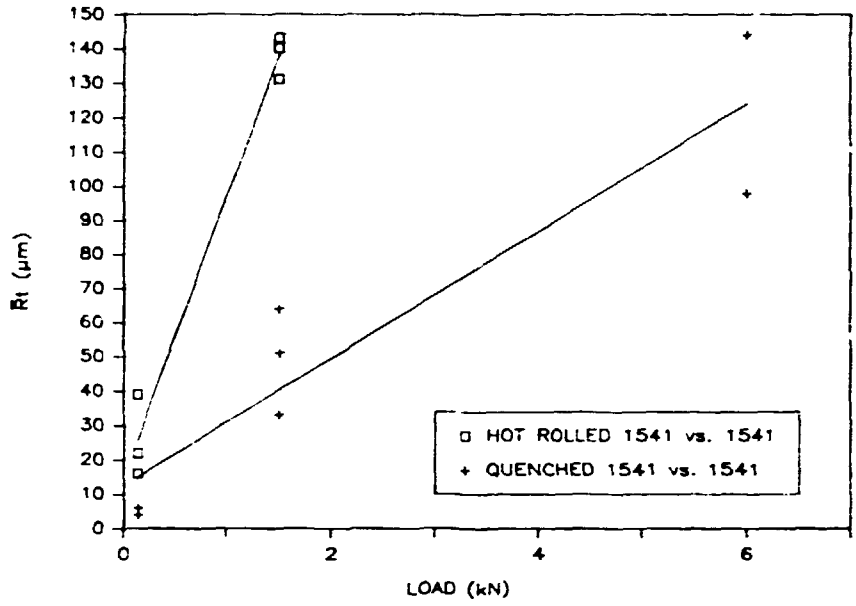

Fig. 12. $\bar{R}_t$ is plotted as a function of load for AISI 1541 steel in the hot rolled (94 HRB) and quenched (54 HRC) conditions.

is plotted as a function of applied load. Here, it is clear that 1541 steel in the quenched condition is much more resistant to galling than it is in the hot rolled condition. Although the high hardness of the quenched material probably contributes to the reduction in damage, as was discussed above in connection with the influence of stacking fault energy, the decrease may not be due just to the increase in hardness. In the hot rolled condition, the microstructure of 1541 steel consists of pearlite and ferrite. After quenching, the structure is martensite with a small amount of retained austenite. The deformation behavior of these two microstructures differs significantly, and this almost certainly will influence the galling response.

It may also be noted in Fig. 12 that the damage measured by $\bar{R}_t$ increases with increasing load. Since the local stresses responsible for galling are proportional to the applied load, this dependence would be expected of a parameter that is used to measure damage severity.

In addition to investigating the influence of heat treatment, the effects of carburizing and nitriding have also been studied.[3,4] Both of these surface treatments were found to result in a significant reduction in galling severity.

Stainless steels are often cited as being susceptible to galling. This is probably because the very thin adherent passive film that forms on the surface of these alloys does not provide the same amount of protection as the thicker, more easily sheared films that are normally present on less corrosion resistant metals. Also, stainless steels do not respond well to many of the lubricants that are used. The galling severity of several stainless steels and a number of other alloys is plotted as a function of hardness in Fig. 13. It can be seen that the stainless steels as a group do not, in fact, behave more poorly than the other metals. Since the surfaces were clean and had not been exposed to conditions that would lead to more than a thin

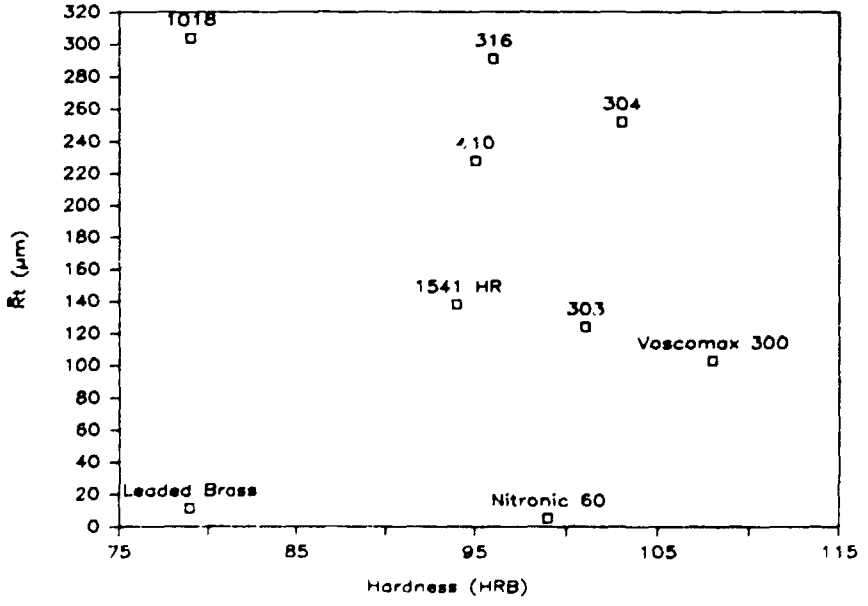

Fig. 13. $\bar{R}_t$ for various commercial alloys tested at a load of 1500 N.

oxide film for all metals, the surface film was not a critical element in differentiating between the galling behavior of these metals.

Two of the metals, Nitronic 60 and leaded brass, stand out as being less severely damaged than the others in Fig. 13. Nitronic 60 is an austenitic stainless steel that is specifically recommended for applications where galling may be a problem.[14]

We have conducted transmission electron microscopy studies on this alloy and have found that it has a low stacking fault energy, considerably less than 304 or 316 stainless steels. It appears that this property is the basis for the improved galling resistance of Nitronic 60.

Leaded brass, on the other hand, is a two phase alloy consisting of small particles of lead in a matrix of alpha brass. It is thought that during sliding the lead may be smeared over the surface and in this way provide what is in effect a thin lubricating film.

CONCLUSIONS

1. Parameters based on surface topography provide a useful means to measure galling behavior
2. Hardness and galling severity do not, in general, correlate for different metals
3. Hexagonal close packed metals are more resistant to galling than body centered cubic and face centered cubic metals
4. Alloys with low stacking fault energies gall less severely than those with high stacking fault energies
5. 1541 steel in the non-hardened, hot rolled condition galls more severely than the same steel in the quenched, hardened condition
6. Galling severity increases with increasing load
7. Carburizing and nitriding increase the resistance to galling

REFERENCES

1. M. B. Peterson, L. K. Ives and K. J. Bhansali, "A Literature Review of the Galling Process", in Metal Transfer and Galling in Metallic Systems, AIME, New York, (to be published)

2. W. J. Schumacher, "New Galling Data Aid in Selecting Stainless Steel," Materials Engr., 4 (1973), 61-63.

3. P. A. Swanson, L. K. Ives, E. P. Whitenton and M. B. Peterson, "A Study of the Galling of Two Steels Using Two Test Methods," in Wear of Materials-1987, K. C. Ludema, ed., ASME, New York (1987) pp. 49-58.

4. L. K. Ives, M. B. Peterson, E. P. Whitenton, "Mechanisms of Galling and Abrasive Wear", in AR&TD Fossil Energy Materials Program Semiannual Progress Report for the Period Ending March 31, 1987, ONRL/FMP-87/1, Oak Ridge National Laboratory, Oak Ridge, TN.

5. M. B. Peterson, K. J. Bhansali, E. P. Whitenton and L. K. Ives, "Galling Wear of Metals," in Wear of Materials-1985, K. C. Ludema, ed., ASME, New York (1985) pp. 293-301.

6. S. B. Ainbinder and A. S. Prancs, "On the Mechanism of the Formation and Destruction of Adhesion Junctions Between Bodies in Frictional Contact", Wear 9 (1966) 209-227.

7. P. Crook and J. H. Richards, "The Effect of Cobalt in Wear Systems", in Proceedings of the Conference on the Production and Applications of Less Common Metals, Hangzhou, Peoples Republic of China, 1982, publ. English Metals Society (1983)

8. E. P. Whitenton, M. B. Peterson, and L. K. Ives, " Method for Quantitative Measurement of Galling Damage," in Proceedings of the TMS/ASTM Symposium on Metal Transfer and Galling in Metallic Systems, Orlando, FL, October 8, 1986, (to be published).

9. M. B. Peterson and W. O. Winer, ed., Wear Control Handbook, ASME, New York (1980) 44.

10. M. Cocks, "Interaction of Sliding Metal Surfaces," J. Appl. Phys. 33 (1962) 2152-61.

11. M. Antler, "Wear, Friction, and Electrical Noise Phenomena in Severe Sliding Systems," ASLE Trans. 5 (1962) pp. 297-307.

12. M. Antler, "Processes of Metal Transfer and Wear", Wear 7 (1964) 181-203.

13. K. J. Bhansali and A. E. Miller, "Role of Stacking Fault Energy on the Galling and Wear Behavior of a Cobalt Base Alloy", in Wear of Materials-1981, ASME, New York (1981) 179-185.

14. W. J. Schumacher, "Metals for Non-Lubricated Wear", Machine Design, March 11, 1976, pp.57-59.

PARTICLE EROSION IN TURBULENT FLOW PAST TUBE BANKS

J.A.C. Humphrey, M.J. Schuh, C. Schuler and M.O. Schweitzer

Mechanical Engineering Department
University of California
Berkeley, CA 94720

ABSTRACT

Measurements and calculations are reported for particle-laden flows past single tubes and two in-line tubes. The measurements are for particle flux in the turbulent flow regime. This is a more fundamental quantity to determine than erosion since the latter is complicated by the nature of the particle-surface interaction and the material properties. The calculations are for fluid and particle motion in the laminar regime. They have required the development and testing of a body-fitted coordinate numerical procedure for determining fluid motion past single tubes, two in-line tubes and a tube in an infinite tube bank. Current work is addressing the extension of the numerical procedure to turbulent flow.

INTRODUCTION

Flows past single tubes or multiple tube arrays arise in numerous engineering applications involving heat transfer. Of special interest here is the case when the bulk flow is aligned normal to the tube(s). Much of the work performed for this configuration, especially for single tubes (or cylinders), has been reviewed by Zukauskas and Ziugzda [1985]. A summary of investigations performed in staggered and in-line tube banks has been given by Chen et al. [1986] for flows in the laminar regime. Corresponding studies for flows in the turbulent regime have been reviewed by Antonopoulos [1985].

Frequently, the flow normal to a tube bank carries solid particles in suspension that erode the tubes. This is the case in the convective zone of a fluidized bed combustor, and in the primary superheaters, reheaters and economizers of coal-fired boilers. These systems present complex erosion problems of great practical consequence and considerable fundamental interest.

In contrast to the relatively large number of experimental and computational investigations conducted to clarify the flow and heat transfer characteristics of tube bank configurations, little work of comparable extent has been done to improve understanding of the corresponding particle-impact erosion problem. While interesting in their own right, numerical studies of particles impacting single tubes, such as have been performed by Tilly [1969], Healy [1970], Laitone [1983] and Vittal and Tabakoff [1986], are of limited value for rendering predictable the erosion of tubes in tube banks. Similarly, the experimental data available, particularly that pertaining to particle motion in turbulent flow, are of limited use for advancing fundamental insight of important basic mechanisms. This is because in attempting to simulate systems of practical (industrial) interest, various factors such as temperature, particle size and concentration, material properties, and fluid flow conditions (especially turbulence, unknowingly) are frequently varied simultaneously. Thus, often the experimental task is reduced to simply obtaining a correlation for erosion, in terms of the independent variables, that is highly specific to the system under investigation. See, for example, Tsai et al. [1981], Bauver et al. [1984], Gilmour et al. [1985] and the various references therein.

To our knowledge, an in-depth study of particle-laden erosive flows in tube banks has not yet been performed. This is not surprising given the complexity of the problem. It is the purpose of this work to partly overcome the knowledge gap by performing an experimental and numerical investigation of a simpler flow configuration.

In the experiment, attention is focused on the flow of air at high speeds through a vertical duct with two in-line tubes of discretely variable spacing aligned normal to the flow. (The single tube configuration is also documented as a reference standard.) The air carries a dilute concentration of glass beads of mass loading $\Gamma < 7 \times 10^{-3}$ and of nominal diameter $d_p = 97\mu m$. The speed and turbulence levels of the air approaching the tubes can be altered to investigate their respective influence on particle flux to the tube surfaces. In addition to particle flux, the study calls for measuring particle and fluid-phase velocities using a laser-Doppler velocimeter. This is part of the plan for continuing work.

The numerical simulation has two principal objectives:

a) to predict as validation test cases the one- and two-tube configurations investigated experimentally;

b) to extrapolate the use of the validated numerical procedure to predict particle-laden gas flows in tube banks.

A related important objective is to calculate the relative erosion in configurations "a" and "b" above, using a cutting wear model as in, for example, Dosanjh and Humphrey [1985].

While turbulent flow conditions are of primary concern, because the laminar flow regime is free of modeling uncertainties and offers valuable qualitative insight, it is also the subject of numerical research. We report here on the laminar flow calculations. Theoretical and numerical work is currently underway that addresses the turbulent motion of the fluid and of the particles in suspension.

The remainder of this report is divided in three parts. First we present ongoing experimental work. This is followed by a description of the ongoing numerical activity. The report concludes with a summary of achievements and plans for continuing work.

DISCUSSION OF CURRENT ACTIVITIES

EXPERIMENTAL WORK

A schematic of the experimental apparatus is provided in Figure 1. Air at high speed is drawn from a stagnation chamber into a vertical duct of square cross-section (hydraulic diameter D = 10cm) by a continuously variable speed, axial-flow, Lansom blower. Measurements of the air velocity through the duct are obtained with a static pressure pitot tube connected to an oil manometer. The air speed range used in the experiments to date is 10-30 m/s, although higher speeds can be achieved. The blower has been sound-proofed for ease of operation.

A 4 to 1 contraction at the duct inlet is followed by two screens of discretely variable spacing. The screen characteristics are: width of grid element, b = 3.175mm; distance between grid element centers, M = 6.845mm. Two in-line tubes of diameter d = 2.32cm are located downstream of the screens in the vertical duct. Their axes are aligned normal to the main flow (as well as to two facing side walls) and contained in the duct center. The spacing between the two tubes is discretely variable. The distance between the second (downstream) screen and the first (upstream) tube determines the level of the turbulence fluctuations at the first tube location. To find this, the experimental correlations given by Naudascher and Farell [1970] are used.

Particles of diameter d_p = 97μm (approximately) are introduced into the duct flow by gravity feed from a hopper whose mass flow versus time has been previously calibrated. The flow of particles is controlled by the size of the orifice through which they pass. The particles fall onto a vibrating screen (isolated from the vertical test section) which distributes them evenly over the duct cross-section. A filter box downstream of the duct test section removes most of the particles from the flow. A cyclone separator removes those particles that have been comminuted and have escaped the screens

in the filter box. Additional filters at the end of the diffuser connected to the blower ensure that very small particles that might damage the blower are removed. The filtered air from the blower is exhausted to the atmosphere.

The upstream tube in the test section is constructed from steel and is perfectly circular. The downstream tube is machined from aluminum. Its cross-section is shown in Figure 2 where it is seen that 36 shallow grooves of triangular cross-section are evenly distributed around the periphery of the tube. Crisco shortening (hydrogenated palm and soy oil) is carefully packed into the grooves and serves to trap any particles that strike a groove cross-section. The Crisco-particle mixture is carefully removed from a groove and placed on a pre-weighed screen after a run. The Crisco is then removed by carefully washing with a warm mixture of isomer hexanes (C_6H_{14}). The mass of particles remaining after washing is dried and then weighed on a Mettler balance to within $\pm$ 4 x 10^{-5} gr. In this way, the circumferential distribution of particles deposited in the grooves around the aluminum tube during an experiment can be determined. Although laborious, the procedure is simple, accurate and inexpensive.

The tubes are positioned at their respective location by insertion through snug-fitting holes in two facing walls of the test section. By aligning two marks, one on a tube and one on a wall, the relative orientation is maintained between a tube and the flow. For experiments involving a single tube, the aluminum tube was always used. For experiments involving two tubes, the aluminum tube was always the second (downstream) tube. The walls of the vertical duct are constructed from 3/8" (9.5mm) thick transparent plexiglass for ease of optical access.

Some of the results obtained to date are shown in Figures 3 - 4. The experimental conditions are given in the figure captions where: x/D denotes the distance in duct hydraulic diameters between the second grid and the first tube;

DISCUSSION OF CURRENT ACTIVITIES

EXPERIMENTAL WORK

A schematic of the experimental apparatus is provided in Figure 1. Air at high speed is drawn from a stagnation chamber into a vertical duct of square cross-section (hydraulic diameter D = 10cm) by a continuously variable speed, axial-flow, Lansom blower. Measurements of the air velocity through the duct are obtained with a static pressure pitot tube connected to an oil manometer. The air speed range used in the experiments to date is 10-30 m/s, although higher speeds can be achieved. The blower has been sound-proofed for ease of operation.

A 4 to 1 contraction at the duct inlet is followed by two screens of discretely variable spacing. The screen characteristics are: width of grid element, b = 3.175mm; distance between grid element centers, M = 6.845mm. Two in-line tubes of diameter d = 2.32cm are located downstream of the screens in the vertical duct. Their axes are aligned normal to the main flow (as well as to two facing side walls) and contained in the duct center. The spacing between the two tubes is discretely variable. The distance between the second (downstream) screen and the first (upstream) tube determines the level of the turbulence fluctuations at the first tube location. To find this, the experimental correlations given by Naudascher and Farell [1970] are used.

Particles of diameter d_p = 97μm (approximately) are introduced into the duct flow by gravity feed from a hopper whose mass flow versus time has been previously calibrated. The flow of particles is controlled by the size of the orifice through which they pass. The particles fall onto a vibrating screen (isolated from the vertical test section) which distributes them evenly over the duct cross-section. A filter box downstream of the duct test section removes most of the particles from the flow. A cyclone separator removes those particles that have been comminuted and have escaped the screens

in the filter box. Additional filters at the end of the diffuser connected to the blower ensure that very small particles that might damage the blower are removed. The filtered air from the blower is exhausted to the atmosphere.

The upstream tube in the test section is constructed from steel and is perfectly circular. The downstream tube is machined from aluminum. Its cross-section is shown in Figure 2 where it is seen that 36 shallow grooves of triangular cross-section are evenly distributed around the periphery of the tube. Crisco shortening (hydrogenated palm and soy oil) is carefully packed into the grooves and serves to trap any particles that strike a groove cross-section. The Crisco-particle mixture is carefully removed from a groove and placed on a pre-weighed screen after a run. The Crisco is then removed by carefully washing with a warm mixture of isomer hexanes (C_6H_{14}). The mass of particles remaining after washing is dried and then weighed on a Mettler balance to within $\pm$ 4 x 10^{-5} gr. In this way, the circumferential distribution of particles deposited in the grooves around the aluminum tube during an experiment can be determined. Although laborious, the procedure is simple, accurate and inexpensive.

The tubes are positioned at their respective location by insertion through snug-fitting holes in two facing walls of the test section. By aligning two marks, one on a tube and one on a wall, the relative orientation is maintained between a tube and the flow. For experiments involving a single tube, the aluminum tube was always used. For experiments involving two tubes, the aluminum tube was always the second (downstream) tube. The walls of the vertical duct are constructed from 3/8" (9.5mm) thick transparent plexiglass for ease of optical access.

Some of the results obtained to date are shown in Figures 3 - 4. The experimental conditions are given in the figure captions where: x/D denotes the distance in duct hydraulic diameters between the second grid and the first tube;

$$\tilde{u} \; (\equiv \sqrt{\overline{u^2}} \times 100/U_B)$$

is the percent turbulence intensity based on the bulk average velocity, U_B, though the duct; Re_d ($\equiv dU_B/\nu$) is the Reynolds number of the flow based on the tube diameter, d; and Re_D ($\equiv DU_b/\nu$) is the Reynolds number of the flow based on the duct diameter D.

The curve in Figure 3-a represents the total particle mass captured by a single tube as a function of time. This shows that after about 10 seconds, for the experimental conditions investigated, a "surface saturation" condition occurs. The figure suggests that after one or two layers of particles are embedded in the grooves, further embedding is inhibited, presumably by rebounding of the particles from encrusted portions of the tube surface. The conclusion is that surface flux measurements using this technique must be limited to short run-times (or, equivalently, low values of the total particle phase mass) to avoid a bias in the measurement of particle surface flux.

Figure 3-b shows the circumferential distribution of particle flux (mass/(time x area)) normalized by the particle flux through the duct (labeled "channel" in the figure) at the end of a 5 second run. It is important to note that the real groove area, as opposed to the projected area, has been used in determining the particle flux to a groove. Results shown for 100, 140 and 180 seconds in Figure 3-c illustrate the problem referred to for long run-times. In particular, the profiles obtained at 140 and 180 seconds display circumferential variations that are absent in the short run-time case in Figure 3-b, due to the cummulative bias in the surface flux measurement.

The particle flux data shown in Figure 3-b is especially interesting for two reasons: i) it shows a maximum flux at 180 degrees, corresponding to the stagnation point on the tube; ii) it shows a small (but measurable) number of particles impacting the tube below 50 and above 270 degrees.

The first point is important because for ductile metals maximum erosion is expected to occur at circumferential locations ± 45 degrees with respect to the normal (180 degree) location; see Bauver et al.

[1984]. Thus, the combined effects of higher speed and sharper angles of attack at these locations must be overcoming the significantly lower particle fluxes there (relative to the stagnation point location.) The second result points to the unavoidable reentrainment of some (albeit few) slower moving particles in the wake region of the tube, which are redirected toward the tube's rear surface where they are embedded.

Results for the flux of particles towards the second of two in-line tubes are shown in Figure 4. The conditions stipulate tubes 2d apart from their centers in a flow with 5% turbulence intensity. The protective influence of the upstream tube is obvious in two ways:

i) first, in the total reduction of mass flux to the second tube (compare with Figure 3-b);

ii) second, in the minimum displayed at 180 degrees, resulting from the upstream tube wake.

Additional experiments are underway to investigate the influence of turbulence intensity and tube spacing on the particle flux to two in-line tubes. The data obtained, of which a representative sample has been shown here, will serve to evaluate the numerical calculation procedure under development. In this regard, it is especially important to note that the measurement of the circumferential particle flux distribution over a tube surface is a much more fundamental experimental quantity to determine than a corresponding measurement of erosion. This is because the prediction of the latter quantity is subject to serious uncertainties related to the specification of material properties, particle-surface interactions and, ultimately, the erosion model used. As a result, erosion measurements are, in general, poor candidates for testing the influence of fluid motion on impacting particle speeds and trajectories.

Continuing work includes making measurements of fluid and particle velocities for the one and two-tube configurations discussed above using a laser-Doppler velocimeter in conjunction with a computerized data acquisition/processing system.

NUMERICAL WORK (LAMINAR FLOW)

The prediction of particle motion and erosion is broken into four stages. First, a nonorthogonal boundary fitted coordinate system is generated for the geometry of interest (single tube, two tubes in-line, a tube in an infinite in-line tube bank). Second, the finite difference method is used to calculate the laminar flow field by solving the steady state Navier Stokes equations of motion on the boundary fitted coordinate system. Third, a Runge-Kutta method is used with a drag model to track the particles through the calculated flow field. Fourth, the particle impact imformation is used with a wear model to predict erosion. This section discusses each of the first three stages and presents the equations and boundary conditons used. The fourth stage is the subject of ongoing work.

Grid Generation

Essentially one type of grid is used for all of the calculations. A typical grid is shown in Figure 5. The grid is generated in two parts. The first part generated is near the tube(s) (approximately the center two quarters in the upstream and downstream direction and from the bottom to the top of the grid). These grid lines are generated by using an elliptic grid generation method as discussed by Thompson et al. [1985]. The second part consists of putting upstream and downstream ends on this grid with a cubic spline. The spline is used to make the grid orthogonal at the inlet and exit planes for ease in implementing boundary conditions; see Figure 6.

In the two dimensional body-fitted curvilinear coordinate system, there are two coordinate lines that will be represented by ζ and η in this report. These lines correspond to x and y respectively in the Cartesian coordinate system. Conceptually, it is easier to solve the conservation equations in what is referred to as the computational domain or transformed field. The computational field is a rectangle

for all of the cases in this report with square cells having sides of unity length. In the computational domain, the curvature of the grid lines in the physical field is accounted for by the metric coefficients which appear in the transformed equations. The elliptic part of the grid generation is accomplished by solving the following Poisson equation in the computational domain, where the derivatives are in terms of the new coordinate lines ζ and η:

$$g_{22}\{r_{\zeta\zeta} + P\, r_{\zeta}\} + g_{11}\{r_{\eta\eta} + Q\, r_{\eta}\} - 2g_{12}r_{\zeta\eta} = 0 \tag{1}$$

where

$$g_{ij} = a_i \cdot a_j \tag{2}$$

and

$$a_i \equiv \underset{\xi}{r_i} \qquad r = xi + yj + zk \tag{3}$$

In all equations (like Equation 1), subscripted coordinates represent partial differentiation. The source terms P and Q are used to control the point distribution of the grid. These source terms are referred to as control functions (functions because they may vary throughout the grid). They can be calculated in a variety of ways. The technique called "derivative line spacing" was used in this work. Derivative line spacing control functions work to maintain the boundary point distribution throughout the grid. P controls the location of vertical lines and Q controls that of the horizontal lines. The control functions are calculated from:

$$P = -\frac{r_{\zeta} \cdot r_{\zeta\zeta}}{|r_{\zeta}|^2} - \frac{r_{\zeta} \cdot r_{\eta\eta}}{|r_{\eta}|^2} \tag{4}$$

$$Q = -\frac{r_{\eta} \cdot r_{\eta\eta}}{|r_{\eta}|^2} - \frac{r_{\eta} \cdot r_{\zeta\zeta}}{|r_{\zeta}|^2} \tag{5}$$

where

$$\left| r_\zeta \right| = \{ r_\zeta \cdot r_\zeta \}^{1/2}$$

and (6)

$$\left| r_\eta \right| = \{ r_\eta \cdot r_\eta \}^{1/2}$$

In Equations 4-6, ζ derivatives are calculated on the top and bottom boundaries and linearly interpolated towards the center of the calculation domain. Similarly, η derivatives are calculated on the left and right boundaries and linearly interpolated towards the center of the domain. These control functions yield consistently smooth grids without further modification.

The use of Equation 1 generates a grid with a suitable point distribution but does not allow the implementation of orthogonality at the boundaries. At the inlet and exit planes, this deficiency was overcome by using a cubic spline to fit horizontal lines that are orthogonal to these boundaries while joining smoothly to the grid generated by the Poisson equation. An additional vertical grid line is added at the inlet and exit plane locations to facilitate the implementation of the fully developed exit flow boundary condition; see Figure 6.

Flow Field Calculation

The steady state continuity and Navier Stokes equations are solved by a finite difference method on the nonorthogonal curvilinear grid. The equations in Cartesian coordinate notation are:

$$\{ \rho u^i \}_{x^i} = 0 \qquad (7)$$

$$\{u^i \rho u - \mu u_{x^i}\}_{x^i} + P_{x^1} = 0 \tag{8}$$

$$\{u^i \rho v - \mu v_{x^i}\}_{x^i} + P_{x^2} = 0 \tag{9}$$

where

$$x^1 = x \quad \text{and} \quad x^2 = y \tag{10}$$

The steady state conservation forms of the continuity and Navier Stokes equations in the computational or transformed region are:

$$\{\sqrt{g}\,\rho U^i\}_{\xi^j} = 0 \tag{11}$$

$$[\sqrt{g}\,\{\rho U^i u - \mu g^{ij} u_{\xi^j}\}]_{\xi^i} + (y_{\xi^2} P)_{\xi^1} - (y_{\xi^1} P)_{\xi^2} = 0 \tag{12}$$

$$[\sqrt{g}\,\{\rho U^i v - \mu g^{ij} v_{\xi^j}\}]_{\xi^i} - (x_{\xi^2} P)_{\xi^1} + (x_{\xi^1} P)_{\xi^2} = 0 \tag{13}$$

where

$$\xi^1 = \zeta \quad \text{and} \quad \xi^2 = \eta \tag{14}$$

$$U^i = \mathbf{a}^i \cdot (ui + vj) \tag{15}$$

$$\mathbf{a}^i \equiv \nabla r \tag{16}$$

$$g^{ij} = \mathbf{a}^i \cdot \mathbf{a}^j \tag{17}$$

The equations are solved by an iterative procedure similar to that in Patankar [1980]. The curvilinear grid requires that all the

variables (u, v, and p) are calculated at the intersection of each grid line rather than at staggered locations as in Patankar's work. The u-momentum equation is discretized and solved with all values taken as constant from the previous iteration except the u velocity. The same procedure is followed for the v-momentum equation. The pressure is calculated by adjusting the pressure from the previous iteration until the velocities calculated by the momentum equations satisfy continuity. This is again similar to the method in Patankar but with two important differences. First, while a central difference is used for the pressure derivatives in the momentum equations in both the present work and in Patankar's work, the central difference has a $2\,\Delta\xi^i$ dependence on the nonstaggered grid but a $\Delta\xi^i$ (Δx^i on a cartesian grid) dependence on a staggered grid. A dependence $2\,\Delta\xi^i$ results in a pressure oscillation when the velocities are averaged to obtain the flux into the control volume used for the pressure calculation. (It is exactly this problem that the staggered grid was created to solve. The staggered grid does not require averages to obtain the fluxes into the control volume used in the pressure calculation.) To obviate velocity averaging at the control volume walls, a linearized version of the momentum equation is solved at each control volume wall. The linearized version of the momentum equation has a $\Delta\xi^i$ dependence in the direction of the two nodes normal to the control volume wall and a $2\,\Delta\xi^i$ dependence in the tangential direction. Solution of the linearized momentum equation eliminates all pressure oscillations in the calculation. The second point is that pressure corrections of the velocities, as performed by Patankar in the pressure equation subroutine, are dispensed with. While this slows down convergence, it does not affect the accuracy of the calculations.

Typical numerical results obtained for the laminar flow regime are shown in Figures 7-9. Figures 7-a and b are complete and close-up views respectively of the 61 x 20 body-fitted coordinate grid used to calculate the flow around a single tube at $Re_d = 26$. This choice of Re_d coincides with flow visualization results presented by Van Dyke [1982]. Figure 8 shows a close-up view of the flow field around the

tube. The separation and reattachment points of the wake agree very well with the flow visualization result. The boundary conditions used for this calculation are indicated in Figure 7-a.

Figure 9 shows the flow past two in-line tubes for three spacings between tubes. Except for the exit plane, the same boundary conditions shown in Figure 7-a were used for these calculations. At the exit plane $v = 0$ and $\partial u/\partial x = 0$ were imposed. For small spacings the wake of the upstream tube projects onto the downstream tube suggesting that in the presence of particles there may be a mitigation of erosion in the vicinity of the stagnation zone of the downstream tube. Although restricted to low Re_d, the results are of qualitative value and considerable practical interest.

Figure 10 illustrates three cases of flows past tubes in an infinite in-line tube bank. In actual fact, it suffices to calculate the flow around one tube with inlet and outlet boundaries located midway between tubes. (The figures show two tubes for ease of presentation). As in the cases shown in Figures 7 - 8, the top and bottom planes are symmetry planes. At the inlet and exit planes, however, periodic boundary conditions are imposed that must be solved for iteratively in the course of calculation. The present case shows wake reattachment between tubes 2d and 3d apart, similar to the in-line two-tube configuration.

Particle Tracking

In this study the following equation is used to describe the motion of an arbitrarily accelerated particle in the fluid flow field

$$m_p \frac{d\vec{U}_p}{dt} = m_p \vec{g} + \frac{1}{2}\pi\left(\frac{d_p}{2}\right)^2 \rho_f C_D \left|\vec{U}_f - \vec{U}_p\right| (\vec{U}_f - \vec{U}_p) \qquad (18)$$

where m_p is the particle mass, $\vec{U}_p$ is its vector velocity, $\vec{U}_f$ is the fluid vector velocity and C_D is the drag coefficient. This equation is the result of a differential force balance where, due to the large

value of the ratio ρ_p/ρ_f (about 2.25×10^3 for glass particles in air), acceleration dependent drag terms (the "added mass" and "Basset history integral" terms) and lift forces (such as "Magnus" and "Saffman" forces) are negligible. Also small are the pressure gradient forces omitted in the equation. Consequently, particle motion is attributed entirely to drag and the gravitational force. Equation (18) is taken from Clift et al. [1978], where it is shown that the terms neglected are indeed small compared to those retained. Furthermore, Eq. (18) is only valid for non-interacting particles.

The particles are assumed to be spherical so that Stoke's drag formula can be used. Since this formula is only valid when the Reynolds number (based on the particle diameter and the relative velocity between the two phases) is much less than unity, an empirically determined correction factor f is employed when the particle Reynolds number is of order unity or larger. As a result, Eq. (18) can be rewritten as

$$\frac{d\vec{U}_p}{dt} = \frac{f}{\tau}(\vec{U}_f - \vec{U}_p) + g \tag{19}$$

where τ is the particle response time given by

$$\tau = \frac{d_p^2 \rho_p}{18 \mu} \tag{20}$$

Since the fluid velocity is calculated at fixed grid points using an eulerian formulation of the equations of motion, the fluid velocity along the trajectory of a particle must be found by interpolation. Special care is required since the grid used for calculating the velocity field is nonorthogonal. In the present study an algorithm embodying the following steps is used:

1. Find the grid point closest to the current particle location. (This is called the search step.)

2. Find the neighboring cell in which the particle is located. (See Figure 11.)
3. Divide the cell found in Step 2 into four triangles, and find the triangle in which the particle is located. (See Figure 12.)
4. Assume that properties at the center of the grid (point c) are the mean of the values at the corners of the cell. Interpolate for properties at the particle location using the values at a, b and c in Figure 12.

This procedure ensures continuity of the interpolated properties from cell to cell. It has also proven to be fast to execute.

Special care is required when the particle approaches the tube surface. Because the solution scheme is parabolic in time, a trial and error scheme has to be implemented to determine the instant and position of impact. For this, a small region around the tube of thickness δ is defined. When the particle first approaches the surface, the solution algorithm is "unaware" of its presence and forces the particle to cross the surface. When this happens, the particle is returned to its previous position, the time step is decreased, and computation is retried. This procedure is repeated until the particle falls into the δ region defined. Assuming that the particle velocity remains constant within δ, Euler's method is used to determine the position and time of particle impaction. Finally, the rebounding particle velocity is calculated assuming specular, elastic reflection. (Of course, more practical, empirical relations can be used.) When the particle is very small ($\tau < 1$), it may rebound from the wall several times. In this case δ must be very small and a very small calculation time step must be used. Consequently, an adaptive time step algorithm is recommended. Work along these lines is in progress.

Extensive testing of the particle-tracking algorithm was performed by reference to the numerical results obtained by Laitone [1983] for the case of a stagnation point flow. Although not shown here, very good agreement was obtained between the two sets of calculations.

Figure 13 shows the trajectories of 200μm glass spheres rebounding specularly and elastically from the surface of a single tube in a flow with $Re_d = 50$. At this low Re_d the particle velocity is strongly influenced by the gravity term in the equation of motion. The particles in this flow are fairly inertial, having momentum equilibrium numbers λ ($\equiv \tau U_B/d$) = 0.44 approximately. The figure also shows how particles crossing the symmetry plane are restored to the flow, as if elastically colliding with the symmetry plane. (This, in fact, is a simple way of ensuring particle mass conservation in the flow field.)

Figure 14 illustrates multiple impacts by a $d_p = 60\mu m$ particle ($\lambda = 0.04$) in a single tube flow with $Re_d = 50$. In this case the particle rebounds three times before clearing the tube. As in the previous case, specular, elastic particle-tube collisions are assumed. Both the particle impact velocity and impact angle vary around the tube, which will affect the secondary erosion. This is a subject of continuing research.

CONCLUSIONS AND CONTINUING WORK

A technique for measuring the particle flux to a tube surface in turbulent gas flows has been successfully developed. Work is underway to obtain measurements of circumferential particle flux distributions on tubes as a function of the turbulence intensity and tube spacing in the flow. Future work includes using a laser-Doppler velocimeter to make corresponding measurements of particle and fluid phase velocities in the vicinity of the tubes.

A numerical procedure has been developed and tested that calculates laminar flow past tubes in body fitted coordinates. Results have been generated for configurations corresponding to a single tube, two in-line tubes and in-line tubes in an infinite tube bank. Work is presently underway to extend the numerical procedure to turbulent flow.

A numerical procedure has been developed and tested that calculates particle trajectories in the laminar flow regime. This has been applied to some of the tube configurations referred to above. The procedure is limited to dilute systems of spherical particles that are denser than the carrier fluid ($\rho_p/\rho_f \gg 1$); a condition characterizing many particle-laden aerodynamic flow configurations. Continuing work will address the extension of the procedure to turbulent flows using a stochastic approach to account for random particle-eddy interactions.

ACKNOWLEDGEMENTS

Thanks go to Mr. J. Lee and Mrs. L. Donahue for the preparation of this report.

REFERENCES

Antonopoulos, K.A. [1985], Heat Transfer in Tube Banks Under Conditions of Turbulent Inclined Flow, International Journal of Heat and Mass Transfer, 28, pp. 1645-1656.

Bauver, W.P., McGough, T.C. and McGowan, J.T. [1984], A Facility for the Characterization of Erosion of Heat Transfer Tubing, in Gas-Solid Flows (J.J. Jurewicz, ed.), FED - Vol. 10, pp. 115-122, American Society of Mechanical Engineers.

Chen, C.K., Wong, K.L. and Cleaver, J.W., [1986] Finite Element Solutions of Laminar Flow and Heat Transfer of Air in a Staggered and an In-Line Tube Bank, Int. J. Heat and Fluid Flow, 7, pp. 291-300.

Clift, R., Grace, J.R. and Weber, M.E. [1978], Bubbles, Drops and Particles, Academic Press, New York.

Dosanjh, S. and Humphrey, J.A.C. [1985], The Influence of Turbulent Erosion by a Particle-Laden Fluid Jet, Wear, 102, pp. 309-330.

Gilmour, J.B., Hindam, H., Liu, A.W. and Briggs, D.C. [1985], the EMR/NSPC/AFBC Materials Program: Evaluation of Probes Removed at the End of Run 5, Physical Metallurgy Research Laboratories Report: ERPR/PMRL 85-12 (TR), Canada Centre for Mineral and Energy Technology, Energy Mines and Resources, Canada.

Healy, J. Val. [1970] Perturbed Two-Phase Cylindrical Type Flows, Phys. Fluids, 13, pp. 551-557.

Laitone, J.A. [1983], Characterization of Particle Rebound Phenomena in the Erosion of Turbomachinery, Journal of Aircraft, 20, pp. 275-281.

Naudascher, E. and Farell, C. [1970], Unified Analysis of Grid Turbulence, J. of the Eng. Mech. Div., Proceedings of the American Society of Civil Engineers, EM 2, pp. 121-141.

Tilly, G.P. [1969], Erosion Caused by Airborne Particles, Wear, 14 pp. 63-79.

Thompson, J.F., Warsi, Z.U.A. and Mastin, C.W. [1985], Numerical Grid Generation, North-Holland, Elsevier Science Publishing Co., Inc., New York.

Tsai, W., Humphrey, J.A.C., Cornet, I. and Levy, A.V. [1981], Experimental Investigation of Accelerated Erosion in a Slurry Pot Tester, Wear, 68, pp. 289-303.

Van Dyke, M. [1982], An Album of Fluid Motion, Parabolic Press, Stanford, California.

Vittal, B.V.R. and Tabakoff, W. [1986], Effect of Solid Particles in Two Phase Flow Around a Two Dimensional Cylinder, paper AIAA-86-0349, presented at the AIAA Aerospace Sciences Meeting, January 6-9, Reno, Nevada.

Zukauskas, A. and Ziugzda, J. [1985], Heat Transfer of a Cylinder in Crossflow, Hemisphere Publishing Corporation, New York.

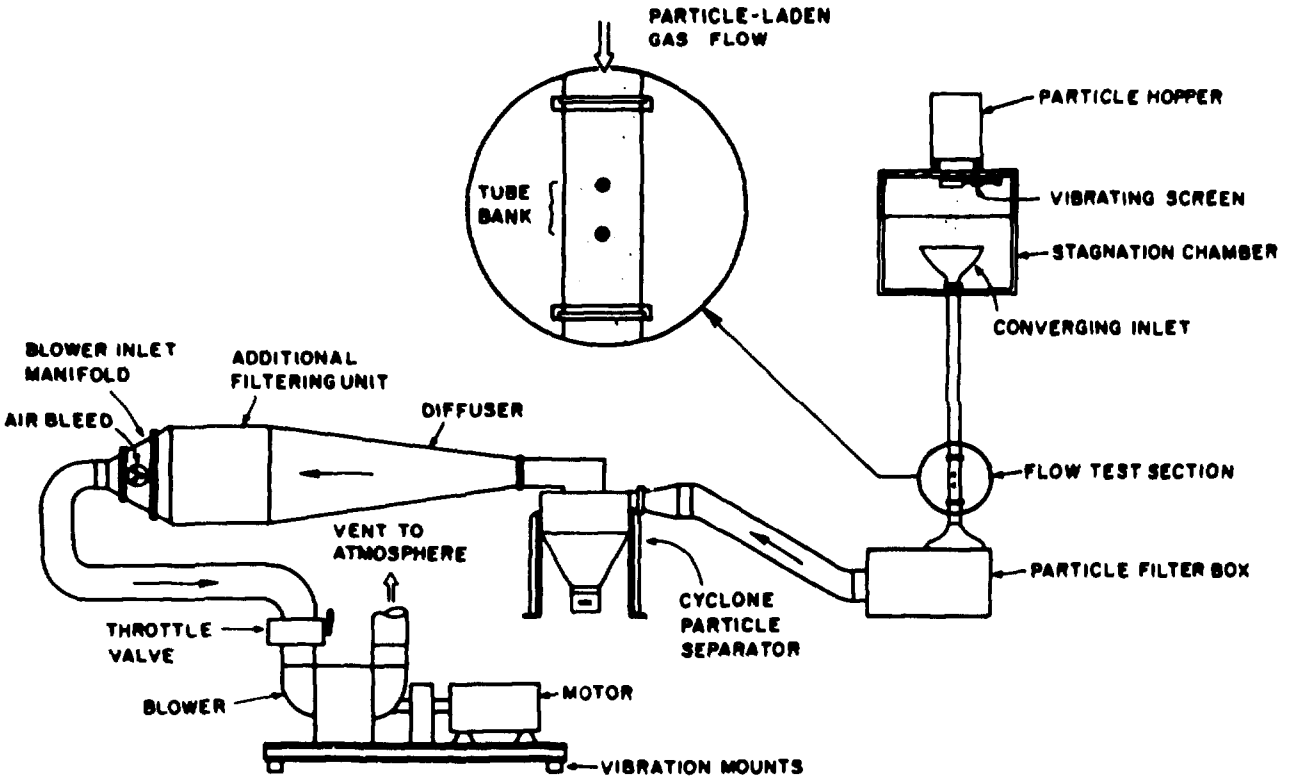

Figure 1: Schematic of experimental apparatus and flow test section

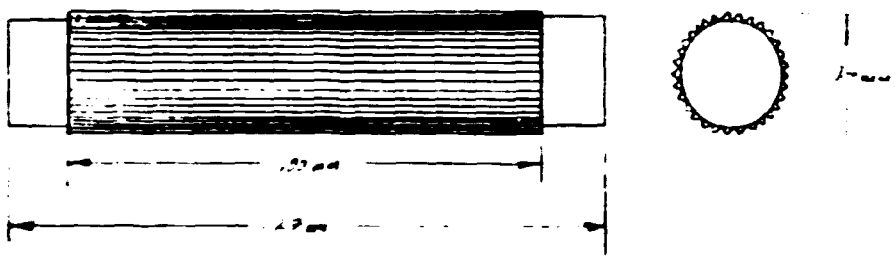

Figure 2: End and side views of machined aluminum tube with triangular grooves for capturing particles.

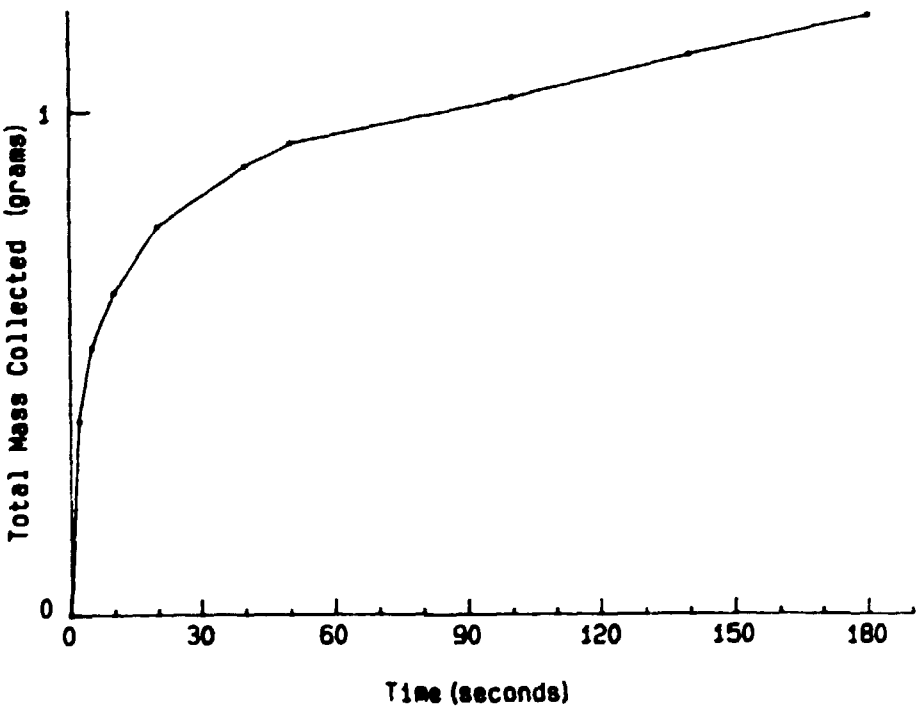

Figure 3-a: Total particle mass collected on a single tube as a function of time. Relevant conditions are: x/D = 8.8; Re_d = 24,000; Re_D = 103,000; $\tilde{u}$ = 1.4%; U_B = 18.49 m/s; d_p = 9μm; $\bar{\Gamma}$ = 6.81 x 10^{-3}.

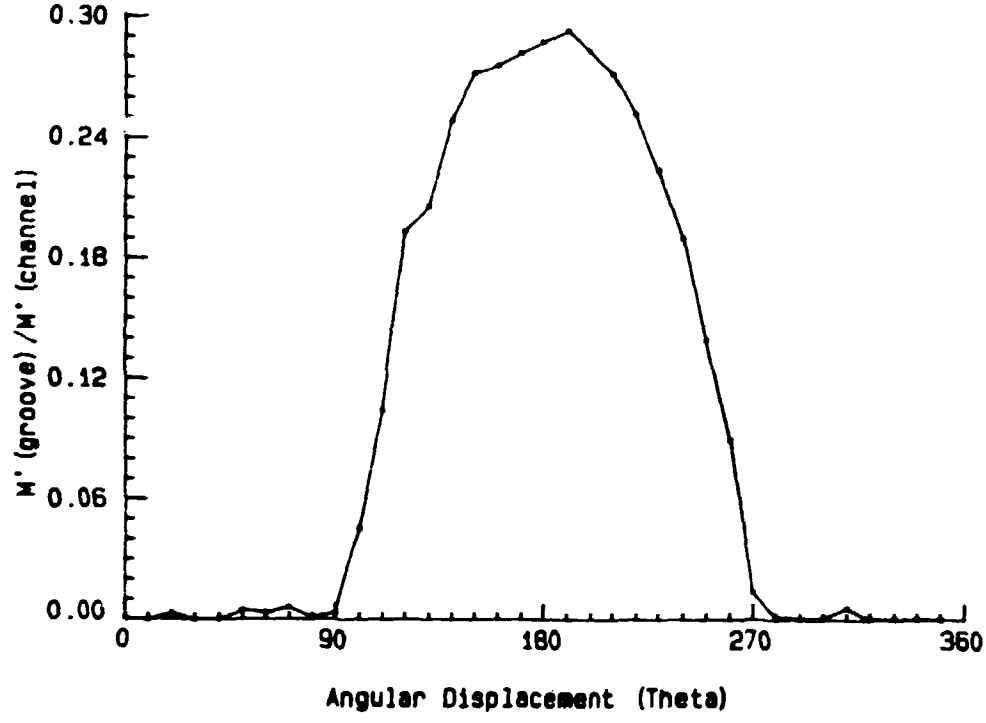

Figure 3-b: Circumferential distribution of normalized particle flux to the surface of a single tube at the end of 5 seconds. Conditions are as specified in caption to Figure 3-a.

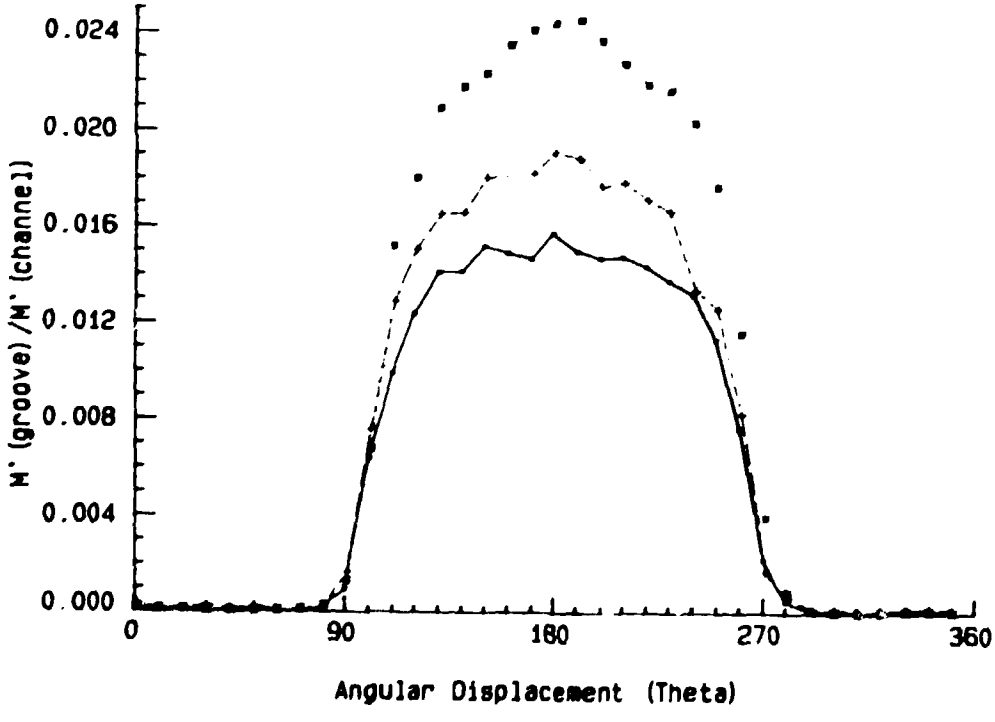

Figure 3-c: Circumferential distributions of normalized particle flux to the surface of a single tube at the end of (— * —) 100 seconds, (— + —) 140 seconds and (—●—) 180 seconds. Conditions are as specified in caption to Figure 3-a.

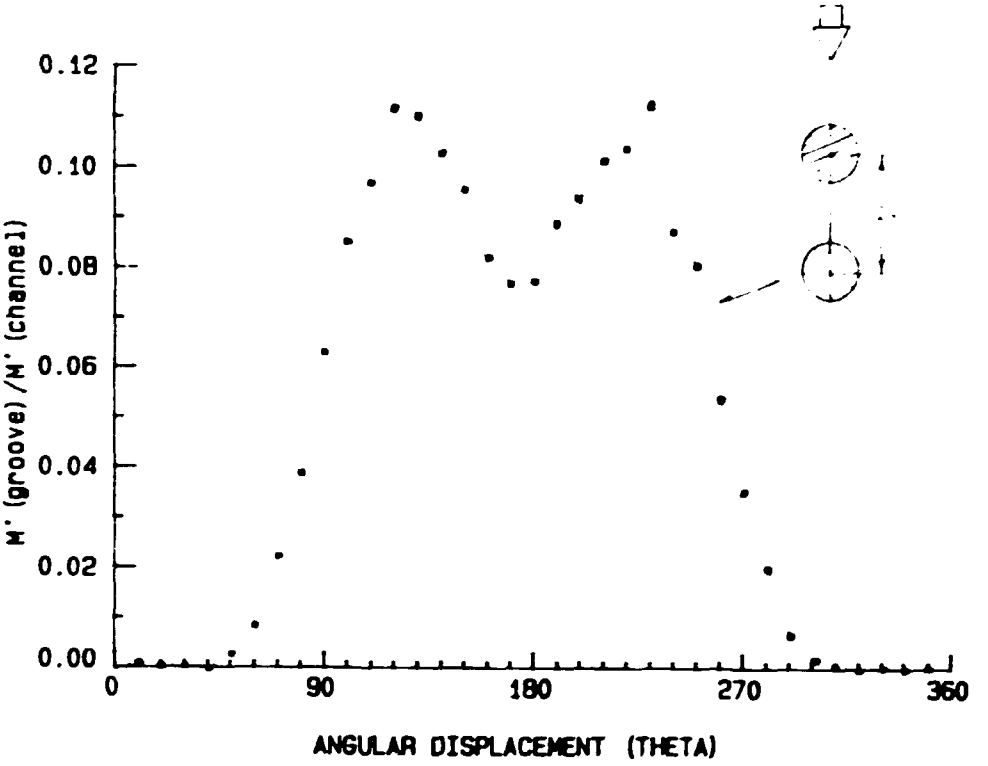

Figure 4: Circumferential distribution of normalized particle flux to the surface of the downstream tube of two in-line tubes. Conditions are as specified in caption to Figure 3-a except that x/D = 0.8 which yields $\widetilde{u}$ = 5%.

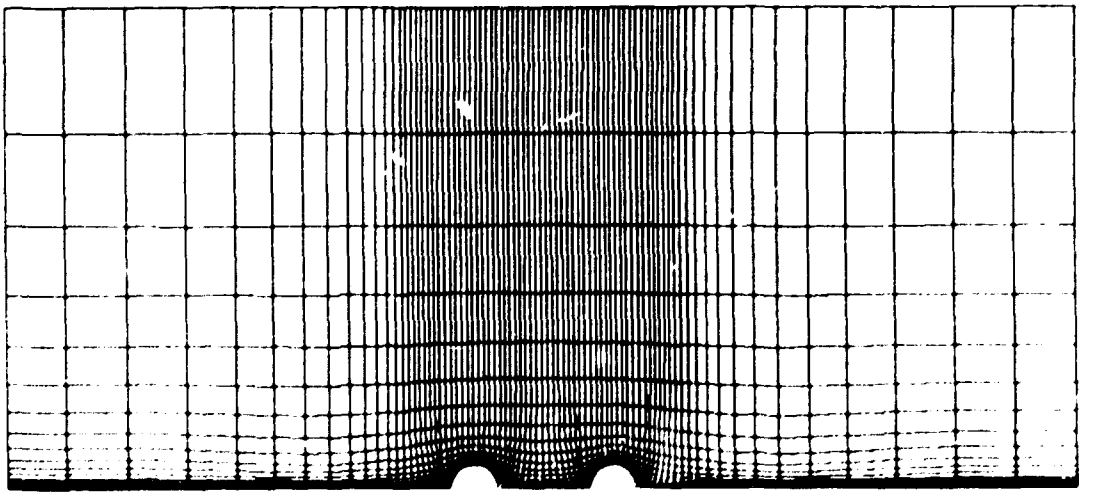

Figure 5: Typical 79 x 18 body-fitted coordinate grid for the case of two in-line tubes.

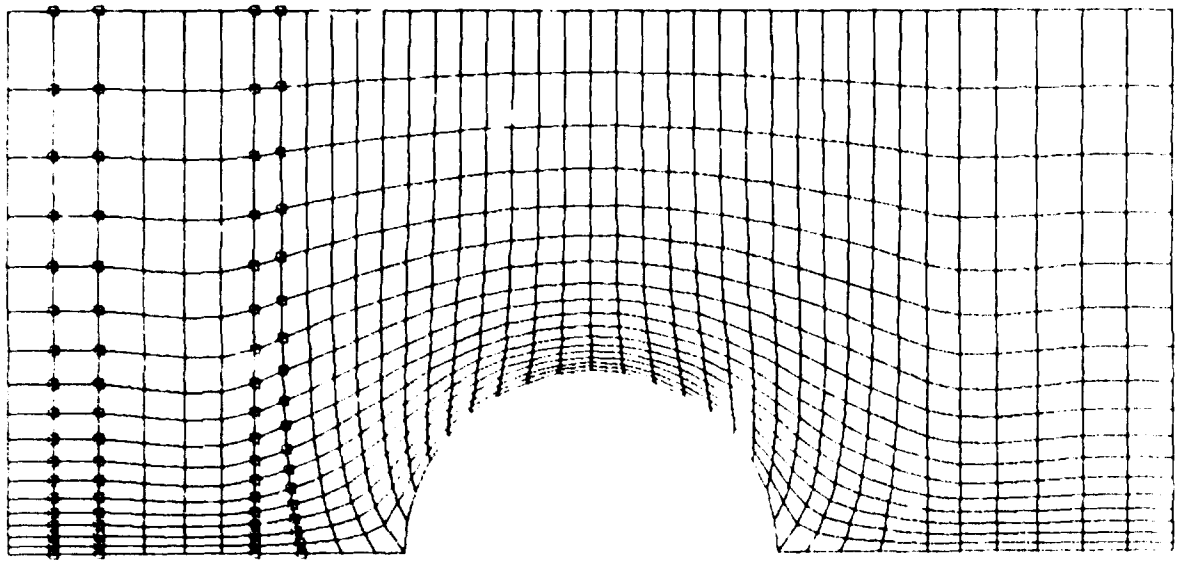

Figure 6: Illustrating the generation of a body-fitted coordinate grid for calculating flow around one tube in an infinite tube bank. Squares in figure mark locations of points used for cubic spline interpolation of horizontal lines (4 points per horizontal line). This procedure ensures a grid that is orthogonal at the inlet and exit planes. In practice, only half the grid is calculated; the other half is generated by reflecting the calculated half with respect to the vertical symmetry plane passing through the tube center.

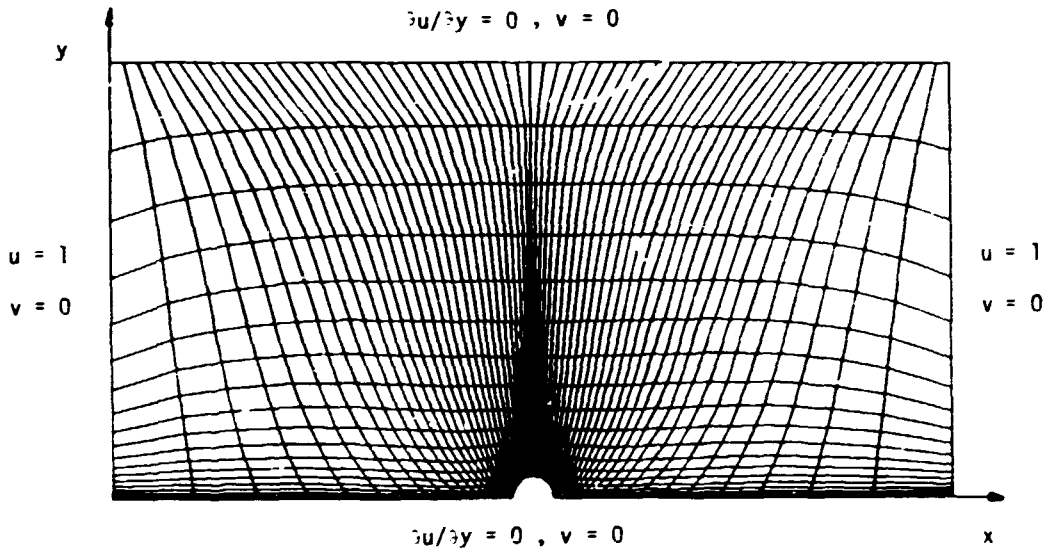

Figure 7-a: Illustrating a 61 x 20 body-fitted coordinate grid for calculating laminar flow around a single tube.

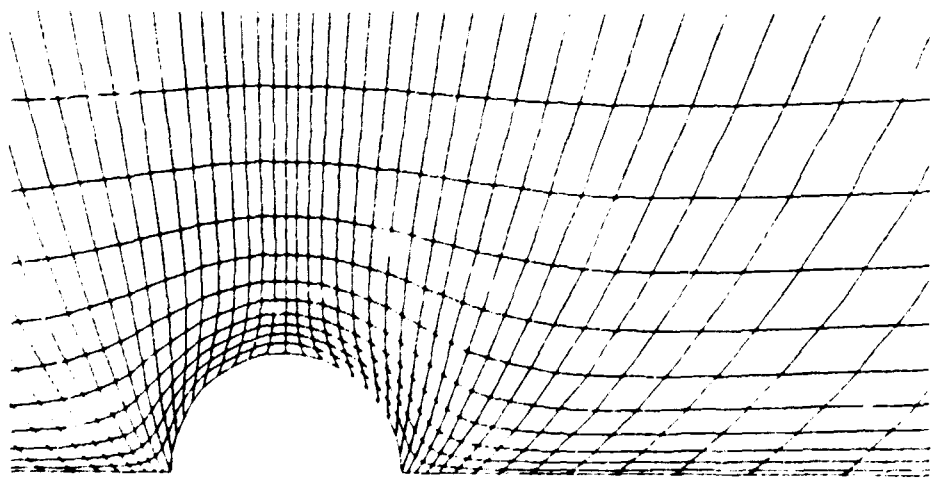

Figure 7-b: Close-up view of Figure 7-a in the vicinity of the tube.

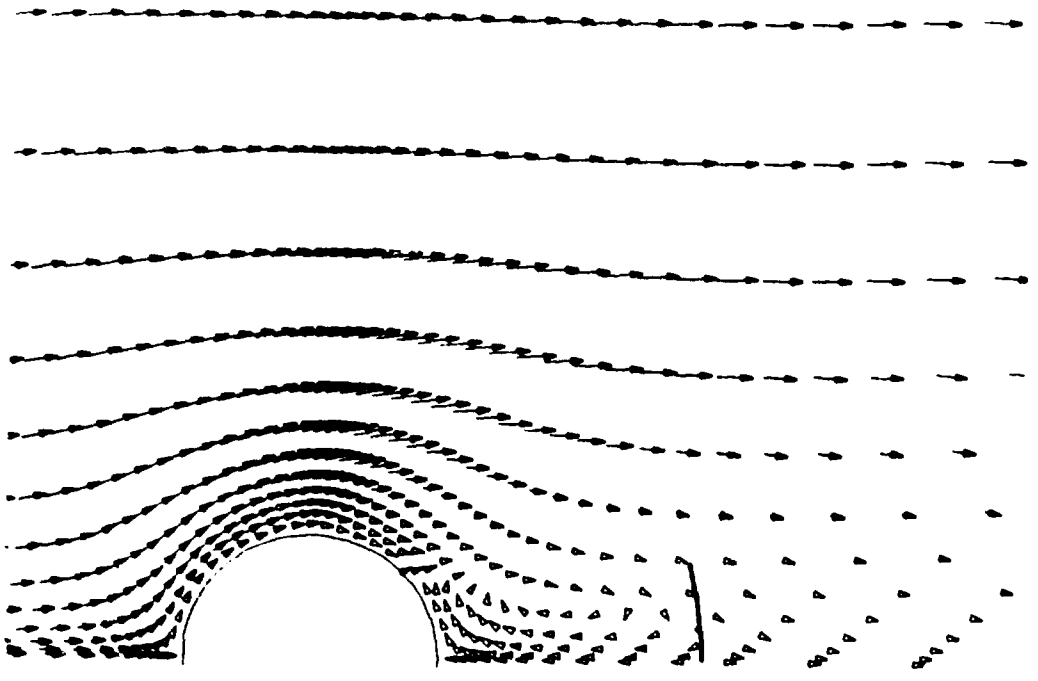

Figure 8: Close-up view of flow around a tube with $Re_d = 26$, calculated on the grid shown in Figure 7-a. Flow is from left to right. Experimentally determined wake length is marked in the figure. Boundary conditions used are given in the figure.

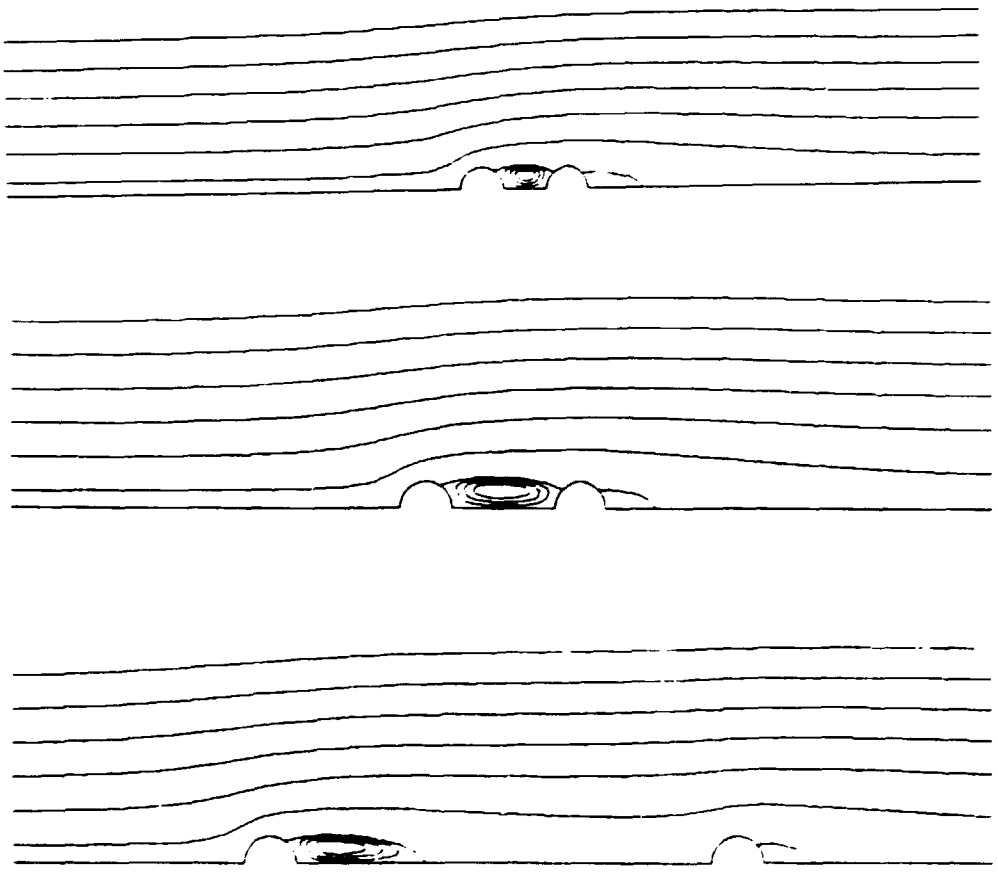

Figure 9: Streamlines for flow around two in-line tubes with centers spaced 2d, 3d and 9d respectively; $Re_d = 50$; flow is from left to right. Boundary conditions are as shown in Figure 7-a except that at exit plane $\partial u/\partial x = 0$ and $v = 0$ are specified.

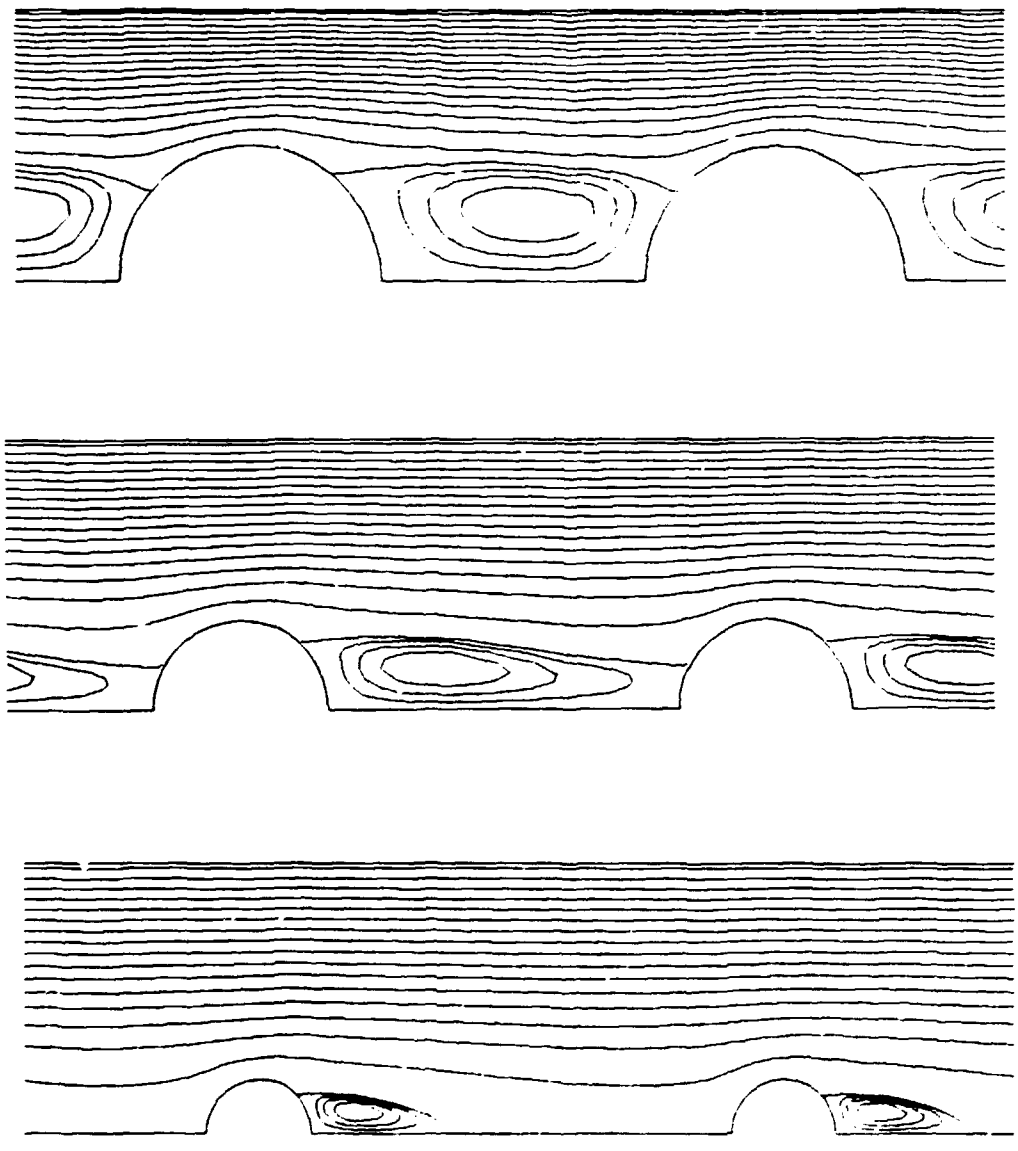

Figure 10: Streamlines for flow around a pair of in-line tubes in an infinite tube bank with spacings 2d, 3d and 9d respectively; Re_d = 50; flow is from left to right. Boundary conditions are as shown in Figure 7-a, except that inlet and exit planes are periodic and boundary conditions there are evaluated iteratively.

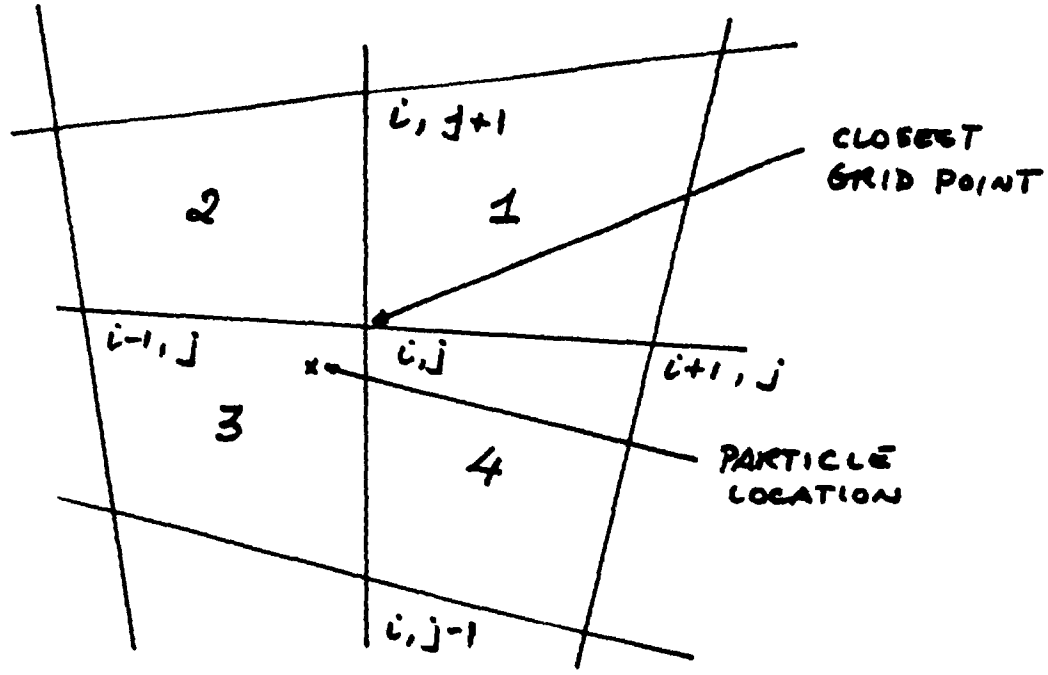

Figure 11: Illustrating the manner for determining the nearest grid node to a particle's location and the cell containing that particle.

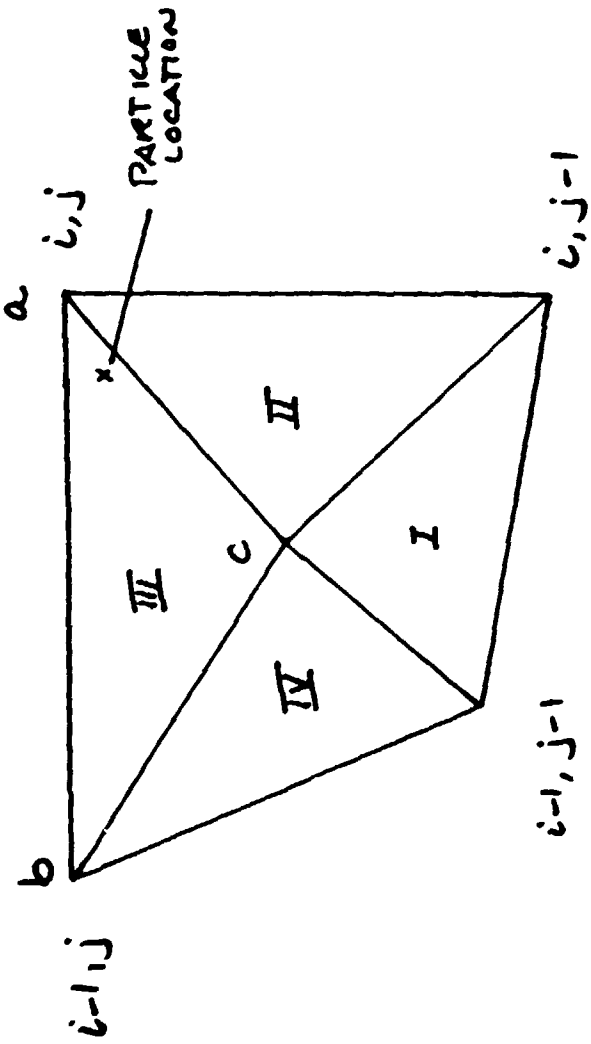

Figure 12: Illustrating the subdivision of the cell in which a particle is located in order to determine the triangular subdomain containing the particle from which 3 points are found for interpolating fluid velocities at the particle's location.

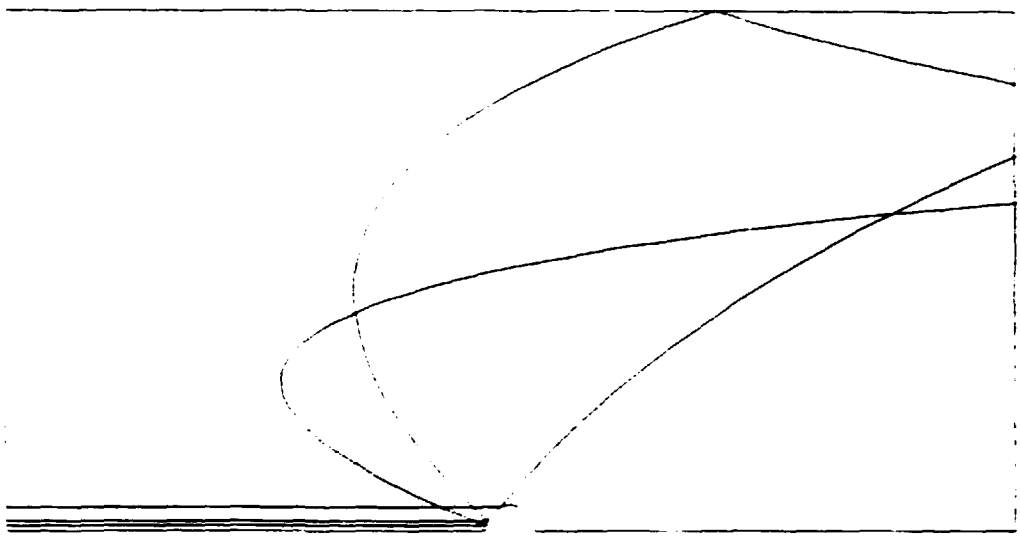

Figure 13: Rebounding trajectories of 200μm glass spheres released in air at different distances from the center-line symmetry plane. Gravity is aligned in the flow direction (left to right) and Re_d = 50.

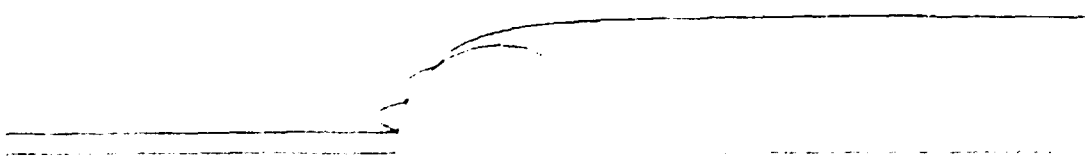

Figure 14: Trajectory of a 60μm glass sphere released in air illustrating multiple rebounding. Gravity is aligned in the flow direction (left to right) and Re_d = 50.

ALKALI ATTACK OF COAL GASIFIER REFRACTORY LININGS

Jesse J. Brown, Jr.

Department of Materials Engineering
Virginia Polytechnic Institute and State University
Blacksburg, Virginia 24061

ABSTRACT

Thermodynamic calculations were used to study the alkali and/or alkali-sulfur species present under coal gasifying conditions and the phases present when alkali and sulfur react with the calcium aluminate cement in the gasifier refractory lining. Phase maps were prepared covering temperatures from 800K to 1900K and pressures from ambient to 10.4 MPa. From a thermodynamic point of view, alkali reactions appear to be inevitable when refractories of the $CaO-Al_2O_3-SiO_2$ system are exposed to alkali-containing coal gasifier environments. Because the total energy of the system is lowered by the formation of alkali compounds, the compounds formed are usually much less dense than the original refractory. The attack may be retarded by slowing the rates of reactions by elevating operating pressures rather than temperatures, minimizing refractory porosity, and maximizing refractory bonding phase maturity prior to initial gasifier operation.

INTRODUCTION

Refractory failure is often the result of alkali attack in many high temperature technologies, including all coal gasification processes where alkalies from the coal are present. Alkali corrosion involves a series of reactions which may either degrade the refractory materials or cause premature failure. In most refractory systems, the presence of alkali tends to lower the liquidus temperature with consequent localized melting. Alternatively, when alkali reacts with refractory linings, compounds with lower densities often form which tend to spall off when subjected to thermal cycling. In cases where the atmosphere is rich in steam, the hydration-dehydration cycle of the alkali compound formed may increase refractory spalling. Alkali impurities also decrease the viscosity of silicate melts; therefore, refractories with high silica contents may show gradual softening

after long exposure to the alkali atmosphere. Alkali corrosion is affected by porosity of the refractory. Either by melt infiltration or vapor penetration through the pores, alkalies may penetrate below the surface and cause even more severe problems.

In addition to alkali, sulfur is constantly present in coal gasifiers. For calcium aluminate bonded refractory castables, which are almost exclusively used in dry ash gasifiers, the presence of sulfur impurities can result in sulfur corrosion. Sulfur impurities have been found to preferentially attack the calcium aluminate bonding phase of refractory castables by forming calcium sulfide.[1] The sulfidation of lime and iron oxide will lead to substantial volume change due to the significant difference in densities of the oxides and sulfides. It appears that sulfur and alkali impurities may act synergistically in attacking the gasifier linings, and lead to a dramatic reduction in the durability of refractory linings.

The mechanism and the state of the release of alkali and sulfur impurities from coal are poorly understood. Experimental identifications of the species existing in the gasifier atmosphere are extremely difficult due to the combined aggressive conditions of high temperature, high pressure, and high chemical reactivity in coal gasification atmospheres. In order to understand the release of alkali and sulfur, a thermodynamic approach is adopted in the present study to calculate the equilibrium states of these impurities under the coal gasification atmosphere using the SOLGASMIX-PV computer program.[2] The SOLGASMIX-PV is capable of calculating chemical equilibrium at various temperatures and pressures. In addition, phases formed from the reactions of alkali and/or alkali-sulfur impurities with the gasifier linings can also be predicted.

It is reasonable that investigations should concentrate on the bonding phase of refractory castables because corrosion generally starts at the bonding phase and the aggregate remains largely unreacted. Although much work has been done on the alkali attack of various refractories,[3-13] very little information has been published on the alkali-cement reactions. Therefore the present study involves:

1. Calculation of equilibrium alkali and sulfur species existing in the coal gasification atmosphere,
2. Calculations of the phases formed from the reactions of alkali and/or alkali-sulfur impurities with calcium aluminate cement.

CALCULATION OF EQUILIBRIUM COMPOSITIONS

The calculation of equilibrium compositions in a given system is based on the minimization of the total Gibbs free energy under the constraint of mass conservation. The basic equations used are:

$$G/RT = \sum_{i=1}^{m} x_i^g[(g_i^o/RT)_i^g + \ln P + \ln (x_i/X)^g] +$$

$$\sum_{i=1}^{n} x_i^\ell[(g_i^o/RT)_i^\ell + \ln (x_i/X)^\ell] + \sum_{i=1}^{s} x_i^c(g_i^o/RT)_i^c \qquad (1)$$

$$\sum_{i=1}^{m} a_{ij}^g x_i^g + \sum_{i=1}^{n} a_{ij}^\ell x_i^\ell + \sum_{i=1}^{s} a_{ij}^c x_i^c = b_j \quad (j = 1, 2, ---, k) \qquad (2)$$

where

G	= Gibbs free energy	a_{ij}	= number of atoms of the j^{th} elements of the i^{th} species
R	= gas content		
x_i	= number of moles of species i	b_j	= total number of moles of the j^{th} element
P	= total pressure	g_i^o	= chemical potential of pure component i
X	= total number of moles		

The indices of g, ℓ, and c represent the gaseous state, liquid state, and solid state, respectively. Equation (1) expresses the total free energy of the system contributed from the gaseous, liquid, and solid components, and equation (2) checks the mass balance relation in the system. By iteration, the equilibrium compositions, x_i, of each species in the system can be determined. The assumptions in the

calculations are that all liquids form ideal solutions and that pure solid phases occur at stoichiometric compositions.

Two series of calculations were carried out in studying alkali and/or alkali-sulfur corrosion. The first series deals with the identification of the alkali and/or alkali-sulfur species existing in the coal gasification atmosphere. The second series predicts the phases formed from the alkali-cement and alkali-sulfur-cement reactions. The thermodynamic data used in the calculations were compiled from various sources.[14-26]

ALKALI AND/OR ALKALI-SULFUR SPECIES

The stable alkali and/or alkali-sulfur species released from coal in gasifier atmospheres were predicted in the first series of calculations. The gasifier atmosphere used in these calculations had the composition (in mole %) - 20 H_2, 20 N_2, 18 CH_4, 17 CO, 12 H_2, 12 CO_2, and 1 alkali impurity. Since the operating conditions of the coal gasifier vary with different processes, calculations were performed at temperatures from 800 K to 1900 K and pressures from ambient to 10.4 MPa.

The species considered corresponding to different impurities are listed in Table 1. In each case, the sodium (or potassium) content was fixed at a level such that when all the sodium (or potassium) species vaporize, the total sodium (or potassium) concentration in the gas phase is approximately 1 mol %. The sulfur content was fixed at a level such that the concentration of H_2S in the gas phase is approximately 0.7 mol %.

ALKALI-CEMENT AND/OR ALKALI-SULFUR-CEMENT REACTIONS

The alkali corrosion, or the combined alkali-sulfur corrosion, is assumed to first start on the surface of the refractory lining. In order to simulate the corrosion process, only the surface layer was considered to participate in the reactions. The successive layers can

Table 1. Chemical Species Considered in Calculations

	Phase State		
Impurity	Gaseous	Liquid	Solid
Sodium	H_2, Na, CH_4, Na^+, CO, Na_2, CO_2, NaO, H_2O, NaO^-, NH_3, NaCN O_2, NaOH, N_2	Na, Na_2O, NaOH, Na_2CO_3, NaCN	C, Na_2O_2, Na_2O, NaO_2, NaOH, Na_2CO_3, NaCN
Sodium & Sulfur	H_2, SO_2, CH_4, SO_3, CO, CO_2, H_2SO_4, NH_3, H_2O, Na, Na_2SO_4, Na^+, O_2, Na_2, N_2, NaO, S_2, NaO^-, CS_2, NaCN, COS, NaOH, H_2S	Na, Na_2O, NaOH, Na_2CO_3, NaCN, H_2SO_4, H_4SO_5, H_6SO_6, H_8SO_7, $H_{10}SO_8$, Na_2SO_4, Na_2S	C, Na_2O_2, NaO_2, NaOH, Na_2CO_3, NaCN, Na_2SO_4, Na_2S
Potassium	H_2, K, CH_4, K^+, CO, K_2, CO_2, KO, H_2O, KO^-, NH_3, KCN, O_2, KOH, N_2	K, KOH, K_2CO_3, KCN	C, K_2O_2, K_2O, KOH, K_2CO_3, KCN
Potassium & Sulfur	H_2, K, CH_4, K^+, CO, K_2, CO_2, KO, H_2O, KO^-, NH_3, KCN, O_2, KOH, N_2, S_2, CS_2, COS H_2S, SO_2, SO_3, H_2SO_4, K_2SO_4	K, KOH, KCN, K_2CO_3, H_2SO_4, H_4SO_5, H_6SO_6, H_8SO_7, $H_{10}SO_8$, K_2SO_4, K_2S	C, K_2O_2, K_2O, KOH, K_2CO_3, KCN, K_2SO_4, K_2S

be treated in the same manner as the surface layer. Therefore, in the simulated system, the amount of the cement tested was taken to be much less than the total gas quantity. This also ensured consistent composition of the gas phase upon reactions with the cement.

Both 53% and 72% alumina cements were tested in this series of calculations. The compositions of the cement are listed in Table 2. In addition to the coal gasification atmosphere, the equilibrium alkali and/or alkali-sulfur species obtained from the previous calculations were also included in the testing atmosphere. Calculations were carried out at ambient pressure.

Table 2. Composition of Alumina Cement (wt%)

	Al_2O_3	CaO	Fe_2O_3	SiO_2
Intermediate purity	53.5	40.5	1.6	4.4
High purity	71.5	27.9	0.17	0.16

Each alumina cement was tested under four different atmospheres corresponding to the type of impurity present in the gasification atmosphere. Therefore, eight sets of results were obtained from this series of calculations. The results show the mineralogical changes of the alumina cement under the influence of alkali and/or alkali-sulfur impurities.

RESULTS AND DISCUSSION

STABLE ALKALI AND/OR ALKALI-SULFUR SPECIES

The stable alkali and/or alkali sulfur species obtained from the calculations are shown in Fig. 1 through 4. The alkali vapors in these cases are likely to be generated by the reactions:

$$Na_2CO_3 + 2C(s) = 2Na(g) + 3CO(g)$$
$$Na_2CO_3(s) + H_2O(g) + C(s) = 2NaOH(g) + 2CO(g)$$

or

$$K_2CO_3(s) + 2C(s) = 2K(g) + 3CO(g)$$
$$K_2CO_3(s) + H_2O(g) + C(s) = 2KOH(g) + 2CO(g)$$

At ambient pressure, the alkali-vapor can exist at a temperature as low as 1270 K for sodium species (Fig. 1), or 1200 K for potassium species (Fig. 3). However, when sulfur impurities are also present, the alkali vapor forming temperatures are increased, while the liquid forming temperatures are decreased, as shown in Fig. 2 and 4. This can be attributed to the eutectic reaction present in the binary system of the alkali carbonate and alkali sulfide, e.g. Na_2CO_3-Na_2S system, and also to the high stability of the liquid alkali sulfide. By increasing pressure, the alkali vapor can be condensed. However, when the temperature is sufficiently high, the presence of the vapor species is independent of pressure. In this case, increasing pressure can only condense part of the vapor species.

At low temperature, carbon is deposited without the presence of an iron catalyst. It should be noted that potassium cyanide is formed at high pressure, as shown in Fig. 3 and 4.

The state of alkali and/or alkali-sulfur species in contact with the refractory lining depends on the local temperature and pressure. If the temperature and pressure distribution in the gasifier are known, the cause and the type of reactions can be understood from the pressure versus temperature (P-T) diagrams.

At low temperatures, alkali corrosion is due to the presence of solid alkali carbonate. The reaction is either diffusion-controlled or interface-controlled. Corrosion in this region is relatively slow and less severe because the reactions involved are solid state and sluggish. If the temperature and pressure are such that liquid alkali is in contact with the refractory lining, corrosion may become serious. Apart from surface reactions, the liquid alkali can infiltrate below the surface and form compounds there which generate

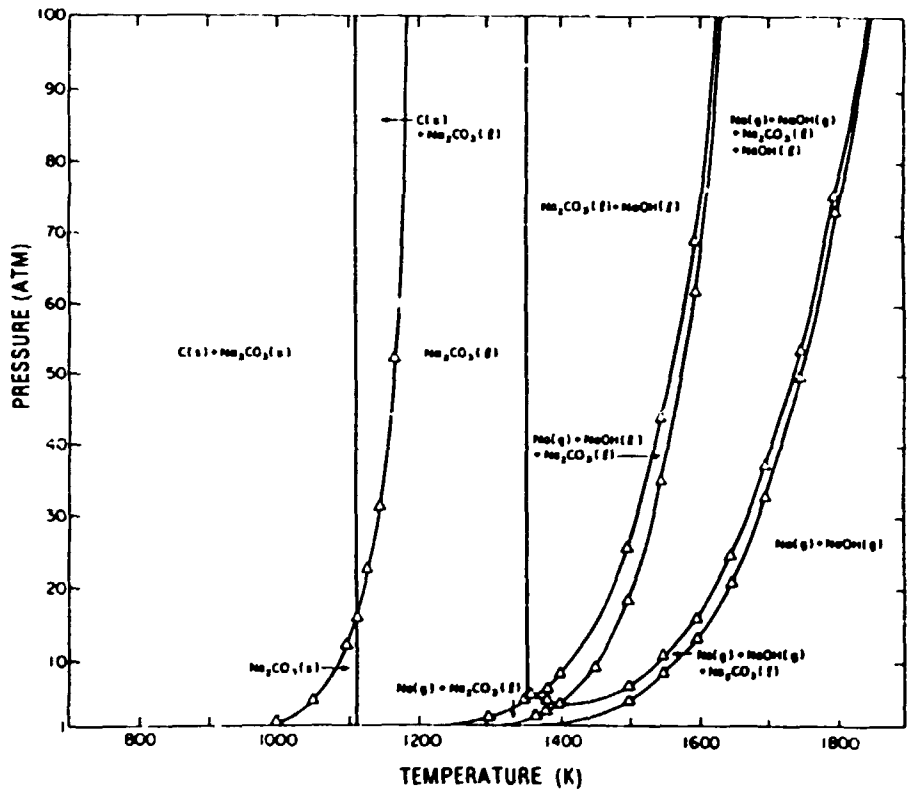

Figure 1. Stable sodium species in coal gasifier atmospheres.

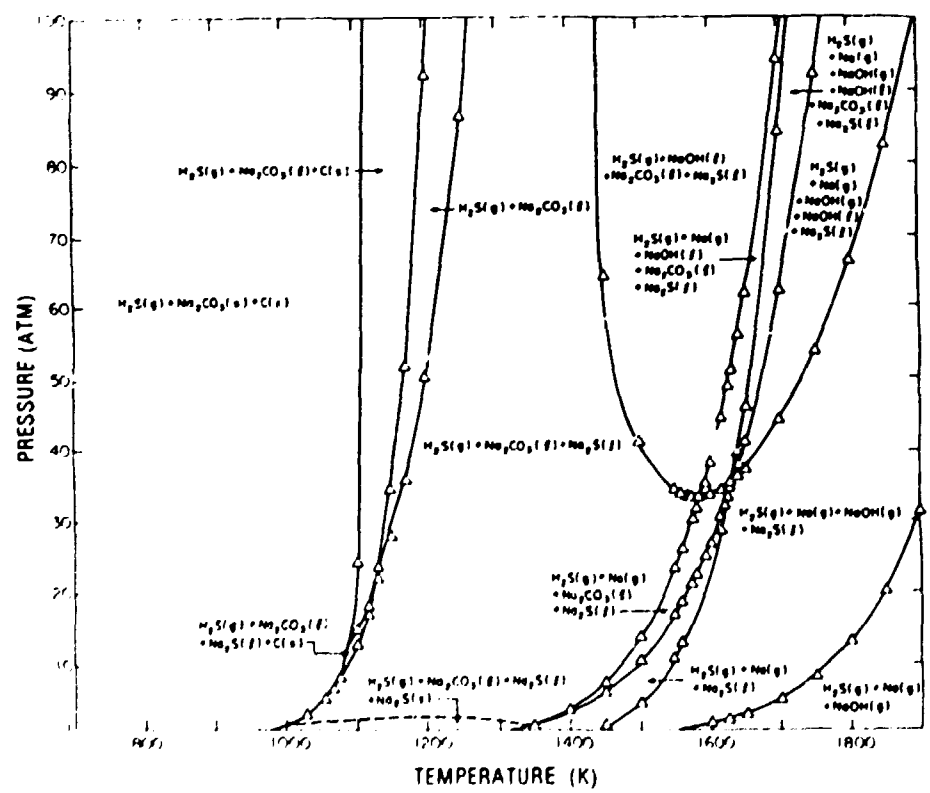

Figure 2. Stable sodium and sulfur species in coal gasifier atmospheres.

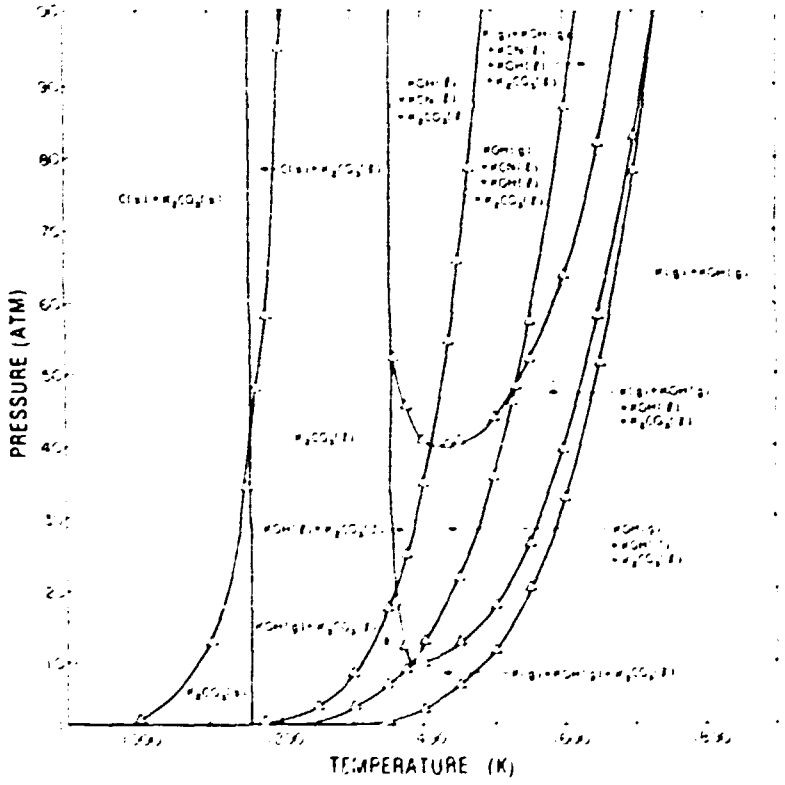

Figure 3. Stable potassium species in coal gasifier atmospheres.

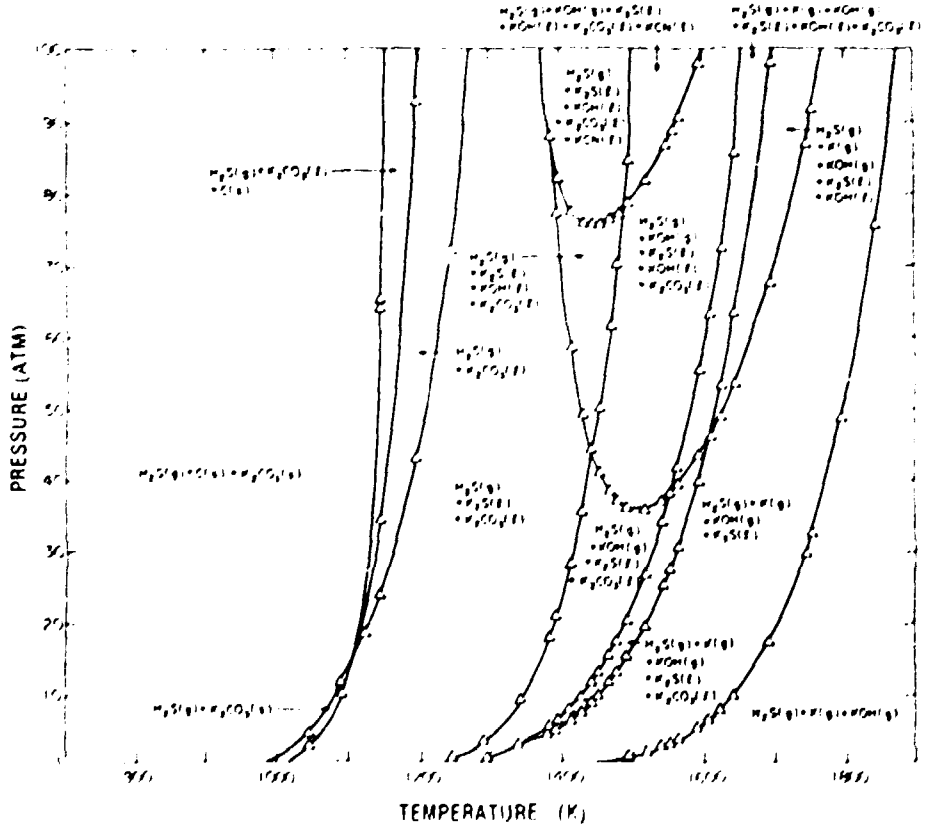

Figure 4. Stable potassium and sulfur species in coal gasifier atmospheres.

internal stresses. In the region where alkali liquid and alkali vapor are in contact with the refractory lining, both liquid infiltration and vapor penetration may occur. In the region where temperature is the highest, the refractory lining is directly exposed to the alkali vapors. The corrosion problem may be threefold at this stage, i.e., undesirable compound formation, direct surface fusion, and alkali circulation through the gasifier. Refractories exposed to this temperature range will undergo the most serious attack.

REACTION PRODUCTS

Using the alkali and/or alkali-sulfur species obtained above, the phases formed for both types of alumina cements upon reaction under different atmospheres are predicted. Table 3 shows the mineralogical changes of the 53% and 72% alumina cement after exposures to the sodium, sodium-sulfur, potassium, and potassium-sulfur atmospheres, respectively. Secondary phases are those present in only minor amounts.

When only sodium or potassium species are present in the atmosphere, calcium aluminate ($CaO \cdot Al_2O_3$) is attacked by the reactions

$$CaO \cdot Al_2O_3 + 2Na + 1/2O_2 = Na_2O \cdot Al_2O_3 + CaO$$

or

$$CaO \cdot Al_2O_3 + 2K + 1/2O_2 = K_2O \cdot Al_2O_3 + CaO$$

For simplicity, Na and K are used to represent the reacting alkali species. The actual alkali species may be solid alkali carbonate, alkali liquid, or alkali vapors, depending on the P-T diagrams. Lime (CaO) is released when either sodium aluminate or potassium aluminate is formed. In a steam-rich atmosphere, the free lime may pick up water and cause the refractory lining to degrade. The formation of sodium aluminate or potassium aluminate is accompanied by a large volume expansion. For example, the volume expansion associated with the formation of sodium aluminate i.

Table 3. Phases Predicted by Thermodynamic Calculations for Reactions at Atmospheric Pressure

		53% Al_2O_3 Cement		72% Al_2O_3 Cement	
Reaction	Temperature(K)	Primary Phase	Secondary Phase	Primary Phase	Secondary Phase
Sodium-	1200	CaO, $Na_2O \cdot Al_2O_3$	Fe, NaOH, Na_2O SiO_2	CaO, $Na_2O \cdot Al_2O_3$	Fe, $Na_2O \cdot SiO_2$
Cement	1300	CaO, $Na_2O \cdot Al_2O_3$	Fe, $Na_2O \cdot SiO_2$	CaO, $Na_2O \cdot Al_2O_3$	Fe, $Na_2O \cdot SiO_2$
	1400	CaO, $Na_2O \cdot Al_2O_3$	Fe, $2CaO \cdot SiO_2$	CaO, $Na_2O \cdot Al_2O_3$	Fe, $2CaO \cdot SiO_2$
Sodium-	1200	CaS, CaO, Na_2S, $Na_2O \cdot Al_2O_3$	Fe, $2CaO \cdot SiO_2$	CaS, Na_2S, $Na_2O \cdot Al_2O_3$	Fe, $Na_2O \cdot SiO_2$
Sulfur- Cement	1300	CaS, CaO, Na_2S, Na_2O Al_2O_3	Fe, $2CaO \cdot SiO_2$	CaS, Na_2S, $Na_2O \cdot Al_2O_3$	Fe, $2CaO \cdot SiO_2$
	1400	CaS, Na_2S, $Na_2O \cdot Al_2O_3$	Fe, $2CaO \cdot SiO_2$	CaS, Na_2S, $Na_2O \cdot Al_2O_3$	Fe, $2CaO \cdot SiO_2$
Potassium-	1200	CaO, $K_2O \cdot Al_2O_3$	Fe, $2CaO \cdot SiO_2$, $K_2O \cdot SiO_2$	CaO, $K_2O \cdot Al_2O_3$	Fe, $K_2O \cdot SiO_2$
Cement	1300	CaO, $K_2O \cdot Al_2O_3$	Fe, $2CaO \cdot SiO_2$	CaO, $K_2O \cdot Al_2O_3$	Fe, $2CaO \cdot SiO_2$
	1400	CaO, $K_2O \cdot Al_2O_3$	Fe, $2CaO \cdot SiO_2$	CaO, $K_2O \cdot Al_2O_3$	Fe, $2CaO \cdot SiO_2$
Potassium-	1200	CaS, K_2S, $K_2O \cdot Al_2O_3$	Fe, $2CaO \cdot SiO_2$	CaS, K_2S, $K_2O \cdot Al_2O_3$	Fe, $K_2O \cdot SiO_2$
Sulfur- Cement	1300	CaS, K_2S, $K_2O \cdot Al_2O_3$	Fe, $2CaO \cdot SiO_2$	CaS, K_2S, $K_2O \cdot Al_2O_3$	Fe, $2CaO \cdot SiO_2$
	1400	CaS, $K_2O \cdot Al_2O_3$	Fe, $2CaO \cdot SiO_2$, $K_2O \cdot SiO_2$	CaS, $K_2O \cdot Al_2O_3$	Fe, $2CaO \cdot SiO_2$

approximately 47% (calculated from specific gravity).

When sulfur impurities are also present, the free lime released from the alkali-cement reaction is sulfidized to form calcium sulfide. The reaction sequence can be reversed, i.e., sulfidation occurs first in the cement matrix and then alkali reacts with the released alumina. Either process will yield the resultant reaction:

$$CaO \cdot Al_2O_3 + 2Na + 1/2S_2 = Na_2O \cdot Al_2O_3 + CaS$$

or

$$CaO \cdot Al_2O_3 + 2K + 1/2S_2 = K_2O \cdot Al_2O_3 + CaS$$

The volume expansion corresponding to the formation of $Na_2O \cdot Al_2O_3$ and CaS is approximately 69%.

The alkali sulfide (Na_2S or K_2S) obtained from the calculations may give the impression that it can decrease the alkali and sulfur concentrations, and therefore reduce the alkali and/or alkali-sulfur attack. However, it was found from the calculations that alkali sulfide exists only when excess alkali and sulfur are present after the alkali and sulfidation reactions have taken place. If the amounts of alkali and sulfur are not sufficient to completely decompose calcium aluminate, alkali sulfide will not form. The phases formed are calcium sulfide, alkali aluminate, and residual calcium aluminate. Based on thermodynamic considerations, adding excess sulfur or alkali to the alkali-containing system will not counteract the alkali or sulfidation reactions.

CONCLUSIONS

The mechanism of alkali and/or alkali-sulfur attack on coal gasifier linings consists of two steps: 1) the release of the alkali and/or alkali-sulfur species from coal, and 2) the reactions with the gasifier lining. The alkali and/or alkali-sulfur species present in the coal gasification atmosphere can be predicted from thermodynamic calculations. The alkali and sulfur compounds formed by the reactions

of these species with the refractory cements can also be calculated. Results strongly depend on the accuracy of the thermodynamic data, especially when handling a system of more than 50 species.

The alkali and/or alkali-sulfur attack can result in:

1. Incipient melting of the hot face due to alkali fluxing;
2. Thermal spalling due to differential thermal expansion of the bulk and the surface compounds;
3. Traverse cracking due to internal stresses generated under the surface; and
4. Surface washout by dissolution of alkali compounds.

When refractories made from the Al_2O_3-SiO_2-CaO system are exposed to alkali atmospheres, alkali reactions appear to be an inevitable consequence from the viewpoint of thermodynamic considerations. Since the total energy of the system will be lowered by the formation of alkali compounds, the compounds formed are usually far less dense than the bulk. The attack can only be retarded by slowing the rate of the reactions. From these results, the recommended methods for retarding alkali attack are:

1. Elevate pressures rather than temperatures in operating conditions;
2. Improve the reactor cooling system;
3. Minimize the refractory porosity; and
4. Maximize the maturity of the bonding phase to develop a strong ceramic bond (this can be done by pre-firing the gasifier without the presence of alkali).

The last point is especially important in that the aggregates remain unreacted to alkali impurity. This is attributed to the larger grain size and smaller surface area of the aggregates when compared to the cement bonding phase. Therefore, with improved bonding phases, the gasifier lining can be expected to last longer.

REFERENCES

1. J. B. Tak and D. J. Young, "Sulfur Corrosion of Calcium Aluminate Bonded Castables," Am. Ceram. Soc. Bull., Vol 61, No. 7, 1982, p. 725.

2. T. M. Besmann, "SOLGASMIX-PV, A Computer Program to Calculate Equilibrium Relationships in Complex Chemical Systems," ORNL/TM-5775, Contract No. W-7405-eng-26, 37 pp., April 1977 (available from NTIS).

3. G. R. Rigby and R. Hutton, "Action of Alkali and Alkali-Vanadium Oxide Slags on Alumina-Silica Refractories," J. Am. Ceram. Soc., Vol. 45, No. 2, 1962, p. 68.

4. R. E. Farris and J. E. Allen, "Aluminous Refractories-Alkali Reactions," Iron and Steel Engineer, Vol. 50, No. 2, 1973, p. 67.

5. C. R. Kennedy, "Alkali Attack on a Mullite Refractory in the Grand Forks Energy Technology Center Slagging Gasifier," J. Materials for Energy Systems, Vol. 3, June, 1981, p. 27.

6. J. T. Shapland and A. F. Lirovich, "Evaluation of Five Commercial Calcium-Aluminate Cements," Am. Ceram. Soc. Bull., Vol. 43, No. 7, 1964, p. 510.

7. S. E. McCune, T. P. Greaney, W. C. Allen, and R. B. Snow, "Reaction Between K_2O and Al_2O_3-SiO_2 Refractories as Related to Blast-Furnace Linings," J. Am. Ceram. Soc., Vol. 40, No. 6, June 1957, p. 187.

8. P. H. Havranek, "Alkali Attack on Blast Furnace Refractories," Trans J. Brit. Ceram. Soc., Vol. 77, 1978, p. 92

9. H. Insley, "Some Observations of Surface Deposits Formed on Glass-Furnace Regenerators," J. Am. Ceram. Soc., Vol. 9, No. 10, 1926, p. 635.

10. C. L. Thompson and E. P. Rexford, "Study of Alumina-Silica Checker-Brick from Regenerator of a Glass Tank," J. Am. Ceram. Soc., Vol. 21, No. 2, 1938, p. 55.

11. E. C. Petrie and D. P. Brown, "Observations on the Shelling of Checker-Brick," J. Am. Ceram. Soc., Vol. 31, No. 1, 1948, p. 14.

12. C. K. Jones and R. L. Hardy, "Petroleum Ash Components and Their Effect on Refractories," Industrial and Engineering Chemistry, Vol. 44, No. 11, Nov., 1952, p. 2615.

13. L. G. Huggett, "The Oil-Ash Problem," Trans. J. Brit. Ceram. Soc., Vol. 80, No. 1, 1981, p. 11.

14. JANAF Joint Army, Navy, Air Force Thermochemical Tables, 2nd ed., 1971, NSRDS-NBS 37, US Government Printing Office. Washington, DC. See also later supplements for 1971-1981.

15. E. T. Turkdogan, "Selected Thermodynamic Functions," Physical Chemistry of High Temperature Technology, Academic Press, 1980.

16. O. Kubaschewski, E. L. Evans, and C. B. Alcok, "Metallurgical Thermochemistry," Pergamon, Oxford, 1967.

17. I. Barin and O. Knacke, "Thermochemical Properties of Inorganic Substances," Springer-Verlag, Berlin and New York, 1973.

18. I. Barin, O. Knacke, and O. Kubaschewski, "Thermochemical Properties of Inorganic Substances, Supplement," Spring-Verlag, Berlin and New York, 1977.

19. O. Kubaschewski, High Temp.-High Pressures, Vol. 4, 1972, p. 1.

20. K. K. Kelley, S. S. Todd, R. L. Orr, E. G. King, and K. R. Bonnickson, "Thermodynamic Properties of Sodium-Aluminum and Potassium-Aluminum Silicates," U. S. Bur. Mines, Report of Investigations 4955, 21 pp., 1953.

21. R. P. Beyer, M. J. Ferrante, R. R. Brown, and G. E. Daut, "Thermodynamic Properties of Potassium Metasilicate and Disilicate," U. S. Bur. Mines, Report of Investigations 5901, 32 pp., 1961.

22. R. P. Beyer, M. J. Ferrante, and R. R. Brown, "Thermodynamic Properties of $KAlO_2$," J. Chem. Thermodynamics, Vol. 12, 1980, p. 985.

23. J. W. Hastie, W. S. Horton, E. R. Plante, and D. W. Bonnell, "Thermodynamic Models of Alkali-Metal Vapor Transport in Silicate Systems," High Temp.-High Pressures, Vol. 14, 1982, p. 669.

24. B. I. Arlynk, "Determination of the Heats of Formation of a Number of Compounds by Quantitative Thermal Analysis," English translation of Zhur. Priklad, Khim., Vol. 41, No. 4, April 1968, p. 783.

25. J. T. Kummer, "β-Alumina Electrolytes," Progr. Solid State Chem., Vol. 7, 1972, p. 141.

26. Y. Y. Skolis, V. A. Levitskii, and V. M. Yanishevskii, "Thermodynamics of Binary Oxides. Thermodynamic Properties of $CaAl_4O_7$ and $CaAl_{12}O_{19}$ at High Temperatures," Russian Journal of Physical Chemistry, Vol. 55, 1981, p. 25.

STUDIES OF MATERIALS EROSION IN COAL CONVERSION AND UTILIZATION SYSTEMS

Alan V. Levy

Lawrence Berkeley Laboratory
University of California
Berkeley, California 94720

ABSTRACT

Investigations have been completed to determine how the mechanical and physical properties of iron, nickel, and cobalt base alloys could be modified by composition changes and mechanical or thermal treatments to improve their solid particle erosion resistance. It has been determined that essentially all structural alloys behave in a very similar manner in near room temperature erosion regardless of their strength or other property levels. No definitive alloy selection criteria for erosion have been established. The addition of hard, carbide particles to metal matrices does not improve erosion resistance until approximately 80 vol. % of the composite is carbide particles.

In combined erosion-corrosion of the type that occurs in coal burning energy generation equipment it is the nature of the scales that form on the metals and not the erosion behavior of the metals that govern metal wastage. Relatively low alloy steels with scale morphologies that are segmented in nature have much lower metal wastage rates than higher alloy content steels whose scales may be more consolidated.

INTRODUCTION

The selection of alloys for use in various types of service environments is generally dependent on various combinations of their microstructures and mechanical and physical properties. Extensive efforts have been made to learn which microstructures and properties of metals enhanced their resistance to erosion by small solid particles.[1-6] It has been determined that structural alloys of iron, nickel and cobalt that are used in elevated temperature applications in energy generation

and utilization equipment have very similar erosion behavior over a broad spectrum of mechanical and physical properties.

The differentiation in their performance occurs when combined erosion-corrosion environments occur at sufficiently elevated temperatures to develop scales on the alloys' surfaces. It is the behavior of the scales that provides a selection criteria for solid particle impact environments and not the mechanical or physical properties of the base metals. The base metal properties can be used to provide for such requirements as load carrying and heat transfer without having to factor in erosion resistance.

The DOE-Fossil Energy Materials Program has supported erosion and erosion-corrosion research at the Lawrence Berkeley Laboratory (LBL) for several years. During that period the relations between properties and erosion behavior have been investigated in depth. Contained in this paper is a brief background of earlier work to provide a summary of what had been learned, a somewhat more detailed but still limited review of the knowledge gained in this past year about the relationship between properties and erosion, and a more extensive presentation of how the oxidation scales that form on alloy surfaces determine the metal wastage rates that occur.

TEST CONDITIONS

All test were carried out in the LBL room and elevated temperature erosion testers.[1,2] The test conditions varied and are indicated on each table or figure

RESULTS

LOW ALLOY STEELS

The initial effort to determine how mechanical properties and hardness affected erosion resistance utilized 1020 plain carbon steel and martensitic hardened AISI 4340 steel. Table 1 shows the erosion rates of annealed and cold worked 1020 steel and Table 2 shows the erosion rates of as-quenched, quenched and tempered and spheroidized annealed AISI 4340 steel. It can be seen that large differences in strength and hardness had, essentially, no effect on erosion rate. If

anything, the more ductile but distinctly softer versions of each steel had lower erosion rates than the stronger, harder conditions.

TABLE 1

Effect of ductility, strength and hardness on erosion behavior of AISI-SAE 1020 steel

Condition	*Ultimate tensile strength* (klbf in^{-2})	*Hardness* (HRB)	*Elongation* (%)	*Erosion mass loss*[a] (mg)
Hot rolled	55	65	25	2.8
Cold rolled	61	70	15	4.0

[a]Statistical average of incremental mass loss per 30 g load of Al_2O_3 particles (average size, 140 μm) at steady state erosion ($\alpha = 30°$; $V = 30$ m s^{-1}; $T = 25$ °C).

TABLE 2

Effect of ductility, strength and hardness on the erosion behavior of AISI-SAE 4340 steel

Heat treatment condition	*Ultimate tensile strength* (klbf in^{-2})	*Hardness* (HRC)	*Elongation* (%)	*Reduction in area* (%)	k_{Ic} (klbf in$^{-3/2}$)	*Charpy impact strength* (ft lbf)	*Erosion mass loss*[a] (mg)
As quenched	307	60	8	24	34	10	1.03
Tempered at 200 °C	273	53	11	36	58	16	0.97
Tempered at 500 °C	182	39	14	47	62	12	0.97
Spheroidized by annealing	≈ 100	≈ 19	≈ 25				0.90

[a]Statistical average of incremental weight loss per 30 gf load of Al_2O_3 particles (average size, 140 μm) at steady state erosion ($\alpha = 30°$; $V = 30$ m s^{-1}; $T = 25$ °C).

HIGHER ALLOY CONTENT ALLOYS

A group of 10 alloys of iron, nickel, or cobalt base from the Cabot Corp. were erosion tested in various annealed, cold worked, or precipitation hardened conditions.[5] Their compositions are listed in Table 3. They were prepared in sevaral different manners, i.e. cast, wrought, deposited, and, as a result, had a wide range of microstructures and resulting properties. The Stellite and Tristelle alloys had 2nd phase carbide particle contents from 8 to 21 vol. %. Table 4 lists the erosion rates of the alloys and their hardnesses. It is rather remarkable that such a wide range of materials of different compositions, microstructures and properties have such similar erosion

rates. In particular the nickel and cobalt base alloys Haynes 188, Hastelloy C-276 and Cabot 718 in both the annealed and strengthened conditions had erosion rates that were nearly identical at each of several different impact angles and eroded by two different, but both angular, erodents.

TABLE 3
Composition of Cabot Alloys

Alloy	Co	Ni	Cr	Fe	W	Mo	C	Si	Mn	Other
										(Nominal)
Haynes 6B	55	3*	30	3*	4	2*	1.2	2*	2*	-
Stellite No.6	Bal.		28		4		1.1			
Tristelle TS-1	12	10	30	42	-	-	1	5	-	-
Tristelle TS-2	12	10	35	36	-	-	2	5	-	-
Tristelle TS-3	12	10	35	35	-	-	3	5	-	-
Ferralium 255	-	5.5	26	61	-	3	0.04*	1*	1.5*	0.2 N 2 Cu
Haynes 188	40	22	22	3*	14	-	0.1	0.35	1.2*	0.08 La
Hastelloy C-276	2.5*	57	16	5	4	16	-	-	1*	-
Cabot 718	1*	52	19	19	-	3	-	-	-	5 (Nb+Ta), 0.9 Ti
Berylco 25	0.25	-	-	-	-	-	-	-	-	Cu - 1.85 Be

* Maximum

TABLE 4

Erosion Rates of Cabot Alloys

Alloy	Elongation	Hardness	Erosion Rate $(cm^3 g^{-1}).10^{-5}$ Silicon Carbide 30°	Silicon Carbide 60°	Silicon Carbide 90°	Quartz 30°	Quartz 60°	Quartz 90°
Haynes 25 (wrought)	11	295x395	2.29	2.26	1.94	1.14	1.28	1.29
Stellite 6B (deposit)	1	461	2.32	2.36	1.96	1.08	1.48	1.34
Stellite 6B-1 (deposit)	1	380	2.24	2.35	2.10	1.50	1.60	1.47
Stellite 6B-2 (wrought)	-	430	-	-	-	1.46	2.11	1.87
Stellite 6B-3 (wrought)	-	460	-	-	-	1.60	2.45	1.91
Stellite 21 (cold rod)	22	407	2.31	1.81	1.45	1.38	1.31	1.08
Haynes 188 annealed	5	320	2.03	1.89	1.54	1.07	1.41	1.16
Haynes 188 cold red.	9	463	2.18	1.89	1.52	1.18	1.38	1.16
Hastelloy X-276 annealed	63	229	2.10	1.78	1.46	1.20	1.22	1.07
Hastelloy X-276 cold red.	15	408	2.13	1.72	1.52	1.17	1.32	1.11
Cabot 718 annealed	30	243	2.13	1.75	1.54	1.22	1.29	1.10
Cabot 718 aged	12	426	2.28	1.93	1.59	1.32	1.40	1.17
Nervico 25 annealed	38	199	2.81	-	-	-	-	-
Nervico 25 aged	4	410	3.02	-	-	-	-	-

Room temperature Erosion
Air carrier gas
60° = impingement
250 µm SiC
135 µm quartz

CARBIDE-DUCTILE METAL MATRIX COMPOSITES

In an effort to increase the erosion resistance of metals by adding hard, carbide particles to a metal matrix, a group of materials was tested and compared. Table 5 (ref. 6) lists the materials and the results. While increasing the carbide content of metal matricies aids in resisting sliding and abrasive wear, until the carbide content exceeds approximately 80 %[6,7] and becomes a continuous skeleton, the erosion resistance decreases with increasing carbide content. Even such high carbide content materials as K90, K3520, and K162B had higher erosion rates than pure iron and low carbon steels at the higher impact angles.

TABLE 5

Erosion Rates of Carbide-Metal Matrix Composites

Alloy	Vol%Carbide	Volume Erosion Rate ($m^3g^{-1}x10^{-12}$)		
		30°	60°	90°
Pure Iron	0	9.70	7.76	5.77
1020	3.1	10.05	7.86	5.67
1080	12.0	9.99	8.19	6.22
Stellite No6	10.4	10.8	14.8	13.4
Haynes 6B	10.4	11.4	12.8	12.9
Tristelle TS-1	8.3	11.78	12.18	11.51
Tristelle TS-2	16.8	14.43	20.87	18.54
Tristelle TS-3	21.4	15.94	24.37	19.02
White Iron	23.1	10.61	13.33	12.27
K90	63.1	7.04	11.47	12.12
K3520	69.5	4.83	10.21	10.73
K3055	83.7	2.21	4.70	4.10
K701	76.2	0.11	0.10	0.20
K801	89.9	0.46	0.77	0.61
K162B	78.5	5.33	10.29	12.59
K165	88.8	1.23	2.51	1.95

SOLUD SOLUTION STRENGTHENED ALLOYS

A number of iron and copper base solid solution strengthened alloys were prepared and tested to determine if solid solution strengthening could enhance the erosion resistance of metals.[8] Tables 6 and 7 lists the alloys and their erosion rates. As in previous efforts to improve the erosion behavior of metals, strengthening by solid solution alloying did not improve the alloys; if anything the stronger alloys had somewhat greater erosion rates.

TABLE 6

Erosion Rates of Iron Base Solid Solution Strengthened Alloys (as cast condition)

Alloy	Hardness Rb	Density g/cm^3	Erosion Rate at Impingement angle					
			30°		60°		90°	
			g/g X 10^{-5}	cm^3/gX 10^{-5}	g/g X 10^{-5}	cm^3/gX 10^{-5}	g/g X 10^{-5}	cm^3/gX 10^{-5}
Fe	69	7.81	8.64	1.106	8.57	1.097	5.50	0.704
Fe-10%Al	99	6.86	7.55	1.161	7.29	1.063	5.01	0.730
Fe-20%Al	100	6.47	7.34	1.134	6.63	1.025	5.20	0.803
Fe-15%Mo	92	8.16	10.14	1.243	9.07	1.110	7.00	0.858
Fe-30%Mo	102	8.71	10.37	1.191	10.14	1.160	8.35	0.959

TABLE 7

Erosion Rates of Copper Base Solid Solution Strengthened Alloys

Alloy	Hardness Rb	Density g/cm^3	Erosion Rate at Impingement angle					
			30°		60°		90°	
			g/g X 10^{-5}	cm^3/g X10^{-5}	g/g X10^{-5}	cm^3/g X10^{-5}	g/g X10^{-5}	cm^3/g X10^{-5}
Cu(10200) Annealed	-30	8.92	11.8	1.32	8.7	0.98	7.40	0.83
Cu(10200) 50%Coldworked	52	8.92	12.1	1.36	9.0	1.01	7.25	0.81
Cu-4%Al*	-15	8.20	12.2	1.49	10.2	1.24	7.76	0.95
Cu-8%Al*	41	7.60	12.5	1.64	9.6	1.26	8.33	1.10
Cu-2%Ti*	68	8.55	13.0	1.52	10.4	1.22	8.30	0.97
Cu-4%Ti*	93	8.11	14.5	1.79	12.4	1.53	9.50	1.17
Cu-2%Ti 50%Hot Rolled	71	8.61	14.8	1.72	11.14	1.29	8.64	1.00
Cu-4%Ti 50%Hot Rolled	99	8.50	15.2	1.79	12.4	1.46	10.28	1.21

* As cast condition

COMBINED EROSION-CORROSION

The metal wastage of steels used in energy generation equipment, such as tube heat exchangers in fluidized bed combustors (FBC's) occurs in an environment where both erosion and corrosion occur simaltaneously. In earlier work[9] it has been determined that the dominant mechanism is corrosion and that the morphology of the scale that forms determines the mechanism and metal lose rates of the alloy steels. The same behavior has been observed in laboratory and actual fluidized bed combustor test environments[10] in the 430° - 850°C temperature range that occurs in FBC's.

When scale forms on a metal surface that is being impacted by small solid particles it nucleates and grows in the form of oxide nodules. A typical nodule is shown in Figure 1. In the lower particle velocity regime that generally occurs in energy generation equipment combustion zones, the size, shape and impact angle of the impacting particles causes the nodular scale to develop in segmented clumps, see Figure 2.

This type of scale is not capable of developing internal stresses from thermal gradients sufficiently high to result in spalling of the scale and it, therefore, loses material by a slow rate, cracking and chipping mechanism.

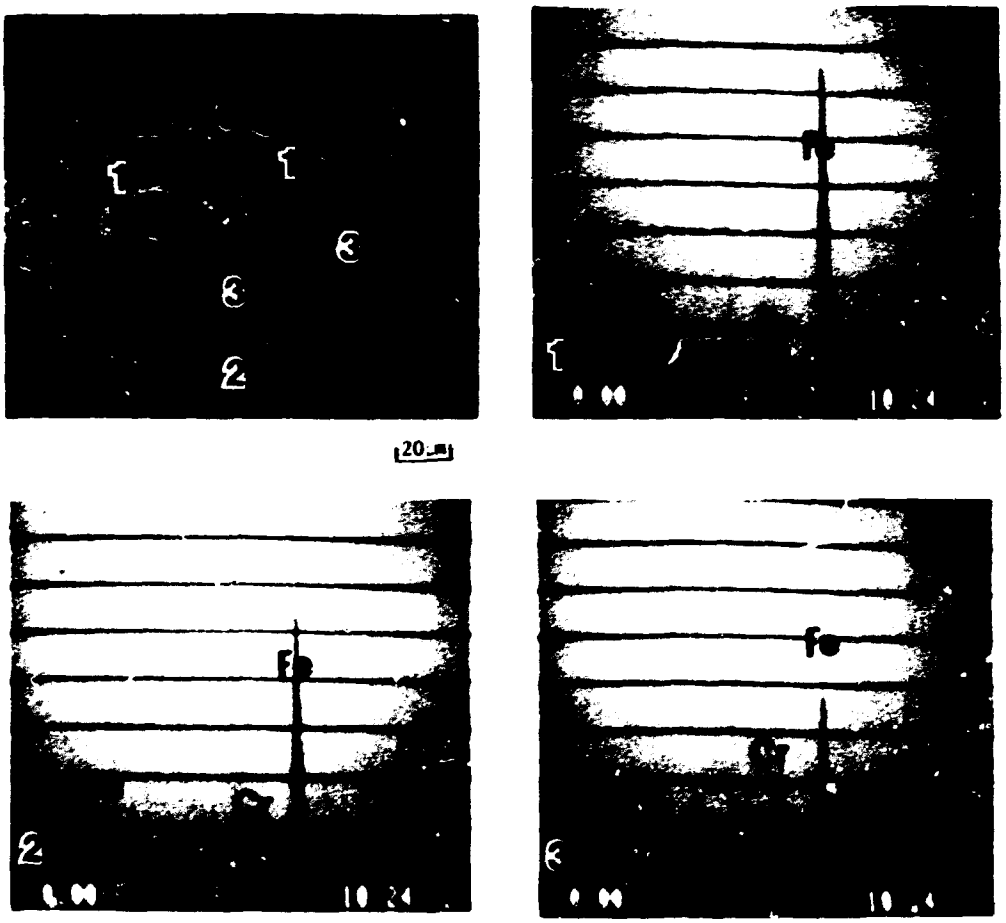

XBB 8411-8502

9Cr-1Mo Steel

Nozzle Tester	T = 850°C
Erosion-Corrosion	ϑ = 30°
Air	V = 35 m/s
130μm Al_2O_3	t = 5 hrs

Fig. 1 Typical oxide nodule formed on 9Cr1Mo steel during erosion-corrosion.

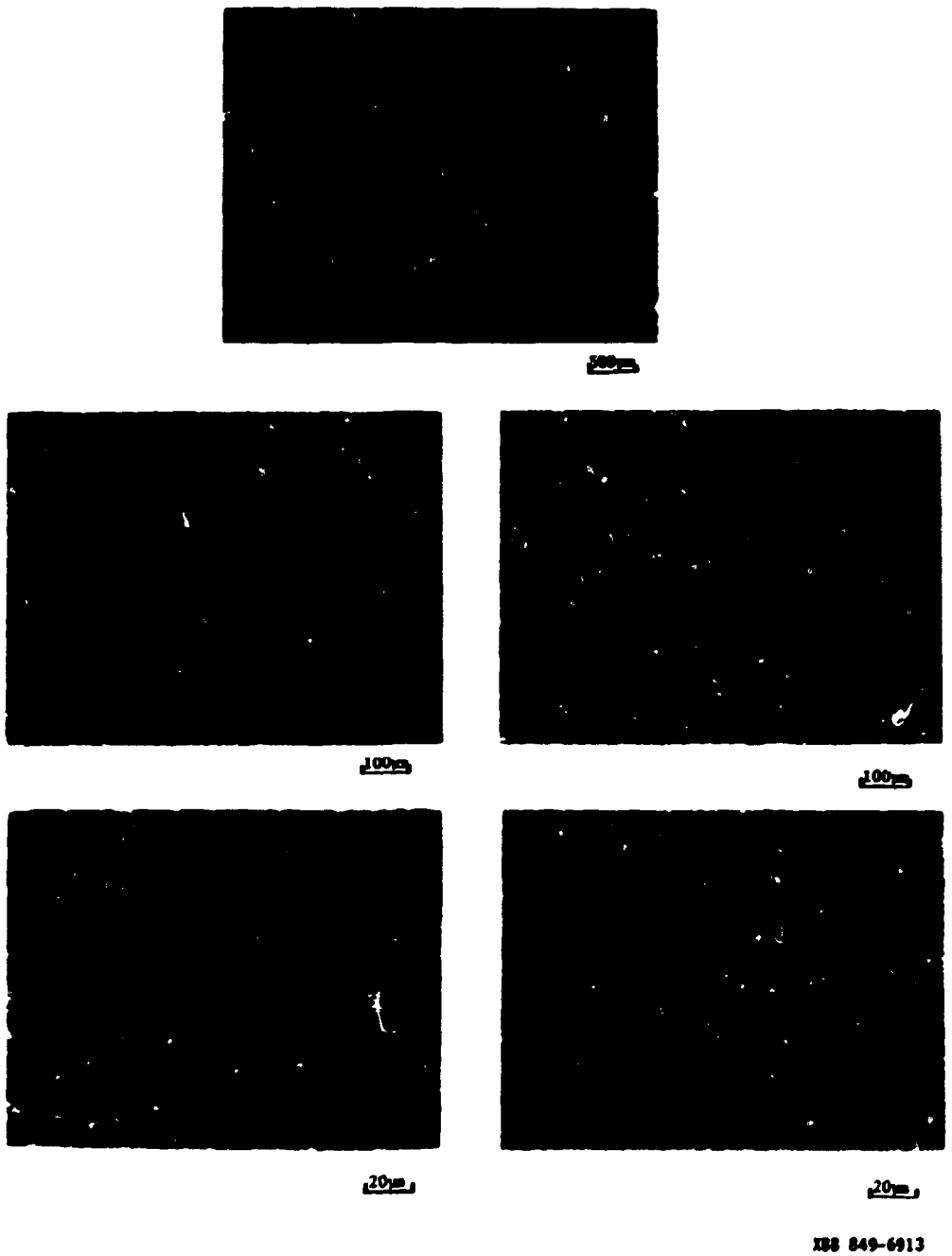

Fig. 2. Morphology of primary zone of 9Cr1Mo steel E-C tested at V=25m/s, α=30°.

When the velocity is somewhat higher and the impact angle of the particles steeper or when the temperature is near the top of the range, the particles striking the growing scale cause it to consolidate, effectively hot pressing it, see Figure 3. In the consolidated condition it can develop internal stresses sufficiently high to cause localized spalling and scale loss occurs at a faster rate as larger pieces are removed.

It is the segmented and the consolidated scales that are eroded in combined erosion-corrosion and not the metal, directly. Metal wastage occurs by the oxidation of the base metal to, in effect, replace the scale that is being removed by either the faster or the slower erosion mechanism. Figure 4 shows the difference in metal thickness loss as a function of particle impact velocity at a shallow impact angle, α=30° and a steep angle, α=90°. The α=90° curve shows that as the particle velocity increases to a level where it can consolidate the scale, the loss of metal changes from the segmented scale's low rate to the much higher rate of the consolidated, spalling scale. The lower, α=30° curve indicates that there is insufficient force at all of the test velocities to consolidate the scale; so it remains segmented and scale loss is by the slower cracking and chipping mechanism at all impact velocities.

EROSION-CORROSION OF ALTERNATE STEELS

The behavior described above has been observed on all of the steels tested to date, even the higher chromium austenitic stainless steels which form thin, yet segmented, scales.[11] An effort was undertaken in the last year to find steels that would form and maintain segmented scales over a wider range of test conditions. Since the mechanism for forming and maintaining segmented scales was not known, four steels that have been produced in pipe form at one time or another were tested. Based upon the results obtained a fifth steel was tested. The compositions of the steels tested are listed in Table 8.

The tests were carried out in the elevated temperature, nozzle type erosion tester. 850°C was used for most of the tests; the 3.5Ni steel was tested at 650°C and 850°C. The erodent particles were rounded,

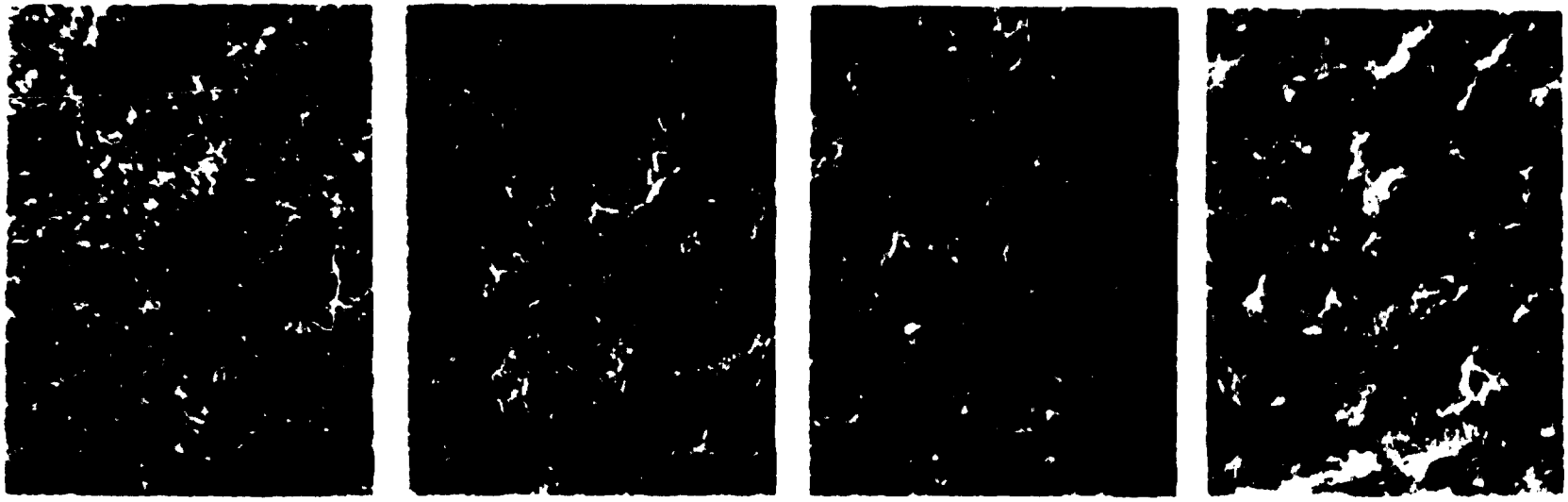

9 Cr 1 Mo Steel

Nozzle Tester	T = 850°C
Erosion-Corrosion	α = 90°
Air	t = 5 Hrs.
130μm Al_2O_3	Primary Zone

Fig. 3. Effect of particle velocity on scale morphology in $\alpha=90^{\circ}$ tests of 9Cr1Mo steel.

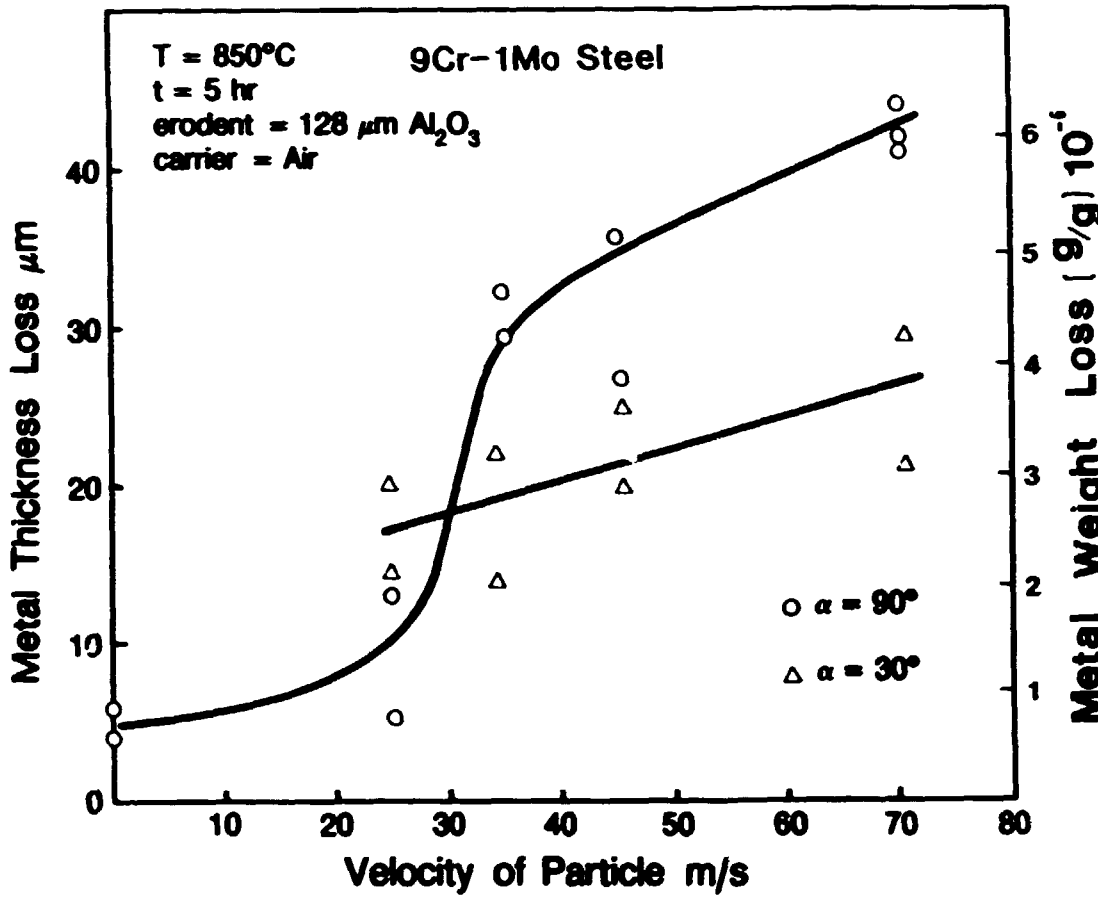

XBL 8410-4619A

Fig. 4. Metal thickness loss v.s. particle velocity for 9Cr1Mo steel at $\alpha=30^{o}$, 90^{o}.

TABLE 8

Compositions of Alternate Steels (wt.%)

ALLOY	Fe	C	Cr	Ni	Mo	Mn	Si	S	P	Others
3.5Ni	Bal	0.15-0.20	----	3.25-3.75	-----	0.40-0.60	0.20-0.35	<0.04	<0.04	
5Cr0.5Mo1.5Si	Bal	0.11	4.84	0.26	0.51	0.51	1.46	0.013	0.013	Cu 0.11
18Cr12Ni2.25Si	Bal	0.07	18.12	12.74	0.01	1.68	2.11			
20Cr2.5Al1Si	Bal	0.047	20.47	0.14	----	0.35	1.02	0.02	0.017	Al 2.47
5Cr0.5Mo	Bal	0.15	5	-----	0.5	<1.0	<1.0	<0.03	<0.04	----------

agglomerated alumina with an average particle size of 90μm. Particle velocities of 30, 40 and 70 m/s were used at a solids loading of 2.5 g/min. at α=90° impact angle. A test time of 5 hours was used which resulted in steady state conditions. The scale compositions of the four kinds of steel tested are listed in Table 9. The Al_2O_3 listed was erodent particles that had adhered to the surface. Table 10 lists the metal losses of the tested specimens.

TABLE 9

X-Ray Diffraction Analysis of Eroded-Corroded Surface of Alternate Steels

ALLOY	PHASE
3.5Ni	α-Fe α-Fe_2O_3 Fe_3O_4 NiO α-Al_2O_3
5Cr0.5Mo1.5Si	α-Fe α-Fe_2O_3 $FeCr_2O_4$ α-Al_2O_3
18Cr12Ni2.25Si	γ-Fe α-Fe_2O_3 $FeCr_2O_4$ Cr_2O_3 Ni_2O_3 α-Al_2O_3
20Cr2.5Al1Si	α-Fe $FeCr_2O_4$ Cr_2O_3 α-Al_2O_3

TABLE 10

Metal Thickness Loss (mm) of Alternate Steels After 5 Hours Exposure

Test Conditions Velocity, m/s	5Cr0.5Mo1.5Si (850°C)	5Cr0.5Mo (850°C)	18Cr12Ni2.25Si (850°C)	20Cr2.5Al1Si (850°C)	3.5Ni (650°C)
30	0.0105	0.096	0.0086	0.034	0.021
	0.0115		0.0095	0.037	0.025
40	0.0140	0.125	0.0105	0.042	0.032
	0.0155		0.0115	0.052	0.026
70	0.0265	0.179	0.0150	0.098	0.042
	0.0295		0.0175	0.089	0.034
n*	1.3	0.93	0.66	1.20	0.55

*$E=V^n$

E = Metal thickness loss
V = Particle velocity
n = exponent

MATERIAL LOSS RATES

Table 10 and the curve in Figure 5 show that a distinct difference in performance occurred that was not a function of chromium content. In fact, the highest chromium content steel with 20% Cr had the highest metal loss rate. The steel with 5% Cr and 1.5% Si was particularly interesting because of its low metal loss rate. At the 30 m/s particle velocity, which is more representative of FBC particle velocities than

the higher velocities used, the steel with 5% Cr had nearly as low a metal loss rate as the 18Cr-12Ni containing steel. It had the same rate of loss at an impact velocity of 30 m/s as that experienced by 9Cr1Mo steel at somewhat lower velocity of 25 m/s.[9] The presence of the 1.5 % silicon in the 5Cr steel can be seen by comparing its behavior to that of the normal Si content 5Cr0.5Mo steel. There was a major reduction in metal thickness loss at all test conditions.

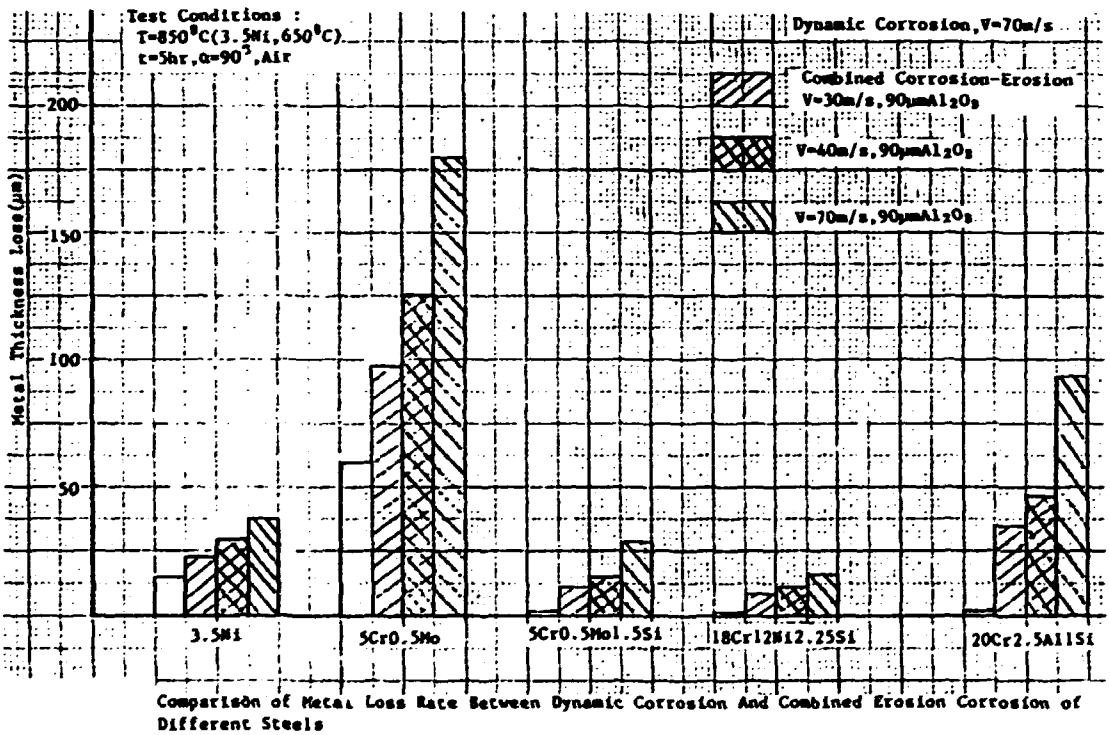

Fig. 5. Effect of velocity on metal loss of alternate steels.

Figure 6 shows the surface morphology of the scale of the 5Cr0.5Mo1.5Si steel. The desired segmented, nodular formation was observed at all test velocities. Many individual nodules of iron oxide in the halo zone can be seen. The scale in the center of the primary zone consists of nodules which are growing together. The occurrence of the clumps of nodules in the center of the primary zone relates to the mechanism of scale loss.[9] The nodules grew together to form a segmented scale rather than a consolidated scale as formed in previous tests on the 9Cr1Mo steel at $\alpha=90°$ at the same particle velocities.

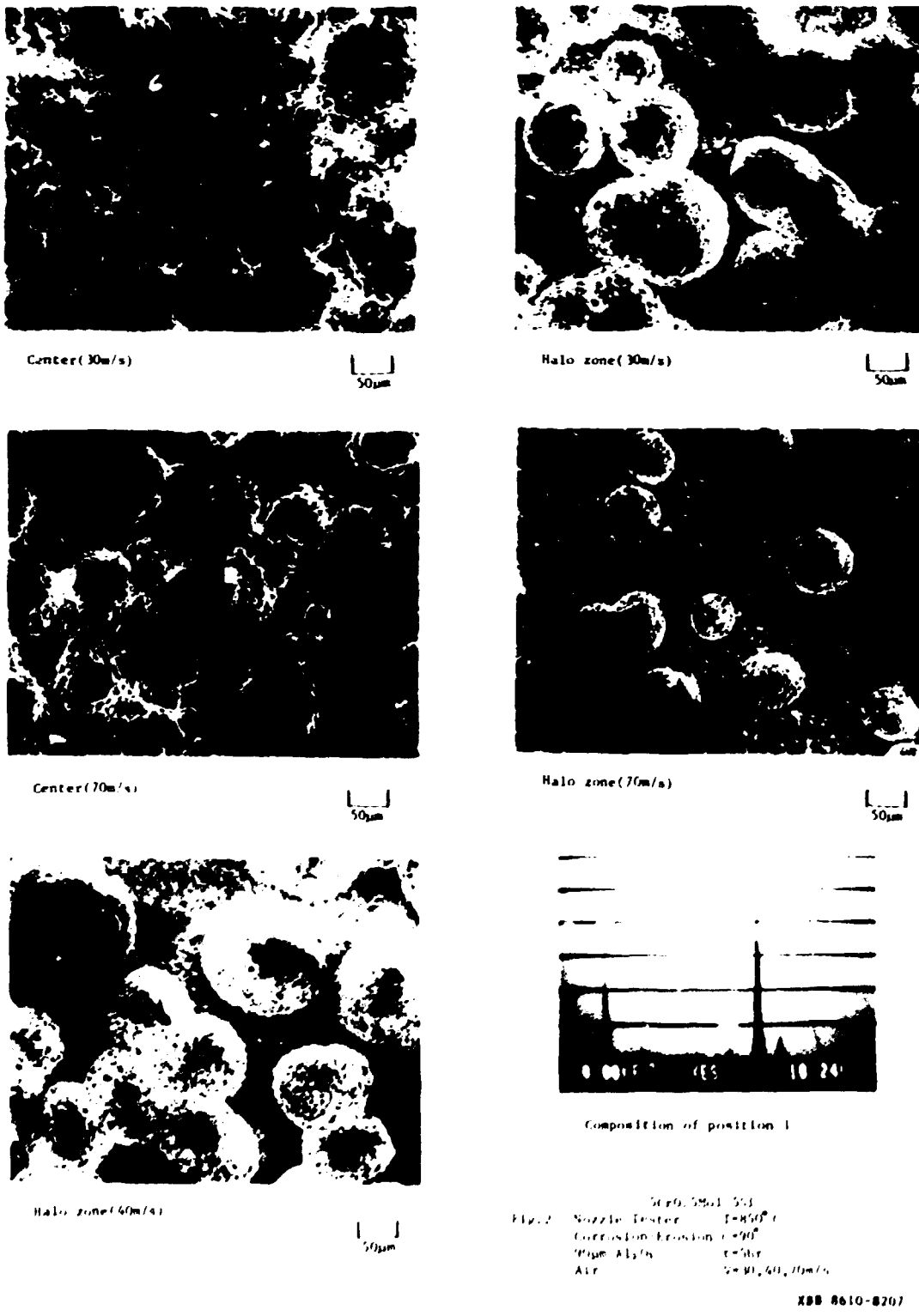

Fig. 6. Surface of 5Cr0.5Mo1.5Si steel after V=30, 70 m/s tests.

These discontinuities are present on the 5Cr0.5Mo1.5Si steel even at V=70 m/s. They account for the inability of the scale to build up the stresses required to cause the faster, periodic spalling scale loss mechanism which occurred in the 9Cr1Mo steel tests at V=70 m/s. The segmented morphology of the scale which caused it to erode slowly is presumed to have caused the lower metal loss of the 5Cr0.5Mo1.5Si steel.

Figure 7 shows the surface morphology of the scale on the 18Cr12Ni2.25Si steel. The scale in both the center of the primary zone and in the halo zone contains many segmented flakes occurring on top of the thin base scale. The EDX peak and x-ray diffraction analyses indicates that the flakes were Fe_2O_3 in the primary zone and $FeCr_2O_4$ in the halo zone with some embedded Al_2O_3 erodent material. In the halo zone, the flakes were relatively dense. In the center zone, the flakes were chipped out. Many small craters occurred which indicated that the base metal was being deformed as well as the scale. This means that the scale was relatively thin, was quite segmented, and had plastically deformed into the base metal. The scale loss mechanism was the slow cracking and chipping one.

The surface morphology of the scale on the 20Cr2.5Al1Si steel is shown in Figure 8. In both the center and halo zones the scale was essentially consolidated with overlapping clumps. This morphology was different from that of the scales that formed on the 5Cr and 18Cr steels. No division or cracks were discernable and individual crystallites could not be observed at the magnification used. The consolidated scale morphology resulted in the generation of stresses in the scale that caused spalling at higher rates of loss than occurred in the other alloy's scales, see Figure 5. Increasing the velocity of the erodent particles caused no distinct changes to occur in the morphology of the scale but the clumps became more dense, thick and bulky.

Figure 9 shows that the morphology of the scale on the 3.5Ni steel at 650°C. The scale in both the center and the halo zones consists of small rounded grains. At V=30 m/s and 40 m/s the morphology of the scale appeared to be the same. At V=70 m/s the round grains became finer and denser. The morphology of the scale on this steel is quite different from that on the Cr-Si steels. Yet the same principle of

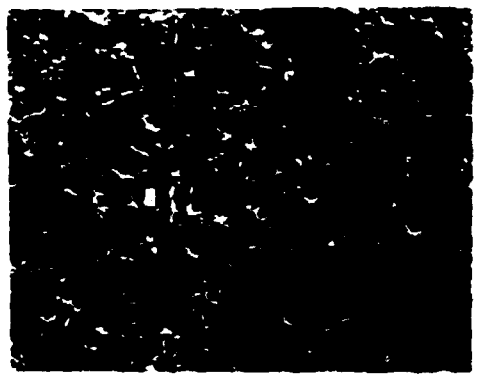

Surface(center, 30m/s)

10μm

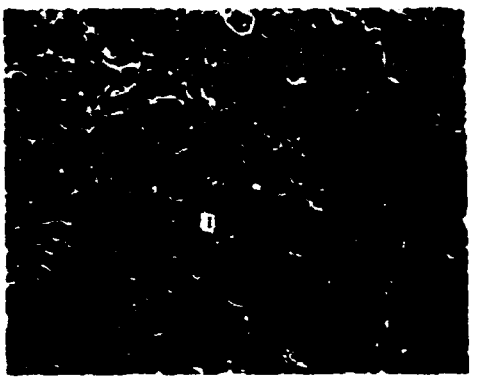

Surface(center, 40m/s)

10μm

Surface(center, 70m/s)

50μm

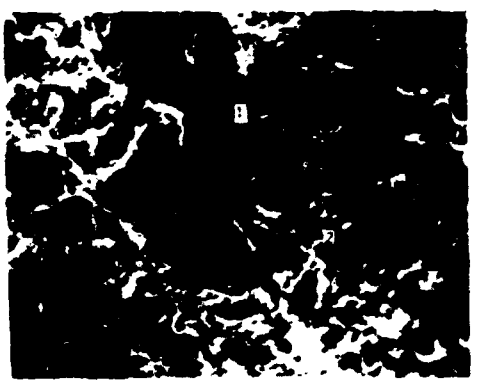

Surface(center, 70m/s)

10μm

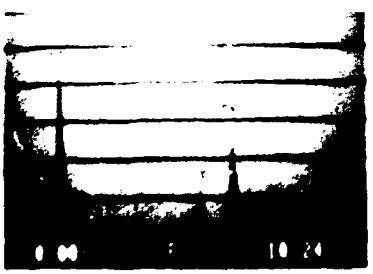

Composition of position 2

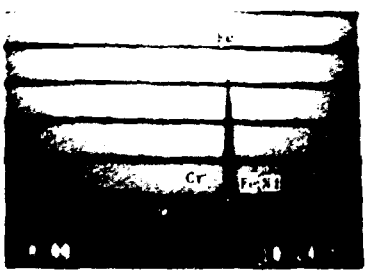

Composition of position 1

18Cr12Ni2.5Si

Sizzle Tester T=850°C

Corrosion-Erosion i=90°

90μm Al_2O_3 t=5hr

Air V=30, 40, 70m/s

X88 8610-8208

Fig. 7. Surface of 18Cr12Ni2.5Si steel after V=30, 40, 70 m/s tests.

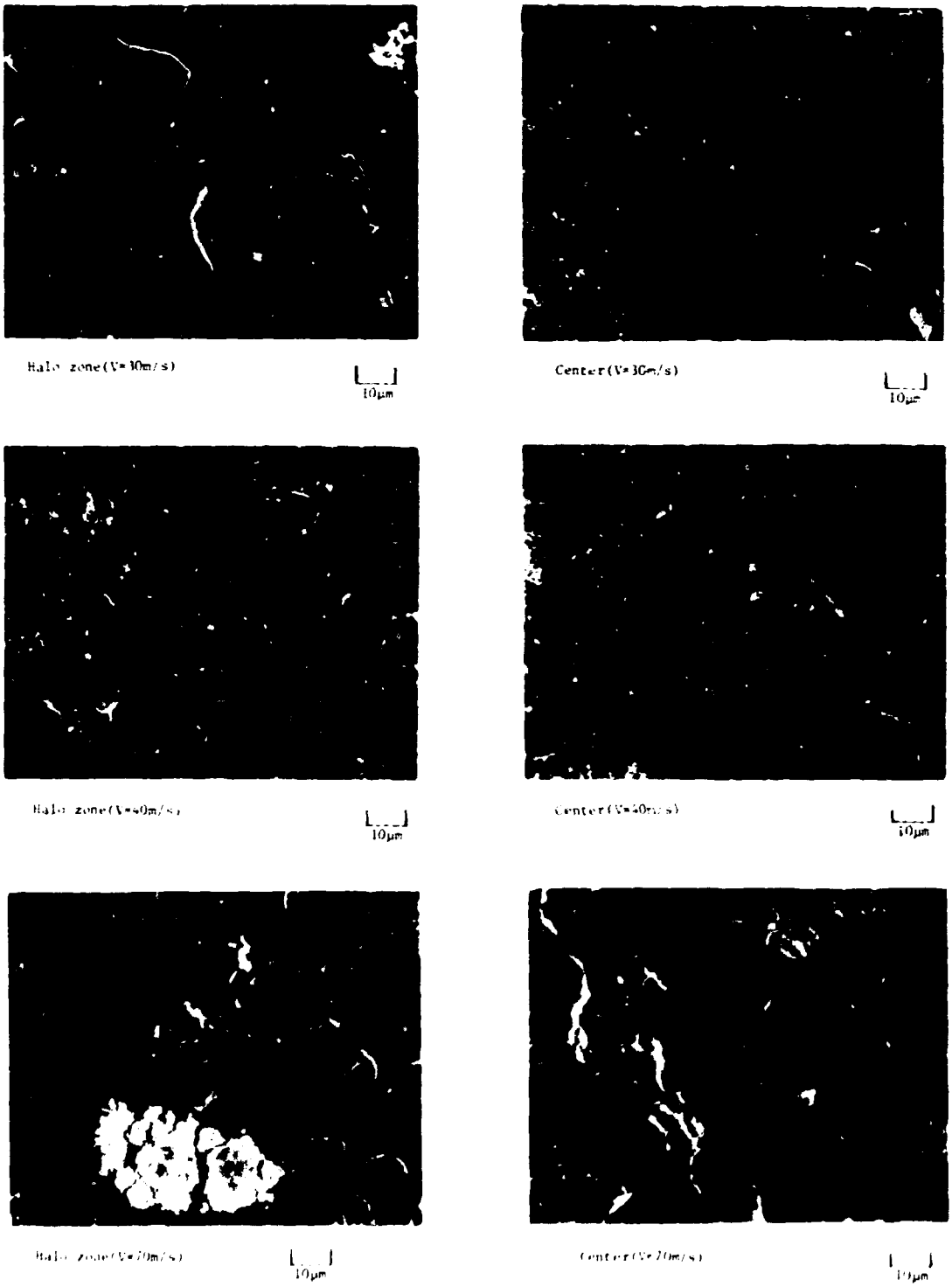

Fig. 8. Surface of 20Cr2.5Si steel after V=30, 40, 70 m/s tests.

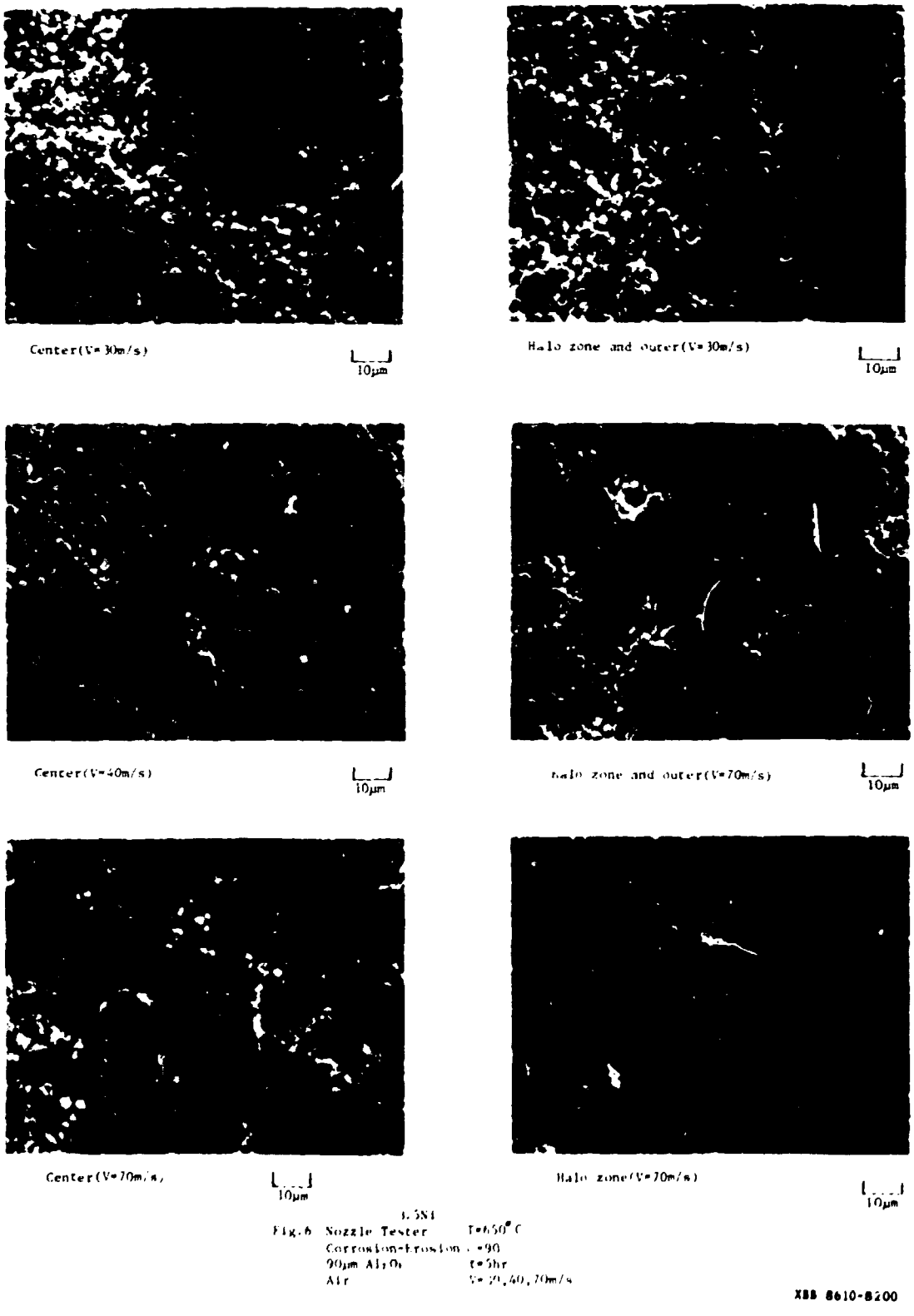

Fig. 9. Surface of 3.5Ni steel after V=30, 40, 70 m/s tests.

scale loss mechanism prevails. The nature of the scale on the 3.5Ni steel is not attractive for use of the alloy in erosion-corrosion environments.

NODULAR OXIDE SCALE FORMATION

Nodules have been observed and reported in the previous work on 9Cr1Mo steel.[9] In the current tests the nodular oxide scale occurred during the E-C of the lowest chromium containing steel, 5Cr0.5Mo1.5Si, at all particle velocities. Figure 6 shows the morphology of the surface of the distinctly nodular scale on the 5Cr0.5Mo1.5Si steel. The composition of the outer surface of the nodule is predominantly Fe_2O_3 with a little Cr dissolved in it. A considerable amount of Al_2O_3 erodent adhered in the surface crevices of the nodules, resulting in an EDX aluminum peak.

The cross section of nodules formed at both V=30 m/s and 70 m/s is shown in Figure 10, along with EDX peak analyses identifying their compositions. The nodules are the same as that shown in Figure 1 which formed on the 9Cr1Mo steel. Each nodule has an upper element above the general plane of the scale and a lower element that extends down into the base metal. It appears that the nodule system must be in direct contact with the base metal to form and grow. Nodules were not observed to grow on top of an already established thick scale layer. The EDX peak analyses, as verified by x-ray diffraction, indicated that the upper element of the nodule is Fe_2O_3 and did not contain any chromium. The lower element of the nodule is shown to be Cr containing Fe_2O_3 which conforms with that reported for the 9Cr1Mo steel.[9]

DISCUSSION

The results presented in this paper cover some of the highlights of the work at LBL to determine and understand the erosion and erosion-corrosion of commercially available steels that are produced in forms that can be used in energy generation equipment. The work was carried out to determine which properties of structural alloys related to their erosion behavior so that alloys could be selected for erosion environments based upon their resistance to erosion. Unfortunately, no useable relationship was ever determined between mechanical or physical properties and the erosion resistance of structural alloys.

cross section (V=70m/s)

cross section (V=30m/s)

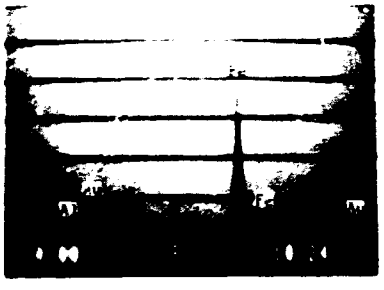

Composition of Cross section Position 2

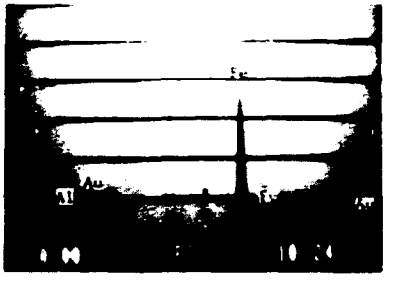

Composition of Cross section Position 1

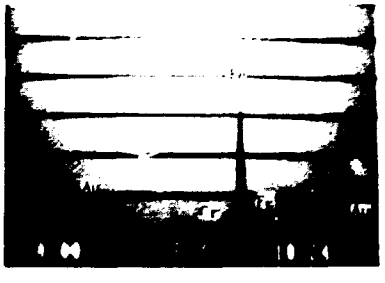

Composition of Cross section Position 5

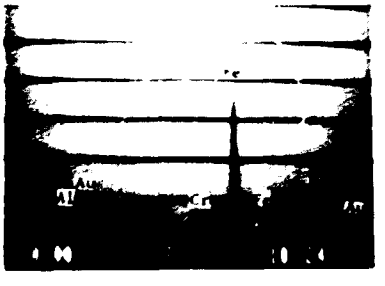

Composition of Cross section Position 3,4

Fig.9 Nozzle Testεv — $5Cr^{1}/_{2}Mo1-^{1}/_{2}Si$
Corrosion-Erosion — T=850°C
90μm Al_2O_3 — α=90°
Air — t=5hr
V=30m/s,70m/s

XBB 8610-8203

Fig. 10. Cross section of nodules formed on 5Cr0.5Mo1.5Si steel during V=30, 70 m/s tests.

The only property that exhibited some relationship was a loosely defined ductility[12] as indicated by the elongation in a normal strain rate tensile test. The obvious difference between the slow strain rate of a standard tensile test and the extremely rapid strain rates which occur when an erodent particle strikes and deforms a metal surface[13] precludes the direct use of any ductility term in indicating the erosion resistance of an alloy.

The data on the erosion of ductile metals presented in this paper has a consistency regarding the inability of any strengthening or hardening mechanism to affect erosion behavior in a positive manner. Work hardening, thermal treatments such as martensitic hardening and precipitation hardening, solid solution strengthening, even the addition of up to 80 vol. % of hard carbides to a ductile matrix did not improve the erosion resistance of the metal for the kind of erosion environments that are present in energy generation equipment.

There is some combination of at least three reasons why iron, nickel and cobalt base structural alloys do not have their room and near room temperature erosion resistance improved by some type of alloying or thermal or mechanical treatment. They are: 1) the temperature rise as the result of the severe straining of the metal's surface that occurs when erodent particles strike, (ref. 12) 2) the extremely high strain rates which occur,(ref. 13) and 3) the large strains which occur.[5] These effects negate any lattice strain or solid solution strengthening present in the alloy.

The carbide-metal matrix composite's hardness increases are overcome by the disruption in plastic deformation which the brittle carbides cause in the immediate vicinity of the impacting particles. This concentrates the particle's force and causes the critical strain to remove metal matrix material along with the carbide particles to be more easily reached.

However, as it turns out, for applications in the elevated temperature regions of energy generation equipment, the erosion behavior of the base metal is of relatively little importance compared to the nature and behavior of the combined erosion-corrosion produced scales

which form on the alloys' surfaces. The metal wastage rate is a direct function of the formation and removal rate of the scale; the metal substrate is never directly impacted by the erodent particles.

The material removal rate of the scale is a function of its morphology, which is determined by a combination of the basic nature of the scale and the particle impact conditions. The composition of the alloy is the primary variable in determining the nature of the scale formation. Therefore, there is an alloy selection criteria that can be used for erosion-corrosion service. In the work presented in this paper, a relatively low chromium content alloy with extra silicon in it, the 5Cr0.5Mo1.5Si alloy, had a scale morphology that resulted in low metal wastage rates compared to higher chromium content alloys and the same 5Cr0.5Mo steel with a normal silicon content.

The knowledge developed on the behavior of alloy steels in combined erosion-corrosion environments hopefully is the beginning of the selection/development of even lower alloy steels whose scales behave in the particular manner that results in low metal wastage rates in coal burning energy generation equipment.

CONCLUSIONS

1. The erosion resistance of commercial iron, nickel and cobalt base alloys cannot be effectively modified by compositional, mechanical or thermal strengthening mechanisms.

2. Until approximately 80 % of the volume of carbide-metal matrix composites consists of carbide particles, carbide additions to ductile metals decreases the erosion resistance of the composites.

3. In combined eroison-corrosion environments, iron base alloys undergo metal wastage rates that are dependent on the nature of the scales that form on their surfaces.

4. The addition of 1.5 wt. % Si to 5Cr0.5Mo steel markedly decreases its metal wastage rate compared to normal 5Cr0.5Mo steel and to higher chromium content steels.

REFERENCES

1. Foley, T. and Levy, A. V., "The Erosion of Heat Treated Steels," WEAR 91 No.1, pp. 45 - 64, October 1983.

2. Levy, A. V., Yan, J., Patterson, J., "Elevated Temperature Erosion of Steels," WEAR 108 No. 1., pp. 43 - 60, March 1986.

3. Nain, M. and Bahadur, S., "Effect of Microstructure and Mechanical Properties on the Erosion of 18Ni (250) Maraging Steel," WEAR 112 No. 2, pp. 217 - 234, November 1986.

4. McCabe, L. P., Sargent, G. A., Conard, H., "Effect of Microstructure on the Erosion of Steel by Solid Particles," WEAR 105 No.3, pp. 257 - 278, October 1985.

5. Ninham, A., "The Effect of Mechanical Properties on Erosion," Proceedings of ASME International Conference on Wear of Materials, pp. 813 - 824, Houston, Texas, April 1987.

6. Ninham, A. and Levy, A. V., "The Erosion of Carbide-Metal Composites," Proceedings of ASME International Conference on Wear of Materials, pp. 825 - 832, Houston, Texas, April 1987.

7. Ball, A. and Patterson, A. W., "Microstructural Design of Erosion Resistant Hard Materials," Proceedings 11th International Plansee Seminar '85 Vol. 2, pp. 377 - 391, Reutte, Austria, Metallwerk Plansee GmbH, Reutte, Austria, 1985.

8. Levy, A. V., Shui, Z. R., Wang, B. Q., "Erosion of Solid Solution Strengthened Alloys," Proceedings of Seventh International Conference on Erosion by Liquid and Solid Impact, Cambridge, England, September 1987.

9. Levy, A. V. and Man Y.-F., "Elevated TEmperature Erosion-Corrosion of 9Cr-1Mo Steel," WEAR 111 No. 2, pp. 135 - 160, September 1986.

10. Levy, A. V., Man, Y.-F., Jee, N., "The Erosion-Corrosion of Heat Exchanger Tubes in Fluidized Bed Combustors," Proceedings of ASME Ninth International Fluidized Bed Combustion Conference, Boston, Mass., May 1987.

11. Levy, A. V. and Man, Y.-F., "Erosion-Corrosion Mechanisms and Rates in Fe-Cr Steels," NACE Corrosion 86, Paper No. 111, Houston, Texas, March 1986.

12. Levy, A. V., "The Platelet Mechanism of Erosion of Ductile Metals," WEAR 108 No. 1, pp. 1 - 22, March 1986.

13. Hutchings, I. M., "A Model for the Erosion of Metals by Spherical Particles at Normal Incidence," WEAR 70 No. 3, pp. 269 - 282, August 1981.

STUDY OF PARTICLE REBOUND CHARACTERISTICS AND MATERIAL EROSION AT HIGH TEMPERATURES

W. Tabakoff

Department of Aerospace Engineering & Engineering Mechanics
University of Cincinnati
Cincinnati, Ohio 45221

ABSTRACT

The Laser Doppler Velocimeter (LDV) system was used to measure the rebounding characteristics of 15 micron mean diameter fly ash particles impacting several target materials. The rebounding velocities and angles were determined for 410 stainless steel, 6Al-4V titanium, INCO 718, RENE 41, AM355, and L605 cobalt target materials at different impact angles. In addition, an erosion study was conducted to measure the erosion rate for the AM355 target material impacted by fly ash and silica sand particles. The effect of the following parameters on erosion was investigated: particle sizes, velocity, impingement angle and temperature.

INTRODUCTION

The use of pulverized coal as fuel in many power plants and industrial establishments is inevitable both at present and in the future. The major problem confronting earlier developers of coal-burning turbines is the serious erosion of turbine blades and other metal parts by the suspension of fly ash in hot combustion gases. Under two-phase flow conditions, the gas and particles experience different degrees of turning as they flow through the blade channels, due to the difference in their inertia. This results in particle concentration gradient across the blade channel, and causes a change in the properties of gas and particles. The net result is a change in the blade surface pressure distribution, which alters the engine performance during the period of particle ingestion.

If the particles are erosive, the problem becomes more complicated. The impact of the blade surfaces by the solid particles can cause severe erosion damage, leading to structural failure of the blades. The maximum erosion damage occurs at the leading and trailing edges of the stator and rotor blades. This damage is manifested by pitting and cutting of the blade leading and trailing edges, and a general increase in the blade surface roughness. The overall effect of the above phenomena, from the aerodynamic viewpoint, is a loss of performance and the deterioration of these engines both structurally and aerodynamically. It is possible to remove approximately 85 percent by weight of the ash in these gases using cyclones. However small particles ranging in size between 1 and 15 microns still pass through the cyclones and enter the turbine. Typical ash concentrations for such a turbine are about 0.000027 mg/cm^3 (7.8 mgm/ft^3) [1].

A thorough knowledge of the various parameters which influence the erosion damage, is required to improve the life and the aerodynamic performance of turbomachinery operating in an ambience of particulate flow. This paper presents an experimental investigation of the particle restitution characteristics for several gas turbine component materials. The restitution coefficients are essential for particle trajectory calculations in turbomachinery, and for the prediction of material erosion using semi-empirical erosion correlations.

EXPERIMENTAL SET-UP

The experimental set-up is shown schematically in Figs. 1 and 2. It consists of the erosion wind tunnel, the laser doppler velocimeter (LDV) system, the data acquisition system and the solid particle feeder.

Erosion Wind Tunnel

In this tunnel, the following variables are controlled: fluid velocity, particle velocity, temperature, particle flow rate and particle sizes in a representative aerodynamic environment. Provisions

were made in the test design to allow for changing the impact angle of the abrasive particle relative to the surface of the test specimen.

A schematic of the tunnel is shown in Fig. 1; it consists of the following components: particle feeder (A), main air supply pipe (B), combustor (C), particle preheater (D), particle injector (E), acceleration tunnel (F), test section (G), and exhaust tank (H).

The equipment functions as follows. A measured amount of abrasive grid of a given constituency is placed into the particle feeder (A). The particles are fed into a secondary air source and blown up to the particle

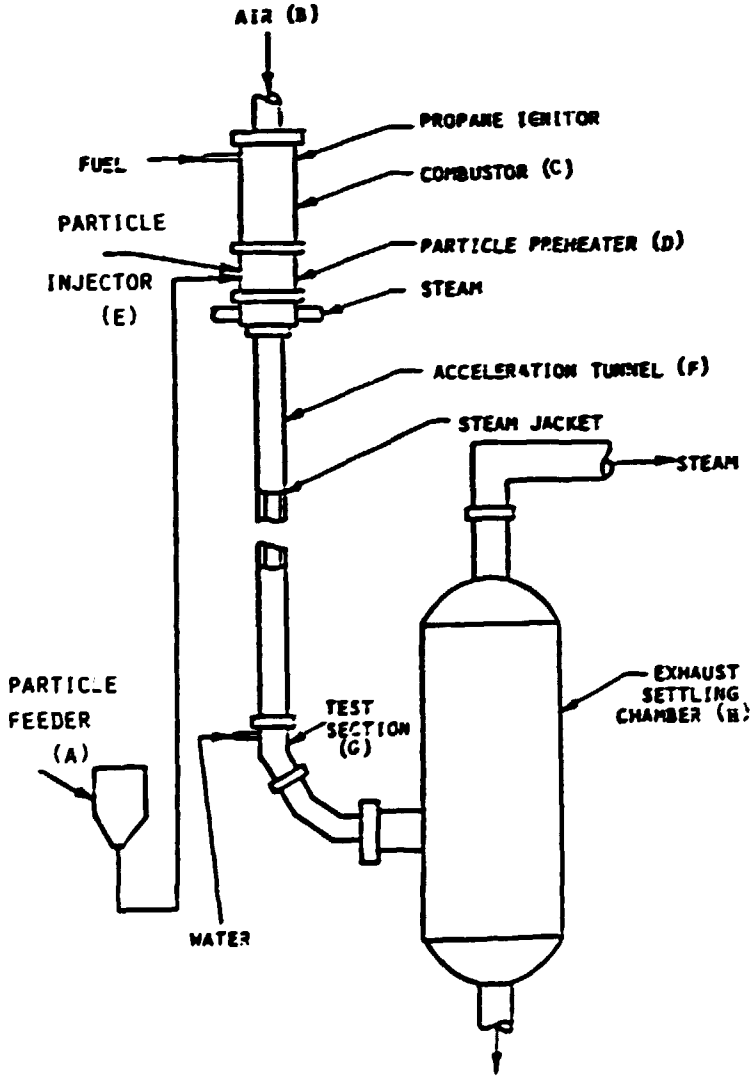

Fig. 1. Schematic of Erosion Test Facility.

preheater (D), and then to the injector (E), where they mix with the main air supply (B), which is heated by the combustor (C). The particles are then accelerated by the high-velocity air in a constant-area steam-cooled duct (F) and impact the specimen in the test section (G). The particulate flow is then mixed with the coolant and dumped in the exhaust tank. This facility is capable of supplying erosion data at temperatures in the range of ambient to 1093°C, and particle velocities from 60 to 450 m/s. In this facility, the particle velocity is controlled by adjusting the tunnel air flow, while the impingement angle is set by rotating the sample relative to the flow stream. The sample temperature is controlled through the combustor heating the flow stream, which in turn affects the material sample temperature. Further description of the facility may be found in reference [2].

The test section is designed such that the particle laden air is channeled over the specimen and the aerodynamics of the fluid surrounding the blade sample is preserved. This section contains several interchangeable inserts such that the fluid profile can be determined using conventional instrumentation and the particle trajectories can be recorded using high speed photography or laser methods.

Particle Feeder

The particles from the feeder A (Fig. 1) are carried up to the particle injector. The feeder was designed as a vessel to operate at high air pressures. However, this pressure is equalized above and below the plunger by a bypass line. This allows the system to be calibrated under gravity feed conditions. Further, an electric eye records the plunger rpm such that the operating conditions are maintained. The metering orifice was designed to be replaceable. In this manner, a larger (or smaller) orifice may be used, along with corresponding rod diameter, to allow versatility of the feeder. In this investigation the air flow was seeded with fly ash particles with the following size distribution: under 5 microns 62%; 5-10 microns 17%; 10-20 microns 20%, and over 20 microns 1%.

Laser and Optics (LDV System)

The optical components of the laser-doppler velocimeter are arranged in the backward scatter mode, Fig. 2, to measure two non-collateral simultaneous velocity components of a single particle. A two-color, 5 watt argon-ion Spectra physics, model 164-09 is used as laser source. The laser beams are brought into one common measuring volume using a transmitting lens of 250 mm focal length. The crossing angle for the incident 1.5 mm diameter beams is 11.05 degrees.

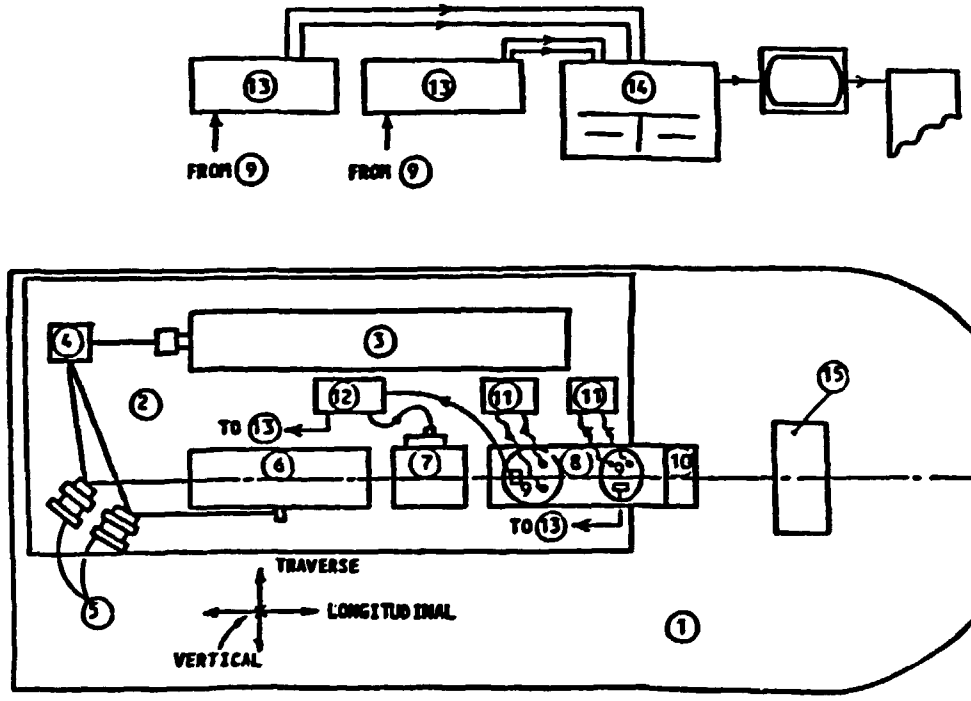

(1) THE PLATFORM
(2) THE OPTICAL SYSTEM TABLE
(3) 5 WATT ARGON LASER
(4) DISPERSION PRISMS
(5) 2 ONE-INCH DIAMETER MIRRORS
(6) BEAMSPLITTERS AND POLARIZATION ROTATORS
(7) FREQUENCY SHIFTER
(8) BACKSCATTER RECEIVING OPTICS WITH COLOR SEPARATORS
(9) PHOTODETECTOR
(10) 250 MM COLLECTING LENS
(11) PHOTOMULTIPLIER
(12) FREQUENCY DOWNMIXER
(13) DATA PROCESSOR
(14) PDP 11/MINC 23 MINI-COMPUTER
(15) THE TEST SECTION

Fig. 2. Schematic Showing the Experimental Set-Up.

Data Acquisition System

Two signal processors TSI model 1990 and on-line Minc 11/23 microcomputer are used to acquire syncronized data for the simultaneous measurements of two non-collateral velocity components. The minimum time for a particle to cross the measuring volume was found to be 1.4 microsec.

Accordingly, the syncronization condition was set to 1 microsec, which is the time out between the two data ready pulses received from both signal processors. A time out of 5 microsec after each valid syncronized data point is tagged in the computer, allows the particle to clear the measuring volume. The data acquisition program thus ensures that the sampling data are not obtained more than once from the same particle.

DEVELOPMENT OF PARTICLE REBOUND CORRELATIONS

The retound characteristics of particles impacting metal targets can only be described in a statistical sense. This becomes obvious when one examines the number of geometric situations that might occur at impact. After a given incubation period, the target material will become pitted with craters, and in fact after a slightly longer period, a regular ripple pattern will form on the eroded surface. Thus, the local impact angle between the small particles and the eroded surface may deviate considerably from the geometric average. Further, the particles themselves are crystalline and irregular in shape with several sharp corners. As the particle approaches the specimen, the orientation of the particle is, for the most part, random. Thus, some particles will impact on a flat surface and do very little work on the target material. Others will impact with a corner oriented in a manner similar to that of a cutting tool and will remove surface material.

The restitution coefficient or restitution ratio is a measure of the kinetic energy exchange between two objects upon impact. In this investigation, an erosive impact occurs when the contaminant particle is much harder than the target material. Therefore, the restitution ratio will be a measure of the distortion of the target material rather than distortion of the erosive particle. In addition, this investigation is mostly for ductile target materials, upon which the particle will create local stresses high enough to cause plastic flow in the target material.

Grant and Tabakoff [3] were the first to investigate thoroughly the rebound characteristics of high speed erosive particles. The study was carried out on annealed 2024 aluminum alloy. The data were described

using histograms to illustrate these statistical distribution. Referring to Fig. 3, the measured particle rebound characteristics are expressed in terms of a normal velocity restitution ratio V_{N2}/V_{N1} (the ratio between the normal component of the particle velocity after impact to that before impact), and a tangential velocity restitution ratio V_{T2}/V_{T1} (the ratio between the tangential component of the particle velocity after impact to that before impact).

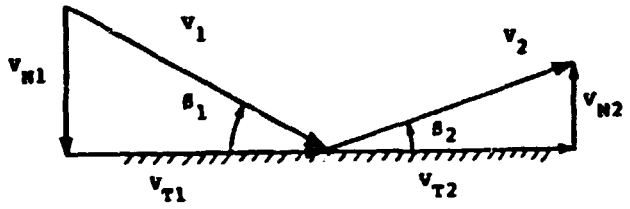

Fig. 3. Velocity and Angle Notations.

MEASUREMENT TECHNIQUE

The LDV system was used to measure two non-collateral velocity components of the impact and rebound velocities for several materials used in turbomachinery. However in this paper only six materials are reported, namely INCO 718, Rene 41, L605 Cobalt, 6Al-4V Titanium, 410 Stainless Steel and AM355. Initially, the impacting particle velocities were measured at four different points above the sample as shown in Fig. 4. It was found that the measured impacting velocities were consistent at points 2 through 4. However the measurements at point 1 were somewhat different. This was attributed to the fact that the data was distorted by the smaller fly ash particles, less than 2 microns, which follow the air flow streamlines without hitting the specimen surface. Therefore point 2 was selected to measure the impingement velocity for the rest of the tests. Measurements for five incidence angles β_1 were performed and a summary of the normalized average and standard deviation of the impingement velocities are shown in Table 1. The velocities are normalized with respect to the particle velocity at the center of the test section which was 98 m/s (320 ft/sec). The standard deviation is large due to the fly

ash particles irregular shapes and the size variation causes the particles to randomly deviate from the air flow path.

The rebounding velocities were measured at four points located on a line 2 mm above and parallel to a specimen surface as shown in Fig. 5. It was found that the variation in the rebounding velocities at these four points were within the standard deviation. The average rebounding velocities were measured and normalized with respect to the corresponding impact velocities for the different impacting angles and the results are shown in Table 1.

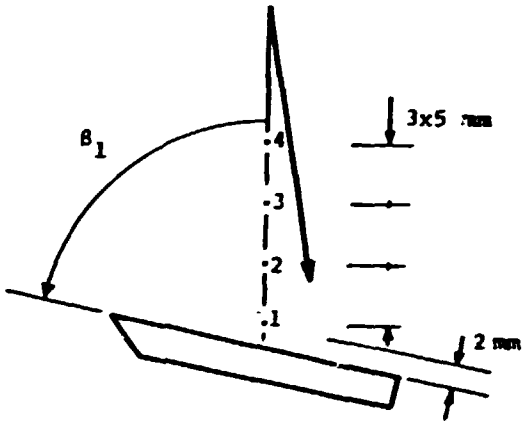

Fig. 4. Impingement Measurements Locations.

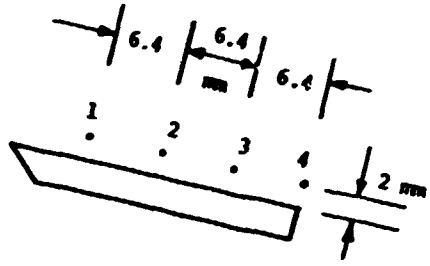

Fig. 5. Rebounding Measurements Locations.

TABLE 1: THE NORMALIZED AVERAGE RESTITUTION COEFFICIENTS FOR 6Al-4V-Ti TARGET MATERIAL AT DIFFERENT INCIDENCE ANGLES

Incidence Angle	Directional Coefficient $\beta=\beta_2/\beta_1$		Velocity Restitution Coefficients				
			Tangential $e_T=V_{T2}/V_{T1}$		Normal $e_N=V_{N2}/V_{N1}$		Total $e_V=V_2/V_1$
β_1	SSM*	SD**	SSM	SD	SSM	SD	SSM
15	1.0	0.4	0.941	0.24	0.95	0.453	0.935
30	0.989	0.217	0.614	0.195	0.589	0.252	0.608
45	0.7	0.158	0.825	0.2	0.523	0.318	0.668
60	0.765	0.128	1.025	0.215	0.628	0.128	0.752
75	0.75	0.114	1.43	0.261	0.526	0.26	0.619

* SSM - Sample Statistical Mean; **SD - Standard Deviation

Figures 6 through 9 illustrate typical histograms of the restitution ratios for the fly ash impacting over a cobalt sample target material at $\beta_1 = 15°$. The vertical axis in these figures represent the frequency of occurrence that the restitution ratio was found to be between the limits designated by the scale at the horizontal axis. The distribution of the data is due to the particle size variation and irregular particle shapes. The ratio of the particle velocity after and before impact, V_2/V_1, is plotted against the impingement angle (β_1) as shown in Fig. 10. Since the statistical distributions are of importance, the shape of these distributions are of importance, the shape of these distributions are cross plotted on the figure. The parameter V_2/V_1 is directly related to the kinetic energy lost during impact. The spread in this data indicates the variable condition of the surfaces and the orientation of the particle at impact. It is evident from this figure that V_2/V_1 decreases as the impact angle β_1 increases from zero to 75 degrees.

Figures 11 and 12 show the normal ($V_{N2}/V_{N1} = V_2\sin\beta_2/V_1\sin\beta_1$) and tangential ($V_{T2}/V_{T1} = V_2\cos\beta_2/V_1\cos\beta_1$) restitution coefficients respectively plotted against the impact angle β_1.

The solid lines in Figs. 10 through 12 represent a least squares polynomial curve fit of the mean value of the restitution parameters which were measured for impingement angles ranging between 15° and 75°. For cobalt, these restitution parameters may be expressed by the equations:

$$e_V = V_2/V_1 = 0.99106 - 0.8048\,\beta_1 + 2.34602\,\beta_1^2 - 3.24094\,\beta_1^3 + 1.26004\,\beta_1^4$$

$$e_T = V_{T2}/V_{T1} = 1.00691 - 1.16164\,\beta_1 + 4.39067\,\beta_1^2 - 5.78692\,\beta_1^3 + 2.24766\,\beta_1^4$$

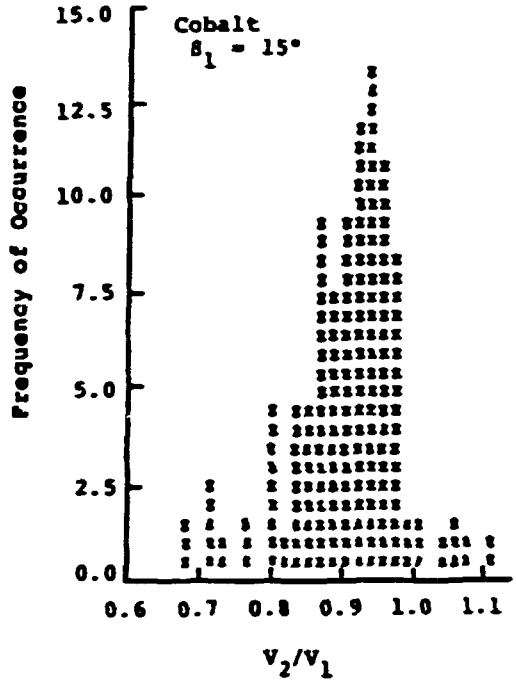

Fig. 6. Erosive Particle Velocity Restitution Ratio Distribution.

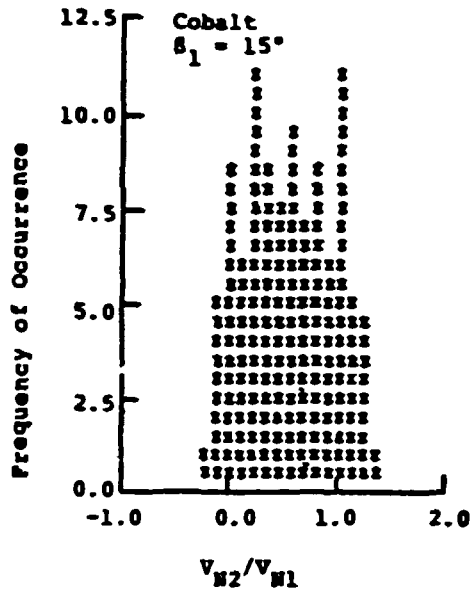

Fig. 8. Erosive Particle Normal Velocity Restitution Ratio Distribution.

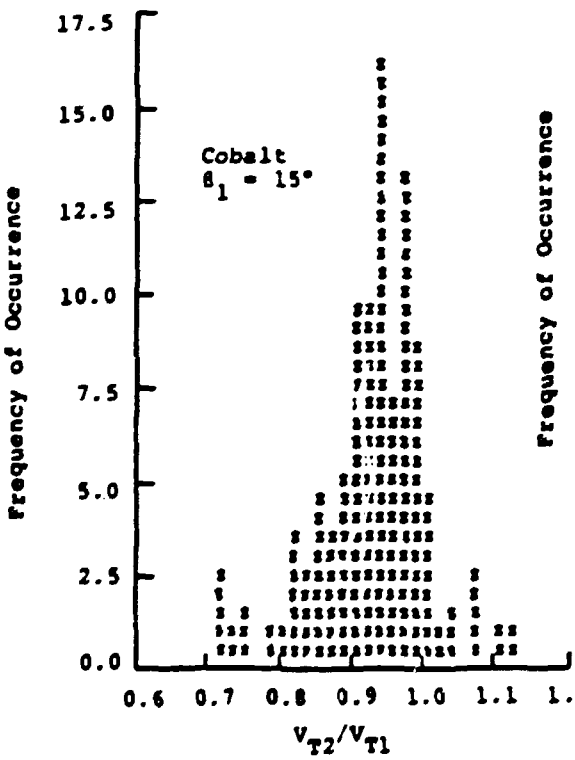

Fig. 7. Erosive Particle Tangential Velocity Restitution Ratio Distribution.

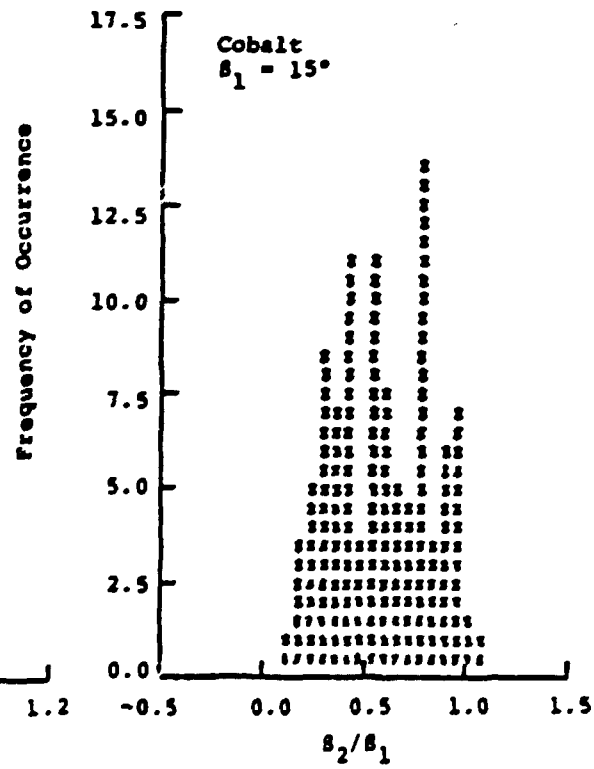

Fig. 9. Erosive Particle Directional Coefficient Distribution.

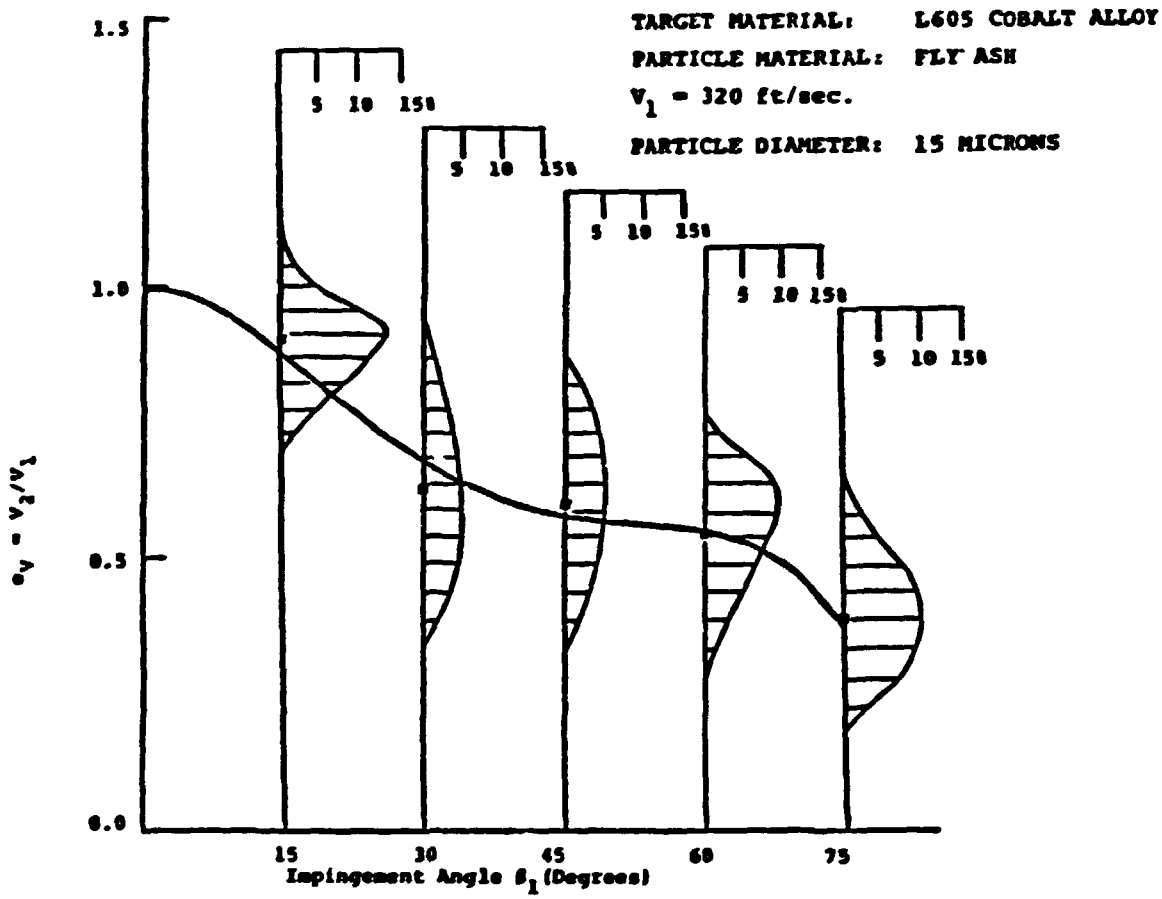

Fig. 10. Influence of β_1 on the Velocity Restitution Coefficient.

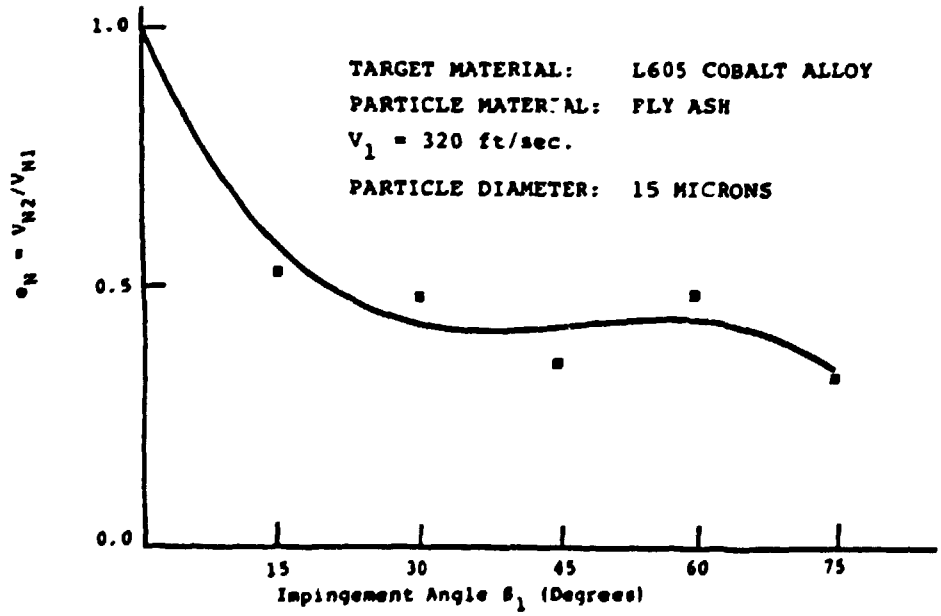

Fig. 11. Influence of β_1 on the Normal Velocity Restitution Coefficient.

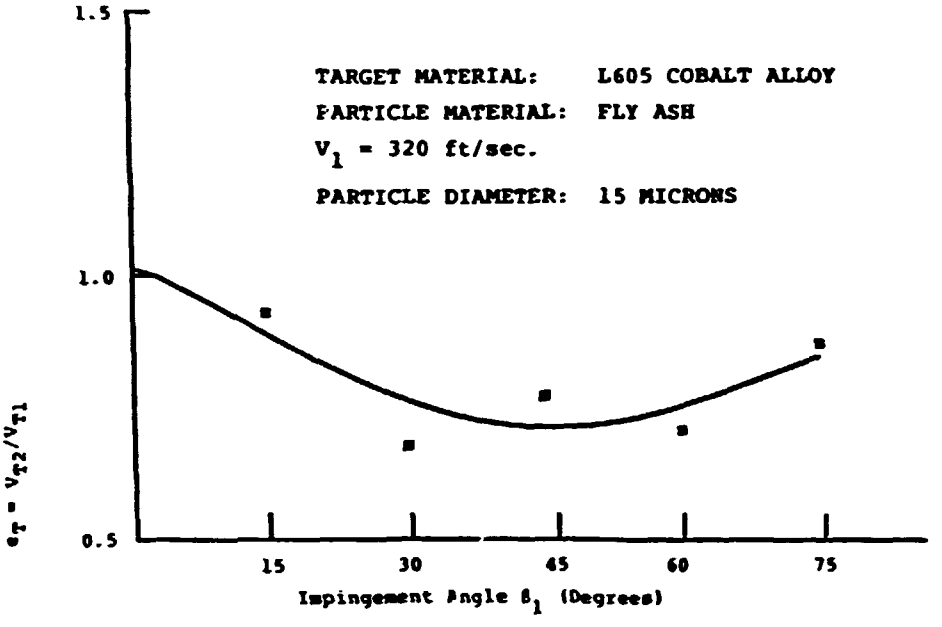

Fig. 12. Influence of β_1 on the Tangential Velocity Restitution Coefficient.

$$e_N = V_{N2}/V_{N1} = 0.96918 - 3.50414\,\beta_1 + 8.14812\,\beta_1^2 - 7.45348\,\beta_1^3 + 2.29569\,\beta_1^4$$

$$e_\beta = \beta_2/\beta_1 = 0.99255 - 2.60506\,\beta_1 + 4.47339\,\beta_1^2 - 2.46638\,\beta_1^3 + 0.38722\,\beta_1^4$$

where β_1 is measured in radians.

Similar measurements and empirical expressions for restitution ratios have been reported by the author in reference [4] for various target materials. Some of the measured experimental data for six different alloys are presented in Figs. 13 through 20. Figures 13 through 16 compare the four restitution parameters for 6Al-4V titanium, 410 stainless steel and AM355 alloys. The same parameters are presented for other three alloys: INCO 718, Rene 41 and L605 Cobalt in Figs. 17 through 20. These data may be used with well documented erosion equation developed by Grant Tabakoff [3] for ambient gas temperatures.

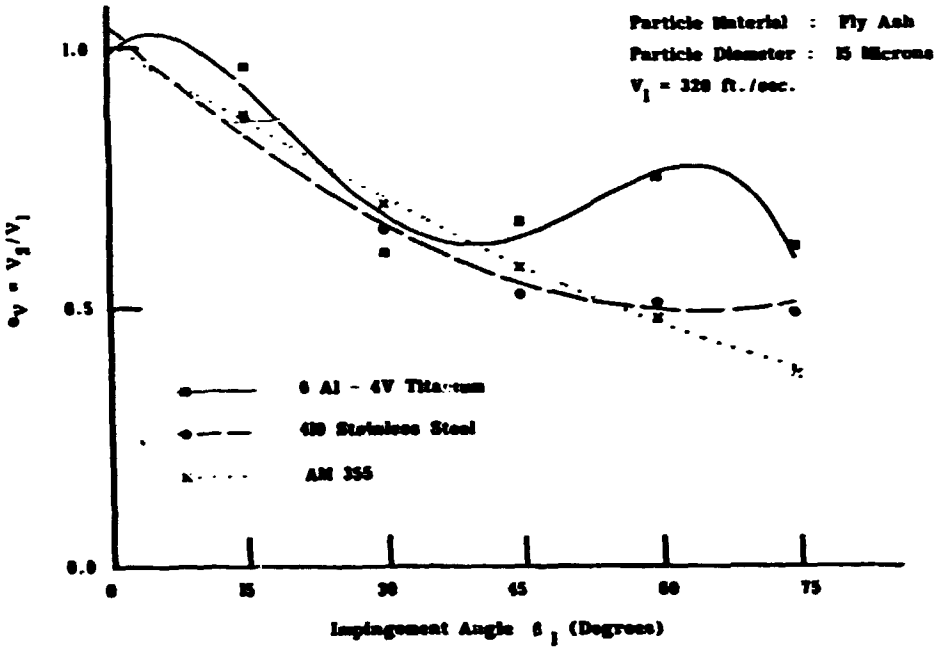

Fig. 13. Comparison of the Velocity Restitution Ratios for Different Target Materials.

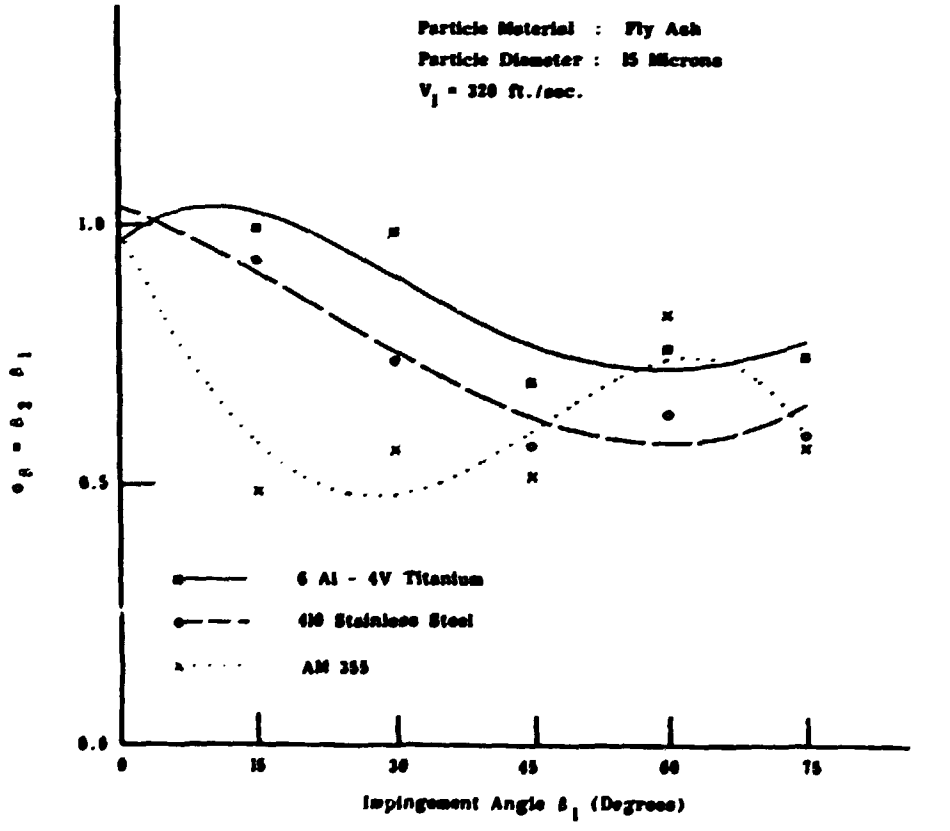

Fig. 14. Comparison of the Directional Coefficient for Different Target Materials.

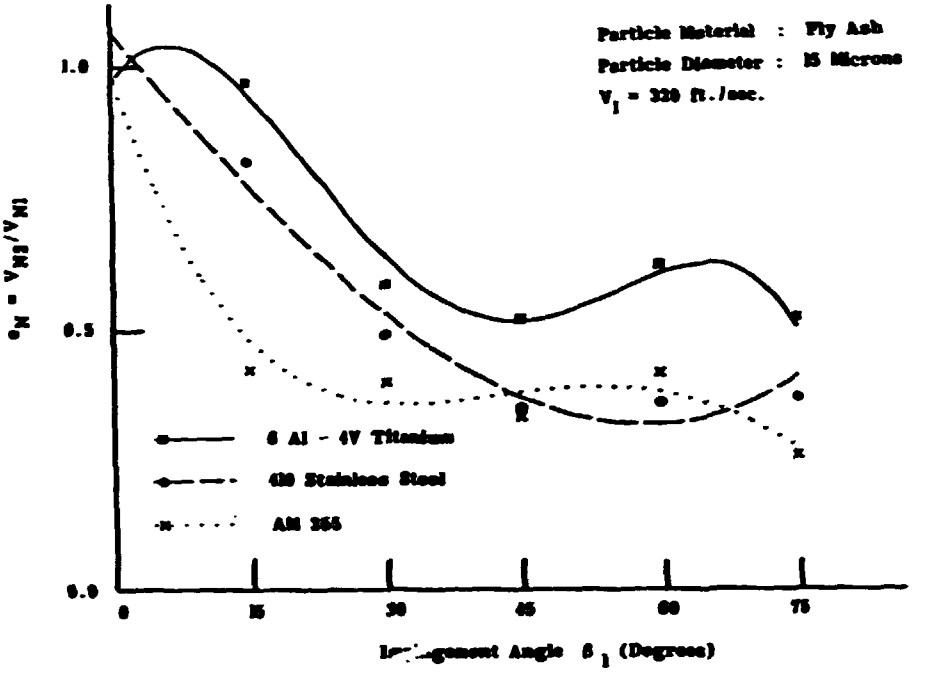

Fig. 15. Comparison of the Normal Velocity Restitution Ratios for Different Target Materials.

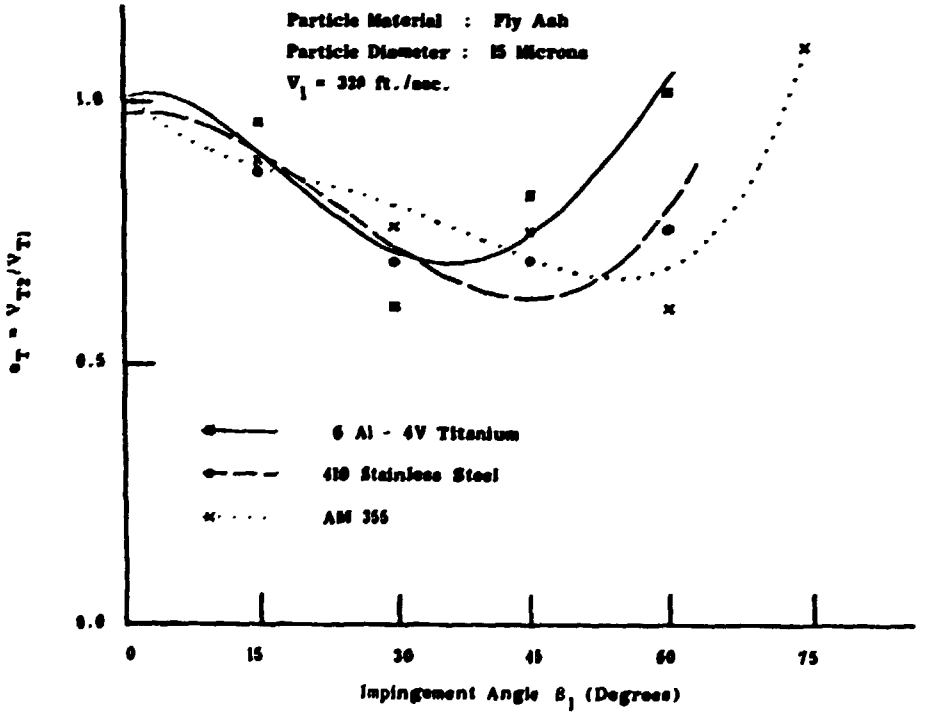

Fig. 16. Comparison of the Tangential Velocity Restitution Ratios for Different Target Materials.

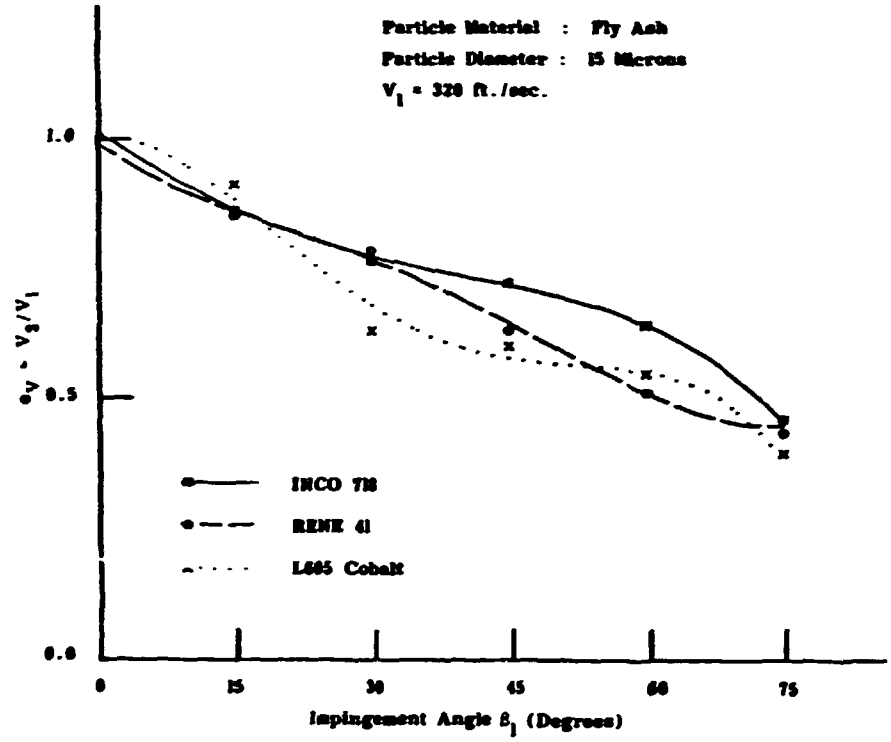

Fig. 17. Comparison of the Velocity Restitution Ratios for Different Target Materials.

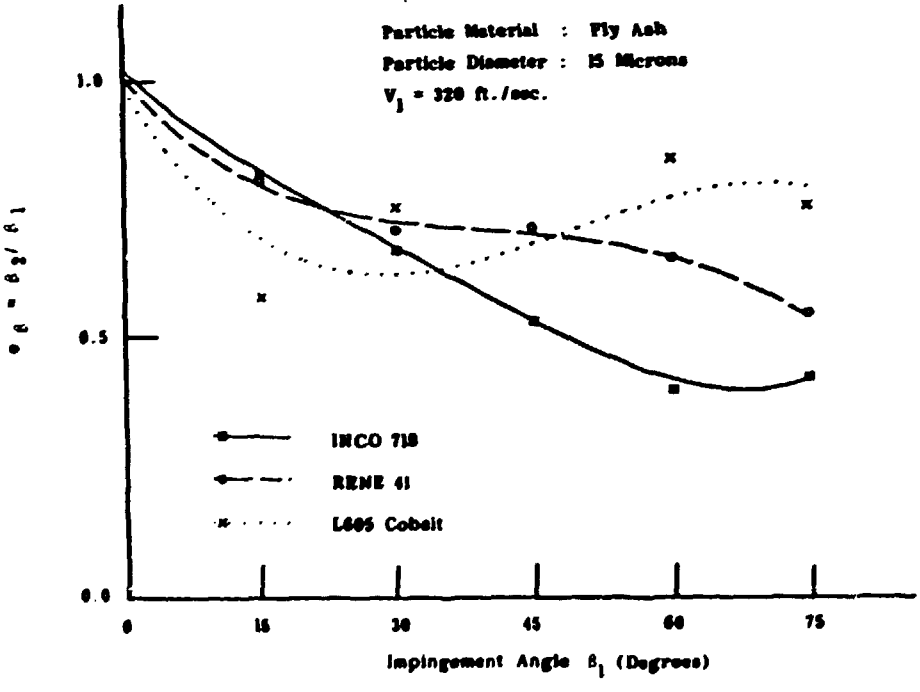

Fig. 18. Comparison of the Directional Coefficients for Different Target Materials.

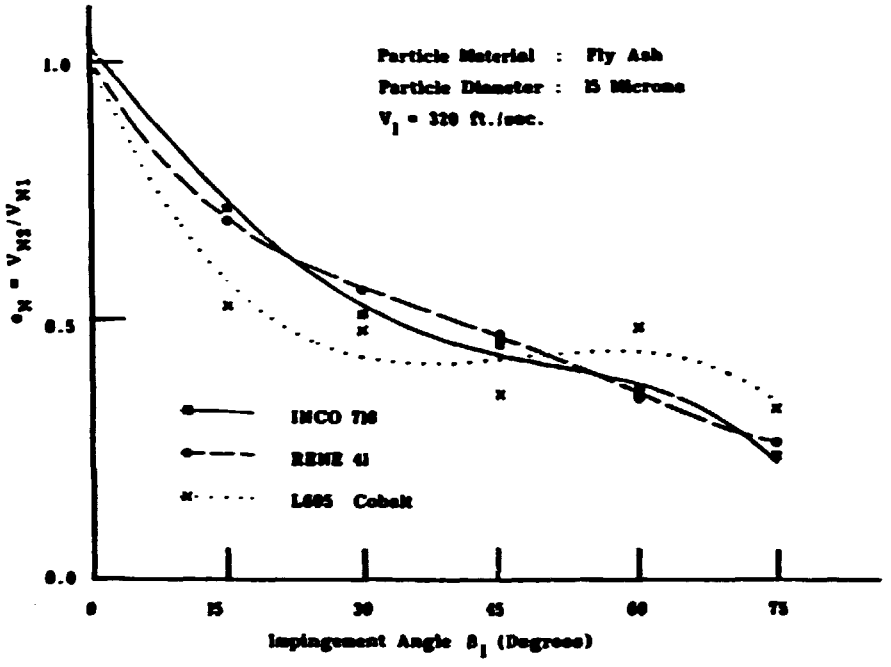

Fig. 19. Comparison of the Normal Velocity Restitution Ratios for Different Target Materials.

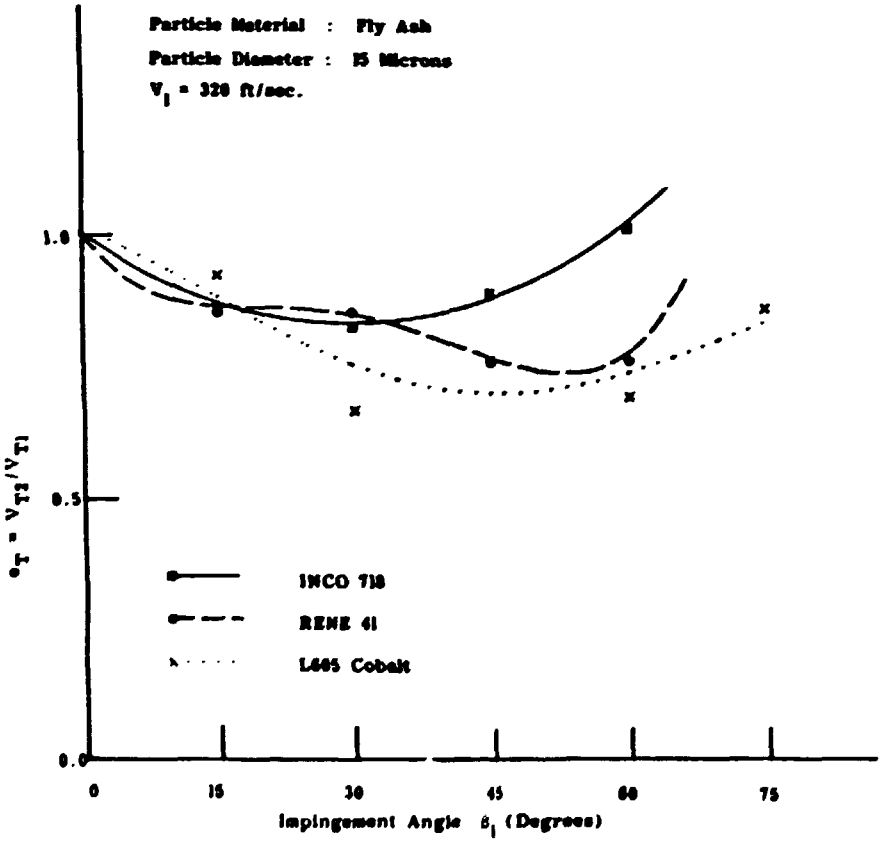

Fig. 20. Comparison of the Tangential Velocity Restitution Ratios for Different Target Materials.

Prediction of Erosion for Different Materials

The following equations were developed by Grant and Tabakoff to predict the erosion of ductile alloys:

$$\varepsilon = K_1 f(\beta_1) V_1^2 \cos^2\beta_1 [1 - R_T^2] + f(V_{IN})$$

$$R_T = 1 - 0.0016 V_1 \sin\beta_1$$

$$f(\beta_1) = [1 + CK \{K_{12} \sin(\frac{90}{\beta_o}) \beta_1\}]^2$$

$$F(V_{IN}) = K_3 (V_1 \sin\beta_1)^4$$

where ε = erosion per unit mass of impacting particles,

β_1 = relative angle between particle path and specimen surface,

β_o = angle of maximum erosion,

V_1 = particle velocity,

R_T = tangential restitution ratio,

$CK = 1$ for $\beta_1 \leq 3\beta_o$

$CK = 0$ for $\beta_1 > 3\beta_o$

The above equation was developed assuming that the erosion process is characterized by two mechanisms at low and high impingement angles. The above equations include the relationship for erosion damage at low angles of impingement, at high angles of impingement and a combination of the two at intermediate approach angles.

The experimental data for ash impacting the aluminum, titanium and stainless steel alloys were substituted into the above equation and from the corresponding results it was possible to determine the empirical constants, K_1, K_{12} and K_3. This was accomplished numerically to obtain a least squares fit to a nonlinear function. The empirical constants for

the different materials erosion by coal ash particles were found to be as follows: (a) For aluminum, $K_1 = 1.56988 \times 10^{-6}$, $K_{12} = 0.3193$ and $K_3 = 2.0 \times 10^{-12}$; (b) For titanium, $K_1 = 1.564951 \times 10^{-6}$, $K_{12} = 0.173636$ and $K_3 = 3.0 \times 10^{-12}$; (c) For stainless steel, $K_1 = 1.505101 \times 10^{-6}$, $K_{12} = 0.296077$ and $K_3 = 5.0 \times 10^{-12}$. These constants were used in the empirical equation and the computed erosion rates are compared to the experimental results. The predicted curves are found to fall generally within the experimental points, but the predicted angle of maximum erosion is slightly higher than the experimentally determined value.

The basic information developed and the empirical relations derived, provide the necessary data for the material removed by erosion. However, presently we are developing new erosion equation based on the restitution ratios for high temperature material erosion. In addition, these restitution ratios are very important for the calculation of particle trajectories in turbomachinery or other industrial systems exposed to particulate flows.

Particle Velocity Effect on Rebounding Characteristics

Experiments were performed using AM355 steel alloy target material and fly ash particles at five different impact velocities. The particle impact velocities for this investigation were 75, 150, 320, 450 and 650 ft/sec. The least squares polynomial curve fits for the mean values of the experimental data restitution parameters are plotted for the five different impact velocities in Figs. 21 and 22. The curves for the different impact velocities exhibit similar trend with respect to the incidence angle. However, the variation of the restitution ratios does not demonstrate specific trend with impact velocities. Further research is needed to have a better understanding of this problem.

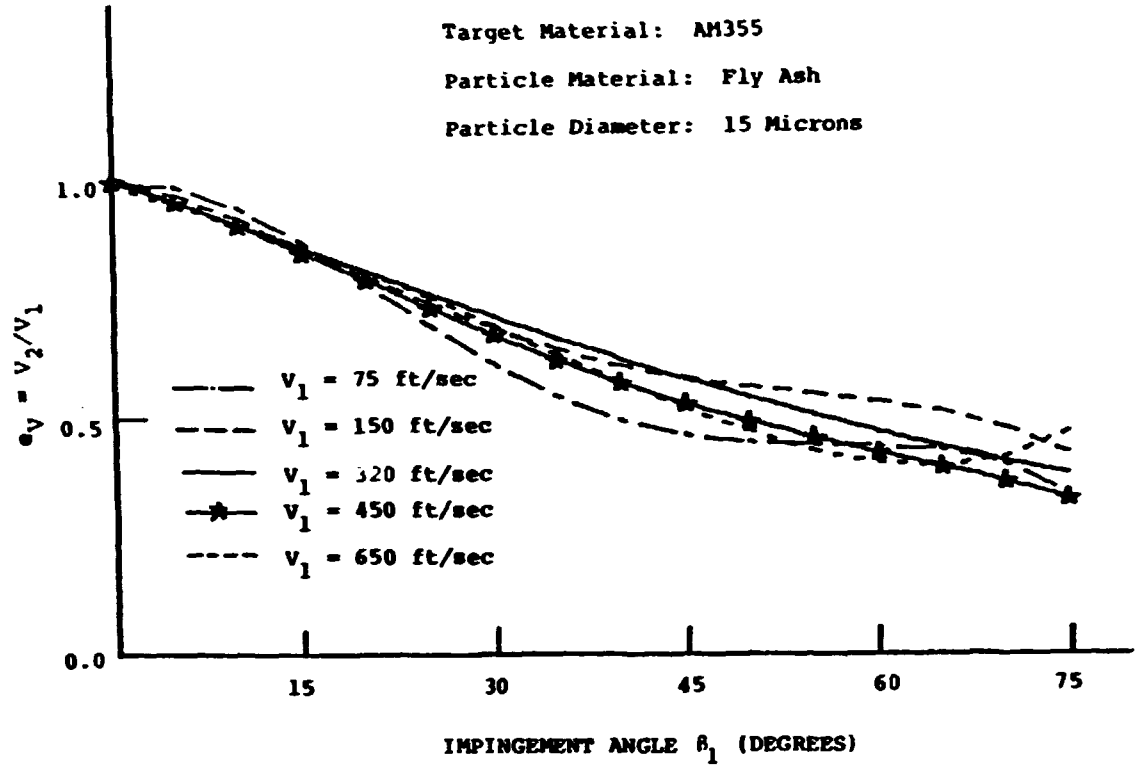

Fig. 21. Influence of β_1 on the Velocity Restitution Coefficient for Different Target Materials.

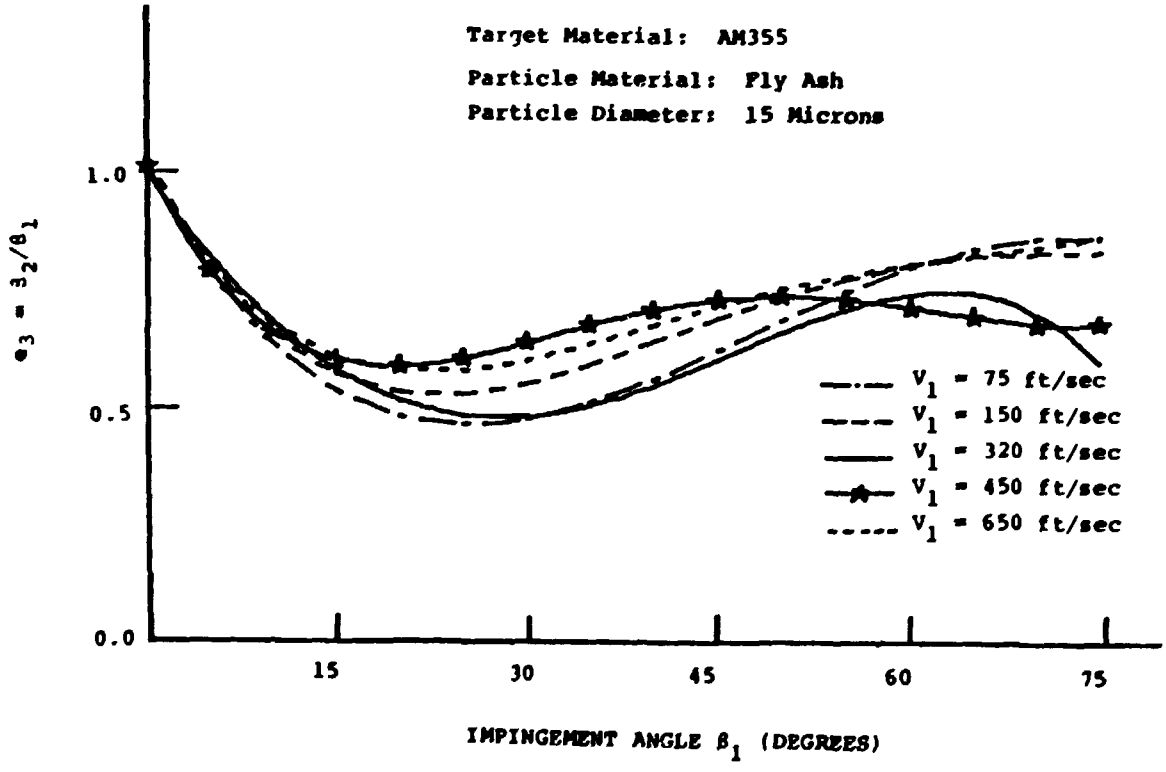

Fig. 22. Influence of β_1 on the Particle Directional Coefficient for Different Particle Impact Velocities.

Effect of Impact Velocity on Erosion at Elevated Temperatures

Some of the experimental results which were obtained for the erosion rate of steel alloy (AM355) at 538°C are shown in Fig. 23 for fly ash. This figure shows plots of the erosion volume parameter versus the impingement angle for different particle velocities. One can observe an increasing trend in the erosion rate with impact velocity. The increase in the erosion rate is much larger at the maximum erosive impingement angle (around 30°) than at all the other impingement angles.

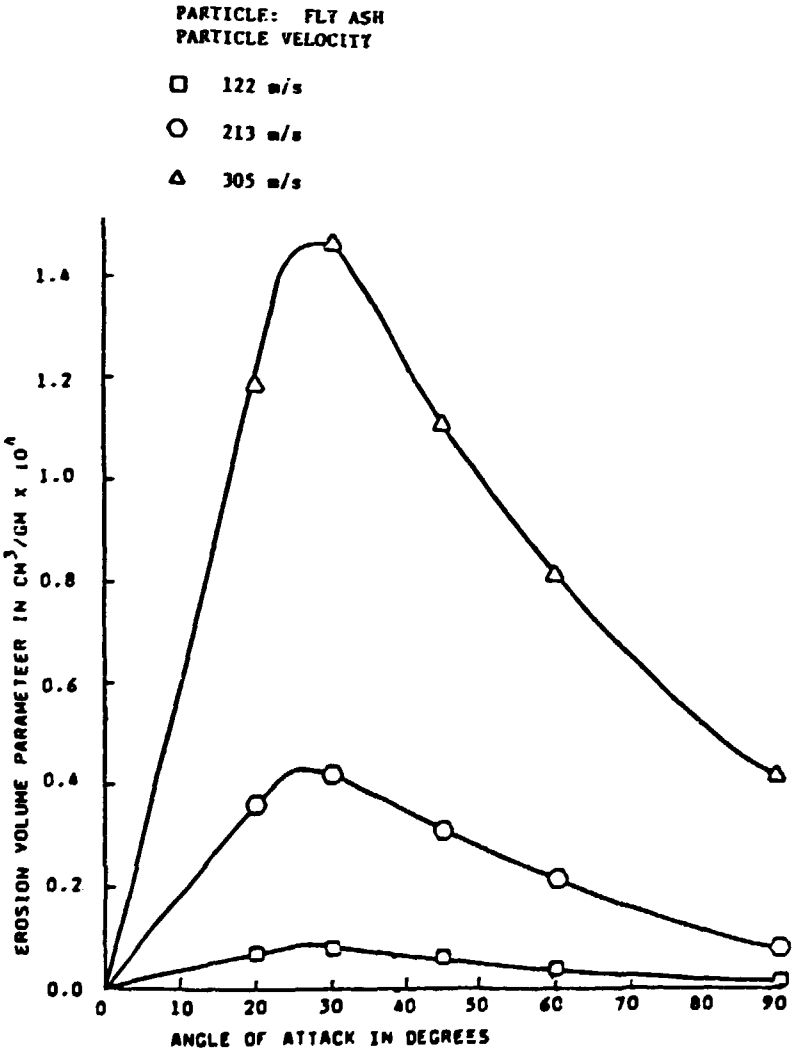

Fig. 23. Effect of Particle Velocity and Impingement Angle on AM355 Alloy at 538°C.

Effect of Particle Size on Erosion at Elevated Temperatures

Some of the experimental erosion results for AM355 alloy impacted by larger silica sand particles at nine different impingement angles are shown in Fig. 24. One can see from this Figure, and also from comparing the same particle velocity, the erosion rate is higher for larger size particles. The same trend was observed in other erosion experiments for particles up to 2,000 microns. An examination of Figs. 23 and 24 reveals that the erosion rate shows a typical trend of ductile behavior with the impingement angle. The erosion rate increases to a maximum at about 25° and then decreases to a residual value at the normal impact. This behavior was always observed in the case of the steel alloy, independent of the particle velocity, the temperature, or the type of impinging particles.

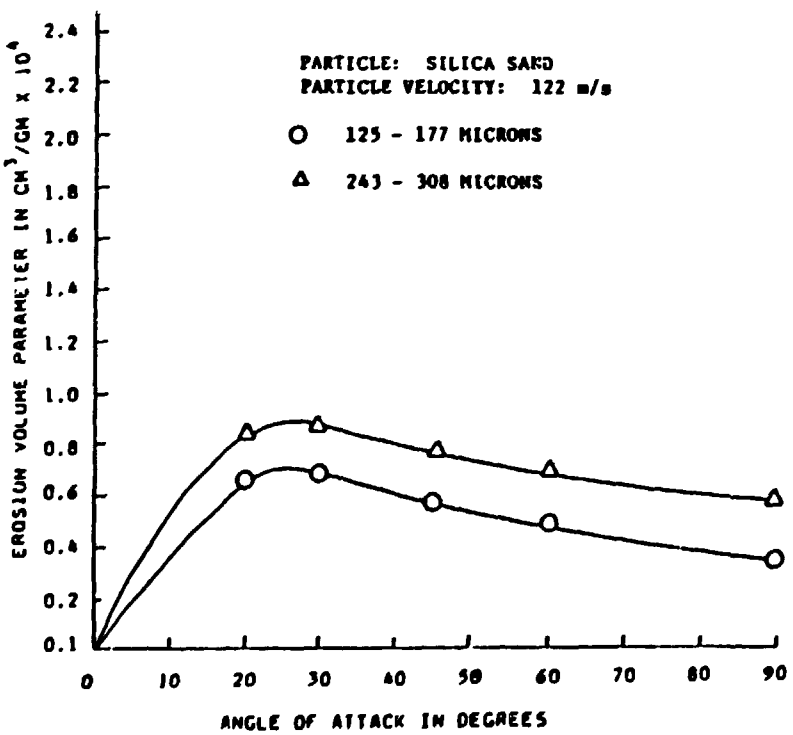

Fig. 24. Effect of Particle Size and Impingement Angle on AM355 at 538°C.

Scanning Electron Microscopy Studies of Abrasive Particles and Eroded Surfaces

One of the objectives of the present study was to observe the abrasive particles, as well as the topography of the eroded specimen. The observations were made using a scanning electron microscope (25 kw Cambridge Stereoscan 600) equipped with an energy dispersive X-ray analyzer (EDAX). Figures 25 and 26 show the scanning electron micrographs of two samples of fly ash, and silica sand particles used in the present study. It is seen from Fig. 25 that the fly ash is composed of discrete, spherical particles. The observations under the microscope revealed that the majority of the particles are smaller than 30 microns. The scanning electron micrograph of the silica abrasive are shown in Fig. 26. The silica particles characteristics were found to be very different depending on the particle sizes. The micrograph of the 150 microns silica particles shows that their corners are not very sharp for this particle size, however, larger particles were found to have sharp corners.

Fig. 25. Scanning Electron Micrograph for Fly Ash Particles (Magnified 500X).

Fig. 26. Scanning Electron Micrograph for 150 Microns Silica Sand Particles (Magnified 500X).

Figures 27 through 29 show the eroded surfaces of three steel alloy (AM355) specimens impacted by fly ash particles at 30° angle of attack. The test temperatures were 20°C, 316°C and 538°C, and the impacting velocities were equal to 99 m/s and 305 m/s. The general appearance of the eroded surfaces is that of intensive surface material flow and plastic deformation. Scanning electron micrograph of steel alloy (AM355) impacted at 30° impingement angle by 150 microns silica sand at 99 m/s and 538°C temperature is shown in Fig. 30. Inspection of this figure demonstrates the increase in the surface erosion damage with increased particle sizes when the rest of the test conditions are unchanged. The last figure shows that the maximum surface damage is produced by the largest particles.

CONCLUSIONS

The dynamic impact characteristics of erosive fly ash particles impacting INCO 718, Rene 41, L605 cobalt, 6A1-4V Titanium, 410 stainless steel and AM355 materials with resulting rebound have been experimentally investigated. The results of this investigation have led to the following conclusions:

1. The kinetic energy lost by the particle can be expressed in terms of restitution coefficients. In theory, this parameter should then be proportional to the resulting erosion.
2. The restitution ratio decreases as the particle impact velocity increases.
3. Directional coefficients (β_2/β_1) and restitution ratios for different alloys are different.
4. Particle restitution coefficients for particle sizes below 40 microns can be measured only with LDV system.
5. The effect of temperature on the erosion rate was found to be dependent on the target material. The steel alloy exhibited an increasing erosion rate with increasing temperature.
6. Scanning Electron Micrographs proved that the volume loss of steel alloy (AM355) is large and proportional to the sizes of the impacting particles.

Fig. 27. Scanning Micrograph of Eroded Surface by Fly Ash at T=20°C, α =30° and V=99 m/s (Magnified 500X).

Fig. 28. Scanning Micrograph of Eroded Surface by Fly Ash at T=316°C, α =30° and V=305 m/s (Magnified 500X).

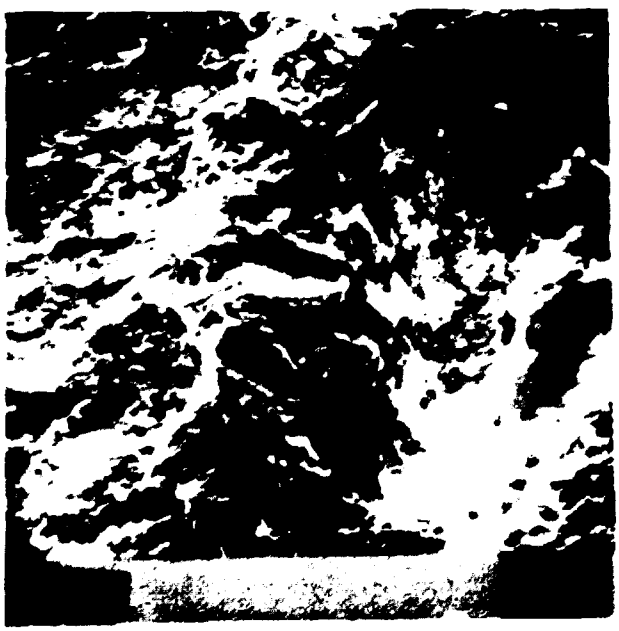

Fig. 29. Scanning Micrograph of Eroded Surface by Fly Ash at T=538°C, α =30° and V=305 m/s (Magnified 500X).

Fig. 30. Scanning Micrograph of Eroded Surface by 150 Microns Silica Sand at T=538°C, α =30° and V=122 m/s (Magnified 500X).

REFERENCES

1. Tabakoff, W., "Review - Turbomachinery Performance Deterioration Exposed to Solid Particulates Environment," Journal of Fluids Engineering, Vol. 106, June 1984, pp. 125-134.
3. Tabakoff, W. and Wakeman, T., "Test Facility for Material Erosion at High Temperature," Erosion-Prevention and Useful Applications, ASTM Special Publication 664, 1979, pp. 123-135.
3. Grant, G. and Tabakoff, W., "Erosion Prediction in Turbomachinery Resulting from Environmental Solid Particles," Journal of Aircraft, Vol. 12, No. 5, 1975, pp. 471-478.
4. Tabakoff, W., Hamed, A. and Eroglu, H., "Study of Particle Rebound Characteristics and Material Erosion at Hign Temperature," Oak Ridge National Laboratory Report ORNL/Sub/84-89628/01, February 1987.

A STUDY OF EROSIVE PARTICLE REBOUND PARAMETERS

T.H. Kosel and T.S. Sairam

Department of Materials Science and Engineering
University of Notre Dame
Notre Dame, IN 46556

ABSTRACT

This paper describes a research project designed to provide a systematic investigation of the effects of materials properties and experimental variables on the rebound directions and velocities of erodent particles. The primary purpose of the project is to develop the capability to accurately predict rebound parameters. The general approach is to develop computer models for the impact of spherical and angular particles, and to compare the predictions with experimental measurements of both single and multiple impact rebound parameters. Initial results are discussed for computer modeling of the impact of spherical particles.

INTRODUCTION

The project discussed herein will meet several needs. First, as has been studied in detail by Tabakoff and coworkers over a period of several years, the rebound problem is an essential component of the calculations required to predict the velocities and directions of the paths of erodent particles as they pass through multi-stage rotating turbines. Tabakoff's group has developed computer techniques[1,2] which allow the calculation of the effect of the complex gas streams within turbines on the paths of erodent particles, and the resultant effect on the distribution of erosive impact damage within the turbine. However, the computer models require experimental data regarding the distribution of rebound directions and velocities when the particles are deflected by surfaces such as turbine blades within the turbine. A model which could correctly predict rebound velocities and directions would preclude the need for the

the many rebound experiments necessary to provide the input to the particle flow models, but most existing models of erosive particle impact have concentrated more on the prediction of the volume of the impact crater than on the rebound problem.

The rebound problem is also of interest from the point of view of predicting erosion rates, since the energy lost during rebound is related to the erosion rate of a material. Erosion is recognized as a significant problem in many energy-production technologies.

Finally, the rebound problem is directly related to the measurement of dynamic hardness or flow stress under the high-strain, high strain-rate conditions pertinent to nearly all types of wear. Thus, part of the work will involve the measurement of the rebound velocities and crater dimensions for the purpose of determining dynamic hardness values, which will serve as input to the computer model for the rebound problem as well as providing a technique and data for dynamic hardness values for correlation with other wear measurements. Dynamic hardness measurements on the work-hardened eroded surface will be included or at least attempted, as well as the more straightforward measurement of dynamic hardness on metallographically prepared specimens.

The computer models which will be developed will calculate the path of a spherical or an angular erodent particle as it moves through the surface material of a planar specimen. In this respect, the models will be similar to several previously published computer models of the erosion impact problem. However, they will also extend the analysis to take into account and evaluate the importance of several effects neglected in previous models. In addition, they will be used to concentrate primarily on the rebound problem, which has not received primary attention in most previous models. The new effects to be evaluated will include the effect of elastic stored energy in the material, the effect of the rotational energy gained by the particle during impact, and the effect of the kinetic energy of the plastically displaced material. All of these effects change the kinetic energy of the particle and affect the direction and velocity of its path through the material, and have been ignored in previous models. The primary goal of most previous models was to calculate the crater volume, since this is assumed to be related to erosion rate. While it

may be that the effects mentioned above will not significantly affect the calculated crater volume, they may significantly affect the calculated rebound direction and velocity. This is particularly true for the effect of elastic stored energy on rebound velocity for angles of incidence near 90^{o}.

The project will include experiments for the determination of the distribution of rebound directions and velocities for multiple-particle, steady-state erosion with typical angular and spherical erodent particles, and measurement of rebound parameters for single-impact tests with spherical particles on flat surfaces. The latter will allow a more direct comparison with the spherical impact model, in which the surface roughness present in realistic erosion experiments will be neglected.

Since the project is relatively new, having begun December 1, 1986, the design of experimental apparatus is still in progress. Optoelectronic time-of-flight measurements will be used to measure rebound velocities. Since some work on the computer modeling of the impact problem for spherical particles has been completed and submitted for publication[3], the present paper will describe the background leading to this modeling work, and summarize the existing results.

COMPUTER MODELING

A number of studies which have appeared in the recent literature on erosion have dealt with single or multiple impacts of spherical erodent particles[4-8]. Unfortunately, in many of these studies the rebound velocity and direction have been ignored or discussed only briefly. A number of studies[4-7] have employed computer calculations of the trajectory of the incident particle through the surface, primarily in order to predict crater dimensions. These models would generally have yielded information concerning the rebound direction and velocity, since they computed the change in the velocity vector due to the forces acting on the particle during successive short time intervals. However, since the rebound parameters were not of primary interest to the authors, they were discussed either briefly or not at all in most of the published results.

Hutchings, Winter and Field[4] experimentally studied the removal of material from solid surfaces by spherical particles, and also numerically solved the equation of motion of the sphere through a planar surface, using two forces exerted on the particle. The first force, due to the flow pressure of the material, was assumed to be normal to the instantaneous area of contact, while the second force was tangential to the contact area and related to the first by a friction coefficient. The validity f the assumption of a constant flow stress during indentation has been discussed in some detail by Tabor in his book on hardness[9], and is reasonably valid for larger indentations. The neglect of work hardening would be especially well justified for steady-state eroded surfaces, by virtue of the very high degree of surface deformation they have undergone. The flow stress should be a dynamic flow stress relevant to the high strain rates and possible temperature rises inherent in the impact process, and will be higher than that measured by conventional hardness test by a factor of about 1.3[9] to 2[5]. The use of a friction coefficient for the tangential force on the particle will be discussed later.

Rickerby and Macmillan[5,6] later developed a computer model which was based on the same concepts as employed by Hutchings et al.[4]. The essential difference between the two models was that the Rickerby and Macmillan model employed a more accurate method for calculation of the area of contact between the sphere and the material, as described later. The agreement between the model and the experiments was quite good for the dependence of crater volume on both velocity and angle of incidence. It is to be noted that Rickerby and Macmillan's model was much more successful in fitting the crater volume vs angle of incidence data than that of Hutchings et al.[4], as was pointed out in a preliminary publication of the model by Rickerby and Macmillan[6]. Some discrepancy existed between Rickerby and Macmillan's[5] calculated and measured cross-sections of impact craters at 30 degrees, in that the model ignored the displacement of material above the original flat surface and that the rebound slopes of the measured craters were steeper than those predicted. No data regarding energy loss or angle of rebound calculations or measurements were discussed by Rickerby and Macmillan[5].

Hutchings, Rickerby and Macmillan[7] published an analysis of many of the results of Hutchings' Ph.D. thesis[10] using the modified computer model developed by Rickerby and Macmillan[5,6]. This paper[7] noted that the existing computer models neglect the elastic energy contribution to the rebound energy of the particle. The neglect of this contribution leads to a prediction of zero rebound velocity for 90° incidence, since no energy is returned to the particle after it stops[4,7-9]. They also noted that neglect of elastic energy only appeared to cause an "appreciable discrepancy" between their model and experiments for 90° incidence.

The elastic energy stored in the material and incident particle have been included in previous analytical treatments of the rebound problem at 90° incidence[8,9]. However, existing computer models of the non-normal impact problem have ignored this. For 90° impact, the elastic energy stored in tne target and erodent particle at the instant when the particle stops its forward motion is released to the erodent particle as the target elastically repels it[7-9]. It is worth noting that while the model of Hutchings et al.[4] incorrectly predicted zero rebound velocity for 90° incidence, this discrepancy did not appear significant in most plots of the data due to the small relative rebound velocities predicted by Tabor's model at the high incident velocities (>200 m/s) used. The discrepancy increases as velocity decreases.

Tabor[9] discussed a treatment of the rebound of a spherically tipped indenter striking a flat specimen, and quoted earlier discussions of the subject. His treatment employed Hertzian analysis to calculate the elastic energy released to the impacting particle, and assumed that the material was purely elastic until a critical indentation depth was reached, and that thereafter it was purely plastic in the sense that the force on the indenter was given simply by P times the area of contact. Actually, between the case of initial elastic indentation and that of purely plastic indentation there is an elastic-plastic range, in which only part of the material immediately under the indenter has reached a high enough stress to yield. This occurs for mean contact pressures P between about 1.1 and 2.8 Y, where Y is the uniaxial yield strength.

Levy and Parry[8] presented a more complete model of 90° rebound than that of Tabor[9] by including an analytical treatment of the elastic-plastic range of indentation sizes. This treatment employed different expressions for the mean contact pressure in the elastic, elastic-plastic and plastic indentation ranges, using an expression given by Johnson[11] for the mean pressure in the elastic-plastic indentation range. In Levy and Parry's model, integration of the resulting force on the particle with respect to the indentation depth gave the energy lost, and yielded better agreement with experiment than the treatment of Tabor for the low range of impact velocities which produce indentations in the elastic-plastic range.

DESCRIPTION OF THE SPHERICAL PARTICLE MODEL

The Rickerby and Macmillan model[5] has been extended in the present project to include the elastic stored energy. This has been done by increasing or decreasing the kinetic energy of the sphere during each iteration so as to compensate for the change in elastic stored energy calculated from the change in contact area during the iteration. In addition, the rotational energy of the particle, which was not included in the previous models, is computed and similarly adjusted for. The present model also differs in that it employs a flow stress term rather than a frictional force tangential to the direction of travel. The predictions of the model are compared with the model and data of Hutchings, Rickerby and Macmillan[7].

A more complete description of the mathematical formulation of the model and the differences between it and that of Rickerby and Macmillan[5] is included in the paper which has already been submitted[3]. It is described here, and its results are compared with some experimental results of Hutchings et al.[7].

The basic principle of the model is to compute the changes in position and velocity of the sphere after successive short (0.2 μs) time increments. During each increment, a force P_N equal to the product of the mean flow pressure and the current area of contact is assumed to act normal to the contact area, while a force P_T tangent to the surface of the sphere and normal to the first force is also included. Figure 1 shows a cross-sectional view of the geometry. In the present

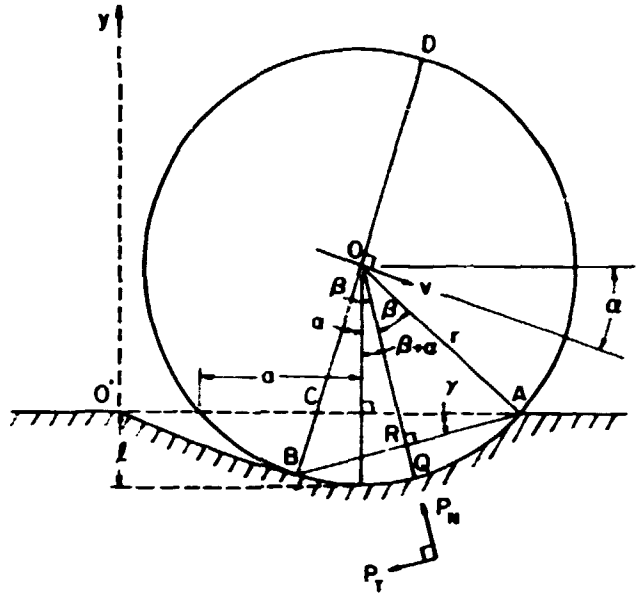

Figure 1. Cross-sectional view of the contact geometry after breakaway; adapted from Rickerby and Macmillan[5].

model, P_T is considered to be due to plastic displacement of the material ahead of the moving particle, and is calculated as the product of P and the area of the spherical sector represented by RQ. In the original Rickerby and Macmillan model[5], the tangential force was taken to be a frictional force μP, which seems less physically justified since this would essentially give the force resisting a sliding rotation of the sphere in a spherical seat.

The model recognizes two regimes of contact. Initially, the entire portion of the sphere which lies below the original surface is in contact, but later (as in Figure 1) it is only in contact along the forward portion. The instant dividing these regimes is termed breakaway, and is defined by the point at which point B first reaches the surface.

The Rickerby and Macmillan model[5] ignored the contribution of the elastic energy stored in the material to the forces on the particle. This leads to a prediction of zero rebound velocity for 90^o incidence, since the sphere simply decelerates due to the work done against the plastic force until it stops. Once it stops, in a real impact the material elastically repels the particle, resulting in a slight increase of the

radius of curvature in the indentation. Tabor[9] presented an elegant analysis of this problem in his 1951 monograph, assuming that the mean contact pressure P over the surface of the indentation could be taken to be simply 2.8Y, where Y is the yield stress of the material. His analysis was discussed in relation to the Scleroscope hardness test, which employs the rebound height of a spherically tipped indenter to determine hardness. Actually, during a quasi-static hardness indentation, between the range of completely elastic contact at extremely low loads and full plasticity at high loads (P=2.8Y) there is a range of elastic-plastic contact during which part of the material under the indenter flows plastically and the rest behaves elastically. This has been discussed at length by Levy and Parry[8], who developed an analytical treatment of the 90° impact of spheres on metal surfaces in a range of velocities ranging from extremely low velocities producing only elastic contact to velocities high enough to reach full plasticity under the indenter. In the present work, it is not necessary to include this sophisticated analysis, since at the velocities in erosion problems of practical interest most metals would reach full plasticity.

In the present model, the elastic energy is taken into account for any angle of incidence, by calculating the change in the area of contact and applying Tabor's analysis[9] to find the change in elastic energy stored in the material. At the end of a time increment in which only the plastic forces P_N and P_T were taken into account, the velocity vector length is increased by an amount which increases the kinetic energy of the particle by an amount equal to the change in stored elastic energy in the material. The direction of the change of the velocity vector due to elastic energy is taken to be normal to the original flat surface.

In addition to the inclusion of the elastic energy, the model includes the change in rotational energy of the particle due to action of P_T during each iteration. This energy is subtracted from the kinetic energy of the particle, along the direction of the existing velocity vector as determined by the plastic forces.

The predictions of the model are compared here with those of the Rickerby and Macmillan model[5] and with the data of the Ph.D. thesis of I. Hutchings as presented by Hutchings, Rickerby and Macmillan[7]. The data

concern the impact of 9.5 mm hardened steel spheres on mild steel. The mean flow pressure of 3.00 GPa used for the steel by Hutchings et al.[4] is also employed here, and is higher than the static hardness due to the fact that it is a dynamic hardness representing high strain rates (and associated temperature effects).

RESULTS OF THE SPHERICAL PARTICLE MODEL

The effect of the inclusion of the increase in rotational energy of the sphere due to the tangential force is very small in all cases. For instance, at 100m/s the final velocity is decreased by only 0.02% by including rotational energy for 30° incidence, and by only 0.04% for 70° incidence. This is qualitatively consistent with the low rotational rates observed for marked spheres by high-speed photography by Hutchings, Winter and Field[4]. The effect was included in the present model as a consistency check, since it is easily shown that if the tangential force were to cause sufficient angular acceleration so that the sphere reached an angular velocity such that it was rolling, the rotational energy would be exactly 40% of the translational kinetic energy. The small effect of rotational energy in the computer model is a reflection of the fact that the surface of the sphere is actually sliding through the impact crater, assuming no initial rotation. The present work thus justifies the exclusion of rotational energy from the work of Hutchings et al.[4] and later workers[5-7], and shows that rebound parameters are affected only slightly.

Under most conditions, the effect of using the flow stress approach of the present model in place of the coefficient of friction approach of Rickerby and Macmillan[5] for the tangential force on the sphere also results in only small changes in predictions. To test this, the model was run using each of these methods separately, with the rotational and elastic energy subroutines turned off. The predicted rebound velocity for 30° incidence is slightly higher for the flow stress approach, by 1% at 100 m/s and 0.3% at 200 m/s. For 70° incidence, the rebound velocity is lower for the flow stress approach by 13% at 100 m/s and by 33% at 200 m/s. The increased magnitude of the effect at high angles and velocities is probably due to the greater depth of penetration, which would

increase the ratio of tangential to normal force for the flow stress approach. The angles of rebound were affected by a maximum of about one degree by the choice of tangential force approach.

The effect of the length of the time interval used was small. Decreasing the interval from the value of 2×10^{-7}s used for the data presented herein to 2×10^{-8}s changed the predicted rebound velocities by at most 1% and the rebound angles by at most 1.5°.

Effect of Elastic Energy

For 90° incidence, it was verified that the discrete interval method of calculation of the elastic energy in the present model predicts the same final rebound velocity as the Tabor model.

The results of the model for the dependence of rebound velocity on incident velocity are summarized in Figure 2, which shows the results of the present model as solid lines, those of the model of the Rickerby and Macmillan model[5] as dashed lines, and the experimental data of Hutchings[7,10]. Both models provide a good fit to the experimental data for angles of incidence up to about 45°. For all angles of incidence, the present model predicts consistently higher rebound velocities, and this effect becomes more significant with increasing angle of incidence. At 75° incidence, the discrepancy is nearly a factor of two. It is natural that the present model should predict a higher rebound velocity than the Rickerby and Macmillan model[5], since the present model includes the elastic energy. For 90° incidence, the neglect of elastic energy causes the older model to predict a zero rebound velocity, while the present model predicts the same value as that obtained from the analytical Tabor model, because it returns the stored elastic energy to the sphere once the velocity reaches zero.

Figure 3 shows a comparison of the model predictions for 75° and 90° incidence, together with the 90° data of Hutchings et al.[7]. The predictions of the model are consistently higher than the experimental data, by a ratio which increases with increasing velocity, since the data show an approximately constant rebound velocity above an incident velocity of about 100 m/s. It can be shown that the discrepancy between the present computer model (which gives the same results as Tabor's

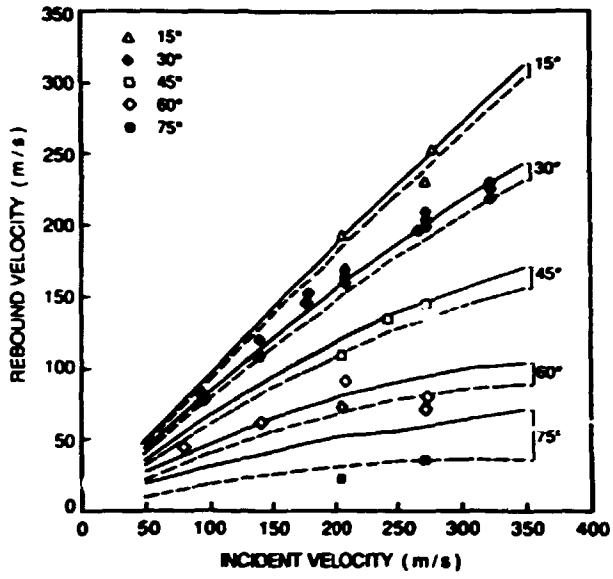

Figure 2. Effect of incident velocity on rebound velocity for angles of incidence up to 75°.

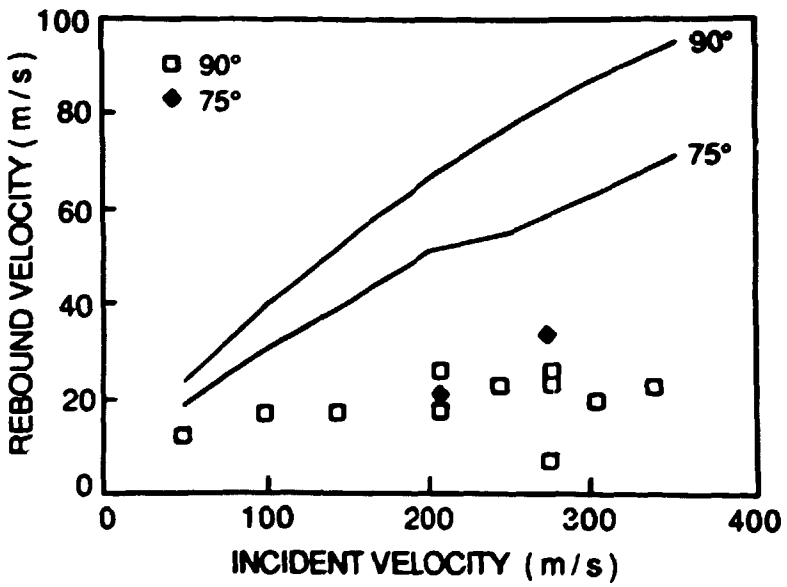

Figure 3. Effect of incident velocity on rebound velocity for 75° and 90° incidence.

analytical model[9]) and the data can be accounted for by taking into account the energy lost to elastic waves in the solid. A method for calculating this energy has been described by Hutchings for the case of 90° incidence[12]. In the actual restitution coefficient (rebound divided by incident velocity) is known, the amount of energy which was dissipated in elastic waves can be calculated. For the 270 m/s data of Hutchings (Figure 3) the restitution coefficient is approximately e = 0.10, which according to Hutchings' model for elastic wave energy[12] would mean that about 9% of the initial energy was lost in elastic waves. Since the fraction of energy lost is easily shown to be $(1-e^2) = 0.99$, in the absence of elastic waves the fraction lost would have been only 0.90, and the restitution coefficient would have been about 0.33. This is quite close to the value of 0.30 predicted by the present model. Since the energy lost to elastic waves decreases with decreasing incident velocity, the model approaches the data more closely as velocity decreases. While it would be possible to take the elastic wave energy into account in the present model for 90° impact, this has not been done since it would not be consistent with the fact that the effect is ignored for non-normal incidence. Development of a model to take elastic waves into account for non-normal incidence would be desirable.

The 75° model predictions are included in Figure 3 because the rebound velocity predicted at 90° is higher than that at 75° by about one third. This is because for 75° the breakaway condition is satisfied, whereas it is not for 90°, and elastic energy is taken into account somewhat differently. As discussed more completely in another paper[3], this is believed to be due to the effect of the neglect of the material ploughed up in front of the sphere on the area of contact.

Rebound Angles

As can be seen from Figure 4, the present model (solid lines) and that of Rickerby and Macmillan[5,7] predict very similar variations of rebound angle on incident velocity for low angles of incidence (up to 45°). At higher angles however, the present model predicts a significantly less rapid rise of rebound angle with velocity, especially at low incident velocities, where a slight decrease is actually predicted.

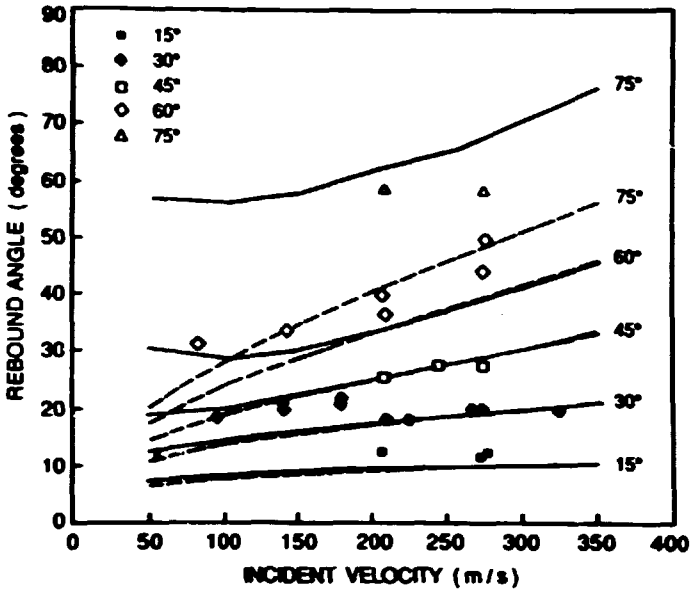

Figure 4. Dependence of rebound angle on incident velocity.

The smaller dependence of rebound on incident angle appears to be more consistent with the data, especially for 60°. Unfortunately, there is insufficient data at 45° and 75° to make a conclusive comparison between the correctness of the models.

Figure 5 compares the predicted dependence of rebound angle on angle of incidence, along with the data of Hutchings et al.[4]. The rebound angle is comparable to but lower than the angle of incidence for angles less than 90°.

Coefficient of Restitution

Figure 6 shows a plot of the model predictions for the coefficient of restitution, defined as the ratio of total final to initial velocity, as a function of incident velocity. Also included are the data of Hutchings et al.[4]; the data and model predictions are both the same as was previously seen in Figure 2, but it is now clear that for the range of velocities from 50 to 350 m/s, the predicted coefficient of restitution is a nearly linear function of incident velocity for angles of incidence up to 60°. This contrasts with the nonlinear behavior seen for 75° and 90° incidence in Figure 7; the 90° behavior is similar to that previously

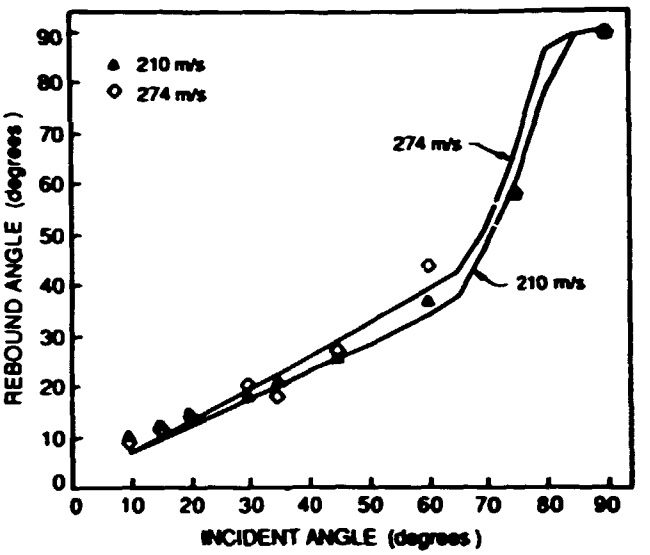

Figure 5. Dependence of rebound angle on angle of incidence.

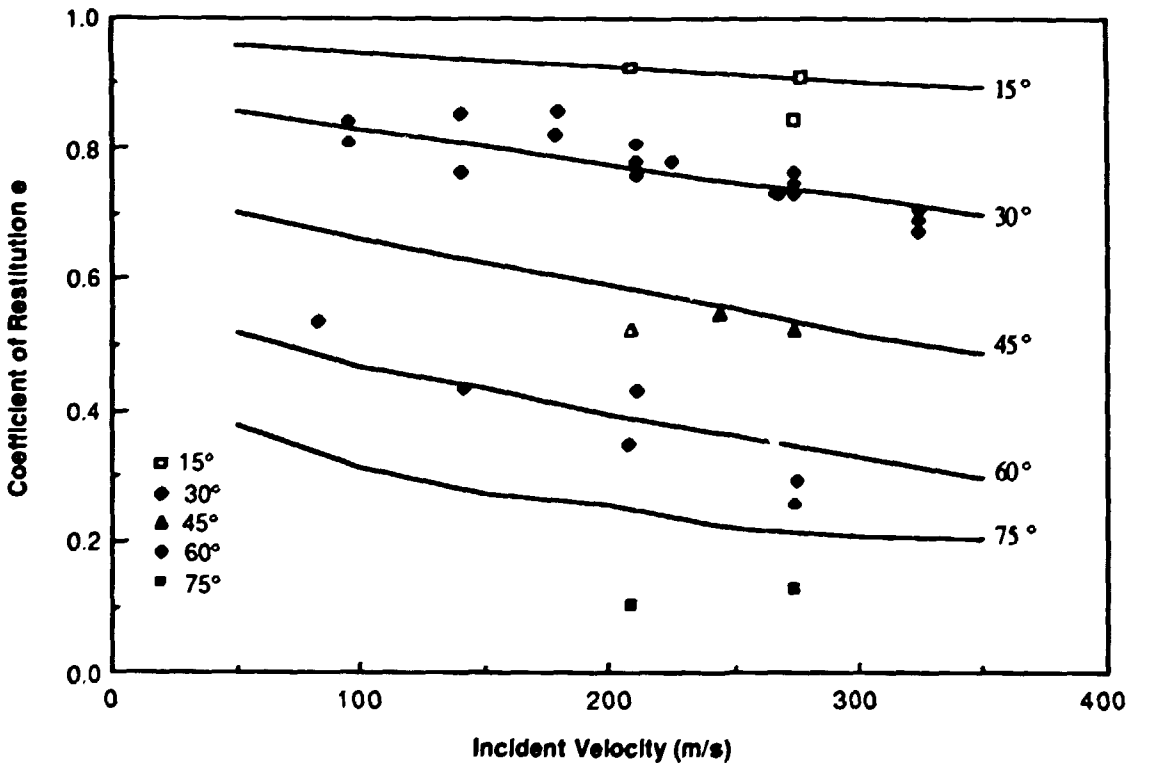

Figure 6. Coefficient of restitution as a function of incident velocity for angles of incidence up to 75°.

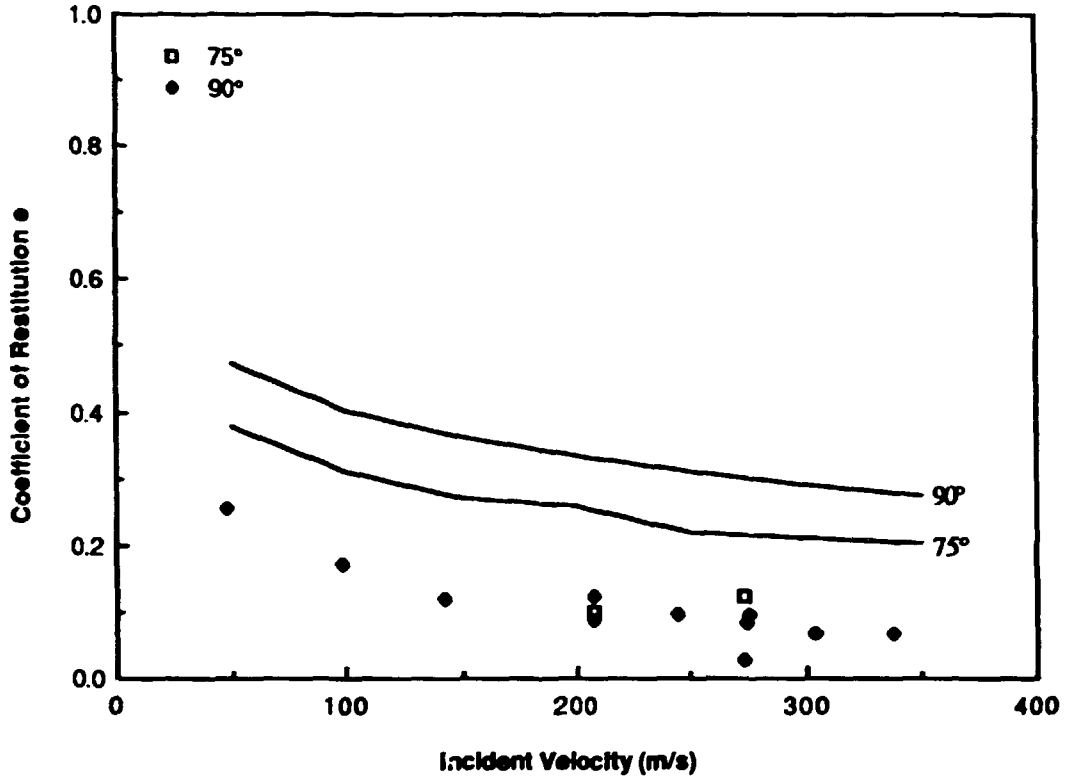

Figure 7. Coefficient of restitution as a function of incident velocity for 75^{o} and 90^{o} incidence.

predicted by Tabor[9] and Levy and Parry[8], and 75^{o} incidence is close enough to 90^{o} to behave similarly. Physically, the dependence of e on velocity is due to the decrease of indentation size with velocity, resulting in smaller energy losses due primarily to the plastic work. The linearity of the predicted value of e for angles below 60^{o} could not in practice extend all the way to zero velocity, since at sufficiently low velocities the indentation would be elastic and the primary energy losses would be due to elastic waves and rotation of the particle. The point at which the curves bend upwards toward 1.0 at low velocity would not be predicted accurately by the present model, since it assumes the force on the particle is given by the fully plastic flow pressure P. This is not accurate for very small indentations, which are elastic-plastic as discussed for the case of 90^{o} incidence by Levy and Parry[8] and give a smaller mean indentation pressure. Thus, for very low velocities, the present model would predict a higher restitution coefficient due to its

overestimate of mean indentation pressure and the resulting shallower indentation. The model predictions for velocities lower than 50 m/s can be compared with experiment later in the project. Qualitatively, the model predicts that the curve for 60^{o} turns upwards just below 50 m/s, while those for lower angles turn much closer to zero velocity.

The plot in Figure 8 of the dependence of coefficient of restitution on angle of incidence for a few velocities shows that the general trend of decreasing e with angle observed by Tabakoff[1,2] is also predicted by the present model and observed for single impacts of spherical particles. The rise predicted at 75^{o} is, as mentioned earlier, due to a difference in the method of computation of contact area before and after breakaway and the neglect of displaced material in computing this area. The coefficient of restitution is seen to be more velocity dependent at higher angles of incidence in both Figures 7 and 8.

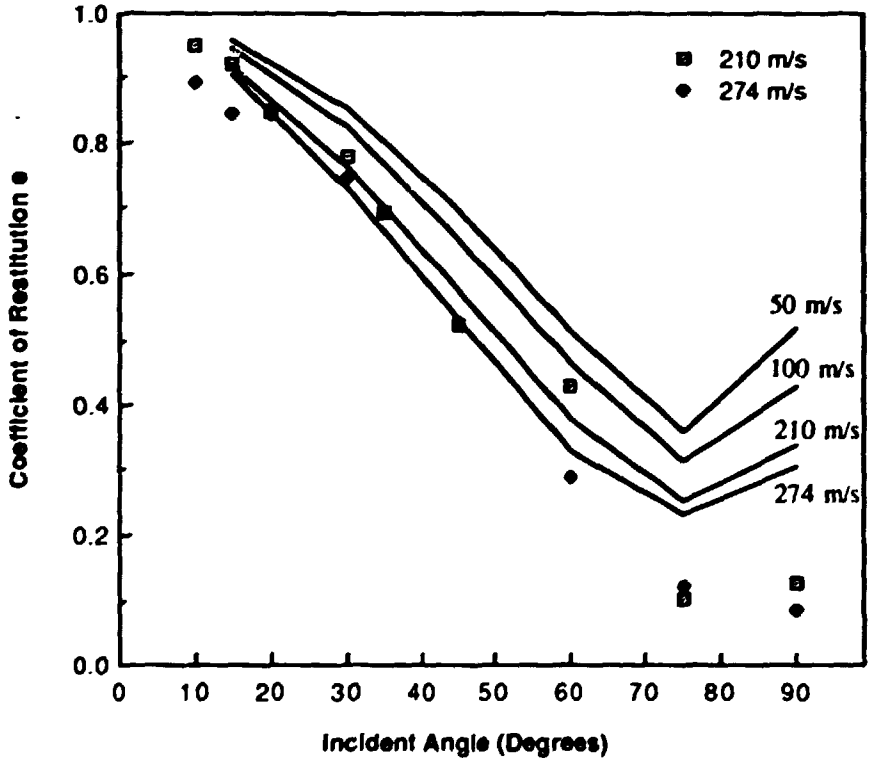

Figure 8. Coefficient of restitution as a function of angle of incidence.

SUMMARY

The spherical-particle model provides a generally suitable prediction of the spherical-particle single impact results. Improvements to the model could include a method for predicting the effect of displaced material on area of contact, correction for the kinetic energy of the displaced material, and possibly inclusion of the effect of elastic wave energy losses. The model must also be tested by further experimental measurements for different materials and impact conditions, and the results of the single-impact spherical particle model should also be compared with modeling and experimental results for angular particles. In addition, the model predictions need to be compared with multiple-impact experiments with spherical particles impinging on surfaces eroded to steady state, and dynamic hardness measurements need to be used tc obtain appropiate input data for the models.

REFERENCES

1. G. Grant and W. Tabakoff, "Erosion Prediction in Turbomachinery Resulting from Environmental Solid Particles," J. Aircraft, Vol. 12, No. 5, 1975, 471-478.
2. W. Tabakoff, M.F. Malak and A. Hamed, "Laser Measurements of Solid Particles Rebound Parameters Impacting on 2024 Aluminum and 6Al-4V Titanium Alloys." AIAA 18th Fluid Dynamics and Plasmadynamics and Lasers Conference, July 16-18, 1985, Cincinnati, Ohio, paper #AIAA-85-1570.
3. "Computer modeling of the Rebound Characteristics of Spherical Erodent Particles," T.S. Sriram and T.H. Kosel, to be published in the Proceedings of the Seventh International Conference on Erosion by Liquid and Solid Impact, Cambridge, England, September 6-10, 1987.
4. I.M. Hutchings, R.E. Winter and J.E. Field, "Solid Particle Erosion of Metals: The Removal of Surface Material by Spherical Projectiles," Proc. Roy. Soc. London A348 (1976) 379-392.

5. D.G. Rickerby and N.H. Macmillan, "Erosion of Aluminum and Magnesium Oxide by Spherical Particles," Proc. Int'l. Conf. on Wear of Materials - 1981, ASME, San Francisco, CA, March 30-April 1, 1981, pp. 548-563.

6. D.G. Rickerby and N.H. Macmillan, "On the Oblique Impact of a Rigid Sphere Against a Rigid-Plastic Sold," Int. J. Mech. Sci. 22 (1980) 491-494.

7. I.M. Hutchings, D.G. Rickerby and N.H. Macmillan, "Further Studies of the Oblique Impact of a Hard Sphere Against a Ductile Solid," Int. J. Mech. Sci. 23 (1981) 639-646.

8. G. Levy and A.A. Parry, "Studies of Impact Phenomena," Wear 64 (1980) 83-99.

9. D. Tabor, The Hardness of Metals, Clarendon Press, Oxford, 1951.

10. I.M. Hutchings, Ph.D. Thesis, University of Cambridge, 1974.

11. K.L. Johnson, "The Correlation of Indentation Experiments," J. Mech. Phys. Solids 18 (1970) 115-126.

12. I.M. Hutchings, "Energy Absorbed by Elastic Waves During Plastic Impact," J. Phys. D: Apl. Phys. 12 (1979) 1819-1824.

IN-SITU SCANNING ELECTRON MICROSCOPY STUDIES OF THE EROSION OF ALLOYS

James R. Keiser

Metals and Ceramics Division
Oak Ridge National Laboratory
P.O. Box X
Oak Ridge, Tennessee 37831

ABSTRACT

Impacts by erosive particles result in the high strain rate deposition of an appreciable amount of energy into the deformed volume of the target material. This energy can be manifested as local heating; softening or even melting has been observed in many materials. Hardening caused by the high strain rate deformation has also been reported for strain hardenable materials. The effect of individual impacts on the surface of selected materials was determined for 343-μm-diam tungsten carbide balls impacting at about 30 m/s and 30° incidence angle. A mechanical properties microprobe was used to measure the hardness of the crater bottom, and just below the original surface. Strain hardening but no evidence of softening was observed in these materials.

INTRODUCTION

During the last decade, considerable effort has been made to develop improved coal conversion and utilization processes in order to make better and more extensive use of our fossil resources. Materials problems involving erosion, corrosion, or both have been encountered, and a significant amount of research has been directed to determine the cause of the problems and to identify suitable materials. The presence of a nontrivial amount of noncombustible mineral matter in coal can result in serious degradation of metallic components of coal conversion plants.

Figure 1 shows a piece of failed steel pipe from a coal liquefaction plant. This pipe carried a mixture of noncombustible material in a hydrocarbon stream, and the wear of the elbow caused by the impacts of the hard particles eroded a hole in the pipe. Erosion failures of pipe and letdown valves were not infrequent occurrences during early operation of coal liquefaction plants, and considerable effort was directed to identifying materials that were more erosion resistant. In addition, the study of erosion mechanisms also received increased attention.

Fig. 1. Cross section of failed steel pipe from a coal liquefaction plant. The pipe carried coal ash in a heavy organic oil at a temperature above 260°C.

As has been well documented in recent papers on erosion, many studies of erosion mechanisms have been performed during the last 30 years. Researchers have tried to relate a material's erosion resistance to one or several of the material's mechanical or physical properties, and a number of mechanistic theories have been proposed. In fact, as demonstrated by Finnie,[1] for pure, annealed materials a good relationship can be demonstrated between erosion resistance and indentation hardness. However, this relationship breaks down when alloys or work hardened metals are included.[2,3] Despite different properties (including greater hardness) in the aged or worked material, no significant increase in erosion resistance of these materials is observed. There are several theories to explain this lack of change in erosion resistance. One is that the properties that control erosion resistance are not changed by aging or

working. Another possible explanation is that multiple particle impacts change the surface of every material to some steady state condition so that the measured erosion resistance is just an indication of this steady state condition.

Because of the lack of correlation between mechanical properties and erosion resistance, other researchers have tried to relate erosion behavior and metal-metal bond energy,[4] melting point,[5] and elastic modulus.[6] Although erosion behavior can be related to some physical or mechanical property for a carefully defined set of materials, none of these relationships holds for materials in all conditions of heat treatment or mechanical working.

A relationship between erosion behavior and some thermal property has been demonstrated by a number of researchers. Ascarelli[7] related erosion behavior to a thermal pressure, $\alpha \times \kappa \times \Delta T$, where α is the coefficient of linear thermal expansion, κ is the bulk modulus, and ΔT is the difference between ambient temperature and the melting point of the target material. Hutchings[8] proposed using the product $\rho \times c_p \times \Delta T$, where ρ is the density, c_p is the specific heat at constant pressure, and ΔT is as previously defined. Malkin[9] related erosion resistance to the specific melting energy $\rho \times \Delta H/a$, where ΔH is the enthalpy change associated with transforming a solid target material at ambient temperature to liquid at the melting temperature, and a is the atomic number. A dimensional analysis was developed by Jennings et al.[10] in which several material properties that might be expected to influence erosion resistance were incorporated. Under certain test conditions, a correlation between any of these thermal parameters and erosion resistance can be shown. However, as in the case with parameters developed using physical properties, none provides a satisfactory correlation for all metals and alloys under all test conditions.

The association of erosion behavior with thermal properties is at least in part related to the observation that significant heating of the surface can occur as the result of a particle impact. Calculations have shown that if a major portion of the energy of the incident particle is transferred to the target, and if adiabatic behavior is assumed, the temperature can be raised appreciably; even to or above the melting point of

the target.[11,12] Melting of the target material has been reported by a number of researchers,[13-15] and there are many reports of annealing or softening of the surface of the target; most likely as a result of heat introduced by the particle impacts.[16-18] Observations of softening were made through hardness measurements and microstructural studies on samples previously exposed to a stream of erosive particles.

Transmission electron microscopy (TEM) has provided evidence of work hardening below eroded surfaces. Ives and Ruff[19] studied annealed 310 stainless steel that had been impacted by angular Al_2O_3 and spherical glass particles approximately 50 μm in diameter and projected at a velocity of 59 m/s at impact angles of 20 and 90°. High dislocation density zones were found around the impact craters. Selected-area electron channeling patterns were also used to study the plastic strain associated with impact craters in 310 stainless steel and copper. The strains appeared to be localized near the impact crater and decreased with distance from the crater.

Edington and Wright[20] studied Stellite 6B that had been eroded by 15 μm diameter Al_2O_3 at velocities of 19 and 52 m/s (63 and 170 ft/s). They found a rapid build-up of a high dislocation density in the surface layer of the eroded material. They also noted that close examination of the dislocation arrays around individual indentations failed to provide any evidence for local heating during impact.

Scattergood and Kosel[21] used TEM to study the density of dislocations beneath eroded surfaces on nickel. They found the highest density was just below the surface, and the density decreased with distance from the surface. For a surface eroded by 130 μm Al_2O_3 particles at 20° incidence angle, the affected material extended to about 70 μm.

There is considerable evidence indicating that appreciable heat is produced as the result of erosive particle impacts. However, as in the papers just cited, there is also a significant collection of data indicating the heat produced by impacts has no measurable effect on the target material. Clearly, for impacts on ductile metals, appreciable energy must be deposited in the target. The manner in which this energy is manifested

is likely controlled by the impact conditions and the properties of the erosive particle and the target; determination of the controlling factors and their limits is a subject that warrants further study.

Unfortunately, there have been few, if any, studies of the effect of appropriately small, single impacts on the properties of the target. In part this has been due to the difficulties associated with making single impacts with very small particles under well controlled conditions and then measuring the change in target properties in such a small volume of material. The work described in this paper has utilized two unique pieces of equipment at our laboratory to study the response (as measured by hardness changes) of a Hastelloy C-276 sample and three aluminum samples to impacts by erosive particles of approximately the same size as particles in coal conversion and utilization plants.

EXPERIMENTAL SYSTEM

The experimental system is based on an ISI Super IIIA scanning electron microscope* (SEM) specially modified to permit in-situ studies of the erosion, corrosion, and erosion-corrosion characteristics of metallic or ceramic surfaces[22,23]. The major additions to the SEM are a gun, which shoots individual particles at a sample at high velocity, and a hot stage, which heats the specimen and the corrosive gas and directs the gas onto the sample surface. For the studies described in this report, the hot stage and hot gas delivery system were not used.

The erosive particle gas gun, shown in Fig. 2, is built on a flange that mounts directly on the SEM chamber. A pulse of carbon dioxide of controlled pressure and duration projects the ball through the barrel. Particle velocities used in experimental studies are generally in the range of 15 to 45 m/s (50–150 ft/s), but velocities as high as 90 m/s (300 ft/s) have been attained.

---

*International Scientific Instruments, Inc., Milpitas, California.

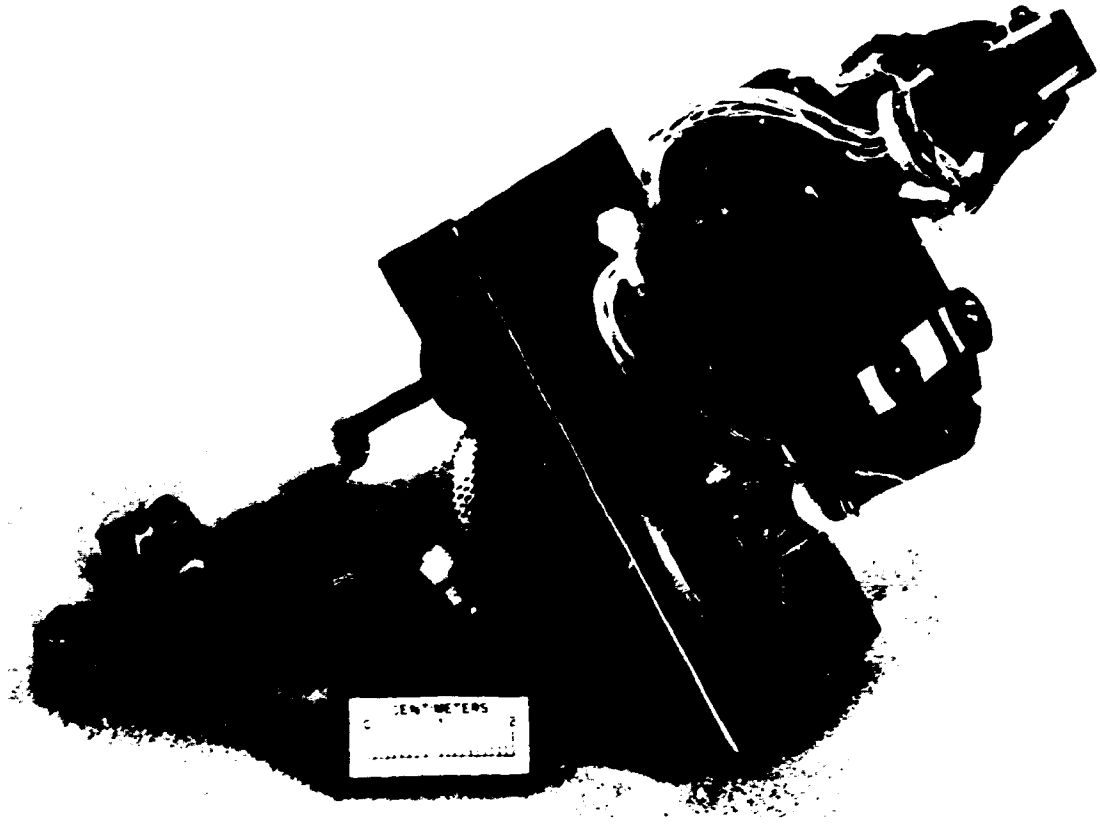

Fig. 2. Miniature air gun used to shoot 0.343-um-diam tungsten carbide balls. The gun is built on a flange that mounts on the side of a SEM.

The tip of the barrel is visible in Fig. 2, which also shows the wiring harness and printed circuit (pc) boards that are mounted on the brass piece that supports the barrel. This wiring harness and the pc boards are components of the velocity measurement system. The barrel for this gun was fabricated from type 316 stainless steel capillary tubing [1.59 mm (0.0625 in.) outside diam, 0.254 mm (0.010 in.) inside diam]. The inside diameter is enlarged by drilling it slightly larger than the ball diameter. The other large pieces of the gun, including the large gear, are made of brass.

The gun is firmly attached to the SEM sample chamber, and the specimen holder and hot stage are tilted to change the angle of impact of the erodent particles on the specimen surface. The impact angle can be varied from 10 to 90° (at 90° the plane of the specimen surface is normal to the flight path of the erodent particles).

As built, this gun shoots standard 0.343-mm-diam (0.0135-in.) tungsten carbide balls, which are purchased from a ball bearing manufacturer. Cobalt-bonded tungsten carbide is used because of its high hardness. The 0.343 mm size was chosen because of the limited availability of smaller sizes, and formidable machining difficulties would be encountered in building a gun for much smaller balls. This size is within the range of particles encountered in most coal conversion and utilization systems.

The velocity of a ball is determined with the commonly used technique of measuring the time it takes the ball to travel between two light beams a known distance apart. The light beams pass through two small holes in the barrel, each 0.25-mm-diam (0.010-in.). This results in a relatively small steady state source of light energy reaching the collector; consequently, the electrical current signal is relatively weak. In addition, a ball traveling 30 m/s totally interrupts the light beam for only about 10 μs; thus, the electrical signal pulse is very short. Fast, high-gain preamplifiers are used to convert the two current pulses into signals that start and stop a 1-MHz clock that is connected to a counter. With this system, the particle's time of flight can be measured with +1-μs accuracy.

The craters produced by the erosive particle impacts are characterized through examination with the SEM and by measurement of the surface profile with a profilometer. Impact crater depths and diameters can be determined from recorder traces of the profilometer scans, and the height and extent of extruded lips can be estimated.

Hardness measurements were made in and around an impact crater with the Nanoindenter mechanical properties microprobe (MPM). This recently developed system is a fully computerized, ultralow load, microindentation hardness tester. The indenter load and displacement are continuously measured as the load is applied and removed, with a resolution of 0.3 μN (30 μg) and 0.16 nm, respectively. Loading was done at a constant displacement rate of 5 nm/s, and hardness was calculated directly from the

load and depth measurement. (Calculated hardness is considered to be only a relative value since the mathematical description for the indenter area does not account for any rounding or blunting of the tip or edges.) A triangular-based diamond indenter similar to a Vickers indenter was used. The hardness measurements at the bottom of the craters were accomplished with a similarly shaped diamond indenter that had been reduced in width to approximately 60 μm. This measuring capability is unique in that the hardness of the surface of these very small craters can be measured as well as the hardness very near the edge of cross-sectioned materials.

EXPERIMENTAL PROCEDURE AND RESULTS

Materials used in this study included Hastelloy C-276, a relatively high melting, ductile, nickel-based alloy, and a series of aluminum alloys that have relatively low melting points and display a wide range of mechanical properties. The aluminum alloys used were annealed 1100, 6061-T6, and 7075-T6. Compositions of these alloys are given in Table 1, and room temperature properties are listed in Table 2. Steady state erosion rates have been previously measured for some of these aluminum alloys, and the results are included in Table 2. The softer, weaker, but higher melting annealed 1100 has a lower erosion rate than 7075-T6.[24,25]

Table 1. Nominal compositions of alloys used in erosion studies

	Hastelloy C-276	1100 Aluminum	6061 Aluminum	7075 Aluminum
Nickel	Balance			
Cobalt	2.0			
Chromium	15.5		0.2	0.23
Molybdenum	15.7			
Tungsten	3.8			
Iron	5.8			
Silicon	0.04		0.6	
Manganese	0.4			
Carbon	0.003			
Aluminum		99.00 min	97.9	90.0
Copper		0.12	0.28	1.6
Magnesium			1.0	2.5
Zinc				5.6

Table 2. Selected properties of alloys used for erosion studies

Material property	Hastelloy C-276 30% cold reduced	Annealed 1100	6061-T6	7075-T6
Hardness 500 kg-10 mm ball	(Rc 35)	23	95	150
Shear strength (MPa)		62	205	330
Yield strength (MPa)	1083	34	275	505
Ductility (%)	15	35	12	11
Solidus temperature (°C)	1323	643	582	477
Relative erosion rate		1.0		1.5

Samples were first polished to a 0.5 μm diamond finish followed by etching for a few seconds in a 10% HF solution to remove most of the work hardened surface created by mechanical polishing. Single, 30° impacts were then made at room temperature with 343-μm-diam tungsten carbide balls. Ball velocity was 30 m/s for the Hastelloy C-276 and was controlled at 28.5 ± 1.0 m/s for the aluminum samples. Hardness measurements were made on the bottom of the impact craters of the Hastelloy C-276 sample and one set of aluminum samples. Another set of aluminum samples was cross-sectioned and polished through the impact crater. The second set was lightly etched as described previously, then the MPM was used to measure the hardness immediately beneath the impact crater. Hardness indentations were made to a depth of 300 nm, and spacing between indentations, in keeping with ASTM recommendations, was generally at least 6 μm center to center.[26] The indentations were limited to 300 nm depth so that measurements could be made fairly close to the unsupported edge without the edge affecting the measurement.

Figure 3 shows two typical impact craters with hardness indentations on the bottom, while Fig. 4 shows cross sections of the impact craters on the aluminum alloys with the array of hardness indentations made around the craters. Although the hardness was determined as a function of depth

Hastelloy C-276

6061-T6

Fig. 3. Photomicrographs of impact craters with a row of hardness indentations along the bottom of the crater. The indentations were made with the Nanoindenter mechanical properties microprobe using a specially modified indenter.

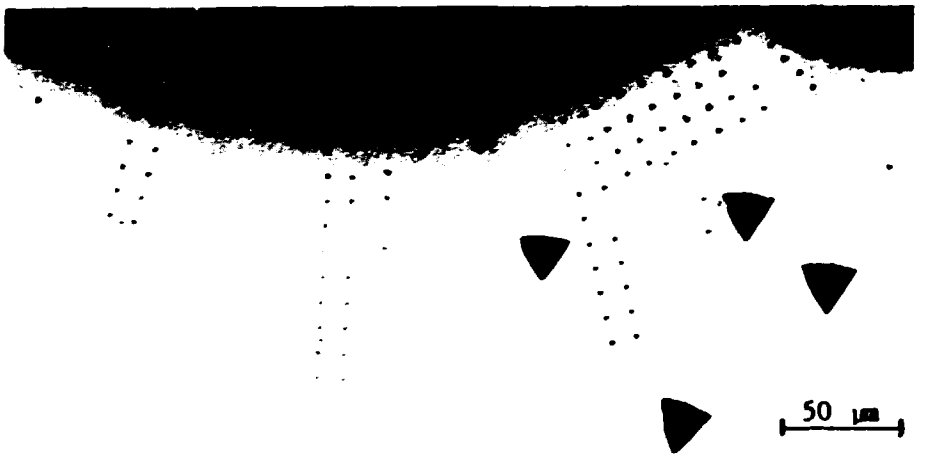

Annealed 1100

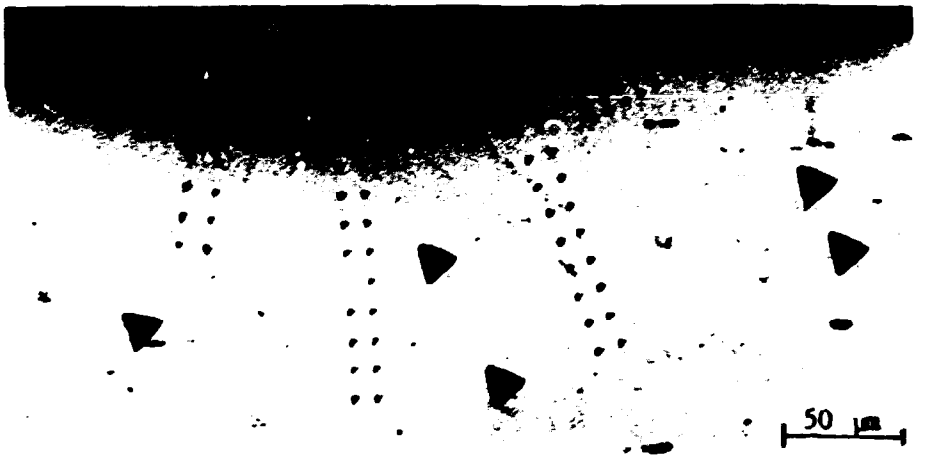

6061-T6

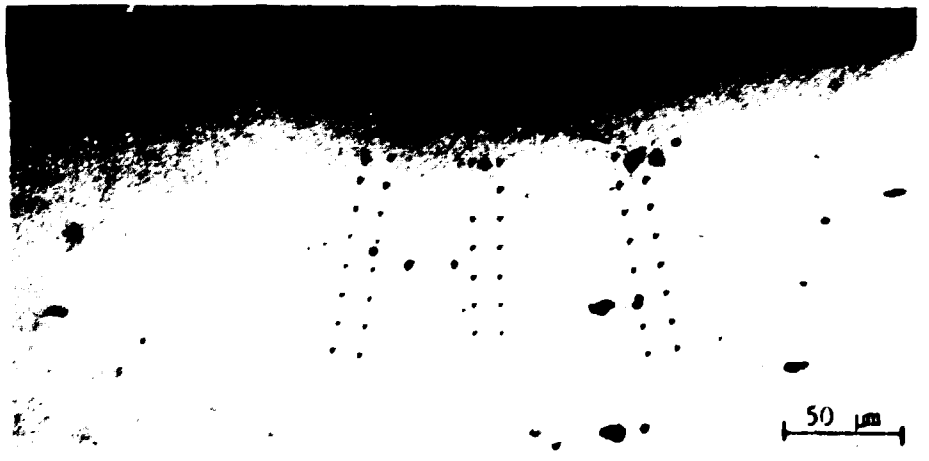

7075-T6

Fig. 4. Cross-sectional view of impact craters showing the array of hardness indentations used to characterize the properties of the material beneath the impact craters.

for the full 300 nm depth of the indentation, only the values of hardness measured at 250 nm were used in the analyses. This depth was chosen over a shallower depth to lessen the error in calculated hardness resulting from the inexact mathematical model used for calculating the indenter tip area. The results of hardness measurements on the aluminum samples are summarized in Figs. 5 through 7. Each of the data points shown is an average. With only a few exceptions, the points shown represent at least five hardness indentations and in some cases as many as 15 indentations. This hardness measuring capability is unique in that the hardness of the surface of these very small craters can be measured and the hardness of the cross-sectioned material can be measured on a smaller scale than previously possible.

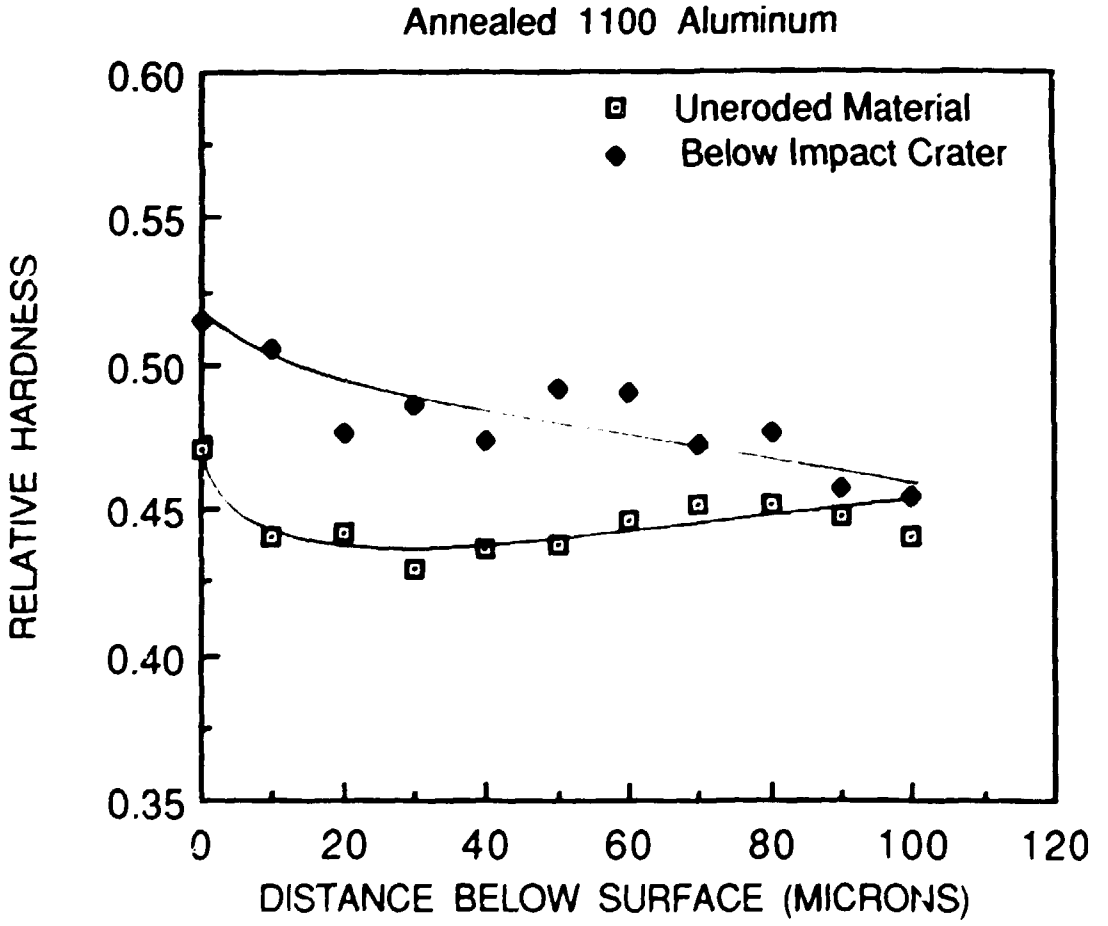

Fig. 5. Relative hardness versus depth below single impact crater on annealed 1100 aluminum.

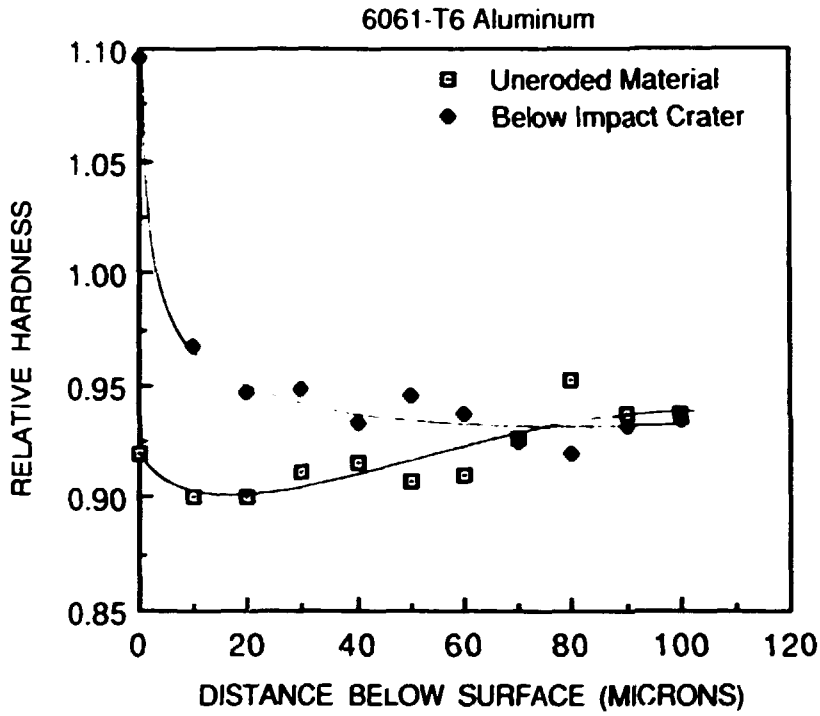

Fig. 6. Relative hardness versus depth below single impact crater on 6061-T6 aluminum.

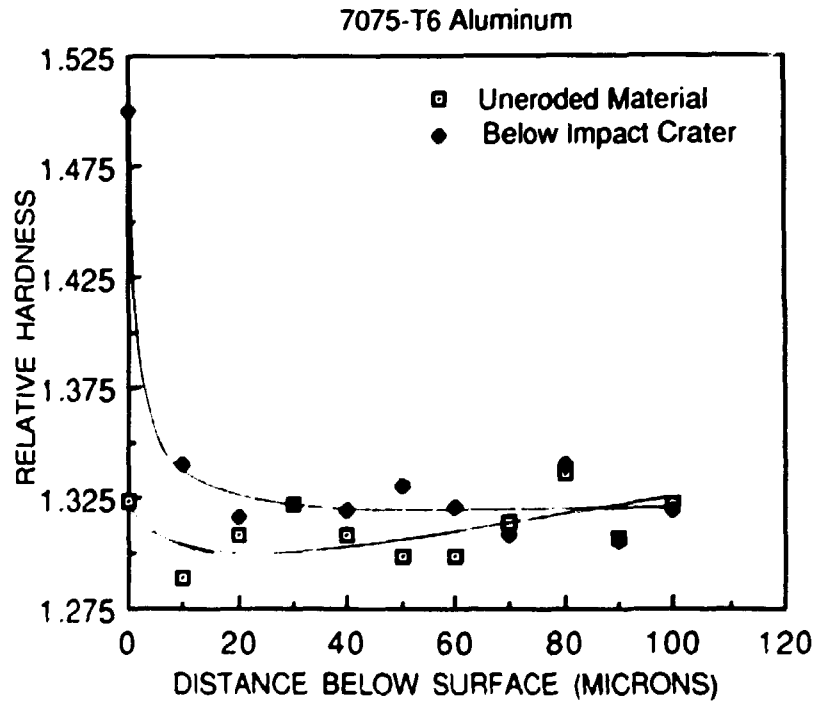

Fig. 7. Relative hardness versus depth below single impact crater on 7075-T6 aluminum.

DISCUSSION

Hardness measurements on the crater bottom of Hastelloy C-276 compared to measurements on the unimpacted surface show that the surface underwent appreciable hardening as a result of the impact even though the sample was already significantly cold worked. The hardness at the bottom of a 30° impact crater on a 30% cold worked sample was about 15% greater than on the unimpacted surface near the crater. Although heating occurs when an erosive particle impacts the surface, no evidence of softening was noted for the relatively high melting Hastelloy C-276. With lower melting point materials (i.e., aluminum alloys), we expected that the effects of local heating would be increased.

As is evident in Figs. 5 through 7, the hardness below the uneroded surface of the aluminum samples was constant or slowly decreased as the surface was approached. In all cases the data from indentations made on the surface showed some hardening, possibly the remnants of work hardening that occurred during polishing. Even though there was only a single impact by a smooth projectile, significant hardening was detected on and beneath the surface of the impact crater. However, the hardening measured on the bottom surface of the crater was appreciably greater than that measured anywhere else.

Table 3 shows that the impact crater was largest on the annealed 1100 aluminum sample. The data shown in Fig. 5 indicate the hardness on and just below the surface of 1100 aluminum increased about 10% as a result of the impact. Hardening by the impact decreased with depth, but affected material extended to about 100 μm. This is on the order of the affected depth reported after multiple particle impacts under somewhat similar impact conditions (30°, 61 m/s, 250–300 μm silicon carbide) on annealed 1100 aluminum.[16] However, unlike the Bellman and Levy work on annealed 1100, our single impact results do not show any evidence of softening at the surface. The Bellman and Levy study utilized a multiply impacted sample that had reached steady state erosion. The possible cumulative effects of the multiple impacts could explain the difference in the hardening and softening observed on the samples. It is also possible that the higher velocity, more angular particles used in the work cited

transferred more energy to the target, but the greater size and density of our particles should have offset most of the velocity and shape effects. Additional study on the effect of particle size and velocity is planned.

Table 3. Length of impact craters formed on aluminum alloys by the 28.5 m/s 30° incidence angle impact of 343-um-diam tungsten carbide balls

Material	Annealed 1100	6061-T6	7075-T6
Crater diameter (um)	175	51	46

The 6061 aluminum alloy is strengthened by heat treating, and the T6 treatment puts the alloy near its maximum strength and hardness. As indicated by the much smaller impact crater, the alloy's resistance to deformation by a high strain rate impact is considerably greater than that of annealed 1100 aluminum. As shown in Fig. 6, 6061-T6 aluminum exhibited a greater increase in surface hardness as well as a decreased depth to which a measurable hardness change could be measured (about 80 μm for this sample). Once again no decrease in hardness was seen indicating no localized overheating or melting had occurred.

The 7075 alloy was also tested in the T6 heat treatment condition that raised its strength and hardness to very high levels. The impact crater formed was somewhat smaller than that on 6061-T6, but it is clear that the high strain rate, single particle impact caused considerable hardening at the surface. Scatter in the data shown in Fig. 6 makes it difficult to determine if the depth of hardening was different for 7075-T6 and 6061-T6. It is apparent that in going from annealed 1100 aluminum to the precipitation strengthened alloys there was a decrease in the depth to which a single impact affects the material. No evidence of softening near the impacted surface was apparent.

Several relationships between erosion resistance and mechanical properties are suggested as a result of this study. The materials that showed greater steady state (multiple impact) erosion resistance developed

larger craters in our single impact tests, and they hardened to a greater depth. The combined results of single and multiple impacts suggest that the weaker, more ductile materials dissipate the energy of the impact over a greater volume and consequently suffer a lower rate of erosion.

For both the high and low melting point materials studied, all single impacts showed hardening; no softening was seen. It is possible that softening does not occur until the surface undergoes more extensive deformation and energy deposition such as would occur from multiple impacts. An answer to this question may be provided by MPM characterization of the material beneath the surface of samples eroded to the steady state condition.

The proposal that thermal properties have a major role in determining erosion resistance is supported in the present study by the observation that the aluminum alloys with the higher solidus temperatures are more erosion resistant. Consequently, additional studies at different velocities and temperatures are planned to apply our unique systems to gain further understanding of erosion behavior.

CONCLUSIONS

The following observations can be drawn from this work.

1. Single impact craters can be made using particles of approximately the size encountered in fossil fuel conversion and utilization systems. Using the specially fabricated indenter, hardness can be measured in the bottom of these single impact craters. By sectioning the sample through the crater, the hardness profile of the material can be determined in the material beneath the crater.

2. Clear evidence of work hardening was observed; we saw no indication of softening as a result of heat produced by single impacts. For the aluminum alloys, the greatest hardening occurred at the bottom of the impact crater with the hardness decreasing with depth; the total depth of hardening was less for the harder, stronger alloys.

3. The high strain rate impacts resulted in localized hardening significantly greater than that accomplished by 50% cold working or by heat treatment designed to optimize the strength of the alloys.

REFERENCES

1. I. Finnie, J. Wolak, and Y. Kabil, J. of Mater. 2, 682 (1967).

2. G. P. Tilly, Wear 14, 241 (1969).

3. G. L. Sheldon, J. Eng. Mater. & Tech., 133–37 (April 1977).

4. A. K. Vijh, Wear 39, 173 (1976).

5. C. E. Smeltzer, M. E. Gulden, and W. A. Compton, J. Basic Eng. 92, 639 (1970).

6. H. Brauer and E. Kriegel, Chemie Ing. Technol. 37, 265 (1965).

7. P. Ascarelli, Relation Between the Erosion by Solid Particles and the Physical Properties of Metals, 71-47, U.S. Army Materials and Mechanics Research Center Technical Report, 1971.

8. I. M. Hutchings, Wear 35, 371 (1975).

9. S. Malkin, Wear 68, 391 (1981).

10. W. H. Jennings, W. J. Head, and C. P. Manning, Jr., Wear 40, 93 (1976).

11. I. M. Hutchings, "Mechanisms of the Erosion of Metals by Solid Particles", pp. 59–76 in Erosion: Prevention and Useful Applications, ASTM STP 664, W. F. Adler, ed., American Society for Testing and Materials, 1979.

12. T. L. Urso, Model for Single-Particle Erosion of Ductile Materials, DOE/METC-86/4066, U.S. Department of Energy, January 1985.

13. T. Christman and P. G. Shewmon, Wear 54, 145 (1979).

14. B. Brown and J. W. Edington, Wear 70, 347 (1982).

15. C. S. Yust and R. S. Crouse, Wear 51, 193 (1978).

16. R. Bellman, Jr. and A. V. Levy, "Platelet Mechanism of Erosion of Ductile Metals," pp. 564–76 in Wear of Materials–1981, S. K. Rhee, A. W. Ruff, and K. C. Ludema, eds., The American Society of Mechanical Engineers, 1981.

17. A. Ninham, "The Effect of Mechanical Properties on Erosion," Wear of Materials–1987, K. C. Ludema, ed., The American Society of Mechanical Engineers, 1987.

18. R. E. Winter and I. M. Hutchings, Wear 34, 141–48 (1975).

19. L. K. Ives and A. W. Ruff, Wear 46, 149 (1978).

20. J. W. Edington and I. G. Wright, Wear 48, 145 (1978).

21. T. H. Kosel, R. O. Scattergood, and A.P.L. Turner, "An Electron Microscope Study of Erosive Wear," Wear of Materials—1979, K. C. Ludema, ed., The American Society of Mechanical Engineers, 1979.

22. J. R. Keiser, Design, Construction, and Initial Results for an Erosion-Corrosion Test System, ORNL/TM-10049, Oak Ridge National Laboratory, May 1986.

23. J. R. Keiser, "The Relationship of an Alloy's Mechanical Properties to Its Response to Individual Erosive Particle Impacts," to be published in Proceedings of the Third Berkeley Conference on Corrosion-Erosion-Wear of Materials at Elevated Temperatures, Berkeley, Calif., January 29–31, 1986.

24. T. Christman and P. G. Shewmon, Wear 52, 57 (1979).

25. A. V. Levy, Wear 108, 1 (1986).

26. "Standard Test Method for Microhardness of Materials, Part 11," ASTM Standard E 384-73 (Reapproved 1979), American Society for Testing and Materials, 1981.

SESSION III - ALLOY DEVELOPMENT AND MECHANICAL PROPERTIES

INVESTIGATION OF CANDIDATE ALLOYS FOR ADVANCED STEAM CYCLE SUPERHEATERS AND REHEATERS

R. W. Swindeman, G. M. Goodwin,
and P. J. Maziasz

Metals and Ceramics Division
Oak Ridge National Laboratory
P.O. Box X
Oak Ridge, Tennessee 37831

ABSTRACT

Screening tests were performed on a series of modified type 316 stainless steels and modified 800H alloys to identify candidates for use as tubing in advanced boiler superheaters/reheaters producing steam at 650°C (1200°F) and 35 MPa (5000 psi) pressure. Alloy evaluations included fabricability, tensile and creep behavior, weldability, metallurgical stability, and response to chromizing. The modified type 316 stainless steels exhibited sufficient strength and ductility to meet a target design strength of 60 MPa at 700°C but were difficult to weld and had very poor oxidation resistance. The compositions based on alloy 800H were weaker than the modified type 316 stainless steels and exhibited similar problems in regard to weldability. All alloys were stronger when cold worked to small strains (2 to 10%). The most promising compositions contained low levels of phosphorus. Based on the results of the screening tests, compositions were selected for the production of small heats of tubing.

INTRODUCTION

In order to be a viable candidate for service as tubing in an advanced steam cycle superheater/reheater, an alloy must have strength exceeding twice that of type 316 stainless steel, fireside corrosion resistance at 700°C equivalent to alloys containing more than 30% chromium, and steamside corrosion resistance equivalent to alloy 800H.[1] The commercial and near-commercial tubing alloys worth consideration have been

investigated by Gold and Jaffee[2] and others.[3,4] They find that the only alloys meeting all requirements are highly alloyed. Examples include alloy 617 and a Nippon-Kokan developmental alloy, CR30A. However, the cladding and surface treatment of lower chromium-bearing alloys provide options that need to be examined.

The program at Oak Ridge National Laboratory investigates the potential of several groups of alloys for service as tubing in advanced steam cycle superheaters and reheaters. One group of alloys consists of "lean" stainless steels, with chromium less than 20%, that have been developed by modifying type 316 stainless steel to produce improved strength and metallurgical stability.[5] A commercial alloy in this category is the 17-14 CuMo stainless steel that is used in the Eddystone Unit 1 Fossil Plant power boiler.[6] Such alloys have good strength but must be surface treated or clad for improved corrosion resistance. A second group of alloys contains 20 to 30% chromium, 20 to 30% nickel, plus strengthening additions, and may be classed as modified 310 stainless steel or modified alloy 800. Near-commercial alloys include the niobium-modified 20-25 stainless steels.[7,8] Such alloys have potentially good strength, weldability, and steamside corrosion resistance. A third group of alloys contains aluminum in the range 4 to 8% and has excellent steam corrosion resistance. These alloys include an aluminum-silicon-modified stainless steel,[9] aluminum-modified stainless steel,[10] and nickel-iron aluminides.[11] A final group of alloys includes commercial nickel-chromium alloys such as Inconel 617,* Inconel 690,* and Inconel 671.*

The program is moving through the logic diagram provided in Fig. 1, which addresses three of the five tasks in the program. The first task involves screening evaluations of laboratory heats from the four alloy groups mentioned above, and ends with the selection of alloys for pilot heats of tubing. The selections are primarily based on results from mechanical, microstructural, and weldability evaluations. The second task involves a broadened experimental program on a smaller number of alloys and includes laboratory fireside and steamside corrosion testing of tubular products. It is expected that the second task will lead to the

---

*Registered trademark of Huntington Alloys, Inc.

a reference location. Here we see that chromium may be increased to levels around 25% for a depth of about 100 μm from the surface. This content may be adequate for the steamside of tubing.

RESEARCH PROGRESS ON MODIFIED ALLOY 800H

Four heats of modified alloy 800H were provided by AMAX; and the chemistries are provided in Table 2. Heats AX1, AX2, and AX3 were procured to examine phosphorus effects; heat AX4 was investigated for high chromium in addition to high phosphorus. The fabricability of the four heats was similar to that of the lean stainless steels, and the same sequence of solution treatment at 1200°C and rolling at 1100°C was followed. The heats were delivered following a 1200°C solution treatment and 10% cold rolling in the mill-annealed condition. Tensile data at 25 and 700°C are compared in Fig. 11. These indicate that all four heats met or exceeded the strength and ductility requirements of ASTM B-409-73. Reannealing at 1200°C decreased the yield strength significantly, but in contrast to the lean stainless steels, the yield strengths exceeded the minimum room temperature requirement (170 MPa).

Table 2. Composition of modified alloy 800H (wt %)

Element	Alloy				
	AX1	AX2	AX3	AX4	800H
C	0.087	0.090	0.092	0.091	0.08
Si	0.20	0.23	0.22	0.22	0.24
Mn	1.99	1.96	2.00	1.97	0.83
Ni	29.8	30.4	30.6	30.3	31.9
Cr	19.6	20.4	20.6	25.2	19.5
Ti	0.27	0.36	0.36	0.36	0.42
Nb	0.21	0.24	0.24	0.24	
V	0.52	0.53	0.52	0.53	
Mo	1.98	1.96	2.00	1.97	
P	0.074	0.045	0.031	0.072	
B	0.005	0.011	0.010	0.011	
S	0.012	0.009	0.010	0.009	0.003
N	0.024	0.028	0.029	0.030	
Cu	0.003				0.54
Al					0.43
Fe	Bal	Bal	Bal	Bal	Bal

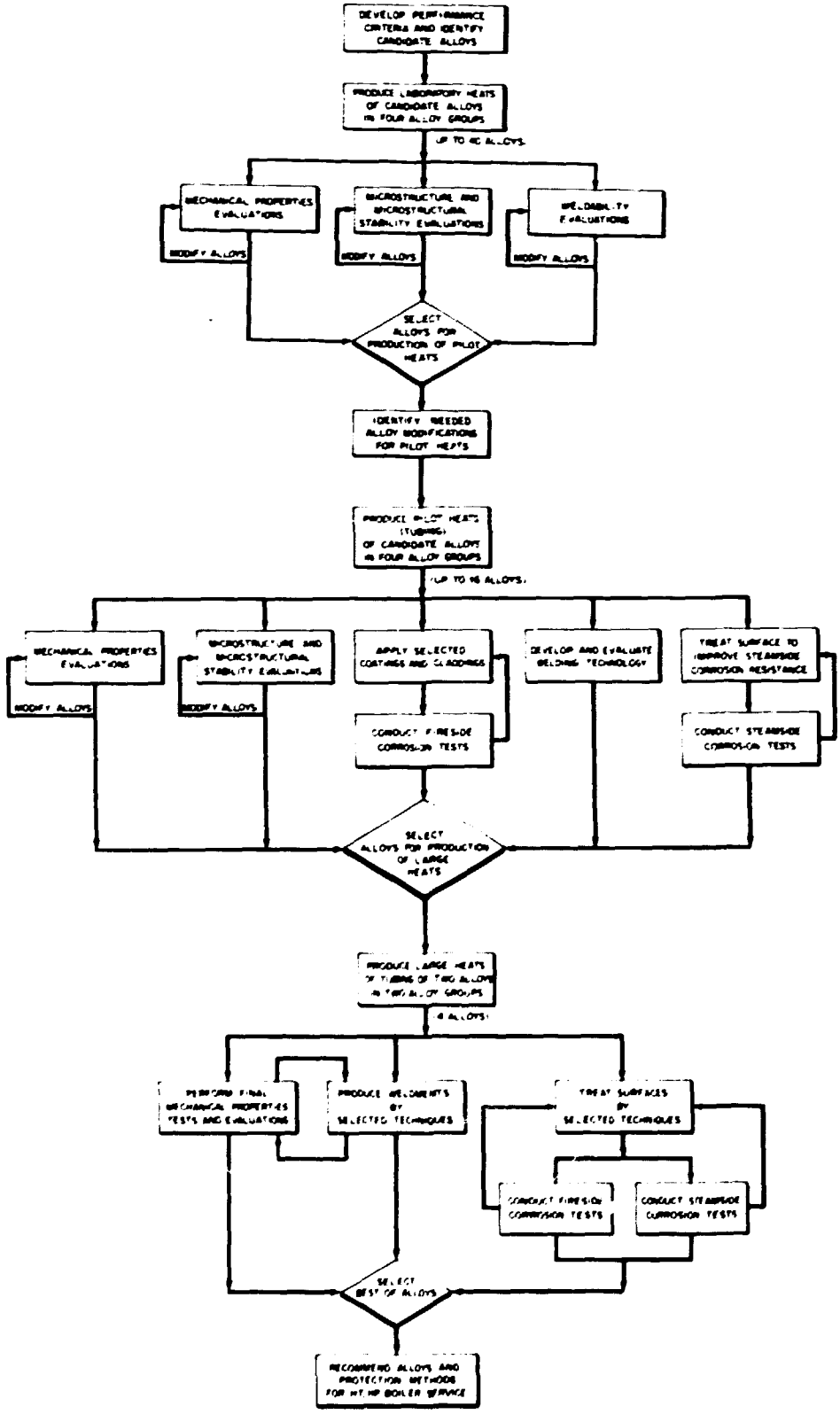

Fig. 1. Logic diagram for the development of alloys for advanced superheater and reheater service.

selection of no more than four alloys for study in a third task. The third task involves a demonstration to show that the major issues concerning fabricability, mechanical behavior, fireside corrosion, and steamside corrosion can be clearly identified and resolved in any commercialization project, should industry decide to proceed with the development of an advanced cycle steam plant. Two additional tasks in the program involve the evaluation of "control alloys" and technology transfer.

RESEARCH PROGRESS ON LEAN STAINLESS STEELS

Eight heats of lean stainless steels were procured for evaluation in the first task. The compositions are identified in Table 1. The first four heats, CE0, CE1, CE2, and CE3, were procured from Combustion Engineering as 25-kg ingots produced by argon-induction melting with electroslag remelting. The reference composition was heat CE1. The other compositions were selected to examine increased silicon content (CE0), increased chromium content (CE2), and a copper addition (CE3). Four other heats were procured from AMAX and are identified in Table 1 as AX5, AX6, AX7, and AX8. Heats AX5 and AX6 were obtained to determine the effects of reduced phosphorus content; heat AX7 was a repeat of CE3, and AX8 was procured to examine the influence of reduced phosphorus and vanadium content. All eight heats were processed by the mills to a 13-mm-thick plate. The "mill annealed" condition involved a 1200°C solution treatment followed by hot or cold rolling to produce the final flattening and surface finish. Except for CE1, the estimated work in the mill-annealed condition was 8 to 10%. The CE1 alloy received 2% equivalent work.

Generally speaking the alloys exhibited satisfactory fabricability; however, some problems were encountered. For example, the centrifugal casting of tube hollows produced the segregation of titanium, and the method could not be used. The CE alloys exhibited centerline delaminations in the rolled plates, and as much as 40% of the plate material had to be scrapped. The CE3 heat produced the highest yield. The AX series

Table 1. Composition of lean stainless steels (wt %)

Element	Alloy								
	CE0	CE1	CE2	CE3	AX5	AX6	AX7	AX8	17-14CuMo
C	0.072	0.085	0.079	0.086	0.076	0.074	0.073	0.074	0.098
Si	0.41	0.21	0.26	0.21	0.12	0.12	0.11	0.12	0.95
Mn	1.80	1.64	1.89	1.75	2.04	1.96	2.0	2.05	0.83
Ni	16.0	16.2	16.0	16.2	16.2	16.0	16.0	15.9	13.9
Cr	14.2	13.1	16.0	14.5	13.9	14.3	14.2	13.9	16.5
Ti	0.24	0.21	0.31	0.27	0.27	0.28	0.28	0.24	0.21
Nb	0.10	0.12	0.11	0.11	0.15	0.15	0.15	0.15	0.45
V	0.57	0.52	0.58	0.56	0.52	0.51	0.53	0.15	0.07
Mo	2.45	2.30	2.26	2.41	2.46	2.48	2.48	2.48	1.96
P	0.071	0.076	0.069	0.071	0.024	0.041	0.073	0.043	0.014
B	0.005	0.005	0.005	0.007	0.005	0.005	0.005	0.005	
S	0.007	0.008	0.008	0.008	0.015	0.015	0.014	0.015	0.005
N	0.015	0.016	0.017	0.012	0.021	0.020	0.024	0.022	0.025
Cu	0.03	0.04	0.03	1.96	0.005	0.004	1.50	0.14	3.07
Fe	Bal	Bal	Bal	Bal	Bal	Bal	Bal	Bal	Bal

of alloys could not be rolled at 1200°C without severe cracking, and ingots had to be machined before rolling in order to produce an acceptable surface finish. Some of the products exhibited variable grain sizes through the section. These problems were not serious; one would expect that they could be resolved in the course of a commercialization effort

Tensile testing of the lean stainless steels was performed at room temperature and 700°C. Data are summarized in Fig. 2, which is a bar chart comparing the yield strength, ultimate strength, elongations, and reduction of area data for alloys in the mill-annealed condition. All alloys met room temperature minimum strengths and ductility requirements per ASTM A-240 specification for H-grade austenitic steels. The type 17-14CuMo stainless steel and heat CE1 had the lowest yield strength.

A few tensile tests were performed on materials reannealed at 1115 and 1200°C, respectively. These tests indicated a significant decrease in yield strength relative to the mill-annealed condition. Some of these data are provided in Fig. 3, which plots flow stress vs nominal strain. The 1200°C reanneal produced a yield strength below the minimum specification (205 MPa) of ASTM A-240; however, this low strength is not unusual for austenitic stainless steels.[12]

The relative creep-rupture behavior of the alloys was evaluated by comparing results from tests at 700°C and 170 MPa. All alloys were tested

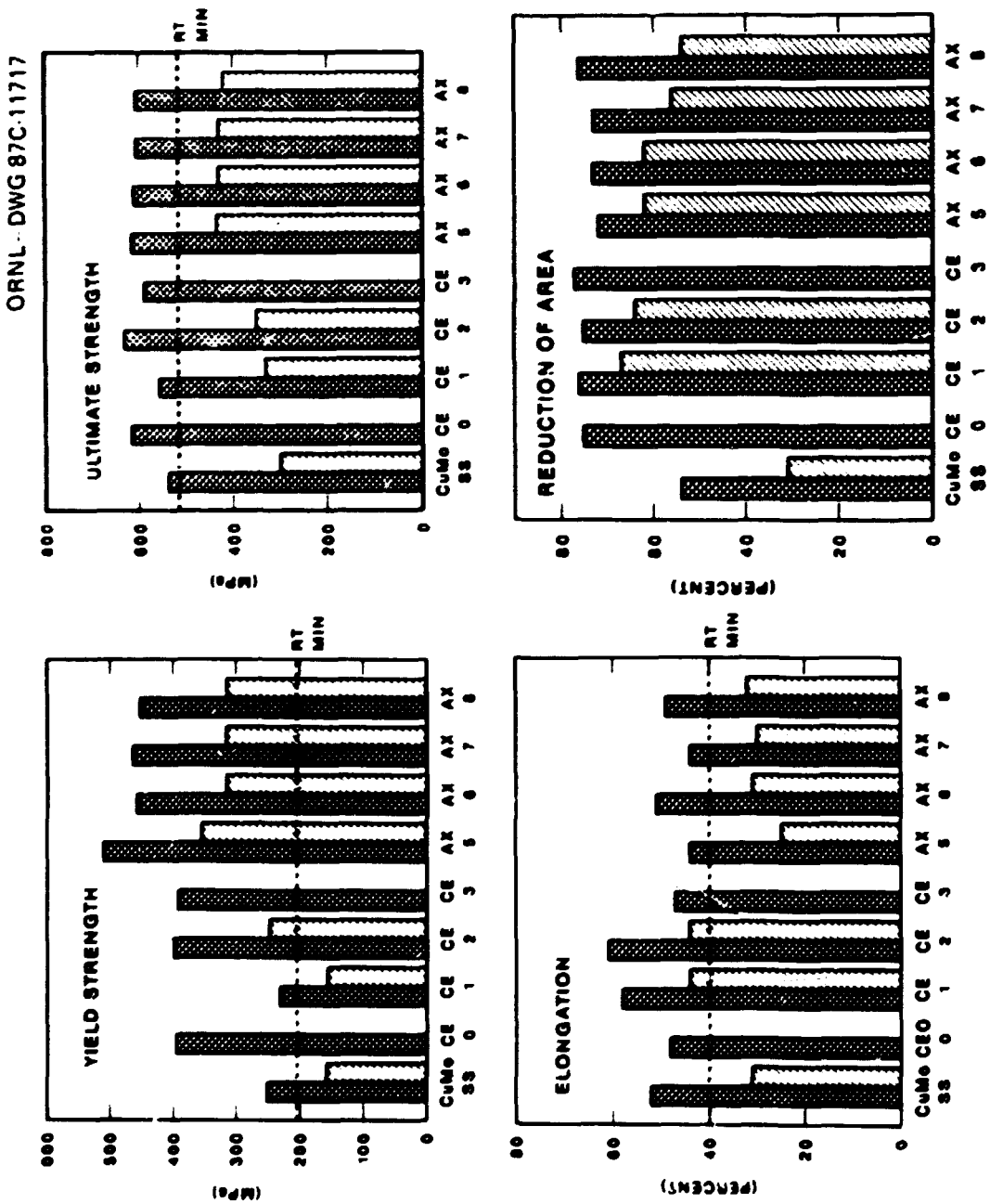

Fig. 2. Tensile properties for experimental lean stainless steels in the mill-annealed condition at 25 and 700°C.

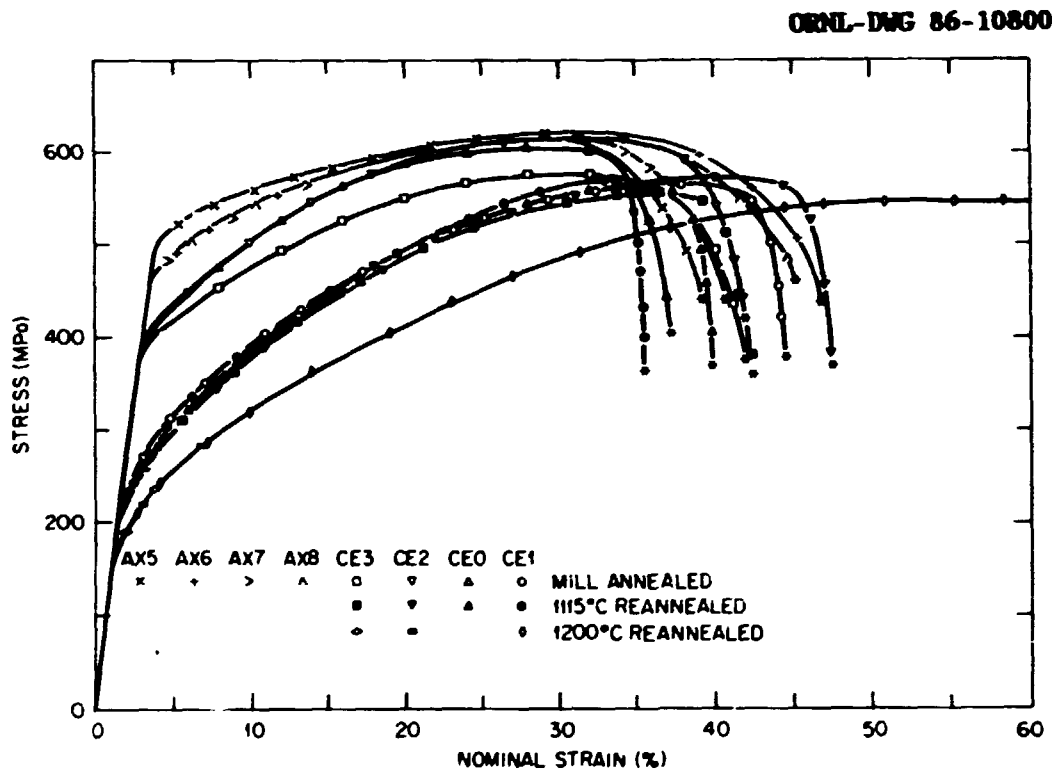

Fig. 3. Effect of reannealing on the tensile curves of lean stainless steel at room temperature.

in two conditions: mill annealed and after reannealing at 1200°C. The CE series of alloys (CE0, CE2, and CE3) was also tested after a reannealing at 1115°C. Aging effects were examined in the CE0 alloy, and stress and temperature effects were examined in the CE2 alloy. These choices were necessary because there was insufficient material of any one alloy to complete a comprehensive program.

A comparison of the creep curves at 170MPa and 700°C is made in Fig. 4 for the CE series of alloys. Data for the "control alloys," 17-14CuMo stainlless steel, alloy 800H, and type 316 stainless steel, are included. The CE alloys varied in rupture life by a factor of 5, with heat CE1 being the weakest and CE0 the strongest. This difference probably reflects differences in the hot or cold work from one heat to another. When reannealed at 1115°C, all of the heats tested (CE0, CE2, and CE3) exhibited similar creep behavior, and curves were similar to those for

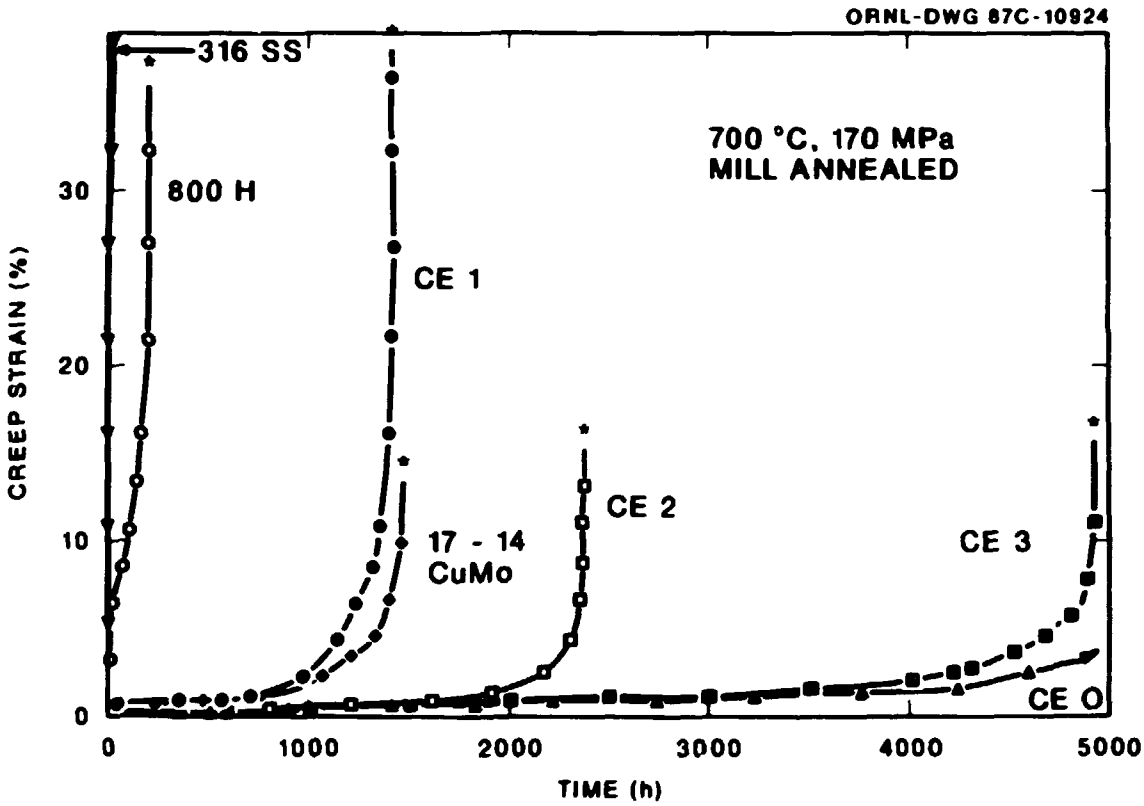

Fig. 4. Creep curves for the mill-annealed CE series of lean stainless steels compared with commerical alloys at 700°C and 170 MPa.

heat CE1 (in the mill-annealed condition) and 17-14CuMo stainless steel. More details are provided elsewhere.[13] When reannealed at 1200°C, the creep strength was improved over the 1115°C annealing treatment; therefore, the screening tests were focused on this reannealing condition for the AX series of alloys. A trend of creep curves is shown in Fig. 5 for the standard condition of 170 MPa and 700°C. Here we see that the eight heats of lean stainless steel fall into a band that covers less than a factor of 2 in time for heats reannealed at 1200°C. The mill-annealed heats of the AX series of alloys exhibited remarkable strengths, with less than 1% creep after 6000 h. Further optimization of the reannealing temperature has been undertaken by Liu and co-workers at Cornell,[14] who are also examining cold work and aging effects in more detail. Some trends showing the cold work and aging effects in heat CE0 are illustrated in Fig. 6, which plots creep curves for mill-annealed, mill-annealed and aged, 1200°C reannealed, 1200°C reannealed plus 5% cold worked, and a series of

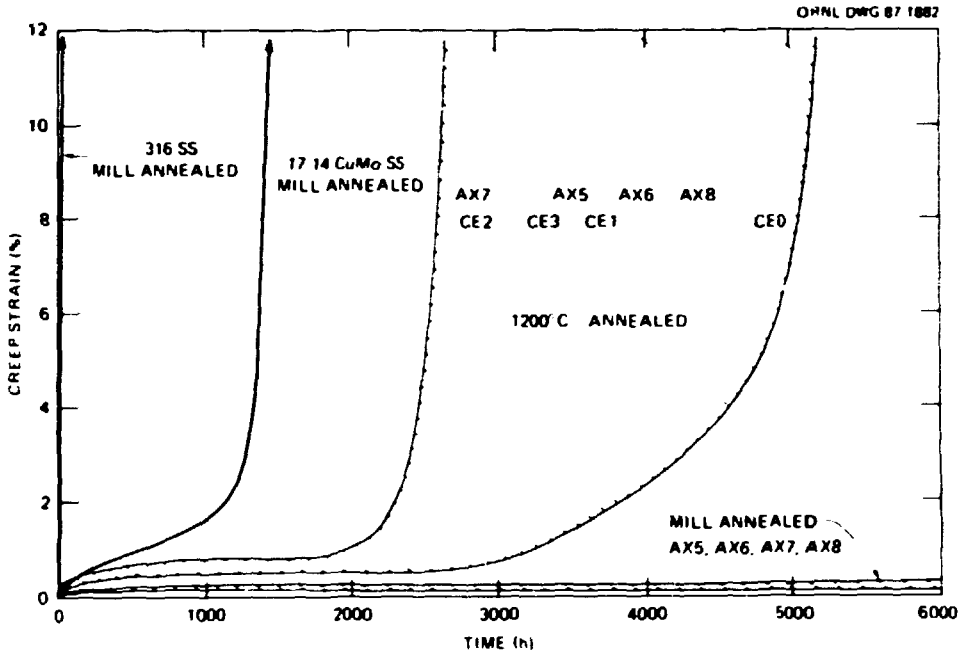

Fig. 5. Trend creep curves for lean stainless steels at 700°C and 170 MPa.

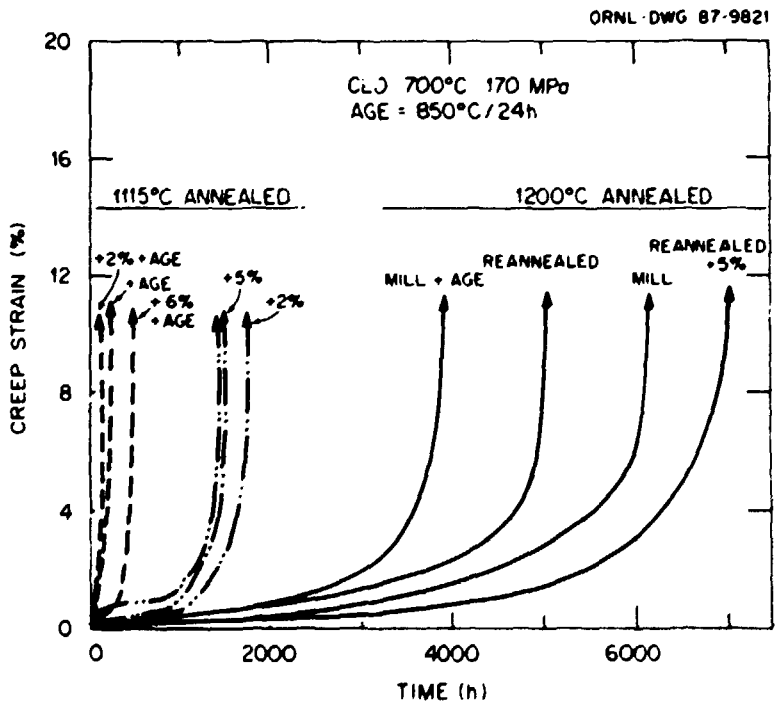

Fig. 6. Effect of reannealing, cold working, and aging on the creep curves of heat CE0 at 700°C and 170 MPa.

cold-worked and aging treatments for the 1115°C annealed condition. Here we see that for all conditions, the 1200°C reannealing is best. The 1115°C reannealing plus aging drastically reduces the creep rupture life for the testing conditions examined. Similar loss in life was observed at a much lower stress (100 MPa).

The effect of stress and temperature on creep rupture is being studied on heat CE3. Testing at 700°C has covered the stress range from 100 to 240 MPa and at times to beyond 10,000 h. Other test temperatures include 650, 730, 760, and 800°C. These data were used to calculate the parameters in models to correlate the time to 1% creep, the minimum creep rate, and the time to rupture with stress and temperature. A typical correlation for rupture life is shown in Fig. 7. Trends indicate that the target strength of 100 MPa at 700°C and at 100,000 h can be met.

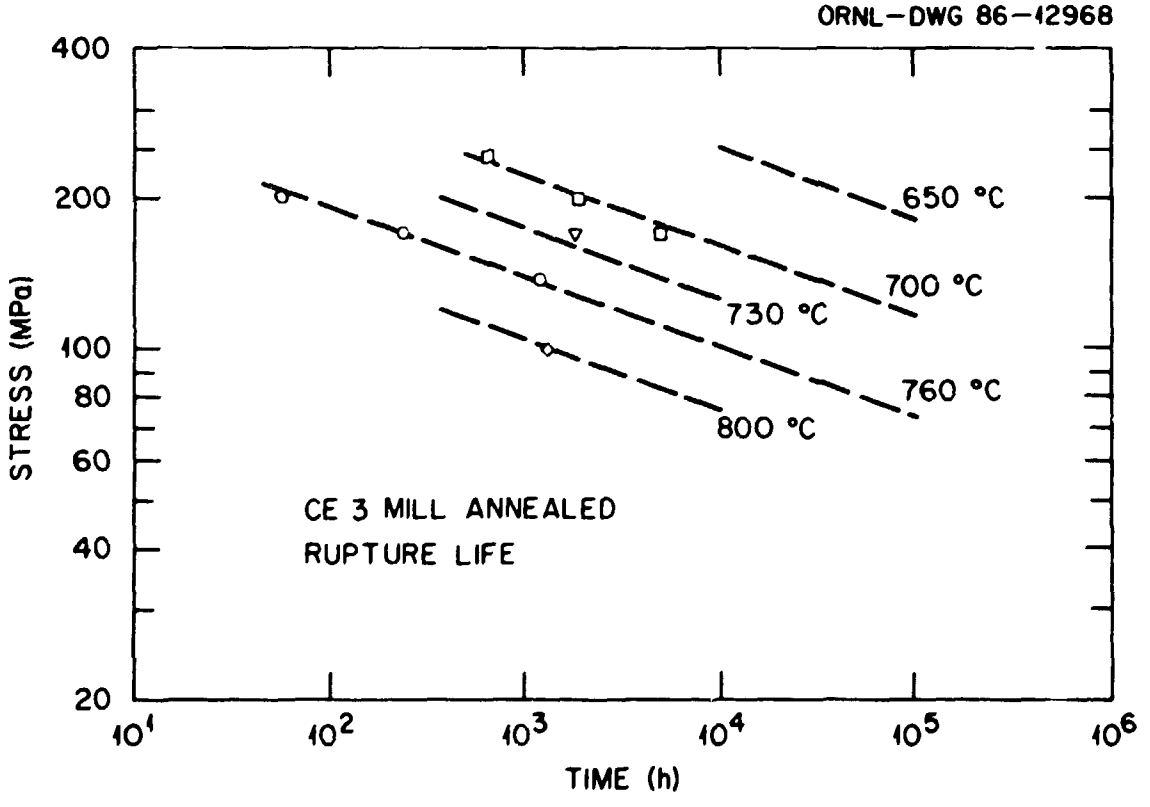

Fig. 7. Long stress vs log rupture life for mill-annealed heat CE3.

Exploratory studies of creep crack growth behavior are under way at 700°C. One test on heat AX5 has been completed. Here, a one-half CT specimen was tested over a period of 1300 h by holding at constant load (starting at 2.6 kN) for 1 week, then increasing the load by 0.53 kN until significant creep crack growth was noticed, which occurred after 1100 h when the load reached 5.3 kN. The data produced at a 5.3-kN load were analyzed on the basis of several parameters of interest in correlating creep crack growth with test parameters. Typical results are provided in Fig. 8, which plots the crack growth rate, da/dt, against the path-independent line integral, C^*, often used to represent creep crack growth.[15] Included in the figure are scatterbands representing experimental data for type 316 stainless steel and alloy 800H.[16] The data for heat AX5 at 700°C are comparable with the trends for type 316 stainless steel in the temperature range 593 to 649°C.

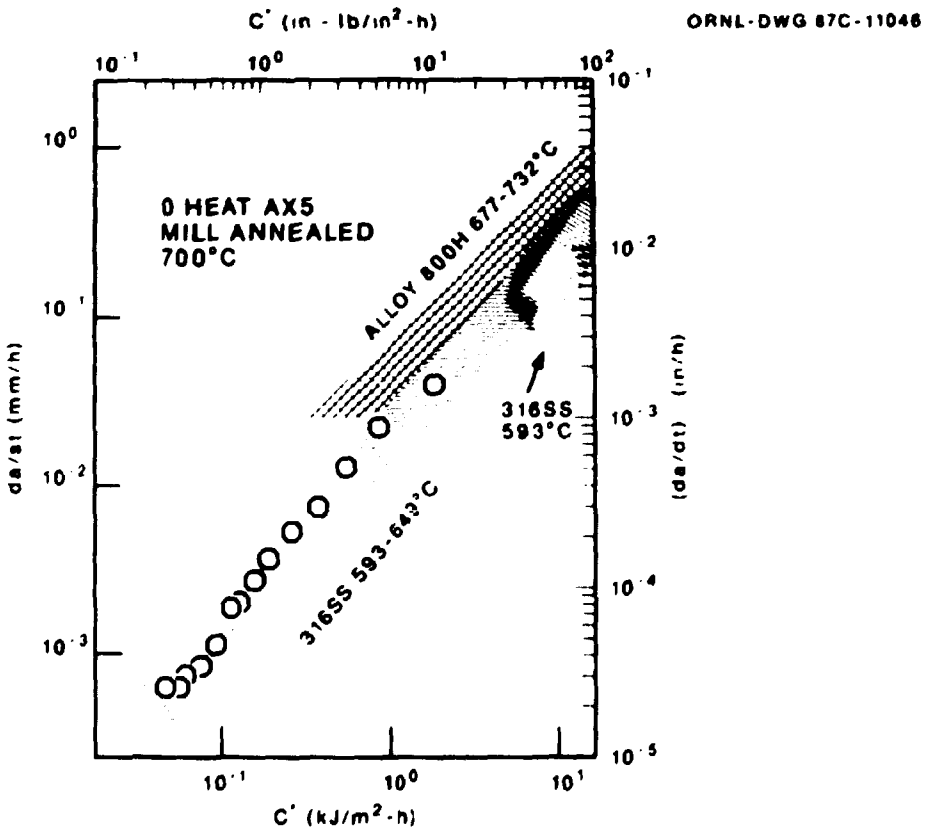

Fig. 8. Comparison of the creep crack growth behavior of heat AX5 with type 316 stainless steel and alloy 800H.

Sigmajig tests indicated that all of the developmental alloys would be susceptable to hot cracking, and even the commercial alloy 17-14CuMo stainless steel was marginal.[13] For this reason, none of the developmental compositions were used to produce filler metal. Heat CE1 was joined with Inconel 82 using the gas tungsten arc (GTA) process, and heat CE2 was joined with a 17-14CuMo stainless steel electrode using the shielded metal arc (SMA) process. The joints exhibited small cracks at the toe of the welds, and a few very small cracks appeared in the fusion line after side bend tests and tensile tests. Heat CE0 was also joined using 17-14 CuMo stainless steel and the GTA process. This weldment exhibited cracking in the weld metal. Heats AX5 through AX8 were joined with the 17-14CuMo stainless steel stick electrodes. The high phosphorus heat, AX7, was badly cracked, and all other heats exhibited some evidence of fusion line cracking when the weldments were examined metallographically. Gleeble data indicated that heat-affected zone cracking would be a problem in all heats.

Tensile heats were performed at 25 and 700°C, and results are summarized in Fig. 9, which is a bar chart showing the ultimate strength and reduction of area data produced on the weldments at 25 and 700°C. All weldments exceeded the minimum ultimate strength for base metal at room temperature, but the GTA weld in heat CE1 and the SMA welds in the AX series of alloys exhibited poor reduction of areas at 700°C. Even at 25°C, where area reduction was good, there was evidence of hot cracking on the fusion line.

Creep rupture tests were performed on weldments of heats CE1, CE0, and AX5 through AX8 at 700°C and 170 MPa. The GTA/I82/CE2 weldment failed in the weld metal in 771 h; the GTA/17-14CuMo stainless steel/CE1 weldment failed in the weld metal after 863 h; the SMA/17-14CuMo stainless steel/CE1 weldment failed in the base metal after 1758 h. The AX5 through AX8 weldment tests are still in progress.

Although task I of the program does not involve fireside and steamside corrosion tests, it was apparent from the condition of the air-tested specimens that the lean stainless steels have very poor oxidation resistance. Some exploratory studies regarding the response to chromizing were performed by Turner.[17] Typical results (obtained on heat AX6) are shown in Fig. 10, which plots weight percent chromium vs distance from

ORNL–DWG 87C-11718

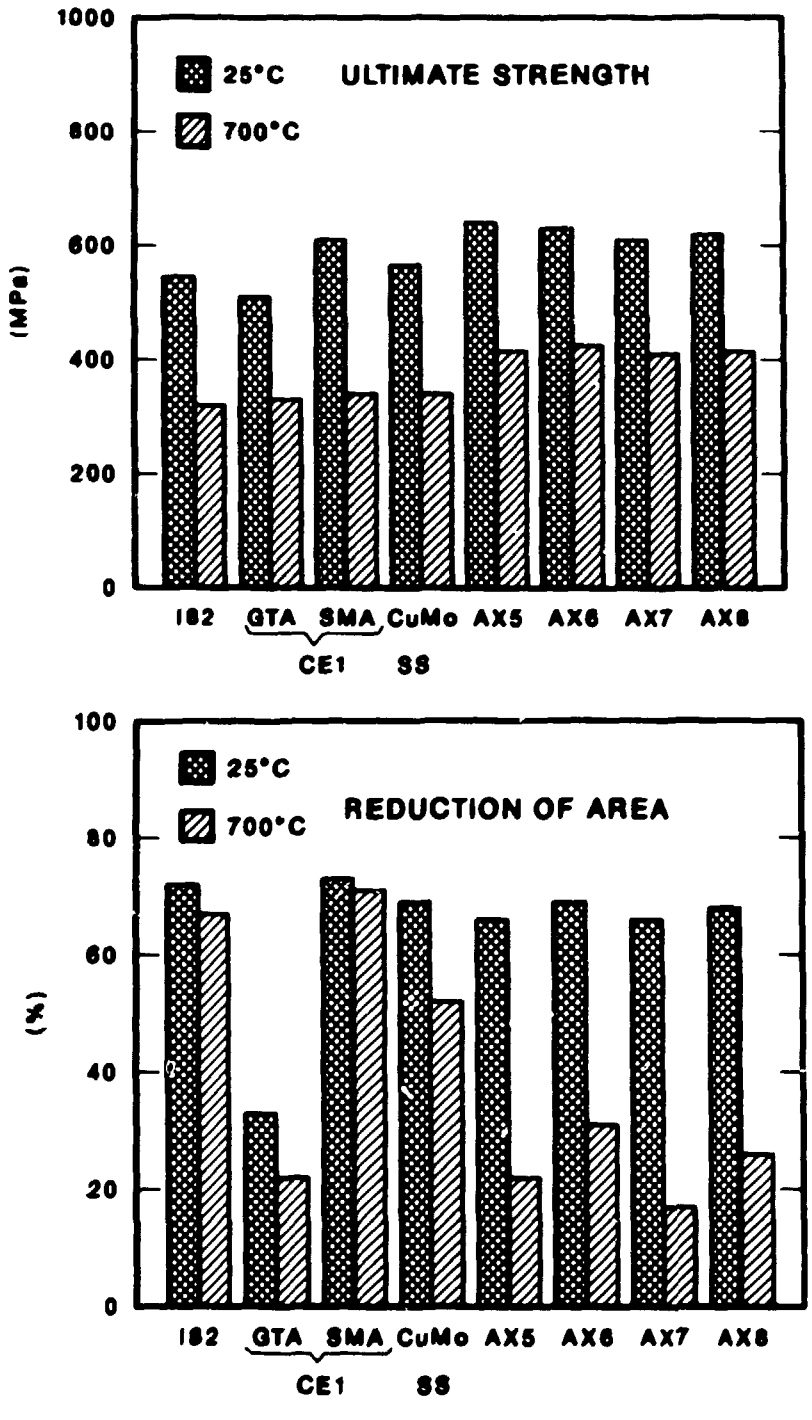

Fig. 9. Tensile data for weldments of the lean stainless steels at 25 and 700°C.

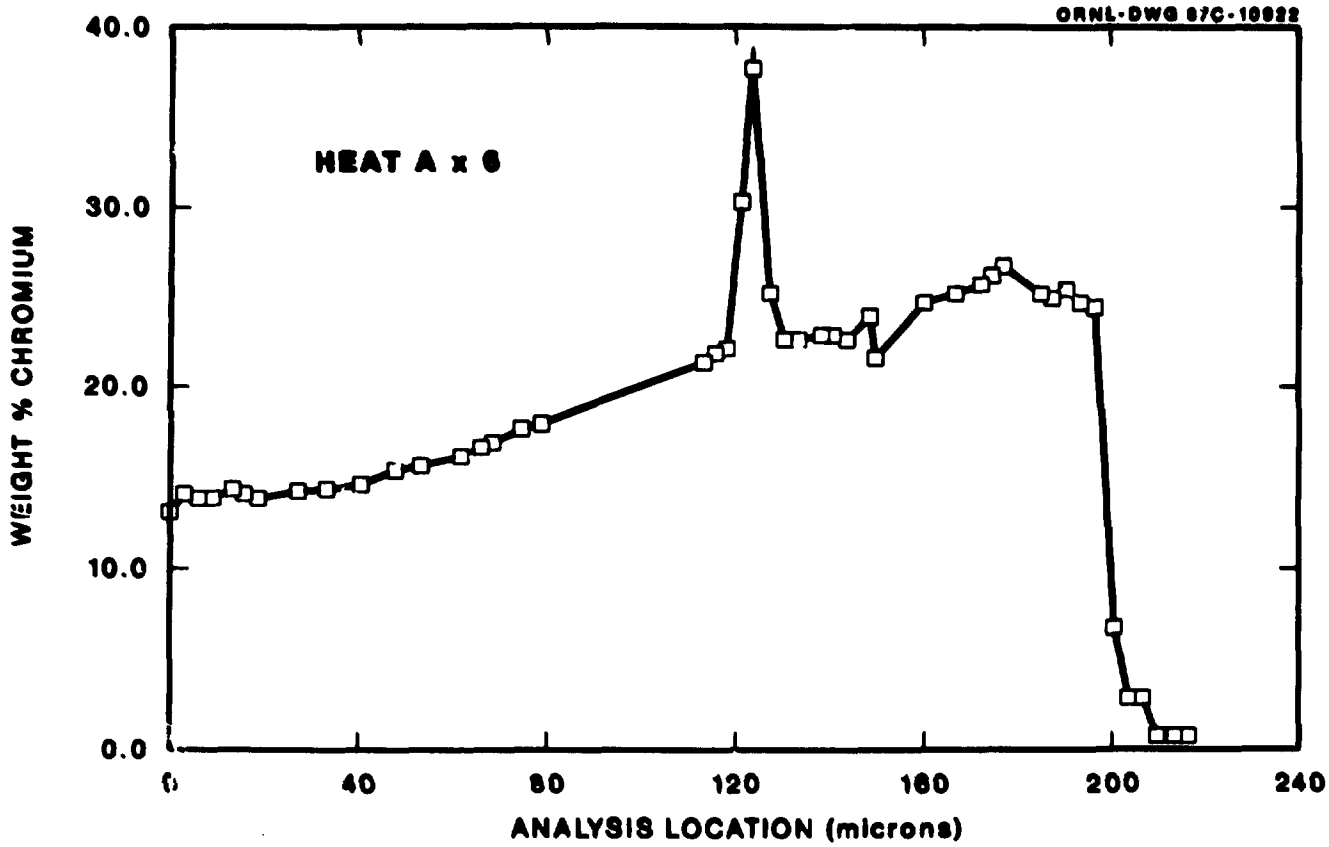

Fig. 10. Chromium profile in chromized heat AX6.

ORNL-DWG 87C-11716

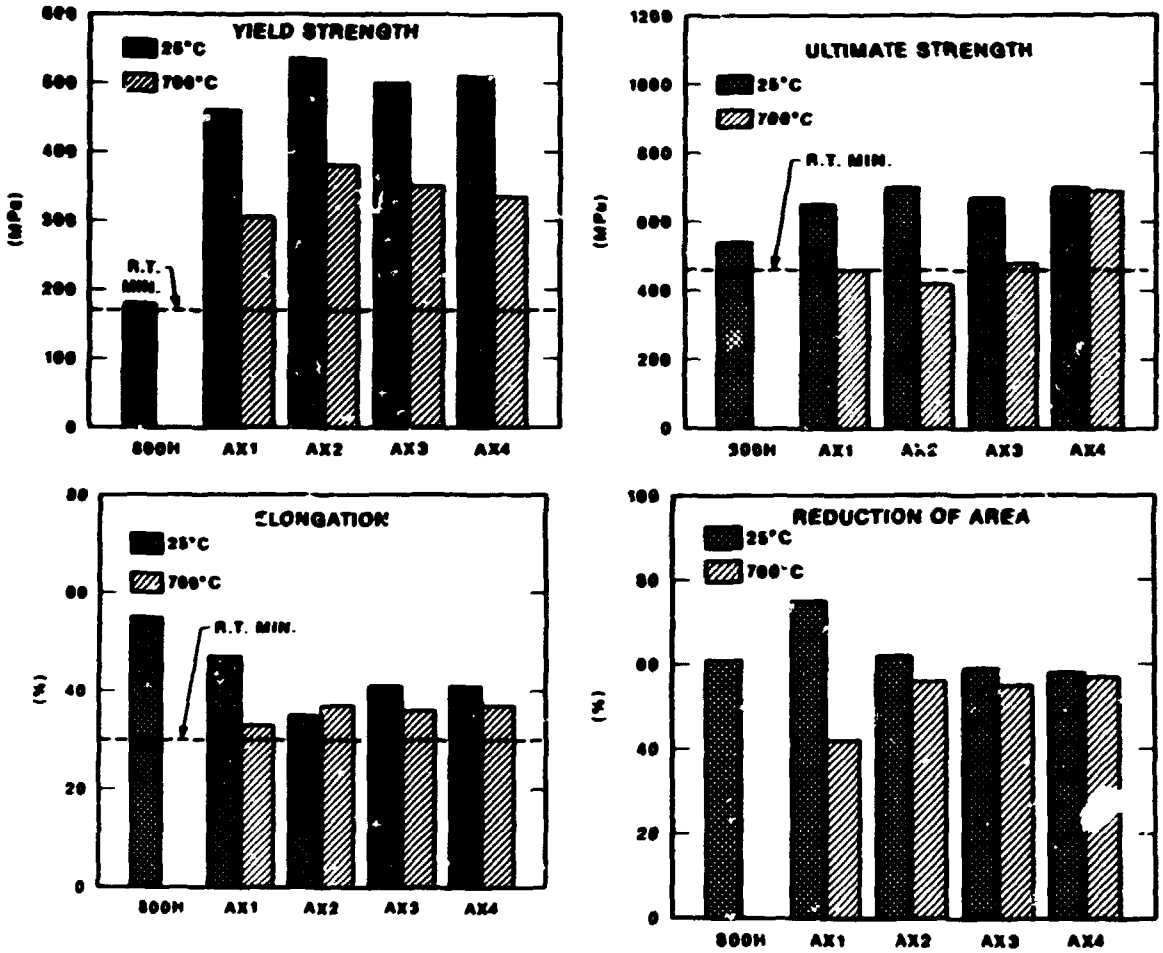

Fig. 11. Tensile properties for experimental heats of modified alloy 800H.

The trend of the creep curves for 700°C and 170 MPa is illustrated in Fig. 12 for heats AX1, AX2, and AX3. Both the mill-annealed and 1200°C reannealed conditions are represented. All show significant improvement in life over the commercial heat of alloy 800H. Heat AX4, with 25% chromium, is not plotted in the figure. The mill-annealed specimen ruptured after 1090 h with a 2.4% reduction of area, and the 1200°C reannealed specimen ruptured in 2232 h with a 9.2% reduction of area. Heats AX1 and AX3 were selected to examine cold work and aging effects. Testing is still in progress, but trends suggest that small amounts of cold work do not improve the creep-rupture strength at 700°C and 170 MPa. Further,

aging at 850°C for 24 h greatly reduces life. Heat AX2 (reannealed at 1200°C) was selected to examine the stress and temperature effects on creep. Stresses ranged from 100 to 240 MPa, and temperatures were from 650 to 800°C. Rupture data are provided in Fig. 13. These data show that the target strength of 100 MPa at 700°C (in 100,000 h) cannot be met for the AX2 alloy in the 1200°C reannealed condition.

Sigmajig tests on heat AX1 indicated the likelihood of severe hot cracking for the modified alloy 800H group; hence, the 17-14CuMo stainless steel stick electrodes were used to produce SMA welds in the plates of AX1 through AX4. Metallography revealed the presence of fusion line cracks, and severe cracking was observed in the fusion line of side bend test specimens. Heats AX1 and AX4 with high phosphorus were the worst. The results from tensile tests at 25 and 700°C, summarized in Fig. 14, revealed low ductility fusion line failures. Heats AX1 and AX4 were the worst failures. Metallography and scanning electron microscopy indicated that both hot cracking and heat-affected zone cracking were present. Heat AX2 exhibited the best weldability and fewest cracks.

RESEARCH PROGRESS ON ALUMINUM-BEARING AUSTENITIC ALLOYS

In their evaluation of materials for the advanced steam cycle superheater/reheater tubing, DiStefano et al.[18] concluded that nickel aluminides have greater potential than lean stainless steels and modified alloy 800H. Partly for this reason, two compositions of nickel aluminide were selected for production into 13-mm (1/2-in.) plate. The aluminides are identified in Table 3, along with the composition of a strong cast nickel aluminide, IC221. Heat NA1 was selected for its good workability and NA2 for its good weldability. Both assessments were based on experience with compositions at ORNL. Ingots of 100 mm diameter, needed to produce the wrought plate products, were cast at Combustion Engineering. Both compositions produced inhomogenuclies that impeded subsequent working by either cold or hot deformation processes. Casting of thinner sections appears possible, as well as powder consolidation methods, which are being examined. Meanwhile, some testing of the investment cast IC221 is in progress. Creep curves plotted in Fig. 15 for tests at 760°C attest to the

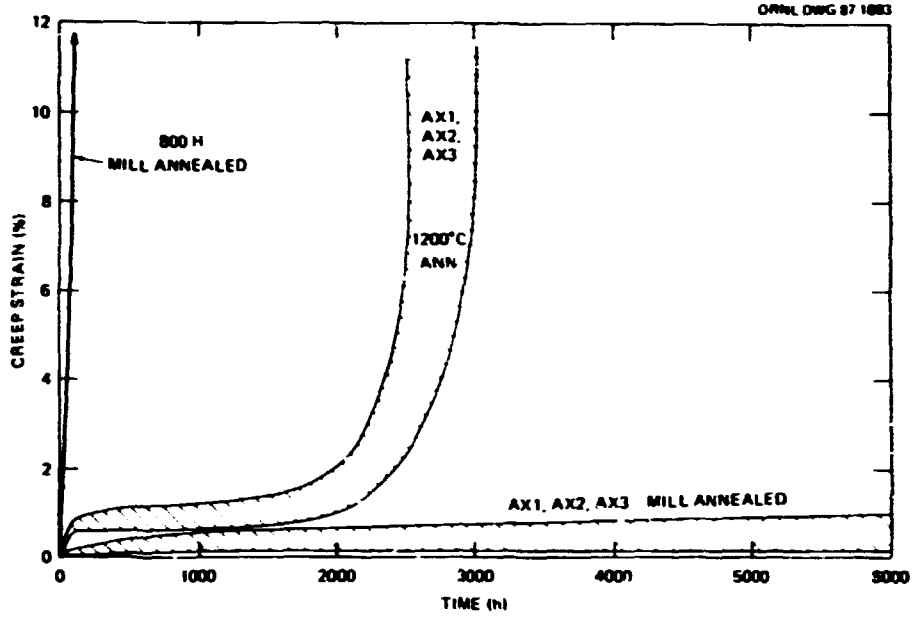

Fig. 12. Trend for creep curves of three heats of modified alloy 800H in the mill-annealed and 1200°C reannealed condition.

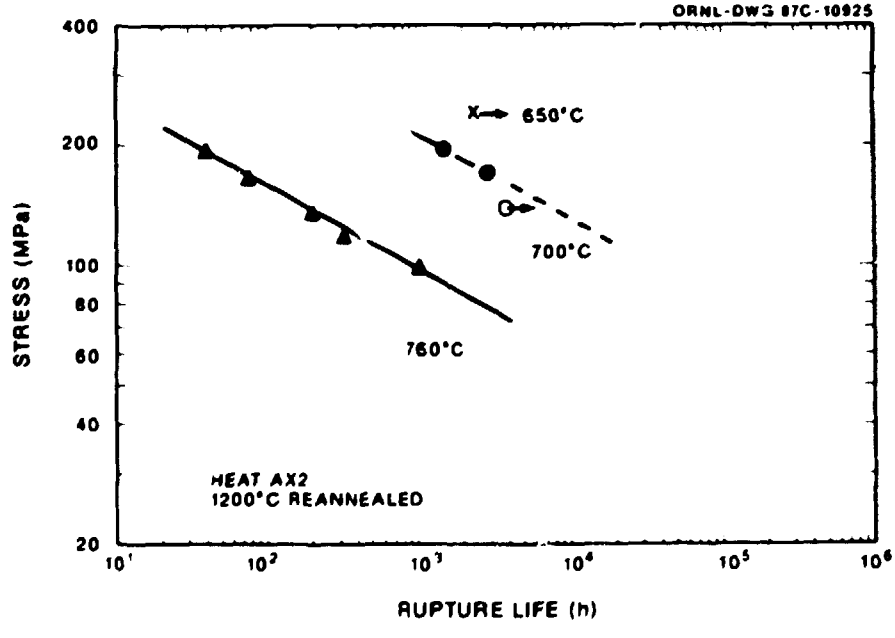

Fig. 13. Log stress vs log rupture life for 1200°C reannealed heat AX2.

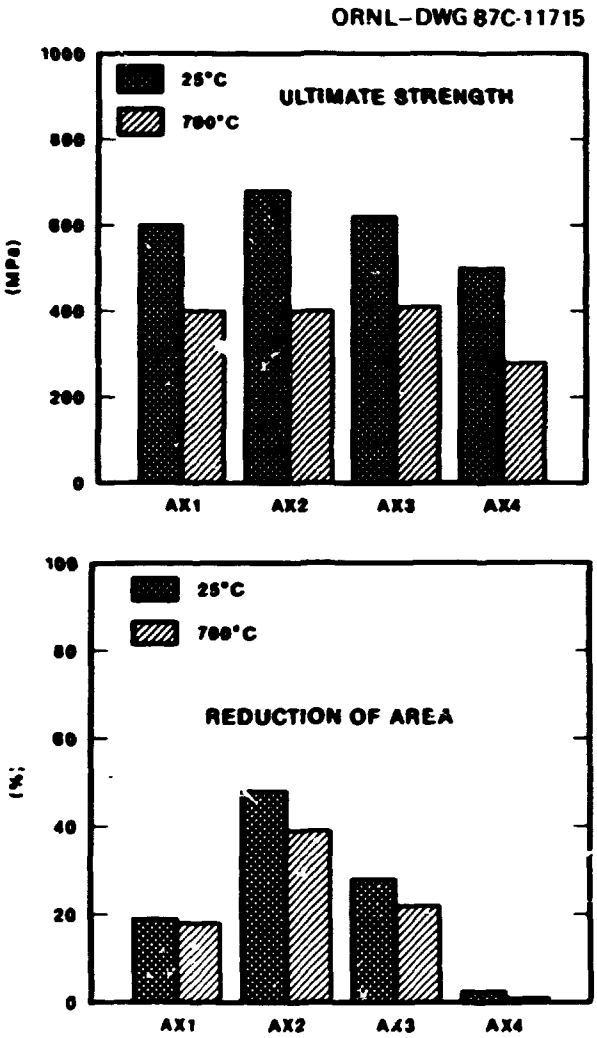

Fig. 14. Tensile data for weldments of modified alloy 800H at 25 and 700°C.

Table 3. Compositions for nickel aluminides (wt %)

Element	Alloy		
	NA1	NA2	IC221*
Cr	6.9	8.3	7.8
Al	9.0	8.5	8.2
Zr	0.35	0.35	1.7
Fe	13.1		
B	0.02	0.02	0.02
Ni	Bal	Bal	Bal

*Cast.

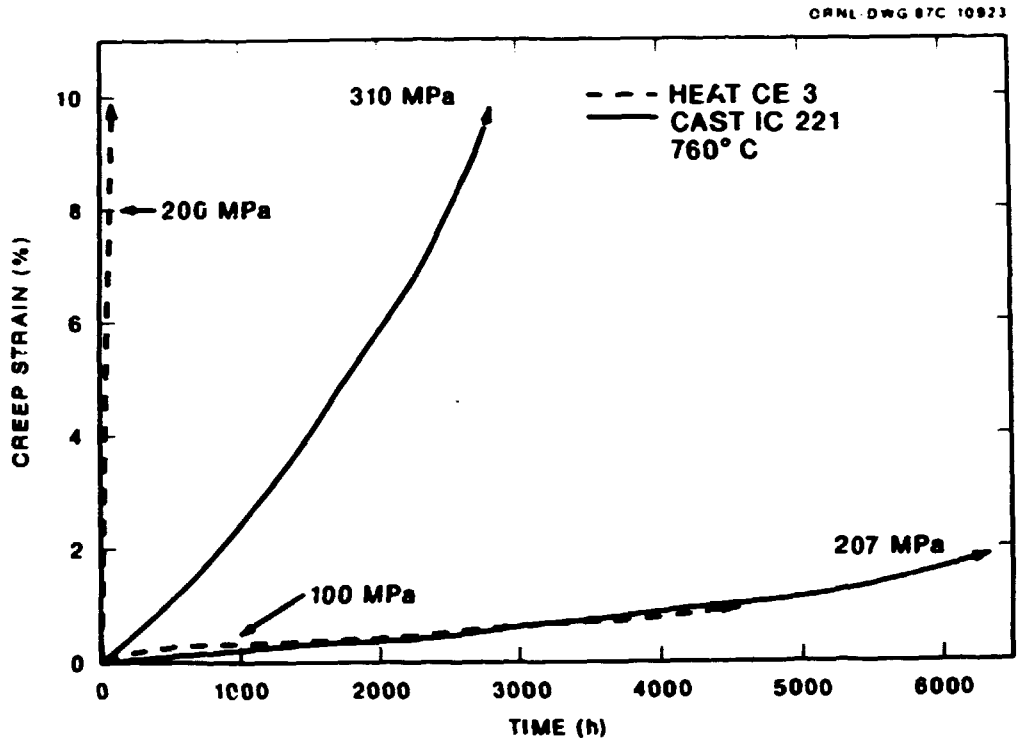

Fig. 15. Comparison of creep curves for nickel aluminides cast IC221 and mill-annealed heat CE3 at 760°C.

excellent strength and ductility of cast nickel aluminide at high temperatures. For example, creep curves for heat CE3 from lean stainless steels are included in Fig. 15 and indicate that cast IC221 has about twice the creep strength.

DISCUSSION AND CONCLUSIONS

Screening tests on various compositions of lean stainless steels is virtually complete, and several of the advantages and disadvantages of this group of alloys have been identified. The alloys were easy to produce and had good crep-rupture strengths in the 1200°C annealed condition, especially when cold or warn working was introduced. Creep rupture ductility was excellent. Relative to the commercial alloy 17-14CuMo stainless steel, there was an improvement in strength and ductility. The dependence of properties on composition was not very pronounced in the eight heats that were produced. Further optimization of heat treatment for strength

and ductility is possible,[14] and microstructural studies may show ways to futher improve the alloys.[5] On the problem side, there is evidence that some combinations of reannealing temperatures and aging conditions degrade strength substantially. Weldability is marginal at best, and even with a suitable filler metal, there is a tendency for hot cracking and heat-affected zone cracking. Reducing the phosphorus content to a maximum of 0.04% may relieve but not eliminate the problem. Poor oxidation resistance makes cladding on the fireside and chromizing on the steamside imperative.

The modified 800H alloys do not appear to offer any advantages over the lean stainless steels, other than improved oxidation resistance. The modified alloys are weaker and less weldable. Optimization of reannealing temperatures could improve creep rupture strength, however, and steels do seem to be stronger than alloy 800H.

Early efforts on nickel aluminides indicate major difficulties must be overcome in fabrication. Additional work on screening of candidate compositions and fabrication methods is needed.

In regard to control and near-commerical alloys, the screening tests on 17-14CuMo stainless steel continue to show this alloy to be a good candidate. Creep-rupture ductility could be improved by boron additions, which would be examined in task 2 of the program.

REFERENCES

1. R. W. Swindeman et al., *Alloy Design Criteria and Evaluation Methods for Advanced Austenitic Alloys in Steam Service*, ORNL-6274 (May 1986).

2. M. Gold and R. I. Jaffee, "Materials for Advanced Steam Cycles," *J. Mater. Energy Syst.*, pp. 138-45 (September 1984).

3. M. Tamura et al., "Promising Alloys for the Heat Exchangers of Advanced Coal-Fired Boilers," paper presented at Industrial Heat Exchanger Technology Conference, Pittsburgh, PA, November 5-8, 1985.

4. P. L. Rittenhouse et al., *Assessment of Materials Needs for Advanced Steam Cycle Coal-Fired Plants*, ORNL/TM-9735, August 1985.

5. P. J. Maziasz, "Microstructural Stability and Control for Improved Irradiation Resistance and High-Temperature Performance of Austenitic Stainless Steels," ASTM MICON Conference, Philadelphia, PA, May 14–16, 1986.

6. J. H. Harlow, "Metallurgical Experience with the Eddystone 5000 lb/in^2/200°F Unit No. 1," paper presented at Joint International Conference on Creep, Institute of Mechanical Engineers, London, 1963.

7. J. T. Venard and J. R. Weir, *In-Reactor Stress Rupture Properties of a 20Cr-25Ni, Niobium-Stabilized Stainless Steel*, ORNL/TM-881, August 1964.

8. H. Masumoti et al., "Development of a High Strength 25Ni-20Cr Austenitic Steel," paper presented at First International Conference on Improved Coal-Fired Power Plants, Palo Alto, CA, November 1986.

9. W. Wolowodirk et al., "Coal-Ash Corrosion Investigations," paper presented at First International Conference on Improved Coal-Fired Power Plants, Palo Alto, CA, November 1986.

10. J. A. McGurty et al., "Introduction of a New Class of High-Aluminum Austenitic Stainless Steel," in *Proceedings of the Conference on High-temperature Alloys: Theory and Design*, Bethesda, MD, April 9–11, 1984.

11. C. T. Liu and J. O. Stiegler, "Ductile Ordered Intermetallic Alloys," *Science* 226, 636–42 (November 1984).

12. R. W. Swindeman, "Variability of Data: Standards for Applications," pp. 71–92 in *Critical Issues in Materials and Mechanical Engineering*, PVP-Vol. 47, American Society of Mechanical Engineers, New York, 1981.

13. R. W. Swindeman, G. M. Goodwin, and P. J. Maziasz, *Procurement and Screening Test Data for Advanced Austenitic Alloys for 650°C Steam Service (Part 1, 14Cr-16Ni Steels and 20Cr-30Ni-Fe Alloys)*, ORNL/TM-10206/P1 (April 1987).

14. R. A. Carolan, B. Coulombe, and C-Y Li, " Mechanical Properties and Stability of Advanced Steam Cycle Materials," *AR&TD Fossil Energy Materials Program Quarterly Progress Report for the Period Ending September 30, 1986*, ORNL/FMP-86/4, (November 1986).

15. D. J. Smith and G. A. Webster, "Estimate of C^* Parameter for Crack Growth in Creeping Materials," *Second International Symposium on Elastic-Plastic Fracture*, American Society for Testing and Materials, Philadelphia, PA, October 1981.

16. A. Saxena, H. A. Ernst, and J. D. Landes, "Creep Crack Growth Behavior in 316 Stainless Steel at 594°C (1100°F)," *Int. J. Fract.* 23, 245–57 (1983).

17. D. L. Turner, Babcock & Wilcox, personal communication to R. W. Swindeman, Oak Ridge National Laboratory, November 18, 1986.

18. J. R. DiStefano, J. H. DeVan, and L. C. Fuller, *Assessment of Material Requirements for Advanced Steam Cycle Systems (<1100°F)*, ORNL/TM, report in preparation.

THE HIGH TEMPERATURE DEFORMATION AND MICROSTRUCTURAL STABILITY OF ADVANCED STEAM CYCLE MATERIALS

R.A. Carolan, B. Coulombe, and Che-Yu Li

Department of Materials Science and Engineering, Cornell University, Ithaca, NY 14853-1501

ABSTRACT

A series of modified austenitic type AISI 316 stainless steels have been evaluated, in terms of high temperature flow strength, for potential use in fossil energy plants. This series includes Ti/V/Nb stabilized 316 steels, and two copper modified 316 steel one stabilized with vanadium, titanium, and niobium, and a second stabilized with titanium and niobium. The effects of thermo-mechanical pre-treatment on alloy flow strength have also been investigated to optimize alloy strength before use. Load relaxation testing has been the primary technique used in this investigation.

INTRODUCTION

This paper reports the evaluation of the deformation characteristics of several candidate, advanced steam cycle materials, which are based on the stabilized AISI type 316 stainless steels strengthened by MC carbides with and without copper additions. These alloys were developed at Oak Ridge National Laboratory.

The mechanical design requirements for advanced steam cycle materials specifies a stress to rupture life of at least 14,000 psi (96 MPa) for 10,000 hrs at 700°C. A more desirable target is a rupture strength of 17,000 psi (117 MPa) for the same conditions. The evaluation of the flow strength of candidate alloys has therefore been a primary concern of this work. Another important objective of this work is to optimize the alloy composition and thermo-mechanical pre-treatment to achieve improved mechanical properties at elevated temperatures.

The high temperature microstructural stability has also been investigated.

The use of refractory metal additions such as Ti, Nb or V, to AISI type 316 stainless steel to form MC type carbides in the grain matrix to enhance creep strength is well known.[1] MC type carbides are more thermodynamically stable than the more common $M_{23}C_6$ type chromium rich carbides; having a higher melting point and a lower free energy of formation. In the normal range of service temperatures for type 316 type steels the lower (more negative) Gibbs free energy of formation of MC carbides[2] ensures small ripening rates.

The addition of copper is also known to improve the creep strength of type 316 steel although the strengthening mechanism is not clear.[3,4,5,6] Possible explanations of the copper effect are solid solution hardening and an increase in the stacking fault energy of the austenite lattice.[4] A representative alloy of this class is the 17/14 CuMo steel.[7]

Additional factors influencing the high temperature strength of type 316 steel include: 1) Solution treatment temperature, which changes the solubility of the MC type carbides and therefore the residual carbide content, as well as the austenite grain size. 2) Segregation effects that are influenced by both solution treatment temperature and quench rate; these effects can reduce matrix precipitation in favor of grain boundary precipitation of MC leading to a loss of matrix strength. 3) Cold work, which introduces a dislocation substructure to provide extra sites for MC nucleation. 4) Prior stabilization aging treatment that is often desired in the case of a stabilized steel to allow the precipitation of MC carbides.

This paper contains experimental results of an investigation of the effects of alloy composition thermo-mechanical pre-treatment and long term aging on the deformation properties at temperatures typical of the service temperatures of these materials. A brief discussion on the mechanisms involved will also be made.

EXPERIMENT

The alloys tested were received in the mill annealed condition, which contains a low level of cold work after casting by the vacuum induction melting process followed by electroslag remelting. Compositions are given in Table 1. CE 3 is a 316 steel that is both copper modified and MC stabilized with Ti, Nb, and V additions. CE 2, CE 1 and CE 0 steels are only stabilized with Ti, V, and Nb additions. The 17/14 CuMo steel is a commercial alloy containing copper additions and the stabilizing elements Nb and Ti. Hence the 17/14 CuMo steel is stabilized by using only two of the usual refractory element additions. CE 3 has three stabilizing additions.

The plates received were solution treated at 1150°C for 45 minutes except in the cases of specimens used to examine the effects of solution treatment temperature. Solution treatment was carried out in an inert atmosphere of argon. An argon gas stream was used to cool the

Table 1. The Compositions of the Modified 316 Alloys Tested.

	Content (wt %)					
Element	CE 0	CE 1	CE 2	CE 3	AX7	17/14 CuMo steel
CR	14.21	13.41	16.13	14.53	14.2	16.29
Ni	16.00	16.19	16.00	16.18	16.0	13.86
Al	0.05	0.03	0.04	0.03	--	--
Mo	2.45	2.30	2.25	2.41	2.48	1.96
Cu	0.03	0.04	0.03	1.96	1.50	3.07
P	0.071	0.076	0.069	0.071	0.073	0.014
B	0.005	0.005	0.005	0.007	0.005	--
N	0.015	0.016	0.017	0.012	0.024	0.025
V	0.57	0.52	0.58	0.56	0.53	0.07
Ti	0.24	0.21	0.31	0.27	0.18	0.21
C	0.072	0.085	0.079	0.086	0.073	0.098
Mn	1.80	1.64	1.89	1.65	1.65	0.83
S	0.007	0.008	0.008	0.008	0.008	0.015
Si	0.41	0.21	0.26	0.21	0.21	0.95
Nb/Ta	0.10	0.12	0.11	0.11	0.15	0.45
Ta	--	--	--	--	--	--
Co	<0.01	<0.01	<0.01	<0.01	0.009	0.04
Fe	bal.	bal.	bal.	bal.	bal.	bal.

specimens to room temperature. Dog-bone type tensile specimens had a gauge length of 2.28 cm (0.9 in), width 0.15 cm (0.06 in) and thickness 0.101 cm (0.04 in). After fabrication the specimens were given a further solution treatment for 15 min at 1150°C both to restore the full solution treatment and remove any cold work effects of fabrication. Precise levels of cold work were introduced by pre-staining with an Instron Universal Mechanical Testing System Model No. 1102 to deform the specimens to nominal tensile strains of 2 and 5%. Some specimens were tested in the solution treated and aged condition without cold work.

All the specimens except those for long term aging were given a stabilization aging treatment of 2 days at 850°C to precipitate MC type carbides. This is a standard heat treatment used for stabilized steels (840-900°C).[1] To examine long term aging effects some materials were given a treatment of 30 days at 800°C. This longer treatment is roughly equivalent to 50,000 hrs at 700°C the expected service temperature of these materials. This equivalence assumes no different phase boundaries are crossed as the aging temperature is decreased.

Load relaxation testing was used as the principle experimental tool for evaluating the flow properties. Testing was performed in the same Instron machine mentioned above. The principles of the load relaxation test and the mechanical data analysis are described elsewhere.[8] The load relaxation test consisted of deforming a tensile specimen at a constant displacement rate to a chosen plastic strain. The displacement rate used throughout this work was 4.23×10^{-3} cm/s (1.667×10^{-4}, in/s). Once a preselected plastic strain was reached, the crosshead of the Instron was fixed. The specimen continued to deform due to the elastic unloading of the test machine. The specimen deformed resulting in relaxation. The output of a load cell, was monitored with respect to time by a digital acquisition system. From the accumulated data the stress/strain rate relationship can be found. The rate of relaxation is related to the plastic strain rate of the specimen through the modulus of the test system including that of the specimen. The data is presented in the form of a logarithmic plot of stress/plastic strain rate or flow curve typically over a strain rate

range of about 10^{-3} to 10^{-8} s^{-1}. To examine the flow properties of a specimen after a given thermo-mechanical pre-treatment, the relaxation runs were made at a plastic state near the yield strain (0.2% strain) so that the effect of work hardening during preloading is negligible.

Comparison of the flow curves produced at the yield strain are used for the purpose of evaluating alloy composition and thermo-mechanical pre-treatment effects. The strain rate of a specimen in load relaxation can be shown to be comparable to the steady state creep rate under similar loads as shown in Fig. 1 provided the specimens have similar thermo-mechanical histories.[9]

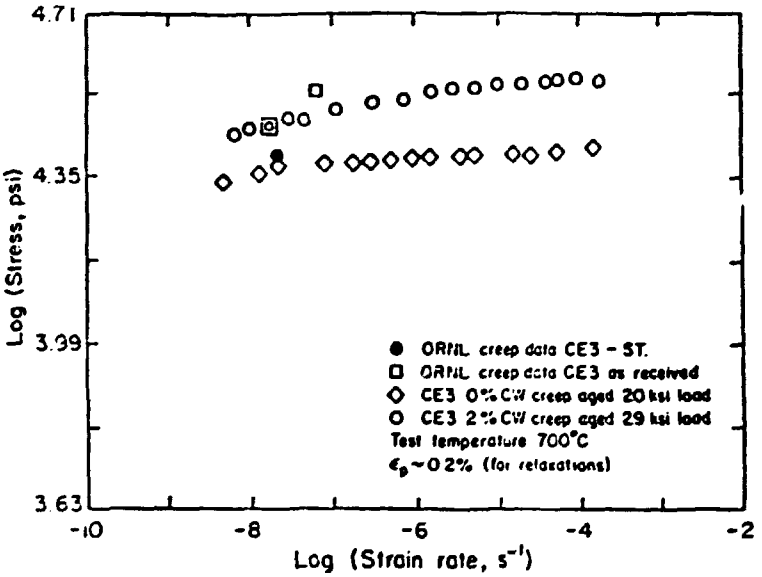

Fig. 1. Comparison of the load relaxation data of alloy CE 3 conditions solution treated for 1 hr, at 1150°C, creep aged for 2 days at 700°C with and without prior cold work and tested at 700°C (ε_p = 0.2% nominally) with creep data.

RESULTS

THE EFFECT OF COLD WORK AND ALLOY COMPOSITION

Figure 2 shows the effect of cold work on alloy CE 3, one of the copper modified and stabilized steels after a solution treatment of 1 hr at 1150°C, cold working, and a stabilization treatment of 2 days at 850°C and testing at 650°C. The load relaxation test was made at the

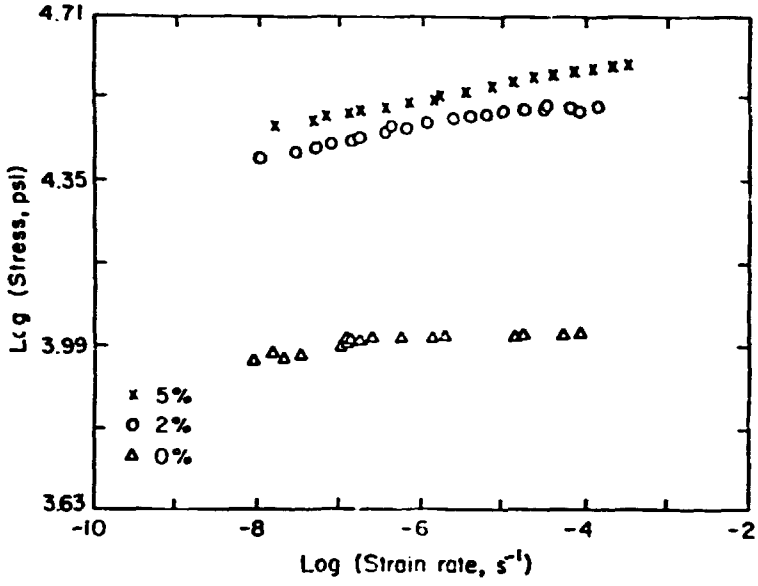

Fig. 2. The effects of cold work on the load relaxation data of alloy CE 3 solution treated for 1 hr at 1150°C, aged for 2 days at 850°C and tested at 650°C (ε_p = 0.2% nominally).

yield strain. The relaxation data shows a large increase in flow strength over the 0-2% cold work interval but a much smaller increase over the 2-5% cold worked interval. Alloy CE 3 is the most promising alloy of the series. It derives its strength mainly from a favorable response to cold work as shown in Fig. 2.[10] Figure 3 compares the

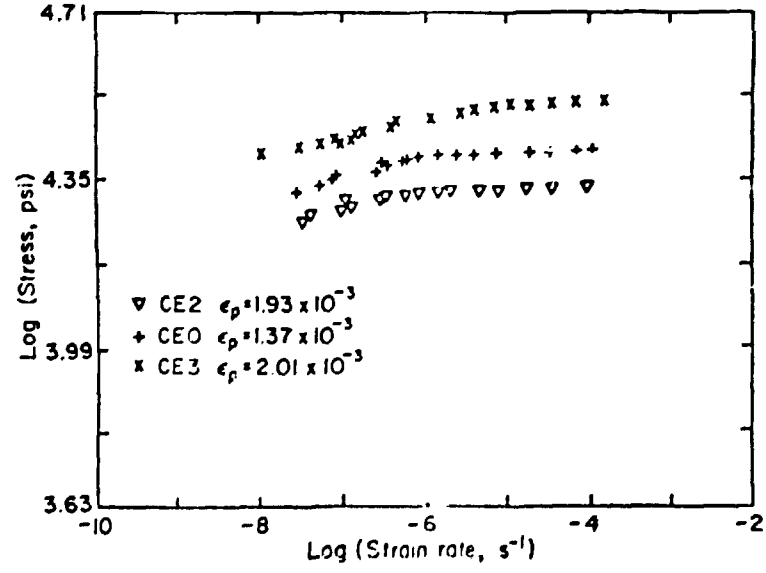

Fig. 3. Comparison of the load relaxation data of alloys CE 0, CE 2, and CE 3 solution treated for 1 hr at 1150°C, 2% cold worked, aged for 2 days at 850°C and tested at 650°C (ε_p = 0.2% nominally).

effects of 2% cold work on alloy CE 3 with the alloys CE 2, and CE 0. CE 2 and CE 0 are MC stabilized 316 stainless steels. The alloys were solution treated for 1 hr at 1150°C, 2% cold worked, stabilized by aging for 2 days at 850°C and tested at 650°C. The load relaxation tests were made at the yield strain. Alloy CE 3, the copper modified and stabilized steel performs better than the other stabilized steels CE 2 and CE 0, after cold working according to Fig. 3. Figures 4 and 5 compare alloy CE 3 with incoloy 800H and another alloy AX7. All specimens were given a solution treatment of 1 hr at 1150°C, 2% cold worked, aged for 2 days at 850°C and tested at 650°C. The load relaxation tests were made at the yield strain. Both figures show that CE 3 has superior flow strength in this condition compared to both incoloy 800H and alloy AX7. It should be noted that alloy AX7 has virtually the same composition as CE 3 except a lower Titanium level. Titanium is one of the stabilizing additions to the steel. Apparently minor compositional changes of this nature can be significant. Incoloy 800H is a higher Ni/Cr austenitic stainless steel that does not have a stabilized structure.

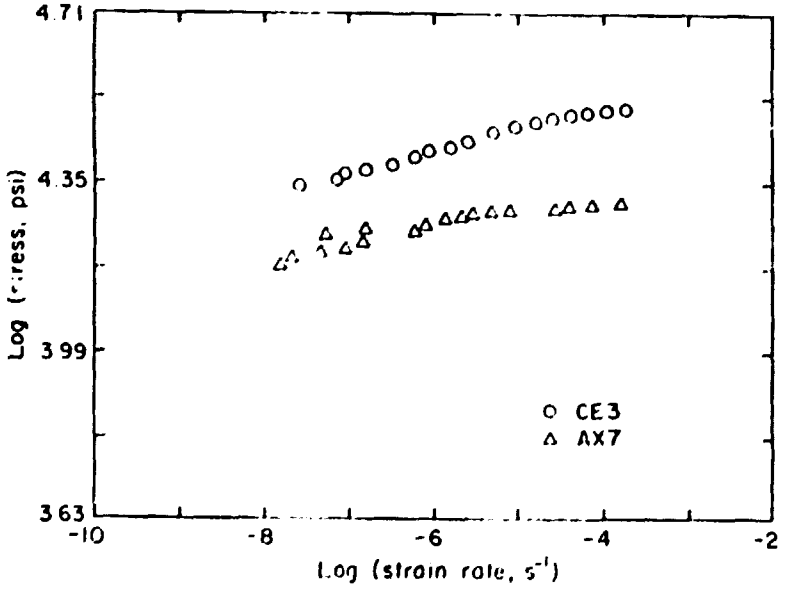

Fig. 4. Comparison of the load relaxation data of alloys AX7 and CE 3 solution treated for 1 hr at 1150°C, 2% cold worked, aged for 2 days at 850°C and tested at 650°C (ε_p = 0.2% nominally).

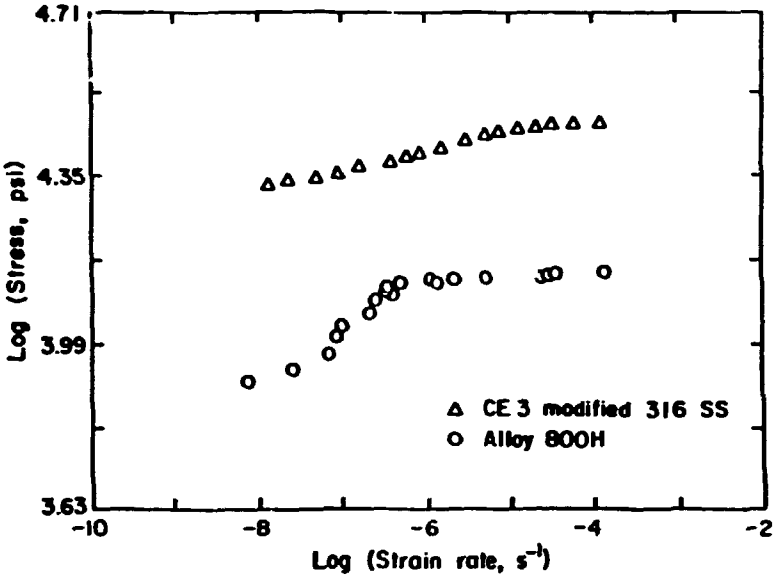

Fig. 5. Comparison of the load relaxation data of alloys 800H and CE 3 solution treated for 1 hr at 1150°C, 2% cold worked, aged for 2 days at 850°C and tested at 650°C (ϵ_p = 0.2% nominally).

THE EFFECTS OF TEST TEMPERATURE

Figure 6 shows the effect of temperature on alloy CE 3. All specimens were solution treated for 1 hr at 1150°C, 2% cold worked, aged for 2 days at 850°C and the load relaxation tests were performed at the yield strain. This data suggests that even at a test temperature of 750°C, the flow strength of this alloy is retained to an adequate level.

THE EFFECTS OF LONG TERM AGING

Figure 7 shows the effect of long term aging on three selected alloys that represent the three classes of stabilized steel tested here. All the alloys received a solution treatment of 1 hr at 1150°C, 5% cold work, and were aged for 30 days at 800°C. The load relaxation data was obtained at 650°C at the yield strain of the specimen. The effects of copper modification/stabilization on the load relaxation properties of CE 3 become more pronounced after a longer aging treatment (compare Figs. 3 and 7). The vertical stress scale in these figures is split so that the data of the three alloys can be included. The left hand scale represents the 17/14 CuMo steel and CE 3, CE 1 is

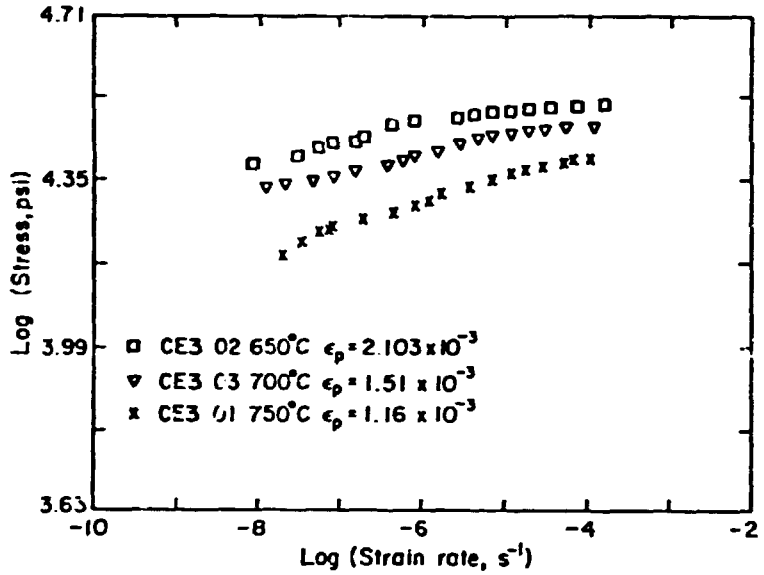

Fig. 6. The effects of test temperature on the load relaxation data of alloy CE 3 solution treated for 1 hr at 1150°C, 2% cold worked, aged for 2 days at 850°C (ϵ_p = 0.2% nominally).

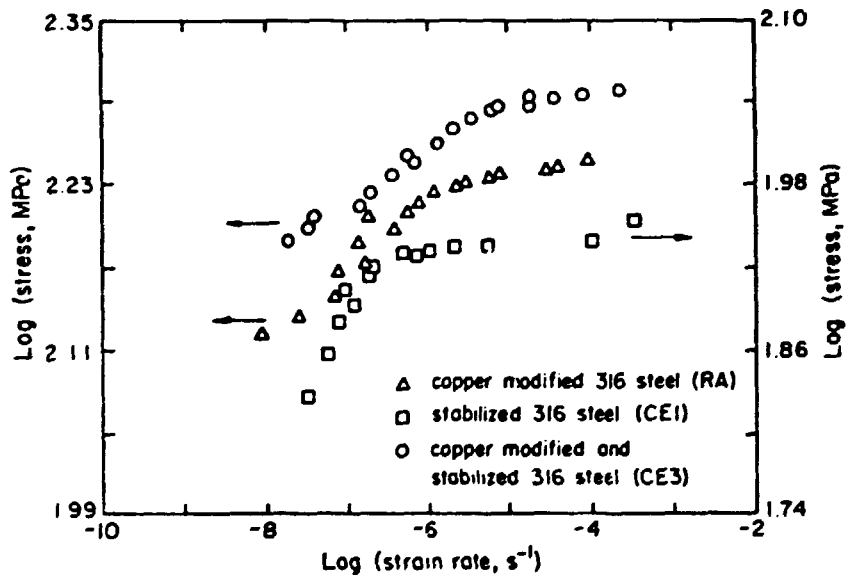

Fig. 7. Comparison of the load relaxation data of alloys CE 3, CE 1 and 17/14 CuMo steel (RA) solution treated for 1 hr at 1150°C, 2% cold worked, aged for 30 days at 800°C (ϵ_p = 0.2% nominally).

represented by the right hand scale. Figure 7 shows that with 5% cold work prior to stabilization aging both the copper containing steels (17/14 CuMo and CE 3) have remaining strength of about twice that of the stabilized steel (CE 1) in the same pre-treated condition. Also

significant is that CE 3 has a higher strength than the 17/14 CuMo steel after long term aging.

Figure 8 shows the effect of long term aging on the 17/14 C· 'o steel. The material was solution treated for 1 hr at 1150°C, 5% cold worked, aged, and then tested at 700°C. The load relaxation tests were performed at the yield strain. It is clear that significant hardening of this alloy occurs compared to the short term agin$_b$. Adequate flow strength is retained apparently at the test temperature of 700°C showing the advantage of combined copper and stabilizing additions.

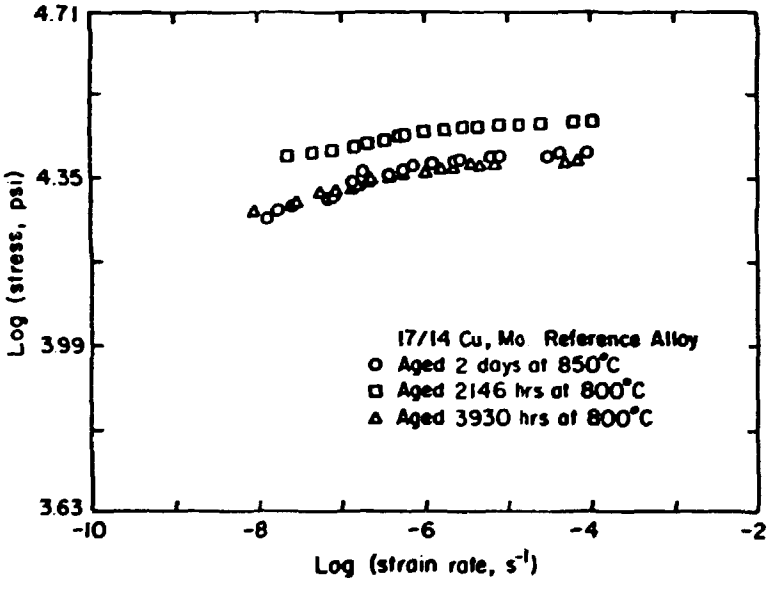

Fig. 8. The load relaxation data of the 17/14 CuMo alloy solution treated for 1 hr at 1150°C, 5% cold worked, aged for various times and tested at 700°C (ε_p = 0.2% nominally).

THE EFFECTS OF SOLUTION TREATMENT TEMPERATURE AND QUENCH RATE

Figure 9 shows the effect of solution treatment temperature on alloy CE 3. All the material was gas quenched from solution treatment temperature to ambient temperature, 2% cold worked, aged for 2 days at 850°C and tested at 700°C. The relaxation tests were performed at the yield strain. Figure 9 shows clearly that the 1150°C solution treatment temperature gives the optimum flow strength. Figure 10 shows the effect of quench rate at the optimum solution treatment temperature

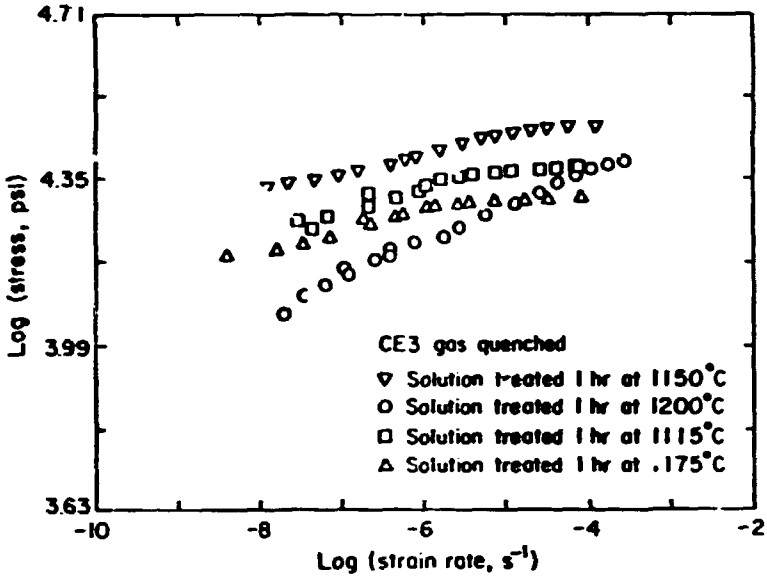

Fig. 9. The effects of solution treatment temperature on the load relaxation data of alloy CE 3, solution treated for 1 hr, with 2% cold work, aged for 2 days at 850°C and tested at 700°C (ε_p = 0.2% nominally).

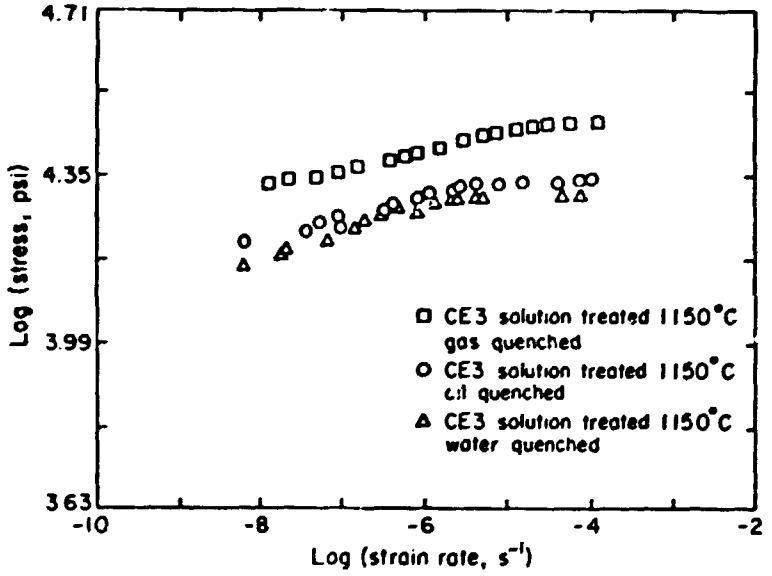

Fig. 10. The effects of quench rate on the load relaxation data of alloy CE 3 solution treated for 1 hr at 1150°C, 2% cold worked, aged for 2 days at 850°C and tested at 700°C (ε_p = 0.2% nominally).

(1150°C). The specimens were solution treated for 1 hour, quenched, 2% cold worked, aged for 2 days at 850°C and tested at 700°C. The load relaxation tests were performed at the yield strain. There is a clear

quench rate effect, the gas quenched material being stronger. No quench rate effect was found at the lower solution treatment temperature of 1115°C.[9]

THE EFFECTS OF STABILIZATION AGING TREATMENT

Figure 11 shows the effect of stabilization treatment on alloy CE 3. The specimens were solution treated at 1150°C for 1 hr, 2% cold worked, stabilized and then tested at 700°C. The relaxation tests were performed at the yield strain. It is clear that the 2 days at 850°C treatment offers the optimum treatment in terms of time and flow strength.

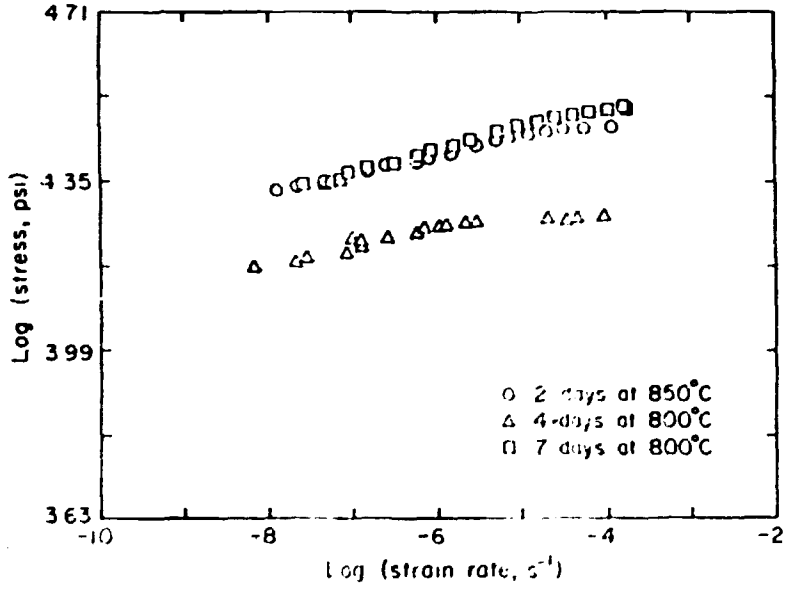

Fig. 11. The effects of stabilization treatment on alloy CE 3 solution treated at 1150°C for 1 hr, 2% cold worked, and tested at 700°C (ε_p = 0.2% nominally).

DISCUSSION

The results of mechanical testing have shown that alloy CE 3 performs better than all the other alloys when given an optimum pretreatment. This involves a solution treatment at 1150°C, gas quenching, a small amount of prior cold work (typically 2%), and stabilization aging of 2 days at 850°C. Alloy CE 3 is a copper modified, Ti,

Nb, V stabilized alloy. The effects of copper addition have been described elsewhere[3,4,5,6,7,13] and will be given a brief discussion here. Basically copper is thought to increase the stacking fault energy of the austenite lattice[4] and make the nucleation of MC stabilizing carbides on stacking faults and dislocations more favorable. Thus the copper containing steels show better flow strengths due to the more heavily MC decorated dislocation networks in the grain matrix after cold work. This proposed mechanism is supported by transmission electron microscopy investigations.[13] That CE 3 performs better than the 17/14 CuMo steel is due to the use of vanadium as an extra stabilizing element and probably due to its lower silicon content. Since the essence of stabilized steels is the formation of a strong MC type precipitate/dislocation network it is clear that they require prior cold work to form the dislocation networks before stabilization aging. The effects of the different stabilization treatments are related to the amount of supercooling, that effects nucleation rates and to diffusion rates which will be lower for the lower stabilization temperatures.

During this work it has also been shown that solution treatment has a strong effect on alloy strength. The reason for the 1150°C peak in flow strength appears to be due to two competing effects. The first is that higher solution treatment temperatures enable better dissolution of any stabilizing element compounds (nitrides, carbonitrides and carbides) that can result in finer re-precipitation of MC carbides during stabilization. However when higher solution treatment temperatures are used alloys are more likely to experience non-equilibrium segregation effects during cooling and it has been shown that the stabilizing elements can segregate particularly to grain boundaries.[14] This leads to the precipitation of grain boundary MC and less grain matrix MC on the dislocations. The effects of quench rate are also related to non-equilibrium segregation.

CONCLUSIONS

1) Alloy CE 3 the copper modified Ti/Nb/V stabilized 316 steel is the strongest alloy tested here when it is used with an optimum pretreatment.

2) The optimum pre-treatment involves solution treatment at 1150°C followed by 2% cold work and a stabilization aging treatment of 2 days at 850°C.
3) The effects of copper are to increase the stacking fault energy of the austenite lattice that favors enhanced nucleation of MC type precipitates on the dislocation structure developed during cold work when the material is given a stabilization aging treatment before use.

REFERENCES

1. Marshall, P. "Austenitic stainless steels; Microstructure and mechanical properties," Elsevier, 1984, p. 48.
2. Beckitt, F.R. and Gladman, T. "British Steel Corporation Res. Rep. SSD 818, 5, 9, 1972.
3. Maziasz, P.G. "Microstructural stability and control for improved irradiation resistance and high temperature performance of austenitic stainless steels," Conf. Proc. Microstructural control 1986 (Micon-86) ASTM-STP, American Society for Testing and Materials, Philadelphia, PA, to be published, 1987.
4. Le May, I and Schetky, L. "Copper in iron and steel," Wiley, 1982, pp. 144-45.
5. Shinoda, T. et al. International Conf., "Creep and Fatigue in Elevated Temperature Applications," I.M.E., London, 1973, pp. 1751-59.
6. Chapman, E.C. and Lorenz, R.E. A.S.M.E. J. Engr. Power, Oct. 1960, pp. 275-85.
7. Smith, G.V. (ed.). "Characterization of materials for service at elevated temperatures," ASME Publication No. MPC 7, 1978.
8. Lee, D. and Hart, E.W. Met. Trans. 2, 1971, pp. 1245-1248.
9. Carolan, R.A. et al. Quarterly Report for the period July-Sept. 1986, Report No. ORNL/FMP-86/4 Cu-2.
10. Carolan, R.A. et al. Quarterly Report for the period Jan.-Mar. 1986, Report No. ORNL/FMP-86/2 Cu-2.
11. Horton, C.A.P. and Gates, R.S. Mat. Sci. and Eng. 27, 1977, pp. 105-133.

12. Askill, J. "Tracer Diffusion Data for Metals, Alloys, and Simple Oxides," Plenum, NY, 1970, p. 34.

13. Carolan, R.A. et al. "The Strengthening Mechanisms in AISI 316 stainless steel," DOE Report No. ORNL/Sub/85-27488/01, Cornell University, 1987.

14. Carolan, R.A. and Faulkner, R.G. In Int. Conf. "Behaviour and Nuclear Applications of Stainless Steels at Elevated Temperatures," Varese, Italy, 1981. Pub.: Inst. of Met., London, 1981.

DEVELOPMENT OF NICKEL-IRON ALUMINIDES*

C. T. Liu, J. V. Cathcart, G. M. Goodwin,
J. A. Horton, E. H. Lee, and J. J. Campbell

Metals and Ceramics Division
Oak Ridge National Laboratory
P.O. Box X
Oak Ridge, TN 37831-6117

ABSTRACT

The objective of this program is to design and characterize new, improved high-temperature materials based on boron-doped Ni_3Al + Fe for structural use in advanced coal conversion systems. Chromium is a key alloying element that promotes a rapid formation of protective oxide scales and improves oxidation and corrosion resistance and environmental embrittlement in nickel-iron aluminides. Alloying with 3 to 7 at. % Cr dramatically reduces dynamic embrittlement in oxidizing environments at 400 to 800°C. Chromium and iron additions increase the stability of the bcc-ordered B2 phase which is brittle at room temperature and weak at elevated temperatures. The formation of the B2 phase in the aluminides leads to lowering the tensile ductility at lower temperatures and the strength at higher temperatures. The study of the alloying effects has led to the development of the aluminide with the composition:
Ni–18.5 ± 0.5% Al–10 ± 1.0% Fe–7 ± 0.5% Cr–0.2% Zr–0.1% B (at. %).

Corrosion studies have demonstrated that chromium additions of 7% or greater were very effective in minimizing sulfur attack on nickel-iron aluminides. Sulfidation protection can also be afforded by oxide films produced in air; however, the oxidation temperature should be 1000 to 1050°C, and the alloys must contain 3% or greater of chromium. The nickel-iron aluminides developed were successfully welded using both the electron beam and gas tungsten arc processes.

---

*Research sponsored by the U.S. Department of Energy (DOE), AR&TD Fossil Energy Materials Program (DOE/FE AA 15 10 10 0), under contract DE-AC05-840R21400 with Martin Marietta Energy Systems, Inc.

INTRODUCTION

Current structural alloys including austenitic stainless steels and nickel-base superalloys generally do not have an adequate combination of strength, ductility, and corrosion resistance required for structural uses in advanced coal conversion systems. Coating materials such as FeCrAl, on the other hand, possess good corrosion resistance but lack adequate strength at high temperatures. There is thus a strong need for the development of new, improved alloys for structural applications in hostile environments at elevated temperatures. The objective of this task is to design and characterize new structural materials based on Ni_3Al alloyed with iron additions.

The ordered intermetallic alloy, Ni_3Al, has unique properties that make it attractive for structural use at elevated temperatures.[1-3] The aluminide is resistant to oxidation because of its ability to form protective oxide scales. Unlike conventional alloys, the yield stress of the aluminide displays an increase rather than a decrease with increased temperature. The major obstacle that limits the use of the aluminide as an engineering material is its low ductility and brittle intergranular fracture in polycrystalline forms. This problem has been solved recently by microalloying the parts-per-million range of boron additions, which dramatically improve the ductility and reduce the tendency for brittle grain-boundary fracture.[4-7] By control of boron content, aluminum level, and thermomechanical treatment, a tensile ductility of greater than 50% was achieved at room temperature.[4,5]

The ductile nickel aluminide was selected as the base material for development of nickel-iron aluminides.[8-15] Iron additions were made to boron-doped Ni_3Al for the purposes of (1) strengthening Ni_3Al by solid-solution hardening, (2) lowering the material cost by reducing the nickel content, and (3) improving the hot ductility of Ni_3Al through formation of a B2 phase (ordered bcc phase). Our previous work showed that alloying with 10% Fe or above effectively increases the strength of Ni_3Al below 800°C.[15] The hot ductility and fabricability of Ni_3Al can be substantially improved by adding about 15 at. % Fe. Hence, the current development of nickel-iron aluminides has focused on Ni–20% Al–15% Fe–0.1% B (at. %).

This alloy development program includes three subtasks. The first one is a basic alloy development effort, which attempts to improve the mechanical and metallurgical properties of nickel-iron aluminides by control of alloy compositions and alloy additions. Both micro- and macroalloying processes were employed to improve the properties of the aluminides, particularly at elevated temperatures. The second subtask is to determine the corrosion behavior of nickel-iron aluminides in sulfidizing environments. This study provides input into the development of corrosion resistant aluminides suitable for use in advanced coal conversion systems. The third subtask is to evaluate the weldability of nickel-iron aluminides. The primary goal of this subtask is to understand and improve the weldability of selected aluminides through control of welding parameters and alloy composition.

BASIC ALLOY DEVELOPMENT

The alloy development started with the composition of Ni—20% Al—15% Fe—0.1% B, in which 15 at. % Fe was added to boron-doped Ni_3Al.* The alloy development involved the following steps: (1) characterization of the mechanical and metallurgical properties of base compositions, (2) identification of problem areas for improvement, and (3) improvement of the properties by alloy additions. The selection of alloy additions was based on empirical relationships and physical metallurgy principles.

Aluminide alloys with nominal compositions were all prepared by arc melting and drop casting, using pure metals and Ni—4 wt % B and Ni—4 wt % Ce master alloys. Cerium at a level of 5 wt ppm was added to tie up sulfur, a trace impurity in nickel-base alloys. The ingots were homogenized for 5 h at 1000°C and then sectioned for cold and hot fabrication. The cold fabrication involved repeated rolling at room temperature with intermediate anneals at 1000 and 1050°C. The hot fabrication was performed by forging or rolling at 1100 to 1200°C in stainless steel jacket. The hot-fabricated alloy plates about 1.5 mm thick were then cold rolled to 0.8 mm for property evaluation.

---

*Unless otherwise noted, all alloy concentrations in this paper are given in atomic percent.

Tensile properties of aluminides were determined at temperatures to 1200°C either in vacuum or in air. Tensile tests were performed on 0.8 mm-thick sheet specimens with a gage section of 12.7 × 3.1 mm at a crosshead speed of 2.5 mm/min. All specimens were heat treated at 1050°C for recrystallization and 1 d at 800°C for fcc ($L1_2$) ordering. The test temperature was monitored by a Pt vs Pt-10% Rh thermocouple located at the center of the gage section. Creep tests were conducted at 760°C at 138 MPa (20 ksi) in air. Limited data were also obtained at 138 and 276 MPa in vacuum.

BORON-DOPED NICKEL-IRON ALUMINIDES CONTAINING 15.5% Fe AND 0.25% Hf(Zr)

Previous studies indicated that the high-temperature properties of Ni_3Al can be improved by alloying with hafnium or zirconium.[2,8,16] Accordingly, small amounts of Hf or Zr were added to the Ni–19.8% Al–15.5% Fe base. The Hf or Zr content is limited to less than 0.3%; otherwise, it lowers the hot fabricability of the nickel-iron aluminides. Extensive characterization was made on two base compositions (at. %):

IC-159: Ni–19.8% Al–15.5% Fe–0.25% Hf–0.07% B,

IC-165: Ni–19.8% Al–15.5% Fe–0.25% Zr–0.07% B.

These two aluminides were successfully fabricated into sheet stock by repeated cold rolling or hot working at 1100°C.

The microstructure of IC-159 was examined by transmission electron microscopy (TEM). Two heat treatments of IC-159 were examined: (1) after a standard anneal for 1 h at 1050°C for recrystallization and (2) after extensive aging at 760°C (e.g., 24 to 200 h) for maximizing the ordered fcc phase ($L1_2$), γ'. The ordered bcc phase (B2), β, is present after the high-temperature age but almost completely transforms to γ' structure upon aging at 760°C (Fig. 1). Some small regions of $\gamma' + \gamma$ (disordered fcc) are present even after aging at 760°C. The composition of the β phase, as compared to the adjacent matrix (γ'), was aluminum enriched by 12%, same iron level, and depleted in Ni by 12% and Hf by 0.2%. A small amount of β particles was observed in IC-159 annealed at 760°C [Fig. 2(a)].

Tensile properties of IC-159 and IC-165 were determined in both vacuum (1×10^{-5} torr) and air. The alloys exhibited an increase in yield strength with temperature, with a peak strength of 680 MPa around 600°C.

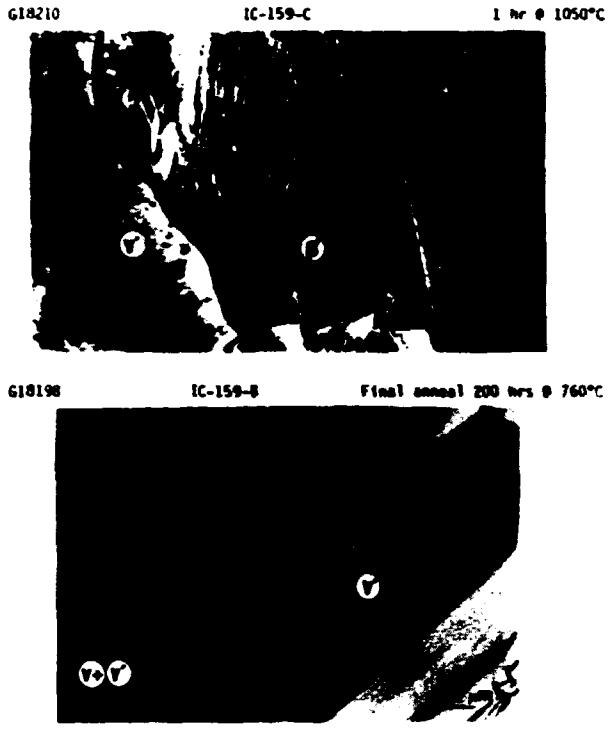

Fig. 1. TEM micrographs of IC-159 annealed for (a) 1 h at 1050°C, and (b) 2 d at 1000°C followed by 200 h at 760°C. Regions marked γ' have the Ll_2 ordered structure, β' have an ordered B2 structure, and γ have a disordered fcc structure. Note that β' region in (a) is twinned with a martensitic appearance.

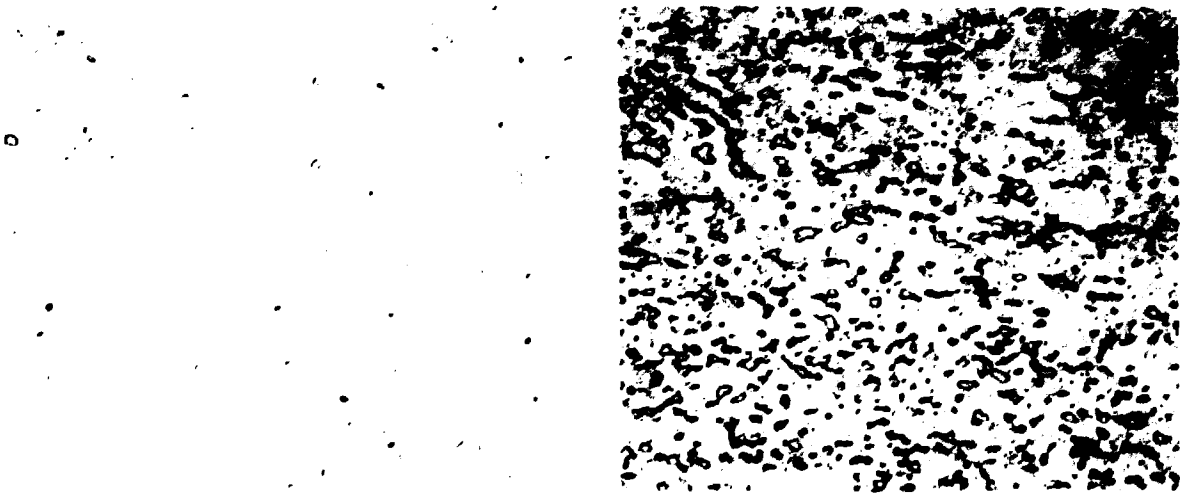

Fig. 2. Optical micrographs of nickel-iron aluminides: (a) IC-159 (0% Cr) annealed 2 d/1000 + 1 d/760°C; 200×. (b) IC-296 (5% Cr) annealed 1 h/1050°C + 1 d/800°C; 300×.

Above that temperature, the strength decreases with temperature, and approaches 200 MPa at 1000°C. Figure 3 compares the tensile ductility of IC-159 tested in air and in vacuum. The alloy has a tensile elongation of about 40% at room temperature. The alloy showed distinctively lower ductility when tested in air than in vacuum at temperatures above 400°C, and the worst embrittlement occurred around 600 to 800°C. The loss in ductility is accompanied by a change in fracture mode from transgranular to intergranular, indicating the embrittlement of grain boundaries during air tests.

In order to understand the embrittlement mechanism, a set of IC-159 specimens was preoxidized in air for 30 min at 1000°C plus 5 h at 850°C and then tensile tested in vacuum at temperatures to 1200°C. The purpose of these tests was to study the effect of preoxidation and oxygen penetration on tensile properties. The test results show that the tensile properties of the aluminides are not much affected by the preoxidation, indicating that the embrittlement is not associated with oxygen penetration along the grain boundaries. A detailed study of environmental

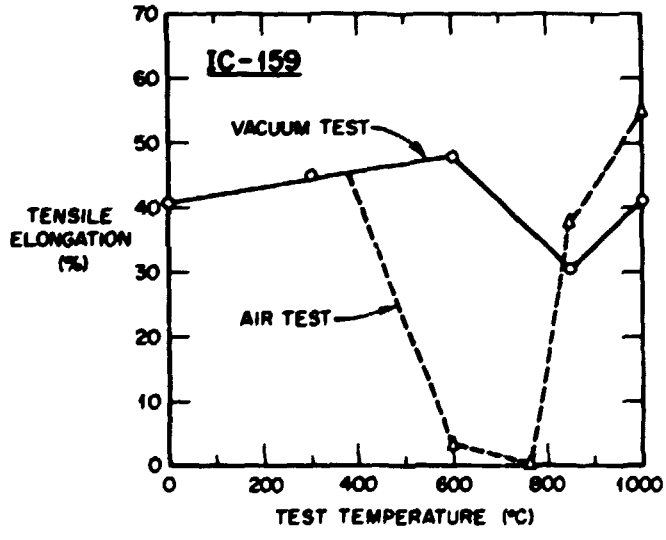

Fig. 3. Comparison of tensile ductility of IC-159 tested in vacuum and air, showing environmental embrittlement in air at temperatures 400 to 800°C.

embrittlement in Ni_3Al alloys[17] reveals that the embrittlement is due to a dynamic effect rather than a static one. The embrittlement mechanism involves chemisorption of oxygen on specimen surfaces and weakening of atomic bonding across grain boundaries during testing of the aluminides in oxidizing environments at elevated temperatures. The localized high stresses, generated during early stages of plastic deformation, nucleate and subsequently propagate microcracks along grain boundaries, leading to a premature failure.

CHROMIUM-MODIFIED NICKEL-IRON ALUMINIDES

15.5% Fe Nickel-Iron Aluminides Containing 0 to 7% Cr

A potential solution to the environmental embrittlement is to add alloy additions that promote a rapid formation of protective oxide films that separate base metal from gaseous oxygen. Our alloy development of nickel aluminides indicates that no elements except chromium have a beneficial effect on reducing dynamic embrittlement in oxidizing environments at elevated temperatures.[17] Accordingly, a series of nickel-iron aluminide alloys was prepared in which chromium was added and the nickel content correspondingly reduced. All the alloys were fabricated into sheet stock without difficulty. Table 1 lists the chromium concentration in the alloys together with tensile properties obtained at temperatures to 850°C in air. The yield strength increases with chromium and reaches a maximum around 3% Cr. The chromium addition has a dramatic effect on the 600 and 760°C ductilities of the nickel-iron aluminide (IC-159), as shown in Fig. 4. The base aluminide containing no chromium elongated less than 4% at these temperatures. The elongations increase sharply with increasing chromium and reach 35% for the alloy with 7% Cr. These results clearly demonstrate that the environmental embrittlement can be effectively reduced by alloying with chromium.

The creep properties of the chromium-modified alloys were determined at 138 MPa and 760°C. Limited creep data in Table 2, Part (a), indicate that the creep resistance of the nickel-iron aluminides decreases with increasing the chromium content. Alloying with 7% Cr lowers the

Table 1. Effect of chromium content on tensile properties of nickel-iron aluminides containing 15.5% Fe (tested in air at a crosshead speed of 2.5 mm/min)

Alloy number	Cr concentration (at. %)	Strength, MPa (ksi)		Elongation (%)
		Yield	Ultimate	
		Room temperature		
IC-159	0 (base alloy)	533 (77.4)	1343 (195)	40.3
IC-197	1.5	531 (77.1)	1323 (192)	41.3
IC-167	3.0	618 (89.7)	1399 (203)	28.0
IC-199	6.0	594 (86.2)	1268 (184)	31.5
IC-168	7.0	624 (90.6)	1357 (197)	24.6
		600°C		
IC-159		648 (94.0)	737 (107)	3.4
IC-197		641 (93.0)	779 (113)	8.3
IC-167		687 (99.7)	965 (140)	22.9
IC-199		650 (94.3)	978 (142)	>16.0
IC-168		515 (74.7)	909 (132)	35.6
		760°C		
IC-159		503 (73.0)	503 (73.0)	0.4
IC-197		562 (81.5)	662 (96.1)	13.0
IC-167		587 (85.2)	663 (96.2)	28.2
IC-199		548 (79.5)	656 (95.2)	22.7
IC-168		548 (79.6)	610 (88.5)	35.4
		850°C		
IC-159		379 (55.0)	402 (58.3)	38.8
IC-197		397 (57.6)	426 (61.9)	37.7
IC-167		360 (52.3)	407 (59.0)	27.1
IC-199		342 (49.7)	393 (57.0)	14.8
IC-168		285 (41.3)	319 (46.3)	34.7

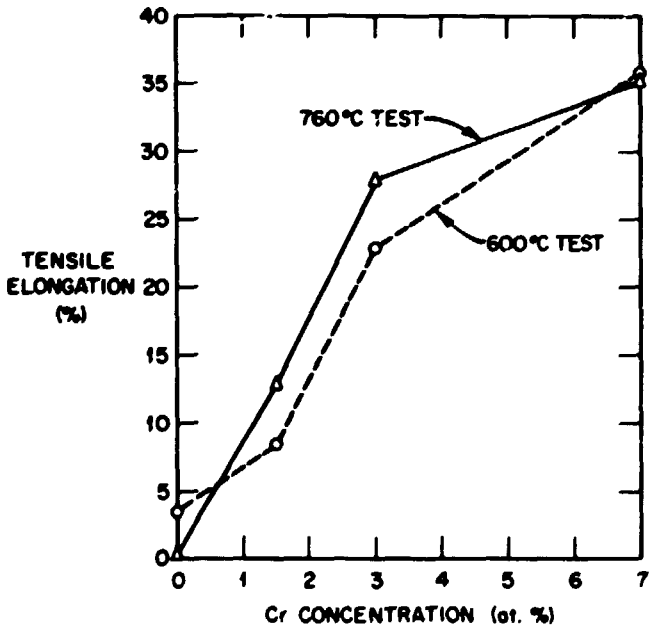

Fig. 4. Plot of tensile elongation as a function of chromium concentration in nickel-iron aluminides containing 15.5 at. % Fe tested in air at 600 and 760°C.

Table 2. Creep properties of nickel-iron aluminides tested at 760°C and 138 MPa (20 ksi)

Alloy number	Alloy addition (at. %)	Creep rupture time (h)	Rupture ductility (%)
	(a) 15% Fe + X% Cr		
IC-165	0 (base composition)	156	25.8
-197	1.5 Cr	—	—
-167	3.0 Cr	61	33.4
-199	6.7 Cr	—	—
-168	7.0 Cr	31	45.4
	(b) 12.0–12.5% Fe + X% Cr		
IC-205	3.0 Cr	289	22.6
-258	3.5 Cr	383	—
-296	5.0 Cr	30	66.2
-297	7.0 Cr	26	52.7
-298	9.0 Cr	—	—
	(c) 3% Cr + X% Fe		
IC-238	12.0 Fe	153	15.3
-205	12.5 Fe	289	22.6
-236	13.0 Fe	71	35.3
-237	14.0 Fe	39	41.0
-167	15.5 Fe	61	33.4
	(d) 7% Cr + X% Fe		
IC-304	12.3 Fe	31	48.9
-333	10.0 Fe	77	60.7
-334	9.0 Fe	89	40.6
-335	8.0 Fe	167	33.5
	(e) 7% Cr + 10 ~ 10.5% Fe + X% Al		
IC-320	20 Al	18	64.0
-331	19.8 Al	40	52.8
-333	19.0 Al	77	60.7
-347	18.5 Al	173	35.7
-336	18.0 Al	245	48.2

creep rupture life by a factor of five. Chromium, although it is beneficial to the tensile ductility in oxidizing environments, is detrimental to the creep resistance of the nickel-iron aluminides.

12.0–12.5% Fe Nickel-Iron Aluminides Containing 3 to 9% Cr

A second series of chromium-modified alloys was prepared that contained 12.0–12.5% Fe instead of the 15.5% as used in the first series. All the alloys here were fabricated into sheet materials by cold or hot rolling

without difficulty. Table 3 summarizes the tensile properties of these aluminides tested at temperatures to 850°C in air. The room-temperature ductility decreases with increasing chromium concentration. At elevated temperatures, the aluminides show a clear trend of increasing ductility with chromium, except for the 9% Cr alloy. The increase in ductility is attributed to a rapid formation of protective chromium oxide scales, which alleviate dynamic embrittlement in nickel-iron aluminides at elevated temperatures in oxidizing environments.

The yield strength at room temperature shows a general trend of increase with the chromium concentration. The strength is relatively less sensitive to chromium content at 600°C. However, the aluminides exhibit a decrease in strength at 760 and 850°C with increasing chromium above 3.5%. The change in mechanical properties can be rationalized by considering the effect of chromium and iron additions on the stability of the B2 phase. The study of microstructure and phase relationship indicates that chromium and iron additions increase the stability of the B2 phase relative to the $L1_2$ phase.[8,15,18,19] Figure 2 shows an increase in B2 particles with increasing chromium concentration in the aluminides. The bcc-ordered B2 phase is more brittle (as compared to the fcc-ordered $L1_2$ phase) at room temperature and is weaker at high temperatures. Hence, the formation of larger amounts of the B2 phase in higher chromium and iron alloys lowers the tensile ductility at room temperature and reduces the tensile strength and creep resistance of nickel-iron aluminides at elevated temperatures.

3% Cr NICKEL-IRON ALUMINIDES CONTAINING 12 TO 15.5% Fe

Tables 1 through 3 indicate that the nickel-iron aluminides containing about 3% Cr have the best combined ductility and strength at room and elevated temperature. To further characterize the iron effect, a series of nickel-iron aluminides containing 3% Cr [see Table 2, Part (c)] was prepared and fabricated into sheets by hot or cold rolling. The tensile results show that the yield strength increases with the iron concentration at room temperature but decreases at 850°C. The room temperature ductility is insensitive to iron concentration to 14%, above which a drop in ductility is

Table 3. Effect of chromium concentration on tensile properties of nickel-iron aluminides containing 12–12.5 at. % Fe (tested in air at crosshead speed of 2.5 mm/min)

Alloy number	Cr concentration (at. %)	Strength, MPa (ksi)		Elongation (%)
		Yield	Ultimate	
		Room temperature		
IC-205	3.0	435 (63.2)	1316 (191)	41.2
IC-258	3.5	506 (73.5)	1461 (212)	38.0
IC-296	5.0	655 (95.1)	1461 (212)	32.8
IC-297	7.0	827 (120)	1102 (160)	11.1
IC-298	9.0	779 (113)	1013 (147)	6.2
		600°C		
IC-205		651 (94.5)	799 (116)	9.4
IC-258		723 (105)	937 (136)	11.0
IC-296		723 (105)	999 (145)	28.5
IC-297		737 (107)	1026 (149)	35.6
IC-298		716 (104)	1013 (147)	18.1
		760°C		
IC-205		637 (92.5)	744 (108)	15.1
IC-258		696 (101)	834 (121)	20.4
IC-296		601 (87.2)	703 (102)	21.2
IC-297		512 (74.3)	581 (84.3)	32.4
IC-298		501 (72.8)	601 (87.2)	21.7
		850°C		
IC-205		486 (70.6)	515 (74.7)	17.9
IC-258		533 (77.4)	576 (83.6)	22.0
IC-296		399 (57.9)	438 (63.5)	35.5
IC-297		--	--	--
IC-298		342 (49.7)	376 (54.6)	23.5

observed. At elevated temperatures, the ductility increases steadily with increasing iron. This increase is clearly demonstrated in Fig. 5, where tensile elongation at 600 and 760°C is plotted as a function of iron concentration. Thus, iron is also beneficial to the ductility of nickel-iron aluminides tested in oxidizing environments. The iron level in these aluminides has to be limited to less than 13%; otherwise, it causes a sharp drop in creep resistance, as indicated in Table 2, Part (c). Microstructural examination also indicates an increase in the B2 phase with iron, resulting in weakening the aluminides at elevated temperatures.

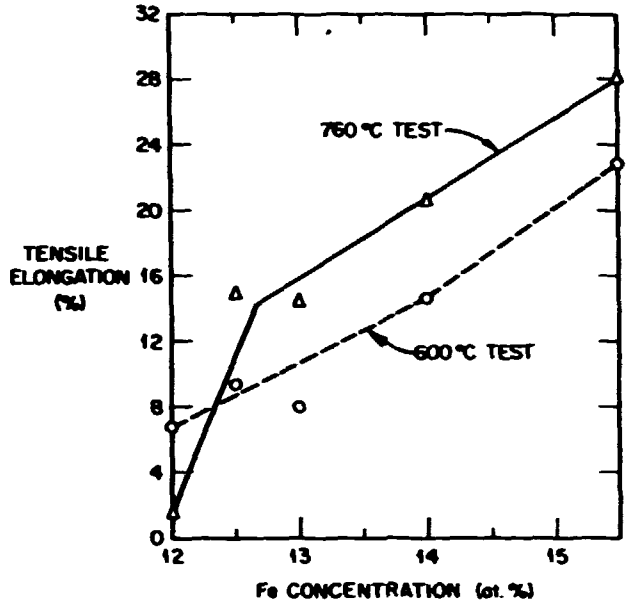

Fig. 5. Plot of tensile elongation as a function of iron concentration in nickel-iron aluminides containing 3% Cr, tested at 760 and 600°C in air.

Figure 6 compares the tensile properties of IC-205 (3% Cr) and IC-258 (3.5% Cr) alloys with the commercial alloy Hastelloy X. The nickel-iron aluminides are much stronger than Hastelloy X, particularly at elevated temperatures. The yield strength of the aluminides is more than double the strength of Hastelloy X at 500 to 800°C. In terms of ductility, the aluminides have the room-temperature ductility comparable to that of Hastelloy X. The ductility of the aluminides is lower at elevated temperatures; however, it is adequate for engineering use.

7% Cr NICKEL-IRON ALUMINIDES CONTAINING 8 TO 12.3% Fe

Corrosion studies discussed in the next section indicate that a 7% Cr addition is needed to protect nickel-iron aluminides in sulfur-bearing environments. We thus studied the effect of iron on 7% Cr nickel-iron aluminides containing 8 to 12.3% Fe [see Table 2, Part (d)]. All alloys were successfully fabricated into sheet materials by hot or cold rolling, except that IC-335 containing the lowest iron (8% Fe) cracked quite badly during hot rolling at 1150°C.

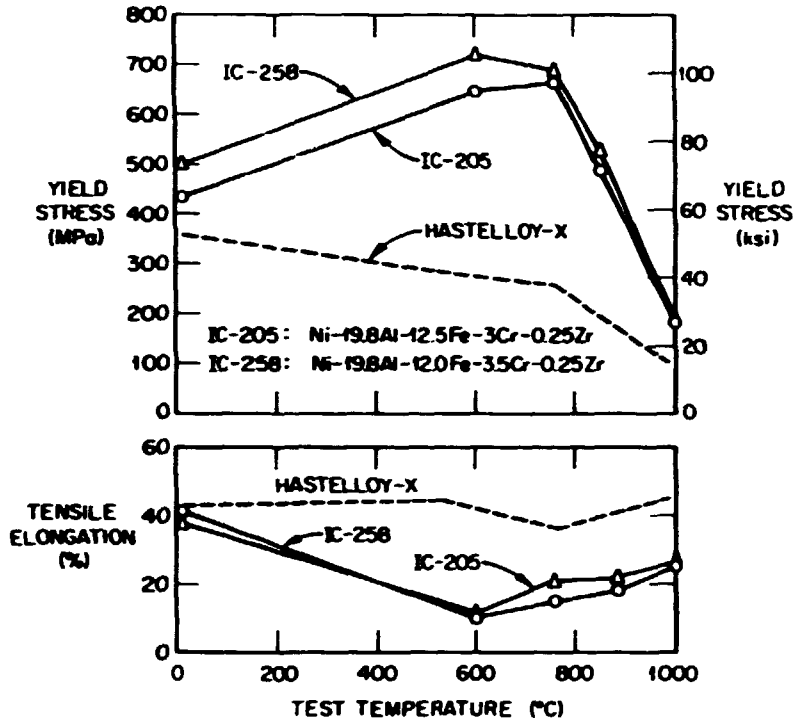

Fig. 5. Comparison of tensile properties of nickel-iron aluminides IC-205 and IC-258 with Hastelloy X.

Tensile tests indicate that IC-304 with the highest iron content (12.3%) has the lowest ductility at room temperature but the highest one at 760 and 850°C. The ductility is not sensitive to iron content in the range of 8 to 10%. The yield strength of the nickel-iron aluminides increases with increasing iron at room temperature but decreases at 850°C. All these results can be rationalized from considering the effect of iron on the stability of the B2 phase formed in nickel-iron aluminides.

The creep properties of this series were also determined at 178 MPa and 760°C, and are listed in Table 2, Part (d). The aluminides show a general trend of increasing creep resistance with decreasing the iron content. Among the alloys, IC-335 with the lowest iron (8%) has the longest creep rupture life.

7% Cr + 10.0–10.5% Fe NICKEL-IRON ALUMINIDES CONTAINING 18 TO 20% Al

The second series of 7% Cr alloys [see Table 2, Part (e)] was prepared for studying the effect of aluminum content on the properties of

nickel-iron aluminides containing 10.0–10.5% Fe and 7% Cr. All alloys were fabricated into sheets by cold or hot rolling without major difficulty. The tensile data indicate that the room-temperature yield strength decreases and the ductility increases with decreasing aluminum content. At elevated temperatures, the alloys show an increase in the strength with decreasing aluminum, with ductility essentially insensitive to aluminum.

The microstructure of IC-336 was examined in detail by TEM. The dark-field micrograph in Fig. 7 was made using a superlattice reflection. Dark areas are disordered fcc (γ) while light areas are ordered with the $L1_2$ structure (γ'). The structure basically consists of ordered regions with patches of disorder (<10% by area) which themselves contain ordered precipitates. Upon cooling from an elevated temperature, the specimen first forms disordered regions with associated elemental partitioning within an ordered matrix. Further cooling results in a precipitation of an ordered phase within the disordered regions. Note that all three regions have the same crystallographic alignment. The interfacial boundaries between the ordered and disordered regions tend to follow {100} planes, suggesting a lower energy on these planes than on a plane with a random orientation.

Fig. 7. TEM dark-field micrograph of IC-336, showing disordered patches with ordered blocky particles within them.

The creep properties of these alloys were summarized in Table 2, Part (e). The results clearly show an increase in rupture life with decreasing aluminum concentration. A decrease in aluminum from 20 to 18% results in an increase in rupture life by more than an order of magnitude. Among all 7% Cr aluminides, IC-336 has the best creep resistance.

CORROSION BEHAVIOR OF NICKEL-IRON ALUMINIDES IN SULFUR BEARING ENVIRONMENTS

Many nickel-base alloys are known to corrode readily in sulfur containing atmospheres because of the tendency for the formation of the low melting eutectic between nickel and Ni_3S_2 (ref. 3). This problem may be overcome either by providing a suitable coating for the alloy or by designing the alloy in such a way that the naturally occurring oxide scale serves to protect the alloy against sulfur attack. The latter solution is obviously the more desirable one, and the goal of this phase of the research is to identify the most promising alloy compositions based on nickel-iron aluminides.

TESTING PROCEDURES

A simple screening test was used to evaluate the alloys. It consisted of exposing a test specimen to the gaseous decomposition products of $CaSO_4$ in a sealed, evacuated quartz capsule.[8] The standard tests lasted for 168 h at 871°C.

This test was chosen because it is both severe and convenient. Any alloy surviving the test is considered worthy of further, more systematic study. It is important to recognize, however, that both oxygen and sulfur pressures inside the capsule change as the test proceeds. A brief description of the sequence of events that occur during the test is helpful in interpreting the results.

The $CaSO_4$ in the capsule will decompose at 871°C according to the equation

$$CaSO_4 = CaO + (1/2)SO_2 + (1/2)SO_3 + (1/4)O_2 = CaO + (1/2)S_2 + (3/2)O_2 ,$$

and the equilibrium constant k is given by

$$k = (P_{S_2})^{1/2} \times (P_{O_2})^{3/2} . \qquad (1)$$

At 871°C the equilibrium partial pressures of S_2 and O_2 are 10^{-26} and 10^{-6} atm, respectively. Corresponding partial pressures for SO_2 and SO_3 are 10^{-6} and 10^{-9} atm, respectively. Thus at the start of a screening test, the sulfur pressure is far too low to form nickel sulfide, but the oxygen pressure is adequate to cause an oxide scale to begin to form on the sample. However, because the reaction is occurring in a closed system, as the oxygen is depleted by the oxidation reaction, the sulfur partial pressure will increase to satisfy the equilibrium constant. Thus while a screening test begins under oxidizing conditions, the sulfur pressure immediately begins to increase relative to oxygen. Experimentally the formation of the Ni-Ni_3S_2 eutectic is observed, indicating that the sulfur pressure must increase at least to the decomposition pressure of Ni_3S_2.

Both alloying additions and preoxidation procedures were investigated as a means of developing an alloy that exhibited significant resistance to sulfur attack. Prior to testing, all alloys were polished mechanically with 4/0 emery paper, washed in water and ethanol, and dried. These samples were subjected to screening tests either in the preoxidized or as-polished condition. The results of screening tests were evaluated in terms of weight gain measurements and through examination of the specimens in a scanning electron microscope (SEM) equipped with an energy dispersive X-ray spectrometer (EDS). While recognizing the need for the use of SEM techniques to identify spalling or crack formation in the oxide scale, we concluded that weight gain measurements are a good general guide to the extent of sulfidation attack.

ALLOYING ADDITIONS TO NICKEL-IRON ALUMINIDES

On the basis of previous studies[17] of the effect of alloying additions to Ni_3Al, it was concluded that only chromium and/or silicon additions to the nickel-iron aluminides were likely to be effective in reducing sulfur attack. The alloy compositions were selected in an effort to determine the optimum concentrations of chromium or silicon that should be added. A second goal was to optimize the relative proportions of aluminum and iron in the alloys.

As described in more detail below, chromium additions above a certain critical level are very effective in preventing sulfur attack. Silicon, on the other hand, was not effective at concentrations (<3%) sufficiently low to avoid adverse effects on the mechanical properties of the alloy. Iron concentrations were varied from 8 to 15.5 at. %. Only a weak dependence of corrosion resistance on the iron concentration was found in tests of as-polished alloys containing 7 at. % Cr; however, a minimum in weight gain occurs in the 10 to 12 at. % range. The screening tests revealed no trend in resistance to sulfur attack when the aluminum content of the alloys was varied from 18 to 20 at. %, but aluminum concentrations near 20 at. % are favored simply to assure an adequate supply of aluminum for the formation of Al_2O_3 scales.

EFFECT OF PREOXIDATION ON SULFIDATION RESISTANCE

Alloy samples were preoxidized in both wet hydrogen and in air in an effort to form an oxide scale that was resistant to sulfur penetration. Oxidation temperature, oxygen partial pressure, and oxide thickness were identified as the three most important parameters in determining the effectiveness of preoxidation procedures. Preoxidation in air can also provide protection, but only if the oxidation temperature is sufficiently high. Figure 8 shows the weight gains during standard screening tests for a series of Ni–19.8% Al–15.5% Fe alloys containing varying concentrations of chromium. Preoxidation at 950°C is useful only for chromium concentration near 7 at. %, but after preoxidation at 1050°C, only a very minor weight gain was observed for alloys containing as little as 1.5 at. % Cr. The higher oxidation temperature again favors the formation of alpha alumina as was demonstrated by both X-ray and EDS measurements.

Preoxidation times were varied from 24 to 168 h, and the oxide scales developed in the longer experiments proved to be roughly an order of magnitude more effective in preventing sulfur attack than scales formed in a 24-h exposure. The thickness of the oxide formed is clearly a function of the total time of oxidation, but as shown below, the morphology of the oxide scales formed on these alloys is complex. The layer of oxide that provides the actual barrier to sulfur penetration can be only a few tenths

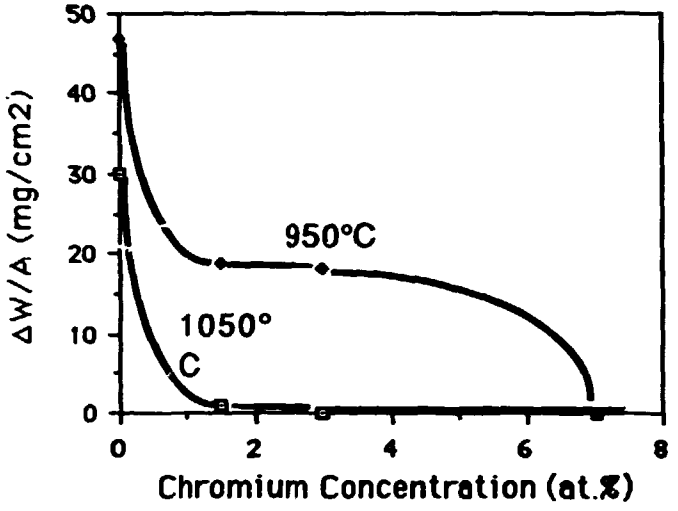

Fig. 8. Screening test weight gain data for a series of preoxidized Ni-19.8Al-15.5Fe alloys containing various amounts of chromium. Preoxidation at 950°C was much less effective than preoxidation at 1050°C.

of a micrometer thick, and the beneficial effects of the longer preoxidation times may relate mainly to the filling up of cracks or pores in this scale rather than to a major increase in its thickness.

SCREENING TESTS OF AS-POLISHED SAMPLES

Neither iron nor chromium additions alone improve the sulfidation resistance of Ni_3Al. Figure 9 shows the weight gains after standard screening tests of a Ni—19.8% Al—15.5% Fe alloy and three nickel-iron alloys containing chromium tested in the as-polished condition. All alloys suffered severe attack. When both iron and chromium are added to the base alloy, however, a dramatic decrease in sulfur attack occurs if the chromium content of the alloy is 7 at. % or higher. Figure 10 illustrates this result in the form of a bar graph showing the weight gains for a series of Ni—20% Al—12.3% Fe alloys containing various amounts of chromium. Although not shown in the figure, tests were also made with an alloy containing 6% Cr. The results were erratic, suggesting that 6% is a marginal level for the chromium content.

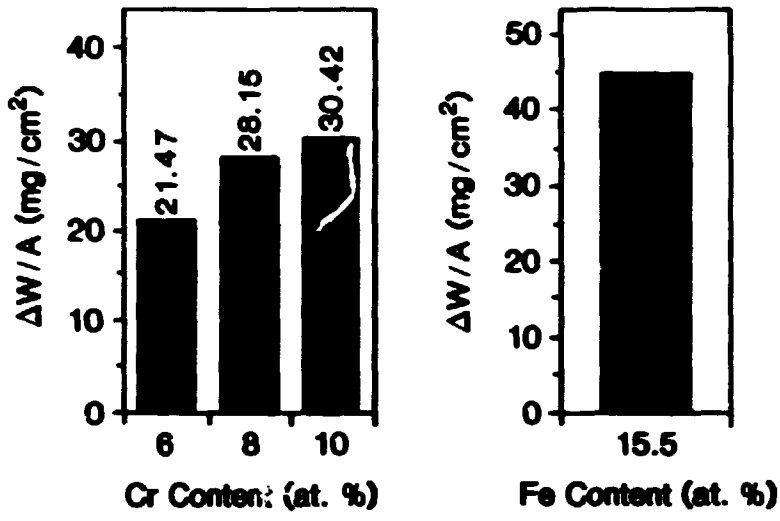

Fig. 9. Weight gain data from screening tests of Ni_3Al alloys with chromium or iron additions. Neither chromium nor iron additions alone improve resistance to sulfur attack.

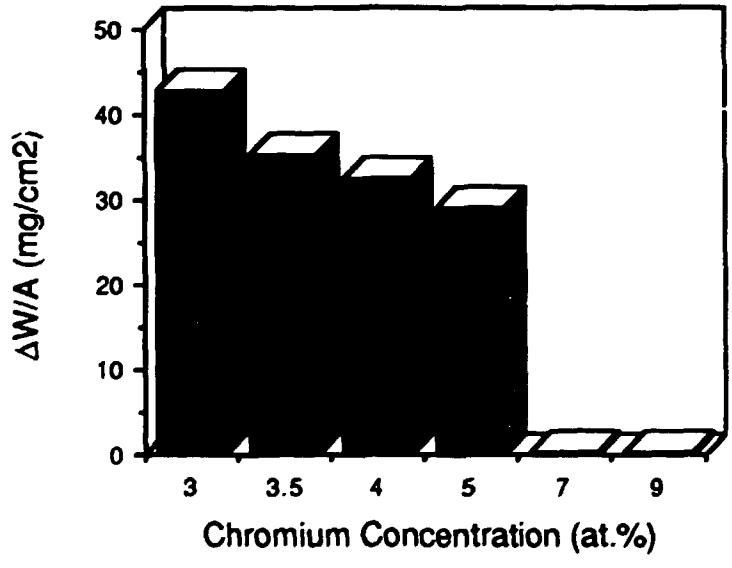

Fig. 10. Weight gain data for screening tests of as-polished Ni-20Al-12.3Fe alloys containing various amounts of chromium. The data show the dramatic decrease in sulfur attack that occurs for chromium additions of 7 at. % or greater.

As shown previously,[8] silicon additions to Ni_3Al can be very effective in preventing sulfur attack on preoxidized specimens because the silicon forms a very thin, amorphous layer of silica on the surface of the sample.

No such effect was observed with silicon additions to nickel-iron aluminides. Additions of 1.5 at. % Si to Ni–19.3% Al–14.5% Fe and of 3.0 at. % Si to Ni–16.8% Al–15.5% Fe produced alloys that were heavily attacked in screening tests even after preoxidation in wet hydrogen at 1100°C.

Silicon was also added to Ni–18.8% Al–12.3% Fe–7% Cr. A sample containing 1 at. % Si was heavily attacked in a standard screening test. An increase of the silicon content to 3 at. % resulted in a large improvement, but the corrosion resistance of the alloy was no better than the same alloy without silicon. It was concluded, therefore, that silicon additions to the nickel-iron aluminides are not likely to be useful.

Figure 11 shows the morphology of the oxide-gas interface of IC-297 (Ni–20% Al–12.3% Fe–7% Cr) after a standard screening test. The oxide surface is covered with raised hillocks that are rich in aluminum (see the X-ray spectrum). The oxide between the hillocks has a much different composition and shows substantial Cr, Fe, and Ni peaks as well as a strong

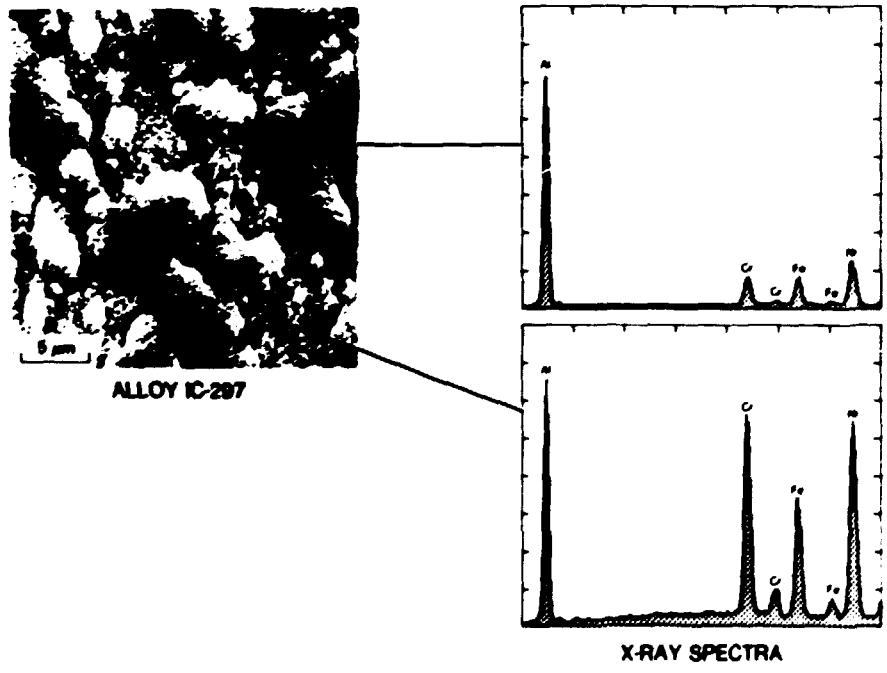

Fig. 11. SEM photograph of the oxide-gas interface of a Ni-20Al-12.3Fe-7Cr alloy after a screening test. The accompanying X-ray spectra are from the energy dispersive spectrometer of the SEM.

aluminum peak. Small particles of the Ni-Ni_3S_2 eutectic are also present on the sample surface. They appear as approximately spherical particles because they were molten at the test temperature. One such particle is the white circular object, 2 μm in diameter, near the top center of the picture. Such features are frequently observed on as-polished specimens after the screening test even on those alloys where only very small weight gains are observed and where the oxide scale remains uncracked. The molten eutectic does not appear to wet the oxide scale, which may be why no appreciable additional attack occurs in tests lasting almost 500 h. X-ray powder diffraction measurements on the oxide scale from this specimen showed the existence of ZrO_2, Ni_3S_2, alpha Al_2O_3, and a Ni-Cr-Al spinel.

WELDING BEHAVIOR OF NICKEL-IRON ALUMINIDES

Although substantially more work has been done on characterizing the weldability of iron-free nickel aluminides, the iron-bearing alloys show good promise in this area based on previous studies[8,9,11,12,13] and limited data available for the current nickel-iron aluminides. The iron-containing alloys which have been studied include IC-205, -261, and -306 and will soon include IC-336 and other 7% Cr aluminides.

Nickel-iron aluminides had been successfully welded using both the electron beam and gas tungsten arc processes. Figure 12 shows metallographic sections of both types of IC-205 weldment. The electron beam weld [Fig. 12(a) and (b)], made at 4.2 mm/s (10 in./min), is full penetration and shows a slight amount of porosity in the fusion zone, but no indication of any cracking in either the fusion zone or heat-affected zone. The gas tungsten arc weld [Fig. 12(c)], made at 14.7 mm/s (35 in./min) shows a substantially different solidification substructure, but also shows no indication of cracking.

Heat IC-306 was available in sufficient quantity that the Sigmajig weldability test could be applied. At a preapplied transverse stress level of 69 MPa (10 ksi), no cracking was observed; even small transverse cracks usually present in un-stressed test specimens were absent. In general, additions of iron at the levels involved here appear to markedly improve the weldability, specifically the resistance to hot cracking, of the nickel aluminides.

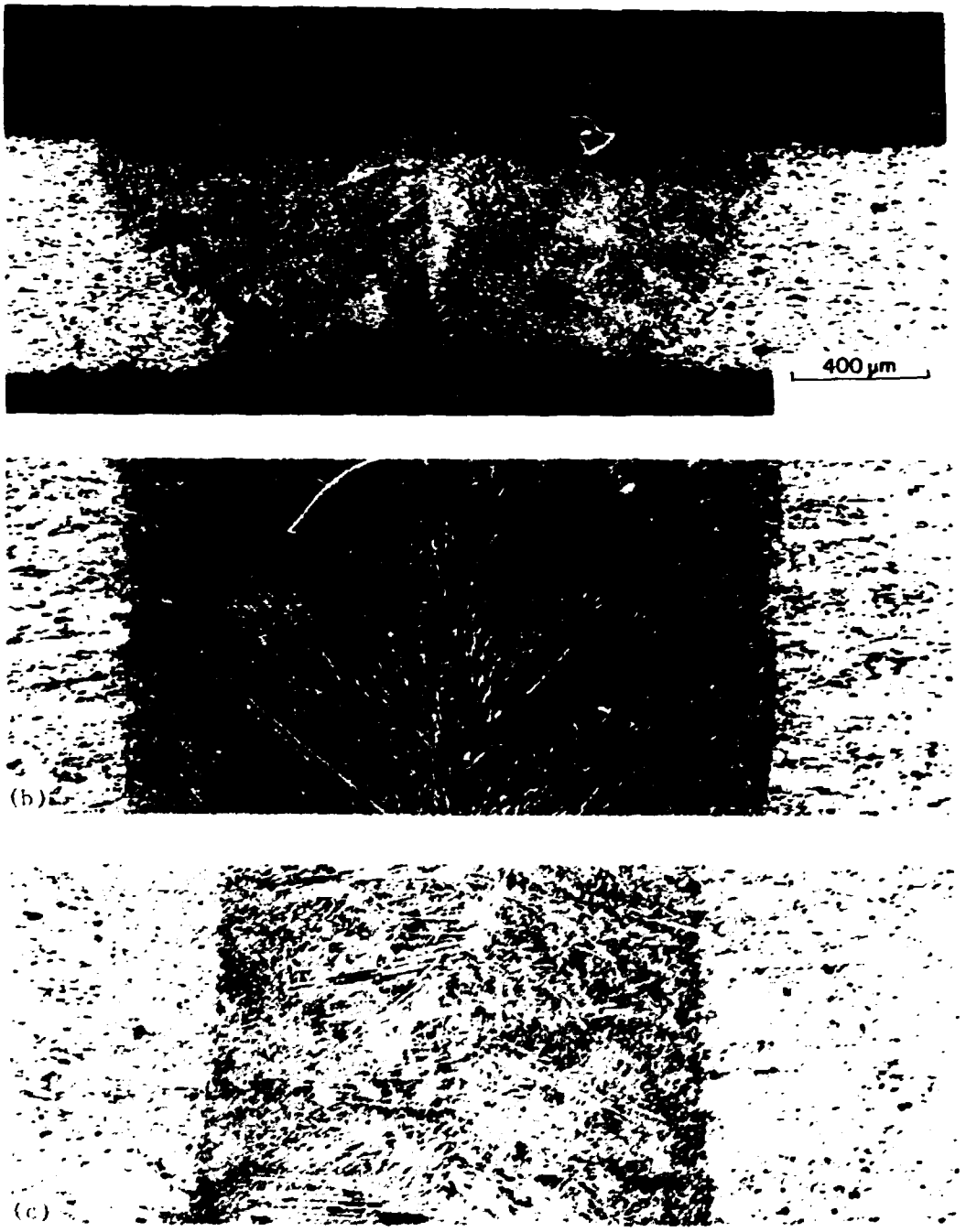

Fig. 12. Metallographic sections of welds made in IC-205; (a) and (b) are transverse and top views of an electron beam weld and (c) is a top view of a gas tungsten arc weld.

SUMMARY AND CONCLUSIONS

We have conducted a systematic study of alloying effects on nickel-iron aluminides based on boron-doped Ni_3Al. The alloying effects of Cr, Fe, and Zr(Hf) on metallurgical and mechanical properties of the aluminides are summarized below.

(1) Chromium — Chromium is a key alloying element, and chromium atoms occupy both nickel and aluminum sublattice sites in Ni_3Al. Chromium has the beneficial effect of promoting a rapid formation of protective oxide scales on alloy surfaces. As a result, alloying with >3% Cr improves air oxidation resistance and reduces dynamic embrittlement in oxidizing environments at intermediate temperatures (400 to 800°C). Alloying with 7% Cr dramatically improves corrosion resistance of nickel-iron aluminides in sulfidizing environments. Chromium increases the stability of the bcc-ordered phase (B2), which is brittle at room temperature and weak at elevated temperatures. The formation of the B2 phase in nickel-iron aluminides leads to lowering the ductility at lower temperatures and the strength at higher temperatures.

(2) Iron — The alloying effect of iron is similar to chromium, both of these elements occupy aluminum and nickel subsites in Ni_3Al. Iron in combination with chromium improves tensile ductility in oxidizing environments and corrosion resistance in sulfur-bearing atmospheres. It also promotes the formation of the B2 phase, and hence improves the hot fabricability of nickel-iron aluminides. The optimum level of (Fe + Cr) depends on the aluminum concentration in nickel-iron aluminides. In general, the level increases with decreasing aluminum; for example, 15.5% of (Fe + Cr) in 19.5% Al aluminides, and 17% of (Fe + Cr) in 18% Al aluminides.

(3) Zr(Hf) — Zirconium and hafnium are the most prominent solid-solution strengtheners in nickel-iron aluminides as well as in nickel aluminides. Alloying with Zr(Hf) effectively improves the high-temperature strength and creep resistance. However, Zr(Hf) has a low solubility limit (<0.3 at. %) in the ordered γ' phase. Excess Zr(Hf) causes an incipient melting of the nickel-iron aluminides at about 1200°C and thus lowers their hot ductility and fabricability. The optimum level of Zr(Hf) is around 0.20 ± 0.05%.

The study of alloying effects has led to the development of nickel-iron aluminides for structural use at elevated temperatures. The optimum composition of the aluminide is determined as follows:

Ni–18.5 ± 0.5% Al–10 ± 0.5% Fe–7 ± 0.5% Cr–0.1% B (at. %).

The aluminide has excellent tensile strength, and is much stronger than commercial alloys such as Hastelloy X and stainless steels, in particular at elevated temperatures. The creep resistance of the aluminides is much better than that of austenitic steels and moderately better than that of Hastelloy X. The aluminide exhibited grain boundary sliding, which leads to high creep rates and formation of intergranular cavities. The future work on alloy design will focus on the strengthening of grain boundaries by alloying with Groups IVA to VIA elements such as molybdenum and titanium.

A simple screening test in which samples are exposed to the decomposition products of $CaSO_4$ was used to evaluate the sulfidation resistance of a variety of nickel-iron aluminides containing chromium and/or silicon. Chromium additions of 7 at. % or greater were very effective in minimizing sulfur attack on as-polished specimens. The optimum iron content for these alloys was found to be between 10 and 12 at. %, and an aluminum concentration near 20 at. % is recommended. Silicon additions, either alone or in combination with chromium, were either ineffective or produced no improvement over chromium additions alone. Sulfidation protection can also be afforded by oxide films preformed in air; however, the oxidation temperature should be 1000 to 1050°C, and the alloys must contain 3 at. % or greater of chromium.

Studies of weldability of nickel-iron aluminides indicate that additions of iron at levels of 10 to 15 at. % appear to improve markedly the weldability of nickel aluminides. The nickel-iron aluminides modified with 3 to 7% Cr were successfully welded using both the electron beam and gas tungsten arc processes. Further studies will emphasize the Sigmajig weldability tests, i.e., evaluation of hot cracking under preapplied stress conditions.

ACKNOWLEDGMENT

The authors thank Connie Dowker for preparation of the manuscript.

REFERENCES

1. C. T. Liu and J. O. Stiegler, "Ductile Ordered Intermetallic Alloys," Science 226, 636–42 (1984).
2. C. T. Liu and C. L. White, "Design of Ductile Polycrystalline Ni_3Al Alloys," pp. 365–80 in Materials Research Society Symposia Proceedings, Vol. 39, High-Temperature Ordered Intermetallic Alloys, symposium held Nov. 26–28, 1984, Boston, Massachusetts, ed. C. C. Koch, C. T. Liu, and N. S. Stoloff, Materials Research Society, Pittsburgh (1985).
3. J. V. Cathcart, "The Oxidation of Ni-Al and Fe-Al Alloys," pp. 445–460 in Materials Research Society Symposia Proceedings, Vol. 39, High-Temperature Ordered Intermetallic Alloys, symposium held Nov. 26–28, 1984, Boston, Massachusetts, ed. C. C. Koch, C. T. Liu, and N. S. Stoloff, Materials Research Society, Pittsburgh (1985).
4. C. T. Liu, C. L. White, C. C. Koch, and E. H. Lee, "Preparation of Ductile Nickel Aluminides for High Temperature Use," Proc. Symp. High Temperature Materials Chemistry – II, ed. Munir et al., The Electrochemical Soc., Inc. (1983).
5. C. T. Liu, C. L. White, and J. A. Horton, "Effect of Boron on Grain Boundaries in Ni_3Al," Acta Metall. 33(2), 213–229 (1985).
6. K. Aoki and O. Izumi, Nippon Kinzoku Gakkaishi 43, 1190 (1979).
7. A. I. Taub, S. C. Huang, and K. M. Chang, Metall. Trans. A 15A, 399 (1984).
8. C. T. Liu, et al., Initial Development of Nickel and Nickel-Iron Aluminides for Structural Uses, ORNL-6067 (1984).
9. S. A. David, W. A. Jemian, C. T. Liu, and J. A. Horton, "Welding and Weldability of Nickel-Iron Aluminides," Weld. J. 64, 22s–28s (1985).

10. M. L. Santella, S. A. David, and J. A. Horton, "Weldability of an Ni_3Al Alloy," pp. 629–633 in Advances in Welding Science and Technology, ed. S. A. David, ASM International (1986).

11. M. L. Santella and S. A. David, "A Study of Heat-Affected Zone Cracking in Fe-Containing Ni_3Al Alloys," Weld. J. 65, 129s–136s (1986).

12. M. L. Santella, et al., Welding Studies of Nickel Aluminide and Nickel-Iron Aluminides, ORNL-6194 (1985).

13. M. L. Santella, S. A. David, and C. L. White, "Weldability of Ni_3Al-Type Aluminide Alloys," pp. 495–504 in Materials Research Society Symposia Proceedings, Vol. 39, High-Temperature Ordered Intermetallic Alloys, symposium held Nov. 26–28, 1984, Boston, Massachusetts, ed. C. C. Koch, C. T. Liu, and N. S. Stoloff, Materials Research Society, Pittsburgh (1985).

14. C. T. Liu, "Development of Ni and Ni-Fe Aluminides for Elevated Temperature Structural Use," to be published in Proc. Symp. MICON (1986).

15. J. A. Horton, C. T. Liu, and M. L. Santella, "Microstructures and Mechanical Properties of Ni_3Al Alloyed with Fe Additions," submitted for publication in Metall. Trans. (1986).

16. Y. Mishima, S. Ochiai, M. Yodogana, and T. Suzuki, Trans. Japan Inst. Metals 27, 41–50 (1986).

17. C. T. Liu and V. K. Sikka, J. Metals 38, 19–21 (1986).

18. S. M. Merchant and M. R. Notis, J. Mater. Sci. 66, 47–60 (1984).

19. S. C. Huang, E. L. Hall, K. M. Chang, and R. P. Laforce, Metall. Trans. A 17A, 1685 (1986).

DEVELOPMENT OF CREEP RESISTANT AUSTENITIC STAINLESS STEELS FOR ADVANCED STEAM CYCLE SUPERHEATER APPLICATION

P. J. Maziasz and R. W. Swindeman

Metals and Ceramics Division
Oak Ridge National Laboratory
P.O. Box X
Oak Ridge, Tennessee 37831

ABSTRACT

The compositions of several 14Cr-16Ni austenitic stainless steels were modified with combinations of minor and residual alloying elements to produce excellent creep strength based on unique precipitate microstructures. These modifications produce fine MC and phosphide precipitates in the matrix for strength and various coarser carbide phases along the grain boundaries for ductility and rupture resistance. Creep-rupture resistance of these modified 14-16 steels is much better than that of type 316 or Inconel 800H and better than that of 17-14CuMo at 700°C in the mill-annealed condition. Analysis of microstruc-ture and correlation with creep properties suggests that precipitate effects are primarily responsible for the properties improvement. The ideas and insight for design of the novel precipitate microstructures stem from microcompositional information obtained using state-of-the-art analytical electron microscopy (AEM).

INTRODUCTION

The desired creep strength requirement for candidate advanced superheater/reheater alloys is that they withstand 100 MPa at 700°C for 100,000 h. Stainless steels like AISI type 316 can withstand only 40 MPa under those conditions. However, these "lean" (i.e., lower Cr and Ni) stainless steels are attractive candidates for alloy development because they provide a lower cost alternative to superalloys like Inconel 617. In another paper in these proceedings, Swindeman et al.[1] describe the overall program to develop advanced superheater/reheater alloys and the various properties evaluations conducted to date. A 14Cr-16Ni austenitic

stainless steel modified with additions of Ti, V, Nb, C, P, and B has been developed at ORNL; this alloy exceeds the creep strength requirements at 700°C and has significantly better creep resistance than the commercially available reference alloy, 17-14CuMo. One purpose of this paper is to provide the background on the ideas and insight that allowed selection of specific precipitate phases and distributions in the matrix and grain boundaries of these new alloys. The minor and residual element compositional modifications were specifically chosen to produce these tailored precipitate microstructures. The other purpose is to show the actual microstructures obtained in heats of the new modified 14-16 steel produced by commercial vendors and to evaluate the role of microstructure in the large improvement observed in creep resistance at 700°C.

BACKGROUND ON ALLOY DESIGN AND DEVELOPMENT

Insight on Microstructural Evolution and Phase Stability in Irradiated Stainless Steels

A substantial portion of the ideas and insight employed in designing the matrix and grain boundary precipitate microstructures came from transmission electron microscopy studies of neutron irradiated type 316 and Ti-modified austenitic stainless steels. These studies were directed at correlating microstructural evolution during irradiation with macroscopic changes in density or mechanical properties. Many detrimental properties changes are induced by irradiation, such as swelling, hardening, and grain-boundary embrittlement. These are either closely related to or directly caused by changes in the microstructure produced by irradiation. Irradiation-induced properties changes often showed varying sensitivity to changes in metallurgical parameters, such as alloy composition or thermal-mechanical pretreatment. It appeared that radiation resistance was linked to the ability to control microstructural evolution during irradiation.[2,3]

From the standpoint of microstructural phenomena, the most severe irradiation environments were the fast breeder reactor (FBR) environment and the mixed fast and thermal neutron light-water reactor environment used to study magnetic fusion reactor (MFR) materials. These environments

subject irradiated materials to elevated temperatures (300 to 750°C), crystalline damage due to point defects created by atomic displacements, varying degrees of insoluble He gas atom generation, and varying rates of radiation-enhanced diffusion and/or induced solute segregation (depending on irradiation temperature).[4] These factors often combined to produce a microstructure of dislocation loops (Frank interstitial) and network dislocations, gas-driven He bubbles, bias-driven voids (net excess vacancy supersaturation), and precipitate phase particles. Each of these microstructural phenomena has a complex sensitivity to the irradiation environment parameters as well as to metallurgical variables. Moreover, they are strongly interrelated. Dramatic changes of one microstructural component will affect the evolution or stability of the others.

The microstructural objectives for irradiation resistance, particularly in a fusion first-wall environment where displacement damage and He generation rates are substantial, are fairly straightforward. Voids are cavities which grow rapidly by absorbing supersaturated vacancies produced by irradiation in the matrix and produce substantial swelling. To achieve swelling resistance, fine, stable He bubbles must be prevented from becoming larger than some critical size at which they convert to unstable voids. The formation of He gas bubbles along grain boundaries can be a major cause of intergranular embrittlement. To achieve resistance to grain boundary He embrittlement, one must either refine the bubble microstructure nucleated by He diffusing into the boundary from the matrix or reduce He diffusion to the boundary by altering its efficiency as a sink.

Precipitate effects are crucial to obtaining either facet of radiation resistance, but precipitation during irradiation is quite difficult to control. Of the various microstructural phenomena produced by irradiation, precipitation has been the last to be properly characterized and understood. The development and application of analytical electron microscopy (AEM) since about 1978 has contributed greatly to unraveling the nature of the various phases formed during irradiation and to sorting out the factors affecting their formation and stability.[4,5]

With regard to identity and nature, the precipitates in neutron-irradiated austenitic stainless steels can be classified as radiation-induced phases or as radiation-enhanced, -modified, or -retarded thermal phases. Characteristic compositions (obtained via X-ray EDS analysis) of the various thermal phases produced in either type 316 or in related Ti/P modified austenitic stainless steels by thermal aging are show in Fig. 1. The thermal phases are $M_{23}C_6$ (tau), M_6C (eta), MC, Laves, sigma, chi, and FeTi-phosphide. Except for M_6C and Laves, the thermal phases are fairly poor in Ni and Si; and except for the MC and phosphide phases, they are quite rich in Cr and Mo. Compositions of the radiation-induced or -modified thermal phases are shown in Fig. 2. For the most part, these phases are rich in Ni and Si, and poor in Cr and Mo compared to the ensemble of thermal phases in Fig. 1. The gamma-prime, G, and A and B type Ni-rich phosphide phases are usually induced by the irradiation environment, while the thermal M_6C and Laves phases undergo compositional modification during irradiation.

Once the phases were properly identified and their compositions were characterized, factors affecting their formation and stability could be identified. Radiation-induced solute segregation (RIS) was found to be the primary driving force for precipitation at 400 to 600°C, concurrent with other radiation-induced phenomena such as void swelling. RIS is a non-equilibrium segregation caused by the coupling of solute atoms to irradiation-produced point defects flowing toward microstructural features that serve as sinks for vacancies and interstitials. RIS in austenitic Fe-Cr-Ni-Mo alloys is an anti-thermal process that causes unnatural demixing of the initially uniform solid solution. During irradiation, elements like Ni that are normally soluble in the austenite segregate to sinks (i.e., dislocations and precipitate particles), while elements like Cr and Mo that are normally supersaturated desegregate. RIS causes abnormally strong segregation of Si during irradiation. RIS was, therefore, identified as one of the dominant factors causing the formation of the irradiation-induced phases and the modification and enhancement of certain thermal phases. Conversely, when RIS was suppressed by conditions favoring radiation resistance, none of these phases formed and the

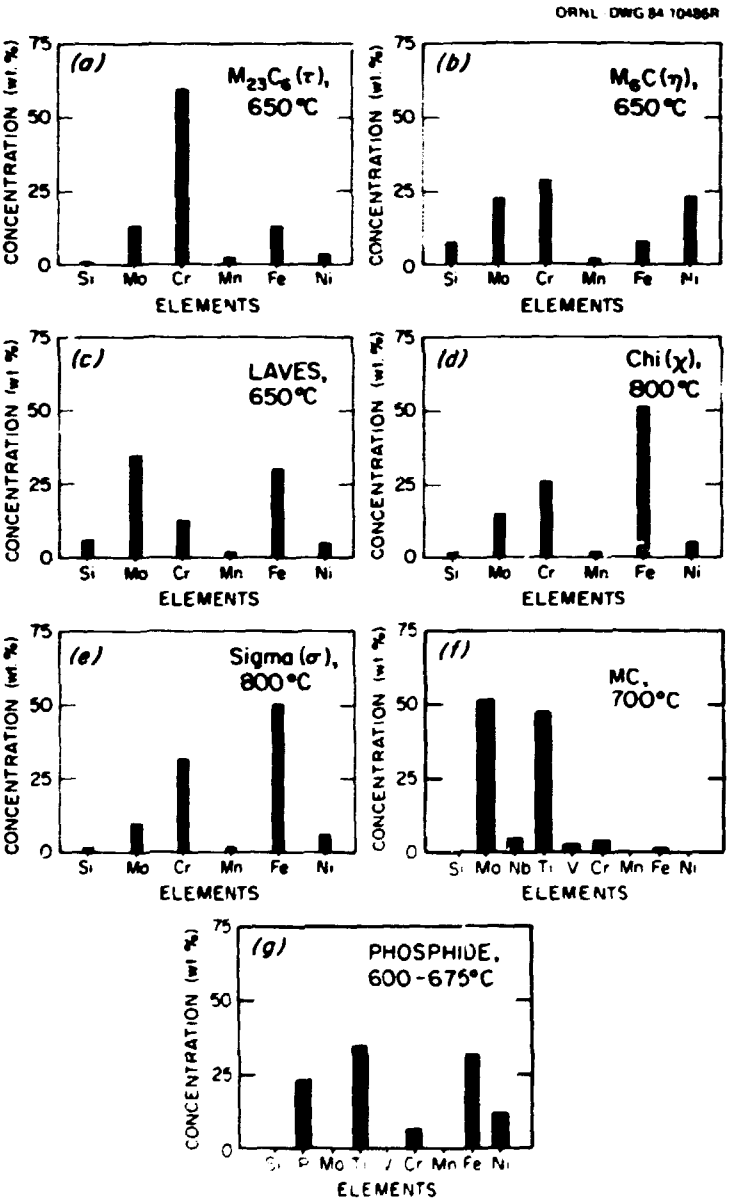

Fig. 1. Histograms of elemental composition of precipitate phases formed during thermal aging in AISI type 316 stainless steel or similar Ti or P modified steels, as determined by quantitative X-ray EDS analysis.

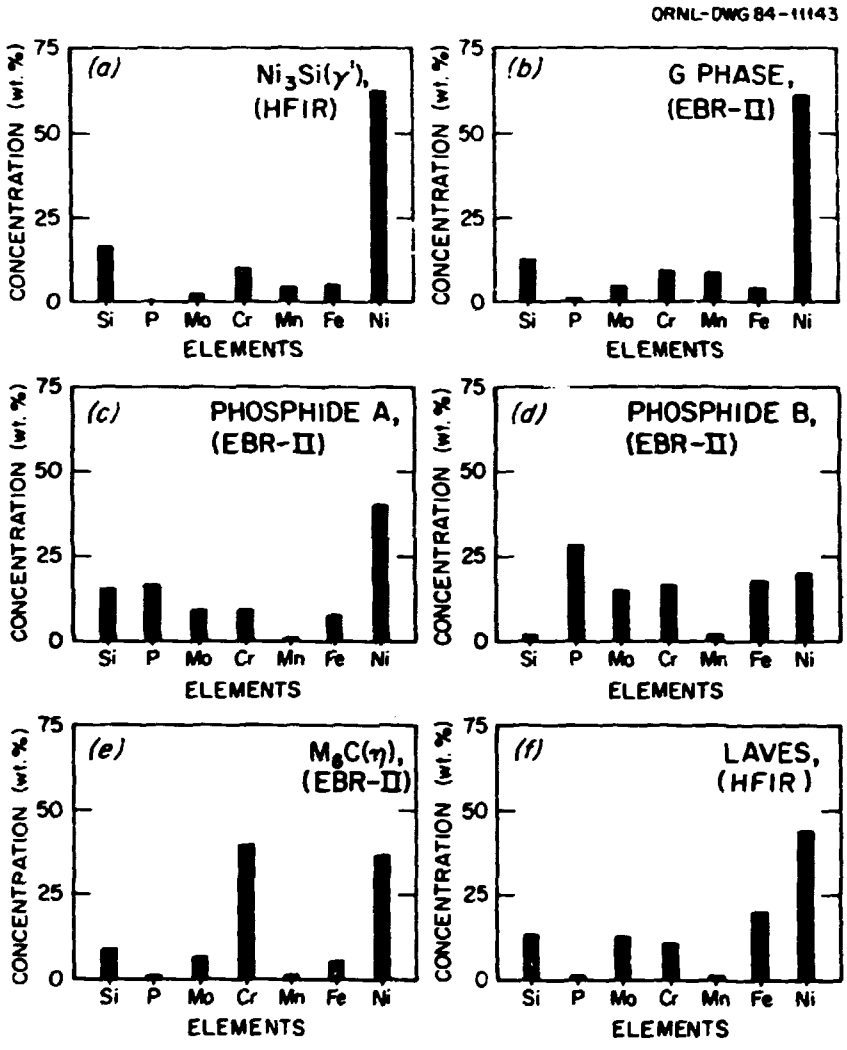

Fig. 2. Histograms of elemental composition of precipitate phases that are either induced or compositionally modified by neutron irradiation of AISI type 316 stainless steel, as determined by quantitative X-ray EDS analysis.

otherwise retarded thermal phases then formed abundantly during irradiation due simply to enhanced thermal diffusion.

This overall picture of precipitation during irradiation suggested that there was always some competition between irradiation-induced effects like RIS and thermal solute supersaturations and diffusion. The net difference between these opposing phenomena then determined which phases formed and which did not, and the degree to which certain phases were compositionally modified. This simplifying assumption then allowed further insight into the basic principles governing phase formation and stability during irradiation. One example of such insight was the fact that compatibility was required between the solubility characteristics of a particular phase and the solute environment of the adjacent surrounding matrix, as illustrated by the lock and key analogy of Fig. 3. If RIS was intense, then phases like gamma-prime (M_3Si) would form during irradiation because of the good match between enrichment/depletion characteristics of that phase and the RIS process. Conversely, the normally dominant $M_{23}C_6$ carbide phase was retarded under the same irradiation conditions, because the enrichment/depletion characteristics of that phase and the RIS process do not match. This concept was further supported by the fact that when RIS was suppressed for the same irradiation conditions (temperature, dose), the radiation-induced phases were not observed, while the otherwise retarded thermal phases were then enhanced.[3] Another example was that most of the radiation-induced, -enhanced, or -retarded phases show very little change in composition despite variations in irradiation conditions. This suggested that these compounds existed over narrow regions of the phase diagram involving the reactant elements, and that they had limited solubility ranges for other solutes in the alloy. By comparison, the compositional flexibility exhibited by the radiation-modified phases suggested wider phase fields for precipitates and larger solubility ranges for other elements. This insight into the nature and the behavior of the various precipitate phases during irradiation then provided useful ideas for carefully manipulating the alloy composition to control their formation characteristics in a nonirradiation environment.

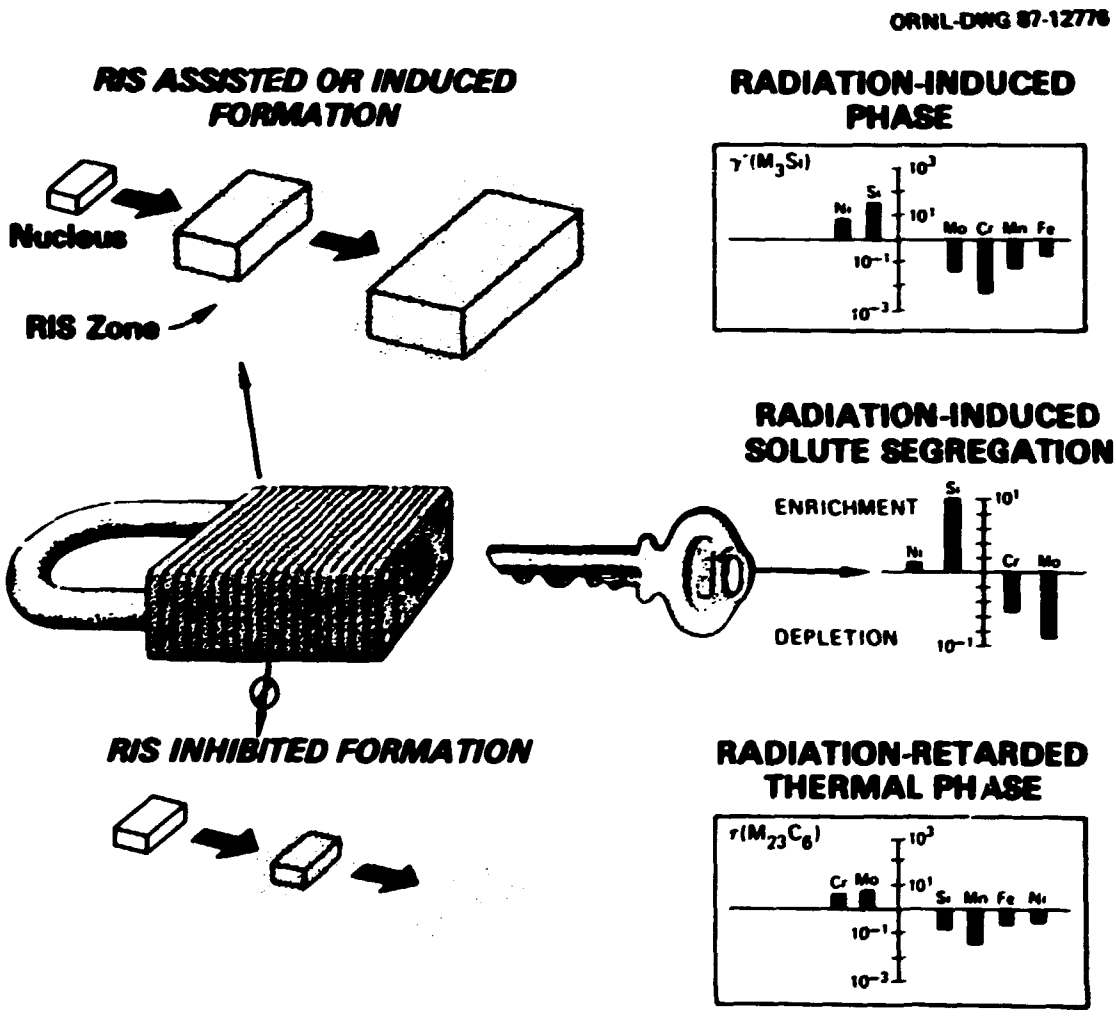

Fig. 3. A schematic diagram to illustrate the idea that phase formation during irradiation is due to compatibility between the solute enrichment/depletion characteristics of various phases and the segregation process driving the precipitation, analogous to a lock and key. When radiation-induced solute-segregation (RIS) is the driving process, a good match between the composition of the radiation-induced gamma-prime phase and the RIS process unlocks formation of that phase. Conversely, a complete mismatch between the normal thermal tau carbide and RIS prevents it from forming during irradiation.

Insight and Ideas for Precipitate Phase Selection for Creep Resistance Through Alloy Compositional Modification

Lean stainless steels for improved thermal creep resistance are a direct spin-off application of alloys originally developed as advanced radiation-resistant steels for fusion first-wall applications. Radiation-resistant steels were developed on the basis of fine matrix MC carbides and fine phosphide needles providing resistance to irradiation-induced void swelling and grain boundary carbides providing resistance to intergranular helium embrittlement.[3] The radiation-resistant alloy composition was the result of ideas developed from the studies on irradiation-produced precipitation and from aging studies on experimental alloys designed to optimize MC and phosphide formation and stability. These alloys were suspected to have good high-temperature creep resistance for several reasons. First, thermal creep resistance in lean stainless steels seems to depend on their precipitate behavior, which appeared non-optimum in the alloys developed to date.[6] Second, radiation resistance in these alloys stems in part from a strong pinning interaction of the fine matrix MC and phosphide particles with irradiation produced dislocations. This interaction ought to carry over to provide resistance to dislocation climb during creep. Third, resistance to radiation embrittlement was due both to the production of carbide phases and to resistance toward formation of coarse intermetallic phases, like sigma and Laves phases, along grain boundaries. Again, these effects were expected to carry over directly to provide enhanced rupture resistance and ductility for improved creep lifetime. Minor element compositional levels and combinations were deliberately chosen to produce these precipitate effects.

Several simple effects summarize the roles envisioned for the various minor alloying elements on precipitate formation and stability, and their manipulation to produce the desired microstructures. These are reactant, catalyst, inhibitor, and interference effects. The matrix composition of 14Cr and 16Ni was selected from earlier studies which indicated that austenite of this composition was more stable against intermetallic phase formation than the 16-18Cr/12-14Ni composition of AISI type 316[7], particularly when Ti is added. The compositions of various heats

of modified 14-16 steel melted by commercial vendors are listed in Table 1. The compositions of various commercially available reference alloys that could be used to produce superheater/reheater components are also listed in Table 1. Comparison of the new modified 14-16 alloys with the commercial alloys shows that both the combinations and levels of minor elements chosen for the former are unique.

The reactant effect is the most straightforward effect. The alloying elements were directly chosen to react and produce the desired precipitate phase. Ti and C were added to produce the MC carbide. Ti and P were added to react with Fe to produce the FeTiP phosphide. Relative to previous work, alloy development studies at ORNL suggested that slightly higher levels of Ti and C could be dissolved in the new lower Cr and higher Ni austenite relative to earlier type 316 + Ti steels (0.25 wt % Ti, 0.05% C).[7]

The catalytic effect is a more subtle effect, but can still be quite easily discerned, particularly when AEM results on phase composition are correlated with microstructural results. Alloying elements that manifest this effect enhance the reaction of other elements to form a particular phase. The precipitate phases are always most enriched in reactant elements. Catalytic elements are either present in the phase to much lower concentrations than the reactant elements (even though they may be enriched in the precipitate phase relative to the matrix) or not present at all (within X-ray EDS detection limits). A schematic diagram of the standard effect of catalysts on chemical reactions in terms of free energy driving forces is shown in Fig. 4a. Catalytic effects were identified for both desirable and undesirable phases, and then manipulated accordingly. Laves phase appears to be catalyzed by Si because its formation is far more sensitive to the concentration of that element than it is to the primary reactants Fe and Mo.[3] Laves formation may also be catalyzed by Nb. Therefore, the Si level was reduced to a very low level to help minimize Laves formation, particularly since Nb was being added for a positive affect on the MC phase. Phosphide formation was found to be catalyzed by V.[3] This was particularly important because P was suspected to cause welding problems if too much was present (above 0.07-0.08%). Catalysis with V appears to contribute to better phosphide

Table 1. Compositions of Commercially Available and New Developmental Candidate Austenitic Stainless Steels for Superheater/Reheater Application

Alloy	COMPOSITION (wt %) (Balance-Fe)											
	Cr	Ni	Mn	Mo	Ti	Nb	V	C	P	B	Si	Other
Commercial Reference Alloys												
316 S S	16	13	2	2.5				.04–.06			0.4–1	
321 S S	17	11	1.5		0.39			0.06			0.4	
Alloy 800H	32	19.5	1		0.4			0.08			0.2	0.4 Al, 0.5 Cu
Alloy 617	23	55	0.2	9	0.5			0.06			0.2	12 Co, 1 Al
17–14 CuMo	16.3	14	0.8	2	0.2	0.45	0.07	0.1			1.0	3 Cu
*Tempaloy-A1	18	11	1.6		0.1	0.15		0.09			0.5	
*Tempaloy-A2	18	14	1.5	1.5	0.16	0.23		0.09		0.003	0.05	
*Tempaloy-CR30A	30	51	0.2	2.1	0.2			0.06			0.3	0.14 Al, 0.05 Zr
Advanced Austenitics from Combustion Engineering (August 1985)												
CE0	14	16	2	2.5	0.3	0.1	0.5	0.08	0.07	0.005	0.4	
CE1	14	16	2	2.5	0.3	0.1	0.5	0.08	0.07	0.005	0.2	
CE2	16	16	2	2.5	0.3	0.1	0.5	0.08	0.07	0.005	0.2	
CE3	14	16	2	2.5	0.3	0.1	0.5	0.08	0.07	0.007	0.2	2 Cu
Advanced Austenitics from AMAX (July 1986)												
AX5	14	16	2	2.5	0.27	0.15	0.5	0.075	0.02	0.005	0.1	
AX6	14	16	2	2.5	0.28	0.15	0.5	0.075	0.04	0.005	0.1	
AX7	14	16	2	2.5	0.18	0.15	0.5	0.075	0.07	0.005	0.1	1.5 Cu
AX8	14	16	2	2.5	0.24	0.09	0.15	0.075	0.04	0.005	0.1	

*Registered trademark of NKK

ORNL-DWG 87 12770

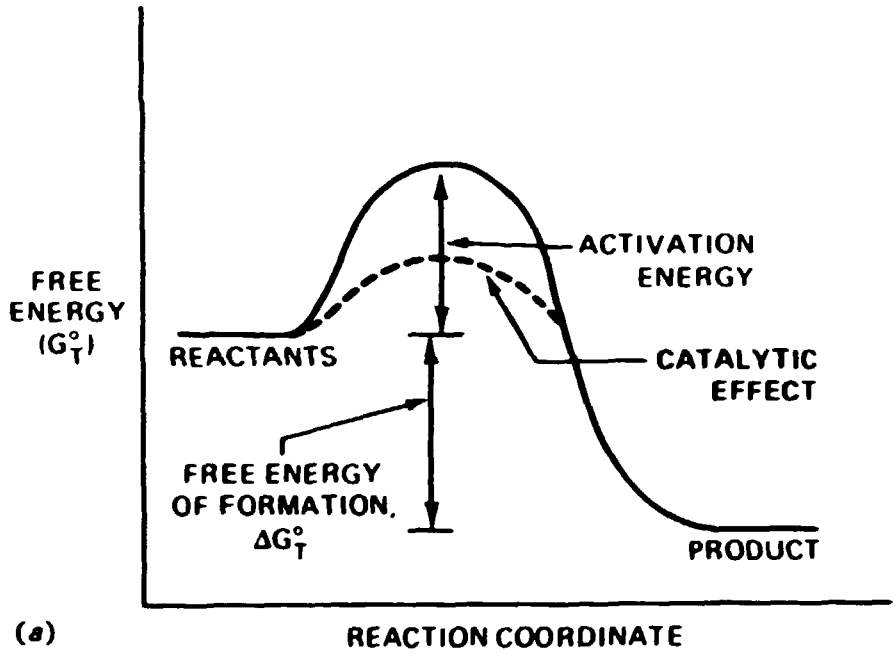

(a)

ORNL-DWG 87-12771A

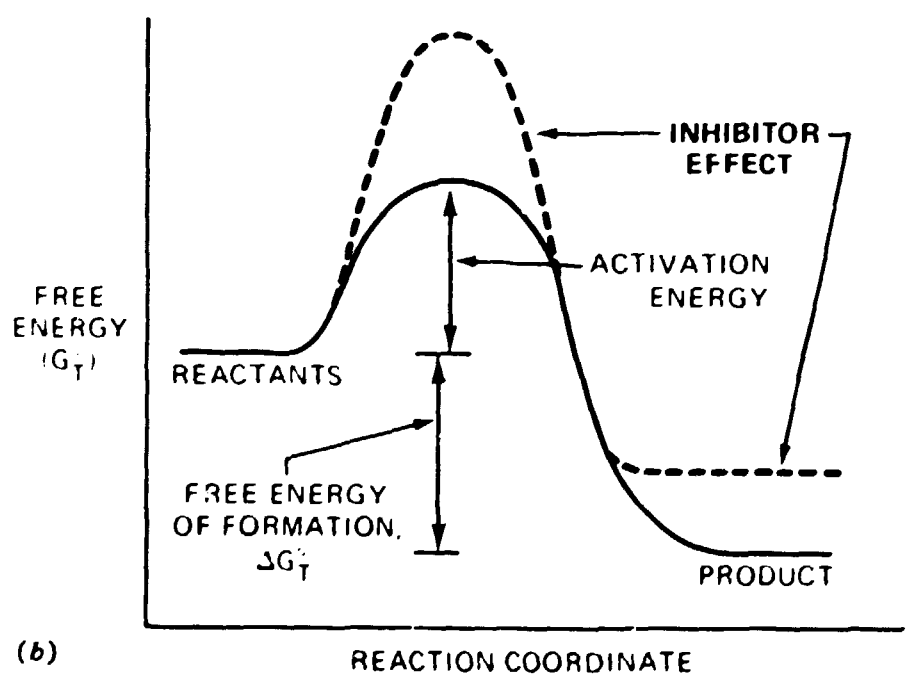

(b)

Fig. 4. Schematic diagrams of free energy changes as a generalized chemical reaction proceeds from the starting components to the final product phase. (a) Illustrates the effect of a catalyst lowering the activation barrier to the forward reaction to allow it to proceed easier or faster, and (b) shows the effects of inhibitors to either make the activation barrier greater or to raise the energy of the product phase to make the reaction more difficult.

formation at lower alloy levels of P, as shown in Fig. 5. Previous studies of similar lean stainless steels suggested that P and B additions to the alloy enhance MC formation and stability[8], suggesting a possible catalytic role of these elements as well. Finally, Ti addition may catalyze the formation of sigma phase.

The inhibitor effect is not obvious at first sight, but is a product of the understanding gained from studying precipitation during irradiation. Alloying elements exhibiting this behavior hinder or block the formation of phases that are the products of other reactant elements. The first hints of such an effect were inferred from the effects of RIS to retard the formation of various thermal phases during irradiation, as depicted in Fig. 3. From the standpoint of reaction energetics, one can visualize inhibition to be by either an increase in the activation barrier to the reaction or by an increase in the free energy of the product phase, which lowers the driving force for the reaction (Fig. 4b). Figure 6 is a a schematic diagram of the composition profile that results from a phase rejecting an insoluble element into the matrix as the particle grows. If rejection must be accomplished before the reaction can proceed, then any difficulty in removing the solute (i.e., low diffusivity or supersaturation in the matrix) would hinder the reaction. This behavior is directly related to the new information provided by AEM which shows little or no concentration of elements in small phase particles that are present in the matrix, like Si or Ni for the MC carbides. Another reason for keeping the Si level in the alloy as low as possible was the idea that Si inhibited formation of most of the carbide phases. However, two important inhibitor effects had to be inferred from a variety of TEM observations because they involved the elements C, P, and B, which are extremely difficult to detect using X-ray EDS. In particular, additions of B and C appear to reduce the formation of Laves phase[3,7,8], and C appears to strongly suppress sigma phase formation. Therefore, higher levels of both of these elements were incorporated to improve the resistance of the new 14-16 alloys to intermetallic phase formation.

The last effect, the interference effect, is a negative effect. An alloying element is either a reactant for more than one precipitate phase so that they compete for it, or it is a soluble element that reduces the

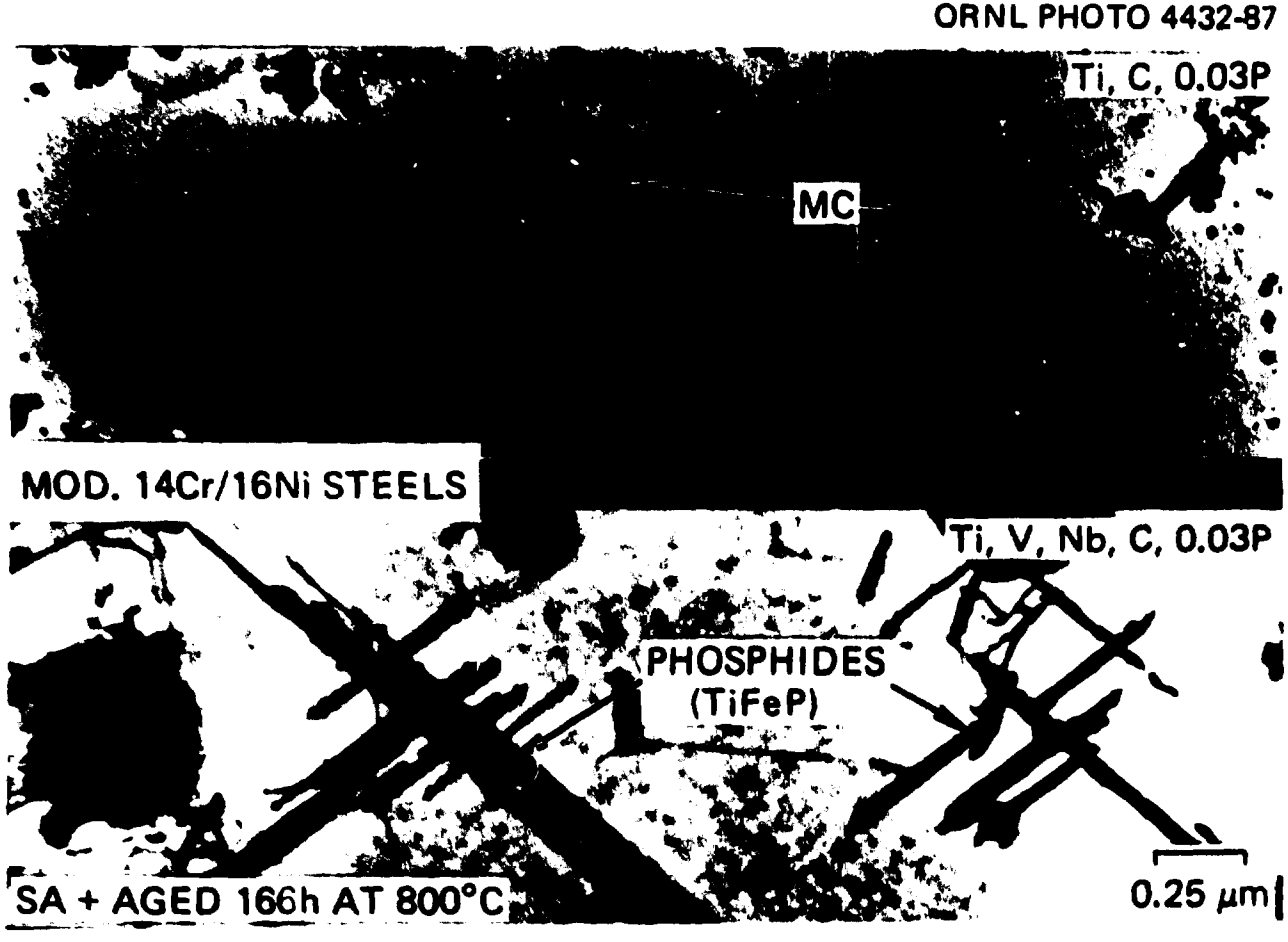

Fig. 5. Comparison of two 14Cr/16Ni alloys after aging in the solution-annealed (SA) condition for 166 h at 800°C shows that phosphide formation is enhanced by V and Nb additions to otherwise identical alloys that contain 0.03 wt % P.

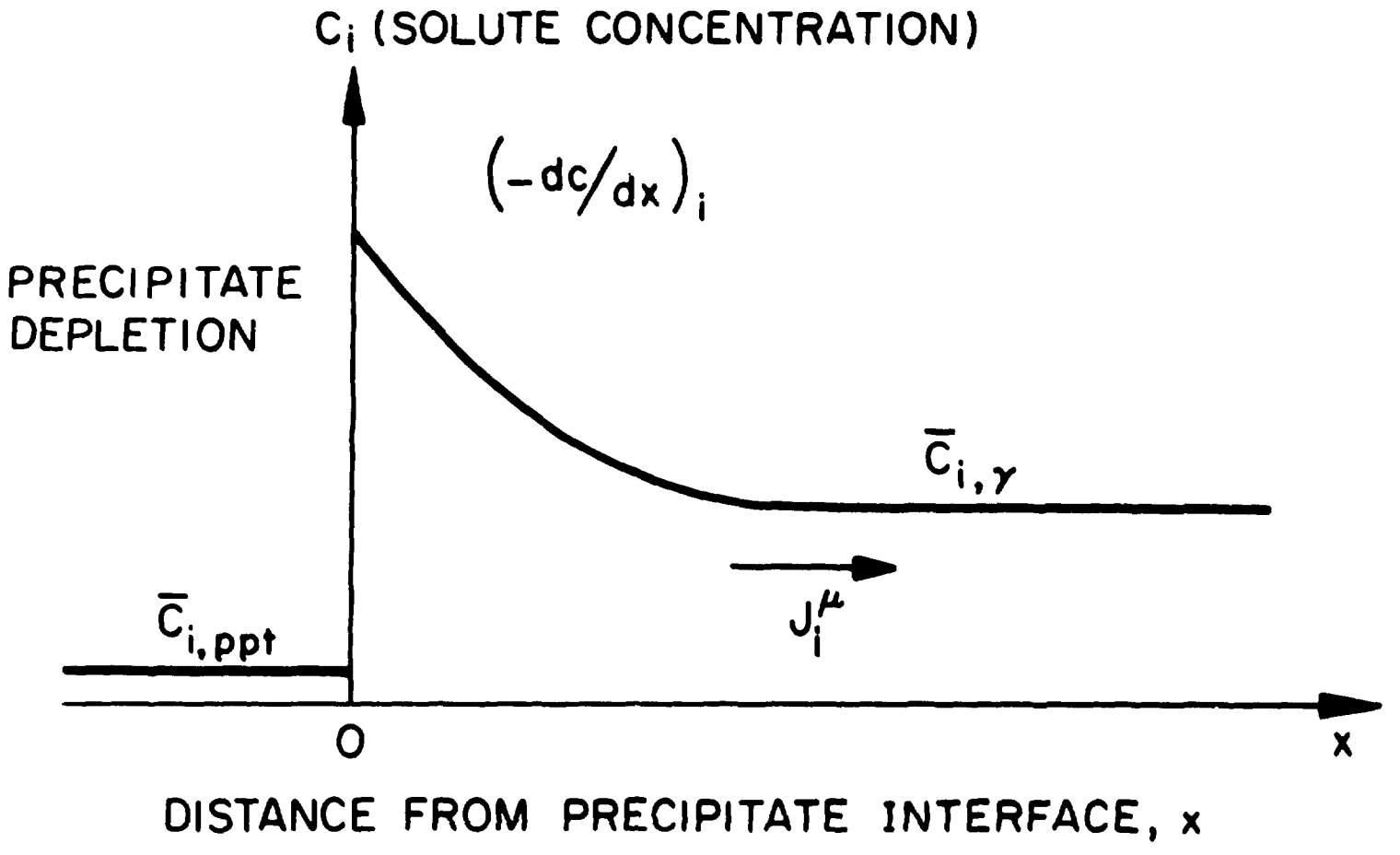

Fig. 6. Schematic diagram of the concentration profile within a precipitate phase and in the matrix adjacent to the advancing interface for a solute that is much less soluble in the new phase than it was in the parent phase.

stability of the precipitate phase. An example of the first case is the competition between the MC and FeTiP phases for Ti. This competition possibly restricts both phases from achieving optimum formation characteristics simultaneously. The idea behind adding V and Nb together with Ti was to substitute these elements for Ti in the MC phase, leaving more Ti free to form the FeTiP phase. The combination of Ti, V, and Nb in the same alloy is one of the unique features of the new modified 14-16 steels[3] (Table 1). An example of the second case was the fact that small MC particles were found to incorporate surprisingly large amounts of Mo and/or Cr, which may not be beneficial to their long-term stability.[3,7] Another reason for adding V and Nb was to have these elements displace Cr and Mo from MC carbide formed when only Ti is present, which could possibly increase the stability of the phase. Such compositional tailoring of an individual precipitate phase forming within a complex alloy does not appear to have been done before.[3]

RESULTS ON CREEP PROPERTIES AND MICROSTRUCTURAL ANALYSIS

The new lean modified 14-16 austenitic stainless steels have substantially improved creep resistance at 700°C relative to other commercially available alloys that could be considered for superheater/reheater application. This can be seen by comparing the creep strain vs time curves shown in Fig. 7 for various alloys tested at 700°C and 170 MPa. Significant improvements in creep strength for the new 14-16 steels relative to the same reference materials can be seen from plots of time to rupture vs applied stress in Fig. 8, for creep testing at 700°C. These new steels approach the creep strength of the superalloy INCONEL 617. More details on the experimental test methods and details of the mechanical property results can be found elsewhere.[1,9] The main focus of this section is to present a portion of the microstructural analyses that has been conducted of creep-tested specimens, and to correlate those with the mechanical properties.

If we look at the TEM microstructure of several of the creep-tested alloys, whose creep are shown in Fig. 7, we can appreciate that the matrix precipitation developed in the new modified 14-16 steels (CEO) is unique.

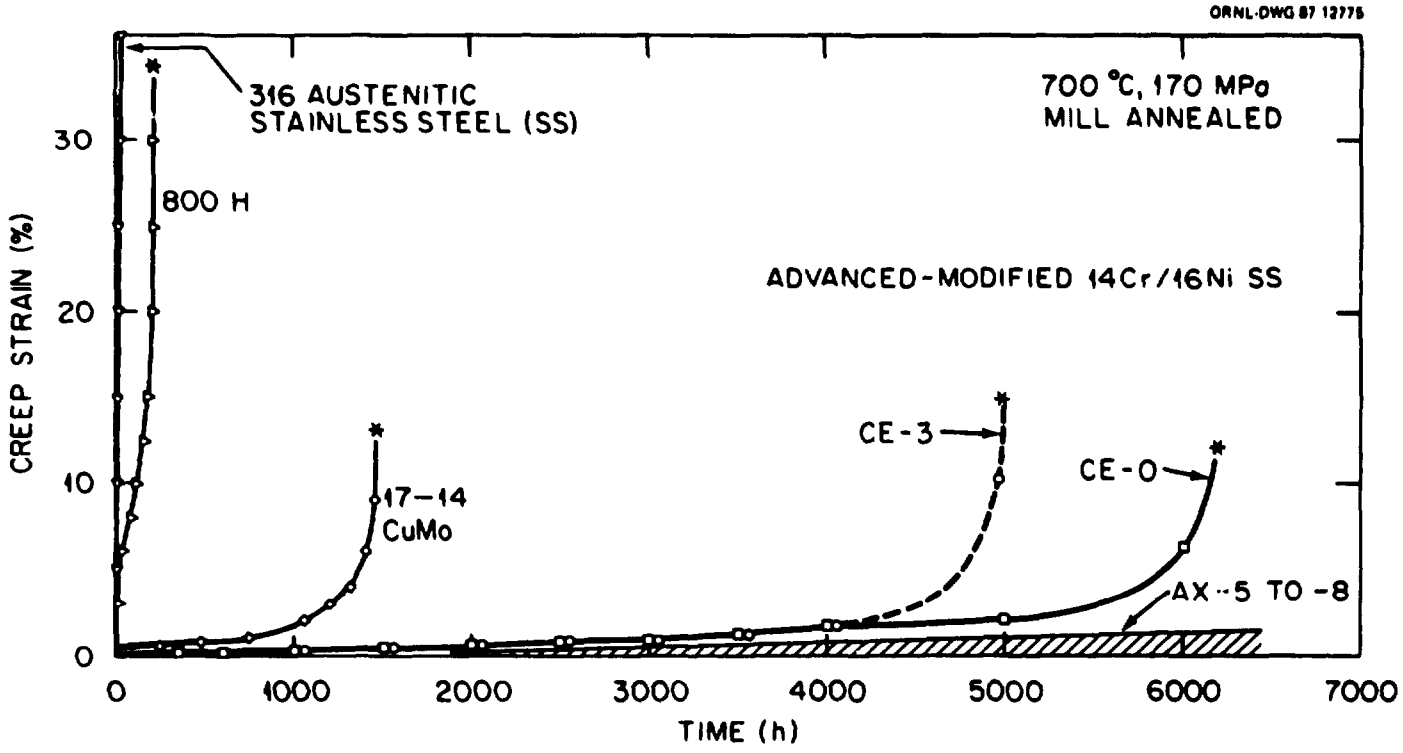

Fig. 7. A plot of creep strain vs time for specimens of various steels tested to rupture in the mill-annealed condition at 700°C and 170 MPa. Alloy compositions are listed in Table 1.

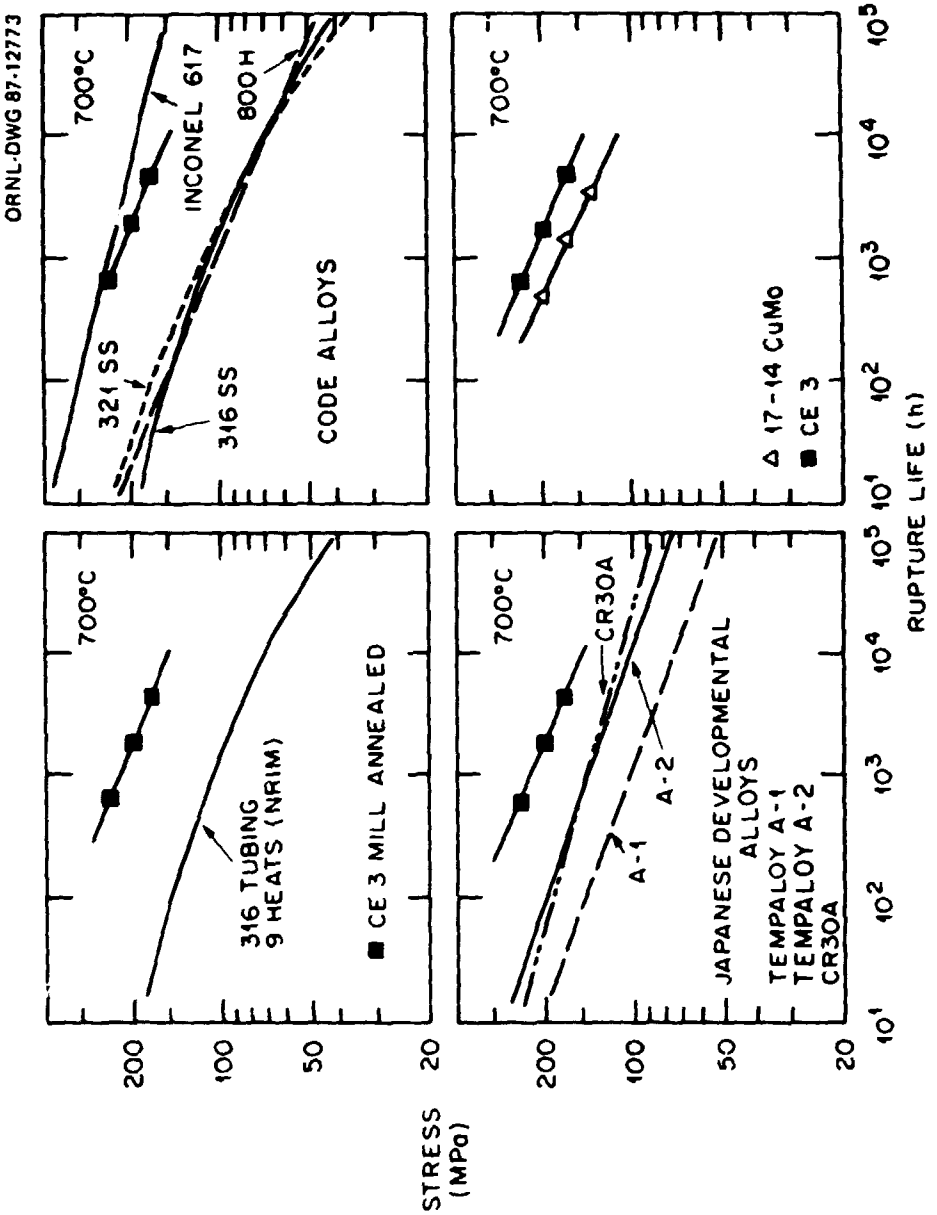

Fig. 8. Plots of creep stress vs time to rupture for various materials tested in the mill-annealed condition at 700°C. Data are separated onto several identical graphs to allow easy comparison without data overlap. Symbols represent data generated at ORNL. Trend curves are drawn from data generated by others.[9] Alloy compositions are listed in Table 1.

The microstructures of mill-annealed type 316, alloy 800H, 17-14 CuMo, and heat CE0 of the modified 14-16 steels developed during creep at 700°C are shown in Fig. 9. The type 316 alloy has virtually no fine-scale matrix precipitation and also has no creep resistance under these conditions. This sample also has large dislocation-free regions adjacent to regions with highly tangled network dislocations (Fig. 9a), suggesting that recovery processes are counteracting dislocation generation processes. Alloy 800H develops a dense dispersion of fine MC carbides together with a coarser distribution of $M_{23}C_6$ (Fig. 9b). Although the dislocations are pinned on some of the precipitates, many dislocations appear to be bowing or climbing past most of the MC particles. The rupture life of alloy 800H exceeds that of type 316 (Fig. 7), but is much less than that of the modified 14-16 steels. The 17-14CuMo develops a microstructure of fine MC particles that appear distributed in coarser clusters, together with particles of an unidentified phase that may be a gamma-prime, during creep at a slightly lower stress of 140 MPa (Fig. 9c). In addition, the 17-14CuMo has many coarse Laves particles distributed throughout the matrix. Many dislocations appear to be pinned at the clusters of finer particles. The 17-14CuMo is significantly more creep resistant than either alloy 800H or type 316 in Fig. 7 at 170 MPa, but it is still 4 to 5 times less creep resistant than CE0. The microstructure produced during creep in CE0 is a fine dispersion of phosphide needles together with a finer dispersion of MC particles, both distributed uniformly throughout the matrix (Fig. 9d). These phases and their distribution and interaction with the dislocation network are different from those found in the other alloys. In particular, the fact that all of the dislocations in the loose network are associated with fine precipitate particles suggests effective pinning is strengthening the modified 14-16 steels.

Interrupted creep tests at 700°C and 100 MPa from another heat (CE3) of the modified 14-16 steels demonstrate that the dislocations are being effectively pinned (Fig. 10). The CE3 heat of steel is modified with Cu, but has a nearly identical precipitate microstructure of fine MC particles and phosphide needles compared to the CE0 heat in either the mill-annealed or the reannealed (1 h at 1200°C) condition. The interruption periods at 700°C, during which the load is removed, should allow dislocations to recover. The fact that creep resumes as though it were following an

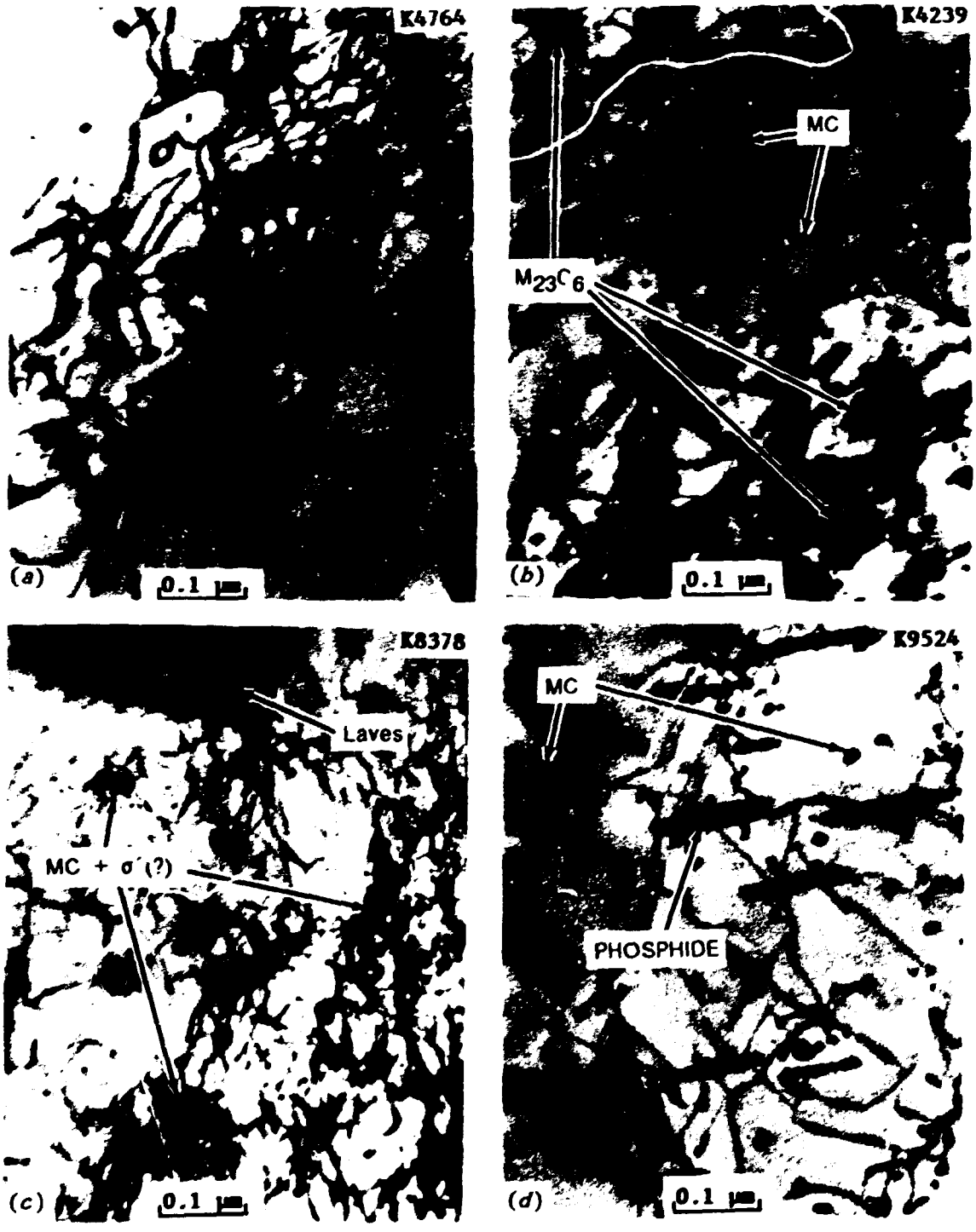

Fig. 9. Matrix microstructure of TEM discs cut from the gage of specimens creep tested in the mill-annealed condition at 700°C. (a) Type 316, 170 MPa, time to rupture(t_r) - 12 h, (b) alloy 800H, 170 MPa, t_r - 120 h, (c) 17-14CuMo, 140 MPa, t_r - 3446 h, (d) modified 14-16 steel (heat CE0), 170 MPa, t_r - 6174 h.

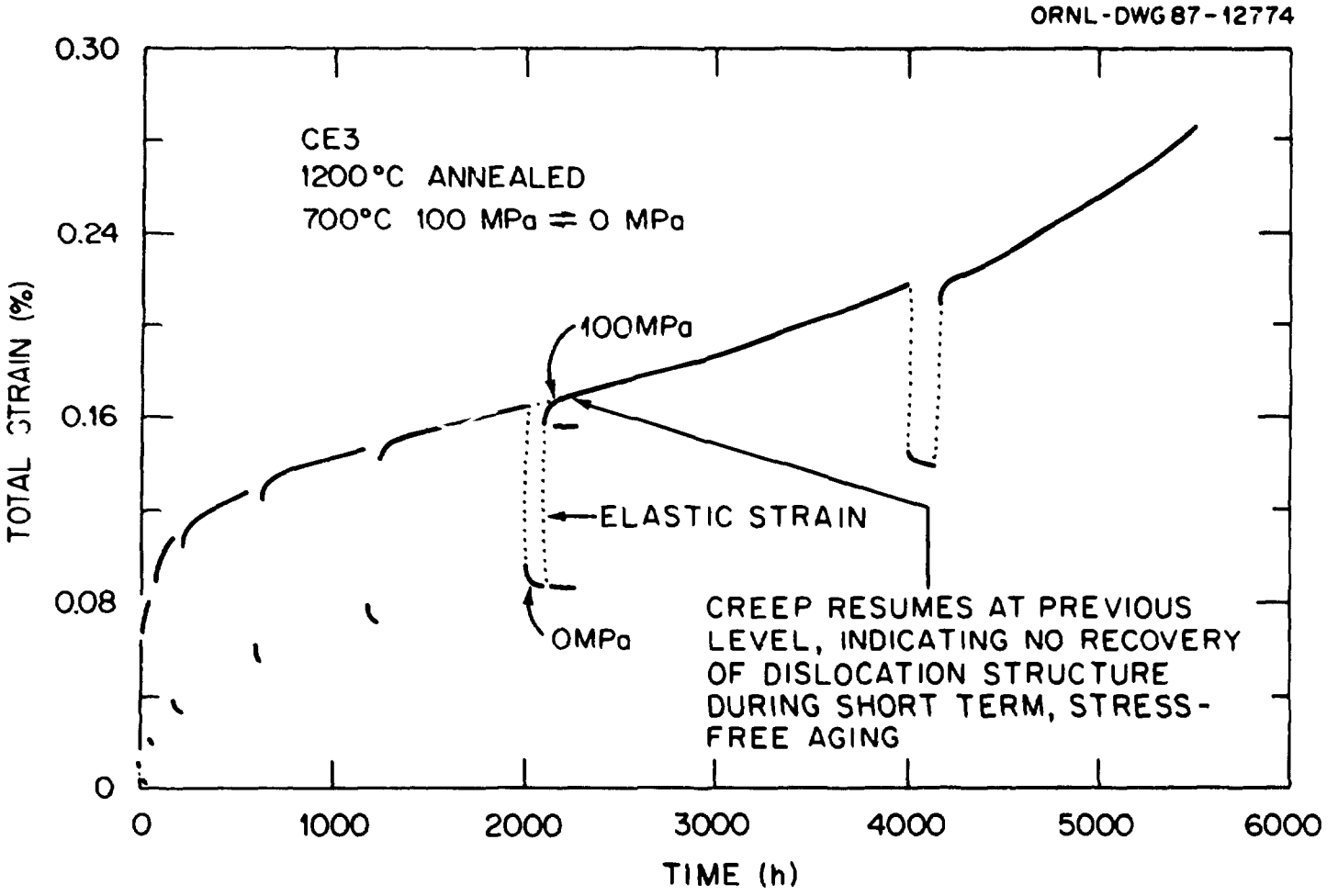

Fig. 10. A plot of total strain vs time for specimen of modified 13-16 steel (heat CE3) creep tested at 700°C and 100 MPa in the reannealed (mill-annealed plus 1 h at 1200°C) condition. The test was interrupted intermittently by removing the load while leaving the specimen at temperature. This short-term anneal was intended to provide an opportunity for dislocation recovery and softening.

uninterrupted creep curve indicates that the material has lost no strength, implying no recovery of the dislocation structure. This suggests very strong pinning of the dislocation structure by the precipitate particles.

Another facet of the improved creep resistance of the modified 14-16 steels is their ductile failure mode, relative to either alloy 800H or 17-14CuMo, despite their increased creep strength. Microstructural comparison of CE3 with 17-14CuMo in Fig. 11 suggests that the differences in fracture behavior correlate with differences in grain boundary precipitation. The 17-14CuMo has only coarse Laves phase particles along the grain boundaries, whereas CE3 has primarily MC and $M_{23}C_6$ and a few Laves particles along the grain boundaries. In terms of fracture behavior, the 17-14CuMo has completely intergranular failure, whereas the CE3 fails by plastic instability in a completely ductile manner. The ductile-failure mode produced by grain boundary carbides may also contribute to the improvements in rupture life observed in Figs. 7 and 8 for the modified 14-16 steels. This difference in grain boundary precipitation and in failure mode punctuates the importance of correctly anticipating the benefits of carbides and then deliberately designing the modified 14-16 steels to enhance carbide formation and minimize intermetallic formation.

The differences in fracture behavior are amplified when crack growth sensitivity during steady state creep is examined. Creep specimens were precracked by room-temperature fatigue prior to creep testing at higher temperatures. Figure 12 shows creep crack growth rates measured at 700°C as a function of stress intensity factor calculated from the applied load. Heat AX5 of the modified 14-16 steels exhibits much better resistance to crack growth than 17-14CuMo when tested at 700°C. Surprisingly, the crack growth resistance is also much better than either types 304 or 316 stainless steels tested at lower temperatures. A crack-resistant material would show less sensitivity to flaws introduced during fabrication than one prone to cracking, and hence promise more reliable service.

Finally, we will touch on one facet of the detailed analysis of precipitates being conducted using AEM on particles extracted from the

ORNL PHOTO 4429-87

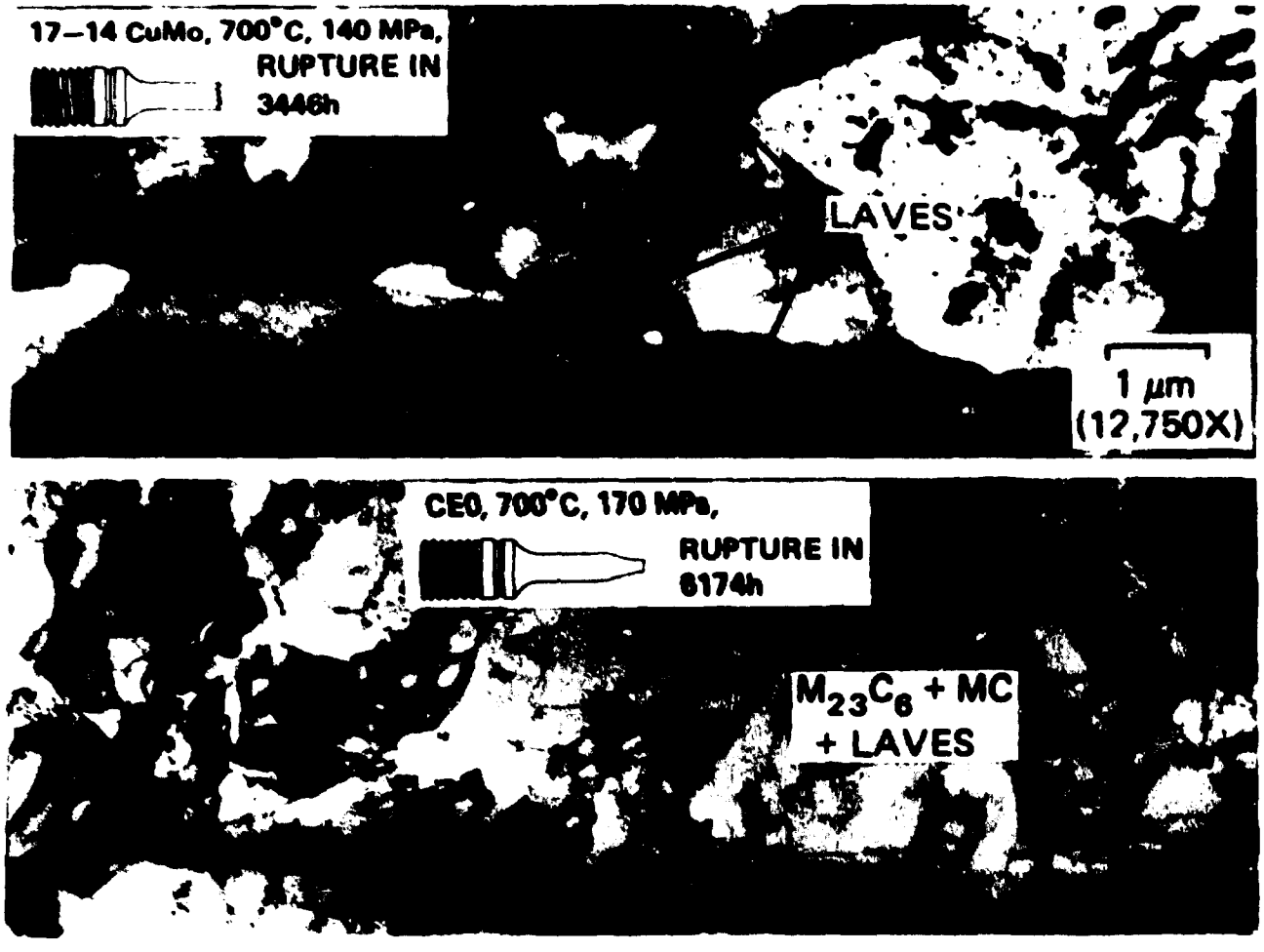

Fig. 11. Grain boundary microstructure of TEM discs cut from the gage lengths of specimens creep tested at 700°C in the mill-annealed condition. Inserts with schematic drawings of the specimen after fracture are included above. (a) 17-14CuMo, 140 MPa, t_r - 3446 h, (b) modified 14-16 steel (heat CE3), 170 MPa, t_r - 4960 h.

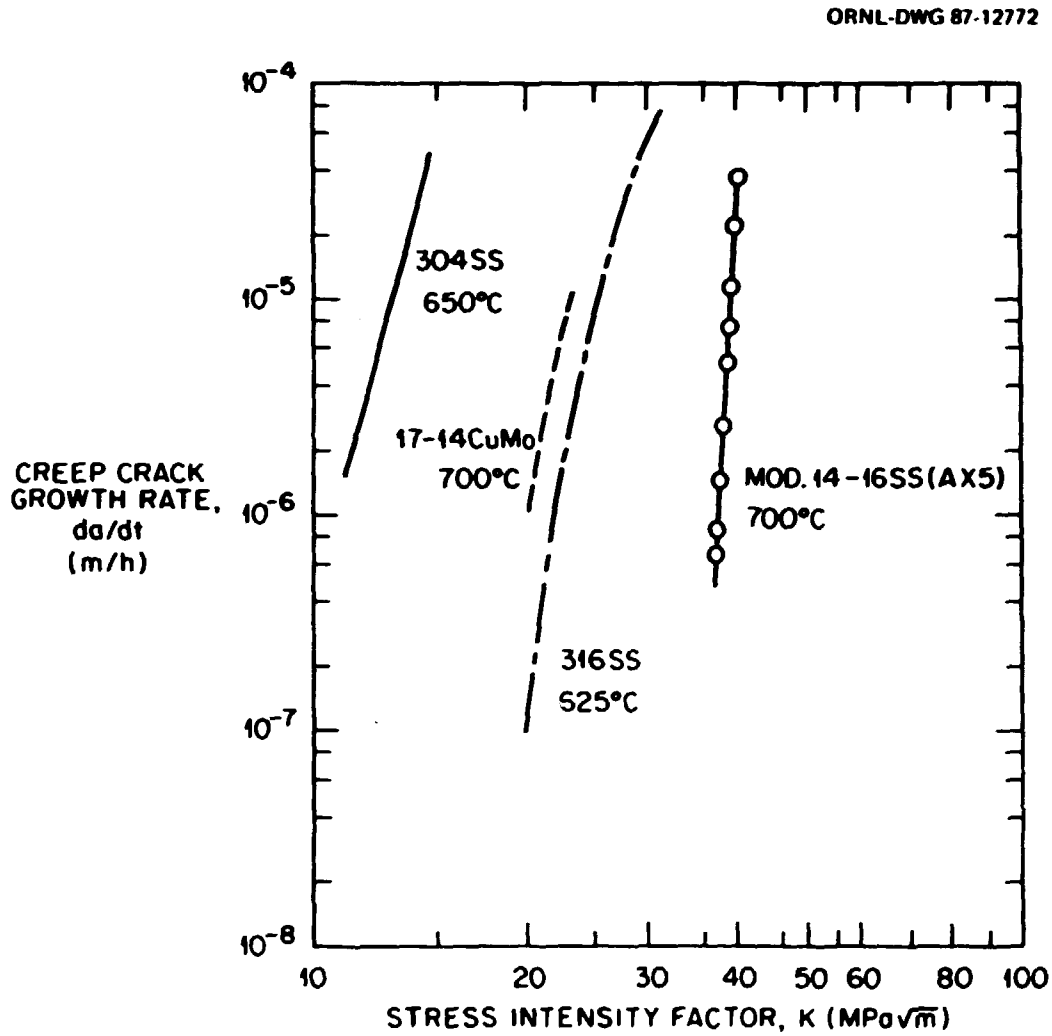

Fig. 12. A plot of creep crack growth rate vs stress intensity factor calculated from the applied load for several austenitic stainless steels. Cracks were introduced prior to creep by room-temperature fatigue. Specimens tested at 700°C had identical geometries, whereas specimens tested at lower temperatures were slightly different.

material on replicas for identification and compositional study. The composition of the fine MC phase in the modified 14-16 steels (CE3) shows that in addition to Ti, Nb and especially V have been incorporated (Fig. 13), as was intended in the desigr of these alloys. The large amount of V in the MC phase is surprising, because it is far more soluble in the austenite than Ti or Nb are. This may indicate an important synergistic effect between Ti and V that causes this behavior. By comparison, the MC carbide found in alloy 800H has mainly Ti with some Cr and Mo, and the MC phase formed in 17-14CuMo has substantial amounts of Ti, Nb, and Mo, in addition to some Cr and Si (Fig. 13). We cannot yet confidently interpret the significance of these MC phase compositional differences. However, it is possible that these differences play a role in making MC formation and stability characteristics and their interaction with dislocations better in the modified 14-16 steels.

Much more mechanical properties and microstructural analysis work has been conducted than is reported here, and a great deal of work is still in progress. More work is needed to confirm the mechanisms suggested for microstructural effects on properties. However, these results do indicate that our alloy development efforts have delivered on their promises and may be even more successful than initially anticipated.[3,6]

SUMMARY AND CONCLUSIONS

The compositions of new modified 14-16 steels developed as advanced steam cycle superheater/reheater materials were selected to produce unique precipitate structures in the matrix and at grain boundaries. Insight for these microstructures and the alloy compositional modifications necessary to produce them are a spin-off from the fast breeder and fusion reactor materials programs. The insight and new ideas for controlling and tailoring precipitation came from studies of precipitate behavior during irradiation and from efforts to develop radiation-resistant steels.

The creep resistance of the new modified 14-16 steels is clearly better than conventional alloys like 316 and alloy 800H, better than

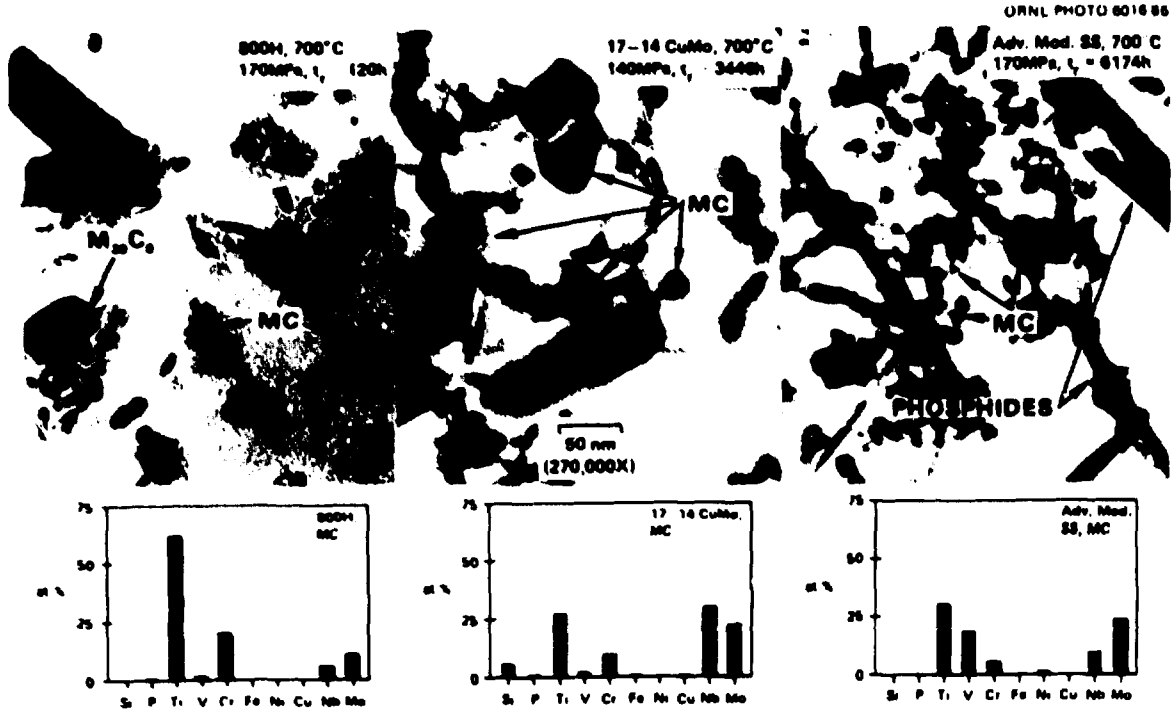

Fig. 13. TEM of precipitates extracted on replicas produced from the gage lengths of various steels creep tested in the mill-annealed condition at 700°C, together with compositions of MC phase particles determined via quantitative X-ray EDS analysis performed on those replicas.

17-14CuMo and approaches the behavior of Inconel 617 at 700°C in the mill-annealed condition. Correlation of microstructure with properties suggests that strong precipitate effects are primarily responsible for the improved creep resistance of the modified 14-16 steels. Fine matrix MC particles and phosphide needles appear to strengthen the material against creep by effectively pinning dislocations. The dispersions of carbides along grain boundaries that form with a minimum of embrittling intermetallic phases appear to contribute to the rupture resistance and ductile-fracture behavior of these steels.

The overall phase selection and the specific compositional tailoring of the MC phase would not be possible without the use of AEM. This work is a general example of how the use of state-of-the-art high technology, in this case compositional microanalysis, can reveal new information, which can then be used to guide precise and efficient alloy development.

REFERENCES

1. R. W. Swindeman, G. M. Goodwin, and P. J. Maziasz, "Investigation of Candidate Alloys for Advanced Steam Cycle Superheaters and Reheaters," elsewhere in this proceedings.

2. P. J. Maziasz, J. Nucl. Mater. 122 & 123 (1984) 472.

3. P. J. Maziasz, "Microstructural Stability and Control for Improved Irradiation Resistance and for High-Temperature Strength of Austenitic Stainless Steel," Proc. Conf. Microstructural Control - 86 (MiCon-86), to be published as an Amer. Soc. for Testing and Matls. - Special Technical Publication (ASTM-STP) in 1987.

4. P. J. Maziasz, Effects of Helium Content on Microstructural Development in Type 316 Stainless Steel Under Neutron Irradiation, ORNL-6121, November 1985.

5. E. H. Lee, P. J. Maziasz, and A. F. Rowcliffe, Conf. Proc. Phase Stability During Irradiation, eds. J. R. Holland, L. K. Mansur, and D. I. Potter, The Metallurgical Society of AIME, Warrendale, Pa., 1981, pp. 257-270.

6. R. W. Swindeman et al., Alloy Design Criteria and Evaluation Methods for Advanced Austenitic Alloys in Steam Service, ORNL-6274, May 1986.

7. P. J. Maziasz and S. Jitsukawa, "Minor Compositional Variations of the Austenitic PCA to Explore MC Formation and Stability Characteristics for Improved Radiation Resistance," ADIP Semiannu. Prog. Rept., DOE/ER-0045/14, U.S. Department of Energy, Washington, D.C., 1985, pp. 37-48.

8. P. J. Maziasz and A. F. Rowcliffe, Oak Ridge National Laboratory, and G. D. Johnson and M. M. Paxton, Hanford Engineering and Development Laboratory, unpublished data from joint work, 1985.

9. R. W. Swindeman, G. M. Goodwin and P. J. Maziasz, Procurement and Screening Test data for Advanced Austenitic Alloys for 650°C Steam Service (Part 1, 14Cr-16Ni Steels and 20Cr-30Ni-Fe Alloys), ORNL/TM-10206/P1, April 1987.

DEVELOPMENT OF A DESIGN METHODOLOGY FOR HIGH-TEMPERATURE CYCLIC APPLICATION OF MATERIALS WHICH EXPERIENCE CYCLIC SOFTENING

D. L. Marriott, J. F. Stubbins, F. A. Leckie,
J. L. Handrock and B. Kschinka

College of Engineering
University of Illinois at Urbana-Champaign
Urbana, Il 61801

ABSTRACT

Consideration is being given to using low alloy steels, such as 2.25 Cr 1 Mo steel, in a heat treated form to produce a bainitic microstructure with improved short term strength compared with the more commonly used annealed form. It has been found, however, that the bainitic structure softens significantly under cyclic loading, as a secondary effect of which the creep strength is also shown to be reduced. Tests in which periodic load reversals were superimposed on a steady load creep test have shown reductions of creep life of an order of magnitude or more. One major mitigating factor is that it appears that cyclic softening only occurs in material subjected to significant strain reversals. In a typical pressure vessel such conditions are only achieved typically in localized areas such as notch-like details and areas experiencing high cyclic thermal gradients. The investigation described here is aimed at determining the effect of local cyclic softening on residual strength of components. This has been done by performing load controlled tests on two types of notched bars, a relatively blunt Bridgman notch with an elastic SCF of 1.6, and a sharper Vee-notch with an SCF of 4.4, together with a small number of uniaxial specimens as controls. Some theoretical results, which attempt to characterize component behavior in a very generalized way, are described, and plans for developing design rules are discussed briefly.

INTRODUCTION

Several CrMo low allow steels are currently being considered for pressure vessel construction in quench and tempered forms. While this provides a considerable enhancement of the monotonic strength characteristics, materials tested in this way suffer a significant loss of strength due to cyclic softening. In simple axial loading, this effect has been found to significantly reduce the long term creep strength, even when the stress range is well below the initial yield strength of the material. On this evidence alone it might be concluded that, where cyclic loading is expected, there may be little or no advantage in using the bainitic structured material in preference to the more common ferritic-pearlitic form. On the other hand, most practical instances of significant stress reversal in components only occur in localized regions such as notch details or surface layers in pipes under cyclic thermal gradients. It is therefore feasible to suppose that conditions may arise where local softening has an insignificant effect on the overall load carrying capacity of the component, thus allowing the full strength attained by heat treatment to be utilized in determining primary stress limits for design.

In order to explore the influence of cyclic softening on component load carrying capacity, a series of tests has been performed on plain and notched, axially loaded specimens. The object was to determine the relative effects of periodic load cycles on creep strength of the material alone as opposed to its response to complex strain reversals in which local behavior is kinematically constrained to some extent by the remainder of the structure.

EXPERIMENTAL WORK

MATERIAL

The material is a 2.25 Cr 1 Mo steel containing reduced residual impurities. The chemical composition of this alloy is given in Table 1. This material was produced by Kawasaki Steel and was supplied to the

University of Illinois by Oak Ridge National Laboratory (ORNL) in the form of sections from a 400 mm thick ring forging.

The heat treatment involved holding the material isothermally at 1070°C for 18 hours followed by a water quench. The material was then tempered at 650°C for 17 hours and air cooled to ambient. This was followed by a simulated post weld heat treatment at 695°C for 19 hours. From this heat treatment the material near to the surface has a coarse ferrite lath structure with local regions that are more equiaxed in shape. The ferrite lath or sub-grain boundaries comprise regular, fine dislocation networks and there is much less evidence of fine scale precipitation at these boundaries. For specimens cut from approximately the center of the 400 mm forging, the microstructure comprises a mixture of fine-structure similar to that observed in surface sections and coarse grains of polygonal ferrite. The coarse ferrite grains contain a uniform fine dispersion of M_2C carbides.

TEST EQUIPMENT

Two 5-ton load capacity screw-driven electromechanical test machines manufactured to an ORNL mechanical design by Applied Test Systems, Inc. (ATS), provide the basis of the creep-fatigue testing performed in this study. The combined stepper-motor screw-jack driven features of this equipment produces low strain rate machine capable of producing strain rates from a maximum of 0.05%/s to as low as 6E-6%/hr. This capability allows the performance of creep-fatigue tests containing very slow ramp loadings and hold times of almost indefinite duration. This ability allows long term creep-fatigue tests to be completed which approach a more realistic representation of actual service conditions. For elevated temperature (up to 1000°C), these test frames are outfitted with three zone resistance split furnaces, each zone containing an independent temperature controller. Further details of the test equipment are given in Ref. 1.

TEST SPECIMENS

Three types of specimens were used in this test program, the dimensions of which are given in Fig. 1

The second two types of specimens consist of notched bars, the first of which contains a Bridgman notch with a moderate stress concentration factor (SCF) of 1.6. The second type of notch is a BS standard Vee-notch having a relatively high SCF of 4.4.

PRESENTATION OF RESULTS

Basic Fatigue Test Results

Strain controlled fully reversed fatigue tests performed by Pejsa[2] show this material to experience significant cyclic softening. Tests were conducted on material in the as-received condition at 565°C for a variety of waveforms at total strain ranges of 0.5% and 1.0%. The softening behavior is a nearly continuous process from initial cycling right up to the point of failure. In all cases though, a significant portion of the softening occurs in the initial portion of the fatigue life.

From Pejsa's original data, it is possible to plot the maximum and minimum stress as a function of log cycles and strain range for each of the waveforms tested. Such a plot is shown in Fig. 2 for selected cyclic conditions. These results in effect represent the strength of the material under conditions of cyclic softening and will later be shown to correlate very well with load control tests performed on both plain and notched bars.

Constant Strain Rate Tests

Constant strain rate tensile tests have also been performed on smooth specimens to obtain elevated temperature strain rate effect data for this material under monotonic loading. For comparison room temperature tests (20°C) were completed at strain rates of 0.5%/min and 0.05%/min from 0 to 10% strain. Elevated temperature tests (565°C) were completed at strain rates of 0.5%/min, 0.05%/min, 0.005%/min, and

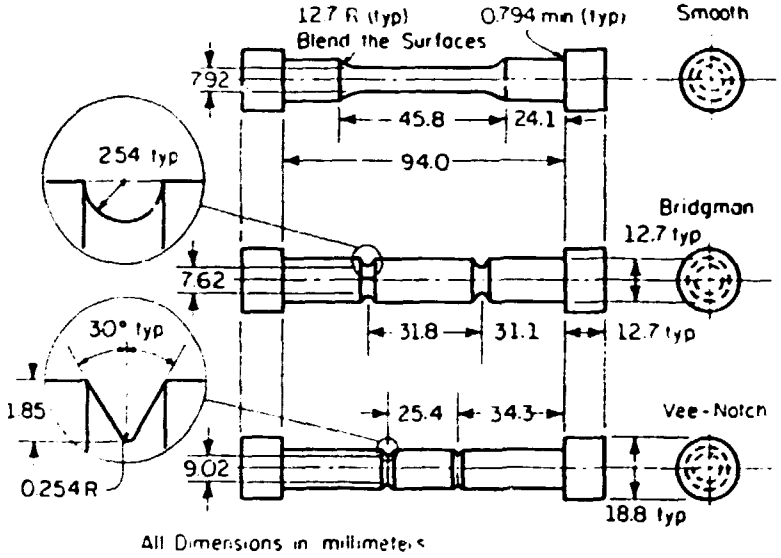

Fig.1 Standard uniform section and notched bars used in test program

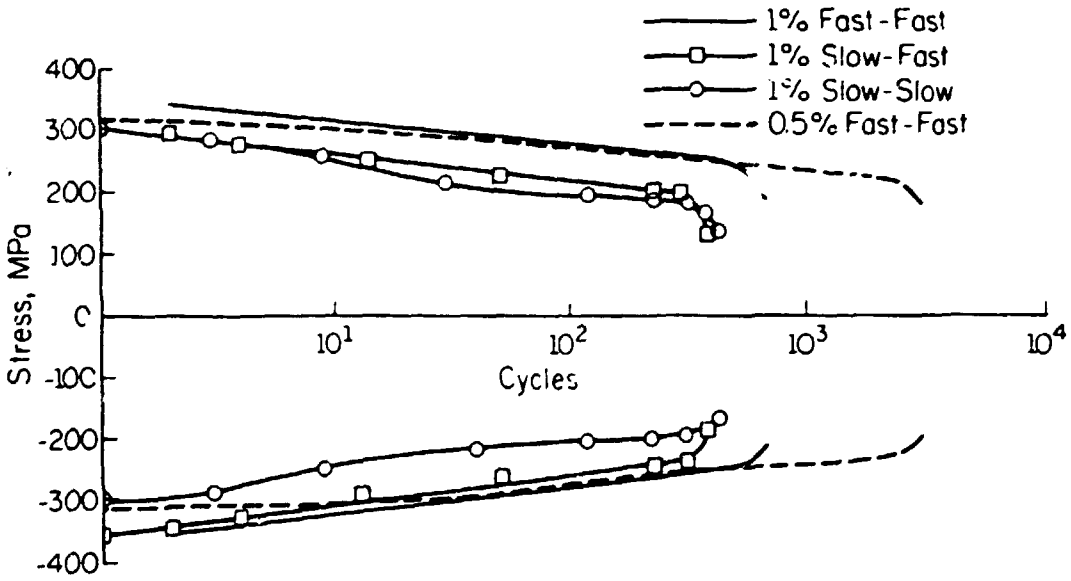

Fig.2 Maximum and minimum stress versus number of cycles for a variety of cyclic conditions

0.0005%/min. The stress versus strain data from these tests are plotted in Fig. 3. The room temperature tests showed essentially no strain rate effect. When tested at elevated temperatures (565°C) this material shows a much different stress-strain response. After reaching the 0.2% yield strength, the material experienced a small amount of hardening after which softening was observed. Not only was the amount of hardening very slight (maximum strength equal to 1.02 to 1.08 times the yield strength), the region over which hardening occurred was much less than that experienced at room temperature.

The elevated temperature tests also show significant strain rate effects. As strain rate increases, both the yield strength and the ultimate strength increase. Figure 3 shows that the rate of increase of the yield and ultimate strengths decreases slightly with increasing strain rate. After reaching the ultimate strength, the material softens at a rate which, to a first approximation, is insensitive to strain rate.

Periodic Load Reversals On Plain And Notched Bars

The phenomenon which focused this program on strain softening is the observation that low alloy steels in quenched and tempered form have been shown by Swindeman[3] to display considerable loss of creep endurance as a result of periodic load reversals even when the stress range is significantly lower than the initial yield stress range.

The effect of cyclic loading on strength is shown clearly by plotting the peak maximum and minimum stresses in strain controlled fatigue tests against the log cycles (see Fig. 2). Unlike the linear plots, these curves show no plateau, but instead a continuous, exponential decrease in strength with time. Cyclic strength appears to be strongly dependent on the frequency of the cycle but only weakly dependent on the wave shape of the strain history or the strain range. This suggests a simple first-order model of cyclic softening in which the current strength is represented as a function of the number of load cycles and the load cycle frequency $\sigma_y(N) = f_1(N) \cdot f_2(f)$ where N = number of load cycles and f = frequency in cycles/unit time.

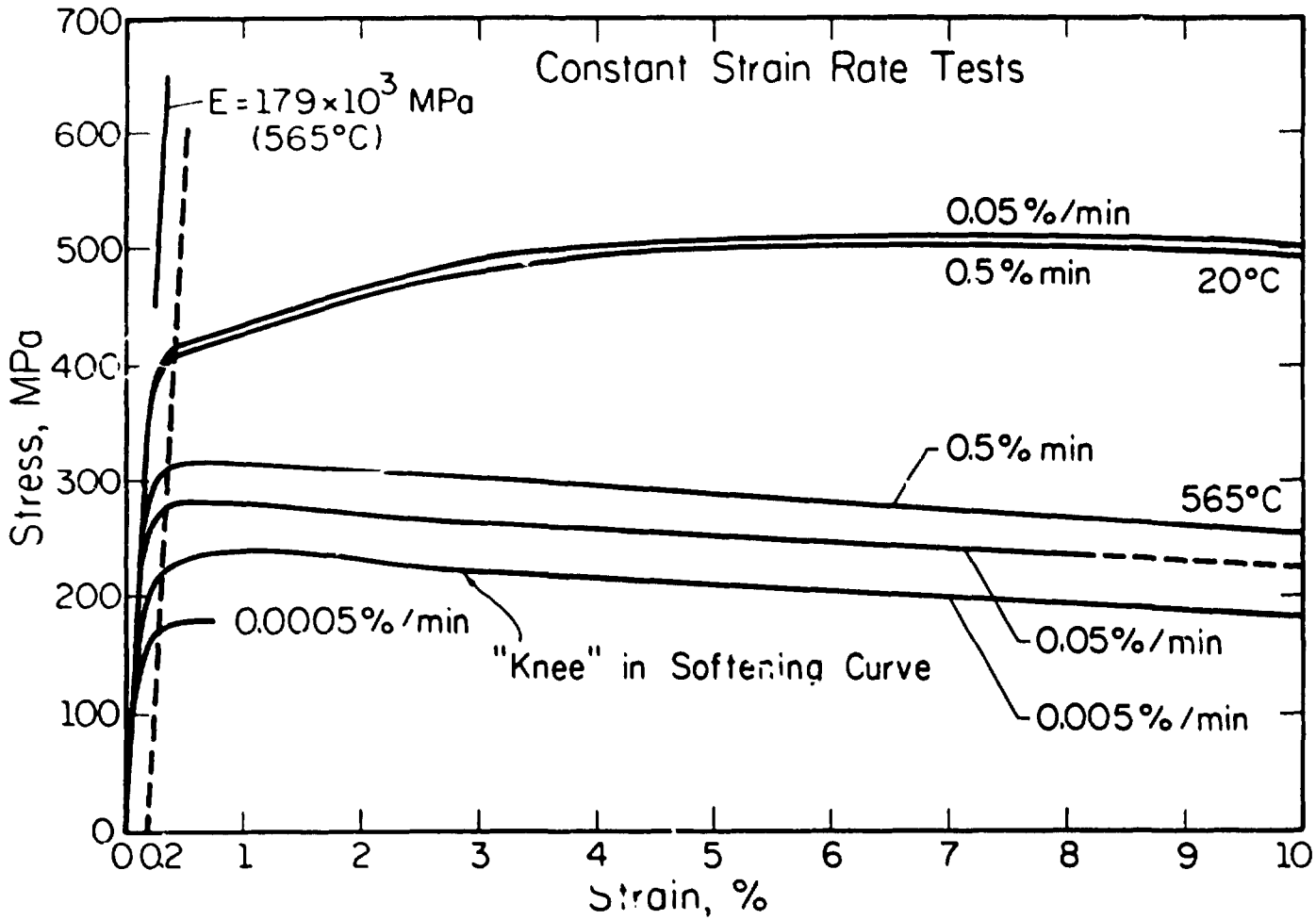

Fig.3 Constant strain rate test results

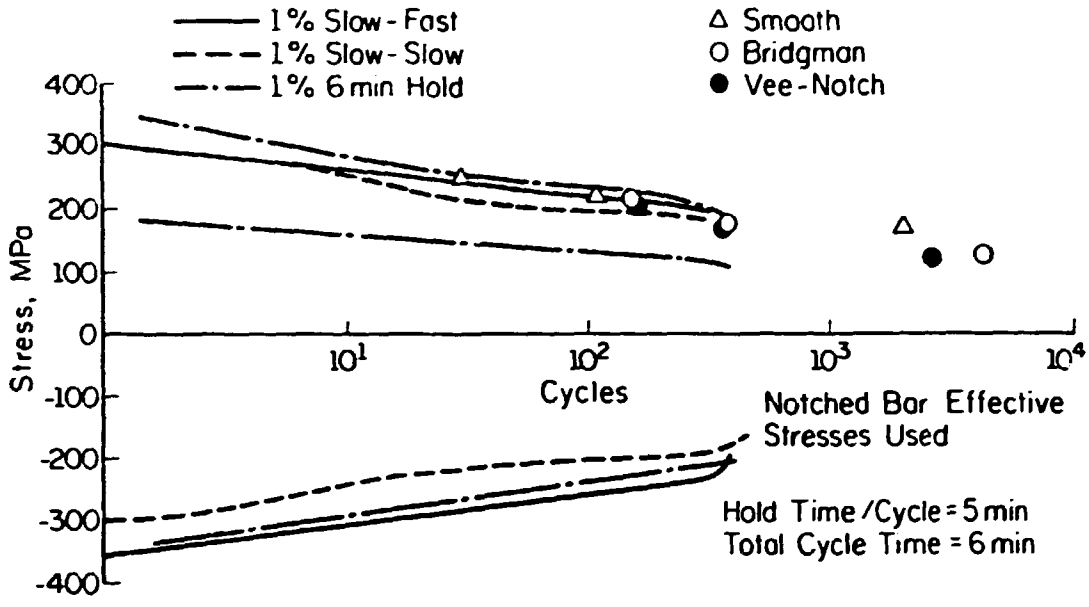

Fig.4 Smooth and notched specimen creep tests with interspersed load reversals test data superimposed on cyclic softening curves

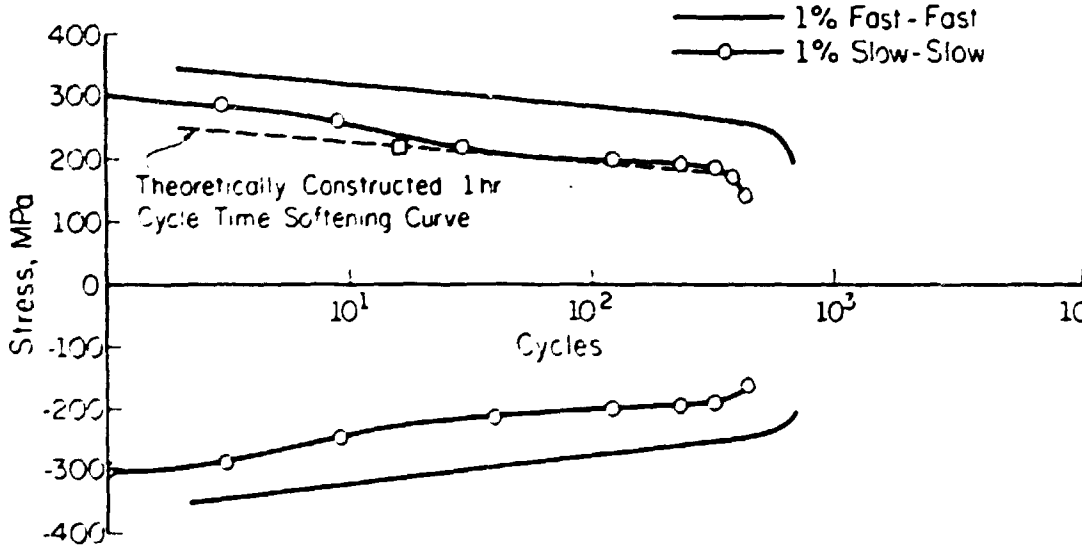

Fig.5 Theoretical versus experimental frequency dependence of cyclic strength. Experimental data point ( ) consists of a Bridgman specimen creep test with superimposed load reversal every 1 hour. Result is plotted using effective stress

To test the hypothesis, the uniaxial creep tests with interspersed load reversals have been plotted on the same graph as the softening curves in Fig. 4. These points fall close to the tensile stress softening line, and the specimen lives would be reasonably accurately predicted by simply assuming the strength to decrease with number of cycles until the tensile strength of the specimen is exceeded.

The same hypothesis holds for more complex stress situations. As also shown in Fig. 4, the lives of all notched specimens undergoing full load reversals are predicted quite well by the number of cycles required to reduce the cyclic strength to the effective stress at the notch net section at the specified cycle frequency.

The frequency dependence of cyclic strength can also be approximated relatively simply. The rate dependence of this material has been examined over a wide range of strain rates, and it is observed that the cycle-dependent softening curves for different frequencies vary in a way similar to the monotonic rate dependence. Figure 5 includes such a curve for a 1-hour cycle time, constructed theoretically on the above hypothesis, which corresponds very well with the one Bridgman specimen tested at that frequency.

From the results of fully reversed load tests on notched bars, it is clear that cyclic softening can have a profound effect on component life, reducing the number of cycles to failure by fatigue and creep life in hours by factors of 10 to 20, and this despite the fact that the cyclic stress range is well below the initial yield range in some cases. For instance, in the testing of a Bridgman notch bar with a nominal net stress at the root of 171 MPa, the Mises effective stress is only 128 MPa, well below the initial yield stress of 310 MPa. The life, however, is only 4372 cycles. From the extrapolation of the rapid cycle data, the cyclic life at this load level is predicted as about 30,000 cycles, and a theoretical prediction based upon initiation at the notch root is nearly 70,000 cycles. Similarly, the creep life predicted from the steady load effective stress at the notch is approximately 3700 hours. In view of the fact that the load reversal is rapid, so that the cyclic stress distribution is approximately elastic, the stress range through most of the notch section is considerably less than the steady

creep effective stress reaching only 124 MPa at the center. This demonstrates that cyclic softening can cause serious reduction of cyclic life at even modest strain levels.

On the basis of this evidence alone, it might be concluded that there is little point in heat treating a low alloy steel to improve its initial strength, if this is to be lost later as a result of cyclic softening. Before accepting this as a general conclusion, it should be observed that a notched bar is a very severe test of stress concentration effects because the entire cross-section of the component is affected by any stress redistribution which may result from plastic deformation at the notch root. In an effort to simulate a more realistic situation, some of the notched bar tests were performed under an R-ratio of 0, thus ensuring that only a small volume of material near the notch root experienced stress reversals. These tests show little or no overall deterioration due to softening. As shown in Table 2, the Bridgman specimen showed no significant reduction in life compared with a similar steadily loaded specimen.

DISCUSSION OF EXPERIMENTAL FINDINGS

It is concluded that the effect of cyclic softening on component behavior is extremely complex and far from being understood well enough to make full use of materials displaying this phenomenon. Clearly there are some situations in which the residual strength is little different from the same material in the annealed form, and in such cases there is no advantage in performing expensive heat treatment. A situation like this might arise, for instance, in a tube wall experiencing severe thermal gradients. On the other hand, there are many practical situations where cyclic stress reversals are confined very locally, to notches or thin surface layers in thick vessels, or where there are clearly no cyclically reversing stresses at all. It would be unjustifiably conservative, in these cases, not to utilize the improved strength gained by heat treatment. It is easy to identify the extremes of the spectrum. What remains to be done is to determine some reliable

criterion for distinguishing between situations in which cyclic softening can be ignored from those in which it cannot.

There are two aspects to the problem just identified, the first relating to material behavior, and the second to component response to cyclic load.

i) Cyclic softening seems to require at least sign reversal of stress. Uniaxial creep tests in which the load was simply removed and replaced have shown no reduction in life compared with steady load tests. On the other hand, the required degree of reversal to cause softening appears to be significantly less than the initial, or even the cyclically softened, yield range as shown by the strong effect displayed by the notched tests under full load reversal. In order to investigate this point further, and to provide some theoretical backing for the simple cycle dependent yield criterion obtained empirically, some progress has been made in developing a constitutive model describing the cyclic softening effect. This work is described briefly in the next section.

ii) The component design problem, which applies not only to cyclic softening but to a wide range of other design situations such as elastic follow-up and inelastic notch strains, is the need for a criterion to judge whether local strain concentrations are strain- or load-controlled. Local strain control amounts to saying that local cyclic softening will not interact with the component load carrying capacity. If conditions in highly strained regions can be determined as a property of the component and the load level only weakly dependent on material strength, then a detailed understanding of cyclic softening is not necessary to evaluate component performance. Some preliminary studies indicate that aspects of local strain behavior in components are, in fact, relatively independent of material constitutive behavior, and that it may be possible to define some classes of problems as insensitive to cyclic softening. These findings are discussed in the section on COMPONENT ANALYSIS.

THEORETICAL MODELING OF SOFTENING

The softening model described in this section is confined for the present to time independent cyclic loading.

The data was obtained from smooth specimen strain controlled fully reversed fatigue tests.[2] Two strain ranges, 0.5 percent and 1.0 percent, were used with both tests performed at a strain rate of 0.004/sec.

In principle, several unified constitutive models are capable of modeling cyclic softening behavior.[4,5] In practice, fitting the form of the constitutive equations to experimental data was found to be more complex than first appearances suggest. This was not simply a case of computational difficulty. The functional forms offered by these constitutive models were inconsistent with the type of behavior observed experimentally. For this reason the model described here is developed as an extension of an existing simple model of stable cyclic inelastic behavior, that has been used extensively and found to represent real material behavior with reasonable fidelity.[6]

The model presented here assumes that the loading and unloading regions of the σ-ε hysteresis loop may be represented by a Ramberg-Osgood form.[7] Full details of the model are given in Ref. 8. For the uniaxial case

Total Strain $$\Delta\varepsilon^* = \Delta\varepsilon^*_e + \Delta\varepsilon^*_p \qquad (1)$$

Elastic Strain $$\Delta\varepsilon^*_e = \frac{\Delta\sigma^*}{E} \qquad (2)$$

Inelastic Strain $$\Delta\varepsilon^*_p = \left(\frac{\Delta\sigma^*}{C}\right)^{1/m} \qquad (3)$$

An asterisk (*) superscript is used to indicate specific stress and strain values in individual hysteresis loops. For notation see Table 3 and Fig. 6. It should be noted that the use of a nonconventional

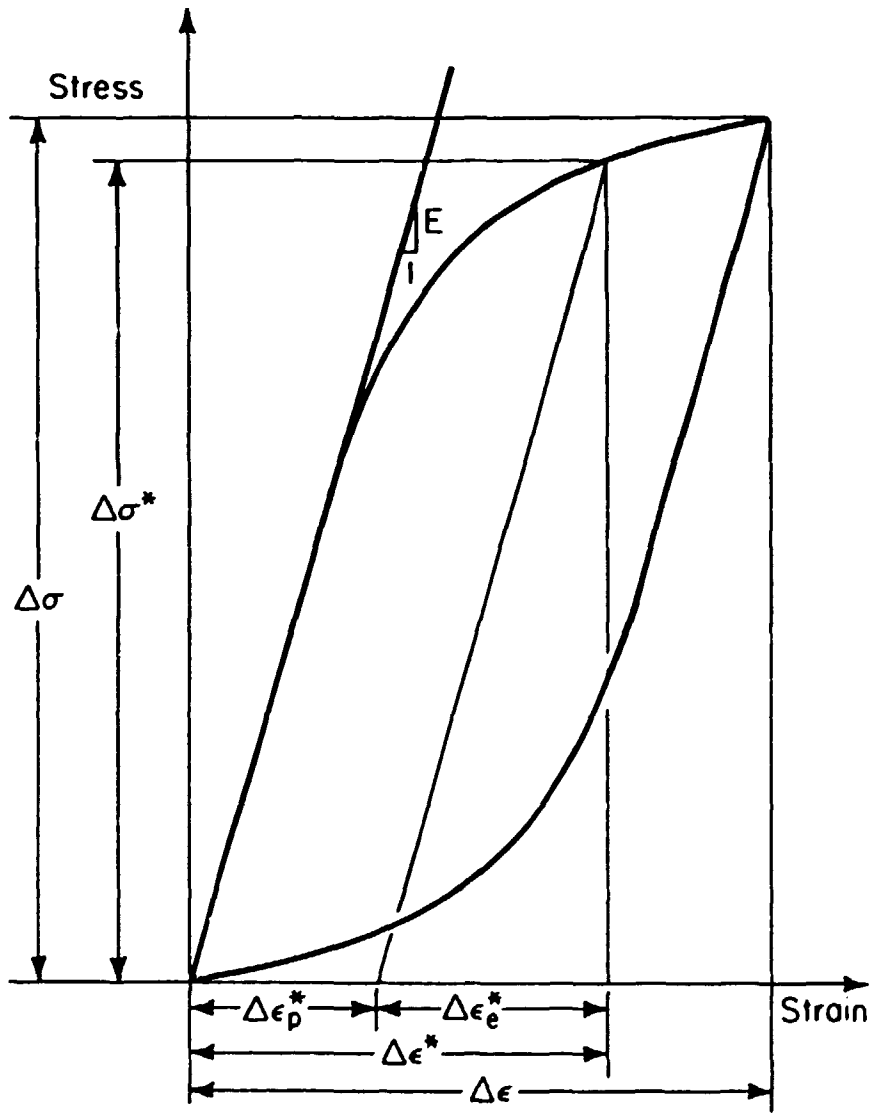

Fig.6 Definition of stress and strain ranges for a typical hysteresis loop

notation for the constants in Eq. (3) above was done deliberately so as to emphasize the difference between these values and those commonly used to describe a materials cyclic σ-ε curve.

To include strain induced softening, it is assumed that C and m are functions of the cumulative plastic strain only. This is an intuitive assumption based on empirical observations of softening behavior in a number of diverse situations[1]. It appears to be the simplest assumption that is capable of capturing the essentials of softening.

This means that

$$\Delta\sigma^* = C(\Sigma\Delta\varepsilon_p) \cdot (\Delta\varepsilon_p^*)^{m(\Sigma\Delta\varepsilon_p)}. \tag{4}$$

Experimental evidence[8] shows that $C(\Sigma\Delta\varepsilon_p)$ has an n-power form,

$$C(\Sigma\Delta\varepsilon_p) = h \cdot (\Sigma\Delta\varepsilon_p)^n \tag{5}$$

where $\Sigma\Delta\varepsilon_p >$ critical strain, and $n < 0$ necessarily, to model softening behavior.

Figure 6 provides a graphical representation of these terms. As shown, the origin of the stress-strain axis is located at the beginning of the reversal. An asterisk (*) superscript is used to differentiate between relative stress/strain values (such as $\Delta\sigma^*$ and $\Delta\varepsilon_e^*$) and absolute stress/strain ranges (such as $\Delta\sigma$ and $\Delta\varepsilon_e$).

It can be shown for the material under consideration, that the relationship between stress range and strain range can be represented by

$$\Delta\sigma^* = h \cdot (\Sigma\Delta\varepsilon_p)^n \cdot (\Delta\varepsilon_p^*)^m \tag{6}$$

where $h = 843$ MPa, $n = -0.0661$, and $m = 0.0905$.

The above relation provides a model of the stress-strain response of a softening material subjected to a cyclic loading. This model was developed from data obtained from a fully reversed 1.0 percent strain range cyclic test. The predictive capability of this model was evaluated by comparing predictions with the experimental results of a fully reversed 0.5 percent strain range cyclic test. In predicting

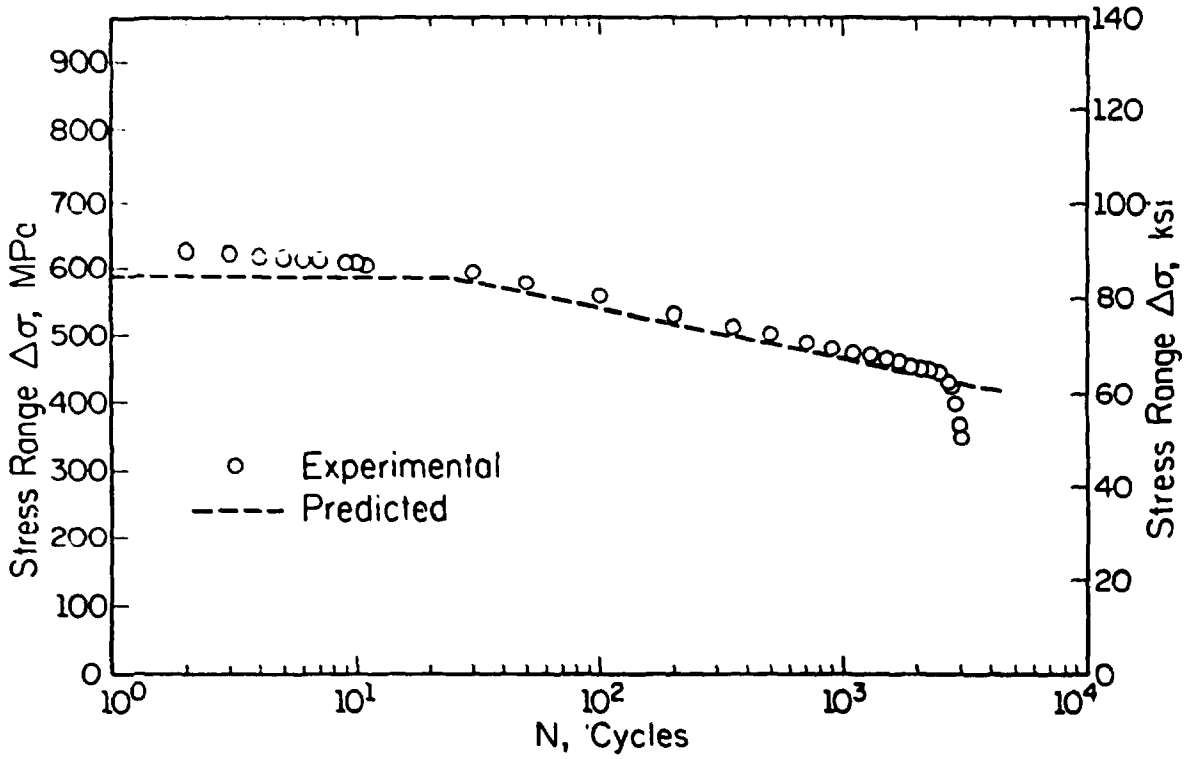

Fig.7 Experimental and predicted results of stress range versus number of cycles for a 0.5% strain range cyclic test

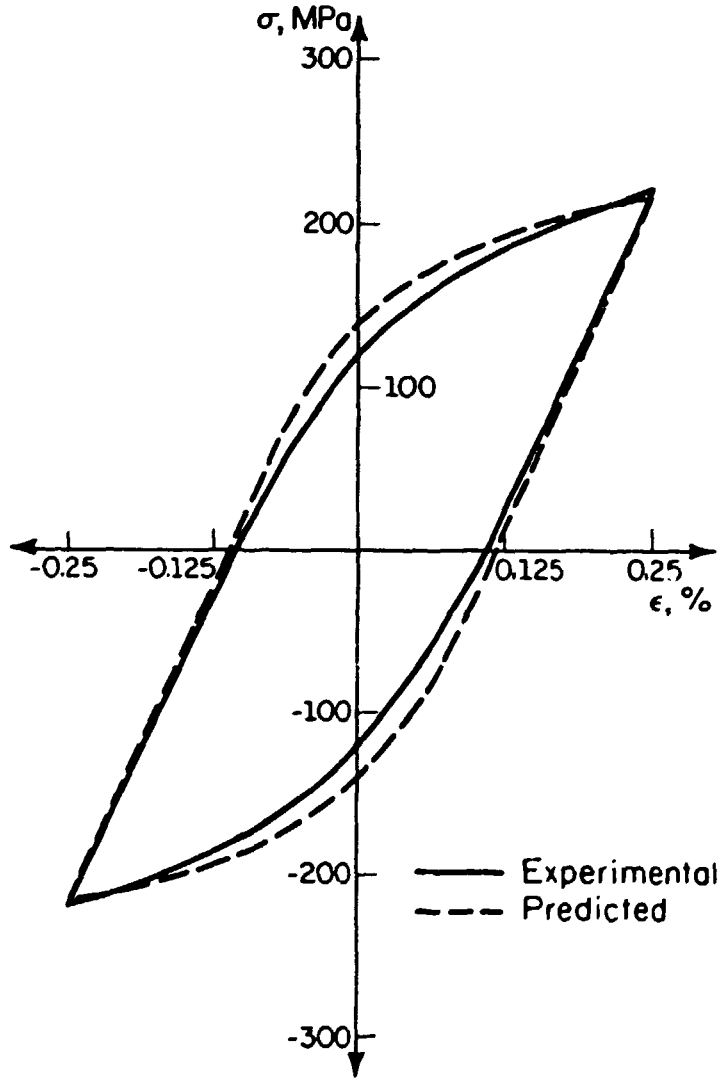

Fig.8 Experimental versus predicted hysteresis loops at cycle no. 2500 for a 0.5% strain range cycle test

material response, a forward solution method was used to estimate the accumulated plastic strain at a variety of cycle numbers. This solution process involves determining, through an iterative procedure, the absolute stress and plastic strain ranges at each of the cycle numbers of interest.

Considering the limited objectives of the work reported here, the approximate constitutive relation appears to work very well indeed. As shown by Fig. 7, the cyclic stress range for a 0.5 percent strain range is predicted very closely from an equation which was derived entirely from 1.0 percent strain range data. Figure 8 shows comparisons between experimental and predicted hysteresis loops which also display good correspondence.

Since creep deformation is indistinguishable from time-independent plastic deformation in this material, even at the microstructural level,[9] the extension of the model to time-dependent conditions should be relatively straightforward. The hypothesis has yet to be tested, but future work in this direction will assume that creep and plastic deformations are additive where strain induced softening is concerned.

COMPONENT ANALYSIS

This section summarizes initial attempts to explore simple methods of analysis for components composed of strain softening material. Finite element analysis of a notched bar and a cylindrical bar containing a spherical cavity has been performed using a linear strain hardening material model in which softening has been represented by a negative hardening coefficient.[10] The object is to determine the extent to which localized plastic deformation may propagate, as the result of strain induced softening, causing the component as a whole to fail by gross yielding.

The approach is an approximate one, in which the cyclic material behavior is summarized as a series of cyclic stress-strain curves, Fig. 9, and the component analyzed for the simple case of monotonic loading into the plastic range, with the assumption of negative strain hardening.

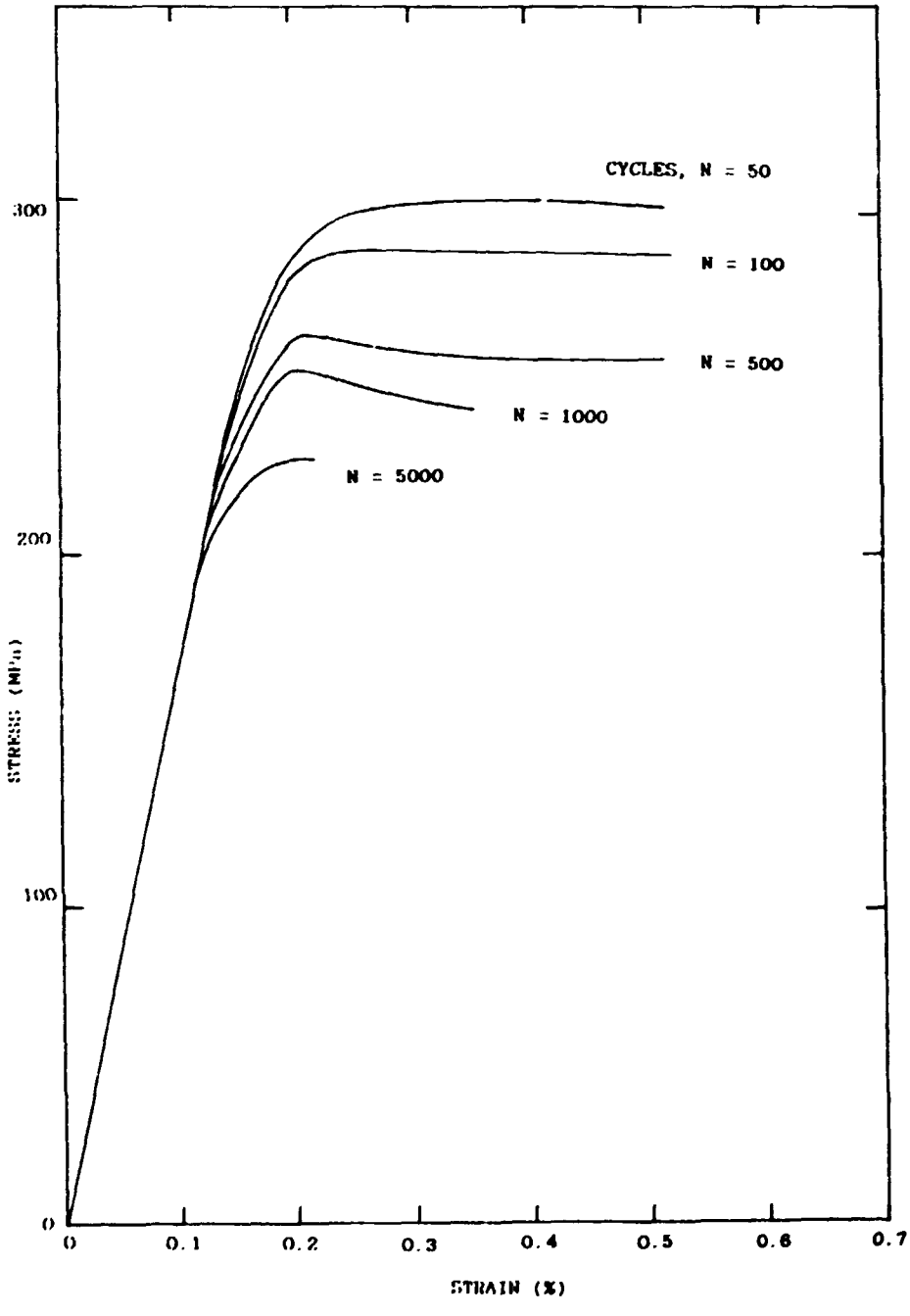

Fig.9 Cyclic stress-strain curves

DESCRIPTION OF EXAMPLE COMPONENTS

The elastic-plastic behavior of two simple component geometries, shown in Fig. 10 are examined.

The constitutive relationship used was an elastic, linear strain hardening model with the degree of hardening or softening defined by a variable strain hardening coefficient, α, which could take negative values to represent softening behavior as illustrated in Fig. 11.

The analyses are described more fully in Ref. 10.

DISCUSSION OF RESULTS OF ANALYSIS

The only result to be discussed here is the relationship between the stress and the strain at the point of maximum strain concentration. As illustrated in Figs. 12 and 13, this relationship traces out a generalized hyperbolic locus, for a fixed load level, as the strain hardening/softening coefficient varies. In the case of a pure strain controlled situation, the locus is a vertical line at constant strain while, for load control (i.e. statically determinate), the locus is a horizontal line at constant stress, Fig. 14. Neuber's hyperbolic rule is intermediate between these extremes and is adopted in this paper as an arbitrary dividing line between local behavior which is strain or load dominated.

Results are summarized in Figs. 12 and 13. The stresses and strains refer to the mid-element Mises effective stresses and strains in the most highly strained element.

In all cases the locus of stress versus strain with changing strain hardening index shows a clear trend which extends continuously from positive to negative values of the hardening coefficient. Not surprisingly, the Neuber rule is not correct for any of the geometries examined although it could present a first-order approximation for initial design scoping calculations. The main observation is, however, that the relaxation characteristics at a point of local inelastic deformation follows a trend which is not strongly dependent on the particular material constitutive relation and applies equally well whether the material hardens or softens as long as the inelastic strain

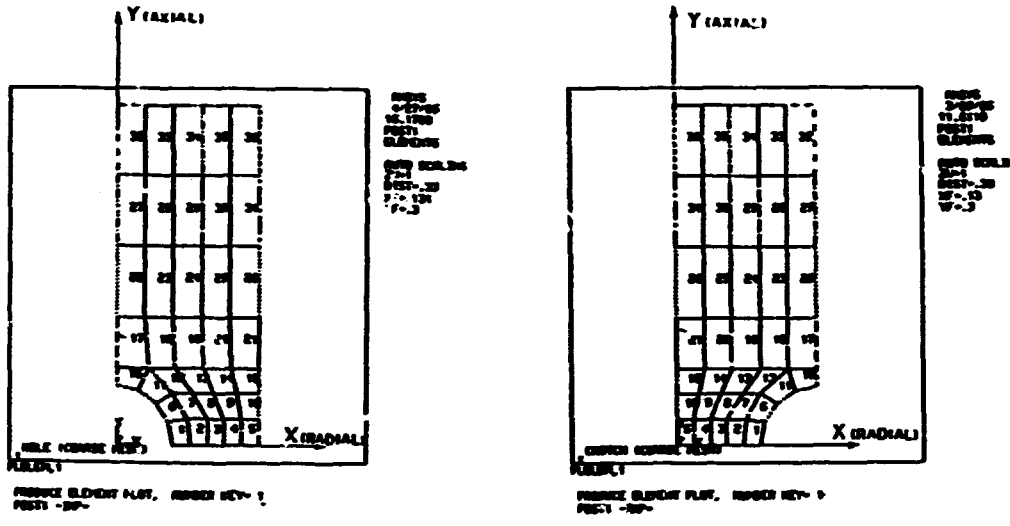

Fig.10 Geometries of notched bar and bar with spherical cavity

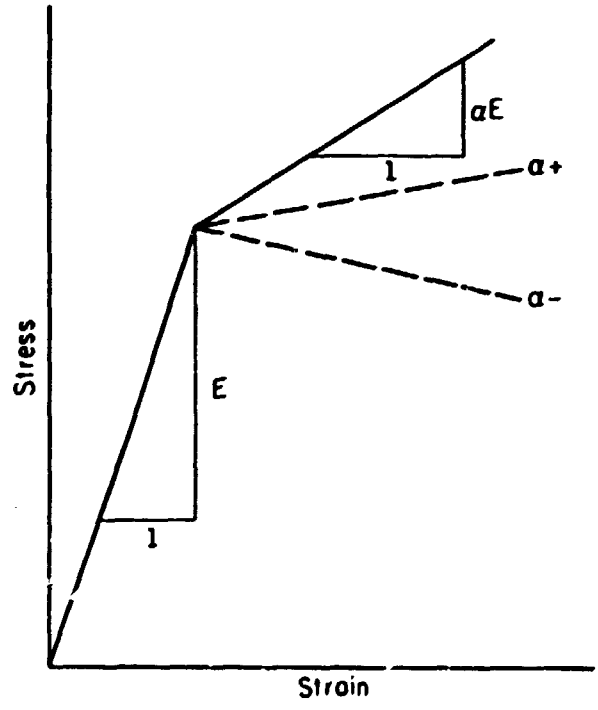

Fig.11 Schematic representation of the constitutive relation (α is the strain hardening coefficient nondimensionalized with respect to Young's modulus, E)

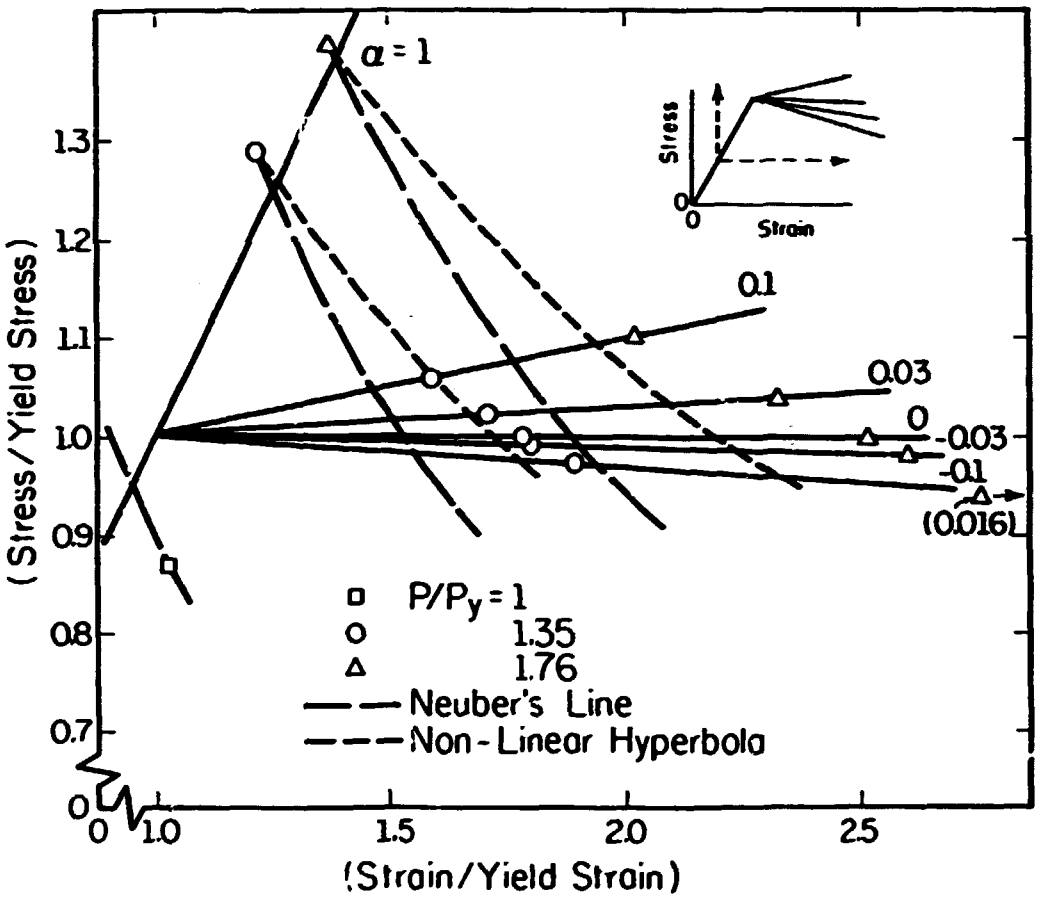

Fig.12 C-notch: peak stress versus peak strain relationship for most highly strained element

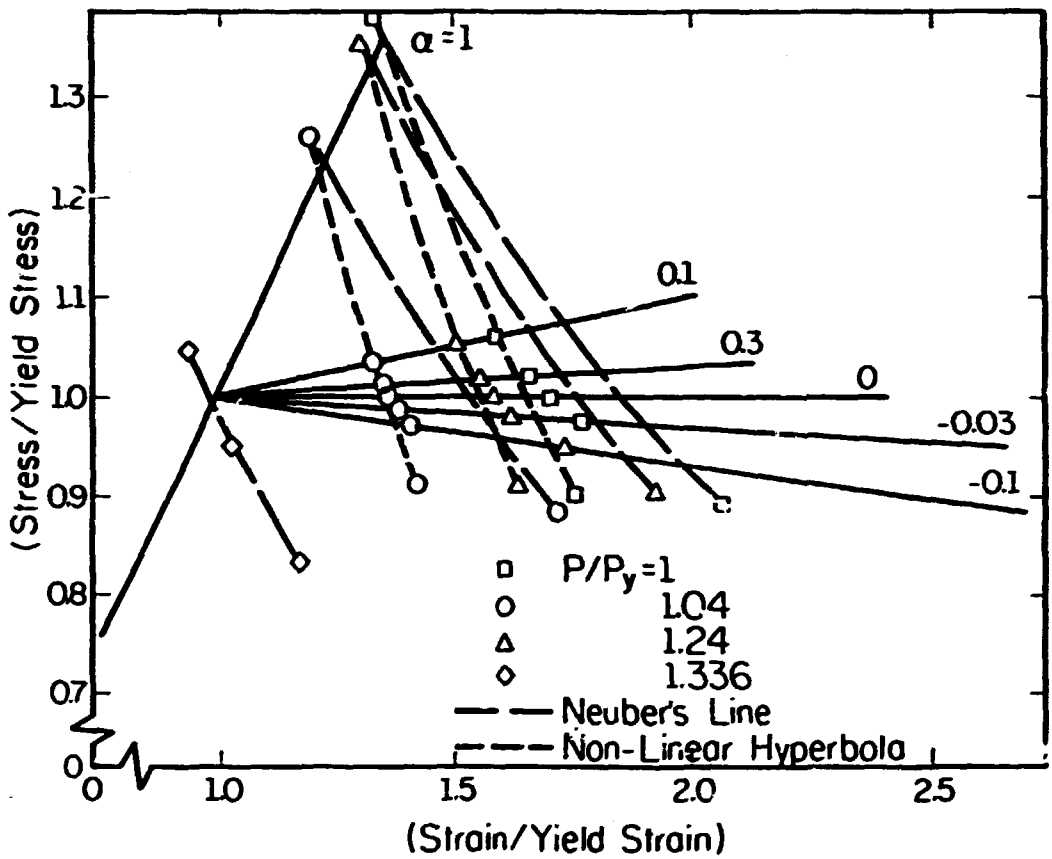

Fig.13 Cavity in cylinder bar: peak stress versus peak strain for most highly strained element

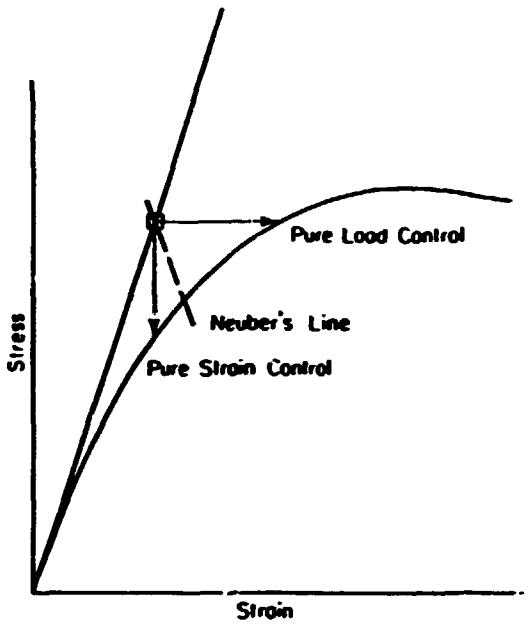

Fig.14 Schematic representation of redistribution behavior at point of peak stress

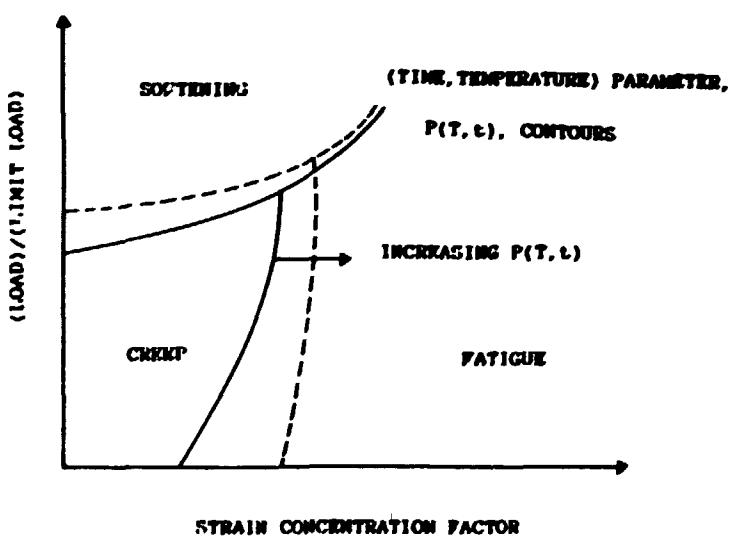

Fig.15 Conceptual form of proposed damage mechanism map

Currently models of an n-bar structure and a beam in bending are under development to examine the cycle-by-cycle progression of softening throughout a component. Simplified models of complex notch geometries, based on the invariance of strain in the notch neck, are also under development.

An important extension of the constitutive model is the inclusion of time dependence or creep. This is being done at present, following the assumption that, in this material, creep and plastic components of inelastic strain are indistinguishable. The resulting model will be a simple one but, since the object is primarily to investigate component sensitivity to softening, the simple model will be adhered to as long as it suffices. If this route encounters difficulties it is possible, once again, to consider a unified, state-variable approach.

In the course of testing this material, it has become apparent that the softening effect has very definite limits of applicability. For instance, it is not experienced to any significant extent at the high temperatures of 565°C used for most of the program, because creep failure occurs rapidly enough for cyclic softening not to have its full effect. In fact, the most dramatic cyclic softening effects have been observed in ambient temperature tests where no creep is experienced. Secondly, it appears that local high strain concentration tend to cause premature failure by fatigue. The window of possible softening failure is therefore defined by an upper temperature and a maximum limit on strain concentration. It is also apparent that softening effects continue down to strain ranges where macroscopic inelastic strains are not observed. There is a need to explore the limits of softening as a problem and present them in a way which is meaningful in material selection and design. A method which is being considered at present is a form of Ashby mechanism map. Figure 15 shows a conceptual form for this proposed map. Work still needs to be done to identify mechanism boundaries.

The current understanding is that cyclic softening is likely to have its greatest impact in relatively uniformly stressed components, such as beams in bending, and tubes under pressure, subject to cyclic strains approaching the yield range. In practice this probably means inelastic strains caused by thermal gradients.

is not too much greater than the elastic strain. To a first approximation, therefore, if a Neuber analysis is considered adequate for dealing with local inelastic deformation of a strain hardening nature, the same form of analysis should be acceptable if the material strain softens.

It can be inferred from the observations described in the previous paragraph that local deformations are largely a function of the component geometry. If so it should be possible to isolate this dependency as a parameter of the component without any reference to the detailed material behavior. So far no clear candidate for this purpose has been identified but work with simpler structures, such as three-bar structures, is being done to develop better understanding.[10]

SUMMARY

Inelastic deformations of a component can be reduced to a small number of elastic calculations to produce the peak stress/strain locus while the constitutive behavior can be considered as a virtually independent problem. Separation of essentially structural behavior from material behavior is a considerable simplification which should significantly reduce the amount of computation needed when complex constitutive relations are involved. More importantly, this separation allows predictions to be made for situations where the current knowledge of material constitutive behavior has not yet advanced to the state where it can be represented in the explicit form required for input to a full analysis - as is the case at present with strain softening.

FUTURE WORK

As yet, understanding of complex component behavior is a long way from complete. However, the simple softening constitutive model will allow theoretical investigation of a range of geometries to be performed. From this work it is expected that some general rules will be forthcoming.

CONCLUSIONS

1. Cyclic softening has been shown, under some circumstances, to cause general loss of component strength, and in others to have only local effects. This introduces the question of how to select allowable design stresses for materials which display this type of behavior.
2. A simple method, based on the empirical observation that cyclic softening is relatively insensitive to anything but number of cycles, has been shown to give reasonable predictions of component life.
3. A constitutive model is presented which predicts strain induced softening very accurately. This model will be used to investigate the effect of complex component geometry.
4. Some theoretical studies of complex geometry have shown that local softening effects can be dealt with by a modified Neuber type analysis. This method has the attribute that complex material and geometric effects can be treated separately.

ACKNOWLEDGMENTS

The authors wish to acknowledge thanks to the U.S. Department of Energy, Advanced Research and Technology Development Fossil Energy Materials Program for the sponsorship of this research under Sub-Contract 19X-55904C. Special thanks is also due to R. W. Swindeman of Oak Ridge National Laboratory, not only for his role as technical monitor of the project, but also for his contributions of a technical nature concerning this work.

REFERENCES

1. Handrock, J. L., and D. L. Marriott, "Cyclic Softening Effects on Creep Resistance of Bainitic Low Alloy Steel Plain and Notched Bars," Properties of High-Strength Steels for High-Pressure Containments, ed., Nisbett, E. G., MPC-27, American Society of Mechanical Engineers, NY, 1986, pp. 93-102.

2. Pejsa, P. N., "Elevated Temperature Low-Cycle Fatigue of Two Bainitic 2.25 Cr - 1 Mo Steels," M.S. Thesis, University of Illinois at Urbana-Champaign, Illinois, 1983.

3. Swindeman, R. W., "Response of Ferritic Steels to Nonsteady Loading at Elevated Temperatures," Research on Chrome-Moly Steels, ed., Swift, R. A., MPC-21, American Society of Mechanical Engineers, NY, 1984, pp. 31-42.

4. Cescotto, S., F. Leckie, and E. Abrahamson, "Unified Constitutive Models for Creep and Plasticity of Metals at High Temperature," University of Illinois at Urbana-Champaign, Illinois, 1982.

5. Slavik, D. C., "An Experimentally Based Unified Model for Isothermal and Thermo-Mechanical Loading," M.S. Thesis, University of Illinois at Urbana-Champaign, Illinois, 1987.

6. Socie, D. F., M. R. Mitchell, and E. M. Caulfield, "Fundamentals of Modern Fatigue Analysis," Fracture Control Program Report No. 26, University of Illinois at Urbana-Champaign, Illinois, 1978.

7. Ramberg, W., and W. R. Osgood, "Description of Stress-Strain Curves by Three Parameters," NACA Technical Note No. 902, July, 1943.

8. Handrock, J. L., D. L. Marriott, and J. F. Stubbins, "Development of a Uniaxial Constitutive Model for a Strain Induced Softening Material," accepted for presentation at the 5th Int. Congress on Pressure Vessels and Piping, ASME, San Diego, CA, June 28 through July 2, 1987.

9. Mehler, M. R., "The Microstructural Changes of Bainitic Two and One Fourth Percent Chromium--One Percent Molybdenum Steel During Creep," M.S. Thesis, University of Illinois at Urbana-Champaign, Illinois, 1985.

10. Marriott, D. L., K. Kloos, and J. L. Handrock, "Approximate Analysis of Components Composed of Strain Softening Material," Properties of High-Strength Steels for High-Pressure Containments, ed , Nisbett, E. G., MPC-27, American Society of Mechanical Engineers, NY, 1986, pp. 103-109.

Table 1 Chemical composition of low alloy steel used in investigation

Component	%
C	0.13
Mn	0.53
P	0.003
S	0.003
Cu	0.16
Si	0.25
Ni	0.15
Cr	2.33
Mo	0.96
Sn	0.001
Al	0.011
V	0.01
As	0.002
Sb	0.0005
Fe	Remainder

Table 2 Low frequency creep-fatigue test results on smooth and notched bars (tests conducted on Arcweld deadweight creep machines)

Specimen Type	σ_{net} Stress MPa	σ_{eff} Stress MPa	Cycles to Failure N_f	Time to Failure Hours	Hold Time Min	R Ratio
S	152	152		1581		1
S	172	172		476		1
B	226	169		665		1
B	226	169	6130	613	5	0
V	232	166		594		1
V	232	166	2250	225	5	0

S = Smooth specimen, B = Bridgman specimen, V = Vee-notch specimen.

Table 3 Nomenclature for cyclic softening constitutive model

C	Hysteresis loop strength coefficient
C_o	Cutoff value of C for small values of accumulated plastic strain (1068 MPa)
E	Young's modulus (159 GPa)
h	Strength coefficient material constart (843 MPa)
log	Common logarithm (base 10)
m	Hysteresis loop strain hardening exponent (0.0905)
n	Strength exponent material constant (-0.0661)
N	Specific cycle number
$\Delta\varepsilon$	Absolute total strain range
$\Delta\varepsilon^*$	Relative total strain range
$\Delta\varepsilon_e$	Absolute elastic strain range
$\Delta\varepsilon_e^*$	Relative elastic strain range
$\Delta\varepsilon_p$	Absolute plastic strain range
$\Delta\varepsilon_p^*$	Relative plastic strain range
$\Delta\sigma$	Absolute stress range
$\Delta\sigma^*$	Relative stress range
$\Sigma\Delta\varepsilon_p$	Accumulated plastic strain
$\Sigma(\lvert\Delta\varepsilon_{eff}\rvert)$	Accumulated Mises plastic strain

PROTECTIVE COATINGS AND CLADDINGS: APPLICATION/EVALUATION

N. Gopalsami, J. A. Ellingson, and R. A. Roberts

Materials and Components Technology Division
Argonne National Laboratory
9700 South Cass Avenue
Argonne, Illinois 60439

ABSTRACT

Nondestructive evaluation (NDE) plays an important role in the development of coatings/claddings for heat recovery systems of coal gasifiers. It must characterize coating defects and establish a relationship between the nature of the defects and observed corrosion behavior in typical heat recovery system environments. A review of potential NDE methods has been made with reference to the type of coatings in this application. The review focuses, in particular, on aluminized, chromized, and simultaneously aluminized/chromized coatings which are produced by pack-diffusion processes on low-alloy and carbon steels. A candidate NDE technique must ideally be capable of detecting fine cracks, inclusions, voids, and Al/Cr concentration profiles. The NDE methods reviewed are thermal-wave imaging, scanning acoustic microscopy, backscattered surface waves, eddy-current testing and X-ray fluorescence. Although each of these methods appears to have applicablity in one respect or the other, we have made an initial selection of thermal-wave imaging and backscattered surface-wave techniques for experimental investigation. Some preliminary results on these methods will be presented.

INTRODUCTION

The primary objective of this program is to develop corrosion-resistant coatings on low-alloy steels for application in downstream waste heat recovery systems of coal gasifiers. A further objective is

to develop nondestructive evaluation (NDE) methods for inspection of the coatings that are developed in this program. The NDE work should play an integral role in formulating the eventual coating specifications.

The previous work on this program[1] included microstructural examination of as-received coated materials and the investigation of the corrosion behavior of these materials in two different gaseous environments under both isothermal and thermal-cycling conditions. One of the conclusions/recommendations arising from this work was that methods must be developed to characterize coating defects and to establish a relationship between the nature of the defects (e.g., type, size, shape and orientation) and the observed corrosion behavior. Consequently, efforts in this fiscal year were directed toward development of NDE techniques for coatings.

The NDE part of this project consists of (i) determining the NDE requirements, (ii) reviewing potential NDE techniques in the literature, and (iii) testing the performance of selected techniques. The nature and size of defects that one must be able to characterize in pack-diffusion coatings by NDE techniques can be seen from micrographs of coated specimens. Figure 1, for example, shows a cross section of an as-received aluminized carbon steel specimen and the corresponding Al concentration profile.[1] The presence of discrete Al oxide particles and oxide colonies has been observed in the outer Al-rich region of several coatings, along with fine cracks extending mainly perpendicularly from the surface.

The above and other microstructural observations suggest that an NDE technique for coatings should ideally be capable of detecting fine cracks, inclusions, voids, and Al/Cr concentration profiles. The defect sizes are on the order of tens of micrometers, and therefore require a high spatial resolution. The NDE system must be adaptable to complex (particularly tubular) geometries and varying surface conditions (a coating surface roughness of up to several tens of micrometers is estimated from visual examination).

Fig. 1. Cross Section of an As-received Aluminized Carbon Steel Specimen Showing Internal Oxide Particles, Acicular (Fe,Al) Carbide Phase, and Al Concentration Profile. From Ref. 1.

RESULTS/ACCOMPLISHMENTS

NDE techniques that hold promise for the present application are reviewed, followed by a discussion of preliminary experimental results on a selected technique.

THERMAL-WAVE IMAGING

Thermal-wave imaging is receiving increased attention as a technique for NDE of surface and subsurface features of opaque solids.[2,3] In this technique, an intensity-modulated, finely focused laser or par-

ticle (electron or ion) beam is used to produce a periodic, localized heating in the specimen. This periodic localized heating generates thermal waves, which propagate from the heated region. In the same way as conventional waves are reflected and scattered at discontinuities, thermal waves are reflected and scattered by surface and subsurface thermal features. The reflected or scattered thermal waves may be detected by a variety of means: optical beam deflection, reflective optical beam deflection, photothermal radiometry, piezoelectric detection, and gas-cell detection.

Thermal-wave imaging is capable of mapping surface and subsurface features with micron-scale resolution. With a wide range of sources and detection methods available, it is possible to image most types of defects. The imaging system can be totally noncontacting and can be adapted to complex surfaces. A major limitation of current thermal-wave imaging systems appears to be the slow speed of imaging. More theoretical development is needed to permit quantitative interpretation of thermal-wave imaging features.

SCANNING ACOUSTIC MICROSCOPY

The scanning acoustic microscope (SAM) is becoming increasingly important in materials research because it offers the possibility of imaging the structural features of materials with high spatial resolution.[4,5] In a reflection-mode SAM, which is appropriate for the present application, a transducer on the top of an acoustic lens launches a pulsed ultrasonic beam and the lens then focuses this beam into a diffraction-limited spot on or below the object surface. The geometry of the lens system is such that it generates Rayleigh waves on the object surface and the leaky Rayleigh waves carrying the object-related information are mode converted and reflected back to the same lens system.

A reasonable imaging speed is possible with the SAM (one commercial vendor quotes approximately 10 seconds per image). The variation of transducer output signal V with respect to the distance z of the object surface from the focal plane, called the V(z) curve, may bear some

relevance to the coating composition of the outer layer. However, features lying deep inside the sample are not imaged with adequate sensitivity and resolution. Also, surface roughness and complex shape may affect the output voltage because of their varying reflection characteristics.

BACKSCATTERED SURFACE WAVES

Like the SAM method, the backscattered surface-wave technique employs leaky Rayleigh waves for imaging near-surface flaws in materials.[6] A focused transducer produces a pulse of longitudinal waves focused at the water-sample interface at an average angle of incidence near the Rayleigh critical angle. A pulse of propagating Rayleigh waves is thereby generated in a small volume below the focal spot. The surface waves, when incident on a flaw near the focal spot, are reflected or backscattered. The backscattered pulse carrying the flaw information, because of its leaky nature, will be received by the transducer. A delay time-gate is used to image a narrow region/volume near the focal spot.

This method may be well suited for detecting a vertical surface-breaking crack because of the normal incidence of the waves on the crack. It is also suited for fast imaging of large inclusions and voids near the surface. The resolution and sensitivity afforded by this method are generally low, compared to SAM or thermal-wave imaging. Surface roughness may be a problem since the coupling of energy to surface waves will be affected by surface scattering.

EXPERIMENTAL INVESTIGATION

Based on the review of potential applicability of the various techniques and the availability of experimental facilities, backscattered surface waves and thermal-wave imaging were chosen for experimentation. Preliminary experiments on the use of backscattered surface waves were conducted with a simultaneously aluminized/chromized sample of tubular geometry and a 25-MHz focused transducer. A rectangular slot

70 μm wide, 8 mm long, and 800 μm deep at the center was made on the sample surface in the transverse direction, and ultrasonic scans were made in the axial direction (perpendicular to the slot orientation). Distinct surface wave echoes were observed when the ultrasonic beam approached the slot as well as the edge of the sample. The peak amplitude of the signal from a narrow-time gate set behind the direct backscattered signal with a delay of about 1 μs was digitized and mapped with respect to x-y movements. Figure 2 gives such a digitized image with a resolution of 100 μm per pixel; both the slot and the end of the sample are seen clearly. The analysis of the data is continuing in an effort to correlate other observable image features with the coating nonuniformities.

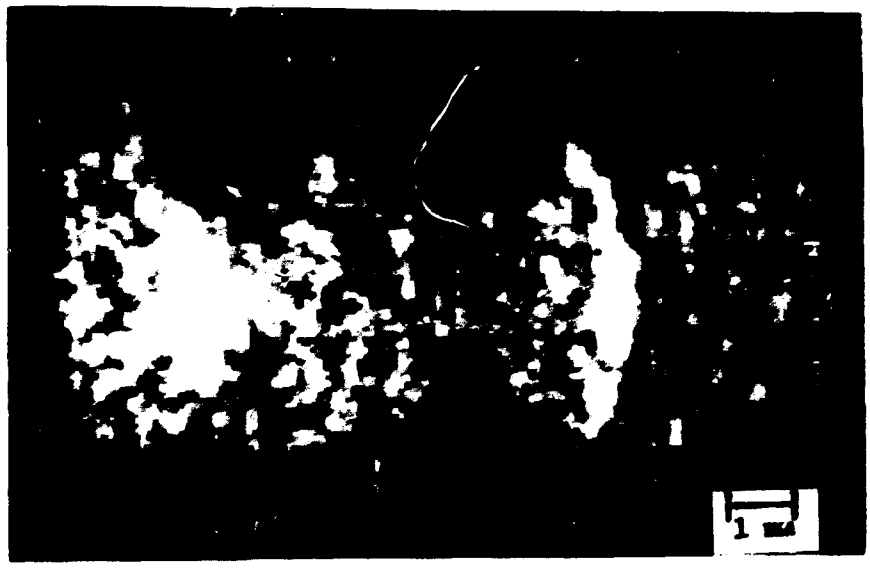

Fig. 2. Backscattered Surface-Wave Image of a Slot in an Aluminized/Chromized Sample.

FUTURE PLANS

Further testing of the backscattered-surface-wave technique will be carried out with an emphasis on determining the type and size of coating defects that can be imaged. Preliminary experiments on thermal-wave imaging of coated samples will be conducted at outside facility (in collaboration with Dr. Doug Rose, U.S. Army Tank-Automotive Command,

Warren, MI). In close coordination with coating vendors, coatings with well-defined defects will be produced to enable efficient testing of the NDE techniques.

ACKNOWLEDGMENTS

The research was supported by the U. S. Department of Energy, Morgantown Energy Technology Center, and Oak Ridge Operations Office, as part of the Surface Gasification Materials Program, under contract W-31-109-ENG-38. Thanks are extended to Jeff Vaitekunas of the Materials and Components Technology Division for helping with surface-wave image processing.

REFERENCES

1. D. J. Baxter, The Corrosion Behavior of Coated Low-Alloy Steels in a Coal Gasifier Environment under Thermal Cycling Conditions, Argonne National Laboratory Report, ANL/FE-86-6 (1986).

2. R. L. Thomas, L. D. Favro, and P. K. Kuo, Thermal-Wave Imaging for Nondestructive Evaluation, Can. J. Phys., Vol. 64, pp. 1234-1237 (1986).

3. J. C. Murphy, J. W. MaClachlan, and L. C. Aamodt, Image Contrast Processes in Thermal and Thermo-Acoustic Imaging, IEEE Trans. Ultrason. Ferroelectrics Frequency Control, Vol. UFFC-33, pp. 529-541 (1986).

4. C. F. Quate, A. Atalar, and H. K. Wickramasinghe, Acoustic Microscopy with Mechanical Scanning, Proc. IEEE, Vol. 67, pp. 1092-1114 (1979).

5. J. M. R. Weaver et al., Applications of the Scanning Reflection Acoustic Microscope to the Study of Materials Science, IEEE Trans. Sonics Ultrason., Vol. SU-32, pp. 302-312 (1985).

6. R. A. Roberts, Focused Ultrasonic Backscatter Technique for Near-Surface Flaw Detection in Structural Ceramics, presented at the 16th Symposium on Nondestructive Evaluation, San Antonio, Texas, April 21-23, 1987.

DEVELOPMENT OF Fe_3Al-BASED ALUMINIDES*

C. G. McKamey, C. T. Liu, S. A. David,
J. A. Horton, and J. V. Cathcart

Metals and Ceramics Division
Oak Ridge National Laboratory
P. O. Box X
Oak Ridge, Tennessee 37831-6116

ABSTRACT

Iron aluminides based on Fe_3Al possess many attractive properties for structural use. However, limited ductility at ambient temperatures and a sharp drop in strength above 600°C restrict their use as structural materials. The goal of the present study is to develop Fe_3Al-based aluminides with optimum combinations of strength, ductility, and corrosion resistance for use as hot components in advanced fossil energy conversion systems.

From a study of the properties of alloys of 24 to 30 at. % Al, it has been determined that the most promising alloy for further development is Fe-28 at. % Al. A discussion of the effect of aluminum concentration on mechanical properties is included in this paper. Initially, 0.5 wt % TiB_2 was added for grain refinement. It has since been determined that these precipitates are deleterious to the weldability, and for future alloy development they will not be added. Alloy additions, have been shown to improve both the high-temperature strength and room-temperature ductility. Results of weldability and tensile and creep tests, as well as the present status of oxidation and aqueous corrosion tests, are reported.

---

*Research supported by the U.S. Department of Energy, Morgantown Energy Technology Center, Surface Gasification Materials Program, under contract DE-AC05-840R21400 with Martin Marietta Energy Systems, Inc.

INTRODUCTION

The objective of this task is to develop low-cost, low-density intermetallic alloys based on Fe_3Al with an optimum combination of strength, ductility, and corrosion resistance for use as components in advanced fossil energy conversion systems. Initial emphasis will be on the development of iron aluminides for heat recovery applications in coal gasification systems. Iron aluminides near the Fe_3Al composition are expected to be resistant to corrosion and sulfidation in high-temperature fossil energy systems because of their ability to form protective aluminum oxide scales. Presently, however, their usefulness is limited by their low room-temperature ductility (~1-2%) and their poor hot strength above 600°C. The current efforts of this task focus on developing alloys with base compositions near Fe_3Al which have improved hot strength and room-temperature ductility, while retaining the oxidation and corrosion properties of the base alloy.

In previous publications[1,2] we have presented results of our preliminary study of the fabricability, microstructures, mechanical properties, oxidation and sulfidation properties, and weldability of several iron-aluminum alloys near the Fe_3Al composition. Since the completion of that work, our program has centered around two technical tasks: (1) a more in-depth study of the correlation between aluminum content, microstructure, and mechanical properties in binary iron-aluminum alloys of 24 to 30 at. % Al; and (2) the effect of macroalloying (<10 at. %) and microalloying (<1 at. %) on the metallurgical and mechanical properties of our selected base alloy, Fe-28 at. % Al. This paper describes recent results of these two tasks.

EXPERIMENTAL PROCEDURES

Alloys with compositions of Fe-24 to 30% Al, each containing 0.5 wt % TiB_2 added for grain refinement, were prepared by arc-melting under argon and drop-casting into water-cooled copper molds. After homogenizing for 5 h at 1000°C, the alloys were hot-rolled to a thickness of approximately 0.9 mm, starting at 1000°C and finishing at 650°C. Final warm rolling

to approximately 0.76 mm was done at 600°C. All multicomponent alloys were prepared in the same manner.

Tensile samples with a gage section of 0.76 × 3.18 × 12.70 mm were punched from the rolled sheet. After a standard heat treatment of 1 h at 850°C (for recrystallization) plus 7 d at 500°C (for ordering), tensile tests were conducted in air on an Instron testing machine at a strain rate of 3.3×10^{-3} s^{-1}. Samples to be tested at less than 400°C were first cleaned and deburred by either electropolishing or vapor blasting.

The creep properties of selected iron aluminide alloys were determined at a stress of 207 MPa (30 ksi) at 593°C in air. The temperature was monitored by a platinum versus platinum-10% rhodium thermocouple located at the center of the gage section, and the creep elongation was measured using a dial gage.

Specimens were prepared for transmission electron microscopy (TEM) by spark discharge machining 3 mm disks from the 0.76 mm tensile samples, grinding to a thickness of 0.3 mm, and electropolishing in one part nitric acid to four parts methanol in a Struers Tenupol jet polishing unit at -28°C. Electron microscopy was performed in a Philips EM430.

EFFECT OF ALUMINUM CONCENTRATION ON MECHANICAL PROPERTIES

Figure 1 shows the room-temperature tensile properties as a function of aluminum concentration. The 0.2% yield strength (σ_y) was highest for the 24 to 26% Al alloys (≈750 MPa) and then decreased rapidly to about 350 MPa for the 30% Al alloy. This transition from high σ_y values at 26% Al to lower values at 27% Al coincides with the boundary between the α+DO_3 and DO_3 phase fields (see phase diagram, ref. 3) at ≈500°C (the temperature used for our ordering heat treatment). Previous studies have shown that, at this temperature, compositions near 24 to 25% can be age-hardened by precipitation of disordered α from the ordered DO_3 phase.[4] Our heat treatment at 500°C for 7 d was sufficient to cause this reaction to occur, as indicated by the presence of the disordered α phase between ordered thermal DO_3 domains in the TEM micrograph shown in Fig. 2. Dark-field images using <111> and <002> diffraction vectors show the dark regions to be disordered and bright region ordered. The higher strength

of these alloys at room temperature may therefore be related to the presence of both disordered and ordered phases, i.e., a precipitation-hardening effect.

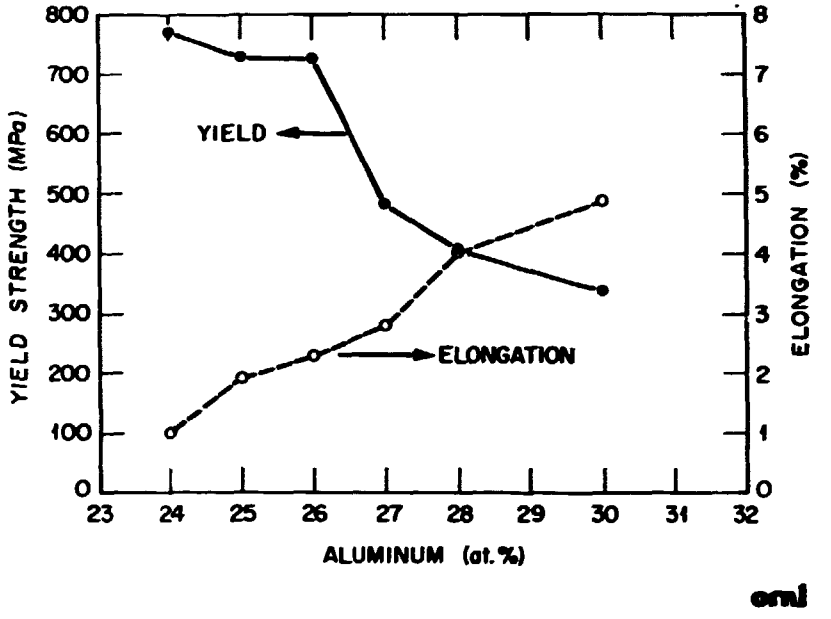

Fig. 1. Room temperature yield strength and elongation versus composition of iron aluminides.

Fig. 2. A <111> dark-field transmission electron micrograph of Fe-24% Al showing its two-phase nature: bright regions are ordered DO_3 phase, dark regions are disordered α phase.

In terms of dislocation structures, the studies of Stoloff and Davies,[5] Morgand et al.,[6] Saburi et al.,[7] and Mendiratta et al.[8] show that the 24 to 26% Al composition is in the range where the dislocation mode changes from the glide of single $1/4a_o'\langle 111\rangle$ dislocations (where a_o' is the lattice parameter for the DO_3 structure) associated with the α phase to glide of $1/4a_o'\langle 111\rangle$ dislocation pairs in the DO_3 superlattice. However, any possible fault contrast associated with slip dislocations in the 24 and 25% Al samples of this study were obscured by the small scale of the ordered and disordered regions. The sharp decrease in σ_y with increasing aluminum above 26% is due to the formation of paired dislocations, i.e., superlattice dislocations which glide easily in the ordered DO_3 lattice.[9] Our study of dislocation structures as a function of composition is continuing.

Figure 1 also shows that the ductility exhibited a fivefold increase from 1% at 24% Al to 5% at 30% Al. This increased ductility is apparently due to the decreased yield stress with increasing aluminum content. Note that all the alloys in this study exhibited essentially intergranular fracture,[10] and this behavior was not affected by the increase in aluminum content.

Figure 3 shows the 0.2% yield strength as a function of temperature for several of the compositions studied. For clarity only the data for the 24, 28, and 30% Al alloys are included. The curve for the 25% Al alloy was similar to the 24%; the curves of the 26 and 27% Al alloys were similar to those of 28 and 30%. It has been shown by other researchers that σ_y near the Fe_3Al composition increases with temperature above 300°C to a maximum value near 550°C and then decreases sharply.[5-7] This temperature corresponds to the second-order phase transformation temperature between the DO_3 and the B2 ordered structures.[3] Morgand et al.[6] showed that this peak in σ_y occurs clearly at compositions from about 23 to 32% Al which coincides with the composition range of the DO_3 phase. This type of yield behavior has been observed in many other ordered systems including Ni_3Al (ref. 11), CuZn (ref. 12), Ni_3Mn (ref. 13), and FeCo (ref. 5).

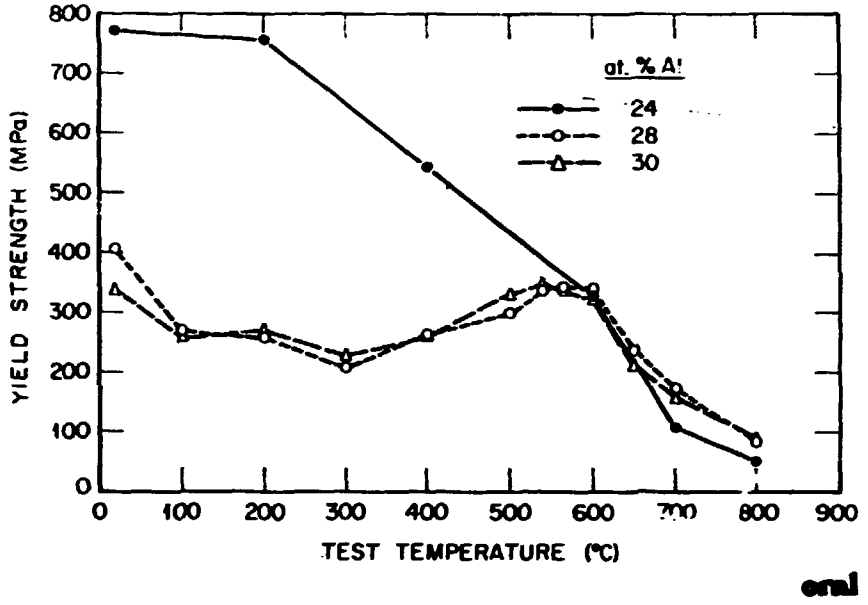

Fig. 3. Yield stress of iron aluminides versus test temperature.

Different mechanisms have been proposed to explain its presence as a function of temperature, including the cross slip model proposed by Kear and Wilsdorf[14] and Takeuchi and Kuramoto[15] and a change in dislocation configuration with degree of order proposed by Stoloff and Davies.[16] However, none of the proposed mechanisms appears to be entirely applicable to the Fe_3Al system. It is seen from this figure that, under the conditions of our test, the alloys containing 24 and 25% Al did not show the same yield behavior as was seen for the 26 to 30% Al alloys. As noted above, Inouye[4] reported that alloys of 24 and 25% Al are age-hardenable above 400°C due to the precipitation of α from the ordered DO_3 phase. The higher yield strength of these alloys at ambient temperatures is a consequence of that age-hardening reaction produced by our ordering heat treatment of 7 d at 500°C. Inouye also showed that by slow cooling from above 550°C, with no aging, the anomalous yield strength peak could be produced at these compositions.

Our data for the 26 to 30% Al alloys showed the expected anomalous yield behavior with a maximum between 550 and 600°C. This composition range coincides with the presence of the DO_3 phase field, as evidenced by

the phase diagram. As noted above, similar maxima, lying at or near the critical ordering temperature, have been reported to occur in other superlattices. However, whether this phenomenon is associated with the presence of the ordered DO_3 lattice is not clear. Our studies have indicated that, even though the DO_3 to B2 transformation can be raised to higher temperatures by alloying with other elements, the anomalous yield peak remains near 550°C (ref. 17). It has also been shown that an alloy of Fe-35% Al, which is outside the DO_3 phase field, exhibits some degree of anomalous yielding.[6]

EFFECTS OF ALLOYING ELEMENTS

From our study of the properties of Fe-Al binary alloys with compositions between 24 and 30 at. % Al (refs. 1,2), we have chosen the Fe-28 at. % Al alloy as our base material for further development. Table 1 lists the alloys which are presently being studied. All were prepared by conventional arc-melting, drop-casting, and hot-rolling procedures, as described above. Only alloy FA-54 containing 2 at. % Zr and 1 at. % Ti_2 experienced difficulty during fabrication. That alloy was very brittle and cracked excessively during rolling at temperatures of less than 800°C.

TENSILE PROPERTIES

Figures 4 and 5 show the room-temperature yield strength and ductility for the iron-aluminium alloys tested. The alloy designated FA-37 is the base alloy of Fe-28 at. % Al with 1 at. % TiB_2 (0.5 wt %). Compared to this alloy, improvements in room-temperature yield strength were seen in alloys FA-56, -80, -82, -59, -66, -79, -60, and -54. Alloys FA-82, -66, -79, and -54 reached yield strengths of above 550 MPa, making them comparable or stronger than modified 9Cr-1Mo alloy. In terms of room temperature ductility, only alloys FA-73, -77, -72, -78, -81, and -83 showed real promise, reaching elongations of more than 7%. With a different heat-treating condition, the elongations of alloys FA-77 and -72 were recently pushed to above 10%.

Table. 1. Alloys presently being studied

Alloy designation FA-	TiB_2 added[a]	Alloying element
37,61	Y,N	Base alloys
52,53,56	Y,Y,Y	Mo
62	N	Mo
69,70	Y,Y	Mn
71	N	Mn
63,64,65	Y,Y,Y	Cr
77,72,78	N,N,N	Cr
59,66	Y,Y	Nb
79	N	Nb
57,58	Y,Y	Ce
67,68	Y,Y	Y
60	Y	B
54	Y	Zr
55	Y	Ti
73,74,75	N,N,N	Combinations of
80,81,82[b]	N,N,N	the above
83	N	

[a]TiB_2 was added to some alloys as precipitates to refine grain size (Y=yes, N=no).

[b]Aluminum concentration was varied from 24 to 28%.

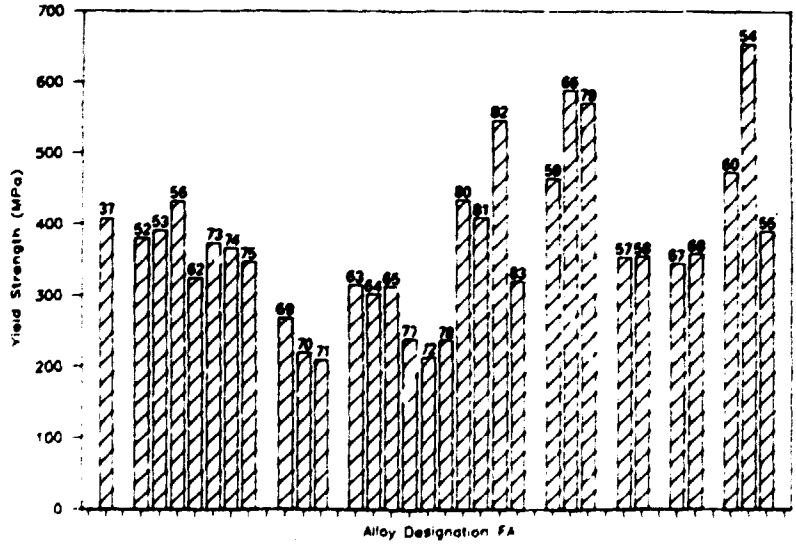

Fig. 4. Room temperature yield stress of multicomponent iron-aluminum alloys.

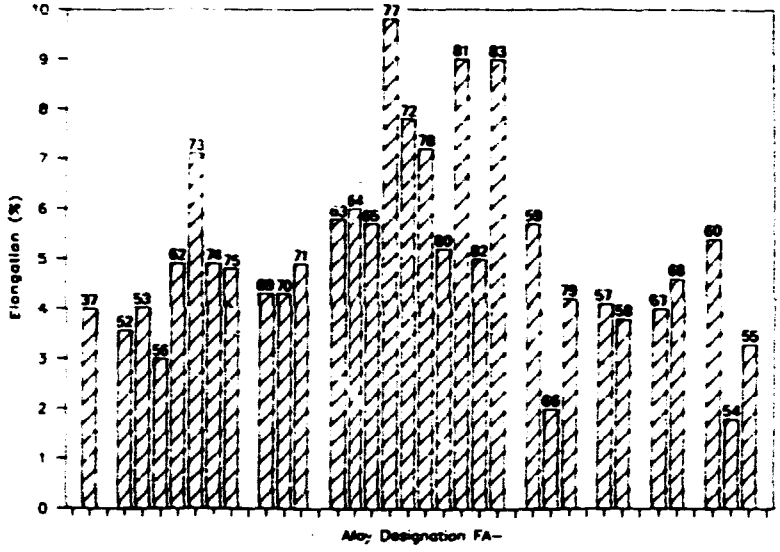

Fig. 5. Room temperature ductility of multicomponent iron-aluminum alloys.

Figure 6 shows the yield strength for alloys tested at 600°C. Values in excess of 300 MPa were seen for all alloys tested, with a maximum of 516 MPa for alloy FA-66. These strengths are much higher than either the modified 9Cr-1Mo alloy or type 316 stainless steel. Elongations at this temperature were in excess of 30% for all alloys except FA-62, -74, and -75.

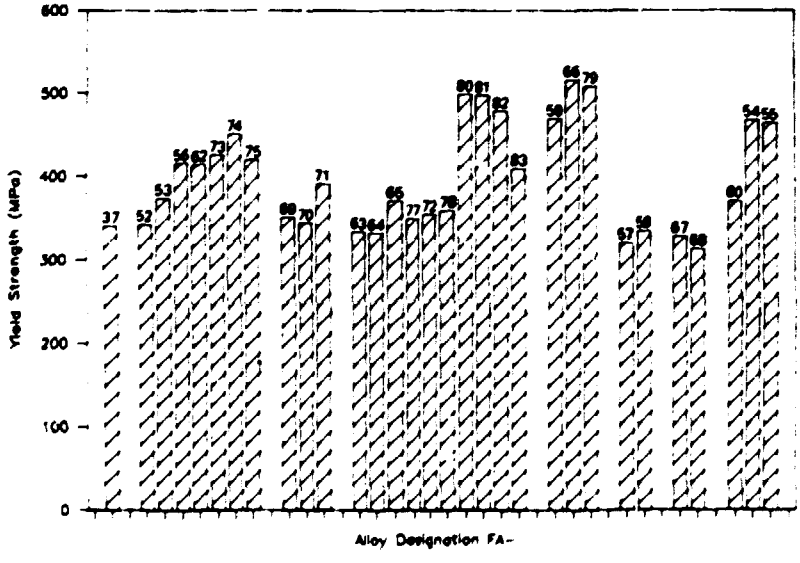

Fig. 6. Yield stress at 600°C for multicomponent iron-aluminum alloys.

CREEP PROPERTIES

Table 2 summarizes the creep results obtained on four alloys. The base alloy FA-61 is weak in creep resistance. The creep properties of the iron aluminides can be improved by alloying additions. The creep properties of FA-73, are comparable to type 304 austenitic stainless steel at the same test condition. All the alloys showed excellent ductilities (>20%) in creep.

Table 2. Creep properties of iron-aluminide alloys[a]

Alloy designation FA-	Rupture life (h)	Creep ductility (%)
61	1.6	33.6
77	3.6	29.2
81	18.8	64.5
73	57.4	24.9

[a]Tested at 207 MPa (30 ksi) and 593°C in air.

OXIDATION AND CORROSION STUDIES

Studies are just beginning of the oxidation resistance of alloys FA-72, -79, -81, and -83. These alloys are being tested in air at temperatures of 800 and 1000°C, with weights being taken every 24 h. After almost 500 h, all alloys have shown excellent resistance to oxidation, with no alloy gaining more than 7 mg/cm^2. Some spalling of the Al_2O_3 film has been observed from alloy FA-72 containing chromium. However, this problem can be corrected easily by alloy additions. This has been corrected in alloys FA-81 and -83. Alloy FA-81 appears to exhibit the best oxidation resistance (<1 mg/cm^2 at both 800 and 1000°C).

Several of our original base alloys (Fe-24 to 30% Al) plus alloys FA-72, -77, and -78 are presently being tested statically in distilled water. These samples were given a recrystallization heat treatment of 1 h

at 800°C followed by polishing with 320 grit emery paper to remove any surface flaws. To date the Fe-Al base alloys have survived 6 months without measurable weight gain (weight changes are measurable to ±0.00005 g) and still show the original shiny polished surface. The ternary alloys being tested in this manner have also shown no weight change and remain shiny after 3 months.

WELDABILITY

Table 3 lists some of the alloys whose weldability has so far been studied. After testing several of the Fe-Al base alloys (alloys FA-36 through -41) using both electron beam (EB) and gas tungsten arc (GTA) welding, it has been determined that the TiB_2 dispersion, which was originally added for grain refinement, is deleterious to the weldability, producing hot cracks along the fusion line (Fig. 7). Most of the ternary and quaternary alloys tested also experienced cracking when TiB_2 was present, but nc cracking otherwise. Note that FA-66 showed no cracks during both EB and GTA welding, indicating that niobium is beneficial to the weldability of iron aluminides, even in the presence of TiB_2.

Table 3. Weldability of iron aluminides

Alloy designation FA-	Weldability[a] EB	GTA
39	C	C
41	C	C
61	NC	NC
64	NC	C
66	NC	NC
69	NC	C
72	NC	NC
79	NC	NC

[a]C = Cracked.
NC = No cracking.

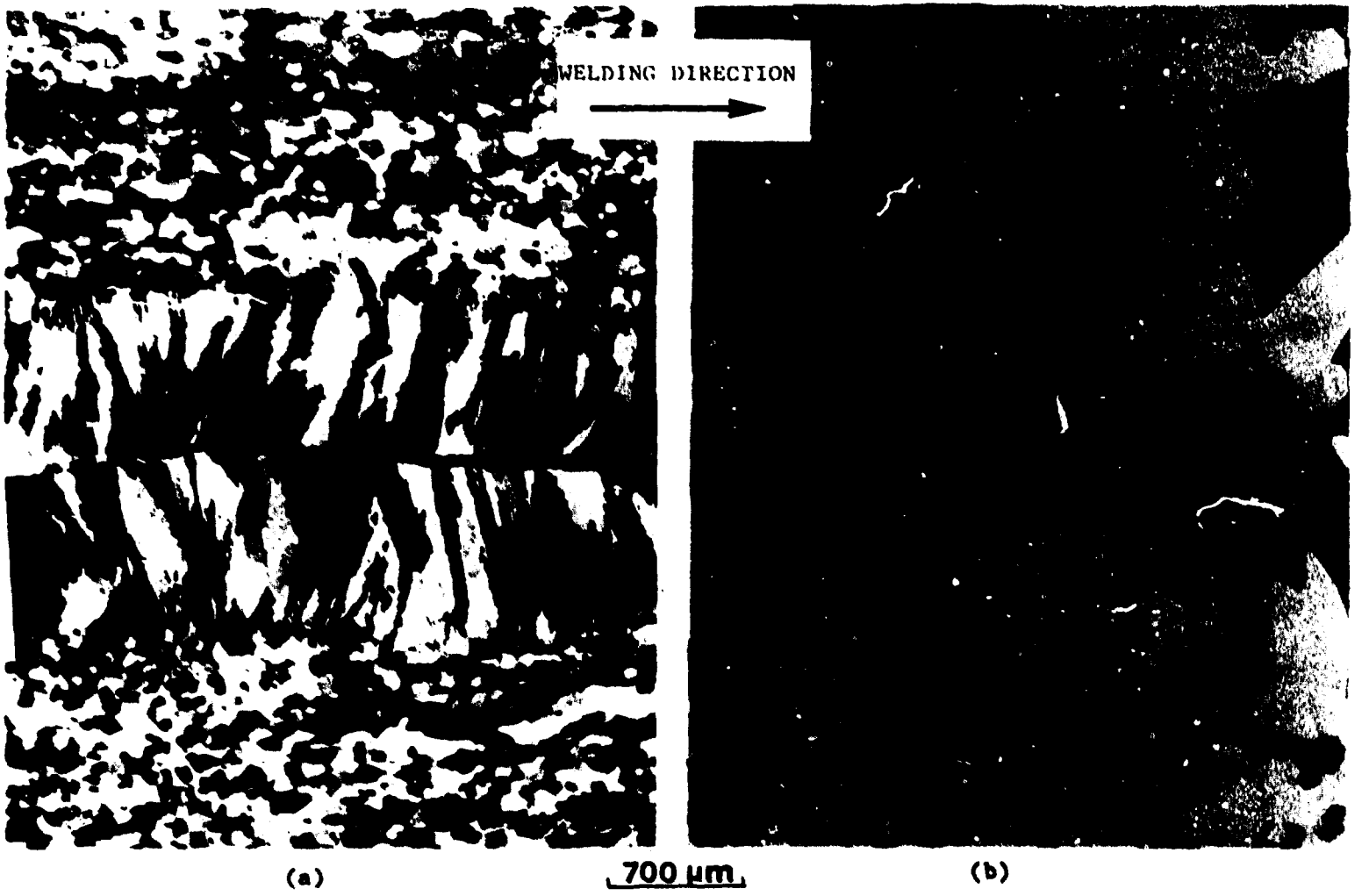

Fig. 7. Effect of the addition of TiB_2 on the electron-beam weldability of iron aluminides. (a) Hot cracking along the fusion line with addition of TiB_2. (b) No cracking when TiB_2 is absent.

CONCLUSIONS

From the studies conducted so far, the following conclusions can be drawn:

1. Using the heat treatment described above, alloys of 24 to 26% Al exhibit a σ_y at room temperature which is much higher than alloys of 27 to 30% Al. This higher σ_y is the result of age-hardening by precipitation of disordered α phase in alloys of 24 and 25% Al. The higher strength of the 26% Al alloy is believed to be related to the low mobility of dislocations in the alloy. The sharp decrease in σ_y above 26% Al can be correlated with the formation of paired superlattice dislocations which glide easily in the ordered DO_3 lattice.[9] The increased ductility with aluminum content is apparently due to the decreased σ_y.

2. The yield strength increases with temperature above 300°C, reaching a maximum around 550 to 600°C, then decreases sharply. This anomalous peak is characteristic of many ordered systems and the reasons for its occurrence in Fe_3Al are still not fully understood. Its presence in iron aluminides occurs near the DO_3 to B2 transformation temperature, but it is still not clear whether it is associated with this transformation.

3. Minor additions of certain elements have been shown to improve properties of iron aluminides.

4. The addition of TiB_2, initially added for grain refinement, is deleterious to the weldability.

5. Iron aluminides have excellent oxidation properties. The testing of alloys at temperatures to 1000°C reveals no serious problems due to the addition of these elements. Also, static aqueous corrosion tests of annealed samples indicate that these alloys are highly resistant to corrosion in atmospheres with high moisture content.

REFERENCES

1. C. G. McKamey and C. T. Liu, pp. 207–217 in Proceedings of the Instrumentation, Components, and Materials Contractors Meeting, DOE/METC-86/6069 (September 1986).

2. C. G. McKamey, C. T. Liu, S. A. David, and J. V. Cathcart, pp. 45-52 in Surface Gasification Materials Program Semiannual Progress Report for the Period Ending September 30, 1986, ORNL/SGMP-86/2 (January 1987).

3. H. Okamoto and P. A. Beck, Metall. Trans. 2, 569 (1971).

4. H. Inouye, in Materials Research Society Symposia Proceedings, Vol. 39, High Temperature Ordered Intermetallic Alloys, ed. C. C. Koch, C. T. Liu, and N. S. Stoloff (Materials Research Society, Pittsburgh, 1985), pp. 255-261.

5. N. S. Stoloff and R. G. Davies, Acta Metall. 12, 473 (1964).

6. P. Morgand, P. Mouturat, and G. Sainfort, Acta Metall. 16, 867 (1968).

7. T. Saburi, I. Yamauchi, and S. Nenno, J. Phys. Soc. Jpn. 32(3), 694 (1972).

8. M. G. Mendiratta, H.-M. Kim, and H. A. Lipsitt, Metall. Trans. A15, 395 (1984).

9. C. G. McKamey, J. A. Horton, and C. T. Liu, to be published in Materials Research Society Symposia Proceedings, Vol. 81, High Temperature Ordered Intermetallic Alloys, II, ed. C. C. Koch, C. T. Liu, N. S. Stoloff, and O. Izumi (Materials Research Society, Pittsburgh, 1987).

10. C. G. McKamey, C. T. Liu, J. V. Cathcart, S. A. David, and E. H. Lee, Evaluation of Mechanical and Metallurgical Properties of Fe_3Al-Based Aluminides, ORNL/TM-10125, Oak Ridge National Laboratory, September 1986.

11. C. T. Liu and J. O. Stiegler, Science 226, 636 (1984).

12. Y. Umakoshi, M. Yamaguchi, Y. Namba, and K. Murakami, Acta Metall. 24, 89 (1976).

13. M. J. Marcinkowski and D. S. Miller, Philos. Mag. 6, 871 (1961).

14. B. H. Kear and H. G. Wilsdorf, Trans. AIME 224, 382 (1962).

15. S. Takeuchi and E. Kuramoto, Acta Metall. 21, 415 (1973).

16. N. S. Stoloff and R. G. Davies, Prog. Mater. Sci. 13, 1 (1966).

17. C. G. McKamey and C. T. Liu, unpublished results.

JOINING OF ADVANCED ALUMINIDES

D. E. Clark

Idaho National Engineering Laboratory
EG&G Idaho, Inc.
P. O. Box 1625
Idaho Falls, Idaho 83415

ABSTRACT

The weldability of four Ni_3Al-8% Cr alloys (IC-218, IC-221, and two low-Zr modifications) was investigated. Solidification segregation during base metal production decreases weldability by creating low-melting regions susceptible to hot cracking during welding. Extrusion, hot rolling, and annealing homogenize the base metal microstructure, solving this problem. Weldability was evaluated with the GTAW process and HAZ simulation (Gleeble testing) as a function of Zr content, preheat temperature, and weld travel speed. Weld cracking occurred in the fusion zone; no cracks originated in base material or HAZ. Cracking increased with Zr content at low Zr levels, increased with welding speed, and decreased with preheat. At higher Zr levels, hot cracking, possibly due to a Zr-Ni eutectic, was severe. An interdendritic phase present at higher welding speeds, apparently β', is strongly enriched in Zr.

INTRODUCTION

Advanced aluminides have substantial potential as high-temperature, high-strength materials. This is a result of the intrinsically good high temperature mechanical properties of ordered intermetallic compounds, the oxidation resistance provided by a high aluminum content, and alloy development work leading to the economical production of boron-modified, relatively ductile polycrystalline alloys.[1]

Applications for these materials will be very limited, however, unless practical methods of joining them are found. The objectives of

the present INEL task are to define the weldability problems limiting the use of the most recently developed ductile aluminides in welded structures, and to develop joining processes to solve these problems. This requires a basic understanding of their metallurgy under welding conditions. Major areas of work include: (a) the characterization of the welding metallurgy of wrought Ni_3Al and modified ORNL advanced alloys; (b) scoping studies on the weldability of rapidly solidified aluminides produced in the concurrent consolidation task; (c) studies of microstructural and residual stress effects on weldability and mechanical properties in heavy section aluminide weldments; and (d) the investigation of criteria for the development of advanced aluminide filler materials.

BACKGROUND

Previous weldability work at ORNL in conjunction with alloy development activities indicates that the advanced aluminides are sensitive to various kinds of weld cracking. Early work on Ni_3Al and nickel-iron aluminides[2] established that (a) an intermediate boron content of approximately 200 ppm was a good compromise between base metal ductility, requiring high B concentrations, and fusion zone hot cracking, which was exacerbated by high B contents; (b) weld cracking was a strong function of welding speed; (c) second phases, notably fusion zone interdentritic and HAZ intergranular β' (a martensitic transformation of the NiAl β phase), are formed by solute partitioning under solidification segregation or HAZ thermal cycles; and (d) most weld cracking was seen in the HAZ rather than the fusion zone. Further work[3] suggested that iron additions improve weldability over the Ni_3Al, and that the β' phase did not seem to cause HAZ cracking. A more comprehensive paper on the weldability of the nickel-iron aluminides[4] (alloys IC-25 and IC-103) showed that boron degrades high temperature ductility by weakening HAZ grain boundaries, the opposite of its effect at room temperature, and again that cracking depends on welding speed. More recent work[5] on IC-50, a Hf-containing alloy based on Ni_3Al, shows that Hf additions improve weldability, although Hf also solid solution

strengthens the matrix and strongly segregates in solidification, forming a eutectic with Ni, both of which were suggested as a cause of weld cracking in thin cast sheet material.

While these welding studies on the Fe- and Hf-containing aluminides were underway, alloy development had progressed to the point that the most promising alloys[6] were the 8 wt.% chromium alloys IC-218 and IC-221, containing 0.9 and 1.8 wt.% Zr, respectively; the Zr was added for high temperature strength and creep resistance. Like iron, Cr replaces both Ni and Al atoms in the ordered lattice,[7] produces an order-disorder transition in the material at 900-1000°C, and, as in stainless steels, might be expected to improve oxidation resistance.

Initial weldability studies on these materials using the Sigmajig[8] showed fusion zone cracking, and suggested not only that the higher-Zr IC-221 was more crack resistant than the IC-218, but that the surface condition of the material made a difference in its crack resistance: after the repeated annealing cycles involved in cold rolling the material to its sheet form, a dark adherent oxide formed; when cleaned electrochemically, the material showed a drastic increase in strength. The amount of material involved in a surface oxide, perhaps of the order of tens of nanometers in thickness, would not appear to be enough to affect bulk properties, even in the relatively thin (~1 mm) material used here. Conclusions as to the weldability effects of Zr, such as whether there is an optimal amount, as with boron, remained to be drawn.

Most recently, further base material studies[9] have shown that even the 0.9 wt.% Zr level might be excessive. The solubility of Zr in the ordered lattice is about 6 at.%, while in the disordered γ phase it is only about 0.3 at.%. This means that as the lattice disorders with increasing temperature, the Zr is rejected by the growing regions of disordered γ, eventually resulting in compositions allowing incipient melting at about 1200°C, leading to a loss of high temperature strength. The apparent solution is to work with Zr levels less than about 0.3 wt.%, and to add an as-yet undetermined other element to recover some of the high temperature strength and creep resistance.

EXPERIMENTAL

MATERIALS

The only compositional difference between IC-218 and IC-221 is the Zr level, yet preliminary welding studies suggested a weldability difference.[8] The weldability effects of zirconium were therefore chosen for study. In addition to IC-218 at 0.9 wt.% Zr and IC 221 at 1.8 wt.% Zr, zero and 0.3 wt.% alloys were obtained, so that a range of Zr levels could be examined.

Alloys were produced by Cabot Corporation by vacuum induction melting and electroslag remelting. Compositions of the modified IC-218 heats are shown in Table 1; an Ni_3Al+B heat was also produced. It had been intended to slice the 4 in. (10 cm) diameter ingots into discs and reduce them to welding study shapes by hot or cold rolling. As shown in Figure 1(a), however, there was a substantial amount of segregation and cracking present, suggesting that such a breakdown would not be possible. The alloys were therefore returned to ORNL where they were

TABLE 1. Modified Reduced-Zr IC-218 Study Alloy Compositions

	Zero Zr		Low Zr	
	wt.% [6]	at.%	wt.%	at.%
Ni	84.18	75.25	83.71	74.72
Al	8.69	16.97	8.69	16.95
Cr	7.67	7.78	8.08	8.18
Zr	<0.01	<0.01	0.25	0.14
B	0.025	0.12	0.022	0.105
C	0.006	0.026	0.014	0.061
N	0.001	0.004	0.001	0.004
O	0.002	0.007	0.002	0.007
S	<0.002	<0.002	<0.002	<0.002

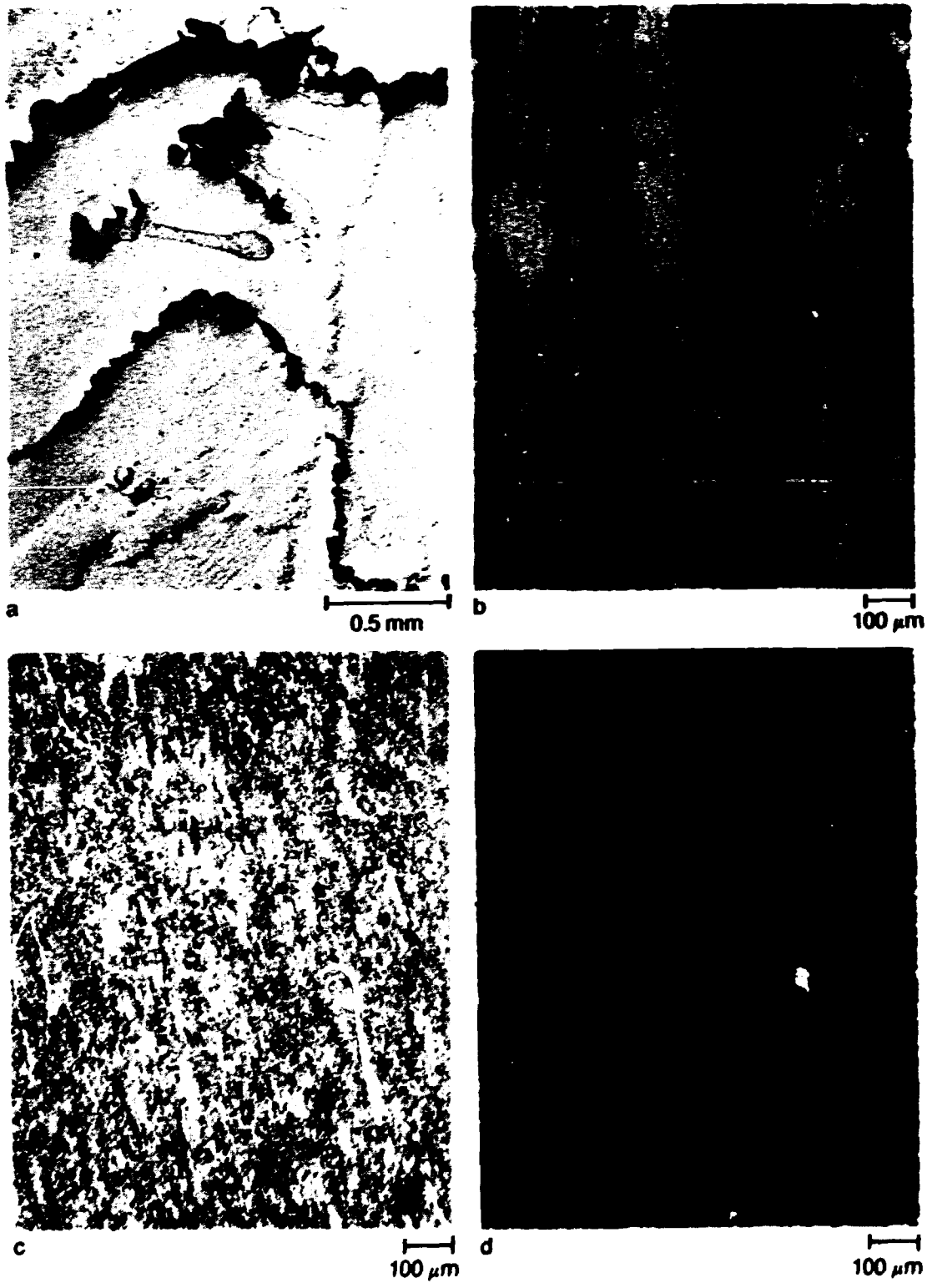

Figure 1. Modified IC-218, Cabot Heat 870, 0.25% Zr. (a) VIM/ESR ingot as received; (b) after hot extrusion; (c) after 50% cold rolling; (d) after 1100°C/1 h heat treatment, the baseline condition for welding studies.

canned in stainless steel and hot extruded at 1000° C to a 1 x 3 in. rectangular cross section. These rectangular shapes were then hot rolled 50% in one pass. The low-Zr alloys hot rolled more successfully than similar IC-218/221 compositions, and, as expected, the Ni_3Al+B compositions were not hot workable. Tensile results indicate that the high temperature strength and ductility of the 0.25% Zr material are comparable to, or exceed, those of IC-218.[10]

Although hot extrusion and rolling successively refined the microstructures, the material was still not completely recrystallized and showed substantial segregation from the original ESR ingot (Fig. 1(b) and (c)). Welds in this material suffered from apparent liquation cracking in the HAZ, which propagated through the fusion zone (Fig. 2(a)). Gleeble tests of this material exhibited zero ductility at 1000°C. Annealing studies showed that 1 h at 1100°C produced a completely recrystallized microstructure with a grain size of 40-50 μm, as shown in Figure 1(d); Gleeble tests under the same conditions showed substantial ductility. Welds in this material showed fusion zone cracking under some circumstances, but the cracks did not propagate into the base material (Fig. 2(b)). This thermal cycle was chosen as the baseline pretreatment for the modified IC-218 alloys.

GTA WELDING

The heat-treated, hot-rolled 0 and 0.25% Zr material was sliced into wafers approximately 12 x 80 mm, including the stainless steel cladding, by about 3 mm thick. GTA welds under argon shielding were made according to the parameters in Table 2. Current was increased along with travel speed to produce welds of approximately the same melted cross sectional area. Each weld was approximately 50 mm long. The coupons were welded on a large copper heat sink to maintain the preheat temperature, with the copper block and specimen equilibrated before welding. Ambient (20°C) and 200°C preheats were used. Similar welding conditions, though at somewhat higher heat inputs, were used for welds in powder metallurgy IC-218 (0.9% Zr) and IC-221 (1.8% Zr).

Figure 3 shows cracked (20 in./min) and uncracked (2 in./min) welds in 0.25% Zr modified IC-218 material. Cracking was quantified by

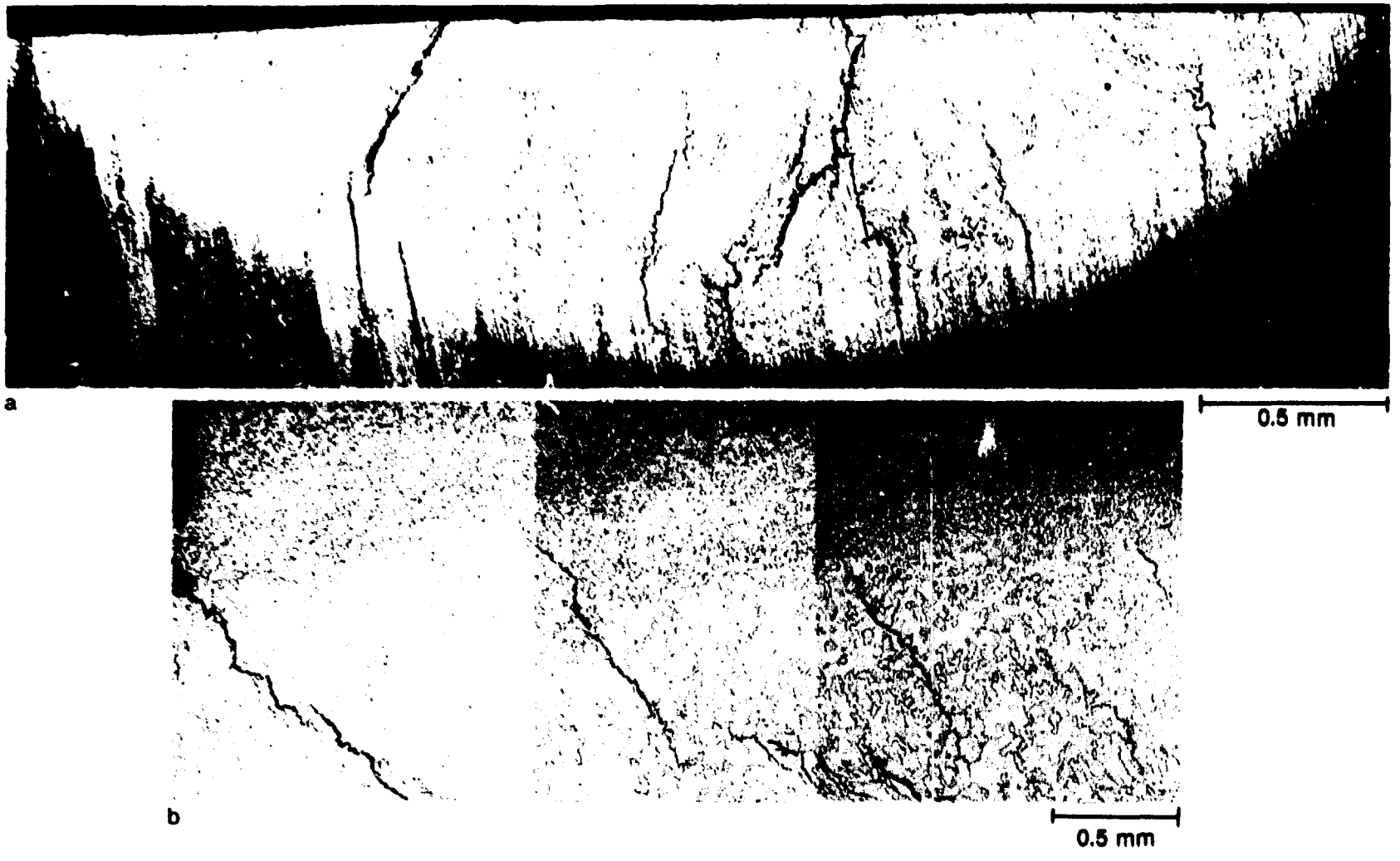

Figure 2. Welds in 0.25% Zr modified IC-218 alloy: (a) as-rolled, showing HAZ liquation cracks extending into the fusion zone; (b) after 1100°C/1 h heat treatment, showing lack of HAZ cracking and arrest of fusion zone cracks at the fusion line.

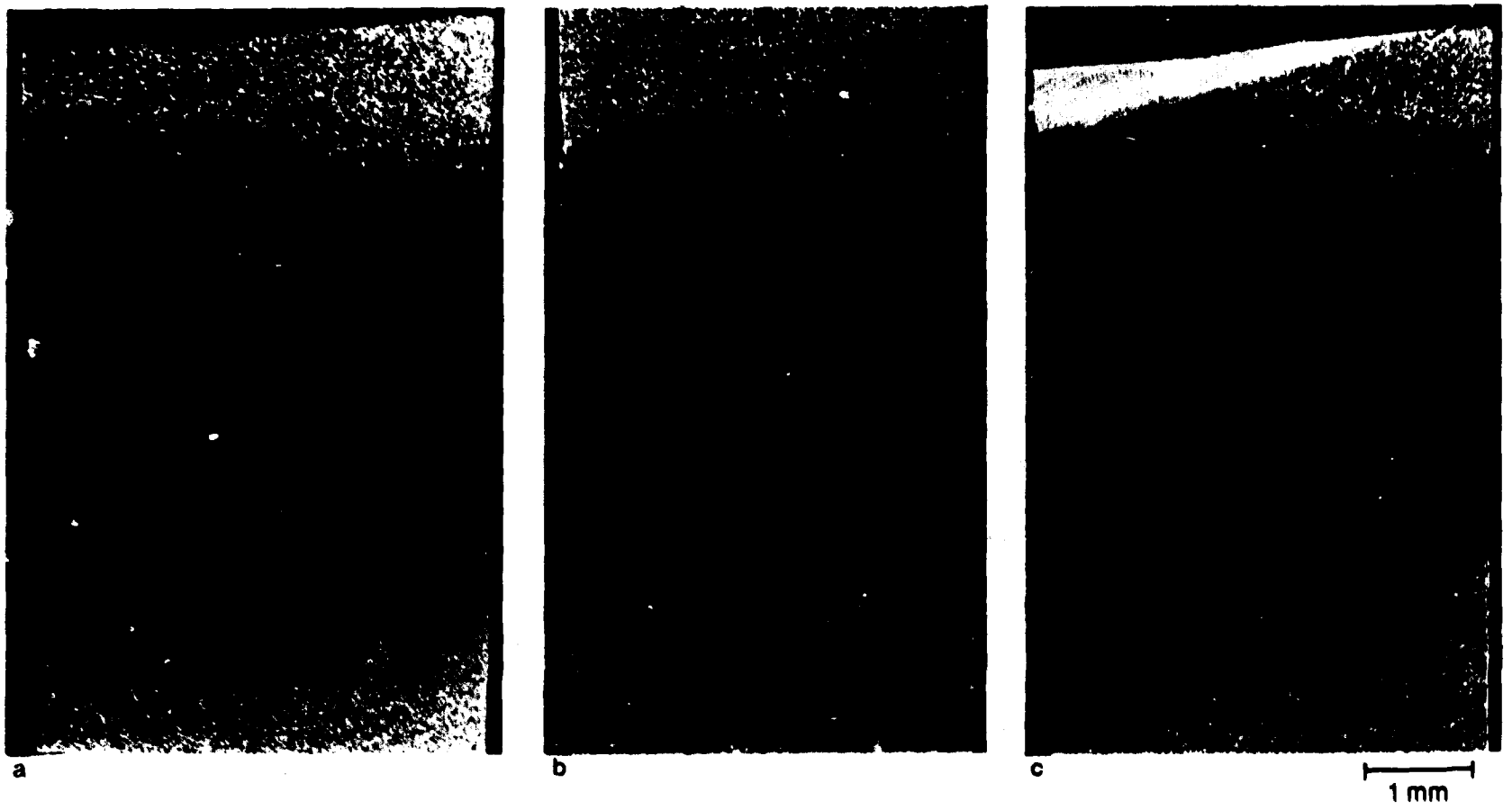

Figure 3. GTA welds in 0.25% Zr modified IC-218 alloy: (a) 20 in./min travel speed, showing extensive cracking; (b) 10 in./min, showing reduced cracking; (c) 2 in./min, showing no cracking.

TABLE 2. GTA Welding Parameters

Travel Speed in./min	Preheat temperature °C	Current (A)
2	20	40
2	200	40
10	20	100
10	200	100
20	20	130
20	200	130

measuring total crack length on a photomacrograph (at approximately 20x) of a polished and etched weld top surface, and dividing by the apparent weld surface area. Multiplying the result by 100 produced a low integer cracking index number ranging from 0 (no cracking) to about 11 in the worst cases observed. This cracking index is nonstandard but useful for comparison among materials and welding parameters.

In addition to standard optical metallography, TEM specimens were taken from those welds where the cracking was not so severe as to prevent the extraction of a whole foil. Since cracking appeared to be confined to the fusion zone, most TEM work was done in this area. The amount of interdendritic phase apparently varied with Zr content; in the 1.8% Zr IC-221 material, the large amount of this phase produced holes during electropolishing, and no foils were obtained.

RESULTS

CRACKING

Figure 4 summarizes the cracking indices for three welding speeds, two preheats, and two Zr levels. It is apparent that at very slow welding speeds none of the alloys cracked; at higher welding speeds the 0.25% Zr material showed much more cracking than the 0% Zr material, though in both cases the amount of cracking was reduced by preheating at 200°C.

The nature of the cracking is not obvious. As seen in Figure 2, HAZ liquation cracking can extend into the fusion zone; this is a result of

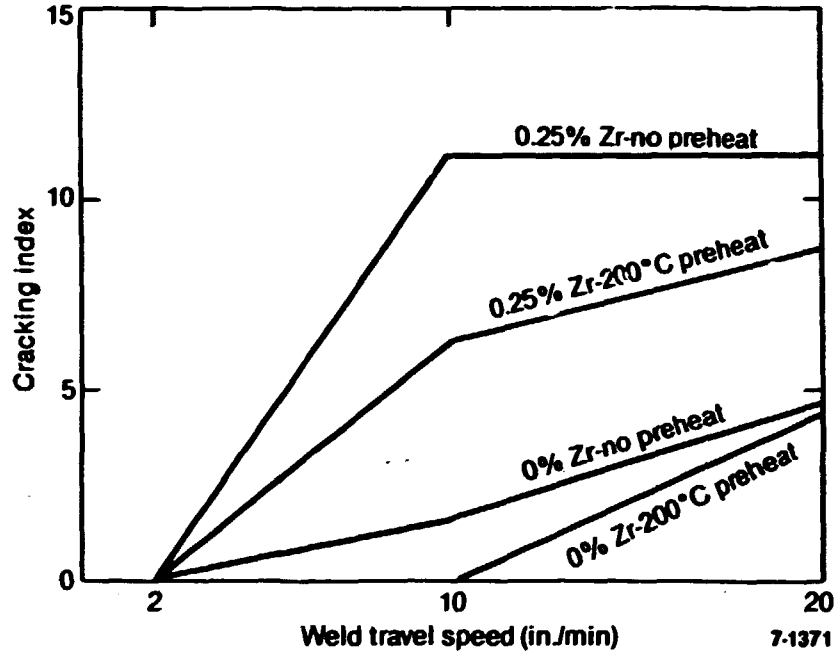

Figure 4. Cracking indices for GTA welds in modified IC-218 alloys as functions of weld travel speed, Zr content, and preheat.

insufficiently homogenized base material. Figure 5 shows the surface of a fusion zone crack in IC-218 (0.9% Zr); the surface has the almost classical melted appearance of a hot crack, with extremely weak bonding between the dendrites, which have broken off as the crack widened. It is highly enriched in Zr (about 7%), suggesting that low-melting eutectics with Ni may be responsible. The cracks in Figure 3 lie between dendrites when seen in plan view, suggesting that they are either hot cracks due to segregation or form in the solid state at weak interdendritic boundaries. Their propagation through the weld metal, however, tends to follow grain boundaries but cross prior interdendritic boundaries, suggesting that grain boundary weakness normal to the residual tensile stresses in the solidified material dominates any interdendritic fracture paths. The cracks may also be due to a combination of mechanisms, for example, a hot crack which concentrates stress along a weak boundary, allowing further crack extension in the solid state. These crack surfaces are presently being examined.

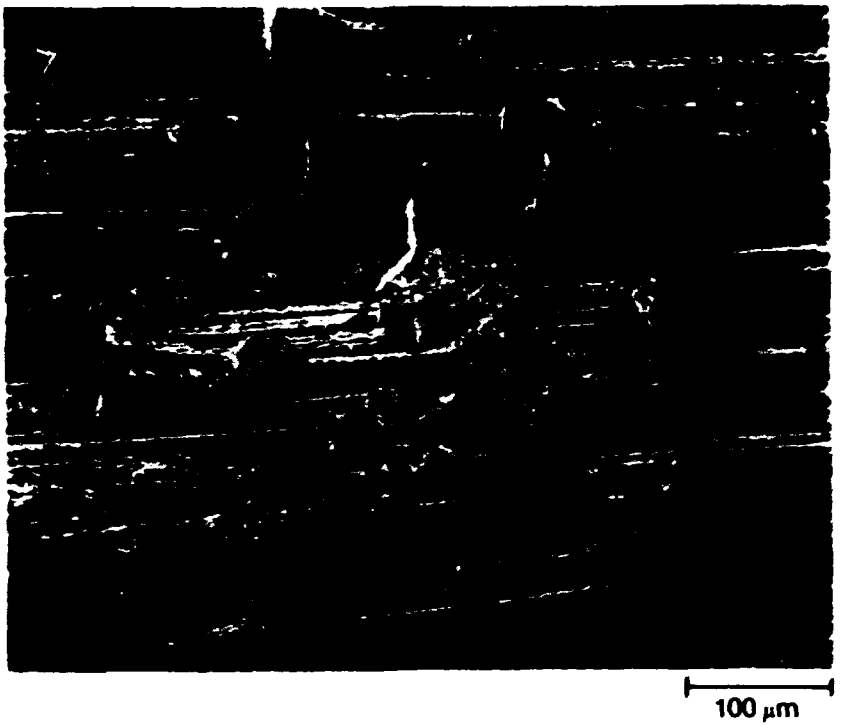

Figure 5. Surface of fusion zone crack in IC-218 alloy, showing surface appearance typical of a hot crack.

MICROSTRUCTURE

Fusion Zone

The fusion zones of all welds showed a dendritic microstructure; the fusion zones of the slower welds, particularly in the 0% Zr material, were recrystallized, but a dendritic pattern was still recognizable. An interdendritic phase was present in the IC-218 (0.9% Zr) and in welds in the 0.25% Zr material made at 10 in./min and above. The appearance and distribution of this phase (Figures 6 and 7) suggest that it is similar to the β' phase seen in nickel-iron aluminides in previous work.[2,4] In the nickel-iron aluminides, the β' phase was found to be depleted in Ni and Fe, and enriched in Al and Mn. STEM analysis of this phase in the IC-218 alloy, however, shows that it has a very high Zr content, as much as 30%. This large proportion of a high-Z element precluded accurate X-ray energy dispersive spectroscopy, and hence accurate chemical analysis, particularly of the low-Z Al.

As expected,[11] the relatively rapid cooling associated with welding quenched in an antiphase domain structure smaller than the grain size.

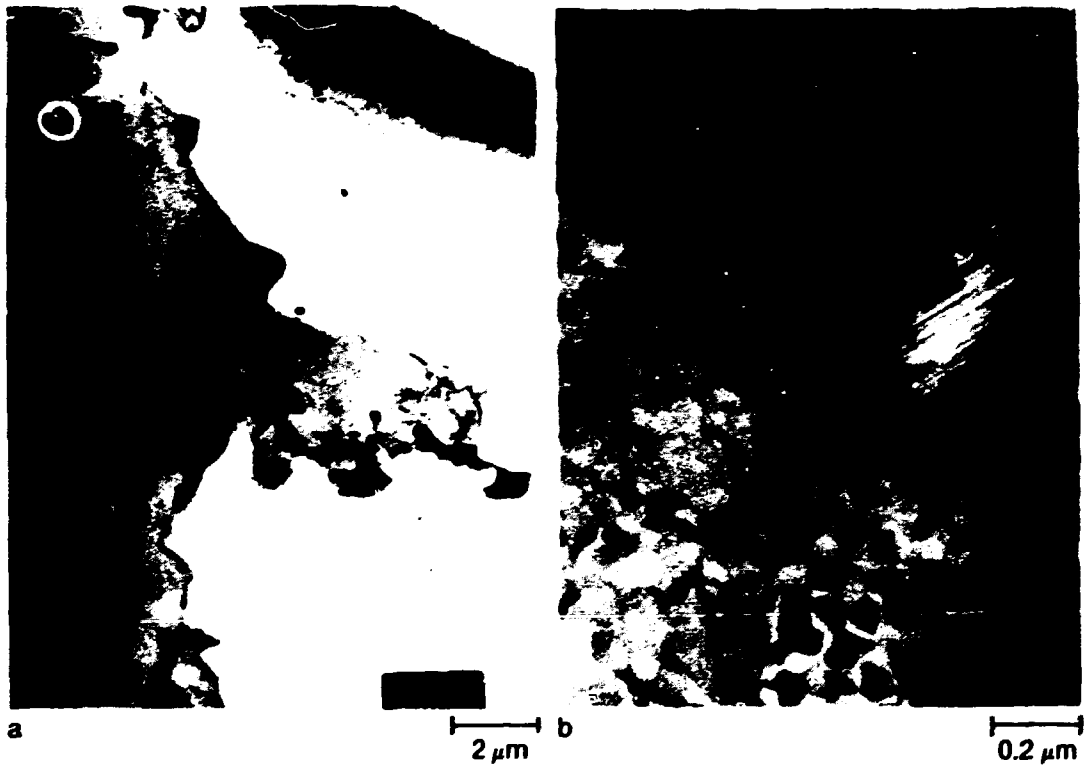

Figure 6. IC-218 GTA weld interdendritic second phase.

Figure 7. Second phase in 0.25% Zr GTA weld, 10 in./min.

As seen in Figure 8, the size of these domains increases with decreasing cooling rate, whether the result of preheat or of welding speed. Figure 9 shows the difference in domain size near the center of the dendrite core for two welding speeds. Figure 10 illustrates the observation that, in general, the domains at the interdendritic boundaries are several times the size of those away from the boundary. As in nickel-iron aluminides, the regions separating the domains are distinct volumes of disordered material, sometimes containing very small ordered regions, rather than planar APB's.

Heat-Affected Zone

Figure 11 shows a transverse section through a weld in IC-218 material produced via powder metallurgy. There is evidence of a second phase at grain boundaries in the HAZ, apparently analogous to the β' precipitate seen in iron-nickel aluminides.[4] There is little or no evidence of this phase in the 0 and 0.25% Zr welds, which were, however, made in ingot metallurgy material at somewhat lower heat inputs.

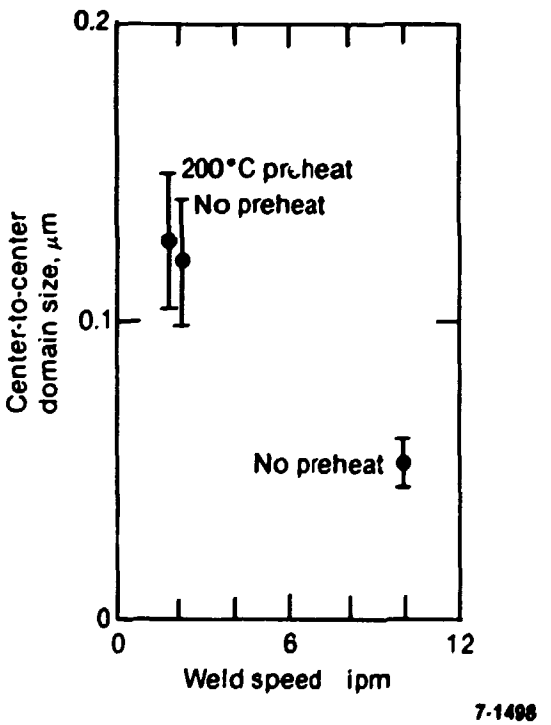

Figure 8. Antiphase domain size (average center-to-center distance) in 0.25% Zr modified IC-218 alloy.

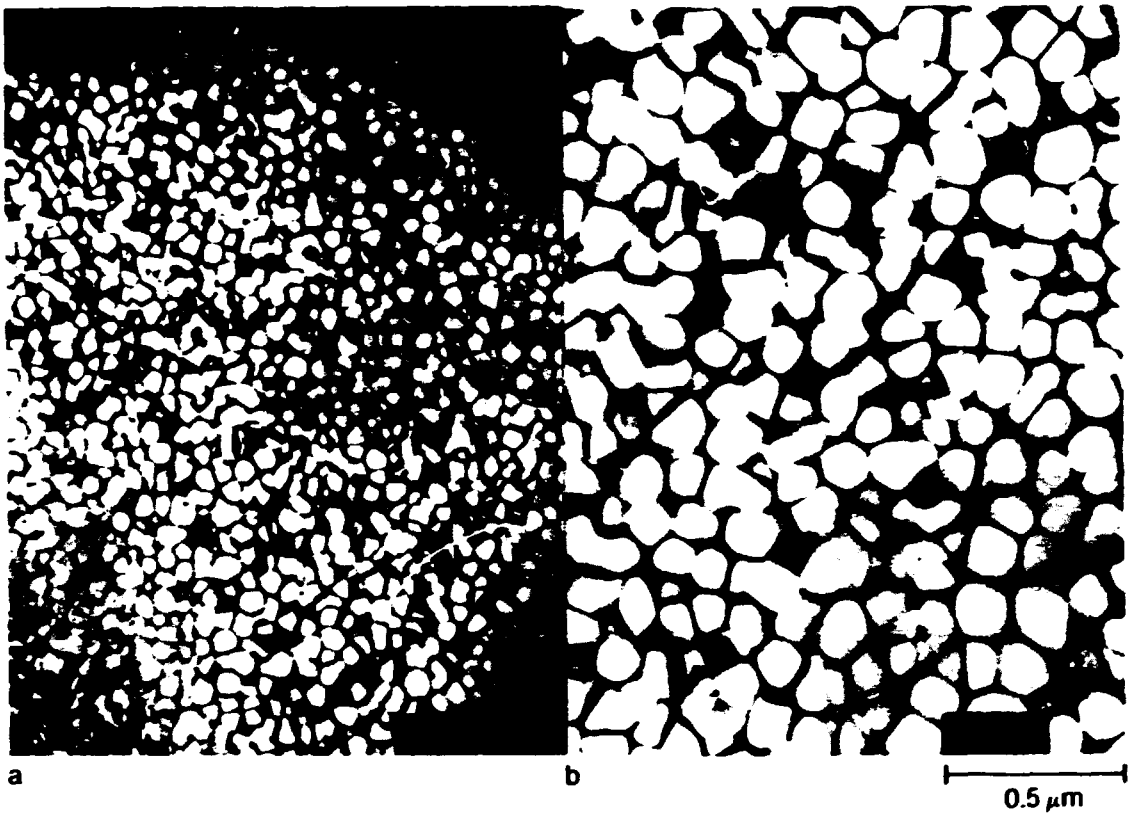

Figure 9. Antiphase domain size in 0.25% Zr modified IC-218 alloy: (a) welded at 10 in./min; (b) welded at 2 in./min

Figure 10. Large r antiphase domains at interdendritic boundary in 0.25% Zr modified IC-218 alloy.

Figure 11. Transverse section of GTA weld in IC-218 powder metallurgy material.

As mentioned previously, the HAZ did not seem susceptible to cracking, whether or not associated with a second phase; fusion zone cracks were generally arrested near the fusion line.

DISCUSSION

BASE METAL

It is evident that zirconium is segregated severely in ingot solidification of the aluminides, and possesses several low-melting eutectics with Ni which could be responsible for hot cracking. Even the severe deformation involved in hot extrusion and rolling preserved evidence of the ingot solidification structure, which, when incorporated into a weld heat-affected zone, showed low-melting zones which nucleated cracks in fusion zone and base material. A 1-h anneal at 1100°C was required to completely recrystallize the material, and may also have served to homogenize it chemically. The lower Zr levels of the study heats prepared for this weldability work do seem, however, to improve the hot workability over the IC-218/221 materials. While extra

processing steps in the breakdown of a material are expensive, in an intrinsically crack sensitive material like the aluminides, such base material processing steps may be crucial for resisting the inevitable thermal and residual stresses encountered in welding. Anticipated work in the weldability of powder metallurgy versions of these same alloys should clarify the benefits of this alloy production route.

FUSION ZONE MICROSTRUCTURE

In some ways, the fusion zone microstructure observed in the IC-218-type alloys is a hybrid of those seen in nickel-iron aluminides on the one hand (e.g., IC-103),[4] and the Hf-containing IC-50 on the other.[5] Like the nickel-iron aluminides, there is an order-disorder phase change at elevated temperatures, solidification segregation appears to promote the formation of β and β' interdendritically, and a β-β' precipitate can appear on HAZ grain boundaries under appropriate thermal conditions. Like Hf in IC-50, the Zr strongly segregates to the interdendritic spaces during solidification, and may influence the ordering reactions, depending on concentration. The unique features of the IC-218 system include the large Zr enrichment of the β' phase, the apparent resistance to heat-affected zone cracking relative to that seen in the nickel-iron aluminides, and the apparently detrimental effects of Zr, whereas Hf appears to improve the weldability of IC-50 over that of straight Ni_3Al.

The change in antiphase domain size was expected from previous work.[2,11] It appears that solidification is complete before ordering occurs, and that cooling rates in the solid state are essentially the same across the very small distances separating different domain size regions. Microchemical analysis is as yet incomplete in the present work, but it is anticipated that chemical segregation will prove to be responsible, by affecting the ordering temperature and hence domain size.

FUSION ZONE CRACKING

Fusion zone cracking, as summarized in Figure 4, appears to depend on interdendritic fracture, whether by hot or cold cracking, or a combination of the two. There are several factors contributing to cracking that are affected by welding parameters, including: (a) thermal

and residual stresses before and after welding; (b) the degree of segregation of both major and minor alloying elements during solidification; (c) the degree of homogenization after solidification, including recrystallization and the possible dissolution of second phases, and (d) the antiphase domain size, to the extent the APBs act like grain boundaries in Hall-Petch strengthening. For example, the presence of the β' interdendritic phase may contribute to fusion zone cracking by forming an incoherent or otherwise crack-sensitive network; this would explain why there was no cracking in the 2 in./min welds, where the β' phase was dissolved, if the nearer-equilibrium solidification conditions ever allowed it to form. Or, rather than the β' itself, excessive solid solution strengthening and a resulting crack sensitivity might result from solidification segregation of strengthening alloying elements such as Hf and Zr. On the other hand, the slower welding speed also means lower thermal gradients during welding and lower residual stresses afterwards, which could also be expected to reduce cracking. While the antiphase domain size shrinks with welding speed, fusion zone mechanics appear to be so influenced by grain and dendrite boundaries that this potential high cooling rate strengthening mechanism does not have a chance to operate.

CONCLUSIONS

1. Fusion zone hot cracking, sometimes propagating into the base metal, occurs in IC-218 and IC-221 at Zr levels of 0.9 and 1.8 %. The strong solidification segregation of Zr, its presence on the crack surfaces, and its low-melting eutectics with Ni suggest that it may be responsible.
2. Weld cracking in reduced-Zr versions of IC-218 occurs in the fusion zone, interdendritically, although the nature of this cracking (hot cracks, or solid state cracks along weak boundaries) is still under investigation. The quantity of weld cracking increases with weld travel speed; no cracks occurred at the slowest speed of 2 in./min. Cracking increases with Zr content between 0 and 0.25% Zr, and decreases with preheat between ambient and 200°C.

3. In both standard and modified low-Zr materials, an interdendritic phase similar to the β' seen in the nickel-iron aluminides is present, but it is highly enriched in Zr. This phase is absent in very slow GTA welds (2 in./min), probably due to solidification closer to equilibrium and chemical homogenization during slow cooling.

REFERENCES

1. Liu, C. T. and J. O. Stiegler, 1984. Ductile Ordered Intermetallic Alloys. Science 226:636-642.

2. David, S. A., W. A. Jemian, C. T. Liu, and J. A. Horton, 1985. Welding and Weldability of Nickel-Iron Aluminides. Welding Journal Research Supplement, 64:22s-28s.

3. Santella, M. L., S. A. David, and C. L. White, 1985. Weldability of Ni_3Al-Type Aluminide Alloys. Mat. Res. Soc. Symp. Proc. Vol. 39:495-503.

4. Santella, M. L. and S. A. David, 1986. A Study of Heat-Affected Zone Cracking in Fe-Containing Ni_3Al Alloys. Welding Journal Research Supplement, 65:129s-137s.

5. Santella, M. L., S. A. David, J. A. Horton, 1986. Weldability of an Ni_3Al Alloy. Advances in Welding Science and Technology. pp. 629-633. ASM, Metals Park, Ohio.

6. Liu, C. T., October 1985. Personal communication.

7. Ochiai, S., Y. Oya and T. Suzuki, 1984. Alloying Behavior of Ni_3Al, Ni_3Ga, Ni_3Si and Ni_3Ge. Acta Met. 32:2 pp. 289-298.

8. Goodwin, G. M., May 1986, personal communication.

9. Liu, C. T., March 1987. Personal communication.

10. Sikka, V. K. March 1987. Personal communication.

11. Horton, J. A. and C. T. Liu 1985. Anisotropic Antiphase Boundaries in Rapidly Solidified Ni_3Al. Acta Met. 33:12 pp. 2191-2198.

HEDL-2 -- INVESTIGATION OF ELECTRO-SPARK DEPOSITED COATING FOR PROTECTION OF MATERIALS IN SULFIDIZING ATMOSPHERES

R. N. Johnson

Westinghouse Hanford Company
P. O. Box 1970
Richland, WA 99352

INTRODUCTION

The objective of this program is to develop candidate coatings, using the electro-spark deposition (ESD) process, for the protection of materials in sulfidizing atmospheres typical of fossil energy applications. Coatings of interest include FeCrAlY, NiCrAlY, chromium, aluminum, niobium, chromium carbide, and titanium diboride. Materials to be protected include low alloy steels, Alloy 800, Type 310 stainless steel and Hastelloy C.*

Background

Electro-spark deposition is a micro-welding process that uses short-duration, high-current electrical pulses to deposit or alloy an electrode material on a metallic substrate. The coating is fused (metallurgically bonded) to the substrate with such a low total heat input that the bulk substrate material remains at or near ambient temperature. Rapid solidification of the deposit typically results in an extremely fine-grained deposit that may be amorphous for some materials. The microstructures produced by ESD can provide exceptional corrosion- and wear-resistance for many materials. Nearly any electrically conductive metal, alloy, or cermet can be applied to metallic substrates.

Further background information on the ESD process is provided in the AR & TD Fossil Energy Materials Program Quarterly Progress Report for the Period

*Trademark, Cabot Corp., Kokomo, IN.

July 1 through September 30, 1985, WBS Element HEDL 6.1, and in References 1 and 2.

DISCUSSION OF CURRENT ACTIVITIES

Two series of ESD coated test specimens were completed and sent to ANL for corrosion testing. The first series consisted of chromium carbide on Type 310 SS prepared at the request of ANL for additional corrosion tests. The second series included pure chromium coatings on Type 310 SS utilizing recently developed deposition parameters.

Corrosion tests were performed by ANL using thermo-gravimetric analysis at 650°C and 875°C in four different environments, consisting of high and low oxygen, and high and low sulfur gases. (Further details are provided in Ref. 3.)

The corrosion rates of the chromium carbide coatings and the chromium coatings on 310 SS were compared to that of bare 310 SS. The chromium carbide exhibited the lowest corrosion rate in both high sulfur and low sulfur environments, with intermediate protection provided by the chromium coating. Similar trends were observed in high temperature air, although differences were not as marked. Hardness measurements showed that the initially hard surface layers of chromium carbide retained their hardness after all the oxidation and sulfidation tests, which should be of benefit under corrosion-erosion conditions.

Another version of the ESD chromium carbide coating has been developed which should offer further improvement in oxidation and sulfidation resistance. The composition of the chromium carbide electrode now used is Cr_3C_2-15% Ni. The nickel makes an excellent binder for the Cr_3C_2 and increases the efficiency of transfer in the ESD process, but the Ni may be susceptible to attack in sulfidizing environments. By further modifying the chromium carbide coating with another ESD treatment using aluminum to alloy with the nickel, a more corrosion resistant surface of chromium carbide plus nickel

aluminide is created. Tests have shown that the Al-modified chromium carbide coating is consistently harder, has a lower corrosion- and wear-rate in both sodium and H_2O, and exhibits better tribological performance than the untreated chromium carbide. Specimens of the new coating applied to 2¼Cr-1Mo steel have been submitted for oxidation and sulfidation tests at ANL.

ESD coating parameters have been developed for applying niobium to 2¼Cr-1Mo steel. The niobium is being used as a diffusion barrier between the substrate and a variety of other corrosion resistant coatings being developed. During attempts to file down some of the initial trial coatings, we discovered that the niobium coating was too hard to file. Subsequent measurements indicated that the niobium coating had alloyed sufficiently with the 2¼Cr-1Mo steel to produce a niobium-base intermetallic with an average hardness of nearly 1500 Knoop, with some readings over 2000 Knoop. (This compares with a normal hardness for pure niobium of about 200 Knoop.) When a chromium coating was applied over the niobium, the hardness of the resulting alloy increased to over 2300 Knoop. Coatings of niobium and niobium plus chromium on 2¼Cr-1Mo steel are being prepared for further ANL testing.

REFERENCES

1. R. N. Johnson, "Coatings for Fast Breeder Reactors," in Metallurgical Coatings, 1984, Elsevier Sequoia, S.A., New York, 1984, p. 31-47.

2. R. N. Johnson and G. L. Sheldon, "Advances in the Electro-Spark Deposition Coating Process," J. Vac. Sci. Technol. A, Vol. 4, No. 6, Nov./Dec. 1986, p. 2740-2746.

3. K. Natesan and R. N. Johnson, "Corrosion Resistance of Chromium Carbide Coatings in Oxygen-Sulfur Environments," presented March 23, 1987 by R. N. Johnson at the 1987 International Conference on Metallurgical Coatings, San Diego, CA; to be published in the proceedings.

INVESTIGATION OF THE WELDABILITY OF DUCTILE ALUMINIDES

M.C. Maguire*, G.R. Edwards*, and S.A. David†

*Center for Welding Research
Colorado School of Mines
Golden, Colorado 80401

†Materials Joining Group
Metals and Ceramics Division
Oak Ridge National Laboratory
Oak Ridge, TN 37831

ABSTRACT

Ni_3Al and alloys based on that composition possess desirable high temperature strength properties. The recent advances in imparting ductility to these alloys by microalloying with boron is not effective at high temperatures, where these alloys fracture in a brittle, intergranular fashion. Consequently, welds made with these alloys are subject to heat-affected zone (HAZ) cracking. This work concerns the improvement of weldability and hot ductility of these alloys through microstructural refinement of the grain structure, and further refinement by production of an antiphase domain structure.

INTRODUCTION

Some intermetallic compounds and long range ordered phases such as Ni_3Al possess unique properties which make them attractive for high temperature use. Alloys based on this composition represent not only a reduction of strategic materials consumption, but potentially improved mechanical properties. Single crystals of Ni_3Al show unusual positive flow strength dependence on temperature up to about 700°C. Yield strengths near 700°C have been observed to increase by a factor of seven with respect to room temperature values[1]. Exploiting this behavior in polycrystalline alloys was generally thought to be impossible owing to grain boundary fracture which produced near-zero ductility at all temperatures, even though single crystals showed good ductility at room temperature. Recent discoveries of the beneficial effect of boron microalloying additions, however, have rekindled the interest in Ni_3Al as a structural material[2,3]. The addition of a few hundred ppm of boron has resulted in the fabrication of Ni_3Al and alloys based on Ni_3Al without the intergranular fracture seen in earlier polycrystalline alloys.

The usefulness of any structural material is strongly dependent on its ability to be joined. Initial weldability studies on Ni_3Al alloys showed that they were susceptible to heat-affected zone (HAZ)

cracking. The cracking was intergranular and occurred transverse to the welding direction. Subsequent alloy modifications have improved the weldability of these alloys, but a fundamental understanding of the mechanism responsible for cracking and the means to reduce this problem is still lacking. The goal of this project is to improve the understanding of the factors affecting the weldability and fabricability of ductile aluminides. The alloys of particular interest here are Ni-Al-Cr alloys with other minor alloy additions.

TECHNICAL APPROACH

The overall goal of this investigation is to obtain a basic understanding of the factors which affect the weldability of Ni-Cr aluminides. Although many alloys are under development, it is clear that a fundamental understanding of the microstructural and mechanical properties which affect weldability is not complete. It is believed that improving the hot ductility is essential to improving the weldability of these alloys.

INITIAL STUDY

The initial work in this area was aimed at investigating the grain size effect on hot ductility of one alloy, designated IC-50. The composition of IC-50 (and that of other alloys to be discussed later) is shown in Table 1.

TABLE 1. Alloy Compositions (atomic percent)

Alloy Designation	Al	Cr	Hf	B	Ni	Al Equivalent
IC-50	23.5	---	0.5	0.10	Bal.	24.0
IC-50-1	21.4	2.0	0.5	0.10	Bal.	22.9
IC-50-2	20.5	5.0	0.5	0.10	Bal.	23.5
IC-50-3	19.6	8.0	0.5	0.10	Bal.	24.1
IC-50-4	19.0	10.0	0.5	0.10	Bal.	24.5
IC-50-5	21.0	2.0	0.5	0.10	Bal.	22.5
IC-50-6	20.0	4.0	0.5	0.10	Bal.	22.5
IC-50-7	19.0	6.0	0.5	0.10	Bal.	22.5
IC-50-8	18.0	8.0	0.5	0.10	Bal.	22.5

This study was conducted in parallel on material prepared by two different means: (1) conventionally cast, cold-worked, and annealed, and (2) rapidly solidified powder which was subsequently hot extruded to a powder compact. Samples from both materials were annealed to produce varying grain sizes. Two grain sizes were chosen for each material, shown in Table 2.

TABLE 2. Grain Sizes of IC-50 Investigated

Cast/Cold Worked	Hot Extruded Powder Compact
22 μm, Annealed 2 hours at 700°C	11 μm, As-received
66 μm, Annealed 1 hour at 900°C at 1100°C	52 μm, Annealed 20 hours

Details of the grain size investigation are discussed elsewhere[4], but the results of the investigation are significant. The hot ductility test records the ductility of a sample undergoing simulated welding conditions when fractured at various temperatures along the HAZ thermal cycle. In materials which are prone to HAZ cracking, increasing the hot ductility will lessen the tendency for cracking. The results of the hot ductility tests are shown in Figs. 1 and 2. The grain size proved to be effective in increasing ductility in the fine-grained PM IC-50, indicating that grain sizes need to be less than 20 μm. A small amount of ductility increase was seen in the fine-grained cast material at 1000°C, but this was due to a dynamic recrystallization occurring during the test. The result of the recrystallization was a local reduction in grain size over a narrow region of the gage length, which was suspected to be the cause of the ductility increase.

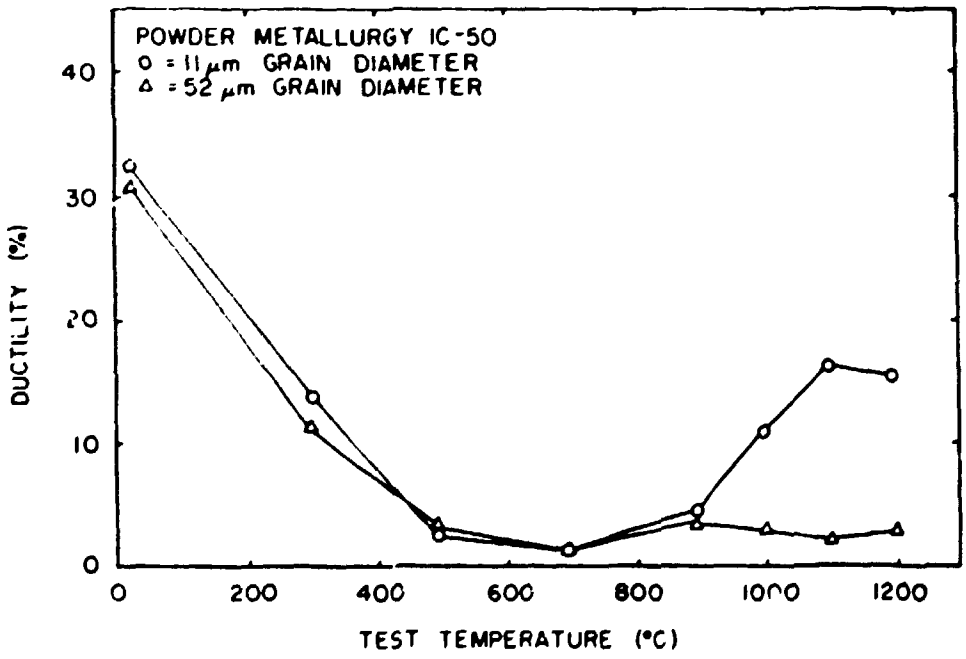

Fig. 1. Hot ductility of powder metallurgy IC 50 for the two grain sizes indicated.

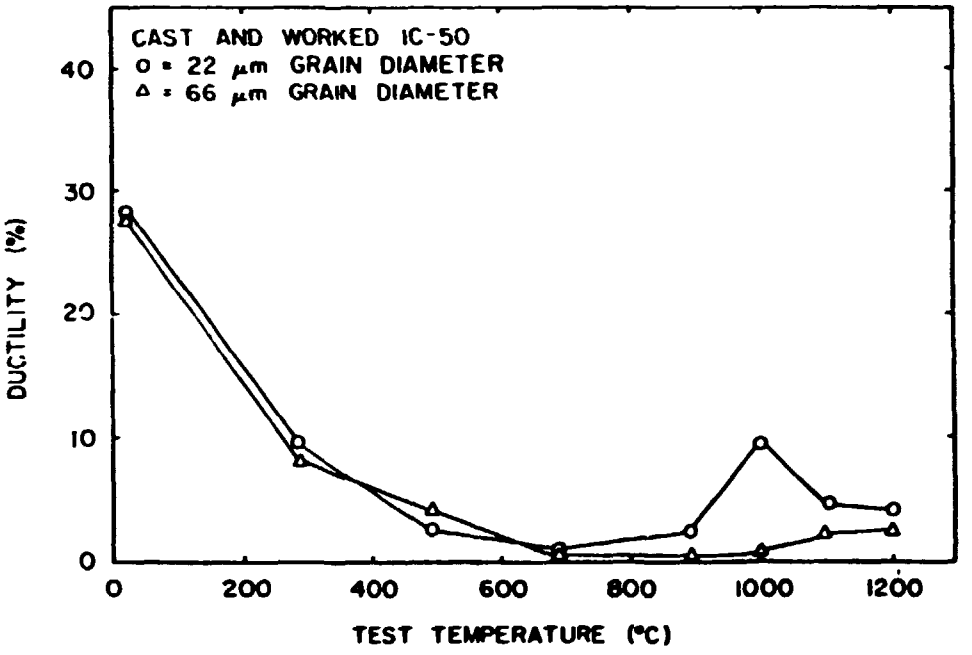

Fig. 2 Hot ductility results for cast IC-50 for the two grain sizes indicated.

CURRENT INVESTIGATION

Refining the grain size was shown to be effective in improving the hot ductility of the IC-50 alloy in the high temperature region. However, by conventional thermomechanical processing, the grain size could not be reduced to less than 20 μm. One would suspect that further microstructural refinement would be beneficial in improving ductility. This can be accomplished in ordered structures by the formation of an antiphase domain boundary (APB) network. The APBs separate regions within a single crystal which are out of phase with each other with respect to the ordering sequence. APBs can originate by either thermal or mechanical means. Four different ordering variants exist in the $L1_2$ crystal structure, which gives rise to the formation of the so-called "foam" network often associated with thermal domains in the $L1_2$ structure. Mechanical APBs exist in the ribbon of material which separates superpartial dislocations. Mechanistically, the spacing between superpartials is balanced by the same forces which dictate Shockley partial spacing in regular FCC alloys. These APBs are important to the motion of dislocation pairs in ordered structures, but are not useful for microstructural refinement.

Thermal domains, which form from thermally cycling above the ordering temperature and cooling quickly, provide barriers to slip. For a dislocation to cut an APB, it must create a new portion of APB -

a process which requires energy and is consequently resisted. Stoichiometric Ni_3Al has an ordering temperature above its melting temperature, so that forming thermal domains from a disordered solid is not possible. However, by perturbing the stoichiometry through the addition of alloying elements, the ordering temperature can be reduced to below the melting temperature. This will allow domain formation, provided cooling is rapid enough.

Forming domains is desirable for the following reason. The results of the hot ductility tests on IC-50 indicate that the grain size, which is proportional to the slip path length, is a key factor in the extent of deformation which can be accomodated prior to fracture initiation. Domains, if produced homogeneously in the microstructure, would then be the secondary source of slip path length refinement. This has been demonstrated in single crystals of Ni_3V, where domains were effective in dispersing slip[5]. More recently, the same principle was applied to rapidly solidified Ni-Cr-Al alloys with no boron additions. These alloys contained well developed domain structures. Despite the lack of boron, which is usually necessary for polycrystalline ductility, the RSP alloys showed measurable ductilities[6].

The alloys prepared for the investigation fell into two classes: high aluminum equivalent and low aluminum equivalent. The aluminum equivalent as defined here consists of the following:

$$\text{Al Equivalence} = \%Al + \%Hf + 0.5\%Cr \qquad (1)$$

This equation assumes that aluminum substitutes equally for nickel and aluminum, which is observed in solubility lobes from ternary sections. Hafnium substitution is uncertain, but it was assumed to substitute strictly for aluminum here. The beneficial effect of boron in imparting ductility is only seen in aluminum lean alloys[3], and the aluminum equivalency should follow the same trend. A set of four chromium containing alloys was prepared by arc melting and drop casting 400 gram ingots. These alloys, designated IC-50-1 through IC-50-4 with compositions shown in Table 1, were then cold-forged, annealed, and cold-rolled. After the rolling operation, the three highest Cr-containing alloys showed extensive cracking and fabrication was stopped. Figure 3 shows the appearance of the ingots after rolling.

The alloys which cracked had the highest aluminum equivalences, and it was suspected that this was part of the cause of the cracking tendency in these alloys. Another source of cracking in these alloys was found to occur during solidification of the primary ingot. Microstructures of the high chromium alloys in the as-cast condition show solidification hot cracks. Figure 4 shows these microstructures. The 8 and 10 percent chromium alloy show the worst cases of hot cracking. The cracks which form in the interdendritic regions serve as further crack nuclei in the rolling operation to worsen the fabricability problems.

Although the fabricability of the high aluminum equivalence alloys was poor, a preliminary welding study was done to evaluate the cracking tendency of the alloys during electron beam welding (EBW). Full penetration EB welds were made on 6.3 mm thick samples. Table 3 summarizes the characteristics of the resulting weldments.

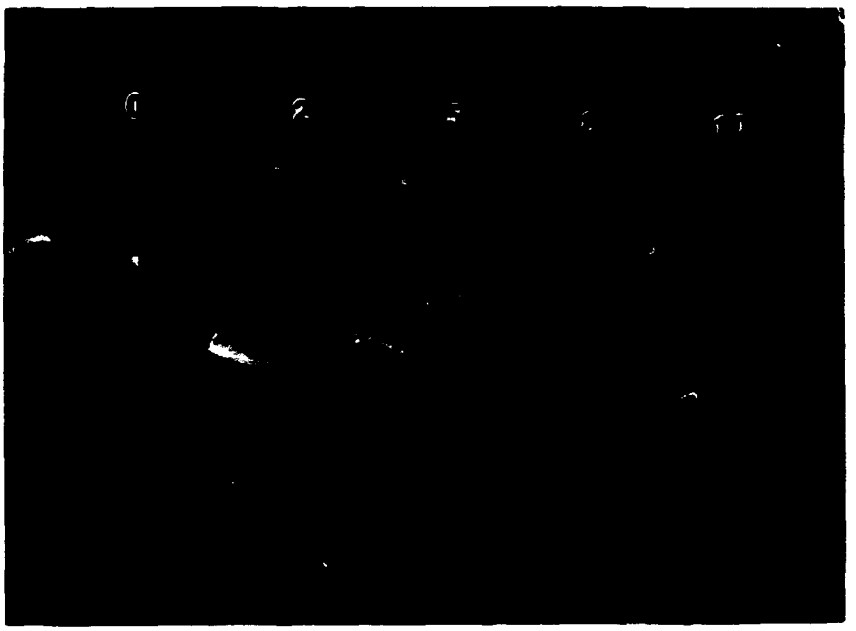

Fig. 3. Ingot appearance after cold-rolling 10 percent alloys IC-50 through IC-50-4. Numbers indicate chromium content.

TABLE 3. Summary of Welding Results for High Aluminum Equivalent Alloys

Alloy	Weld Characteristics
IC-50	Sound Welds
IC-50-1	Minimal HAZ Cracking
IC-50-2	Hot Tearing, HAZ Cracking
IC-50-3	Hot Tearing, HAZ Cracking
IC-50-4	Hot Tearing, HAZ Cracking

The hot tearing observed in these alloys consisted of centerline cracking. Figure 5 shows the crack face on a center line crack in IC-50-4. The HAZ cracking occurred as cold cracking and in some cases extended into the fusion zone but not as a solidification hot crack. This sort of behavior is shown in Fig. 6.

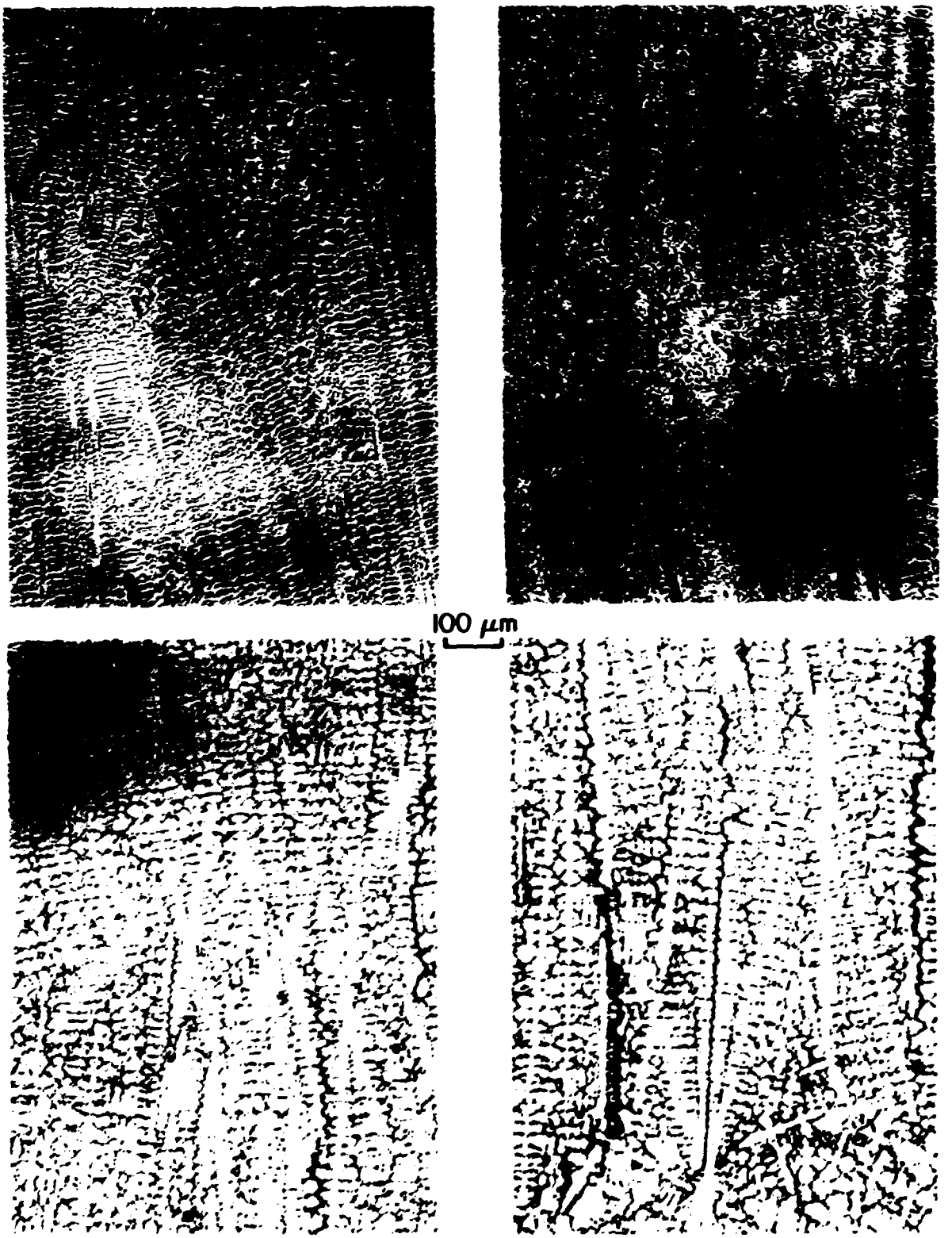

Fig. 4. Optical micrographs of as-cast structures for (a) IC-50-1, (b) IC-50-2, (c) IC-50-3, and (d) IC-50-4 showing solidification hot cracking in the latter two alloys.

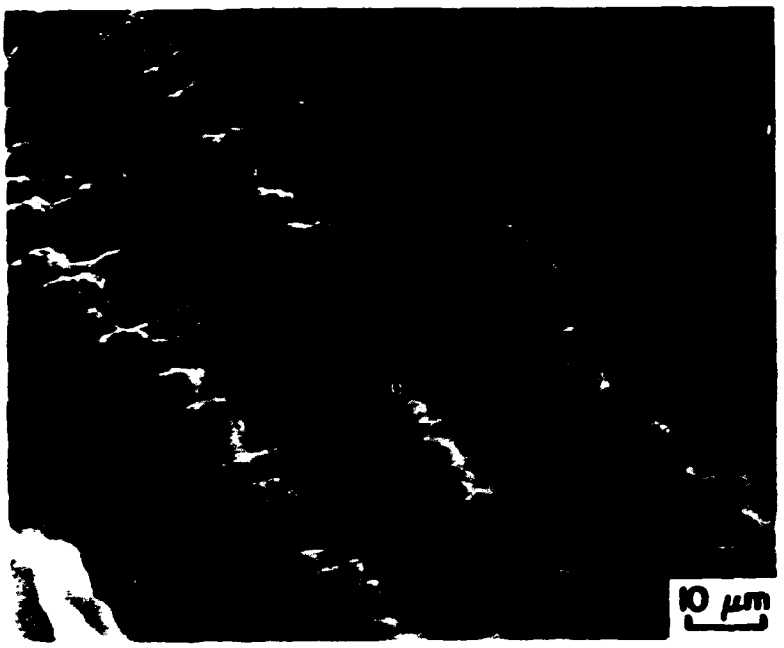

Fig. 5. Crack face of centerline crack in IC-50-4.

Fig. 6. Transverse section of an EB weld in IC-50-4 showing HAZ cracking and fusion zone cracking.

A second set of chromium containing alloys with a lower aluminum equivalence was prepared. These alloys, designated IC-50-5 through IC-50-8 had a constant aluminum equivalence of 22.5. The phase stability of the low aluminum equivalence alloys was estimated from available data in the literature[7]. The compositions of alloys IC-50 and IC-50-5 through IC-40-8 is shown in Fig. 7.

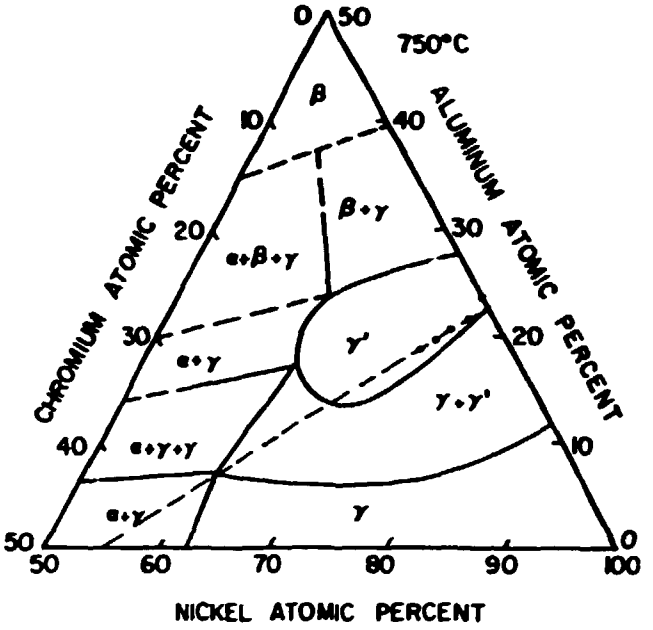

Fig. 7. Ternary isotherm of nickel-rich section of the Ni-Al-Cr systrem at 750°C showing compositions of IC-50 and low aluminum equivalence alloys (After Ref. 7).

Cold-rolling operations on the low aluminum equivalence alloys resulted in only minor incidences of cracking. These alloys were then investigated to determine the feasibility of producing thermal domains under the type of thermal conditions encountered during welding. An estimated pseudobinary, shown in Fig. 8, indicates that these alloys should disorder fully prior to melting. An attempt to determine the transformation temperatures using dilatometry proved unsuccessful. The volumetric expansion associated with the transformation was below the limits of detection of the dilatometer. To detect the disordering reaction after the fact, 0.7 mm thick samples of the four alloys were subjected to HAZ simulations matching the thermal excursion used in the hot ductility test. The peak temperature in the cycle was 1250°C. These samples were then examined by transmission electron microscopy to determine the resulting microstructures. Figure 9 to 12 show the base plate and thermally cycled regions of the low aluminum equivalent alloys. The 2 and 4 percent chromium alloys show the development of a higher dislocation density due to the thermally

induced stresses present when cooling the sample in the Gleeble 1500. No disordering appeared to have taken place. The two higher chromium alloys show the development of disordered material by the regions which contain domains after the cooling cycle. Alloy IC-50-7 showed small regions of the base plate which contained a small amount of disordered gamma with ordered precipitates. This observation indicated that either the phase equilibria predicted by the pseudobinary was slightly in error, or that casting inhomogeneities still existed in the structure. Since optical metallography showed a relatively uniform distribution of the disordered phase, it was concluded that there was some error in the published phase equilibria for compositions near the phase field boundaries. The 8 percent chromium alloy showed a microstructure completely dominated by a domain structure. This indicated that the microstructure became completely disordered at 1250°C and that the cooling rate was sufficient to keep the growing domains from coarsening to encompass a single grain, the typical behavior when cooling from a recrystallization anneal.

CONCLUSIONS

1. High aluminum equivalent alloys experienced severe problems during fabrication and welding.

2. As predicted by phase equilibria, increasing the chromium content produced increasing fractions of disordered material at 1250°C and hence a larger fraction of anti-phase domains in the microstructure.

3. Since the lower chromium alloys did not disorder at 1250°C, equilibrium temperatures appear to be higher than the published values.

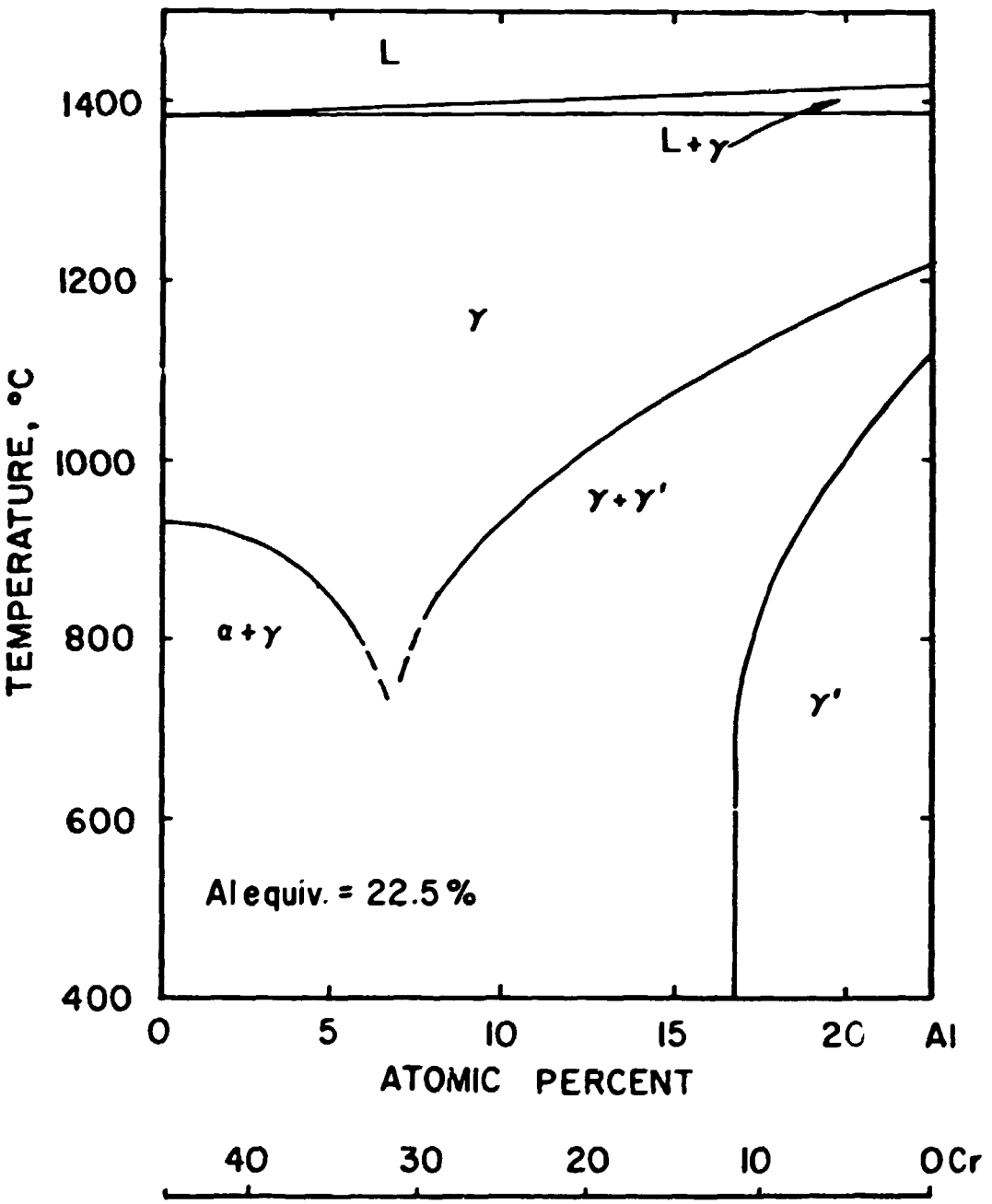

Fig. 8. Estimated pseudobinary for alloys with 22.5 percent Al equivalence (After Ref. 7).

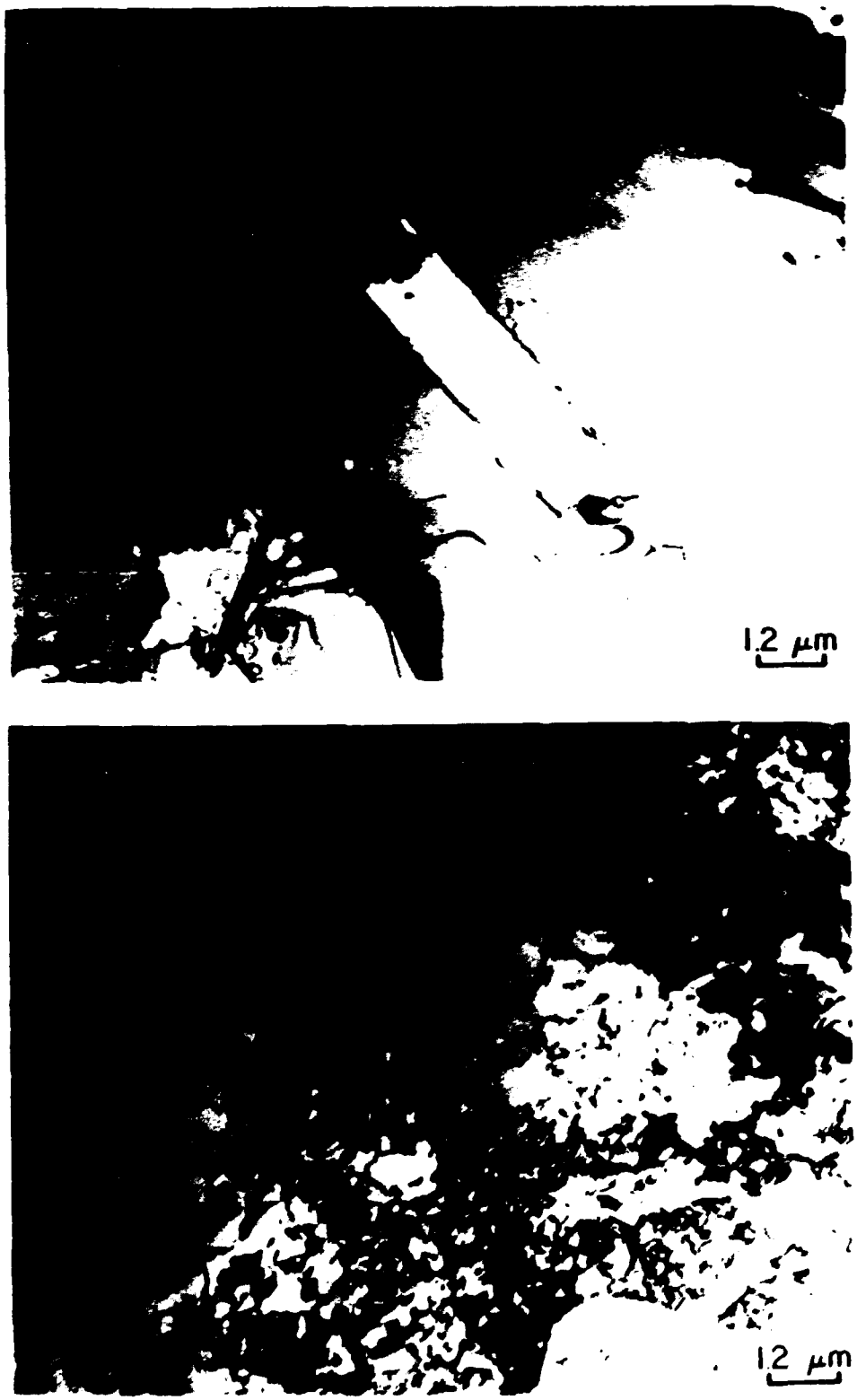

Fig. 9. TEM micrographs of alloy IC-50-5 showing (a) base plate microstructure (bright field), and (b) simulated HAZ (bright field).

Fig. 10. TEM micrographs of alloy IC-50-6 showing (a) base plate microstructure (bright field), and (b) simulated HAZ (bright field).

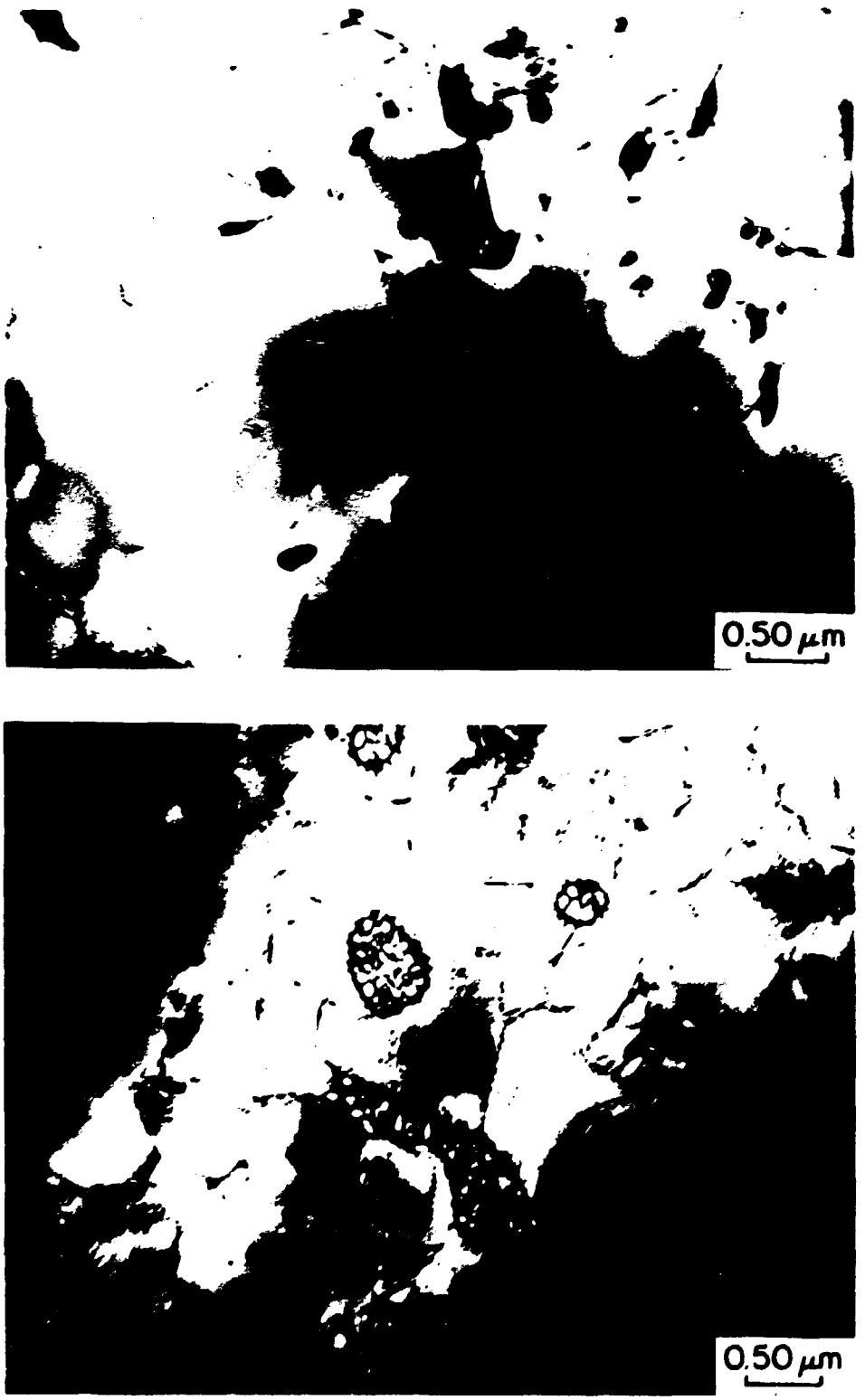

Fig. 11. TEM micrographs of alloy IC-50-7 showing (a) base plate microstructure (bright field), and (b) simulated HAZ (superlattice dark field).

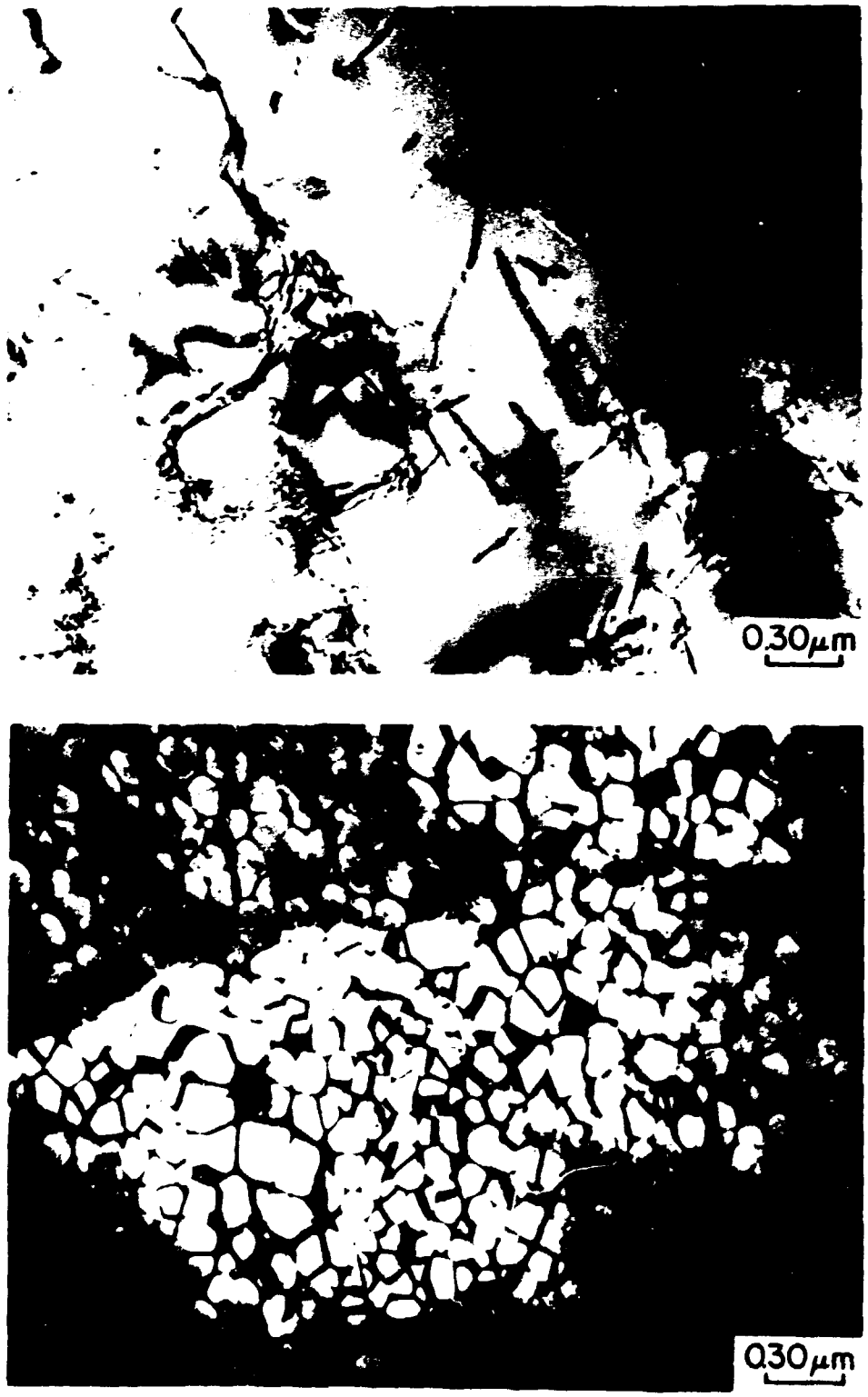

Fig. 12. TEM micrographs of alloy IC-50-8 showing (a) base plate microstructure (bright field), and (b) simulated HAZ (superlattice dark field).

REFERENCES

1. S.M. Copley and B.H. Kear, "Temperature and Orientation Dependence of the Flow Stress in Off-Stoichiometric Ni_3Al (γ' Phase)", Trans. TMS-AIME, 239, 977-984, (1967).

2. K. Aoki and O. Izumi, Nippon Kizoku Gakkaishi, 43 (12), 1979, 1190-1195.

3. C.T. Liu, C.L. White, and J.A. Horton, "Effect of Boron on Grain Boundaries in Ni_3Al", Acta. Metall. 33 (2), 213-229 (1985).

4. M.C. Maguire, G.R. Edwards, and S.A. David, "Investigation of the Weldability of Ductile Aluminides", Technical Report No. ORNL/Sub/85-27421/01, Oak Ridge National Laboratory, Oak Ridge, TN 37831.

5. G. Vanderschaeve, T. Sarrazin, and B. EScaig, "Effect of Domain Size on the Mechanical Properties of Ni_3V", Acta. Met., 27, 1251-1260, (1979).

6. S.C. Huang, E.L. Hall, K.M. Chang, and R.P. Laforce, "Ll_2-Type Ni-Al-Cr Alloys Processed by Rapid Solidification", Metall. Trans. A, 17A, 1685-1692, (1986).

7. S.M. Merchant and M.R. Notis, "A Review: Constitution of the Al-Cr-Ni System", Mat. Sci. Eng., 66, 46-60, (1984).

CONSOLIDATION OF RAPIDLY SOLIDIFIED NICKEL ALUMINIDE POWDERS

R. N. Wright and J. E. Flinn
Idaho National Engineering Laboratory
EG&G Idaho, Inc.
P. O. Box 1625
Idaho Falls, ID 83415

ABSTRACT

The microstructure and mechanical properties of boron microalloyed rapidly solidified Ni-22.6Al and Ni-18.4Al-8.3Cr powders that have been consolidated by hot extrusion and hot isostatic pressing have been investigated. Vacuum gas and centrifugal atomization have both been found to produce relatively clean powders with a thin oxide that does not hinder bonding during consolidation. Extruded materials produced from the powders have very fine grain sizes which resist coarsening at elevated temperatures. The powder materials have good room temperature strength and ductility and exhibit relatively little increase in flow stress with increasing temperature. Both of the alloys are very strain rate sensitive above 900°C. The Cr-containing alloy is found to exhibit superplastic behavior. The properties of the hot isostatically pressed material are very sensitive to the consolidation parameters and post-consolidation heat treatment.

INTRODUCTION

Alloys based on the intermetallic compound Ni_3Al have been known for many years to have attractive high temperature properties. In addition to good resistance to oxidation and sulfidation, the low bulk diffusion rates intrinsic to ordered intermetallic compounds and the well-known increase in yield strength with increasing temperature suggest that these alloys should exhibit excellent elevated temperature mechanical properties.[1] Although quite ductile in single crystal form, commercial application of these materials has been hindered by their inherent tendency to fail in a brittle manner by intergranular fracture. The recent observation that polycrystalline nickel aluminides could be rendered ductile by microalloying with boron has resulted in renewed interest. It has been

shown in several studies that alloys with 200 to 500 parts per million by weight of boron exhibit significant ductility at room temperature in cast polycrystalline form.[2,3] However, it is generally very difficult to fabricate these alloys by conventional ingot metallurgy methods due to limited ductility during hot working processes.

Powder metallurgy appears to have several advantages over the conventional ingot metallurgy approach, including refined microstructures, suppression of macrosegregation, and the possibility of applying near net shape technology. The purpose of this paper is to present the results of a study of the microstructure and mechanical properties of rapidly solidified powders of nominal Ni-22.6Al and Ni-18.4Al-8.3Cr composition (atomic percentages), alloyed with 200 parts per million by weight of boron, consolidated by hot extrusion and hot isostatic pressing. The extreme sensitivity of the ductility of these alloys to the segregation of boron, and impurity atoms such as sulfur and oxygen, requires careful control of the processing parameters and the resulting microstructure.[4,5]

PROCEDURE

Powders of boron microalloyed nickel aluminide and nickel aluminide alloyed with chromium were produced using vacuum gas atomization (VGA) and centrifugal atomization (CA) by Homogeneous Metals, Clayville NY, and Pratt and Whitney Government Products Division, West Palm Beach, FL, respectively. The vendors supplied starting material of two alloy compositions for atomization. A binary alloy that is slightly hypostoichiometric with respect to Al and an alloy containing Cr with approximately the same stoichiometry were selected for this study. A boron concentration of approximately 200 weight ppm was desired for both alloys. Chemical analyses of both alloys from each vendor are given in Table 1. In addition to the bulk chemistries shown in the table, the surface chemistry of the powders was examined by sputtering experiments in a scanning Auger spectrometer. It was found that there is carbon and

TABLE 1. CHEMICAL ANALYSIS OF POWDERS[a]

Powder	Ni	Al	Cr	C	S	P	N_2[b]	O_2[b]	B[c]
CA Ni_3Al	--	12.40	--	0.003	0.001	0.006	--	--	242
VGA Ni_3Al	86.72	12.80	--	0.006	0.001	0.003	0.002	0.010	199
CA Ni_3Al + Cr	80.85	10.50	8.11	0.004	0.001	0.010	0.005	0.006	231
VGA Ni_3Al + Cr	80.08	9.71	8.18	0.007	0.001	0.005	0.002	0.007	270

a. Weight percent.
b. From hot extruded powder.
c. Weight ppm.

sulfur enrichment on the outermost few atomic layers of the powder particles and there is an aluminum-rich oxide layer approximately 2.0 nm thick.

The particle size distribution of the powders was determined by screening, and the morphology of the powder particles was examined using scanning electron microscopy. The microstructure of the particles and the degree of order were determined using optical microscopy and x-ray diffraction, respectively.

The powders were consolidated by hot extrusion and hot isostatic pressing (HIPping). Extrusion was carried out by the vendors at 1100°C in an eight-to-one reduction from the original diameter of the evacuated stainless steel cans used to contain the powder. Several size fractions of each powder were also consolidated by hot isostatic pressing using several combinations of temperature and pressure. The powder was contained in evacuated stainless steel containers for HIPping. The microstructure and mechanical properties of the consolidated materials were determined in the as-consolidated condition and after subsequent heat treatments.

RESULTS

Both the centrifugally atomized and vacuum gas atomized powders were found to consist primarily of spherical particles. The VGA particles exhibit many satellites, particularly in association with the larger particles. While the aluminide powders were generally similar to Type 304 stainless steel and nickel-base superalloy powders produced by the same methods,[6,7] the aluminides tended to have many more particles which were cracked and many fragments of broken particles were observed. Based on a cumulative 50%-finer-than basis, the average particle sizes are 65 and 60 μm for the CA and VGA powders, respectively, and did not seem to be a function of the alloy chemistry.

The microstructures of several size fractions of each powder were examined using optical microscopy. The chromium-containing CA powder had a well developed dendritic microstructure, the remaining CA powder and both VGA alloys solidified in a cellular manner. There was no qualitative difference in the microstructure of the powders as a function of the particle size. Centrifugal atomization resulted in a generally finer microstructure compared to vacuum gas atomization.

The degree of order, described by the Bragg-Williams long range order parameter, was determined as a function of particle size for each of the powders using x-ray diffraction. The results indicate that a significant degree of disorder is quenched into both the CA and VGA powders. The degree of order is nearly identical for powder from the two processes and is independent of the particle size. The Bragg-Williams long range order parameter is shown as a function of the particle size in Figure 1 for the CA powder. It can be seen from the figure that the degree of order is lower when measured from the (100) superlattice reflection compared to that measured from the (110) superlattice reflection. This result is consistent with the antiphase domain boundary energy having a minimum value on the (100) planes.[1] It can also be seen from the figure that the Cr-containing alloy in general has a lower degree of order.

The microstructures of the as-extruded materials were examined using optical microscopy. The grain growth behavior and microstructural evolution were examined after a series of heat treatments using optical

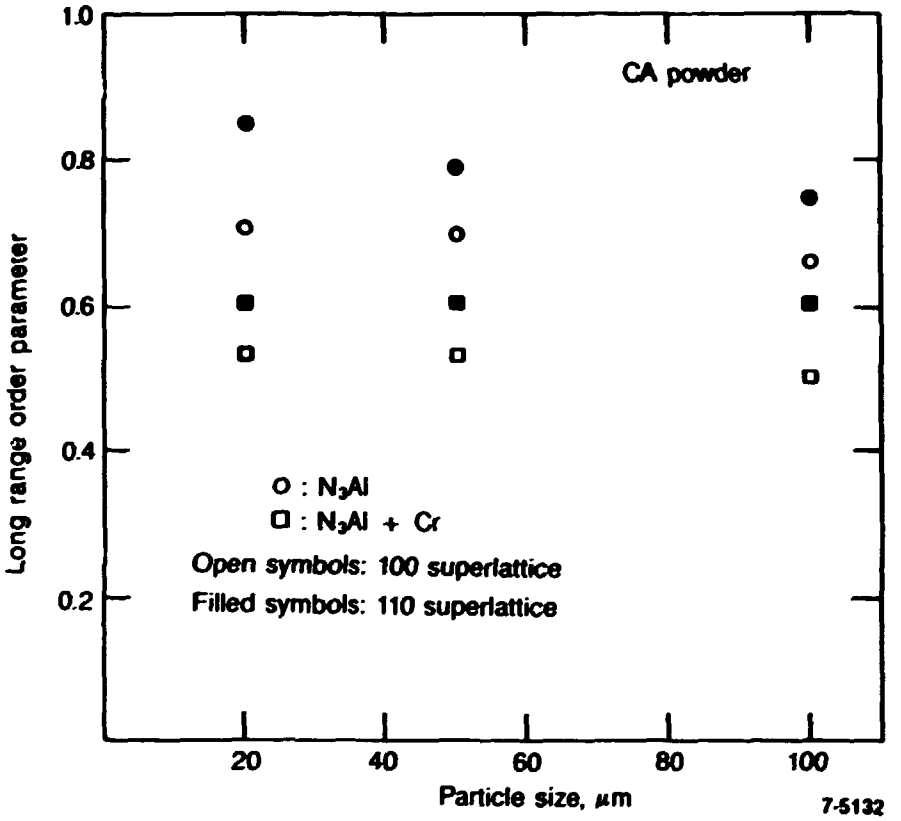

Figure 1. Bragg-Williams long range order parameter for the CA powder as a function of particle size.

and transmission electron microscopy. All of the extrusions were found to have nearly equiaxed single phase structures and were crack free. There was some porosity elongated in the extrusion direction for all of the materials. The extrusions from the CA powders had a greater amount of porosity which seemed to increase with distance from the centerline.

The grain growth behavior and microstructures were examined after annealing over a temperature range from 900 to 1200°C for one hour; longer time grain growth studies were conducted at 900 and 1100°C. The unalloyed aluminide from both types of powder was found to have a single phase equiaxed microstructure after all of the annealing treatments. Both the CA and VCA chromium-containing alloys exhibit a very fine single phase microstructure after the lower temperature anneals and develop a two-phase structure after one hour at 1100 and 1200°C. The microstructure of the VCA material after annealing at 1200°C is shown in Figure 2. TEM examination of the materials after annealing showed that

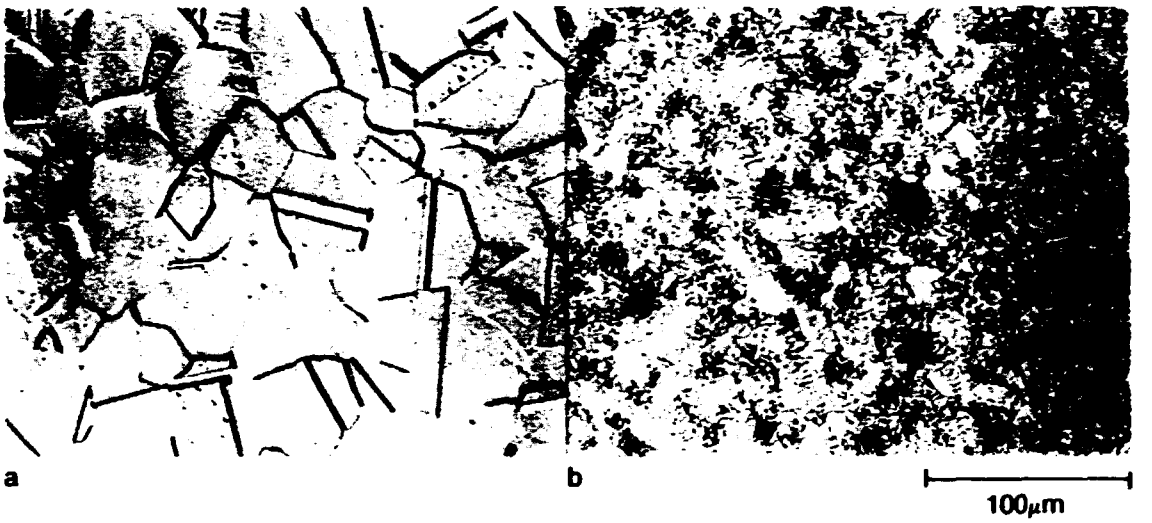

Figure 2. The microstructure of VGA (a) Ni_3Al and (b) Ni_3Al + Cr after annealing at 1200°C for 1 h.

the chromium-containing alloys were fully ordered up to 1000°C and had numerous Cr-rich particles along the grain boundaries; a bright field electron micrograph of the VGA sample after annealing at 1000°C is shown in Figure 3. The second phase that appeared after higher temperature anneals was found to be composed of ordered islands contained within wells of disordered material. A dark field electron micrograph from the 1200°C sample formed with a superlattice reflection is shown in Figure 4, (ordered regions appear bright in this micrograph). The disordered material was found to be epitaxial with the ordered matrix and the ordered islands have the same orientation as the matrix. The interface between the disordered material and the matrix is formed by widely spaced dislocations to maintain coherency across the {100} planes.

The average grain diameters of extruded VGA and CA materials are shown as a function of temperature in Figure 5. It can be seen that the Cr-containing materials have very limited grain growth and even the unalloyed aluminide shows restricted grain growth compared to conventional ingot metallurgy stainless steels.[8] For lower annealing temperatures it appears that the Cr-rich particles tend to restrict grain growth in the alloyed material. Electron microscopy has shown that these particles go into solution at 1100 and 1200°C, and therefore the restricted grain growth at these temperatures is presumably related to the formation of the

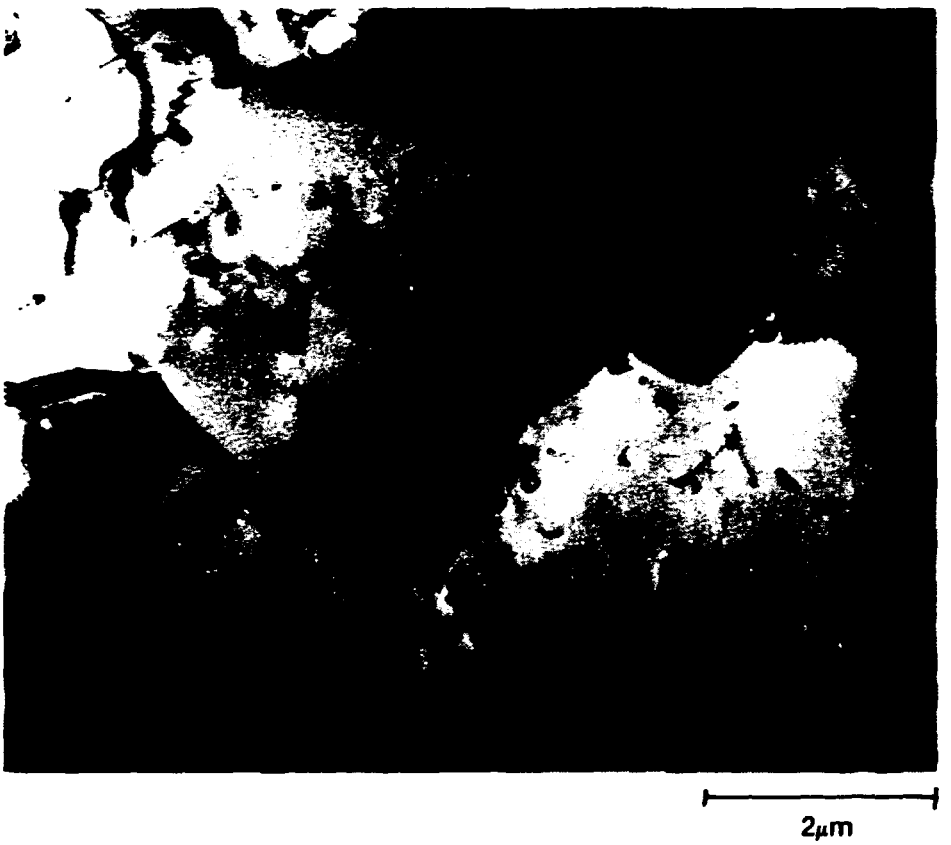

Figure 3. Bright field electron micrograph of Cr-rich particle on a grain boundary in VGA Ni_3Al + Cr.

two-phase microstructure. Grain growth measurements after annealing for 10 and 100 h at 900 and 1100°C showed that the Cr containing alloys continued to exhibit sharply reduced grain growth compared to the unalloyed material.

The tensile properties of extruded CA and VGA materials have been determined at room temperature after post-consolidation heat treatments of one hour at temperatures from 900 to 1200°C. Elevated temperature tensile properties have also been determined for the VGA materials after heat treatments of one hour at 1000°C. All of the tests were done in air at a nominal strain rate of 5×10^{-4} s^{-1}. At room temperature all of the materials show large yield drops, followed by Luders strains of as large as 5% before uniform elongation begins. The magnitude of the yield drop and extent of Luders deformation were found to decrease with increasing annealing temperature. The room temperature upper yield stress

Figure 4. Superlattice dark field of disordered webs in Ni_3Al + Cr after annealing at 1200°C for 1 h.

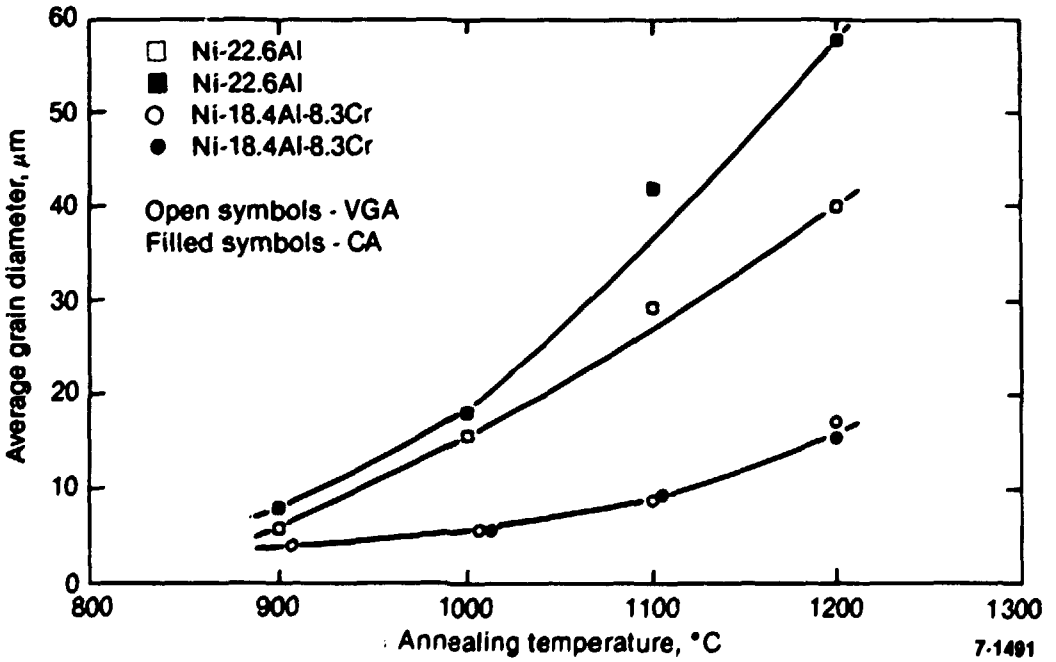

Figure 5. Grain size of extruded powders as a function of temperature for 1 h anneals.

is shown as a function of the annealing temperature for all of the materials in Figure 6. Repeated tests for the same annealing treatment gave quite consistent ductility and ultimate tensile stress values for the extruded VGA material. Data for the CA material, however, showed a large amount of scatter, ranging from values comparable to the VGA samples to significantly reduced values. This effect seems to reflect the relatively large amount of inhomogeneous porosity in the CA extrusions. The room temperature total elongation and ultimate tensile stress are shown as a function of the annealing temperature for the VGA materials in Figures 7 and 8, respectively. Data for the extruded CA material have not been included due to uncertainty in the values.

The yield stress of extruded VGA material is shown as a function of the test temperature in Figure 9. Included in this figure for comparison are data for coarse grained cast Ni_3Al.[9] It is apparent from the figure that the powder materials have considerably higher room temperature strength than the cast material, however, the cast material has a much larger increment of increase in the flow stress up to about 700°C. The Cr-containing alloy is also consistently stronger than the unalloyed aluminide up to about 800°C. Above this temperature the unalloyed material has higher flow stress. The corresponding total elongation values are shown for the powder material in Figure 10. It can be seen that at this strain rate the powder materials exhibit considerable embrittlement. The Cr-containing alloy retains about 10% ductility at the minimum at 700°C, but the fracture surface shows almost complete intergranular fracture.

The strain rate sensitivity of the VGA materials, defined by the equation $\sigma = k\dot{\epsilon}^m$, was determined as a function of the test temperature up to 1000°C. For convenience in displaying the data, the log of the flow stress is plotted as a function of the log of the strain rate in Figure 11. The strain rate sensitivity parameter, m, is the slope of the log-log plot. It can be seen that there are generally two regimes in the log-log plots, and a change in slope occurs at higher strain rates. If just the slope of the curves between the two lowest strain rates is considered, then it can be seen that there is a monotonic

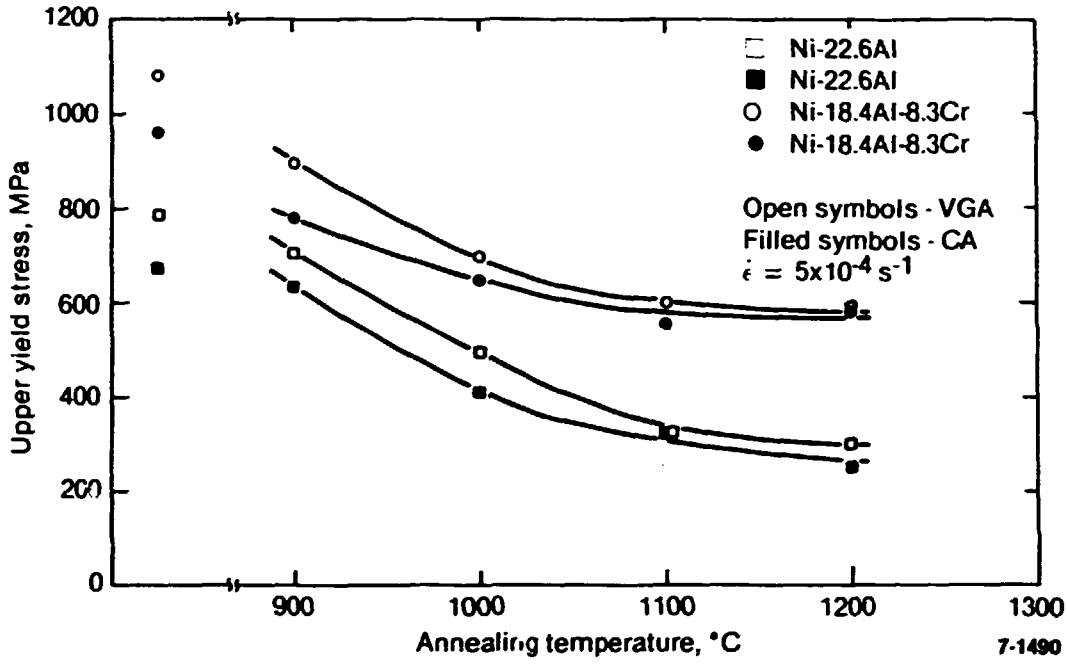

Figure 6. Upper yield stress for extruded powders as a function of temperature.

increase in m as the temperature is increased, with no apparent influence of the anomalous strength peak. It was not possible to test the unalloyed material over the whole temperature range because of the sharply reduced ductility near 700°C. At 900 and 1000°C the Cr-containing material has an m value above 0.5 and the unalloyed aluminide has a value approaching 0.5.

Tensile samples of the VGA material were strained in tension at several temperatures and unloaded prior to failure and the dislocation structures were examined using TEM. The dislocation structures of the two alloys were very similar after testing at room temperature; the dislocations were mainly partials separated by stacking faults. The substructure of the Cr-containing alloy strained to about 5% plastic strain after Luders deformation at room temperature is shown in Figure 12a and the substructure of the same alloy tested to a similar strain at 600°C is shown in Figure 12b. Analysis of the nature of the dislocation structures is not yet complete for the elevated temperature tests, however, it can be seen from the micrographs that there are few stacking faults in the substructure after testing at 600°C. The

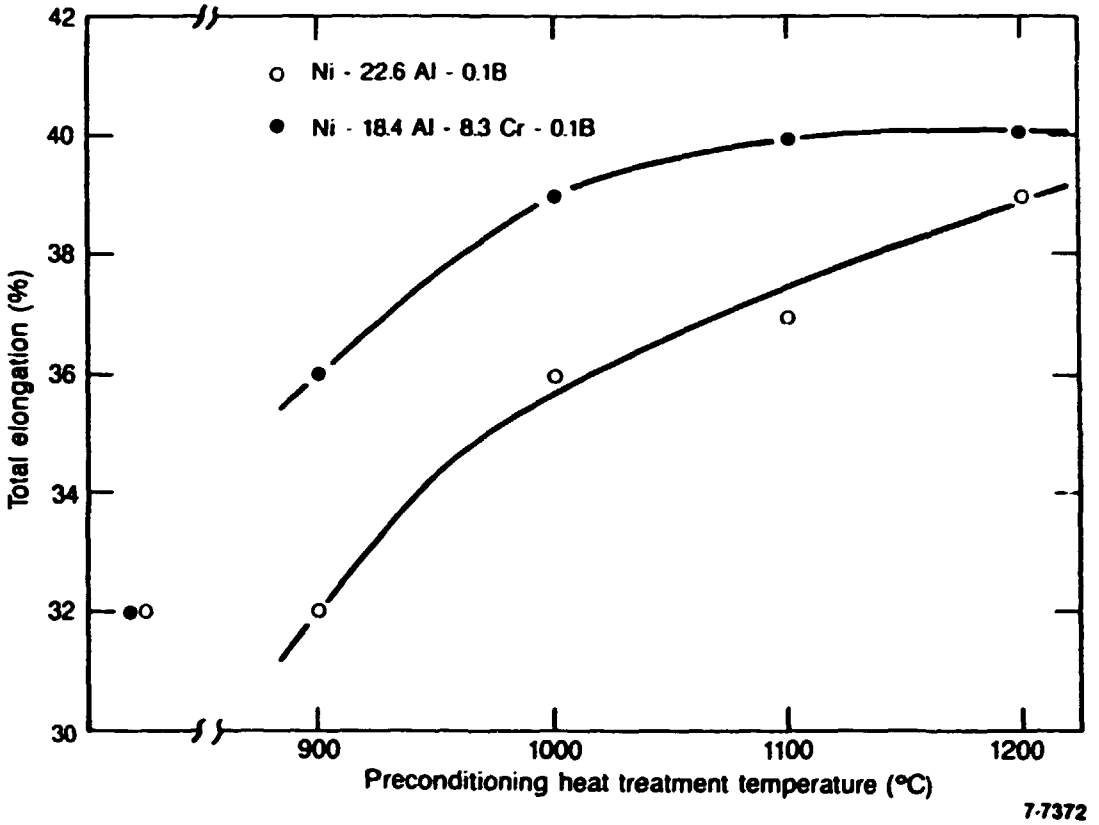

Figure 7. Total tensile elongation for extruded VGA powders as a function of annealing temperature.

micrographs in Figure 13a and b are a bright field and superlattice dark field pair from the Cr-containing alloy which was deformed at 800°C. Comparing the two figures it can be seen that there are some curved APBS that appear to be the result of the passage of dislocations.

A series of HIP consolidation experiments was conducted to study the influence of temperature and pressure for a fixed holding time of 2.5 h on the densification of the powders. The results of the various parameters on the density of two nominally monosize powder fractions and "grab" samples that are expected to represent the average size distribution are given in Table 2. It was found that full density can be achieved by a number of combinations of temperature and pressure while the resulting microstructure can be quite different. In general, the Cr-containing alloy consolidates more rapidly than the unalloyed powder. These results are consistent with the Cr-containing alloy having a lower flow stress at the temperatures of interest for HIPping. Optical micrographs of the

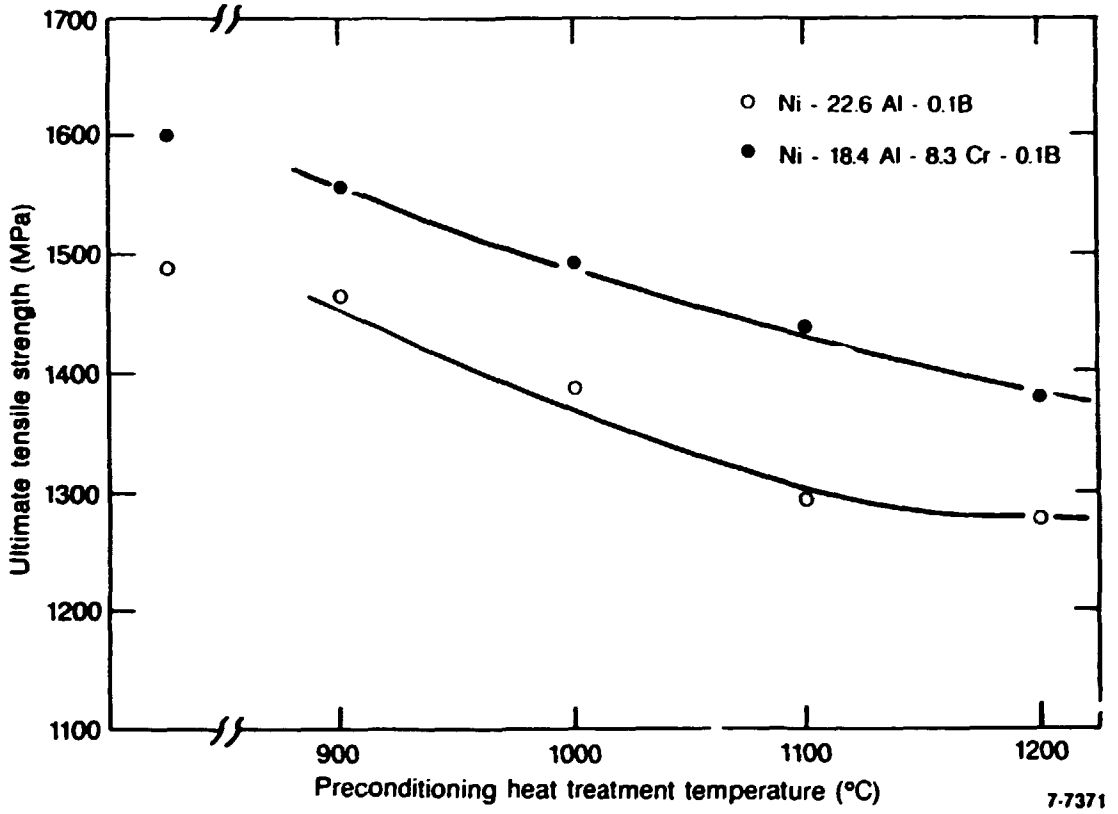

Figure 8. Ultimate tensile strength of extruded VGA powders as a function of annealing temperature.

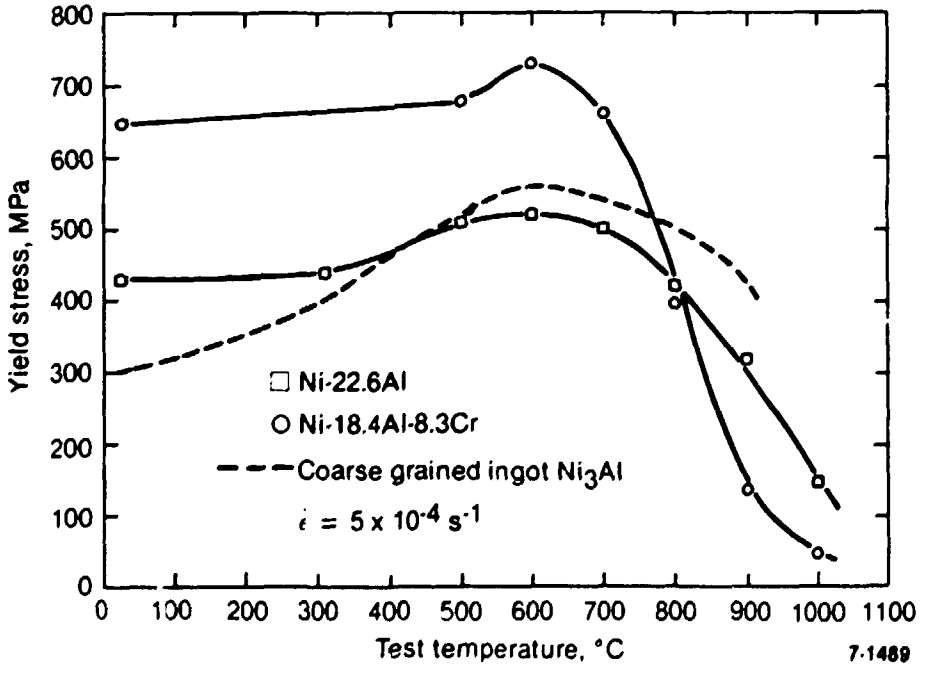

Figure 9. Yield stress of extruded VGA powder as a function of test temperature.

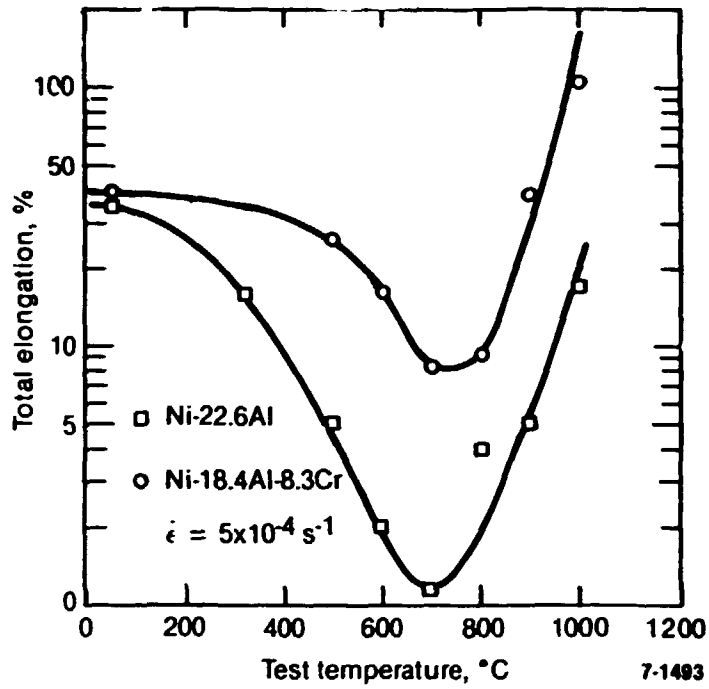

Figure 10. Total tensile elongation of extruded VGA powders as a function of test temperature.

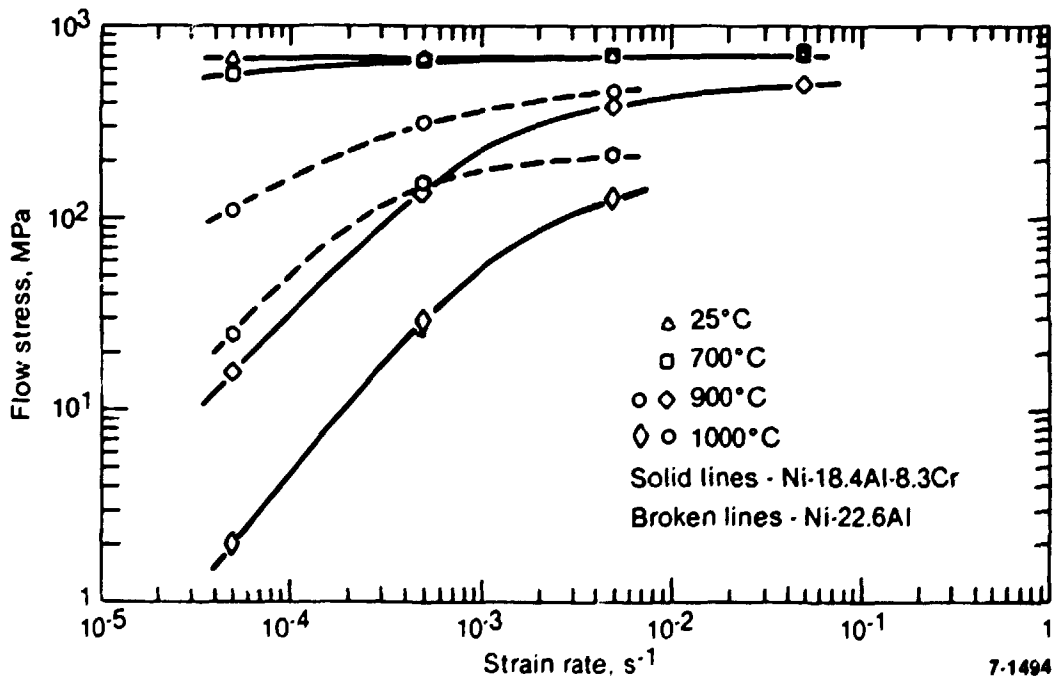

Figure 11. Log flow stress vs log strain rate as a function of test temperature for extruded VGA powders.

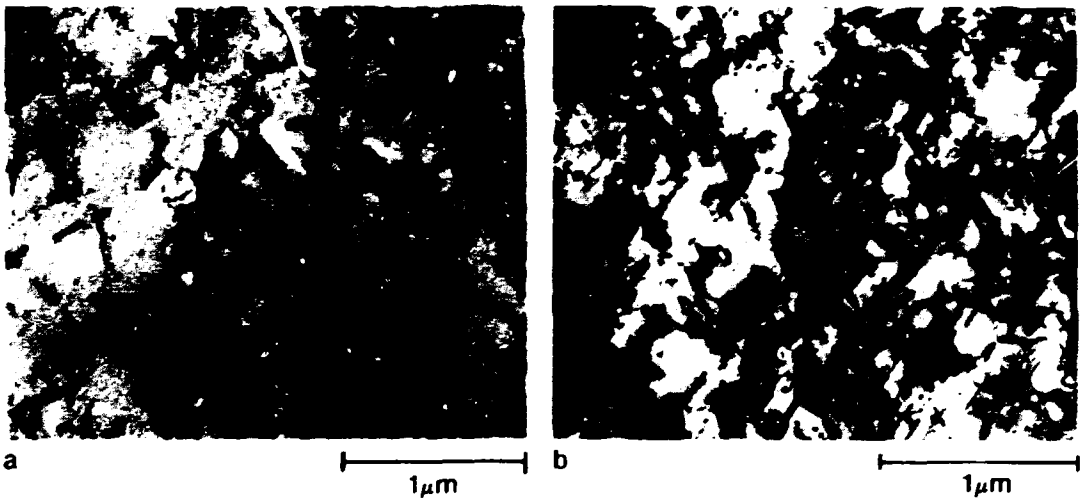

Figure 12. Bright field micrographs of dislocation structures in extruded VGA Ni_3Al deformed to 5% strain at (a) room temperature and (b) 600°C.

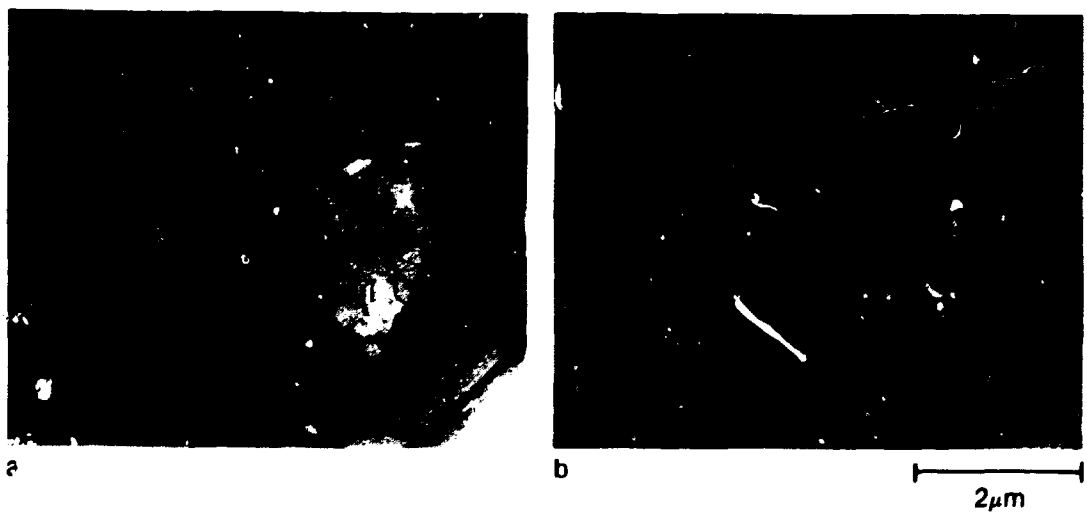

Figure 13. Bright field (a) and superlattice dark field (b) of extruded VGA Ni_3Al + Cr deformed to 5% strain at 800°C.

microstructure of the Cr-containing VGA powder after two HIPping treatments are shown in Figure 14. Room temperature tensile properties were measured for grab samples of all of the powders after consolidating at 207 MPa pressure at 1000°C for 2.5 h. The upper yield stress is shown as a function of post-consolidation heat treatment temperature in Figure 15, and the corresponding total elongation values are shown in Figure 16. Yield strength and total elongation values for the extrusion

TABLE 2. EFFECTS OF HIP PARAMETERS ON DENSIFICATION FOR 2.5 h HIP CYCLES

Material	Particle Size (μm)	Temperature (°C)	Pressure (MPa)	Density (%)
CA Ni_3Al	30	900	35	85.3
	100			83.1
	Grab			84.6
CA Ni_3Al + Cr	30	900	35	92.8
	100			83.8
	Grab			84.8
VGA Ni_3Al	30	900	35	90.03
	100			88.2
	Grab			92.7
VGA Ni_3Al + Cr	30	900	35	95.1
	100			90.4
	Grab			94.6
CA Ni_3Al	30	1100	35	98.5
	100			96.5
	Grab			97.8
CA Ni_3Al + Cr	30, 100, Grab	1100	35	100
VGA Ni_3Al	30	1100	35	99.2
	100			97.5
	Grab			99.3
VGA Ni_3Al + Cr	30, 100, Grab	1100	35	100
CA Ni_3Al	30	900	103	93.3
	100			95.8
	Grab			96.3
CA Ni_3Al + Cr	30	900	103	97.2
	100			96.1
	Grab			94.3
VGA Ni_3Al	30	900	103	99.8
	100			99.4
	Grab			99.5
VGA Ni_3Al + Cr	30	900	103	99.9
	100			99.0
	Grab			99.3
CA Ni_3Al	30, 100, Grab	900	207	100
CA Ni_3Al + Cr	30, 100, Grab	900	207	100

TABLE 2. Continued

Material	Particle Size (μm)	Temperature (°C)	Pressure (MPa)	Density (%)
VGA Ni_3Al	30, 100, Grab	900	207	100
VGA Ni_3Al + Cr	30, 100, Grab	900	207	100
CA Ni_3Al	30, 100, Grab	1000	207	100
CA Ni_3Al + Cr	30, 100, Grab	1000	207	100
VGA Ni_3Al	30, 100, Grab	1000	207	100
VGA Ni_3Al + Cr	30, 100, Grab	1000	207	100

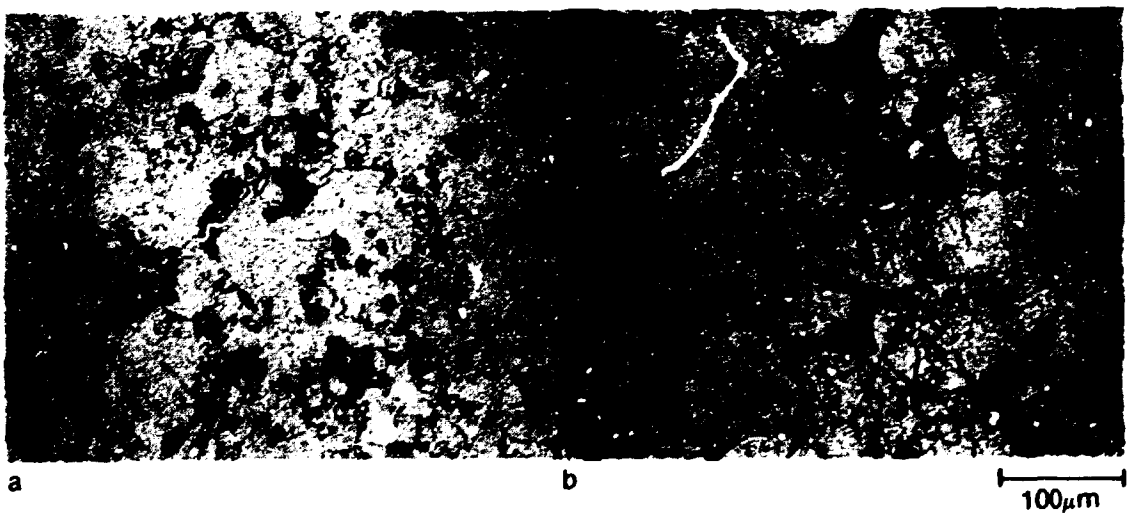

Figure 14. Microstructure of VGA Ni_3Al + Cr HIPped at (a) 100°C and (b) 900°C at 35 MPa pressure for 2.5 h.

consolidated Cr-containing VGA material are included in the figures for comparison. The HIPped material has generally lower yield strength and ductility compared to the extruded material. Post-consolidation heat treatments seem to improve the ductility of the HIPped material.

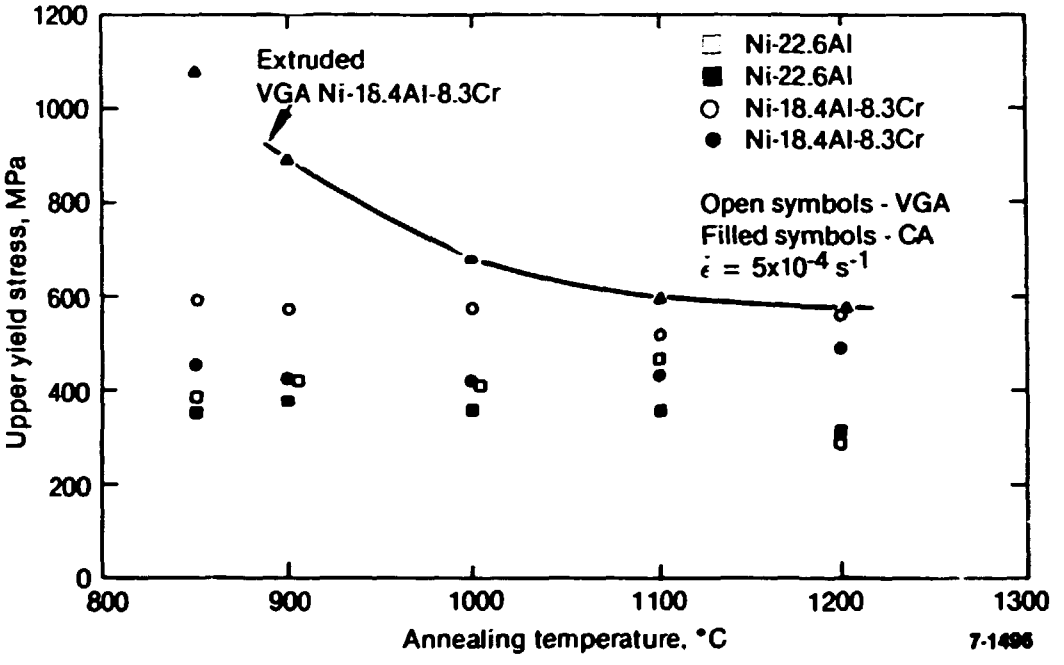

Figure 15. Upper yield stress of HIP consolidated powders as a function of annealing temperature.

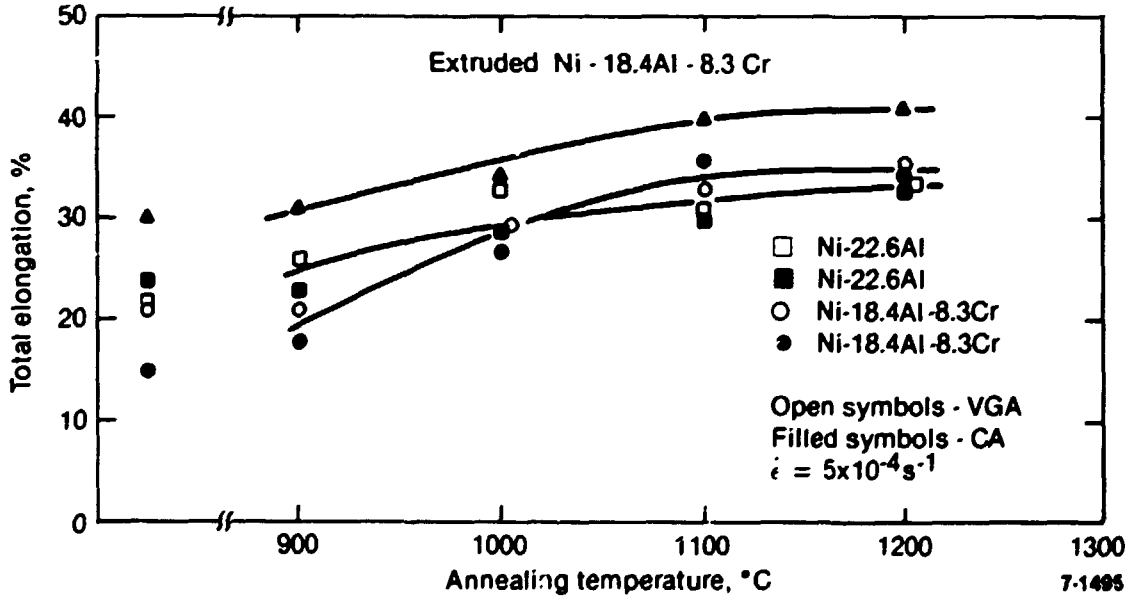

Figure 16. Total tensile elongation of HIP consolidated powders as a function of annealing temperature.

DISCUSSION

The general particle shape and size distributions observed for the powders used in this study are similar to previous work reported in the literature.[6,7] The x-ray diffraction results indicating that there is a significant amount of disorder quenched into the powders are also in agreement with several studies on melt spun ribbons and CA powders of slightly different composition.[10,11] It has been reported that sulfur tends to segregate to the surface of nickel-based superalloy powders during solidification.[5] It was noted above that sulfur enrichment was found on the outermost few atomic layers of the powders investigated in this study. It is not clear from the current work whether the surface enrichment is a result of segregation during solidification or results from contamination subsequent to atomization. The very thin oxide layer which forms on the powders is apparently quite stable even after exposure to laboratory air. The microstructure and property studies on extruded and HIPped material indicate that the oxide is not a hindrance to interparticle bonding during consolidation.

The fine grained material which results from extrusion of the powders has good room temperature strength compared to large grain size material which often results from casting, while retaining adequate ductility. The addition of chromium results in a finer grain size and also in considerable solid solution strengthening. The powder metallurgy materials tend to have a smaller increment of anomalous strengthening on increasing the test temperature compared to cast material.[1,9] In single crystal Ni_3Al there is nearly a fivefold increase in the flow stress on raising the test temperature from room temperature to 700°C.[1] If the single crystal data are taken as a measure of the tendency for matrix strengthening, the relatively flat flow stress behavior of the powder metallurgy material can be interpreted as a competition between the decreased effectiveness of grain boundaries as barriers to slip and increased matrix strengthening due to dislocation cross slip onto (100) planes as the temperature is increased. Experiments with samples of varying grain size from casting or recrystallization of single crystals indicate that in general the magnitude of the strength peak tends to increase with increasing grain size.[1,9]

The reversal in strength between the Cr-containing and the unalloyed materials above 800°C and the higher values for the strain rate sensitivity parameter at very slow strain rates indicate that the Cr-containing material probably undergoes a transition in flow mechanism from dislocation glide to diffusion controlled at a relatively low temperature. The Cr-containing alloy also begins to show evidence of disordering from dislocation motion at 800°C. While it was not possible to examine the unalloyed material due to embrittlement at elevated temperature, it is expected that the Cr-containing alloy is less stable with respect to disordering since it begins to form a two-phase microstructure above 1000°C.

The fine, stable, grain size of the powder materials and high strain rate sensitivity values indicate that these materials should exhibit superplastic behavior. The Cr-containing alloy has been deformed in tension to strains greater than 100% at a strain rate of 5×10^{-4} s^{-1}, and greater strains are likely at lower strain rates. Superplastic behavior is probably not observed in the unalloyed material due to premature fracture caused by oxygen embrittlement. The mechanism of deformation during superplastic flow has not yet been determined for these alloys but is likely due in part to grain boundary sliding.

The HIPping study indicates that full density can be achieved in these materials at relatively low temperature, however, it has been observed previously that consolidation at 900°C can cause severe interparticle embrittlement due to sulfur segregation.[12] The tensile results from the powder materials consolidated at 1000°C also show reduced ductility compared with extruded material. Examination of the fracture surfaces using scanning electron microscopy showed a preponderance of interparticle fracture. It appears that it might be advantageous to HIP these materials at a higher temperature, e.g., 1100°C, to ensure complete particle bonding and a fully recrystallized microstructure. The grain growth studies indicate that this should not result in substantial coarsening of the microstructure, and a lower pressure would also be required.

The relatively low ductility of the HIPped material and the variability in properties in the extruded CA material that appears to be

due to inhomogeneous distribution of porosity emphasize the need for careful control of the consolidation processing parameters to achieve optimum properties from powder metallurgy nickel aluminides.

CONCLUSIONS

Vacuum gas and centrifugal atomization both produce relatively clean, spherical, powders of nickel aluminides. The powders do not need special handling and the relatively thin oxide layer on the particles does not hinder bonding during consolidation.

The materials consolidated from powder by extrusion have good room temperature strength and ductility. The as-extruded grain size is very fine and resistant to coarsening. Alloying with 8% Cr improves the strength, ductility, and resistance to grain growth.

The powder metallurgy materials show relatively little increase in flow stress with increasing temperature compared to single crystal or coarse grained cast material. The Cr-containing material is stronger than the unalloyed aluminide up to 900°C. Above that temperature there is a reversal in the relative strengths.

Both of the alloys have high strain rate sensitivities above 900°C. Combined with the resistance to grain growth, the high strain rate sensitivity values indicate that these materials should exhibit superplastic behavior. The Cr-containing alloy has been deformed in tension to strains greater than 100% and higher strains should be possible at very low strain rates.

Careful selection of HIPping parameters is required to achieve optimum properties. These materials also appear to be very sensitive to porosity in the consolidated forms.

ACKNOWLEDGMENTS

The assistance of G. L. Fletcher, V. L. Toth, and M. D. Harper in conducting the experimental efforts is greatly appreciated.

REFERENCES

1. N. S. Stoloff and R. G. Davies, "The Mechanical Properties of Ordered Alloys", Progress in Materials Science, Vol. 13, 1966, pp. 3-84.

2. C. T. Liu and J. O. Stiegler, "Ductile Ordered Intermetallic Alloys", Science, Vol. 226, 1984, pp. 636-642.

3. C. T. Liu, C. L. White and J. A. Horton, "Effect of Boron on Grain-Boundaries in Ni_3Al", Acta Metallurgica, Vol. 33, 1985, pp. 213-229.

4. C. L. White, R. A. Padgett, C. T. Liu and S. M. Yalisove, "Surface and Grain Boundary Segregation in Relation to Intergranular Fracture: Boron and Sulfur in Ni_3Al", Scripta Metallurgica, Vol. 18, 1984, pp. 1417-1420.

5. P. H. Poss and B. H. Kear, "Surface Segregation in Rapidly Solidified Superalloy Powders", Rapid Solidification Processing--Principles and Technologies, R. Mehrabian, B. H. Kear and M. Cohen (eds.), Baton Rouge, LA, Claitor's Publishing Division, 1978.

6. B. H. Kear, P. R. Holiday and A. R. Cox, "On the Microstructure of Rapidly Solidified IN-100 Powders", Metallurgical Transactions, Vol. 10A, 1979, pp. 191-197.

7. R. N. Wright, J. E. Flinn and G. E. Korth, Characterization of Rapidly Solidified Type 304 Stainless Steel Powders, EGG-SCM-7133, 1986.

8. J. K Stanley and A. J. Perrotta, "Grain Growth in Austenitic Stainless Steels", Metallography, Vol. 2, 1969, pp. 349-362.

9. S. Hanada, S. Watanabe and O. Izumi, "Deformation Behavior of Recrystallized Ni_3Al", Journal of Materials Science, Vol. 21, 1986, pp. 203-210.

10. J. A. Horton and C. T. Liu, "Anisotropic Antiphase Boundaries in Rapidly Solidified Ni_3Al", Acta Metallurgica, in press.

11. I. Baker, J. A. Horton and E. M. Schulson, "Transmission Electron Microscopy of Rapidly Solidified Powders of Ni_3Al", Metallography, Vol. 19, 1986, pp. 63-74.

12. R. N. Wright and J. E. Flinn, "Microstructure and Mechanical Properties of Hot Isostatically Pressed Nickel Aluminides", Proceedings of the International Conference on Hot Isostatic Pressing, 1987, to be published.

APPENDIX A - CONFERENCE PROGRAM AND SESSION AGENDA

FOSSIL ENERGY MATERIALS PROGRAM CONFERENCE

Session I - Structural Ceramics

May 19, 1987

7:30	Registration Desk Opens Coffee and Rolls	
8:45	Welcome and Introductory Remarks	E. E. Hoffman R. A. Bradley R. R. Judkins
9:00	Fabrication of Fiber-Reinforced Composites by Chemical Vapor Infiltration and Deposition	D. P. Stinton Oak Ridge National Laboratory
9:30	Modeling of Fibrous Preforms for CVD Infiltration	T. L. Starr Georgia Tech Research Institute
10:00	Structural Reliability of Ceramic Composites	E. R. Fuller National Bureau of Standards
10:30	Break	
10:50	Poster Presentations	
	Assessment of Causes of Failure of Ceramic Filters	R. L. S. Chang Acurex Corporation
	Improved Ceramic Composites Through Controlled Fiber-Matrix Interaction	W. J. Weber Pacific Northwest Laboratory
	Effects of Flaws on the Fracture Behavior of Ceramics	J. P. Singh Argonne National Laboratory
	Thermomechanical Modeling of Refractory Linings for Slagging Gasifiers	O. Buyukozturk and F. Tamer Massachusetts Institute of Technology
12:00	Lunch (Energy Conference Room)	

FOSSIL ENERGY MATERIALS PROGRAM CONFERENCE

Session I - Structural Ceramics

May 19, 1987

1:00	**Poster Presentations**	
	Materials for a Solid Oxide Oxygen Pump	T. E. Easler Argonne National Laboratory
	Ceramic Fiber-Ceramic Matrix Filters for Hot Gas Cleaning	R. A. Lowden Oak Ridge National Laboratory
	Nondestructive Evaluation of Ceramic Composites	J. B. Walter Idaho National Engineering Laboratory
	Advanced Materials for Solid Oxide Fuel Cells	W. J. Weber Pacific Northwest Laboratory
2:30	Break	
2:50	Preparation of SiC Whiskers by the Vapor-Liquid-Solid Process	W. J. Parkinson Los Alamos National Laboratory
3:20	Development of Advanced Fiber-Reinforced Ceramics	T. L. Starr Georgia Tech Research Institute
3:50	Joining of Silicon Carbide Fiber-Silicon Carbide Matrix Composites	D. N. Coon Idaho National Engineering Laboratory
4:20	Nondestructive Evaluation of Structural Ceramics	W. A. Ellingson Argonne National Laboratory
5:00	Adjourn	
6:30-8:30	Reception (Garden Plaza Ballroom)	

FOSSIL ENERGY MATERIALS PROGRAM CONFERENCE

Session II - Corrosion and Erosion

May 20, 1987

7:30	Registration Desk Opens Coffee and Rolls	
8:00	Introductory Remarks	E. E. Hoffman R. A. Bradley R. R. Judkins
8:15	Corrosion of Alloys in Mixed-Gas and Combustion Environments	K. Natesan Argonne National Laboratory
9:00	Corrosion-Resistant Scales on Iron-Based Alloys	H. S. Hsu Oak Ridge National Laboratory
9:30	Mechanisms of Corrosion of Alloys and Coatings by Coal Combustion Products	G. H. Meier University of Pittsburgh
10:00	Break	
10:20	Poster Presentations	
	Development and Breakdown of Protective Oxide Scales	I. G. Wright Battelle Columbus Laboratories
	Development and Breakdown of Protective Oxide Scales	K. M. Vedula Case Western Reserve University
	Development and Breakdown of Protective Oxide Scales	V. Srinivasan Universal Energy Systems
12:00	Lunch (Energy Conference Room)	

FOSSIL ENERGY MATERIALS PROGRAM CONFERENCE

Session II - Corrosion and Erosion

May 20, 1987

1:00	**Poster Presentations**	
	Mechanisms of Galling and Abrasive Wear	L. K. Ives National Bureau of Standards
	Solid Particle Erosion in Turbulent Flows Past Tube Banks	J. A. C. Humphrey University of California
	Alkali Attack of Coal Gasifier Refractories	J. J. Brown Virginia Polytechnic Institute
2:30	Break	
2:50	Studies of Materials Erosion in Coal Conversion and Utilization Systems	A. V. Levy Lawrence Berkeley Laboratory
3:20	Study of Particle Rebound Characteristics and Material Erosion at High Temperature	W. Tabakoff University of Cincinnati
3:50	A Study of the Relationships of Particle Rebound Parameters, Materials Properties, and Erosion	T. H. Kosel University of Notre Dame
4:20	In-Situ Scanning Electron Microscopy Studies of the Erosion of Alloys	J. R. Keiser Oak Ridge National Laboratory
4:50	Adjourn	

FOSSIL ENERGY MATERIALS PROGRAM CONFERENCE

Session III - Alloy Development and Mechanical Properties

May 21, 1987

7:30	Registration Desk Opens Coffee and Rolls	
8:45	Welcome and Introductory Remarks	E. E. Hoffman R. A. Bradley R. R. Judkins
9:00	Advanced Steam Cycle Superheater Alloys	R. W. Swindeman Oak Ridge National Laboratory
9:30	Mechanical Properties of Advanced Steam Cycle Alloys	C. Y. Li Cornell University
10:00	Development of Nickel-Iron Aluminides	C. T. Liu Oak Ridge National Laboratory
10:30	Break	
10:45	Poster Presentations	
	Development of Advanced Steam Cycle Superheater Alloys	P. J. Maziasz Oak Ridge National Laboratory
	Design Methodology for High-Temperature Cyclic Applications	D. L. Marriott University of Illinois
	Protective Coatings and Claddings	N. Gopalsami Argonne National Laboratory
12:00	Lunch (Energy Conference Room)	

FOSSIL ENERGY MATERIALS PROGRAM CONFERENCE

Session III - Alloy Development and Mechanical Properties

May 21, 1987

1:00	**Poster Presentations**	
	Development of Iron Aluminides	C. G. McKamey Oak Ridge National Laboratory
	Joining of Nickel-Iron Aluminides	D. E. Clark Idaho National Engineering Laboratory
	Electrospark Deposited Coatings for Protection of Materials	R. N. Johnson Hanford Engineering Development Laboratory
2:30	Break	
3:00	Weldability and Ductility of Nickel-Iron Aluminides	G. R. Edwards Colorado School of Mines
3:30	Consolidation of Aluminide Powders	R. N. Wright Idaho National Engineering Laboratory
4:00	Adjourn	

765 | 766

APPENDIX B - LIST OF ATTENDEES

FOSSIL ENERGY MATERIALS PROGRAM CONFERENCE
OAK RIDGE, TENNESSEE

May 19-21, 1987

FINAL LIST OF ATTENDEES

Allard, L. F.
Oak Ridge National Laboratory
P. O. Box X
Oak Ridge, TN 37831-6064
(615) 574-0811

Beatty, R. L.
Oak Ridge National Laboratory
P. O. Box X
Oak Ridge, TN 37831-6088
(615) 574-4536

Besmann, T. M.
Oak Ridge National Laboratory
P. O. Box X
Oak Ridge, TN 37831-6063
(615) 574-6852

Blough, J. L.
Foster Wheeler Development
12 Peach Tree Hill Road
Livingston, NJ 07039

Bradley, R. A.
Oak Ridge National Laboratory
P. O. Box X
Oak Ridge, TN 37831-6098
(615) 574-6094

Brown, J. J.
Virginia Polytechnic Institute
and State University
Department of Materials Engineering
Blacksburg, VA 24061
(703) 961-6777

Buyukozturk, O.
Massachusetts Institute
of Technology
Civil Engineering
77 Massachusetts Avenue
1-280
Cambridge, MA 02139
(617) 253-7186

Carlson, P. T.
Oak Ridge National Laboratory
P. O. Box X
Oak Ridge, TN 37831-6098
(615) 574-5135

Carolan, R. A.
Cornell University
Materials Science and Engineering
Bard Hall
Ithaca, NY 14853-1501
(607) 255-4315

Carr, J. P.
Department of Energy
FE-23, GTN
Germantown, MD 20545

Chang, R. L. S.
Acurex Corporation
Environmental Systems Division
485 Clyde Avenue
P. O. Box 7044
Mountain View, CA 94039
(415) 961-5700

Clark, D. E.
Idaho National Engineering
Laboratory
EG&G Idaho, Incorporated
P. O. Box 1625
Idaho Falls, ID 83415
(208) 526-0746

Clark, J. W.
University of Alabama
Mineral Resources Institute
P. O. Drawer AY
Tuscaloosa, AL 35485
(205) 348-1582

Coon, D. A.
Idaho National Engineering
Laboratory
EG&G Idaho, Incorporated
P. O. Box 1625
Idaho Falls, ID 83415
(208) 526-9738

Corey, R. G.
University of Louisville
KECL, P. O. Box 13015
Ironworks Pike
Lexington, KY 40512-3025
(606) 252-5535

Daniel, M.
Oak Ridge National Laboratory
P. O. Box X
Oak Ridge, TN 37831-6156
(515) 574-4453

David, S. A.
Oak Ridge National Laboratory
P. O. Box X
Oak Ridge, TN 37831-6095
(615) 574-4804

DeVan, J. H.
Oak Ridge National Laboratory
P. O. Box X
Oak Ridge, TN 37831-6157
(615) 576-2449

Devine, T. J.
Wisconsin Centrifugal
905 E. St. Paul Avenue
Waukesha, WI 53188
(414) 544-7700

DiStefano, J. R.
Oak Ridge National Laboratory
P. O. Box X
Oak Ridge, TN 37831-6157
(615) 574-4452

Doychak, J.
Babcock & Wilcox
R&D Division
1562 Beeson Street
Alliance, OH 44601
(216) 821-9110, Ex. 760

Easler, T. E.
Argonne National Laboratory
Materials and Components Technology
9700 South Cass Avenue
Argonne, IL 60439
(312) 972-4250

Eaton, H. E.
United Technologies
Research Center
Silver Lane
East Hartford, CT 06108

Edwards, G. R.
Colorado School of Mines
Center for Welding Research
Golden, CO 80401
(303) 273-3773

Ellingson, W. A.
Argonne National Laboratory
9700 S. Cass Avenue
Argonne, IL 50439
(312) 972-50690

Fuller, Jr., E. R.
National Bureau of Standards
Ceramics Division
Bldg. 223, Room A258
Gaithersburg, MD 20899
(301) 975-5795

Gac, F. D.
Los Alamos National Laboratory
P. O. Box 1663, MST-6, MS G770
Los Alamos, NM 87545

Goodwin, G. M.
Oak Ridge National Laboratory
P. O. Box X
Oak Ridge, TN 37831-6096
(615) 574-4809

Gopalsami, N.
Argonne National Laboratory
9700 S. Cass Avenue
Argonne, IL 50439
(312) 972-5078

Groves, M. T.
General Electric Company
Aircraft Engine Group
1 Neumann Way M-87
Cincinnati, OH 45215

Harrison, R. W.
General Electric Company
Aircraft Engine Group
1 Neumann Way M-87
Cincinnati, OH 45215
(513) 243-3666

Heidersbach, R. S.
Oak Ridge National Laboratory
P. O. Box X
Oak Ridge, TN 37831-6156
(615) 574-4453

Hoffman, E. E.
Department of Energy
Federal Building
Room 2039
Oak Ridge, TN 37830
(615) 576-0735

Holland, J. R.
University of Alabama
Mineral Resources Institute
P. O. Box 6282
Tuscaloosa, AL 35487
(205) 348-4963

Horton, J. A.
Oak Ridge National Laboratory
P. O. Box X
Oak Ridge, TN 37831-6376
(615) 574-5575

Hsu, H. S.
Oak Ridge National Laboratory
P. O. Box X
Oak Ridge, TN 37831-6156
(615) 576-4810

Humphrey, J. A. C.
University of California
Mechanical Engineering
6177 Etcheverry Hall
Berkeley, CA 94720
(415) 642-6463

Ives, L. K.
National Bureau of Standards
Metallurgy Division
Bldg. 225, Room B266
Gaithersburg, MD 20899
(301) 975-6013

Johnson, T. I.
Babcock & Wilcox
Contract Research Division
1562 Beeson Street
P. O. Box 835
Alliance, OH 44601
(216) 821-9110, Ex. 355

Johnson, R. N.
Hanford Engineering
Development Laboratory
P. O. Box 1970
Richland, WA 99352
(509) 376-0715

Jones, R. H.
Pacific Northwest Laboratory
P. O. Box 999
Richland, WA 99352
(509) 376-4276

Judkins, R. R.
Oak Ridge National Laboratory
P. O. Box X
Oak Ridge, TN 37831-6098
(615) 574-4572

Keiser, J. R.
Oak Ridge National Laboratory
P. O. Box X
Oak Ridge, TN 37831-6156
(615) 574-4453

King, R. T.
Office of Technical Coordination
Department of Energy
FE14, GTN
Washington, DC 20545
(301) 353-2786

Kosel, T. H.
University of Notre Dame
Department of Materials Science
and Engineering
384 Fitzpatrick Hall
Notre Dame, IN 46556
(219) 239-5642

Lawton, C. W.
Lawton Scientific, Inc.
52 Chapman Road
West Hartford, CT 06107
(203) 521-4326

Levy, A. V.
Lawrence Berkeley Laboratory
MCSD M.S. 62-203
University of California
Berkeley, CA 94720
(415) 486-5822

Li, Che-Yu
Cornell University
Materials Science and Engineering
Bard Hall
Ithaca, NY 14853
(607) 255-4349

Liu, C. T.
Oak Ridge National Laboratory
P. O. Box X
Oak Ridge, TN 37831-6117
(615) 574-4459

Liu, Y. Y.
Argonne National Laboratory
9700 South Cass Avenue
Argonne, IL 60439
(312) 972-5127

Long, L. M.
Tennessee Eastman Company
B-54D
Kingsport, TN 37662
(615) 229-6177

Lowden, R. A.
Oak Ridge National Laboratory
P. O. Box X
Oak Ridge, TN 37831-6090
(615) 574-4559

Lundin, C. D.
University of Tennessee
Materials Science and Engineering
Knoxville, TN 37916
(615) 974-5310

Marriott, D. L.
University of Illinois
Department of Mechanical
and Industrial Engineering
Urbana, IL 61801

Maziasz, P. J.
Oak Ridge National Laboratory
P. O. Box X
Oak Ridge, TN 37831-6376
(615) 574-5082

McClung, R. W.
Oak Ridge National Laboratory
P. O. Box X
Oak Ridge, TN 37831-6151
(615) 574-4466

McKamey, C. G.
Oak Ridge National Laboratory
P. O. Box X
Oak Ridge, TN 37831-6116
(615) 574-6917

Meier, G. H.
University of Pittsburgh
Materials Science and Engineering
848 Benedum Hall
Pittsburgh, PA 15261
(412) 624-9741

Michal, G. M.
Case Western Reserve University
Metallurgy and Materials Science
10900 Euclid Avenue
Cleveland, OH 44106
(216) 368-5070

Morishige, M.
Ishikawajima-Harima Heavy
Industries Co., Ltd.
1, Shinnakahara-Cho. Isogo-Ku
Yokohama, Japan 235
(045) 751-1231, Ext. 6053

Muan, A.
Penn State University
212 Deike Building
University Park, PA 16802
(814) 865-7042

Natesan, K.
Argonne National Laboratory
Materials and Components Technology
9700 South Cass Avenue
Argonne, IL 60439
(312) 972-5103

Nolan, T. A.
Oak Ridge National Laboratory
P. O. Box X
Oak Ridge, TN 37831-6064
(615) 574-0811

Puentes, E. A.
University of Louisville
KECL, P. O. Box 13015
Ironworks Pike
Lexington, KY 40512-3025
(606) 252-5535

Santella, M. L.
Oak Ridge National Laboratory
P. O. Box X
Oak Ridge, TN 37831-6096
(615) 574-4805

Schuh, M. J.
University of California
Mechanical Engineering
5119 Etcheverry Hall
Berkeley, CA 94720
(415) 642-1006

Sherman, S. K.
University of Louisville
KECL, P. O. Box 13015
Ironworks Pike
Lexington, KY 40512-3025
(606) 252-5535

Singh, J. P.
Argonne National Laboratory
Materials and Components Technology
9700 South Cass Avenue
Argonne, IL 60439
(312) 972-5123

Slaughter, G. M.
Oak Ridge National Laboratory
P. O. Box X
Oak Ridge, TN 37831-6152
(615) 574-4267

Srinivasan, V.
Universal Energy Systems
4401 Dayton-Xenia Road
Dayton, OH 45432
(513) 426-6900

Starr, T. L.
Georgia Institute of Technology
Energy and Materials
Sciences Laboratory
Room 113, Baker Building
Atlanta, GA 30332
(404) 894-3678

Stinton, D. P.
Oak Ridge National Laboratory
P. O. Box X
Oak Ridge, TN 37831-6090
(615) 574-4556

Stubbins, J. F.
University of Illinois
214 NEL
103 S. Goodwin
Urbana, IL 61801

Swindeman, R. W.
Oak Ridge National Laboratory
P. O. Box X
Oak Ridge, TN 37831-6155
(615) 574-5108

Tabakoff, W.
University of Cincinnati
Aerospace Engineering and
Engineering Mechanics, ML 70
Clifton Avenue
Cincinnati, OH 45221
(513) 475-2849

Tamer, F.
Massachusetts Institute
of Technology
Civil Engineering
77 Massachusetts Avenue
1-053
Cambridge, MA 02139
(617) 253-3084

Tennery, V. J.
Oak Ridge National Laboratory
P. O. Box X
Oak Ridge, TN 37831-6062
(615) 574-5123

Tortorelli, P. F.
Oak Ridge National Laboratory
P. O. Box X
Oak Ridge, TN 37831-6156
(615) 574-5119

Vedula, K. M.
Case Western Reserve University
Department of Materials
Science and Engineering
10900 Euclid Avenue
Cleveland, OH 44106
(216) 731-1760

Walter, J. B.
Idaho National Engineering
Laboratory
EG&G Idaho, Incorporated
P. O. Box 1625
Idaho Falls, ID 83415
(208) 526-0033

Weber, W. J.
Pacific Northwest Laboratory
P. O. Box 999
Richland, WA 99352
(509) 375-2299

White, M. J.
University of Tennessee
Space Institute
Tullahoma, TN 37388

Williams, R. O.
Oak Ridge National Laboratory
P. O. Box X
Oak Ridge, TN 37831-6117
(615) 576-2631

Wilson, D. R.
University of Louisville
KECL, P. O. Box 13015
Ironworks Pike
Lexington, KY 40512-3025
(606) 252-5535

Wright, I. G.
Battelle Columbus Laboratories
505 King Avenue
Columbus, OH 43201
(614) 424-4377

Wright, R. N.
Idaho National Engineering Laboratory
EG&G Idaho, Incorporated
P. O. Box 1625
Idaho Falls, ID 83415
(208) 526-f127

ORNL/FMP-87/4

INTERNAL DISTRIBUTION

1. L. F. Allard
2. R. L. Beatty
3. T. M. Besmann
4-5. R. A. Bradley
6. P. T. Carlson
7. M. D. Daniel
8. S. A. David
9. J. H. DeVan
10. J. R. DiStefano
11. G. M. Goodwin
12. R. S. Heidersbach
13. J. A. Horton
14. H. S. Hsu
15. D. R. Johnson
16-25. R. R. Judkins
26. J. R. Keiser
27. C. T. Liu
28. R. A. Lowden
29. P. J. Maziasz
30. R. W. McClung
31. C. G. McKamey
32. T. A. Nolan
33. A. R. Olsen
34. M. L. Santella
35. A. C. Schaffhauser
36. G. M. Slaughter
37. J. O. Stiegler
38. D. P. Stinton
39. R. W. Swindeman
40. V. J. Tennery
41. P. T. Thornton
42. P. F. Tortorelli
43. R. O. Williams
44. Central Research Library
45. Document Reference Section
46. ORNL Patent Section
47-48. Laboratory Records Department
49. LRD - RC

EXTERNAL DISTRIBUTION

50. J. L. Blough, Foster Wheeler Development, 12 Peach Tree Hill Road, Livingston, NJ 07039

51. J. W. Byam, Morgantown Energy Technology Center, Department of Energy, P. O. Box 880, Morgantown, WV 26505

52. J. J. Brown, Virginia Polytechnic Institute & State University Department of Materials Engineering, Blacksburg, VA 24061

53. Richard J. Bullock, Rolled Alloys, P. O. Box 590, Kingston, NJ 08528/0590

54. O. Buyukozturk, Massachusetts Institute of Technology, Civil Engineering, 77 Massachusetts Ave. 1-280, Cambridge, MA 02139

55. R. A. Carolan, Cornell University, Materials Science and Engineering, Bard Hall, Ithaca, NY 14853-1501

56. J. P. Carr, Department of Energy, FE-23, GTN, Germantown, MD 20545

57. R. L. S. Chang, Acurex Corporation, Environmental Systems Div., 485 Clyde Ave., P. O. Box 7044, Mountain View, CA 94039

58. D. E. Clark, Idaho National Engineering Laboratory, EG&G Idaho Inc., P. O. Box 1625, Idaho Falls, ID 83415

59. J. W. Clark, University of Alabama, Mineral Resources Institute, P. O. Drawer AY, Tuscaloosa, AL 35485

60. D. A. Coon, Idaho National Engineering Laboratory, EG&G Idaho Inc., P. O. Box 1625, Idaho Falls, ID 83415

61. R. G. Corey, University of Louisville, KECL, P. O. Box 13015, Ironworks Pike, Lexington, KY 40512-3025

62. T. J. Devine, Wisconsin Centrifugal, 905 E. St. Paul Avenue, Waukesha, WI 53188

63. J. Doychak, Babcock & Wilcox, R&D Division, 1562 Beeson Street Alliance, OH 44601

64. D. Dubis, Morgantown Energy Technology Center, Department of Energy, P. O. Box 880, Morgantown, WV 26505

65. T. E. Easler, Argonne National Laboratory, Materials and Components Technology, 9700 S. Cass Ave., Argonne, IL 60439

66. H. E. Eaton, United Technologies, Research Center, Silver Lane, East Hartford, CT 06108

67. G. R. Edwards, Colorado School of Mines, Center for Welding Research, Golden, CO 80401

68. W. A. Ellingson, Argonne National Laboratory, 9700 S. Cass Avenue, Argonne, IL 50439

69. E. R. Fuller, Jr., National Bureau of Standards, Ceramics Division, Bldg. 223, Room A258, Gaithersburg, MD 20899

70. K. N . Frye, Office of Technical Coordination, Department of Energy, Office of Fossil Energy, FE-14, GTN, Washington, DC 20545

71. F. D. Gac, Los Alamos National Laboratory, P. O. Box 1663, MST-6, MS G770, Los Alamos, NM 87545

72. C. W. Garrett, Office of Fossil Energy, Department of Energy, FE-14, GTN, Washington, DC 20545

73. M. Ghate, Morgantown Energy Technology Center, Department of Energy, P. O. Box 880, Morgantown, WV 26505

74. F. M. Glaser, Office of Fossil Energy, Department of Energy, FE-14, GTN, Washington, DC 20545

75. N. Gopalsami, Argonne National Laboratory, 9700 S. Cass Avenue, Argonne, IL 50439

76. M. T. Groves, General Electric Company, Aircraft Engine Group, 1 Neumann Way M-87, Cincinnati, OH 45215

77. J. S. Halow, Morgantown Energy Technology Center, Department of Energy, P. O. Box 880, Morgantown, WV 26505

78. R. W. Harrison, General Electric Company, Aircraft Engine Group, 1 Neumann Way M-87, Cincinnati, OH 45215

79. J. R. Holland, University of Alabama, Mineral Resources Institute, P. O. Box 6282, Tuscaloosa, AL 35487

80. J. A. C. Humphrey, University of California, Mechanical Engineering, 6177 Etcheverry Hall, Berkeley, CA 94720

81. L. K. Ives, National Bureau of Standards, Metallurgy Division, Bldg. 223, Room B266, Gaithersburg, MD 20899

82. D. M. Jewell, Morgantown Energy Technology Center, Department of Energy, P. O. Box 880, Morgantown, WV 26505

83. T. I. Johnson, Babcock & Wilcox, Contract Research Division, 1562 Beeson St., P. O. Box 835, Alliance, OH 44601

84. R. N. Johnson, Hanford Engineering, Development Laboratory, P. O. Box 1970, Richland, WA 99352

85. R. H. Jones, Pacific Northwest Laboratory, P. O. Box 999, Richland, WA 99352

86. R. T. King, Office of Technical Coordination, Department of Energy, FE-14, GTN, Washington, DC 20545

87. T. H. Kosel, University of Notre Dame, Dept. of Materials Science & Engineering, 384 Fitzpatrick Hall, Notre Dame, IN 46556

88. C. W. Lawton, Lawton Scientific, Inc., 52 Chapman Road, West Hartford, CT 06107

89. A. V. Levy, La[illegible] Berkeley Laboratory, MCSD M.S. 62-203, University of [illegible], Berkeley, CA 94720

90. Che-Yu Li, Cornell University, Materials Science and Engineering, Bard Hall, Ithaca, NY 14853

91. Y. Y. Liu, Argonne National Laboratory, 9700 South Cass Avenue, Argonne, IL 60439

92. L. M. Long, Tennessee Eastman Company, B-54D, Kingsport, TN 37662

93. C. D. Lundin, University of Tennessee, Materials Science and Engineering, Knoxville, TN 37916

94. K. E. Markel, Morgantown Energy Technology Center, Department of Energy, P. O. Box 880, Morgantown, WV 26505

95. D. L. Marriott, University of Illinois, Department of Mechanical and Industrial Engineering, Urbana, IL 61801

96. G. H. Meier, University of Pittsburgh, Materials Science and Engineering, 848 Benedum Hall, Pittsburgh, PA 15261

97. G. M. Michal, Case Western Reserve University, Metallurgy and Materials Science, 10900 Euclid Avenue, Cleveland, OH 44106

98. Peter Mohr, Lawrence Livermore National Laboratory, L144, Box 808, Livermore, CA 94550

99. N. Morishige, Ishikawajima-Harima Heavy Industries Co., Ltd., 1, Shinnakahara-Cho. Isogo-Ku, Yokohama, Japan 235

100. A. Muan, Penn State University, 212 Deike Building, University Park, PA 16802

101. K. Natesan, Argonne National Laboratory, Materials & Components Technology, 9700 South Cass Avenue, Argonne, IL 60439

102. F. V. Nolfi, Dept. of Energy, Office of Basic Energy Sciences, Materials Sciences Division., ER-131, GTN, Washington DC 20545

103. E. A. Puentes, University of Louisville, KECL, P. O. Box 13015, Ironworks Pike, Lexington, KY 40512-3025

104. M. J. Schuh, University of California, Mechanical Engineering, 5119 Etcheverry Hall, Berkeley, CA 94720

105. S. K. Sherman, University of Louisville, KECL, P. O. Box 13015, Ironworks Pike, Lexington, KY 40512-3025

106. T. B. Simpson, Office of Fossil Energy, Department of Energy, FE-34, GTN, Washington, DC 20545

107. M. I. Singer, Office of Fossil Energy Department of Energy, FE-30, GTN, Washington, DC 20545

108. J. P. Singh, Argonne National Laboratory, Materials & Components Technology, 9700 South Cass Avenue, Argonne, IL 60439

109. V. Srinivasan, Universal Energy Systems, 4401 Dayton-Zenia Road, Dayton, OH 45432

110. T. L. Starr, Georgia Institute of Technology, Energy & Materials, Sciences Laboratory, Room 113, Baker Building, Atlanta, GA 30332

111. J. F. Stubbins, University of Illinois, 214 NEL, 103 S. Goodwin, Urbana, IL 61801

112. W. Tabakoff, University of Cincinnati, Aerospace Engineering & Engineering Mechanics, ML 70, Clifton Ave., Cincinnati, OH 45221

113. F. Tamer, Massachusetts Institute of Technology, Civil Engineering, 77 Massachusetts Ave., 1-053, Cambridge, MA 02139

114. K. M. Vedula, Case Western Reserve University, Dept. of Materials Science & Engineering, 10900 Euclid Avenue, Cleveland, OH 44106

115. J. B. Walter, Idaho National Engineering Laboratory, EG&G Idaho, Inc., P. O. Box 1625, Idaho Falls, ID 83415

116. W. J. Weber, Pacific Northwest Laboratory, P. O. Box 999, Richland, WA 99352

117. Department of Energy, Oak Ridge Operations Office, Assistant Manager for Energy Research & Development, P. O. Box E, Oak Ridge, Oak Ridge, TN 37831

118-147. Department of Energy, Technical Information Center, P. O. Box 62, Oak Ridge, TN 37831

For distribution by microfiche as shown in DOE/TIC-4500, Distribution Category UC-114 (Coal Based Materials and Components).

☆U.S. GOVERNMENT PRINTING OFFICE 1987-748 168/60083